WILEY-VCH

Edited by
Landong Li and Justin S. J. Hargreaves

Heterogeneous Catalysis for Sustainable Energy

Heterogeneous Catalysis for Sustainable Energy

Heterogeneous Catalysis for Sustainable Energy

Edited by Landong Li and Justin S. J. Hargreaves

WILEY-VCH

Editors

Prof. Landong Li
Nankai University
School of Materials Science and Engineering
38# Tongyan Road
Haihe Education Park
Jinnan District
300350 Tianjin
China

Prof. Justin S. J. Hargreaves
University of Glasgow
School of Chemistry
Joseph Black Building
G12 8QQ Glasgow
United Kingdom

Cover Image: © skegbydave/Getty Images

Library of Congress Card No.: applied for

British Library Cataloguing-in-Publication Data
A catalogue record for this book is available from the British Library.

Bibliographic information published by the Deutsche Nationalbibliothek The Deutsche Nationalbibliothek lists this publication in the Deutsche Nationalbibliografie; detailed bibliographic data are available on the Internet at <http://dnb.d-nb.de>.

Print ISBN: 978-3-527-34485-7
ePDF ISBN: 978-3-527-81589-0
ePub ISBN: 978-3-527-81591-3
oBook ISBN: 978-3-527-81590-6

Typesetting Straive, Chennai, India

Printed on acid-free paper

10 9 8 7 6 5 4 3 2 1

Contents

Preface

Energy can be defined as the ability to do work. Specifically, energy exists in various forms such as chemical energy, thermal energy, and radiant energy. Moreover, the controllable transformation of one form to another is of great significance for modern civilization. With the development of human society, the demand for energy has been increasing generally each year, and energy and its interconversion have become a highly topical issue. Nowadays, there are growing concerns not only about accessible energy reserves but also about the energy infrastructure necessary to maintain sustainable development of society. The concept of sustainable energy, which represents energy that can meet current demand and not cause harmful repercussions for the future, is increasingly recognized. Sustainable energy depends upon not only its origin but also how it is utilized.

Catalysis is a process in which a catalyst can change, generally increase, the rate of a chemical reaction without being consumed in the process. It has had huge impact on society, and the rapid development of human society is always accompanied by notable breakthroughs in catalysis, for example, the well-known catalytic ammonia synthesis, catalytic polymerization, and catalytic cracking processes. Catalysis has an indispensable role in industrial production. It is involved in about 90% of chemical processes and the manufacture of over 60% of industrial products.

Catalysis is closely related to energy. In a general catalytic process, a chemical reaction can proceed much faster than that in the absence of a catalyst, and therefore, less energy may be consumed. More intuitively, catalysis can directly participate in the energy transformation processes, for example, converting thermal energy to chemical energy via thermal catalysis, converting photo energy to chemical energy via photocatalysis, and converting electrical energy to chemical energy via electrocatalysis. A key issue in energy transformation is efficiency, and catalysis undoubtedly plays an essential role in promoting the energy efficiency for more sustainable development. It is well known that the energy structure for society is undergoing distinct changes: i.e. the proportion of traditional energy sources like petroleum and coal applied is gradually declining, the proportion of greener energy is gradually increasing, and, correspondingly, the proportion of sustainable energy is gradually increasing. However, society presently must rely on the traditional fossil energy sources of petroleum (~32%), coal (~27%), and natural gas (~24%). Improvements in the transformation of fossil energy or resources via catalysis

can make a significant contribution to modern requirements. On the other hand, the direct generation of sustainable energy from renewable resources via the development of routes involving heterogeneous catalysis might provide a possible solution to the global energy challenges.

Under such circumstances, it is meaningful and desirable to summarize current research progress in heterogeneous catalysis for sustainable energy. Related to this, this book provides a summary relating to the fundamental science of heterogeneous catalysis and sustainable energy, and it is timely to encourage further research activity in this highly topical research field. In this book, two different aspects are summarized, namely, i) the more efficient transformation of fossil resources using heterogeneous catalysis as a tool and ii) the exploitation of renewable energy through heterogeneous catalysis. Specifically, aspects related to hydrogen energy, methane activation, alkane activation, zeolite catalysis, the application of carbon dioxide as building block, and biomass conversion have been included. The authors of the various chapters included in this book are all active researchers in the field of heterogeneous catalysis and sustainable energy. Authors from around the world, including China, the United Kingdom, Australia, Mexico, and Singapore, have contributed.

Nankai University and
Glasgow Unversity
October, 2021

By *Landong Li and Justin S. J. Hargreaves*

Part I

Hydrogen Economy

1

Catalytic Hydrogen Production

Xingyuan Gao and Sibudjing Kawi

National University of Singapore, Department of Chemical and Biomolecular Engineering, 4 Engineering Drive 4, 117585 Singapore, Singapore

1.1 Introduction

Currently and in the near future, fossil fuels are/will be the major source of hydrogen production [1, 2]. As shown in Figure 1.1, almost all the industrial manufacturing processes for hydrogen rely on fossil fuels directly or indirectly [1]. Among the fossil fuels like coal, heavy hydrocarbons, and natural gas, methane is mostly studied due to its high abundance in the world, such as in the United States and Malaysia [4–8]. On the other hand, around 48% of hydrogen gas is generated from natural gas [9–11]. Moreover, methane is easy to handle and has a high H/C ratio [12]. Therefore, we focus on the thermocatalytic conversion of methane first in this part, followed by the conversion of other fossil fuels to produce hydrogen gas.

1.1.1 Thermocatalytic Decomposition of Methane

Only hydrogen gas and carbon are produced in the thermal decomposition of hydrocarbons. This CO-free process is promising for industry [13, 14]. As the major component of hydrocarbons, methane has drawn much interest in the recent years in the production of hydrogen gas via thermal decomposition. The reaction mechanisms are shown below [9]. Initially, methane is chemisorbed on the exposed face of catalyst crystals; secondly, C—H bonds are broken in gaseous methane molecules to produce methyl groups and hydrogen atoms, followed by stepwise dissociations to generate CH_x and more hydrogen atoms; thirdly, two hydrogen atoms combine to generate hydrogen molecules, which are released in gaseous form; fourthly, atomic carbon aggregates and diffuses onto the surface of catalyst particles; fifthly, nucleation and growth of carbon filaments occur in the trailing face of catalyst particles.

Among several methane cracking technologies like plasma, pyrolytic, thermocatalytic, and photocatalytic routes, we focus on thermocatalytic decomposition due to the simultaneous formation of carbon nanofibers or carbon nanotubes

Heterogeneous Catalysis for Sustainable Energy, First Edition. Edited by Landong Li and Justin S. J. Hargreaves.

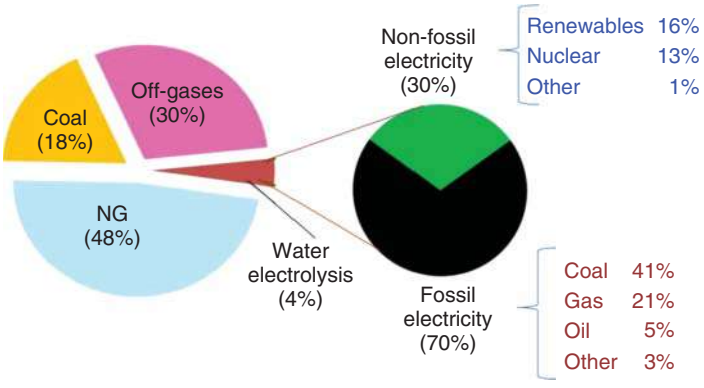

Figure 1.1 The major sources of the industrial hydrogen manufacturing. Source: Reproduced with permission: © 2007, International Energy Agency [3].

that can be potentially used in various applications [14, 15]. Because of the very inactive C—H bond in methane molecules, the activation energy is high, and the reaction is strongly endothermic [16]. Therefore, catalysts are necessary to lower the reaction temperatures and promote the kinetics, including metal- and carbon-based catalysts [1].

1.1.1.1 Metal Catalysts

Since the 1960s, transition metals (Ni, Fe, Co) have been extensively studied and show good catalytic performance in methane decomposition, which occurs at 500–800 °C, much lower than 1200 °C required without a catalyst [17–20]. However, the industrialization of this catalytic system is impeded due to the carbon deposits covering the active sites, leading to rapid deactivation [16, 21]. Modifications have been made to improve the reactivity and stability of transition metal-based catalysts using other transition metals and rare earth metals [22–26].

Bayat et al. [22] studied the Ni–Fe alloy derived from the reduction of the spinel $NiFe_2O_4$ phase. Below 650 °C, the addition of Fe inhibited the encapsulation of carbon by facilitating the carbon diffusion. However, the active sites become fewer with increasing Fe content due to the lower degree of reducibility. To offset the negative effect of Fe, Bayat et al. [23] doped Cu into the Ni–Fe alloy to enhance the methane adsorption and Ni dispersion on alumina. The optimal ratio of Ni/Fe/Cu was 5 : 1 : 1.

Instead of adding Fe, Lua and Wang [24] doped Co into Ni–Cu to form a tri-metallic alloy. Since Co possesses a high melting point, the quasi-liquid phenomenon occurring between 650 and 775 °C was effectively inhibited, leading to enhanced stability. However, phase separation may be an issue with the further addition of Co. Following this work, a series of catalysts comprising Co and W in different ratios were developed [25]. When Co/W equaled 4 : 1, hydrogen gas and multiwall carbon nanotubes were simultaneously produced, showing the highest conversion of methane. It was found that non-interacted Co_3O_4 was responsible for the superior catalytic performance.

Besides doping of transition metals, a series of rare earth metals were added to Ni to form bimetallic catalysts. Among the additives La, Sr, Nd, Pr, Y, and Sm, Ni-La

Table 1.1 Summary of metal catalysts in methane decomposition.

Catalyst	Conditions	Findings	References
Ni–Fe/Al_2O_3	700 °C for 3 h; 30 vol% CH_4 and 70 vol% N_2.	Fe inhibited the encapsulation of carbon by facilitating the carbon diffusion	[22]
Ni–Fe–Cu/Al_2O_3	700 °C for 3 h; 30 vol% CH_4 and 70 vol% N_2.	Cu enhanced methane adsorption and improved the reducibility and nickel dispersion	[23]
Ni–Co–Cu	500–850 °C; 20 vol% CH_4 and 80 vol% N_2.	The high melting point of Co inhibited the quasi-liquid phenomenon, leading to an enhanced stability	[24]
Co–W/MgO	700 °C; CH_4 at a flow rate of 50 sccm.	When Co/W equaled to 4 : 1; non-interacted Co_3O_4 was responsible for the highest conversion of methane	[25]
Ni–La–Si	300~750 °C; CH_4 at a flow rate of 10 ml min^{-1}	The high activity and low solid carbon formation were attributed to the good thermal stability and small Ni particle size	[26]

exhibited the highest activity and lowest solid carbon formation due to their good thermal stability and small Ni particle size [26] (Table 1.1).

1.1.1.2 Carbon Catalysts

Due to the low cost, resistance to sulfur, and temperature, various carbon materials have been studied as alternatives to transition metals in methane decomposition [1, 16], including active carbon particles [27–30], ordered mesoporous carbons [31, 32], carbon black particles [33], and commercial carbon materials [34]. However, gradual deactivation occurred on carbon catalysts resulting from the coverage of inactive turbostratic carbon. To alleviate this issue, Muradov et al. [35] prolonged methane decomposition by generating active carbon aerosols continuously in a non-thermal plasma device. Besides, Dufour et al. [36] discovered that the addition of small amounts of oxidizing agents like oxygen, CO_2, and steam in the feedstock could effectively enhance the sustainability. Furthermore, the gaseous form of carbon particles derived from partial gasification could inhibit the deactivation of catalyst in a fluid state and cyclic process between the reactor and heater [37].

1.1.2 Partial Oxidation of Methane

Partial oxidation of methane (POM) has drawn much attention recently due to the compactness, good response time, and lower sensitivity to the type of fuels. In the

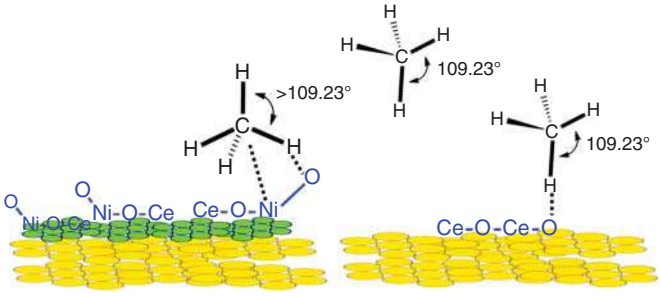

Figure 1.2 Schematic representation of Ni/CeO_2 and CeO_2 surface having surface defects with under coordinated oxygen atoms. Source: Reproduced with permission from Pal et al. [40]; © 2015, American Chemical Society.

presence of oxygen, POM is considered as a fast and highly exothermic reaction to produce syngas as shown in Eq. (1.1) [38]:

$$CH_4 + \frac{1}{2}O_2 \rightarrow CO + 2H_2 \quad \Delta H^{\circ}_{298\ K} = -35.6\ kJ\ mol^{-1} \tag{1.1}$$

The reaction can occur at a very high temperature without catalysts. However, the use of catalysts can lower the reaction temperature greatly that saves the energy input. The commonly studied catalysts for POM include transition metals, noble metals, and perovskites as shown in Table 1.2.

Amongst the transition metals, Ni with different supports is widely applied in POM. Pantaleo et al. [39] compared the catalytic performance of CeO_2 and La_2O_3 single oxide supports and CeO_2–La_2O_3 mixed oxide supports prepared by wet impregnation and coprecipitation. Interestingly, coke only deposited on the single oxide supported catalysts. The enhanced anti-coking property of mixed oxide supported catalyst was attributed to the formation of a series of Ni–La_2O_3 species with different oxidation states of Ni. Besides, in another study regarding Ni/CeO_2 [40], the surface and point defects with undercoordinated oxygen atoms in CeO_2 originating from the formation of O–Ni–O–Ce superstructures promoted the activation of C—H bonds (Figure 1.2). In addition to Ni-based catalysts, Co/ZrO_2 exhibited a very high conversion of methane and selectivity to hydrogen gas, out-performing many other catalysts [41].

Noble metals are also used in POM. A comparison among Pt, Pd, and bimetallic catalysts was conducted by Abbasi et al. [42]. It was found that Pd performed the best in this comparison, followed by the mixture and Pt alone. On the other hand, supports can also affect the performance of Rh-based catalysts [43]. Due to the oxygen spillover from $Ce_{0.5}Zr_{0.5}O_2$, Rh was easily reoxidized and lost active sites; however, this spillover effect could be alleviated by Al_2O_3.

Perovskite structures present superior anti-coking properties due to the reaction of carbon deposits and oxygen species derived from the structure [60]. $Sr_{0.8}Ni_{0.2}ZrO_3$ exhibited a highly stable conversion of methane at 900 °C under a reducing atmosphere [44]. Similarly, $LaGa_{0.65}Mg_{0.15}Ni_{0.2}O_3$ achieved 81% conversion of methane and 100% selectivity to hydrogen gas at 900 °C. This excellent catalytic property may be attributed to the existence of La_2O_3 and $La_2O_2CO_3$ besides the perovskite structure [45].

Table 1.2 Summary of catalysts in partial oxidation of methane.

Catalyst	Conditions	Findings	References.
$Ni/CeO_2–La_2O_3$	700 °C; WHSV = 60 000; O/C = 0.5	Over 90% methane conversion; the formation of a series of $Ni–La_2O_3$ species with different oxidation states of Ni inhibited cokes	[39]
Ni/CeO_2	750 °C; WHSV = 50 000; O/C = 0.5	Over 85% methane conversion and 65% H_2 selectivity; the surface and point defects originated from the formation of O–Ni–O–Ce structures activated the C—H bonds	[40]
Co/ZrO_2	800 °C; WHSV = 60 000; O/C = 0.5	Co/ZrO_2 exhibited 100% conversion of methane and 98.1% selectivity to hydrogen gas	[41]
$Pd/\gamma\text{-}Al_2O_3$	650 °C; WHSV = 38 400; O/C = 2	Pd performed the best (nearly 100%), followed by Pt–Pd and Pt alone	[42]
Rh/Al_2O_3 and $Rh/Ce_{0.5}Zr_{0.5}O_2$	600 °C; WHSV = 252 000; O/C = 2	Rh was easily reoxidized by oxygen spillover in $Ce_{0.5}Zr_{0.5}O_2$; this spillover effect could be alleviated by Al_2O_3, maintaining 60% methane conversion for 10 h	[43]
$Sr_{0.8}Ni_{0.2}ZrO_3$	900 °C; WHSV = 66 000; O/C = 0.5	Over 94% methane conversion; a highly stable conversion of methane at 900 °C under reducing environment	[44]
$LaGa_{0.65}Mg_{0.15}Ni_{0.20}O_{3-\delta}$	900 °C; WHSV = 3300; O/C = 0.5	81.2% methane conversion and 100% H_2 selectivity were attributed to the existence of La_2O_3 and $La_2O_2CO_3$ besides the perovskite structure	[45]
$Pt–NiO/Al_2O_3$	800 °C; WHSV = 7200; O/C = 0.5	91.8% methane conversion and 98.4% H_2 selectivity; Ni reduction was promoted by Pt	[46]
Co/Al_2O_3	850 °C; WHSV = 60 000; O/C = 0.5	95% methane conversion and 93.6% H_2 selectivity were attributed to the formation of Co_3O_4 as the major phase after 500 °C calcination	[47]
$Ni/12CaO{\cdot}7Al_2O_3$	800 °C; WHSV = 30 000; O/C = 0.5	Over 90% methane conversion and 95% H_2 selectivity were attributed to the active oxygen ions and high dispersion of Ni.	[48]

Table 1.2 (Continued)

Catalyst	Conditions	Findings	References.
Co/MgO	850 °C; WHSV = 20 000; O/C = 0.5	95% methane conversion, little coke formation, and sintering were attributed to small crystals embedded in the support derived from CoO–MgO solid solution	[49]
$Ni/CeO_2/Al_2O_3$	800 °C; WHSV = 152 432; O/C = 0.5	Low loading of CeO_2 (1%) generated a highly dispersed CeO_2 particle, enhancing the reducibility and obtaining 80.3% methane conversion with less carbon deposition	[50]
$Ni–Cr/Al_2O_3$	700 °C; WHSV = 195 000; O/C = 0.5	85% methane conversion and enhanced stability were realized by the more dispersed Ni particles and surface basicity with addition of Cr	[51]
$Ni–Rh/Al_2O_3–MgO$	750 °C; WHSV = 354 044; O/C = 0.5	93% methane conversion and 95% H_2 selectivity; Rh prevented the oxidation of Ni	[52]
Rh/CeO_2	700 °C; WHSV = 60 000; O/C = 0.5	The Rh ions in the surface lattice of CeO_2 were active in POM and obtained 95.2% methane conversion and 92.9% H_2 selectivity	[53]
$Ni/ZrO_2@SiO_2$ core shell	750 °C; WHSV = 50 000; O/C = 0.5	Over 90% methane conversion and 75% H_2 selectivity were obtained with strong coke resistance due to the high oxygen storage capacity and steric hindrance	[54]
Ni/zeolite catalysts	750 °C; WHSV = 90 000; O/C = 0.5	100% methane conversion with strong anti-deactivation ability was attributed to less surface acidity and higher thermal stability	[55]
Ni/TiO_2	800 °C; WHSV = 4800; O/C = 0.5	86.3% methane conversion and 99.7% H_2 selectivity were obtained, but serious deactivation was observed, resulting from the NiO and $NiTiO_3$ formation	[56]
$LaCoO_3/\gamma\text{-}Al_2O_3$	800 °C; WHSV = 899 550; O/C = 0.25	Over 35% methane conversion and 40% H_2 selectivity; excellent stability was caused by highly dispersed Co and carbon removal by La_2O_3	[57]

Table 1.2 (Continued)

Catalyst	Conditions	Findings	References.
$La_{0.08}Sr_{0.92}Fe_{0.20}Ti_{0.80}O_3$	900 °C; WHSV = 30 000; O/C = 0.5	Over 50% methane conversion and 60% H_2 selectivity; high oxygen vacancy concentration was responsible for the high activity	[58]
$La_{0.5}Sr_{0.5}CoO_3$	850 °C; WHSV = 30 000; O/C = 0.5	Over 70% methane conversion and 75% H_2 selectivity were realized with highly dispersed Co particles in the La_2O_3 and SrO matrix	[59]

WHSV, weight hour space velocity (unit: ml h^{-1} $g_{cat}{}^{-1}$); O/C, O_2-to-carbon ratio.

1.1.3 Catalytic Reforming of Methane

The popular syngas production methods consist of steam reforming of methane (SRM), oxidative steam reforming of methane (OSRM), and dry reforming of methane (DRM). The following will respectively introduce the reaction mechanism, issues to be overcome, and catalytic systems. Kinetic modeling will also be included.

1.1.3.1 Steam Reforming of Methane (SRM)

SRM possesses many advantages, including high hydrogen yield and low cost to obtain hydrogen gas [61, 62]. The reaction equation is shown as below:

$$CH_4 + H_2O \rightarrow CO + 3H_2 \quad \Delta H^{\circ}_{298\ K} = 206.2\ kJ\ mol^{-1} \tag{1.2}$$

Due to the endothermic nature of this reaction, a high reaction temperature is preferred to generate a high yield of H_2 [63]. However, a simultaneous water–gas shift (WGS) reaction occurs, and the CO conversion is inhibited at high temperatures since WGS reaction is exothermic according to Eq. (1.3) [64]:

$$CO + H_2O \rightarrow CO_2 + H_2 \quad \Delta H^{\circ}_{298\ K} = -41\ kJ\ mol^{-1} \tag{1.3}$$

To solve this issue in industry, a two-reactor system has been adopted to achieve both a high conversion of methane and a high yield of H_2. In detail, the reactants, methane and steam, are passed through the first reactor operated at 300–450 °C where the reaction is accelerated kinetically and more methane is converted thermodynamically according to Eq. (1.2) in spite of the low conversion of CO according to Eq. (1.3). Afterward, the intermediate products are continuously fed to the second low-temperature reactor (175–250 °C) with a high ratio of steam to convert more CO to form CO_2 and H_2 [65, 66].

To further purify or enhance the yield of hydrogen gas in the final products, CO_2 and H_2 is required to be removed *in situ* respectively by sorbents and selective membranes as shown in Figure 1.3 [67].

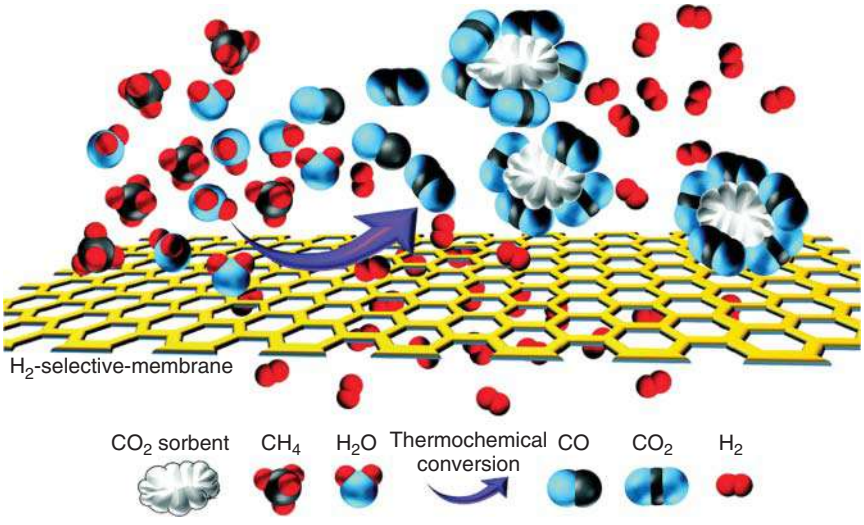

Figure 1.3 Representation of H_2 and CO_2 removal by H_2-selective membranes and using CO_2 sorbents. Source: Reproduced with permission from Ji et al. [67]: © 2018, The Royal Society of Chemistry.

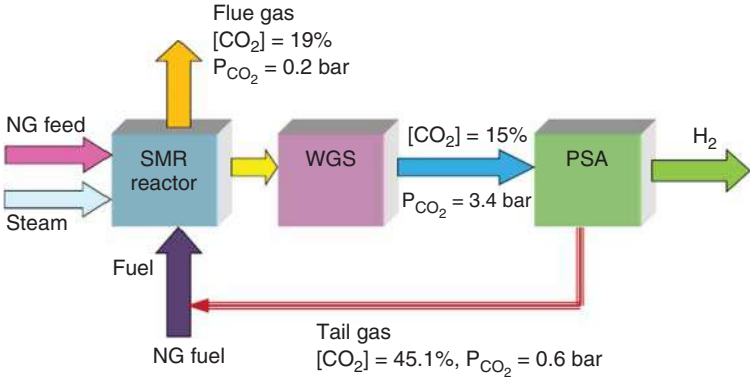

Figure 1.4 Simplified block diagram of a modern SMR plant with major CO_2 containing streams. SMR, steam methane reforming; WGS, water–gas shift reactor; PSA, pressure swing adsorption unit. Source: Reproduced with permission from Muradov [1]: © 2017, Elsevier.

Specifically for CO_2 sorbents, different from the hot potassium carbonate or amine scrubber used about two to three decades ago, pressure swing adsorption (PSA), a physical adsorption technology, is widely adopted in modern SRM plants, achieving an ultrahigh purity of 99.999% for H_2 (shown in Figure 1.4) [1]. In this process, CO_2 is not selectively separated from other gases, but used together with CH_4 and CO to provide heat for the reformer with CO_2 as an exhaust vented out of the reactor system in the end [68].

Besides the design of the reactor system, SRM catalysts should possess the follow stringent features: high catalytic stability, high conversion of methane, superior

mechanical strength, excellent thermal stability, low pressure drop, and good heat transfer [69]. Ni-based catalysts are commonly studied due to their high conversion and selectivity. However, carbon deposition hinders their large-scale application in industry. Additives and support materials have been used to alleviate this issue, including rare earth metals, noble metals, and perovskites as summarized in Table 1.3. For example, with the addition of Sn into Ni/YSZ, the activation energy of CH_4 increased, and the binding of carbon to the low-coordinated Ni sites was weakened, thus inhibiting the nucleation of carbon at Ni sites [78]. Similarly, Cu can potentially block the sites for carbon formation when forming Ni–Cu alloy, achieving 98% methane conversion and 99% H_2 selectivity [75]. When perovskite oxides were used as the supports or precursors, the catalytic stability could be enhanced, and coke formation could be diminished due to their high thermal stability under a wide range of oxygen partial pressures and also the formation of finely dispersed metal nanoparticles [60]. For example, $La_{0.8}Ce_{0.2}Fe_{0.7}Ni_{0.3}O_3$ exhibited stable catalytic performance regardless of the S/C ratio and only 0.2 wt% coke formed after a 20 hour test. This superior performance was attributed to the oxygen vacancy, which promoted the dissociation of steam and coke gasification [79]. Similarly, the lattice oxygen provided by $LaAlO_3$ and $SrTiO_3$ were located near the Ni surface, which migrated easily to the CH_x fragments and oxidized the CH_x [80].

In addition to the modifications mentioned above, preparation methods can also affect the physicochemical properties of Ni-based catalysts. For example, dielectric barrier discharge (DBD) was adopted together with the impregnation method in the preparation of Ni/SiO_2 catalysts, forming a smaller Ni particle size than that prepared with the conventional impregnation method [74]. For core–shell $Ni–Al_2O_3$/silicalite zeolite catalysts, repeated calcinations at elevated temperatures generated $NiAl_2O_4$ spinel phase in the core, the catalytic performance of which was 10% higher than that prepared with traditional method [74]. Regarding Ni/CeO_2 catalysts, a hierarchical structure was formed with a template synthesis process, where the nanoporous and interwoven ceramic fiber template was loaded with NiO nanoparticles and supported on the CeO_2 scaffold. After thermal treatment, the microstructure of the nanocatalyst increased the conversion of methane up to 98% at 800 °C, which remained stable for five hours [81].

Besides Ni-based catalysts, noble metals with different supports have been tested in SRM. With ZrO_2 and Al_2O_3 as mixed support materials, Pd–Rh metal foams presented excellent catalytic stability over 200 hours with little coke formation at 800 °C [70]. Ru also proved to be highly active and selective in SRM. By using γ-Al_2O_3 as the support, the catalyst outperformed commercial Ni/Al_2O_3 by 2 orders of magnitude for methane conversion. However, when the Ru loading was lower than 0.15 wt%, the oxidation of sub-nanometer Ru clusters caused a rapid decline in the conversion [71]. Despite the size limitations, Ru-based catalysts could maintain stable perfomance with a low S/C ratio (=1), while Ni/α-Al_2O_3 catalyst deactivated very rapidly when S/C = 2 [71]. Another noble metal, Pd, was found to be sensitive to the type of support material. Compared with Al_2O_3, La_2O_3 promoted the formation of $Pd^0[Pd^{\delta+}O_xLa]$ species due to the metal–support interaction (MSI). La_2O_3 could also enhance the interaction between Pt and Al_2O_3 because of the improved thermal stability of Al_2O_3 [72].

Table 1.3 Summary of catalysts in steam reforming of methane.

Catalyst	Conditions	Findings	References
Pd–Rh/metal foam	300 °C; GHSV = 2000 h^{-1}; S/C = 2.5.	96.7% CH_4 conversion for 200 h was attributed to the absence of pore diffusion limitations, stable structure, and small loading of active metals	[70]
Ru/γ-Al_2O_3	600 °C; WHSV = 750; S/C = 1.	75% methane conversion and 68% H_2 selectivity; when the Ru loading was lower than 0.15 wt%, the oxidation of sub-nanometer Ru clusters caused the fast drop of the conversions	[71]
Pd/La_2O_3–Al_2O_3	510 °C; S/C = 3.	La_2O_3 promoted the formation of Pd° [$Pd^{\delta+}O_xLa$] species and enhanced the interaction between Pt and Al_2O_3	[72]
Ni-nano-CaO/Al_2O_3	600 °C; WHSV = 2 700; S/C = 4.	86% methane conversion, 92% H_2 selectivity, and enhanced stability were attributed to high-temperature pretreatment and formation of $Ca_{12}Al_{14}O_{33}$	[73]
Ni/SiO_2	800 °C; WHSV = 24 000; S/C = 0.5.	Enhanced methane conversion was obtained by the smaller catalyst size prepared by dielectric barrier discharge (DBD) plasma	[74]
Ni–Cu/Al_2O_3	500 °C; WHSV = 2 000; S/C = 3.	Cu could possibly block the sites for carbon formation when forming Ni–Cu alloy, realizing over 85% methane conversion and 97% H_2 selectivity	[75]
Ni/$Ce_{1-x}Gd_xO_2$	700 °C; WHSV = 560 000; S/C = 3.	75% methane conversion; Ga enhanced MSI so metal sintering was inhibited and carbon deposits were more reactive	[76]
Ru/MgO–Nb_2O_5	700 °C; WHSV = 20 000; S/C = 4.	Over 95% methane conversion, 72% H_2 selectivity; tetragonal Nb_2O_5 and metallic Ru were formed *in situ* from amorphous niobic acid and Ru^{4+} during the reaction	[77]

Table 1.3 (Continued)

Catalyst	Conditions	Findings	References
Sn/Ni/YSZ	740 and 850 °C; S/C = 1.	The binding of carbon to the low-coordinated Ni sites was weakened with Sn addition, thus inhibiting the nucleation of carbon at Ni sites	[78]
$La_{0.8}Ce_{0.2}Fe_{0.7}Ni_{0.3}O_3$	500–800 °C; WHSV = 108 000; S/C = 3.	Only 0.2 wt% coke formation after a 20 h test, which was attributed to the oxygen vacancy, promoting the dissociation of steam and coke gasification	[79]
$Ni/LaAlO_3$ and $Ni/SrTiO_3$	800 °C; W/F = 1.58 g h mol^{-1}. S/C = 2.	91.7% and 88.4% methane conversions with longer stabilities were achieved due to the lattice oxygen in perovskites, promoting the oxidation of CH_x species	[80]

WHSV, weight hour space velocity (unit: ml h^{-1} $g_{cat}{}^{-1}$); S/C, steam-to-carbon ratio.

1.1.3.2 Oxidative Steam Reforming of Methane (OSRM)

OSRM is a combination of POM and SRM, which is also called autothermal reforming of methane. OSRM has the advantages of the heat generated from POM and hydrogen gas produced by SRM [82]. Compared with SRM, less methane is burnt, and thus the carbon efficiency is higher for OSRM [83]. Another merit of OSRM is that the process can be stopped and started rapidly, and the amount of hydrogen gas produced is large [38]. Owing to these advantages, OSRM is widely applied in the syngas production units in Fischer–Tropsch plants [84]. However, to reduce the carbon in the spent catalysts, an expensive process needs to run to separate C_{2+} from methane [85]. Also, considering the high temperature of the burner, the high cost of operation is another concern [86]. To run the reaction properly, the S/C and O_2/fuel ratios need to be controlled carefully to prevent the by-product formation, optimize the reaction temperature, and tune the gas compositions [82, 87, 88].

Due to the good activation of C—C bonds and low cost, Ni-based catalysts are widely studied for this reaction [38]. The $MgAl_2O_4$ spinel material has been widely applied as the support material for Ni [84]. Besides, Ce–ZrO_2 mixed oxides have been popularly applied because of their high oxygen storage capacity (OSC). Together with the metal surface area of Ni, cubic phase $Ce_{0.75}Zr_{0.25}O_2$-supported Ni catalyst exhibited high catalytic performance [89]. In detail, mobile oxygen species formed through a redox cycle inhibited coke deposition on the Ni active sites. As shown in Figure 1.5, a three-layer model was proposed comprising a layer of Ni–Ce–Zr–O_x in the middle of free Ni metal and Ce–ZrO_2 support. The lattice oxygen consumed was replenished by the O_2 [90].

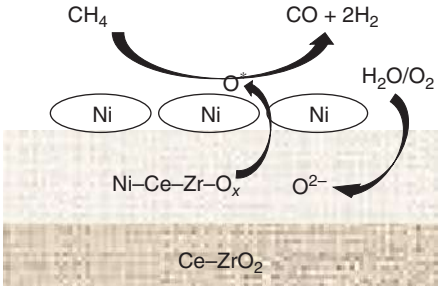

Figure 1.5 Schematic of synthesis gas production over Ni/Ce–ZrO_2 catalyst. Source: Reproduced with permission from Roh et al. [90]: © 2001, Springer.

Several promoters were added to the above catalyst and Ag was shown to be better than Fe, Pt, and Pd due to its greater redox property. Compared with 0.1 wt%, higher loading of Ag (1 wt%) presented a higher reactivity [91]. Ce–ZrO_2 can also promote the catalytic properties of noble metals. The high reducibility and OSC enhanced the reactivity of Rh catalyst. Compared with mixed phase of $Ce_{0.5}Zr_{0.5}O_2$, single cubic phase led to superior performance [92]. Similar effect was exerted on Pt catalyst, where the carbon deposits were continuously removed at the metal–support interface due to the OSC of the $Ce_{0.5}Zr_{0.5}O_2$ support [93]. When Ce–ZrO_2 was adopted as the support, the addition of Al_2O_3 could enhance the metal dispersion and reduce the size of particles. Besides the carbon inhibition effect, Zr in the support could prevent the formation of inactive $NiAl_2O_4$ [94, 95].

Different opinions existed that considering the high reaction temperature, deactivation or poisoning of the catalysts in OSRM may not be as serious as the catalysts in steam reforming. Therefore, instead of focusing on the catalyst design, however, more attention should be paid to the optimization of pellet shape and minimizing the pressure drop [84].

1.1.3.3 CO_2/Dry Reforming of Methane

Among the two greenhouse gases – methane and CO_2 – though the concentration of methane is much lower than that of CO_2, methane's global warming potential is 28–36 times higher than CO_2. DRM can effectively reduce these greenhouse gases [96, 97]. Besides, syngas (mixture of CO and H_2) as the product of this reaction acts as both a sustainable fuel alternative to fossil fuel and a precursor to produce high value-added chemicals such as ammonia and methanol [98–105]. The main reaction equation is shown below:

$$CH_4 + CO_2 \rightarrow 2CO + 2H_2 \quad \Delta H^{\circ}_{298\,K} = 248\ \text{kJ mol}^{-1} \tag{1.4}$$

The Fischer–Tropsch reaction will be benefited from this low H_2/CO ratio because of the suppression of methanation and the promotion of chain growth. In addition, the endothermic nature promotes the Solchem process since solar energy is converted to chemical energy. Furthermore, the storage of seasonal energy is applicable in the form of H_2 and CO [106–111]. In the long term, however, a more sustainable way to supply the heat for DRM reaction is to use renewable energy [112].

Based on the stoichiometry in Eq. (1.4), the conversion of CH_4 and CO_2 will be equal. Considering the reverse WGS reaction as shown in Eq. (1.5), more CO_2 will

be converted to form CO and water; thus generally CO_2 conversion should be higher than that of methane [112, 113]. In terms of the yield of H_2, however, this side reaction needs to be inhibited:

$$H_2 + CO_2 \rightarrow CO + H_2O \quad \Delta H^{\circ}_{298\ K} = 41\ kJ\ mol^{-1} \tag{1.5}$$

In spite of the environmental and economic potential, DRM is still industrially immature because of the relatively high cost and problems related to the development of robust catalysts with a long lifespan. Especially for the catalyst design, two factors hinder the large-scale applications in industry: coke formation based on Eqs. (1.6, 1.7) and metal sintering at high temperatures [112–117]. Therefore, it is crucial to develop a highly active and stable catalyst with economic feasibility and excellent anti-deactivation ability [112]:

$$CH_4 \rightarrow C + 2H_2 \qquad \Delta H^{\circ}_{298\ K} = 75\ kJ\ mol^{-1} \tag{1.6}$$

$$2CO \rightarrow C + CO_2 \quad \Delta H^{\circ}_{298\ K} = -172\ kJ\ mol^{-1} \tag{1.7}$$

The commonly investigated catalysts include noble metals and non-noble metals. Noble metals such as Pt, Pd, and Rh exhibit outstanding catalytic performance [118]. In the catalytic tests of a series of noble metals, the order of the activity was found to be Rh, Ru > Ir > Pd, Pt. Ru and Rh performed better than other noble metals, and in industry, Ru may be more suitable considering its lower cost than that of Rh. The high activity and coke resistance derived from the dissociation of CO_2 to form CO and O species that subsequently activated methane molecules and oxidized CH_x species to prevent the carbon deposition [119]. In another study regarding the support effect on Pt catalysts, Pt/TiO_2 and Pt/ZrO_2 exhibited long-term stability with negligible coke formation during 80 hours on stream. The excellent performance of Pt/TiO_2 was attributed to the coverage of TiO_x on the surface of Pt, which prevented the growth of Pt nanoparticles. It was reported that small Pt particles inhibited both CO and methane dissociation, thus reducing carbon formation on the metal surface [120–122]. A similar mechanism was speculated to occur for Pt/ZrO_2. Besides, the strong Pt–Zr interaction inhibited coke formation by blocking the active sites [123, 124]. In the absence of this strong interaction, Pt/Cr_2O_3 and Pt/SiO_2 deactivated rapidly [125].

Despite the high activity and coke resistance for noble metals, their application is hindered by their high cost and also the occurrence of metal sintering [104]. Ni and Co catalysts are proven to be the most suitable candidates considering their high intrinsic activity and affordable cost [104, 126]. Co-based catalysts have been investigated based on the interaction with different supports. Due to the strong sintering of SrO and BaO, Co active sites were covered and exhibited very low activity. Although the initial conversions were acceptable for SiO_2-, CaO-, and Al_2O_3-supported Co catalysts, deactivation was rapid. With MgO as the support, activity, stability, and anti-sintering properties were enhanced up to 50 hours, which might be caused by the strong interaction between CoO and MgO and low reducibility of the catalyst [127, 128].

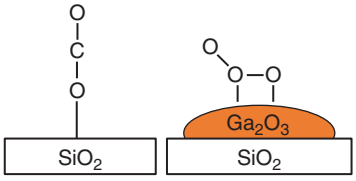

Figure 1.6 Activation of CO_2 on Ga_2O_3-promoted SiO_2 support. Source: Reproduced with permission from Pan et al. [138]: © 2010, The Royal Society of Chemistry.

Compared with Co and noble metals, Ni-based catalysts are more widely studied due to their low cost and good activity [104]. However, metal sintering and coke formation impede further application in industry. In the following section, catalyst design will be introduced based on surface regulation, oxygen defects, interfacial engineering, and structural optimization.

Surface Regulation In the DRM reaction, CO_2 and CH_4 are adsorbed, dissociated, and recombined to form CO and H_2 on the catalyst surface. Modifications of the surface acidity and basicity exert great effects on performance and coke resistance [104].

It was reported that Lewis acidic sites could balance the removal of carbon and the activation of CH_4, thus inhibiting the coke formation and improving stability [129]. Also, surface basicity could dissociate CO_2 to form CO and O species that oxidized CH_x to form CO and H_2 [104]. To enhance the surface basicity, alkali metals, alkali earth metals, and rare earth metal oxides have been investigated [104, 130–133].

Rare earth metal oxide La_2O_3 promoted the adsorption of CO_2 to form La oxycarbonate ($La_2O_2CO_3$) [134], which subsequently reacted with CH_4 molecules to produce CO and prevented coke formation based on the *in situ* DRIFT study [135]. MgO could further enhance the surface basicity of Ni/La_2O_3 catalyst so that more CO_2 adsorption occurred and monoclinic $La_2O_2CO_3$ was formed by reacting with La_2O_3. This monoclinic phase reacted more efficiently with carbon deposits than hexagonal La_2O_3 and $La_2O_2CO_3$ mixtures produced with a low Mg/La ratio [136]. The promotional effect of La_2O_3 is derived from the oxygen atoms of $La_2O_2CO_3$ that could react with CH and C species, while La–Ni accelerated the dissociation of C—H bond and intensified the coke formation. In summary, La metal dopant was not effective as its oxide [137].

In addition to La_2O_3 and MgO, the enhanced surface basicity of Ni/SiO_2 catalyst was achieved by doping with Ga_2O_3, leading to greater carbonate or bicarbonate formation along with the CO_2 adsorption as shown in Figure 1.6. The coke formed on the SiO_2 surface reacted more easily with the carbonate species than the physically or linearly adsorbed CO_2 [138].

In some circumstances, however, if the surface basicity is too strong, more coke deposits will generate due to less CO_2 adsorption [139]. In this case, Y_2O_3 was doped to offer weak and medium basic sites, leading to a higher activity and stability than pristine MgO/Al_2O_3 [140].

Besides the surface basicity, the concentration of surface hydroxyl groups can affect the oxidation of carbon deposits. The addition of B_2O_3 into Ni/Al_2O_3 can effectively increase the amount of hydroxyl groups on the surface, thus inhibiting the coke formation [141].

Oxygen Defects The generation of oxygen defects influences the oxygen mobility, thus determining the carbon resistance of the Ni-based catalysts [104]. Several promoters can form the oxygen defects, including rare earth metal oxides, transition metal oxides, mixed oxides, and perovskite oxides.

As representative of rare earth metal oxides, CeO_2 can produce lattice oxygen defects and promote surface oxygen mobility, thus scavenging carbon species. Typically, the reversible conversion of Ce^{4+} and Ce^{3+} determined the formation of oxygen defects, enhancing the adsorption of CO_2 or O_2 molecules that oxidized the surface coke and maintained the active metal sites. However, excessive doping of CeO_2 may block the access of reactant molecules and decrease conversion [104, 113, 142, 143].

The activation sites for CH_4 and CO_2 were investigated in a theoretical study as demonstrated in Figure 1.7. In detail, CH_4 molecules were preferably activated on the oxygen vacancies at the metal–support interfaces, metal vacancies, and metal–support interfaces. For CO_2, oxygen vacancies on the support or metal–support interfaces were more available for the activation of the molecules. Moreover, the interfacial oxygen of CeO_2 could regenerate the active sites. It can be seen that oxygen vacancies played a dominant role in both CH_4 and CO_2 activation [144].

ZrO_2 can further enhance the oxygen vacancy concentration when added to CeO_2. The cubic phase of $Ce_xZr_{1-x}O_2$ exhibited a higher OSC and oxidized the carbon more easily to form CO [145]. Interestingly, the loading of Ni in this mixed oxide also affected the oxygen vacancy concentration. With a 9.3 mol% Ni amount, CH_4 and CO_2 were converted with a higher percentage than other ratios [146].

Another two rare earth metal oxides, Y_2O_3 and La_2O_3, were also applied as the support to adjust the oxygen vacancy. α-Oxygen derived from Y_2O_3 presented very effective activation of CH_4 and removal of carbon. However, a small amount of oxygen may be fed considering the limited concentration of α-oxygen. For La_2O_3, oxycarbonate formation could adsorb more CO_2 while the addition of Sr could further enhance the oxygen vacancy concentration and oxidize the coke more effectively [147, 148].

Similarly to the rare earth metal oxides, transition metal oxides like ZrO_2 and TiO_2 could also provide oxygen vacancies because of their incompletely occupied *d* orbitals [149–152]. Due to the strong interaction between Ni and ZrO_2, CH_x originated from the CH_4 activation could be effectively converted to CO and H_2 by reacting with the lattice oxygen in ZrO_2. Moreover, CO_2 adsorption was promoted by the oxygen defects, thus inhibiting the coke formation [153]. Similarly, two types of oxygen species were observed in TiO_2, i.e. the lattice oxygen in the interface and oxygen ions inside TiO_2. The lattice oxygen could react with the coke on the surface of Ni to form CO and regenerated Ni for the continuous conversion [149].

Different from rare earth metal and transition metal oxides, perovskite oxides with ABO_3 structure generated oxygen defects by lattice distortions. The promoted oxygen fluidity enhanced the catalytic performance in DRM reaction [154–156]. A variety of elements have been used to substitute the A or B sites to form lattice defects [157–160]. When La was used in the A-site, Sr and Ce were doped to enhance the

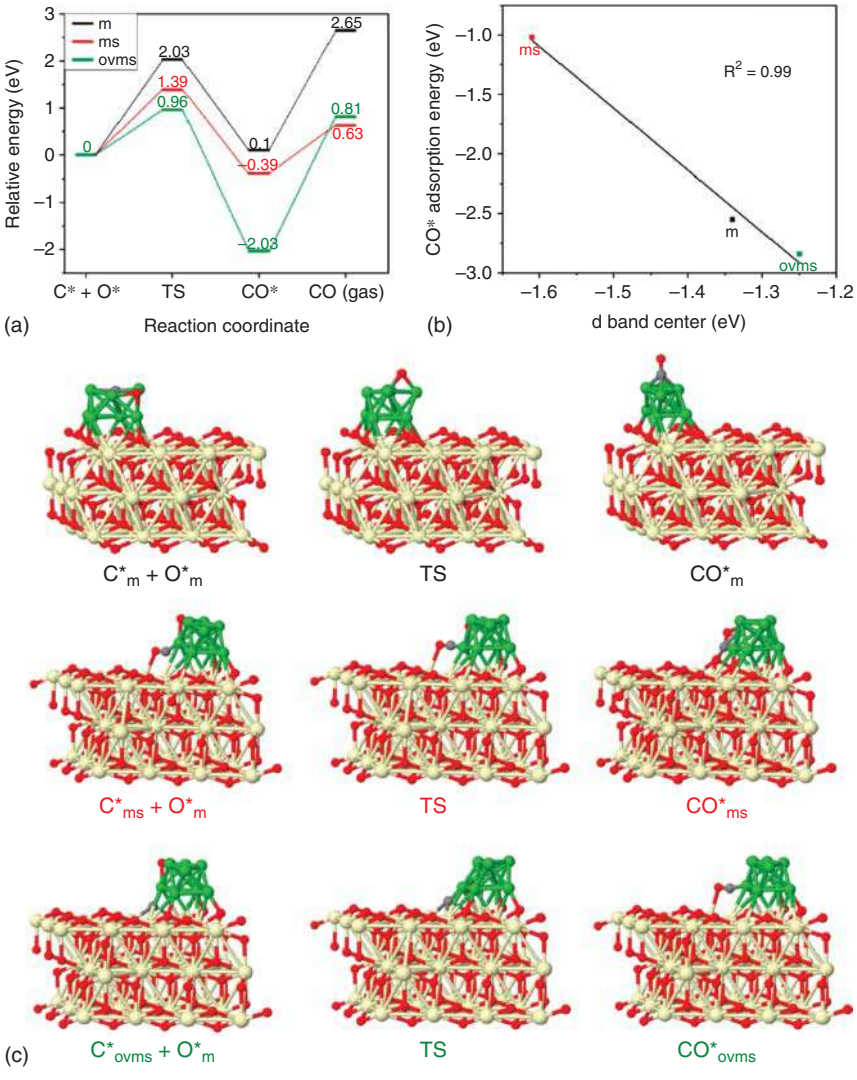

Figure 1.7 Three paths of C* elimination. (a) Relative energy of C* elimination at m, ms, and ovms sites. (b) Relation of d band center with CO* adsorption energy. (c) Corresponding configurations of part a. Gray spheres represent C, red spheres represent O, green spheres represent Ni, and cream-colored spheres represent Ce. Source: Reproduced with permission from Lian et al. [144]: © 2020, American Chemical Society.

oxygen vacancies in the $LaNiO_3$ perovskite structure. Due to the different oxidation states and size of Sr and La ions, lattice distortions occurred, and oxygen vacancies were generated. Differently, Ce^{3+} and La^{3+} have the same valence state, while the oxygen vacancies were derived from local redox fluctuations of Ce ions. For B-site replacement, Cu and Fe both promoted the formation of oxygen vacancies. However, Ni agglomeration occurred with copper substitution, while for Fe-substituted Ni perovskite, higher stability was accomplished due to the stronger MSI [160].

Interfacial Engineering The interfacial engineering for both Ni-metal and Ni-support interfaces influences the electron density, metal dispersion, and surface composition, thus affecting the reactant activation and catalyst deactivation behavior [161, 162]. When Cu formed a Ni–Cu alloy with Ni, the environment of Ni was changed, and coke formation was prevented [163]. A similar effect was observed for Ni–Co alloy catalysts [164]. When noble metals were doped to form alloys with Ni, metal dispersion was enhanced, and the oxidation of CH_x species was promoted instead of dehydrogenation [165, 166].

Besides the strategy to tune the alloy interface, the modification of MSI can determine the size, dispersion, surface area, and reducibility. For the inert SiO_2 support, the formation of Ni phyllosilicate was promising to enhance the MSI. Several methods were used to prepare the phyllosilicate structure, such as ammonia evaporation and sequential two-step calcination [167, 168]. Compared with the inert SiO_2, basic support MgO or $MgAl_2O_4$ could produce highly dispersed Ni nanoparticles with CO_2 adsorptions. However, too strong MSI may lead to the metal sintering at a high reduction temperature [169–171]. Besides the inert and basic oxides, CeO_2 can form Ni–Ce solid solutions, which changed the electronic or chemical state of Ni and adsorbed CH_4 by both Ni and O atoms, thus inhibiting carbon formation, proven by the lack of C or NiC_x peaks as shown in Figure 1.8 [142].

Structural Optimization Both porous materials and hierarchical structures can prevent the Ni sintering at high temperatures [101, 104, 105]. Porous carbon support synthesized from renewable hydrochar effectively anchored the Ni^{2+} ions on the surface, controlling the average diameter of Ni particles within 8 nm. Mesoporous active carbon with mesopores and high surface area provided strong MSI and enhanced the methane conversion [172, 173]. Similarly, with ordered structures and high porosities, porous silica materials are also applied as supports to control the Ni dispersion [174–179]. With the help of amine groups of polyethylenimine (PEI), SBA-15 with ordered channels and surface silanol groups could trap Ni ions by physical confinement effect and chemical bonding (Figure 1.9) [176].

Other metal oxides with mesoporous structures also draw attention due to their multifunctional nature [180–183]. For example, NiO–MgO–Al_2O_3 mesoporous frameworks provided both the mesopores to anchor the active metals and prevent sintering and the basic sites to adsorb more CO_2 to form CO and O radicals, thus removing coke on the metal surface [180]. In another case of mesoporous NiO–CeO_2–Al_2O_3 material, the only difference was apparent in the redox property offered by CeO_2 that oxidized the coke instead of by the basic nature of MgO [184].

In addition to the usage of porous support, architecture designs of catalysts also alleviate metal sintering and coke formation. Following the first core–shell nanoreactor Pt@CoO, various nanostructures have been developed recently to control metal distribution and enhance the dispersion [104, 185–193].

Ni@SiO_2 core–shell structures have been widely studied in the DRM reaction. When a thick shell of silica was used, the core–shell structure was transformed into

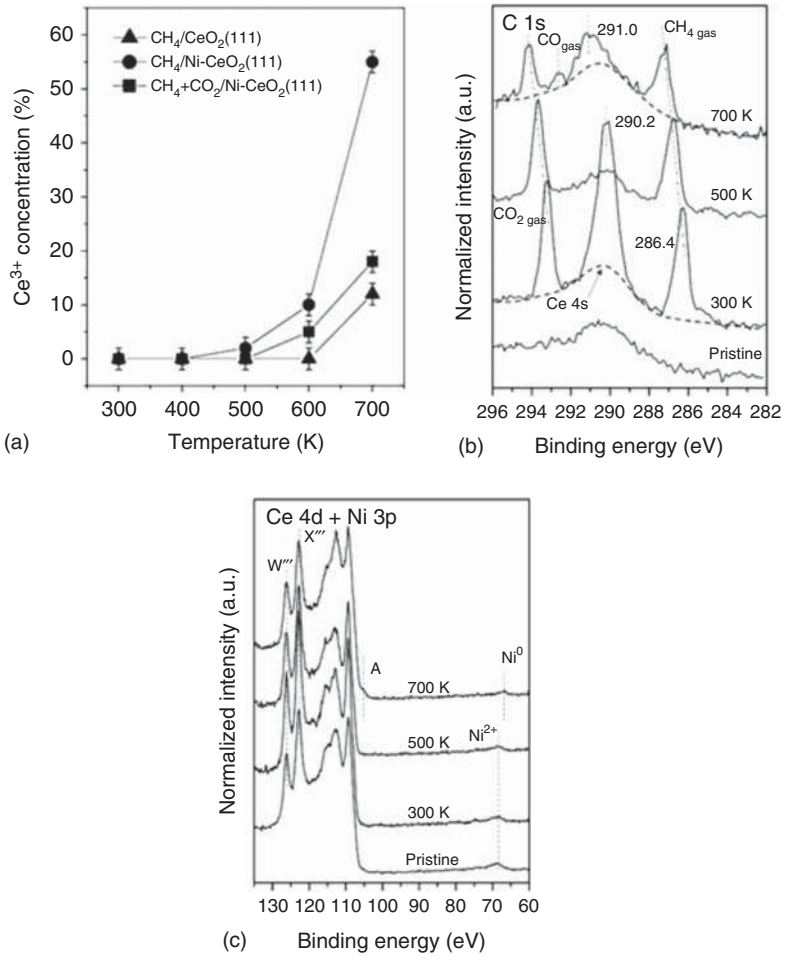

Figure 1.8 (a) Ce^{3+} concentration measured in XPS as a function of temperature under reaction conditions (i.e. exposure to 100 mTorr of methane or a mixture of 100 mTorr of methane and 100 mTorr of CO_2). (b) and (c) C 1s and Ce 4d + Ni 3p spectra of the Ni–CeO_2 (111) ($\theta_{Ni} \approx 0.1$ ml) surface under 100 mTorr CH_4 + 100 mTorr of CO_2 at 300, 500, and 700 K. Source: Reproduced with permission from Liu et al. [142]: © 2016, Wiley.

a yolk–shell structure with Ni metal as the core surrounded by Ni embedded in the SiO_2 shell (Figure 1.10). The excellent conversion and stability were attributed to the small satellite Ni particles and the strong MSI [194].

To further enhance the catalytic performance, Ni–Mg phyllosilicate was adopted as the shell to provide strong MSI, basicity, and modified pore structures. With this synergistic effect, both Ni sintering and coke formation were inhibited [195, 196]. Similarly, NiMgAl layer double hydroxide was prepared first, followed by being coated with another mesoporous silica layer. After thermal treatment, Ni metal was confined by MgO and SiO_2, leading to suppressed carbon deposition [197] (Table 1.4).

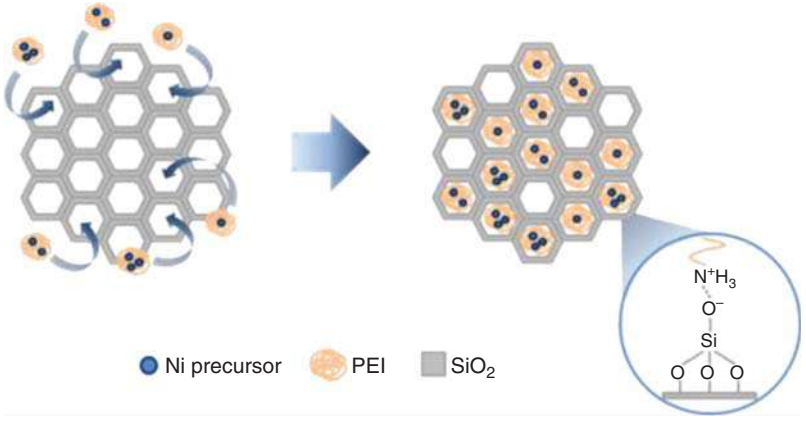

Figure 1.9 Schematic diagram of PEI-aided route. Source: Reproduced with permission from Kang et al. [176]: © 2017, Elsevier.

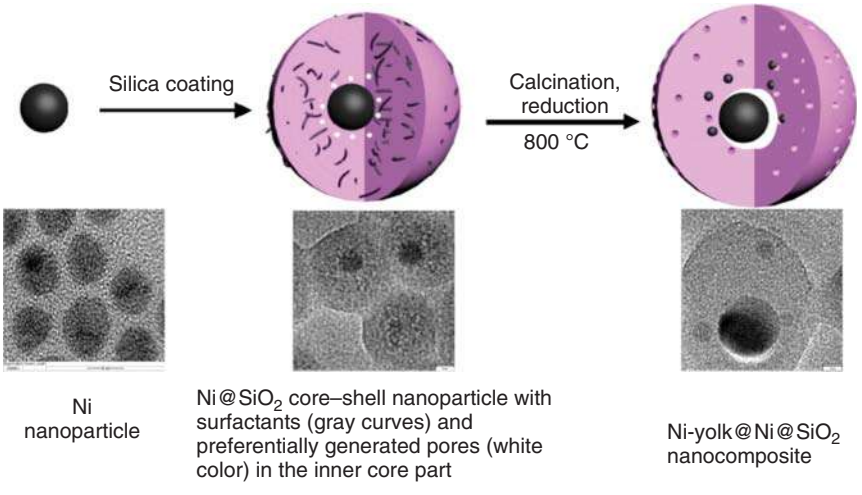

Figure 1.10 Schematic illustration of the formation process of Ni–yolk@Ni@SiO_2 nanocomposite. Source: Li et al. [194]/with permission of American Chemical Society.

1.1.4 Thermocatalytic Conversion of Other Fossil Fuels

According to US DOE, 95% of the overall hydrogen production was based on fossil fuels [2]. Besides the methane reforming discussed above, catalytic steam reforming of LPG was studied as another way to generate hydrogen gas. Noble metal catalysts were mainly investigated with oxides as the supports. When $Ru/CeO_2–Al_2O_3$ was applied, the products were mainly H_2, CO, and CO_2 while the decomposition of LPG and methanation were responsible for methane, ethane, and ethylene production [198]. Addition of oxygen was effective in the elimination of higher hydrocarbons, reduction of coke, and enhancement of stability [199, 200]. Besides Ru, other noble metals such as Pd, Rh, and Pt exhibited good anti-coking ability in steam reforming of LPG [201, 202].

Table 1.4 Summary of catalysts in dry reforming of methane.

Catalyst	Conditions	Findings	References
$Ru/MgO–Al_2O_3$	500 and 650 °C; $CO_2/CH_4 = 4$.	The dissociation of CO_2 to form CO and O species that subsequently activated methane molecules and oxidized CH_x species to prevent the carbon deposition	[119]
Pt/ZrO_2	600 °C; $CO_2/CH_4 = 1$	The strong Pt–Zr interaction inhibited coke formation by blocking the active sites	[123]
Ni/La_2O_3	700 °C; $CH_4/CO_2 = 1$	70% CH_4 and 75% CO_2 conversion; La oxycarbonate reacted with carbon to form CO	[134]
$Ni/MgO–La_2O_3$	700 °C; $CH_4/CO_2 = 1$	63% CH_4 and 65% CO_2 conversion; more CO_2 adsorbed on the surface with MgO	[136]
$Ni/SiO_2–Ga_2O_3$	700 °C; $CH_4/CO_2 = 1$	70% CH_4 and 79% CO_2 conversion; carbonate or bicarbonate was formed by CO_2 adsorption promoted by Ga_2O_3	[138]
HTNi–Y	700 °C; $CH_4/CO_2 = 1$	74% CH_4 and 78% CO_2 conversion; weak and medium basic sites were introduced to the surface by addition of Y_2O_3	[140]
$5\%Ni/B_2O_3–Al_2O_3$	700 °C; $CH_4/CO_2 = 1$	75% CH_4 and 67% CO_2 conversion; more hydroxyl groups were formed on borated surface, oxidizing the carbon	[141]
$NiRhCe_2Zr_{1.51}$	700 °C; $CH_4/CO_2 = 7:3$	16% CH_4 and 37.5% CO_2 conversion; more oxygen vacancies were generated by the cubic phase of $Ce_xZr_{1-x}O_2$	[145]
Ni-SDL (Sr doped La)	600 °C; $CH_4/CO_2 = 1$	78% CH_4 and 60% CO_2 conversion; surface oxygen species mobility was enhanced by Sr	[148]
$Ni–CaO–ZrO_2$	700 °C; $CH_4/CO_2 = 1$	73% CH_4 and 83% CO_2 conversion; CH_x species on Ni surface reacted with the lattice oxygen in ZrO_2 to form CO and H_2	[153]
$La_{0.8}Sr_{0.2}Ni_{0.8}Cu_{0.2}O_3$	600–800 °C; $CH_4/CO_2 = 1$	80% CH_4 and 80% CO_2 conversion; lattice oxygen mobility was promoted with the addition of Sr and Cu	[160]
$NiPt/Al_2O_3$	700 °C; $CH_4/CO_2 = 1$	85.8% CH_4 and 91.2% CO_2 conversion; CH was oxidized by Pt layer in the core–shell structure	[166]

Table 1.4 (Continued)

Catalyst	Conditions	Findings	References
Ni@Ni embedded SiO_2	700 °C; $CH_4/CO_2 = 1$	74% CH_4 and 82% CO_2 conversion; interaction with SiO_2 and dispersion of Ni were both enhanced by phyllosilicate	[167]
Ni/SiO_2	700 °C; $CH_4/CO_2 = 1$	80% CH_4 and 85% CO_2 conversion; metal dispersion and metal–support interaction were enhanced by sequential calcination	[168]
$AuNi/MgAl_2O_4$	650 °C; $CH_4/CO_2 = 69 : 30$	20% CH_4 and 48% CO_2 conversion; $MgAl_2O_4$ spinel phase enhanced the surface basicity and CO_2 adsorption, thus inhibiting the coke formation	[171]
Ni/CeO_2	450 °C; $CH_4/CO_2 = 1$	10^{-7} Torr CH_4 and 10^{-7} Torr CO_2; Ni–Ce solid solution promoted the adsorption of CH_4 on Ni and O	[142]
Ni@C	700 °C; $CH_4/CO_2 = 1$	68% CH_4 and 80% CO_2 conversion; Ni dispersion was enhanced due to the confinement effect of pore structure	[172]
Ni/SBA-15	750 °C; $CH_4/CO_2 = 1$	85% CH_4 and 88% CO_2 conversion; the steric hindrance of ordered channels inhibited the metal sintering	[176]
$NiO–MgO–Al_2O_3$	700 °C; $CH_4/CO_2 = 1$	78% CH_4 and 83% CO_2 conversion; coke formation and metal agglomeration were alleviated by the pore structure and enhanced basicity	[180]
$NiO–CeO_2–Al_2O_3$	700 °C; $CH_4/CO_2 = 1$	78% CH_4 and 73% CO_2 conversion; thermally stable mesoporous support confined Ni in the matrix and redox CeO_2 prevented coke formation	[184]
$Ni@SiO_2$	800 °C; $CH_4/CO_2 = 1$	90% CH_4 and 95% CO_2 conversion; small satellite Ni particles and strong metal–support interaction enhanced the catalytic performance with appropriate shell thickness	[194]
NiMgAl–(LDH)@ mesoporous–SiO_2	750 °C; $CH_4/CO_2 = 1$	79% CH_4 and 88% CO_2 conversion; MgO and SiO_2 layers confined Ni particles in the cavity	[197]

However, considering the high cost of raw materials, noble metals may not be suitable candidates for commercial use. Due to the high OSC, redox property, and strong metal–support interaction, CeO_2-based catalysts are promising alternatives [201–207]. Compared with traditional Ni/Al_2O_3, the redox property of CeO_2 prepared with the surfactant-assisted approach presented excellent activity and coke resistance.

In addition to steam reforming, dry reforming of hydrocarbons draws attention since it can alleviate the greenhouse gas effect. For dry reforming of ethane, with the increase of Mn concentration, the conversion of ethane increased accordingly. When SiO_2 was replaced by Al_2O_3, the conversion of ethane increased while the yield of ethylene decreased. To obtain a higher selectivity to ethylene, the CO_2/ethane ratio should be kept at a high value [208]. When Rh/ZSM-5 was adopted as the catalyst, the reaction rate of dry reforming of ethane was five times higher than DRM, which may be attributed to the easier dissociation of the C—H bond in ethane than methane. However, the coke formation was considerably higher than DRM [209–212]. Two different mechanisms were proposed, i.e. (i) CH_x generated from the decomposition of C_2H_6 reacting with the absorbed oxygen to form CH_xO, which decomposes to produce CO and H_2 [209–211, 213], and (ii) CO_2 and H_2 reacting to form hydroxyl species, which subsequently react with CH_x [214, 215].

The yield and selectivity in dry reforming of propane also depended on the catalysts used. When a series of noble metals were supported on Al_2O_3, the reactivity order was shown as Ru > Rh, Pd > Pt, Ir. Among them, Ru/Al_2O_3 exhibited the highest H_2 selectivity. As for the support activity with Rh as the active metal, Al_2O_3 performed the best, followed by TiO_2, MgO, and SiO_2 [209–211]. In addition to noble metals, Ni supported on Mg and Al support derived from a hydrotalcite precursor presented excellent stability due to the continuous supply of oxygen from CO_2 to Ni metal [216].

Other hydrocarbons such as *n*-butane, *iso*-butane, *neo*-pentane, *n*-heptane, ethylene, and *n*-dodecane could be converted to syngas, short hydrocarbon molecules, and coke when CO_2 was fed into the reactor. MnO exhibited high catalytic performance, especially when promoted by Cr and K and supported on La_2O_3 and ZrO_2. Similarly, Ni or Rh as the active metals performed well in heavier hydrocarbon dry reforming reactions [208, 213, 217, 218].

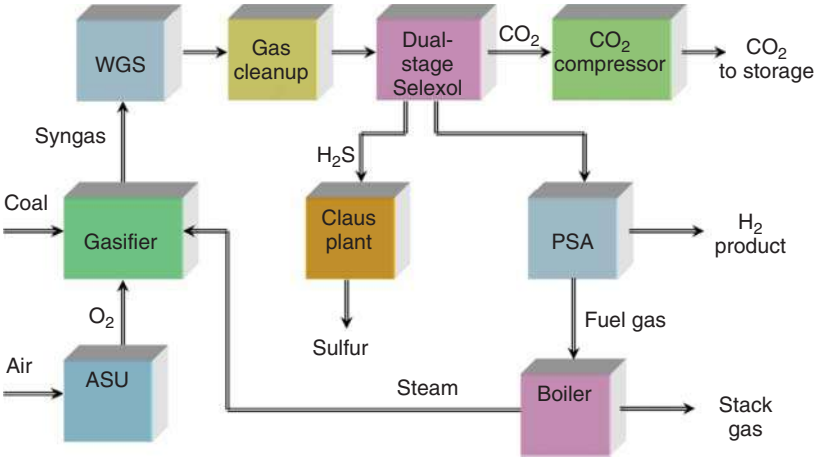

Figure 1.11 A simplified block diagram of a coal gasification hydrogen plant with CO_2 capture. ASU; air separation unit. Source: Reproduced with permission from Muradov [1]: © 2017, Elsevier.

Besides the reforming of hydrocarbons, coal gasification was another pathway to generate hydrogen gas, where coal reacted with an O_2–steam mixture at high temperature [219]. Despite the low hydrogen content (H/C = 0.1), the specific importance of integrated gasification cycle lies in the simultaneous production of hydrogen gas and electricity [1]. As shown in Figure 1.11, the produced syngas flowed into a WGS reactor with a sulfur-tolerant catalyst to produce a H_2–CO_2 mixture. Then, a double-stage Selexol unit was equipped to remove the H_2S and CO_2, generating an acidic gas-free stream that was directed to PSA for H_2 purification [220].

1.2 Conclusions and Prospects

In this chapter, we summarized the catalytic routes for production of hydrogen gas, by converting fossil fuels such as methane. Both the reaction mechanisms and values of the reactions are included. To realize a more efficient and cost-effective industry process, we have covered the recent progress of catalyst design for each reaction.

The main routes of hydrogen production are still those related to the catalytic processing of methane. Among the several approaches, methane decomposition is still at the lab scale and work has has to explore the way to industrialization. SRM is dominant in producing hydrogen gas, along with ATR and POM as the efficient and economical technologies for the large-scale production of hydrogen gas. Furthermore, due to the increasing concern toward environmental issues, DRM attracts much attention. To further enhance the catalytic performance and stability, it is necessary to modify the catalysts using promoters, dopants, novel architectures, and regulated morphologies and structures. Besides, operation parameters and reactor designs can be further refined to meet industry requirements.

In addition to the issues above, advanced characterization methods and simulation techniques are needed to elucidate mechanisms of catalyst formation, the interaction between the catalyst and the reactant, and the kinetics. Moreover, it is crucial and urgent to refine the existing "good" catalysts at the lab-scale level to be capable at industry level where the mass diffusion and energy transfer are both different from the lab experiments. In the meanwhile, optimization of the existing industry system and parameters should also be considered.

References

1 Muradov, N. (2017). *Int. J. Hydrogen Energy* 42: 14058–14088.
2 Navarro, R., Pena, M., and Fierro, J. (2007). *Chem. Rev.* 107: 3952–3991.
3 International Energy Agency (2007). *Hydrogen Production and Distribution: IEA Energy Technology Essentials*. Paris: OECD/IEA.
4 Ball, M. and Wietschel, M. (2009). *Int. J. Hydrogen Energy* 34: 615–662.
5 Balat, M. and Balat, M. (2009). *Int. J. Hydrogen Energy* 34: 3589–3603.
6 Ong, H., Mahlia, T., and Masjuki, H. (2011). *Renew. Sustain. Energy Rev.* 15: 639–647.

7 Wang, Q., Chen, X., Jha, A.N., and Rogers, H. (2014). *Renew. Sustain. Energy Rev.* 30: 1–28.
8 Konieczny, A., Mondal, K., Wiltowski, T., and Dydo, P. (2008). *Int. J. Hydrogen Energy* 33: 264–272.
9 Ashik, U.P.M., Daud, W.M.A.W., and Abbas, H.F. (2015). *Renew. Sustain. Energy Rev.* 44: 221–256.
10 Voldsund, M., Jordal, K., and Anantharaman, R. (2016). *Int. J. Hydrogen Energy* 41: 4969–4992.
11 Ball, M. and Weeda, M. (2015). *Int. J. Hydrogen Energy* 40: 7903–7919.
12 Zhang, J.B., Li, X., Chen, H.Y. et al. (2017). *Int. J. Hydrogen Energy* 42: 19755–19775.
13 Gaudernack, B. (1998). Hydrogen production from fossil fuels. In: *Hydrogen Power: Theoretical and Engineering Solutions* (ed. T.O. Saetre), 75–89. Netherlands: Springer.
14 Muradov, N. (2002). Hydrogen from fossil fuels without CO_2 emissions. In: *Advances in Hydrogen Energy* (ed. P.C.E. Grégoire and F. Lau), 1–16. USA: Springer.
15 Teo, K.B., Singh, C., Chhowalla, M., and Milne, W.I. (2003). Catalytic synthesis of carbon nanotubes and nanofibers. In: *Encyclopedia of Nanoscience and Nanotechnology*, vol. 10 (ed. H.S. Nalwa), 1–22. USA: American Scientific Publishers.
16 Baharudin, L. and Watson, M.J. (2018). *Rev. Chem. Eng.* 34: 43–72.
17 Lobo, L. and Trimm, D. (1973). *J. Catal.* 29: 15–19.
18 Robertson, S. (1972). *Carbon* 10: 221–229.
19 Bayat, N., Rezaei, M., and Meshkani, F. (2016). *Korean J. Chem. Eng.* 33: 490–499.
20 Ibrahim, A.A., Fakeeha, A.H., Al-Fatesh, A.S. et al. (2015). *Int. J. Hydrogen Energy* 40: 7593–7600.
21 Aiello, R., Fiscus, J., Loye, H., and Amiridis, M. (2000). *Appl. Catal., A* 192: 227–234.
22 Bayat, N., Rezaei, M., and Meshkani, F. (2016). *Int. J. Hydrogen Energy* 41: 1574–1584.
23 Bayat, N., Meshkani, F., and Rezaei, M. (2016). *Int. J. Hydrogen Energy* 41: 13039–13049.
24 Lua, A.C. and Wang, H.Y. (2014). *Appl. Catal., B* 156: 84–93.
25 Awadallah, A.E. and Aboul-Enein, A.A. (2015). *Egypt. J. Pet.* 24: 299–306.
26 Yu, Y., Cui, M.S., Li, M.L. et al. (2014). *J. Rare Earths* 32: 709–714.
27 Liu, F., Chen, L., Yang, L. et al. (2016). *Int. J. Hydrogen Energy* 41: 4592–4602.
28 Kim, M., Lee, E., Jun, J. et al. (2004). *Int. J. Hydrogen Energy* 29: 187–193.
29 Bai, Z., Chen, H., Li, B., and Li, W. (2005). *J. Anal. Appl. Pyrolysis* 73: 335–341.
30 Moliner, R., Suelves, I., Lazaro, M., and Moreno, O. (2005). *Int. J. Hydrogen Energy* 30: 293–300.
31 Shen, Y. and Lua, A.C. (2016). *J. Colloid Interface Sci.* 462: 48–55.
32 Serrano, D., Botas, J., Pizarro, P. et al. (2008). *Chem. Commun.* 6585–6587.
33 Dunker, A., Kumar, S., and Mulawa, P. (2006). *Int. J. Hydrogen Energy* 31: 473–484.

34 Serrano, D., Botas, J., and Guil-Lopez, R. (2009). *Int. J. Hydrogen Energy* 34: 4488–4494.

35 Muradov, N., Smith, F., Bockerman, G., and Scammon, K. (2009). *Appl. Catal., A* 365: 292–300.

36 Dufour, A., Celzard, A., Fierro, V. et al. (2008). *Appl. Catal., A* 346: 164–173.

37 Muradov, N., Chen, Z., and Smith, F. (2005). *Int. J. Hydrogen Energy* 30: 1149–1158.

38 Chaubey, R., Sahu, S., James, O.O., and Maity, S. (2013). *Renew. Sustain. Energy Rev.* 23: 443–462.

39 Pantaleo, G., La Parola, V., Deganello, F. et al. (2015). *Appl. Catal., B* 164: 135–143.

40 Pal, P., Singha, R.K., Saha, A. et al. (2015). *J. Phys. Chem. C* 119: 13610–13618.

41 Bi, X.-J., Hong, P.-J., Xie, X.-G., and Dai, S.-S. (1999). *React. Kinet. Catal. Lett.* 66: 381–386.

42 Abbasi, R., Huang, G., Istratescu, G.M. et al. (2015). *Can. J. Chem. Eng.* 93: 1474–1482.

43 Santis-Alvarez, A.J., Büchel, R., Hild, N. et al. (2014). *Appl. Catal., A* 469: 275–283.

44 Staniforth, J., Evans, S.E., Good, O.J. et al. (2014). *Dalton Trans.* 43: 15022–15207.

45 Meng, B., Zhang, H., Zhao, Z. et al. (2016). *Catal. Today* 259: 388–392.

46 Ji, Y., Li, W., Xu, H., and Chen, Y. (2001). *Catal. Lett.* 71: 45–48.

47 Wang, H.Y. and Ruckenstein, E. (2001). *Catal. Lett.* 75: 13–18.

48 Yang, S., Kondo, J.N., Hayashi, K. et al. (2004). *Appl. Catal., A* 277: 239–246.

49 Wang, H.Y. and Ruckenstein, E. (2001). *J. Catal.* 199: 309–317.

50 Wang, H.-T., Li, Z.-H., and Tian, S.-X. (2004). *React. Kinet. Catal. Lett.* 83: 245–252.

51 González, M.G., Nichio, N.N., Moraweck, B., and Martin, G. (2000). *Mater. Lett.* 45: 15–18.

52 Basile, F., Fornasari, G., Trifirò, F., and Vaccari, A. (2001). *Catal. Today* 64: 21–30.

53 Zhu, Y., Zhang, S., Shan, J.-J. et al. (2013). *ACS Catal.* 3: 2627–2639.

54 Ding, C., Ai, G., Zhang, K. et al. (2015). *Int. J. Hydrogen Energy* 40: 6835–6843.

55 Chalupka, K.A., Jozwiak, W.K., Rynkowski, J. et al. (2014). *Appl. Catal., B* 146: 227–236.

56 Yan, Q.G., Weng, W.Z., Wan, H.L. et al. (2003). *Appl. Catal., A* 239: 43–58.

57 Brackmann, R., Perez, C.A., and Schmal, M. (2014). *Int. J. Hydrogen Energy* 39: 13991–14007.

58 Yoon, J.S., Lim, Y.-S., Choi, B.H., and Hwang, H.J. (2014). *Int. J. Hydrogen Energy* 39: 7955–7962.

59 Morales, M., Espiell, F., and Segarra, M. (2014). *Int. J. Hydrogen Energy* 39: 6454–6461.

60 Sengodan, S., Lan, R., Humphreys, J. et al. (2018). *Renew. Sustain. Energy Rev.* 82: 761–780.

61 Abad, A.V. and Dodds, P.E. (2017). *Production of Hydrogen*, vol. 3. Elsevier.

62 Acar, C. and Dincer, I. (2013). *Int. J. Hydrogen Energy* 39: 1–12.

63 Akamatsu, K., Murakami, T., Sugawara, T. et al. (2011). *AlChE J.* 57: 1882–1888.
64 Iulianelli, A., Liguori, S., Wilcox, J., and Basile, A. (2016). *Catal. Rev.* 58: 1–35.
65 Utaka, T., Sekizawa, K., and Eguchi, K. (2000). *Appl. Catal., A* 194–195: 21–26.
66 Ginés, M.J.L., Amadeo, N., Laborde, M., and Apesteguía, C.R. (1995). *Appl. Catal., A* 131: 283–296.
67 Ji, G.Z., Yao, J.G., Clough, P.T. et al. (2018). *Energy Environ. Sci.* 11: 2647–2672.
68 Collodi, G. ()2010. Hydrogen production via steam reforming with CO_2 capture. http://www.audic.it/CICAP4/webpapers/7Collodi.pdf.
69 Angeli, S.D., Monteleone, G., Giaconia, A., and Lemonidou, A.A. (2014). *Int. J. Hydrogen Energy* 39: 1979–1997.
70 Roy, P.S., Park, N.-K., and Kim, K. (2014). *Int. J. Hydrogen Energy* 39: 4299–4310.
71 Simakov, D.S.A., Luo, H.Y., and Román-Leshkov, Y. (2015). *Appl. Catal., B* 168–169: 540–549.
72 Cassinelli, W.H., Damyanova, S., Parizotto, N.V. et al. (2014). *Appl. Catal., A* 475: 256–269.
73 Xue, X. and Wu, S. (2015). *Int. J. Hydrogen Energy* 40: 5617–5623.
74 Zhang, Y., Wang, W., Wang, Z. et al. (2015). *Catal. Today* 256: 130–136.
75 Khzouz, M., Wood, J., Pollet, B., and Bujalski, W. (2013). *Int. J. Hydrogen Energy* 38: 1664–1675.
76 Andrade, M.L., Almeida, L., do Carmo Rangel, M. et al. (2014). *Chem. Eng. Technol.* 37: 343–348.
77 Amjad, U., Gonçalves, G., Camargo Fernandes-Machado, N.R.C., and Specchia, S. (2015). *Catal. Today* 257: 122–130.
78 Nikolla, E., Schwank, J., and Linic, S. (2009). *J. Catal.* 263: 220–227.
79 Choi, S.O. and Moon, S.H. (2009). *Catal. Today* 146: 148–153.
80 Urasaki, K., Sekine, Y., Kawabe, S. et al. (2005). *Appl. Catal., A* 286: 23–29.
81 Wang, Z., Shao, X., Hu, X. et al. (2014). *Catal. Today* 228: 199–205.
82 Krumpelt, M., Krause, T.R., Carter, J.D. et al. (2002). *Catal. Today* 77: 3–16.
83 Ma, R.S., Xu, B., and Zhang, X. (2019). *Catal. Today* 338: 18–30.
84 Horn, R. and Schlögl, R. (2015). *Catal. Lett.* 145: 23–39.
85 Dybkjær, I. (1995). *Fuel Process. Technol.* 42: 85–107.
86 Bharadwaj, S. and Schmidt, L. (1995). *Fuel Process. Technol.* 42: 109–127.
87 Aasberg-Petersen, K. and Christensen, T.S. (2004). Synthesis gas production for FT synthesis. In: *Fischer–Tropsch Technology* (ed. A. Steynberg and M. Dry), 258–352. Amsterdam: Elsevier.
88 Bellows, R.J. (1999). Technical challenges for hydrocarbon fuel reforming. In: *Proceedings of the joint DOE/ONR FuelCell workshop*, Baltimore, 6.
89 Lisboa, J.S., Terra, L.E., Silva, P.R.J. et al. (2011). *Fuel Process. Technol.* 92: 2075–2082.
90 Roh, H.-S., Jun, K.-W., Dong, W.-S. et al. (2001). *Catal. Lett.* 74: 31–36.
91 Dantas, S.C., Escritori, J.C., Soares, R.R., and Hori, C.E. (2010). *Chem. Eng. J.* 156: 380–387.
92 Cao, L., Pan, L., Ni, C. et al. (2010). *Fuel Process. Technol.* 91: 306–312.

93 Ruiz, J.A.C., Passos, F.B., Bueno, J.M.C. et al. (2008). *Appl. Catal. A* 334: 259–267.

94 Escritori, J.C., Dantas, S.C., Soares, R.R., and Hori, C.E. (2009). *Catal. Commun.* 10: 1090–1094.

95 Cai, X., Dong, X., Lin, W., and Nat, J. (2006). *Gas Chem.* 15: 122–126.

96 Elvidge, C.D., Bazilian, M.D., Zhizhin, M. et al. (2018). *Energy Strateg. Rev.* 20: 156–162.

97 Song, C., Liu, Q., Ji, N. et al. (2018). *Renew. Sustain. Energy Rev.* 82: 215–231.

98 Zain, M.M. and Mohamed, A.R. (2018). *Renew. Sustain. Energy Rev.* 98: 56–63.

99 Paksoy, A.I., Selen, B., and Aksoylu, A.E. (2015). *Appl. Catal., B* 168–169: 164–174.

100 Bian, Z.F., Das, S., Wai, M.H. et al. (2017). *ChemPhysChem* 18: 3117–3134.

101 Li, Z.W., Li, M., Bian, Z.F. et al. (2016). *Appl. Catal., B* 188: 324–341.

102 Kathiraser, Y., Oemar, U., Saw, E.T. et al. (2015). *Chem. Eng. J.* 278: 62–78.

103 Bian, Z.F. and Kawi, S. (2020). *Catal. Today* 339: 3–23.

104 Kawi, S., Kathiraser, Y., Ni, J. et al. (2015). *ChemSusChem* 8: 3556–3575.

105 Li, Z.W., Das, S., Hongmanorom, P. et al. (2018). *Catal. Sci. Technol.* 8: 2763–2778.

106 Bradford, M.C.J. and Vannice, M.A. (1996). *Appl. Catal. A* 142: 73–96.

107 Gadalla, A.M. and Bower, B. (1988). *Chem. Eng. Sci.* 43: 3049–3062.

108 Chubb, T.A. (1980). *Sol. Energy* 24: 342–345.

109 McCrary, J.H., McCrary, C.E., Clark, D.H., and Chubb, T.A. (1980). *Proc. Meet. Am. Sect. Int. Sol. Eng. Soc.* 3: 99–103.

110 McCrary, J.H., McCrary, G.E., Chubb, T.A. et al. (1982). *Sol. Energy* 29: 141–151.

111 Peral, J.M.A. (1986). *Proc. Intersoc. Energy Convers. Engng Conf.* 21: 695–701.

112 Jang, W.-J., Shim, J.-O., Kim, H.-M. et al. (2019). *Catal. Today* 324: 15–26.

113 Abdulrasheed, A., Jalil, A.A., Gambo, Y. et al. (2019). *Renew. Sustain. Energy Rev.* 108: 175–193.

114 Gould, T.D., Izar, A., Weimer, A.W. et al. (2014). *ACS Catal.* 4: 2714–2717.

115 Xie, X., Otremba, T., Littlewood, P. et al. (2013). *ACS Catal.* 3: 224–229.

116 Lavoie, J.-M. (2014). *Front. Chem.* 2: 1–17.

117 Von der Assen, N., Voll, P., Peters, M., and Bardow, A. (2014). *Chem. Soc. Rev.* 43: 7982–7994.

118 Singh, R., Dhir, A., Mohapatra, S.K., and Mahla, S.K. (2020). *Biomass Convers. Biorefin.* 10: 567–587.

119 Rostrup-Nielsen, J. and Hansen, J.-H. (1993). *J. Catal.* 144: 38–49.

120 Bradford, M.C.J. and Vannice, M.A. (1998). *J. Catal.* 173: 157–171.

121 Van Santen, R.A. and Neurock, M. (1995). *Catal. Rev. Sci. Eng.* 37: 557–698.

122 Koster, A.D.E. and van Santen, R.A. (1991). *J. Catal.* 127: 141–166.

123 Bitter, J.H., Hally, W., Seshan, K. et al. (1996). *Catal. Today* 29: 349–353.

124 Roberts, S. and Gorte, R.J. (1991). *J. Phys. Chem.* 95: 5600–5604.

125 van Keulen, A.N.J., Seshan, K., Hoebink, J.H.B.J., and Ross, J.R.H. (1997). *J. Catal.* 166: 306–314.

126 Wittich, K., Krämer, M., Bottke, N., and Schunk, S.A. (2020). *ChemCatChem* 12: 2130–2147.

127 Ruckenstein, E. and Wang, H.Y. (2000). *Appl. Catal. A* 204: 257–263.

128 Stevenson, S.A., Dumesic, J.A., Baker, R.T.K., and Ruckenstein, E. (ed.) (1987). *Metal-Support Interactions in Catalysis, Sintering, and Redispersion*, 141. New York: Van Nostrand Reinhold.

129 Ni, J., Zhao, J., Chen, L.W. et al. (2016). *ChemCatChem* 8: 3732–3739.

130 Wang, C., Sun, N., Kang, M. et al. (2013). *Catal. Sci. Technol.* 3: 2435–2443.

131 Al-Fatesh, A.S., Arafat, Y., Atia, H. et al. (2017). *J. CO_2 Util.* 21: 395–404.

132 Phan, T.S., Sane, A.R., de Vasconcelos, B.R. et al. (2018). *Appl. Catal., B* 224: 310–321.

133 Zhang, L., Lian, J., Li, L. et al. (2018). *Microporous Mesoporous Mater.* 266: 189–197.

134 Li, X.Y., Li, D., Tian, H. et al. (2017). *Appl. Catal., B* 202: 683–694.

135 Zhang, Z., Verykios, X.E., MacDonald, S., and Affrossman, S. (1996). *J. Phys. Chem.* 100: 744–752.

136 Ni, J., Chen, L.W., Lin, J.Y. et al. (2013). *Int. J. Hydrogen Energy* 38: 13631–13642.

137 Li, K., He, F., Yu, H.M. et al. (2018). *J. Catal.* 364: 248–261.

138 Pan, Y.-X., Kuai, P., Liu, Y. et al. (2010). *Energy Environ. Sci.* 3: 1322–1325.

139 Dębek, R., Motak, M., Galvez, M.E. et al. (2017). *Int. J. Hydrogen Energy* 42: 1–12.

140 Świrk, K., Gálvez, M.E., Motak, M. et al. (2018). *J. CO_2 Util.* 27: 247–258.

141 Ni, J., Chen, L., Lin, J., and Kawi, S. (2012). *Nano Energy* 1: 674–686.

142 Liu, Z.Y., Grinter, D.C., Lustemberg, P.G. et al. (2016). *Angew. Chem. Int. Ed.* 55: 7455–7459.

143 Macario, A., Frontera, P., Candamano, S. et al. (2019). *J. Nanosci. Nanotechnol.* 19: 3135–3147.

144 Lian, Z., Olanrele, S.O., Si, C.W. et al. (2020). *J. Phys. Chem. C* 124: 5118–5124.

145 Horváth, A., Stefler, G., Geszti, O. et al. (2011). *Catal. Today* 169: 102–111.

146 Safavinia, B., Wang, Y.M., Jiang, C.Y. et al. (2020). *ACS Catal.* 10: 4070–4079.

147 Oemar, U., Hidajat, K., and Kawi, S. (2011). *Appl. Catal., A* 402: 176–187.

148 Sutthiumporn, K. and Kawi, S. (2011). *Int. J. Hydrogen Energy* 36: 14435–14446.

149 Yang, W.Q., Wang, Z.B., Tan, W.Z. et al. (2020). *Sci. China Mater.* 63: 364–374.

150 Lou, Y., Steib, M., Zhang, Q. et al. (2017). *J. Catal.* 356: 147–156.

151 Wang, Y., Yao, L., Wang, Y. et al. (2018). *ACS Catal.* 8: 6495–6506.

152 Liu, W.M., Li, L., Zhang, X.H. et al. (2018). *J. CO_2 Util.* 27: 297–307.

153 Sun, N., Wen, X., Wang, F. et al. (2011). *Appl. Surf. Sci.* 257: 9169–9176.

154 Kang, D., Lim, H.S., Lee, M., and Lee, J.W. (2018). *Appl. Energy* 211: 174–186.

155 Fan, M.S., Abdullah, A.Z., and Bhatia, S. (2009). *ChemCatChem* 1: 192–208.

156 Pakhare, D., Schwartz, V., Abdelsayed, V. et al. (2014). *J. Catal.* 316: 78–92.

157 Wang, H.Q., Dong, X.L., Zhao, T.T. et al. (2019). *Appl. Catal., B* 245: 302–313.

158 Yang, E.H., Noh, Y.S., Hong, G.H., and Moon, D.J. (2018). *Catal. Today* 299: 242–250.

159 Rynkowski, J., Samulkiewicz, P., Ladavos, A., and Pomonis, P. (2004). *Appl. Catal., A* 263: 1–9.

160 Sutthiumporn, K., Maneerung, T., Kathiraser, Y., and Kawi, S. (2012). *Int. J. Hydrogen Energy* 37: 11195–11207.

161 Ruckenstein, E. and Hu, Y.H. (1996). *J. Catal.* 162: 230–238.

162 Foley, H.C., Hong, A.J., Brinen, J.S. et al. (1990). *Appl. Catal.* 61: 351–375.

163 Lee, J.H., Lee, E.G., Joo, O.S., and Jung, K.D. (2004). *Appl. Catal., A* 269: 1–6.

164 Fan, M.S., Abdullah, A.Z., and Bhatia, S. (2011). *ChemSusChem* 4: 1643–1653.

165 Kambolis, A., Matralis, H., Trovarelli, A., and Papadopoulou, C. (2010). *Appl. Catal., A* 377: 16–26.

166 Li, L., Zhou, L., Ould-Chikh, S. et al. (2015). *ChemCatChem* 7: 819–829.

167 Li, Z., Kathiraser, Y., and Kawi, S. (2015). *ChemCatChem* 7: 160–168.

168 Gao, X.Y., Hidajat, K., and Kawi, S. (2016). *J. CO_2 Util.* 15: 146–153.

169 García-Vargas, J.M., Valverde, J.L., Lucas-Consuegra, A.D. et al. (2013). *Int. J. Hydrogen Energy* 38: 4524–4532.

170 Tomishige, K., Yamazaki, O., Chen, Y.G. et al. (1998). *Catal. Today* 45: 35–39.

171 Horváth, A., Guczi, L., Kocsonya, A. et al. (2013). *Appl. Catal., A* 468: 250–259.

172 Li, Y.M., Wang, Z.J., Zhang, B. et al. (2020). *Catalysts* 10: 501.

173 Wang, H.Q., Han, J., Zhao, B. et al. (2019). *Mol. Catal.* 475: 110486.

174 Zhang, Q., Zhang, T., Shi, Y. et al. (2017). *J. CO_2 Util.* 17: 10–19.

175 Zhang, Q.L., Sun, M.H., Ning, P. et al. (2019). *Appl. Surf. Sci.* 469: 368–377.

176 Kang, D., Lim, H.S., and Lee, J.W. (2017). *Int. J. Hydrogen Energy* 42: 11270–11282.

177 Baktash, E., Littlewood, P., Pfrommer, J. et al. (2015). *ChemCatChem* 7: 1280–1284.

178 Qian, L., Huang, K., Wang, H. et al. (2017). *Microporous Mesoporous Mater.* 243: 301–310.

179 Wang, M., Zhang, Q., Zhang, T. et al. (2017). *Chem. Eng. J.* 313: 1370–1381.

180 Xu, L., Song, H., and Chou, L. (2011). *Appl. Catal., B* 108–109: 177–190.

181 Xu, L., Song, H., and Chou, L. (2012). *Int. J. Hydrogen Energy* 37: 18001–18020.

182 Xu, L., Miao, Z., Song, H. et al. (2014). *Catal. Sci. Technol.* 4: 1759–1770.

183 Ashcroft, A.T., Cheetham, A.K., Green, M.L.H., and Vernon, P.D.F. (1991). *Nature* 352: 225–226.

184 Wang, N., Xu, Z., Deng, J. et al. (2014). *ChemCatChem* 6: 1470–1480.

185 Yin, Y., Rioux, R.M., Erdonmez, C.K. et al. (2004). *Science* 304: 711–714.

186 Park, J.C., Bang, J.U., Lee, J. et al. (2010). *J. Mater. Chem.* 20: 1239–1246.

187 Kim, D.H., Kim, S.Y., Han, S.W. et al. (2015). *Appl. Catal., A* 495: 184–191.

188 Lu, Y., Guo, D., Ruan, Y.Z. et al. (2018). *J. CO_2 Util.* 24: 190–199.

189 Li, Z.W. and Kawi, S. (2018). *ChemCatChem* 10: 2994–3001.

190 Cao, Y., Lu, M.R., Fang, J.H. et al. (2017). *Chem. Commun.* 53: 7549–7552.

191 Tian, J.Q., Ma, B., Bu, S.Y. et al. (2018). *Chem. Commun.* 54: 13993–13996.

192 Dou, J., Zhang, R.G., Hao, X.B. et al. (2019). *Appl. Catal., B* 254: 612–623.

193 Bian, Z.F. and Kawi, S. (2018). *ChemCatChem* 10: 320–328.

194 Li, Z., Mo, L., Kathiraser, Y., and Kawi, S. (2014). *ACS Catal.* 4: 1526–1536.

195 Li, Z.W., Kathiraser, Y., Ashok, J. et al. (2014). *Langmuir* 30: 14694–14705.

196 Bian, Z.F., Suryawinata, I.Y., and Kawi, S. (2016). *Appl. Catal., B* 195: 1–8.

197 Du, X., Zhang, D., Gao, R. et al. (2013). *Chem. Commun.* 49: 6770–6772.

198 Ahmed, K., Gamman, J., and Föger, K. (2002). *Solid State Ionics* 152–153: 485–492.

199 Wang, X. and Gorte, R.J. (2002). *Appl. Catal., A* 224: 209–218.

200 Suzuki, T., Iwanami, H.-I., Iwamoto, O., and Kitahara, T. (2001). *Int. J. Hydrogen Energy* 26: 935–940.

201 Laosiripojana, N. and Assabumrungrat, S. (2006). *J. Power Sources* 158: 1348–1357.

202 Ramírez-Cabrera, E., Atkinson, A., and Chadwick, D. (2004). *Appl. Catal., B* 47: 127–131.

203 Fornasiero, P., Balducci, G., Monte, R.D. et al. (1996). *J. Catal.* 164: 173–183.

204 Miki, T., Ogawa, T., Haneda, M. et al. (1990). *J. Phys. Chem.* 94: 6464–6467.

205 Imamura, S., Shono, M., Okamoto, N. et al. (1996). *Appl. Catal., A* 142: 279–288.

206 Kacimi, S., Barbier, J. Jr., Taha, R., and Duperz, D. (1993). *Catal. Lett.* 22: 343–350.

207 Pijolat, M., Prin, M., and Soustelle, M. (1995). *J. Chem. Soc., Faraday Trans.* 91: 3941–3948.

208 Krylov, O.V., Mamedov, A.K., and Mirzabekova, S.R. (1995). *Ind. Eng. Chem. Res.* 34: 474–482.

209 Solymosi, F., Tolmacsov, P., and Kedves, K. (2003). *J. Catal.* 216: 377–385.

210 Solymosi, F. and Tolmacsov, P. (2002). *Catal. Lett.* 83: 183–186.

211 Solymosi, F., Szõke, A., and Ovári, L. (1999). *J. Catal.* 186: 269–278.

212 Futamura, S., Kabashima, H., and Einaga, H. (2004). *IEEE Trans. Ind. Appl.* 40: 1476–1481.

213 Puolakka, J. (2007). *CO_2 reforming; Thesis for the Degree of Licentiate of Science and Technology*. Helsinki, Finland: Helsinki University of Technology.

214 Bradford, M.C.J. and Vannice, M.A. (1996). *Appl. Catal. A* 142: 97–122.

215 Bradford, M.C.J. and Vannice, M.A. (1999). *Catal. Rev. Sci. Eng.* 41: 1–42.

216 Olafsen, C., Daniel, Y., Schuarman, L. et al. (2006). *Catal. Today* 115: 179–185.

217 Mirzabekova, S.R., Farkhadovs, G.T., Mamedov, A.K., and Rustamov, M.I. (1993). *Kinet. Catal.* 34: 841–843.

218 Fujimura, S., Nakagawa, K., Ikenaga, N., and Suzuki, T. (1997). *Sekiyu Gakkaishi* 40: 179–184.

219 Wang, H., Huang, H., Xue, D., and Ouyang, M. (2013). Hydrogen and fuel-cell vehicle technology. In: *Sustainable Automotive Energy System in China*, 301–333. Berlin, Heidelberg: Springer.

220 US DOE National Energy Technology Laboratory. (2010). Assessment of Hydrogen Production with CO_2 Capture Volume 1: Baseline State-of-the-Art Plants. DOE/NETL Final report 2010/1434.

2

Catalytic Reforming of Oxygen-Containing Chemicals

Wei Luo[1], Song Song[1], Tong Ding[1], Ye Tian[1], and Xingang Li[1,2]

[1] Tianjin University, Collaborative Innovation Center of Chemical Science and Engineering (Tianjin), School of Chemical Engineering and Technology, State Key Laboratory of Chemical Engineering, Tianjin Key Laboratory of Applied Catalysis Science and Engineering, Department of Applied Catalysis Science and Engineering, No.135 Yaguan Road, Haihe Education Park, Tianjin 300350, P. R. China
[2] Lanzhou Jiaotong University, School of Chemistry and Chemical Engineering, Department of Chemical Engineering, No.88 Anningxi Road, Anning District, Lanzhou, Gansu Province 730070, P. R. China

2.1 Introduction

Hydrogen (H_2) has been identified as promising clean fuel and energy carrier for the future [1]. It can be used in fuel cells to generate electricity or power with water as the only product. Currently, H_2 is mainly produced from fossil fuels [2, 3]. Considering the huge CO_2 emissions from fossil fuels, developing efficient technology for H_2 production from renewable sources such as biomass is more promising. There are many ways to produce H_2 from biomass or biomass-derived molecules [4], such as catalytic reforming. For example, Dumesic and coworkers pioneered aqueous-phase reforming (APR) of biomass-derived resources to generate H_2 and alkanes in liquid water [5]. In the past decade, great breakthroughs have been achieved on catalytic reforming of biomass-derived oxygen-containing chemicals for hydrogen production. However, there are still many challenges that have not been fully addressed [6].

In this chapter, we mainly focus on the hydrogen production by catalytic reforming of biomass-derived oxygen-containing chemicals including methanol, ethanol, DME, and polyols such as glycerol, ethylene glycol (EG), and sorbitol (Figure 2.1). We summarize the effects of metal nanoparticle size, metal dispersion, acid–base properties of catalysts, metal–support interaction, and promoters on the catalytic activity, as well as the related reaction mechanisms.

2.2 Catalytic Hydrogen Production from Methanol

Methanol is considered as a promising feedstock for hydrogen production by catalytic reforming due to its high hydrogen/carbon (H/C) ratio and low reaction temperature, which is easily derived from syngas, natural gas, and biomass.

Heterogeneous Catalysis for Sustainable Energy, First Edition. Edited by Landong Li and Justin S. J. Hargreaves.

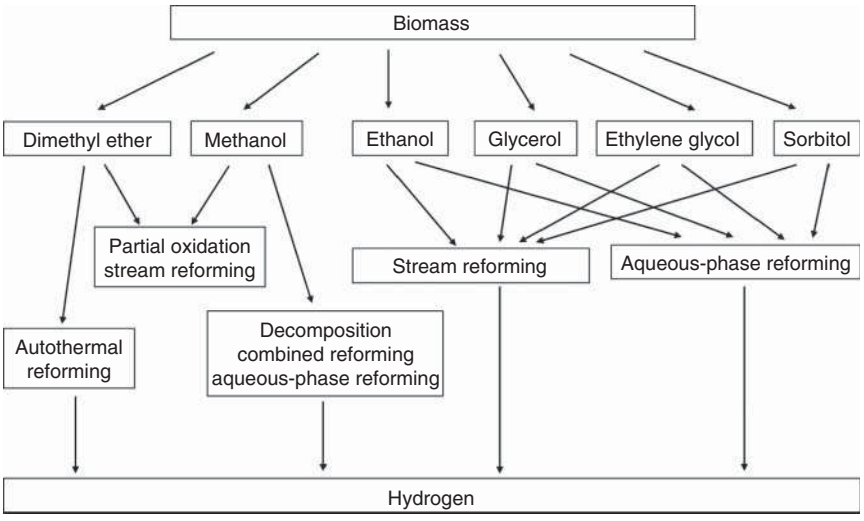

Figure 2.1 Graphic overview of hydrogen production by catalytic reforming of oxygen-containing chemicals.

In general, the catalytic reforming of methanol includes the following methods: the decomposition of methanol (MD), the partial oxidation of methanol (POM), the steam reforming of methanol (SRM), and the combined reforming of methanol (CRM). The equation for each process is given below [7]:

$$\text{MD: } CH_3OH \rightarrow CO + 2H_2 \quad \Delta H_{298\ K} = 92\ \text{kJ mol}^{-1}$$

$$\text{SRM: } CH_3OH + H_2O \rightarrow CO_2 + 3H_2 \quad \Delta H_{298\ K} = 49.7\ \text{kJ mol}^{-1}$$

$$\text{POM: } CH_3OH + 0.5O_2 \rightarrow CO_2 + 2H_2 \quad \Delta H_{298\ K} = -192.3\ \text{kJ mol}^{-1}$$

$$\text{CRM: } CH_3OH + 0.5H_2O + 0.25O_2 \rightarrow CO_2 + 2.5H_2 \quad \Delta H_{298\ K} = -71.4\ \text{kJ mol}^{-1}$$

2.2.1 Catalytic Hydrogen Production from Decomposition of Methanol

Although the MD is an endothermic reaction, the utilization of engine exhaust heat makes it available to be applied in internal combustion engines. Both metal catalysts and metal oxide catalysts have been studied for the MD reaction (Table 2.1). It is well known that supports can significantly influence catalytic properties of metal catalysts. Usami et al. investigated the effect of different supports on the activity of Pd-based catalysts [8]. The catalytic behavior followed the order of $Pd/ZrO_2 > Pd/Pr_2O_3 > Pd/CeO_2 > Pd/Fe_3O_4 > Pd/TiO_2 > Pd/SiO_2 > Pd/ZnO$. The excellent catalytic activity of Pd/ZrO_2 catalyst was attributed to the strong interaction between Pd nanoparticles and ZrO_2 and the presence of Pd^+ cations. For non-noble metal Ni/SiO_2 catalysts, the catalytic performance was structure-sensitive, and the turnover frequency (TOF) decreased with the enlarged size of Ni nanoparticles [9]. Metal oxide catalysts are also applied in the MD reaction. Li et al. studied the

Table 2.1 Catalytic hydrogen production from decomposition of methanol over metal catalysts.

Catalyst	Temperature (K)	CH_3OH (vol%)	Space velocity (ml h^{-1} g^{-1})	Conversion (%)	H_2 selectivity (%)	References
Pd/ZrO_2	573	15	10 000	90	—	[8]
Ni/SiO_2	511	1.6	0.75[a)]	90	—	[9]
$CuAl_2O_4$	543	—	2.63[a)]	80	—	[10]

a) Weight hourly space velocity (WHSV), h^{-1}.

catalytic hydrogen production from MD reaction over Cu–Al oxides. The catalysts with spinel $CuAl_2O_4$ structure were more stable and exhibited higher catalytic activity than non-spinel Cu–Al oxides [10].

A brief summary of catalytic hydrogen production from the MD over metal catalysts is listed in Table 2.1.

2.2.2 Catalytic Hydrogen Production from Partial Oxidation of Methanol

POM is an exothermic reaction with the main product of CO_2 rather than CO. It is beneficial to resolve the poisoning problem of platinum electrode in fuel cells. Thereupon, the POM reaction shows great potential for onboard hydrogen production.

The POM reaction has been extensively studied over supported noble metal catalysts, especially for Au-based catalysts [11–13]. Chang et al. studied this reaction over Au/TiO_2–MO_x (M = Fe, Co, and Zn) catalyst. X-ray photoelectron spectroscopy (XPS) analysis results revealed the existence of metallic gold and Au_2O_3 species in the calcined samples. The most active one was Au/TiO_2–Fe_2O_3, which resulted from a synergistic effect of different active sites [14]. Hernández-Ramírez et al. synthesized Au catalysts by the deposition–precipitation method [15]. It was found that the ratio of Au^0/Au^+ was critical for H_2 production on the Au/ZrO_2 catalyst. As a result, the catalyst exhibited better catalytic performance at low temperatures due to the stronger adsorption of oxygen and methoxy groups. Besides, bimetallic Au–Cu/TiO_2 and Au–Cu/TiO_2–Fe_2O_3 catalysts were investigated for SRM, and the latter catalyst showed higher activity than the former one. The main reason was that Fe_2O_3 support could supply reactive oxygen atoms to stabilize active gold species ($Au^{\delta+}$) during the reaction [16, 17].

As for non-noble metal catalysts, Cu-based catalysts are more active and selective for the POM reaction. Catalytic activity in the POM reaction-strongly depends on the Cu species. Araiza et al. [18] studied the POM reaction over Cu/CeO_2. Cu supported on polyhedral CeO_2 with exposed (111) and (100) planes contained a higher ratio of Cu^0/Cu^+ and showed higher H_2 selectivity. Huang et al. investigated the POM reaction over Au-modified CuO/ZnO catalysts [19]. The addition of Au changed the reducibility of Cu species and generated more active sites, i.e. Cu^0 and Cu^+, on the catalytic surface, thereby enhancing the catalytic activity.

Table 2.2 Catalytic hydrogen production from partial oxidation of methanol over metal catalysts.

Catalyst	Temperature (K)	O_2/C[a)]	Space velocity (ml h^{-1} g^{-1})	Conversion (%)	H_2 selectivity (%)	References
Ag/ZnO	623	0.5	12 870[b)]	100	100	[12]
Pt/Al_2O_3	688	0.7	20 000[b)]	100	—	[13]
Au/TiO_2–Fe_2O_3	548	0.3	90 000	95	76	[14]
Au–Cu/TiO_2–Fe_2O_3	523	0.3	48 000[b)]	95	93	[16]
Cu/CeO_2	493	0.3	192 000	50	—	[18]
Au/CuO/ZnO	463	0.5	60 000	95	97	[19]

a) O_2/C, O_2/CH_3OH.
b) Gas hourly space velocity (GHSV), h^{-1}.

The results of catalytic hydrogen production from POM over metal catalysts are summarized in Table 2.2.

2.2.3 Catalytic Hydrogen Production from Steam Reforming of Methanol

SRM is a promising process for catalytic hydrogen production due to its high H_2 yield and relatively mild reaction conditions. Different kinds of supported metal catalysts have been studied for the SRM reaction.

Noble metal catalysts normally exhibit high catalytic activities in the SRM reaction. Karim et al. [20] observed the formation of a PdZn alloy in Pd/ZnO due to the hydrogen spillover effect, which improved the activity and selectivity compared with monometallic Pd catalysts. For $PdZn/Al_2O_3$ catalyst, metal nanoparticles were stabilized by the Al_2O_3 support to improve sintering resistance at high temperatures [21].

For non-noble metal catalysts, Cu-based catalysts have been extensively studied. Generally, Cu^0 species are regarded as the main active sites in the SRM reaction. The function of Cu^+ species is to improve the selectivity toward CO_2 by promoting the water–gas shift (WGS) reaction, while Cu^{2+} species are inactive [22]. The addition of ZrO_2 to CuO/CeO_2 catalyst promoted generation of surface oxygen vacancies, and Cu_2O was formed by electron transfer between Cu species and oxygen vacancies. The coexistence of Cu_2O and metallic Cu enhanced the activity for the SRM reaction [23].

The dispersion of active copper species also affects the catalytic performance of Cu-based catalysts. Yao et al. [24] found that a Cu/ZrO_2 catalyst prepared by oxalate gel-coprecipitation method showed superior activity, which was attributed to the high Cu dispersion and stronger interaction between copper and zirconia. Similarly, a Cu/ZnO catalyst synthesized by homogeneous precipitation method showed higher catalytic performance than that synthesized by the traditional wet-chemical precipitation method. The extraordinary catalytic activity resulted from the high Cu

Table 2.3 Catalytic hydrogen production from steam reforming of methanol over non-noble metal-based catalysts.

Catalyst	Temperature (K)	S/C[a)]	Space velocity (ml h^{-1} g^{-1})	Conversion (%)	H_2 selectivity (%)	References
$Cu/CeO_2/ZrO_2$	523	1.5	16 380	>80	350[b)]	[23]
Cu/ZrO_2	533	1.3	3 600	100	—	[24]
Cu/ZnO	523	3.0	21 600	70	93	[25]
CuO/CeO_2	523	1.2	800[c)]	95	—	[26]
$CuO/ZnO/Al_2O_3$	513	1.5	10 000	93	63	[27]

a) S/C, steam/CH_3OH.
b) mmol h^{-1} g^{-1}.
c) GHSV, h^{-1}.

dispersion and the formation of a Cu–Zn alloy [25]. Especially, the combined effect of high metal dispersion, enhanced metal–support interaction, and active copper species could significantly improve the activity of CuO/CeO_2 catalysts in the SRM reaction [26].

In addition, Shokrani et al. [27] prepared a series of $CuO/ZnO/Al_2O_3$ catalysts by a combustion method using urea as fuel, in which catalyst surface areas were significantly enlarged by increasing the amount of alumina. The as-synthesized catalysts with large surface areas showed good catalytic performance for the SRM reaction.

Thus, the type of Cu species, the dispersion of Cu active sites, and the surface area of catalysts are the main factors controlling the catalytic activity of Cu-based catalysts. A brief summary of catalytic hydrogen production for SRM reaction over non-noble metal-based catalysts is presented in Table 2.3.

2.2.4 Catalytic Hydrogen Production from Combined Reforming of Methanol

The H_2 productivity in the POM reaction is relatively low owing to the dilution of O_2 in feed gas. The SRM reaction normally requires external energy. CRM is more prevalent and can overcome the disadvantages of the SRM and POM reactions. The ratio of H_2O/CH_3OH plays an important role in the CRM reaction. Agrell et al. [28] concluded that the optimized ratio of H_2O/CH_3OH and O_2/CH_3OH was 1.3 and 0.2, respectively. It was also found that the concentration of CO produced over CuO/ZnO catalyst was much lower in the CRM reaction than that in the SRM reaction. In addition, Ni/CeO_2–ZrO_2 catalyst is a good choice for the CRM reaction due to its inhibition of the reverse water–gas shift (RWGS) reaction [29].

2.2.5 Catalytic Hydrogen Production from Aqueous-Phase Reforming of Methanol

The process for the APR of methanol includes the cleavage of C—H/O—H bond and the WGS reaction. It is important to take advantage of the WGS reaction to effectively

suppress the selectivity toward by-product CO. Therefore, developing catalysts with strong ability for C—H/O—H bond cleavage and high activity in the WGS reaction is highly desirable for the APR of methanol.

APR of methanol has been investigated using Pt- and Ru-based catalysts. Lin et al. [30] reported that Pt atomically dispersed on α-MoC was able to catalyze APR of methanol at very lower temperatures of 423–463 K. The excellent catalytic performance of Pt/α-MoC was attributed to the outstanding water dissociation ability of α-MoC and the synergistic effect between Pt and α-MoC to activate methanol. Li et al. [31] studied the catalytic performance of $Pt/NiAl_2O_4$ and Pt/Al_2O_3 catalysts in the APR of methanol. Due to the presence of oxygen vacancies in $Pt/NiAl_2O_4$, PtO_x was readily reduced to metallic Pt, leading to improved activity in the dehydrogenation of methanol. Awasthi et al. [32] developed a homogeneously dispersed Ru/L1 catalyst that comprised ligand-stabilized ruthenium nanoparticles, which exhibited a very high H_2 production rate.

The promoter effect on supported noble metal catalysts has been investigated in the APR of methanol. Sakamoto et al. [33] investigated the effect of metal promoters on Pt/TiO_2 catalyst. The addition of Mo or Fe significantly promoted the catalytic performance for H_2 production. The formation of a low-valence thin oxide layer over the TiO_2 surface could be verified after adding Mo or Fe element. Similarly, Re or Mo promoter showed an enhancement effect on the catalytic activities of SiO_2, ZrO_2, and TiO_2 supported Ir catalysts [34]. By adding Re to Ir/SiO_2 and Ir/ZrO_2 catalysts, the particle sizes of Ir increased, and the formation of nanocomposites with Ir and Re was observed, which remarkably accelerated the formation rate for H_2. For $Mo–Ir/TiO_2$ catalyst, the formation of a MoO_2 monolayer on TiO_2 surface could promote the hydration reaction of partially dehydrogenated methanol on the catalyst surface.

Ni-based catalysts with high catalytic activity and low cost have been widely studied in the APR of methanol. Coronado et al. [35] investigated the effect of support and promoter on catalytic performance of Ni-based catalysts. γ-Al_2O_3 was demonstrated to be the best support for Ni-based catalysts. The addition of Cu or Ce to the Ni-based catalysts showed enhanced catalytic performance compared with the monometallic catalysts. Lin et al. [36] developed a Ni/α-MoC catalyst with remarkable H_2 production activity. It was demonstrated that the single-site Ni_1 on α-MoC was stabilized by the formation of $Ni_1–C_x$ motifs through a carbon bridge bond, which maximized active site density and enhanced structural stability. In addition, Stekrova et al. [37] found that strengthened metal–support interactions of $Ni/CeO_2–ZrO_2$ were effective for inhibiting Ni migration and carbon deposition, which improved catalytic performance in methanol conversion.

2.3 Catalytic Hydrogen Production from Ethanol

Ethanol is a promising feedstock for hydrogen production by catalytic reforming due to its renewable nature, low toxicity, and ease of transport. Although ethanol can be directly used in internal combustion engines, the results of economic analysis show

that the energy efficiency of hydrogen production from ethanol is much higher than burning [38]. There are two main processes for catalytic hydrogen production from ethanol reforming, including steam reforming of ethanol (ESR) and APR of ethanol. The catalytic hydrogen production from reforming of ethanol can be described as follows:

$$CH_3CH_2OH + 3H_2O \rightarrow 6H_2 + 2CO_2 \quad \Delta H^{\theta}_{298\ K} = 174.2\ kJ\ mol^{-1}$$

2.3.1 Catalytic Hydrogen Production from Steam Reforming of Ethanol

ESR is a complex process, and the catalytic activity highly depends on the types of catalysts. Both metal oxide catalysts and supported metal catalysts have been extensively studied. To maximize H_2 production and inhibit carbon deposition, catalyst with strong ability to break C—C/C—H bond is an ideal choice for the ESR reaction.

Llorca et al. [39] explored the catalytic activity of different metal oxide catalysts in ESR, including MgO, γ-Al_2O_3, SiO_2, V_2O_5, ZnO, La_2O_3, CeO_2, and Sm_2O_3. The catalytic performance of MgO, La_2O_3, SiO_2, CeO_2, and Sm_2O_3 was very low. Although ethanol was totally consumed over γ-Al_2O_3, the major product was C_2H_4 due to ethanol dehydration. On the contrary, ethanol dehydration on ZnO was not observed. The high selectivity toward H_2 and CO_2 was attributed to the basic and redox nature of ZnO.

ESR has been mainly investigated using Pt-, Rh-, and Ru-based noble metal catalysts. The nature of both metal and support strongly affects the catalytic activity and stability. Pt-based catalysts show strong ability of C—C bond cleavage and high activity in the WGS reaction, which are suitable for the ESR reaction. Ciambelli et al. [40] compared the catalytic performance of Pt/CeO_2 and Pt/Al_2O_3 catalysts in ESR reaction. The larger oxygen storage capacity of CeO_2 support resulted in higher catalytic stability. In contrast, more stable carbonaceous species were detected on Pt/Al_2O_3 catalyst. Due to the large oxygen storage capacity of the $CeZrO_2$ support, the Pt/$CeZrO_2$ catalyst showed excellent activity for ethanol conversion [41]. However, the catalytic performance of Pt/$CeZrO_2$ decreased significantly at 773 K, owing to the presence of acetate-like surface species. When increasing reaction temperature to 1073 K, these carbonaceous species could be removed.

The properties of supports show significant impact on the catalytic performance of Rh-based catalysts in the ESR reaction. ZrO_2 has good thermal stability and possesses tunable acidic properties. Zhong et al. demonstrated that two kinds of acid sites existed on Rh/ZrO_2–HT prepared by hydrothermal method. Lewis acidic sites facilitated absorption of ethanol, while Brønsted acidic sites catalyzed dehydration of ethanol. It was also found that high reaction temperatures were beneficial to improve the stability of Rh/ZrO_2–HT by the removal of metastable carbonaceous species [42]. The strong oxidizing ability of the Y_2O_3 support benefited hydrogen atom abstraction from ethanol, promoting the full conversion of ethanol during 923–1073 K [43]. In addition, the large oxygen storage capacity and abundant surface oxygen vacancies of the CeO_2 support helped to remove surface carbonaceous species. As a result, ceria-supported noble metal catalysts normally

Table 2.4 Catalytic hydrogen production from steam reforming of methanol over noble metal catalysts.

Catalyst	Temperature (K)	S/C[a)]	Space velocity (h^{-1})	Conversion (%)	H_2 selectivity (%)	References
Pt/CeO_2	573	2.0	15 000[b)]	100	29	[40]
$Pt/CeZrO_2$	773	3.0	170[b)]	98	65	[41]
$Pt/CeZrO_2$	1073	3.0	170[b)]	100	74	[41]
Rh/ZrO_2	673	10.0	54 000[c)]	100	5.7[d)]	[42]
Rh/Y_2O_3	973	3.0	69 600[c)]	100	90	[43]
Rh/CeO_2	773	3.0	—	100	60	[44]
$Rh/SiCeO_2$	1073	3.5	70 297[b)]	100	70	[45]
$Rh–Fe/Ca–Al_2O_3$	623	3.0	34 000[c)]	100	65	[46]
Ru–C	723	5.0	7 243[b)]	100	—	[47]

a) S/C, steam/C_2H_6O.
b) WHSV.
c) GHSV.
d) $molH_2/mol_{EtOH}$.

showed high catalytic stability in ESR [44]. Recently, Moraes et al. [45] reported that a monolithic $Rh/SiCeO_2$ catalyst displayed high activity and stability in the ESR reaction. The extraordinary catalytic stability was attributed to the high structural stability of the monolith support. CO poisoning is notorious for Rh-based catalysts in the ESR reaction. Chen et al. [46] developed a novel $Rh–Fe/Ca–Al_2O_3$ catalyst with Fe as the auxiliary agent. No CO was detected in the reaction temperature range of 623–673 K. Characterization results confirmed that the presence of iron oxide species promoted the conversion of CO to CO_2 and H_2 via the WGS reaction.

Considering the high cost of Pt- and Rh-based catalysts, it is important to develop cheap and highly efficient Ru-based catalysts for the ESR reaction. Bosko et al. developed highly dispersed Ru on C, i.e. Ru/C catalyst, by electroless deposition method. The typical morphology of carbon fibers was beneficial for the uniform distribution of Ru nanoparticles, which remarkably improved the catalytic activity and stability in the ESR reaction [47].

We summarize recent development of catalytic hydrogen production from ESR over noble metal catalysts, as listed in Table 2.4.

Due to the high cost and low abundance of noble metals, the development of alternative non-noble metal catalysts for the ESR reaction is highly desirable.

Ni-based catalysts are suitable for the ESR reaction owing to their strong ability to break C—C/C—H bonds and form H—H bonds [48]. The strong metal–support interaction plays an important role in the Ni-catalyzed ESR reaction. Li et al. [49] found that Ni/ZrO_2 with small support size showed good performance in H_2 production due to enhanced metal–support interaction. Compared with monoclinic ZrO_2, tetragonal ZrO_2-supported Ni catalysts showed higher catalytic activity, resulting

from the promoted WGS reaction and the inhibited methane steam reforming (SR) reaction. Zhang et al. developed a Ni/SiO_2 catalyst by the ammonia evaporation method. The as-synthesized catalyst with enhanced metal–support interaction showed high dispersion of Ni nanoparticles, facilitating ethanol conversion and inhibiting carbon deposition [50]. Moreover, Xu et al. [51] found that Ni/CeO_2 showed the good catalytic activity and stability toward H_2 production. Ce^{3+} species promoted dissociation of H_2O to OH, which could react with methyl groups to inhibit production of methane during ESR reaction.

The catalytic performance of Co-based catalysts highly depends on the size of Co nanoparticles and supports. Llorca et al. [52] prepared Co/ZnO catalyst with ultra-small cobalt oxide nanoparticles by using $Co_2(CO)_8$ precursor. No CO was generated on Co/ZnO during the reaction, and H_2 selectivity could reach up to 73%. Soykal et al. [53] investigated the effect of support size on the ESR reaction over Co/CeO_2. Compared with micro-CeO_2, Co catalysts supported on nano-CeO_2 were highly resistant to coke formation.

Ni and Co-based catalysts generally suffer from deactivation due to coke formation and catalyst sintering. The addition of alkali metal is effective to improve the stability of these catalysts. For $Co/K/\gamma\text{-}Al_2O_3$ catalyst, the addition of K species resulted in the formation of Co^0–CoO core–shell structure, which helped to stabilize adsorbed acetate species and suppress coke formation [54]. Bimetallic catalysts are also developed to improve the sintering resistance. Wang et al. [55] synthesized perovskite-type Ni–Co bimetallic catalysts with formation of a Ni–Co alloy. Due to the synergistic effect between Ni and Co, this catalyst exhibited higher catalytic performance and sintering resistance than the monometallic catalysts.

2.3.2 Catalytic Hydrogen Production from Aqueous-Phase Reforming of Ethanol

Developing efficient catalysts for the APR of ethanol requires improving the ability of C—C bond cleavage, inhibiting the methanation reaction, and meanwhile facilitating the WGS reaction.

Nozawa et al. [56] studied APR of ethanol on TiO_2-supported noble metal catalysts, and the catalytic activity followed the order of Ru > Rh > Pt > Ir > Pd. It was found that small Ru nanoparticles on Ru/TiO_2 could prevent the undesirable CO_2 methanation. Subsequently, the effect of promoter on the catalytic performance of supported noble metal catalysts was investigated [57]. When Re was added to Rh/TiO_2, remarkable improvement ethanol conversion and H_2 yield could be obtained. The average particle sizes of Rh were decreased by adding Re due to the anchoring effect of ReO_x overlayers on the TiO_2 surface. However, the presence of partially oxidized ReO_x sites on $Re–Rh/TiO_2$ would improve the hydration of acetaldehyde to form acetic acid.

In addition, many researchers have disclosed that the formation of bimetallic active sites was beneficial for ethanol dehydrogenation and acetaldehyde decomposition. For example, due to the formation of the intermetallic $PdZn_\beta$ phase and pore confinement effects, bimetallic PdZn/CNTs was more active and selective for

CO-free H_2 production from ethanol reforming at low temperatures [58]. Similarly, it was reported that the synergistic behavior of the bimetallic Ru–Pt catalyst resulted in higher H_2 production rate, higher C—C bond cleavage ability, and lower methanation rate than the monometallic Ru or Pt catalyst [59].

Roy et al. [60] studied the effect of surface modification on Ni/Al_2O_3 catalyst in the APR of ethanol. The catalytic activity of Ni/Al_2O_3 increased after plasma modification. The modified catalysts displayed larger metal surface areas, higher metal dispersion, lower active metal particle sizes, and enhanced metal–support interactions. Subsequently, it was found that a Ni–Ce–O catalyst prepared by a sol–gel method exhibited higher activity in ethanol conversion than that prepared by a combustion synthesis method. The improved oxygen mobility induced by Ni doping promoted CO oxidation and catalytic activity thereof [61].

2.4 Catalytic Hydrogen Production from Dimethyl Ether

DME, as the simplest ether, does not contain a high-energy C—C bond, and the energy of C—O bond is only 349 kJ mol^{-1}, which is even lower than methanol (386 kJ mol^{-1}) [62]. Besides, the energy of the C—H bond in DME (401 kJ mol^{-1}) is lower compared with that in methane (440 kJ mol^{-1}). Lower bond energy results in milder operation conditions and less coke deposition during the DME reforming reaction. Thus, DME is a more suitable feedstock for hydrogen production via catalytic reforming compared with methane and methanol.

Catalytic hydrogen production from DME reforming can be divided into three categories: partial oxidation (PO) of DME, autothermal reforming (ATR) of DME, and SR of DME:

$$\text{PO of DME: } (CH_3)_2O + 1.5O_2 \rightarrow 2CO_2 + 3H_2 \quad \Delta H_{298} = -25 \text{ kJ mol}^{-1}$$

$$\text{ATR of DME: } (CH_3)_2O + O_2 + H_2O(g) \rightarrow 2CO_2 + 4H_2 \quad \Delta H_{298} = 85 \text{ kJ mol}^{-1}$$

$$\text{SR of DME: } (CH_3)_2O + 3H_2O(g) \rightarrow 2CO_2 + 6H_2 \quad \Delta H_{298} = 135 \text{ kJ mol}^{-1}$$

2.4.1 Catalytic Hydrogen Production from Partial Oxidation of Dimethyl Ether

During the PO of DME reaction, DME first decomposes into methoxy (CH_3O-) and methyl (CH_3-) species, which are then decomposed to form CO and H_2 with the help of oxygen [63]. The air-to-DME ratio is a key factor in the PO of DME [64]. The conversion of DME is incomplete at low oxygen concentrations, while excessive oxygen will lead to over-oxidation. Wang et al. [65] studied the PO of DME over Al_2O_3-supported catalysts. It was found that the catalytic activity decreased in the order of $Ni/\gamma\text{-}Al_2O_3 > Rh/\gamma\text{-}Al_2O_3 > Co/\gamma\text{-}Al_2O_3 \gg Ru/\gamma\text{-}Al_2O_3 > Fe/\gamma\text{-}Al_2O_3 > Pt/\gamma\text{-}Al_2O_3 \gg Ag/\gamma\text{-}Al_2O_3$. Currently, studies of the PO of DME are relatively limited due to the fast catalyst deactivation caused by high reaction temperatures.

2.4.2 Catalytic Hydrogen Production from Autothermal Reforming of Dimethyl Ether

The presence of H_2O in the ATR of DME has the advantage to avoid temperature runaway compared with the PO of DME. The process for the ATR of DME is very complex and might include the following reactions:

DME SR: $(CH_3)_2O + 3H_2O(g) \rightarrow 2CO_2 + 6H_2 \quad \Delta H_{298\ K} = 135\ kJ\ mol^{-1}$

DME PO: $(CH_3)_2O + 1.5O_2 \rightarrow 2CO_2 + 3H_2 \quad \Delta H_{298\ K} = -25\ kJ\ mol^{-1}$

DME hydrolysis: $(CH_3)_2O + H_2O(g) \rightarrow 2CH_3OH \quad \Delta H_{298\ K} = 37\ kJ\ mol^{-1}$

MeOH SR: $CH_3OH + H_2O(g) \rightarrow CO_2 + 3H_2 \quad \Delta H_{298\ K} = 49\ kJ\ mol^{-1}$

Water–gas shift: $CO + H_2O \rightarrow CO_2 + 3H_2 \quad \Delta H_{298\ K} = -41\ kJ\ mol^{-1}$

DME decomposition: $(CH_3)_2O \rightarrow CO + H_2 + CH_4 \quad \Delta H_{298\ K} = -1\ kJ\ mol^{-1}$

MeOH decomposition: $CH_3OH \rightarrow CO + H_2 \quad \Delta H_{298\ K} = 90\ kJ\ mol^{-1}$

DME oxidation: $(CH_3)_2O + 3O_2 \rightarrow 2CO_2 + 3H_2O \quad \Delta H_{298\ K} = -1330\ kJ\ mol^{-1}$

For Pd-based catalysts, besides CO_2 and H_2, alcohols, ethers, hydrocarbons, and other by-products are also produced in the ATR of DME. Nilsson et al. [66] found that Pd/γ-Al_2O_3 exhibited superior activity among Pd catalysts supported on ceramic monolith. Besides, the addition of Zn to Pd/γ-Al_2O_3 could promote the oxidation of CO to CO_2. However, the complex process for the ATR of DME limits its practical application.

2.4.3 Catalytic Hydrogen Production from Steam Reforming of Dimethyl Ether

In general, the SR of DME reaction includes three processes [67, 68]: DME hydrolysis, SRM, and RWGS. The equations for each process are shown as follows:

DME hydrolysis: $(CH_3)_2O + H_2O \rightarrow 2CH_3OH \quad \Delta H_{298\ K} = 37\ kJ\ mol^{-1}$

SRM: $CH_3OH + H_2O \rightarrow CO_2 + 3H_2 \quad \Delta H_{298\ K} = 49\ kJ\ mol^{-1}$

RWGS: $CO_2 + H_2 \rightarrow CO + H_2O \quad \Delta H_{298\ K} = 41\ kJ\ mol^{-1}$

Reaction parameters, like the H_2O/DME ratio, the reaction temperature, and the pressure, significantly influence H_2 production efficiency in the SR of DME reaction [69]. According to Le Chatelier's principle, high concentration of H_2O and high reaction temperature and pressure can accelerate the reaction rate of H_2 production.

For the SR of DME reaction, DME hydrolysis and methanol reforming are two elementary reactions. Solid acid catalysts are an ideal choice for DME hydrolysis,

and metal catalysts are widely used in methanol reforming. Thus, fabrication of bifunctional catalysts, like mixed bifunctional catalysts and supported bifunctional catalysts, are widely studied in the SR of DME reaction.

2.4.3.1 Mixed Bifunctional Catalysts

The mixture of solid acid and steaming reforming catalysts shows excellent activity in the SR of DME reaction.

Zeolites are efficient heterogeneous solid acid catalysts for DME hydrolysis, and their catalytic activity is highly dependent on their acidic property [70–72]. Gao et al. [73] found that ZnO/H–ZSM-5 exhibited higher DME conversion and H_2 yield than H–ZSM-5. Strong Brønsted acid sites of H–ZSM-5 gradually decreased with the increased content of ZnO, while weak acid sites had little change. Long et al. [74] found that the concentration of the strong acid sites of H–ZSM-5 reduced with the increased content of MgO, which inhibited side reactions. Phosphorus modification is another effective method to adjust acid density of zeolite. The H–ZSM-5/CuZnAlO modified with 5% P displayed much better catalytic stability than the parent one due to the loss of strong acid sites [75]. Besides zeolite, γ-Al_2O_3 can be employed for DME hydrolysis due to its high activity and stability. The moderate acid strength of γ-Al_2O_3 caused only a small amount of coke on the catalyst surface [76].

Cu-based catalysts are excellent candidates for steam reforming [77, 78], and both Cu^+ and Cu^0 species have been demonstrated to be active [79]. Especially, the ratio of Cu^0/Cu^+ is crucial to the catalytic performance [79]. Wang et al. [80] confirmed that the catalytic activity of Cu/SiO_2 was related to the synergistic effect between Cu^0 and Cu^+ species. When the ratio of Cu^0/Cu^+ was close to 1, the Cu/SiO_2 catalyst showed the highest reaction rate. Similarly, Huang et al. [81] developed the La_2O_3-modified Cu/SiO_2 catalyst for the SR of DME. It was demonstrated that the addition of lanthanum species inhibited transformation of Cu^+ to Cu^0 to maintain a constant ratio of Cu^+/Cu^0. In addition, the ZnO-modified copper phyllosilicate catalyst was also developed [82]. The amount of ZnO affected the concentration of Cu^0 and Cu^+, and the strong interaction between ZnO and Cu prevented carbon deposition by inhibiting the RWGS reaction. A brief summary of catalytic hydrogen production from the SR of DME over the mixed bifunctional catalysts is listed in Table 2.5.

2.4.3.2 Supported Bifunctional Catalysts

Supported bifunctional catalysts are also studied in the SR of DME reaction, as summarized in Table 2.6. Alumina-supported catalysts are commonly used due to their good selectivity towards CO_2 and H_2.

Cu/γ-Al_2O_3 is an effective catalyst for the SR of DME reaction. Kim et al. [83] investigated the stability of Cu/γ-Al_2O_3 and found that the coke resistance of catalysts was dependent on the surface area of the γ-Al_2O_3 support. The decreased surface area of γ-Al_2O_3 would induce severe carbon deposition. The promoter shows remarkable effect on the catalytic performance of Cu/γ-Al_2O_3 catalyst. Sun et al. [84] synthesized a Cu–ZnO/γ-Al_2O_3 catalyst with low Cu loading (~3%) by a sputtering method. The thermal aggregation of Cu nanoparticles was inhibited by strong interactions between Cu and ZnO. The as-synthesized Cu–ZnO/γ-Al_2O_3

Table 2.5 Catalytic hydrogen production from steam reforming of dimethyl ether over mixed bifunctional catalysts.

Catalyst 1	Catalyst 2[a]	Temperature (K)	S/C[b]	Space velocity (ml h^{-1} g^{-1})	Conversion (%)	H_2 yield (%)	References
H–ZSM-5	Cu/Zn/Al	563	4.0	4 000[c]	100	85	[70]
ZnO/ H–ZSM-5	Cu/Zn/Al	563	1.5	4 000	100	93	[73]
MgO/ H–ZSM-5	Cu/Zn/Al	563	4.0	4 000[c]	97	93	[74]
P–H–ZSM-5	CuO/Zn/Al	623	2.5	12 000	84	84	[75]
γ-Al_2O_3	Zn_9Ga_1O	723	2.5	12 000	95.4	95	[76]
γ-Al_2O_3	Ga-Cu/SiO_2	653	2.5	12 000	100	99	[77]
γ-Al_2O_3	CuNi-PS	648	2	18 000[b]	100	92	[78]
γ-Al_2O_3	Cu-AE	673	2	18 000[b]	100	95	[79]
γ-Al_2O_3	Cu/SiO_2	653	2.5	12 000	96	92	[80]
γ-Al_2O_3	La–Cu/SiO_2	653	2.5	12 000	99	98	[81]
γ-Al_2O_3	Cu–ZnO/SiO_2	653	2.5	12 000	96	97	[82]

a) Cu, CuO; Zn, ZnO; Al, Al_2O_3.
b) S/C, steam/DME.
c) GHSV, h^{-1}.

Table 2.6 Catalytic hydrogen production from steam reforming of dimethyl ether over supported bifunctional catalysts.

Catalyst	Temperature (K)	S/C[a]	Space velocity (ml h^{-1} g^{-1})	Conversion (%)	H_2 yield (%)	References
Cu/γ-Al_2O_3	723	3.0	7 700[b]	96	72	[83]
Cu–ZnO/γ-Al_2O_3	653	2	12 000	100	97.7	[84]
Cu–Zn/γ-Al_2O_3	623	3.0	—	100	11[c]	[85]
Cu–Ni/γ-Al_2O_3	623	3.0	3 240	100	62	[86]
Pt–Mo_2C/γ-Al_2O_3	623	5.0	5 500	100	96[c]	[87]
(K + Au)/ (CeO_2 + γ-Al_2O_3)	773	3.0	8 000	100	87	[88]

a) S/C, steam/DME.
b) GHSV, h^{-1}.
c) mmol h^{-1} g^{-1}.

catalyst exhibited high catalytic activity. Takeishi and Suzuki reported that the addition of Zn or Pd to Cu/γ-Al_2O_3 could improve H_2 production in the SR of DME reaction [85]. For Cu–Ni/γ-Al_2O_3 catalyst, the addition of Ni improved dispersion of Cu and suppressed the WGS reaction [86].

Cu-based spinel catalysts, like $CuFe_2O_4$, also exhibit excellent catalytic performance in the SR of DME reaction, due to the formation of a new Cu–Fe–AlO_4 phase

by solid-state reaction between $CuFe_2O_4$ and Al_2O_3. Importantly, the spinel-type catalysts can be easily regenerated through calcination [89, 90].

2.5 Catalytic Hydrogen Production from Glycerol

Glycerol is one of major by-products in biodiesel production [91]. The production of 10 tons of biodiesel is normally accompanied by 1 ton of glycerol, so catalytic reforming of glycerol to hydrogen is very promising. The equations for glycerol reforming are given below [92]:

$$C_3H_8O_3 + 3H_2O \rightarrow 3CO_2 + 7H_2 \quad \Delta H_{298\ K} = 128\ kJ\ mol^{-1}$$

$$C_3H_8O_3 \rightarrow 3CO + 4H_2 \quad \Delta H_{298\ K} = 250\ kJ\ mol^{-1}$$

$$CO + H_2O \rightarrow CO_2 + H_2 \quad \Delta H_{298\ K} = -41\ kJ\ mol^{-1}$$

2.5.1 Catalytic Hydrogen Production from Steam Reforming of Glycerol

Steam reforming of glycerol (GSR) is an endothermic reaction, mainly including C—C bond cleavage and the WGS reaction. However, there exist many side reactions due to the complex structure of glycerol. Thus, an ideal catalyst should facilitate C—C bond cleavage to ensure high catalytic activity and inhibit the side reactions to reduce carbon deposition.

2.5.1.1 Noble Metal Catalysts

Noble metal (Pt, Ru, and Rh)-based catalysts are investigated in the GSR reaction. Among them, Pt-based catalysts are more active and selective owing to their stronger ability to break C—C bond and higher activity in the WGS reaction. The catalytic activity of Pt-based catalysts is strongly influenced by the acid–base properties of their supports. Pompeo et al. [93] reported that Pt catalysts with acidic supports such as Pt/ZrO_2 and $Pt/\gamma\text{-}Al_2O_3$ were easily deactivated due to the formation of coke. In contrast, Pt catalysts supported on inert SiO_2 showed high H_2 selectivity and stability. Moreover, Wei et al. [94] studied the catalytic performance of Pt/C and Pt–Re/C catalysts in the GSR reaction. Characterization results demonstrated the formation of ReO_x species on Pt–Re/C catalyst surface during the reaction, which accelerated the desorption of CO. The spillover of CO from Pt to ReO_x facilitated CO desorption, thereby enhancing the catalytic activity.

For Ru-based catalysts, Gallo et al. [95] studied the effect of reaction temperature and glycerol/water ratio on the activity of Ru/Mg(Al)O and found that the catalyst deactivated quickly at low reaction temperatures (<723 K). Nevertheless, the activity could remain stable for at least 20 hours at high temperatures with close to 100% H_2 yield. Moreover, Fe, Co, Ni, and Mo could be added as promoters to improve the catalytic performance of Ru-based catalysts [96]. The addition of Ni had a positive effect on the conversion of glycerol over $Ru–Ni/Ce_{0.5}Zr_{0.5}O_2$ and $Ru–Ni/Y_2O_3$. Also,

Table 2.7 Catalytic hydrogen production from steam reforming of glycerol over noble metal catalysts.

Catalyst	Temperature (K)	S/C[a)]	Space velocity (ml h^{-1} g^{-1})	Conversion (%)	H_2 selectivity (%)	References
Pt/SiO_2	623	9.0	3 000	100	69	[93]
3%Pt/C	498	9.0	20 000[b)]	36	48	[94]
3%Pt–3%Re/C	—	—	25 000[b)]	59	45	[94]
Ru/Mg(Al)O	823	15.3	—	97	96	[95]
$Ru–Ni/Y_2O_3$	823	12.0	—	22[c)]	70	[96]
Rh/Al_2O_3	923	3.0	30 000[b)]	88	—	[98]

a) S/C, steam/$C_3H_8O_3$.
b) GHSV, h^{-1}.
c) μmol s^{-1} g^{-1}.

$Ru–Mo/Ce_{0.5}Zr_{0.5}O_2$ and $Ru–Mo/Y_2O_3$ exhibited superior catalytic stability because MoO_x moieties effectively inhibited mobility of Ru clusters on the catalyst surface.

Several studies studied activity of Rh-based catalysts for the GSR reaction. Shanmugam et al. [97] found that the high dispersion of Rh nanoparticles and large oxygen storage–release capacity of CeO_2 resulted in a strong interaction between Rh and CeO_2, which improved the sintering resistance of Rh/CeO_2 catalyst. Moreover, Chiodo et al. [98] found that Rh/Al_2O_3 was more active and stable than Ni/Al_2O_3 in the GSR reaction.

The results for catalytic hydrogen production from GSR reaction over noble metal catalysts are summarized in Table 2.7.

2.5.1.2 Non-noble Metal Catalysts

Ni-based materials are the most suitable catalysts among non-noble metal catalysts for the GSR reaction because of their strong ability to break C—C, C—H, and O—H bonds and to catalyze the WGS reaction. The successful application of alumina in hydrocarbon SR makes it widely used as a support in GSR reaction. Wu et al. [92] prepared a series of Ni/Al_2O_3 catalysts using four different Ni precursors. Ni/Al_2O_3 synthesized using $Ni(CH_3COO)_2$ displayed small Ni nanoparticle size, moderate Ni reduction degree, and high Ni dispersion, thereby achieving superior activity in the GSR reaction. Senseni et al. [99] synthesized a series of Ni/Al_2O_3 catalysts with different Ni loadings ranging from 5 to 20 wt%. Amongst them, 15 wt% Ni/Al_2O_3 with the largest surface area and smallest Ni size showed the highest activity with good stability. To further improve the performance of Ni-based catalysts, bimetallic catalysts are developed. When Co was introduced into Ni/Al_2O_3, much higher H_2 and CO_2 yields could be obtained in comparison with Ni/Al_2O_3 alone [100, 101].

Besides Al_2O_3, SBA-15, TiO_2, and ZrO_2 have been applied to investigate the influence of supports on the catalytic performance of Ni-based catalysts [102]. The Ni/TiO_2 catalyst exhibited negligible activity due to the oxidation of metallic Ni

Table 2.8 Catalytic hydrogen production from steam reforming of glycerol over non-noble metal catalysts.

Catalyst	Temperature (K)	S/C[a)]	Space velocity (ml h^{-1} g^{-1})	Conversion (%)	H_2 selectivity (%)	References
15%Ni/Al_2O_3	823	4.0	50 000	80	—	[99]
Ni/ZrO_2	923	9.0	—	72	90	[102]
Ni/CeO_2	723	9.0	15[b)]	100	45	[104]
3%Mg–Ni/Al_2O_3	873	6.0	57[c)]	95	80	[105]
Ni–Cu–Al	923	3.0	—	91	93	[106]

a) S/C, steam/$C_3H_8O_3$.
b) WHSV, h^{-1}.
c) GHSV, h^{-1}.

active sites during reaction. Ni/ZrO_2 was more active and stable than Ni/SBA-15 and Ni/TiO_2, resulting from the strengthened metal–support interaction and high thermal stability of ZrO_2 support. Al Salihi et al. [103] reported that the mesoporous structure of SBA-15 would be gradually destroyed during glycerol SR at high temperatures. Wang et al. [104] prepared Ni/CeO_2 catalyst by glow discharge plasma method and discovered that formation of Ni–O–Ce linkage in Ni/CeO_2 was the reason for the high H_2 yield obtained.

The main disadvantage of Ni-based catalysts is their rapid deactivation. Adding Mg can improve the catalytic stability of Ni/Al_2O_3 by inhibiting metal nanoparticle aggregation and reducing catalyst surface acidity [105]. The addition of Cu to Ni/Al_2O_3 catalyst inhibited carbon deposition, further enhancing catalytic stability [106]. In addition, Bobadilla et al. [107] developed a robust Ni monolithic catalyst for the GSR reaction. This catalyst was more active and stable than powder and spherical pellet catalysts, due to strong interaction between catalyst particles and support layers in the monolith.

A brief summary of catalytic hydrogen production from GSR over non-noble metal catalysts is provided in Table 2.8.

2.5.2 Catalytic Hydrogen Production from Aqueous-Phase Reforming of Glycerol

Currently, Pt- and Ni-based catalysts are widely investigated in the APR of glycerol reaction. The acid–base properties of supports significantly influence the catalytic activity of Pt-based catalysts [108]. The order of the catalytic activity of Pt-based catalysts followed the sequence of SAPO-11 < activated carbon < H-USY < SiO_2 < MgO < Al_2O_3. Pt/Al_2O_3 showed high activity toward H_2 production but unfortunately suffered from a high concentration of alkane side products. In contrast, basic supports promoted the activity of Pt catalysts by strongly adsorbing CO_2. Similarly, Guo et al. [109] found that supports with strong basicity

would promote the WGS reaction, thereby enhancing the catalytic activity of the APR of glycerol.

For Ni-based catalysts, Bastan et al. developed Ni/$Ce_xZr_{1-x}O_2$ catalysts for APR of glycerol reaction. It was found that the catalytic activity strongly depended on the Ce/Zr ratio, which influenced the Ni dispersion and the surface area of the catalysts [110]. Morales-Marín et al. [111] synthesized Ni-based catalysts by the reduction of nickel aluminate ($NiAl_2O_4$). The size of Ni nanoparticles was adjusted by changing the reduction temperatures from 573 to 1123 K. NiAl-850 with the smallest particle size showed the best catalytic performance.

Bimetallic catalyst systems were developed to further improve the catalytic activity of Ni-based catalysts. Rahman [112] found that the bimetallic Cu–Ni catalyst showed the higher H_2 selectivity and glycerol conversion than the monometallic Ni catalyst. Adding Cu to Ni-based catalysts to induce strong Cu–Ni interactions can improve the reducibility of Ni, inhibit methanation, and enhance WGS. Moreover, the formation of Pt–Ni alloy can improve the dehydrogenation–decarboxylation and dehydration–hydrogenation steps, which are beneficial for the APR of glycerol reaction [113].

2.6 Catalytic Hydrogen Production from Ethylene Glycol

EG is one of the main products from cellulose hydrolysis. The reforming of EG includes C—C bond cleavage and WGS reaction. The reforming of EG is described as follows [114]:

$$C_2H_6O_2 + 2H_2O \rightarrow 5H_2 + 2CO_2 \quad \Delta H_{298\,K} = 85.9\,kJ\,mol^{-1}$$

2.6.1 Catalytic Hydrogen Production from Steam Reforming of Ethylene Glycol

The SR of EG includes dehydrogenation and WGS. Ni-based catalysts have been extensively investigated in this reaction. Li et al. [115] studied the influence of supports on the catalytic performance of Ni catalysts. The highest H_2 yield was observed over the Ni catalyst supported on basic support. Acidic sites on the supports of ZrO_2 and γ-Al_2O_3 promoted the formation of the ethanol and ethylene by-products. The abundant surface-active oxygen of the CeO_2 support could increase the selectivity toward CO_2 by promoting the WGS reaction. Attapulgite (ATP) is a natural hydrated magnesium aluminum silicate mineral with needle-shaped structure. It is a good catalyst support due to its high hydrothermal stability, large specific surface area, and unique structure. Wang et al. [116] reported that ATP-supported Ni catalysts showed good anti-sintering and anti-coking properties because of enhanced metal–support interactions.

Bimetallic catalysts have been developed to further improve the catalytic performance of Ni catalysts. Zhao et al. [117] found that the introduction of Pt could stabilize Ni^0 sites and suppress coke formation by electron transfer and hydrogen

Table 2.9 Catalytic hydrogen production from steam reforming of ethylene glycol over metal catalysts.

Catalyst	Temperature (K)	S/C[a)]	Space velocity (ml h^{-1} g^{-1})	Conversion (%)	H_2 selectivity (%)	References
Ni/MgO	873	3	—	93	64	
Ni/CeO_2				96	50	
$Ni/\gamma\text{-}Al_2O_3$				97	47	
Ni/ZrO_2				94	50	[115]
Ni/ATP	873	2	9 600	97	73	[116]
$Pt–Ni/SiO_2$	573	10[b)]	—	90	72	[117]
$Pt–Ni/\gamma\text{-}Al_2O_3$	723	10[b)]	80.8[c)]	96	80	[118]

a) S/C, steam/$C_2H_6O_2$.
b) wt% EG.
c) WHSV, h^{-1}.

spillover. Thus, both $Pt\text{-}Ni/SiO_2$ and $Pt\text{-}Ni/CeO_2$ showed more than 80% EG conversion and 70% H_2 selectivity at 573 K. Kiadehi and Taghizadeh [118] also found that bimetallic $Pt–Ni/\gamma\text{-}Al_2O_3$ catalyst exhibited the higher catalytic activity and stability than $Pt/\gamma\text{-}Al_2O_3$ or $Ni/\gamma\text{-}Al_2O_3$ alone.

The results of catalytic hydrogen production from the SR of EG are summarized in Table 2.9.

2.6.2 Catalytic Hydrogen Production from Aqueous-Phase Reforming of Ethylene Glycol

An efficient catalyst for APR of EG requires high activity for C—C bond cleavage and the WGS reaction. To select a suitable active component, Davda et al. [119] studied the APR of EG reaction over a series of SiO_2-supported noble metal catalysts. Pt- and Pd-based catalysts were demonstrated to be more promising for H_2 production due to their strong activity towards C—C cleavage.

The properties of supports can remarkably affect the activity of noble metal catalysts in this reaction. For example, Liu et al. [120] prepared Pd/Fe_2O_3 catalysts by a coprecipitation method, which showed much higher catalytic activity than Pd/SiO_2. Full EG conversion was achieved over Pd/Fe_3O_4, and only 20% conversion was lost after 120 hours. The excellent catalytic activity of Pd/Fe_3O_4 was attributed to enhanced metal–support interactions. Porous carbon supports for Pt-based catalysts are more prevalent than with conventional supports due to larger specific surface areas, larger pore volumes, and higher chemical stability. A Pt/CMK-9 catalyst with a hollow-type and 3D mesoporous structure showed high catalytic performance for H_2 production in the APR of EG. The enhanced activity was attributed to the improved mass transfer and high Pt dispersion on Pt/CMK-9 [121]. Besides, bimetallic catalysts have also been developed to improve the performance

Table 2.10 Catalytic hydrogen production from aqueous-phase reforming of ethylene glycol over metal catalysts.

Catalyst	Temperature (K)	*P* (bar)	EG (wt%)	Catalyst (g)	Conversion (%)	H_2 selectivity (%)	References
Pt/SiO_2	483	22	10	—	—	50	[119]
Pd/Fe_3O_4	498	26	5	1.3	100	94	[120]
Pt/CMK-9	523	45	10	0.3	89	94[a)]	[121]
Pt–Mn/CMK-3	523	45	10	—	40	40	[122]
Ni /Sn/Al–HT	498	26	5	1.5	—	100	[124]
Ni/Zn/Al	498	26	20	0.2	100	99	[125]
Ni/Fe/Co	498	26	20	0.2	95	100	[126]

a) Yield.

of noble metal catalysts [122]. The TOF value for H_2 formation over bimetallic $PtNi/Al_2O_3$ was much higher than the monometallic catalysts. The enhancement of catalytic activity was attributed to the formation of more active Pt–Ni alloy species [123].

The development of efficient non-noble metal catalysts is highly desirable for this reaction. Ni-based catalysts have been extensively studied due to their strong ability for C—C bond cleavage. Pan et al. [124] prepared a Ni/Sn/Al-HT catalyst by a coprecipitation method. Formation of Ni_3Sn alloy enhanced the Ni reducibility, thereby improving catalytic activity and H_2 selectivity in the APR of EG. Due to the acceleration effect of ZnO, Ni/Zn/Al catalyst with the ratio of Ni/Zn = 1 showed 99% EG conversion and 100% H_2 selectivity at EG concentration as high as 20 wt% [125]. To further improve the activity of Ni-based catalysts, Tao et al. [126] added Fe and Co to Ni-based catalysts to prepare Ni/Fe/Co catalysts. The role of Fe was to promote the WGS reaction, while Co could promote adsorption of EG and inhibit adsorption of H_2 on the surface of catalysts. The as-synthesized Ni/Fe/Co catalysts displayed the much higher activity than the monometallic Ni catalysts.

The summary of catalytic hydrogen production from APR of EG reaction over metal catalysts has been provided in Table 2.10.

2.7 Catalytic Hydrogen Production from Sorbitol

Sorbitol ($C_6H_{14}O_6$) is a biomass-derived intermediate, which is mainly produced from hydrogenation of glucose. The reforming of sorbitol is described as follows [127]:

$$C_6H_{14}O_6 + 6H_2O \rightarrow 13H_2 + 6CO_2 \quad \Delta H_{298\,K} = 598\,kJ\,mol^{-1}$$

Tanksale et al. [128] studied the influence of impregnation method on Pt–Ni bimetallic catalysts for aqueous reforming of sorbitol. It was claimed that co-impregnation of Pt and Ni increased the Ni reducibility by forming a Pt–Ni

alloy, which could not be formed by the sequential impregnation of Pt after Ni. The co-impregnated Ni–Pt catalysts showed the much higher H_2 formation rate than the sequentially impregnated Pt/Ni and monometallic Ni catalysts. He and Chen [129] found that integrating CO_2 capture into the sorbitol SR reaction could improve H_2 yield and selectivity, resulting from CO_2 sorption. It was predicted that the combining CO_2 capture and sorbitol reforming reactions under suitable operating conditions could achieve as high as 98.8 mol% purity H_2 by thermodynamic analysis.

2.8 Conclusions and Future Outlook

The development of efficient technology for hydrogen production is of great significance to achieve green and sustainable energy development. The catalytic reforming of biomass-derived oxygen-containing chemicals is promising for hydrogen production, which can be conducted by various techniques like SR, aqueous reforming, PO, decomposition, and APR. At present, biomass-derived oxygen-containing chemicals used for hydrogen production mainly include methanol, dimethyl ether, ethanol, glycerol, EG, and sorbitol.

Steam reforming has been demonstrated to be one of the most effective techniques for catalytic hydrogen production. The SR process mainly involves C—C/C—H bond cleavage and the WGS reaction. Pt- and Ni-based catalysts are commonly used catalysts due to their strong ability for C—C/C—H bond cleavage and high activity in WGS. Metal nanoparticle size, metal dispersion, acid–base properties, and metal–support interaction are key factors influencing the catalytic activity and stability in reforming. The addition of promoters to metal catalysts can improve catalytic activity by increasing hydrogen yield and/or inhibiting coke formation.

So far, significant progress has been achieved in catalytic reforming for hydrogen production. However, there still are many challenges to be overcome. More attention should be focused on developing catalysts with high efficiency, long-term stability, and low cost. Also, the catalytic reforming of biomass-derived oxygen-containing chemicals for hydrogen production currently is only on a laboratory scale, and pilot-scale studies are highly desirable in the near future.

References

1 Sharma, S. and Ghoshal, S.K. (2015). *Renewable Sustainable Energy Rev.* 43: 1151–1158.
2 Muradov, N. (2017). *Int. J. Hydrog. Energy* 42: 14058–14088.
3 Sengodan, S., Lan, R., Humphreys, J. et al. (2018). *Renewable Sustainable Energy Rev.* 82: 761–780.
4 Song, S., Qu, J., Ha, P. et al. (2020). *Nat. Commun.* 11: 4899.
5 Cortright, R.D., Davda, R.R., and Dumesic, J.A. (2002). *Nature* 418: 964–967.
6 Parthasarathy, P. and Narayanan, K.S. (2014). *Renewable Energy* 66: 570–579.

7 Azenha, C.S.R., Mateos-Pedrero, C., Queiros, S. et al. (2017). *Appl. Catal., B* 203: 400–407.
8 Usami, Y., Kagawa, K., Kawazoe, M. et al. (1998). *Appl. Catal., A* 171: 123–130.
9 Mihaylov, M., Tsoncheva, T., and Hadjiivanov, K. (2011). *J. Mater. Sci.* 46: 7144–7151.
10 Li, G.J., Gu, C.T., Zhu, W.B. et al. (2018). *J. Clean. Prod.* 183: 415–423.
11 Chen, W.H. and Guo, Y.Z. (2018). *Fuel* 222: 599–609.
12 Sun, Q., Men, Y., Wang, J. et al. (2018). *Inorg. Chem. Commun.* 92: 51–54.
13 Chen, W.H., Shen, C.T., Lin, B.J., and Liu, S.C. (2015). *Energy* 88: 399–407.
14 Chang, F.W., Yu, H.Y., Roselin, L.S. et al. (2006). *Appl. Catal. A* 302: 157–167.
15 Hernández-Ramírez, E., Wang, J.A., Chen, L.F. et al. (2017). *Appl. Surf. Sci.* 399: 77–85.
16 Chang, F.W., Ou, T.C., Roselin, L.S. et al. (2009). *J. Mol. Catal. A-Chem.* 313: 55–64.
17 Chang, F.W., Roselin, L.S., and Ou, T.C. (2008). *Appl. Catal. A* 334: 147–155.
18 Araiza, D.G., Gomez Cortes, A., and Diaz, G. (2017). *Catal. Today* 282: 185–194.
19 Huang, Y.J., Ng, K.L., and Huang, H.Y. (2011). *Int. J. Hydrog. Energy* 36: 15203–15211.
20 Karim, A., Conant, T., and Datye, A. (2006). *J. Catal.* 243: 420–427.
21 Conant, T., Karim, A.M., Lebarbier, V. et al. (2008). *J. Catal.* 257: 64–70.
22 Chi, H., Andolina, C.M., Li, J. et al. (2018). *Appl. Catal. A* 556: 64–72.
23 Oguchi, H., Nishiguchi, T., Matsumoto, T. et al. (2005). *Appl. Catal. A* 281: 69–73.
24 Yao, C.Z., Wang, L.C., Liu, Y.M. et al. (2006). *Appl. Catal. A* 297: 151–158.
25 Sanches, S.G., Huertas Flores, J., de Avillez, R.R., and Pais da Silva, M.I. (2012). *Int. J. Hydrog. Energy* 37: 6572–6579.
26 Yang, S.Q., Zhou, F., Liu, Y.J. et al. (2019). *Int. J. Hydrog. Energy* 44: 7252–7261.
27 Shokrani, R., Haghighi, M., Jodeiri, N. et al. (2014). *Int. J. Hydrog. Energy* 39: 13141–13155.
28 Agrell, J., Birgersson, H., Boutonnet, M. et al. (2003). *J. Catal.* 219: 389–403.
29 Perez Hernandez, R., Gutierrez Martinez, A., Palacios, J. et al. (2011). *Int. J. Hydrog. Energy* 36: 6601–6608.
30 Lin, L., Zhou, W., Gao, R. et al. (2017). *Nature* 544: 80–96.
31 Li, D., Li, Y., Liu, X. et al. (2019). *ACS Catal.* 9: 9671–9682.
32 Awasthi, M.K., Rai, R.K., Behrens, S., and Singh, S.K. (2021). *Cat. Sci. Technol.* 11: 136–142.
33 Sakamoto, T., Kikuchi, H., Miyao, T. et al. (2010). *Appl. Catal. A* 375: 156–162.
34 Sakamoto, T., Miyao, T., Yoshida, A., and Naito, S. (2010). *Int. J. Hydrog. Energy* 35: 6203–6209.
35 Coronado, I., Stekrova, M., Moreno, L.G. et al. (2017). *Biomass Bioenergy* 106: 29–37.
36 Lin, L., Yu, Q., Peng, M. et al. (2021). *J. Am. Chem. Soc.* 143: 309–317.
37 Stekrova, M., Paavola, A.R., and Karinen, R. (2018). *Catal. Today* 304: 143–152.
38 Song, H. and Ozkan, U.S. (2010). *Int. J. Hydrog. Energy* 35: 127–134.

39 Llorca, J., de la Piscina, P.R., Sales, J., and Homs, N. (2001). *Chem. Commun.* 641–642.

40 Ciambelli, P., Palma, V., and Ruggiero, A. (2010). *Appl. Catal. B* 96: 18–27.

41 de Lima, S.M., da Cruz, I.O., Jacobs, G. et al. (2008). *J. Catal.* 257: 356–368.

42 Zhong, Z., Ang, H., Choong, C. et al. (2009). *Phys. Chem. Chem. Phys.* 11: 872–880.

43 Wu, X. and Kawi, S. (2010). *Energy Environ. Sci.* 3: 334–342.

44 da Silva, A.M., de Souza, K.R., Jacobs, G. et al. (2011). *Appl. Catal. B* 102: 94–109.

45 Moraes, T.S., Borges, L.E.P., Farrauto, R., and Noronha, F.B. (2018). *Int. J. Hydrog. Energy* 43: 115–126.

46 Chen, L., Choong, C.K.S., Zhong, Z. et al. (2010). *J. Catal.* 276: 197–200.

47 Bosko, M.L., Ferreira, N., Catena, A. et al. (2018). *Catal. Commun.* 114: 19–23.

48 Ogo, S. and Sekine, Y. (2020). *Fuel Process. Technol.* 199: 106238.

49 Li, S., Li, M., Zhang, C. et al. (2012). *Int. J. Hydrog. Energy* 37: 2940–2949.

50 Zhang, C., Yue, H., Huang, Z. et al. (2013). *ACS Sustain. Chem. Eng.* 1: 161–173.

51 Xu, W., Liu, Z., Johnston-Peck, A.C. et al. (2013). *ACS Catal.* 3: 975–984.

52 Llorca, J., de la Piscina, P.R., Dalmon, J.A. et al. (2003). *Appl. Catal. B* 43: 355–369.

53 Soykal, I.I., Sohn, H., and Ozkan, U.S. (2012). *ACS Catal.* 2: 2335–2348.

54 Ogo, S., Shimizu, T., Nakazawa, Y. et al. (2015). *Appl. Catal. A* 495: 30–38.

55 Wang, Z., Wang, C., Chen, S., and Liu, Y. (2014). *Int. J. Hydrog. Energy* 39: 5644–5652.

56 Nozawa, T., Mizukoshi, Y., Yoshida, A., and Naito, S. (2014). *Appl. Catal. B* 146: 221–226.

57 Nozawa, T., Yoshida, A., Hikichi, S., and Naito, S. (2015). *Int. J. Hydrog. Energy* 40: 4129–4140.

58 Xiong, H., DeLaRiva, A., Wang, Y., and Datye, A.K. (2015). *Cat. Sci. Technol.* 5: 254–263.

59 Zhao, Z., Zhang, L., Tan, Q. et al. (2019). *AIChE J.* 65: 151–160.

60 Roy, B., Loganathan, K., Pham, H.N. et al. (2010). *Int. J. Hydrog. Energy* 35: 11700–11708.

61 Roy, B. and Leclerc, C.A. (2015). *J. Power Sources* 299: 114–124.

62 Sun, J., Yang, G., Yoneyama, Y., and Tsubaki, N. (2014). *ACS Catal.* 4: 3346–3356.

63 Badmaev, S.D., Akhmetov, N.O., Belyaev, V.D. et al. (2020). *Int. J. Hydrog. Energy* 45: 26188–26196.

64 Song, L., Li, X., and Zheng, T. (2008). *Int. J. Hydrog. Energy* 33: 5060–5065.

65 Wang, S.Z., Ishihara, T., and Takita, Y. (2002). *Appl. Catal. A* 228: 167–176.

66 Nilsson, M., Jozsa, P., and Pettersson, L.J. (2007). *Appl. Catal. B* 76: 42–50.

67 Faungnawakij, K., Shimoda, N., Viriya-empikul, N. et al. (2010). *Appl. Catal. B* 97: 21–27.

68 Oar Arteta, L., Aguayo, A.T., Remiro, A. et al. (2016). *Chem. Eng. J.* 306: 401–412.

69 Oar Arteta, L., Remiro, A., Aguayo, A.T. et al. (2015). *Ind. Eng. Chem. Res.* 54: 9722–9732.
70 Li, J., Zhang, Q.J., Long, X. et al. (2012). *Chem. Eng. J.* 187: 299–305.
71 Song, S., Di, L., Wu, G. et al. (2017). *Appl. Catal. B* 205: 393–403.
72 Song, S., Yuen, V.F.K., Di, L. et al. (2020). *Angew. Chem. Int. Ed.* 59: 19846–19850.
73 Gao, T.Y., Zhao, Y.H., Zhang, Q.J. et al. (2019). *React. Kinet. Mech. Catal.* 128: 235–249.
74 Long, X., Zhang, Q.J., Liu, Z.T. et al. (2013). *Appl. Catal. B* 134: 381–388.
75 Lu, J.H., Zhou, S., Ma, K. et al. (2015). *Chin. J. Catal.* 36: 1295–1303.
76 Zhou, S., Ma, K., Tian, Y. et al. (2016). *RSC Adv.* 6: 52411–52420.
77 Huang, J.J., Cai, J.M., Ma, K. et al. (2019). *Acta Phys. -Chim. Sin.* 35: 431–441.
78 Ma, K., Cui, Z., Zhang, Z. et al. (2018). *ChemCatChem* 10: 4010–4017.
79 Ma, K., Tian, Y., Zhao, Z.J. et al. (2019). *Chem. Sci.* 10: 2578–2584.
80 Wang, X.-L., Ma, K., Guo, L.-H. et al. (2017). *Acta Phys.-Chim. Sin.* 33: 1699–1708.
81 Huang, J.J., Ding, T., Ma, K. et al. (2018). *ChemCatChem* 10: 3862–3871.
82 Wang, X.L., Ma, K., Guo, L.H. et al. (2017). *Appl. Catal. A* 540: 37–46.
83 Kim, D., Choi, B., Park, G. et al. (2020). *Chem. Eng. Sci.* 216: 10.
84 Sun, Z., Tian, Y., Zhang, P. et al. (2019). *Ind. Eng. Chem. Res.* 58: 7085–7093.
85 Takeishi, K. and Suzuki, H. (2004). *Appl. Catal. A* 260: 111–117.
86 Wang, X.L., Pan, X.M., Lin, R. et al. (2010). *Int. J. Hydrog. Energy* 35: 4060–4068.
87 Lian, J.H., Tan, H.Y., Guo, C.Q. et al. (2020). *Int. J. Hydrog. Energy* 45: 31523–31537.
88 Gazsi, A., Ugrai, I., and Solymosi, F. (2011). *Appl. Catal. A* 391: 360–366.
89 Oar-Arteta, L., Remiro, A., Aguayo, A.T. et al. (2016). *J. Ind. Eng. Chem.* 36: 169–179.
90 Oar Arteta, L., Remiro, A., Vicente, J. et al. (2014). *Fuel Process. Technol.* 126: 145–154.
91 Wang, Y., Furukawa, S., Song, S. et al. (2020). *Angew. Chem. Int. Ed.* 59: 2289–2293.
92 Wu, G.W., Zhang, C.X., Li, S.R. et al. (2013). *ACS Sustain. Chem. Eng.* 1: 1052–1062.
93 Pompeo, F., Santori, G., and Nichio, N.N. (2010). *Int. J. Hydrog. Energy* 35: 8912–8920.
94 Wei, Z., Karim, A.M., Li, Y. et al. (2015). *J. Catal.* 322: 49–59.
95 Gallo, A., Pirovano, C., Ferrini, P. et al. (2012). *Appl. Catal. B* 121: 40–49.
96 Kim, J. and Lee, D. (2013). *Int. J. Hydrog. Energy* 38: 11853–11862.
97 Shanmugam, V., Zapf, R., Hessel, V. et al. (2018). *Appl. Catal. B* 226: 403–411.
98 Chiodo, V., Freni, S., Galvagno, A. et al. (2010). *Appl. Catal. A* 381: 1–7.
99 Senseni, A.Z., Meshkani, F., and Rezaei, M. (2016). *Int. J. Hydrog. Energy* 41: 20137–20146.
100 Sanchez, E.A. and Comelli, R.A. (2014). *Int. J. Hydrog. Energy* 39: 8650–8655.

101 Cheng, C.K., Foo, S.Y., and Adesina, A.A. (2010). *Ind. Eng. Chem. Res.* 49: 10804–10817.

102 Nichele, V., Signoretto, M., Menegazzo, F. et al. (2012). *Appl. Catal. B* 111: 225–232.

103 Al Salihi, S., Abrokwah, R., Dade, W. et al. (2020). *Int. J. Hydrog. Energy* 45: 14183–14198.

104 Wang, B., Xiong, Y., Han, Y. et al. (2019). *Appl. Catal. B* 249: 257–265.

105 Dieuzeide, M.L., Laborde, M., Amadeo, N. et al. (2016). *Int. J. Hydrog. Energy* 41: 157–166.

106 Wang, C., Dou, B., Chen, H. et al. (2013). *Int. J. Hydrog. Energy* 38: 3562–3571.

107 Bobadilla, L.F., Alvarez, A., Dominguez, M.I. et al. (2012). *Appl. Catal. B* 123: 379–390.

108 Wen, G., Xu, Y., Ma, H. et al. (2008). *Int. J. Hydrog. Energy* 33: 6657–6666.

109 Guo, Y., Azmat, M.U., Liu, X. et al. (2012). *Appl. Energy* 92: 218–223.

110 Bastan, F., Kazemeini, M., and Larimi, A.S. (2017). *Renew. Energy* 108: 417–424.

111 Morales-Marín, A., Ayastuy, J.L., Iriarte-Velasco, U. et al. (2019). *Appl. Catal. B* 244: 931–945.

112 Rahman, M.M. (2015). *Int. J. Hydrog. Energy* 40: 14833–14844.

113 He, C., Zheng, J., Wang, K. et al. (2015). *Appl. Catal. B* 162: 401–411.

114 Wang, N., Perret, N., and Foster, A. (2011). *Int. J. Hydrog. Energy* 36: 5932–5940.

115 Li, S., Zhang, C., Zhang, P. et al. (2012). *Phys. Chem. Chem. Phys.* 14: 4066–4069.

116 Wang, Y., Chen, M., Li, X. et al. (2018). *Int. J. Hydrog. Energy* 43: 20438–20450.

117 Zhao, X., Wu, K., Liao, W. et al. (2019). *Green Energy Environ.* 4: 300–310.

118 Kiadehi, A.D. and Taghizadeh, M. (2018). *Int. J. Hydrog. Energy* 43: 4826–4838.

119 Davda, R.R., Shabaker, J.W., Huber, G.W. et al. (2003). *Appl. Catal. B* 43: 13–26.

120 Liu, J., Sun, B., Hu, J. et al. (2010). *J. Catal.* 274: 287–295.

121 Kim, H.D., Kim, T.W., Park, H.J. et al. (2012). *Int. J. Hydrog. Energy* 37: 12187–12197.

122 Kim, H.D., Park, H.J., Kim, T.W. et al. (2012). *Int. J. Hydrog. Energy* 37: 8310–8317.

123 Huber, G.W., Shabaker, J.W., Evans, S.T., and ADumesic, J. (2006). *Appl. Catal. B* 62: 226–235.

124 Pan, G., Ni, Z., Cao, F., and Li, X. (2012). *Appl. Clay Sci.* 58: 108–113.

125 Chen, G., Xu, N., Li, X. et al. (2015). *RSC Adv.* 5: 60128–60134.

126 Tao, J., Hou, L., Yan, B. et al. (2020). *Energy Fuel* 34: 1153–1161.

127 Sladkovskiy, D.A., Godina, L.I., Semikin, K.V. et al. (2018). *Chem. Eng. Res. Des.* 134: 104–116.

128 Tanksale, A., Zhou, C.H., Beltramini, J.N., and Lu, G.Q. (2009). *J. Incl. Phenom. Macrocycl. Chem.* 65: 83–88.

129 He, L. and Chen, D. (2012). *ChemSusChem* 5: 587–595.

3

Advances in Fischer–Tropsch Synthesis for the Production of Fuels and Chemicals

Liangshu Zhong

Shanghai Advanced Research Institute, Chinese Academy of Sciences, CAS Key Laboratory of Low-Carbon Conversion Science and Engineering, No.99 Haike Road, Zhangjiang Hi-Tech Park, Pudong, Shanghai 201203, P. R. China

3.1 Introduction

The petrochemical industry provides the majority of liquid fuels and building block chemicals required for human activity. However, the reserves of petroleum are limited, and, accordingly, it is necessary to search for non-petroleum-based resources as alternative feedstocks. The non-petroleum carbon-containing resources include coal, natural gas, shale gas, biomass, solid organic waste, and even CO_2. Various value-added products can be obtained via the efficient utilization of non-petroleum carbon-containing resources. C1 chemistry, which focuses on the catalytic conversion of simple molecules comprising a single carbon atom (such as CO, CO_2, methane, and methanol), has attracted more and more attention from both the industrial and academic communities. One of the most active research fields in C1 chemistry is the conversion of syngas ($CO + H_2$) into different target products including high-purity solid wax (C_{21+} hydrocarbons), liquid fuels ($C_{5–11}$ hydrocarbons as gasoline; $C_{8–16}$ hydrocarbons as jet fuel; $C_{10–20}$ hydrocarbons as diesel fuels), and various chemicals (olefins, aromatics, and oxygenates) as shown in Figure 3.1.

Fischer–Tropsch synthesis (FTS) has been known for almost one century, and it is applied for the effective conversion of syngas to fuels and chemicals [1, 2]. The product spectrum of FTS is rather complicated, and the catalytic mechanism remains an issue of debate. Both hydrocarbons and oxygenates can be directly produced through the FTS route [3]. However, the product range typically follows the so-called Anderson–Schulz–Flory (ASF) distribution: $M_n = (1-\alpha)^2 n\alpha^{n-1}$ [4]. According to the classical ASF model (Figure 3.2), the maximum fractions of $C_{2–4}$, $C_{5–11}$ (gasoline-range fuel), $C_{8–16}$ (jet-range fuel), and $C_{10–20}$ (diesel-range fuel) hydrocarbon are estimated to be 58%, 48%, 41%, and 40%, respectively. Obviously, as the carbon distribution of FT products is rather broad, it remains a significant challenge to obtain a specific range of useful C_{2+} products with high selectivity.

Heterogeneous Catalysis for Sustainable Energy, First Edition. Edited by Landong Li and Justin S. J. Hargreaves.

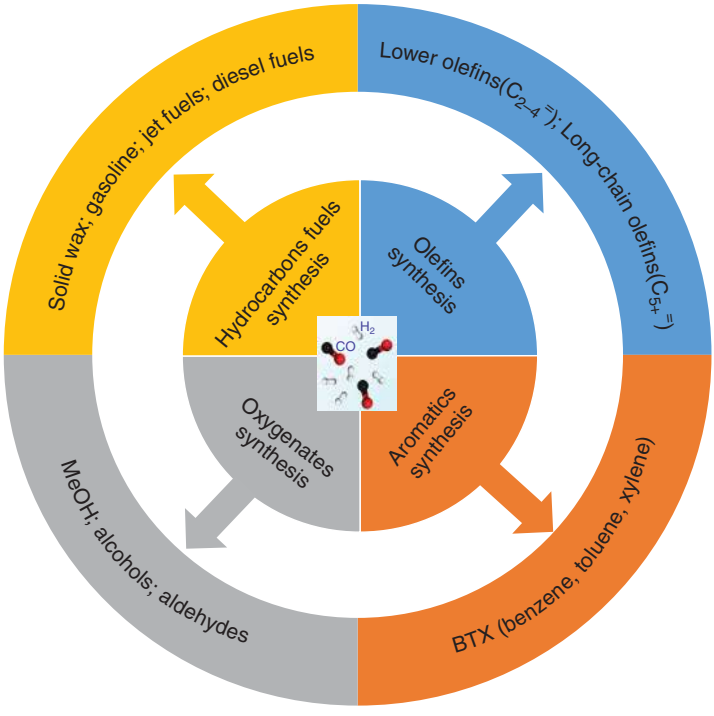

Figure 3.1 Syngas conversion to various fuels and chemicals via different catalytic processes.

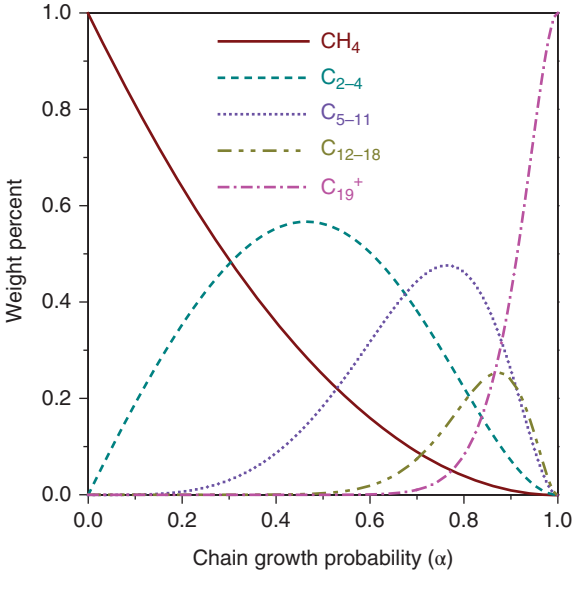

Figure 3.2 Product distributions based on the Anderson–Schulz–Flory (ASF) model.

Although the FTS technology has been commercialized, there are still many fundamental aspects that remain to be further clarified. Most of the current investigations on FTS focus on the improvement of C_{5+} selectivity via the synthesis of efficient catalysts and optimizing reaction conditions. Key catalyst factors that affect the catalytic performance include the active site structure, the presence of promoters, and the nature of the support. The microenvironment has been investigated in detail and also reviewed in detail in recent publications [5–8]. Moreover, the synthesis of C_{2+} oxygenates from syngas via the FTS route is rather economically favorable [3]. Dual active sites (one site for dissociative CO adsorption and C–C coupling and the other for associative CO adsorption and insertion) are required for C_{2+} oxygenate formation. However, the complex reaction network involved makes it difficult to elucidate detailed structure–performance relationships [9, 10].

Detailed studies have been carried out to break the product selectivity limitation for high value-added hydrocarbons and oxygenates in syngas conversion. Over the past decade, significant progress has been achieved, including the identification of active site structures and the preparation of efficient catalytic systems with high selectivity. Some novel strategies, concepts, and methodologies, such as reaction coupling, relay catalysis, and tandem catalysis, have been proposed [11]. In addition, benefiting from the rapid development of advanced synthesis methods, characterization techniques, and powerful computational simulation capabilities, the key factors affecting the catalytic performance have been explored in depth to provide improved understanding of structure–performance relationships. This chapter will mainly describe the great achievements made in selectivity control for the production of hydrocarbon products (i.e. fuels, olefins, and aromatics) and C_{2+} oxygenates through the FTS route. Some key advances achieved via non-FTS route will also be introduced, such as the development of bifunctional catalytic systems comprising oxide/zeolite. The currently existing challenges for selective syngas conversion and some perspectives for future research directions will also be presented.

3.2 Catalyst Development for Fischer–Tropsch Synthesis

The common FT catalysts are based upon Fe, Co, and Ru. A large number of FT catalysts based on these three types of metal have been developed to improve the C_{5+} selectivity. Some catalysts based on Fe or Co have been employed in large-scale industrial processes, while the high cost of Ru precludes its commercial application. Therefore, this section will focus upon the advances made on the development of Fe-based and Co-based catalysts.

3.2.1 Fe-Based FTS

Iron is the cheapest transition metal and is most promising for large-scale commercial application for FTS. Iron carbide is usually regarded as the active phase for Fe-based FTS [8]. However, various iron carbide phases including χ-Fe_5C_2, ξ-Fe_xC,

and θ-Fe_3C may coexist with other iron species (i.e. Fe_3O_4, Fe^0) during the reaction process. The formation of iron carbide and its stability in FTS process are highly dependent on many factors including the catalyst composition, the reduction process and reaction conditions employed, and the local chemical environment and crystallite structure [12–14]. In addition, the phase transformation of iron species usually takes place under FT reaction conditions. It is difficult to study the catalytic performance of individual phases of iron carbide, and it remains a challenge to prepare a Fe-based catalyst with well-defined structure for FTS with high C_{5+} selectivity and low selectivity to undesirable products. Recent studies evidence significant advances in controlling the synthesis of specific iron carbides through the development and application of novel synthetic methodology. The structure evolution of iron species during the whole FTS process can be monitored through advanced *in situ*/*operando* characterization techniques. It should be noted that the Fe-based FT catalysts are prone to deactivation, which may be due to the strong binding of C atoms on the surface of iron species [15].

With regard to the various types of iron carbides, most studies have suggested that χ-Fe_5C_2 is responsible for FTS [16, 17], while in some cases it has been proposed that the ξ-iron carbide (ξ-Fe_2C, ξ-$Fe_{2.2}C$) [18–20] exhibits better catalytic performance for FTS. The θ-Fe_3C phase and amorphous Fe_xC display high metallic nature and are more susceptible to the buildup of surface graphitic carbonaceous deposits during FTS [12]. As different types of iron carbides show different catalytic performance [14], the preparation of Fe-based catalysts with phase-pure iron carbide is the key step to elucidate the structure–performance relationship of Fe-based FT catalysts. Yang and coworkers developed a facile wet-chemical route for the synthesis of χ-Fe_5C_2 nanoparticles with controlled size (~20 nm) through the reaction of $Fe(CO)_5$ and octadecylamine at 350 °C [16]. It was found that bromide (Br^-) was a key directing agent for the conversion of $Fe(CO)_5$ to χ-Fe_5C_2, and the as-obtained χ-Fe_5C_2 exhibited high intrinsic catalytic activity in FTS, demonstrating it to be an active phase for FTS. In another study, Xu and coworkers successfully prepared a ξ-Fe_2C-dominant catalyst (73.1%) for low-temperature FTS. It was found that the as-obtained ξ-Fe_2C-dominant catalyst was more active than χ-Fe_5C_2 at low temperature, and the selectivity to transportation fuels (C_5–C_{21}) reached up to 73% at 150 °C [18]. Theoretical predication has suggested that ξ-Fe_2C becomes thermodynamically the most stable among the TP- and O-carbides at low temperature [12]. For the traditional Fe-based FTS process, a large amount of CO_2 is produced due to the high activity for the water–gas shift (WGS) reaction. However, a recent study reported the preparation of phase-pure ε-Fe_2C catalysts by carefully controlling the pretreatment and carburization conditions, producing catalysts that could suppress the WGS activity (5% CO_2 selectivity) and showed a high C_{5+} selectivity and excellent stability for at least 150 hours of testing [19].

The catalyst structure of Fe-based catalysts may change during the FTS reaction process. The development of modern characterization techniques provides a chance to observe the structural evolution of iron species under working conditions [21–23]. de Smit et al. performed a comprehensive experiments combining *in situ* X-ray absorption fine structure (XAFS), X-ray diffraction (XRD), and Raman

Table 3.1 *In situ* characterization results for Fe-based catalysts (starting from Fe_2O_3) after different pretreatments [12].

Status	XRD (vol%)	XAFS (mol%)	Raman
After pretreatment[a)]	χ-Fe_5C_2 (90%)	χ-Fe_5C_2 (70%)	Some graphitic carbon
	ε-carbides (10%)	Fe_xC (24%)	
After FTS[a)]	χ-Fe_5C_2 (57%)	χ-Fe_5C_2 (76%)	No significant increase in graphitic carbon
	ε-carbides (5%)	Fe_xC (12%)	
	Fe_3O_4 (38%)	Fe_3O_4 (14%)	
After pretreatment[b)]	χ-Fe_5C_2 (56%)	χ-Fe_5C_2 + θ-Fe_3C (51%)	Some graphitic carbon
	θ-Fe_3C (44%)	Fe_xC (49%)	
After FTS[b)]	χ-Fe_5C_2 (61%)	χ-Fe_5C_2 + θ-Fe_3C (50%)	Incremental graphitic C formation
	θ-Fe_3C (39%)	Fe_xC (50%)	

Reaction conditions: 240 °C, 10 bar, $H_2/CO = 1$.
a) Pretreatment in pure CO flow at 280 °C.
b) Pretreatment in 1% CO/H_2 flow at 350 °C.

spectroscopy and density functional theory (DFT) calculations to investigate the evolution of iron species starting from a α-Fe_2O_3 precursor during pretreatment and under realistic FTS conditions [12], as depicted in Table 3.1. They found that Fe_xC (χ-Fe_5C_2 and θ-Fe_3C) mixtures of different composition were obtained as the α-Fe_2O_3 was reduced under different conditions (pure CO or 1% CO/H_2). No additional iron carbide phases were detected except for the appearance of a large fraction of the Fe_3O_4 phase for the spent sample. They speculated that the χ-Fe_5C_2 and amorphous carbide phase are susceptible to oxidation. For the 1% CO/H_2-reduced catalyst, the characterization results suggested the iron species remained almost unchanged during the reaction process. However, the Raman spectra indicated a significant buildup of graphitic carbon on the surface of 1% CO/H_2-treated catalysts. In addition, a slow transformation of θ-Fe_3C to χ-Fe_5C_2 was observed under high-pressure FTS conditions. This study suggested that the different carbon chemical potentials (μ_C) imposed by the reaction atmosphere and reaction temperature exert significant influence on the formation of iron carbide.

The addition of suitable promoters and supports is necessary to achieve promising catalytic performance for the FT reaction. Promoters such as manganese, calcium, zinc, copper, alkali metals, and alkali-earth metals are often introduced to modify catalyst properties [24–26]. For the alkali metal-promoted Fe-based catalysts, the carburization rate typically follows this order: unpromoted < Li < Na < K = Rb = Cs. K is the most reported alkali promoter and can effectively weaken the C—O bond and promote the CO dissociation [26]. In addition, supported Fe-based catalysts are always employed to obtain better mechanical stability and a high dispersion of active sites. The commonly used supports include SiO_2, Al_2O_3, TiO_2, and zeolites [27, 28]. Recently, a type of novel carbon support has attracted great interest. Carbon nanofibers (CNFs), carbon nanotubes (CNTs), and graphene have been exploited

due to their inert property and high specific surface area [1, 29]. It was suggested that the carbon-based supports can enhance the dispersion of the iron phase and favor the reduction/carburization of iron oxide precursors to form iron carbide. In addition, the surface defects or surface-functionalized groups can create sites for anchoring metal precursors on carbon-based supports, thus creating a positive chemical microenvironment for iron carbide formation and for tailoring the product distribution [30].

3.2.2 Co-Based FTS

Compared with Fe, Co-based FTS catalysts typically show higher activity and produce more long-chain hydrocarbons with lower fraction of CH_4 and CO_2. The metallic Co is generally recognized to be the active phase for FTS, and the transformation of Co^0 to Co_xO or Co-based spinel composite (i.e. CoAl, CoSi) may lead to catalytic deactivation [31–33]. Due to the high cost of Co, supported Co-based catalysts with high dispersion, reducibility, and stability are highly desirable. Over the last decade, nanoeffects of Co-based FT catalysts relating to the influence of active phase, particle size, crystallographic structure, and exposed facet on the catalytic performance have attracted significant attention [8], and the nature of the metal–support interaction (MSI) is another very important issue [34].

There exist both hexagonal close-packed (HCP) phase and face-centered cubic (FCC) phases for metallic Co. Many studies have confirmed that the HCP Co is more active than FCC Co for the FT reaction [35–37]. Based on DFT calculations, Liu and coworkers found that HCP Co and FCC Co nanoparticles showed different surface topological structures and exposed facets (Figure 3.3) [35]. Most of the exposed facets of HCP Co showed lower CO dissociation barriers than those for FCC Co. Further investigation suggested that the HCP Co favored the direct CO dissociation, while the H-assisted CO dissociation was preferred on FCC Co. The above conclusion may provide important insights for the rational preparation of supported Co-based catalyst with a high fraction of the HCP Co crystallographic structure. Generally, the reduction of the precursor with H_2 will lead to the formation of FCC Co, and the classical way to obtain HCP Co is to follow the reduction–carburization–reduction (RCR) strategy via Co_2C as intermediate [38, 39].

FTS is a structure-sensitive reaction, and the particle size greatly influences the catalytic performance for Co-based FTS catalysts [5, 8]. Various types of Co-based catalysts including Co/CNF, Co/α-Al_2O_3, Co/γ-Al_2O_3, Co/CNT, Co/carbon spheres, Co/SiO_2, and Co/ITQ-2 zeolite were employed to investigate the size effect of Co nanoparticles [1]. It has been concluded that the turnover frequency (TOF) increases with increasing Co particle size (typically in the range of 5–10 nm) and then remains almost unchanged as the particle size further increases. The C_{5+} product slates follow a similar trend to that of the TOF, while the CH_4 selectivity presents the opposite trend. In addition, the cobalt time yield (CTY) reaches a maximum at a critical size of the Co nanoparticles.

MSI for supported Co-based catalysts is a key parameter and can affect the catalytic activity and stability. Strong metal–support interaction (SMSI) will cause

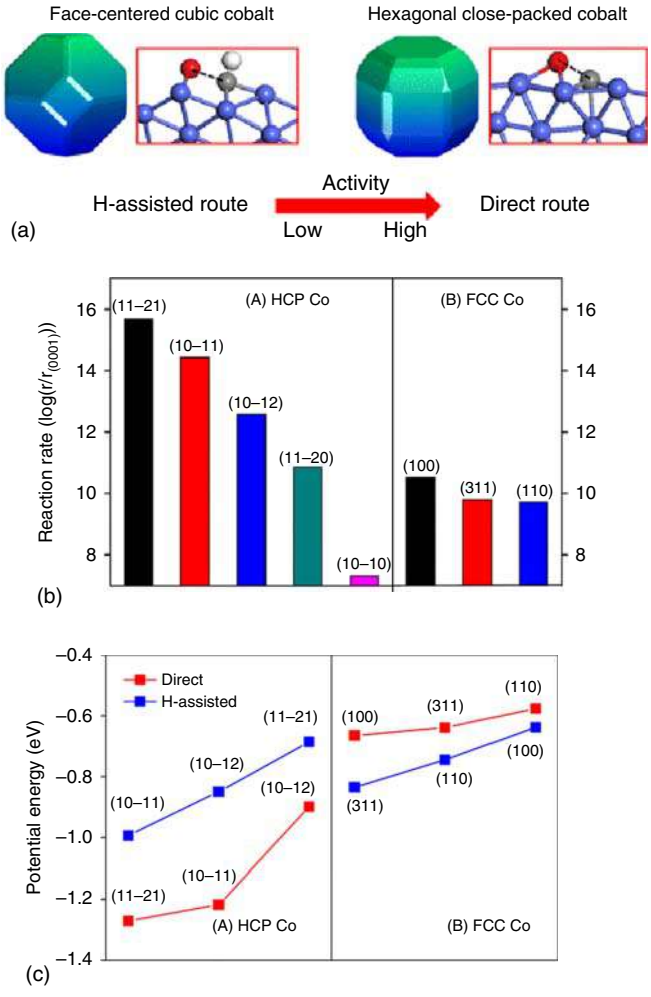

Figure 3.3 (a) Equilibrium morphology of FCC Co and HCP Co based on the Wulff construction from DFT, (b) calculated reaction rates for CO dissociation on exposed HCP and FCC Co facets at the low coverage (all rates are normalized by that of HCP (0001) with units of s^{-1}·site^{-1}), and (c) calculated potential energy for CO activation at the transition states for breaking the C=O bond. Source: Reproduced with permission from Liu et al. [35]; © 2013, American Chemical Society.

low reducibility of Co species while too weak MSI may lead to poor dispersion of Co nanoparticles and possible particle aggregation. By tuning the MSI, a highly efficient Co-based catalysts can be prepared. de Jong and coworkers developed a reduction–oxidation–reduction (ROR) treatment strategy to tuning the SMI for metallic Co nanoparticles supported on reducible oxidizing supports to improve the catalytic performance without the addition of noble metal promoters [34]. They firstly obtained hollow cobalt oxide nanoparticles via the Kirkendall effect. After the second reduction, the treated Co/TiO_2 and Co/Nb_2O_5 catalysts showed

doubled activity in FTS compared with their untreated counterparts and a slightly decreased activity for Co/α-Al_2O_3. They found that the temperature in the oxidation and reduction steps should be well-controlled. Recently, Ellis et al. fabricated a supported Co/α-Al_2O_3 with high Co dispersion for slurry-phase FTS [40]. It was suggested that the method for metal addition into inert supports played a decisive role for FTS performance. Liu et al. successfully introduced a thin layer of TiO_2 on β-SiC to increase the MSI of Co and support, thus enhancing the dispersion of active Co phase [41]. The as-obtained Co/TiO_2-SiC showed about twofold activity compared with Co/SiC, and the C_{5+} selectivity was also higher than for the latter.

Investigation of the fundamental mechanism of FTS at an atomic level and direct visualization of catalyst evolution under working conditions have become hot research directions [42–46]. Powerful computer simulation and the recent development of *in situ* or *operando* characterization techniques provide important tools to elucidate these issues. Recently, Navarro et al. reported the self-assembled behavior of hydrocarbon molecules on Co surfaces during the FTS process by using a purpose-built *in situ* scanning tunneling microscope (STM) [47]. They claimed that short molecules were mainly formed in the very first stage of the FT reaction, which were easy to desorb from Co surface. As the reaction proceeded, the surface terrace sites were gradually covered by parallel arrays of stripes. These stripes were formed by the self-assembly of linear hydrocarbon product molecules. Further study suggested that the width of the stripes corresponded to molecules with 14 or 15 carbon atoms long. Very recently, Böller et al. carried *operando* STM to identify the nature of active site at atomic scale on a working Co-based catalyst [44]. It was suggested that atomic steps were the active sites of the FTS on a Co(0001) as model catalyst. They also suggested that the step sites might leave sufficient space for the dissociation process and would not be poisoned although various surface reaction intermediates might preferentially bind to the step sites.

3.3 Selectivity Control for the Production of Hydrocarbon Liquid Fuels

The traditional FTS process produces a mixture of hydrocarbons with a broad distribution, obeying the classical ASF distribution. Under such circumstances, the selectivity to middle-distillate hydrocarbons as liquid fuels through FTS is very limited. To break the selectivity limitation and improve the quality and fraction of specific liquid fuels, the development of highly efficient catalytic systems is needed [11].

As shown in Figure 3.4, there are two typical routes for the selectivity control of liquid fuels. One is based on modified FTS catalysts, and the other uses bifunctional catalysts that compose of an FTS catalyst (i.e. Fe_xC_y, Co, and Ru) for FTS to heavy hydrocarbons and a solid acid catalyst (typically a zeolite) for the hydrocracking/isomerization of hydrocarbons to target products. Another bifunctional catalyst via the non-FT route is based on the configuration of metal oxides and zeolites [48].

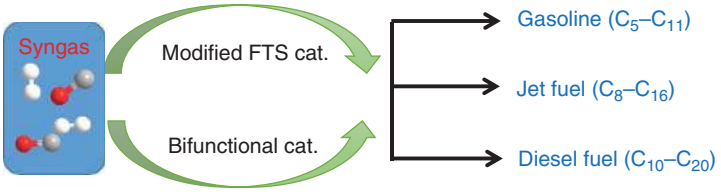

Figure 3.4 Direct conversion of syngas to liquid fuels over modified FTS catalysts or bifunctional catalysts.

3.3.1 Modified FTS Catalysts for Selectivity Control of Liquid Fuels

The modified FTS catalysts are similar to the traditional FTS catalysts. The product distribution is always tuned by adding promoters and supports or tailoring the active site structure and the microenvironment. Kang et al. reported a supported Ru/CNT catalyst for the selective production of diesel-range fuel (C_{10}–C_{20}) with selectivity of 65% at CO conversion of 34% [49], and the methane selectivity was only 8.3%. They found that the supports, CNT pretreatment, and Ru particle size played key roles in determining the product distribution. A Ru/CNT catalyst with a mean Ru size of ~7 nm showed the highest TOF and selectivity to C_{10}–C_{20} hydrocarbons. Smaller Ru particles (<6 nm) exhibited lower activity than the larger ones. They speculated that CNTs with acidic functional groups on surface could adsorb hydrogen species, which might favor the mild hydrocracking process. Recently, the group of Tsubaki successfully fabricated a size-uniformed Co nanoparticles embedded in mesoporous SiO_2 [50]. By changing the confined Co particle size from 7.2 to 11.4 nm, the FTS product distribution can be easily tuned from the diesel fraction (66.2%) to the gasoline fraction (62.4%) at a very high CO conversion (~80%). It was found that the confined structure can prevent the aggregation of Co nanocrystals and the escape of reaction intermediates during FTS. The C* species can be strongly adsorbed and captured on the smaller Co particles, which further form a large amount of CH_x intermediates in the confined space, and the heavy hydrocarbons are generated easily. It should be noted that this phenomenon is quite different from the traditional recognition that larger Co crystallites are of benefit for the carbon chain growth to form heavier hydrocarbons.

3.3.2 Bifunctional Catalysts for Selectivity Control of Liquid Fuels

The bifunctional catalytic route is the most reported in highly selective production of a specific range of liquid fuels. The tandem catalysis route is especially often investigated as it can enable the occurrence of the FTS and hydrocracking/isomerization processes in one reactor. FT metal (Co, Ru) and metal carbide can be applied for the FTS process, while zeolites can be used as acid sites for the hydrocracking/isomerization process. Different catalyst configurations have been investigated for the optimization of reaction coupling, such as the dual-bed model (up, FTS catalyst; down, zeolite), the mixed bed model (i.e. physical mixture), the core–shell structure model (FT catalyst as core and zeolite as shell), and the

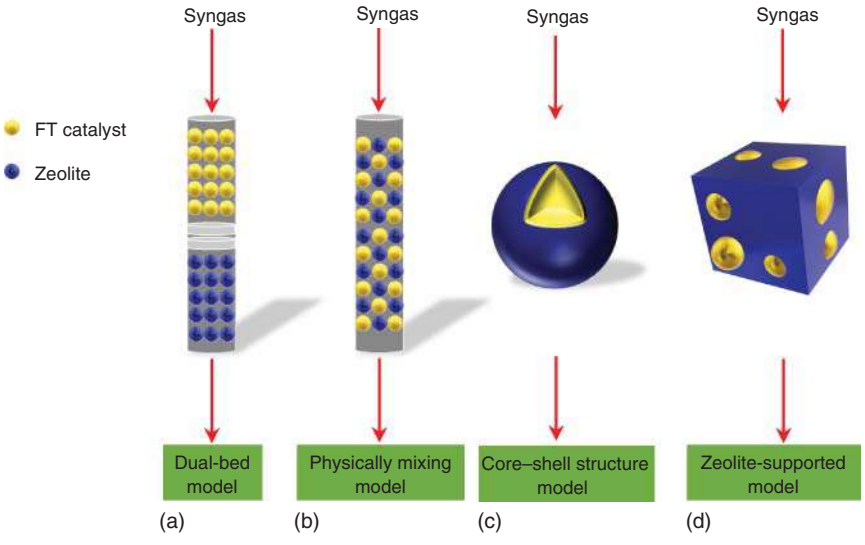

Figure 3.5 Configurations for two components of bifunctional catalysts. (a) Dual-bed model, (b) physically mixing model, (c) core–shell structure model, and (d) zeolite-supported model.

zeolite-supported FT catalyst component model, as shown in Figure 3.5 [1, 51]. The latter two models attract the greatest attention with great breakthroughs in recent years, and these will be discussed in this section.

Generally, for syngas conversion to middle-distillate liquid fuels with high selectivity, bifunctional catalysts with mesoporous or hierarchical zeolites are more preferred than microporous zeolites. The presence of mesopores not only promotes mass transport but also improves both metal dispersion and proximity between the metal and acid sites, which contributes to the enhancement of CO conversion and suppression of the production of short chain paraffins. In addition, the mesoporous zeolite enhances the catalytic stability by inhibiting coke deposition. With respect to the acidic property, the zeolites with relatively stronger Brønsted acidity favor the cleavage of C—C bonds to produce gasoline-range fuels. In addition, the Brønsted acid sites can catalyze the isomerization reaction to form iso-paraffins, thus increasing the iso-paraffin/*n*-paraffin ratio and thus the research octane number (RON), which is desired for the commercial gasoline fuels. For the purpose of diesel-range fuels, zeolites with relatively lower densities of Brønsted acid sites are required. The main concern is how to inhibit the formation of CH_4 and short-chain hydrocarbons due to the over-cracking of hydrocarbons. In addition, the proximity between FT metal and acid sites exhibits a profound influence upon the catalytic performance. Close proximity between these two types of active sites may promote the hydrocracking and isomerization of heavier hydrocarbons [52], and thus the proximity should be precisely controlled according to the target liquid fuels desired.

Promoters have also been incorporated into bifunctional catalysts to moderate the hydrocarbon distribution [53].

As far as the core–shell structure bifunctional catalysts are concerned, traditional FTS catalysts, such as Co/Al_2O_3, Co/SiO_2, fused Fe, $Fe_3O_4@SiO_2$, and RANEY® Fe, are always used as the core, while the shell is a zeolitic component, such as ZSM-5 or β. The heavier hydrocarbons produced on the FT active sites can diffuse out through the zeolite channel, where the hydrocracking/isomerization reactions take place on the acid sites. The thickness of the zeolite shell should be controlled precisely as the mass transport and proximity between these two kinds of active sites should be considered. Typically, the zeolite shell grows easily around the FT catalyst core, and the challenge is to prevent the FT metal being destroyed by the strong alkaline conditions required for zeolite crystallization. An efficient strategy is to prepare Si- or Al-coated FT catalysts as core in the first step [54]. The Si or Al layer can not only protect the FT metal but also induce the formation of zeolite shell. The group of Tsubaki has developed different types of core–shell structure bifunctional catalysts for syngas conversion to gasoline-range fuels, and a maximum selectivity of about 72% can be obtained using Co/SiO_2@H-ZSM-5 as catalyst [55]. Sun and coworkers reported a RANEYFe@H-ZSM-5 with ∼4.1 μm of shell thickness for CO hydrogenation, and the selectivity of C_5–C_{11} slate reached 71% with 1.9 of C_{iso}/C_n at CO conversion of 93% [56].

Zeolite-supported FT catalysts were also studied to obtain high selectivity to the special range of fuels. The group of Wang successfully developed a series of efficient supported bifunctional catalysts for the highly selective production of gasoline, jet, and diesel fuel at a higher CO conversion (>30%) [53, 57–61]. In their study, the fraction of C_5–C_{11} hydrocarbons is typically higher than 70%, and the C_{iso}/C_n ratio is >2.3 using Ru/meso-ZSM-5 [59], Ru/meso-β [58], and Co/meso-ZSM-5 [57] as bifunctional catalysts. The selectivity of C_{10}–C_{20} hydrocarbons typically exceeded 58% using Co/K-meso-Y, Co/Na-meso-Y [61], and Co-Mn/Na-meso-Y [53] as catalysts. In addition, Kim reported a similar C_5–C_{11} selectivity (77.3%) and C_{iso}/C_n ratio (2.9) but at a much higher CO conversion (79%) over a Co/NS-MFI bifunctional catalyst [62]. They found that mesoporous zeolites with medium mean size of ∼5 nm benefited the production of C_5–C_{11} hydrocarbons [59]. They further found that the Co/Na-meso-Y catalyst exhibited superior diesel fuel selectivity compared with the Co/H-meso-Y counterpart. Further studies suggested that the mean Co size of 8.4 nm, average mesopore size of 15 nm, and addition of Mn as promoters could greatly increase the selectivity to C_{10}–C_{20} hydrocarbons. Recently, Li et al. successfully fabricated a series of Co/M-meso-Y bifunctional catalyst for syngas conversion [60]. By modifying the meso-Y zeolite with Ce^{4+}, La^{3+}, and K^+ ions via the ion exchange method, the acidity of zeolite could be readily tuned, and the as-obtained Co/Ce-meso-Y, Co/La-meso-Y, and Co/K-meso-Y catalysts showed outstanding selectivity toward gasoline, jet fuel, and diesel fuel with selectivities of 74%, 72%, and 58%, respectively. They proposed that the porous and acidic properties of meso-Y zeolites played a determining role in regulating the product distribution.

3.4 Selectivity Control for Production of Chemicals

3.4.1 Syngas to Olefins

Olefins, including lower olefins ($C_{2-4}^{=}$) and long-chain olefins ($C_{5+}^{=}$), are one of the most important building blocks in the chemical industry. Currently, lower olefins are mainly produced from naphtha cracking or fluid catalytic cracking. In China, lower olefins are also produced through methanol-to-olefin (MTO) route. However, it is still very desirable to develop one-step transformation routes for syngas to olefins, which are more energy and cost efficient.

In the latest decade, significant advances have been achieved in this filed. Generally, there are two classical routes for the direct conversion of syngas to olefins: one is the well-known Fischer–Tropsch-to-olefin (FTO) process [63], and the other is the oxide–zeolite bifunctional route with methanol or ketene as the intermediates [11], as shown in Figure 3.6. Most of these investigations focus on the maximization of the selectivity to lower olefins meanwhile hindering the formation of methane with high catalytic stability.

3.4.1.1 Fe-Based FTO

Fe-based catalysts are prevailing for FTO reaction due to the higher proportion of olefins and less reactive for the secondary hydrogenation reaction compared with Co-based counterparts. SASOL has produced various fuels and chemicals including lower olefins by FT industrial process. However, only 6% selectivity to $C_{2-4}^{=}$ was formed in the low-temperature FT process (LTFT), and the maximum selectivity to lower olefins was about 24% for the high-temperature FT process (HTFT).

Similar to the Fe-based FTS, the χ-Fe_5C_2 is generally accepted as the active site for FTO [64, 65]. The structure evolution of iron species under working conditions and the corresponding reaction mechanism are the research interests of academic community. As the traditional bulk iron catalysts are mechanically unstable at high temperature, supported iron-based catalysts are usually applied for the FTO reaction [63]. To avoid the SMSI, inert supports or carbon materials and modified carbon materials have been widely reported recently. Examples include α-Al_2O_3 [66], SiC [66], CNFs [66], CNTs [67], N-doped carbon materials [68], activated carbon (AC), graphene [69], and graphene oxide [70]. Additionally, promoters such as S, Na, K, Mn, and Zn are often added to the Fe-based catalysts. These supports and promoters

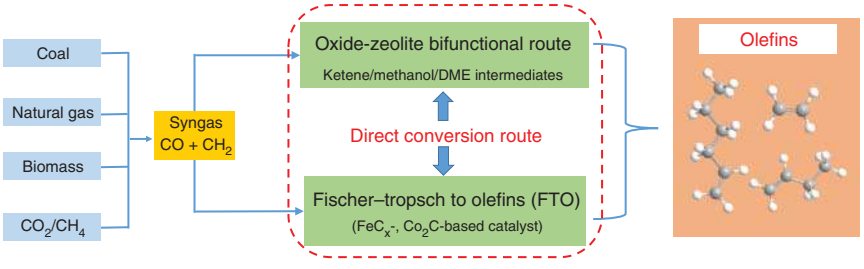

Figure 3.6 Direct conversion of syngas into olefins via different catalytic processes.

play a vital role in obtaining excellent FTO performance with high selectivity to olefins via promoting the formation of iron carbide. Among them, K-promoted FeMn-based catalysts are the most widely studied for FTO [63]. Although some papers reported that Fe-based catalysts showed very high activity and olefin selectivity under some circumstances, poor stability is one of the most widely encountered problems. With the use of inert supports, the weak physical binding between iron particles and the support surface may lead to particle aggregation.

A major breakthrough in Fe-based FTO was reported with CNF or α-Al_2O_3 supported iron carbide nanoparticles in the presence of Na and S as promoters [66]. The lower olefin selectivity reached 61% at a very low CO conversion. The methane selectivity, however, was as high as ~23%. The weak MSI promoted the formation of iron carbide. The sulfur promoter can selectively block the hydrogenation site, thus suppressing methane production and increasing olefin selectivity.

As for the effect of iron carbide particle size, Galvis et al. proposed that small particles possessed abundant highly active low coordination sites residing at corners and edges, where methane formation preferentially takes place, while the terrace sites of particles are available for the production of lower olefins, which would be affected by the addition of Na and S promoters [64]. Steady-state isotopic transient kinetic analysis (SSITKA) indicated that the coverage of CH_x and H species on iron carbide surface increased with decreasing particle size from 6.9 to 2.2 nm, resulting in higher TOF and methane selectivity on smaller particles. In addition, the formation rate of CH_4 would be accelerated on the edges and terraces of unpromoted χ-Fe_5C_2 according to the measurement of CH_x residence time. The addition of Na/S promoter decreased the coverage of H species, significantly suppressing the formation of CH_4 on the terraces site [71].

As for the iron carbide phase, Cheng and coworkers reported a K-promoted Fe/rGO (reduced graphene oxide) catalyst for the FTO reaction, which showed a very high lower olefin selectivity (68%) with O/P ratio of 11% and 20% of CH_4 selectivity [70]. Synchrotron radiation XRD verified that the χ-Fe_5C_2 was the predominant iron phase. The addition of K promoted the formation of χ-Fe_5C_2 carbide while a negative effect was also observed. In a very recent work, Zhai et al. prepared a Na and Zn-modulated Fe_5C_2 catalyst for syngas conversion to long-chain olefins [65]. The selectivity to total olefins and C_{5+} olefins was as high as 79% and 51%, respectively, with 9.7% CH_4 selectivity and 23.8% CO_2 selectivity at CO conversion of 77.2%. It is suggested that the Zn as structural promoter can greatly influence the size of iron species, while the Na as the electronic promoter can enhance the desorption of olefins and suppress the secondary hydrogenation of olefins.

3.4.1.2 Co-Based FTO

In the traditional FTS reaction, metallic Co is recognized to be the active phase for FTS, and the cobalt oxides and cobalt carbide are often considered as inactive or lower activity phase during FT process. Recently, significant progress has been made in the development of Co_2C for FTO reaction. Zhong et al. successfully prepared Co_2C nanoprisms derived from CoMn composite oxide catalysts via a coprecipitation method and found that it exhibited excellent FTO performance (Figure 3.7) [72]. At

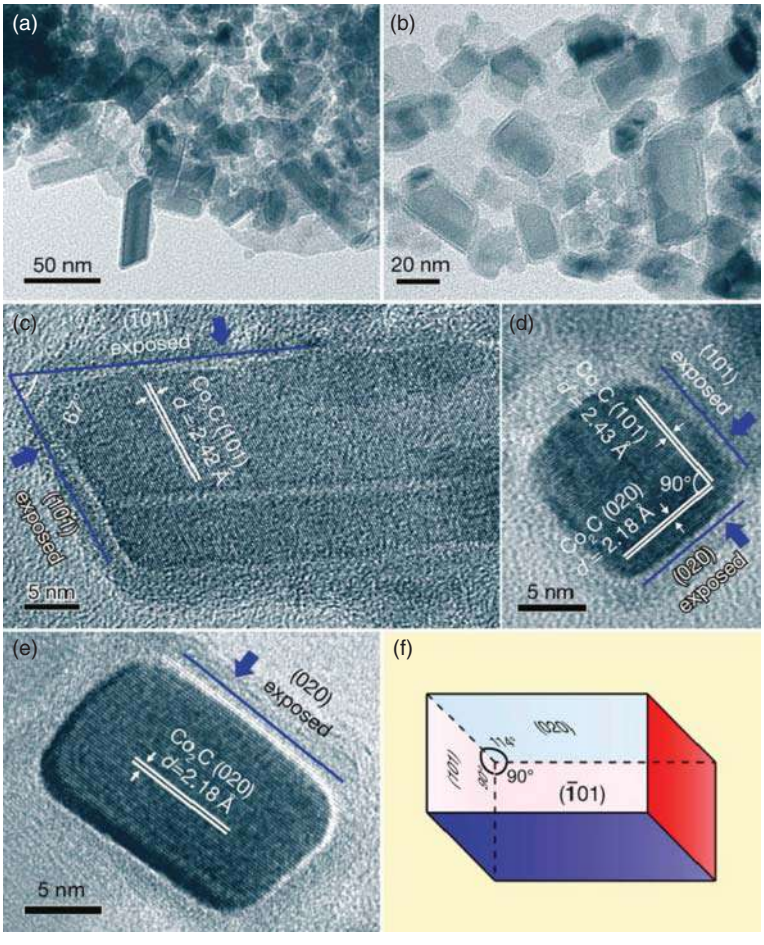

Figure 3.7 TEM characterization of the CoMn catalysts at the steady stage of reaction. (a, b) Low-resolution TEM images, (c–e) high-resolution images of Co_2C nanoprisms with exposed facets of (101), (−101), and (020), (d) distance (length) of the lattice fringes, and (f) Co_2C nanoprisms model with four rectangular faces and two rhomboid faces. Source: Reproduced with permission from Zhong et al. [72]; © 2016, Springer Nature.

250 °C, 1 bar, H_2/CO ratio of 2, and 2000 ml h^{-1} g^{-1}, the lower olefin selectivity was as high as 60.8% with very low selectivity to methane (5%) at CO conversion of 31.8%. The hydrocarbon distribution significantly deviated away from the classical ASF distribution, and the O/P ratio of C_{2-4} reached 30, which increased to 51 when a lower H_2/CO ratio ($H_2/CO = 0.5$) was applied. This catalyst showed very good stability at least for 600 hours under industrially relevant operating conditions. Combined with DFT theory calculations and advanced characterization techniques, a significant morphology and facet effect for Co_2C was reported. The Co_2C nanoprism structure with specific exposed facets of (101) and (020) could gradually evolve during reaction, and the as-obtained facet could effectively suppress the formation of methane and favor the C–O activation and C–C coupling. In-depth studies suggested that the

Na promoter, acting as electronic donor to cobalt, could enhance the formation of Co_2C via accelerating the carburization rate [73]. The Mn promoter mainly worked as a structural promoter and combined with Co to form CoMn composite oxides (i.e. spinel structure, $Co_xMn_{1-x}O$), which played a vital role in formation of Co_2C nanoprisms [74]. This proposal was further confirmed by the work of Liu, where they deduced that the value of x in $Co_xMn_{1-x}O$ was in the range of 0.6–0.85 [75]. In addition, the addition of Mn could be used to tune the exposed facet proportion of the Co_2C nanostructures, with higher Mn loading resulting in a higher facet proportion of $Co_2C(020)$, which exhibited higher intrinsic activity and lower methane selectivity [76]. However, the addition of CO_2 into the feed could inhibit the formation of olefins, which was quite different from that reported for Na–FeZn catalyst in Fe-based FTO process [77]. It was found that increasing CO_2 content hindered the adsorption of CO and surface intermediates, creating a CO-lean and H-rich surface microenvironment, which changed the morphology of Co_2C nanostructures from nanoprisms to nanospheres and induced the appearance of metallic Co through decomposition of Co_2C. Correspondingly, the formation of olefins was suppressed, and the methane production was promoted.

The morphological control of Co_2C is a key parameter in determining its superior performance for syngas conversion to olefins. Further studies in Zhong's group suggested that the control of reduction conditions (Figure 3.8), and the nature of supports could effectively construct the Co_2C nanoprisms [78, 79]. Using 10% CO-300 °C, 10% H_2-300 °C, and 10% H_2-250 °C as the reduction conditions, Co_2C nanoprisms were formed with high $C_{2-4}^=$ selectivity and low CH_4 selectivity. However, a mixture of Co_2C nanoprisms and nanospheres was obtained in the spent sample using 10% H_2-350 °C. If the catalyst was reduced by CO-300°C and 10% H_2-400 °C, a large fraction of Co_2C nanospheres were obtained, which showed low FTS activity and high selectivity to methane. Besides, the impregnation method with CNF as support could fabricate Co_2C nanoprisms, which showed higher

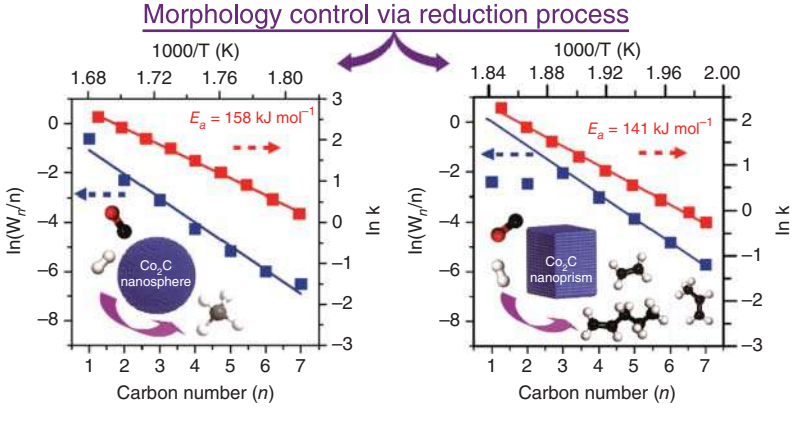

Figure 3.8 Morphology control of Co_2C nanostructures via reduction process for direct production of lower olefins from syngas. Source: Reproduced with permission from An et al. [78]; © 2018, Elsevier.

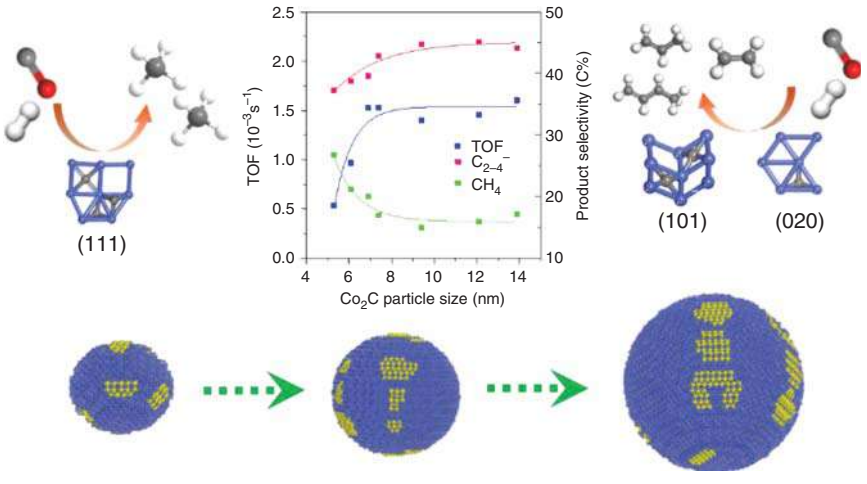

Figure 3.9 Particle size effect of Co_2C on FTO catalytic performance. Source: Reproduced with permission from Dai et al. [80]; © 2018, American Chemical Society.

selectivity to value-added chemicals (olefins and oxygenates) than the SiO_2- and γ-Al_2O_3-supported catalysts. They concluded that a relative weak cobalt-support interaction was necessary for obtaining CoMn composite oxides during calcination, which acted as a prerequisite for the formation of Co_2C nanoprisms with excellent catalytic performance for olefin production via syngas.

The particle size effect of Co_2C on FTO catalytic performance was also investigated, as shown in Figure 3.9 [80]. The TOF, lower olefins, and olefin-to-paraffin ratio increased while CH_4 selectivity decreased as the size of Co_2C increased from 5.3 to 7 nm. However, when the Co_2C nanoparticles were larger than 7 nm, both the intrinsic activity and product selectivity were independent of the particle size. DFT calculations revealed a strong correlation between Co_2C particle size and exposed facets. The smaller Co_2C particle size (<6 nm) mainly exposed the (111) facet, and increasing particle size resulted in the appearance of a large number of Co_2C(101) and Co_2C(020) facets, which favored the formation of olefins while suppressing the methane production.

Besides Co_2C, a very recent study from the group of de Jong showed that a Co/Mn/Na/S catalyst catalyzed CO hydrogenation to C_2–C_4 olefins with selectivity of 54% at 240 °C and 1 bar. Characterization results suggested that the HCP Co metal particles of size of 10 nm constituted the active site for FTO reaction, and the synergistic effect of Na plus S, acting as electronic promoters, promoted the selective production of lower olefins [81].

3.4.1.3 Bifunctional Catalysts for Syngas to Olefins

The FTS route over iron carbide or cobalt carbide catalysts can produce at most ~60% of lower olefins ($C_{2-4}^{=}$) due to the limitation of the ASF distribution. To further enhance the olefin selectivity, many attentions have been directed toward the development of non-FTS routes to break the selectivity limitation. Recent

progress showed that by adopting a reaction-coupling strategy [82] and an OX-ZEO concept [83], highly efficient bifunctional catalysts composed of two separate components could be fabricated, which exhibited very high selectivity to lower olefins (>75%) in hydrocarbon during CO hydrogenation process. The bifunctional catalysts are usually prepared by physically mixing of the two components. The reducible oxide component (i.e. $ZnCrO_x$ [83, 84], $ZnO\text{-}ZrO_2$ [85], MnO_x [86], and ZnO [87]) is responsible for the CO activation to carbon-containing intermediates such as methanol/dimethyl (CH_3OH/DME) or ketene, while the zeolite component is responsible for C–C coupling. SAPO-34 is highly suitable for the diffusion of lower olefins and is usually used for C—C bond formation. Other zeolites such as SSZ-13 [88] with a similar CHA-topology to SAPO-34 and AlPO-18 [84] possessing the AEI framework have also been reported to show excellent performance for the selective coupling of the intermediates to lower olefins. The selective synthesis of ethylene with high selectivity (76%) can be achieved with mordenite (MOR) as the zeolite component [89]. Thermodynamically, the CH_3OH/DME or ketene synthesis is feasible at temperatures ≤400 °C, while olefin formation on zeolites (i.e. the MTO reaction) typically requires temperatures of ≥400 °C. The reported optimal reaction temperature is therefore around 400 °C for the bifunctional catalysts.

Bao and coworkers developed a bifunctional catalyst composed of $ZnCrO_x$ and MSAPO (mesoporous SAPO) that enabled the conversion of syngas to lower olefins with selectivity of 80% at CO conversion of 17% at 400 °C, 2.5 MPa pressure, and a H_2/CO ratio of 1.5 [83]. The group of Wang integrated a CH_3OH/DME synthesis catalyst and MTO catalyst into a single bifunctional catalyst and achieved direct syngas conversion to lower olefins (Figure 3.10). The reported $ZnO\text{-}ZrO_2$/SAPO-34 catalyst provided 74% selectivity to lower olefins at a CO conversion of 11% under 400 °C, 1.0 MPa, and a H_2/CO ratio of 2 [82]. By replacing SAPO-34 with SSZ-13 as the zeolite component while retaining $ZnO\text{-}ZrO_2$ as the oxide component, the as-obtained catalyst achieved 87% of selectivity to lower olefins at CO conversion of 10%. Increasing CO conversion to 29% slightly decreased the olefin selectivity to 77% [88]. It was found that the Zn/Zr molar ratio, the density of zeolite Brønsted acid site, the metal oxide/zeolite weight ratio and their proximity played a crucial role in the catalytic performance of the bifunctional catalysts. In-depth studies revealed that CH_3OH/DME was the key intermediate, the production of which constituted the rate-determining step over the bifunctional catalyst.

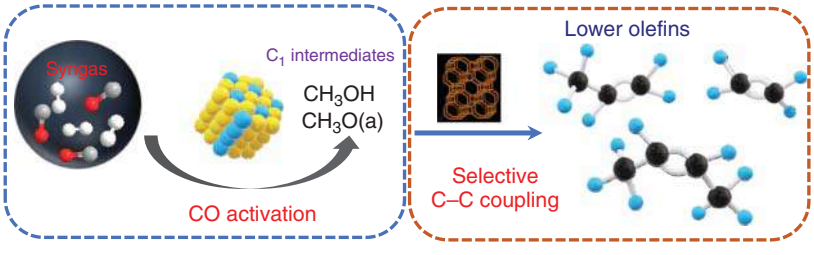

Figure 3.10 Reaction coupling of methanol synthesis and methanol to olefins for direct production of lower olefins via syngas.

3.4.2 Syngas to Aromatics

Aromatics are one of the most important bulk chemicals that are widely applied for fuel additives and the production of polymers. With the depletion of petroleum resources and the gradual shift of cracking feedstock from naphtha to ethane derived from shale gas, the coproduction of aromatics based on the petroleum route will be affected in the future, and it is necessary to develop alternative green routes for the production of aromatics.

Recently, syngas to aromatics (STA) over bifunctional catalysts has attracted much attention, and some significant advances have been achieved [11, 90]. According to the category of intermediates, the STA process can be classified into two classical routes as shown in Figure 3.11, i.e. (i) STA via olefins as intermediates (syngas to olefins and further to aromatics, denoted as SOA) by combining FTS catalysts and zeolite catalysts, and (ii) STA via methanol/dimethyl ether as intermediates (syngas to methanol/dimethyl ether and further to aromatics, denoted as SMA) with oxide–zeolite as combined catalysts [91]. These highly efficient catalysts are generally prepared by a simple physical mixture, and they are loaded into a single reactor and run under uniform reaction conditions.

3.4.2.1 STA via Olefins as Intermediates (SOA)

In the process of SOA, a bifunctional catalyst is usually prepared comprising an FTO catalyst for olefin formation and a zeolite for olefin dehydrogenative aromatization. HZSM-5 is the most widely reported zeolite to convert olefins to aromatic hydrocarbons, and the reaction temperature is usually higher than 300 °C. To match the working temperature of zeolites, high-temperature Fe-based FTO catalysts are the preferred choice for olefin formation [92–94]. Current research mainly focuses on regulating the total reaction network to obtain aromatics with high selectivity by designing a highly efficient Fe-based FTO catalyst and a HZSM-5 zeolite with a unique hierarchical pore structure and moderate acidity.

Zhao and coworkers successfully fabricated a tandem catalyst including components of Na-Zn-Fe_2C_5 and hierarchical H-ZSM-5 for one-step syngas conversion to aromatics via olefins as intermediates, and the aromatics selectivity could be up to 51% at CO conversion >85% [92]. They reported that almost all of the olefins participated in the aromatization process and the long-chain olefins could directly cyclize producing aromatics without oligomerization. The acid sites provided by the zeolite directly crack the C_{12+} hydrocarbon into olefins, which were further transformed into aromatics and light paraffins through the complex process of oligomerization, cyclization and hydrogen transfer. The mild density and strength of Brønsted acid

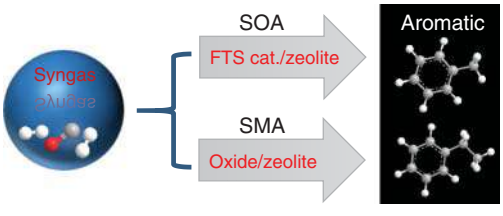

Figure 3.11 Bifunctional catalysts for direct conversion of syngas into aromatics.

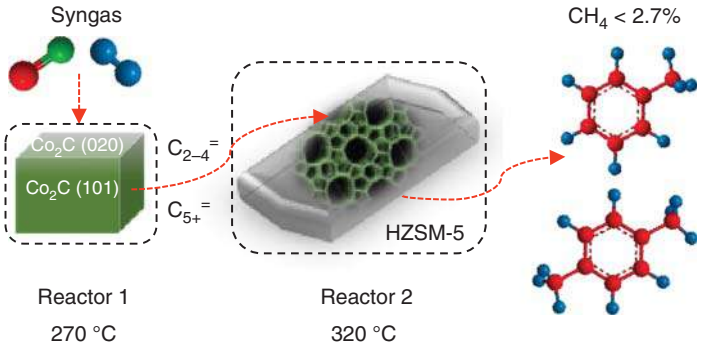

Figure 3.12 Syngas conversion to aromatics over Co_2C-based catalyst and HZSM-5 via tandem system. Source: Reproduced with permission from Sun et al. [95]; © 2020, American Chemical Society.

sites and the hierarchical pore structure of HZSM-5 contribute to the outstanding performance for aromatic production from syngas conversion. Xu et al. fabricated a bifunctional catalyst composed of core–shell Fe_3O_4@MnO_2 and hollow HZSM-5 (granule mixing) enabled the conversion of STA with 57% selectivity at >90% CO conversion. No obvious catalyst deactivation could be observed for 180 hours of reaction testing [93].

As Co_2C catalysts show high selectivity toward olefins and can effectively inhibit the CH_4 formation, the combination of Co_2C with zeolites has also been used to produce aromatics [95]. Recently, Sun et al. reported that a two-stage tandem reactor system with Co_2C in the upstream reactor and HZSM-5 zeolite in the downstream reactor exhibited better performance in aromatics production compared with other catalyst configurations (Figure 3.12). The aromatics selectivity was as high as 55.5% with trace amounts of methane being produced at a CO conversion of 34.9%. This work provides an effective route for the direct production of aromatics via the conversion of syngas derived from alternative non-petroleum feedstock.

It should be noted that the aromatics selectivity depends on the content of olefin intermediates, which is determined by the FTO catalysts. In the process of SOA, it is also hard to avoid the hydrogenation of olefins intermediates, which will decrease the aromatics selectivity for majority of the bifunctional catalysts reported.

3.4.2.2 STA via Methanol/Dimethyl Ether as Intermediates (SMA)

As a non-FTS route, the SMA process requires a bifunctional catalyst composed of a methanol synthesis (MS) catalyst and a CHA zeolite component for methanol or dimethyl ether to aromatics (MTA). For the reported efficient SMA catalysts, metal oxides with solid solution or spinel structure are generally applied for MS at high temperatures, such as ZnZr [96], ZnCr [97], CeZr [98], and MoZr [91]. These metal oxides with oxygen defect sites combined with HZSM-5 can obtain very good STA performance, and the aromatic selectivity is generally >70%. The composition and size of the metal oxides, the concentration of oxygen defect,

and the proximity between the two components are key parameters controlling the catalytic performance. For HZSM-5, the density of Brønsted acid sites, the distribution of acid sites, and the pore structure are also very important factors. Typically, a close contact between oxides and zeolites is preferred. It is recognized that a lower density of Brønsted acid sites of HZSM-5 (higher Si/Al ratio) is more favorable for the SMA process than the MTA process alone. Selectively poisoning the external acid site of zeolite by silica deposition [96] or coating the zeolite with a silica shell [99] can effectively increase the fraction of BTX (benzene, toluene, and xylene) fraction in the aromatic product distribution. It is demonstrated that the methanol or dimethyl ether formed on these oxides will transform into aromatics on HZSM-5 zeolite, where they are firstly converted into lower olefins with the subsequent oligomerization to higher olefins. The as-obtained higher olefins are further converted into aromatics by dehydrogenative cyclization [96]. One of the core concerns is to control the hydrogen transfer and alleviate or avoid the hydrogenation of olefin intermediates to paraffins.

Cheng et al. combined the $ZnO\text{-}ZrO_2$ and HZSM-5 zeolite to construct a bifunctional catalyst for the one-step conversion of STA [96]. The aromatic selectivity was as high as 80% at CO conversion of 20% under 400 °C, 3 MPa, $H_2/CO = 2$, and space velocity of 1500 ml g^{-1} h^{-1}. This catalyst showed very good catalytic stability over 1000 hours of testing. The relatively lower density of Brønsted acid sites of zeolite and the thermal stability of $ZnO\text{-}ZrO_2$ oxides and the appropriate proximity between two components contributed to the excellent STA performance. In addition, they observed the self-promotion effect of CO, which acted as a "hydrogen acceptor" to remove the hydrogen species formed during the aromatization process. The fraction of BTX in aromatics could also be tuned to more than 60% by selectively passivating external Brønsted acid sites of H-ZSM-5.

Recently, Arslan et al. prepared a bifunctional catalyst comprising nanosized $ZnCr_2O_4$ and coffin-shaped HZSM-5 with short straight channels [010] along the *b*-axis via physically mixing. The reported that the tetramethylbenzene (TeMB) selectivity was as high as ~70% in hydrocarbons at CO conversion of 37% for a H_2-deficient syngas ($H_2/CO = 1$) feedstock. When the H_2/CO ratio was tuned to 2, the total selectivity toward aromatics could reach up to 83.3% with a reduced TeMB selectivity (~52%) at a higher CO conversion (~48%). No obvious catalyst deactivation was observed for 600 hours of testing [100].

3.4.3 Syngas to C_{2+} Oxygenates

C_{2+} oxygenates are herein defined as linear alcohols or aldehydes with two or more carbon atoms and are also referred to as higher alcohols (HA, $C_{2+}OH$). The direct transformation of syngas into C_{2+} oxygenates (denoted as higher alcohol synthesis (HAS)) is highly attractive. In the synthesis of hydrocarbons via the syngas conversion route, almost all of the oxygen atoms in the gas feedstock (i.e. CO) are transformed into undesired CO_2 or H_2O, while these O-atoms in the HAS process are partially utilized in the form of oxygenate products, making it more economically favorable and conforming to the key principles of green chemistry [101].

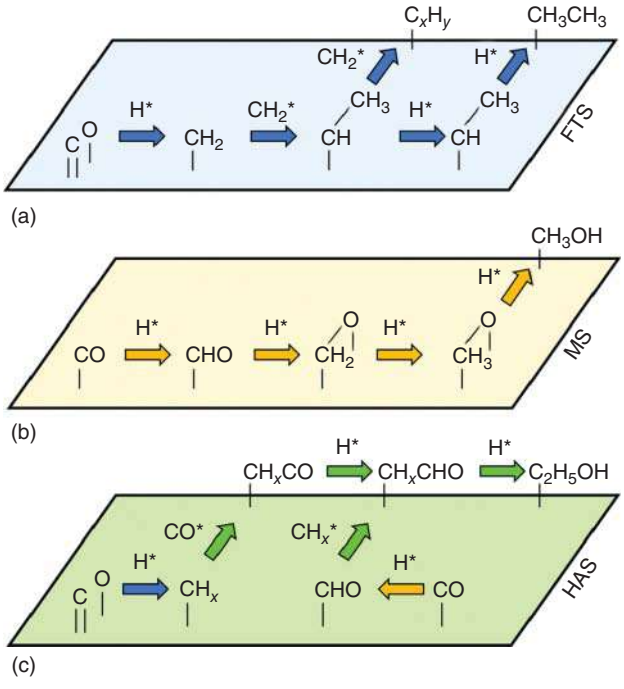

Figure 3.13 Simplified reaction process for (a) FTS, (b) methanol synthesis (MS), and (c) HAS involving a CO or CHO insertion step. Source: Reproduced with permission from Luk et al. [3]; © 2016, The Royal Society of Chemistry.

The reaction network for HAS is very complex and it is commonly accepted to follow the CO insertion mechanism as illustrated in Figure 3.13 [3]. A dual-site structure in close proximity with different functions is thus required as is widely recognized. In this concept, one active site catalyzes CO dissociation and carbon chain propagation, while the other active site works for CO non-dissociative activation and subsequent insertion, also denoted as an oxygen-containing process. To obtain C_{2+} oxygenates with high selectivity, the synergistic effect between dual-site structures is required [9, 102, 103]. However, the $C_nH_z^*$ intermediates tend to be hydrogenated to form hydrocarbons instead of coupling with CO^* (or CHO^*) species to form oxygenates, resulting in the relatively low selectivity to C_{2+} oxygenates.

Generally, the reported HAS catalysts can be classified into four types: modified MS catalysts, modified Fischer–Tropsch (FT) catalysts, molybdenum-based catalysts, and rhodium-based catalysts [3]. Among them, the modified FTS catalysts attract special attention and have been extensively studied over the past decade due to their superior performance for both selectivity and yield of C_{2+} oxygenates. We herein mainly review the significant advances made for the modified FTS catalysts with the emphasis on understanding the nature of active sites and the efforts made in strengthening the insertion process of oxygen-containing species by modifying the reaction network and catalyst design.

3.4.3.1 Co_2C-Containing Co-Based Catalyst for Syngas to C_{2+} Oxygenates

The promotional effect of Co_2C on the formation of oxygenates was reported prior to 2010 [104]. Recent studies provide a deeper understanding on the role of Co_2C and propose that Co_2C-Co work as dual active sites for HAS [105–110]. The metallic Co is responsible for the dissociative adsorption of CO and subsequent C–C coupling, while the Co_2C functions for the associative adsorption of CO and insertion to form oxygenates. Optimizing the Co_2C/Co ratio and tuning the formation of interface with high intimacy is one of the research directions. In addition, some work suggests that the Co_2C–oxide interface provides excellent selectivity to C_{2+} oxygenates [109].

Numerous studies focus on the promotional effects of supports and promoters on the formation and stability of Co_2C and the Co-Co_2C interface by combing experimental study and theoretical calculations. Carbon materials are the most widely reported supports due to their promotional effects on the formation of Co_2C [106, 107, 111], similar to that reported for Fe-based FT/FTO catalysts. Common promoters include Mn [108, 112], alkali metals [108, 109, 113], alkaline earth metals [114], La [106, 111], and Zn [115].

In 2011, Lebarbier et al. reported that the La_2O_3 promoter and AC support played an important role for the formation of Co_2C and enhancement of the C_{2+} oxygenate selectivity [106]. DFT calculations suggest that the CO insertion into CH_x species over Co_2C is energetically favorable with a very low activation energy barrier, while CO dissociation and carbon chain growth are favored on Co metal. These CH_x species can exist stably at the interfacial boundary between Co/Co_2C and oxide phase, which also show lower-energy barrier for C–C coupling with either CO or CH_x species. The authors therefore proposed that the selectivity to oxygenates could be improved by increasing the Co_2C/Co ratio and by tuning the structure of the boundary sites. Zhang and coworkers claimed that Co_2C crystal facets played an important role in C_2 species formation through elaborate DFT calculations [105]. The Co_2C (111) facet is very efficient for the production of C_2 oxygenates, while the Co_2C(101) and (110) facets show high selectivity to C_2 hydrocarbon. In addition, the Co/Co_2C(111) interface catalyst is the most favorable for C_2 oxygenate synthesis compared with the other catalysts. Controlling the exposed facet of Co_2C and the interface structure of Co/Co_2C can regulate the FTS products from hydrocarbons to alcohols.

Ding and coworkers successfully prepared highly active unsupported and AC-supported Co-Co_2C catalysts for HAS via the FT reaction (Figure 3.14) [107]. For the Co-Co_2C/AC catalyst, the CO conversion was as high as 71.4% with alcohol selectivity of 38.4%, where more than 91.6% of the produced oxygenates are $C_{2+}OH$, which was better than the bulk Co-Co_2C catalyst. In combination with DFT calculations, they demonstrated that the (111) surface of Co_2C could serve as the active site for the non-dissociative adsorption of CO and the formation of stable Co_2C and the Co-Co_2C interface were very efficient in strengthening CO insertion to CH_2 intermediates to form oxygenates.

Recently, Xiang et al. prepared a highly efficient CoMnK catalyst and the sum selectivity of aldehydes and alcohols is about 50 wt% at a very low CO conversion (<3%) over $Co_4Mn_1K_{0.1}$ catalyst under 200 °C and at 4.0 MPa pressure. Upon

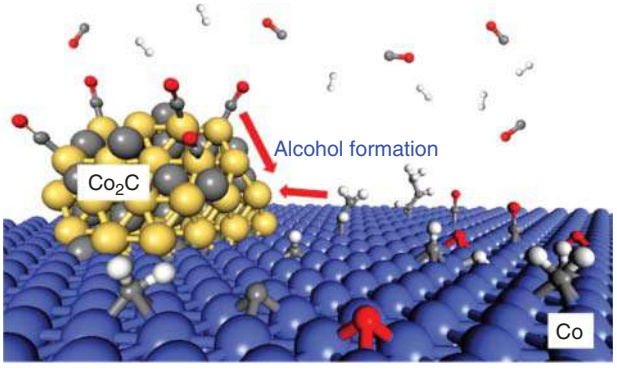

Figure 3.14 Schematic depiction of the formation of higher alcohols via syngas conversion over cobalt metal/carbide interface. Source: Reproduced with permission from Pei et al. [107]; © 2015, American Chemical Society.

elevating the reaction temperature to 280 °C, the CO conversion was enhanced to more than 40% while the oxygenates selectivity remained at about 50 wt% (CO_2-free). It is surprising to note that no metallic Co could be detected under this harsh reaction conditions, and the bulk Co_2C constituted the main Co phase. They suggested that the synergistic interaction between Co_2C and Mn_5O_8 resulted in the unique product distribution [109].

Yang et al. synthesized a NaCoMn catalyst to catalyze CO hydrogenation to C_{2+} oxygenates [108]. Over a CoMn-SC (0.8 Na) catalyst, the selectivity to $C_{2+}OH$ was as high as 33.0% (CO_2-free) at a CO conversion of 11.4%. Studies suggested that the Na promoter could benefit the carburization of Co^0 to Co_2C and the occurrence of Co-Co_2C as bifunctional dual-site contributing to the increasing C_{2+} oxygenates. A similar phenomenon was observed by varying the reaction pressure from 0.1 to 4.0 MPa. At atmospheric pressure, pure Co_2C nanoprisms were constructed and showed very high selectivity to olefins with negligible amounts of oxygenates. Increasing pressure, however, led to increasing oxygenate selectivity. Further structural characterization verified that the evolution from Co_2C to a mixture of Co/Co_2C could tune the product distribution from characteristic FTS to HAS [116].

In addition to adding promoters or supports to tune the structure of Co-Co_2C, the regulation of the reaction network by constructing several types of active sites with complementary properties is another novel strategy to tailor the production of C_{2+} oxygenates. Very recently, a significant advance in converting syngas to C_{2+} oxygenates with high selectivity and high stability was reported by Lin et al. via fabricating a multifunctional catalyst composed of CoMn oxides and CuZnAlZr oxide (Figure 3.15) [110]. The total selectivity to value-added chemicals (oxygenates and olefins) reached 80.6 wt% at CO conversion of 29.0%. The proximity between CoMn and CuZnAlZr component plays a crucial role in tuning the product distribution. The CoMn|CuZnAlZr catalyst with granule stacking configurations showed the best HAS performance, and the C1 product slates including methanol, CH_4, and CO_2 were strongly suppressed. The fraction of $C_{2+}OH$ in the oxygenate distribution was always above 98.0 wt% at reaction temperature of 200–240 °C, and

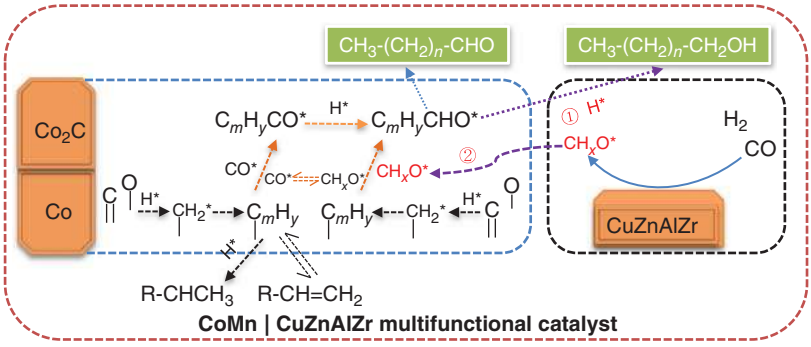

Figure 3.15 Proposed reaction pathways for oxygenate formation over CoMn|CuZnAlZr multifunctional catalyst. Source: Reproduced with permission from Lin et al. [110]; © 2019, Wiley-VCH.

that of $C_{5+}OH$ could even reach 87.6 wt%. This work suggests that the insertion process of oxygen-containing species can be effectively strengthened to allow the preferential production of C_{2+} oxygenates by increasing the concentration of CH_xO^* species. A similar strategy was also recently reported by fabricating $ZnCrAlO_x$|KNiMoSMMO-5 as multifunctional catalyst for HAS, and the CH_xO^* species obviously promoted the production of C_{2+} oxygenates [117].

3.4.3.2 Cu-Modified FTS Catalysts

Cu-modified FTS catalysts, denoted as CuCo- or CuFe-based catalysts, are generally used to produce C_{2+} oxygenates via syngas conversion. It is typically recognized that the Cu component can facilitate the dissociative adsorption of H_2 and enable the molecular adsorption of CO and subsequent insertion, while the FTS components, i.e. Co^0 and Fe_xC (mainly referring to Fe_5C_2), are responsible for the CO dissociative adsorption and carbon chain growth. The intimate contact between highly dispersed Cu and FTS components and their synergistic effect play a crucial role in obtaining higher selectivity to C_{2+} oxygenates. Any agglomeration behavior or phase separation between dual site will cause the deactivation [9], as illustrated in Figure 3.16. Although extensive studies were conducted for CuCo- or CuFe-based catalysts, many key scientific issues are still required to be further explored. For example, the nature of active site remains unclear, the role of Cu is controversial, and the rapid deactivation due to the unstable dual-site structure should be solved. It remains challenging to construct a CuCo or CuFe catalyst with stable and higher degree of interfacial boundary to shift the products from hydrocarbons to C_{2+} oxygenates. To solve these problems, many studies focus on the exploration of the effect of supports, promoters (i.e. Mn and Nb), and preparation methods via combining experimental design, theory calculation, kinetic studies, and advanced characterization techniques [3, 10, 103, 118]. Generally, CuCo core–shell structures and CuCo alloys were successfully prepared, and the catalyst derived from layered double hydroxide (LDHs) precursors [119–121] exhibited promising performance for HAS. Xiang and coworkers reported that a Co@Cu structure, comprising a Co-rich core structure and Cu-dominated

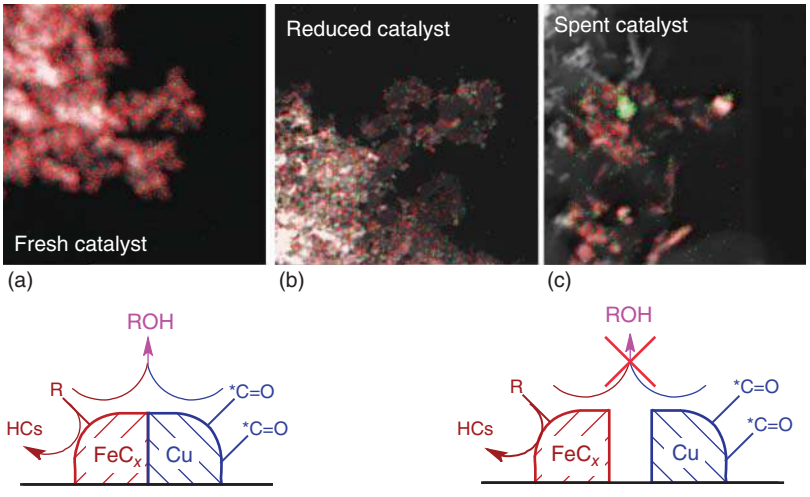

Figure 3.16 Structure evolution of CuFe-based catalyst during HAS reaction process. In the mapping EDS images of (a) fresh, (b) reduced, and spent (c) CuFe catalyst, the red denotes Fe distribution, and green denotes Cu distribution. Source: Reproduced with permission from Xiao et al. [102]; © 2013, Elsevier.

CoCuMn mixed shell, could effectively catalyze syngas to long-chain terminal alcohols (C_{7+} slate) [122]. They claimed that the catalyst preparation via oxalate route had a great influence on obtaining the core–shell structures with high specific surface areas.

Combing the DFT and microkinetic modeling, Prieto and coworkers predicted that the CuCo alloy with Co-rich surfaces was the preferred surface structure for HAS [123]. Gao et al. fabricated a highly efficient core–shell Cu@(CuCo-alloy)/Al_2O_3 catalyst for CO hydrogenation to HA, and the fraction of $C_{2+}OH$ in alcohols distribution reached 80.2 wt% (~40 C% of $C_{2+}OH$ selectivity). They claimed that the unique electronic/geometric interaction between Cu and Co could effectively avoid phase separation and elevate the selectivity to C_{2+} oxygenates [119]. Lu et al. reported that Cu^0-χ-Fe_5C_2 (510) derived from three-dimensionally ordered macroporous (3DOM) Cu_2-Fe_1 binary catalyst showed 58.4% of CO conversion and 26.2% of $C_{2+}OH$ selectivity [124]. The synergistic geometric and electronic interactions between Cu^0 and χ-Fe_5C_2 on the interface contributed to the enhanced HAVE performance. Very recently, the group of Ma successfully prepared an interfacial Fe_5C_2–Cu catalyst derived from $Cu_4Fe_1Mg_4$-LDH precursor for low-pressure CO hydrogenation to HA [121]. The Fe_5C_2–Cu interfacial catalyst exhibited CO conversion of 53.2% with selectivity of 27.2% and 14.8% for $C_{2+}OH$ and $C_{5+}OH$, respectively.

To strengthen the proximity of Cu and Fe, Luk and coworkers prepared a CNF-supported Cu_2Fe_1 catalyst by the sol–gel route, associated with 0.01 wt% of K content (CNF-2-0.01), the selectivity toward C_{2+} oxygenates was as high as 47%, and that of space time yield reached 220 mg g^{-1} h^{-1} at CO conversion of 8% under 270 °C, 5 MPa, 16 000 ml g^{-1} h^{-1}, and $H_2/CO = 2$ [125]. Upon changing the reaction conditions to 320 °C and 32 000 ml g^{-1} h^{-1}, the CNF-2-0.005 catalyst exhibited a

space time yield of 530 mg g^{-1} h^{-1} with 11% of CO conversion and 37% of $C_{2+}OH$ selectivity. The choice of carrier, preparation method, Cu/Fe ratio, and K amount could effectively tune the metal particle size and their proximity, which finally contributed to the enhanced HAS performance.

3.5 Summary and Outlook

Over the past decade, FTS to various value-added products such as clean liquid fuels, olefins, aromatics, and C_{2+} oxygenates has become one of the most interesting research topics in heterogeneous catalysis due to the rising concerns of energy consumption and the expected depletion of nonrenewable petroleum reserves. This chapter highlights some significant advances made in the field of FTS to fuels and chemicals via the development of highly efficient catalysts and novel reaction process, which can break the selectivity imposed by the ASF distribution limitation. Key catalyst factors affecting the catalytic performance in terms of activity, selectivity, and stability are summarized, and the nature of active sites for various reactions has been discussed. Benefiting from the development of advanced characterization techniques and powerful computer simulation, the evolution of active site structures and the fundamental mechanism can be more clearly elucidated, providing greater input into rational catalyst design with promising catalytic performance. Some novel catalytic systems composed of oxide–zeolite bifunctional catalysts based on non-FTS route are also included in this chapter for their milestone progress in tailoring product distribution to produce a specific range of fuels and chemicals with a very high selectivity, which may open up a new horizon in syngas chemistry.

Although industrial application has been successfully achieved for the traditional FTS process using Fe-based or Co-based catalysts, efforts are still required to further improve the C_{5+} hydrocarbon selectivity and catalytic stability by preparing a solid catalyst with well-defined active phase with the aid of promoters and supports or employing novel synthesis methods. For Fe-based catalysts, further studies should focus on the role of each iron carbide phase and the structure evolution of the iron species throughout the whole process. Currently, experimental studies about the particle size effect and facet effect of specific phase of iron carbide remain scarce due to the facile nature of phase transformation. In addition, the lifetime of Fe-based catalysts under industrial reaction conditions should be further improved. For Co-based FT catalysts, the nanoeffect of metallic Co nanoparticles has been investigated well, and it is desirable to control the preparation to form pure-HCP Co with determined exposed facets and suitable crystallite size. The main concern is related to the tuning of MSI to obtain a robust supported Co-based catalyst with high dispersion, easy reducibility, and long stability.

Direct selective production of gasoline-, jet fuel-, and diesel-range hydrocarbons with high selectivity can be achieved over bifunctional catalysts combining an FTS catalyst for heavy hydrocarbon formation and a zeolite catalyst for hydrocracking/isomerization of hydrocarbons to achieve target products. The major target is to reduce the selectivity to CH_4 and light paraffins by optimizing the mesoporous

zeolite structure. Future efforts are needed to elucidate the reaction mechanism and improve the quality of liquid fuels produced. For example, the fraction of iso-paraffins in gasoline-range fuels should be further enhanced to increase the RON value.

Lower olefins and long-chain olefins can be produced both through FTS route over the iron carbide-based or Co_2C-based catalysts. The Fe-based FTO catalysts is very similar to Fe-based FTS catalysts. The relative high CH_4 selectivity and rapid deactivation due to the coke deposition are the main limitations for Fe-based FTO catalysts. Much effort should be devoted to suppress the formation of CH_4 and improve the catalytic stability by careful catalyst design. The major breakthrough in Co-based FTO is the construction of Co_2C nanoprisms, mainly exposing the (101) and (020) facets. Intensive studies have suggested the nanoeffect of Co_2C plays a determining role in breaking the ASF distribution and obtaining high lower olefin selectivity. As for the bifunctional catalyst composed of metal oxide–zeolite via non-FTS route, C_2–C_4 olefins can be obtained with a selectivity higher than 80%. Various key parameters for this process have been investigated. Coke deposition over the zeolites should be considered at such high reaction temperature (~400 °C) although no deactivation within 500 hours of testing has been reported.

Direct transformation of STA has performed over bifunctional catalysts via FTS route with olefins as intermediates (SOA) or non-FTS route with CH_3OH/DME as intermediates (SMA). A complicated reaction network including olefins/methanol formation, oligomerization, cyclization, dehydrogenation, and hydrogen transfer is contained in the whole STA process, making it hard to explore the reaction mechanism. Fe-based FTO catalysts are always employed to produce olefins as intermediates as a high reaction temperature is required in the aromatization process. The challenges encountered for Fe-based FTO catalysts also exist for SMA. In addition, the SOA process typically produces aromatics with selectivity less than 60%, and much remains to be done to further optimize Fe-based component and zeolite component. For the SMA process, a very high aromatic selectivity can be obtained. However, the CO conversion is rather low for the SMA process at high reaction temperature.

Direct syngas conversion to C_{2+} oxygenates with high selectivity remains the greatest challenge in syngas chemistry. The modified FTS catalysts seem most promising for long-chain linear oxygenates as target products. Less information is available for understanding of the nature of the active sites to improve the selectivity of C_{2+} oxygenates. The current consensus is that dual active sites are required. The synergistic effect between dual-site structures is crucial. Modification of the ratio of dual active sites and increasing the interfacial boundary and the ratio of non-dissociative CO-containing species to alkyl species, i.e. increasing the CH_xO^* intermediates concentration, have been demonstrated to be efficient to improve the selectivity of C_{2+} oxygenates. Recent studies also demonstrate significant progress in producing ethanol as specific oxygenates from syngas based on RhMn@Zeolite [126] or tandem catalytic systems [127, 128] via non-FTS routes. The confined structure is a promising methodology to tune the product distribution. However, kinetic mismatching in each step is the biggest challenge. Further studies should

focus on the careful design of the corresponding catalyst at each step, and a positive functional synergism between different components is crucial to obtain higher C_{2+} oxygenates for multifunctional catalytic systems.

References

1 Cheng, K., Kang, J., King, D.L. et al. (2017). Advances in catalysis for syngas conversion to hydrocarbons. *Adv. Synth. Catal.* 60: 125–208.
2 Martinez-Vargas, D.X., Sandoval-Rangel, L., Campuzano-Calderon, O. et al. (2019). Recent advances in bifunctional catalysts for the Fischer–Tropsch process: one-stage production of liquid hydrocarbons from syngas. *Ind. Eng. Chem. Res.* 58 (35): 15872–15901.
3 Luk, H.T., Mondelli, C., Ferré, D.C. et al. (2017). Status and prospects in higher alcohols synthesis from syngas. *Chem. Soc. Rev.* 46 (5): 1358–1426.
4 Schulz, H. and Claeys, M. (1999). Kinetic modelling of Fischer–Tropsch product distributions. *Appl. Catal., A* 186 (1-2): 91–107.
5 Zhang, Q., Deng, W., and Wang, Y. (2013). Recent advances in understanding the key catalyst factors for Fischer–Tropsch synthesis. *J. Energy Chem.* 22 (1): 27–38.
6 Zhang, Q., Cheng, K., Kang, J. et al. (2014). Fischer–Tropsch catalysts for the production of hydrocarbon fuels with high selectivity. *ChemSusChem* 7 (5): 1251–1264.
7 Zhai, P., Sun, G., Zhu, Q., and Ma, D. (2013). Fischer–Tropsch synthesis nanostructured catalysts: understanding structural characteristics and catalytic reaction. *Nanotechnol. Rev.* 2 (5): 547–576.
8 Chen, W., Lin, T., Dai, Y. et al. (2018). Recent advances in the investigation of nanoeffects of Fischer–Tropsch catalysts. *Catal. Today* 311: 8–22.
9 Xiao, K., Bao, Z., Qi, X. et al. (2013). Advances in bifunctional catalysis for higher alcohol synthesis from syngas. *Chin. J. Catal.* 34 (1): 116–129.
10 An, Y., Lin, T., Yu, F. et al. (2017). Advances in direct production of value-added chemicals via syngas conversion. *Sci. China Chem.* 60 (7): 887–903.
11 Zhou, W., Cheng, K., Kang, J. et al. (2019). New horizon in C1 chemistry: breaking the selectivity limitation in transformation of syngas and hydrogenation of CO_2 into hydrocarbon chemicals and fuels. *Chem. Soc. Rev.* 48: 3193–3228.
12 de Smit, E., Cinquini, F., Beale, A.M. et al. (2010). Stability and reactivity of $\varepsilon-\chi-\theta$ iron carbide catalyst phases in Fischer–Tropsch synthesis: controlling μ_C. *J. Am. Chem. Soc.* 132 (42): 14928–14941.
13 Zhang, Q., Kang, J., and Wang, Y. (2010). Development of novel catalysts for Fischer–Tropsch synthesis: tuning the product selectivity. *ChemCatChem* 2 (9): 1030–1058.
14 Wezendonk, T.A., Sun, X., Dugulan, A.I. et al. (2018). Controlled formation of iron carbides and their performance in Fischer–Tropsch synthesis. *J. Catal.* 362: 106–117.

15 Cheng, J., Hu, P., Ellis, P. et al. (2010). Density functional theory study of iron and cobalt carbides for Fischer–Tropsch synthesis. *J. Phys. Chem. C* 114 (2): 1085–1093.

16 Yang, C., Zhao, H., Hou, Y., and Ma, D. (2012). Fe_5C_2 nanoparticles: a facile bromide-induced synthesis and as an active phase for Fischer–Tropsch synthesis. *J. Am. Chem. Soc.* 134 (38): 15814–15821.

17 Chen, B., Wang, D., Duan, X. et al. (2018). Charge-tuned CO Activation over a χ-Fe_5C_2 Fischer–Tropsch catalyst. *ACS Catal.* 8 (4): 2709–2714.

18 Xu, K., Sun, B., Lin, J. et al. (2014). ε-iron carbide as a low-temperature Fischer–Tropsch synthesis catalyst. *Nat. Commun.* 5: 5783.

19 Wang, P., Chen, W., Chiang, F.K. et al. (2018). Synthesis of stable and low-CO_2 selective epsilon-iron carbide Fischer–Tropsch catalysts. *Sci. Adv.* 4 (10): eaau2947.

20 Teng, X., Huang, S., Wang, J. et al. (2018). Fabrication of Fe_2C embedded in hollow carbon spheres: a high-performance and stable catalyst for Fischer–Tropsch synthesis. *ChemCatChem* 10 (17): 3883–3891.

21 Chang, Q., Zhang, C., Liu, C. et al. (2018). Relationship between iron carbide phases (ε-Fe_2C, Fe_7C_3, and χ-Fe_5C_2) and catalytic performances of Fe/SiO_2 Fischer–Tropsch catalysts. *ACS Catal.* 3304–3316.

22 Xu, J., Yang, Y., and Li, Y.-W. (2013). Fischer–Tropsch synthesis process development: steps from fundamentals to industrial practices. *Curr. Opin. Chem. Eng.* 2 (3): 354–362.

23 Wezendonk, T.A., Santos, V.P., Nasalevich, M.A. et al. (2016). Elucidating the nature of Fe species during pyrolysis of the Fe-BTC MOF into highly active and stable Fischer–Tropsch catalysts. *ACS Catal.* 6 (5): 3236–3247.

24 Wang, H., Huang, S., Wang, J. et al. (2019). Effect of Ca promoter on the structure and catalytic behavior of FeK/Al_2O_3 catalyst in Fischer–Tropsch synthesis. *ChemCatChem* 11 (14): 3220–3226.

25 Niu, L., Liu, X., Liu, J. et al. (2019). Tuning carburization behaviors of metallic iron catalysts with potassium promoter and CO/syngas/C_2H_4/C_2H_2 gases. *J. Catal.* 371: 333–345.

26 Huo, C.-F., Wu, B.-S., Gao, P. et al. (2011). The mechanism of potassium promoter: enhancing the stability of active surfaces. *Angew. Chem. Int. Ed.* 50 (32): 7403–7406.

27 Cheng, K., Virginie, M., Ordomsky, V.V. et al. (2015). Pore size effects in high-temperature Fischer–Tropsch synthesis over supported iron catalysts. *J. Catal.* 328: 139–150.

28 Abello, S. and Montane, D. (2011). Exploring iron-based multifunctional catalysts for Fischer–Tropsch synthesis: a review. *ChemSusChem* 4 (11): 1538–1556.

29 Xiong, H.F., Jewell, L.L., and Coville, N.J. (2015). Shaped carbons as supports for the catalytic conversion of syngas to clean fuels. *ACS Catal.* 5 (4): 2640–2658.

30 Xiong, H.F., Moyo, M., Motchelaho, M.A. et al. (2014). Fischer–Tropsch synthesis: iron catalysts supported on N-doped carbon spheres prepared by chemical vapor deposition and hydrothermal approaches. *J. Catal.* 311: 80–87.

31 Khodakov, A.Y., Chu, W., and Fongarland, P. (2007). Advances in the development of novel cobalt Fischer–Tropsch catalysts for synthesis of long-chain hydrocarbons and clean fuels. *Chem. Rev.* 107 (5): 1692–1744.

32 Tsakoumis, N.E., Ronning, M., Borg, O. et al. (2010). Deactivation of cobalt based Fischer–Tropsch catalysts: a review. *Catal. Today* 154 (3–4): 162–182.

33 Fischer, N., Clapham, B., Feltes, T. et al. (2014). Size-dependent phase transformation of catalytically active nanoparticles captured in situ. *Angew. Chem. Int. Ed.* 53 (5): 1342–1345.

34 Hernandez Mejia, C., van Deelen, T.W., and de Jong, K.P. (2018). Activity enhancement of cobalt catalysts by tuning metal–support interactions. *Nat. Commun.* 9 (1): 4459.

35 Liu, J.-X., Su, H.-Y., Sun, D.-P. et al. (2013). Crystallographic dependence of CO activation on cobalt catalysts: HCP versus FCC. *J. Am. Chem. Soc.* 135 (44): 16284–16287.

36 Karaca, H., Hong, J., Fongarland, P. et al. (2010). In situ XRD investigation of the evolution of alumina-supported cobalt catalysts under realistic conditions of Fischer–Tropsch synthesis. *Chem. Commun.* 46 (5): 788–790.

37 Karaca, H., Safonova, O.V., Chambrey, S. et al. (2011). Structure and catalytic performance of Pt-promoted alumina-supported cobalt catalysts under realistic conditions of Fischer–Tropsch synthesis. *J. Catal.* 277 (1): 14–26.

38 Patanou, E., Tsakoumis, N.E., Myrstad, R., and Blekkan, E.A. (2018). The impact of sequential H_2-CO-H_2 activation treatment on the structure and performance of cobalt based catalysts for the Fischer–Tropsch synthesis. *Appl. Catal., A* 549: 280–288.

39 Braconnier, L., Landrivon, E., Clémençon, I. et al. (2013). How does activation affect the cobalt crystallographic structure? An in situ XRD and magnetic study. *Catal. Today* 215: 18–23.

40 Ellis, P.R., Enache, D.I., James, D.W. et al. (2019). A robust and precious metal-free high performance cobalt Fischer–Tropsch catalyst. *Nat. Catal.* 2: 623–631.

41 Liu, Y.F., Florea, I., Ersen, O. et al. (2015). Silicon carbide coated with TiO_2 with enhanced cobalt active phase dispersion for Fischer–Tropsch synthesis. *Chem. Commun.* 51 (1): 145–148.

42 Pestman, R., Chen, W., and Hensen, E. (2019). Insight into the rate-determining step and active sites in the Fischer–Tropsch reaction over cobalt catalysts. *ACS Catal.* 9 (5): 4189–4195.

43 Cats, K.H., Gonzalez-Jimenez, I.D., Liu, Y. et al. (2013). X-ray nanoscopy of cobalt Fischer–Tropsch catalysts at work. *Chem. Commun.* 49 (41): 4622–4624.

44 Böller, B., Durner, K.M., and Wintterlin, J. (2019). The active sites of a working Fischer–Tropsch catalyst revealed by operando scanning tunnelling microscopy. *Nat. Catal.* 2 (11): 1027–1034.

45 Weststrate, C.J., Sharma, D., Garcia Rodriguez, D. et al. (2020). Mechanistic insight into carbon–carbon bond formation on cobalt under simulated Fischer–Tropsch synthesis conditions. *Nat. Commun.* 11 (1): 750–760.

46 Yang, J., Tveten, E.Z., Chen, D., and Anders, H. (2010). Understanding the effect of cobalt particle size on Fischer–Tropsch synthesis: surface species and mechanistic studies by SSITKA and kinetic isotope effect. *Langmuir* 26 (21): 16558–16567.

47 Navarro, V., van Spronsen, M.A., and Frenken, J.W. (2016). In situ observation of self-assembled hydrocarbon Fischer–Tropsch products on a cobalt catalyst. *Nat. Chem.* 8 (10): 929–934.

48 Li, N., Jiao, F., Pan, X. et al. (2019). High-quality gasoline directly from syngas by dual metal oxide–zeolite (OX-ZEO) catalysis. *Angew. Chem. Int. Ed.* 58 (22): 7400–7404.

49 Kang, J., Zhang, S., Zhang, Q., and Wang, Y. (2009). Ruthenium nanoparticles supported on carbon nanotubes as efficient catalysts for selective conversion of synthesis gas to diesel fuel. *Angew. Chem. Int. Ed.* 48 (14): 2565–2568.

50 Cheng, Q., Tian, Y., Lyu, S. et al. (2018). Confined small-sized cobalt catalysts stimulate carbon-chain growth reversely by modifying ASF law of Fischer–Tropsch synthesis. *Nat. Commun.* 9 (1): 3250.

51 Sun, B., Qiao, M., Fan, K. et al. (2011). Fischer–Tropsch synthesis over molecular sieve supported catalysts. *ChemCatChem* 3 (3): 542–550.

52 Carvalho, A., Marinova, M., Batalha, N. et al. (2017). Design of nanocomposites with cobalt encapsulated in the zeolite micropores for selective synthesis of isoparaffins in Fischer–Tropsch reaction. *Catal. Sci. Technol.* 7 (21): 5019–5027.

53 Kang, J., Wang, X., Peng, X. et al. (2016). Mesoporous zeolite Y-supported Co nanoparticles as efficient Fischer–Tropsch catalysts for selective synthesis of diesel fuel. *Ind. Eng. Chem. Res.* 55 (51): 13008–13019.

54 Yang, G., Wang, D., Yoneyama, Y. et al. (2012). Facile synthesis of H-type zeolite shell on a silica substrate for tandem catalysis. *Chem. Commun.* 48 (9): 1263–1265.

55 Yamane, N., Wang, Y., Li, J. et al. (2017). Building premium secondary reaction field with a miniaturized capsule catalyst to realize efficient synthesis of a liquid fuel directly from syngas. *Catal. Sci. Technol.* 7 (10): 1996–2000.

56 Sun, B., Yu, G., Lin, J. et al. (2012). A highly selective Raney Fe@HZSM-5 Fischer–Tropsch synthesis catalyst for gasoline production: one-pot synthesis and unexpected effect of zeolites. *Catal. Sci. Technol.* 2 (8): 1625–1629.

57 Cheng, K., Zhang, L., Kang, J. et al. (2015). Selective transformation of syngas into gasoline-range hydrocarbons over mesoporous H-ZSM-5-supported cobalt nanoparticles. *Chem. Eur. J.* 21 (5): 1928–1937.

58 Cheng, K., Kang, J., Huang, S. et al. (2012). Mesoporous beta zeolite-supported ruthenium nanoparticles for selective conversion of synthesis gas to C_5–C_{11} isoparaffins. *ACS Catal.* 2 (3): 441–449.

59 Kang, J., Cheng, K., Zhang, L. et al. (2011). Mesoporous zeolite-supported ruthenium nanoparticles as highly selective Fischer–Tropsch catalysts for the production of C_5–C_{11} isoparaffins. *Angew. Chem. Int. Ed.* 50 (22): 5200–5203.

60 Li, J., He, Y., Tan, L. et al. (2018). Integrated tuneable synthesis of liquid fuels via Fischer–Tropsch technology. *Nat. Catal.* 1 (10): 787–793.

61 Peng, X.B., Cheng, K., Kang, J.C. et al. (2015). Impact of hydrogenolysis on the selectivity of the Fischer–Tropsch synthesis: diesel fuel production over mesoporous zeolite-Y-supported cobalt nanoparticles. *Angew. Chem. Int. Ed.* 54 (15): 4553–4556.

62 Kim, J.-C., Lee, S., Cho, K. et al. (2014). Mesoporous MFI zeolite nanosponge supporting cobalt nanoparticles as a Fischer–Tropsch catalyst with high yield of branched hydrocarbons in the gasoline range. *ACS Catal.* 4 (11): 3919–3927.

63 Galvis, H.M.T. and de Jong, K.P. (2013). Catalysts for production of lower olefins from synthesis gas: a review. *ACS Catal.* 3 (9): 2130–2149.

64 Torres Galvis, H.M., Bitter, J.H., Davidian, T. et al. (2012). Iron particle size effects for direct production of lower olefins from synthesis gas. *J. Am. Chem. Soc.* 134 (39): 16207–16215.

65 Zhai, P., Xu, C., Gao, R. et al. (2016). Highly tunable selectivity for syngas-derived alkenes over zinc and sodium-modulated Fe_5C_2 catalyst. *Angew. Chem. Int. Ed.* 55 (34): 9902–9907.

66 Galvis, H.M.T., Bitter, J.H., Khare, C.B. et al. (2012). Supported iron nanoparticles as catalysts for sustainable production of lower olefins. *Science* 335 (6070): 835–838.

67 Trepanier, M., Dalai, A.K., Abatzoglou, N. et al. (2010). Synthesis of CNT-supported cobalt nanoparticle catalysts using a microemulsion technique: role of nanoparticle size on reducibility, activity and selectivity in Fischer–Tropsch reactions. *Appl. Catal., A* 374 (1): 79–86.

68 Lu, J., Yang, L., Xu, B. et al. (2014). Promotion effects of nitrogen doping into carbon nanotubes on supported iron Fischer–Tropsch catalysts for lower olefins. *ACS Catal.* 4 (2): 613–621.

69 Chen, X., Deng, D., Pan, X. et al. (2015). N-doped graphene as an electron donor of iron catalysts for CO hydrogenation to light olefins. *Chem. Commun.* 51 (1): 217–220.

70 Cheng, Y., Lin, J., Xu, K. et al. (2016). Fischer–Tropsch synthesis to lower olefins over potassium-promoted reduced graphene oxide supported iron catalysts. *ACS Catal.* 6 (1): 389–399.

71 Xie, J., Yang, J., Dugulan, A.I. et al. (2016). Size and promoter effects in supported iron Fischer–Tropsch catalysts: insights from experiment and theory. *ACS Catal.* 6 (5): 3147–3157.

72 Zhong, L., Yu, F., An, Y. et al. (2016). Cobalt carbide nanoprisms for direct production of lower olefins from syngas. *Nature* 538 (7623): 84–87.

73 Li, Z., Zhong, L., Yu, F. et al. (2017). Effects of sodium on the catalytic performance of CoMn catalysts for Fischer–Tropsch to olefin reactions. *ACS Catal.* 7 (5): 3622–3631.

74 Li, Z., Lin, T., Yu, F. et al. (2017). Mechanism of the Mn promoter via CoMn spinel for morphology control: formation of Co_2C nanoprisms for Fischer–Tropsch to olefins reaction. *ACS Catal.* 7 (12): 8023–8032.

75 Liu, S., Sun, B., Zhang, Y. et al. (2019). The role of intermediate $Co_xMn_{1-x}O$ ($x = 0.6$–0.85) nanocrystals in the formation of active species for the direct production of lower olefins from syngas. *Chem. Commun.* 55 (46): 6595–6598.

76 An, Y., Lin, T., Gong, K. et al. (2020). Tuning the facet proportion of Co_2C nanoprisms for Fischer–Tropsch synthesis to olefins. *ChemCatChem* 12: 1630–1638.

77 Lin, T., Gong, K., Wang, C. et al. (2019). Fischer–Tropsch synthesis to olefins: catalytic performance and structure evolution of Co_2C-based catalysts under a CO_2 environment. *ACS Catal.* 9 (10): 9554–9567.

78 An, Y., Zhao, Y., Yu, F. et al. (2018). Morphology control of Co_2C nanostructures via the reduction process for direct production of lower olefins from syngas. *J. Catal.* 366: 289–299.

79 Wang, X., Chen, W., Lin, T. et al. (2018). Effect of the support on cobalt carbide catalysts for sustainable production of olefins from syngas. *Chin. J. Catal.* 39 (12): 1869–1880.

80 Dai, Y., Zhao, Y., Lin, T. et al. (2018). Particle size effects of cobalt carbide for Fischer–Tropsch to olefins. *ACS Catal.* 9 (2): 798–809.

81 Xie, J., Paalanen, P.P., van Deelen, T.W. et al. (2019). Promoted cobalt metal catalysts suitable for the production of lower olefins from natural gas. *Nat. Commun.* 10 (1): 1–10.

82 Cheng, K., Gu, B., Liu, X. et al. (2016). Direct and highly selective conversion of synthesis gas to lower olefins: design of a bifunctional catalyst combining methanol synthesis and carbon–carbon coupling. *Angew. Chem. Int. Ed.* 55: 1–5.

83 Jiao, F., Li, J., Pan, X. et al. (2016). Selective conversion of syngas to light olefins. *Science* 351 (6277): 1065–1068.

84 Su, J., Zhou, H., Liu, S. et al. (2019). Syngas to light olefins conversion with high olefin/paraffin ratio using $ZnCrO_x$/AlPO-18 bifunctional catalysts. *Nat. Commun.* 10 (1): 1297–1305.

85 Cheng, K., Gu, B., Liu, X. et al. (2016). Direct and highly selective conversion of synthesis gas into lower olefins: design of a bifunctional catalyst combining methanol synthesis and carbon–carbon coupling. *Angew. Chem. Int. Ed.* 55 (15): 4725–4728.

86 Zhu, Y., Pan, X., Jiao, F. et al. (2017). Role of manganese oxide in syngas conversion to light olefins. *ACS Catal.* 7 (4): 2800–2804.

87 Li, N., Jiao, F., Pan, X. et al. (2019). Size effects of ZnO nanoparticles in bifunctional catalysts for selective syngas conversion. *ACS Catal.* 9 (2): 960–966.

88 Liu, X., Zhou, W., Yang, Y. et al. (2018). Design of efficient bifunctional catalysts for direct conversion of syngas into lower olefins via methanol/dimethyl ether intermediates. *Chem. Sci.* 9 (20): 4708–4718.

89 Jiao, F., Pan, X.L., Gong, K. et al. (2018). Shape-selective zeolites promote ethylene formation from syngas via a ketene intermediate. *Angew. Chem. Int. Ed.* 57 (17): 4692–4696.

90 Kasipandi, S. and Bae, J.W. (2019). Recent advances in direct synthesis of value-added aromatic chemicals from syngas by cascade reactions over bifunctional catalysts. *Adv. Mater.* 31 (34): 1803390.

91 Zhou, W., Shi, S., Wang, Y. et al. (2019). Selective conversion of syngas to aromatics over a Mo–ZrO_2/H-ZSM-5 bifunctional catalyst. *ChemCatChem* 11 (6): 1681–1688.

92 Zhao, B., Zhai, P., Wang, P. et al. (2017). Direct transformation of syngas to aromatics over Na–Zn–Fe_5C_2 and hierarchical HZSM-5 tandem catalysts. *Chem* 3 (2): 323–333.

93 Xu, Y., Liu, J., Wang, J. et al. (2019). Selective conversion of syngas to aromatics over Fe_3O_4@MnO_2 and hollow HZSM-5 bifunctional catalysts. *ACS Catal.* 9 (6): 5147–5156.

94 Wang, T., Xu, Y., Shi, C. et al. (2019). Direct production of aromatics from syngas over a hybrid FeMn Fischer–Tropsch catalyst and HZSM-5 zeolite: local environment effect and mechanism-directed tuning of the aromatic selectivity. *Catal. Sci. Technol.* 9 (15): 3933–3946.

95 Sun, T., Lin, T., An, Y. et al. (2020). Syngas conversion to aromatics over the Co_2C-based catalyst and HZSM-5 via a tandem system. *Ind. Eng. Chem. Res.* 59 (10): 4419–4427.

96 Cheng, K., Zhou, W., Kang, J. et al. (2017). Bifunctional catalysts for one-step conversion of syngas into aromatics with excellent selectivity and stability. *Chem* 3 (2): 334–347.

97 Yang, J., Pan, X., Jiao, F. et al. (2017). Direct conversion of syngas to aromatics. *Chem. Commun.* 53 (81): 11146–11149.

98 Huang, Z., Wang, S., Qin, F. et al. (2018). Ceria-zirconia/zeolite bifunctional catalyst for highly selective conversion of syngas into aromatics. *ChemCatChem* 10 (20): 4519–4524.

99 Zhang, P.P., Tan, L., Yang, G.H., and Tsubaki, N. (2017). One-pass selective conversion of syngas to para-xylene. *Chem. Sci.* 8 (12): 7941–7946.

100 Arslan, M.T., Qureshi, B.A., Gilani, S.Z.A. et al. (2019). Single-step conversion of H_2-deficient syngas into high yield of tetramethylbenzene. *ACS Catal.* 9 (3): 2203–2212.

101 He, M., Sun, Y., and Han, B. (2013). Green carbon science: scientific basis for integrating carbon resource processing, utilization, and recycling. *Angew. Chem. Int. Ed.* 52 (37): 9620–9633.

102 Xiao, K., Bao, Z., Qi, X. et al. (2013). Structural evolution of CuFe bimetallic nanoparticles for higher alcohol synthesis. *J. Mol. Catal. A: Chem.* 378: 319–325.

103 Ao, M., Pham, G.H., Sunarso, J. et al. (2018). Active centers of catalysts for higher alcohol synthesis from syngas: a review. *ACS Catal.* 8 (8): 7025–7050.

104 Volkova, G.G., Yurieva, T.M., Plyasova, L.M. et al. (2000). Role of the Cu–Co alloy and cobalt carbide in higher alcohol synthesis. *J. Mol. Catal. A: Chem.* 158 (1): 389–393.

105 Zhang, R., Wen, G., Adidharma, H. et al. (2017). C_2 oxygenate synthesis via Fischer–Tropsch synthesis on Co_2C and Co/Co_2C interface catalysts: how to control the catalyst crystal facet for optimal selectivity. *ACS Catal.* 7 (12): 8285–8295.

106 Lebarbier, V.M., Mei, D., Kim, D.H. et al. (2011). Effects of La_2O_3 on the mixed higher alcohols synthesis from syngas over Co catalysts: a combined theoretical and experimental study. *J. Phys. Chem. C* 115 (35): 17440–17451.

107 Pei, Y.P., Liu, J.X., Zhao, Y.H. et al. (2015). High alcohols synthesis via Fischer–Tropsch reaction at cobalt metal/carbide interface. *ACS Catal.* 5 (6): 3620–3624.

108 Yang, Y., Lin, T., Qi, X. et al. (2018). Direct synthesis of long-chain alcohols from syngas over CoMn catalysts. *Appl. Catal., A* 549: 179–187.

109 Xiang, Y. and Kruse, N. (2016). Tuning the catalytic CO hydrogenation to straight- and long-chain aldehydes/alcohols and olefins/paraffins. *Nat. Commun.* 7: 13058.

110 Lin, T., Qi, X., Wang, X. et al. (2019). Direct production of higher oxygenates by syngas conversion over a multifunctional catalyst. *Angew. Chem. Int. Ed.* 58 (14): 4627–4631.

111 Zhao, Z., Lu, W., Zhu, H.J. et al. (2018). Tuning the Fischer–Tropsch reaction over Co_xMn_yLa/AC catalysts toward alcohols: effects of La promotion. *J. Catal.* 361: 156–167.

112 Zhao, Z., Lu, W., Yang, R. et al. (2018). Insight into the formation of $Co@Co_2C$ catalysts for direct synthesis of higher alcohols and olefins from syngas. *ACS Catal.* 8 (1): 228–241.

113 Anton, J., Nebel, J., Song, H. et al. (2016). The effect of sodium on the structure–activity relationships of cobalt-modified $Cu/ZnO/Al_2O_3$ catalysts applied in the hydrogenation of carbon monoxide to higher alcohols. *J. Catal.* 335: 175–186.

114 Du, H., Zhu, H.J., Chen, X.K. et al. (2016). Study on CaO-promoted Co/AC catalysts for synthesis of higher alcohols from syngas. *Fuel* 182: 42–49.

115 Singh, J.A., Hoffman, A.S., Schumann, J. et al. (2019). Role of Co_2C in ZnO-promoted Co catalysts for alcohol synthesis from syngas. *ChemCatChem* 11 (2): 799–809.

116 An, Y., Lin, T., Yu, F. et al. (2018). Effect of reaction pressures on structure–performance of Co_2C-based catalyst for syngas conversion. *Ind. Eng. Chem. Res.* 57 (46): 15647–15653.

117 Luan, X., Ren, Z., Dai, X. et al. (2020). Selective conversion of syngas into higher alcohols via a reaction-coupling strategy on multifunctional relay catalysts. *ACS Catal.* 10 (4): 2419–2430.

118 Puga, A.V. (2018). On the nature of active phases and sites in CO and CO_2 hydrogenation catalysts. *Catal. Sci. Technol.* 8 (22): 5681–5707.

119 Gao, W., Zhao, Y.F., Chen, H.R. et al. (2015). Core–shell $Cu@(CuCo\text{-alloy})/Al_2O_3$ catalysts for the synthesis of higher alcohols from syngas. *Green Chem.* 17 (3): 1525–1534.

120 Ning, X., An, Z., and He, J. (2016). Remarkably efficient CoGa catalyst with uniformly dispersed and trapped structure for ethanol and higher alcohol synthesis from syngas. *J. Catal.* 340: 236–247.

121 Li, Y., Gao, W., Peng, M. et al. (2020). Interfacial Fe_5C_2–Cu catalysts toward low-pressure syngas conversion to long-chain alcohols. *Nat. Commun.* 11 (1): 61.

122 Xiang, Y., Chitry, V., Liddicoat, P. et al. (2013). Long-chain terminal alcohols through catalytic CO hydrogenation. *J. Am. Chem. Soc.* 135 (19): 7114–7117.

123 Prieto, G., Beijer, S., Smith, M.L. et al. (2014). Design and synthesis of copper–cobalt catalysts for the selective conversion of synthesis gas to ethanol and higher alcohols. *Angew. Chem. Int. Ed.* 53 (25): 6397–6401.

124 Lu, Y., Zhang, R., Cao, B. et al. (2017). Elucidating the copper–Hägg iron carbide synergistic interactions for selective CO hydrogenation to higher alcohols. *ACS Catal.* 7 (8): 5500–5512.

125 Luk, H.T., Mondelli, C., Mitchell, S. et al. (2018). Role of carbonaceous supports and potassium promoter on higher alcohols synthesis over copper–iron catalysts. *ACS Catal.* 8 (10): 9604–9618.

126 Wang, C., Zhang, J., Qin, G. et al. (2020). Direct conversion of syngas to ethanol within zeolite crystals. *Chem* 6 (3): 646–657.

127 Zhou, W., Kang, J., Cheng, K. et al. (2018). Direct conversion of syngas into methyl acetate, ethanol, and ethylene by relay catalysis via the intermediate dimethyl ether. *Angew. Chem. Int. Ed.* 57 (37): 12012–12016.

128 Kang, J., He, S., Zhou, W. et al. (2020). Single-pass transformation of syngas into ethanol with high selectivity by triple tandem catalysis. *Nat. Commun.* 11: 827.

Part II

Methane Activation

4

Steam and Dry Reforming of Methane

José Luis Rico

Michoacan University, Catalysis Laboratory, Department of Chemical Engineering, V1 Building, C.U., Ave. F. J. Múgica S/N, Morelia, Michoacán C.P. 58030, México

4.1 Introduction

The present chapter is focused on the generation of hydrogen and CO, a mixture of gases known as synthesis gas, by the steam reforming of methane (SRM) and dry reforming of methane (DRM). More precisely, the center of attention of this review will be on the heterogeneous catalysts useful in both processes. Synthesis gas is used as a feed in large-scale processes such as methanol synthesis, oxo-synthesis, and Fischer–Tropsch processes. In addition, two very important uses of hydrogen are related to the synthesis of ammonia, which is then utilized in the production of fertilizers and in the processing of crude oil. In the case of CO, it is also a very useful compound utilized in various industrial processes, such as a raw material in the synthesis of aldehydes, in the production of phosgene that is then used for the production of polyurethanes, polycarbonates, and isocyanates and also in the metallurgical industry.

4.1.1 Steam Reforming of Methane

Although hydrogen is the most abundant molecule in the known universe, it is not directly available on earth. Hydrogen is mainly obtained from the SRM [1, 2]. In the classical process, methane reacts with steam at high temperature to produce mainly H_2 and CO. The reaction is endothermic and proceeds at high temperature, typically 800–1000 °C, and pressures of 1.5–3 MPa. The transformation can be represented as follows:

$$CH_4 + H_2O \leftrightarrow 3H_2 + CO \; \Delta H^\circ_{298} = 205.8 \text{ kJ mol}^{-1}$$

$$CO + H_2O \leftrightarrow H_2 + CO_2 \; \Delta H^\circ_{298} = -41 \text{ kJ mol}^{-1}$$

Nearly half of the world demand of hydrogen is supplied by the SRM process [3]. In the above reactions, the latter is known as the water–gas shift (WGS) reaction.

Heterogeneous Catalysis for Sustainable Energy, First Edition. Edited by Landong Li and Justin S. J. Hargreaves.

It is exothermic and further increases the production of hydrogen. During the SRM, the following unwanted side reactions occur:

$$2CO \leftrightarrow C + CO_2 \; \Delta H^\circ_{298} = -171 \text{ kJ mol}^{-1}$$

$$CH_4 \leftrightarrow C + 2H_2 \; \Delta H^\circ_{298} = +75 \text{ kJ mol}^{-1}$$

The former is known as the Boudouard reaction, and the latter is methane decomposition or the cracking of methane reaction.

4.1.2 Dry Reforming of Methane

Fischer and Tropsch observed as early as 1928 that the DRM reaction proceeds on various metals of the Group VIII that show different activities [4]. Nowadays, the DRM is gaining renewed interest due to the fact that CO_2, which is consumed in this reaction, is a significant atmospheric pollutant. Both CO_2 and CH_4 are considered as greenhouse gases and are abundant, which make them attractive reactants for the production of synthesis gas. A difference between DRM and SRM is that the former route produces a low H_2/CO ratio suitable for the production of oxygenated hydrocarbons, such as alcohols and aldehydes [5]. The DRM is also an endothermic catalytic transformation. It can be represented by the following equation:

$$CH_4 + CO_2 \leftrightarrow 2CO + 2H_2 \; \Delta H^\circ_{298} = 247 \text{ kJ mol}^{-1}$$

Some essential reaction steps for this transformation were proposed by Wang and Lu using the standard free energies: the activation of methane on the surface of the catalysts and reaction with the adsorbed oxygen species [6]:

$$CH_4 + * \leftrightarrow CH_{4-x}* + xH*$$

$$CO_2 \leftrightarrow CO + O*$$

$$CO_2 + * \leftrightarrow C + 2O*$$

$$C* + O* \leftrightarrow CO$$

$$H* + H* \leftrightarrow H_2$$

According to the stoichiometry for the DRM, a 1 : 1 mol ratio of H_2 and CO is expected. However, due to the side reactions occurring during DRM, the final H_2/CO mole ratio tends to be less than unity [7]. Decomposition of methane on the surface forms carbon species that cover the active sites and eventually deactivate the catalyst. Moreover, carbon monoxide can react to produce CO_2 and carbon through the Boudouard reaction contributing to carbon deposition on the surface of the catalyst. Furthermore, another side transformation is the WGS. Such reactions were shown previously.

As mentioned, the SRM and DRM are strongly endothermic and therefore very energetically demanding processes. Other alternatives for the generation of synthesis gas are the oxidative reforming (OR) and the autothermal reforming (ATR) (coupling the OR and the SRM) [8]. However, such processes are outside of the scope of the current review.

4.1.3 Thermodynamic Analysis of the SRM and DRM Reactions

Although this review deals with heterogeneous catalysts used in both DRM and SRM, it is worth commenting upon some of the thermodynamic details of these reactions. The species involved in thermodynamic equilibrium for the SRM and the DRM are CH_4, H_2O, H_2, CO, CO_2, and $C_{(s)}$ deposited on the catalyst surface [9]. Ávila-Neto et al. [10] have performed thermodynamic calculations upon the SRM and DRM. According to the analysis performed corresponding to 1 atm pressure and with a H_2O/CH_4 mol ratio of 2, the first reaction to occur during the SRM as the reaction temperature is increased is the methane decomposition reaction, generating $C_{(s)}$ and H_2. At about 327 °C, the SRM and WGS start to occur, and at about 550 °C, a maximum in the methane decomposition, and consequently the highest deposition of coke, is observed. Above this temperature, both SRM and WGS prevail. Other studies about equilibrium data in the literature for SRM were reported by Lutz et al. [11].

In the case of DRM [10], the calculations performed corresponding to 1 atm pressure and a CO_2/CH_4 mol ratio of 1 indicate that at 100 °C, 87.5% of the methane is consumed by the CO_2 reforming of methane and by methane decomposition. As the temperature is increased, these reactions decrease gradually, and the reaction of H_2 with CO_2 to form water and CO (the reverse WGS) becomes significant. However, as the temperature is further increased, at about 700 °C, the WGS is favored. Furthermore, at about 1000 °C, the WGS is the main reaction responsible for the generation of H_2. Other studies about equilibrium data in the literature for the DRM are reported by Akpan et al. [12]. There is greater potential for coke formation during the DRM, primarily due to the low H/C ratio of this system. The thermodynamic analysis on the DRM shows that coke formation is possible over a wide range of reaction conditions.

4.2 Heterogeneous Catalysts for the SRM

The harsh experimental conditions for the SRM and DRM strongly influence the activity of catalysts. Formation of coke, sintering of the metal particles, and poisoning are the main problems of deactivation of catalysts in both processes. Poisoning of the catalysts can be related to sulfur in the feed, and all sulfur compounds are transformed to hydrogen sulfide in the reformer. H_2S severely poisons and deactivates the metal catalyst forming metal sulfides that are inactive for the methane reforming [13]. Contrarily, the morphology and properties of the coke formed on the surface of a catalyst are influenced by several factors such as composition of the

support; the presence of promoters; the nature, size, and morphology of the catalytic particles; the feed composition; and the experimental conditions used in the reactor. Furthermore, the deactivation of catalysts due to coke deposition depends on its morphology: encapsulating carbon produces the fouling of the metal surface, whereas whisker-like carbon blocks the pores of the catalyst and breaks the structure of the support, causing an increase of pressure in the reformer furnace tubes [14].

As will be observed below, much of the research work reported in the literature on this subject present different alternatives to reduce the deactivation and extend the life of catalysts during SRM or DRM.

4.2.1 Ni-Based and Other Catalysts

Although noble metal catalysts show high activity and stability for the SRM [15], the reaction is performed preferentially on nickel-based catalysts due to their lower cost and reasonable activity [16]. However, nickel-based catalysts are also prone to deactivate [17]. The problem of deactivation of catalysts due to carbon species deposition has been addressed a long time ago. Reitmeier et al. determined interesting experimental conditions to decrease coking and to produce syngas of ratio H_2/CO less than 3 through the DRM [18].

The first step before the SRM is the reduction of the catalyst. It was reported by Holm and Clark [19] that nickel supported on alumina prepared by coprecipitation was more difficult to reduce than impregnated nickel samples, due to the fact that the difficulty of reduction is increased when increasing the metal–support interaction. Furthermore, they also observed that high-temperature treatment of catalysts increases the difficulty for reduction. The reduction depends also upon the nature of the support, as found by Lo Jacono et al. [20] using α- and γ-Al_2O_3 with the aim of studying the properties of Ni by reflectance spectroscopy and X-ray diffraction. The authors found the formation of $NiAl_2O_4$ and reported that the relative occupancy of tetrahedral and octahedral sites of the spinel is affected by the atmosphere of firing, the nickel content, and the nature of the supports. Zielińsky [21] found by temperature-programmed reduction that nickel on alumina is present in two forms, namely, free and fixed to the support. The fixed nickel was related to the formation of $NiAl_2O_4$ that was more difficult to reduce due to its strong chemical interaction with the support. Bartholomew and Pannell [22, 23] found that the interactions of nickel with the support were strong or weak by performing adsorption experiments of H_2 and CO on alumina- and silica-supported catalysts. Roman and Delmon [24] investigated the influence of promoters (Cu, Pd, and Pt) on the reduction of nickel on NiO/SiO_2. The authors reported three nickel species on silica that were partially reduced by hydrogen even at temperatures higher than 400 °C. They also reported that copper was the most efficient promoter enhancing the reduction of nickel.

In another study, Agnelli et al. investigated the deactivation of Ni/alumina catalysts during the SRM and found that the presence of water during reduction affects negatively the reducibility of nickel. They also observed by programmed temperature reduction three features for this catalyst. The first two, appearing in the temperature range of 400–490 °C, resulted from the presence of water during reduction retarding

the reaction rate. When water was removed before reduction, only one signal appeared at about 400 °C and was assigned to NiO similarly to the one observed in the unsupported NiO profile. The third signal at about 660 °C was attributed to NiO that has interacted with the support [25]. In another research report, Xua et al. [26] pretreated a Ni/honeycomb catalyst with steam at 900 °C followed by reduction with hydrogen at this temperature and before the SRM. The authors found that this procedure improved the performance of the catalyst at temperatures below 800 °C, due to the oxidation of nickel atoms with water followed by a total reduction with hydrogen. Such treatment resulted in small reduced nickel particles suitable for SRM. The catalysts were characterized by scanning electron microscopy (SEM) equipped with energy-dispersive X-ray spectroscopy (EDS), *in situ* X-ray absorption fine structure (XAFS), and Brunauer-Emmett-Teller (BET) measurements.

Numaguchi and Kikuchi [27] reported the deactivation of Ni/α-Al_2O_3 bimodal catalysts. The samples were calcined at 873 K, sample B, or 1173 K, sample N. The catalysts were used in the SRM for 160 and 600 hours, B and N, respectively. The former was strongly deactivated, whereas the latter ran for longer time. In addition, sample N showed five times greater quantity of carbon deposition than sample B. The authors found that the Ni crystallites were 163 and 65 nm in B and N, respectively, and these differences influenced the size of the carbon particles that severely blocked the pores in sample B, contrary to the observation in sample N. In another study, Sardar et al. [28] reported the synthesis of nickel nanoparticles supported on silica-functionalized alumina which were then tested in the SRM. They found that the catalyst showed good catalytic activity and stability and no coke was observed during 48 h under the reaction conditions employed, whereas the conventional nickel catalyst showed severe deactivation due to the formation of filamentous carbon on the surface. The authors concluded that silica-functionalized alumina improved the dispersion of Ni nanoparticles and prevented sintering and aggregation at high temperatures during the SRM.

Matsumura and Nakamori [29] tested Ni-based catalysts supported on γ-Al_2O_3, ZrO_2, and SiO_2 on the SRM conducted at low reaction temperatures. Nickel supported on zirconia was the most effective catalyst for this reaction at 500 °C. It was also reported that in the initial stage of the reaction solely with methane at this temperature, surface hydroxyl groups on these catalysts react with methane to produce H_2 and CO_2, suggesting that the these groups play an important role during the SRM.

Vogt et al. [30] reported a series of catalysts with well-defined Ni particle sizes between 1.2 and 6 nm supported on silica that were tested in the SRM and the DRM. The catalysts were characterized by *operando* infrared spectroscopy to determine the active mechanism over Ni and its kinetic dependence on Ni particle size. The authors found that Ni particles below 2.5 nm led to different structure sensitivity. Isotopically labeled experiments with CH_xD_x indicated that the activation of methane is not the only rate-limiting step in both the SRM and DRM. In the DRM, the recombination of C and O or the activation of CO is likely also a rate-limiting step, whereas desorption of CO becomes more kinetically limiting for the SRM. In addition, the optimal Ni particle size in terms of activity was 2–3 nm for both reactions at 500 and 600 °C and

5 bar. An increase in the Ni particle size enhances the carbon whisker formation for both methane reactions.

Metal–support interactions play an important role to obtain a suitable catalyst with small particle size and thermal stability under severe reaction conditions, as those required for the SRM. It has been reported that bimetallic oxides such as $NiMO_3$ or NiM_2O_4 could be attractive precursors for synthesis of catalysts to be used in the SRM. In this respect, $NiAl_2O_4$ spinel can be a promising precursor to synthesize Ni/Al_2O_3 [31, 32]. For the synthesis of catalysts from $NiAl_2O_4$ for the SRM, the precursor is typically reduced at high temperature to induce nickel extraction and produce an attractive catalyst comprising metallic crystallites. The synthesis of such a solid resulted in a better catalyst for SRM than those obtained from $CuAl_2O_4$, $NiFe_2O_4$, or $NiMn_2O_4$ [32, 33]. Jiménez-González et al. [34] reported that the best catalyst for SRM among the samples prepared was that obtained from the reduction of $NiAl_2O_4$ (17 wt% Ni) previously prepared by coprecipitation. This sample showed a methane conversion of 78–80% and a yield of hydrogen close to 1.63 at 650 °C and 38.4 l of CH_4 g^{-1} h^{-1}.

Aghayan et al. reported the synthesis of Ni-based catalysts supported on alumina nanofibers for the methanation of CO_2 and steam reforming by wet-combustion synthesis. The procedure yields homogeneous NiO nanoparticles of about 4 nm size on alumina nanofibers covered with $NiAl_2O_4$. In addition, the catalysts showed outstanding performance in the SRM due to the low density, high gas permeability, and nickel dispersion. The support was stable and prevented the sintering of the nickel nanoparticles. Furthermore, the catalysts showed a relatively low activity in the CO_2 methanation [35].

In a recent research, Rogers et al. [36] studied various nickel aluminate samples such as $NiAl_4O_7$, $NiAl_2O_4$, and $Ni_2Al_2O_5$ prepared by Pechini synthesis and tested in the SRM and DRM reactions in reduced/unreduced form. Due to the presence of fourfold coordinated oxidized nickel, the reduced or unreduced $NiAl_2O_4$ and also the reduced $NiAl_4O_7$ catalysts were active and stable for DRM. The authors commented that due to the limited amount of metallic Ni present on these catalysts, carbon deposition was minimized. The best catalysts for the SRM were the reduced and unreduced $Ni_2Al_2O_5$ and the reduced $NiAl_2O_4$ catalysts due to the presence of metallic nickel that is required for methane steam reforming. Interestingly and due to the small nickel nanoparticles, few carbonaceous deposits were observed during SRM. These catalysts are promising for high-temperature reforming reactions and could be regenerated after the formation of some coking during reaction. Table 4.1 presents the methane conversion.

Park et al. [37] reported the synthesis of NiO–MgO from a solid solution. Upon reduction, the nickel nanoparticles are exsoluted from a $Ni_{0.4}Mg_{0.6}O$ powder. Characterization indicates that the size and dispersion state of the nickel nanoparticles strongly depend on the homogeneity of the parent solid solution. The authors found also that the homogeneity of the solid solution is increased when the sample is sintered at high temperatures. High homogeneity decreases the reducibility of the nickel ions, and consequently, well-distributed nickel nanoparticles are obtained. In response to specific atmospheric conditions, the metallic nickel moves reversibly

Table 4.1 Methane conversion over $NiAl_4O_7$, $NiAl_2O_4$, $Ni_2Al_2O_5$, and commercial 50 wt% Ni/α-Al_2O_3 at 700 °C after six hours on stream for SRM and DRM.

	$X(CH_4)$[a] (%) initial/final			
	Reduced CH_4 dry reforming	**Unreduced CH_4 dry reforming**	**Reduced CH_4 steam reforming**	**Unreduced CH_4 steam reforming**
$NiAl_4O_7$	43	12	Not active	Not active
$NiAl_2O_4$	32	32	78	Not active
$Ni_2Al_2O_5$	Rapidly coked	Rapidly coked[b]	82	78
50 wt% NI/α-Al_2O_3	Coked[c]	Rapidly coked[b]	Rapidly coked[b]	85

a) Methane conversions were assessed at six hours.
b) Coke requiring reactor shutdown at $t < 1$ hours.
c) Coke requiring reactor shutdown at $t < 3$ hours.
Source: Reprinted from Table 4 with permission from the American Chemical Society [36].

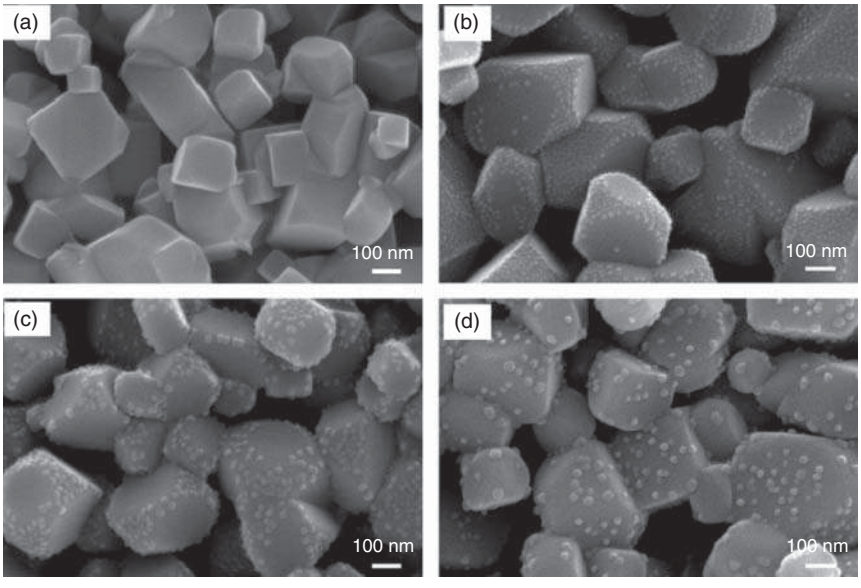

Figure 4.1 SEM images of (a) parent solid solution powder and catalyst samples reduced at (b) 700 °C, (c) 800 °C, and (d) 900 °C for five hours. All samples were sintered at 1000 °C for three hours before reduction. Source: From Park et al. [37]/with permission of Elsevier.

to and out from the parent solid solution. The nickel sample sintered at 1000 °C and subsequently reduced at 800 °C showed a negligible deactivation in the SRM during 1000 hours on stream. Figure 4.1 shows SEM images of the prepared samples.

Some promoters such as Zr, B, La, Mg, and Ce are also used to increase catalytic activity. Ceria and doped ceria supports are also reported in the literature due to the ability to store and release oxygen, decreasing coke formation and allowing therefore operation of the reactor at lower reaction temperatures. Roh et al. [38] reported two series of Ni-based catalysts tested in the SRM and oxy-steam

reforming. Ni/θ-Al_2O_3 and Ni/Ce–ZrO_2/θ-Al_2O_3 catalysts with Ni content from 0 to 15 wt% were prepared. The authors synthesized Ni/Ce–ZrO_2/θ-Al_2O_3 catalysts. Ce–ZrO_2-modified θ-Al_2O_3 support was prepared by the incipient wetness method with a weight ratio of $CeO_2/ZrO_2/Al_2O_3$ equal to 1/4/95. It was found that the high activity and high coke resistance of the Ni/Ce–ZrO_2/θ-Al_2O_3 catalyst containing 12 wt% of Ni were due to the Ce–ZrO_2 layer precoated on θ-Al_2O_3 that formed stable NiO_x species rather than free NiO or inactive $NiAl_2O_4$ and gave mobile oxygen species. Roh et al. reported the synthesis of various Ni–$Ce_{(1-x)}$ $Zr_{(x)}$ O_2 catalysts by coprecipitation with the aim to find a suitable catalyst best for the SRM at severe reaction conditions. The authors found that at 600 °C and using a feed of $CH_4/H_2O = 1$, a Ni–$Ce_{0.8}Zr_{0.2}O_2$ catalyst of 15 wt% of Ni exhibited the highest catalytic activity and stability during the SRM. The authors then concluded that this effect was due to the high oxygen storage capacity of this sample [39]. Duarte et al. [40] studied the SRM on atomically dispersed rhodium/$x$$Sm_2O_3$–$y$$CeO_2$–$Al_2O_3$ catalysts and found that their activities depend on the dispersion of metal and this on the support composition. The authors found using scanning transmission electron microscopy (STEM) that a 12CeO_2–Al_2O_3 support (12 wt% Ce) imparts partial stability to rhodium, resulting in the formation of dispersed atoms of rhodium and rhodium nanoparticles during SRM at 500 °C. In presence of these metal atoms and in the absence of rhodium nanoparticles, lower reaction rates were observed since the formation of CO was inhibited. In another study, Iglesias et al. [41] synthesized and characterized various Ni/$Ce_{1-x}Zr_xO_{2-\delta}$ catalysts that were tested in the SRM at mild experimental conditions. The presence of zirconium enhances nickel reducibility and oxygen mobility. As a result, higher CO/CO_2 molar ratios were observed. Among the samples studied, the Ni/$Ce_{0.85}Zr_{0.15}O_{2-\delta}$ catalyst with 5 wt% of Ni was the best, which showed a conversion above 70% and hydrogen yield of 65% at 600 °C and contact time of 1 mg min (N ml)$^{-1}$. The authors also reported that ceria retains the cubic structure in presence of Zr up to 15 at%. In another research study, Iglesias et al. [42] reported that Zr improved the stability of nickel and reduced coke formation on Ni/Ce–Zr catalysts for the SRM. Based on previous research works, the authors have synthesized and tested Ni/$CeO_{2-\delta}$ and Ni/$Ce_{0.85}$ $Zr_{0.15}$ $O_{2-\delta}$. The percentages of nickel and zirconium were 5 and 15 wt%, respectively.

Lin et al. [43] reported the synthesis of Ni samples supported on $MgAl_2O_4$ and $CaTiO_3/MgAl_2O_4$. The $CaTiO_3$ films were deposited on $MgAl_2O_4$ by atomic layer deposition (ALD). Nickel (1 or 20 wt%) was impregnated on the supports by incipient wetness. The catalysts were characterized and tested in the DRM and SRM reactions. The authors found that reduction of nickel in the Ni/$CaTiO_3/MgAl_2O_4$ catalysts required higher temperatures to achieve activities comparable with those for Ni/$MgAl_2O_4$ samples. However, the exhibited carbon deposition on the former catalysts drastically decreases compared with those on Ni/$MgAl_2O_4$ during the reforming reaction.

Boudjeloud et al. [44] studied 10 wt% Ni–La catalysts supported on α-Al_2O_3 and tested in the SRM from 500 to 800 °C. The nickel/lanthanum weight ratios were 9 : 1, 2 : 8, and 7 : 3. The authors concluded that the addition of La leads to smaller

and well-dispersed NiO particles with strong metal–support interaction (SMSI) that enhance the dissociative adsorption of CH_x species. The highest hydrogen yield of 98% at 800 °C was observed for 7Ni–3La/Al with 7 wt% of nickel and 3 wt% of La.

There are some other recent research reports involving noble metals. Among catalysts based on Ru, Re, and Pt supported on alumina and CeO_2, Amjad et al. [45] found that 1.5% Rh/CeO_2 and 1.5% Rh/Al_2O_3 were the best samples for the oxidative steam reforming and SRM. The 1.5% Rh/CeO_2 catalyst showed complete methane conversion, higher selectivity for CO_2 (87.5%), and H_2 concentration (74.4% dry volume). The catalysts were prepared by combustion of a solution and characterized by various techniques. Duarte et al. [46] synthesized and tested CeO_2-promoted Rh/Al_2O_3 catalysts. The samples were run in the SRM using *in situ* X-ray absorption spectroscopy and online mass spectrometry at 773 K, allowing the determination of the Ce oxidation state during reaction. The catalysts were also characterized by electron microscopy and X-ray diffraction. The authors concluded that 25% of Ce^{4+} was reduced to Ce^{3+} under a flow of CH_4/H_2O/He and a slight reoxidation occurred when the catalysts are exposed to a mixture of steam and He, indicating that only small fraction of CeO_{2-x} may be involved in the water activation step. The presence of Sm_2O_3 further increased the reduction of ceria. In contrast, the reduction of Rh during the SRM is complete. A significant amount of Ce was incorporated into alumina during the SRM forming $CeAlO_3$ species, which impart stability to alumina.

Other alternatives to enhance the SRM are presented in the literature. Carvill et al., Barelli et al., and Harrison [47–49] reported the sorption-enhanced steam methane reforming (SESMR) to intensify the in situ capturing of CO_2 using high-temperature solid sorbent and therefore enriching the production of H_2. Giuliano et al. [50] reported the use of nickel nitrate hexahydrate, nickel acetate, and calcium acetate hydrate as precursors for the preparation of Ni and CaO/mayenite catalysts that were tested in the SRM and SESMR. With the aim to capture CO_2, the authors also tested combined sorbent-catalyst materials (CSCMs) for the methane reforming. Better catalysts for SRM were obtained using nickel nitrate instead of nickel acetate. The CaO54Ni(N)10 sample containing 54 wt% of CaO and 10 wt% of Ni/mayenite obtained from nickel nitrate precursor showed a stable CH_4 conversion. In addition, the presence of calcium enhances the dry hydrogen concentration at the reactor outlet to about 90 vol%, diluent-free.

Wang [51] reported Ni–Re catalysts for the production of H_2 from the SRM. The catalysts were prepared using Ni nanowires that were impregnated with $Ni(NO_3)_2$ and NH_4ReO_4 solutions followed by drying, calcination, and reduction with H_2. Stable CH_4 conversion was observed during 8 h on stream at various reaction temperatures. At 723 K, a CH_4 conversion of about 25% was noticed, and H_2 and CO_2, free of CO, were the main products.

Cobalt supported on alumina is also a good catalyst for the SRM; however, cobalt oxides on this support are more difficult to reduce than nickel species on alumina due to stronger metal–support interactions [52]. In this respect, Profeti et al. [53] reported various Co/Al_2O_3 catalysts promoted with noble metals in low amount (0.3 wt%). The loading of Co in the catalyst was 18% (w/w). The presence of a noble

metal enhances the reducibility of cobalt species. The resultant catalysts were stable and less susceptible to deactivation during the SRM. In addition, the formation of cobalt aluminate was undetectable. The best catalyst found was Co/Al_2O_3 promoted with Pt, which showed high stability and selectivity for H_2.

4.2.2 Theoretical Studies on the SRM

van Grootel et al. [54] studied three reaction pathways for the formation of CO from CH and O species during the SRM on planar and stepped Rh surfaces by quantum-chemical density functional theory (DFT). They found that the barriers for C—O bond formation for planar and stepped Rh surfaces were 180 and 90 kJ mol^{-1}, respectively. In addition, the conventional pathway for CO competes with that for CHO species.

By combining reaction and activation energies with a microkinetic modeling approach, Xu et al. [55] reported a theoretical study to screen a large number of transition metal and transition metal alloy catalysts to predict their rates and selectivities in the SRM reaction. Since the energetics of the intermediates are not strongly structure sensitive, the authors simplified the analysis by considering the stepped (211) facets as a model for open surfaces, since generally more open surfaces are more active. In addition, the adsorption energies, described as function of surface coverage, and the interaction between adsorbates were also considered in the microkinetic model. The theoretical procedure that includes filters related to stability and cost enables the screening of novel, active, stable, and low-cost catalysts for the SRM reaction. The results indicate that Co_3Ni, Co_3Ge and Ni_3Sn, Ni_3Fe, Ni_3Ge, Ni_3Sb, Ni_3As, Co_3Ni, and Co_3Ge are potential catalysts for the inlet and outlet experimental conditions of the steam reforming reactor.

Arevalo et al. [56] studied the energetics of the SRM on Ru catalysts by first-principles calculations based on dispersion-corrected density functional theory (DFT-D2). Their calculation suggests that after activation of methane via an exothermic dissociative adsorption process, it forms CH_y and zH surface-bound state species ($y+z=4$), with C and CH being the most stable adsorbates. The oxidation of C is kinetically slow indicating a possible rate-determining step.

The SRM mechanism on metal-free titania (101) surface has been investigated by Hook et al. [57] using periodic DFT. The authors found that water acts as co-catalyst since it reduces the CH_4 activation barrier from 4.96 to 2.95 eV and lowers the most difficult barrier of dehydrogenation in 2–3 eV. The pathways involving high-energy intermediates were neglected in the calculation. Due to the high barrier for the dehydrogenation of CHO, CO_2 would be the preferred product of the WGS reaction.

In a theoretical study using DFT by Liang et al. [58], the addition of Ca to a Ni (111) surface for SESMR was investigated. The authors found that the presence of Ca enhances water dissociation, the mobility of oxygen, and the oxidation of carbon to CO. The incorporation of Ca to a nickel surface could therefore decrease the rate of coke formation.

Fu et al. [59] have reported first-principles simulations of the adsorption of water on the MnO–Co catalyst. It is known that Co surfaces show weak adsorption for

water, which is unfavorable when this metal is used as catalyst in the SRM. In the present research work, the authors compare the H_2O adsorption properties of MnO–Co, Co (111) surface, and pristine Co clusters. The incorporation of manganese in the Co catalyst strongly enhances the adsorption of water compared with other surfaces, which is crucial for inhibiting coke formation and improving the SRM.

More recently, Niua et al. [60] reported a monolayer of Pt on the Ni surface by DFT coupled with a kinetic study to elucidate and compare the performance of this sample with Pt and Ni catalysts in the SRM. The authors found that the core–shell Ni@Pt catalyst significantly decreased the carbon formation and slightly reduced the catalytic activity compared to other surfaces. Although methane activation is the rate-limiting reaction step for all catalysts, the reaction mechanisms differ. The direct methane activation was the reaction pathway on Ni while methane activation assisted by OH* was on Pt and Ni@Pt catalysts. In addition, the presence of Ni in a bimetallic catalyst modified the electron density of Pt and shifted the d-band center away from Fermi level compared with Pt(111) and Ni(111) surfaces, leading to the formation of strong basic surface OH* that reacts with CH_x species and finally reduces coke formation. The effective activation energy determined by DFT agrees well with the experimental value for Pt and Ni@Pt catalysts.

4.3 Heterogeneous Catalysts for the DRM

4.3.1 Noble Metal Catalysts

Although noble metals are catalytically active for this reaction, the formation of coke and sintering of the metal particles at the high temperatures required for this transformation deactivate the catalysts. Solymosi et al. [61] studied the DRM using Pt metals/Al_2O_3 and the dissociation of CH_4 and CO_2. The catalysts were prepared by impregnation to finally obtain a nominal 1 wt% of metal. The samples were reduced at 500 °C for one hour. The DRM was performed using a CH_4/CO_2 ratio equal to 1 in the reactor feed. The specific activities decreased in the order Ru, Pd, Rh, Pl, and Ir, which agreed with their activity order toward the dissociation of CO_2. Bitter et al. [62] reported that not all the accessible platinum contributes equally to the reforming of methane. The catalytic activity is determined by the accessible Pt located on the perimeter of Pt–ZrO_2. The authors concluded that methane is activated on Pt but CO_2 on the support, forming carbonate species, and that both sites must be in the proximity of each other for the reaction to occur. In addition, the authors reported low activity for Pt black and Pt/SiO_2, which were incapable of forming carbonate species, highlighting the importance of ZrO_2 in the DRM. The authors also concluded that SMSI exist for Pt/ZrO_2 during high-temperature reduction. However, such a state does not persist during the DRM due to the presence of adsorbed oxygen during reaction. Other studies using transition metals as catalysts were reported by Rostrup-Nielsen and coworkers [63] and Nakamura et al. [64]. Pakhare and Spivey [65] recently published a review on DRM with noble metal catalysts.

4.3.2 Ni-Based Catalysts

Due to lower cost and availability, Ni is preferred as the catalyst for this transformation. However, similar to SRM, it also deactivates by coking, sintering, and poisoning. As will be shown below, much of the current related research work is aimed at extending the life of catalysts.

García-Diéguez et al. [66] reported the synthesis of Ni–Pt/alumina catalysts for the DRM. The authors used nanofibrous Al_2O_3 or commercial alumina for the preparation of mono- and bimetallic samples. In addition to the DRM, the catalysts were characterized by X-ray diffraction (XRD), transmission electron microscopy (TEM), X-ray photoelectron spectroscopy (XPS), Raman spectroscopy, and elemental analysis. The authors observed that Pt avoids the sintering of Ni and the formation of $NiAl_2O_4$, improves Ni reduction during activation, decreases the Ni particle size when its concentration increases, and inhibits coke deposition during the DRM. The Pt–Ni/nanofibrous alumina catalyst improves the CH_4 and CO_2 conversions. The Pt content was 0.0, 0.4, 2, or 4 wt%, whereas that for Ni was 0 or 10 wt%. In another study aimed to reduce the coke formation during the DRM reaction, $LaNi_{1-x}\ Ru_xO_3$ perovskite-type oxides of different composition were synthesized, characterized, and tested for this reaction at atmospheric pressure and 750 °C. The authors found that filamentous carbon was formed in all samples but was not harmful. In addition, they found that nickel was more selective to hydrogen but ruthenium formed less carbon. Among their samples, the best catalyst found with the lowest coke formation was the $LaNi_{0.8}Ru_{0.2}O_3$ sample [7]. Dalin et al. [67] published a review on the effect of Ni-based catalysts modified with noble metals on the methane reforming. The authors commented that Ni catalysts suitable for SRM need to present improved properties when used as catalysts in the DRM or OR, such as high resistance to oxidation and coke formation and hot spot reduction. The doping of noble metals to the Ni-based catalysts improves those properties. However, the synthesis method that influences the final catalytic performance is a very important step to achieve this goal.

With the aim to reduce the sintering of Ni nanoparticles, Gould et al. [68] synthesized Ni/Al_2O_3 catalysts by ALD. These catalysts were stabilized by molecular layer deposition (MLD) with a hybrid polymer–inorganic alucone that was then calcined to form a porous alumina film over the Ni particles. The MLD layer, the amount of Ni exposed, and its activity were strongly affected by the calcination and reduction temperatures. The catalyst with 5-MLD cycles yielded the highest steady-state DRM rate, whereas that with 10-MLD was stable even after repeated calcination and reduction. The authors found that the porous alumina MLD layers effectively stabilized the Ni particles reducing sintering. The schematic representation of the process and some TEM images are presented in Figure 4.2.

Salhi et al. [69] reported the synthesis of $NiAl_2O_4$, x-$NiO/NiAl_2O_4$ (x = 5, 10, 15 wt% of NiO). The samples were characterized by XRD, SEM, TEM, BET, and temperature-programmed reduction (TPR) and tested as catalysts in the DRM. The $NiAl_2O_4$ spinel showed relevant catalytic performance, high CH_4 conversion, a H_2/CO ratio equal to 3, and low carbon formation. The presence of Ni inside the $NiAl_2O_4$ spinel leads to high stability and high dispersion of the Ni particles. The

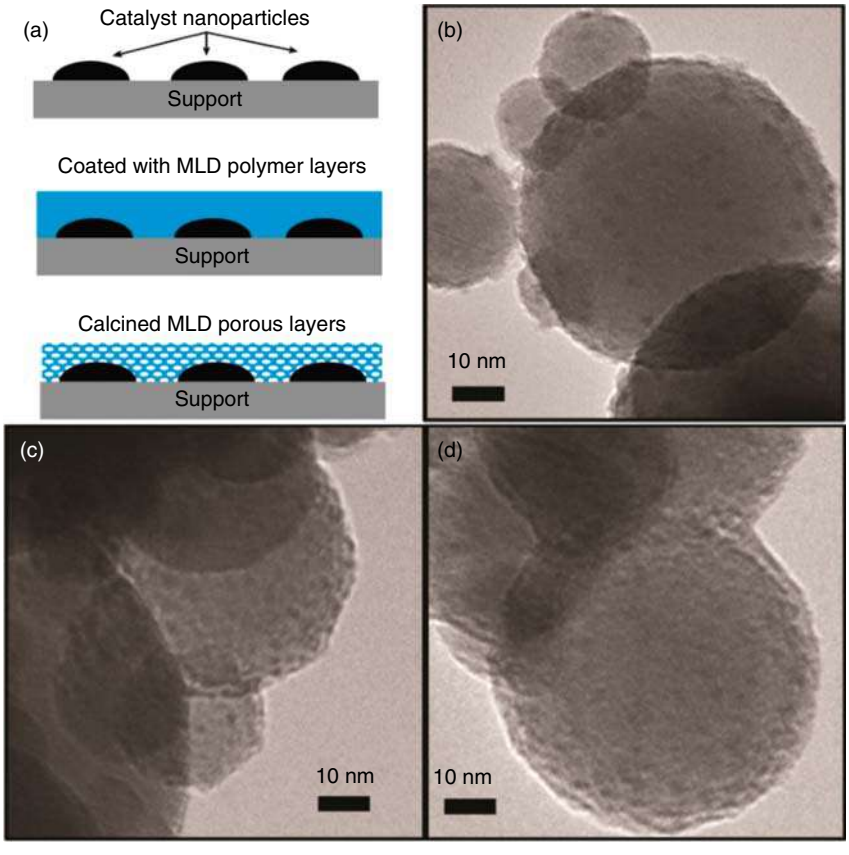

Figure 4.2 (a) Schematic representation of MLD coating process to produce porous alumina overlayers. (b) Ni nanoparticles (2–5 nm dark particles) deposited on spherical alumina; Ni/Al_2O_3 nanoparticles coated by (c) 5-MLD cycles and (d) 10-MLD cycles. The hybrid polymer–inorganic MLD layer is the lighter layer encircling the spheres in (c) and (d). Source: Troy et. [68]/with permission of American Chemical Society.

low coke formation on this catalyst was due to the limited growth of the Ni particles. An increase of the free NiO species decreases the CH_4 conversion and the CO yield, due to sintering of Ni particles, favoring coke formation.

González-Delacruz et al. [70] synthesized Ni/ZrO_2 catalysts reduced under CO or H_2 and tested in the DRM reaction. The nickel content was 3 or 26 wt%. The samples were further characterized by X-ray absorption spectroscopy (XAS) and diffuse reflectance infrared Fourier transform spectroscopy (DRIFTS). The reduction of samples was performed with 5% H_2/Ar or 5% CO/He at 500 °C for one hour using 50 ml min^{-1} and applying a ramp of 10 °C min^{-1} to reach the set temperature. The results indicate that high-temperature reduction with CO reduces the nickel particle sizes and increases the metal dispersion, compared with those results using H_2 as a reducing agent. As a consequence, the methane conversion was higher for the Ni/ZrO_2 sample reduced under CO than that reduced with H_2.

Xie et al. [71] reported the synthesis of $Ni_{0.2}Mn_{0.8}O/SiO_2$ catalyst by a one-pot approach and then evaluated it in the DRM reaction. As a reference catalyst, a bulk material prepared by conventional coprecipitation was used. The catalysts were first reduced in a pure H_2 flow of 15 ml min^{-1} before the DRM reaction. During reforming, a feed of CH_4:CO_2:N_2 = 2 : 2 : 1 was chosen. The $Ni_{0.2}Mn_{0.8}O/SiO_2$ catalyst showed remarkable activity at 500 °C, much higher than that observed for the reference sample.

Zanganeh et al. reported the synthesis and application of various $Ni_xMg_{1-x}O$ ($x = 0.03, 0.07, 0.10, 0.15, 0.25$) on the DRM [72]. The $Ni_{0.03}Mg_{0.97}O$ catalyst showed relative low methane and CO_2 conversions in the temperature range from 600 to 700 °C compared with other catalysts but excellent coke resistance that was attributed to the high dispersion of small Ni species showing SMSI and to the basicity of the support. The difficulty in the reduction of Ni from a NiMgO solid solution generates small Ni particles. Coke deposition increased when the Ni particle size was increased.

Margossian et al. [73] reported the preparation of NiFe supported on MgAl mixed oxide catalysts through colloid synthesis, and the samples were then tested in the DRM reaction. The catalysts prepared following this procedure were $Ni_{0.5}Fe_{0.5}$, $Ni_{0.75}Fe_{0.25}$, Fe, Ni, and Ni/Mg(Al)O used as reference. In addition, the samples were reduced at 650 or 850 °C prior to the reforming reaction. The catalysts were characterized by Fourier transform infrared (FTIR) spectroscopy, energy-dispersive X-ray (EDX) spectroscopy, and *operando* XAS at the Ni K-edge and the Fe K-edge, TEM, and high-angle annular dark field scanning transmission electron microscopy (HAADF-STEM). They found that supported 3–4 nm NiFe particles with a Ni/Fe ratio of 3 showed an enhanced stability compared with the corresponding pure Ni-based catalyst and a higher activity in comparison to conventional NiFe catalysts. NiO are the active sites for the DRM, and FeO effectively removed the coke, enhancing the nickel catalyst performance. TEM images are presented in Figure 4.3.

Kambolis et al. [74] have synthesized and characterized Ni/(CeO_2–ZrO_2) catalysts that were tested in the DRM. The CeO_2–ZrO_2 supports contained 28–100% CeO_2. The catalysts were characterized by N_2 adsorption–desorption, XRD, UV-Vis diffuse reflectance spectroscopy (DRS), TPR, SEM-EDS, and temperature-programmed hydrogenation (TPH). XRD indicated the formation of $Ce_xZr_{1-x}O_2$ in all samples, whereas the formation of lattice defects in binary solid solutions was detected by UV–Vis DR. The presence of Zr increases the reducibility of the support and catalysts and improves the catalytic activity, attributed to an increase in the active sites. It was also observed that the amount of coke depends on the Ce/Zr ratio rather than on the catalytic activity. The higher the Zr content in the catalysts, the greater the catalytic activity and the resistance to coke formation.

Wang et al. [75] studied the DRM under the presence of Ni–Si/ZrO_2 or Ni–Zr/SiO_2 at 400 and 450 °C. In addition, the samples were characterized by H_2-TPR, XRD, TEM, thermogravimetric analysis combined with mass spectrometry (TGA-MS), Raman, *in situ* XPS, and DRIFTS. The initial CO_2 and CH_4 conversions at 400 °C were higher for the Ni–Si/ZrO_2 than for Ni–Zr/SiO_2. In the former catalyst, the coke species (C_1 coke) were easy removed, contrary to those formed at 450 °C (C_2 coke).

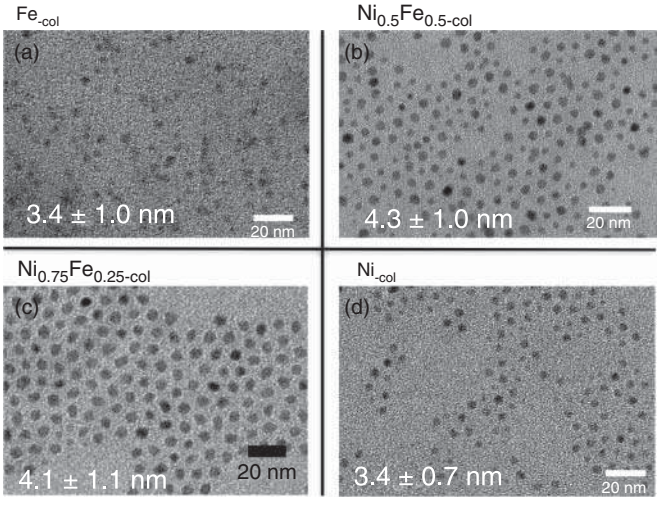

Figure 4.3 TEM images of the different colloids: (a) Fe, (b) $Ni_{0.5}Fe_{0.5}$, (c)$Ni_{0.75}Fe_{0.25}$, and (d) Ni. Source: Margossian et al. [73]/with permission of American Chemical Society.

In contrast, the NiO species on Ni–Zr/SiO_2 were oxidized to NiO species at 400 °C, could not be restored, and led to deactivation.

Horiuchi et al. [76] reported the use of Na, K, Mg, and Ca oxides on the Ni/Al_2O_3 in the DRM aimed to reduce coke formation. These oxides strongly suppress coke formation that was attributed to the ability of the catalytic surface to reduce the decomposition of methane. The amount of coke formed on the Ni/Al_2O_3 (10 wt% of Ni) and on the modified catalysts after 5 h in the DRM at 800 °C was reduced about 90%, showing the positive effect of the use of Na, K, Mg, and Ca oxides (10 wt% on Ni/Al_2O_3).

Among various supports, MgO is commonly used due to its high thermal stability and low cost that maintains a relative large surface area at high temperatures, compared with other supports [77]. In addition, MgO imparts Lewis basicity causing strong adsorption of CO_2 and reduces the coke deposition [78]. Shen et al. [79] reported and characterized mesoporous Ni–Al and Ni–Mg–Al samples that were then tested as catalysts in the DRM. The catalysts were prepared by the evaporation-induced self-assembly (EISA) method, using Pluronic P123 or not, as a soft template. The authors observed that the ordered mesoporous samples showed higher activity and durability for the DRM and were stable after 30 h at 750 °C, as observed by TEM and surface area determination. In addition, the mesoporous samples avoid the sintering of Ni particles and suppress the formation of coke. The activity of the catalysts was not enhanced with the addition of Mg, but coke formation during the DRM was suppressed. Xua et al. [80] studied the DRM in the presence of Ni–Mg–Al oxides as catalysts. The mesoporous samples with various Ni and Mg loadings were synthesized following the EISA procedure. The framework stabilized the Ni nanoparticles and showed a confinement effect. Among the prepared samples, the 15Ni–2Mg–83Al catalyst (coefficients in mol%)

showed attractive catalytic activity, low coke formation (small Ni nanoparticles), and high stability over 100 h in the DRM. Mette et al. [81] studied the influence of the structural and compositional nickel catalysts on the activity in the DRM reaction and on the formation of coke during this reaction. They reported a series of Ni/MgAl catalysts of different Ni content obtained from a hydrotalcite-like precursors $Ni_xMg_{0.67-x}Al_{0.33}(OH)_2(CO_3)_{0.17} \cdot mH_2O$. High-resolution transmission electron microscopy (HRTEM) showed that the diameter of the nickel particles varies from 7 to 20 nm. In addition, the formation of nickel aluminate overgrowth on the nickel particles was observed. The catalyst with 5 mol% Ni showed that the formation of coke effectively decreases, due to the overgrowth of nickel aluminate, while the catalytic activity on the DRM was preserved. Contrarily, large metallic nickel surfaces at high nickel contents (50 mol%) showed significant coke formation during the DRM reaction. In a different report, Guczi et al. [82] studied the surface carbon species formed during the DRM on $NiMgAl_2O_4$ catalysts containing 8.8 wt% of Ni. A feed of 29% CO_2 and 71% CH_4 was used during catalytic tests. The performance was studied doing sequential reactions. Characterization indicates that after the first reaction, Ni carbide is possibly formed and after several sequential reactions, the surface is graphitized forming carbon nanotubes. The addition of 0.5 wt% of gold to $NiMgAl_2O_4$ improved the catalytic activity and inhibited the formation of carbon nanotubes. Margossian et al. [83] synthesized and characterized nickel-based catalyst by tailoring the Ni precursor and the support for the DRM reaction. The authors demonstrated that Ni dispersions as high as 33% could be achieved by using a precursor, namely $[\{Ni(\mu_2\text{-}OCHO)(OCHO)\text{-}(tmeda)\}_2(\mu_2\text{-}OH_2)]$ (tmeda = tetramethylethylenediamine) that is soluble in a broad range of solvents and can be dispersed on supports. The reduced samples showed good dispersion of Ni and particle sizes of about 2.0 ± 1.0 nm. Such small Ni particles increased the catalytic activity and reduced coke formation. However, *operando* X-ray absorption near-edge structure (XANES) spectroscopy confirmed that deactivation largely occurred by the migration of such nanoparticles forming $NiAl_2O_4$ when γ-alumina was used as the support. On the contrary, modification of alumina with magnesium mitigates the reactivity of nanoparticles with alumina, and the resulting catalyst showed good activity and stability for the DRM reaction over 20 h on stream. In another study, Bu et al. [84] prepared a series of samples, mainly Ni–Mg–Al and Ni–Mg–Al–BN catalysts with various Ni content that were tested in the DRM. The best catalyst found was the reduced Ni–Mg–Al–BN catalyst containing 5 wt% of nickel. The results indicate that Ni nanoparticles are well-dispersed and embedded in the structure, preventing the sintering of nickel during DRM. Boron nitride improved the thermal stability and hindered the collapse of the $(Ni,Mg)Al_2O_4$ at high temperature. The stability was related to the fast formation of carbonate and hydroxyl species, reducing coke during the DRM reaction. The study also suggested that the SMSI avoided the sintering of nickel particles.

The presence of cerium led to a catalyst with higher activity in the DRM, better stability, and lower coke formation compared to the counterpart Ni catalyst. Liu et al. [85] studied the activity of Ni–CeO_2 catalyst in the DRM. The catalyst contained very small NiO particles dispersed on a solid solution of Ce_{1-x} Ni_xO_{2-y}.

The overall composition of the catalyst was 20% NiO/80% CeO_2.The authors found by XPS that at ambient temperature, CH_4 can be dissociated at temperatures as low as 27 °C, generating adsorbed CH_x and CO_x species on the surface of the Ni/CeO_2 catalyst. No signals assigned to carbon or nickel carbide were noticed in this experiment. In addition, the DFT calculation indicates that the effective barrier for the activation of methane on the Ni(111) surface and on the $Ni/CeO_{2-x}(111)$ is 0.9 and 0.15 eV, respectively, showing a significant decrement by the presence of ceria. The authors observed that the DRM occurs efficiently on this catalyst. In another work, Wang et al. [86] prepared Ni–Ce–Al samples following the EISA method that were tested in the DRM reaction. Following this method, the Ni nanoparticles were stabilized inside of the channels of the alumina matrix. The catalyst with a Ce/(Ce + Al) ratio of 1% exhibited the highest and stable catalytic activity at 700 °C and showed conversions of 70% and 68% for CO_2 and CH_4, respectively. The improved catalytic activity was explained by the large surface area, high dispersion, and stability of the nickel nanoparticles in the alumina framework. In addition, the catalyst showed high resistance to carbon deposition, contrarily to the nickel impregnated alumina catalyst, used as a reference. Chen et al. [87] studied the carbon resistance of the Ni/Ce–AlO catalysts during the DRM reaction. The authors found that after reduction at 900 °C, cerium is present as $CeAlO_3$ and was expected to be under the DRM reaction conditions. This phase improves the resistance to carbon formation without decreasing the catalytic activity. All tested catalysts with or without $CeAlO_3$ showed good catalytic activities at 700 °C during 250 h on stream and using 20 l $(h\,g_{cat})^{-1}$ but presented different coke formation. A decrease from 0.92 to 0.29 g g_{cat}^{-1} in carbon deposition was measured, along with the increase in the $CeAlO_3$ phase. Graphitic carbon was retarded by this phase, whereas amorphous carbon was independent of it. The $CeAlO_3$ species were able to decompose CO_2 to form active surface oxygen, and this oxidative environment of nickel particles could be responsible for the carbon-resistance enhancement. In another study, Zhang et al. [88] reported the synthesis of Ni–Ce/SBA-16 samples that were tested in the DRM. The presence of Ce (Ni/Ce = 1) facilitates the reduction of nickel and resulted in the formation of stable nanoparticles of about 5.7 nm with high activity in the DRM at 700 °C over 100 h. Ce also imparts stability to the SBA-16. The authors also found by Ce L_{III}-edge XANES that Ce^{3+} species were predominant in the fresh and spent catalysts. Nandini et al. [89] studied the carbon formation during DRM using $13.5Ni–2K/10CeO_2–Al_2O_3$ (the coefficients indicate the wt% in the sample) as a catalyst at 650, 700, and 750 °C over 60 h. The sample was characterized by thermogravimetric analysis (TGA), XRD, XPS, BET, and TEM. The authors observed that at 700 and 750 °C, the carbon was well distributed on the surface of the catalysts and was not seen, whereas at 650 °C, the sample presented a significant amount of coke of graphitic form. However, this high coke content did not affect its catalytic activity. The authors proposed that this deposited carbon is probably active in the formation of CO. It is suggested that both DRM and CO disproportionation contribute to carbon deposition. XPS results indicated that carbon was present as carbonaceous (-C-C-) and oxidized carbon species. The effect of ceria is related to the high mobility of oxygen and the redox properties imparted

to the catalyst. In another study, Ocsachoque et al. [90] prepared and tested mono- and bimetallic Rh–Ni/CeO_2–Al_2O_3 catalysts in the DRM. The alumina support was modified with 3 and 5 wt% of Ce. In addition, the catalysts were characterized by hydrogen chemisorption, TPR, XRD, XPS, BET, and TEM. The authors studied the influence of calcination temperature and Ce loading on the activity and stability of the catalysts for the DRM. The addition of Rh and Ce to nickel improves the catalytic activity. The promoted Rh–Ni/CeO_2–Al_2O_3 catalyst containing 3 wt% of Ce calcined at 650 °C presented the highest catalytic and stability for the DRM, which was attributed to the interaction of the Rh and Ce phases that improved Rh dispersion. Furthermore, Rh increases the resistance to deactivation. Other studies have also reported the positive effect of ceria when added to Ni catalysts [91–93] that was attributed to the excellent redox properties of ceria by releasing lattice oxygen under reducing conditions, creating anionic vacancies, which are correlated to the high lattice oxygen mobility [94].

In a study related to Ni/La_2O_3/γ-Al_2O_3 and Ni/La_2O_3/α-Al_2O_3 catalysts on the DRM, Junke et al. [95] found three morphologies of carbon species: amorphous (polymeric), filamentous, and graphitic carbon. The amount and morphology of the carbon species depended on the size of the Ni particle and the texture of the support. The authors also commented that the sample with metallic Ni particles smaller than 15 nm suppressed the formation and deposition of filamentous carbon, decreased carbon deposition, and showed therefore a better catalytic activity and higher stability due to the presence of more active C_α species. Al-Fatesh et al. [96] studied the effect of La_2O_3 as a support and promoter on Ni-based catalysts. The following samples were prepared and studied: Ni/La_2O_3, Ni/Al_2O_3 and Ni/(La_2O_3 + Al_2O_3) with 10, 20, and 30 wt% La_2O_3. The Ni content was 5 wt% in all catalysts. The authors found that the addition of La to the catalyst alumina matrix improves the dispersion of Ni and the adsorption of CO_2 enhancing the catalytic activity and stability. The DRM was studied in the temperature range of 500–700 °C.

Fujita et al. [97] studied the DRM reaction at 450 °C using Ni/Y_2O_3 composites dealloyed from $Ni_{12.5}Y_{12.5}Al_{75}$ and Ni_{25} Y_{25} Al_{50} and compared their catalytic activities with the Ni/Al_2O_3 and Ni/Y_2O_3 catalysts prepared via chemical routes. At low temperature, coke formation tends to be significant on Ni catalysts. The authors found that at such experimental conditions, the composites showed remarkable activities and stabilities compared with the performance of the Ni/Al_2O_3 and Ni/Y_2O_3 catalysts. The good performances of the composites were attributed to the aluminum oxide remaining in these materials that suppressed coarsening of the pores. The inert Y_2O_3 nanowires were useful as substrate. Figure 4.4 shows some STEM images of the spent catalysts.

Li et al. [98] have previously found that Y_2O_3 behaves as a promoter when added to the NiO/SBA-15 catalyst for the DRM. The authors noticed that among the catalysts tested in the DRM, the best was the Y–NiO/SBA-15 sample containing Ni/Y weight ratio of 1 : 1, which showed good stability, low carbon deposition, and excellent catalytic activity. The authors also reported strong interaction of Ni particles and the support as a result of Y_2O_3 segregation. The samples were prepared by sol–gel using 9 wt% of Ni and Ni/Y weight ratios of 9 : 0, 3 : 1, 3 : 2, and 1 : 1.

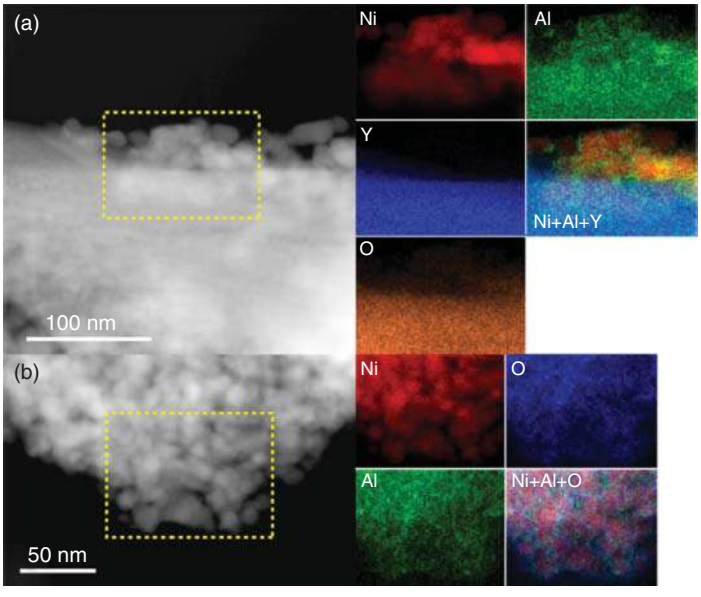

Figure 4.4 STEM image and EDS chemical maps of the selected area, showing the elemental distributions after the DRM tests of the nanoporous Ni/Y_2O_3 composite (i.e. dealloyed $Ni_{12.5}Y_{12.5}Al_{75}$): (a) 650 °C for three hours and (b) 450 °C for 100 hours. Source: Fujita et al. [97]/with permission of American Chemical Society.

Ibrahim et al. [99] prepared various Ni-based catalysts that were tested in the DRM reaction at 800 °C. Ni, Co, and Ni–Co supported on SBA-15 and SBA-15 doped with Zn or Ce were synthesized. The metal content was 5 wt% of mono- or bimetallic samples. Ni/SBA-15 showed the best activity and selectivity (high H_2/CO), followed by Co–Ni/SBA-15 and Co–Ni/Ce–SBA-15 and finally by Co/SBA-15 and Co–Ni/Zn–SBA-15. Ce and Zn influenced the reducibility of the catalysts and increased the acidic sites as determined by temperature-programmed desorption (TPD) of ammonia. In another research report, Chotirach et al. [100] studied various Ni-based catalysts supported on SBA-15 and promoted with TiN on the DRM. The samples were prepared in two steps: synthesis of SBA-15 in the presence of TiN followed by the impregnation of Ni. The Ni content was 2.5, 5, 7.5, or 10 wt%, whereas that of TiN was 5, 10, 15, or 18 wt%. The authors found that the presence of TiN enhances the catalytic activity during DRM and reduces coke formation by increasing the basicity of the surface, compared with those samples without TiN. Among the prepared samples, the Ni/TiN–SBA-15 catalyst with 10 wt% of Ni and 5 wt% of TiN showed good stability, high methane and CO_2 conversions of about 70%, H_2/CO ratios of about 0.8, and over 800 h on stream at 700 °C. In another study, Zhicheng et al. [101] reported the synthesis of Ni supported on KIT-6, a mesoporous silica, and tested as catalysts in the DRM. The Ni particles of less than 5 nm were highly dispersed on the pore walls of the support. The pores of this silica structure are open and accessible to reactants. The Ni particles present strong interaction with the support and showed high catalytic activity and selectivity. In addition, the

catalysts exhibit high resistance to coke formation during DRM, contrarily to the performance of a Ni conventional catalyst.

Theofanidis et al. [102] synthesized and characterized a series of Ni–Fe/$MgAl_2O_4$ catalysts, using various Fe/Ni ratios from 0 to 1.5. The samples were then tested in the DRM at atmospheric pressure, from 650 to 800 °C using a ratio of $CH_4/CO = 1$ in the feed. The catalysts structure during H_2-TPR, CO_2–TPO (temperature-programmed oxidation), and DRM were studied by time-resolved in situ XRD. The H_2–TPR results indicate that above 700 °C, the reduction of NiO and Fe_2O_3 formed a Ni–Fe alloy. This alloy was stable under CO_2 during reoxidation and decomposed to Ni and Fe_3O_4 above 627 °C. The authors commented that the Ni–Fe alloy is the active phase during the DRM. From pulse experiments with CO_2 and CH_4 throughout the DRM and over Ni–Fe/$MgAl_2O_4$, Ni/$MgAl_2O_4$, and Fe/$MgAl_2O_4$, the authors noted that this reaction can be described by a Mars–van Krevelen mechanism. A catalyst with 0.7 Fe/Ni ratio showed high selectivity to CO and a CO/H_2 ratio close to 1. The experiments indicate that the activity of the catalysts can be restored after regeneration and that the effect of Fe on the Ni/$MgAl_2O_4$ catalyst depends on the employed Fe/Ni ratio.

Subhasis et al. [103] reported interesting nickel nitride catalysts for the DRM. The samples were highly efficient in the reforming reaction. In addition, the catalysts were also very resistant to coke formation. Mesoporous alumina was first synthetized using Pluronic 123, aluminum isopropoxide, and anhydrous ethanol. Nickel nanoparticles were deposited in mesoporous alumina by an organic matrix decomposition technique and further nitrided under NH_3. The samples were characterized by XRD, XPS, and TEM. The final catalysts contained 2.5%, 5%, 7.5%, and 10% nickel nitride/aluminum nitride, or alumina mixed phase. The samples were tested in the DRM without reduction at 700 °C under various contact times. The authors noted that short contact times favor the DRM over side reactions and produce H_2/CO ratios close to unity. A further decrease in contact times diminishes the methane conversion. At 700 °C, 10 l h^{-1} g^{-1}, and 200 h under stream, the best catalyst found was 5% nickel nitride/aluminum nitride showing feed conversions of 90% and 89% of methane and carbon dioxide, respectively, and a stable H_2/CO ratio of about 0.98. On the contrary, a rapid deactivation due to coke deposition was observed using a commercial NiO/silica catalyst. A DFT study on nickel nitride was also performed. The authors concluded that the small nickel nitride particles into the support show remarkable stability due to the contact with both aluminum nitride and alumina, whereas those at the surface and in contact only with aluminum nitride are rapidly oxidized and prone to deactivate through coke deposition during the DRM reaction.

4.3.3 Co-Based and Other Catalysts

Cobalt supported on alumina is also a promising catalyst for the DRM [104, 105]. Ji et al. [105] prepared Co catalysts supported on alumina from various sources and applied them in DRM. The Co content was 10 wt% in all samples and was impregnated on commercial alumina (CoAlco-im) and sol–gel made alumina (CoAlsg-im). In addition, another sample with the same Co loading was prepared by direct sol–gel processing from organometallic compounds (CoAlsg). The latter

sample showed a lower catalytic activity than other samples due to the formation of $CoAl_2O_4$ but presented the lowest coking rate and a lifetime 24 times longer than CoAlco-im at 700 °C using a CO_2/CH_4 ratio equal to 0.88 in the feed. The catalyst on commercial alumina showed heavy and fast deposition of coke. The great catalytic performance of CoAlsg was due to the presence of smaller Co particles with SMSI and abundant OH species on the surface. Ruckenstein and Wang [106] studied the DRM in the presence of supported Co catalysts. The authors tested the following supports: MgO, CaO, SrO, BaO, γ-Al_2O_3, and SiO_2. It was found that only MgO showed a high activity and stability during 50 h on stream, with yields of 93% and 90% for CO and H_2, respectively. The Co/γ-Al_2O_3 catalyst showed also a high initial CO yield, but it deactivated quickly. The formation of a solid solution of Co–Mg on the Co/MgO catalyst was detected by XRD. Such a solid solution is less reducible than pure CoO and forms small clusters of Co^0 partially embedded in the substrate, reducing sintering and coke formation. The interaction of Co with the MgO was suggested to be responsible for the high activity and selectivity in the DRM.

In another study, the effect of La, Ce, Mn, Mg, and K as promoters for the Co/ZrO_2 catalysts employed in the DRM was studied by Özkara-Aydınoğlu and Aksoylu [107]. Among the catalysts prepared, the Co/ZrO_2 doped with Ce showed the highest activity and a small loss in activity over 6 h in the DRM at 650 °C with a CH_4/CO_2 ratio of 1 : 1. In the case of Co/ZrO_2 doped with La, it presented a moderate activity, less coke formation, and high stability. The Co content was 5 wt%, and that of the promoter was 2 wt%. Wang et al. [108] reported the doping effect of Mn on the Co–Ce–Zr–O_x catalysts in the DRM. The samples were prepared by coprecipitation and characterized by various techniques. The highest catalytic activity and selectivity in the DRM were observed using a catalyst with a Mn/(Ce + Zr + Mn) molar ratio equal to 10 that was attributed to the surface oxygen species and oxygen mobility. Characterization of the coke formed on the Mn-doped catalyst indicated the easy removal of coke from the surface due to the high oxygen mobility. In addition, Mn increased the dispersion of Co species.

Nagaoka et al. [109] studied the effect of the addition of Pt or Ru on 0.5 wt% Co/TiO_2 and the replacement of Co by Ni in the DRM. The atomic Pt/Co ratios used varied from 0.005 to 0.05, and those for Ru/Co from 0.01 to 0.05. Furthermore, for the replacement of cobalt by nickel, Ni/Co atomic ratios equal to 1 : 99 and 100 : 0 were explored. Due to the oxidation of Co during the DRM, the Co/TiO_2 reduced at 850 °C showed slow deactivation. Contrarily, the presence of noble metals in the Co/TiO_2 enhanced the Co reducibility and drastically improved the stability of the catalyst during reaction. Strong coke formation resulted when Ni replaced Co in high content, whereas in small amount, a further enhancement of the catalytic stability of Co/TiO_2 was observed. A Co/Ni ratio of 90 : 10 was found to be optimum, showing high stability and small coke deposition of the Co–Ni/TiO_2 catalyst during the DRM at 2 MPa where coke formation is highly enhanced.

In the work reported by Mirzaei et al. [110], the authors presented a study of the DRM in the presence of Co–MgO catalysts with various Co loading. They found that the catalyst with 10 wt% Co was very stable and active for the DRM. The samples

were characterized by XRD, BET, TEM, TPR, SEM, and TPO. The catalysts were prepared by coprecipitation.

Asami et al. [111] performed the DRM using ceria-supported metal catalysts. Fe, Co, and Ni were used as active metal. The loading was 5 wt% for each metal. The DRM was performed at 850 °C and used 500 mg of catalyst and 100 ml min^{-1} (standard temperature and pressure [STP]) of $CH_4/CO_2 = 1$. Coke formation was not observed, and the activity and selectivity were stable during 24 h under stream. The reduction of the catalyst at 850 °C is very important to obtain an excellent catalytic performance. Ni catalyst showed the highest activity for the DRM.

Liu et al. [112] reported a high active and stable catalyst for the DRM. The remarkable catalytic performance of a ceria-supported Ru nanocluster (<1 nm) was characterized by in situ XRD and XAFS while the surface by ambient-pressure X-ray photoelectron spectroscopy (AP-XPS) and DRIFTS. The authors found that methane activates on the surface at temperatures as low as 150 °C. During the DRM reaction, the formation of $Ru^{\delta+}$–CeO_{2-x} occurred that differs from that when large Ru nanoparticles are supported on ceria. The oxidation of surface carbon was correlated with the oxygen transfer governed by $Ru^{\delta+}$–CeO_{2-x} interactions at temperatures higher than 300 °C. Ruthenium carbonyls, carboxylate species, surface −OH groups, and polydentate carbonates were identified by DRIFTS.

Mounfield et al. [113] studied the morphological effects of tungsten carbide nanoparticles (β-W_2C) and nanorods (α-WC) on the catalytic activity and coke formation during the DRM. The authors found that β-W_2C nanoparticles maintained high activity and exhibited less coke formation for more than 40 000 turnovers than α-WC nanorods that deactivated after only 8000 turnovers. The dissimilarity in coke formation was attributed to the difference of the exposed facets present in both morphologies.

Wu et al. [114] reported effective Ni–Co/Al_2O_3 catalysts for the DRM. The catalyst showed good activity in the DRM even at 350 °C. All samples were characterized by XRD, XAS, HRTEM, extended X-ray absorption fine structure (EXAFS), XPS, and DRM reaction. The authors found that a Ni–Co alloy was formed after calcination under H_2 flow, which was extremely active for the DRM at various temperatures. The lattice of the Ni–Co alloy showed good ability for the dissociation of CO_2 and weak chemisorption for H_2 inhibiting the reverse water–gas shift (RWGS) reaction. The electron microscopy characterization is shown in Figure 4.5.

Fan et al. [115] prepared a series of Ni–Co catalysts supported on Mg–Zr oxide (Zr/Mg = 9 : 1) that were tested in the DRM. The total metal content was 6 wt% of any metal or 3 wt% for both Ni and Co in the case of bimetallic catalysts. The samples were characterized by XRD, XPS, N_2 physisorption, H_2 chemisorption, thermogravimetric analysis coupled with differential thermal analysis (TGA-DTA), HRTEM, H_2-TPR, TPH, SEM, and DRM at 750 °C, 1 atm, using a CH_4/CO_2 feed ratio of 1. The authors found that the best catalyst was the bimetallic sample with methane and CO_2 conversions of 80% and 84%, respectively, and a constant activity during 60 h showing gradually deactivation at longer times. In addition, the sample recovered its initial activity after regeneration in air for one hour. The authors concluded that the high catalytic performance of the bimetallic catalyst

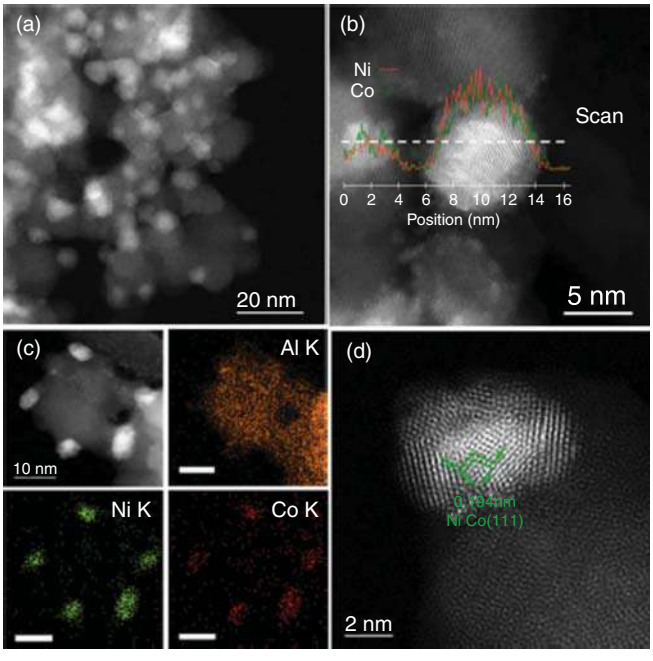

Figure 4.5 Electron microscope characterization of Ni–Co/Al_2O_3–S catalyst (-S means stepwise impregnation method): low- (a) and high-magnification (b) high-angle annular dark field (HAADF)-STEM images. The inset profile in (b) shows the intensity of nickel and cobalt along the white dashed line, collected via energy-dispersive X-ray spectroscopy (EDS). (c) Elemental analysis: STEM Z-contrast image and corresponding elemental maps of Al, Ni, and Co using Kα peaks (1.49, 7.47, and 6.92 keV, respectively) from the whole region (the scale bars represent 10 nm). (d) High-resolution STEM Z-contrast image. The green label marks the measured interplanar spacing (0.194 nm), which could be assigned to the (111) plane of Ni–Co alloy. Source: Zhaoxuan et al. [114]/with permission of American Chemical Society.

was attributed to better metal dispersion, small particle size, a synergetic effect of Ni and Co, and stabilization of the *t*-phase of ZrO_2.

Bhavani et al. [116] reported the synthesis of lanthanum-substituted barium manganite $La_{1-x}Ba_xMnO_3$ ($x = 0.10$–0.50). The solids were then tested as catalysts in the DRM. The authors reported that the optimal level of Ba/Mn = 0.1, 0.15 resulted in a catalyst with high surface area, uniform particles, and highly ordered pores that showed high conversions, high syngas selectivity, and low coke formation. The catalysts showed enhanced reducibility of Mn^{3+}/Mn^{4+} to Mn^{2+} and a rapid migration of oxygen from the bulk to the surface. The authors concluded that this facility of donating lattice oxygen to the catalytic surface seems to be responsible for the decomposition and dissociation of CH_4 and CO_2, which resulted in a high catalytic performance. The catalytic experiments were performed during 25 h at 800 °C over reduced perovskites and used a feed with a mole ratio of $CH_4/CO_2 = 1/0.8$. The best catalysts showed stable methane and CO_2 conversions of about 90% and 80%, and selectivities for H_2 and CO were about 70% and 60%, respectively.

Recently, a review on catalysts used in the DRM was published by Singh et al. [117].

4.3.4 Theoretical Studies on the DRM

The reaction mechanism of the DRM on Pt^{4+}/ZrO_2 was investigated by DFT together with the periodic slab model. Wang and Gao [118] found that the preferential pathway is the decomposition of CO_2/CH_4 to form CH species that react with carbonate to produce formate species to further decompose, producing CO and OH. The study indicates that ZrO_2 provides a unique site for adsorption of CO_2, a very important step to form carbonate and formate species. In addition, it was also found that formate species is the key intermediate and its transformation to CO and OH is the rate-determining step.

In another work, Zuo et al. [119] studied the reactivity of a single-atom Ni_1/MgO_2 (100) site and the Ni_4/MgO_2 (100) single site in the DRM by DFT and kinetic Monte-Carlo simulation. In addition, the calculations were accomplished by DRM experiments. The theoretical calculations indicate that a single-atom Ni/MgO site is unable to produce H_2, CO, and H_2O, whereas Ni_4/MgO_2(110) site is capable to break the CH_4 and CO_2 bonds under the DRM experimental conditions. The predictions from theory were confirmed by experimental studies on DRM.

Fan et al. [120] studied the microkinetic of the DRM on nickel surfaces by DFT. The adsorption and the activation energies were evaluated for the elemental reaction steps on three facets of nickel, Ni(111), Ni (100), and Ni(211) as flat, open, and stepped surfaces, respectively. The information was then used for the evaluation of the reaction rate coefficients at realistic reaction temperatures and pressures. The authors found that at low partial pressure of CH_4 and CO_2, both the dissociative adsorption of CH_4 and the carbon oxidation would dominate the overall reaction rate. However, at high pressures, it is suggested that the oxidation of carbon or CH is the rate-limiting step in the DRM.

Huygh et al. [121] performed DFT calculations on the resistance of the TiO_2 anatase (001) surface for coke formation during the DRM reaction. The authors found that the stability of C and CH is significantly lower than those of CH_2 and CH_3. In addition, the hydrogenation rates are higher than dehydrogenation for various species in the temperature range of 27–727 °C. Appreciable dehydrogenation rates of CH_3, CH_2, and CH only occur at 327, 627, and 627 °C, respectively. The authors concluded that anatase titania (001) is a high coke-resistance surface that will be likely stable during the DRM reaction.

4.4 Comments on Both SRM and DRM Processes

Both technologies for the production of syngas are well established and play an important role in the production of hydrogen. The CO generated from the SRM or DRM processes is also a very valuable product. However, after utilization of the CO in different processes, it frequently ends up as CO_2. To reduce the contamination

of the atmosphere by this gas, it is urgent to capture and reuse it. According to the United Nations Intergovernmental Panel on Climate Change (IPCC), atmospheric concentrations of CO_2 equivalent must be limited to 450 ppm by 2100 to prevent global warming of greater than 2 °C [122]. However, as reported by the International Energy Agency (IEA), the energy sector will increase the CO_2 emissions from 50% in 2030 to 80% in 2050 [123]. The monthly average level of CO_2 in the earth atmosphere was 416.71 ppm in December 2021. Furthermore, an annual mean growth rate of 2.31 ppm of CO_2 yr^{-1} was measured in 2020 [124].

4.5 Final Remarks

As observed in this review, the challenge in relation to the catalysts utilized in the DRM and SRM is still the design and development of a cheap, environmental-friendly, stable, and active catalyst to reduce coke formation, expand the lifetime of the catalysts, and prolong therefore the operation of the reactor reducing the frequency of shutdown. In addition, a reduction in the reaction temperature might be achieved by designing a suitable catalyst, which is also very desirable, since both the SRM and DRM are highly energetically demanding processes. Some reports in the literature show that the synthesis of tailored catalysts is possible that allow the dispersion of metal particles of few nanometers in size. Such small nanostructures reduce coke formation and present high catalytic surface area leading to more efficient catalysts. In addition, confinement of the nanoparticles to reduce sintering is also highly desirable to obtain a high catalytic performance. Furthermore, the facilities to perform theoretical studies are nowadays commonly available. This is of great importance since the catalytic synthesis of H_2 and CO can be simulated on different metal surfaces. Theoretical and experiment approaches would ultimately lead to the design and development of optimal catalysts for these reactions.

References

1 Holladay, J.D., Hu, J., King, D.L., and Wang, Y. (2009). An overview of hydrogen production technologies. *Catal. Today* 139: 244–260.

2 Kothari, R., Buddhi, D., and Sawhney, R.L. (2008). Comparison of environmental and economic aspects of various hydrogen production methods. *Renewable Sustainable Energy Rev.* 12: 553–563.

3 da Silva Veras, T., Mozer, T.S., da costa Rubim Messeder dos Santos, D., and da Silva Cesar, A. (2017). Hydrogen: trends, production and characterization of the main process worldwide. *Int. J. Hydrogen Energy* 42: 2018–2033.

4 Fischer, V.F. and Tropsch, H. (1928). Conversion of methane into hydrogen and carbon monoxide. *Brennst.-Chem.* 3 (9): 39–46.

5 Aasbrg-Petersen, K., Bak Hansen, J.H., Christensen, T.S. et al. (2001). Technologies for large-scale gas conversion. *Appl. Catal., A* 221: 379.

6 Wang, S. and Lu, G.Q. (1996). Carbon dioxide reforming of methane to produce synthesis gas over metal-supported catalysts: state of the art. *Energy Fuel* 10: 896–904.

7 Araujo, G.C., Lima, S.M., Assaf, J.M. et al. (2008). Catalytic evaluation of perovskite-type oxide La–Ni–Ru–O_3 in methane dry reforming. *Catal. Today* 133–135: 129–135.

8 Rostrup-Nielsen, J.R. (2002). Syngas in perspective. *Catal. Today* 71: 243–247.

9 Seo, Y.-S., Shirley, S.T., and Kolaczkowski, S.T. (2002). Evaluation of thermodynamically favourable operating conditions for production of hydrogen in three different reforming technologies. *J. Power Sources* 108: 213–225.

10 Ávila-Neto, C.N., Dantas, S.C., Silva, F.A. et al. (2009). Hydrogen production from methane reforming: thermodynamic assessment and autothermal reactor design. *J. Nat. Gas Sci. Eng.* 1: 205–215.

11 Lutz, A.E., Bradshaw, R.W., Keller, J.O., and Witmer, D.E. (2003). Thermodynamic analysis of hydrogen production by steam reforming. *Int. J. Hydrogen Energy* 28: 159–167.

12 Akpan, E., Sun, Y., Kumar, P. et al. (2007). Kinetics experimental and reactor modelling studies of the carbon dioxide reforming of methane (CDRM) over a new Ni/CeO_2–ZrO_2 catalyst in a packed bed tubular reactor. *Chem. Eng. Sci.* 62: 4012–4024.

13 Rostrup-Nielsen, J.R. (1984). Catalytic steam reforming. In: *Catalysis, Science and Technology*, Chap. 1, vol. 5 (ed. J.R. Anderson and M. Boudart). Berlin: Springer-Verlag.

14 Rostrup-Nielsen, J.R. (1975). *Steam Reforming Catalysis: An Investigation of Catalysts for Tubular Steam Reforming of Hydrocarbons*. Copenhagen: Danish Technical Press.

15 Kikuchi, E., Tanaka, S., Yamazaki, Y., and Morita, Y. (1974). Steam reforming of hydrocarbons on noble metal catalysts (Part 1). *Bull. Jpn. Pet. Inst.* 16: 95–98.

16 Rostrup-Nielsen, J.R. (1973). Activity of nickel catalysts for steam reforming of hydrocarbons. *J. Catal.* 31: 173–199.

17 Sehested, J. (2006). Four challenges for nickel steam-reforming catalysts. *Catal. Today* 111: 103–110.

18 Reitmeier, R.E., Atwood, K., Bennett, H.A., and Baugh, H.M. (1948). Production of synthesis gas by reacting light hydrocarbons with steam and carbon dioxide. *Ind. Eng. Chem.* 40: 4.

19 Holm, V.C.F. and Clark, A. (1968). Reduction studies on supported metal oxide catalysts. *J. Catal.* 11: 305–316.

20 Lo Jacono, M., Schiavedo, M., and Cimino, A. (1971). *J. Phys. Chem.* 75 (8): 1044.

21 Zielińsky, J. (1982). Morphology of nickel/alumina catalysts. *J. Catal.* 76: 157–163.

22 Bartholomew, C.H., Pannell, R.B., and Butler, J.L. (1980). Support and crystallite size effects in CO hydrogenation on nickel. *J. Catal.* 65: 335–347.

23 Bartholomew, C.H. and Pannell, R.B. (1980). The stoichiometry of hydrogen and carbon monoxide chemisorption on alumina- and silica-supported nickel. *J. Catal.* 65: 390–401.

24 Roman, A. and Delmon, B. (1973). Promoter and carrier effects in the reduction of $NiOSiO_2$. *J. Catal.* 30: 333.

25 Agnelli, M.E., Demicheli, M.C., and Ponzi, E.N. (1987). Catalytic deactivation of methane steam reforming catalysts. 1. Activation. *Ind. Eng. Chem. Res.* 26: 1704–1707.

26 Xua, Y., Harimoto, T., Wang, L. et al. (2018). Effect of steam and hydrogen treatments on the catalytic activity of pure Ni honeycomb for methane steam reforming. *Chem. Eng. Process. Process Intensif.* 129: 63–70.

27 Numaguchi, T. and Kikuchi, K. (1991). Deactivation of bimodal nickel catalyst for steam methane reforming eeaction. *Ind. Eng. Chem. Res.* 30 (3): 447–453.

28 Ali, S., Al-Marri, M.J., Abdelmoneim, A.G. et al. (2016). Catalytic evaluation of nickel nanoparticles in methane steam reforming. *Int. J. Hydrogen Energy* 41: 22876–22885.

29 Matsumura, Y. and Nakamori, T. (2004). Steam reforming of methane over nickel catalysts at low reaction temperature. *Appl. Catal., A* 258: 107–114.

30 Vogt, C., Kranenborg, J., Monai, M., and Weckhuysen, B.M. (2020). Structure sensitivity in steam and dry methane reforming over nickel: activity and carbon formation. *ACS Catal.* 10: 1428–1438.

31 Enger, B.C., Lodeng, R., Walmsley, J., and Holmen, A. (2010). Inactive aluminate spinels as precursors for design of CPO and reforming catalysts. *Appl. Catal., A* 383: 119–127.

32 Pinheiro, A.L., Pinheiro, A.N., Valentini, A. et al. (2009). Analysis of coke deposition and study of the structural features of MAl_2O_4 catalysts for the dry reforming of methane. *Catal. Commun.* 11: 11–14.

33 Muroyama, H., Nakase, R., Matsui, T., and Eguchi, K. (2010). Ethanol steam reforming over Ni-based spinel oxide. *Int. J. Hydrogen Energy* 35: 1575–1581.

34 Jiménez-González, C., Boukha, Z., de Rivas, B. et al. (2014). Behavior of coprecipitated $NiAl_2O_4/Al_2O_3$ catalysts for low-temperature methane steam reforming. *Energy Fuels* 28: 7109–7121.

35 Aghayan, M., Potemkin, D.I., Rubio-Marcos, F. et al. (2017). Template-assisted wet-combustion synthesis of fibrous nickel-based catalyst for carbon dioxide methanation and methane steam reforming. *ACS Appl. Mater. Interfaces* 9: 43553–43562.

36 Rogers, J.L., Mangarella, M.C., D'Amico, A.D. et al. (2016). Differences in the nature of active sites for methane dry reforming and methane steam reforming over nickel aluminate catalysts. *ACS Catal.* 6: 5873–5886.

37 Park, Y.S., Kang, M., Byeon, P. et al. (2018). Fabrication of a regenerable Ni supported NiO–MgO catalyst for methane steam reforming by exsolution. *J. Power Sources* 397: 318–324.

38 Roh, H.-S., Jun, K.-W., and Park, S.-E. (2003). Methane-reforming reactions over $Ni/Ce\text{-}ZrO_2/\theta\text{-}Al_2O_3$ catalysts. *Appl. Catal., A* 251: 275–283.

39 Roh, H.-S., Eum, I.-H., and Jeong, D.-W. (2012). Low temperature steam reforming of methane over $NieCe_{(1-x)}Zr_{(x)}O_2$ catalysts under severe conditions. *Renewable Energy* 42: 212–216.

40 Duarte, R.B., Krumeich, F., and van Bokhoven, J.A. (2014). Structure, activity, and stability of atomically dispersed Rh in methane steam reforming. *ACS Catal.* 4: 1279–1286.

41 Iglesias, I., Baronetti, G., Alemany, L., and Mariño, F. (2019). Insight into $Ni/Ce_{1-x}Zr_xO_2$-δ support interplay for enhanced methane steam reforming. *Int. J. Hydrogen Energy* 44: 3668–3680.

42 Iglesias, I., Forti, M., Baronetti, G., and Mariño, F. (2019). Zr-enhanced stability of ceria based supports for methane steam reforming at severe reaction conditions. *Int. J. Hydrogen Energy* 44: 8121–8132.

43 Lin, C., Jang, J.B., Zhang, L. et al. (2018). Improved coking resistance of "intelligent" Ni catalysts prepared by atomic layer deposition. *ACS Catal.* 8: 7679–7687.

44 Boudjeloud, M., Boulahouache, A., Rabia, C., and Salhi, N. (2019). La-doped supported Ni catalysts for steam reforming of methane. *Int. J. Hydrogen Energy* 44: 9906–9913.

45 Amjad, U.-E.-S., Vita, A., Galletti, C. et al. (2013). Comparative study on steam and oxidative steam reforming of methane with noble metal catalysts. *Ind. Eng. Chem. Res.* 52: 15428–15436.

46 Duarte, R.B., Safonova, O.V., Krumeich, F. et al. (2013). Oxidation state of Ce in CeO_2-promoted Rh/Al_2O_3 catalysts during methane steam reforming: H_2O activation and alumina stabilization. *ACS Catal.* 3: 1956–1964.

47 Carvill, B.T., Hufton, J.R., Anand, M., and Sircar, S. (1996). Sorption-enhanced reaction process. *AIChE J.* 42: 2765–2772.

48 Barelli, L., Bidini, G., Gallorini, F., and Servili, S. (2008). Hydrogen production through sorption-enhanced steam methane reforming and membrane technology: a review. *Energy* 33: 554–570.

49 Harrison, D.P. (2008). Sorption-enhanced hydrogen production: a review. *Ind. Eng. Chem. Res.* 47: 6486–6501.

50 Di, G., Gallucci, K., Foscolo, P.U., and Courson, C. (2019). Effect of Ni precursor salts on Ni-mayenite catalysts for steam methane reforming and on Ni-CaO mayenite materials for sorption enhanced steam methane reforming. *Int. J. Hydrogen Energy* 44: 6461–6480.

51 Wang, L. (2020). Novel highly active Ni–Re super-alloy nanowire type catalysts for CO-free hydrogen generation from steam methane reforming. *Bull. Mater. Sci.* 43: 93.

52 Ji, L., Lin, J., and Zeng, H.C. (2000). Metal–support interactions in Co/Al_2O_3 catalysts: a comparative study on reactivity of support. *J. Phys. Chem. B* 104: 1783–1790.

53 Profeti, L.P.R., Ticianelli, E.A., and Assaf, E.M. (2008). Co/Al_2O_3 catalysts promoted with noble metals for production of hydrogen by methane steam reforming. *Fuel* 87: 2076–2081.

54 van Grootel, P.W., Hensen, E.J.M., and van Santen, R.A. (2010). The CO formation reaction pathway in steam methane reforming by rhodium. *Langmuir* 26 (21): 16339–16348.

55 Xu, Y., Lausche, A.C., Wang, S. et al. (2013). In silico search for novel methane steam reforming catalysts. *New J. Phys.* 15: 125021.

56 Arevalo, R.L., Meñez Aspera, S., Sison Escaño, M.C. et al. (2017). Ru-catalyzed steam methane reforming: mechanistic study from first principles calculations. *ACS Omega* 2: 1295–1301.

57 Hook, A., Nuber, T.P., and Celik, F.E. (2018). Density functional theory investigation of the role of cocatalytic water in methane steam reforming over anatase TiO_2 (101). *Ind. Eng. Chem. Res.* 57: 8131–8143.

58 Liang, L., Hong, D., and Guo, X. (2019). Insight into CaO addition on coking resistance of Ni surface for sorption enhanced methane steam reforming: a density functional study. *Appl. Surf. Sci.* 475: 887–895.

59 Fu, Z., Liu, M., Sun, Q. et al. (2019). Cooperative activation effect on H_2O adsorption in MnO–Co catalysed steam methane reforming. *Phys. Lett. A* 383: 1357–1361.

60 Niua, J., Wang, Y., Qi, Y. et al. (2020). New mechanism insights into methane steam reforming on Pt/Ni from DFT and experimental kinetic study. *Fuel* 266: 117143.

61 Solymosi, F., Kutsán, G., and Erdöhelyi, A. (1991). Catalytic reaction of CH_4 with CO_2 over alumina-supported Pt metals. *Catal. Lett.* 11: 149–156.

62 Bitter, J.H., Seshan, K., and Lercher, J.A. (1997). The state of zirconia supported platinum catalysts for CO_2/CH_4 reforming. *J. Catal.* 171: 279–286.

63 Rostrup-Nielsen, J. and Hansen, J.-H. (1993). CO_2-reforming of methane over transition metals. *J. Catal.* 144: 38–49.

64 Nakamura, J., Aikawa, K., Sato, K., and Uchijima, T. (1994). Role of support in reforming of CH_4 with CO_2 over Rh catalysts. *Catal. Lett.* 25: 265–270.

65 Pakhare, D. and Spivey, J.Y. (2014). A review of dry (CO_2) reforming of methane over noble metal catalysts. *Chem. Soc. Rev.* 43: 7813–7837.

66 García-Diéguez, M., Pieta, I.S., Herrera, M.C. et al. (2010). Nanostructured Pt- and Ni-based catalysts for CO_2-reforming of methane. *J. Catal.* 270: 136–145.

67 Li, D., Nakagawa, Y., and Tomishige, K. (2011). Methane reforming to synthesis gas over Ni catalysts modified with noble metals. *Appl. Catal., A* 408: 1–24.

68 Gould, T.D., Izar, A., Weimer, A.W. et al. (2014). Stabilizing Ni catalysts by molecular layer deposition for harsh, dry reforming conditions. *ACS Catal.* 4: 2714–2717.

69 Salhi, N., Boulahouache, A., Petit, C. et al. (2011). Steam reforming of methane to syngas over $NiAl_2O_4$ spinel catalysts. *Int. J. Hydrogen Energy* 36: 11433–11439.

70 González-Delacruz, V.M., Pereñiguez, R., Ternero, F. et al. (2011). Modifying the size of nickel metallic particles by H_2/CO treatment in Ni/ZrO_2 methane dry reforming catalysts. *ACS Catal.* 1: 82–88.

71 Xie, X., Otremba, T., Littlewood, P. et al. (2013). One-pot synthesis of supported, nanocrystalline nickel manganese oxide for dry reforming of methane. *ACS Catal.* 3: 224–229.

72 Zanganeh, R., Rezaei, M., and Zamaniyan, A. (2013). Dry reforming of methane to synthesis gas on NiO–MgO nanocrystalline solid solution catalysts. *Int. J. Hydrogen Energy* 38: 3012–3018.

73 Margossian, T., Larmier, K., Min Kim, S. et al. (2017). Supported bimetallic NiFe nanoparticles through colloid synthesis for improved dry reforming performance. *ACS Catal.* 7: 6942–6948.

74 Kambolis, A., Matralis, H., Trovarelli, A., and Papadopoulou, C. (2010). Ni/CeO_2–ZrO_2 catalysts for the dry reforming of methane. *Appl. Catal., A* 377: 16–26.

75 Wang, Y., Lu, Y., Wang, Y. et al. (2018). Low-temperature catalytic CO_2 dry reforming of methane on Ni-Si/ZrO_2 catalyst. *ACS Catal.* 8: 6495–6506.

76 Horiuchi, T., Sakuma, K., Fukui, T. et al. (1996). Suppression of carbon deposition in the CO_2-reforming of CH_4 by adding basic metal oxides to a Ni/Al_2O_3 catalyst. *Appl. Catal., A* 144: 111–120.

77 Hu, Y.H. (2009). Solid-solution catalysts for CO_2 reforming of methane. *Catal. Today* 148: 206–211.

78 Kuzminy, A. and Mironova, N. (1998). Composition dependence of the lattice parameter in $Ni_cMg_{1-c}O$ solid solutions. *J. Phys.: Condens. Matter* 10: 7937–7944.

79 Shen, W., Momoi, H., Komatsubara, K. et al. (2011). Marked role of mesopores for the prevention of sintering and carbon deposition in dry reforming of methane over ordered mesoporous Ni–Mg–Al oxides. *Catal. Today* 171: 150–155.

80 Xua, L., Song, H., and Chou, L. (2011). Carbon dioxide reforming of methane over ordered mesoporous NiO–MgO–Al_2O_3 composite oxides. *Appl. Catal., B* 108–109: 177–190.

81 Mette, K., Kühl, S., Tarasov, A. et al. (2016). High-temperature stable Ni nanoparticles for the dry reforming of methane. *ACS Catal.* 6: 7238–7248.

82 Guczi, L., Stefler, G., Geszti, O. et al. (2010). Methane dry reforming with CO_2: a study on surface carbon species. *Appl. Catal., A* 375: 236–246.

83 Margossian, T., Larmier, K., Min Kim, S. et al. (2017). Molecularly tailored nickel precursor and support yield a stable methane dry reforming catalyst with superior metal utilization. *J. Am. Chem. Soc.* 139: 6919–6927.

84 Kankan, B., Kuboon, S., Deng, J. et al. (2019). Methane dry reforming over boron nitride interface-confined and LDHs derived Ni catalysts. *Appl. Catal., B* 252: 86–97.

85 Liu, Z., Grinter, D.C., Lustemberg, P.G. et al. (2016). Dry reforming of methane on a highly-active Ni–CeO_2 catalyst: effects of metal–support interactions on C–H bond breaking. *Angew. Chem. Int. Ed.* 55: 7455–7459.

86 Wang, N., Shen, K., Huang, L. et al. (2013). Facile route for synthesizing ordered mesoporous Ni–Ce–Al oxide materials and their catalytic performance for methane dry reforming to hydrogen and syngas. *ACS Catal.* 3: 1638–1651.

87 Chen, W., Zhao, G., Xue, Q. et al. (2013). High carbon-resistance $Ni/CeAlO_3$-Al_2O_3 catalyst for CH_4/CO_2 reforming. *Appl. Catal., B* 136–137: 260–268.

88 Zhang, S., Muratsugu, S., Ishiguro, N., and Tada, M. (2013). Ceria-doped Ni/SBA-16 catalysts for dry reforming of methane. *ACS Catal.* 3: 1855–1864.

89 Pechimuthu, N.A., Pant, K.K., and Dhingra, S.C. (2007). Deactivation studies over Ni-K/CeO_2-Al_2O_3 catalyst for dry reforming of methane. *Ind. Eng. Chem. Res.* 46: 1731–1736.

90 Ocsachoque, M., Pompeo, F., and Gonzalez, G. (2011). Rh–Ni/CeO_2–Al_2O_3 catalysts for methane dry reforming. *Catal. Today* 172: 226–231.

91 Daza, C.E., Gallego, J., Mondragon, F. et al. (2010). High stability of Ce-promoted Ni/Mg–Al catalysts derived from hydrotalcites in dry reforming of methane. *Fuels* 89: 592–603.

92 Wang, N., Chu, W., Zhang, T., and Zhao, X. (2012). Synthesis, characterization and catalytic performances of Ce-SBA-15 supported nickel catalysts for methane dry reforming to hydrogen and syngas. *Int. J. Hydrogen Energy* 37: 19–30.

93 Laosiripojana, N., Sutthisripok, W., and Assabumrungrat, S. (2005). Synthesis gas production from dry reforming of methane over CeO_2 doped Ni/Al_2O_3: influence of the doping ceria on the resistance toward carbon formation. *Chem. Eng. J.* 112: 13–22.

94 Campbell, C.T. and Peden, C.H.F. (2005). Oxygen vacancies and catalysis on ceria surfaces. *Science* 309: 713–714.

95 Xu, J., Wei, Z., Jihui, W. et al. (2009). Characterization and analysis of carbon deposited during the dry reforming of methane over $Ni/La_2O_3/Al_2O_3$ catalysts. *Chin. J. Catal.* 30 (11): 1076–1084.

96 Al-Fatesh, A.S., Naeem, M.A., Fakeeha, A.H., and Abasaeed, A.E. (2014). Role of La_2O_3 as promoter and support in Ni/γ-Al_2O_3 catalysts for dry reforming of methane. *Chin. J. Chem. Eng.* 22 (1): 28–37.

97 Fujita, T., Peng, X., Yamaguchi, A. et al. (2018). Nanoporous nickel composite catalyst for the dry reforming of methane. *ACS Omega* 3: 16651–16657.

98 Li, J.F., Xia, C., Au, C.T., and Liu, B.S. (2014). Y_2O_3-promoted NiO/SBA-15 catalysts highly active for CO_2/CH_4 reforming. *Int. J. Hydrogen Energy* 39: 10927–10940.

99 Ibrahim, A.A., Amin, A., Al-Fatesh, A.S. et al. (2019). Nanosized Ni/SBA-15 catalysts for CO_2 reforming of CH_4. *Appl. Sci.* 9: 1926.

100 Chotirach, M., Tungasmita, S., Nuntasri Tungasmita, D., and Tantayanon, S. (2018). Titanium nitride promoted Ni-based SBA-15 catalyst for dry reforming of methane. *Int. J. Hydrogen Energy* 43: 21322–21332.

101 Liu, Z., Zhou, J., Cao, K. et al. (2012). Highly dispersed nickel loaded on mesoporous silica: one-spot synthesis strategy and high performance as catalysts for methane reforming with carbon dioxide. *Appl. Catal., B* 125: 324–330.

102 Theofanidis, S.A., Galvita, V.V., Poelman, H., and Marin, G.B. (2015). Enhanced carbon-resistant dry reforming Fe–Ni catalyst: role of Fe. *ACS Catal.* 5: 3028–3039.

103 Das, S., Bag, A., Gupta, R.K. et al. (2018). Facile nitridation of NiO/Al_2O_3: an efficient approach to design an extraordinarily stable catalyst for dry reforming of methane. *ACS Appl. Energy Mater.* 1: 4414–4419.

104 Osaki, T., Masuda, H., Horiuchi, T., and Mori, T. (1995). Highly hydrogen-deficient hydrocarbon species for the CO_2-reforming of CH_4 on CO/Al_2O_3 catalyst. *Catal. Lett.* 34: 59–63.

105 Ji, L., Tang, S., Zeng, H.C. et al. (2001). CO_2 reforming of methane to synthesis gas over sol–gel-made $CO/\gamma\text{-}Al_2O_3$ catalysts from organometallic precursors. *Appl. Catal., A* 207: 247–255.

106 Ruckenstein, E. and Wang, H.Y. (2000). Carbon dioxide reforming of methane to synthesis gas over supported cobalt catalysts. *Appl. Catal., A* 204: 257–263.

107 Özkara-Aydınoğlu, Ş., A. and Aksoylu, E. (2010). Carbon dioxide reforming of methane over $Co\text{-}X/ZrO_2$ catalysts (X = La, Ce, Mn, Mg, K). *Catal. Commun.* 11: 1165–1170.

108 Wang, N., Chua, W., Zhang, T., and Zhao, X.-S. (2011). Manganese promoting effects on the Co–Ce–Zr–Ox nano catalysts for methane dry reforming with carbon dioxide to hydrogen and carbon monoxide. *Chem. Eng. J.* 170: 457–463.

109 Nagaoka, K., Takanabe, K., and Aika, K. (2004). Modification of Co/TiO_2 for dry reforming of methane at 2MPa by Pt, Ru or Ni. *Appl. Catal., A* 268: 151–158.

110 Mirzaei, F., Rezaei, M., Meshkani, F., and Fattah, Z. (2015). Carbon dioxide reforming of methane for syngas production over Co–MgO mixed oxide nanocatalysts. *J. Ind. Eng. Chem.* 21: 662–667.

111 Asami, K., Li, X., Fujimoto, K. et al. (2003). CO_2 reforming of CH_4 over ceria-supported metal catalysts. *Catal. Today* 84: 27–31.

112 Liu, Z., Zhang, F., Rui, N. et al. (2019). Highly active ceria-supported Ru catalyst for the dry reforming of methane: in situ identification of $Ru^{\delta+}\text{–}Ce^{3+}$ interactions for enhanced conversion. *ACS Catal.* 9: 3349–3359.

113 Mounfield, W.P., Harale, A., and Román-Leshkov, Y. (2019). Impact of morphological effects on the activity and stability of tungsten carbide catalysts for dry methane reforming. *Energy Fuels* 33 (6): 5544–5550.

114 Wu, Z., Yang, B., Miao, S. et al. (2019). Lattice strained Ni-Co alloy as a high-performance catalyst for catalytic dry reforming of methane. *ACS Catal.* 9: 2693–2700.

115 Fan, M.-S., Zuhairi Abdullah, A., and Bhatia, S. (2010). Utilization of greenhouse gases through carbon dioxide reforming of methane over $Ni\text{–}Co/MgO\text{–}ZrO_2$: preparation, characterization and activity studies. *Appl. Catal., B* 100: 365–377.

116 Bhavani, A.G., Kim, W.Y., and Lee, J.S. (2013). Barium substituted lanthanum manganite perovskite for CO_2 reforming of methane. *ACS Catal.* 3: 1537–1544.

117 Singh, R., Dhir, A., Mohapatra1, S.K., and Mahla, S.K. (2020). Dry reforming of methane using various catalysts in the process: review. *Biomass Convers. Biorefin.* 10: 567–587. https://doi.org/10.1007/s13399-019-00417-1.

118 Wang, Y. and Gao, H. (2017). Mechanism of CO_2 reforming of CH_4 on a $Pt^4/ZrO^2(101)$ surface: a density functional theory study. *J. Phys. Chem. B* 121: 5238–5246.

119 Zuo, Z., Liu, S., Wang, Z. et al. (2018). Dry reforming of methane on single-site Ni/MgO catalysts: importance of site confinement. *ACS Catal.* 8: 9821–9835.

120 Fan, C., Zhu, Y.-A., Yang, M.-L. et al. (2015). Density functional theory-assisted microkinetic analysis of methane dry reforming on Ni catalyst. *Ind. Eng. Chem. Res.* 54: 5901–5913.

121 Huygh, S., Bogaerts, A., Bal, K.M., and Neyts, E.C. (2018). High coke resistance of a TiO_2 anatase (001) catalyst surface during dry reforming of methane. *J. Phys. Chem. C* 122: 9389–9396.

122 Pachauri, R.K. and Meyer, L.A. (ed.) (2014). *Climate Change 2014: Synthesis Report. Contribution of Working Groups I, II and III to the Fifth Assessment Report of the Intergovernmental Panel on Climate Change*. Geneva, Switzerland: United Nations Intergovernmental Panel on Climate Change.

123 IEA-International Energy Agency (2009). *Transport, energy and CO_2*. Paris: International Energy Agency.

124 https://www.esrl.noaa.gov/gmd/ccgg/trends/ (accessed 23 January 2022).

5

Methane Activation Over Zeolites

Meera A. Shah and Russell A. Taylor

Durham University, Department of Chemistry, South Road, Durham DH1 3LE, UK

5.1 Introduction

Methane, the principal component of natural gas, is the fastest growing fossil fuel. It accounts for almost one-third of total energy demand growth through the last decade, more than any other fuel [1]. Energy production is the primary use of methane, but it is also the feedstock for some of the most important inorganic and organic bulk chemicals produced by the chemical industry [2]. A few bulk chemicals are produced directly from methane (radical chlorination to form CH_3Cl, CH_2Cl_2, and $CHCl_3$; methane partial combustion or electrothermal pyrolysis to acetylene; reaction with ammonia to hydrogen cyanide), but most chemicals are produced indirectly through synthesis gas (syngas), a mixture of carbon monoxide and hydrogen. Scheme 5.1 shows some of the diverse bulk chemicals that are produced from synthesis gas, either by utilizing hydrogen or carbon monoxide alone or by using syngas. While syngas can be produced from methane in a number of ways [3], steam reforming (SR) and autothermal reforming (ATR) (a combination of SR and partial oxidation) are the most commonly practiced methods [4, 5]. Historically, it is SR that has been most commonly implemented for producing syngas for the manufacture of important basic chemicals (e.g. ammonia and methanol), for use in oil refining processes, and in many other industrial applications [6].

Despite the syngas mediated route to chemicals from methane being industrially practiced, there are still a number of drawbacks. Both SR and ATR of methane utilize catalysts and operate at elevated temperature (1073 K and above) and pressures (30 bar and above) [6]. Due to these challenging conditions, the construction costs of the plant are high, and the catalysts are also prone to deactivation due to sintering or the formation of carbonaceous deposits [3]. Additionally, it is estimated that between 20% and 50% of the natural gas feedstock is consumed through energy losses to reach the high reaction temperatures required during SR. [4] Trying to further improve the energy efficiency of SR has been reported to detrimentally impact the syngas production cost [7]. To maximize the return on investment of the high costs associated with syngas production plants, they are typically constructed at large scales to optimize

Heterogeneous Catalysis for Sustainable Energy, First Edition. Edited by Landong Li and Justin S. J. Hargreaves.

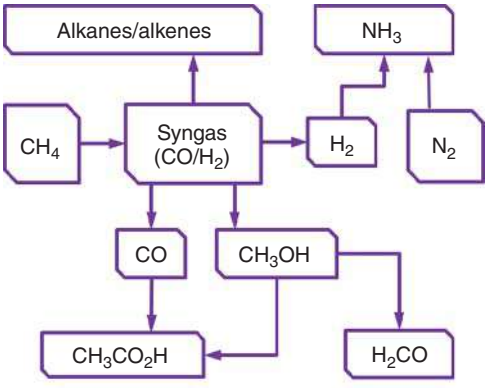

Scheme 5.1 Flow scheme showing some of the primary products formed from syngas.

material throughput. As such, indirect methane conversion is therefore limited in where it can be deployed due to the multistep, large-scale approach required.

Oil is the primary natural resource used for the production of chemicals [8]. There are of course serious concerns regarding the exploitation of coal, oil, and gas for fuels and chemicals, mainly due to the risks of global warming and other environmental issues [8–10]. However, natural gas is regarded as the cleanest of all the fossil-based resources and is championed to be the preferred resource in the global transition to lower carbon economies [2, 11]. Therefore, developing technologies that enhance the portfolio of products derived from methane will help to alleviate our reliance on oil for chemical production [12].

5.1.1 The Direct Conversion of Methane

In the effort to develop new industrial processes for the direct production of chemicals from methane, there have been three main conversions that have been intensely studied: (i) oxidative coupling of methane (OCM) to ethylene, (ii) methane dehydraomatization (MDA) to aromatics, and (iii) partial oxidation of methane to methanol (direct methane to methanol [dMtM]) (Scheme 5.2) [13]. Progress has been made in all three areas, but it is probably the OCM reaction that shows the greatest promise of a commercial process [2, 14] given recent announcements from Siluria Technologies that they have been running a one ton of ethylene per day demonstration plant since 2015 [15].

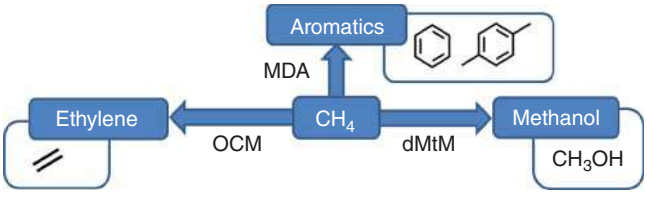

Scheme 5.2 Main products of interest from direct methane conversion processes.

Catalytic methane dehydroaromatization (MDA) has received significant attention since Wang et al. demonstrated high selectivity to benzene, via non-oxidative methane upgrading at 700 °C, using a Mo-modified H-ZSM-5 zeolite catalyst [16]. Unfortunately rapid catalyst deactivation and high selectivity to coke hinder commercialization, but recent scientific developments have given great insight into the active species and reaction mechanism and novel strategies to avoid deactivation.

dMtM has been intensely investigated by both homogeneous [17, 18] and heterogeneous [18, 19] catalyst practitioners and has been described as the holy grail of catalysis [20]. Perhaps what makes dMtM so tantalizing is the fact that nature has already been able to master this challenging chemistry in the form of methantropic bacteria. These bacteria contain an enzyme, methane monooxygenase (MMO), which is capable of converting methane to methanol at physiological conditions [21]. Two types of MMO enzymes exist, so-called *particulate* and *soluble* forms, pMMO and sMMO, respectively. The sMMO enzyme contains a dinuclear Fe center in the active site, while pMMO contains Cu [22]. The proposed structures of these active sites have inspired much research to develop laboratory mimics and have been a significant source of inspiration in the development of catalysts for dMtM.

Zeolite-based catalysts have been utilized in all three research areas and form the basis of the most cutting edge materials used in MDA and dMtM reactions. However, they have been much less successfully applied in the OCM reaction. After briefly introducing zeolites to the reader, the remainder of the chapter will look at each of the three reactions and key findings regarding methane activation and conversion with zeolite-based catalysts.

5.1.2 Introduction to Zeolites

Zeolites are crystalline, microporous, aluminosilicate materials, though the term zeolites is often more liberally taken to include microporous framework materials that do not solely contain oxygen, aluminum, and silicon in the framework. The term zeolite, from the Greek *zeo* that means to boil and *lithos* that means stone, was coined in 1756 by Cronstedt. Cronstedt discovered stilbite, a naturally occurring zeolite, which when rapidly heated produced large amounts of steam from adsorbed water [23]. However, it was not until Richard Barrer prepared the first solely synthetic zeolite in the mid-twentieth century that research into zeolites accelerated [24]. Since the early reports concerning synthetic zeolites, there has been extensive research into developing and understanding zeolite materials, from synthetic methodology to the widespread applications for which they are now used.

Since Barrer's initial discovery, over 253 unique zeolite frameworks have been reported [25]. These frameworks are made up of corner-sharing $[SiO_4]$ and $[AlO_4]^-$ tetrahedra, which form a continuous three-dimensional structure with interconnecting pores, channels, or cages. It is the framework that makes zeolites particularly valuable as molecular sieves, ion exchange (IE) materials, and, in particular,

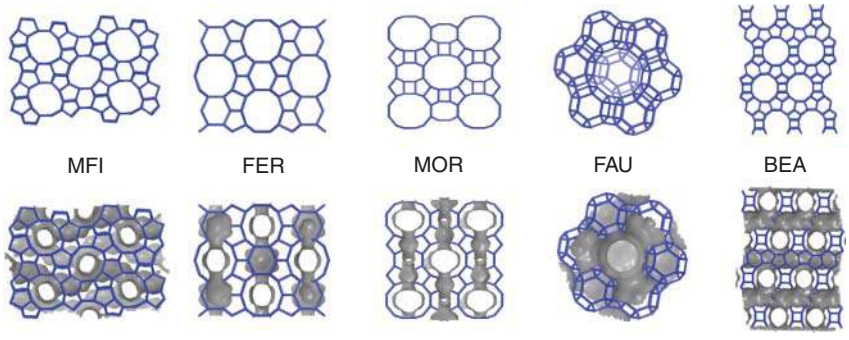

Figure 5.1 The "Big Five" zeolite topologies with channel systems highlighted in gray. Source: Images from IZA Structure database based on [25].

catalysts. Shown in Figure 5.1 are five framework types (MFI, FER, MOR, FAU, and Beta, sometimes known as the "Big Five") that are widely commercially available and frequently used in scientific research, particularly in catalytic applications.

Hydrothermal synthesis methods [26, 27] form the foundation of most modern zeolite syntheses, where a source of silica and alumina is combined and dissolved in the presence of a mineralizer to form a gel. This gel phase is subsequently placed in an autoclave at elevated temperature to crystallize. The resulting zeolite structure that is formed is dependent on factors such as temperature (80–200 °C), time for crystallization (hours to weeks), structure-directing agent (SDA), and pressure. Figure 5.2 illustrates these factors and many other synthesis parameters that may control the outcome of a zeolite synthesis. While neutral, all-silica zeolites can be formed, the presence of negatively charged $[AlO_4]^-$ tetrahedra require a charge

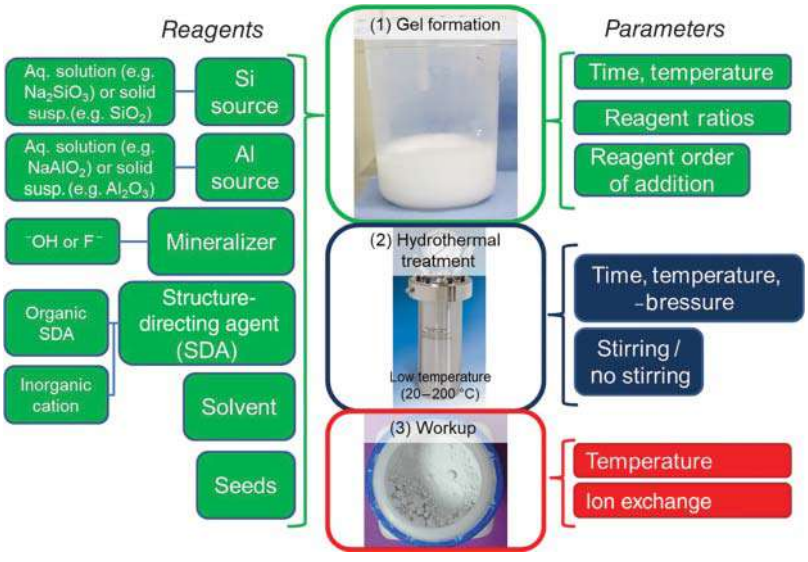

Figure 5.2 Factors effecting zeolite formation under hydrothermal synthesis conditions.

balancing extra-framework cation, which drastically changes the properties of the materials. During synthesis, inorganic cations and/or organic structure-directing agents (OSDAs) (such as tetraalkylammonium cations) are used in synthesis to balance this charge. However, additional post-synthetic treatments [28] are commonly carried out to produce a zeolite material in the state required for the desired application. These steps include calcination to remove the OSDA and/or IE to introduce the desired extra-framework cation.

Zeolites have three main industrial applications: catalysis, gas cleanup and separation, and IE. The largest volume use for zeolites is in detergent formulations where the IE properties are exploited to remove calcium and magnesium from hard water [29]. As the microporous structures have similar kinetic diameters to small molecules, this allows tunable molecular sieving properties that enable molecular separation and selective adsorption, for example, in removing impurities such as CO_2 and SO_2 from natural gas streams [30]. However, the introduction of zeolites into refinery operations was groundbreaking, and since their success in catalytic cracking, zeolites have found many applications in refinery and petrochemical processes [31–33]. Fluidized catalytic cracking (FCC) uses USY to convert high-boiling fractions of crude oil primarily into gasoline with around 15 million barrels processed around the world per day [29, 31]. The combination of molecular sieving properties and catalytic properties gives rise to the well-known reactant, product, and transition state selectivity [34–36]. These modes of reaction selectivity are able to induce reaction selectivities that differ to those predicted by thermodynamics alone. Additionally zeolites can impart remarkable reaction selectivity through confinement, where the free energy of the transition state is lowered by interactions with the framework, commonly van der Waals interactions and charge stabilization by anionic T-sites [37]. The capacity to alter reaction selectivities through subtle substrate–framework interactions has drawn parallels with enzymes [38], exemplified by the carbonylation of dimethyl ether to methyl acetate, which has been shown to selectively take place in the eight membered ring (MR) side pockets of MOR [39, 40]. As zeolites already find utility at industrial scales in challenging catalytic environments and also demonstrate a remarkable capacity to control reaction selectivity, they are touted to be disruptive materials in future catalytic conversion processes [41] and have the potential to be instrumental in the challenging conversions posed by OCM, MDA, and dMtM processes.

5.2 Oxidative Coupling of Methane over Zeolite Catalysts

The OCM to ethane and ethylene has been intensely researched since first being reported in the early 1980s by Keller and Bhasin [42] of Union Carbide and Hinsen and Baerns [43] and being the subject of patents from Exxon Research and Engineering Co. [44, 45]. Very typically, these catalysts are based on doped metal oxides (e.g. Li/MgO, Sr/La_2O_3) where ethane and ethylene are formed from methane and oxygen at temperatures between 500 and 1000 °C. The accepted

pathway to the formation of C2 products involves initial abstraction of a hydrogen atom from methane by an oxygen atom at the surface of the catalyst [19]. Methyl radicals [46, 47] combine in the gas phase to give ethane (the primary product), which subsequently undergoes hydrogen atom abstraction and conversion to ethylene. As such, the mechanism occurs in homogeneous and heterogeneous phases. A key limitation to the OCM process is the radical nature of the process as the C—H bond of the C2 products is weaker than methane, giving an inherent kinetic limitation of per pass yield of 30% [48, 49], a yield that is rarely surpassed without engineering intervention [13]. Additionally, despite the negative Gibbs free energy for the OCM reaction, the formation of CO and CO_2 are substantially more favorable [50]. As such the process has inherent kinetic and thermodynamic limitations. Despite these issues, substantial effort has gone into further developing the process through reactor design and engineering solutions (e.g. membrane reactors) and the development of new catalysts [51]. For further information on recent developments in the field, the reader is suggested to see the following reviews [13, 50–53].

Initial research into the OCM reaction included using zeolites as supports. However, activity in the area has been very limited in the last few decades. Natural and synthetic mordenites with varying degrees of Brønsted acid sites (BASs) and Groups 1 and 2 extra-framework cations were shown to give up to 5.6% yield of C2 products at 973 K using a CH_4/O_2 ratio of 2. Methane conversion ranged from 18% to 24% depending on pretreatment condition of the MOR catalyst [54]. Shepelev and Ione studied the rate and selectivity of OCM oxidative synthesis over different framework types and compositions, as well as exploring the efficacy of different oxidants (O_2, N_2O, NO, NO_2, SO_3) [55]. Using dioxygen as the terminal oxidant (600 °C, $CH_4/O_2 = 5$), they reported that only ZSM-5 with BAS gave rise to the formation of higher hydrocarbons; Na/ZSM-5, H/MOR, and H/Y gave carbon oxides (CO, CO_2) only. The selectivity to higher hydrocarbons correlated with the aluminum content of the H/ZSM-5 material, with hydrocarbon yields ranging from 1% ($SiO_2/Al_2O_3 = 121$) to 3% ($SiO_2/Al_2O_3 = 28$). For the reaction over H/ZSM-5 ($SiO_2/Al_2O_3 = 28$), 4.85% CH_4 conversion and 96.9% O_2 conversion were reported. The authors also showed that using NO, NO_2, or SO_3 as oxidants gave only carbon oxides under the same reaction conditions when H/ZSM-5 ($SiO_2/Al_2O_3 = 28$) was used as a catalyst. Conversely, the greatest selectivity to higher hydrocarbons (87.5%) was given through the use N_2O as oxidant, giving rise to 9.64% CH_4 conversion. Again, the authors showed that only H/ZSM-5 materials gave rise to higher hydrocarbons when using N_2O as oxidant, with H/MOR and H/Y only producing carbon oxides. Additionally, the interaction of methane with the different catalysts was explored by ^{13}C NMR and IR spectroscopy. The authors reported that methane interacts more strongly with the BAS sites of ZSM-5 than with MOR or Y, as gauged by the relative changes in vibrational frequency and NMR chemical shift of adsorbed methane. The authors conclude that the MFI zeolite framework is beneficial for the formation of higher hydrocarbons, regardless of the oxidant [55].

Zeolites impregnated with basic oxides, somewhat mimicking the traditional active phases in OCM, have also been explored. MgO impregnated on ZSM-5

has been tested and shown that the zeolite basic sites play an active role in the chemistry [56]. At 800 °C, a feed of CH_4/O_2 (4.5/1) over ZSM-5 (Si/Al = 22) impregnated with increasing loadings of MgO (1, 5, 10, 20 wt%) gave increasing selectivity to C2 products (approximately 70–80%) at the expense of decreasing CH_4 conversion (3% to 2%). Notably, the additional impregnation of NaCl to the MgO/ZSM-5 materials eliminated the formation of CO_x but further reduced the CH_4 conversion. Comparison with pure MgO showed that dispersing MgO onto the zeolite support marginally improved the observed C2 selectivity [56].

Weitkamp and coworkers studied OCM over NaY zeolites treated with sodium azide, the aim of the latter treatment reportedly being to increase the Na content and overall basicity of the materials [57]. They reported a maximum yield of 13.4% for C2 products at 19.9% CH_4 conversion, from a CH_4/O_2/He (7.5/2.5/90) feed at 1073 K over NaY treated with NaN_3. The authors noted that the high-temperature activation procedure was critical to the optimized performance of the catalyst. For example, pretreatment in air at 1073 K was beneficial to the yield of C2 products (10.3%) compared to pretreatment under He (5.6%). A time-on-stream (TOS) study showed that the azide-treated material gave steady CH_4 conversion and selectivity to C_2H_6 over approximately 17 hours, while selectivity to CO_x increased at the expense to the selectivity to C_2H_4 [57].

Additionally, CsX materials prepared by IE, solid-phase IE, and impregnation have been tested for OCM [58]. Both the impregnated and solid-phase IE gave notably higher activity in OCM over the IE material. The different synthetic methods led to different levels of basicity of the materials that correlated with the activity for OCM [58]. In a related study, it was reported the equivalent LiX materials gave lower performance than the CsX materials owing to the lower basicity of the material [59].

A NaCl–MnO/H–ZSM-5 catalyst demonstrated 58.5% selectivity to C2 products at 713 K with a feed 4 : 1 (CH_4:O_2) feed and 31.2% CH_4 conversion over 20 hours OCM activity [60]. NaCl–MnO/SiO_2(aerogel) gave very similar performance, though at 775 K. NaCl–MnO supported on MgO and on SiO_2 are reported in this chapter, but the reported conversions are too disparate to make meaningful selectivity comparisons due to the strong dependence of selectivity and conversion in the OCM reaction.

Overall, the superior performance of doped metal oxide catalysts (e.g. Li/MgO, Sr/La_2O_3), giving up to 30% per pass yields of C2 products, has curtailed investigations of using zeolites as catalysts or catalyst supports for OCM. As the standard OCM catalyst technology improves, it seems that zeolites will be unlikely to form the basis of this methane conversion reaction.

5.3 Methane Dehydroaromatization (MDA)

Aromatics, such as benzene, toluene, and xylene (BTX), are in high demand as feedstocks for fine chemicals, commodity chemicals, and plastic industry [53]. These products are predominantly derived from the cracking and reforming of fractions obtained from the distillation of oil. The direct production of methane to

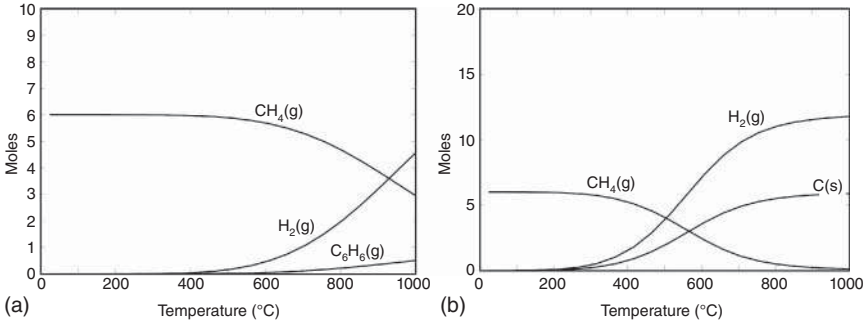

Figure 5.3 (a) Equilibrium amounts (mol), 1 bar, starting with 6 mol CH_4 and allowing only H_2 and benzene as components. Calculated using HSC 7.1 software. (b) Equilibrium amounts (moles), 1 bar, starting with 6 mol CH_4 and allowing $C_{(s)}$, H_2, and benzene as components. Source: Reproduced with permission from Spivey and Hutchings [61]; © 2014 Royal Society of Chemistry.

BTX via direct, non-oxidative conversion, commonly known as MDA, is extremely attractive to the chemical industry. However, the reaction is hindered by thermodynamic limitations [61, 62]. It is clear from the highly positive Gibbs free energy of reaction (Eq. (5.1)) that the formation of benzene is thermodynamically unfavorable. The graph in Figure 5.3a shows the equilibrium composition for the conversion of methane to benzene and hydrogen only, and it is clear that appreciable amounts of benzene are formed only at very high temperatures. Additionally, the formation of solid carbon (C_s), also known as coke, is more thermodynamically favored than the formation of benzene. Figure 5.3b shows the equilibrium distribution of methane to solid carbon, benzene, and hydrogen, and negligible quantities of benzene are formed. As such, MDA should suffer from unfavorable reaction thermodynamics and very poor reaction selectivities.

A balanced equation for benzene formation from methane with ΔG and ΔH energy values is given below [61].

$$6CH_{4\,(g)} \rightarrow 9H_{2\,(g)} + C_6H_{6\,(g)} \qquad \Delta G_r^\circ = +433\ \text{kJ mol}^{-1}$$

$$\Delta H_r^\circ = +531\ \text{kJ mol}^{-1} \tag{5.1}$$

It is therefore surprising that zeolites, when modified with metals (Zn, Ga, Pt, Re, and Cr), were reported in the 1980s to give yields of benzene up to 14%, at up to 18% methane conversion, in a pulsed microreactor [63, 64]. While pioneering, these reports gave few details and did not discuss catalyst synthesis or catalyst characterization. In 1993, Wang et al. reported that Mo-modified ZSM-5 is a particularly efficient MDA catalyst and that the catalyst was stable over a three-hour period, producing benzene with 100% selectivity under continuous flow conditions [16]. Following these results, numerous studies have been undertaken using a variety of main group metals and transition metals (e.g. V, Cr, Fe, Mo [65], Co [66], Ni [67], W [68], Re [69], Zn [16, 70, 71], Mn [72, 73], Ga [74]). However, it is Mo-based catalysts that have by far and away been the most studied systems. This is due to the fact that the most promising systems to date, Mo/H–ZSM-5 and Mo/H–MCM-22,

achieve 10–12% methane conversion with 60–70% benzene selectivity at 700 °C [75]. Unsurprisingly, the catalyst performance is sensitive to many factors other than the nature of metal. Key factors that modify catalyst performance include the level of Brønsted acidity of the zeolite; the state, location, and method of Mo introduction; and the pretreatment steps though the underlying origin of these effects is beginning to be understood [62, 66, 67]. A number of studies into the effects of dopants have been conducted [76–79], and in spite of the domination of Mo/zeolite catalysts in the field, significant attention has also been turned to mixed metal systems [80]. Overall, the development of zeolite-based MDA catalysts is a field that continues to attract more interest year on year that is exemplified by the number of excellent reviews dedicated to MDA chemistry that have appeared recently [52, 61, 62, 81–83]. In a notable boost to the future large-scale applicability of the MDA reaction, a recent techno-economic assessment of MDA indicated that it would indeed be a profitable enterprise giving an MDA plant a profitability index of 1.17 [84].

Although the mechanism of MDA over Mo/ZSM-5 has yet to be fully clarified, there are two different mechanisms proposed: (i) a bifunctional pathway and (ii) a hydrocarbon pool-like pathway. In the bifunctional pathway, methane is converted to C_2 hydrocarbons (C_2H_y) over Mo sites within the catalyst (ethylene or acetylene has been proposed as intermediates). The C_2H_y species are subsequently oligomerized on the BAS sites of the zeolite support [85]. Alternatively, in the hydrocarbon pool-like mechanism, activation of methane occurs at Mo sites to give C_xH_y species that react with carbonaceous species in the micropore network (Figure 5.4). While this is similar in nature to the hydrocarbon pool mechanism for the methanol-to-hydrocarbon (MTH) reaction, the MDA reaction proceeds through polyaromatic radical intermediates [86], not via carbocations as the MTH reaction does. Traditionally, the first pathway has been widely accepted, but there

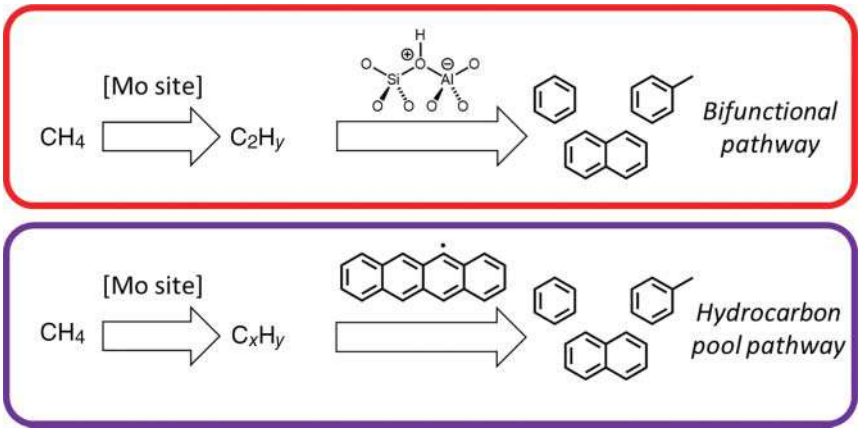

Figure 5.4 Different proposed pathways for MDA over Mo/zeolites. Top: The bifunctional pathway involving CH_4 activation over Mo sites and aromatization over BAS. Bottom: The hydrocarbon pool pathway involving CH_4 activation over Mo sites and aromatization over radical polyaromatic species.

is a growing body of evidence highlighting that the hydrocarbon pool-like pathway is dominant, as will be discussed further below.

Although the mechanism is clearly complex, some important mechanistic factors have been established in the MDA reaction over Mo/Zeolites. There is a notable activation period before the detection of aromatic molecules, and this is associated with the reduction of Mo (most likely present as $[MoO_x(OH)_y]$) by methane to form molybdenum carbide species. The induction period also accompanies the formation of the hydrocarbon pool within the micropore network of the zeolite [75, 87]. This results in some carbonaceous deposit, which can lead to catalyst deactivation. The non-innocence of the hydrocarbon pool has been established by several recent studies. Hensen and coworkers used ^{13}C isotope studies and pulse reactions to demonstrate that benzene is synthesized from secondary reactions of confined polyaromatic carbon species with the initial products of methane activation [88]. Gascon and coworkers also used isotope labeling studies to evidence that carbon from the hydrocarbon pool is incorporated into the detected aromatic products [75]. A recent computational study also identified the hydrocarbon pool-like radical reaction pathway to be more energetically favorable than an alternative Mo-only ethylene production path [89]. The study concluded that the radical path involves methane activation over MoC_x, which acts cooperatively with the neighboring confined aromatic species to form C—C bonds and ultimately generate the desirable aromatic products via cracking [89].

The main intermediate of the reaction, i.e. the initial product of methane activation, is usually considered to be ethylene. Xu et al. suggest ethylene as the initial product as they observed the formation of ethylene at similar times to benzene. Moreover, with increasing space velocity, ethylene selectivity increased [16, 90]. Furthermore, Rosynek and coworkers established that when using ethylene as the reactant, a similar hydrocarbon product distribution to methane over Mo/H–ZSM-5 was observed [91]. However, Meriaudeau and coworkers consider acetylene as an important intermediate in MDA as the amount of acetylene formed decreases with increased contact time while the yields of ethylene and benzene increased [92]. They reported that the bifunctional mechanism is less important, and the principle route for the aromatization of methane is the formation of C_2H_2 over Mo_2C that forms benzene over the same Mo_2C sites. Kapteijn and coworkers also conclude that ethylene is not likely to be the primary product of MDA, as upon reaction of ethylene under MDA conditions, the hydrocarbon pool formed was more dense and contained less hydrogenated species than when using methane [93]. Furthermore, the coke deposits formed from MDA when using methane were found to be more reactive than those formed from ethylene. A very recent paper by Bhan and coworkers reports that ethane is the sole primary product of MDA and this is subsequently dehydrogenated to ethylene and acetylene before aromatization to benzene occurs [94]. Overall, the mechanism of MDA over Mo/H–ZSM-5 has not yet been fully understood, and questions such as the exact involvement of carbonaceous deposits in the formation of benzene still require answers.

Substantial efforts have gone into trying to understand the state of the Mo species within the zeolite to form structure–activity relationships and with the aim of

improving catalyst performance. Mo/zeolite catalysts are usually prepared through impregnation using $(NH_4)_6Mo_7O_{24}$ as the Mo source (2–5 wt% Mo) [85]. Presumably, Mo species in the form of $[Mo_7O_{24}]^{6-}$ are located on the external surfaces of the zeolite during this stage. Upon calcination, mononuclear MoO_3 is formed and migrates into the zeolite channels [90]. This migration has been evidence by numerous techniques: BET, NH_3-TPD, powder X-ray diffraction (PXRD), X-ray absorption spectroscopy (XAS), and NMR spectroscopy [95–98].

Iglesia and coworkers reported that at 623 K, MoO_x species are distributed over the external surface of the zeolite [95]. Upon heating, these species migrate into the zeolite channels and can undergo IE at BAS, resulting in the formation of mononuclear $[MoO_2(OH)]^+$ species. Further condensation can form dimers $[Mo_2O_5]^{2+}$ (Scheme 5.3a) that Iglesia showed were reduced to the active MoC_x species upon exposure to CH_4 [96]. The $[MoO_2(OH)^+]$ species can also react with another BAS to form a $[MoO_2]^{2+}$ cation bridging two framework oxygen atoms (Scheme 5.3b).

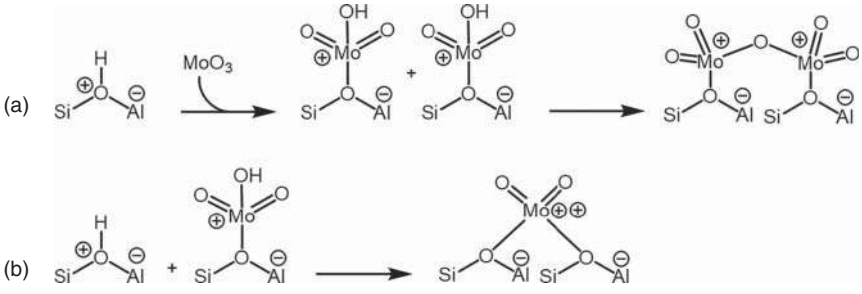

Scheme 5.3 Interactions between Mo species and BAS resulting in Mo dimers and bridged species.

X-ray photoelectron spectroscopy (XPS) studies by Rosynek and coworkers demonstrate that following calcination, Mo exists principally as Mo^{6+}, likely as MoO_3 [91]. Exposure to CH_4 at 973 K resulted in the gradual reduction of the Mo^{6+} until complete transformation to Mo_2C occurred. PXRD analysis indicated that the carbide was highly dispersed within the zeolite channels, and this Mo_2C species was found to be critical for the activation of methane [91, 99].

Using combined *operando* X-ray absorption fine structure (XAFS) and high-resolution PXRD, with additional online reactor effluent analysis, Beale and coworkers made a highly detailed and complete study of Mo speciation during activation and catalytic MDA (Figure 5.5) [98]. Very importantly, their observations confirm that the Mo must be fully carburized before aromatics production begins, hence confirming molybdenum carbides as the active sites for MDA. Additionally, the results show that the neutral MoC_3 and Mo_xC_y clusters are no longer bound to the zeolite framework and migrate to the external surface of the crystal, where they catalyze the formation of carbon deposits [98]. These observations are also in line with another study that showed that the degree of Al pairs in the ZSM-5 framework could control the Mo species introduced into the micropore but had no

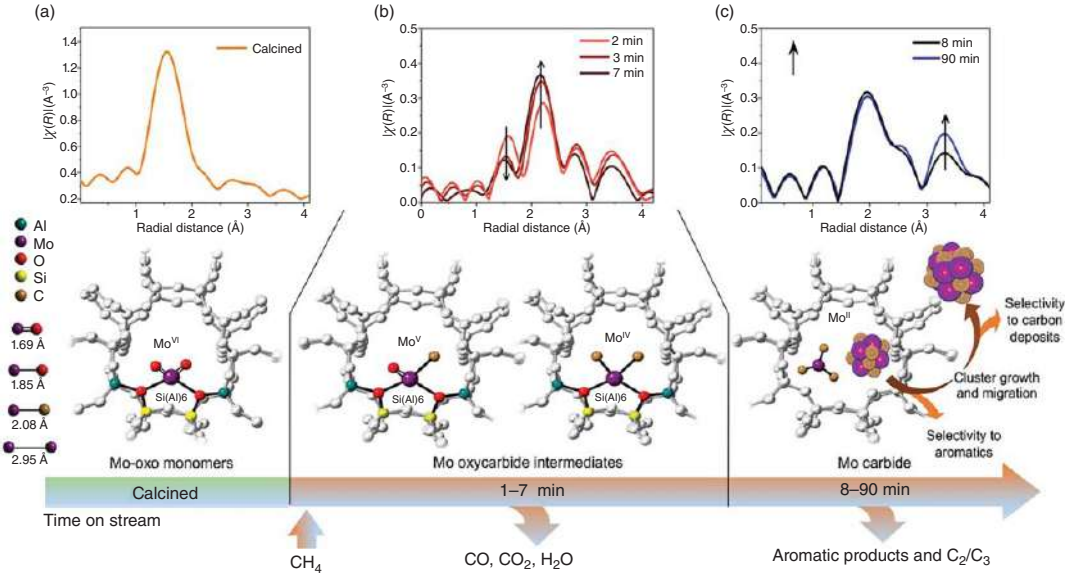

Figure 5.5 Schematic representation of Mo species evolution during MDA reaction on Mo/H-ZSM-5 catalyst as determined by operando XAS studies. The image shows the phase-corrected FT-EXAFS spectra, the corresponding Mo species proposed, and the reaction products are pictured for the (a) calcined sample, (b) sample during the first one to seven minutes of reaction (induction period), and (c) sample between 8 and 92 minutes of reaction (aromatization stage). Source: Liu et al. [98]/with permission of John Wiley & Sons, Inc.

effect on the catalytic performance [100]. Both these studies show that without the ability to anchor the active site in the micropore, the migration and deactivation is an inherent problem for the MDA reaction. In a subsequent study, Beale and coworkers showed that a Mo/silicalite-1 catalyst underwent more rapid deactivation than Mo/ZSM-5 due to faster Mo carbide migration [101]. This illustrates that the negative framework charge does have a stabilizing effect on the active molybdenum carbide catalysts, but cannot prevent the deactivation process. Hensen and coworkers have shown that molybdenum carbide hosted on non-zeolitic supports mainly produces carbon under MDA conditions while showing that Mo/silicalite-1 is active for MDA [102]. The groups study determined that aromatization of methane is an intrinsic ability of molybdenum carbides dispersed in the ten-membered ring (10-MR) micropores of the MFI framework, with the zeolite solely providing a BTX shape selecting capacity.

In 2020, Han and coworkers used integrated differential phase-contrast scanning transmission electron microscopy (iDPC-STEM) to demonstrate the presence of atomically dispersed molybdenum species in ZSM-5 (Si/Al = 40) after impregnation with $(NH_4)_6Mo_7O_{24}{\cdot}4H_2O$ and subsequent thermal treatment at 973 K (Figure 5.6) [103]. The absence of bulk MoO_3 was also confirmed by PXRD analysis. When the same procedure was conducted with silicalite-1 as the support-only bulk, MoO_3 clusters were formed. Energy-dispersive spectroscopy (EDS) elemental mapping performed under STEM also supported these observations, showing highly dispersed Mo on the ZSM-5 sample and clusters in the silicalite-1 sample. Additionally, the authors were able to model the Mo location and subsequently determine the Al occupancy of T-sites in the ZSM-5 sample (Figure 5.6f). Using MOR (Si/Al = 6) as the support, highly dispersed Mo species were also formed, though the study was unable to determine whether monomeric or dimeric species dominated, the latter possibly more likely given the high Al content of the MOR sample used [103].

Recent work has concluded that BAS sites do not catalyze any rate- or selectivity-determining steps in the benzene formation pathway, which suggests that the main benefits of BAS sites are only to disperse Mo during the preparation of the catalyst [104]. Furthermore the study determined that Mo carbide was the only kinetically relevant species in the MDA reaction.

In order to maximize benzene selectivity while minimizing the effects from coking, numerous Mo-exchanged zeolite and zeotype frameworks have been studied for MDA. Lin and coworkers screened several frameworks and concluded that protic silica–alumina zeolites, such as ZSM-5, ZSM-8, ZSM-11, and Beta, containing 2D channel structures (at least) with pore diameters close to the dynamic diameter of benzene (6 Å) were the best supports for the MDA reaction [105]. No hydrocarbon products were formed from Mo/H-SAPO-5 or Mo/SAPO-11 catalysts [105]. Other frameworks (X, Y, MOR) demonstrated low levels of methane conversion and were rapidly deactivated due to the formation of coke [106]. However, only Mo-loaded H–MCM-22 and H–MCM-49 produced high MDA activity that was comparable with Mo/H–ZSM-5 [85]. Hence, MCM-22 and ZSM-5 have been studied extensively. H–MCM-22 consists of two independent pore systems: a 2D sinusoidal

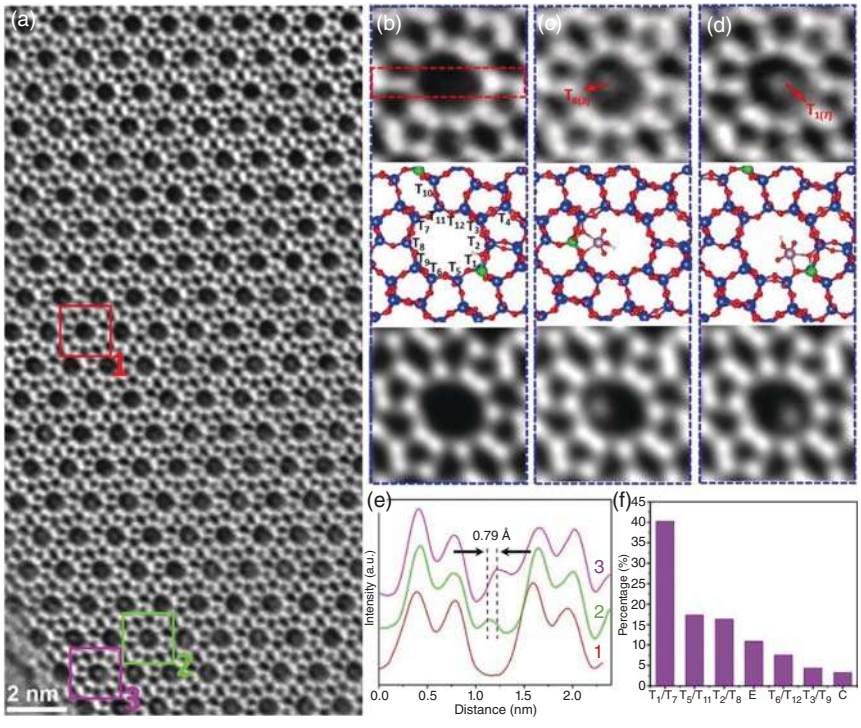

Figure 5.6 A representative iDPC-STEM image of Mo/ZSM-5, showing the presence of off-center contrast in many 10-MR channels. (b)–(d) Zoomed-in areas 1, 2, and 3 of (a), respectively, corresponding to three scenarios: empty channel (b) and channels containing a MoO_3H cluster bound at the T8 site (c) and at the T1 site (d). Each panel includes the raw image (top), the calculated structural model (middle), and the simulated projected electrostatic potential (bottom). Si, blue; O, red; Al, green; Mo, pink; and H, white. (e) Intensity line profiles of the images in (b), (c), and (d) across the areas as represented by the red dashed rectangle. (f) Statistics of Al occupancy at different T-sites, based on the results of one hundred channels. The labels (e) and (c) represent empty channels and channels with an on-center extra contrast, respectively. Source: Reproduced with permission from Liu et al. [103]; © Copyright 2018 Wiley.

10-MR pore system and a larger 3D 12-MR super-cage system interconnected by 10-MR windows. The smaller sinusoidal system is not dissimilar to the 3D channel structure of ZSM-5 (Figure 5.7). This pore structure and the presence of supercages allow MCM-22 to accommodate high levels of coke while retaining shape selectivity for benzene. Hence, high MDA activity is achieved using Mo/H–MCM-22 with higher catalyst stability than Mo/H–ZSM-5 [107, 108].

Although the exact nature of the active species and mechanism for MDA has not yet been established, one fact is clear for MDA reactions over Mo/zeolites: severe carbon deposition is a major source of deactivation. Three types of coke have been observed on Mo/H–ZSM-5 using XPS: graphite-like carbon in the zeolite channels, carbidic coke as a component of Mo_2C on the zeolite surface, and hydrogen poor sp-type coke that gradually covers the zeolite surface [53, 85]. Evidence for these types of coke is supported by temperature-programmed techniques performed by

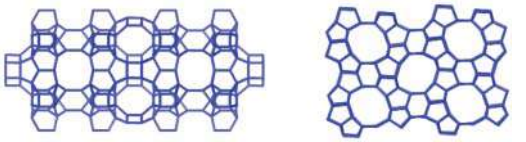

Figure 5.7 Structure and channel dimensions of (a) MCM-22 and (b) ZSM-5, both promising catalysts for MDA. Source: Images and dimensions from IZA Structure database based on [25].

Bao and coworkers [107, 109, 110] and UV-Raman spectroscopy [111]. The coke levels increase with TOS and with temperature [112]. Generally, the dehydrogenation of CH_x on the metal catalyst results in amorphous coke, while the polymerization of C_2H_x and C_6H_5 on the BAS sits results in polyaromatic deposits [113]. It is this polyaromatic type carbon that is thought to be the main cause of catalyst deactivation [53, 85]. Furthermore, under excessive Mo loading and extended TOS, the zeolite framework can collapse forming $Al_2(MoO_4)_3$, and under the harsh reaction conditions, sintering of the Mo_2C species can also cause deactivation [114].

While the formation of carbon deposits is somewhat inevitable, catalyst deactivation within a few hours of contact with methane under MDA reaction conditions is not suitable for practical applications. Therefore, a number of groups are working on regeneration protocols and also reducing the deposition of coke during MDA reactions. The catalysts can be regenerated by oxidation or hydrogenation of the coke. Oxidative treatments result in the removal of coke by forming CO_x, but very high-temperature air calcination cannot be carried out as this results in zeolite dealumination [85]. Low-temperature (300–500 °C) oxidation can remove polyaromatic deposits, and Hensen and coworkers have developed a novel isothermal air regeneration protocol for MDA [115]. Periodic oxygen pulses into the methane feed resulted in full restoration of catalytic activity, doubled cumulative benzene yield, and considerably lower overall coke formation. However, the regenerative effects diminish with TOS as harder-to-oxidize polyaromatic coke, which cannot be removed at 973 K under oxidative conditions, forms. Other groups have also developed pulsing methods, under oxygen or hydrogen, leading to the enhanced benzene yields and more stable catalyst performances [116–118]. This method shows great potential in tackling the coking issues of the MDA reaction.

Mintova and coworkers recently succeeded in synthesizing a ZSM-5 material with framework Mo sites, [Mo,Al]ZSM-5, where the Mo sites were active for the MDA reaction [119]. Interestingly the material had improved thermal stability (up to 1000 °C), hydrothermal stability, and substantially longer MDA lifetime than a reference material where Mo was introduced via impregnation. Notably [Mo,Al]ZSM-5 also produced a greater fraction of alkenes than the reference material. Post-mortem analysis showed that the Mo remained in the framework after the MDA reaction though dealumination was observed. It was reported that the increased stability of [Mo,Al]ZSM-5 was due to the healing of framework defects by Mo during the synthesis procedure [119]. This unexpected result indicates

isolated framework active sites may well provide the appropriate anchoring to the zeolite framework resulting in preventing migration and sintering of Mo. Developing zeolites with high-temperature stability [120] will be useful for the MDA reaction, due to the need for high-temperature conditions resulting from the thermodynamic limitations of the reaction. In that regard, it should be noted that stabilizing aluminosilicate zeolites by the healing of silanol defects was reported by Wakihara and coworkers using an aqueous treatment of TEAOH and NH_4F at 443 K for 24 hours [121]. Remarkably the high-silica ZSM-5 treated with this defect healing method retained 97% crystallinity after steaming at 1423 K.

To overcome poor benzene yield caused by the thermodynamic limitations of the reaction, a number of different strategies have been employed. Hydrogen-selective membrane reactors have been used to remove hydrogen from the product stream and have successfully managed to enhance the methane conversion by nearly 200% (up to 12.7% CH_4 conversion) and enhance the benzene yield by up to 350% [122]. Bhan and coworkers have employed an *in situ* H_2 chemisorption method to improve the MDA product yield [123]. By adding Zr to pre-carburized Mo/H-ZSM-5 formulations, they were able to achieve 27 % maximum single-pass CH_4 through the formation of ZrH_x species during MDA at 700 °C. A composite catalyst of doped cerium oxide and Mo/ZSM-5 was reported to give a 62% increase in methane conversion through *in situ* oxidation of H_2 to water by the doped cerium oxide [124].

Since the initial report of MDA over Mo/H–ZSM-5 in 1993, substantial progress has been made in understanding various aspects of the reaction. However, the inherent inertness of methane, rapid catalyst deactivation, and thermodynamic limitations of the reaction hinder the industrialization of MDA. Mo/H–ZSM-5 and Mo/H–MCM-22 remain the most active and selective catalysts due to their 10-MR channels giving high selectivities to BTX. Though the exact mechanistic details remain debated, it is generally accepted that Mo migrates into the zeolite channels during calcination where the molybdenum carbide phases are formed upon methane exposure. There is growing evidence that hydrocarbons formed in the micropore network during the induction period play an active role in the catalytic mechanism while results from Beale and coworkers [98], Hensen and coworkers [102], and Meriaudeau and coworkers [92] demonstrate that BAS sites are not necessarily required for MDA activity. Further advances in reaction procedure, reactor design, and fundamental understanding of mechanism and active sites will hopefully lead to future improvements in the MDA process.

5.4 Metal-Modified Zeolites for dMtM

The partial oxidation of methane to methanol with oxygen (dMtM) is thermodynamically favorable but suffers from poor selectivity as the over oxidation to carbon dioxide is even more thermodynamically favorable still [125]. As such, low reaction selectivity is observed at higher methane conversion levels, much like the OCM reaction. Additionally, radical based mechanisms also hamper the reaction selectivity as

the product of the reaction, methanol, has a weaker C—H bond than methane [49]. This gives rise to an inherent kinetic limitation, resulting in a best obtainable yield of 5% due to the large differences in C—H bond enthalpy [49, 126]. Despite the kinetic and thermodynamic challenges of the reaction, nature has mastered this conversion in the form of an enzyme, MMO, which is capable of converting methane to methanol at physiological conditions [21] and provides inspiration to develop a synthetic system that is able to overcome these limitations [127].

Early reports on dMtM can be traced to the very early part of the twentieth century. Articles by Bone and Wheeler were published in 1902 and 1903 concerning homogeneous (gas phase) partial oxidation of methane [128, 129]. In 1905, Lance and Elworthy described the oxidation methane to methanol with hydrogen peroxide in the presence of ferrous sulfate [130]. Early research into dMtM was dominated by efforts in homogeneous (gas phase) conversion though some notable work using heterogeneous catalysts was reported in 1928 [131]. By the 1960s, a range of different supported metals had been tested for dMtM [18]. In particular, much effort has been gone into applying early transition metal oxides for dMtM as they find use as oxidation catalysts through Mars–van Krevelen-type mechanisms [132]. For instance, the commercial production of maleic anhydride via partial oxidation of either benzene or *n*-butane has utilized oxides of molybdenum or vanadium as catalysts [133]. Heterogenized oxides of molybdenum and vanadium catalysts are indeed active for the partial oxidation of methane though the catalysts typically produce formaldehyde rather than methanol [134–137]. In 2008, an Fe/SiO_2 catalyst was reported to give high methane conversion and very high selectivity (13.2% and 78.8%, respectively) [138], but no further articles on the system have been reported. Heterogeneous catalysis remains an important area of research into improving dMtM, with a number of recent reviews highlighting the progress made [13, 18, 19, 139–142] but also the challenges that need to be addressed for future commercialization [126, 143–146].

Metal-modified zeolites have featured extensively in the modern era of dMtM research [142, 147, 148]. In early pioneering work, a patent filed in 1989 from the Sun Refining and Marketing Company reported that a ferrosilicate (SOD framework) was competent for the catalytic, direct, partial oxidation of methane to methanol with molecular oxygen under flow conditions (64% selectivity at 4.6% conversion, 407 °C) [149]. The relevant control experiment gave 47% selectivity at 0.2% conversion over glass beads. Articles from the Mobil Research and Development Corporation reported less inspiring results, 16.7% selectivity at 5.2% conversion over H/ZSM-5 at 450 °C [150], while a H/ZSM-5 material impregnated with Zn (most likely ZnO) gave 20.6% selectivity at 5.5% conversion at 465 °C [151]. While the Mobil results were less promising, these early results showed that methanol could be formed under continuous flow conditions, albeit within the theoretical 5% yield limitation later determined by Labinger [49]. In 1995, Panov and coworkers showed that methanol could be formed from methane by contact with the so-called α-Fe site, supported on ZSM-5 [152]. While the structure of the active site was unknown at this stage, the selectivity (after aqueous extraction) was shown to be 75%. This inspired others to further study these stoichiometric reactions in a bid to uncover

the mechanism and active site requirements such that the yield and selectivity of the catalytic reaction may be improved.

Despite substantial progress in dMtM using heterogeneous catalysts, no system has yet been commercialized (though a pilot plant running dMtM is reportedly in operation in the United States), indicative of the significant barriers that remain. In evaluating a dMtM production plant using recent catalyst technologies, de Klerk highlighted the areas where improvements need to be made to challenge the syngas route: (i) improving MeOH selectivity/reducing CO_2 selectivity, (ii) reducing the need for pure oxygen (which introduces an air fractionation step), and (iii) keeping the reaction pressure to a minimum to reduce the compressor duty [153]. In a positive outlook for the future of dMtM, it should be noted that these areas can be tackled by catalyst improvement and should be targets within future research.

5.4.1 Fe-Modified Zeolites

A substantial research effort has been applied to understanding the speciation and mechanism of extra-framework Fe sites in zeolite catalysis [154, 155]. In the early 1990s, Panov et al. studied the activation of extra-framework iron species in ZSM-5 with N_2O and showed that the resultant activated iron was able to oxidize benzene to phenol stoichiometrically [156–158]. Early reports determined that Fe/ZSM-5 is able to decompose N_2O at low temperatures (<300 °C) forming a highly reactive iron/oxygen species bound to the zeolite surface, but as the structure was unknown, it was simply termed α-oxygen (α-O). It was later shown to be the active species in direct partial oxidation of methane to methanol [152].

The nature of the active site and factors determining reactivity were difficult to prove due to the presence of inactive spectator iron species. Similar to MMO enzymes, it was originally thought that the active precursor associated with the decomposition of N_2O (known as α-Fe) was a binuclear iron species [159]. However, the α-Fe site was later determined to be a mononuclear Fe^{II} species formed via auto-reduction of impregnated Fe^{III} species upon thermal treatment [160, 161]. Recently, a study managed to elucidate significant structural and electronic information about both the α-Fe and α-O sites in zeolite beta (β), showing that α-Fe is a mononuclear, high-spin Fe^{II} species residing within a square planar coordination environment, while the α-O site is a mononuclear, high-spin species that contains an Fe^{IV}=O center adopting a square pyramidal geometry [161]. Additional density functional theory (DFT) studies support the square planar site resides within a β–6-MR (Figure 5.8). Very similar α-Fe and α-O sites have also been identified to be formed in SSZ-13 (CHA framework); equally the α-O species was able to oxidize methane stoichiometrically at room temperature and was formed from reaction of α-Fe with N_2O [162]. The activation of N_2O by extra-framework iron species is not experimentally limited to MFI, CHA, and beta framework types alone. Evidence for N_2O decomposition over MOR, FER, and FAU has also been reported [163–166]. In the case of Fe/BEA and Fe/CHA, methanol was recovered by liquid extraction [161, 162].

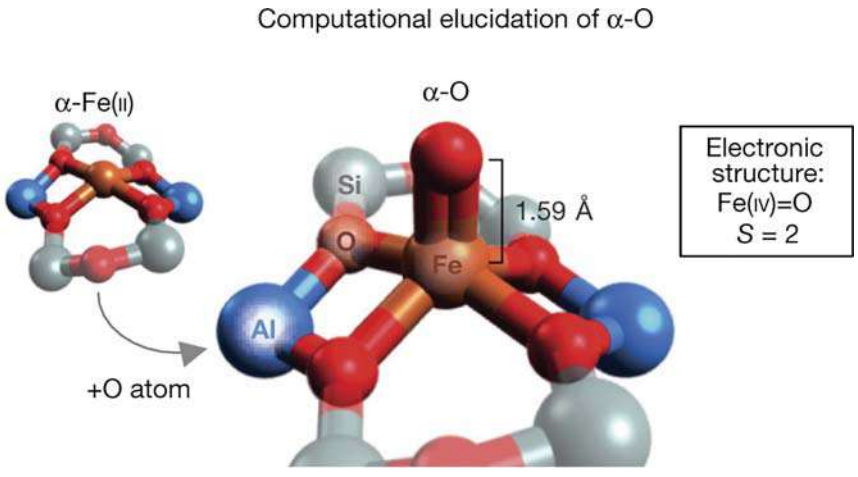

Figure 5.8 DFT-optimized structure of α–Fe(IV)=O in the $S = 2$ ground state and its formation. Source: Reproduced with permission from Snyder et al. [161]; © Copyright 2016 Springer Nature.

It is generally agreed that the methane-to-methanol reaction pathway over α-O sites begins with a radical based hydrogen atom abstraction mechanism, although steps following this first step are debated. A hydrogen atom abstraction from methane by the α-O results in a Fe^{III}–O–H fragment and a CH_3 radical. The CH_3 radical then either reacts with a further α-O to form Fe^{III}–O–CH_3, or the CH_3 radical may "rebound" to form Fe^{II}–O(H)–CH_3 (Figure 5.9) [160, 167]. The formation of dimethyl ether (DME, CH_3OCH_3) has also been reported to occur via the reaction of a CH_3 radical with a Fe^{III}–O–CH_3 group [160]. Experiments to study kinetic isotope effects suggest that the first step (C—H bond cleavage of methane) is the rate-limiting step [159]. Computational experiments strongly support a radical based mechanism for C—H bond cleavage; the Fe^{IV}=O species elongates and gains significant radical character at the transition state, becoming closer to a Fe^{III}–$O^{\cdot -}$ species [161]. It has also been shown by computational studies that the high activity of the α-O site is partially attributed to confinement effects within the zeolite channels [167, 168]. One of these studies determined that the confining effect of zeolite channels on the α-O site in SSZ-13 may reduce the energetic barrier to methane activation by over 50% [167]. The effect is predominantly electrostatic in nature and stabilizes the reaction intermediates and transition states to a further degree than that of the initially adsorbed methane molecule [167].

A limitation of iron-modified zeolites is that most materials can only form the α-O site from N_2O and not from O_2. In a work echoing the pioneering patent filed in 1989 from the Sun Refining and Marketing Company [149], a ferrisilicate (MFI framework) has been reported to be active in the direct conversion of methane to methanol using O_2 as the terminal oxidant [169]. The ferrisilicate (MFI) required elevated temperatures giving low-to-medium conversion, 523–903 K for 0.1–30% conversion, respectively, although the higher temperatures were detrimental to methanol selectivity. The need for higher temperatures to achieve low-level

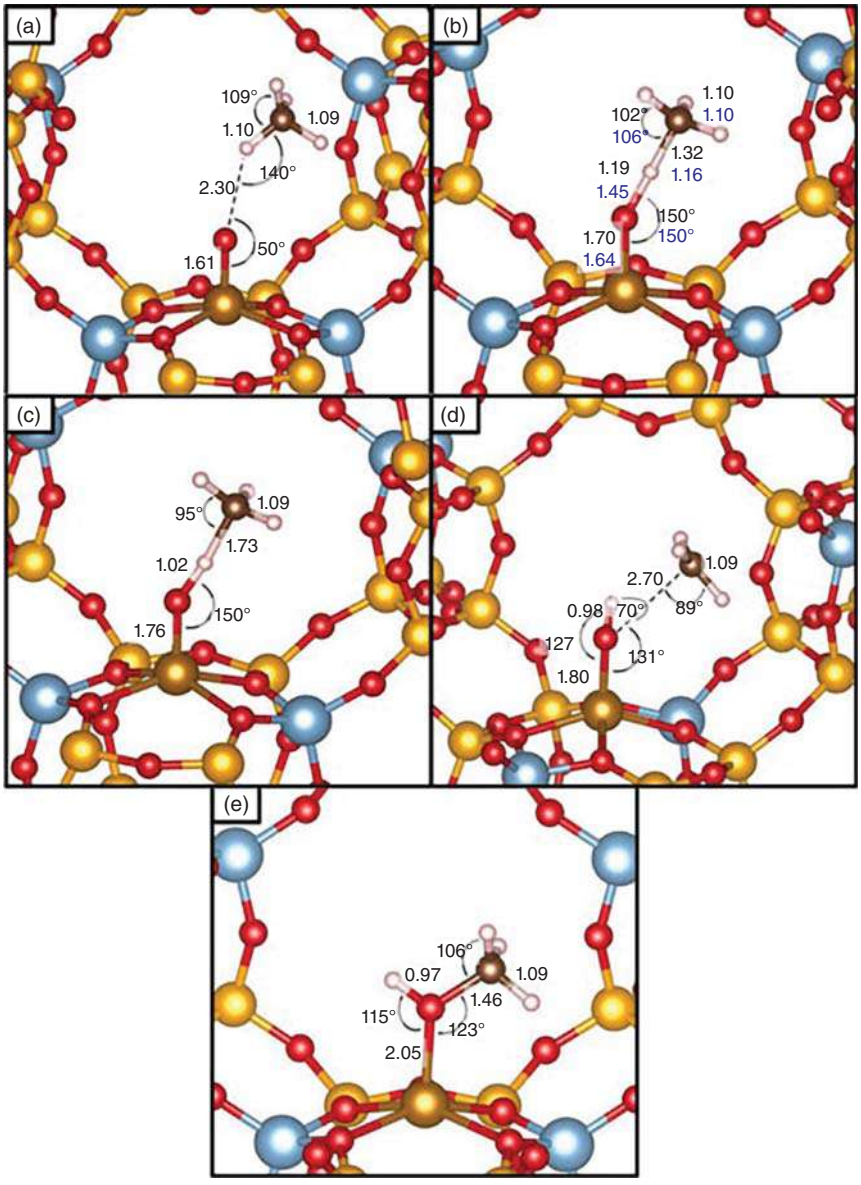

Figure 5.9 Structures and the most important intermediates (adsorbed molecule (a), reaction intermediate (c), and adsorbed methanol (e)) and transition states (abstraction transition state (b) and rebound transition state (d)) along the reaction pathway of dMtM over the α–O site. Color legend: Si atoms, yellow; O atoms, red; Al atoms, blue-gray; Fe atoms, gold; H atoms, white; and C atoms, brown. Black numbers represent PBE-D2 distances (in Å) and angles (in degrees); blue numbers in panel (b) show the optimized RPA geometry. Source: Reproduced with permission from Göltl et al. [167]; © Copyright 2016 American Chemical Society.

conversion suggests that ferrisilicates contain an active site that is different to the Fe-modified aluminosilicate zeolites. As a mechanism for methane oxidation over ferrisilicates has not been suggested, it is not possible to compare and contrast with respect to the α-O site.

Very recently, dioxygen activation to form the α-O site has been shown to occur over proximate binuclear Fe^{II} centers in ferrierite, at room temperature. Exposure of these α-O sites gave methanol as the major product [170]. The authors reported that the two cooperating Fe cations carry out a four-electron process of dioxygen dissociation in an $M^{II} \rightarrow M^{IV}$ cycle, similar to the redox processes occurring over Fe active sites in MMO. DFT calculations with additional framework types have shown that for the iron(II) sites to activate dioxygen, certain geometric criteria need to be met with regard to the distance and orientation of the proximate binuclear site [171]. Furthermore, in a landmark discovery, the same research team has also reported that proximate binuclear Ni, Mn, and Co centers in ferrierite are also able to activate dioxygen and affect methane oxidation, with proximate binuclear Ni sites giving the highest yield of methanol per metal [172]. These recent important papers show that subtle changes in the zeolite framework and composition can result in new mechanisms of reactivity and lead to new avenues of chemistry for the partial oxidation of methane.

5.4.2 Cu-Modified Zeolites

The dMtM reaction has been intensely investigated over copper-modified zeolites [141] ever since the first study on the selective formation of methanol utilizing copper-modified ZSM-5 was reported in 2005 [173]. Since then, a wide range of copper-modified zeolite frameworks have been shown to yield methanol in the dMtM reaction, including MFI, MOR, FER, CHA, FAU, BEA, LTL, EON, MAZ, MEI, BPH, HEU, SZR, AFX, ERI, and AEI [174–177]. Moreover, a wide variety of active sites have been proposed for this transformation, including mononuclear and multinuclear copper species, which has recently been summarized in a recent comprehensive review [141].

5.4.2.1 Active Sites for Methane Partial Oxidation in Copper-Modified Zeolites

In contrast to iron-modified zeolites where only one site (the so-called α-Fe site) is reported to be active for dMtM, multiple active sites proposed to exist in copper-modified zeolites [141, 155]. The first site to be proposed for methane C—H bond activation in Cu/ZSM-5 was the bis(μ-*oxo*)dicopper core (Figure 5.10a) that had previously been identified for the decomposition of NO [178] and was thought to be characterized by a strong absorption band at $22\,700\,cm^{-1}$ in the ultraviolet/visible/near-infrared (UV/Vis/NIR) spectrum [173]. Another active site, a (μ-η^2:η^2-peroxo)dicopper core (Figure 5.10b), which is active in nature for O_2 transport by the protein hemocyanin, was also suggested, but was not observed to be active in NO reduction [173, 178, 179].

By utilizing resonance-enhanced Raman spectroscopy (rR) to identify the active site from spectator species, the structure of the active site in Cu/ZSM-5 has

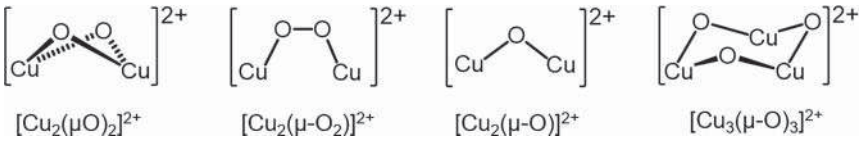

Figure 5.10 Cu-oxo complexes proposed as the active sites for methane activation in Cu-containing high-silica zeolites.

been determined to be a bent mono(μ-oxo)dicopper species (Figure 5.10c) [180]. The assignment was in part based on a series of isotope-sensitive fundamental vibrations at 456 cm^{-1} ($\Delta^{18}O_2 = 8\ cm^{-1}$) and 870 cm^{-1} ($\Delta^{18}O_2 = 40\ cm^{-1}$) alongside an intense overtone of the latter at 1725 cm^{-1} ($\Delta^{18}O_2 = 83\ cm^{-1}$) that closely resembles that seen for mono(μ-oxo)diferric cores [180, 181]. The active site is suggested to reside within the 10-MR channel of ZSM-5, with each copper atom of the mono(μ-oxo)dicopper core ligated by two oxygen atoms. Normal coordinate analysis predicts a Cu–O–Cu bridging angle of 140°. The copper species are proposed to be formally Cu^{II}, as Cu^{III} cannot be stabilized without coordination of a further –OH group of which no evidence was detected by IR spectroscopy [180].

It should be noted that the mono(μ-oxo)dicopper core in ZSM-5 can be formed by activation in both N_2O and O_2 as evidenced by observation of the UV/Vis/NIR band at 22 700 cm^{-1} that is associated with this active site [182, 183]. However, the formation of the active site by N_2O and O_2 takes different pathways. Activation by N_2O leads directly to the oxygen bridging mode (μ-1,1-O) [184], while activation by O_2 first in the formation of a (μ-η^2:η^2-peroxo)dicopper core followed by formation of the mono(μ-oxo)dicopper core from approximately 448 K onward (Figure 5.10) [183].

Larger copper clusters have been both evidenced and predicted as active sites for the partial oxidation of methane in copper-modified zeolite systems. A trinuclear copper core, $[Cu_3(\mu O)_3]^{2+}$ (Figure 5.10d), has been proposed to reside at the entrance of the 8-MR side pocket of Cu/MOR [185]. Extended X-ray absorption fine structure (EXAFS) measurements suggest that more than one Cu–Cu scattering path exists within the cluster, suggesting a nuclearity of >2. By studying the BAS/Cu stoichiometry during IE, it was shown that two BASs are displaced for every three Cu atoms, supporting the formation of a divalent, trinuclear copper site.

DFT simulations of mono(μ-oxo)dicopper and $[Cu_3(\mu O)_3]^{2+}$ cores in Cu/ZSM-5 have shown that high-temperature calcination in O_2 leads to the formation of the trinuclear species, whereas the binuclear species is preferentially formed under low partial pressures of O_2 [186]. Other multinuclear sites ($[Cu_nO_{n-1}]^{2+}$ and $[Cu_n(\mu O)_n]^{2+}$, where $n = 2, 3, 4, 5$) in Cu/MOR have been simulated by DFT calculations to compare their stability and reactivity [187]. It was reported that as the cluster increases in size, it becomes both more stable as a cluster and that the initial product of reaction with methane (the formation of Cu–O–H and CH_3 fragments) was also more stable. However, it is not clear if the activation energy was also reduced in the process.

In small-pore zeolites such as CHA, mononuclear extra-framework Cu cations have been identified both experimentally [188, 189] and using DFT calculations [190]. However, *operando* XAS studies have excluded the involvement of mononuclear $[CuOH]^+$ species as the active sites for the partial oxidation of methane in Cu/SSZ-13, instead showing that the mono(μ-oxo)dicopper site is most likely the active site [189]. Through UV/Vis and resonance Raman spectroscopy, a very recent study supports the identification of mono(μ-oxo)dicopper being the active site in Cu/SSZ-13 [191]. Notably the study showed through *operando* UV/Vis spectroscopy that the mono(μ-oxo)dicopper site in ZSM-5 is less reactive than the same site in SSZ-13, which was determined (from DFT calculations) to be due to the relative binding orientations of the framework oxygen atoms to the mono(μ-oxo)dicopper site in each framework. This study neatly highlights the subtle differences that zeolite lattice constraints can have on active site reactivity [191].

5.4.2.2 Reaction Mechanism for the Partial Oxidation of Methane over Copper-Modified Zeolites

Studies of the dMtM reaction over copper-modified zeolites have typically been conducted in a multistep process, with each step conducted under very different conditions [192, 193]. In the first step, the copper-exchanged zeolite is activated in an oxidative atmosphere using either O_2 (at elevated temperature, typically 723–823 K) or N_2O (at room temperature or higher) [194]. The activated material is then exposed to methane at approximately 473 K followed by subsequent extraction of the strongly bound products through contact with water vapor or another suitable solvent [192, 193].

It is widely accepted that methane activation over copper-modified zeolites occurs via radical type mechanisms as strongly supported by kinetic isotope experiments, along with DFT calculations [141, 180, 186, 194, 195]. The mono(μ-oxo)dicopper core in ZSM-5, formally denoted as $Cu^{2+}–O^{2-}–Cu^{2+}$, is thought to be in resonance with what is effectively a cupric-oxyl species, $Cu^{2+}–O^{\cdot -}–Cu^{+}$ (Figure 5.11), which possesses significant radical character owing to its singly occupied molecular orbital (SOMO) [180, 186]. This latter resonance form is poised to perform hydrogen atom

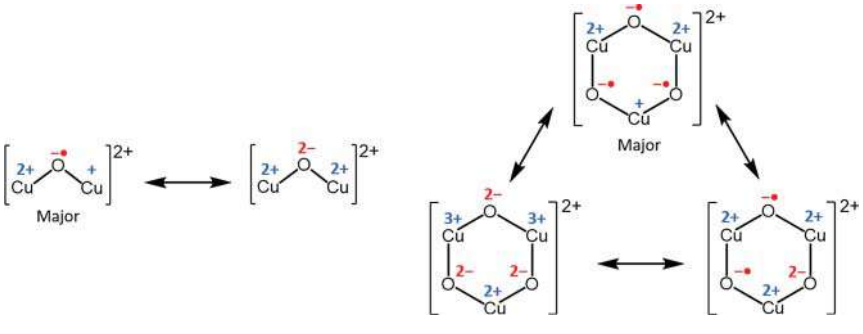

Figure 5.11 Possible resonance structures that could be proposed to describe the formal charge configuration in the extra-framework copper species.

abstraction from methane to form an intermediate Cu–OH–Cu species and a CH_3 radical and gives an H/D kinetic isotope effect (KIE) of 3.1 at 448 K when the activation energies of CH_4 and CD_4 are compared [180]. In a separate study, an H/D KIE of 1.6 was determined when CH_4 was substituted by CD_4 in the extracting gas at 483 K over Cu/Na–ZSM-5 [196]. These observations alongside DFT predictions show that hydrogen abstraction is the rate-limiting step in methanol formation from methane.

After hydrogen atom abstraction over the mono(μ-oxo)dicopper core in ZSM-5, the resultant "free" CH_3 radical intermediate has been predicted to collapse in several ways to form intermediates of various stability (Figure 5.12a) [186]. Two potential pathways can result in the formation of a strongly bound methanol molecule. The first, known as the "rebound mechanism," sees the CH_3 radical reacts with the bridging Cu–OH–Cu and forms Cu–OH(CH_3)–Cu. Alternatively, the CH_3 radical can also react with one of the copper atoms forming an intermediate CH_3–Cu–OH–Cu species prior to migration to the bridging oxygen atom. The most stable product however was the formation of a framework methoxy species, where the CH_3 radical has reacted with a framework oxygen atom. This results in formation of a reduced copper cluster, Cu^I–O–Cu^I. Formation of methanol from here is not expected to be favorable in the absence of water as the reformation of the CH_3 radical would be required [186]. Recent experimental evidence from solid-state NMR and FTIR spectroscopy supports the occurrence of these different reaction pathways over Cu/ZSM-5 [197]. A complementary investigation utilizing solid-state NMR and FTIR spectroscopy into the activity of Cu/MOR detected the additional presence of formate and dimethyl ether species, and notably it was also concluded that the Si/Al ratio of the host MOR zeolite affects the structure of the copper species that is in turn responsible for the formation of different products [198].

The mechanism of methane activation over the trinuclear $[Cu_3(\mu O)_3]^{2+}$ core in ZSM-5 has been calculated to occur along a similar pathway (Figure 5.12b) to the binuclear equivalent. Theoretical calculations suggest that the trinuclear species in

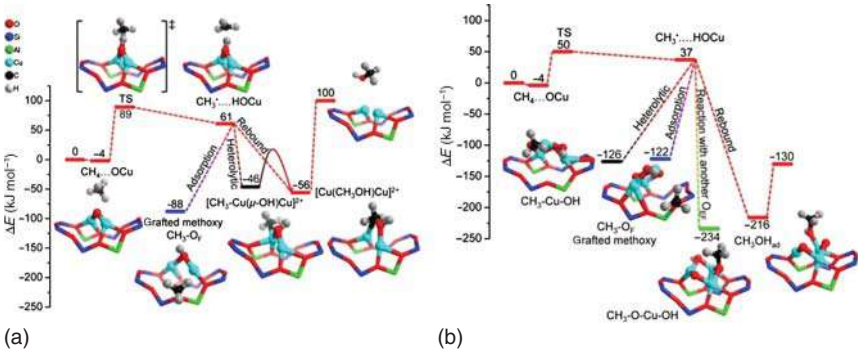

Figure 5.12 Reaction pathways for methane oxidation to methanol and alternative CH_3 recombination routes over binuclear $[Cu_2(\mu O)]^{2+}$ (a) and trinuclear $[Cu_3(\mu O)_3]^{2+}$ (b) sites. Source: Reproduced with permission from Li et al. [186]; © Copyright 2016 Elsevier.

ZSM-5 is most accurately described as a radical species, similar to that seen for the binuclear equivalents [185, 186]. As such, this species is reported to exist as a mixed Cu^{II}/Cu^{I} system possessing radical anionic oxygen ligands in resonance with the formally charged species (Figure 5.12b).

Regardless of the mechanistic descriptions highlighted above, the product of the reaction (methanol) is strongly adsorbed in all cases, and the co-adsorption/reaction of water is required to liberate the formed methanol. In general, it is not considered possible to thermally desorb methanol as the increased reaction temperature may result in further oxidation to CO_2.

5.4.2.3 Alternatives to Stepwise Methanol Production: Isothermal and Direct Catalytic Conversion of Methane to Methanol over Copper-Modified Zeolites

As discussed above, most copper-modified zeolites that are active for methane to methanol go through three distinct steps that are executed over a variable temperature range. This is a barrier to commercial use as substantial temperature changes reduce the production efficiency as time is wasted during heat cycles, and thermal efficiency as heat is wasted during the heating and cooling of the reactor [199]. Recently, a number of papers have reported the ability to run the dMtM reaction in a stepwise, isothermal mode using O_2 as terminal oxidant over a number of different frameworks [177, 199, 200]. It is found in the case of isothermal activation with O_2 over Cu/MOR that methanol yield depends on methane pressure with increasing pressure from 50 mbar to 37 bar resulting in two orders of magnitude change in methanol yield (per gram of catalyst). This strongly indicates that the active sites present in Cu/MOR are nonuniform in nature [199]. This may be either due to the presence of multiple active species, possibly with a higher nuclearity clusters or possibly in the distribution of active sites within different areas of the framework (e.g. in 8-MR SP or the 12-MR channel in MOR).

One of the main goals of research into the dMtM reaction is to develop methanol production under continuous flow conditions using O_2 as the terminal oxidant. The first report of copper-exchanged zeolites achieving this feat was published in 2016 using a feed gas mixture of $CH_4/O_2/H_2O$ at moderate temperatures (483–498 K) and giving methanol production values of approximately 0.30–3.12 $\mu mol_{MeOH}\ g_{cat}^{-1}\ h^{-1}$, depending on the framework [196]. However, approximately 300 hours of TOS was required to give 1.4 $mol_{MeOH}\ mol_{Cu}^{-1}$ for a Cu/ZSM-5 material, highlighting the poor performance of the reaction. In 2019, a copper-exchanged CHA was reported to give up to 18 $\mu mol_{MeOH}\ g_{cat}^{-1}\ h^{-1}$, under a feed mix of $CH_4/O_2/H_2O$ at 543 K [201]. Intriguingly, a recent complementary isotope study points to the fact that the water is the source of oxygen in the formation of methanol over Cu/CHA under continuous flow conditions, with a reported productivity of 6 $\mu mol_{MeOH}\ g_{cat}^{-1}\ h^{-1}$ [202]. This finding could open new avenues of research in developing dMtM in the future. A very recent breakthrough has been reported concerning dMtM under continuous flow conditions with a Cu/CHA achieving over 500 $mol_{MeOH}\ mol_{Cu}^{-1}\ h^{-1}$, for 500 hours TOS [203]. Catalyst screening with MOR, CHA, and MFI frameworks showed CHA to optimal while the ideal reaction conditions were shown to be 98% CH_4/2% H_2O/400 ppm O_2. Spectroscopic studies suggest that the fast redox

cycling of $Cu^{2+}/Cu^{+}/Cu^{2+}$ is important for the high catalytic activity, while DFT calculations suggest that both monomeric and dimeric copper sites were active for the reaction [203]. This groundbreaking report heralds much promise for the development of continuous flow dMtM reaction using copper-exchanged zeolites.

5.4.2.4 Effect of Framework Topology and Composition on Methane Partial Oxidation over Copper-Modified Zeolites

The nature of the copper active site and the methanol yield are both affected by the zeolite topology and composition. In general, more aluminous topologies readily stabilize multinuclear copper clusters, while more siliceous topologies with highly dispersed Al atoms are more likely to support monomeric active sites [204]. Like most dMtM literature, Cu/ZSM-5 was the first framework to be studied for dMtM, but confinement effects in MOR frameworks, leading to the higher methanol yields, have been thoroughly explored [173]. Most recently, frameworks containing small cages and pores, such as CHA, MAZ, and MOR, have shown remarkable methanol yields and have been studied intensely (Figure 5.13).

Although the yield of methanol obtained from Cu/ZSM-5 is considerably lower than other frameworks, this material has been used to characterize the formation of the Cu active sites and the reaction mechanism involved. The Cu loading and Al distribution of the Cu/ZSM-5 can affect the nature of the active site that in turn impacts the methanol yield [205]. Nevertheless, the major active site within Cu/ZSM-5 is suggested to be the bent mono(μ-oxo)dicopper species (Figure 5.10c), illustrated by the UV/Vis/NIR band at 22 700 cm^{-1} [88]. However, the local environment of the Cu species can impact the reactivity toward methane, i.e. Cu species within the channel and at channel intersections demonstrate different reactivity [205].

This impact of local environment has been studied extensively in Cu/MOR. Both binuclear and trinuclear clusters capable of performing methane partial oxidation have been suggested to be present at the 8-MR windows of the MOR

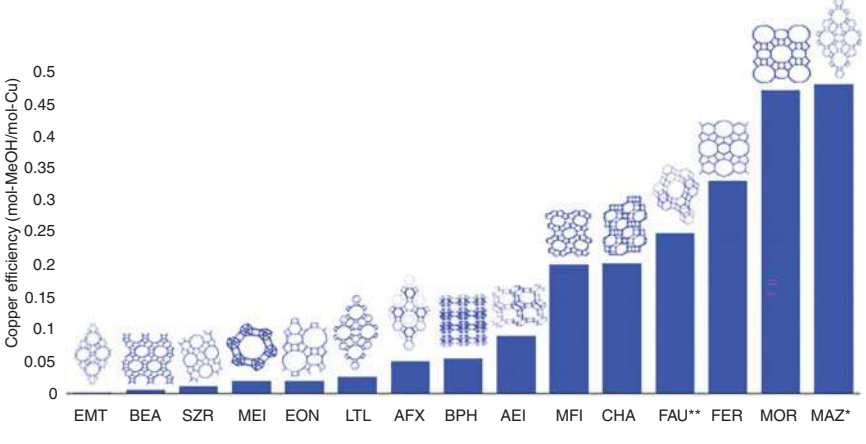

Figure 5.13 Performance of copper zeolite systems tested for methane to methanol. Source: Reproduced with permission from Newton et al. [141]; © Copyright 2020 Royal Society of Chemistry.

side pockets [173, 185]. Furthermore, recent spectroscopic observations [206] and DFT simulations [207] have further suggested that Cu/MOR possesses two mono(μ-oxo)dicopper species (Figure 5.10c) predicted to be distinct with respect to their siting within the 8-MR side pocket [207]. Although the two sites have similar geometric and electronic structures, they demonstrate significant reactivity differences. Additionally, only one of the two active sites is stable above 603 K [206]. These two species have recently been determined to be the result of confinement within the multidimensional structure of MOR [208]. The confinement of $[Cu_2O]^{2+}$ dimer in the 8-MR side pocket of MOR results in a lower activation barrier due to the stabilization of the transition state through van der Waals contacts with the framework. Although this confinement effect (sometimes known as the nest effect) [209] is less well known than other zeolite shape-selective effects, the Iglesia group has studied its role within a number of catalytic systems [30, 210, 211]. Furthermore, confinement in the 8-MR side pockets of MOR has been shown to give rise to a notable increase in reaction rate, and therefore selectivity, in the carbonylation of carbon monoxide to form methyl acetate [39, 212]. Using confinement to selectivity enhance the rate of one reaction (formation of methanol in this case) through transition state stabilization could be the mechanism needed to overcome the thermodynamic limitation on methane partial oxidation.

Solomon and coworkers determined from methanol yields that 5% of Cu atoms were active in the conversion of methane to methanol over Cu/ZSM-5 [180]. However, 60% of Cu^{II} species were found to be reduced to Cu^{I} upon methane exposure in Cu/MOR through X-ray absorption near-edge structure (XANES) studies [213, 214]. More recently, it has been established that the ratio of copper species that is reduced correlates well to the quantity of methanol formed in Cu/MOR [215]. Furthermore, it was observed that multiple oxidation/reduction cycles were necessary to obtain a representative view of the overall performance of dMtM over Cu/MOR, as it is indicated that the copper species present equilibrate over many cycles.

Borfecchia and coworkers reported a very high yielding Cu/MOR with a Si/Al = 7 and Cu/Al = 0.18 that produced 170 $\mu mol_{MeOH}\ g_{cat}^{-1}$ (only very recently outperformed by SSZ-13) [216]. Importantly, their *operando* XAS and high-energy-resolution fluorescence-detected (HERFD) XANES spectroscopy investigations strongly indicated that a dicopper species is likely active in Cu/MOR [216]. The authors observed that for every two Cu ions in the material, approximately one methane molecule was activated. Furthermore, the methanol productivity across a variety of materials and reaction procedures was observed to increase with a slope of 0.5 as the concentration of the active Cu species (identified spectroscopically) increases.

Recently, copper-modified small-pore zeolites, such as SSZ-13, have gained considerable interest as methane partial oxidation catalysts [176, 203, 217, 218]. The highest yield of methanol to date, 195 $\mu mol_{MeOH}\ g_{cat}^{-1}$, has recently been reported by Li and coworkers over Cu/SSZ-13 (Si/Al = 11.4, Cu/Al = 0.23) [203]. The authors suggest that the confinement provided by the CHA cage appears to be ideal for the partial reduction of Cu^{2+} to Cu^{+} but hinders subsequent reduction to inactive Cu^{0}. Much of

the recent literature on SSZ-13 suggests isolated copper ions in the form of $[CuOH]^+$ are responsible for the conversion of methane to methanol in SSZ-13, unlike the multinuclear clusters present in larger-pore zeolites [188, 190, 216]. However, as mentioned above, certain *operando* XAS studies have excluded the involvement of mononuclear $[CuOH]^+$ species as the active sites for the partial oxidation of methane in Cu/SSZ-13, instead showing that a mono(μ-oxo)dicopper site is most likely the active site [189].

Given the high yield of methanol observed for SSZ-13 and the obvious benefits of confinement in the promotion of the partial oxidation of methane, it is likely that subsequent progress in dMtM using copper-modified zeolites will exploit small-pore zeolites or small channels and side pockets as in MOR.

5.4.3 Zn-Modified Zeolites

Unlike iron- and copper-modified zeolites, zinc-based systems have been shown to form active species without an initial high-temperature oxidation step, indicating the potential of an isothermal processes. Since the initial findings of Kazansky and Serykh, which demonstrated heterolytic CH_4 bond dissociation over Zn exchanged zeolites [219], a number of groups have shown the partial oxidation of methane, in the presence of dioxygen, over zinc-modified zeolites though no catalytic systems have been developed to date.

Incipient wetness impregnation and IE using a decomposable zinc salt are two easy methods of introducing zinc into zeolites. However, these methods can introduce a variety of zinc species into the zeolite, making it difficult to determine which exact species is responsible for C–H activation. Consequently, a variety of different mechanisms have been proposed. Impregnation introduces the biggest variety of species: Zn^{2+} ions that sit at cation exchange sites within the zeolite, $[Zn–O–Zn]^{2+}$ clusters formed through the condensation of partially hydrolyzed $[Zn–OH]^+$ extra-framework ions, and ZnO clusters. Comparatively, IE methods result in predominantly the introduction of Zn^{2+} cations [220, 221].

Unlike the other metals previously discussed in this chapter, chemical vapor deposition (CVD) methods can be used to introduce zinc into zeolites. Vapor deposition with Zn^0 powder involves the exchange of BASs for Zn^{2+} ions via a redox reaction evolving H_2 [222]. A small fraction of paramagnetic isolated Zn^+ ions have also been detected by EPR spectroscopy upon contact of metallic zinc vapors with H–ZSM-5, but these have not been reported to react with methane [223]. In 2015, Kuroda and coworkers were able to stabilize a $[Zn_2]^{2+}$ species in the pores of ZSM-5 through introduction of zinc by CVD where an excess of metallic zinc was present [224]. However, the reactivity of this dimeric species has not yet been explored in the confines of a zeolite micropore. Finally, CVD of dimethyl zinc leads to surface-grafted $[Zn–CH_3]^+$ species that can be converted to Zn^{2+} ions through reaction with H_2 or oxidized to ZnO clusters [220].

Alongside the variety of species present, the levels of zinc exchange vary with the method of zinc introduction. Vapor deposition techniques have been shown to result in full exchange of BAS, while other methods normally result in lower exchange

levels, particularly for high-silica zeolites [219, 220]. Reduced zinc loading is often attributed to the difficulty of stabilizing the formal 2+ charge associated with the Zn^{2+} ions in high-silica zeolites where there is low framework charge and possibly a high level of separation between framework Al tetrahedra [221, 225].

5.4.3.1 Mechanism of C–H Activation in Zinc-Exchanged Zeolites

The initial report of methane activation over zinc-modified zeolites, as demonstrated through diffuse reflectance infrared Fourier transform spectroscopy (DRIFTS), concluded that heterolytic CH_4 bond dissociation occurs on isolated Zn^{2+} sites in Zn/ZSM-5 at room temperature [226]. A zinc methyl species, $[Zn–CH_3]^+$, and a framework BAS were observed as illustrated in Scheme 5.4.

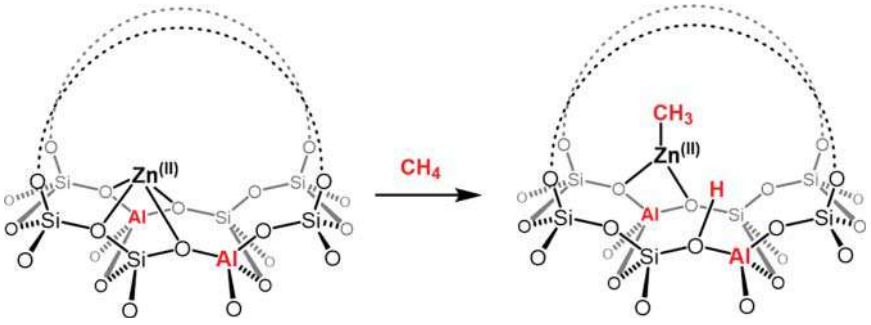

Scheme 5.4 C–H activation step for dissociative adsorption of methane over Zn^{2+} forming a $Zn–CH_3$ and new BAS.

The heterolytic dissociation of CH_4 has been corroborated by a number of solid-state NMR spectroscopic studies that confirm the presence of the $[Zn–CH_3]^+$ species due to the distinctive upfield chemical shift ($\delta = -20$ ppm) of this organometallic fragment [227]. Furthermore, the signal observed from the $[Zn–CH_3]^+$ species was more intense in the $^1H–^{13}C$ CP/MAS NMR than in the direct excitation MAS NMR spectra, indicating that the species has reduced mobility and is therefore strongly attached to the surface [227]. This spectroscopic evidence strongly suggests that C—H bond cleavage of methane at ambient temperature occurs by dissociative adsorption over Zn sites, forming a framework $[Zn–CH_3]^+$ species and a framework BAS (Scheme 5.4). Complementary DFT studies have reported that isolated extra-framework Zn^{2+} sites act as Lewis acids (the CH_4 σ(C–H) orbital donating electron density into the empty Zn–4s orbital), while the framework oxygen atom acts as a Lewis base, resulting in the C—H bond cleavage [228]. The same active site has also been shown to effect H_2 dissociation into a $[Zn–H]^+$ and a BAS as shown through IR spectroscopic studies [219, 228].

However, Xu et al. observed a ^{13}C NMR signal at $\delta = 58$ ppm corresponding to a zinc methoxy species ($ZnOCH_3$) that suggests homolytic C—H bond cleavage is possible over a $[Zn–O–Zn]^{2+}$ dimer [229]. The authors suggest that the activation mechanism involved the formation of a methyl radical ($\cdot CH_3$), which could interact with the zinc cluster to produce the zinc methoxy species observed in the ^{13}C

NMR spectra. However, this zinc methoxy species was reportedly formed in a 3 : 1 ratio to the zinc methyl species. The presence of both species indicates that both heterolytic cleavage over Zn^{2+} sites forming the zinc methyl species and homolytic cleavage forming the zinc methoxy species on $[Zn–O–Zn]^{2+}$ dimer can occur simultaneously [229]. It should be noted that the Zn/ZSM-5 sample was prepared by Zn vapor deposition that should lead to the presence of predominantly Zn^{2+} ions only, not $[Zn–O–Zn]^{2+}$ dimers.

Wang and coworkers also suggested that both heterolytic and homolytic cleavages of methane at Zn sites can occur as they observed the presence of oxygenated species (zinc methoxy and zinc formate groups) in ^{13}C NMR spectra after methane activation over Zn/ZSM-5 [230]. However, the predominant species observed was still zinc methyl species, and the signals from the zinc methoxy and zinc formate groups disappeared upon further heating of the sample, implying additional reactions occurring at higher temperatures. In this case, the zinc was introduced through incipient wetness impregnation, which can lead to a variety of zinc species within the zeolite, perhaps explaining the theory of simultaneous activation mechanism [230].

Nevertheless, Stepanov and coworkers have provided strong evidence that the appearance of zinc methoxy and formate species are in fact not due to the radical based homolytic cleavage suggested above, but are due to the presence of adventitious oxygen, as shown in Scheme 5.5 [222]. When Zn/ZSM-5 prepared by vapor deposition was exposed to labeled methane ($^{13}CH_4$) at room temperature, two signals at $\delta = -4$ and -6 ppm, corresponding to physisorbed methane, were observed in the ^{13}C NMR spectrum [222]. The two signals correspond to two Zn^{2+} sites of different Lewis acidity caused by a nonhomogeneous aluminum distribution [219]. Upon heating to 250 °C, the zinc methyl signal is observed as expected, while no zinc methoxy or zinc formate species are formed. Similar observations were made by Taylor and coworkers over Zn/ZSM-5, Zn/MOR, and Zn/FER prepared by zinc vapor deposition [231]. Only through the addition of molecular oxygen were additional methoxy or formate species observed. These studies support heterolytic cleavage as the principal method of CH_4 activation by Zn^{2+} ions contrary to the findings above.

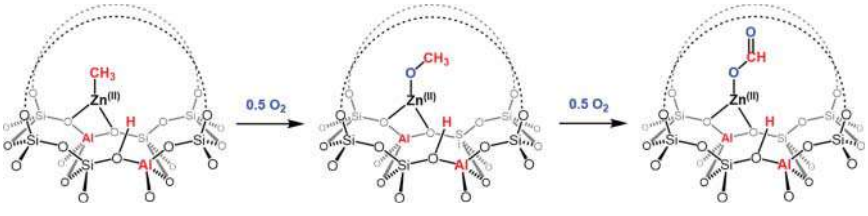

Scheme 5.5 Formation of zinc methoxy and zinc formate species upon addition of O_2 to $[Zn^{II}–CH_3]$ species.

Very recently, Kuroda and coworkers have reported room-temperature activation of methane over a Zn^{II}–oxyl species in ZSM-5 [232]. The Zn^{II}–oxyl species is formed

by irradiation of a Zn^{II}–H species using UV light under an O_2 atmosphere [233]. The photoreaction results in the formation of Zn^{II}–(O_3·) that liberates O_2 resulting in a Zn^{II}–O_t· species. This radical Zn^{II}–O· species is able to oxidize methane to methanol with a very high selectivity of 94% and a methanol yield of 29 μmol g^{-1} at room temperature [232], remarkable for zinc species at room temperature.

It has been determined that as few as 5–15% of ion-exchanged sites are active for CH_4 heterolysis in MFI zeolites [234]. Hence, understanding the role of Al distribution in zeolites is key to maximizing metal IE levels. DFT studies have suggested this reactivity is dependent on a specific Al array within the zeolite [235]. A recent theoretical paper by Kuroda and coworkers examines the spontaneous heterolytic cleavage of H_2 on Zn^{2+}/MFI to investigate this dependence [236]. It was found that heterolysis was more favorable on a circumferentially arrayed Al–Al site compared with a straight channel axis in MFI as shown in Figure 5.14. This is due to the formation of a favorably aligned Lewis base–Zn^{2+} pair, resulting in a suitable position to activate H_2, even at room temperature. Therefore, the Al arrangement alongside the curvature created by the zeolite pores can have an impact on the activity of metal ions within zeolite frameworks. This has been further established recently through the selective oxidation of methane to methanol using Zn/MOR reported by Taylor and coworkers [231]. They report that under similar (oxidative) conditions, zinc formate and methanol are formed when using Zn/FER and Zn/ZSM-5, highlighting that zeolite topology impacts product selectivity. Furthermore, the percentage of active zinc sites, determined through quantitative NMR spectroscopy studies, was found to be dependent on the zeolite framework [231].

5.4.3.2 Zinc Oxide Clusters in Zeolites

Zinc oxide clusters have been shown to be active for propane aromatization and ethane activation [237–239]. Propane aromatization over zinc-impregnated BEA is proposed to occur via dissociative adsorption of propane over the ZnO species within the pores of the zeolite via cleavage of a C—H bond [237]. However, ZnO is ineffective for the aromatization of ethylene that takes place primarily over Lewis acidic

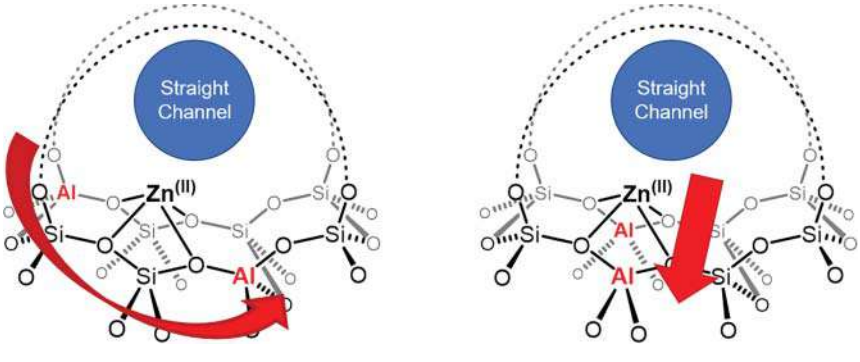

(a) Circumferential Al–Al pair (b) Straight channel Al–Al pair

Figure 5.14 Representation of Al array direction within a zeolite framework: (a) circumferential and (b) straight channel directions.

Zn^{2+} or $[Zn–O–Zn]^{2+}$ sites [239], and systemic studies of zinc oxide and Zn^{2+} in Beta show that zinc oxide is unable to activate methane to form zinc methyl species $[Zn–CH_3]^+$ [238].

Nevertheless, ZnO clusters have been found to be active for H/D exchange of CH_4/CD_4 in Zn/H-BEA [238]. The reactivity was found to be dependent on the nature of the zinc site with isolated Zn^{2+} cations demonstrating a rate constant of $65 \times 10^{-5}\,g\,mol^{-1}\,min^{-1}$, while ZnO clusters were less reactive at $1.2 \times 10^{-5}\,g\,mol^{-1}\,min^{-1}$. This reactivity, however, was found to be limited to H/D exchange with no reaction observed for the alkylation of benzene with methane over these ZnO clusters, dissimilar to Zn^{2+} cations that showed further reactivity with benzene to form substituted aromatics [238]. Furthermore, Kazansky et al. have found that ZnO clusters in Zn/Na–Y are unable to perform heterolytic dissociative adsorption of methane [240]. The ZnO clusters in Zn/Na–Y can be reduced to form isolated Zn^{2+}, but this new site is also inactive for C–H cleavage of methane, further indicating that the framework plays an important role in mediating the reaction [240]. Equally, DRIFTS studies show that methane does adsorb at Zn^{2+} sites on Zn/Y (where Zn^{2+} has been introduced by zinc vapor deposition), though C—H bond cleavage was also not observed to occur (in contrast to Zn/ZSM-5) [226]. The authors indicated that the high Al content of Y strongly stabilizes the Zn^{2+} cations and is the root cause for the lack of bond cleavage [226].

5.4.3.3 The Role of Brønsted Acid Sites in C–H Activation

The effect of BAS on C–H activation has been found to be dependent on the method of zinc introduction. Stepanov and coworkers have shown that if BAS are present after zinc exchange, through zinc vapor deposition, on H–ZSM-5, CH_4 activation has been shown to be reversible under reduced pressure [222]. Note that in a fully zinc-exchanged ZSM-5, the $Zn–CH_3$ fragments remain intact after exposure to vacuum [222, 241]. On the other hand, Wu et al. found that there is no reformation of methane with evacuation on a bifunctional Zn/H–ZSM-5 zeolite prepared by impregnation methods [242]. This highlights that different methods of zinc introduction can have different reactivity or distribution of zinc species.

The synergic effect between BAS and zinc Lewis acid sites also supposedly impacts the temperature required for C–H activation. It has been observed that fully zinc-exchanged zeolites require temperatures of 523 K for activation to take place, whereas partially exchanged systems are able to form zinc methyl species at room temperature indicating mechanistic differences caused by the presence of BAS [222].

Deng and coworkers also suggest that the relationship between the BAS and zinc species can enhance H/D exchange [243]. The authors suggest that an increase in Brønsted acidity through the spatial proximity between the Zn^{2+} ions and the Brønsted acidic protons of the zeolite leads to enhanced activity. However, the spatial proximity of these sites is crucial, requiring a BAS–Zn distance <3.5 Å [243]. However, this has once again been disputed by Stepanov and coworkers who find no evidence for BAS with enhanced acid strength in the presence of Zn^{2+} compared

with the pure acid form when using solid-state NMR and FTIR techniques to probe the strength of the Brønsted acidic protons in H- and Zn/ZSM-5 [244].

5.4.3.4 Reactivity of Methane with Small Molecules on Zinc-Modified Zeolites

The reactivity of zinc methyl species with molecules such as O_2, CO, CO_2, and H_2O has been found to be very similar to that of organozinc compounds and has been explored by a number of groups [222, 230, 231, 242]. For example, the formation of zinc methoxy and zinc formate groups is observed when the zinc methyl species are exposed to dioxygen at ambient temperature. Additional heating of the sample results in the formation of higher oxygenates such as acetic acid [222, 230]. Through *in situ* NMR spectroscopy studies, Deng and coworkers established that proton donors such as water, methanol, and HCl readily convert the zinc methyl species to methane at room temperature [230].

Furthermore, the addition of CO and CO_2 to methane over zinc-exchanged zeolites has been studied in the context of the formation of acetic acid, demonstrated in Figure 5.15 [245]. Acetic acid can be formed through two different pathways: CO reacting with surface zinc methoxy species or CO_2 reacting with zinc methyls [246]. The BAS play a key role in the formation of acetic acid via proton transfer to the surface acetate species formed upon addition of CO_2 [242].

5.4.4 Other *d*-Block Metals in Zeolites

Methane activation over Co-, Ni-, and Mo-modified zeolites has been reported, but the available literature is somewhat scarce. For Co-modified zeolites, the product of methane partial oxidation is dependent on the nature of the Co active species. Cobalt oxide species, Co_3O_4 and CoO, within the zeolite are typically selective toward methanol production while Co^{2+} cations in the zeolite channels are generally selective toward formaldehyde production [247]. Therefore, similar to

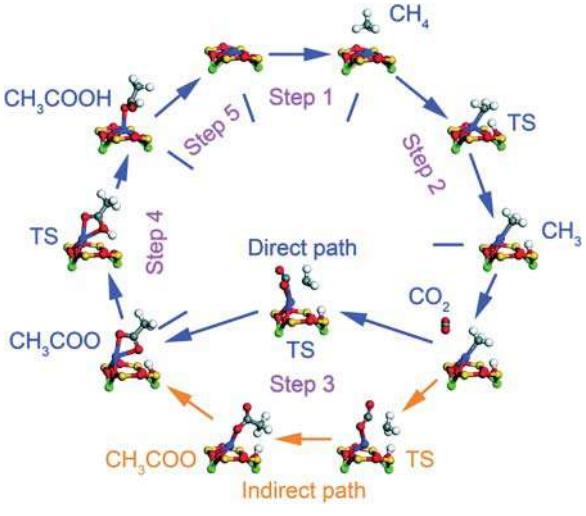

Figure 5.15 Catalytic cycle for the conversion of CH_4 and CO_2 to acetic acid on Zn/H-ZSM-5. TS indicates transition states. The green, blue, red, orange, gray, and white spheres represent Al, Zn, O, Si, C, and H atoms, respectively. Source: Reproduced with permission from Zhang et al. [245]; © Copyright 2019 Royal Society of Chemistry.

Zn in particular, the method of Co introduction can dramatically affect methanol selectivity. Consequently, Co/ZSM-5 prepared by incipient wetness impregnation (IWI) typically contains more surface Co oxide species and is more selective toward methanol, while Co/ZSM-5 prepared via IE contains more Co^{2+} species within the zeolite channel system and is more selective toward formaldehyde [247].

Furthermore, modifications to the zeolite such as the introduction of mesoporisity via alkaline treatment can increase the number of Co oxide species improving methanol selectivity [248, 249]. This was established by Beznis et al. who demonstrated that a linear correlation is observed between zeolite surface area and the number of Co oxide species and thus methanol selectivity [248]. Additionally, the authors suggested that the increased methanol selectivity could be attributed to the reduced ability to form Co^{2+} sites as a result of extra-framework alumina blocking the channel system. Therefore, after acid treatment to remove extra-framework alumina was carried out before Co introduction, an increase in Co^{2+} species within the zeolite channels was observed, and methanol selectivity decreased [248].

The mechanism of methane to methanol over Co/ZSM-5 in the presence of N_2O has been established to be similar to that observed for α-Fe species through DFT studies [250]. As for Fe, the Co–ZSM-5 is predicted to decompose N_2O resulting in an α-O species that is highly reactive toward radical hydrogen abstraction from methane. While the reaction pathway may be similar to Fe (*vide supra*), it should be noted that lower activation barriers are present for each step with Co. Nevertheless, as with Fe, the presence of water substantially decreases the energy barrier to the methanol formation step.

Partial oxidation of methane using O_2 as an oxidant has also been studied [251]. The reaction was conducted in a small-scale batch reactor at 423 K under an atmosphere of methane (0.75 bar) and 5% oxygen in nitrogen (2 bar) using a Co-impregnated mesoporous H–ZSM-5 catalyst [251]. A preliminary calcination step is required to introduce active oxygen species (similar to Cu and Fe, *vide supra*) before being exposed to methane at 150 °C. It was found that the optimum extracted methanol yield (79%) was obtained at a reaction time of 60 minutes. Longer reaction times resulted in a substantial decrease in yield likely due to the complete oxidation of methane to CO_2 and water. Furthermore, the authors suggest that the presence of molecular oxygen as an oxidant causes an increased reaction rate when compared with the base reaction in which oxygen (O^{2-}) from cobalt oxides or the ZSM-5 surface acts as the oxidizing agent. However, it is worth noting that the reaction products remain strongly adsorbed to the catalyst and must be extracted into the liquid phase resulting in a process that, at present, has not been demonstrated to run in a continuous regime.

The nature of the Ni active site in ZSM-5 for dMtM has been somewhat controversial since initial exploration by Tao and coworkers [252]. The authors reported that an anchored mono(μ-oxo)dinickel $[Ni_2(\mu O)]^{2+}$ site in Ni-modified ZSM-5 was the active site for dMtM, analogous to Cu–ZSM-5. As for other metals, the Ni-modified zeolite must be thermally activated in O_2 before methane introduction, but the

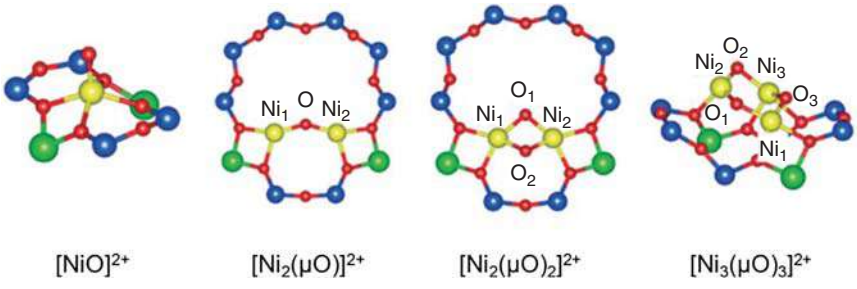

Figure 5.16 Optimized ground state structures of (a) $[NiO]^{2+}$, (b) $[Ni_2(\mu O)]^{2+}$, (c) $[Ni_2(\mu O)_2]^{2+}$, and (d) $[Ni_3(\mu O)_3]^{2+}$ in MFI. Source: Reproduced with permission from Mahyuddin and Yoshizawa [254]; © Copyright 2018 Royal Society of Chemistry.

catalyst was able to produce methanol as the major product at 150 °C, after aqueous extraction into the liquid phase from the catalyst. However, DFT studies suggest that this active site motif is not reasonable as no activity in methane-to-methanol conversion was able to be simulated under sensible reaction conditions [253]. This was further corroborated with a recent study by Yoshizawa and coworker that used a combination of DFT with Coulomb interaction potential calculations to simulate an array of plausible Ni-oxo motifs in the periodic MFI framework structure, specifically $[NiO]^{2+}$, $[Ni_2(\mu O)]^{2+}$, $[Ni_2(\mu O)_2]^{2+}$, and $[Ni_3(\mu O)_3]^{2+}$ (Figure 5.16) [254]. The authors suggested that the $[Ni_2(\mu O)]^{2+}$ center could not be the active site for dMtM due to its respective energy of activation for hydrogen atom abstraction from methane being both considerably higher than that observed experimentally and that calculated for the other motifs examined [252, 254]. On the other hand, the energy of activation for hydrogen atom abstraction calculated for the $[Ni_2(\mu O)_2]^{2+}$ and $[Ni_3(\mu O)_3]^{2+}$ centers is in good agreement with that observed experimentally highlighting that these are more likely the Ni active sites in ZSM-5. The use of experimental resonance Raman spectroscopy (rR) (as used to distinguish the active species in Cu-modified zeolites) could prove invaluable in assigning the true nature of the active Ni species.

Mn/ZSM-5 has been shown to be active in the decomposition of N_2O resulting in the suggested formation of an α-O species [255]. Similar to Fe/ZSM-5, this site cannot be generated directly using O_2. However, as mentioned earlier in the chapter, Tabor and coworkers have very recently demonstrated the splitting of dioxygen over distant binuclear transition metal (M = Ni, Mn, and Co) cationic centers in FER [172]. Analogous to Fe/FER [170], the dioxygen is split to form a pair of α-oxygen sites. Methane was found to react with the α-oxygen on the M(II) sites at room temperature, and the products (methanol) were easily released from the cationic centers without the use of a supplementary extraction step [172]. The yield of methanol was higher for Ni/FER (0.68 mol_{CH3OH} $mol_M{}^{-1}$) than Fe/FER, Mn/FER, or Co/FER (0.63, 0.12, and 0.08 mol_{CH3OH} $mol_M{}^{-1}$, respectively) highlighting that the Ni/FER sample oxidized with dioxygen has the best performance in the direct oxidation of methane to methanol in this system [170, 172].

5.5 Outlook

The direct conversion of methane to higher-value products is seen as a way to reduce the global reliance on oil-based chemical feedstocks, as well as monetizing stranded and associated natural gas. Furthermore, as natural gas is determined to be a cleaner fossil feedstock than oil (or coal), utilizing natural gas for chemicals is seen as a stepping stone on the journey to fuller utilization of bio-derived feedstocks for chemicals [2, 11].

Methane activation over zeolite-based materials shows great promise in the development of a dMtM process, and for the MDA reaction to produce BTX products. In both cases, it is metal-modified zeolites that are the most active catalysts, but residual BAS can play important roles in methane activation and the subsequent steps in forming the desired products. Both dMtM and MDA reactions need to overcome a major challenge in that the desired product is not the thermodynamically most stable product under the reaction conditions. For dMtM, carbon oxides (CO, CO_2) are thermodynamically more favored than the desired methanol, and for MDA, the formation of carbon is thermodynamically more favored than BTX. However, through their ability to control reaction selectivity through size exclusion principles, and through more subtle effects such as confinement, zeolites have the capacity to give reaction products that differ from thermodynamic calculations (e.g. toluene alkylation with methanol to *p*-xylene over ZSM-5) [256].

Through advanced characterization methods, coupled with *in situ* and *operando* methods, great advances have been made in understanding the nature and evolution of the active sites in both dMtM and MDA reactions. The structures of both α-Fe and α-O sites have been determined in zeolite beta [161] and in the CHA [191] framework. The location and single-site nature of the Mo/ZSM-5 pre-catalyst have been determined by TEM [103] while the evolution of the Mo sites has been followed in detail by *operando* XAS [98].

Remarkable advances in dMtM performance have been achieved in a very short space of time. The best catalytic performance of dMtM with copper-exchanged zeolites under continuous flow conditions has risen from 3.1 $\mu mol_{MeOH}\ g_{cat}^{-1}\ h^{-1}$ in 2016 [196] to 195 $mmol_{MeOH}\ g_{cat}^{-1}\ h^{-1}$ in 2021 [203], an increase of nearly 5 orders of magnitude in productivity. Notably, it was a small-pore, copper-modified CHA that gave optimal performance in both studies, outperforming the other medium- and large-pore frameworks tested in each study. This may point to confinement effects leading to the enhanced selectivity in dMtM. Further, water has been reported to be able to act as the terminal oxidant in continuous flow dMtM over a Cu/CHA material [202] that opens up new avenues as to the role water can play in this chemistry. With this in mind, we note that in the industrial production of acetaldehyde from ethylene and dioxygen (the Wacker process), the C—O bond is in fact formed from water, not dioxygen, in a dual catalytic cycle that utilizes Pd and Cu chloride salts in an acidic, aqueous solution [257]. Likewise, in Shilov chemistry where the conversion of methane to methanol in aqueous solution is mediated by homogeneous platinum salts, it is water that gives rise to the formation of the C—O bond in the methanol [258].

Given the promising developments of the last few years concerning methane activation over zeolite materials, it is anticipated that the direct conversion of methane to higher-value products has a promising future over metal-modified zeolites.

References

1 IEA (2019). *The Role of Gas in Today's Energy Transitions*, IEA, Paris https://www.iea.org/reports/the-role-of-gas-in-todays-energy-transitions.
2 Zichittella, G. and Pérez-Ramírez, J. (2021). Status and prospects of the decentralised valorisation of natural gas into energy and energy carriers. *Chem. Soc. Rev.* 50: 2984–3012.
3 Aasberg-Petersen, K., Dybkjær, I., Ovesen, C.V. et al. (2011). Natural gas to synthesis gas–catalysts and catalytic processes. *J. Nat. Gas Sci. Eng.* 3: 423–459.
4 Aasberg-Petersen, K., Bak Hansen, J.H., Christensen, T.S. et al. (2001). Technologies for large-scale gas conversion. *Appl. Catal., A* 221: 379–387.
5 Reyes, S.C., Sinfelt, J.H., and Feeley, J.S. (2003). Evolution of processes for synthesis gas production: recent developments in an old technology. *Ind. Eng. Chem. Res.* 42: 1588–1597.
6 Reimert, R., Marschner, F., Renner, H.-J. et al. (2011). Gas production, 2. Processes. In: *Ullmann's Encyclopedia of Industrial Chemistry*. Wiley-VCH https://pubs.acs.org/doi/10.1021/acs.est.7b04573.
7 Bhat, S.A. and Sadhukhan, J. (2009). Process intensification aspects for steam methane reforming: an overview. *AlChE J.* 55: 408–422.
8 Levi, P.G. and Cullen, J.M. (2018). Mapping global flows of chemicals: from fossil fuel feedstocks to chemical products. *Environ. Sci. Technol.* 52: 1725–1734.
9 Foster, G.L., Royer, D.L., and Lunt, D.J. (2017). Future climate forcing potentially without precedent in the last 420 million years. *Nat. Commun.* 8: 14845.
10 OECD (2008). OECD Environmental Outlook to 2030, OECD Publishing, Paris. https://doi.org/10.1787/9789264040519-en (accessed 12 November 2018).
11 IEA (2017). World Energy Outlook 2017, IEA, Paris. https://www.iea.org/reports/world-energy-outlook-2017.
12 Yuan, S., Li, Y., Peng, J. et al. (2020). Conversion of methane into liquid fuels—bridging thermal catalysis with electrocatalysis. *Adv. Energy Mater.* 10 (40): 2002154.
13 Kondratenko, E.V., Peppel, T., Seeburg, D. et al. (2017). Methane conversion into different hydrocarbons or oxygenates: current status and future perspectives in catalyst development and reactor operation. *Catal. Sci. Technol.* 7: 366–381.
14 Schüth, F. (2019). Making more from methane. *Science* 363: 1282–1283.
15 Siluria Technologies. http://siluria.com/Technology/Demonstration_Plant (accessed 2 April 2021).
16 Wang, L., Tao, L., Xie, M. et al. (1993). Dehydrogenation and aromatization of methane under non-oxidizing conditions. *Catal. Lett.* 21: 35–41.

17 Gunsalus, N.J., Koppaka, A., Park, S.H. et al. (2017). Homogeneous functionalization of methane. *Chem. Rev.* 117: 8521–8573.

18 Ravi, M., Ranocchiari, M., and van Bokhoven, J.A. (2017). The direct catalytic oxidation of methane to methanol—a critical assessment. *Angew. Chem. Int. Ed.* 56: 16464–16483.

19 Horn, R. and Schlögl, R. (2015). Methane activation by heterogeneous catalysis. *Catal. Lett.* 145: 23–39.

20 Arndtsen, B.A., Bergman, R.G., Mobley, T.A., and Peterson, T.H. (1995). Selective intermolecular carbon-hydrogen bond activation by synthetic metal complexes in homogeneous solution. *Acc. Chem. Res.* 28: 154–162.

21 Wang, V.C.C., Maji, S., Chen, P.P.Y. et al. (2017). Alkane oxidation: methane monooxygenases, related enzymes, and their biomimetics. *Chem. Rev.* 8574–8621.

22 Ross, M.O. and Rosenzweig, A.C. (2017). A tale of two methane monooxygenases. *J. Biol. Inorg. Chem.* 22: 307–319.

23 Dyer, A. (1988). *An Introduction to Zeolite Molecular Sieves*. Chichester: Wiley.

24 Flanigen, E.M. (1991). Zeolites and molecular sieves an historical perspective. In: *Studies in Surface Science and Catalysis*, Chapter 2, vol. 58 (ed. H. van Bekkum, E.M. Flanigen and J.C. Jansen), 13–34. Elsevier.

25 Database of Zeolite Structures. http://www.iza-structure.org/databases (accessed 2 April 2021).

26 Cundy, C.S. and Cox, P.A. (2003). The hydrothermal synthesis of zeolites: history and development from the earliest days to the present time. *Chem. Rev.* 103: 663–702.

27 Davis, M.E. and Lobo, R.F. (1992). Zeolite and molecular sieve synthesis. *Chem. Mater.* 4: 756–768.

28 Valtchev, V., Majano, G., Mintova, S., and Perez-Ramirez, J. (2013). Tailored crystalline microporous materials by post-synthesis modification. *Chem. Soc. Rev.* 42: 263–290.

29 Li, Y., Li, L., and Yu, J. (2017). Applications of zeolites in sustainable chemistry. *Chemistry* 3: 928–949.

30 Jensen, N.K., Rufford, T.E., Watson, G. et al. (2012). Screening zeolites for gas separation applications involving methane, nitrogen, and carbon dioxide. *J. Chem. Eng. Data* 57: 106–113.

31 Komvokis, V., Tan, L.X.L., Clough, M. et al. (2016). Zeolites in fluid catalytic cracking (FCC). In: *Zeolites in Sustainable Chemistry: Synthesis, Characterization and Catalytic Applications* (ed. F.-S. Xiao and X. Meng), 271–297. Berlin, Heidelberg: Springer-Verlag.

32 Primo, A. and Garcia, H. (2014). Zeolites as catalysts in oil refining. *Chem. Soc. Rev.* 43: 7548–7561.

33 Vermeiren, W. and Gilson, J.-P. (2009). Impact of zeolites on the petroleum and petrochemical industry. *Top. Catal.* 52: 1131–1161.

34 Csicsery, S.M. (1984). Shape-selective catalysis in zeolites. *Zeolites* 4: 202–213.

35 Davis, M.E. (1991). Zeolites and molecular sieves: not just ordinary catalysts. *Ind. Eng. Chem. Res.* 30: 1675–1683.

36 Millini, R. and Bellussi, G. (2017). Zeolite science and perspectives. In: *Zeolites in Catalysis: Properties and Applications*, Chapter 1, 1–36. The Royal Society of Chemistry.

37 Gounder, R. and Iglesia, E. (2013). The catalytic diversity of zeolites: confinement and solvation effects within voids of molecular dimensions. *Chem. Commun.* 49: 3491–3509.

38 Corma, A. (2003). State of the art and future challenges of zeolites as catalysts. *J. Catal.* 216: 298–312.

39 Bhan, A., Allian, A.D., Sunley, G.J. et al. (2007). Specificity of sites within eight-membered ring zeolite channels for carbonylation of methyls to acetyls. *J. Am. Chem. Soc.* 129: 4919–4924.

40 Li, B., Xu, J., Han, B. et al. (2013). Insight into dimethyl ether carbonylation reaction over mordenite zeolite from in-situ solid-state NMR spectroscopy. *J. Phys. Chem. C* 117: 5840–5847.

41 Abate, S., Barbera, K., Centi, G. et al. (2016). Disruptive catalysis by zeolites. *Catal. Sci. Technol.* 6: 2485–2501.

42 Keller, G.E. and Bhasin, M.M. (1982). Synthesis of ethylene via oxidative coupling of methane: I. Determination of active catalysts. *J. Catal.* 73: 9–19.

43 Hinsen, W. and Baerns, M. (1983). Oxidative coupling of methane to C_2 hydrocarbons in the presence of different catalysts. *Chem. Ztg.* 107: 223–226.

44 Mitchell, H.L. III, and Waghorne, R.H. (1979). Catalysts for the conversion of relatively low molecular weight hydrocarbons to high molecular weight hydrocarbons and the regeneration of the catalysts. US4172810A, filed 08 May 1978.

45 Mitchell, H.L. III, and Waghorne, R.H. (1980). Catalysts for the conversion of relatively low molecular weight hydrocarbons to higher molecular weight hydrocarbons and the regeneration of the catalysts. US4239658A.

46 Driscoll, D.J., Martir, W., Wang, J.X., and Lunsford, J.H. (1985). Formation of gas-phase methyl radicals over magnesium oxide. *J. Am. Chem. Soc.* 107: 58–63.

47 Luo, L., Tang, X., Wang, W. et al. (2013). Methyl radicals in oxidative coupling of methane directly confirmed by synchrotron VUV photoionization mass spectroscopy. *Sci. Rep.* 3: 1625.

48 Labinger, J.A. (1988). Oxidative coupling of methane: an inherent limit to selectivity? *Catal. Lett.* 1: 371–375.

49 Labinger, J.A. (2004). Selective alkane oxidation: hot and cold approaches to a hot problem. *J. Mol. Catal. A: Chem.* 220: 27–35.

50 Farrell, B.L., Igenegbai, V.O., and Linic, S. (2016). A viewpoint on direct methane conversion to ethane and ethylene using oxidative coupling on solid catalysts. *ACS Catal.* 6: 4340–4346.

51 Gao, Y., Neal, L., Ding, D. et al. (2019). Recent advances in intensified ethylene production—a review. *ACS Catal.* 9: 8592–8621.

52 Kondratenko, E.V. and Baerns, M. (2011). Chapter 3 Catalysis of oxidative methane conversions. In: *Nanostructured Catalysts: Selective Oxidations*, 35–55. The Royal Society of Chemistry.

53 Schwach, P., Pan, X., and Bao, X. (2017). Direct conversion of methane to value-added chemicals over heterogeneous catalysts: challenges and prospects. *Chem. Rev.* 117: 8497–8520.

54 Ilchenko, N.I., Il'in, V.G., Raevskaya, L.N. et al. (1989). Oxidative condensation of methane on modified natural mordenites. *React. Kinet. Catal. Lett.* 38: 141–146.

55 Shepelev, S.S. and Ione, K.G. (1989). Oxidative synthesis of higher hydrocarbons from methane on zeolites. *J. Catal.* 117: 362–370.

56 Kovacheva, P., Davidova, N., and Weiss, A.H. (1994). Oxidative conversion of methane over MgO/ZSM-5 catalysts. In: *Studies in Surface Science and Catalysis*, vol. 82 (ed. V.C. Corberán and S.V. Bellón), 403–409. Elsevier.

57 Ernst, S. and Weitkamp, J. (1991). Oxidative coupling of methane: activities and selectivities of modified zeolite catalysts. In: *Studies in Surface Science and Catalysis*, vol. 61 (ed. A. Holmen, K.J. Jens and S. Kolboe), 25–31. Elsevier.

58 Kovacheva, P., Arishtirova, K., and Davidova, N. (1997). Effect of preparation of a CsX zeolite catalyst on the oxidative conversion of methane. *Appl. Catal., A* 163: 255–260.

59 Kovacheva, P., Arishtirova, K., and Davidova, N. (1997). Characterization of lithium and cesium modified zeolite catalysts in the oxidative conversion of methane. *Appl. Catal., A* 149: 277–287.

60 Levinbuk, M.I., Usachev, N.Y., Pavlov, M.L. et al. (1997). Performance of catalytic properties of reagent catalyst in the processes such as methane oxidative coupling and hydrogen production by methane conversion. In: *Studies in Surface Science and Catalysis*, vol. 110 (ed. R.K. Grasselli, S.T. Oyama, A.M. Gaffney and J.E. Lyons), 731–736. Elsevier.

61 Spivey, J.J. and Hutchings, G. (2014). Catalytic aromatization of methane. *Chem. Soc. Rev.* 43: 792–803.

62 Kosinov, N. and Hensen, E.J.M. (2020). Reactivity, selectivity, and stability of zeolite-based catalysts for methane dehydroaromatization. *Adv. Mater. (Weinheim, Ger.)* 32: 2002565.

63 Bragin, O.V., Vasina, T.V., Isakov, Y.I. et al. (1982). Catalytic aromatization of methane and ethane. *Bull. Acad. Sci. USSR, Div. Chem. Sci. (Engl. Transl.)* 31: 847–847.

64 Bragin, O.V., Vasina, T.V., Preobrazhenskii, A.V., and Minachev, K.M. (1989). Aromatization of methane on pentasil-containing catalysts. *Bull. Acad. Sci. USSR, Div. Chem. Sci. (Engl. Transl.)* 38: 680.

65 Weckhuysen, B.M., Wang, D., Rosynek, M.P., and Lunsford, J.H. (1998). Conversion of methane to benzene over transition metal ion ZSM-5 zeolites: II. Catalyst characterization by X-ray photoelectron spectroscopy. *J. Catal.* 175: 347–351.

66 Xu, Y., Chen, M., Wang, T. et al. (2020). Probing cobalt localization on HZSM-5 for efficient methane dehydroaromatization catalysts. *J. Catal.* 387: 102–118.

67 Xu, Y., Chen, M., Liu, B. et al. (2020). CH_4 conversion over Ni/HZSM-5 catalyst in the absence of oxygen: decomposition or dehydroaromatization? *Chem. Commun.* 56: 4396–4399.

68 Yang, J., Deng, F., Zhang, M. et al. (2003). W/HZSM-5 catalyst for methane dehydroaromatization: a multinuclear MAS NMR study. *J. Mol. Catal. A: Chem.* 202: 239–246.

69 Shu, Y., Ohnishi, R., and Ichikawa, M. (2003). Improved methane dehydrocondensation reaction on HMCM-22 and HZSM-5 supported rhenium and molybdenum catalysts. *Appl. Catal., A* 252: 315–329.

70 Yungchieh, L. and Götz, V. (2016). Zn-HZSM-5 catalysts for methane dehydroaromatization. *Environ. Prog. Sustain. Energy* 35: 334–344.

71 Abdelsayed, V., Smith, M.W., and Shekhawat, D. (2015). Investigation of the stability of Zn-based HZSM-5 catalysts for methane dehydroaromatization. *Appl. Catal., A* 505: 365–374.

72 Tan, P.L., Au, C.T., and Lai, S.Y. (2006). Methane dehydrogenation and aromatization over 4 wt% Mn/HZSM-5 in the absence of an oxidant. *Catal. Lett.* 112: 239–245.

73 Lim, T.H. and Kim, D.H. (2019). Characteristics of Mn/H-ZSM-5 catalysts for methane dehydroaromatization. *Appl. Catal., A* 577: 10–19.

74 Luzgin, M.V., Gabrienko, A.A., Rogov, V.A. et al. (2010). The "alkyl" and "carbenium" pathways of methane activation on Ga-modified zeolite BEA: ^{13}C solid-state NMR and GC-MS study of methane aromatization in the presence of higher alkane. *J. Phys. Chem. C* 114: 21555–21561.

75 Vollmer, I., van der Linden, B., Ould-Chikh, S. et al. (2018). On the dynamic nature of Mo sites for methane dehydroaromatization. *Chem. Sci.* 9: 4801–4807.

76 Ismagilov, Z.R., Matus, E.V., and Tsikoza, L.T. (2008). Direct conversion of methane on Mo/ZSM-5 catalysts to produce benzene and hydrogen: achievements and perspectives. *Energy Environ. Sci.* 1: 526–541.

77 Burns, S., Hargreaves, J.S.J., Pal, P. et al. (2006). The effect of dopants on the activity of MoO_3/ZSM-5 catalysts for the dehydroaromatisation of methane. *Catal. Today* 114: 383–387.

78 Xu, Y., Wang, J., Suzuki, Y., and Zhang, Z.-G. (2011). Effect of transition metal additives on the catalytic stability of Mo/HZSM-5 in the methane dehydroaromatization under periodic CH_4-H_2 switch operation at 1073 K. *Appl. Catal., A* 409–410: 181–193.

79 Ramasubramanian, V., Lienhard, D.J., Ramsurn, H., and Price, G.L. (2019). Effect of addition of K, Rh and Fe over Mo/HZSM-5 on methane dehydroaromatization under non-oxidative conditions. *Catal. Lett.* 149: 950–964.

80 Menon, U., Rahman, M., and Khatib, S.J. (2020). A critical literature review of the advances in methane dehydroaromatization over multifunctional metal-promoted zeolite catalysts. *Appl. Catal., A* 608: 117870.

81 Kiani, D., Sourav, S., Tang, Y. et al. (2021). Methane activation by ZSM-5-supported transition metal centers. *Chem. Soc. Rev.* 50: 1251–1268.

82 Vollmer, I., Yarulina, I., Kapteijn, F., and Gascon, J. (2019). Progress in developing a structure-activity relationship for the direct aromatization of methane. *ChemCatChem* 11: 39–52.

83 Sun, K., Ginosar, D.M., He, T. et al. (2018). Progress in nonoxidative dehydroaromatization of methane in the last 6 years. *Ind. Eng. Chem. Res.* 57: 1768–1789.

84 Corredor, E.C., Chitta, P., and Deo, M.D. (2019). Techno-economic evaluation of a process for direct conversion of methane to aromatics. *Fuel Process. Technol.* 183: 55–61.

85 Ma, S., Guo, X., Zhao, L. et al. (2013). Recent progress in methane dehydroaromatization: from laboratory curiosities to promising technology. *J. Energy Chem.* 22: 1–20.

86 Kosinov, N., Uslamin, E.A., Coumans, F.J.A.G. et al. (2018). Structure and evolution of confined carbon species during methane dehydroaromatization over Mo/ZSM-5. *ACS Catal.* 8: 8459–8467.

87 Jiang, H., Wang, L., Cui, W., and Xu, Y. (1999). Study on the induction period of methane aromatization over Mo/HZSM-5: partial reduction of Mo species and formation of carbonaceous deposit. *Catal. Lett.* 57: 95–102.

88 Kosinov, N., Wijpkema, A.S.G., Uslamin, E. et al. (2018). Confined carbon mediating dehydroaromatization of methane over Mo/ZSM-5. *Angew. Chem. Int. Ed.* 57: 1016–1020.

89 Li, G., Vollmer, I., Liu, C. et al. (2019). Structure and reactivity of the Mo/ZSM-5 dehydroaromatization catalyst: an operando computational study. *ACS Catal.* 9: 8731–8737.

90 Xu, Y., Liu, S., Guo, X. et al. (1994). Methane activation without using oxidants over Mo/HZSM-5 zeolite catalysts. *Catal. Lett.* 30: 135–149.

91 Wang, D., Lunsford, J.H., and Rosynek, M.P. (1996). Catalytic conversion of methane to benzene over Mo/ZSM-5. *Top. Catal.* 3: 289–297.

92 Ha, V.T.T., Tiep, L.V., Meriaudeau, P., and Naccache, C. (2002). Aromatization of methane over zeolite supported molybdenum: active sites and reaction mechanism. *J. Mol. Catal. A: Chem.* 181: 283–290.

93 Vollmer, I., Abou-Hamad, E., Gascon, J., and Kapteijn, F. (2020). Aromatization of ethylene - main intermediate for methane dehydroaromatization? *ChemCatChem* 12: 544–549.

94 Razdan, N.K., Kumar, A., Foley, B.L., and Bhan, A. (2020). Influence of ethylene and acetylene on the rate and reversibility of methane dehydroaromatization on Mo/H-ZSM-5 catalysts. *J. Catal.* 381: 261–270.

95 Borry, R.W., Kim, Y.H., Huffsmith, A. et al. (1999). Structure and density of Mo and acid sites in Mo-exchanged H-ZSM5 catalysts for nonoxidative methane conversion. *J. Phys. Chem. B* 103: 5787–5796.

96 Ding, W., Li, S., Meitzner, G.D., and Iglesia, E. (2001). Methane conversion to aromatics on Mo/H-ZSM5: structure of molybdenum species in working catalysts. *J. Phys. Chem. B* 105: 506–513.

97 Kim, Y.-H., Borry, R.W., and Iglesia, E. (2000). Genesis of methane activation sites in Mo-exchanged H–ZSM-5 catalysts. *Microporous Mesoporous Mater.* 35–36: 495–509.

98 Agote-Aran, M., Kroner, A.B., Islam, H.U. et al. (2019). Determination of molybdenum species evolution during non-oxidative dehydroaromatization

of methane and its implications for catalytic performance. *ChemCatChem* 11: 473–480.

99 Solymosi, F., Cserényi, J., Szöke, A. et al. (1997). Aromatization of methane over supported and unsupported Mo-based catalysts. *J. Catal.* 165: 150–161.

100 Vollmer, I., Li, G., Yarulina, I. et al. (2018). Relevance of the Mo-precursor state in H-ZSM-5 for methane dehydroaromatization. *Catal. Sci. Technol.* 8: 916–922.

101 Agote-Aran, M., Fletcher, R.E., Briceno, M. et al. (2020). Implications of the molybdenum coordination environment in MFI zeolites on methane dehydroaromatisation performance. *ChemCatChem* 12: 294–304.

102 Kosinov, N., Coumans, F.J.A.G., Uslamin, E.A. et al. (2017). Methane dehydroaromatization by Mo/HZSM-5: mono- or bifunctional catalysis? *ACS Catal.* 7: 520–529.

103 Liu, L., Wang, N., Zhu, C. et al. (2020). Direct imaging of atomically dispersed molybdenum that enables location of aluminum in the framework of zeolite ZSM-5. *Angew. Chem. Int. Ed.* 59: 819–825.

104 Razdan, N.K. and Bhan, A. (2020). Carbidic Mo is the sole kinetically-relevant active site for catalytic methane dehydroaromatization on Mo/H-ZSM-5. *J. Catal.* 389: 667–676.

105 Zhang, C.-L., Li, S., Yuan, Y. et al. (1998). Aromatization of methane in the absence of oxygen over Mo-based catalysts supported on different types of zeolites. *Catal. Lett.* 56: 207–213.

106 Liu, S., Wang, L., Ohnishi, R., and Ichikawa, M. (1999). Bifunctional catalysis of Mo/HZSM-5 in the dehydroaromatization of methane to benzene and naphthalene XAFS/TG/DTA/MASS/FTIR characterization and supporting effects. *J. Catal.* 181: 175–188.

107 Bai, J., Liu, S., Xie, S. et al. (2003). Shape selectivity in methane dehydroaromatization over Mo/MCM-22 catalysts during a lifetime experiment. *Catal. Lett.* 90: 123–130.

108 Bai, J., Liu, S., Xie, S. et al. (2004). Comparison of 6Mo/MCM-22 and 6Mo/ZSM-5 in the MDA process. *React. Kinet. Catal. Lett.* 82: 279–286.

109 Liu, H., Shen, W., Bao, X., and Xu, Y. (2005). Methane dehydroaromatization over Mo/HZSM-5 catalysts: the reactivity of MoC_x species formed from MoO_x associated and non-associated with Brönsted acid sites. *Appl. Catal., A* 295: 79–88.

110 Liu, H., Su, L., Wang, H. et al. (2002). The chemical nature of carbonaceous deposits and their role in methane dehydro-aromatization on Mo/MCM-22 catalysts. *Appl. Catal., A* 236: 263–280.

111 Yuan, S., Li, J., Hao, Z. et al. (1999). The effect of oxygen on the aromatization of methane over the Mo/HZSM-5 catalyst. *Catal. Lett.* 63: 73–77.

112 Matus, E.V., Ismagilov, I.Z., Sukhova, O.B. et al. (2007). Study of methane dehydroaromatization on impregnated Mo/ZSM-5 catalysts and characterization of nanostructured molybdenum phases and carbonaceous deposits. *Ind. Eng. Chem. Res.* 46: 4063–4074.

113 Song, Y., Xu, Y., Suzuki, Y. et al. (2014). A clue to exploration of the pathway of coke formation on Mo/HZSM-5 catalyst in the non-oxidative methane dehydroaromatization at 1073 K. *Appl. Catal., A* 482: 387–396.

114 Lezcano-González, I., Oord, R., Rovezzi, M. et al. (2016). Molybdenum speciation and its impact on catalytic activity during methane dehydroaromatization in zeolite ZSM-5 as revealed by operando X-ray methods. *Angew. Chem. Int. Ed.* 55: 5215–5219.

115 Kosinov, N., Coumans, F.J.A.G., Li, G. et al. (2017). Stable Mo/HZSM-5 methane dehydroaromatization catalysts optimized for high-temperature calcination-regeneration. *J. Catal.* 346: 125–133.

116 Xu, Y., Lu, J., Wang, J. et al. (2011). The catalytic stability of Mo/HZSM-5 in methane dehydroaromatization at severe and periodic CH_4–H_2 switch operating conditions. *Chem. Eng. J. (Lausanne)* 168: 390–402.

117 Rodrigues, A.C.C. and Monteiro, J.L.F. (2008). The use of CH_4/H_2 cycles on dehydroaromatization of methane over MoMCM-22. *Catal. Commun.* 9: 1060–1065.

118 Toosi, M.R., Sabour, B., Hamuleh, T., and Peyrovi, M.H. (2010). Methane dehydroaromatization over Mo and W catalysts supported on HZSM-5: the effect of preactivation and use of the CH_4/H_2 cycle. *React. Kinet. Mech. Catal.* 101: 221–226.

119 Konnov, S.V., Dubray, F., Clatworthy, E.B. et al. (2020). Novel strategy for the synthesis of ultra-stable single-site Mo-ZSM-5 zeolite nanocrystals. *Angew. Chem. Int. Ed.* 59: 19553–19560.

120 Clatworthy, E.B., Konnov, S.V., Dubray, F. et al. (2020). Emphasis on the properties of metal-containing zeolites operating outside the comfort zone of current heterogeneous catalytic reactions. *Angew. Chem. Int. Ed.* 59: 19414–19432.

121 Iyoki, K., Kikumasa, K., Onishi, T. et al. (2020). Extremely stable zeolites developed via designed liquid-mediated treatment. *J. Am. Chem. Soc.* 142: 3931–3938.

122 Natesakhawat, S., Means, N.C., Howard, B.H. et al. (2015). Improved benzene production from methane dehydroaromatization over Mo/HZSM-5 catalysts via hydrogen-permselective palladium membrane reactors. *Catal. Sci. Technol.* 5: 5023–5036.

123 Kumar, A., Song, K., Liu, L. et al. (2018). Absorptive hydrogen scavenging for enhanced aromatics yield during non-oxidative methane dehydroaromatization on Mo/H-ZSM-5 catalysts. 57: 15577–15582.

124 Zhang, Y. and Jiang, H. (2018). A novel route to improve methane aromatization by using a simple composite catalyst. *Chem. Commun.* 54: 10343–10346.

125 Jocz, J.N., Medford, A.J., and Sievers, C. (2019). Thermodynamic limitations of the catalyst design space for methanol production from methane. *ChemCatChem* 11: 593–600.

126 Latimer, A.A., Kakekhani, A., Kulkarni, A.R., and Nørskov, J.K. (2018). Direct methane to methanol: the selectivity–conversion limit and design strategies. *ACS Catal.* 8: 6894–6907.

127 Shteinman, A.A. (2020). Bioinspired oxidation of methane: from academic models of methane monooxygenases to direct conversion of methane to methanol. *Kinet. Catal.* 61: 339–359.

128 Bone, W.A. and Wheeler, R.V. (1902). LVIII.—The slow oxidation of methane at low temperatures. *J. Chem. Soc., Trans.* 81: 535–549.

129 Bone, W.A. and Wheeler, R.V. (1903). CV.—The slow oxidation of methane at low temperatures. Part II. *J. Chem. Soc., Trans.* 83: 1074–1087.

130 Lance, D. and Elworthy, S.H. (1905). Procédé de fabrication d'aldéhyde formique, d'acide formique, d'alcool méthylique et de leurs dérivés. FR352687.

131 Layng, T.E. and Soukup, R. (1928). Partial oxidation of methane and ethane in the presence of catalysts. *Ind. Eng. Chem.* 20: 1052–1055.

132 Grant, J.T., Venegas, J.M., McDermott, W.P., and Hermans, I. (2018). Aerobic oxidations of light alkanes over solid metal oxide catalysts. *Chem. Rev.* 118: 2769–2815.

133 Lohbeck, K., Haferkorn, H., Fuhrmann, W., and Fedtke, N. (2000). Maleic and fumaric acids. In: *Ullmann's Encyclopedia of Industrial Chemistry*. Wiley-VCH https://doi.org/10.1002/14356007.a16_053.

134 Spencer, N.D. (1988). Partial oxidation of methane to formaldehyde by means of molecular oxygen. *J. Catal.* 109: 187–197.

135 Kiyoshi, O. and Masaharu, H. (1992). Boron, phosphorus, and alkaline earth-metal mixed oxides as active catalysts in partial oxidation of methane into formaldehyde. *Chem. Lett.* 21: 2397–2400.

136 Weng, T. and Wolf, E.E. (1993). Partial oxidation of methane on Mo/Sn/P silica supported catalysts. *Appl. Catal., A* 96: 383–396.

137 Fait, M.J.G., Ricci, A., Holena, M. et al. (2019). Understanding trends in methane oxidation to formaldehyde: statistical analysis of literature data and based hereon experiments. *Catal. Sci. Technol.* 9: 5111–5121.

138 Fajardo, C.A.G., Niznansky, D., N'Guyen, Y. et al. (2008). Methane selective oxidation to formaldehyde with Fe-catalysts supported on silica or incorporated into the support. *Catal. Commun.* 9: 864–869.

139 Zakaria, Z. and Kamarudin, S.K. (2016). Direct conversion technologies of methane to methanol: an overview. *Renewable Sustainable Energy Rev.* 65: 250–261.

140 Taifan, W. and Baltrusaitis, J. (2016). CH_4 conversion to value added products: potential, limitations and extensions of a single step heterogeneous catalysis. *Appl. Catal., B* 198: 525–547.

141 Newton, M.A., Knorpp, A.J., Sushkevich, V.L. et al. (2020). Active sites and mechanisms in the direct conversion of methane to methanol using Cu in zeolitic hosts: a critical examination. *Chem. Soc. Rev.* 49: 1449–1486.

142 Raynes, S., Shah, M.A., and Taylor, R.A. (2019). Direct conversion of methane to methanol with zeolites: towards understanding the role of extra-framework d-block metal and zeolite framework type. *Dalton Trans.* 48: 10364–10384.

143 Dinh, K.T., Sullivan, M.M., Serna, P. et al. (2018). Viewpoint on the partial oxidation of methane to methanol using Cu- and Fe-exchanged zeolites. *ACS Catal.* 8306–8313.

144 Lange, J.-P., Sushkevich, V.L., Knorpp, A.J., and van Bokhoven, J.A. (2019). Methane-to-methanol via chemical looping: economic potential and guidance for future research. *Ind. Eng. Chem. Res.* 58: 8674–8680.

145 Jovanovic, Z.R., Lange, J.-P., Ravi, M. et al. (2020). Oxidation of methane to methanol over Cu-exchanged zeolites: scientia gratia scientiae or paradigm shift in natural gas valorization? *J. Catal.* 385: 238–245.

146 Ravi, M., Sushkevich, V.L., Knorpp, A.J. et al. (2019). Misconceptions and challenges in methane-to-methanol over transition-metal-exchanged zeolites. *Nat. Catal.* 2: 485–494.

147 Kulkarni, A.R., Zhao, Z.J., Siahrostami, S. et al. (2018). Cation-exchanged zeolites for the selective oxidation of methane to methanol. *Catal. Sci. Technol.* 8: 114–123.

148 Mahyuddin, M.H., Shiota, Y., and Yoshizawa, K. (2019). Methane selective oxidation to methanol by metal-exchanged zeolites: a review of active sites and their reactivity. *Catal. Sci. Technol.* 9: 1744–1768.

149 Durante, V.A., Walker, D.W., Gussow, S.M., and Lyons, J.E. (1990). Silicometallate molecular sieves and their use as catalysts in oxidation of alkanes. US4918249A.

150 Walsh, D.E., Han, S., and Palermo, R.E. (1991). Partial oxidation of methane to liquid hydrocarbons over ZSM-5 catalyst. *J. Chem. Soc., Chem. Commun.* 1259–1260.

151 Han, S., Kaufman, E.A., Martenak, D.J. et al. (1994). Direct partial oxidation of methane over ZSM-5 catalyst: Zn–ZSM-5 catalyst studies. *Catal. Lett.* 29: 27–32.

152 Sobolev, V.I., Dubkov, K.A., Panna, O.V., and Panov, G.I. (1995). Selective oxidation of methane to methanol on a Fe–ZSM-5 surface. *Catal. Today* 24: 251–252.

153 Klerk, A. (2015). Engineering evaluation of direct methane to methanol conversion. *Energy Sci. Eng.* 3: 60–70.

154 Bols, M.L., Rhoda, H.M., Snyder, B.E.R. et al. (2020). Advances in the synthesis, characterisation, and mechanistic understanding of active sites in Fe-zeolites for redox catalysts. *Dalton Trans.* 49: 14749–14757.

155 Snyder, B.E.R., Bols, M.L., Schoonheydt, R.A. et al. (2018). Iron and copper active sites in zeolites and their correlation to metalloenzymes. *Chem. Rev.* 118: 2718–2768.

156 Panov, G.I., Sobolev, V.I., and Kharitonov, A.S. (1990). The role of iron in N_2O decomposition on ZSM-5 zeolite and reactivity of the surface oxygen formed. *J. Mol. Catal.* 61: 85–97.

157 Panov, G.I., Sheveleva, G.A., Kharitonov, A.S. et al. (1992). Oxidation of benzene to phenol by nitrous oxide over Fe–ZSM-5 zeolites. *Appl. Catal., A* 82: 31–36.

158 Sobolev, V.I., Kharitonov, A.S., Paukshtis, Y.A., and Panov, G.I. (1993). Stoichiometric reaction of benzene with α-form of oxygen on Fe–ZSM-5 zeolites. Mechanism of aromatics hydroxylation by N_2O. *J. Mol. Catal.* 84: 117–124.

159 Panov, G.I., Sobolev, V.I., Dubkov, K.A. et al. (1997). Iron complexes in zeolites as a new model of methane monooxygenase. *React. Kinet. Catal. Lett.* 61: 251–258.

160 Starokon, E.V., Parfenov, M.V., Pirutko, L.V. et al. (2011). Room-temperature oxidation of methane by α-oxygen and extraction of products from the Fe–ZSM-5 surface. *J. Phys. Chem. C* 115: 2155–2161.

161 Snyder, B.E.R., Vanelderen, P., Bols, M.L. et al. (2016). The active site of low-temperature methane hydroxylation in iron-containing zeolites. *Nature* 536: 317–321.

162 Bols, M.L., Hallaert, S.D., Snyder, B.E.R. et al. (2018). Spectroscopic identification of the α-Fe/α-O active site in Fe–CHA zeolite for the low-temperature activation of the methane C—H bond. *J. Am. Chem. Soc.* 140: 12021–12032.

163 Valyon, J., Millman, W.S., and Hall, W.K. (1994). The desorption of O_2 during NO and N_2O decomposition on Cu- and Fe-zeolites. *Catal. Lett.* 24: 215–225.

164 Leglise, J., Petunchi, J.O., and Hall, W.K. (1984). N_2O decomposition over iron-exchanged mordenite. *J. Catal.* 86: 392–399.

165 Andrikopoulos, P.C., Sobalik, Z., Novakova, J. et al. (2013). Mechanism of framework oxygen exchange in Fe–zeolites: a combined DFT and mass spectrometry study. *ChemPhysChem* 14: 520–531.

166 Fu, C.M., Korchak, V.N., and Hall, W.K. (1981). Decomposition of nitrous oxide on FeY zeolite. *J. Catal.* 68: 166–171.

167 Göltl, F., Michel, C., Andrikopoulos, P.C. et al. (2016). Computationally exploring confinement effects in the methane-to-methanol conversion over iron-oxo centers in zeolites. *ACS Catal.* 6: 8404–8409.

168 Mahyuddin, M.H., Staykov, A., Shiota, Y., and Yoshizawa, K. (2016). Direct conversion of methane to methanol by metal-exchanged ZSM-5 zeolite (metal = Fe, Co, Ni, Cu). *ACS Catal.* 6: 8321–8331.

169 Michalkiewicz, B. (2004). Partial oxidation of methane to formaldehyde and methanol using molecular oxygen over Fe–ZSM-5. *Appl. Catal., A* 277: 147–153.

170 Tabor, E., Dedecek, J., Mlekodaj, K. et al. (2020). Dioxygen dissociation over man-made system at room temperature to form the active α-oxygen for methane oxidation. *Sci. Adv.* 6: eaaz9776.

171 Tabor, E., Lemishka, M., Olszowka, J.E. et al. (2021). Splitting dioxygen over distant binuclear Fe sites in zeolites. Effect of the local arrangement and framework topology. *ACS Catal.* 11: 2340–2355.

172 Mlekodaj, K., Lemishka, M., Sklenak, S. et al. (2021). Dioxygen splitting at room temperature over distant binuclear transition metal centers in zeolites for direct oxidation of methane to methanol. *Chem. Commun.* 57: 3472–3475.

173 Groothaert, M.H., Smeets, P.J., Sels, B.F. et al. (2005). Selective oxidation of methane by the bis(μ-oxo)dicopper core stabilized on ZSM-5 and mordenite zeolites. *J. Am. Chem. Soc.* 127: 1394–1395.

174 Park, M.B., Ahn, S.H., Mansouri, A. et al. (2017). Comparative study of diverse copper zeolites for the conversion of methane into methanol. *ChemCatChem* 9: 3705–3713.

175 Smeets, P.J., Groothaert, M.H., and Schoonheydt, R.A. (2005). Cu based zeolites: a UV–vis study of the active site in the selective methane oxidation at low temperatures. *Catal. Today* 110: 303–309.

176 Wulfers, M.J., Teketel, S., Ipek, B., and Lobo, R.F. (2015). Conversion of methane to methanol on copper-containing small-pore zeolites and zeotypes. *Chem. Commun.* 51: 4447–4450.

177 Zhu, J., Sushkevich, V.L., Knorpp, A.J. et al. (2020). Cu-Erionite zeolite achieves high yield in direct oxidation of methane to methanol by isothermal chemical looping. *Chem. Mater.* 32: 1448–1453.

178 Groothaert, M.H., van Bokhoven, J.A., Battiston, A.A. et al. (2003). Bis(μ-oxo)dicopper in Cu–ZSM-5 and its role in the decomposition of NO: a combined in situ XAFS, UV–Vis–near-IR, and kinetic study. *J. Am. Chem. Soc.* 125: 7629–7640.

179 Groothaert, M.H., Lievens, K., van Bokhoven, J.A. et al. (2003). Bis(μ-oxo)dicopper as key intermediate in the catalytic decomposition of nitric oxide. *ChemPhysChem* 4: 626–630.

180 Woertink, J.S., Smeets, P.J., Groothaert, M.H. et al. (2009). A $[Cu_2O]_2^+$ core in Cu–ZSM-5, the active site in the oxidation of methane to methanol. *Proc. Natl. Acad. Sci. U.S.A.* 106: 18908–18913.

181 Czernuszewicz, R.S., Sheats, J.E., and Spiro, T.G. (1987). Resonance Raman spectra and excitation profile for bis(acetato)bis(hydrotripyrazolylborato) oxodiiron, a hemerythrin analog. *Inorg. Chem.* 26: 2063–2067.

182 Groothaert, M.H., Lievens, K., Leeman, H. et al. (2003). An operando optical fiber UV–vis spectroscopic study of the catalytic decomposition of NO and N_2O over Cu–ZSM-5. *J. Catal.* 220: 500–512.

183 Smeets, P.J., Hadt, R.G., Woertink, J.S. et al. (2010). Oxygen precursor to the reactive intermediate in methanol synthesis by Cu–ZSM-5. *J. Am. Chem. Soc.* 132: 14736–14738.

184 Tsai, M.L., Hadt, R.G., Vanelderen, P. et al. (2014). $[Cu_2O]_2^+$ Active site formation in Cu–ZSM-5: geometric and electronic structure requirements for N_2O activation. *J. Am. Chem. Soc.* 136: 3522–3529.

185 Grundner, S., Markovits, M.A.C., Li, G. et al. (2015). Single-site trinuclear copper oxygen clusters in mordenite for selective conversion of methane to methanol. *Nat. Commun.* 6: 7546.

186 Li, G., Vassilev, P., Sanchez-Sanchez, M. et al. (2016). Stability and reactivity of copper oxo-clusters in ZSM-5 zeolite for selective methane oxidation to methanol. *J. Catal.* 338: 305–312.

187 Palagin, D., Knorpp, A.J., Pinar, A.B. et al. (2017). Assessing the relative stability of copper oxide clusters as active sites of a CuMOR zeolite for methane to methanol conversion: size matters? *Nanoscale* 9: 1144–1153.

188 Paolucci, C., Parekh, A.A., Khurana, I. et al. (2016). Catalysis in a cage: condition-dependent speciation and dynamics of exchanged Cu cations in SSZ-13 zeolites. *J. Am. Chem. Soc.* 138: 6028–6048.

189 Pappas, D.K., Borfecchia, E., Dyballa, M. et al. (2017). Methane to methanol: structure–activity relationships for Cu–CHA. *J. Am. Chem. Soc.* 139: 14961–14975.

190 Kulkarni, A.R., Zhao, Z.-J., Siahrostami, S. et al. (2016). Monocopper active site for partial methane oxidation in Cu-exchanged 8MR zeolites. *ACS Catal.* 6: 6531–6536.

191 Rhoda, H.M., Plessers, D., Heyer, A.J. et al. (2021). Spectroscopic definition of a highly reactive site in Cu–CHA for selective methane oxidation: tuning a mono-μ-oxo dicopper(II) active site for reactivity. *J. Am. Chem. Soc.* 143: 7531–7540.

192 Tomkins, P., Ranocchiari, M., and van Bokhoven, J.A. (2017). Direct conversion of methane to methanol under mild conditions over Cu–zeolites and beyond. *Acc. Chem. Res.* 50: 418–425.

193 Tao, L., Lee, I., and Sanchez-Sanchez, M. (2020). Cu oxo nanoclusters for direct oxidation of methane to methanol: formation, structure and catalytic performance. *Catal. Sci. Technol.* 10: 7124–7141.

194 Vanelderen, P., Vancauwenbergh, J., Sels, B.F., and Schoonheydt, R.A. (2013). Coordination chemistry and reactivity of copper in zeolites. *Coord. Chem. Rev.* 257: 483–494.

195 Zhao, Z.-J., Kulkarni, A., Vilella, L. et al. (2016). Theoretical insights into the selective oxidation of methane to methanol in copper-exchanged mordenite. *ACS Catal.* 6: 3760–3766.

196 Narsimhan, K., Iyoki, K., Dinh, K., and Román-Leshkov, Y. (2016). Catalytic oxidation of methane into methanol over copper-exchanged zeolites with oxygen at low temperature. *ACS Cent. Sci.* 2: 424–429.

197 Kolganov, A.A., Gabrienko, A.A., Yashnik, S.A. et al. (2020). Nature of the surface intermediates formed from methane on Cu–ZSM-5 zeolite: a combined solid-state nuclear magnetic resonance and density functional theory study. *J. Phys. Chem. C* 124: 6242–6252.

198 Sushkevich, V.L., Verel, R., and van Bokhoven, J.A. (2020). Pathways of methane transformation over copper-exchanged mordenite as revealed by in situ NMR and IR spectroscopy. *Angew. Chem. Int. Ed.* 59: 910–918.

199 Tomkins, P., Mansouri, A., Bozbag, S.E. et al. (2016). Isothermal cyclic conversion of methane into methanol over copper-exchanged zeolite at low temperature. *Angew. Chem. Int. Ed.* 55: 5467–5471.

200 Knorpp, A.J., Newton, M.A., Mizuno, S.C.M. et al. (2019). Comparative performance of Cu-zeolites in the isothermal conversion of methane to methanol. *Chem. Commun.* 55: 11794–11797.

201 Dinh, K.T., Sullivan, M.M., Narsimhan, K. et al. (2019). Continuous partial oxidation of methane to methanol catalyzed by diffusion-paired copper dimers in copper-exchanged zeolites. *J. Am. Chem. Soc.* 141: 11641–11650.

202 Koishybay, A. and Shantz, D.F. (2020). Water is the oxygen source for methanol produced in partial oxidation of methane in a flow reactor over Cu-SSZ-13. *J. Am. Chem. Soc.* 142: 11962–11966.

203 Sun, L., Wang, Y., Wang, C. et al. (2021). Water-involved methane-selective catalytic oxidation by dioxygen over copper zeolites. *Chemistry* 7: 1557–1568.

204 Sushkevich, V.L., Palagin, D., and Bokhoven, J.A.V. (2018). The effect of the active-site structure on the activity of copper mordenite in the aerobic and anaerobic conversion of methane into methanol. *Angew. Chem. Int. Ed.* 57: 8906–8910.

205 Markovits, M.A.C., Jentys, A., Tromp, M. et al. (2016). Effect of location and distribution of Al sites in ZSM-5 on the formation of Cu-oxo clusters active for direct conversion of methane to methanol. *Top. Catal.* 59: 1554–1563.

206 Vanelderen, P., Snyder, B.E.R., Tsai, M.-L. et al. (2015). Spectroscopic definition of the copper active sites in mordenite: selective methane oxidation. *J. Am. Chem. Soc.* 137: 6383–6392.

207 Mahyuddin, M.H., Tanaka, T., Shiota, Y. et al. (2018). Methane partial oxidation over $[Cu_2(\mu\text{-}O)]_2^+$ and $[Cu_3(\mu\text{-}O)_3]_2^+$ active species in large-pore zeolites. *ACS Catal.* 8: 1500–1509.

208 Snyder, B.E.R., Vanelderen, P., Schoonheydt, R.A. et al. (2018). Second-sphere effects on methane hydroxylation in Cu-zeolites. *J. Am. Chem. Soc.* 140: 9236–9243.

209 Derouane, E.G. (1986). Shape selectivity in catalysis by zeolites: the nest effect. *J. Catal.* 100: 541–544.

210 Jones, A.J., Zones, S.I., and Iglesia, E. (2014). Implications of transition state confinement within small voids for acid catalysis. *J. Phys. Chem. C* 118: 17787–17800.

211 Sarazen, M.L., Doskocil, E., and Iglesia, E. (2016). Effects of void environment and acid strength on alkene oligomerization selectivity. *ACS Catal.* 6: 7059–7070.

212 Cheung, P., Bhan, A., Sunley, G.J., and Iglesia, E. (2006). Selective carbonylation of dimethyl ether to methyl acetate catalyzed by acidic zeolites. *Angew. Chem. Int. Ed.* 45: 1617–1620.

213 Alayon, E.M.C., Nachtegaal, M., Ranocchiari, M., and van Bokhoven, J.A. (2012). Catalytic conversion of methane to methanol using Cu-zeolites. *CHIMIA Int. J. Chem.* 66: 668–674.

214 Newton, M.A., Knorpp, A.J., Pinar, A.B. et al. (2018, 140). On the mechanism underlying the direct conversion of methane to methanol by copper hosted in zeolites; braiding Cu K-edge XANES and reactivity studies. *J. Am. Chem. Soc.* 10090–10093.

215 Bozbag, S.E., Alayon, E.M.C., Pecháček, J. et al. (2016). Methane to methanol over copper mordenite: yield improvement through multiple cycles and different synthesis techniques. *Catal. Sci. Technol.* 6: 5011–5022.

216 Pappas, D.K., Martini, A., Dyballa, M. et al. (2018, 140). The nuclearity of the active site for methane to methanol conversion in Cu-mordenite: a quantitative assessment. *J. Am. Chem. Soc.* 15270–15278.

217 Ipek, B. and Lobo, R.F. (2016). Catalytic conversion of methane to methanol on Cu–SSZ-13 using N_2O as oxidant. *Chem. Commun.* 52: 13401–13404.

218 Oord, R., Schmidt, J.E., and Weckhuysen, B.M. (2018). Methane-to-methanol conversion over zeolite Cu–SSZ-13, and its comparison with the selective catalytic reduction of NO_x with NH_3. *Catal. Sci. Technol.* 8:1028–1038.

219 Kazansky, V.B. and Serykh, A.I. (2004). Unusual localization of zinc cations in MFI zeolites modified by different ways of preparation. *Phys. Chem. Chem. Phys.* 6: 3760–3764.

220 Almutairi, S.M.T., Mezari, B., Magusin, P.C.M.M. et al. (2012). Structure and reactivity of Zn-modified ZSM-5 zeolites: the importance of clustered cationic Zn complexes. *ACS Catal.* 2: 71–83.

221 Pinilla-Herrero, I., Borfecchia, E., Holzinger, J. et al. (2018). High Zn/Al ratios enhance dehydrogenation vs hydrogen transfer reactions of Zn–ZSM-5 catalytic systems in methanol conversion to aromatics. *J. Catal.* 362: 146–163.

222 Gabrienko, A.A., Arzumanov, S.S., Luzgin, M.V. et al. (2015). Methane activation on Zn_2^+–exchanged ZSM-5 zeolites. The effect of molecular oxygen addition. *J. Phys. Chem. C* 119: 24910–24918.

223 Morra, E., Berlier, G., Borfecchia, E. et al. (2017). Electronic and geometrical structure of Zn^+ ions stabilized in the porous structure of Zn-loaded zeolite H-ZSM-5: a multifrequency CW and pulse EPR study. *J. Phys. Chem. C* 121: 14238–14245.

224 Oda, A., Ohkubo, T., Yumura, T. et al. (2015). Synthesis of an unexpected $[Zn_2]_2^+$ species utilizing an MFI-type zeolite as a nano-reaction pot and its manipulation with light and heat. *Dalton Trans.* 44: 10038–10047.

225 Dyer, A. and Emms, T.I. (2005). Cation exchange in high silica zeolites. *J. Mater. Chem.* 15: 5012–5021.

226 Kazansky, V.B., Serykh, A.I., and Pidko, E.A. (2004). DRIFT study of molecular and dissociative adsorption of light paraffins by H–ZSM-5 zeolite modified with zinc ions: methane adsorption. *J. Catal.* 225: 369–373.

227 Kolyagin, Y.G., Ivanova, I.I., Ordomsky, V.V. et al. (2008). Methane activation over Zn-modified MFI zeolite: NMR evidence for Zn-methyl surface species formation. *J. Phys. Chem. C* 112: 20065–20069.

228 Oda, A., Torigoe, H., Itadani, A. et al. (2013). Mechanism of CH_4 activation on a monomeric Zn_2^+-ion exchanged in MFI-type zeolite with a specific Al arrangement: similarity to the activation site for H_2. *J. Phys. Chem. C* 117: 19525–19534.

229 Xu, J., Zheng, A., Wang, X. et al. (2012). Room temperature activation of methane over Zn modified H–ZSM-5 zeolites: insight from solid-state NMR and theoretical calculations. *Chem. Sci.* 3: 2932–2940.

230 Wu, J.F., Wang, W.D., Xu, J. et al. (2010). Reactivity of C_1 surface species formed in methane activation on Zn-modified H–ZSM-5 zeolite. *Chem. Eur. J.* 16: 14016–14025.

231 Shah, M.A., Raynes, S., Apperley, D.C., and Taylor, R.A. (2020). Framework effects on activation and functionalisation of methane in zinc-exchanged zeolites. *ChemPhysChem* 21: 673–679.

232 Oda, A., Ohkubo, T., Yumura, T. et al. (2019). Room-temperature activation of the C—H bond in methane over terminal Zn^{II}–oxyl species in an MFI zeolite: a combined spectroscopic and computational study of the reactive frontier molecular orbitals and their origins. *Inorg. Chem.* 58: 327–338.

233 Oda, A., Ohkubo, T., Yumura, T. et al. (2017). Identification of a stable Zn^{II}–oxyl species produced in an MFI zeolite and its reversible reactivity with O_2 at room temperature. *Angew. Chem. Int. Ed.* 56: 9715–9718.

234 Akira, O., Hiroe, T., Atsushi, I. et al. (2012). Unprecedented reversible redox process in the ZnMFI—H_2 system involving formation of stable atomic Zn0. *Angew. Chem. Int. Ed.* 51: 7719–7723.

235 Pidko, E.A. and van Santen, R.A. (2007). Activation of light alkanes over zinc species stabilized in ZSM-5 zeolite: a comprehensive DFT study. *J. Phys. Chem. C* 111: 2643–2655.

236 Oda, A., Ohkubo, T., Yumura, T. et al. (2017). Why do zeolites induce an unprecedented electronic state on exchanged metal ions? *Phys. Chem. Chem. Phys.* 19: 25105–25114.

237 Gabrienko, A.A., Arzumanov, S.S., Freude, D., and Stepanov, A.G. (2010). Propane aromatization on Zn-modified zeolite BEA studied by solid-state NMR in situ. *J. Phys. Chem. C* 114: 12681–12688.

238 Gabrienko, A.A., Arzumanov, S.S., Toktarev, A.V. et al. (2017). Different efficiency of Zn_2^+ and ZnO species for methane activation on Zn-modified zeolite. *ACS Catal.* 7: 1818–1830.

239 Mehdad, A. and Lobo, R.F. (2017). Ethane and ethylene aromatization on zinc-containing zeolites. *Catal. Sci. Technol.* 7: 3562–3572.

240 Kazansky, V.B., Borovkov, V.Y., Serykh, A.I. et al. (1999). On the role of zinc oxide nanometric clusters in preparation of ZnNaY zeolite by ion exchange. *Phys. Chem. Chem. Phys.* 1: 2881–2886.

241 Stepanov, A.G., Arzumanov, S.S., Gabrienko, A.A. et al. (2008). Significant influence of Zn on activation of the C—H bonds of small alkanes by Bronsted acid sites of zeolite. *ChemPhysChem* 9: 2559–2563.

242 Wu, J.-F., Yu, S.-M., Wang, W.D. et al. (2013). Mechanistic insight into the formation of acetic acid from the direct conversion of methane and carbon dioxide on zinc-modified H–ZSM-5 zeolite. *J. Am. Chem. Soc.* 135: 13567–13573.

243 Qi, G., Wang, Q., Xu, J. et al. (2016). Synergic effect of active sites in zinc-modified ZSM-5 zeolites as revealed by high-field solid-state NMR spectroscopy. *Angew. Chem. Int. Ed.* 55: 15826–15830.

244 Gabrienko, A.A., Danilova, I.G., Arzumanov, S.S. et al. (2020). Does the Zn_2^+ species introduced into H–ZSM-5 zeolite affect the strength of Brønsted acid sites? *ChemCatChem* 12: 478–487.

245 Zhang, P., Yang, X., Hou, X. et al. (2019). Active sites and mechanism of the direct conversion of methane and carbon dioxide to acetic acid over the zinc-modified H–ZSM-5 zeolite. *Catal. Sci. Technol.* 9: 6297–6307.

246 Wang, X., Qi, G., Xu, J. et al. (2012). NMR-Spectroscopic evidence of intermediate-dependent pathways for acetic acid formation from methane

and carbon monoxide over a ZnZSM-5 zeolite catalyst. *Angew. Chem. Int. Ed.* 51: 3850–3853.

247 Beznis, N.V., Weckhuysen, B.M., and Bitter, J.H. (2010). Partial oxidation of methane over Co–ZSM-5: tuning the oxygenate selectivity by altering the preparation route. *Catal. Lett.* 136: 52–56.

248 Beznis, N.V., van Laak, A.N.C., Weckhuysen, B.M., and Bitter, J.H. (2011). Oxidation of methane to methanol and formaldehyde over Co–ZSM-5 molecular sieves: tuning the reactivity and selectivity by alkaline and acid treatments of the zeolite ZSM-5 agglomerates. *Microporous Mesoporous Mater.* 138: 176–183.

249 Krisnandi, Y.K., Putra, B.A.P., Bahtiar, M. et al. (2015). Partial oxidation of methane to methanol over heterogeneous catalyst Co/ZSM-5. *Procedia Chemistry* 14: 508–515.

250 Fellah, M.F. and Onal, I. (2010). Direct methane oxidation to methanol by N_2O on Fe- and Co–ZSM-5 clusters with and without water: a density functional theory study. *J. Phys. Chem. C* 114: 3042–3051.

251 Krisnandi, Y.K., Samodro, B.A., Sihombing, R., and Howe, R.F. (2015). Direct synthesis of methanol by partial oxidation of methane with oxygen over cobalt modified mesoporous H–ZSM-5 catalyst. *Indonesian J. Chem.* 15: 263–268.

252 Shan, J., Huang, W., Nguyen, L. et al. (2014). Conversion of methane to methanol with a bent mono(μ-oxo)dinickel anchored on the internal surfaces of micropores. *Langmuir* 30: 8558–8569.

253 Arvidsson, A.A., Zhdanov, V.P., Carlsson, P.-A. et al. (2017). Metal dimer sites in ZSM-5 zeolite for methane-to-methanol conversion from first-principles kinetic modelling: is the $[Cu–O–Cu]_2^+$ motif relevant for Ni, Co, Fe, Ag, and Au? *Catal. Sci. Technol.* 7: 1470–1477.

254 Mahyuddin, M.H. and Yoshizawa, K. (2018). DFT exploration of active site motifs in methane hydroxylation by Ni–ZSM-5 zeolite. *Catal. Sci. Technol.* 8: 5875–5885.

255 Radu, D., Glatzel, P., Gloter, A. et al. (2008). Geometric and electronic structure of α-oxygen sites in Mn–ZSM-5 zeolites. *J. Phys. Chem. C* 112: 12409–12416.

256 Breen, J.P., Burch, R., Kulkarni, M. et al. (2007). Improved selectivity in the toluene alkylation reaction through understanding and optimising the process variables. *Appl. Catal., A* 316: 53–60.

257 Keith, J.A. and Henry, P.M. (2009). The mechanism of the Wacker reaction: a tale of two hydroxypalladations. *Angew. Chem. Int. Ed.* 48: 9038–9049.

258 Labinger, J.A. and Bercaw, J.E. (2015). Mechanistic studies on the Shilov system: a retrospective. *J. Organomet. Chem.* 793: 47–53.

6

The Selective Oxidation of Methane to Oxygenates Using Heterogeneous Catalysts

James H. Carter, Nicholas F. Dummer, Ying Kit Chow, Christopher Williams, Ali Nasrallah, David J. Willock, Graham J. Hutchings, and Stuart H. Taylor

Cardiff University, Cardiff Catalysis Institute, Max Planck-Cardiff Centre on the Fundamentals of Heterogeneous Catalysis FUNCAT, School of Chemistry, Main Building, Park Place, Cardiff CF10 3AT, UK

6.1 Introduction and Historical Context

Methane, an abundant natural resource found in oil and gas fields around the world, is the major component of shale gas. The utilization of methane, particularly in remote areas, remains a challenge as transportation and on-site conversion are not economically viable. Hence, hundreds of billions of cubic meters of methane are flared into the environment as CO_2 every year [1]. Current industrial methane conversion processes are based on steam reforming methane into syngas (CO and H_2) that can then be further converted into platform chemicals and higher hydrocarbons via processes such as methanol synthesis and Fischer–Tropsch synthesis. Reforming is an energy-intensive process, typically operated at 800 °C using a Ni/Al_2O_3 catalyst that, although efficient, is only feasible at large-scale operation. Methanol is currently synthesized from syngas at c. 220 °C and 20 bar over CuZnO-based catalysts and is therefore generated indirectly from methane. The development of a direct process for converting methane to methanol or other C_1 oxygenates would be of considerable practical value, and demand for such processes has soared in the recent years since the emergence of shale gas, which means a vast supply of methane is guaranteed in the coming decades.

In contrast to steam reforming and other methane conversion processes, the selective oxidation of methane to C_1 oxygenates is considerably more challenging. Although any of the commonly reported oxygenates (methanol, formaldehyde, and formic acid) would be of value, methanol in particular has been targeted due to its current scale of production and central role as a platform chemical [2]. Providing a valuable non-crude oil source for the production of olefin-based petrochemicals, methanol is transformed industrially by the methanol-to-olefin (MTO) or methanol-to-propylene (MTP) processes [3, 4]. Alternatively acetic acid can be produced from methanol using processes based on earlier Monsanto technologies and other processes such as the Cativa process developed by British Petroleum (BP) [5, 6]. Additionally, formaldehyde [7], dimethyl ether [8], and methyl *tert*-butyl

Heterogeneous Catalysis for Sustainable Energy, First Edition. Edited by Landong Li and Justin S. J. Hargreaves.

ether [9], important chemicals for production of plastics and pharmaceutical solvents, require methanol as a precursor. Furthermore, methanol remains a clean and renewable energy-dense liquid fuel, capable of direct application as a transportation fuel, or blended with gasoline for automobiles [10]. Methanol may also provide an intermediate source of green energy by application of direct methanol fuel cell technology [10], offering high power and energy generated at ambient conditions with low emissions while requiring only renewable methanol [10]. In addition, methanol is a potential solution for H_2 storage, which is a key developing technology. The reduction of CO_2 by H_2 is projected to produce 40–70 million tons of methanol by 2050 [2]. Subsequently, methanol production provides an important technological and economic challenge for both industry and academia [11].

Initially demonstrated in the publications of Bone and Wheeler [12, 13], at the beginning of the twentieth century, the direct oxidation of methane to oxygenates has captured the interest of academics and industrialists alike. The first half of the twentieth century contains sporadic advances in methane oxidation chemistry, most made after the 1930s and often in the absence of a catalyst. However, in the second half of the twentieth century with the cementation of natural gas as a feedstock to many industrial processes, interest in valorizing methane gained renewed interest. This has further increased in the wake of the discovery of vast global shale gas reserves, particularly in North America. Despite this interest, methanol production is still carried out by industrial steam reforming of natural gas followed by subsequent methanol synthesis, and no known process comes close to replacing it.

In nature, the conversion of CH_4 is efficiently achieved at ambient conditions by methanotrophic bacteria with molecular oxygen [14]. In these bacteria, CH_4 is utilized as a primary source of carbon or energy by assimilation of formaldehyde or formation of CO_2 [14]. They occupy the interface of aerobic and anaerobic boundaries in wet soils or lakes or near ocean vents, where methane is supplied by the anaerobic metabolism of methanogens [15]. It is from these enzymes that many of the most promising heterogeneous catalysts have been inspired.

Methane monooxygenase (MMO) exists in two distinct forms: particulate methane monooxygenase (pMMO) and soluble methane monooxygenase (sMMO), which involve copper and iron active centers, respectively [16]. Although demonstrating high efficiency for the oxidation of methane to methanol, crucially, overall methanol productivity is low. Turnover frequencies TOFs for sMMO and pMMO present in *Methylococcus capsulatus* (Bath) for the oxidation of methane by O_2 are 0.19 and 1 s^{-1}, respectively [17]. The economic viability of harnessing these natural processes for the methane-to-methanol reaction is hampered by the requirement of costly reductants (NADH) while only achieving low productivities. In addition, the extraction and isolation of MMO enzymes from methanotrophs is still too costly for an alternative compared with the application of methanotrophic bacteria themselves [18].

Even so, mechanistic understanding from MMO studies provides opportunities for the design of novel catalysts. The seminal studies of Dalton and coworkers highlighted this importance, with sMMO shown to be non-specific and capable of oxidizing a range of *n*-alkanes, from C_1 to C_8 [19]. Additionally,

sMMO selectively epoxidizes alkenes and hydroxylated cyclic alkanes and aromatics. Importantly, the oxidation of methane by O_2 achieved a productivity of 5.05 $mol_{(methanol)}$ $kg_{(protein)}^{-1}$ h^{-1}, becoming an academic target for low-temperature methane oxidation [19, 20].

6.2 Liquid-Phase Reactions

The liquid-phase oxidation of methane is typically characterized by relatively low reaction temperatures (<150 °C) and is typically carried out in batch reactors at elevated pressure (30–50 bar). Water is commonly used as a solvent for these reactions, as most organic solvents with C—H bonds are more reactive than methane. In the following sections, we describe the most promising catalytic systems for the partial oxidation of methane in the liquid phase.

6.2.1 Zeolite Catalysts

The microporous, crystalline structure of zeolites is composed of an aluminosilicate framework [21]. The three-dimensional network of SiO_4 and AlO_4^- units linked via bridging O atoms produces pores and cavities with dimensions ranging 3–14 Å [21, 22]. Producing a uniform array of well-defined micropores, the resulting large-surface-area environments act as reaction channels [21, 22]. Furthermore, the presence of negative charge from framework AlO_4^- units results in interchangeable extra-framework cations (such as Na^+, H^+) to maintain charge neutrality [23]. The resulting ion exchange of cations produces a diverse chemistry, allowing for tunable activity and selectivity [23]. The confined architecture of zeolites has been likened to that found in the active centers of an enzyme. Hence, active catalytic centers supported in zeolites have been of great interest.

Using both Fe–ZSM-5 and Cu–ZSM-5, Hammond et al. demonstrated the liquid-phase oxidation of CH_4 using H_2O_2 [24]. Building upon previous works for H–ZSM-5 by Ishihara and coworkers, pre-activated by high-temperature calcination (550 °C), H_2O_2 was utilized for CH_4 oxidation to HCOOH with c. 68% selectivity at 100 °C [25]. Identifying trace impurities of Fe, Hammond et al. investigated ion-exchanged Fe–ZSM-5 at 50 °C, achieving oxygenate selectivity of 83%, producing predominantly HCOOH (c. 72%) [24]. Similarly, Cu–ZSM-5 produced 88% oxygenate selectivity but drastically improved methanol selectivity, increasing to 83% of total oxygenates. Producing higher selectivity, Fe–ZSM-5 demonstrated greater activity with 0.7% CH_4 conversion in comparison with 0.3% of initial 30.3 mmol CH_4. Formation of bimetallic CuFe–ZSM-5 produced remarkably improved activity and selectivity. Further investigation revealed the presence of Cu^{2+} minimized hydroxyl radical ($HO^{\cdot}$) formation, reducing the consecutive oxidation of CH_3OH to HCOOH. Subsequently, methanol selectivity reached 93% while maintaining comparable CH_4 conversion with Fe–ZSM-5 [26]. Chadwick and coworkers identified that formaldehyde, hydrogen, and polyoxomethylene

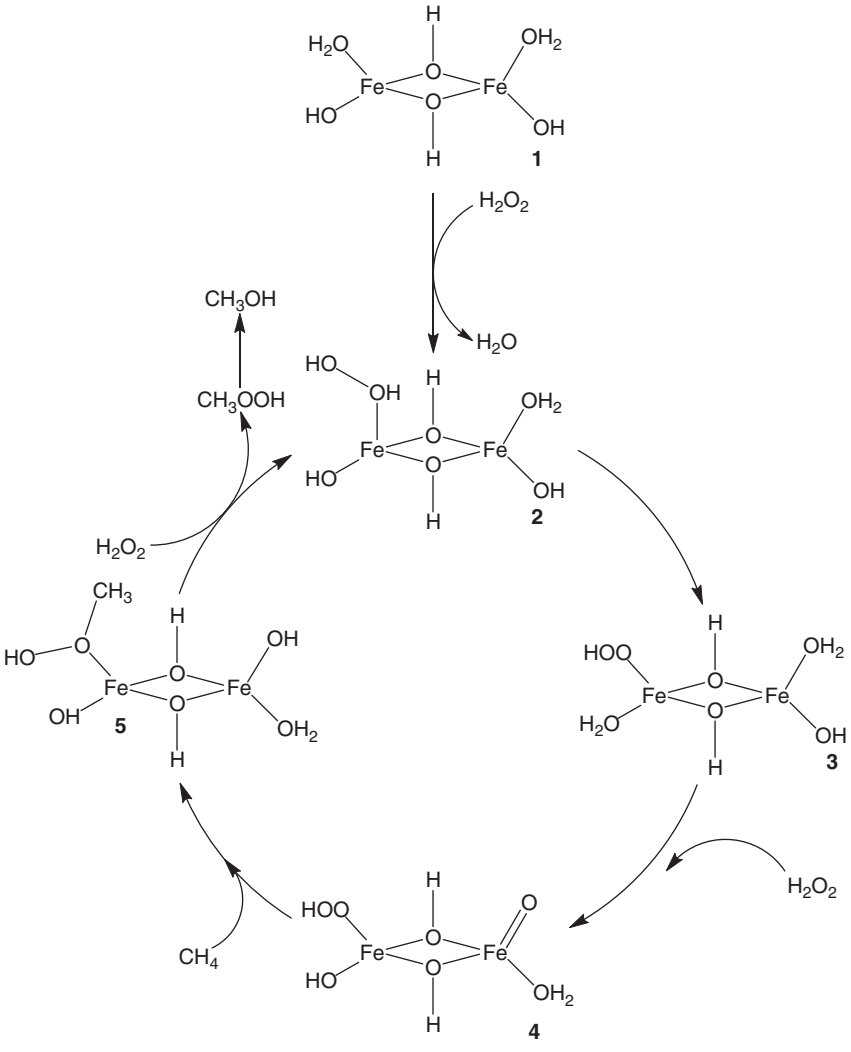

Figure 6.1 Proposed catalytic cycle for the oxidation of methane to methanol catalyzed by a binuclear Fe species in ZSM-5 [24].

were also produced, clarifying the reaction pathways involved in the oxidation of methane with H_2O_2 [27].

The proposed reaction mechanism is shown in Figure 6.1 [24]. Density functional theory (DFT) calculations were performed using the Vienna Ab initio Simulation Package (VASP) to study the mechanism of the reaction. Transition-state calculations were carried out for species 4 to species 5 to determine the barrier for hydrogen abstraction from methane to form methyl hydroperoxide. The barrier determined computationally was found to be 50 kJ mol^{-1}, which is in good agreement with the activation energy determined experimentally (61 kJ mol^{-1}).

Electron paramagnetic resonance (EPR) spectroscopy was used to confirm the validity of the model described in Figure 6.1. The EPR spectra obtained confirmed the absence of methyl radicals, indicating that the reaction does indeed go through methyl hydroperoxide as the primary intermediate. Upon its generation, the methyl hydroperoxide desorbs into the solution, thereby closing the catalytic cycle [24, 26].

Similarly, Ayodele investigated CH_4 conversion to CH_3OH over ferrous oxalate-supported ZSM-5 (FeO_x/ZSM-5) [28]. They identified $Fe^{(II)}$ as the active phase generating highly reactive HO· from H_2O_2 during a Fenton-like process, which resulted in the CH_4 activation. Methanol formation was reported to proceed via methoxy radical formation, as suggested by Hammond et al. [26].

Although water is often used as a solvent in methane oxidation reactions, the solubility of methane and oxygen is poor (1.9 mg CH_4 in 100 g H_2O at 30 °C and 1 bar). Yokoi and coworkers very recently described a reaction in sulfolane/water mixture over Fe–MFI catalysts where around 900 μmol of methanol was produced after two hours at 30 bar. The extremely high productivity was related to the use of sulfolane in the reaction, which also prevented over-oxidation of methanol to CO_2 [29].

6.2.2 Noble Metal Catalysts

The application of cheaper and cleaner oxidants are recurring themes for methane oxidation, and despite aims to utilize O_2, preformed H_2O_2 is often used instead. As a strong oxidant, H_2O_2 represents a reactive oxygen species [30]. Providing an alternative to current environmentally unfriendly methods of H_2O_2 formation, the *in situ* generation of an environmentally benign oxidant is industrially attractive [31]. Palladium and gold–palladium alloy catalysts are well known for their activity in the direct synthesis of hydrogen peroxide and have been widely applied to selective methane oxidation catalysis using preformed H_2O_2 or O_2 and H_2 to generate H_2O_2 *in situ*.

Lin and Sen first demonstrated the oxidation of alkanes with H_2O_2 generated *in situ* using a Pd/C catalyst [32]. Initial investigations were carried out by successful oxidation of ethane to predominantly ethanol at 30 °C [32]. Investigating temperatures ranging from 70 to 110 °C, lower temperatures, in addition to small quantities of acidic media, were required to minimize Pd-catalyzed H_2O_2 decomposition. As illustrated, direct synthesis of H_2O_2 was produced from O_2 and H_2 over the Pd catalyst, with the H_2 source formed from the water–gas shift reaction of CO and H_2O. Attempts to oxidize methane succeeded and produced formic acid (HCOOH), with a turn over number (TON) ranging from 80 to 160. Experiments carried out using H_2 and O_2 only rapidly produced H_2O_2. However, high rates of Pd-catalyzed decomposition were observed. Similarly, the formation of unstable HCOOH from CH_4 was observed and resulted in over-oxidation to carbon dioxide and water.

This initial report proved that preformed H_2O_2 and *in situ* generated H_2O_2 could be used to generate oxygenates from methane. Subsequent studies have simplified the reaction mixture, opting to use H_2 and O_2 directly (rather than $CO + H_2O$) or preformed H_2O_2.

Ab Rahim et al. reported that bimetallic 2.5 wt%Au–2.5 wt%Pd/TiO_2 catalysts could oxidize CH_4 using preformed H_2O_2 to produce methyl hydroperoxide and methanol [33, 34]. High oxygenate selectivity (>80%) at 50 °C and 30 bar CH_4 after 30 minutes was observed, although H_2O_2 consumption was high, with 10% of the initial 5000 μmol H_2O_2 remaining. When the catalysts were applied to *in situ* generation of H_2O_2, improved methanol selectivity was observed when compared with experiments using preformed H_2O_2 (68% vs 49%) while maintaining similar productivity. Importantly, the theoretical maximum quantity of H_2O_2 produced was calculated at c. 250 μmol, representing a threefold increase in H_2O_2 reactivity compared with the similar quantities of preformed H_2O_2. However, low productivities for H_2O_2 synthesis from H_2 and O_2 resulted in a low overall rate of CH_4 oxidation, while the use of preformed H_2O_2 requires excess H_2O_2 despite the high selectivity to oxygenates.

The addition of Cu to produce a trimetallic AuPdCu/TiO_2 catalyst enhanced methanol selectivity to c. 83% while operating under similar condition with preformed H_2O_2 for 2.5 wt%Au–2.5 wt%Pd–1.0 wt%Cu (AuPdCu) [35]. However, this increase in the performance was not realized in the *in situ* generation of H_2O_2; oxygenate productivity decreased from 0.11 $mol_{oxygenates}$ kg_{cat}^{-1} h^{-1} for bimetallic AuPd to 0.04 $mol_{(oxygenates)}$ kg_{cat}^{-1} h^{-1} for AuPdCu catalysts [35]. This effect is likely due to the decreased H_2O_2 synthesis rate of the Cu-containing catalyst.

Recently, Williams et al. investigated the effect of Pd oxidation state, particle size, and metal concentration for selective methane oxidation using supported AuPd catalysts [36]. It was found that a complex relationship between all three of these parameters existed, and for high activity and selectivity, all three must be optimized. Specifically, highly active and efficient catalysts featured large mean particle diameter (>10 nm), a higher concentration of Pd^{2+} species, and low metal loadings. The tuning of these parameters led to the preparation of a catalyst with a TOF of 103 h^{-1}, significantly higher than previously prepared supported AuPd catalysts.

Recent work by Agarwal et al. [37] reported that unsupported colloidal AuPd nanoparticles significantly improved upon the oxygenate productivity demonstrated by earlier supported AuPd catalysts. Utilizing 1000 μmol H_2O_2, oxygenate productivity of 29.4 $mol_{(oxygenates)}$ kg_{cat}^{-1} h^{-1} was achieved, consuming 28% of initial H_2O_2 concentration with 6.6 μmol AuPd metal. Importantly, productivity was enhanced to 39.4 $mol_{(oxygenates)}$ kg_{cat}^{-1} h^{-1} further by the reduction of H_2O_2 concentration to 50 μmol in combination with O_2 (5 bar) addition. The incorporation of O_2 in the partial oxygenate products was evidenced by isotopically labeled $^{18}O_2$ experiments, which demonstrated that ^{18}O was present in c. 70% of the primary products [37].

The incorporation of O_2 into primary CH_4 oxidation products represents significant progress toward direct CH_3OH formation using O_2 as oxidant [37]. At present, the ability to utilize O_2 as a direct and readily available oxidant is very limited. Instead, activation of O_2 by reduction with NADH or H_2 is required [38]. Additionally, homogeneous catalyst performance is greatly superior to their heterogeneous counterparts in terms of CH_4 conversion and selectivity [18]. The challenge for a commercial low-temperature process is the requirement of a highly

active catalytic system, which remains stable while producing methanol in high concentration [38, 39].

Recently, Flytzani-Stephanopoulos and coworkers reported the oxidation of CH_4 to CH_3OH and acetic acid (CH_3CO_2H) using mononuclear rhodium species anchored on ZSM-5 [40]. Utilizing O_2 and CO at 150 °C, two independent pathways were proposed for the formation of CH_3CO_2H or CH_3OH. Optimization of conditions for CH_3CO_2H production by varying P_{O_2} at constant CH_4 concentrations gave yields of c. 22 000 μmol g_{cat}^{-1}, reached in three hours, with 60% selectivity. Additionally, zeolite acidity was modified, having previously been demonstrated to promote CH_3CO_2H selectivity for Cu–ZSM-5 [41]. Instead, the application of Na–ZSM-5 was used to suppress HCOOH formation, tuning selectivity toward methanol. Resulting in CH_3OH yields of 430 μmol g_{cat}^{-1} at c. 55% selectivity, the introduction of homogeneous $Cu^{(II)}$ species enhanced yields to 550 μmol g_{cat}^{-1} with c. 70% CH_3OH selectivity [40]. In a similar approach, Tang et al. also reported the formation of acetic acid, formic acid, and methanol from isolated Rh_1O_5 species anchored on ZSM-5. The activation of methane was proposed to occur over the Rh species to generate a methyl species that subsequently couples with CO and OH [42].

Developing a polymer-based covalent triazine framework comprising a coordinated $Pt^{(II)}$ center (Pt-covalent triazine framework [CTF]), Palkovits et al. successfully demonstrated the heterogeneous equivalent to Periana's Pt catalyst for methane oxidation [43]. Achieving a TON of c. 245, methanol selectivity of greater than 75% was reached under similar H_2SO_4/SO_3 conditions to Periana [43, 44]. However, pre-activation under reaction conditions was required to improve the initial TON from 26 to c. 245 in. successive cycles. Proving to be reusable, the initial advantage of heterogeneous Pt-CTF is lost due to the catalyst instability, leading to Pt leaching. Subsequently, Wang and coworkers were able to convert 25% CH_4 to methanol with 72% selectivity by using an ionic liquid ([Bmim]Cl) and trifluoroacetic acid as the solvent and Au/SiO_2 as the catalyst, at 90 °C [45]. In this system, the product was methyl trifluoroacetate, which in water readily hydrolyzes to form methanol and trifluoroacetic acid. Such techniques to protect methanol from further reaction are not common, but are clearly effective in some cases and result in the highest methanol yields reported.

6.3 Gas-Phase Reactions

The liquid-phase reactions described thus far were carried out in high-pressure batch reactors. However, much attention has been focused on developing a continuous process, where methane and an oxidant are co-fed in the gas-phase. This approach is more desirable than a batch process as continuous operation can afford high productivity. Zeolite catalysts comprise a significant proportion of the literature on gas-phase catalyzed methane to oxygenate research, and so this section has been divided into studies with and without zeolites. Non-zeolite catalysts frequently consist of mixed metal oxides, sometimes with supported transition metals and more often than not pre-date the zeolite literature.

6.3.1 Non-zeolite Catalysts

Early investigations of gas-phase methane oxidation were often carried out in the absence of a catalyst. Typically operating at temperatures between 500 and 800 °C and pressures of 30–60 bar, product formation was dictated by radical reaction pathways [46]. Subsequently, the moderately selective formation of methanol was controlled by considering reactor setup, residence time, and product capture by quenching of unstable oxygenates [46–48]. Despite the difficulties associated with controlling this radical process, only low yields have been reported for methanol and formaldehyde formation [49]. Zhang et al. report yields of methanol c. 8%, converting 13% of methane to methanol with 60% selectivity [50]. Operating at high temperatures (450–500 °C) and pressures (30–60 bar), several studies also reported similar CH_4 conversion (5–10%) with methanol selectivities of 30–40% [51–54].

Alternatively, Hargreaves et al. demonstrated an improvement to C_1 oxygenate selectivity by using high space velocities over MgO catalysts [55]. Operating at high temperatures, MgO was demonstrated as an effective catalyst for the oxidative coupling of methane, generating C_{2+} species [56]. Careful control of reaction conditions by reduction of contact time allowed control of competing coupling and oxidation reactions occurring in the gas phase and upon the catalyst surface. Subsequently, reduction of methane partial pressure reduced the concentration of methyl radicals produced, improving selectivity and yielding formaldehyde as the major product. Importantly, the reduction in pressure afforded the ability to tune product yield and selectivity using solid catalysts.

Silica-supported MoO_x and VO_x have also been reported with yields of 3–4% for formaldehyde synthesis while operating at temperatures between 350 and 500 °C [57]. Initially reported by Dowden and Walker [58], the importance of the presence of a metal oxide catalyst was described, with $Fe_2O_3(MoO_3)_3$ being most active for methanol production [59]. Further work by Spencer and coworkers examined the application of SiO_2-supported MoO_3, forming primarily formaldehyde (HCHO), CO, and CO_2. Selectivity to HCHO was dependent upon methane conversion, with low CH_4 conversion producing 71% HCHO selectivity. High specific activity was determined to originate from isolated penta-coordinated $Mo^{(VI)}O_x$, demonstrating high selectivity toward HCHO and CH_3OH [60, 61]. Meanwhile, Taylor et al. investigated MoO_3-catalyzed CH_4 partial oxidation using a range of metal oxides [62]. Experiments at 450 °C indicated Ga_2O_3/MoO_3 catalysts were able to form methanol from O_2 with 22% selectivity, while Ga_2O_3 and MoO_3 showed 3% and 11% selectivity to methanol. The synergy of this catalyst was attributed to the high activity of Ga_2O_3 and the high selectivity of MoO_3 [62].

Alternatively, Parmaliana et al. demonstrated the partial oxidation of CH_4 using SiO_2-supported V_2O_5 catalyst [63]. Operating at 650 °C, the application of a continuous flow recycle reactor allowed 10–18% yields of formaldehyde to be obtained [64]. Addition of NO to the reaction feed was also investigated by Barbero et al. using low-surface-area V_2O_5/SiO_2 [65]. The introduction of low amounts of NO (0–2.92 vol%) promoted the activation of methane at moderate temperatures, with C_1 oxygenate selectivity reaching 40% of the products at c. 40% methane conversion.

Most of the work described above dates back at least two decades; the focus has since shifted toward zeolite-based heterogeneous catalysts and noble metals used at lower temperatures in solvents. However, there are some promising recent reports of metal oxide-catalyzed methane activation. Rodriguez and coworkers demonstrated that over $CeO_2/Cu_2O/Cu(111)$ surfaces, methane could be selectively converted into methanol in the presence of water at 177 °C [66]. DFT calculations suggested that an Eley–Rideal mechanism was likely, where initially water dissociates, generating OH groups on Ce cation sites. Then methane interacts with these surface hydroxyl groups to dissociate, directly forming methanol. The facile dissociation of water on the surface was proposed to inhibit deleterious further reaction of intermediates and products.

Nørskov and coworkers recently used DFT calculations to study hydrogen abstraction from methane on both pure and oxygen-promoted FCC(111) metal surfaces [67, 68]. Their calculations were used to determine whether it is possible for the hydrogen abstraction step to proceed via a radical-like transition state on the pure (111) surfaces. The radical transition-state energy was approximated to be that of $CH_3(g) + H^*$, where "*" indicates a surface adsorption site. When repeated for oxygen-promoted metals, it was found that the reaction mechanism for Au and Ag proceeded through a radical-like transition state but that a surface-stabilized transition state could not be determined. This was unexpected as both Au(111) and Ag(111) surfaces were expected to be capable of a surface-stabilized transition state. A key finding of this investigation was that oxygen-promoted noble metal catalysts had the more favorable hydrogen abstraction energies than the clean metallic surface. This was explained by considering the effect of the promoting species on the catalyst. A promoter on a noble metal catalyst (oxygen in this case) is weakly bound, making the hydrogen abstraction energy favorable. Moreover, the transition-state barriers for the oxygen-promoted Au and Ag were quite low, with energies very similar to that of Pd(111) or Pt(111) metallic surfaces. This method of studying hydrogen abstraction can be used as a universal indicator in determining which catalysts are fit for this reaction. This is an important contribution to the catalysis community as it would allow identification of which reaction pathway a given catalyst is likely to promote. After the screening process is performed, other factors such as selectivity of product formation can then be further examined.

Xi and Heyden studied the partial oxidation of methane to methanol using DFT calculations on Rh-doped graphene supported on Ni(111) surfaces using molecular oxygen as an oxidant [69]. The reaction mechanism was compared on two different surfaces at 200 °C: (i) Rh-doped graphene supported on Ni(111) surface and (ii) Rh-doped graphene. The reaction mechanism proposed for the first model involves the adsorption of two molecular oxygen molecules on the Rh atom present on graphene. One of the oxygen molecules then abstracts a hydrogen atom from methane resulting in a Rh—C bond with the methyl group and the cleavage of the O—O bond leaving an O–H connected to the Rh atom. The hydrogen abstraction process has a barrier of 132.18 kJ mol^{-1}. The formation of the first methanol group then occurs rapidly with a barrier of 8.68 kJ mol^{-1}. The oxygen atom left on the

surface then reacts with another methane molecule with a free energy barrier of 92.63 kJ mol^{-1}. The catalytic cycle is then closed upon the desorption of the second methanol molecule. The energy barrier of the hydrogen abstraction for the freestanding graphene–Rh model was found to be significantly higher with an energy barrier of 194.90 kJ mol^{-1}. This marked difference highlighted the importance of the Ni(111) support. Since Cu-containing zeolites have shown remarkable activity for this reaction, Cu-doped graphene supported on a Ni(111) surface was considered, but was calculated to be about 460 times less active at 200 °C. The interaction between the Rh-doped graphene and the Ni(111) surface was described as an electronic atomic monolayer metal–support interaction (EAMSI). The general nature of EAMSI was explored further by comparing the adsorption of CO, C_2H_4, and OH on Cu-, Fe-, Ir-, Mn-, and Rh-doped graphene on Ni(111) and the freestanding structures. In all cases, the adsorption energy was stronger on the catalysts that were supported on the Ni(111) surface. This suggests that the presence of a metal support can stabilize the adsorption energy of small molecules by forming covalent bonds with the transition metal doped atomic monolayer. This computational study showed that it is possible to alter the catalytic properties of single-atom catalysts through the EAMSI model.

6.3.2 Zeolite Catalysts

As described above, zeolites are of particular interest in methane oxidation catalysis for their structural confinement, which has been postulated to mimic one important feature of nature's MMOs.

6.3.2.1 Copper as the Active Component

In general, the formation of methanol in Cu/zeolite catalysts has been described by several groups as a stepwise process. Initially, copper species are dispersed over the surface of the zeolite under a high-temperature treatment with oxygen. The proposed active site, which facilitates methane adsorption, is generated and often described as a bis-(μ-oxo) di-copper core or more simply as Cu_xO_y. Excess oxygen is removed by an inert gas and the catalyst bed cooled prior to the introduction of methane. Methane reacts at this oxygenated copper site to form a bound alkoxy species; this is then removed through a further treatment step. Illustrated in Figure 6.2 is the stepwise process of methane oxidation and extraction of methanol

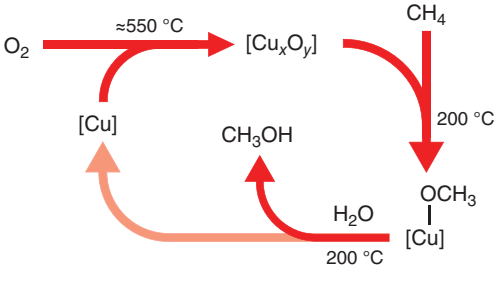

Figure 6.2 Proposed stepwise methane-to-methanol reaction over Cu/zeolite catalysts. (i) Oxidation of Cu, (ii) methane adsorption and methoxy formation, and (iii) methanol extraction with water. Source: Adapted from [70–72].

with water following formation of the methoxy species. Water is used to extract methanol, often with high selectivity from the copper-containing active site. However, the conditions for the two steps are quite different. Other treatment conditions whereby either inert gas or methanol are flowed over the catalyst bed result in the formation of CO_x, H_2, and H_2O or DME.

The structure and formation of the active site remains under debate; however, the role of framework aluminum in the zeolite structure and in the development of this copper site has been investigated [73, 74]. The aluminum has been proposed to be necessary to stabilize the Cu_xO_y active site, and two aluminum atoms located about the framework ring structure of the zeolite are required to balance the charge. Sushkevich et al. investigated the Si/Al ratio and hence the Cu/Al ratio on both aerobic and anaerobic reactions to form methanol [73]. Under an aerobic activation step, the Cu–mordenite catalyst with the highest relative Si/Al ratio and interestingly the highest Cu/ratio of the materials studied achieved the greatest methanol yield of 0.316 mol_{MeOH} $mol_{Cu}{}^{-1}$. This was ascribed to the potential to form different Al pairs in the structure and in turn stabilize the formation of Cu_xO_y, where $x \geq 2$. More recently, Yokoi et al. have reported on the possibility to prepare zeolite structures in which the location of the Al can be controlled [75]. They investigated the role that Al presents as a lone species in zeolite ring structures has, compared with an equivalent CHA structure containing a greater density of two Al within a ring structure. The close proximity of two Al atoms can promote greater methanol selectivity and reduce over-oxidation products. Their conclusion that Cu/CHA rich with these Al species, denoted as Q4(2Al), resulted in higher selectivity to methanol is compelling for future catalyst design in this area.

Pappas et al. utilized X-ray adsorption spectroscopy to explore the Cu active site of a Cu/ferririte catalyst, which was effective for the methanol from methane reaction [74]. The catalyst studied comprised ratios of Si/Al of 11 and Cu/Al of 0.20. Methanol was formed on the order of c. 0.33 mol_{MeOH} $mol_{Cu}{}^{-1}$ at a selectivity of c. 88%. The X-ray absorption near edge structure (XANES) and X-ray absorption spectra (XAS) linear combination fit study concluded that during activation, Cu(II) is observed as a framework-coordinated species. Under cooling, further rearrangement was noted, and under methane, a Cu(I) species evolved. Water, used to extract methanol, was reported to assist the partial oxidation of Cu(I) to Cu(II).

In contrast to the majority of reports on the Cu_xO_y/zeolite system, Le et al. reported a CuO/SBA-15 system [70]. They were inspired by earlier reports by Groothaert et al., in which methanol was produced over an amorphous silica catalyst impregnated with $Cu(OAc)_2{\cdot}H_2O$, albeit at a low concentration [76]. The catalyst described by Le et al. comprises CuO nanoclusters dispersed over a mesoporous silica support (SBA-15). Methanol was extracted in both *ex situ* and *in situ* manners, following an initial high-temperature oxygen treatment and then cooling under an inert gas before methane was introduced in a similar fashion to those reports using Cu/zeolites above. Despite this, high selectivity to methanol and DME of >84% was observed over the CuO/SBA-15 system with a yield of methanol in the order of 30 μmol/g of catalyst.

6.3.2.2 Iron as the Active Component

The sMMO system has also inspired many studies focusing on using the binuclear Fe center embedded in different types of support. An interesting approach using N_2O as the oxidant over Fe–ZSM-5 has been extensively investigated by Panov and coworkers [77–80]. They reported that methane was activated over Fe–ZSM-5 by α-oxygen species formed on the Fe center when using N_2O as the oxidant. The catalyst is typically pretreated under a range of temperatures, between 200 and 900 °C, under oxygen to convert the Fe^{3+} to Fe^{2+}, also called an α-Fe site. The radical anionic nature of the α-oxygen species allows the cleavage of the methane C—H bond via hydrogen abstraction to occur at room temperature [81]. Additionally, it was also observed that the surface α-oxygen species cannot be generated using molecular oxygen due to the strong stabilization of the parent ZSM-5 zeolite.

It follows a structural rearrangement to allow the α-oxygen to be generated by decomposing N_2O over the reversible redox α-Fe sites, which switch back to Fe^{3+}. An overall equation of this catalytic N_2O conversion is shown in Eq. (6.1):

$$N_2O + (Fe^{2+})_\alpha \rightarrow (Fe^{3+} - O^-)_\alpha + N_2. \tag{6.1}$$

From their early work, Panov and coworkers have shown a three-step process that involves the following: step 1 is the N_2O pretreatment over Fe–ZSM-5 to set up α-oxygen, step 2 is switching over to methane to perform stoichiometric methane-to-methanol oxidation, and step 3 is the methanol extraction from the methane-treated catalyst. It was reported that the methoxy and hydroxyl groups formed are subsequently adsorbed on the α-Fe sites, even at room temperature, which can yield methanol directly on the surface of the zeolite [81]. This process is quasi-catalytic as methanol must be extracted from the catalyst surface via hydrolysis using a solvent system consisted of a mixture of acetonitrile and water and achieved 94% selectivity to methanol. However, if operated at an appropriate temperature, it can be fully catalytic. It was found also that the co-feeding water with CH_4 and N_2O aided the desorption of methanol from the catalyst, boosting stability and minimizing selectivity to coke [79].

Chow et al. investigated the influence of acidity on catalytic methane oxidation over MFI zeolites [82]. It was found that the presence of Al was essential to form the active Fe species but methanol was unstable over Brønsted acid sites found in ZSM-5, forming coke via the hydrogen pool mechanism and limiting significant methanol selectivity and yield. A later study used the Delplot method to investigate the reaction pathways and effect of water on the reaction mechanism [83]. It was shown that water does not affect the reaction pathway, but simply aids the desorption of methanol, and the deactivation of the catalyst was due to the loss of active Fe iron sites and the subsequently diminished N_2O activation.

While the original motivation for loading Fe into ZSM-5 was to mimic the MMOs, which feature dinuclear Fe, the structure of the active Fe site is still a matter of debate. It is considered to be either mononuclear Fe^{4+}=O (or Fe^{3+}–O^-) or dinuclear Fe as an oxo-bridged $Fe^{3+}O^{2-}Fe^{3+}$ species [79]. Snyder et al. recently reported that a mononuclear α-Fe^{2+} in an extra-lattice site was present in Fe-beta zeolite (BEA), using magnetic circular dichroism spectroscopy [84]. A high-spin Fe^{4+}=O was

described as the reactive intermediate with the confinement of the zeolite lattice facilitating the reactivity observed. Furthermore, Dubkov et al. [85] employed Mössbauer spectroscopy to reveal that the active oxygen species with adjacent Fe^{2+} atoms existed as mononuclear sites upon decomposition of N_2O in Fe–ZSM-5. Interestingly, Sklenak and coworkers recently reported that methane activation with N_2O was possible using binuclear Co and Ni supported in a ferrierite zeolite [86]. Such transition metal structures have generally been overlooked compared with the supported iron and copper zeolite catalysts.

Fellah and Onal studied the direct methane-to-methanol oxidation on Fe–ZSM-5 and Co–ZSM-5 clusters using N_2O as an oxidant [87]. The group used DFT implemented using the Gaussian program to identify the mechanistic steps through which this reaction occurs. The effect of water on methanol formation was also studied. The ZSM-5 was modeled as a cluster ($(SiH_3)_4AlO_4M$) where M is either Fe or Cu. The reaction mechanism proposed involves the decomposition of the N_2O molecule forming α-oxygen on a Fe/Cu–ZSM-5 cluster. The second and third steps involve the abstraction of hydrogen from methane followed by the formation of a hydroxy complex. The energy barrier for the hydrogen abstraction step on Fe–ZSM-5 and Cu–ZSM-5 was found to be 66.90 and 62.80 kJ mol^{-1}, respectively. Even though the activation barrier for the hydrogen abstraction step was relatively low, the methanol formation step had barriers that were significantly higher. The methanol formation step was found to be the rate-determining step with activation barriers of 205 and 222 kJ mol^{-1} for Cu–ZSM-5 and Fe–ZSM-5, respectively.

6.4 Conclusions and Outlook

The selective oxidation of methane to oxygenates over heterogeneous catalysts continues to be one of the most challenging problems in chemistry. As the vast reserves of shale gas are extracted, demand for efficient methane conversion technologies will continue to increase. Despite significant effort from researchers around the globe, no catalyst or process has been reported that comes close to commercial application. The limitations of the current state-of-the-art catalysts are typically (i) low methane conversion, (ii) low selectivity to oxygenates, and (iii) prohibitively expensive oxidants.

The mechanisms of methane activation using N_2O or H_2O_2 as the oxidant are relatively well understood. However, despite this knowledge, only marginal increases in the oxygenate yields have been made in several years of research. Novel methane activation mechanisms and catalysts continue to emerge, including single-site catalysts [40] and by the incorporation of O_2 [37] and H_2O into the product [88]. These advances are undoubtedly important, but as important are the strategies to protect methanol from over-oxidation at appreciable methane conversion. Nørskov and coworkers recently analyzed a large library of experimental data, recognizing the selectivity–conversion limit associated with continuous processes. They proposed design strategies to move beyond this limit, which included the removal of methanol from the reaction via "collectors," the use of aqueous conditions to limit

the free energy of the methanol, and the use of diffusion-limited systems to prevent over-oxidation [89]. In the case of a collector, methanol is strongly adsorbed onto a surface, lowering the partial pressure of methanol in the reactor and limiting readsorption of methanol onto the active site of the catalyst. Once saturated, the methanol would be desorbed and the collector recycled. Lange et al. recently evaluated the feasibility of chemical looping technologies against industrial performance criteria. Based on typical methanol yields ($3\,mg\,g^{-1}$ of material), it was concluded that current production rates fall short by a factor of 50 compared with what would be required for an industrial process. This demonstrates that this technology still requires significant advances. Future research efforts must address in both methane activation and methanol protection if a process with acceptable yields is to be developed. Additionally, abundant and inexpensive oxidants must be used.

References

1 Elvidge, C.D., Zhizhin, M., Baugh, K. et al. (2016). Methods for global survey of natural gas flaring from visible infrared imaging radiometer suite data. *Energies* 9 (1): 14.

2 Iaquaniello, G., Centi, G., Salladini, A., and Palo, E. (2018). Methanol economy: environment demand, and marketing with a focus on the waste-to-methanol process. In: *Methanol*, 595–612. Elsevier.

3 Tian, P., Wei, Y., Ye, M., and Liu, Z. (2015). Methanol to olefins (MTO): from fundamentals to commercialization. *ACS Catal.* 5 (3): 1922–1938.

4 Khanmohammadi, M., Amani, S., Garmarudi, A.B., and Niaei, A. (2016). Methanol-to-propylene process: perspective of the most important catalysts and their behavior. *Chin. J. Catal.* 37 (3): 325–339.

5 Smejkal, Q., Linke, D., and Baerns, M. (2005). Energetic and economic evaluation of the production of acetic acid via ethane oxidation. *Chem. Eng. Process. Process Intensif.* 44 (4): 421–428.

6 Maitlis, P.M., Haynes, A., Sunley, G.J., and Howard, M.J. (1996). Methanol carbonylation revisited: thirty years on. *J. Chem. Soc., Dalton Trans.* (11): 2187–2196.

7 dos Santos, R.O., de Sousa Santos, L., and Prata, D.M. (2018). Simulation and optimization of a methanol synthesis process from different biogas sources. *J. Cleaner Prod.* 186: 821–830.

8 Hankin, A. and Shah, N. (2017). Process exploration and assessment for the production of methanol and dimethyl ether from carbon dioxide and water. *Sustainable Energy Fuels* 1 (7): 1541–1556.

9 Olah, G.A. (2005). Beyond oil and gas: the methanol economy. *Angew. Chem. Int. Ed.* 44 (18): 2636–2639.

10 Achmad, F., Kamarudin, S.K., Daud, W.R.W., and Majlan, E.H. (2011). Passive direct methanol fuel cells for portable electronic devices. *Appl. Energy* 88 (5): 1681–1689.

11 Tang, P., Zhu, Q., Wu, Z., and Ma, D. (2014). Methane activation: the past and future. *Energy Environ. Sci.* 7 (8): 2580–2591.

12 Bone, W.A. and Wheeler, R.V. (1903). CV.—The slow oxidation of methane at low temperatures. Part II. *J. Chem. Soc. Trans.* 83: 1074–1087.

13 Bone, W.A. and Wheeler, R.V. (1902). LVIII.—The slow oxidation of methane at low temperatures. *J. Chem. Soc. Trans.* 81: 535–549.

14 Trotsenko, Y.A. and Murrell, J.C. (2008). Metabolic aspects of aerobic obligate methanotrophy. *Adv. Appl. Microbiol.* 63: 183–229.

15 Hanson, R.S. and Hanson, T.E. (1996). Methanotrophic bacteria. *Microbiol. Rev.* 60 (2): 439–471.

16 Ross, M.O. and Rosenzweig, A.C. (2017). A tale of two methane monooxygenases. *J. Biol. Inorg. Chem.* 22 (2–3): 307–319.

17 Semrau, J.D., Dispirito, A.A., and Yoon, S. (2010). Methanotrophs and copper. *FEMS Microbiol. Rev.* 34 (4): 496–531.

18 Kondratenko, E.V., Peppel, T., Seeburg, D. et al. (2017). Methane conversion into different hydrocarbons or oxygenates: current status and future perspectives in catalyst development and reactor operation. *Cat. Sci. Technol.* 7: 366–381.

19 Colby, J., Stirling, D.I., and Dalton, H. (1977). The soluble methane mono-oxygenase of *Methylococcus capsulatus* (Bath). Its ability to oxygenate *n*-alkanes, *n*-alkenes, ethers, and alicyclic, aromatic and heterocyclic compounds. *Biochem. J.* 165 (2): 395–402.

20 Merkx, M., Kopp, D.A., Sazinsky, M.H. et al. (2001). Dioxygen activation and methane hydroxylation by soluble methane monooxygenase: a tale of two irons and three proteins. *Angew. Chem. Int. Ed.* 40 (15): 2782–2807.

21 Moshoeshoe, M., Nadiye-Tabbiruka, M.S., and Obuseng, V. (2017). A review of the chemistry, structure, properties and applications of zeolites. *Am. J. Mater. Sci.* 7 (5): 196–221.

22 Corma, A. (2003). State of the art and future challenges of zeolites as catalysts. *J. Catal.* 216 (1–2): 298–312.

23 Townsend, R.P. and Coker, E.N. (2001). Ion exchange in zeolites. *Stud. Surf. Sci. Catal.* 137 (9): 467–524.

24 Hammond, C., Forde, M.M., Ab Rahim, M.H. et al. (2012). Direct catalytic conversion of methane to methanol in an aqueous medium by using copper-promoted Fe-ZSM-5. *Angew. Chem. Int. Ed.* 51 (21): 5129–5133.

25 Rahman, A.K.M.L., Kumashiro, M., and Ishihara, T. (2011). Direct synthesis of formic acid by partial oxidation of methane on H-ZSM-5 solid acid catalyst. *Catal. Commun.* 12 (13): 1198–1200.

26 Hammond, C., Jenkins, R.L., Dimitratos, N. et al. (2012). Catalytic and mechanistic insights of the low-temperature selective oxidation of methane over Cu-promoted Fe-ZSM-5. *Chem. Eur. J.* 18 (49): 15735–15745.

27 Al-Shihri, S., Richard, C.J., and Chadwick, D. (2017). Selective oxidation of methane to methanol over ZSM-5 catalysts in aqueous hydrogen peroxide: role of formaldehyde. *ChemCatChem* 9 (7): 1276–1283.

28 Ayodele, O.B. (2016). Structure and reactivity of ZSM-5 supported oxalate ligand functionalized nano-Fe catalyst for low temperature direct methane conversion to methanol. *Energy Convers. Manage.* 126: 537–547.

29 Xiao, P., Wang, Y., Nishitoba, T. et al. (2019). Selective oxidation of methane to methanol with H_2O_2 over an Fe-MFI zeolite catalyst using sulfolane solvent. *Chem. Commun.* 55: 2896–2899.

30 Tang, J., Yin, H.Y., and Zhang, J.L. (2017). Luminescent zinc complexes as bioprobes for imaging molecular events in live cells. In: *Inorganic and Organometallic Transition Metal Complexes with Biological Molecules and Living Cells*, 1–53. Elsevier Inc.

31 Edwards, J.K., Solsona, B.E., Landon, P. et al. (2005). Direct synthesis of hydrogen peroxide from H_2 and O_2 using TiO_2-supported Au–Pd catalysts. *J. Catal.* 236 (1): 69–79.

32 Lin, M. and Sen, A. (1992). A highly catalytic system for the direct oxidation of lower alkanes by dioxygen in aqueous medium. A formal heterogeneous analog of alkane monooxygenases. *J. Am. Chem. Soc.* 114 (18): 7307–7308.

33 Ab Rahim, M.H., Forde, M.M., Jenkins, R.L. et al. (2013). Oxidation of methane to methanol with hydrogen peroxide using supported gold–palladium alloy nanoparticles. *Angew. Chem. Int. Ed.* 52 (4): 1280–1284.

34 Ab Rahim, M.H., Forde, M.M., Hammond, C. et al. (2013). Systematic study of the oxidation of methane using supported gold palladium nanoparticles under mild aqueous conditions. *Top. Catal.* 56 (18–20): 1843–1857.

35 Ab Rahim, M.H., Armstrong, R.D., Hammond, C. et al. (2016). Low temperature selective oxidation of methane to methanol using titania supported gold palladium copper catalysts. *Cat. Sci. Technol.* 6: 3410–3418.

36 Williams, C., Carter, J.H., Dummer, N.F. et al. (2018). Selective oxidation of methane to methanol using supported AuPd catalysts prepared by stabilizer-free sol-immobilization. *ACS Catal.* 8 (3): 2567–2576.

37 Agarwal, N., Freakley, S.J., McVicker, R.U. et al. (2017). Aqueous Au-Pd colloids catalyze selective CH_4 oxidation to CH_3OH with O_2 under mild conditions. *Science* 358 (6360): 223–227.

38 Hammond, C., Conrad, S., and Hermans, I. (2012). Oxidative methane upgrading. *ChemSusChem* 5 (9): 1668–1686.

39 Ravi, M., Ranocchiari, M., and van Bokhoven, J.A. (2017). A critical assessment of the direct catalytic oxidation of methane to methanol. *Angew. Chem. Int. Ed.* 56 (52): 16464–16483.

40 Shan, J., Li, M., Allard, L.F. et al. (2017). Mild oxidation of methane to methanol or acetic acid on supported isolated rhodium catalysts. *Nature* 551 (7682): 605–608.

41 Narsimhan, K., Michaelis, V.K., Mathies, G. et al. (2015). Methane to acetic acid over Cu-exchanged zeolites: mechanistic insights from a site-specific carbonylation reaction. *J. Am. Chem. Soc.* 137 (5): 1825–1832.

42 Tang, Y., Li, Y., Fung, V. et al. (2018). Single rhodium atoms anchored in micropores for efficient transformation of methane under mild conditions. *Nat. Commun.* 9: 1231.

43 Palkovits, R., Antonietti, M., Kuhn, P. et al. (2009). Solid catalysts for the selective low-temperature oxidation of methane to methanol. *Angew. Chem. Int. Ed.* 48 (37): 6909–6912.

44 Periana, R.A., Taube, D.J., Gamble, S. et al. (1998). Platinum catalysts for the high-yield oxidation of methane to a methanol derivative. *Science* 280 (5363): 560–564.

45 Li, T., Wang, S.J., Yu, C.S. et al. (2011). Direct conversion of methane to methanol over nano-[Au/SiO_2] in [Bmim] Cl ionic liquid. *Appl. Catal., A* 398 (1–2): 150–154.

46 Otsuka, K. and Wang, Y. (2001). Direct conversion of methane into oxygenates. *Appl. Catal., A* 222 (1): 145–161.

47 Burch, R., Squire, G.D., and Tsang, S.C. (1989). Direct conversion of methane into methanol. *J. Chem. Soc., Faraday Trans.* 1 85 (10): 3561–3568.

48 Walker, G.S., Lapszewicz, J.A., and Foulds, G.A. (1994). Partial oxidation of methane to methanol-comparison of heterogeneous catalyst and homogeneous gas phase reactions. *Catal. Today* 21 (2–3): 519–526.

49 Feng, W., Knopf, F.C., and Dooley, K.M. (1994). Effects of pressure, third bodies, and temperature profiling on the noncatalytic partial oxidation of methane. *Energy Fuels* 8 (4): 815–822.

50 Zhang, Q., He, D., Li, J. et al. (2002). Comparatively high yield methanol production from gas phase partial oxidation of methane. *Appl. Catal., A* 224 (1–2): 201–207.

51 Foulds, G.A., Gray, B.F., Miller, S.A., and Walker, G.S. (1993). Homogeneous gas-phase oxidation of methane using oxygen as oxidant in an annular reactor. *Ind. Eng. Chem. Res.* 32 (5): 780–787.

52 Chun, J.W. and Anthony, R.G. (1993). Partial oxidation of methane, methanol, and mixtures of methane and methanol, methane and ethane, and methane, carbon dioxide, and carbon monoxide. *Ind. Eng. Chem. Res.* 32 (5): 788–795.

53 Rytz, D.W. and Baiker, A. (1991). Partial oxidation of methane to methanol in a flow reactor at elevated pressure. *Ind. Eng. Chem. Res.* 30 (10): 2287–2292.

54 Holmen, A. (2009). Direct conversion of methane to fuels and chemicals. *Catal. Today* 142 (1–2): 2–8.

55 Hargreaves, J.S.J., Hutchings, G.J., and Joyner, R.W. (1990). Control of product selectivity in the partial oxidation of methane. *Nature* 348 (6300): 428–429.

56 Ito, T. and Lunsford, J.H. (1985). Synthesis of ethylene and ethane by partial oxidation of methane over lithium-doped magnesium oxide. *Nature* 314: 721.

57 de Vekki, A.V. and Marakaev, S.T. (2009). Catalytic partial oxidation of methane to formaldehyde. *Russ. J. Appl. Chem.* 82 (4): 521–536.

58 Dowden, D.A.; Walker, G.T. (1971). Br. Patent 1,244,001.

59 Zhang, Q., He, D., and Zhu, Q. (2003). Recent progress in direct partial oxidation of methane to methanol. *J. Nat. Gas Chem.* 12: 81–89.

60 Ohler, N. and Bell, A.T. (2006). Study of the elementary processes involved in the selective oxidation of methane over MoO_x/SiO_2. *J. Phys. Chem. B* 110 (6): 2700–2709.

61 Banares, M.A., Dauphin, L., Calvoperez, V. et al. (1995). Activity and characterization of self-supported model catalysts derived from cobalt-based clusters of clusters: hydrogenation of 1,3-butadiene. *J. Catal.* 152 (2): 396–409.

62 Taylor, S.H., Hargreaves, J.S.J., Hutchings, G.J. et al. (1998). The partial oxidation of methane to methanol: an approach to catalyst design. *Catal. Today* 42 (3): 217–224.

63 Parmaliana, A., Frusteri, F., Mezzapica, A. et al. (1993). Novel high activity catalyst for partial oxidation of methane to formaldehyde. *J. Chem. Soc., Chem. Commun.* (9): 751–753.

64 Frusteri, F., Arena, F., Martra, G. et al. (2001). Mechanistic evidences of the synthesis of methyl formate from methane and air on oxide catalysts. *Catal. Today* 64 (1–2, 102): 97.

65 Barbero, J.A., Alvarez, M.C., Banares, M.A. et al. (2002). Breakthrough in the direct conversion of methane into C_1-oxygenates. *Chem. Commun.* (11): 1184–1185.

66 Zuo, Z., Ramírez, P.J., Senanayake, S.D. et al. (2016). Low-temperature conversion of methane to methanol on CeO_x/Cu_2O catalysts: water controlled activation of the C–H bond. *J. Am. Chem. Soc.* 138 (42): 13810–13813.

67 Latimer, A.A., Aljama, H., Kakekhani, A. et al. (2017). Mechanistic insights into heterogeneous methane activation. *Phys. Chem. Chem. Phys.* 19: 3575–3581.

68 Latimer, A.A., Kulkarni, A.R., Aljama, H. et al. (2017). Understanding trends in C-H bond activation in heterogeneous catalysis. *Nat. Mater.* 16 (2): 225–229.

69 Xi, Y. and Heyden, A. (2019). Direct oxidation of methane to methanol enabled by electronic atomic monolayer–metal support interaction. *ACS Catal.* 9 (7): 6073–6079.

70 Le, H.V., Parishan, S., Sagaltchik, A. et al. (2018). Stepwise methane-to-methanol conversion on CuO/SBA-15. *Chem. Eur. J.* 24 (18): 12592–12599.

71 Narsimhan, K., Iyoki, K., Dinh, K., and Román-Leshkov, Y. (2016). Catalytic oxidation of methane into methanol over copper-exchanged zeolites with oxygen at low temperature. *ACS Cent. Sci.* 2 (6): 424–429.

72 Le, H.V., Parishan, S., Sagaltchik, A. et al. (2017). Solid-state ion-exchanged Cu/mordenite catalysts for the direct conversion of methane to methanol. *ACS Catal.* 7 (2): 1403–1412.

73 Sushkevich, V.L., Palagin, D., and van Bokhoven, J.A. (2018). The effect of the active-site structure on the activity of copper mordenite in the aerobic and anaerobic conversion of methane into methanol. *Angew. Chem. Int. Ed.* 57 (29): 8906–8910.

74 Pappas, D.K., Martini, A., Dyballa, M. et al. (2018). The nuclearity of the active site for methane to methanol conversion in Cu-mordenite: a quantitative assessment. *J. Am. Chem. Soc.* 140 (45): 15270–15278.

75 Yokoi, T., Kunitake, Y., Osuga, R., et al. (2019). Effect of framework Al location in metal cation-exchanged zeolites on methane conversion. Abstract Paper 257th ACS National Meeting & Exposition, Orlando, FL, United States (31 March–4 April 2019).

76 Groothaert, M.H., Smeets, P.J., Sels, B.F. et al. (2005). Selective oxidation of methane by the bis(μ-oxo)dicopper core stabilized on ZSM-5 and mordenite zeolites. *J. Am. Chem. Soc.* 127 (5): 1394–1395.

77 Sobolev, V.I., Kharitonov, A.S., Panna, O.V., and Panov, G.I. (1995). Room temperature oxidation of methane to methanol on FeZSM-5 zeolite surface. *Stud. Surf. Sci. Catal.* 98: 159–160.

78 Starokon, E.V., Parfenov, M.V., Arzumanov, S.S. et al. (2013). Oxidation of methane to methanol on the surface of FeZSM-5 zeolite. *J. Catal.* 300: 47–54.

79 Parfenov, M.V., Starokon, E.V., Pirutko, L.V., and Panov, G.I. (2014). Quasicatalytic and catalytic oxidation of methane to methanol by nitrous oxide over FeZSM-5 zeolite. *J. Catal.* 318: 14–21.

80 Ovanesyan, N.S., Shteinman, A.A., Dubkov, K.A. et al. (1998). The state of iron in the Fe-ZSM-5-N_2O system for selective oxidation of methane to methanol from data of Mössbauer spectroscopy. *Kinet. Catal.* 39 (6): 792–797.

81 Starokon, E.V., Parfenov, M.V., Pirutko, L.V. et al. (2011). Room-temperature oxidation of methane by α-oxygen and extraction of products from the FeZSM-5 surface. *J. Phys. Chem. C* 115 (5): 2155–2161.

82 Chow, Y.K., Dummer, N.F., Carter, J.H. et al. (2018). Investigating the influence of acid sites in continuous methane oxidation with N_2O over Fe/MFI zeolites. *Cat. Sci. Technol.* 8: 154–163.

83 Chow, Y.K., Dummer, N.F., Carter, J.H. et al. (2018). A kinetic study of methane partial oxidation over Fe-ZSM-5 using N_2O as an oxidant. *ChemPhysChem* 19 (4): 402–411.

84 Snyder, B.E.R., Vanelderen, P., Bols, M.L. et al. (2016). The active site of low-temperature methane hydroxylation in iron-containing zeolites. *Nature* 536: 317–321.

85 Dubkov, K.A., Ovanesyan, N.S., Shteinman, A.A. et al. (2002). Evolution of iron states and formation of α-sites upon activation of FeZSM-5 zeolites. *J. Catal.* 207 (2): 341–352.

86 Tabor, E., Lemishka, M., Sobalik, Z. et al. (2019). Low-temperature selective oxidation of methane over distant binuclear cationic centers in zeolites. *Commun. Chem.* 2: 71.

87 Fellah, M.F. and Onal, I. (2010). Direct methane oxidation to methanol by N_2O on Fe- and Co-ZSM-5 clusters with and without water: a density functional theory study. *J. Phys. Chem. C* 114 (7): 3042–3051.

88 Sushkevich, V.L., Palagin, D., Ranocchiari, M., and Van Bokhoven, J.A. (2017). Selective anaerobic oxidation of methane enables direct synthesis of methanol. *Science* 356 (6337): 523–527.

89 Latimer, A.A., Kakekhani, A., Kulkarni, A.R., and Nørskov, J.K. (2018). Direct methane to methanol: the selectivity-conversion limit and design strategies. *ACS Catal.* 8 (8): 6894–6907.

Part III

Alkane Activation

7

Catalytic Cracking of Hydrocarbons to Light Olefins

Xia Xiao[1] *and Zhen Zhao*[1,2]

[1] *Shenyang Normal University, Institute of Catalysis for Energy and Environment, College of Chemistry and Chemical Engineering, 253#, Huanghe North Street, Huanggu District, Shenyang, 110034, P.R. China*
[2] *China University of Petroleum Beijing, State Key Laboratory of Heavy Oil Processing, 18#, Fuxue Road, Changping District, Beijing 102249, P.R. China*

7.1 Background Introduction

Ethylene, propylene, and butylene are important building blocks for the production of various polymers and other value-added chemicals in the chemical industry, an industry of around 500 billion dollars and expected to grow to over 958 billion by 2025 [1, 2]. Therefore, studies on enhancing the production of light olefins have attracted more and more interest. Light olefins can be produced by many important industrial pathways such as steam cracking [2], light alkane dehydrogenation [3, 4], Fischer–Tropsch synthesis to olefins [5, 6], and methanol to olefins [7, 8]. Through more than 90 years of development, steam cracking has become the main technology for the production of light olefins because of its wide range of feedstocks, ranging from ethane to gas oil [9]. However, steam cracking suffers from multiple limitations: high reaction temperature (over 800 °C, requiring expensive construction materials and leading to very high energy consumption), inflexibility of the product slate and, in particular, low propylene/ethene (P/E) ratios (which are strongly determined by the feed composition), high investment costs to benefit from economy of scale, etc.

In addition to the traditional steam cracking technology, catalytic cracking of naphtha to light olefins in the presence of a highly selective catalyst has been considered as a promising alternative because of its ability to reduce energy consumption and CO_2 emissions and its ease of controlling product distribution [10–12]. There is a rising enthusiasm for petrochemical enterprises to develop the technology of direct catalytic cracking of crude oil to produce value-added products such as light olefins and aromatics, with the challenges of energy shortage and the increasing demand for low-carbon economy [13]. It is not difficult to imagine that the reaction conditions for the cracking of crude oil to produce olefins and aromatics are relatively harsh, and the reaction mechanism is complicated [14, 15]. In the process of producing low-carbon olefins by catalytic cracking, in addition to

Heterogeneous Catalysis for Sustainable Energy, First Edition. Edited by Landong Li and Justin S. J. Hargreaves.

the design of the reactor and the optimization of the process, the development of high-efficiency catalysts is the key technology.

Different catalytic cracking processes require different catalysts, and the development of catalysts needs to be matched with process operating parameters. In thermodynamic terms, the catalytic cracking reaction is an endothermic reaction, and high temperature is conducive to the cracking reaction. In addition, the kinetics of the catalytic cracking reaction follows the characteristics of parallel sequential reactions. While the main cracking reaction is proceeding, a series of side reactions such as hydrogen transfer, dehydrogenation aromatization, and coking occur. Moreover, many staggered reactions occur at the same time, producing a very complex reaction network. Therefore, it is desirable to design an efficient cracking catalyst with high catalytic activity, stability, and selectivity to olefins and aromatics simultaneously under harsh reaction conditions.

7.2 Reaction Mechanism of Catalytic Cracking over Zeolites

In the past, the mechanism of hydrocarbon catalytic cracking has been extensively studied [16, 17]. There are three well-recognized reaction mechanisms: the free radical mechanism, the carbenium ion mechanism, and the free radical and carbenium ion mechanism. Catalytic cracking in the presence of solid acid catalysts follows the carbenium ion reaction mechanism. Generally speaking, the catalytic cracking process is characterized by both catalytic reaction and thermal reaction. Oxide catalysts are dominated by the free radical reaction mechanism under high-temperature steaming conditions. However, solid acid zeolite catalysts are dominated by the carbocation reaction mechanism under low-temperature conditions [18].

Bloch et al. observed that *n*-butane isomerized to isobutane under the influence of pure aluminum chloride only in the presence of HCl [19]. Thus, they proposed that the ionization step occurred through the initial hydrolysis of the alkanes, as evidenced by the formation of hydrogen in the initial stage of the reaction. Paraffin has high stability and low reactivity, and it is difficult to give functional groups to paraffin directly. Although many studies agree that the carbocations are key intermediates for isomerization, cracking, and alkylation reactions over solid acids, the mode of their formation from low reactivity hydrocarbons is still under debate.

7.2.1 Monomolecular or α-Protolytic Cracking Mechanism

As is known, the activation of alkane molecules and the generation of carbonium ions or carbenium ion intermediate species are the key steps in the pathways of hydrocarbon cracking. The cracking reaction network is quite complex and involves several consecutive-parallel reactions, such as dehydrogenation, cracking, isomerization, alkylation, and aromatization, for the formation of light olefins and by-product alkanes and coke [20]. Meanwhile, light olefins are much easier to activate and transform than paraffins of naphtha on zeolite catalysts via secondary reactions, resulting in a low atomic economy of the naphtha transformation process [21].

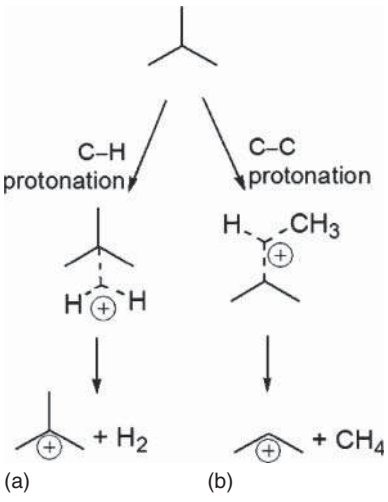

Figure 7.1 Protonation of saturated alkanes over acid zeolites. Source: Reproduced with permission from Blay et al. [2]; © 2017 American Chemical Society.

Various reaction pathways such as protolysis [22], hydride abstraction by preexisting carbenium ions [23], hydride abstraction by Lewis acids [24–26], oxidation by traces of metal impurities, and protonation of alkene impurities or of those formed through thermal cracking [27] have been proposed, due to the longstanding debate about the initial steps of hydrocarbon conversion on solid acid catalysts. Today, it is widely accepted that the first mode of alkane activation occurs in many cases through the Haag–Dessau mechanism, also known as the monomolecular or α-protolytic cracking mechanism [28] (Figure 7.1). The Haag–Dessau mechanism involves the formation of high-energy pentacoordinated carbonium-like species. Meanwhile, the formation of hydrogen (dehydrogenation) and methane/ethane (cracking) through carbonium-like intermediates collapses.

Boronat and Corma proposed that both carbenium and carbonium ions might exist as the true reaction intermediates in zeolite-catalyzed processes only when the positive charge is not easily accessible to framework oxygen atoms [29]. As shown in Figure 7.2, carbonium ions can be directly formed from adsorbed olefins and paraffins, following a concerted mechanism that involves the simultaneous protonation of the olefin by the bridging hydroxyl group and the interaction of the resulting positively charged fragment with the paraffin.

Figure 7.3 shows that the catalytic cracking of hydrocarbons under relevant conditions can proceed through a monomolecular mechanism [2]. The monomolecular cracking involves the direct protonation of paraffin to form a high-energy transition state that may resemble a pentacoordinated carbonium ion, which is subsequently cracked or dehydrogenated to produce light olefins. The monomolecular mechanism is dominant at a low partial pressure of reactants [30], low concentration of alkenes in the reaction environment, high temperature, and low conversion [31].

Haag et al. demonstrated the acid-catalyzed cracking of simple paraffins at high temperature and low partial pressure did not occur by the classical bimolecular carbenium chain reaction, but by the protonation of paraffins to produce pentacoordinated carbonium ion intermediates [32]. Moreover, the pore diameter of

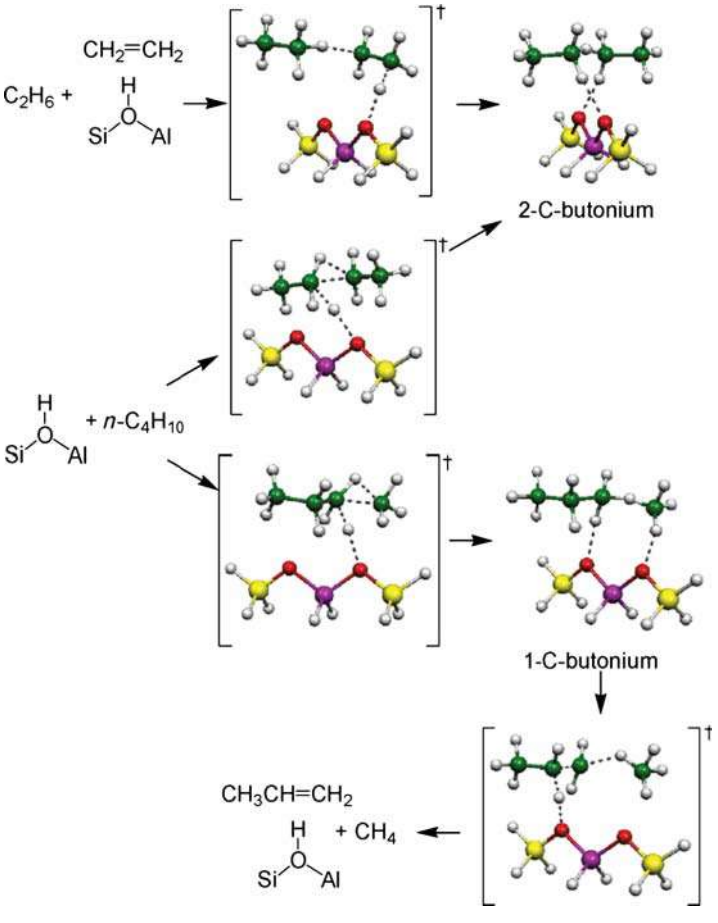

Figure 7.2 Zeolite-catalyzed formation, rearrangements, and dissociation of $C_4H_{11}^+$ carbonium ions. Source: Reproduced with permission from Boronat and Corma [29]; © 2008 Elsevier.

zeolite catalysts influences the reaction mechanism. Generally speaking, narrow- or medium-pore zeolites, such as H–ZSM-5 [33–35], favor monomolecular cracking, whereas large-pore zeolites and amorphous silica alumina favor classical bimolecular cracking. Notably, the medium-pore zeolites with high Si/Al ratio [36], i.e. protons well-dispersed throughout the zeolite (low acid site density) [37], favor the monomolecular cracking.

7.2.2 Bimolecular Cracking Mechanism

Bimolecular cracking is the classical chain process involving the formation of carbenium-like species by hydrogen transfer between a paraffin molecule and a preexisting (shorter) chemisorbed carbenium ion intermediates. Figure 7.4 shows catalytic cracking of hydrocarbons under relevant conditions can proceed through

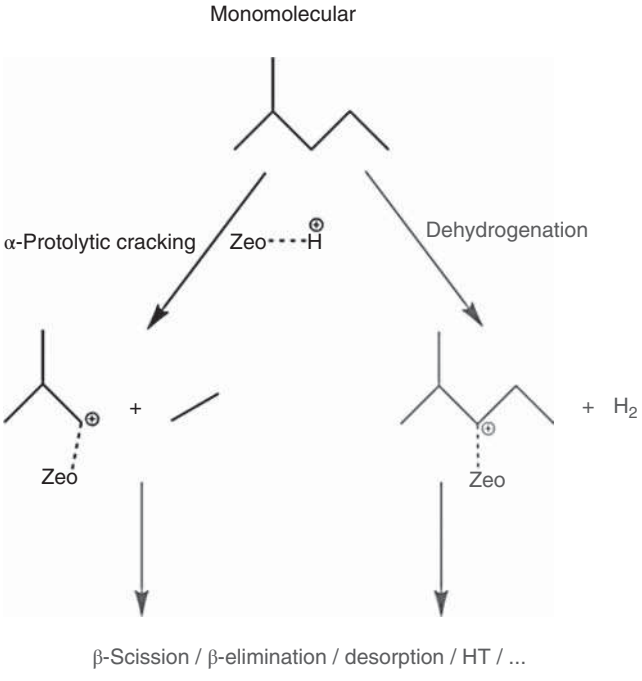

Figure 7.3 Monomolecular cracking mechanisms of alkanes over acid zeolites. Source: Reproduced with permission from Blay et al. [2]; © 2017 American Chemical Society.

Figure 7.4 Bimolecular cracking mechanisms of alkanes over acid zeolites. Source: Reproduced with permission from Blay et al. [2]; © 2017 American Chemical Society.

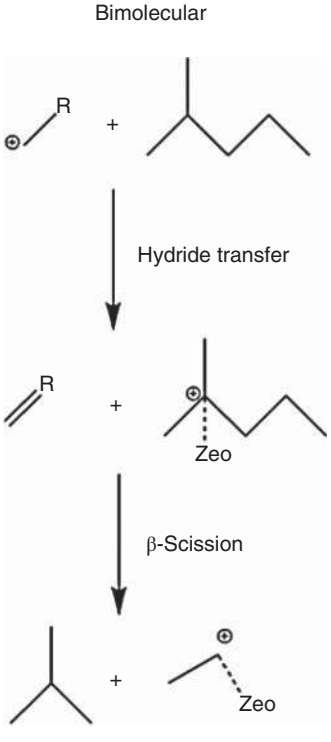

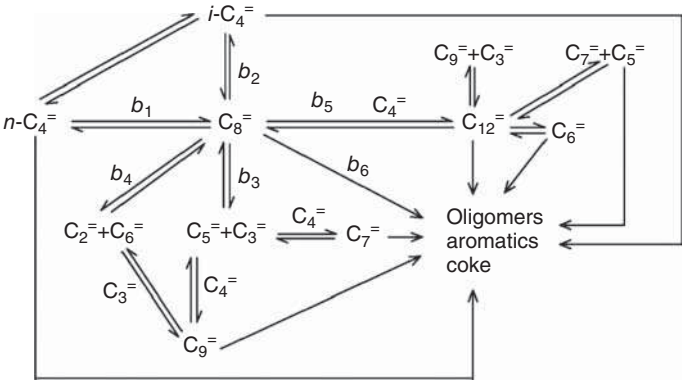

Figure 7.5 Dimolecular mechanism of *n*-butene pyrolytic cracking over H–ZSM-5 zeolite. Source: Reproduced with permission from Li et al. [39]; © 2006 Elsevier.

the bimolecular mechanism. The formation of a new carbenium ion is followed by skeletal isomerization prior to β-scission to avoid the formation of primary carbenium ions and their cracking by β-scission to yield ethylene and propylene.

The bimolecular cracking predominates at mild temperatures (usually below 350 °C) and high olefin concentration, i.e. high conversion. The catalytic cracking of alkene into shorter olefins is a very complex reaction process, including oligomerization, disproportionation, isomerization, cracking, hydrogen transfer, and aromatization and other parallel and continuous reactions [38].

Li et al. reported that the catalytic thermal cracking of *n*-butene only follows the bimolecular reaction mechanism [39]. As shown in Figure 7.5, the catalytic thermal cracking of *n*-butene includes two consecutive reactions: the dimerization of *n*-butene and the cracking of the intermediate dimer. Each of these species can also participate in hydrogen transfer reactions, leading to different alkane, cyclic, and aromatic molecules. Meng et al. suggested a bimolecular mechanism based on the experiments for the catalytic pyrolysis of *n*-butene in the temperatures range between 480 and 560 °C [40]. Similar bimolecular reaction pathways have been observed in commercial Omega processes. Tsunoda and Sekiguchi [41] reported that a range of olefins with different chain lengths were available to oligomerize with butenes, leading to intermediate carbenium-like species of different chain lengths adsorbed on zeolite acid centers, which contributed to the observation of pentenes, hexenes, heptenes, and so on, in addition to the most abundant octenes.

Al-Khattaf and coworkers [42] revealed the formation of alkenes, including propylene, increased and those of alkanes and aromatics decreased with decreasing Al content. Moreover, the silicalite-1 was an efficient catalyst for the production of propylene in the catalytic cracking of alkenes. As shown in Figure 7.6, the 1-butene is protonated by Brønsted acid site to form 2-butyl cation, and then it converts to *trans*- and *cis*-2-butene by deprotonation, octane and dodecene isomers by oligomerization, and isobutene by skeletal isomerization. Octene and dodecene isomers undergo cracking to form alkenes. At last alkenes undergo hydrogen transfer to form alkanes

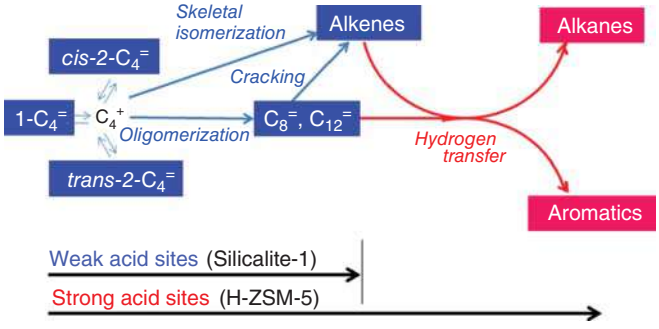

Figure 7.6 Simplified reaction pathway of reaction of 1-butene over H–ZSM-5 and silicalite-1. Source: Reproduced with permission from Arudra et al. [42]; © 2014 American Chemical Society.

and aromatics. Among these reactions, the double-bond isomerization is the easiest reaction, which proceeds at low temperatures.

Lin et al. found that the reaction pathways for the catalytic cracking of 1-butene to propylene could be controlled by adjusting the acid strength distribution of ZSM-5 zeolite [43]. This was achieved by different treatments. For instance, phosphoric acid treatment allowed very preferential removal of weak acid sites, a HNO_3 treatment (6 M) removed both strong and weak acid sites, while treatment with HNO_3 (2 M) allowed increasing the proportion of strong/weak acid centers. The P/E ratio increased with the decreased amount of strong acid sites, due to the activation energies of different reaction pathways influenced by acid strength to a different extent. Pathway II occurred through a primary cation, while pathway III proceeded through a secondary or tertiary carbenium ion. Strong acid sites could favorably promote the pathways I and II, while the weak acid sites preferred the pathway III, since pathway II required strong acid sites to overcome the energy barrier (Figure 7.7). The P/E

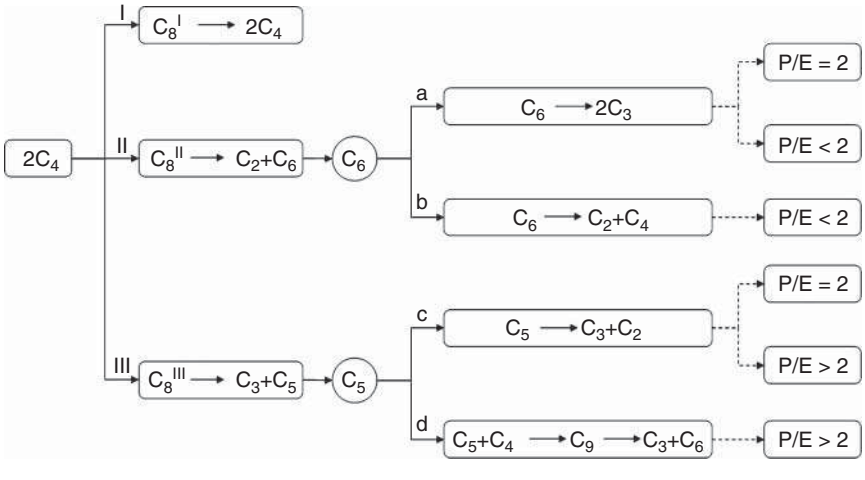

Figure 7.7 Three dimolecular dimerization cracking reaction pathways of 1-butene over ZSM-5. Source: Reproduced with permission from Lin et al. [43]; © 2014 Elsevier.

ratio and selectivity to propylene could be significantly improved through reducing the amount of strong acid sites on H–ZSM-5.

7.2.3 Monomolecular and Bimolecular Cracking Mechanism

Krannila et al. [17] observed the occurrence of two simultaneous mechanisms: (i) a monomolecular mechanism proceeding through the pentacoordinated carbonium ion formed by protonation of the *n*-butane at the two position and (ii) a bimolecular hydride transfer proceeding through carbenium ion intermediates for *n*-butane cracking catalyzed by H–ZSM-5. Haag et al. [32] also reported the mechanism of paraffin cracking and proposed that cracking of *n*-hexane and of 3-methylpentane proceeded by two simultaneous pathways, i.e. the bimolecular cracking mechanism and the monomolecular cracking mechanism. Taking the catalytic cracking of naphtha model compound *n*-octane as an example, the possible reaction pathways of *n*-octane cracking over ZSM-5 zeolite catalyst are summarized in Figure 7.8.

Alkane activation occurs mainly through the Haag–Dessau mechanism, also known as monomolecular or α-protolytic cracking mechanism, and bimolecular mechanism [30, 44, 45]. The monomolecular reactions occur on zeolite Brønsted acid sites, where alkanes are protonated to form pentacoordinated carbonium ion transition states that can undergo either protolytic cracking of a C—C bond yielding alkanes (including methane and ethane) or protolytic dehydrogenation of the carbonium ion yielding hydrogen and carbenium ions [46]. These carbenium ions subsequently form alkenes via back-donation of a proton to the zeolite catalyst. Instead, bimolecular mechanism involves the formation of carbenium ion by hydride transfer to preexisting chemisorbed intermediates and their cracking by *β*-scission to produce alkenes. In paraffin cracking pathways, the monomolecular and bimolecular pathways always coincide and battle with each other in the chain reaction mechanism, and which mechanism is preferable mainly depends on relevant conditions [47]. According to Figure 7.8, for a monomolecular mechanism, a *n*-octane molecule obtains a H^+ from ZSM-5 catalyst to produce a C_8^+ carbonium ion, which immediately isomerizes to reach dynamic balance. Then, the C_8^+ carbonium ion converts to $C_2^=\sim C_6^=$ light olefins and $C_2^0\sim C_6^0$ alkanes by *β*-scission, hydride transfer, and deprotonation reactions. Another monomolecular pathway is C_8^+ carbonium ion converted to hydrogen and C_8^+ carbenium ions by protolytic dehydrogenation reaction. However, for a bimolecular mechanism, a *n*-octane molecule undergoes hydride transfer to preexisting $C_2^+\sim C_6^+$ intermediates to produce a C_8^+ carbenium ion and $C_2^=\sim C_6^=$ light olefins. Moreover, $C_2^=\sim C_6^=$ light olefin products obtained from cracking main reactions will undergo secondary reaction to produce a series of by-products. It can be seen that the *n*-octane cracking reaction network is relatively complicated, and various side reactions are accompanied by the main cracking reaction. Hydrogen and aromatic BTX (the total of benzene, toluene, and xylene) are resulted from the dehydrogenation–aromatization and deprotonation reaction. Methane and ethane are generated by hydrogenation and dealkylation. $C_3^0\sim C_4^0$ alkanes and another part of aromatics are produced by hydride transfer reaction. Aromatics will continue to form coke by oligomerization,

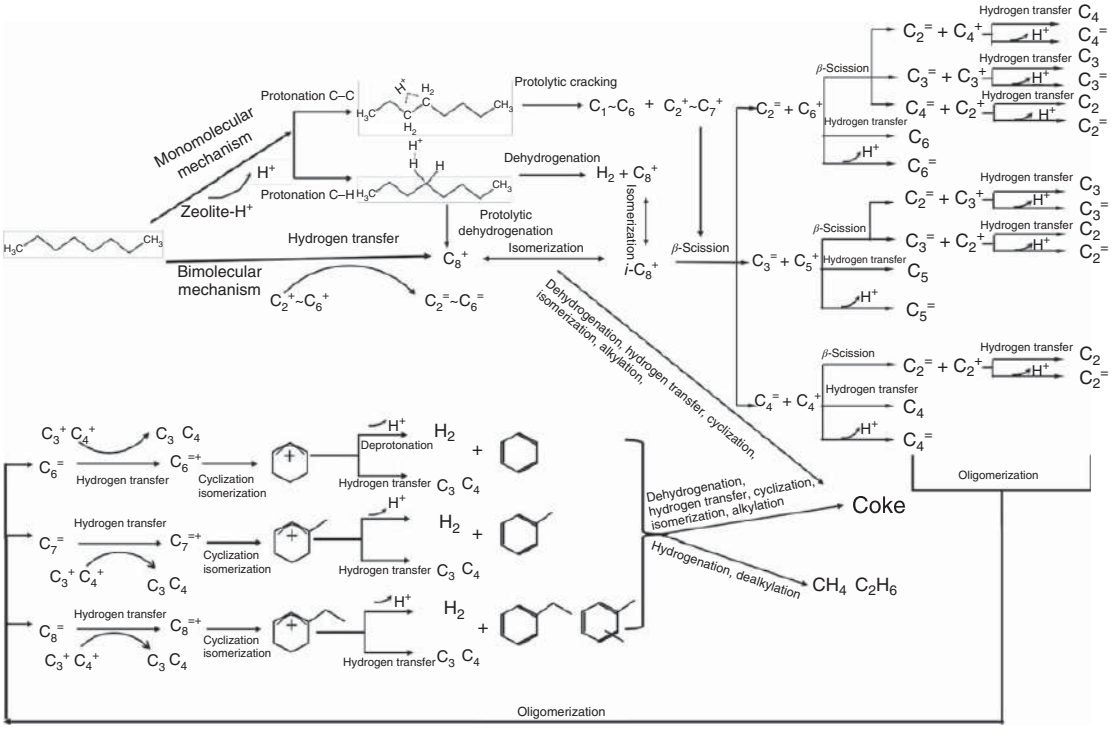

Figure 7.8 Possible reaction routes for the *n*-octane cracking over ZSM-5 catalysts.

hydride transfer reactions, alkylation, cyclization, aromatization, and dehydrogenation. Apparently, to improve the selectivity of ethylene, propylene, and light olefins, side reactions should be suppressed, and the main reactions should be strengthened through regulating the reaction conditions and the physicochemical properties of catalysts.

7.3 Development of Zeolite Catalysts

Zeolites are microporous inorganic materials with regular intracrystalline cavities and channels of molecular dimensions [48]. The crystallinity is a major feature of zeolites, which imparts them with a high thermal and hydrothermal stability. Moreover, the micropore sizes of zeolites are usually below 1 nm, which render large surface areas and unique size/shape selectivity properties that are advantageous for catalysis [49]. The existence of strong and tunable acidity is another important feature of zeolites, which guarantee their utilization as catalysts in a large number of acid catalyzed reactions, mainly in processes of interest to the oil refining and petrochemical industries [50]. The Brønsted/Lewis acid ratio may be varied over a wide range by changing the composition (Si/Al molar ratio), pretreatment conditions, and zeolite structure. Currently, various zeolites with different topologies (channels/cavities), framework compositions (strength and density of acidic sites), and morphologies (crystal dimensions and microporosity and mesoporosity) have been studied in the catalytic cracking of hydrocarbons to light olefins.

7.3.1 Zeolites with Different Framework Structures

Zeolites with the different topologies and compositions such as ZSM-5, SAPO-34, MCM-22, ferrierite, mordenite, MCM-49, ZSM-48, ZSM-11, ZSM-23, and IM-5 zeolite have been studied for the purpose of propylene production by cracking. Representative zeolites are summarized in Table 7.1.

Among these materials, the presence of pores of different sizes can affect the diffusion of certain molecules through different pores (so-called molecular traffic control) or the location of active sites in certain crystallographic positions, hence influencing the catalytic results. To maximize the selectivity to light olefins in catalytic cracking, small-pore zeolites have attracted more and more attention [51]. Some relevant examples from the literature are discussed below.

The FER zeolite is used industrially for the isomerization of 1-butene [52]. Some researchers also reported the use of FER for the production of light olefins from the cracking of naphtha-related compounds [53, 54]. In these cases, FER was shown to be more selective for the production of olefins than other zeolites such as ZSM-5. Bastiani et al. observed that H-FER exhibited higher selectivity to methane, ethane, propylene, and butenes, whereas ethylene, propane, and butane selectivity was higher for H–ZSM-5 (Figure 7.9). H-FER seems to inhibit the hydrogen transfer reactions involving the C3 and C4 fractions, and the cracking reaction via the

Table 7.1 Representative zeolites with the different topologies and compositions employed in the catalytic cracking of hydrocarbons to light olefins.

Framework	Material	Channel system	Membered rings	Pore size (nm)	Framework density (T/1000 Å^3)
TON	ZSM-22	1D	10	0.46 × 0.57	18.1
MTT	ZSM-23	1D	10	0.45 × 0.52	18.2
MRE	ZSM-48	1D	10	0.56 × 0.56	19.7
EUO	EU-1	1D	10	0.41 × 0.54	17.1
ITH	ITQ-13	3D	10	0.48 × 0.53	17.4
			10	0.48 × 0.51	
			9	0.40 × 0.48	
FER	Ferrierite	2D	10	0.54 × 0.43	17.6
			8	0.48 × 0.34	
CHA	SAPO-34	3D	8	0.38 × 0.38	15.1
MTW	ZSM-12	1D	12	0.59 × 0.60	18.2
FAU	Y	3D	12	0.74 × 0.74	13.3
MOR	Mordenite	1D	12	0.65 × 0.70	17.2
			8	0.26 × 0.57	
AEI	SAPO-18	3D	8	0.38 × 0.38	15.1
MFI	ZSM-5	3D	10	0.51 × 0.55	18.4
				0.53 × 0.56	
MWW	MCM-22	2D	10	0.40× 0.55	15.9
				0.41 × 0.51	
MEL	ZSM-11	3D	10	0.53 × 0.54	17.4
IMF	IM-5	3D	10	0.55 × 0.56	17.5
				0.48 × 0.54	
BEA	β	3D	12	0.66 × 0.67	15.3
				0.56 × 0.56	

protolytic route is favored in H-FER due to its more restricted porous structure. The use of a zeolite such as ferrierite (FER) is more restricted than that of ZSM-5, which might be a good strategy to increasing the production of light olefins while restricting the aromatic formation. However, the lower catalytic activity of H-FER zeolite along with experimental limitations prevents the comparison of some of its conversion levels to those observed for H–ZSM-5. Komatsu et al. [55] observed that the H-ferrierite had the highest alkene selectivity in heptane cracking due to its smaller pore size. Ca^{2+} exchange into H-ferrierite improved the selectivity and controlled coke formation. Ca^{2+} ions located at the center of the eight-membered ring (8MR) converted ferrierite pores into one-dimensional channels of 10-MRs, which suppressed the bimolecular hydride transfer to form alkanes and coke

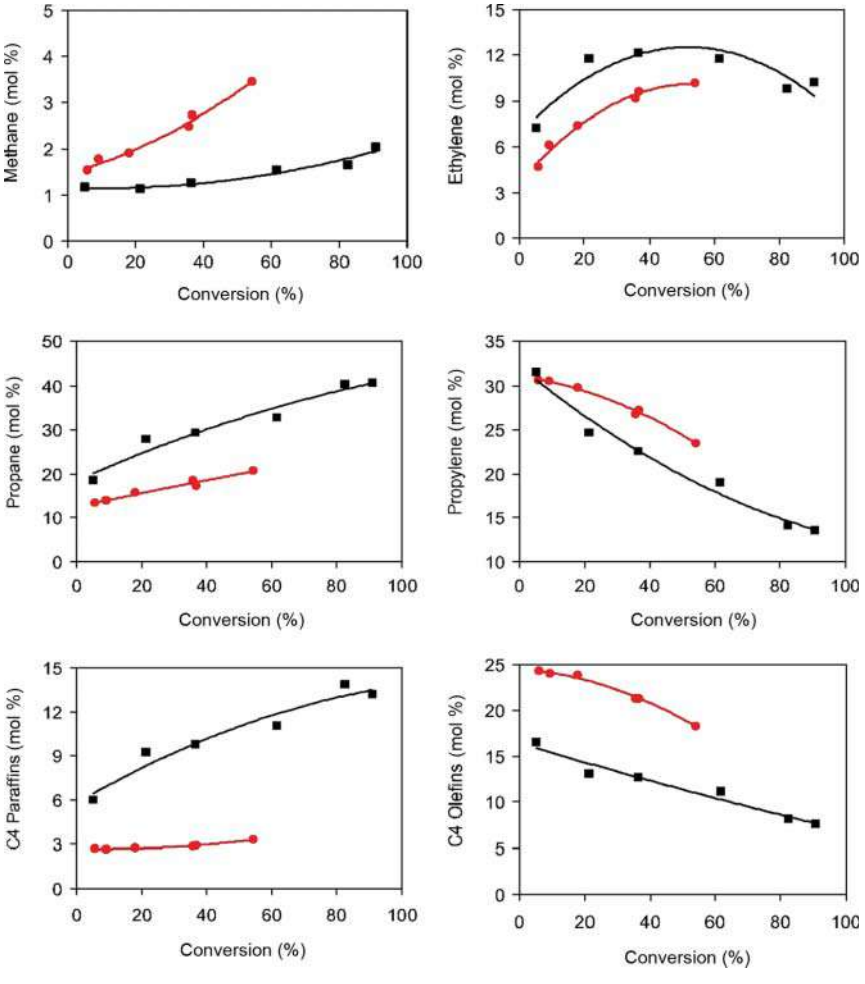

Figure 7.9 Selectivity for methane, ethylene, propane, propylene, C4 paraffins, and olefins as a function of the conversion at 500 °C. Zeolites: ■ H–ZSM-5; □ H-FER. Source: Reproduced with permission from Bastiani et al. [54]; © 2013 Elsevier.

precursors. However, the stability of H–ZSM-5 with smaller crystallite size is better than that of H-ferrierite.

Natural mordenite was treated with different concentrations of nitric acid to obtain hierarchical mordenite for naphtha cracking using *n*-hexane as a model compound [56]. High selectivity to propylene with a propylene/ethylene ratio of 1.26 was achieved over mordenite treated to mild dealumination by HNO_3 (1 M). However, one-dimensional mordenite deactivated quickly due to the pore blockage in the cracking of naphtha. The initial selectivity to propylene was higher over the hierarchical mordenite in the first 80 minutes due to the presence of mesopores.

The EUO framework has a one-dimensional 10-MR pore system periodically interrupted by 12-MR side pockets. Gong's group developed a seed-assisted method to

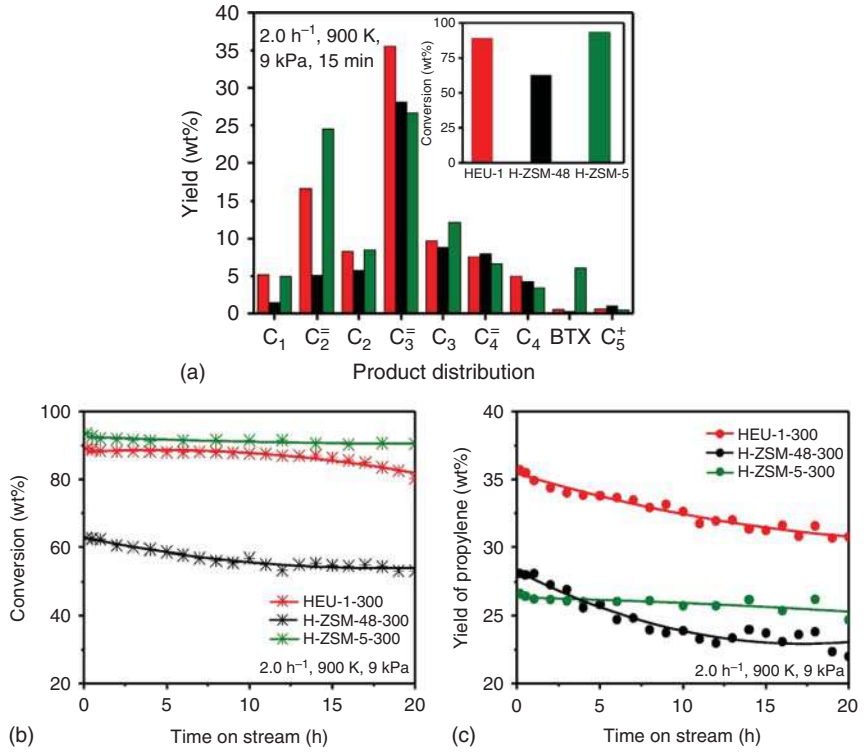

Figure 7.10 Initial products yields and *n*-hexane conversion over HEU-1-300, H–ZSM-48-300, and H–ZSM-5-300 zeolites (a). The *n*-hexane conversion (b) and propylene yield (c) with time on stream over HEU-1-300, H–ZSM-48-300, and H–ZSM-5-300 zeolites. Source: Reproduced with permission from Zhang et al. [58]; © 2016 Elsevier.

prepare pure EU-1 (EUO) zeolite with a high Si/Al ratio [57]. The prepared EU-1 zeolite was studied in the cracking of *n*-hexane [58]. H-EU-1 zeolite, displayed significant product shape selectivity due to its confined channel system, even though the large void space favored the formation of large intermediate species or aromatics precursors. Interestingly, H-EU-1-300 zeolite exhibited the highest propylene yield of about 35.6%, higher than that over H–ZSM-48 and H–ZSM-5 by 7.5% and 9.0% points, respectively (Figure 7.10a). Moreover, H-EU-1-300 showed much lower BTX selectivity in gas effluent than H–ZSM-5. H–ZSM-48-300 zeolite presented the higher propylene yield than H–ZSM-5-300 before four hours but subsequently decreased to the lowest one due to its lowest conversion (Figure 7.10b,c). H-EU-1 topological structure also showed pronounced effect on the formation and oxidation of coke deposition. It can be concluded that high-silica H-EU-1 zeolite is a preferential material for the formation of light olefins, especially propylene in paraffin catalytic cracking reaction.

ZSM-48 zeolite is also a one-dimensional 10-MR zeolite, but it does not have side pockets like EU-1, which will affect its transition-state shape selectivity. A series of ZSM-48 samples with different SiO_2/Al_2O_3 ratios were applied in the

C4-olefin cracking reactions [59]. The results showed that ZSM-48 would be more attractive than ZSM-5 for the production of propylene due to its appropriate acidity. Coking was the main reason for the deactivation of H–ZSM-48 in C4-olefin cracking reactions. Consequently, better stability and higher propylene selectivity were accomplished over hierarchical ZSM-48 zeolite [60]. Parent ZSM-48 showed the same textural and acidic properties after regeneration while the structure of the posttreated sample suffered from serious defects. The defects severely decreased the number of active sites and caused major structural collapse.

MCM-22 zeolite has a set of 10-MR channels similar to the ZSM-5 and also has a super cage system composed of 12-MR. Zhu et al. reported that MCM-22 zeolite showed high initial cracking activity and light olefin selectivity [61]. The 10-MR channels led to the high yields of ethylene and propylene. However, due to the existence of super cages, the catalyst was prone to carbon deposition and deactivation, and the stability was poor. Xu et al. synthesized a high-silicon MCM-22 zeolite using a one-step method and investigated the performance of 1-butene catalytic cracking to propylene [62]. They found that the selectivity of propane and aromatics decreased with the increase of Si/Al molar ratio and the highest selectivity of propylene was obtained at Si/Al ratio of 79. Wang et al. also found that MCM-22 zeolite with higher Si/Al ratios exhibited better catalytic performance due to the lower amount and strength of acid sites [63]. Dealuminated MCM-22 zeolites by using ammonium hexaflurosilicate treatment improved the catalytic life and propylene selectivity at very high *n*-hexane conversions, due to the smaller amount of Lewis acid sites.

IM-5 presents strong acidity, high hydrothermal stability, and excellent catalytic cracking activity. Corma et al. thought that IM-5 could be an excellent candidate for steam catalytic cracking (SCC) of hydrocarbons [64]. The use of IM-5 instead of ZSM-5 zeolite for SCC process slightly improved the yield to ethene, keeping constant the yield of propylene. IM-5 zeolite allowed obtaining higher ethylene and propylene yield than ZSM-5. Mesoporous IM-5 exhibited higher light olefin yield (especially propylene) and catalyst lifetime in catalyzing *n*-alkane than conventional IM-5 and ZSM-5. Interestingly, compared with ZSM-5 with identical Si/Al ratio, the higher acid strength and more Brønsted acid site endowed IM-5 better catalytic performance with higher catalytic activity and higher yields of light olefins [65]. In the reaction of naphtha SCC to produce ethylene and propylene, IM-5 has achieved a catalytic effect comparable with ZSM-5, becoming one of the most promising new catalysts to replace ZSM-5 zeolite [66].

Zhu et al. comparatively studied the catalytic cracking reaction performance of C4 olefins on zeolites with different topological structures [67]. It was found that the conversion of C4 olefins and the selectivity of light olefins were affected by the pore structure, acid properties, and Si/Al ratio of zeolites. The smaller pore size of zeolite was more "shape selective" for the production of propylene and ethene in butene cracking. The hydrogen transfer index also decreased with the pore size of the zeolite (Figure 7.11).

The shape selectivity of SAPO-34 is a key factor for the high propylene selectivity giving way to high olefin (propylene) selectivity [68]. However, this catalyst shows

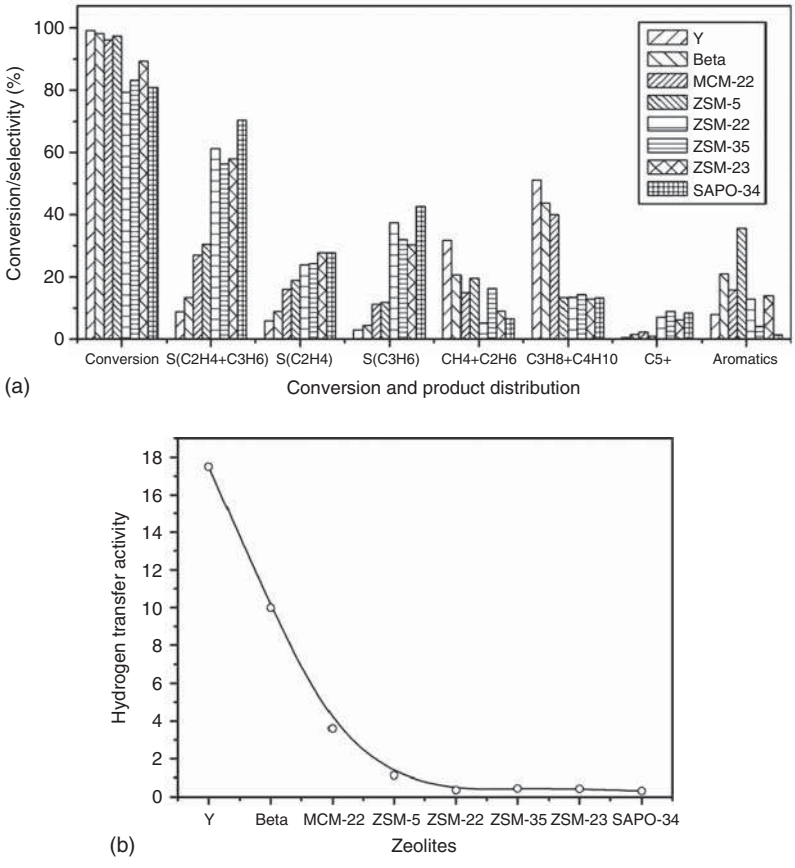

Figure 7.11 Butene conversion and product distribution on zeolites with different structures (a). Hydrogen transfer index on zeolites with different structures (b). Source: Reproduced with permission from Zhu et al. [67]; © 2005 Elsevier.

a fast deactivation rate caused by the pore blockage due to the alkylated aromatic retained in the internal cages of microporous intersections, giving way to coke with a high amount of non-condensed rings and of olefinic nature. The coke deposited on H–ZSM-5 zeolite catalyst has a higher external coke fraction and is mainly composed of condensed aromatics and long aliphatic chains. The ability for the internal circulation of coke precursors is favored by agglomerating the H–ZSM-5 zeolite in a mesoporous matrix, which allows the deposition and evolution of the coke on the outside of the zeolite, thus avoiding the blockage of catalytic acid sites (Figure 7.12).

Corma et al. [69] observed that the selectivity to iso-butane strongly depended on zeolite catalysts, which had different pore volumes in the cracking of *n*-heptane. They pointed out the importance and possibility of controlling product selectivity not only by the pore size but also by the pore volume of zeolite. Miyaji et al. studied the influence of the pore structures of zeolites on their selectivity to the formation of ethylene and propylene in the conversion of 2-methyl-2-butene and 2-pentene over

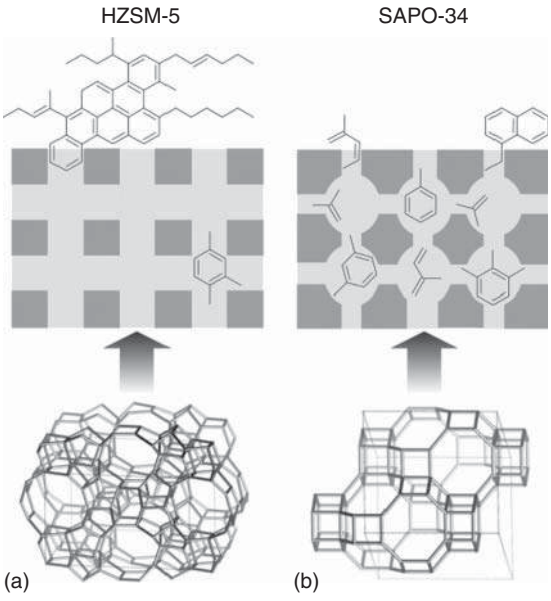

Figure 7.12 Scheme of the internal coke precursor retention and of the composition of the external coke deposited on (a) H–ZSM-5 zeolite and (b) SAPO-34. Source: Reproduced with permission from Epelde et al. [68]; © 2014 Elsevier.

various proton-exchanged zeolites [70]. They reported that the selectivity to ethylene and propylene was highly dependent on both the spatial volume of the zeolite cavity and the dimensionality of the pore structure. Only when the specific space volume of the zeolite with one- or two-dimensional pore structure was almost the same as the volume of the pentyl cations, the selective production of both ethylene and propylene could proceeds via the monomolecular cracking of pentene.

Numerous studies have demonstrated that ZSM-5, with its unique shape selectivity, proper acid properties, well-ordered pore network, and high thermal and hydrothermal stability, is an excellent heterogeneous catalyst for naphtha cracking in the petrochemical industry [10, 12]. However, due to the relatively complex reaction network for the catalytic cracking of hydrocarbons, the ZSM-5 zeolite still suffers from significant diffusion limitations, hindering the accessibility of active sites by large reactant molecules and causing catalyst deactivation due to coke deposition in microporous channels. Many studies have been devoted to improving the catalytic performance of ZSM-5 through a wide variety of approaches, such as introduction of P [71], transition metal elements [72, 73], or rare earth (RE) elements [74–76] to modify the acidity of ZSM-5 zeolite, and construction of nanocrystals [77, 78] or hierarchical zeolites [79–82].

7.3.2 Adjustment of Acid Properties of ZSM-5 Zeolite

The acid properties of ZSM-5 zeolite, including acid amount, acid strength, and acid types, are significant for hydrocarbon cracking since the catalytic cracking of hydrocarbons is dominant by acid catalysis. All of these factors have significant impacts on the catalytic activity, product selectivity, and carbon deposition during hydrocarbon cracking.

7.3.2.1 Effect of Si/Al Ratio of ZSM-5 Zeolite

The Si/Al ratio of zeolites is an important factor affecting the catalytic cracking performance, owing to its influence on the density of the acid sites and on their strength. The adjustment of the Si/Al ratio of H–ZSM-5 zeolite has been proved to be a feasible tool to modulate the catalytic activity, selectivity to propylene, and stability of catalysts in catalytic cracking of hydrocarbon reactions [83–85].

Xu and coworkers [67] have investigated the cracking of 1-butene to propylene and ethene over H–ZSM-5 zeolite with different Si/Al ratios. They observed that the amounts of both the Brønsted acid sites and the Lewis acid sites and the acid strength gradually decreased with the increasing of the Si/Al ratio of H–ZSM-5 zeolite from 25 to 183. The H–ZSM-5 sample with the highest Si/Al ratio of 183 exhibited the best catalytic performance and lowest coking due to the suppression of the hydrogen transfer and aromatization reactions, although this increase also entailed a decrease in conversion. For the ZSM-5 (Si/Al = 25), the conversion decreased from an initial value of 96.6% to 67.5%, i.e. 29% lower in 10 hours of running, while for the ZSM-5 (Si/Al = 183), the conversion changed from 84.5% to 81.4% (a decrease of only 3%) (Figure 7.13).

Generally speaking, the catalysts with lower acidity are preferred for the cracking of alkenes like butene due to the reactive nature of alkenes. Therefore, the main work in alkene cracking is to suppress the secondary reactions by decreasing the acidity of the zeolites. Furthermore, the stabilities of the catalysts are effectively prolonged with enhancing the Si/Al ratios, and the coke deactivation rate of H–ZSM-5 zeolite catalysts is considerably attenuated, because the decrease in the acid strength attenuates acid site activity for the condensation reaction of coke precursors [83]. Corma and coworkers [84] reported that Si/Al ratios around 300 showed maximum propylene yield in 1-butene cracking while decreasing the Si/Al ratio to below 300 enhanced the initial activity of the catalyst due to the larger amounts of active sites.

Al-Khattaf and coworkers [42] reported that the yield of propylene and the molar ratio of propylene/ethylene increased with increasing Si/Al molar ratio of H–ZSM-5 zeolites (Figure 7.14a). The yield of propylene (39.1 C-wt%) and propylene/ethylene molar ratio (6.5) was the highest for the cracking of 1-hexene reaction over silicalite-1. In contrast to the yields of propylene, the yields of aromatics decreased with increasing Si/Al ratio for the reactions of all alkenes (Figure 7.14b). Moreover, the yield of propylene could be improved through the removal of a part of Al contained in silicalite-1 as an impurity and the enrichment of surface silanol groups on silicalite-1.

The influence of Si/Al ratio on light olefin production in the catalytic cracking of alkanes is different from that in alkene cracking, because the reactant molecules have different reactivities. In alkane cracking, relative stronger acidity is required to activate the alkane molecules; however, the secondary reaction of alkene products is also prompted for the same reason, resulting in much lower propylene and ethene selectivity than that in alkene cracking. Zhao and coworkers [85–87] studied the effects of Si/Al ratio (25, 38, 50, 80, and 150) of H–ZSM-5, Fe/H–ZSM-5, and Cr/H–ZSM-5 zeolites on the performance of ZSM-5 catalysts for light olefin formation in C4 alkane catalytic cracking. The total acid amounts, density, and strength of

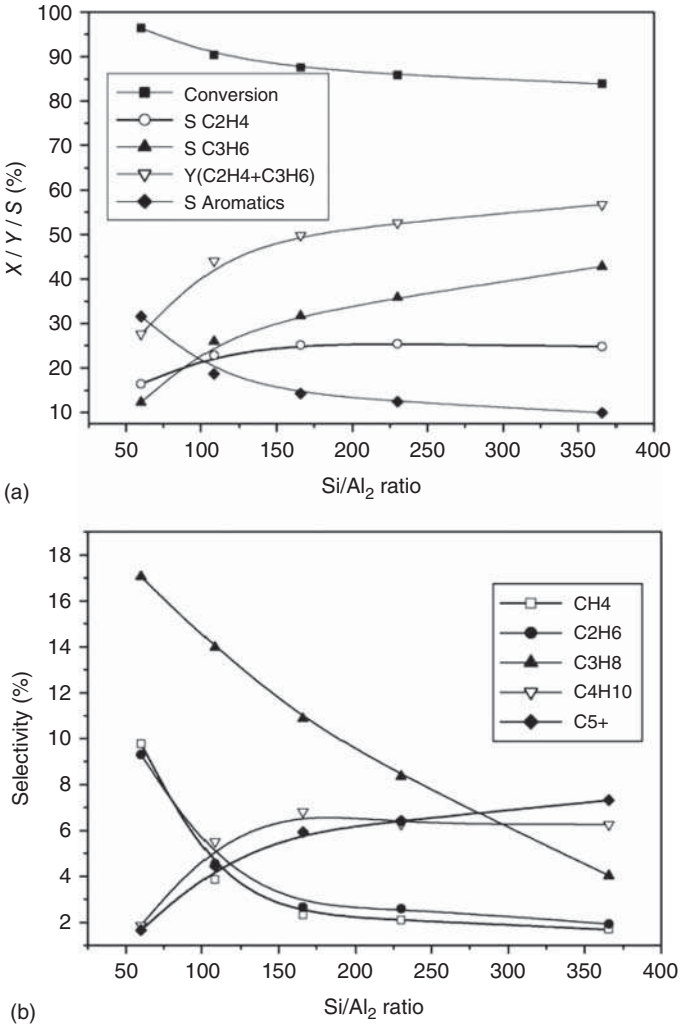

Figure 7.13 Butene conversion and product distributions on ZSM-5 zeolites with different Si/Al_2 ratios (a). Stability of ZSM-5 zeolites with different Si/Al_2 ratios (b). Source: Reproduced with permission from Zhu et al. [67]; © 2005 Elsevier.

H–ZSM-5, Fe/H–ZSM-5, and Cr/H–ZSM-5 zeolites obviously decreased, while those of weak acid sites increased with reducing Si/Al molar ratios. The higher ratios of Si/Al (≥80) were beneficial to improving the yields of light olefins. Furthermore, the optimum Si/Al ratio that favors the yield of specific light olefin was different among the three catalyst systems. The highest yield of light olefins (59.8 wt%) over Cr/H–ZSM-5 zeolite was achieved using Si/Al ratio of 150, while over Fe/H–ZSM-5 and H–ZSM-5, the ratios of 80 and 50 resulted in the highest yields of light olefins (54.6 wt% and 50.8 wt%, respectively). The yield of BTX decreased in all the samples by enhancing the Si/Al molar ratio of ZSM-5; therefore, the hydride transfer and aromatization were suppressed by keeping the number of acid sites low.

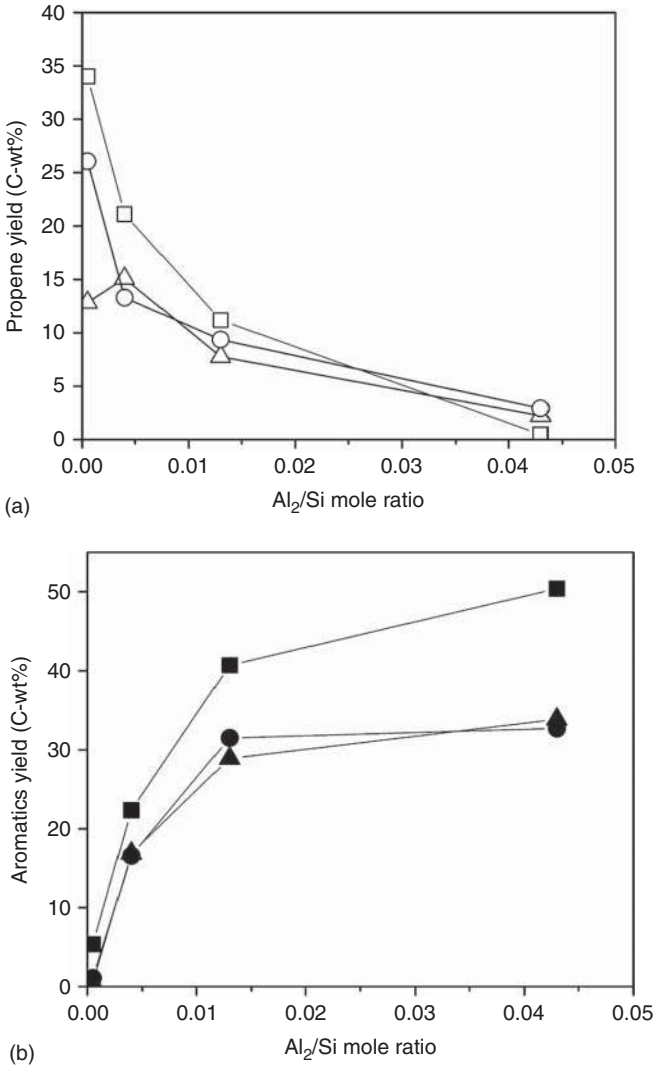

Figure 7.14 Variations in the yield of propylene as a function of Al_2/Si ratio of catalyst at 550 °C. Propylene from reactions of 1-butene (□), 1-pentene (Δ), and 1-hexene (○) at a GHSV of 900 h^{-1} for 1-butene and LHSV of 6 h^{-1} for 1-pentene and 1-hexene; time on stream = 1 hours; total pressure, atmospheric pressure (a). Variations in the yield of aromatics as a function of the Al_2/Si ratio of catalyst at 550 °C (b). Aromatics from reactions of 1-butene (■), 1-pentene (▲), and 1-hexene (●). Source: Reproduced with permission from Arudra et al. [42]; © 2014 American Chemical Society.

Komatsu and coworkers [88] investigated the cracking of *n*-hexane over H–ZSM-5 zeolite with different Si/Al ratios. They discussed the effect of Si/Al ratio on the product distribution and the model of coke deactivation over H–ZSM-5 zeolite. Although the initial conversions on all the catalysts were higher than 95%, the conversions decreased with time on stream. In eight hours running, the extent

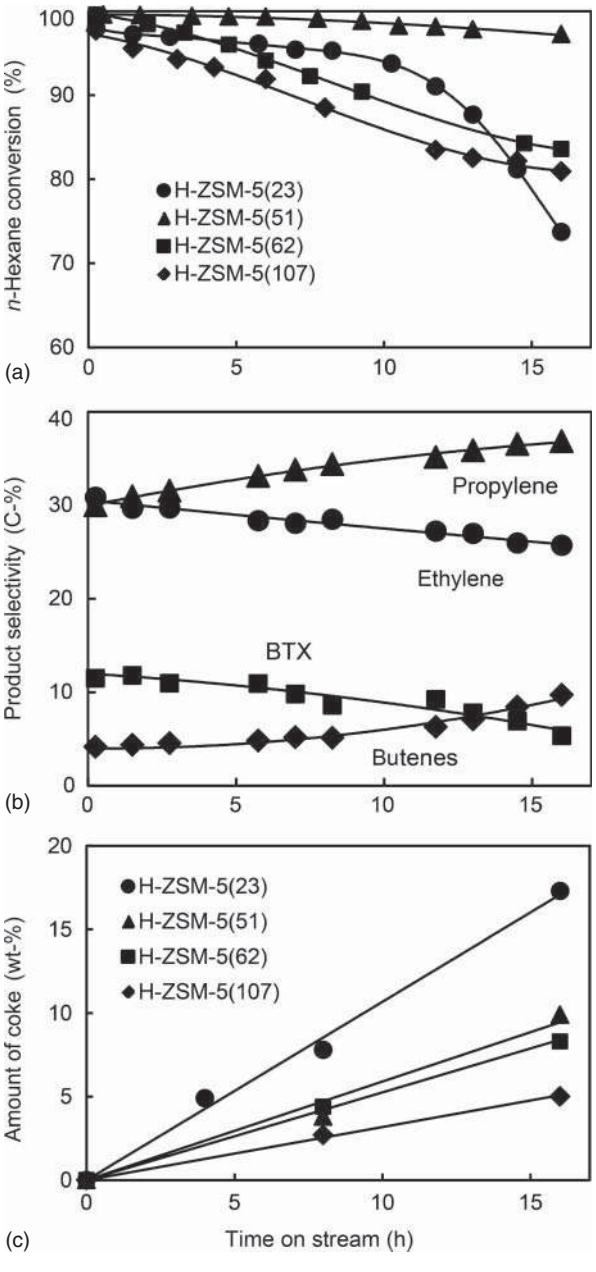

Figure 7.15 Time courses of (a) *n*-hexane conversion on various H–ZSM-5, (b) product distribution on H–ZSM-5(23), and (c) coke amount on various H–ZSM-5. Source: Reproduced with permission from Urata et al. [88]; © 2014 Elsevier.

of deactivation was in the following order H–ZSM-5(107) > H–ZSM-5(62) > H–ZSM-5(23) > H–ZSM-5(51) (Figure 7.15a). The product selectivity also gradually changed accompanied by the slight decline in the conversion (Figure 7.15b). Figure 7.15c showed that the coke formation rate was in the following order of H–ZSM-5(23) > H–ZSM-5(51) > H–ZSM-5(62) > H–ZSM-5(107). Thus, the rate of the deactivation did not depend apparently on the rate of coke formation.

However, the amount of coke per acid site was almost the same, demonstrating that the mechanism of coke formation did not depend on the Si/Al ratio of H–ZSM-5 zeolite.

Igarashi and coworkers [89] reported that the H–ZSM-5 zeolite with a lower Si/Al ratio exhibited higher activity because the activation energy for *n*-heptane cracking reaction decreased with decreasing Si/Al molar ratio of H–ZSM-5 catalysts. However, all the H–ZSM-5 zeolites with various Si/Al molar ratios exhibited almost the same selectivity, olefin/paraffin (O/P) ratios, and *i*-butene/*n*-butenes at the similar conversion of 70% (Table 7.2), indicating that the Si/Al molar ratios showed negative impacts on the product selectivity at relatively high conversions.

CMR ratios, which are defined as a parameter of the ratio of the monomolecular cracking to the classical bimolecular cracking by Post and coworkers, increase significantly with increasing Si/Al ratios [90]. Akira Igarashi and coworkers found that the CMR ratio increased with increasing Si/Al molar ratio of H–ZSM-5 catalysts in the catalytic cracking of *n*-heptane [89]. Moreover, the fact that the Si/Al ratio did not affect the selectivity suggested that the CMR ratios would not change considerably with Si/Al ratios. Nevertheless, there existed controversies over the effects of Si/Al molar ratio on the CMR ratios. The CMR ratios might not be a suitable parameter at high reaction temperatures. Consequently, it is difficult to determine the effect of Si/Al ratio on the ratio of the monomolecular cracking to the classical bimolecular cracking.

Table 7.2 Effect of acid site density of H–ZSM-5 on selectivity (mol%) of cracking of *n*-heptane at c. 70% conversion (reaction temperature = 923 K, TOS = 15 min).

Si/Al[a)]	31	34	51	106	200
C_2H_4	32.5	33.0	34.0	32.3	31.9
C_3H_6	28.7	26.3	29.9	29.3	28.3
n-C_4H_8	6.0	5.2	5.8	6.0	6.2
i-C_4H_8	3.2	2.8	3.2	3.3	3.4
BTX	1.5	2.5	1.0	1.0	0.7
CH_4	6.4	8.4	5.9	6.4	7.6
C_2H_6	8.2	9.2	7.1	8.4	9.0
C_3H_8	8.2	7.9	7.8	7.7	7.1
n-C_4H_{10}	3.5	3.1	3.5	3.6	3.6
i-C_4H_{10}	0.4	0.4	0.3	0.3	0.2
C_{5+}	1.5	1.4	1.5	1.7	2.1
CMR[b)]	118	131	158	174	202
O/P[c)]	3.47	3.28	3.90	3.54	3.50
i-C_4H_8/*n*-C_4H_8	0.54	0.55	0.55	0.55	0.55

a) Determined by ICP measurement.
b) $(C_1 + \sum C_2)/i\text{-}C_4$ (as described).
c) C_nH_{2n}/C_nH_{2n+2} $(n = 2–4)$.
Source: Reproduced with permission from Kubo et al. [89]; © 2012 Elsevier.

ZSM-5 zeolite with low Si/Al molar ratio can promote the catalytic activity but facilitate the coking simultaneously, resulting in the quick deactivation, owing to the coverage of acid sites and pore blockage by carbon deposition. Jung et al. [91] observed that the increases in the Si/Al molar ratio of MFI zeolites induced a significant decrease in the conversion of *n*-octane. However, the selectivity for olefin slowly increased with reaction temperature regardless of their Si/Al molar ratio. It means that the Si/Al molar ratio does considerably influence the conversion, but it does not strongly affect the selectivity to light olefins. Thus, a stable catalytic activity with less carbon deposition can be obtained by increasing the Si/Al ratio moderately.

7.3.2.2 Tuning of Al Siting and Distribution in ZSM-5 Zeolite

The location of Brønsted acid sites within zeolites influences the catalytic rates and selectivity due to diverse intrachannel environments, which guide the stabilization of transition states to different extents [92]. One of the most prototypical examples is that of mordenite zeolite. In this section, some recent examples on the effect of different aluminum sitings or distributions on the catalytic behaviors are surveyed, as well as the very interesting strategies that are being developed to control this distribution and that can improve the performance for catalytic cracking by zeolites.

At present, the research on the microscopic acid properties of ZSM-5 zeolite is divided into two levels. The first level is to study the position of Al atoms, which are located in straight channels (α-position), intersections (β-position), or sinusoidal channels (γ-position) [93, 94]. The second level is the relative position of Al atoms, that is, the position of two Al atoms in the basic structural unit ring of the zeolites. There are currently three classifications [93, 94]: (i) Al pair refers to Al–O–(Si–O)*n*–Al, where $n \leq 2$, and can be located in a five-membered ring or a six-membered ring. However, it should be pointed out that the connection sequence of Al–O–Si–O only appears in zeolites with Si/Al < 12 (the zeolites synthesized by different methods may be different). (ii) Al unpair refers to Al–O–(Si–O)*n*–Al, where $n > 2$, and is located in different rings but must face the same pores. (iii) Single Al refers to Al–O–(Si–O)*n*–Al, where $n \geq 3$.

As early as 1991, Wielers et al. proposed that in the catalytic cracking reaction, isolated acid sites are conducive to the protonation of hydrocarbons, while adjacent acid sites are conducive to hydrogen transfer and other reactions [90]. Wichterlová and coworkers studied the effect of Al distribution on the cracking reaction path of *n*-butene using ZSM-5 zeolites with different Al distributions as the catalyst for the reaction of *n*-butene [95]. The experimental results were consistent with the view of Wielers et al. When the content of "single Al" in the zeolite was higher, it was more conducive to the cracking reaction of *n*-butene. On the contrary, when the content of "close Al" in the zeolite was higher, it was more conducive to the hydrogen transfer reaction. Janda and Bell [96] reported the influence of the Si/Al ratio of zeolite on the position of Al (such as intersections, straight channels or sinusoidal channels) and correlated it with the monomolecular cracking and dehydrogenation process of *n*-butane. The results showed that with increasing Al content in ZSM-5 zeolite, the Al content at the intersection increased compared with the Al in the straight channel and the sinusoidal channel. The selectivity to dehydrogenation over cracking and to

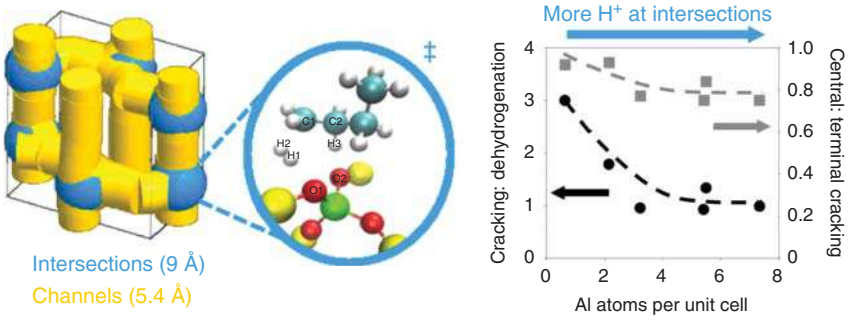

Figure 7.16 Schematic of Al atoms in ZSM-5 zeolite straight channel and sinusoidal channel intersections. Source: Reproduced with permission from Janda and Bell [96]; © 2013 American Chemical Society.

terminal cracking over central cracking increased nearly monotonically with the Al content (Figure 7.16). Thus, the terminal cracking and dehydrogenation of *n*-butane occurred preferentially on Brønsted acid protons located at channel intersections, due to the higher intrinsic entropies of activation and consequently lowers Gibbs free energies attainable at these sites.

Of particular interest may be those approaches aiming to introduce Al concentration gradients (zoning) along the zeolite crystals. It is well established that the cracking activity is proportional to the aluminum concentration in the zeolite catalysts, which can be further attributed to strong Brønsted acid sites [97]. Additionally, the local environment of the Brønsted acid sites in ZSM-5 has profound influences on the catalytic activity of *n*-pentane cracking. Schallmoser et al. reported that the turnover frequency (TOF) of tetrahedrally coordinated extra-lattice alumina in close proximity to strong Brønsted acid sites was approximately 40 times higher than that of normal Brønsted acid sites [97]. However, high Brønsted acid site density promoted undesired secondary reactions of hydrogen transfer and aromatization, thus decreasing the selectivity to light olefins. The P/E ratio and selectivity of propylene could be significantly improved by manipulating the acid strength distribution and the concentration of acid sites in different confined positions in ZSM-5 zeolites [98]. Very recently, Yokoi et al. [99] reported that the use of pentaerythritol (PET) as a pore-filling agent in combination with Na cations in the synthesis of ZSM-5 with Si/Al = 25 led to a unique Al distribution in the MFI framework. Since PET has no charges (unlike TPA cations), Al^{3+} species would be located near Na^{+} species. This would lead to the preferential location of Al atoms at straight and sinusoidal channels rather than channel intersections in the MFI framework.

7.3.2.3 Modification of ZSM-5 Zeolites with Different Elements

The innovative fine control of the zeolite acidity, that is, acid type, acid strength, and acid distribution, has attracted extensive attention because zeolite acidity is crucial for the overall performance of hydrocarbon cracking. Alkali metal, alkaline earth metal, RE metal, transition metal, and P element modification can effectively modulate the acid properties of the zeolite, and the proper adjustment of the acid

properties of the catalyst can appropriately improve the catalytic performance [100–103]. Until now, the catalytic cracking of various types of hydrocarbons has been investigated with the modified H–ZSM-5 zeolite to enhance light olefin production.

7.3.3 Alkaline Metal- and Alkali Earth Metal-Modified ZSM-5

Wakui et al. [100, 101] investigated the cracking of *n*-butane to propylene and ethene over modified H–ZSM-5 catalysts with different alkali earth metals (Mg, Ca, Sr, Ba). The H–ZSM-5 zeolite was modified by the addition of carbonate salt of each alkali earth metals to the aqueous solution used for the synthesis of the zeolite. The NH_3-TPD curves of modified ZSM-5 samples showed that the strong acid sites were transformed to weak acid sites by the introduction of alkaline earth metals. The non-modified H–ZSM-5 showed the highest activity, a large amount of benzene, toluene, xylenes (BTX) products, and the lowest ethylene and propylene yields. The higher yields of ethylene and propylene were observed with Mg-, Ca-, and Ba–ZSM-5, and the yields of BTX on the modified H–ZSM-5 were lower than those on non-modified H–ZSM-5 (Figure 7.17). Moreover, the ethylene/ethane and the C2/other product ratios over the alkaline earth-modified H–ZSM-5 were higher than those on non-modified H–ZSM-5. In this study, the highest yield of ethylene and propylene was obtained over Ba–ZSM-5 due to the dehydrogenation cracking stimulated by Ba modification [100].

Wang et al. [102] studied the conversion of C3–C9 paraffins to light olefins over modified H–ZSM-5 with the different alkaline metals. They reported that the modification of ZSM-5 zeolite catalysts with K and Ba elements enhanced the dehydrogenation activity of catalysts and minimized bimolecular hydrogen transfer reactions. C2–C4 olefin selectivity of 70.4% and 66.8% could be obtained for propane and *n*-hexane oxidative cracking, respectively, at a temperature of 873 K. The presence of Li^+ and Na^+ decreased the concentration of strong Brønsted acid

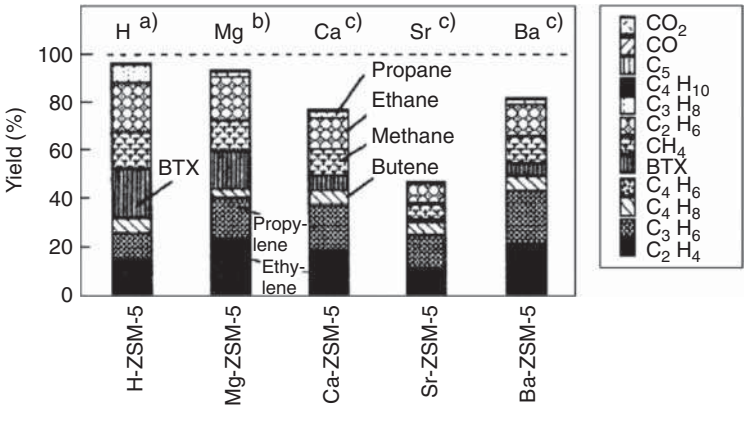

Figure 7.17 Product distribution in cracking of *n*-butane on alkaline earth-modified H–ZSM-5. Source: Reproduced with permission from Wakui et al. [100]; © 2002 Springer.

sites, whereas K^+ affected acid centers of different strength. Xu et al. [103] reported that the cracking activity of the various alkaline metal (Li, Na, K)-modified ZSM-5 catalysts decreases slowly with the extension of reaction. However, the selectivity to ethylene and propylene did not increase accordingly [103]. The three metals could be incorporated in different amounts to finely tune the selectivity to ethylene and propylene, and the highest selectivity to light olefins was obtained over 0.5 wt% Li-, 1.5 wt% Na-, and 1.5 wt% K-modified zeolite catalysts [103].

7.3.4 Transition Metal-Modified ZSM-5

The modifications of ZSM-5 zeolite with transition metals can adjust the catalyst acidity because these metals have partially occupied *d*-orbitals, several stable oxidation states, and different coordination numbers. Generally speaking, the incorporation of transition metal ions into H–ZSM-5 zeolites leads to the formation of Lewis acid sites. However, the impacts of Lewis acid sites the catalytic performance of ZSM-5 zeolite in hydrocarbons cracking reaction are still ambiguous [104].

Transition metals, such as Ni, Co, Zn, Cu, Cr, and Ga, introduced into ZSM-5 zeolites are generally used as active centers for hydrogenation or dehydrogenation or aromatization reactions [73, 87, 105, 106]. Zhao and coworkers investigated the cracking of butane to propylene and ethene over modified H–ZSM-5 zeolites with different transition metals [85–87]. It was observed that the acidic amount of the Fe/H–ZSM-5 catalysts first increased with the introduction of a small amount of Fe, but it decreased with further increasing quantity of Fe(III). The acid site density of the Cr/H–ZSM-5 catalysts increased with the increasing loading of Cr(III), while the strength of strong acid sites decreased obviously. The high catalytic activity and selectivity to light olefins in the catalytic cracking of iso-butane were attained over Fe/H–ZSM-5 [85] and Cr/H–ZSM-5 [87] catalysts loaded with a trace amount of Fe (0.010 mmol/g) and Cr (0.004 mmol/g), respectively. The presence of a small amount of Fe or Cr elements could be favorable for the dehydrogenation of *iso*-butane to *iso*-butene, which was easily cracked to light olefins. On the one hand, the catalytic cracking reactivity of Fe/H–ZSM-5 and Cr/H–ZSM-5 catalysts decreased by loading high amounts of Fe and Cr, due to the existence of a majority of Fe(III) and Cr(III) species with large domain sizes and the coverage of zeolite outer surface or acid sites [85, 87]. Meanwhile, the selectivity to the total olefins decreased with the further increasing quantity of Fe or Cr in H–ZSM-5, which might be due to the improving oligomerization and cyclization reactions [85, 87]. It was demonstrated that the incorporation of transition metal ions into zeolites could lead to interesting bifunctional catalysts in which metallic and acidic active sites played roles simultaneously [73]. Consequently, the cracking activity and selectivity toward light alkenes could be modified by tailoring both metallic and acidic active sites.

Hensen and coworkers [105] prepared a series of Ga/H–ZSM-5 zeolites via wet impregnation, ion exchange, and chemical vapor deposition methods for the catalytic cracking of *n*-heptane. They found that the Ga/H–ZSM-5 catalysts with a lower Ga/Al ratio displayed improved activity and the product distribution depends on the contributions of Brønsted acid sites (protolytic cracking, olefin

cracking) and of Ga sites (dehydrogenation, aromatization, olefin cracking). The synergy between Ga dehydrogenation sites and Brønsted acid sites was proposed to improve the dehydrogenation rate. Altogether, the combination of Ga Lewis sites for the dehydrogenation of the paraffinic feedstock with Brønsted acid sites for the cracking of subsequent higher olefins to light olefins could enhance the yield of light olefins [105]. The Ga_2O_3/ZSM-5 hollow fibers with hierarchical macro/meso/microporosities showed excellent catalytic conversion of *n*-butane and the highest yield of light olefins plus aromatics, because the hierarchical macro/meso/microporosities effectively enlarge the bifunctionality by enhancing the accessibility of active sites and the diffusion behaviors [107]. The simultaneous presence of Brønsted acid sites and transition metal sites could influence on the selectivity to the catalytic cracking products.

The incorporation of Zr on ZSM-5 zeolite enhanced the hydride transfer reactions and led to higher catalytic activity accompanied with the proximate stability [106]. The incorporation of Ag into ZSM-5 zeolite resulted in the dehydrogenation cracking over Ag sites, and the cracking over redox sites selectively promoted cleavage of C—H bond and the formation of light olefins [106]. The light olefin yields of 58 and 81% were obtained at 500 °C over Zr–ZSM-5 and Ag–ZSM-5, respectively, which were higher than that over the parent H–ZSM-5. However, some side reactions were also promoted, resulting in a rapid coke formation and catalyst deactivation over Ag–ZSM-5 [106].

7.3.5 Rare Earth Element-Modified ZSM-5

RE elements comprise the lanthanide elements with atomic number from 57 to 71 and scandium and yttrium, which have similar electronic structures and chemical properties to lanthanide elements. RE elements possess 4*f* orbitals without full electron occupancy and the lanthanide contraction. These characteristics result in their unique chemical properties when being used as catalysts or catalytic components [108]. As early as the 1960s, RE-exchanged Y zeolites (REY) catalysts have been successfully employed in FCC technology to improve the hydrothermal stability of the Y zeolite, overall activity, and gasoline selectivity. The introduction of RE^{3+} such as La^{3+} and Ce^{3+} into zeolites can be used to adjust the amount and intensity of the acid sites [74]. Moreover, the influence of RE modification on the catalytic performance of ZSM-5 zeolite in the cracking of hydrocarbon is still under discussion.

It is thought that the addition of RE elements into H–ZSM-5 has a great impact on its acidic properties, thus affecting its catalytic performance for the cracking of hydrocarbon [109, 110]. As early as in 1989, Hartford et al. reported that lanthanum exchange could reduce the number of strong acid sites and increase the number of weak acid sites in H–ZSM-5 catalyst, suggesting that La ions (or ionic complexes) acted as weak acid sites. Moreover, the result of hexane adsorption indicated that La exchange did not reduce the effective free pore volume or enlarge the steric hindrances for the passage of linear molecules through the pores of catalyst. The activity of La-exchanged H–ZSM-5 catalyst in hexane cracking decreased with the increasing La content [109]. Xue et al. also deduced that adding La to H–ZSM-5 zeolite reduced

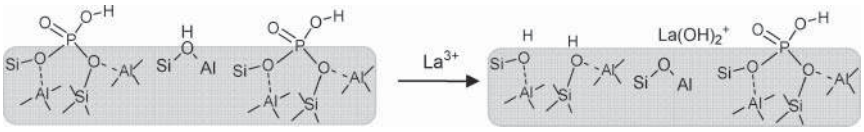

Figure 7.18 Schematic show of the La ions that are introduced into the P/H–ZSM-5. Source: Reproduced with permission from Xue et al. [111]; © 2010 Elsevier.

the total amount of Brønsted acid sites in zeolite and the density of Brønsted acid sites in La/H–ZSM-5 decreased with the increasing La loadings [111]. It is believed that the exchange of La^{3+} ion with bridged hydroxyls in zeolite may cause the elimination of Brønsted acid sites, in spite of some new acid sites being created by splitting the coordinated water molecules with La^{3+} ions (Figure 7.18).

Wang et al. systematically studied the effect of different RE (RE = La, Ce, Pr, Nd, Sm, Eu, or Gd) element-modified H–ZSM-5 zeolite on its acidity and catalytic performance in the catalytic cracking of mixed butane to light olefins [110]. On the contrary, they claimed that the total amount of acid sites of light RE-modified H–ZSM-5 samples increased, except for the Gd-modified ZSM-5 sample, compared with the parent H–ZSM-5. Moreover, the orders of the amount of weak acid, strong acid, and total acid were as follows: Sm > Nd > Pr > Eu > Ce > La > H–ZSM-5 > Gd, Nd > Eu > La > Sm > Ce > Pr > Gd > H–ZSM-5, and Nd > Sm > Eu > Pr > Ce > La > H–ZSM-5 > Gd, respectively. The addition of Ce and Nd to H–ZSM-5 catalyst greatly enhanced the selectivity to olefins, especially to propylene, thus increasing the total yield of olefins in the catalytic cracking of mixed butane to light olefins [110]. The highest total alkene yield was achieved over Ce/H–ZSM-5 at 600 °C (57.2 wt%) and Nd/H–ZSM-5 at 650 °C (60.0 wt%).

The RE compounds, especially oxides, possess both acidity and basicity, especially Lewis acidity, due to the presence of valence electrons and empty f orbitals in RE elements. Wang et al. illustrated that the introduction of RE elements into H–ZSM-5 sample not only modified the amount of acid sites of H–ZSM-5 but also altered the acid type. That is, the ratio of Lewis acid/Brønsted acid could be altered, which showed significant impact on the catalytic performance of H–ZSM-5 [110]. The introduction of RE metals to H–ZSM-5 sample promoted the performance of H–ZSM-5 in the catalytic cracking of butane, while the product P/E ratio differed obviously according to the reaction temperature and the type of incorporated RE elements.

On the other hand, it is generally accepted that the introduction of RE elements can modify the basicity of ZSM-5 zeolite, as RE oxides usually possess some basic character [110]. Wakui et al. [112] investigated the effect La, Ce, Pr, and Sm on the acid/base properties and the catalytic behavior of H–ZSM-5 zeolite in *n*-butane cracking. The NH_3-TPD and CO_2-TPD results of RE-loaded H–ZSM-5 catalysts indicated that the basic sites could be created on the catalyst surface by RE element loading, although the acidity of the parent H–ZSM-5 catalyst was almost not affected. Yoshimura et al. [113] also observed the similar results that the acid amount and strength of the ZSM-5 zeolite were almost the same before and after the La loading (10 wt% loading). This indicates that the La loading did not affect the acid

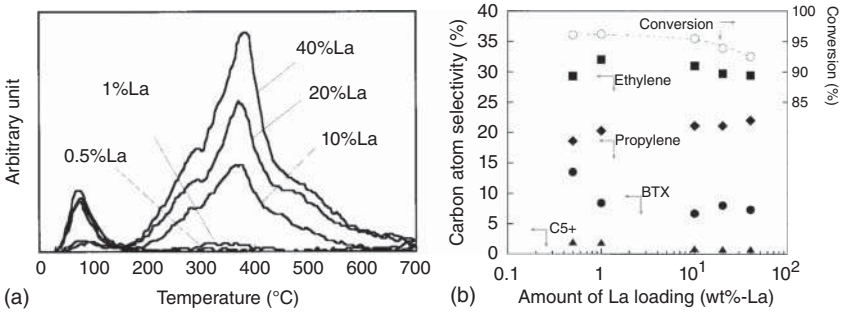

Figure 7.19 CO_2-TPD spectra of ZSM-5 catalysts modified with La (a). Effect of La loading on conversion of *n*-butane and product selectivity (b). Source: Reproduced with permission from Yoshimura et al. [113]; © 2001 Springer.

properties of the ZSM-5 catalyst. However, the amount of CO_2 adsorption calculated from the peak at 70 °C increased with increasing amount of La, suggesting the generation of basic sites on the ZSM-5 catalyst surface as a result of La loading (Figure 7.19). The modification of ZSM-5 zeolite catalysts with the RE elements enhanced the surface basicity, and thus it reduced the readsorption of the basic compounds of the cracking products, such as ethylene, propylene, and butenes. This is apparently the major cause of the lower aromatics and higher light olefin formation [110, 112, 113].

Wakui et al. [114] reported that a dehydrogenation-cracking double-stage (tandem) reaction of *n*-butene employing a Pt–Sn type dehydrogenation catalyst and a cracking catalyst (RE-loaded H–ZSM-5). The highest yield of light olefins (ethylene + propylene) was 58% at 650 °C. It was proved that the introduction of 10% RE element Pr to ZSM-5 played an important role in inhibiting the bimolecular reactions, deriving the high yield of ethylene and propylene.

7.3.6 Phosphorus-Modified ZSM-5

Phosphorus modification remains as the most widely used ZSM-5 modification for hydrocarbon cracking in industrial practice. The benefits of phosphorus for improving the hydrothermal stability and shape selectivity of ZSM-5 zeolites were firstly reported by the researchers at Mobil [115]. Phosphorus stabilizes the lattice aluminum ions by retarding aluminum from leaving the zeolite framework. Thus, it hinders framework collapse of zeolite that significantly results in enhancing the stability of the catalyst [115]. The performance and mechanism for P on H–ZSM-5 catalysts have been extensively investigated for the cracking of hydrocarbons to light olefins.

It is generally accepted that the addition of P element into H–ZSM-5 has a great impact on its hydrothermal stability and acidic properties, thus affecting its catalytic activity and light alkene selectivity for the cracking of hydrocarbon. As early as in 1986, Lercher and Rumplmayr [116] proposed that when phosphorus reacts with zeolite, the phosphorus species interact with the oxygen of

the bridging hydroxyl groups on the ZSM-5 zeolite surfaces and result in the cleavage of the Al—O bonding and the opening of the zeolite framework. Thus, the strong Brønsted acid sites convert into weak Brønsted acid sites without changing the overall acid/base properties. Blasco et al. [117] found that the introduction of P on H–ZSM-5 would increase the hydrothermal stability of framework aluminum and the selectivity to propylene and butenes. The acidity and cracking activity for the cracking of *n*-decane of steamed samples reached an optimum for a P/Al molar ratio of c. 0.5–0.7. The framework aluminum pairs are stabilized by extra-framework cationic species formed by protonation of orthophosphoric acid. Zhao et al. [118] and Xue et al. [119] reported that the strong acidity of P modification H–ZSM-5 was weakened by dealumination and the stability and selectivity to propylene of catalyst was better than that of the unmodified H–ZSM-5. The results suggested that the enhanced performance of the catalysts possibly related to the incorporated phosphorus species was stabilized by some non-framework aluminum species. It was found that the framework Al—O coordination bond can be replaced by coordinative bonds between water molecules and the aluminum [120]. One to three water molecules can form coordinative bonds with framework Al and release energy. The P modification restrains the dealumination [120]. Jiang et al. [121] found that phosphorus addition not only modulated the amounts of acidic sites, the percentage of weak acidic sites in total acidic sites, and the acid type, i.e. the ratio of Lewis/Brønsted, but also regulated the basic characteristics of H–ZSM-5 zeolites that in turn promoted its catalytic performance. The maximum yields of propylene and ethylene were 25.6% and 33.9% at 650 °C, which were higher than that over parent H–ZSM-5 by 7% and 4.5%, respectively. The yield of aromatics was reduced with increasing P loading due to the reduction of strong acid and the formation of new basic sites that inhibited the hydrogen transfer reaction [121]. P modification of nano-sized H–ZSM-5 zeolite by trimethyl phosphate impregnation was employed to enhance the hydrothermal stability of zeolites, which exhibited excellent catalytic performance for the full-range fluid catalytic cracking gasoline [122].

On the other hand, even though modification of acid strength may not affect substantially the selectivity in alkane cracking under usual conditions, its impact on activity and catalyst stability is being increasingly demonstrated. Corma et al. [123] studied the effects of P introduction into ZSM-5 zeolite on the catalytic performance for the SCC of naphtha. It was observed that irreversible catalyst deactivation by dealumination occurred in the reactor when the cracking was carried out in the presence of steam. Interestingly, the post-synthesis impregnation with P could slow down the steam deactivation rate of catalyst. The optimum amount of P depended on the Al content of zeolite. Much more stable catalyst could be achieved with enhanced activity and without penalty for production of ethene and propylene. Ji et al. [124] also found that the amount of carbon deposition decreased with increasing P content, resulting in a stable catalytic activity with high light alkene selectivity in supercritical catalytic cracking of *n*-dodecane. Typically, ZSM-5-0.5P zeolite showed the highest catalytic activity.

The co-modification of ZSM-5 zeolite with P and metal cation has been regarded as an effective method to enhance the catalytic activity and stability in the cracking of hydrocarbons. It was found that when Mg, Ca, La, and Zr were introduced into the P-modified ZSM-5 zeolite, the carbon deposition was suppressed and the catalytic activity was higher than that of the parent ZSM-5 zeolite [125]. When a small amount of La was introduced into the P-modified ZSM-5 zeolites, its acidity decreased with the increasing La content, while the basicity increased with the increasing La content [126, 127]. Introducing La to P/H–ZSM-5 not only modified the Brønsted acid sites in H–ZSM-5 but also enhanced the hydrothermal stability of H–ZSM-5 zeolite, which might be assigned to the synergistic effect of P and the formed $LaPO_4$ species in the zeolite channel [111]. For the steamed catalysts, the highest activity was observed on the ZSM-5 co-modified by P and La, in which the introduced La stabilized P species in the zeolite from leaching in steam at high temperatures (Figure 7.20) [111]. The Ni and Fe were introduced into P-modified ZSM-5 zeolite via an impregnating method [128, 129]. In the cracking of butene and pentene, the performance of

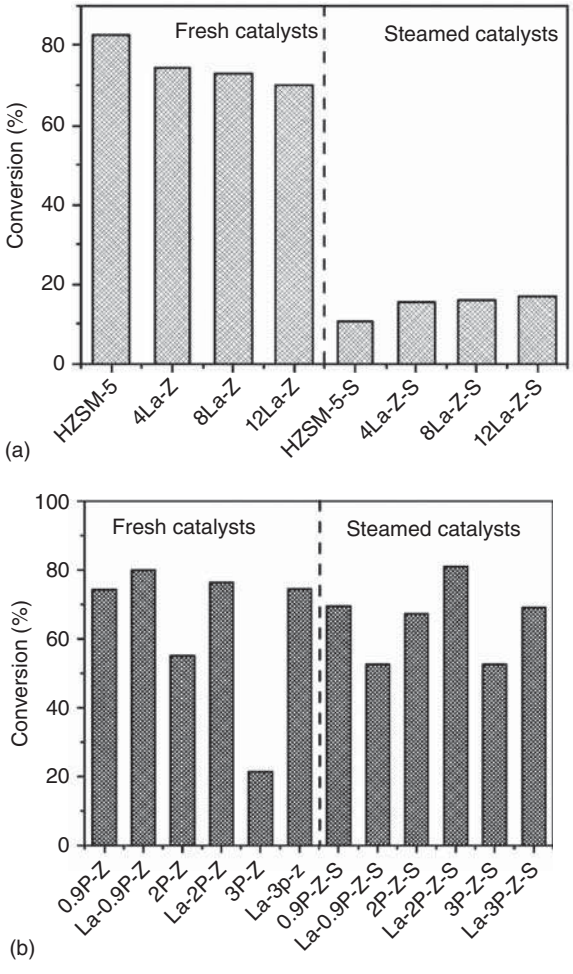

Figure 7.20 (a) Conversion of 1-butene over La/H–ZSM-5 catalysts at 570 °C (N_2/butene = 3 : 1 atm). (b) Conversion of 1-butene over P- and/or La-modified H–ZSM-5 catalysts at 570 °C (N_2/butene = 3 : 1 atm). Source: Reproduced with permission from Xue et al. [111]; © 2010 Elsevier.

catalysts was strongly dependent on the content of Ni and Fe. The Ni and Fe interacted with P and increased the content of tetrahedral framework aluminum, resulting in the recovery of partial Brønsted acid sites that were previously neutralized by P modification [129]. In addition, introducing Ni and Fe created some Lewis acid sites, which significantly promoted the conversions of butene and pentene. The pentene conversion, ethylene selectivity, and propylene selectivity increased with the increasing Ni content in the cracking of pentene [128]. Furthermore, the ethylene selectivity increased with the increasing Fe loading in P-modified H–ZSM-5, while propylene selectivity decreased [129].

Moreover, Inagaki et al. proposed a HNO_3 treatment of ZSM-5 zeolite to dealuminate on its external surface [130]. The resulting ZSM-5 zeolite catalyst with very few acid sites on its external surface exhibited high durability and less coke formation in the cracking of hexane or other paraffin molecules. To date, the regulations of zeolite acidity mentioned above mainly rely on P modification [122], while acid-dealumination and B-assistance [131] techniques have their own pertinence and limitations. Therefore, it is urgent and necessary to develop a new one-pot method for the construction of zeolite catalysts with tunable acidity.

7.4 Nano-ZSM-5 Zeolite

In general, the crystal sizes of ZSM-5 zeolite (about 1∼3 μm) are much larger than the micropore size. When ZSM-5 zeolite is used as a shape-selective catalyst for hydrocarbon cracking, the diffusion and transfer of reactants and product molecules within the pores are limited, leading to low product selectivity [132, 133]. Moreover, owing to the effective active sites, mostly acid sites, for cracking reactions distributed on the internal surfaces of the microporous channels and on the external surfaces of the crystal, coke tends to be deposited in the pore mouths and blocks the micropores, resulting in short catalyst lifetime [134–137]. To alleviate the diffusion limitations, the strategy of shortening the length of pore diffusion path has been widely used by reducing the zeolite crystal size to the nanoscale [138, 139]. Tago et al. [138] summarized the size-controlled preparation of nano-sized zeolites via hydrothermal synthesis in water/surfactant/organic solvent (emulsion method) and their applications as heterogeneous catalysts for light olefin synthesis. As shown in Figure 7.21, the adsorption of surfactants on zeolite precursor and the surface of the nuclei affect the nucleation rate, growth rate, and crystallinity of zeolite.

Alipour summarized the progresses of nano-ZSM-5 zeolite in the catalytic cracking of naphtha to light olefins [12].The nano-zeolites not only provide more external surface area and thus more active sites but also reduce the resistance to pore diffusion. Konno et al. [140] reported that the nano-sized ZSM-5 zeolite catalyst exhibited high cracking activity and provided high yields of light olefins. As shown in Figure 7.22, the total yield of light olefins over the nano-sized zeolite (32.4%) was much higher than that over the macro-sized zeolite (23.2%) at the *n*-hexane conversion of approximately 95%. Moreover, this value could be maintained for 18 hours, whereas the BTX and olefin yields over the macro-sized zeolite monotonically

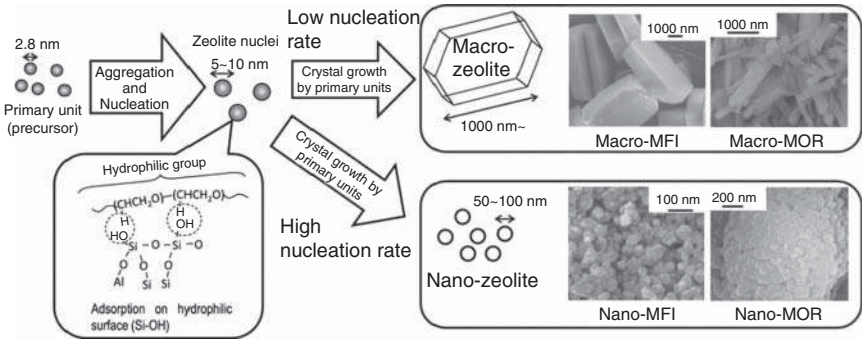

Figure 7.21 Schematic diagram showing zeolite nucleation, crystal growth, and possible relation between the surfactant and zeolite surface. Source: Tago et al. [138]/with permission of Springer Nature.

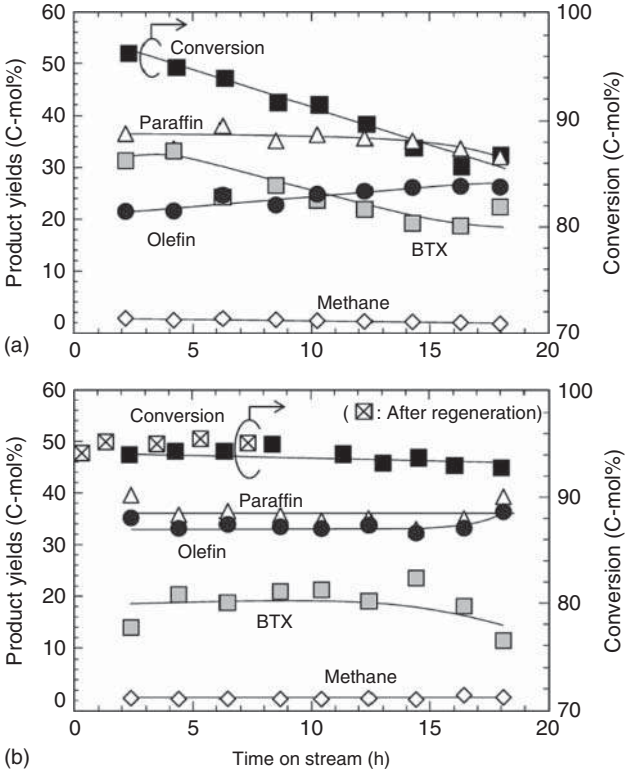

Figure 7.22 Changes in *n*-hexane conversion and product yields with time on stream over (a) macro- and (b) nano-sized zeolites (Si/Al = 50). Source: Reproduced with permission from Konno et al. [140]; © 2012 Japan Petroleum Institute.

changed with time on stream. The amount of coke formed on the nano-sized zeolite was approximately three times smaller than that on the macro-sized zeolite, and the H/C atomic ratio (an index of the aromaticity of the coke) on the nano-sized zeolite was smaller than that on the macro-sized zeolite. Accordingly, the nano-sized zeolite exhibited higher and more stable activity with lower coke formation than the macro-sized zeolite, leading to the higher yield of light olefins.

Teng et al. studied the effect of crystal size on the catalytic performance of ZSM-5 zeolite for cracking of C4 olefins to propylene [141]. It was found that small-crystal ZSM-5 (0.2∼0.3 μm) exhibited excellent stability against coke deposition and the catalytic performance remained stable after regeneration for 10 times in the catalytic cracking of C4 olefins. Similar results on high cracking ability and long lifetime of nano-ZSM-5 zeolite catalysts were obtained by Rownaghi et al. [142]. Under similar conditions, nano-sized H–ZSM-5 produced higher amount of light olefin and less coke in *n*-hexane cracking reaction. The order of conversion of *n*-hexane and selectivity to light olefin was observed as H–ZSM-5-100 > H–ZSM-5-500 > H–ZSM-5-2000, which was the same order as external surface area and the reverse order of crystal size (Figure 7.23). This is because that the nano-sized crystals have a larger external surface area, which offers a higher number of pore entrances and enhances the reaction occurring inside the pore channels compared with large micro-sized crystals. The experimental results show that *n*-hexane cracking activity and selectivity to light olefins are related to the crystal size and the ratio of surface acid sites to total acid sites. Moreover, the selectivity can be improved by reducing the number of acid sites on the external surface. Therefore, decreasing the sizes of the crystals and reducing the acid sites on the external surface are key strategies to improve the catalytic activity and selectivity, respectively.

Ji et al. [143] also prepared ZSM-5 samples with different crystal sizes. It was found that the total yield of propylene and ethylene in the naphtha cracking over the ZSM-5 zeolites increased with the decrease of crystal sizes. The reason is the shorter distance for molecular diffusion, which is conducive to the diffusion of the ethylene and propylene to the outside of the channel; the probability of the secondary cracking reaction and hydrogen transfer is therefore reduced. The smaller the crystal size of ZSM-5 zeolite, the more easily the ethylene and propylene are diffused from the zeolite channel. This reduces the probability of hydrogen transfer reaction and the further cleavage of light olefin to form CH_4.

Tago and coworkers believed that nanocrystal ZSM-5 zeolites were more effective in the catalytic cracking of naphtha and the size of the zeolite must be less than several hundred nanometers for the reaction to proceed under reaction-control conditions [133, 144]. The nano-sized ZSM-5 zeolites exhibited higher *n*-hexane conversion than the macro-sized zeolite and stable activity for 50 hours (Figure 7.24). The reason is that the cracking reaction over nano-zeolite proceeds under reaction limiting conditions, whereas the reaction over macro-sized zeolite proceeds under transition between reaction-limiting and diffusion-limiting conditions. Moreover, the nano-zeolites with large external surface area and low diffusion resistance can reduce the coke deposition.

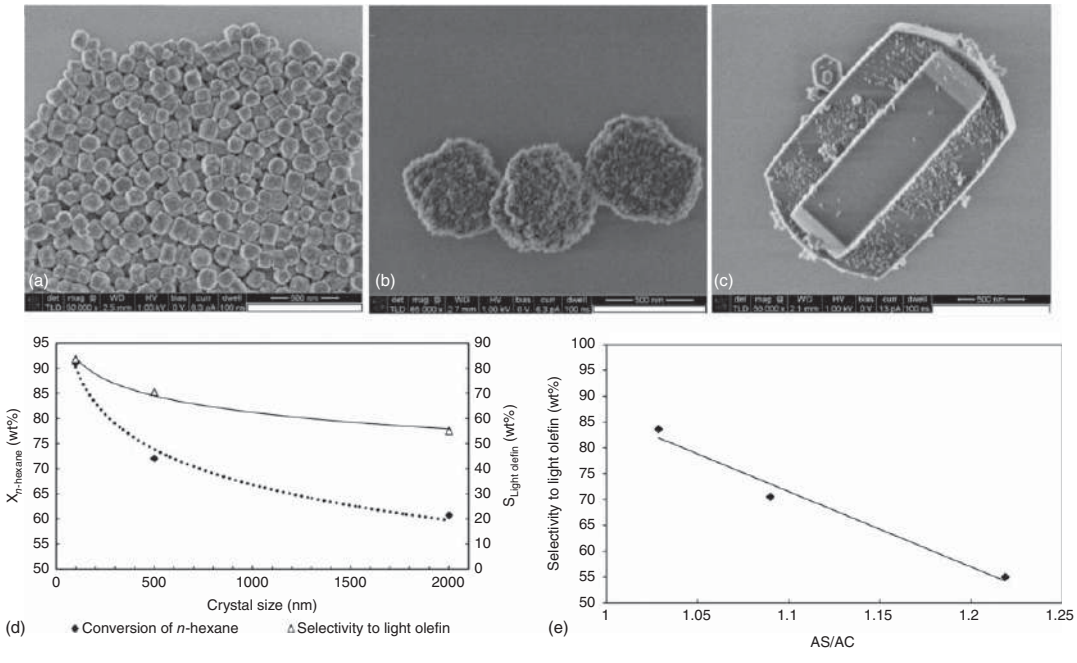

Figure 7.23 FE-SEM images of the H–ZSM-5 crystals synthesized by different methods (a)–(c). Correlation between conversion of *n*-hexane and selectivity to light olefin on the three different-sized H-ZSM-5 catalysts (d). Correlation between selectivity to light olefin and the external acid sites/intercrystalline acid site ratio (AS/AC). Reactant, *n*-hexane; reaction temperature, 470 °C; WHSV, 3 h^{-1}; time on stream, 15 hours; pressure, 1.1 bar (e). Source: Rownaghi et al. [142]/with permission of Elsevier.

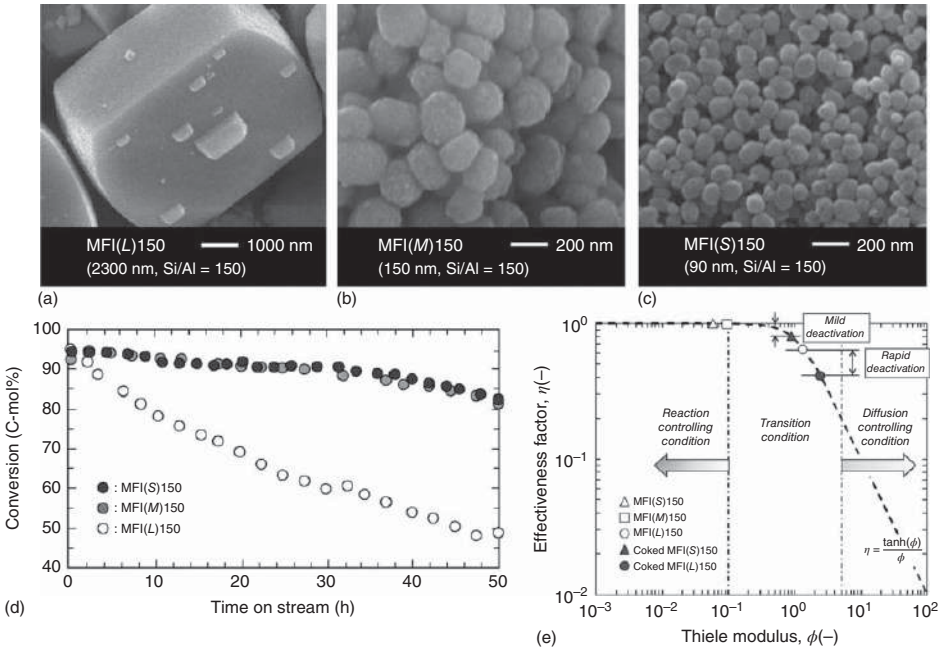

Figure 7.24 FE-SEM images of the H–ZSM-5 crystals (a)–(c). *n*-Hexane conversion over time in *n*-hexane cracking reaction over the ZSM-5 zeolite (Si/Al = 150) with different crystal sizes. Reaction conditions: $T = 650\,°C$, W/F = 0.125 hours, $P = 22.1$ kPa (d). Relationship between the Thiele modulus and effectiveness factor in the *n*-hexane cracking at 650 °C over ZSM-5 zeolites (Si/Al = 150) with different crystal sizes (e). Source: Konno et al. [137]/ with permission of Elsevier.

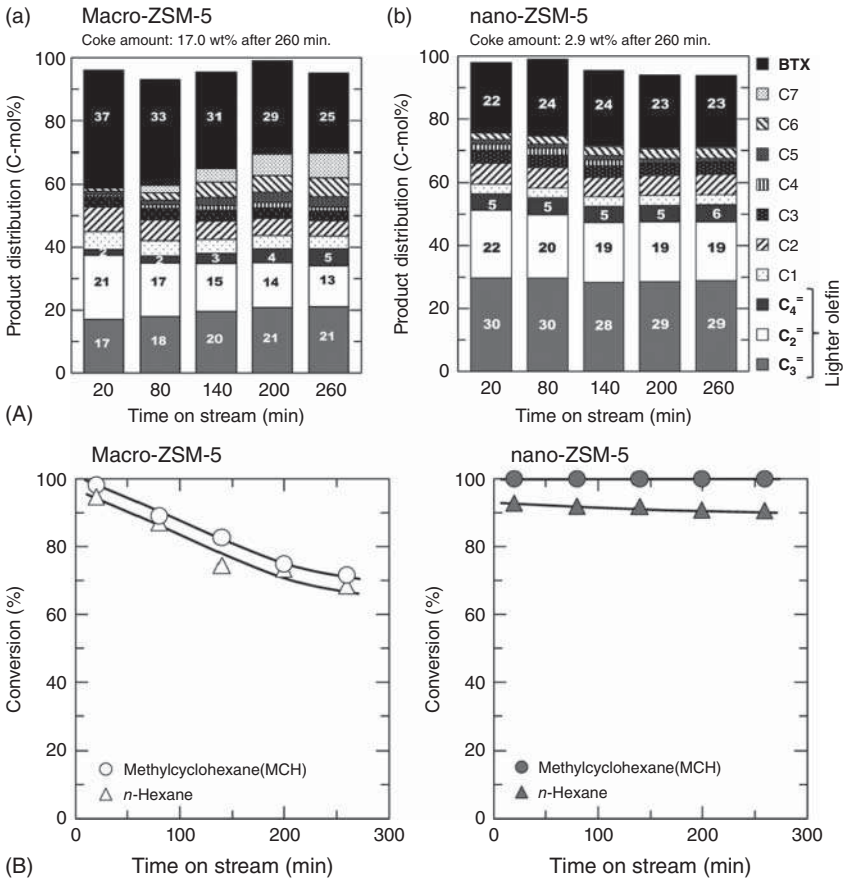

Figure 7.25 (A) Product distribution of the catalytic cracking of model naphtha over micro-ZSM-5 (a) and nano-ZSM-5 (b). (B) Conversion of *n*-hexane and methylcyclohexane in the cracking of model naphtha over micro-ZSM-5 (a) and nano-ZSM-5 (b). Source: Reproduced with permission from Konno et al. [132]; © 2014 Royal Society of Chemistry.

The nano-ZSM-5 zeolite can not only increase the selectivity to light olefins but also increase the lifetime of catalysts. Konno et al. confirmed that the nano-ZSM-5 had relatively higher catalyst stability [132, 133]. The diffusion resistance of both reactants and products within the macro-ZSM-5 was approximately 400 times larger than that in the nano-ZSM-5 [132]. It is evident that nano-ZSM-5 has a higher yield of olefins (approximately 57 C-mol%) and exhibits more stable activity than macro-ZSM-5 (Figure 7.25). The difference in diffusion resistance presumably was the main factor affecting both the product distributions and the catalyst lifetime. Since the cracking of the naphtha representatives takes place under reaction-limiting conditions over nano-ZSM-5, the acid sites of the nano ZSM-5 located at near the external surface and deep inside the crystal are fully used in the cracking reaction. In a multicomponent diffusion system, such as naphtha cracking, hydrocarbons with low diffusability such as naphthenes impose constraints on molecules with higher diffusability such as alkanes and alkenes. This prevents the generated olefins from diffusing inside the zeolite pores, thus

prolongs the residence time, and leads to the production of BTX and coke within the micropores. Moreover, the low diffusion resistance of naphthene reactants and products in nano-ZSM-5 zeolite crystals significantly reduces the amount of coke during the cracking process (2.9 wt% after 260 min). Accordingly, the nano-ZSM-5 exhibits high olefin yields and stable activity in model naphtha cracking.

Mochizuki et al. [136] reported a facile method for preparing nano-sized H–ZSM-5 (c. 65 nm) by mixing the mother gel under mild conditions before crystallization. The crystallite size of the H–ZSM-5 could be controlled by changing the amount of water in the mother gel. It was pointed out that in the catalytic cracking reaction of *n*-hexane, the crystallite size of H–ZSM-5 showed little impacts on the initial activity but considerably influenced the deactivation rate. The nanocrystalline ZSM-5 zeolite deactivated more slowly probably owing to the high pore density and the suppression of coke formation on the surface and/or in the pore. Moreover, nano-ZSM-5 had more pore openings, and the blockage of zeolite channels by coking could be avoided, leading to improved catalyst lifetime.

The difference in catalytic performance and deactivation mechanism between nanoscale and macroscale ZSM-5 zeolites in the cracking of alkane (*n*-hexane) and naphthene (methyl-cyclohexane) was investigated by Konno et al. [133]. It was found that the product selectivity and catalyst lifetime of the ZSM-5 zeolite catalyst depended on the type of reactant. However, the nanoscale ZSM-5 exhibited a high conversion and high light olefin yields with stable activity, regardless of the type of reactant due to the large external surface area and low diffusion resistance to the reactant/product hydrocarbons as compared with the macroscale ZSM-5. The catalyst stability of the zeolite in the cracking of *n*-hexane was greater than that in the cracking of naphthenes (Figure 7.26). This was due to the different mechanisms of coking that deactivated the acid sites available both on the external surface and within the crystal pores. The coke produced from *n*-hexane cracking was mainly deposited on the outer surface of zeolite crystal, while that from methyl cyclohexane cracking was deposited on the outer surface and inside of zeolite crystal.

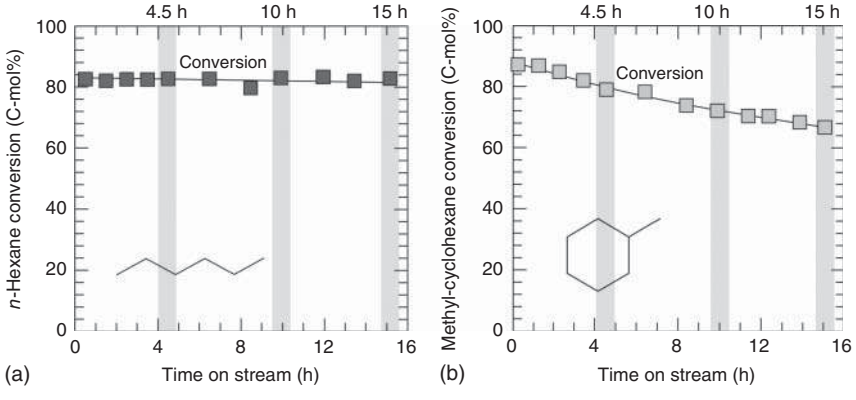

Figure 7.26 (a) *n*-Hexane and (b) methylcyclohexane conversions with time on-stream (W/F = 0.125 hours) over the nanoscale ZSM-5 zeolite (Si/Al = 150). Source: Reproduced with permission from Konno et al. [133]; © 2013 Elsevier.

7.5 Hierarchical ZSM-5 Zeolites

H–ZSM-5 zeolites show good activity with their unique channels and suitable acid properties for the catalytic cracking of hydrocarbons, but they still suffer from the diffusion limitation due to their single microporosity. Hierarchically structured zeolites integrate at least two levels of porosity and present the advantages associated with each level of porosity, from selectivity to mass transport. The hierarchical zeolites that contain both mesopores and macropores to allow for the rapid diffusion of bulky molecules and zeolitic micropores to provide catalytic activity and selectivity are therefore desirable. Hence, they are categorized into three distinctly different types according to their hierarchical porosities: mesostructured zeolites, macrostructured zeolites, and micro/meso/macroporous structured zeolites. Furthermore, the synthesis of hierarchical zeolites with multiple levels of porosity, with combined advantages of the acidity and stability of micropores and the enhanced diffusion of larger pores, is considered one of the best approaches and has been widely employed in heterogeneous catalysis [145–148]. Several strategies have been proposed to generate mesopores in zeolite crystals such as post-synthesis modification based on desilication or dealumination [149, 150] and direct synthesis [151]. The latter can be accomplished either by carbon templating [152] or by soft templating [153, 154], which is attracting more and more attention because of its ability to better control mesoporosity. To improve the mass transfer capability and enhance the accessibility of acid sites in zeolites, great efforts have been made [147, 149, 151, 155]. In this section, we will review some interesting advances in hierarchical ZSM-5 zeolites in the cracking of naphtha model compounds.

7.5.1 Mesoporous/Microporous ZSM-5 Zeolites

7.5.1.1 Hard Template Method

The most direct way to introduce mesopores into zeolite crystals is to use a hard template. Nanoparticles, such as carbon nanotubes or polymers, can be contained in synthesis and occluded in zeolite crystals. After the removal of carbon particles by combustion, zeolite crystals with controllable pore size distribution and highly crystalline micro/mesoporous hierarchical structure can be formed [152]. The generation of mesopores by secondary templating with carbon particles during synthesis increases the accessibility of acid sites in ZSM-5 and meanwhile shortens diffusion path.

Chou et al. [156] synthesized the mesoporous ZSM-5 zeolite by using a carbon hard template combined with dry gel conversion method and studied its catalytic performance in the cracking of *n*-hexane. The results showed that the introduction of mesopores led to the decrease in the catalytic activity in the cracking reaction due to the decreases in crystallinity of the zeolite and the amount of acid sites.

Siddiqui et al. [157] found that a novel mesoporous ZSM-5 zeolite with enhanced diffusion rates of FCC naphtha and products could significantly increase the selectivity to light olefins and BTX. The yield of ethylene and propylene was up to 24%, which was significantly higher than that of conventional ZSM-5. The mesoporosity

of ZSM-5 significantly enhanced the production of aromatics, showing a twofold increase in BTX yields compared with conventional ZSM-5 catalyst (Figure 7.27).

Lee et al. [158] used the carbon templating method to synthesize mesoporous ZSM-5 zeolite and used it in the catalytic cracking of C5 raffinate. The results showed that the conversion of C5 raffinate and yield of light olefins increased with increasing carbon template content during synthesis, while the selectivity to ethylene and propylene was kept unchanged (Figure 7.28). The mesoporosity played an important role in determining the catalytic performance because the presence of mesopores increased the diffusion of reactant to access the active sites of zeolites.

7.5.1.2 Post-treatment Method

Among a variety of strategies studied, post-treatment methods such as typical desilication and dealumination are more effective and convenient to construct hierarchical zeolite. Desilication of the conventional ZSM-5 zeolite has been proven to be a relatively more straightforward method to introduce mesoporosity.

Zhao et al. [159] found that in the cracking of heavy oil, the catalytic activity and the yield of light olefins on ZSM-5 zeolite alkali treated in 0.2 M NaOH solution were higher than those on untreated ZSM-5 and industry catalyst CEP-1. The alkali-treated ZSM-5 zeolites with Si/Al ratio of 25 presented higher catalytic cracking performance and selectivity of light olefin due to their optimized hierarchical pores. A possible mechanism of desilication during alkali treatment was proposed and show in Figure 7.29.

Gao et al. [160] also found that new mesopores could be created with the removal of siliceous species by alkali treatment. The ZSM-5 zeolite treated with NaOH exhibited a significantly higher conversion, selectivity, and yield of ethylene and propylene than those over parent ZSM-5 sample in the catalytic cracking of *n*-butene. When the treated concentration of NaOH solution was 0.1 M, the highest yield of ethylene and propylene could reach 81.76%. The excellent catalytic performance was attributed to the integrated zeolite structure, suitable acid amount, and abundant mesopores.

Sazama et al. [79] observed that the dealuminated micro/mesoporous ZSM-5 zeolite showed higher conversion of *n*-hexane and higher selectivity to light olefins and lower selectivity to aromatic compounds (Figure 7.30). A reasonable explanation was that the mass transport in shorter microporous channels could be improved and the shorter contact time of the intermediates inside the microporous channels could limit the further transformation of olefins to aromatic compounds.

7.5.1.3 Soft Template Method

Soft templating method is a more generalized method that uses large organic molecules as the mesopore template along with a structure-directing agent (SDA) for the synthesis of zeolites. Figure 7.31 illustrates the synthetic strategy for templating uniform mesopores within a zeolite matrix [154]. As the zeolite crystal grows, the incorporated polymer becomes phase-segregated from the zeolite matrix, forming an intracrystal polymer network that is covalently linked to the zeolite framework. The polymer porogen can be removed by calcination of the composite crystals, and zeolites with uniform intracrystal mesopores can be obtained.

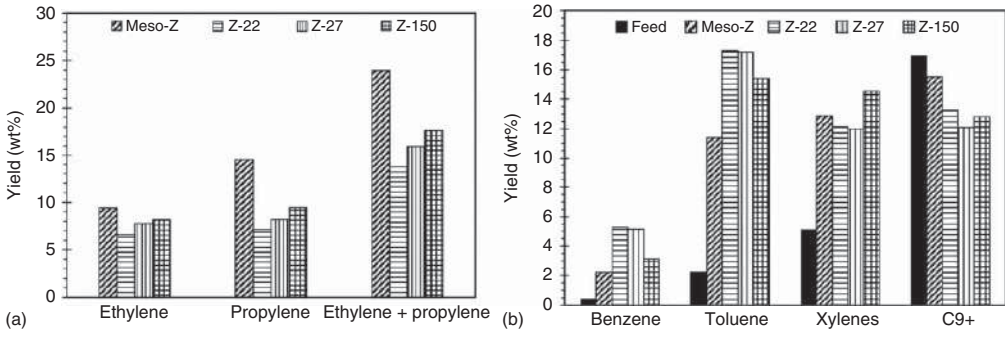

Figure 7.27 Comparison of ethylene and propylene yields (a) and BTX content (b) in cracked naphtha for Meso-Z, Z-22, Z-27, and Z-150 at constant catalyst/naphtha ratio of 3.0 and 600 °C. Source: Reproduced with permission from Siddiqui et al. [157]; © 2010 Springer.

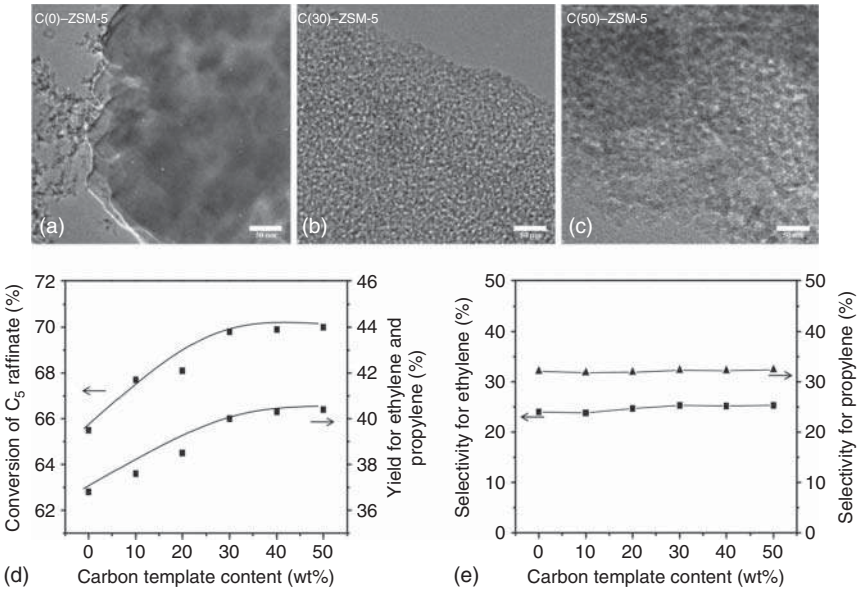

Figure 7.28 HR-TEM images of (a) C(0)–ZSM-5, (b) C(30)–ZSM-5, and (c) C(50)–ZSM-5 catalysts. (d) and (e) Catalytic performance of C(X)–ZSM-5 (X = 0, 10, 20, 30, 40, and 50) catalysts in the catalytic cracking of C5 raffinate to light olefins performed at 500 °C after a three hours-catalytic reaction, plotted as a function of carbon template content. Source: Lee et al. [158]/with permission of Elsevier.

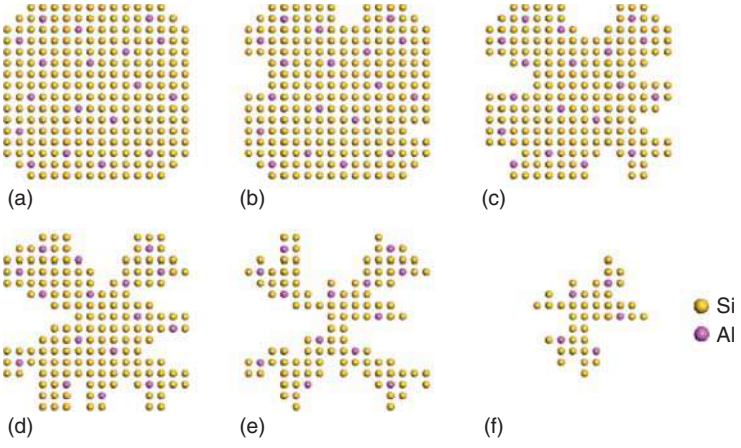

Figure 7.29 The proposed desilication mechanism of ZSM-5 zeolite. Source: Reproduced with permission from Zhao et al. [159]; © 2011 Elsevier.

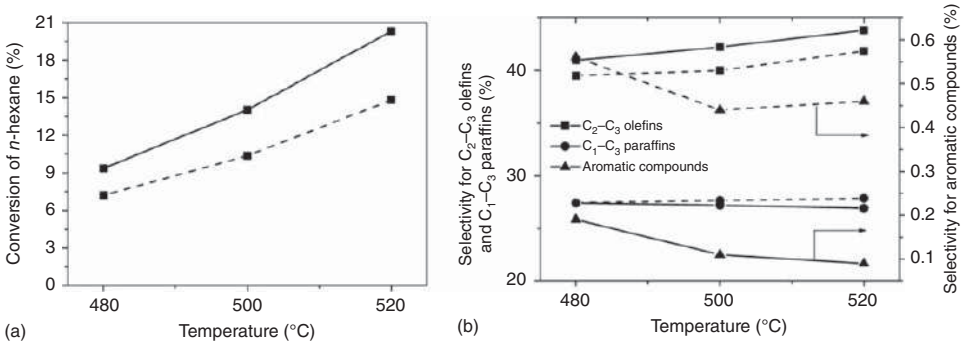

Figure 7.30 Cracking of *n*-hexane over deAlmm-ZSM-5(I) (solid line) and microporous ZSM-5(II) (dashed line). (a) Conversion of *n*-hexane and (b) selectivity for C2–C3 olefins, C1–C3 paraffins, and aromatic compounds as a function of temperature. Source: Reproduced with permission from Sazama et al. [79]; © 2013 Wiley-VCH.

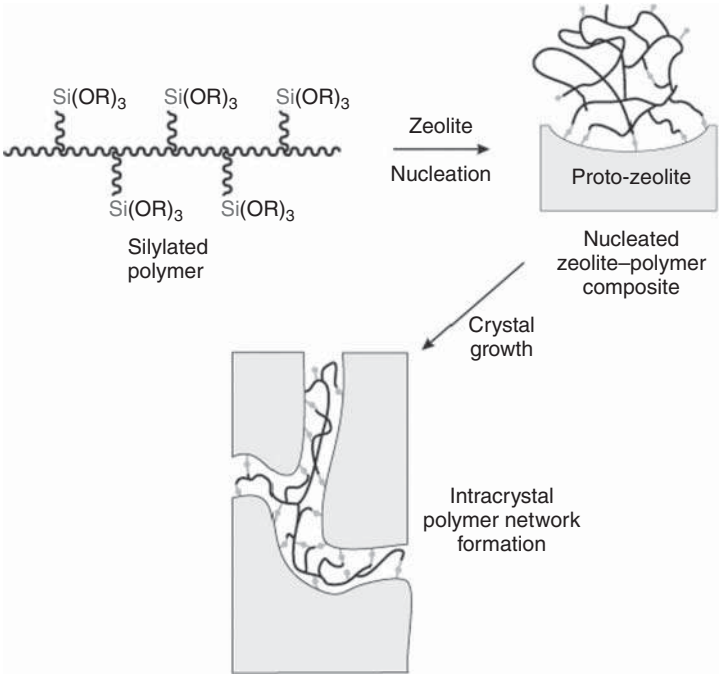

Figure 7.31 Conceptional approach to the synthesis of a zeolite with intracrystal mesopores using a silylated polymer as the mesoporogen. Source: Reproduced with permission from Wang and Pinnavaia [154]; © 2006 Wiley-VCH.

The hierarchical ZSM-5 zeolites with similar acidity were prepared by hydrothermal synthesis with organosilane ((3-aminopropyl) triethoxysilane [APTES]) and tetrapropylammonium hydroxide (TPAOH) as dual templates to investigate the effect of pore structure on the catalytic cracking of *n*-heptane [161]. Zhang et al. found that the selectivity to ethylene and propylene increased with the increase of mesopore volume and the selectivity to ethylene and propylene had a well-linear dependence with HF [161]. This was attributed to the existence of mesopore that could significantly enhance the diffusion rate and decrease the residence time of light olefins in the reaction. The products could move out of pore channels immediately, and the excessive reaction of the ethylene and propylene could be suppressed, as illustrated in Figure 7.32.

Ding et al. [162] also pointed out that the hierarchical ZSM-5 zeolite showed higher heavy oil cracking activity due to the increased accessibility of the active sites by the presence of the hierarchical structure and higher olefin selectivity due to the suppress of secondary reactions with shorter residence time.

7.5.1.4 Other Methods

Li et al. [163] reported a general strategy for the green synthesis of MFI zeolite nanocrystals with controllable intercrystalline mesopores and studied the catalytic performance in hexane cracking reaction. The results showed that the mesopores of MFI zeolite varied with the nanocrystals size by changing the sodium salt

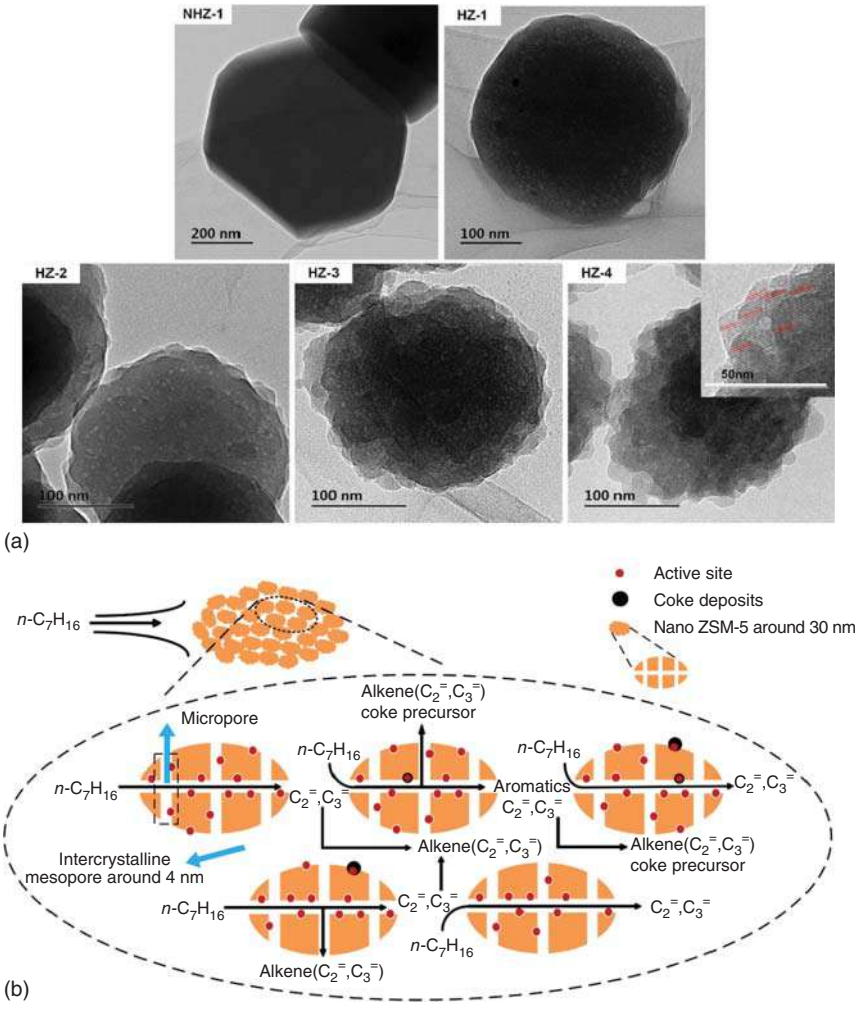

Figure 7.32 (a) TEM images of the hierarchical ZSM-5 samples and traditional ZSM-5 zeolite. (b) The model of catalytic cracking of *n*-heptane over hierarchical ZSM-5. Source: Zhang et al. [161]/with permission of Elsevier.

concentration or sodium salt type in the aluminous silicate gel during hydrothermal crystallization. The introduction of mesopores significantly improved the stability of catalyst against carbon deposition and the shortening of the diffusion path slowed down the rate of carbon deposition. The lifetime of mesoporous ZSM-5 catalysts could be about twice longer than that of highly dispersed MFI zeolite nanocrystals (Figure 7.33).

Recently, Zhao and Jiang's research group prepared a series of core–shell H–ZSM-5@mesoSiO$_2$ for *n*-butane catalytic cracking [164]. The diffusion time constant continually increased with the increasing shell thickness of SiO$_2$. The linear positive correlation between diffusion property and catalytic performance was directly established for the first time. It was found that the H–ZSM-5@mesoSiO$_2$

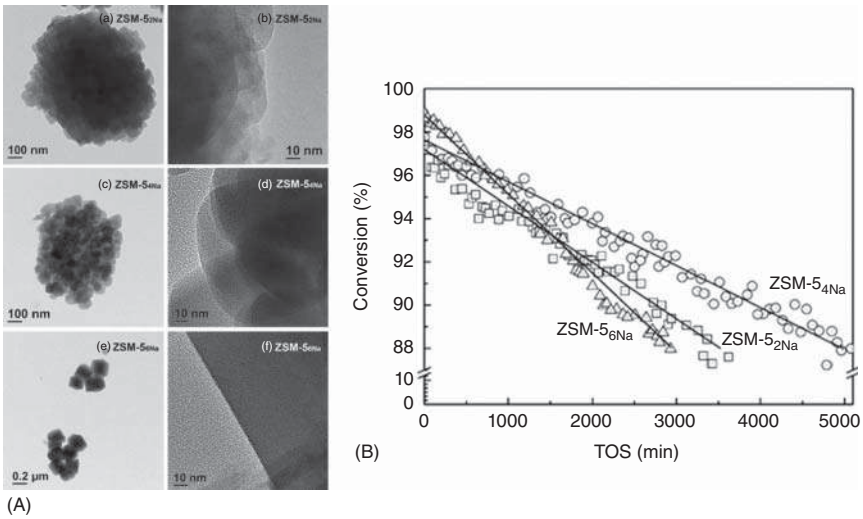

Figure 7.33 (A) TEM and (B) HRTEM images of ZSM-5*x*-Na ($x = 2$, 4, and 6) samples. The conversion of *n*-hexane cracking over ZSM-5*x*-Na ($x = 2$, 4, and 6) samples. Source: Li et al. [163]/with permission of Royal Society of Chemistry.

(1 : 4) sample showed optimized *n*-butane conversion rate per Al site of 2.43 min^{-1}, which was nearly twice as that over parent H–ZSM-5 (1.34 min^{-1}) (Figure 7.34).

7.5.2 Macroporous/Mesoporous/Microporous ZSM-5

Great progress in the preparation of hierarchical zeolites has been made in the past few decades. However, most of the work focuses on the bimodal porous structure on micro/mesoscale, which are still limited for efficient diffusion. Therefore, hierarchically macro/meso/microporous materials are expected to further enhance the mass transport and thus maximize the benefits of hierarchy in some catalytic reactions. The critical issue in the preparation of macro/meso/microporous zeolites is how to construct well-interconnected pores with multilevels in a versatile and controlled manner and further tailor the catalytic performance of cracking reaction.

Louis and coworkers [165] prepared a ZSM-5 zeolite/glass-based composite catalyst material with macroporous/mesoporous/microporous trimodal pore size distributions. Starting from the glass monomer with mesopores and macropores, the ZSM-5 zeolite entered through partial recrystallization of the glass support, allowing the zeolite crystal growth and introducing additional micropores. Zeolite crystals in intimate contact with the glass support, featuring micropores in addition to the mesopores (Figure 7.35). Therefore, the composite materials exhibited strong acidic properties and enhanced diffusion properties in comparison with purely microporous zeolite materials, which also exhibited high catalytic activity and selectivity to light olefins in the *n*-hexane cracking reaction.

Zhao's group developed ZSM-5 zeolite fibers with hierarchical macro/meso/microporosities by an electrospinning method [166]. The as-prepared ZSM-5 zeolite fibers

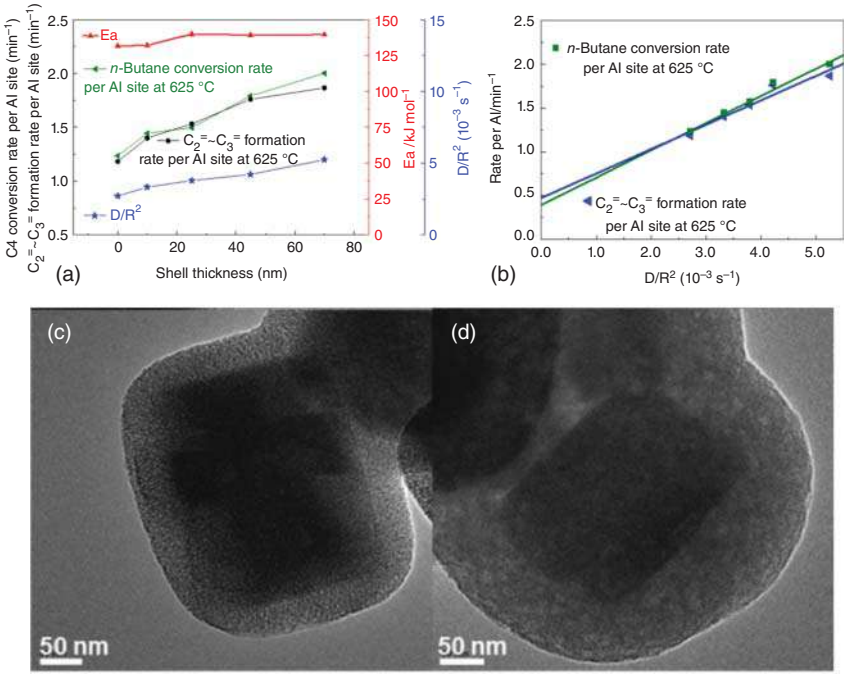

Figure 7.34 *n*-Butane conversion rate per Al site versus reaction temperature (a) and the apparent energy activation calculation (b) over prepared samples for cracking of *n*-butane. TEM images of H–ZSM-5@meso SiO_2 (1 : 2) (c) and H–ZSM-5@meso SiO_2 (1 : 4) (d). Source: Yang et al. [164]/with permission of John Wiley & Sons, Inc.

retained the micropore structure of ZSM-5 zeolite building block; meanwhile macro/mesoporosity structures originating from the crystal self-assembly were introduced (Figure 7.36). Consequently, the zeolite fibers included both the excellent catalytic properties of small crystal ZSM-5 zeolite and the mass transfer properties of hierarchical porosity. The hierarchical ZSM-5 zeolite fibers showed superior *iso*-butane conversion and yield to propylene and good catalyst stability in the cracking of *iso*-butane reaction. The further structure–property relationship study indicated that the excellent catalytic performance of the ZSM-5 hollow fibers was attributed to the hierarchical macro/meso/microporosities, which improved the accessibility of active sites for enhanced reactivity and also promoted the efficiency of mass transfer to suppress the secondary reaction, leading to the high yield to light olefins and good anti-coking stability.

The pioneering work by Ryoo and coworkers demonstrated that resembling small cations in conventional synthetic systems, local functional groups of a large molecule could act as SDAs to direct the crystallization of zeolite framework on the mesoporous and microporous length scales simultaneously and thus yield MFI zeolite nanosheets [167]. The MFI nanosheets were only 2 nm thick, which corresponded to the *b*-axis dimension of a single MFI unit cell (Figure 7.37). The large number of acid sites on the external surface of these zeolites rendered them highly active for the catalytic conversion of large organic molecules. The long

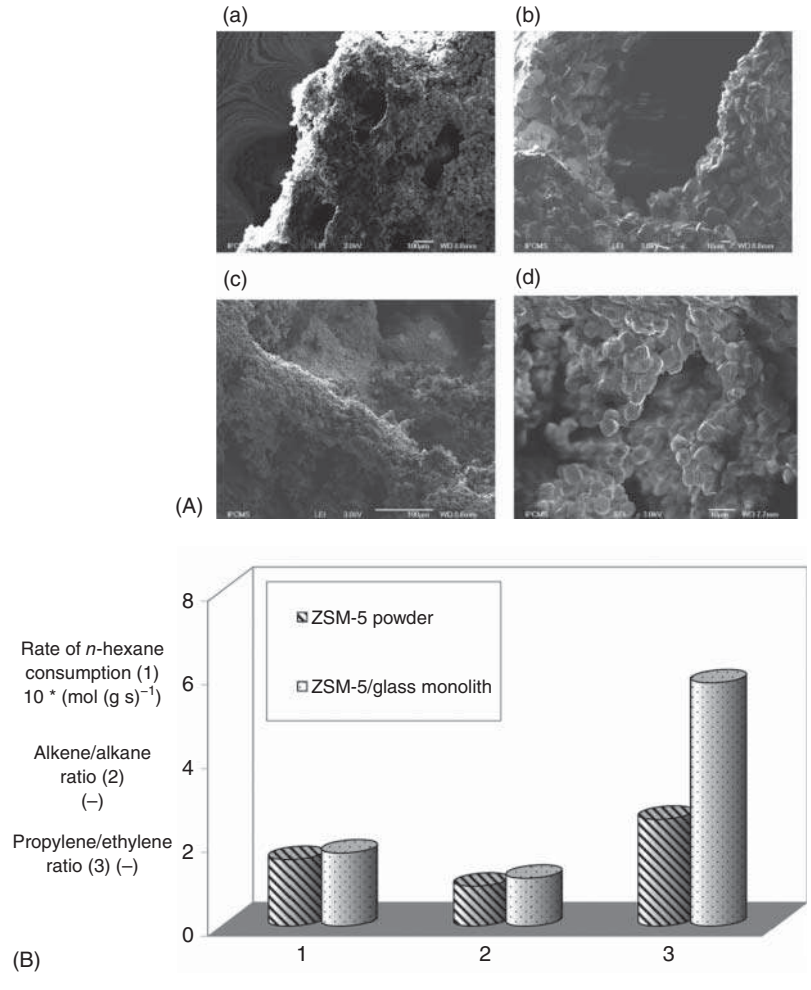

Figure 7.35 (A) SEM images of ZSM-5 crystals coated on mesoporous glass using TEOS (a) and (b) and using Aerosil 200 (c) and (d) as silicon source. (B) Activity and selectivity of H–ZSM-5/glass monolith (using TEOS) in *n*-hexane cracking reaction. Source: Ocampo et al. [165]/with permission of American Chemical Society.

catalytic lifetime of the MFI nanosheets was due to the slow deposition of coke exclusively at the external zeolite surfaces.

ZSM-5 nanosheets with macro/meso/microporosities and highly exposed (010) crystal planes were also reported, which exhibited high catalytic activity and good anti-coking stability simultaneously for *n*-heptane catalytic cracking [168]. The conversion of *n*-heptane was remarkably higher over nanosheet ZSM-5 than that over conventional ZSM-5, especially at low reaction temperatures, due to the unique diffusion characteristics and accessibility of the acid sites of nanosheet ZSM-5. High catalytic activity and stability were also demonstrated. The conversion of *n*-heptane on the nanosheet ZSM-5 sample decreased from 96.6% to 86.5%, with a reduction of 10% after 100 hours on stream, while conventional ZSM-5 conversion was reduced

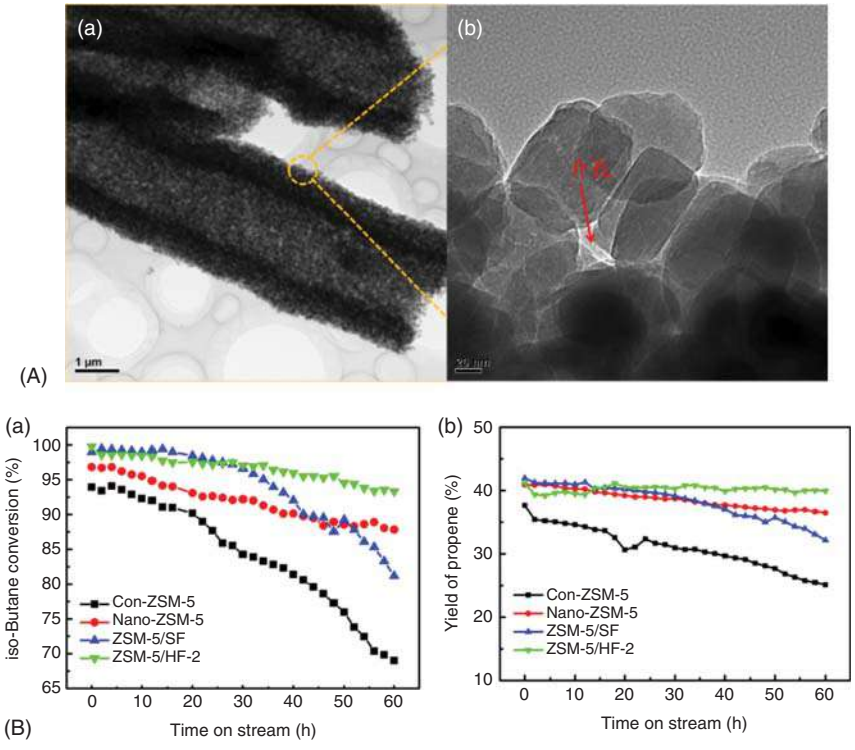

Figure 7.36 (A) TEM and HRTEM images of ZSM-5/HF-2 sample, showing the mesopores created from the stacking of ZSM-5 nanoparticles. (B) Catalytic stability of the test results of con-ZSM-5, nano-ZSM-5, ZSM-5/SF, and ZSM-5/HF-2 zeolite fibers during 60 hours on stream at 625 °C by monitoring the conversion of *iso*-butane (a) and the yield of propylene (b). Source: Liu et al. [166]/Springer Nature/CC by 4.0.

by 28.4%, almost three times the value of that on nanosheet ZSM-5 (Figure 7.38). The outstanding catalytic performance was attributed to the synergy of high external surface area and acid sites, fully accessible channel intersections acid sites, and hierarchical porosity by the unique morphology.

Hierarchical ZSM-5 combines the high activity, shape selectivity, and hydrothermal stability of conventional ZSM-5, and thus it shows improved catalytic performance in the cracking of model compounds due to the hierarchical porosity of the pore walls and to the easier transport and access to the active sites. Recently, Sun et al. [169] reported that hierarchically porous zeolite single-crystal reactors with fully interconnected and highly ordered multimodal porosity showed excellent catalytic efficiency and lifetime in the conversion of bulky molecules (Figure 7.39). However, the synthesis of mesoporous zeolite single crystals often required expensive porogens such as CTAB, P123, and F127 [170]. Therefore, an environmentally friendly and low-cost synthesis strategy remains a great challenge in the field of single-crystal mesoporous zeolites.

Three-dimensional (3D) printing manufacturing has attracted much attention in various fields due to its rapid accomplishment, cost-effectiveness, approach

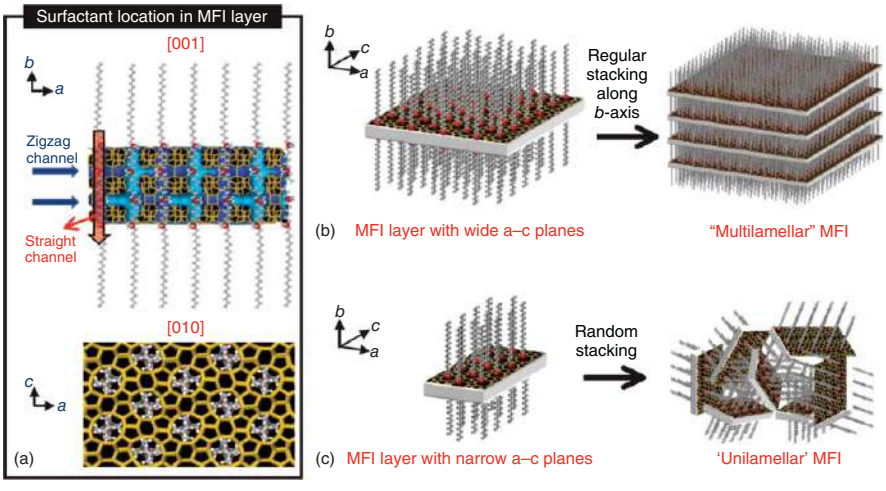

Figure 7.37 Crystallization of MFI nanosheets. (a) Proposed structure model for the single MFI nanosheet. Surfactant molecules are aligned along the straight channel of MFI framework. Two quaternary ammonium groups (indicated as a red sphere) are located at the channel intersections: one is inside the framework, and the other is at the pore mouth of the external surface. Many MFI nanosheets form either multilamellar stacking along the *b*-axis (b) or a random assembly of unilamellar structure (c). Source: Reproduced with permission from Choi et al. [167]; © 2009 Springer Nature.

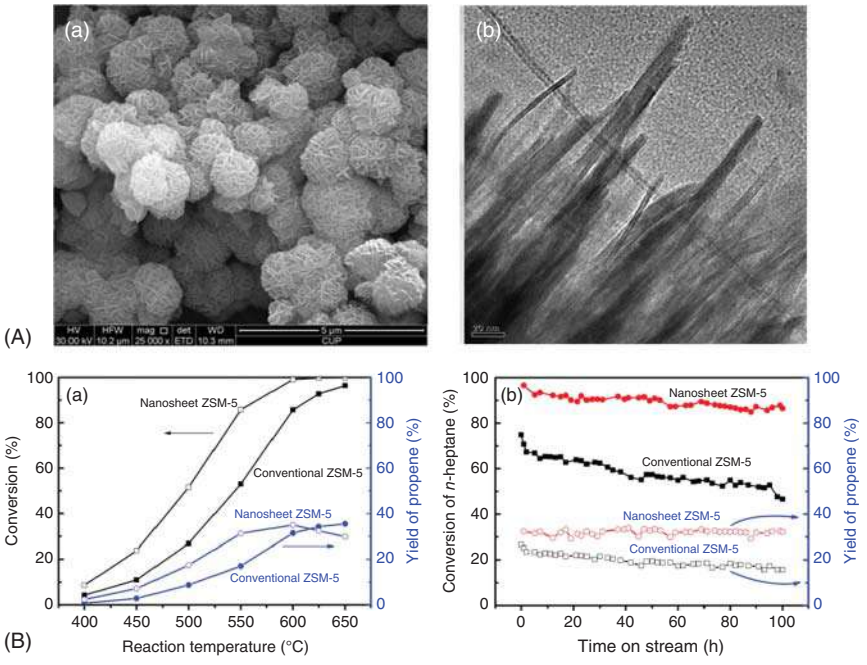

Figure 7.38 (A) SEM and HRTEM images of nanosheet ZSM-5 zeolite. (B) The conversion of *n*-heptane and the yield of propylene on the ZSM-5 catalysts plotted as a function of reaction temperature (a); the conversion of *n*-heptane and the yield of propylene on the ZSM-5 catalysts plotted as a function of time on stream (b). Source: Xiao et al. [168]/with permission of Royal Society of Chemistry.

facilities, and structure controllability [171, 172]. Motivated by the advantages offered by the 3D-printed technique, Li et al. reported a novel and facile approach for fabrication of MFI and FAU monolith catalysts with macro/meso/micorporosities via 3D printing and as heterogeneous catalysts for the *n*-hexane cracking reaction [173]. Besides, SAPO-34 molecular sieves were grown on the surface via a secondary growth method to modify and improve the performance of the monolithic catalysts (Figure 7.40). The results indicated that the 3D-printed H-ZSM-5 monolith exhibited more stable activity in *n*-hexane cracking and higher selectivity to light olefins than its powder counterpart as a result of hierarchical pores and moderated acidity.

7.5.3 Composite Zeolites

In addition to the hierarchical zeolite discussed above, ordered mesoporous materials usually lack the hydrothermal stability and acid strength typical of crystalline zeolites, although they have shown improved ability for cracking large-size molecules. However, their application to reactions less demanding in acid strength, such as olefin cracking, might be possible if better stability is achieved. Progress in these materials has led to the development of micro/mesoporous zeolite composites,

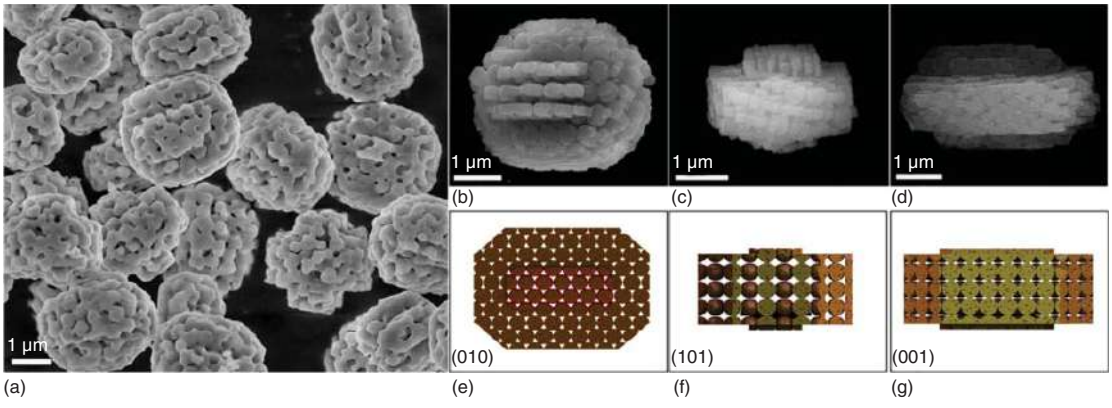

Figure 7.39 SEM images of OMMS–ZSM-5(400,30). Source: Sun et al. [169]/with permission of Elsevier.

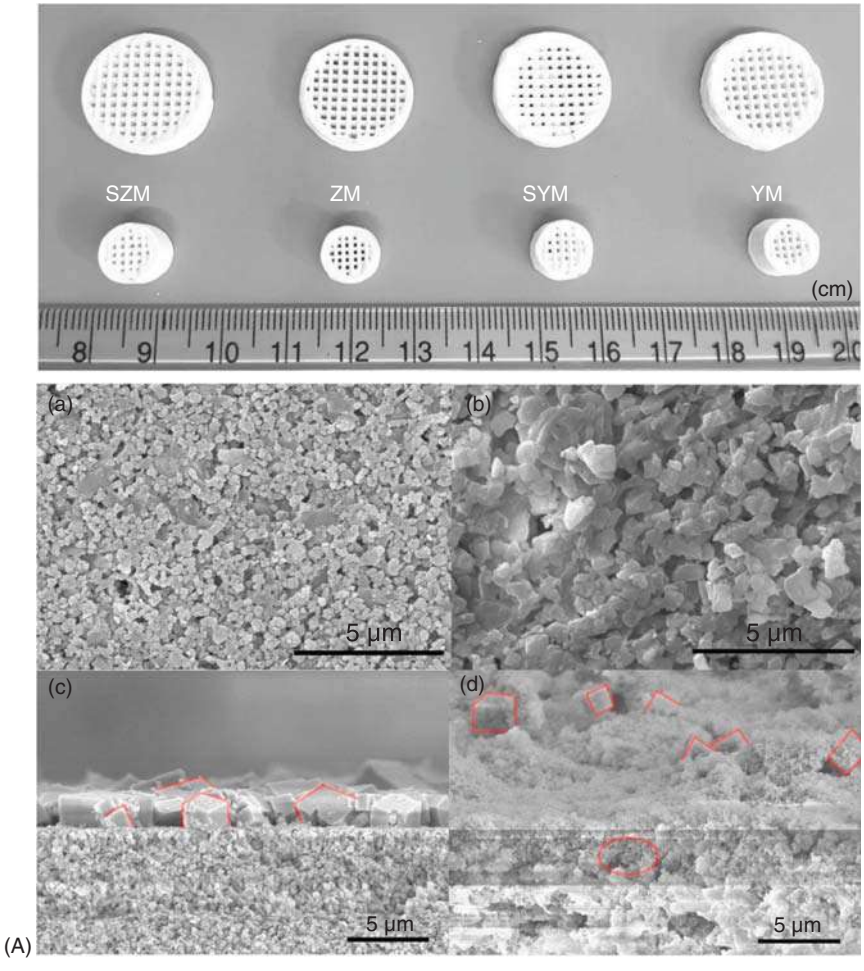

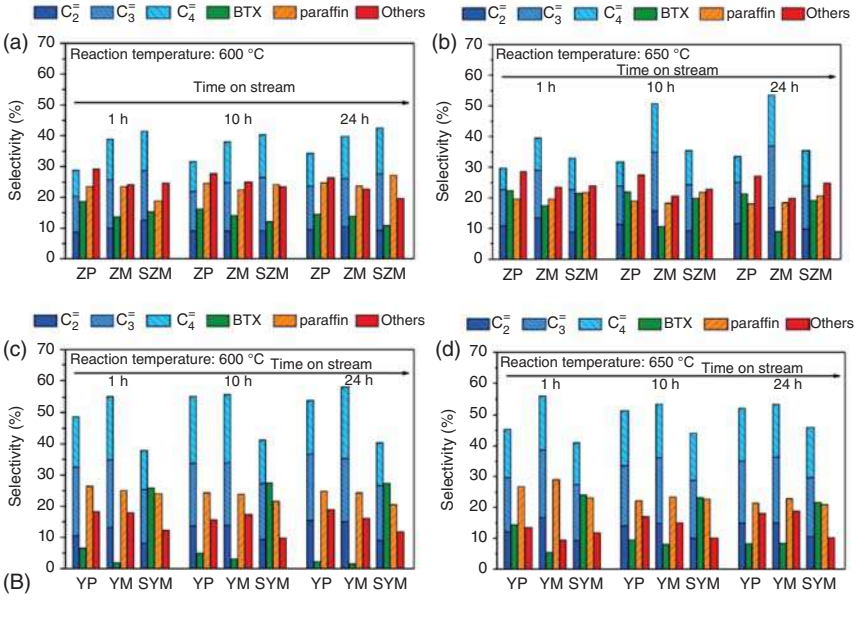

Figure 7.40 Optical image of the 3D printed monoliths. (A) SEM images of the surface of (a) H–ZSM-5 monolith, (b) HY monolith, (c) H–ZSM-5 monolith with SAPO-34 growth, and (d) HY monolith with SAPO-34 growth. (B) Product distribution on the investigated H–ZSM-5 and HY zeolites at (a), (c) 600 °C and (b), (d) 650 °C. Reactant, *n*-hexane; WHSV, 5 h^{-1}; time on stream, 24 hours; pressure, 1.01 bar. Source: Li et al. [173]/with permission of Elsevier.

which hold great promise for cracking catalysis. These comprise a mesoporous material wherein zeolite crystals are embedded, thus improving their acid strength and shape selectivity. These composites can be achieved by (i) direct synthesis, incorporating protozeolites or zeolite nanocrystals to the surfactant-driven synthesis of the mesophase, (ii) partial dissolution and recrystallization in the presence of surfactant, or (iii) zeolitization of preformed mesoporous materials. This last approach is difficult given the thin wall thickness of mesoporous materials, often leading to phase segregation unless steam-assisted crystallization is used.

The H–ZSM-5/MCM-41 composite zeolite exhibited a microporous/mesoporous structure with nano-sized H–ZSM-5 particles and controllable acidity [174]. The mesoporous structure and nano-sized H–ZSM-5 particles improved the diffusion of the reactants and products in the pores, and the H–ZSM-5 nanoparticles uniformly dispersed in the MCM-41 matrix supplied proper acidity, shorter channels, and higher total specific surface area (Figure 7.41). These resulted in high catalytic activity, high selectivity to light olefins, and long lifetime for *n*-decane catalytic cracking.

A series of hierarchical porous zeolites (ZSM-5-ZRP-1) was synthesized by adding different contents of ZRP-1 to the procedure of hydrothermal synthesis of

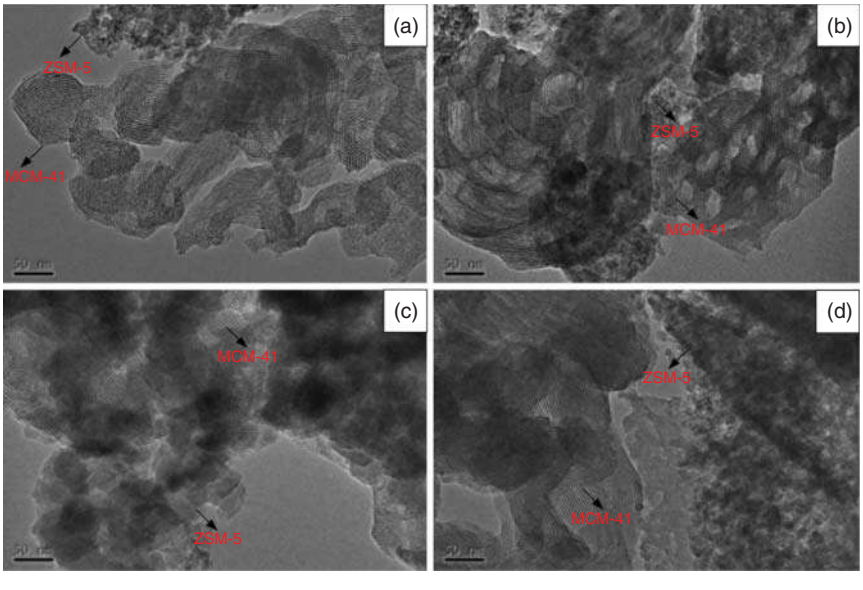

Figure 7.41 TEM images of (a) HZM-N (50), (b) HZM-N (100), (c) HZM-N (150), and (d) HZM-l (50). Source: Sang et al. [174]/with permission of Springer Nature.

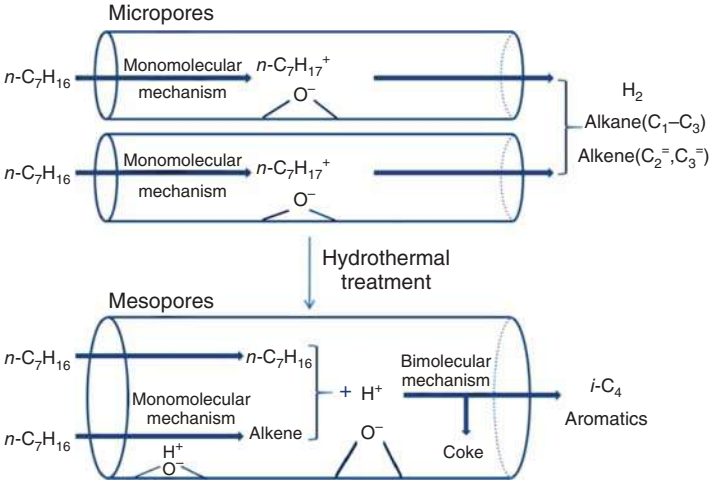

Figure 7.42 The brief model of catalytic cracking of *n*-heptane over ZSM-5/MOR zeolites in micropores and mesopores. Source: Reproduced with permission from Zhu et al. [176]; © 2009 Elsevier.

ZSM-5 [175]. The results indicated that physicochemical properties and catalytic performance of ZSM-5-ZRP-1 samples were quite different from that of H–ZSM-5 or ZRP-1. ZSM-5–ZRP-1 samples had a lot of mesopores and a suitable amount of acid sites and higher Lewis/Brønsted ratio than H–ZSM-5 or ZRP-1 and also showed medium acid amount and strength. All these characteristics led to higher selectivity to olefins (ethylene and propylene) in the cracking of *n*-heptane.

A ZSM-5/MOR composite zeolite with the hierarchical porous structure of 10-MR and 12-MR channels was prepared by Zhu et al. [176]. They investigated the catalytic cracking of *n*-heptane over the fresh and steamed ZSM-5/MOR zeolites by *in situ* DRIFTS. It was found that the content of mesopores increased while that of micropores decreased after hydrothermal treatment. The increased mesopores enhanced bimolecular pathways, and the decreased micropores constrained monomolecular pathways (Figure 7.42). Therefore, the initial activity of the steamed sample was boosted, and the *i*-C4/C3 ratio increased. The enhanced activity but low propylene selectivity over ZSM-5/MOR composite zeolite was caused by the decreased diffusion limitation due to the generation of mesopores during hydrothermal treatment.

7.6 Outlook

The cracking of crude oil-derived feedstocks to provide building blocks for the petrochemical industry (ethene, propylene, and butenes) is an attractive pathway and interesting research and development direction. Being the most important ingredient of catalytic cracking processes, zeolite-based catalysts and additives are destined

to be in the spotlight as they are the key contributors to this process. Hydrocarbon catalytic cracking catalysts generally need to have three characteristics: (i) increased selectivity to ethylene and propylene while reducing the cracking reaction temperature, (ii) excellent thermal and hydrothermal stability because the cracking reaction temperature is too high and some processes need to introduce a large amount of steam, and (iii) high stability and strong anti-coking ability.

Zeolites, especially MFI zeolite catalysts, have been playing a key role in the catalytic cracking process for years due to their high thermal and hydrothermal stability, large surface areas, tunable acidity, and unique size/shape selectivity properties. Most alternative zeolites still lack the high stability and activity needed for the hydrocarbon cracking reaction. Moreover, some synthesis processes of zeolites face limited availability, expensive organic structure-directing agents (OSDAs), and so on. Therefore, it is also necessary to develop cost-friendly synthesis methods, like OSDA-free syntheses, solvent-free syntheses, and other environmental-friendly methods for accelerating zeolite crystallizations.

Obviously, the hydrocarbon catalytic cracking reaction network is relatively complicated; various side reactions are accompanied with the main cracking route. The suitable catalysts for the catalytic cracking of naphtha fractions should contain strong acid sites to initiate the cracking reaction by producing reactive intermediates, the specific pore structures, and the short diffusion paths to suppress the formation of coke precursor. It is also important to note that hierarchical zeolites and composite zeolite catalysts show promising results in naphtha cracking reaction. However, their practical application is still limited due to most of the synthesis methods being on the laboratory scale and in the fundamental research stage. Considering the improving impact of zeolites on the various process parameters, it is worthwhile to investigate the production and application of these materials on a larger scale than the laboratory.

It is our belief that in-depth understanding of the catalytic reaction mechanism over zeolite catalysts can provide guidance for catalyst design and performance improvement. The monomolecular and bimolecular pathways always coincide and compete with each other in the chain reaction mechanism in paraffin cracking pathways. Furthermore, which mechanism is favored mainly depends on the specific conditions. The catalytic activity, selectivity to light olefins, and stability of the catalysts can be controlled by tuning the density, dispersion, and chemical environments of acid sites. Future catalyst research and development should focus on better hydride transfer control and on high activity for high conversion. A control of active sites especially the Al siting and distribution in the zeolite framework might be a core technology to achieve higher selectivity and longer catalyst lifetime. It is desired to develop the methods for incorporating desired amounts of heteroatoms into specific T sites at will and also to accurately evaluate their location and the associated catalytic performance to establish structure–activity relationships. This will allow us to use zeolites in catalysis to their maximum potential in the future.

References

1 Grand View Research (2016). Petrochemicals Market Analysis by Product (Ethylene, Propylene, Butadiene, Benzene, Xylene, Toluene, Vinyls, Styrene, Methanol) By Region (North America, Europe, China, Middle East, Africa, Latin America) And Segment Forecasts, 2014–2025. *Report No. 978-1-68038-560-1*, pp. 1–110.

2 Blay, V., Louis, B., Miravalles, R. et al. (2017). Engineering zeolites for catalytic cracking to light olefins. *ACS Catal.* 7 (10): 6542–6566.

3 Sheng, J., Yan, B., Lu, W.D. et al. (2021). Oxidative dehydrogenation of light alkanes to olefins on metal-free catalysts. *Chem. Soc. Rev.* 50: 1438–1468.

4 Sattler, J.J.H.B., Ruiz-Martinez, J., Santillan-Jimenez, E., and Weckhuysen, B.M. (2014). Catalytic dehydrogenation of light alkanes on metals and metal oxides. *Chem. Rev.* 14: 10613–10653.

5 Zhong, L.S., Yu, F., An, Y.L. et al. (2016). Cobalt carbide nanoprisms for direct production of lower olefins from syngas. *Nature* 538: 84–87.

6 Jiao, F., Li, J.J., Pan, X.L. et al. (2016). Selective conversion of syngas to light olefins. *Science* 351: 1065–1068.

7 Yarulina, I., Chowdhury, A.D., Meirer, F. et al. (2018). Recent trends and fundamental insights in the methanol-to-hydrocarbons process. *Nat. Catal.* 1 (6): 398–411.

8 Zhang, W.N., Chen, J.R., Xu, S.T. et al. (2018). Methanol to olefins reaction over cavity-type zeolite: cavity controls the critical intermediates and product selectivity. *ACS Catal.* 8: 10950–10963.

9 Bellussi, G. and Pollesel, P. (2005). Industrial applications of zeolite catalysis: production and uses of light olefins. *Stud. Surf. Sci. Catal.* 158: 1201–1212.

10 Blay, V., Epelde, E., Miravalles, R., and Perea, L.A. (2018). Converting olefins to propene: ethene to propene and olefin cracking. *Catal. Rev. Sci. Eng.* 60: 278–335.

11 Ishihara, A., Kodama, Y., and Hashimoto, T. (2020). Effect of matrix on aromatics production by cracking and dehydrocyclization of *n*-pentane using Ga ion-exchanged ZSM-5-alumina composite catalysts. *Fuel Process. Technol.* 213 (4): 106679.

12 Alipour, S.M. (2016). Recent advances in naphtha catalytic cracking by nano ZSM-5: a review. *Chin. J. Catal.* 37 (5): 671–680.

13 Alabdullah, M., Rodriguez-Gomez, A., Shoinkhorova, T. et al. (2021). One-step conversion of crude oil to light olefins using a multi-zone reactor. *Nat. Catal.* 4: 1–9.

14 Soni, D.S., Shorey, S., and Rao, M.R. (2008). Maximizing propylene through catalytic cracking: indmax fluid catalytic cracking (I-FCC) process. *AICHE Spring National Meeting*. New York: AICHE.

15 Fujiyama, Y., Okuhara, T., Saeed, M.R. et al. (2006). Technology: high-severity FCC: a new process to maximize refinery propylene. *Hydrocarbon Asia* 16 (3): 20–25.

16 Zhang, X., Chen, Z.Z., Liu, Z.Y., and Liu, Q.Y. (2021). Radical induced cracking of naphtha model compound: using bibenzyl as a novel radical initiator. *J. Anal. Appl. Pyrolysis* 156 (3111): 105101.

17 Krannila, H., Haag, W.O., and Gates, B.C. (1992). Monomolecular and bimolecular mechanisms of paraffin cracking: *n*-butane cracking catalyzed by H-ZSM-5. *J. Catal.* 135 (1): 115–124.

18 Wojciechowski, B.W. (1996). Chain mechanisms in catalytic cracking. *Arabian J. Sci. Eng.* 21 (2): 165.

19 Bloch, H.S., Pines, H., and Schmerling, L. (1946). The mechanism of paraffin isomerization. *J. Am. Chem. Soc.* 68 (1): 153–153.

20 Lin, L.F., Qiu, C.F., Zhuo, Z.X. et al. (2015). Acid strength controlled reaction pathways for the catalytic cracking of 1-pentene to propene over ZSM-5. *ACS Catal.* 5 (7): 4048–4059.

21 Xiao, X., Xu, Z.L., Wang, P. et al. (2021). Solvent-free synthesis of SAPO-34 zeolite with tunable SiO_2/Al_2O_3 ratios for efficient catalytic cracking of 1-butene. *Catalysts* 11 (7): 835–848.

22 Stefanadis, C., Gates, B.C., and Haag, W.O. (1991). Rates of isobutane cracking catalysed by H-ZSM-5: the carbonium ion route. *J. Mol. Catal.* 67 (3): 363–367.

23 Huang, J., Jiang, Y., Marthala, V.R.R., and Hunger, M. (2008). Insight into the mechanisms of the ethylbenzene disproportionation: transition state shape selectivity on zeolites. *J. Am. Chem. Soc.* 130: 12642–12644.

24 Marczewski, M. (1986). Mechanism of *n*-alkane transformations over a solid superacid of Lewis character, $Al_2O_3/AlCl_3$. *J. Chem. Soc., Faraday Trans.* 82 (6): 1687–1701.

25 Narbeshuber, T.F., Brait, A., Seshan, K., and Lercher, J.A. (1997). Dehydrogenation of light alkanes over zeolites. *J. Catal.* 172 (1): 127–136.

26 Narbeshuber, T.F., Brait, A., Seshan, K., and Lercher, J.A. (2003). Three-coordinate aluminum in zeolites observed with in situ X-ray absorption near-edge spectroscopy at the Al K-edge: flexibility of aluminum coordinations in zeolites. *J. Am. Chem. Soc.* 125 (24): 7435.

27 Louis, B., Pereira, M.M., Santos, F.M. et al. (2010). Alkane activation over acidic zeolites: the first step. *Chem. Eur. J.* 16 (2): 573–576.

28 Corma, A., Melo, F.V., Sauvanaud, L., and Ortega, F. (2005). Light cracked naphtha processing: controlling chemistry for maximum propylene production. *Catal. Today* 107: 699–706.

29 Boronat, M. and Corma, A. (2008). Are carbenium and carbonium ions reaction intermediates in zeolite-catalyzed reactions? *Appl. Catal., A* 336 (1–2): 2–10.

30 Xu, B., Sievers, C., Hong, S.B. et al. (2006). Catalytic activity of Brønsted acid sites in zeolites: intrinsic activity, rate-limiting step, and influence of the local structure of the acid sites. *J. Catal.* 244 (2): 163–168.

31 Jentoft, F.C. and Gates, B.C. (1997). Solid-acid-catalyzed alkane cracking mechanisms: evidence from reactions of small probe molecules. *Top. Catal.* 4 (1): 1–13.

32 Haag, W.O., Dessau, R.M., and Lago, R.M. (1991). Kinetics and mechanism of paraffin cracking with zeolite catalysts. *Stud. Surf. Sci. Catal.* 60: 255–265.

33 Altwasser, S., Welker, C., Traa, Y., and Weitkamp, J. (2005). Catalytic cracking of *n*-octane on small-pore zeolites. *Microporous Mesoporous Mater.* 83 (1–3): 345–356.

34 Shen, H., Liu, M., Li, J.J. et al. (2021). Promising strategy to synthesize ZSM-5@silicalite-1 with superior catalytic performance for catalytic cracking reactions. *Ind. Eng. Chem. Res.* 60 (25): 9098–9106.

35 Jolly, S., Saussey, J., Bettahar, M.M. et al. (1997). Reaction mechanisms and kinetics in the *n*-hexane cracking over zeolites. *Appl. Catal., A* 156: 71–96.

36 Corma, A. and Orchilles, A.V. (2000). Current views on the mechanism of catalytic cracking. *Microporous Mesoporous Mater.* 35: 21–30.

37 Caeiro, G., Carvalho, R.H., Wang, X. et al. (2006). Activation of C2–C4 alkanes over acid and bifunctional zeolite catalysts. *J. Mol. Catal. A: Chem.* 255 (1–2): 131–158.

38 Corma, A., Mengual, J., and Miguel, P.J. (2015). Catalytic cracking of *n*-alkane naphtha: the impact of olefin addition and active sites differentiation. *J. Catal.* 330: 520–532.

39 Li, L., Gao, J.S., Xu, C.M., and Meng, X.H. (2006). Reaction behaviors and mechanisms of catalytic pyrolysis of C4 hydrocarbons. *Chem. Eng. J.* 116 (3): 155–161.

40 Meng, X.H., Xu, C.M., Li, L., and Gao, J.S. (2010). Kinetic study of catalytic pyrolysis of C4 hydrocarbons on a modified ZSM-5 zeolite catalyst. *Energy Fuels* 24: 6233–62380.

41 Tsunoda, T. and Sekiguchi, M. (2008). The omega process for propylene production by olefin interconversion. *Catal. Surv. Asia* 12 (1): 1–5.

42 Arudra, P., Bhuiyan, T.I., Akhtar, M.N. et al. (2014). Silicalite-1 as efficient catalyst for production of propene from 1-butene. *ACS Catal.* 4 (11): 4205–4214.

43 Lin, L., Qiu, C., Zhuo, Z. et al. (2014). Acid strength controlled reaction pathways for the catalytic cracking of 1-butene to propene over ZSM-5. *J. Catal.* 309: 136–145.

44 Fu, J., Feng, X., Liu, Y.B. et al. (2018). Mechanistic insights into the pore confinement effect on bimolecular and monomolecular cracking mechanisms of *n*-octane over HY and H-ZSM-5 zeolites: a DFT study. *J. Phys. Chem. C* 122 (23): 12222–12230.

45 Maihom, T., Pantu, P., Tachakritikul, C. et al. (2010). Effect of the zeolite nanocavity on the reaction mechanism of *n*-hexane cracking: a density functional theory study. *J. Phys. Chem. C* 114 (17): 7850–7856.

46 To, A.T. and Resasco, D.E. (2015). Hydride transfer between a phenolic surface pool and reactant paraffins in the catalytic cracking of M-cresol/hexanes mixtures over an HY zeolite. *J. Catal.* 329: 57–68.

47 Anderson, B.G., Schumacher, R.R., Van Duren, R. et al. (2002). An attempt to predict the optimum zeolite-based catalyst for selective cracking of naphtha-range hydrocarbons to light olefins. *J. Mol. Catal. A: Chem.* 181 (1–2): 291–301.

48 Cejka, J., Corma, A., and Zones, S. (2010). *Zeolites and Catalysis: Synthesis, Reactions and Applications*. Weinheim: Wiley-VCH.

49 Chen, L.H., Li, X.Y., Rooke, J.C. et al. (2012). Hierarchically structured zeolites: synthesis, mass transport properties and applications. *J. Mater. Chem.* 22 (34): 17381–17403.

50 Li, K., Valla, J., and Garcia-Martinez, J. (2014). Realizing the commercial potential of hierarchical zeolites: new opportunities in catalytic cracking. *ChemCatChem* 6 (1): 46–66.

51 Moliner, M., Martínez, C., and Corma, A. (2014). Synthesis strategies for preparing useful small pore zeolites and zeotypes for gas separations and catalysis. *Chem. Mater.* 26: 246–258.

52 Xu, W.Q., Yin, Y.G., Suib, S.L. et al. (1996). Modification of non-template synthesized ferrierite/ZSM-35 for *n*-butene skeletal isomerization to isobutylene. *J. Catal.* 163 (2): 232–244.

53 Komatsu, T., Ishihara, H., Fukui, Y., and Yashima, T. (2001). Selective formation of alkenes through the cracking of *n*-heptane on Ca^{2+}-exchanged ferrierite. *Appl. Catal., A* 214 (1): 103–109.

54 Bastiani, R., Lam, Y.L., Henriques, C.A., and da Silva, V.T. (2013). Application of ferrierite zeolite in high-olefin catalytic cracking. *Fuel* 107: 680–687.

55 Komatsu, T. (2018). Coke formation on zeolite catalysts in naphtha cracking. *J. Jpn. Pet. Inst.* 61 (1): 28–36.

56 Nasser, G.A., Kurniawan, T., Tago, T. et al. (2016). Cracking of *n*-hexane over hierarchical MOR zeolites derived from natural minerals. *J. Taiwan Inst. Chem. Eng.* 61: 20–25.

57 Xu, Q., Gong, Y., Xu, W. et al. (2011). Synthesis of high-silica EU-1 zeolite in the presence of hexamethonium ions: a seeded approach for inhibiting ZSM-48. *J. Colloid Interface* 358 (1): 252–260.

58 Zhang, Y.F., Liu, X.L., Sun, L.Y. et al. (2016). Catalytic cracking of *n*-hexane over HEU-1 zeolite for selective propylene production: optimizing the SiO_2/Al_2O_3 ratio by *in-situ* synthesis. *Fuel Process. Technol.* 153: 163–172.

59 Zhao, G., Teng, J., Zhang, Y. et al. (2006). Synthesis of ZSM-48 zeolites and their catalytic performance in C4-olefin cracking reactions. *Appl. Catal., A* 299: 167–174.

60 Ahmed, M.H.M., Muraza, O., Nakaoka, S. et al. (2017). Stability assessment of regenerated hierarchical ZSM-48 zeolite designed by post-synthesis treatment for catalytic cracking of light naphtha. *Energy Fuels* 31 (12): 14097–14103.

61 Zhu, X., Liu, S., Song, Y. et al. (2005). Catalytic cracking of 1-butene to propene and ethene on MCM-22 zeolite. *Appl. Catal., A* 290 (1): 191–199.

62 Xu, G., Zhu, X., Niu, X. et al. (2009). One-pot synthesis of high silica MCM-22 zeolites and their performances in catalytic cracking of 1-butene to propene. *Microporous Mesoporous Mater.* 118 (1–3): 44–51.

63 Wang, Y., Yokoi, T., Namba, S. et al. (2014). Catalytic cracking of *n*-hexane for producing propylene on MCM-22 zeolites. *Appl. Catal., A* 504: 192–202.

64 Corma, A., Martı´ nez-Triguero, J., Valencia, S. et al. (2002). IM-5: A highly thermal and hydrothermal shape-selective cracking zeolite. *J. Catal.* 206 (1): 125–133.

65 Yu, Q., Sun, H., Sun, H. et al. (2018). Highly mesoporous IM-5 zeolite prepared by alkaline treatment and its catalytic cracking performance. *Microporous Mesoporous Mater.* 273: 297–306.

66 Corma, A., Mengual, J., and Miguel, P.J. (2013). IM-5 zeolite for steam catalytic cracking of naphtha to produce propene and Ethene. An alternative to ZSM-5 zeolite. *Appl. Catal., A* s460–461 (11): 106–115.

67 Zhu, X., Liu, S., Song, Y., and Xu, L. (2005). Catalytic cracking of C4 alkenes to propene and ethene: influences of zeolites pore structures and Si/Al_2 ratios. *Appl. Catal., A* 288 (1–2): 134–142.

68 Epelde, E., Ibaez, M., Aguayo, A.T. et al. (2014). Differences among the deactivation pathway of H-ZSM-5 zeolite and SAPO-34 in the transformation of ethylene or 1-butene to propylene. *Microporous Mesoporous Mater.* 195 (9): 284–293.

69 Corma, A., Davis, M., Fornés, V. et al. (1997). Cracking behavior of zeolites with connected 12- and 10 member ring channels: the influence of pore structure on product distribution. *J. Catal.* 167 (2): 438–446.

70 Miyaji, A., Sakamoto, Y., Iwase, Y. et al. (2013). Selective production of ethylene and propylene via monomolecular cracking of pentene over proton-exchanged zeolites: pentene cracking mechanism determined by spatial volume of zeolite cavity. *J. Catal.* 302: 101–114.

71 Abbasizadeh, S. and Karimzadeh, R. (2018). Effect of framework single and close (pairs and un-pairs) aluminum atoms on phosphorous modification of H-ZSM-5 in cracking of liquefied petroleum gas to ethylene and propylene. *Microporous Mesoporous Mater.* 266: 132–140.

72 Kubo, K., Iida, H., Namba, S., and Igarashi, A. (2018). Selective formation of light olefins by catalytic cracking of naphtha components over ZSM-5 zeolite catalysts. *J. Jpn. Pet. Inst.* 61 (1): 10–19.

73 Maia, A.J., Louis, B., Lam, Y.L., and Pereira, M.M. (2010). Ni-ZSM-5 catalysts: detailed characterization of metal sites for proper catalyst design. *J. Catal.* 269 (1): 103–109.

74 Sousa-Aguiar, E., Trigueiro, F.E., and Zotin, F. (2013). The role of rare earth elements in zeolites and cracking catalysts. *Catal. Today* 218–219: 115–122.

75 Momayez, F., Darian, J.T., and Sendesi, S.M.T. (2015). Synthesis of zirconium and cerium over H-ZSM-5 catalysts for light olefins production from naphtha. *J. Anal. Appl. Pyrolysis* 112: 135–140.

76 Hou, X., Qiu, Y., Tian, Y. et al. (2018). Reaction pathways of *n*-pentane cracking on the fresh and regenerated Sr, Zr and La-loaded ZSM-5 zeolites. *Chem. Eng. J.* 349: 297–308.

77 Tian, Y.J., Zhang, B.F., Liang, H.R. et al. (2018). Synthesis and performance of pillared H-ZSM-5 nanosheet zeolites for *n*-decane catalytic cracking to produce light olefins. *Appl. Catal., A* 572: 24–33.

78 Hao, J., Cheng, D.G., Chen, F.Q., and Zhan, X.L. (2021). *n*-Heptane catalytic cracking on ZSM-5 zeolite nanosheets: effect of nanosheet thickness. *Microporous Mesoporous Mater.* 310: 110647–110654.

79 Sazama, P., Sobalik, Z., Dedecek, J. et al. (2013). Enhancement of activity and selectivity in acid-catalyzed reactions by dealuminated hierarchical zeolites. *Angew. Chem. Int. Ed.* 52 (7): 2038–2041.

80 Han, L., Wang, R.Y., Wang, P. et al. (2021). Hierarchical hollow Al-rich nano ZSM-5 crystals for highly selective production of light olefins from naphtheness. *Catal. Sci. Technol.* https://doi.org/10.1039/d1cy00772f.

81 Zheng, J.J., Zhang, X.W., Zhang, Y. et al. (2009). Structural effects of hierarchical pores in zeolite composite. *Microporous Mesoporous Mater.* 122 (1–3): 264–269.

82 Abildstrøm, J.O., Kegnæs, M., Hytoft, G. et al. (2016). Synthesis of mesoporous zeolite catalysts by in situ formation of carbon template over nickel nanoparticles. *Microporous Mesoporous Mater.* 225: 232–237.

83 Epelde, E., Gayubo, A.G., Olazar, M. et al. (2014). Modified H-ZSM-5 zeolites for intensifying propylene production in the transformation of 1-butene. *Chem. Eng. J.* 251: 80–91.

84 Campo, P.D., Navarro, M.T., Shaikh, S.K. et al. (2020). Propene production by butene cracking. Descriptors for zeolite catalysts. *ACS Catal.* 10 (20): 11878–11891.

85 Lu, J.Y., Zhao, Z., Xu, C.M. et al. (2006). FeH-ZSM-5 molecular sieves–highly active catalysts for catalytic cracking of iso-butane to produce ethylene and propylene. *Catal. Commun.* 7 (4): 199–203.

86 Lu, J.Y., Zhao, Z., Xu, C.M. et al. (2008). Catalytic cracking of iso-butane over H-ZSM-5, FeH-ZSM-5 and CrH-ZSM-5 catalysts with different SiO_2/Al_2O_3 ratios. *J. Porous Mater.* 15 (2): 213–220.

87 Lu, J.Y., Zhao, Z., Xu, C.M. et al. (2006). CrH-ZSM-5 zeolites – highly efficient catalysts for catalytic cracking of iso-butane to produce light olefins. *Catal. Lett.* 109 (1–2): 65–70.

88 Urata, K., Furukawa, S., and Komatsu, T. (2014). Location of coke on H-ZSM-5 zeolite formed in the cracking of *n*-hexane. *Appl. Catal., A* 475: 335–340.

89 Kubo, K., Iida, H., Namba, S., and Igarashi, A. (2012). Selective formation of light olefin by *n*-heptane cracking over H-ZSM-5 at high temperatures. *Microporous Mesoporous Mater.* 149 (1): 126–133.

90 Wielers, A., Vaarkamp, M., and Post, M. (1991). Relation between properties and performance of zeolites in paraffin cracking. *J. Catal.* 127 (1): 51–66.

91 Jung, J.S., Kim, T.J., and Seo, G. (2004). Catalytic cracking of *n*-octane over zeolites with different pore structures and acidities. *Korean J. Chem. Eng.* 21 (4): 777–781.

92 Liu, R.H., Sarker, M., Rahman, M.M. et al. (2020). Multi-scale complexities of solid acid catalysts in the catalytic fast pyrolysis of biomass for bio-oil production-a review. *Prog. Energy Combust. Sci.* 80: 100852.

93 Dedecek, J., SobalÍK, Z., and Wichterlová, B. (2012). Siting snd distribution of framework aluminium atoms in silicon-rich zeolites and impact on catalysis. *Catal. Rev. Sci. Eng.* 54 (2): 135–223.

94 Dedecek, J., Balgová, V., Pashkova, V. et al. (2012). Synthesis of ZSM-5 zeolites with defined distribution of Al atoms in the framework and multinuclear

MAS NMR analysis of the control of Al distribution. *Chem. Mater.* 24 (16): 3231–3239.

95 Sazama, P., Dedecek, J., Gábová, V. et al. (2008). Effect of aluminium distribution in the framework of ZSM-5 on hydrocarbon transformation. Cracking of 1-butene. *J. Catal.* 254 (2): 180–189.

96 Janda, A. and Bell, A.T. (2013). Effects of Si/Al ratio on the distribution of framework Al and on the rates of alkane monomolecular cracking and dehydrogenation in H-MFI. *J. Am. Chem. Soc.* 135 (51): 19193–19207.

97 Schallmoser, S., Ikuno, T., Wagenhofer, M.F. et al. (2014). Impact of the local environment of Brønsted acid sites in ZSM-5 on the catalytic activity in *n*-pentane cracking. *J. Catal.* 316: 93–102.

98 Li, C.G., Vidal-Moya, A., Miguel, P.J. et al. (2018). Selectively introducing acid sites in different confined positions in ZSM-5 and its catalytic implications. *ACS Catal.* 8: 7688–7697.

99 Yokoi, T., Mochizuki, H., Biligetu, T. et al. (2017). Unique Al distribution in the MFI framework and its impact on catalytic properties. *Chem. Lett.* 46: 798–800.

100 Wakui, K., Satoh, K., Sawada, G. et al. (2002). Cracking of *n*-butane over alkaline earth-containing H-ZSM-5 catalysts. *Catal. Lett.* 84 (3): 259–264.

101 Wakui, K., Satoh, K., Sawada, G. et al. (2002). Dehydrogenative cracking of *n*-butane over modified H-ZSM-5 catalysts. *Catal. Lett.* 81 (1): 83–88.

102 Wang, L., Xie, M., and Tao, L. (1994). Conversion of light paraffins for preparing small olefins over ZSM-5 zeolites. *Catal. Lett.* 28 (1): 61–68.

103 Xu, R.F., Liu, J.X., Liang, C.C. et al. (2011). Effect of alkali metal ion modification on the catalytic performance of Nano-H-ZSM-5 zeolite in butene cracking. *J. Fuel Chem. Technol.* 39 (6): 449–454.

104 Rahimi, N. and Karimzadeh, R. (2011). Catalytic cracking of hydrocarbonsover modified ZSM-5 zeolites to produce light olefins: a review. *Appl. Catal., A* 398 (1–2): 1–17.

105 Rane, N., Kersbulck, M., Santen, R., and Hensen, E. (2008). Cracking of *n*-heptane over Brnsted acid sites and Lewis acid Ga sites in ZSM-5 zeolite. *Microporous Mesoporous Mater.* 110 (2–3): 279–291.

106 Hou, X., Qiu, Y., Yuan, E.X. et al. (2017). Promotion on light olefins production through modulating the reaction pathways for *n*-pentane catalytic cracking over ZSM-5 based catalysts. *Appl. Catal., A* 543: 51–60.

107 Han, J., Jiang, G.Y., Han, S.L. et al. (2016). The fabrication of Ga_2O_3/ZSM-5 hollow fibers for efficient catalytic conversion of *n*-butane into light olefins and aromatics. *Catalysts* 6 (1): 13.

108 Zhan, W.C., Guo, Y., Gong, X.Q. et al. (2014). Current status and perspectives of rare earth catalytic materials and catalysis. *Chin. J. Catal.* 35 (8): 1238–1250.

109 Hartford, R.W., Kojima, M., and O'Connor, C.T. (1989). Lanthanum ion exchange on H-ZSM-5. *Ind. Eng. Chem. Res.* 28 (12): 1748–1752.

110 Wang, X.N., Zhao, Z., Xu, C.M. et al. (2007). Effects of light rare earth on acidity and catalytic performance of H-ZSM-5 zeolite for catalytic cracking of butane to light olefins. *J. Rare Earth* 25 (3): 321–328.

111 Xue, N.H., Liu, N., Nie, L. et al. (2010). 1-Butene cracking to propene over P/H-ZSM-5: effect of lanthanum. *J. Mol. Catal. A: Chem.* 327 (1–2): 12–19.

112 Wakui, K., Satoh, K., Sawada, G. et al. (1999). Catalytic cracking of *n*-butane over rare earth-loaded H-ZSM-5 catalysts. *J. Jpn. Pet. Inst.* 42 (5): 449–456.

113 Yoshimura, Y., Kijima, N., Hayakawa, T. et al. (2001). Catalytic cracking of naphtha to light olefins. *Catal. Surv. Asia* 4: 157–167.

114 Wakui, K., Satoh, K., Sawada, G. et al. (2002). Dehydrogenative cracking of *n*-butane using double-stage reaction. *Appl. Catal., A* 230 (1): 195–202.

115 Degnan, T.F., Chitnis, G.K., and Schipper, P.H. (2000). History of ZSM-5 fluid catalytic cracking additive development at mobil. *Microporous Mesoporous Mater.* 35 (2): 245–252.

116 Lercher, J.A. and Rumplmayr, G. (1986). Controlled decrease of acid strength by orthophosphoric acid on ZSM5. *Appl. Catal.* 25 (1–2): 215–222.

117 Blasco, T., Corma, A., and Martínez-Triguero, J. (2006). Hydrothermal stabilization of ZSM-5 catalytic-cracking additives by phosphorus addition. *J. Catal.* 237 (2): 267–277.

118 Zhao, G.L., Teng, J.W., Xie, Z.K. et al. (2007). Effect of phosphorus on H-ZSM-5 catalyst for C4-olefin cracking reactions to produce propylene. *J. Catal.* 248 (1): 29–37.

119 Xue, N.H., Chen, X.K., Nie, L. et al. (2007). Understanding the enhancement of catalytic performance for olefin cracking: hydrothermally stable acids in P/H-ZSM-5. *J. Catal.* 248 (1): 20–28.

120 Yang, J. and Sun, H. (2009). A theoretical study of hydrothermal stability of P-modified ZSM-5 zeolites. *Sci. China Chem.* 52 (003): 282–287.

121 Jiang, G.Y., Zhang, L., Zhao, Z. et al. (2008). Highly effective P-modified H-ZSM-5 catalyst for the cracking of C4 alkanes to produce light olefins. *Appl. Catal., A* 340 (2): 176–182.

122 Zhao, Y., Liu, J.X., Xiong, G., and Guo, H.C. (2017). Enhancing hydrothermal stability of nano-sized H-ZSM-5 zeolite by phosphorus modification for olefin catalytic cracking of full-range FCC gasoline. *Chin. J. Catal.* 38 (1): 138–145.

123 Corma, A., Mengual, J., and Miguel, P.J. (2012). Stabilization of ZSM-5 zeolite catalysts for steam catalytic cracking of naphtha for production of propene and ethene. *Appl. Catal., A* S421–422: 121–134.

124 Ji, Y.J., Yang, H.H., Zhang, Q., and Yan, W. (2017). Phosphorus modification increases catalytic activity and stability of ZSM-5 zeolite on supercritical catalytic cracking of *n*-dodecane. *J. Solid State Chem.* 251: 7–13.

125 Tsunoji, N., Sonoda, T., Furumoto, Y. et al. (2014). Recreation of Brønsted acid sites in phosphorus-modified H-ZSM-5(Ga) by modification with various metal cations. *Appl. Catal., A* 481: 161–168.

126 Lee, J., Hong, U.G., Hwang, S. et al. (2013). Catalytic cracking of C5 raffinate to light olefins over lanthanum-containing phosphorous-modifiied porous ZSM-5: effect of lanthanum content. *Fuel Process. Technol.* 109: 189–195.

127 Rahimi, N., Moradi, D., Sheibak, M. et al. (2016). The influence of modification methods on the catalytic cracking of LPG over lanthanum and phosphorus modified H-ZSM-5 catalysts. *Microporous Mesoporous Mater.* 234: 215–223.

128 Li, J.W., Li, T., Ma, H.F. et al. (2017). Effect of nickel on phosphorus modified H-ZSM-5 in catalytic cracking of butene and pentene. *Fuel Process. Technol.* 159: 31–37.

129 Li, J.W., Li, T., Ma, H.F. et al. (2015). Effect of impregnating Fe into P-modified H-ZSM-5 in the coupling cracking of butene and pentene. *Ind. Eng. Chem. Res.* 54 (6): 1796–1805.

130 Inagaki, S., Shinoda, S., Kaneko, Y. et al. (2013). Facile fabrication of ZSM-5 zeolite catalyst with high durability to coke formation during catalytic cracking of paraffins. *ACS Catal.* 3 (1): 74–78.

131 Li, C., Vidal-Moya, A., Miguel, P.J. et al. (2018). Selective introduction of acid sites in different confined positions in ZSM-5 and its catalytic implications. *ACS Catal.* 8: 7688–7697.

132 Konno, H., Ohnaka, R., Nishimura, J. et al. (2014). Kinetics of the catalytic cracking of naphtha over ZSM-5 zeolite: effect of reduced crystal size on the reaction of naphthenes. *Catal. Sci. Technol.* 4: 4265–4273.

133 Konno, H., Tago, T., Nakasaka, Y. et al. (2013). Effectiveness of nano-scale ZSM-5 zeolite and its deactivation mechanism on catalytic cracking of representative hydrocarbons of naphtha. *Microporous Mesoporous Mater.* 175 (13): 25–33.

134 Mohammadparast, F., Halladj, R., and Askari, S. (2015). The crystal size effect of nano-sized ZSM-5 in the catalytic performance of petrochemical processes: a review. *Chem. Eng. Commun.* 202 (4): 542–556.

135 Alipour, S.M., Halladj, R., Askari, S., and BagheriSereshki, E. (2016). Low cost rapid route for hydrothermal synthesis of nano ZSM-5 with mixture of two, three and four structure directing agents. *J. Porous Mater.* 23 (1): 145–155.

136 Mochizuki, H., Yokoi, T., Imai, H. et al. (2011). Facile control of crystallite size of ZSM-5 catalyst for cracking of hexane. *Microporous Mesoporous Mater.* 145 (1–3): 165–171.

137 Konno, H., Okamura, T., Kawahara, T. et al. (2012). Kinetics of *n*-hexane cracking over ZSM-5 zeolites-effect of crystal size on effectiveness factor and catalyst lifetime. *Chem. Eng. J.* S207–208 (10): 490–496.

138 Tago, T., Konno, H., Nakasaka, Y., and Masuda, T. (2012). Size-controlled synthesis of nano-zeolites and their application to light olefin synthesis. *Catal. Surv. Asia* 16 (3): 148–163.

139 Li, S.Y., Li, J.F., Dong, M. et al. (2019). Strategies to control zeolite particle morphology. *Chem. Soc. Rev.* 48: 885–907.

140 Konno, H., Okamura, T., Nakasaka, Y. et al. (2012). Effects of crystal size and Si/Al ratio of MFI-type zeolite catalyst on *n*-hexane cracking for light olefin synthesis. *J. Jpn. Pet. Inst.* 55 (4): 267–274.

141 Teng, J.W., Zhao, G.L., Xie, Z.K., and Chen, Q.L. (2004). Effect of ZSM-5 zeolite crystal size on propylene production from catalytic cracking of C4 olefins. *Chin. J. Catal.* 25 (8): 602–606.

142 Rownaghi, A.A., Rezaei, F., and Hedlund, J. (2012). Selective formation of light olefin by *n*-hexane cracking over H-ZSM-5: influence of crystal size and acid sites of nano- and micrometer-sized crystals. *Chem. Eng. J.* 191: 528–533.

143 Ji, Y.Y., Wang, H.R., Man, Y., and Si, Y.C. (2010). Effect of crystal size of ZSM-5 zeolite on catalytic cracking of naphtha. *Petrochem. Technol.* 39 (8): 844–848.

144 Nakasaka, Y., Okamura, T., Konno, H. et al. (2013). Crystal size of MFI-type zeolites for catalytic cracking of *n*-hexane under reaction-control conditions. *Microporous Mesoporous Mater.* 182: 244–249.

145 Zhou, J.M., Zheng, F., Li, H. et al. (2020). Optimization of post-treatment variables to produce hierarchical porous zeolites from coal gangue to enhance adsorption performance. *Chem. Eng. J.* 381: 122698.

146 Zhang, J.S., Ding, H., Zhang, Y.X. et al. (2018). An efficient one-pot strategy for synthesizing hierarchical aluminosilicate zeolites using single structure directing agent. *Chem. Eng. J.* 335: 822–830.

147 Serrano, D.P., Escolac, J.M., and Pizarroab, P. (2013). Synthesis strategies in the search for hierarchical zeolites. *Chem. Soc. Rev.* 42: 4004–4035.

148 Christensen, C.H., Schmidt, I., Carlsson, A. et al. (2005). Crystals in crystals-nanocrystals within mesoporous zeolite single crystals. *J. Am. Chem. Soc.* 127 (22): 8098–8102.

149 Tao, Y.S., Kanoh, H., Abrams, L., and Kaneko, K. (2010). Mesopore-modified zeolites: preparation, characterization, and applications. *Chem. Rev.* 37 (21): 896–910.

150 Su, L.L., Liu, L., Zhuang, J.Q. et al. (2003). Creating mesopores in ZSM-5 zeolite by alkali treatment: a new way to enhance the catalytic performance of methane dehydroaromatization on Mo/H-ZSM-5 catalysts. *Catal. Lett.* 91 (3–4): 155–167.

151 Na, K., Jo, C., Kim, J. et al. (2011). Directing zeolite structures into hierarchically nanoporous architectures. *Science* 333 (6040): 328.

152 Schmidt, I., Boisen, A., Gustavsson, E. et al. (2001). Carbon nanotube templated growth of mesoporous zeolite single crystals. *Chem. Mater.* 13 (12): 4416–4418.

153 Liu, F.J., Willhammar, T., Wang, L. et al. (2012). ZSM-5 zeolite single crystals with b-axis-aligned mesoporous channels as an efficient catalyst for conversion of bulky organic molecules. *J. Am. Chem. Soc.* 134 (10): 4557–4560.

154 Wang, H. and Pinnavaia, T.J. (2006). MFI zeolite with small and uniform intracrystal mesopores. *Angew. Chem. Int. Ed.* 118 (45): 7765–7768.

155 Wei, Y., Parmentier, T.E., Jonga, K.P.D., and Zečević, J. (2015). Tailoring and visualizing the pore architecture of hierarchical zeolites. *Chem. Soc. Rev.* 44: 7234–7261.

156 Chou, C., Cundy, C.S., and Garforth, A.A. (2005). A dry gel synthesis route to mesoporous ZSM-5 catalysts. *Stud. Surf. Sci. Catal.* 156: 393–400.

157 Siddiqui, M.A.B., Aitani, A.M., Saeed, M.R., and Al-Khattaf, S. (2010). Enhancing the production of light olefins by catalytic cracking of FCC naphtha over mesoporous ZSM-5 catalyst. *Top. Catal.* 53 (19–20): 1387–1393.

158 Lee, J., Hong, U.G., Hwang, S. et al. (2013). Production of light olefins through catalytic cracking of C5 raffinate over carbon-templated ZSM-5. *Fuel Process. Technol.* 108: 25–30.

159 Zhao, L., Gao, J.S., Xu, C., and Shen, B.J. (2011). Alkali-treatment of ZSM-5 zeolites with different SiO_2/Al_2O_3 ratios and light olefin production by heavy oil cracking. *Fuel Process. Technol.* 92 (3): 414–420.

160 Gao, X.H., Tang, Z.C., Lu, G.X. et al. (2010). Butene catalytic cracking to ethylene and propylene on mesoporous ZSM-5 by desilication. *Solid State Sci.* 12 (7): 1278–1282.

161 Zhang, X., Cheng, D.G., Chen, F.Q., and Zhan, X.L. (2017). *n*-Heptane catalytic cracking on hierarchical ZSM-5 zeolite: the effect of mesopores. *Chem. Eng. Sci.* 168: 352–359.

162 Ding, J.J., Liu, H.Y., Yuan, P. et al. (2013). Catalytic properties of a hierarchical zeolite synthesized from a natural aluminosilicate mineral without the use of a secondary mesoscale template. *ChemCatChem* 5 (8): 2258–2269.

163 Li, W.L., Ma, T., Zhang, Y.F. et al. (2015). Facile control of inter-crystalline porosity in the synthesis of size-controlled mesoporous MFI zeolites via in situ conversion of silica gel into zeolite nanocrystals for catalytic cracking. *CrystEngComm* 17 (30): 5680–5689.

164 Yang, Q.X., Li, Y.M., Chen, Z.T. et al. (2020). Core-shell structured HZSM@MesoSiO_2 catalysts with tunable shell thickness for efficient *n*-butane catalytic cracking. *AlChE J.* 3: 1–10.

165 Ocampo, F., Yun, H.S., Pereira, M.M. et al. (2009). Design of MFI zeolite-based composites with hierarchical pore structure: a new generation of structured catalysts. *Cryst. Growth Des.* 9 (9): 3721–3729.

166 Liu, J., Jiang, G.Y., Liu, Y. et al. (2014). Hierarchical macro-meso-microporous ZSM-5 zeolite hollow fibers with highly efficient catalytic cracking capability. *Sci. Rep.* 4: 7276–7281.

167 Choi, M., Na, K., Kim, J. et al. (2009). Stable single-unit-cell nanosheets of zeolite MFI as active and long-lived catalysts. *Nature* 461: 246–249.

168 Xiao, X., Zhang, Y.Y., Jiang, G.Y. et al. (2016). Simultaneous realization of high catalytic activity and stability for catalytic cracking of *n*-heptane on highly exposed (010) crystal planes of nanosheet ZSM-5 zeolite. *Chem. Commun.* 52: 10068–10071.

169 Sun, M.H., Zhou, J., Hu, Z.Y. et al. (2020). Hierarchical zeolite single-crystal reactor for excellent catalytic efficiency. *Matter* 3: 1226–1245.

170 Jian, Z., Hua, Z., Liu, Z. et al. (2011). Direct synthetic strategy of mesoporous ZSM-5 zeolites by using conventional block copolymer templates and the improved catalytic properties. *ACS Catal.* 1 (4): 287–291.

171 Li, X., Alwakwak, A.A., Rezaei, F., and Rownaghi, A.A. (2018). Synthesis of Cr, Cu, Ni, and Y-doped 3D-printed ZSM-5 monoliths and their catalytic performance for *n*-hexane cracking. *ACS Appl. Energy Mater.* 1 (6): 2740–2748.

172 Couck, S., Cousin-Saint-Remi, J., Van der Perre, S. et al. (2018). 3D-printed SAPO-34 monoliths for gas separation. *Microporous Mesoporous Mater.* 255: 185–191.

173 Li, X., Li, W.B., Rezaeia, F., and Rownaghi, A. (2018). Catalytic cracking of *n*-hexane for producing light olefins on 3D-printed monoliths of MFI and FAU zeolites. *Chem. Eng. J.* 333: 545–553.

174 Sang, Y., Jiao, Q., Li, H.S. et al. (2014). H-ZSM-5/MCM-41 composite molecular sieves for the catalytic cracking of endothermic hydrocarbon fuels: nano-ZSM-5 zeolites as the source. *J. Nanopart. Res.* 16 (12): 1–11.

175 Chen, F.Q., Ma, L.Y., Cheng, D.G., and Zhan, X.L. (2012). Synthesis of hierarchical porous zeolite and its performance in *n*-heptane cracking. *Catal. Commun.* 18 (1): 110–114.

176 Zhu, N., Wang, Y., Cheng, D.G. et al. (2009). Experimental evidence for the enhanced cracking activity of *n*-heptane over steamed ZSM-5/mordenite composite zeolites. *Appl. Catal., A* 362 (1–2): 26–33.

8

Catalytic Dehydrogenation of Light Alkanes

An-Hui Lu

Dalian University of Technology, State Key Laboratory of Fine Chemicals, Liaoning Key Laboratory for Catalytic Conversion of Carbon Resources, School of Chemical Engineering, LingGong Road 2#, Dalian 116024, P. R. China

8.1 Introduction

Light olefins, including ethylene, propylene, and butylene, are the most important feedstocks to produce polymers (e.g. polyethylene, polypropylene), oxygenates (e.g. ethylene glycol, propylene epoxide), and other derivatives (e.g. ethylbenzene, acrylonitrile) in the chemical industry. The worldwide consumption of ethylene and propylene has been continuously increasing to approximately 160 and 115 million tonnes, respectively, in 2019 (https://www.chyxx.com/research/201805/644700.html). Petroleum-derived steam cracking, fluid catalytic cracking (FCC), methanol to olefins (MTO), and Fischer–Tropsch to olefins (FTO) are mainly applied as the industrial technologies for the production of olefins [1, 2]. Nevertheless, extensive energy consumption and enormous carbon emission of these technologies drive researchers to investigate more environmentally friendly routes to produce olefins.

On the other hand, the reserves of natural gas and shale gas are found to be worldwide abundant. For example, the proved reserves of natural gas were up to 197 trillion cubic meters in 2018. In addition to methane, these gas resources are composed of considerable amounts of light alkanes, such as ethane and propane, which are easily separated from the natural gas [3]. Light alkanes have acted as Cinderella molecules in chemical feedstocks in long past years because of their inert chemical properties, including strong and localized C=H and C—C bonds, and they are usually employed as fuel. Facing the abundant, cheap, and less used alkane reserves and the huge market demand for olefins in the follow-up industry chains, concentration of technical strength to develop light alkane conversion technology can effectively use multisource light alkanes, prompting humans to gradually get rid of traditional fossil energy and alleviating the global energy crisis in future energy development.

Converting these light alkanes into high-value-added olefins, namely, catalytic dehydrogenation (DH) of light alkanes, is an important part of light alkane conversion technology, including direct dehydrogenation (DH) and oxidative dehydrogenation (ODH) processes. The key issue is the activation of C—H bond of alkanes

Heterogeneous Catalysis for Sustainable Energy, First Edition. Edited by Landong Li and Justin S. J. Hargreaves.

and selectivity control toward olefins. Harsh reaction conditions are required to activate alkane molecules due to the bond energy strength of C—H bonds which is as high as 400 kJ mol^{-1} in propane. For example, under non-oxidative conditions, the reaction temperature of propane dehydrogenation (PDH) to propylene is usually up to 600 °C. Side reactions, such as cracking, hydrogenolysis, polymerization, and deep dehydrogenation, also occur at this time, causing a low olefin selectivity. In the case of oxidative conditions (ODH), the higher reactivity of the olefin products or intermediates is vulnerable to be deeply oxidized to CO_x even at lower temperatures (<600 °C), resulting in low selectivity for high-value-added olefins or oxygenated products. Taking propane as an example, from the thermodynamics aspect, there is a complicated reaction network under both non-oxidative and oxidative conditions (Scheme 8.1). The non-catalytic dehydrogenation inevitably suffers from the problem of low olefin selectivity; thus, catalysts are required to promote the target reaction channel by regulating the reaction kinetics to obtain higher olefin selectivity. In this chapter, we review the recent advances made for dehydrogenation catalysts.

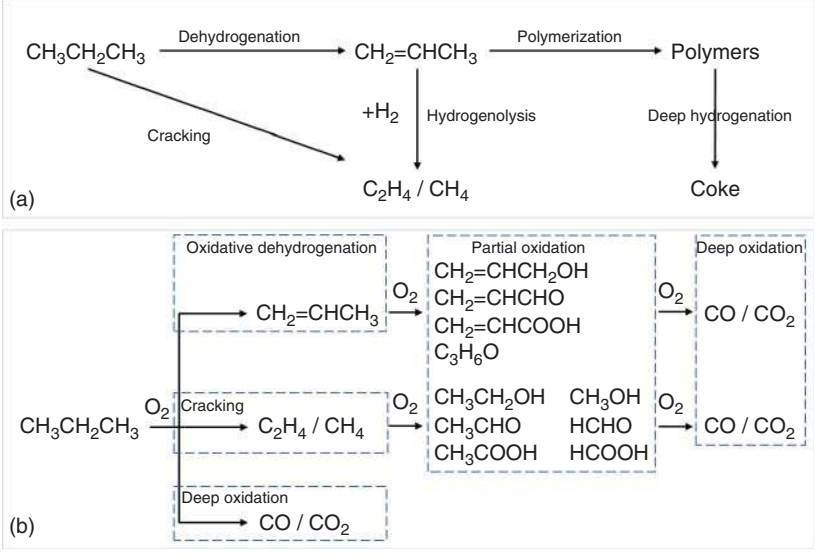

Scheme 8.1 Reaction networks of catalytic dehydrogenation of propane under non-oxidative (a) and oxidative (b) conditions.

8.2 Direct Dehydrogenation

8.2.1 Commercial Dehydrogenation Processes

Compared with oil-based steam cracking, catalytic cracking, and coal-based MTO, catalytic dehydrogenation technology of light alkanes has a single feed and a single product, which reduces the operation costs of reactant pretreatment and product post-treatment, and has a high target olefin yield. Moreover, the by-produced hydrogen makes the catalytic dehydrogenation of low-carbon alkanes, possess advantages

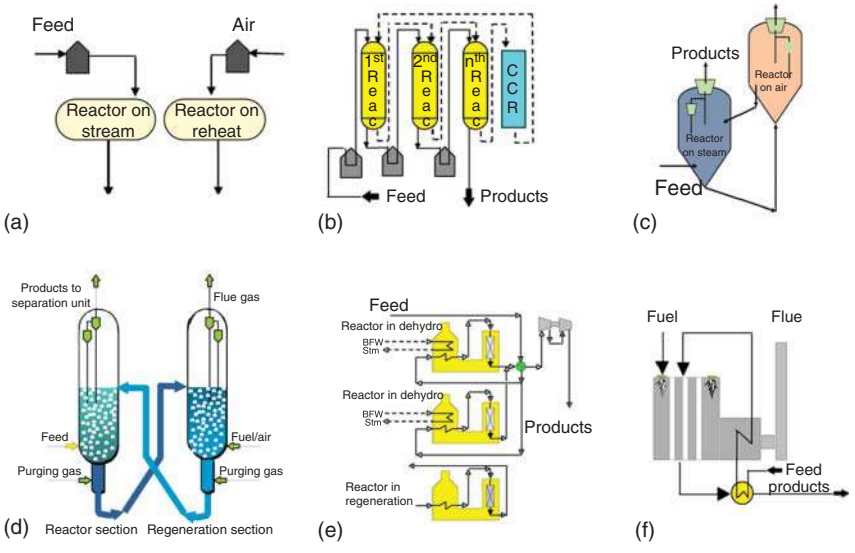

Figure 8.1 Different dehydrogenation processes for light hydrocarbons. (a) Catofin, (b) Oleflex, (c) ADHO, (d) FBD, (e) PDH, and (f) STAR. Source: Reproduced with permission from Sanfilippo and Miracca [10]; © 2006, Elsevier.

of low investment requirements and high return prospects. The present commercial dehydrogenation processes, as shown in Figure 8.1, mainly include the Catofin process (ABB Lummus, US) [4], the Oleflex process (UOP, US) [5], the alkane dehydrogenation to olefin (ADHO) technology developed by the China University of Petro [6], the fluidized bed dehydrogenation (FBD) process (Snamprogetti, Italy) [7, 8], the PDH process (Linde, BASF, and Statoil), and the Star process (Krupp Wood, Germany (Uhde)) [9]. Table 8.1 lists the technical features of each different dehydrogenation process. Among them, the Oleflex process and the Catofin process dominate the alkane dehydrogenation to olefins market [10–12].

8.2.1.1 Catofin Process

In the 1940s, Houdry Company developed Catadiene technology to produce butadiene from butane. Based on this technology, ABB Lummus developed Catofin technology for the catalytic dehydrogenation of C_3~C_5 alkanes to produce single olefins. Catofin technology uses chromium-based catalysts and fixed-bed reactors (Figure 8.1a). The catalytic process cycles through the catalytic dehydrogenation of low-carbon alkanes, cleaning and purging of the dehydrogenation reactor, catalyst pretreatment, and roasting regeneration. Each cycle is about 23 minutes, of which the life of the chromium-based catalyst is about 36 months. To ensure continuous production, the Catofin process requires five reactors (production*2, regeneration*2, purge*1).

8.2.1.2 Oleflex Process

In the 1980s, UOP combined and renovated two existing processes (the Pacol process and the continuous catalyst regeneration [CCR] continuous reforming process)

Table 8.1 Technical features of each different industrial dehydrogenation process.

Items	**Catofin**	**Oleflex**	**ADHO**	**FBD**	**PDH**	**STAR**
Reactor	**Fixed bed**	**Moving bed**	**Fluidized bed**	**Fluidized bed**	**Multitube fixed bed**	**Multitube fixed bed**
Structure	**Adiabatic**	**Adiabatic**	**Adiabatic**	**Adiabatic**	**Adiabatic**	**Adiabatic**
Reaction temperature (°C)	560–650	525–705	500–650	550–600	550–650	480–620
Reaction pressure (MPa)	0.02–0.05	0.1–0.3	—	0.11–0.15	≥0.10	0.5–0.6
Propylene selectivity (%)	82–87	85.5–88	~90	80–85	95	80–90
Propane conversion (%)	40–45	30–40	~50	45–50	40–45	~35
Consumption ($t\,t^{-1}$)	1.18	1.22	—	—	—	1.25
Catalyst	Cr_2O_3/Al_2O_3	$Pt–Sn/Al_2O_3$	Refractory mixed oxides	Cr_2O_3/Al_2O_3	$Pt–Ca–Zn–Al_2O_3$	Noble metal/$Zn–Al_2O_3$
Lifes (yr)	2–3	4–5	—	—	>2	>5
Regenerative way	Switch, air burning, 15–30 min	Continuously move out of regeneration	Continuous removal from the regenerated fluidized bed, air burning	Continuous removal from the regenerated fluidized bed, air burning	Switch, air burning, reaction for 6 h, regeneration for 3 h	Switch, air burning, reaction for 7 h, regeneration for 1 h
Dilution condition	Undiluted	Diluted with H_2	Undiluted	Undiluted	Undiluted	Diluted with H_2O

and developed the Oleflex process. The Pacol process uses a fixed-bed reactor to dehydrogenate heavy alkanes to produce olefins under relatively mild conditions. The reaction–regeneration cycle is about one to two months. However, the use of the Pacol process for the dehydrogenation of light alkanes needs operation under stricter conditions. Coke deposition and deactivation of the catalyst commonly occurred. Thus, frequent catalyst regeneration operations are required, which increases the operating cost of the Oleflex process. Therefore, a continuous reforming process similar to CCR is used to achieve continuous cycle regeneration of the catalyst.

Oleflex technology uses platinum-based catalysts and moving bed reactors (Figure 8.1b). The catalytic process cycle mainly includes catalytic dehydrogenation of low-carbon alkanes, product separation, and catalyst roasting regeneration. The Oleflex process takes hydrogen as a diluent to inhibit high-temperature thermal cracking of alkanes and deactivation of catalyst coking and carbon deposits and as a heating medium to maintain the dehydrogenation reaction temperature. The continuous reforming process is adopted to realize the continuous cycle regeneration of the catalyst.

8.2.1.3 ADHO Technology

In 2016, the China University of Petroleum announced new propane/butane dehydrogenation (ADHO) technology (Figure 8.1c), which was successfully industrialized by Shandong Hengyuan Petrochemical Company Limited. The dehydrogenation technology adopts nontoxic and noncorrosive non-noble metal oxide catalyst, equipped with a high-efficiency circulating fluidized bed reactor, and the continuous dehydrogenation reaction and burning the catalyst for regeneration.

The new propane/butane dehydrogenation (ADHO) technology has the following characteristics [6]: raw materials can be directly fed into the device for reaction without pretreatment, eliminating the need for complex technical processes such as desulfurization, arsenic removal, and lead removal. The ADHO technology is suitable not only for the individual dehydrogenation of propane or butane but also for the dehydrogenation of gas mixtures consisting of propane and butane. The reaction and catalyst regeneration are carried out continuously, and the production efficiency is high. The catalyst is a refractory oxide, which has the advantages of high mechanical strength, low cost, noncorrosiveness owing to the absence of oxychlorination for catalyst regeneration, low reagent consumption, and long and stable operation. Besides, the heat of catalyst regeneration can be returned to the system for recycling, the reaction temperature can be controlled according to the circulation amount, and the entire reaction does not require hydrogen, showing low energy consumption and high heat transfer efficiency.

8.2.1.4 Other Processes

In the 1960s, the Italian company Snamp developed the FBD process (Figure 8.1d), which includes a reactor–regeneration system, using a chromium-based catalyst and a fluidized-bed reactor. In the 1980s, Linde and BASF cooperated to develop the PDH process (Figure 8.1e), which includes a hydrocarbon–hot air circulation

system, using chromium-based and platinum-based catalysts, and a fixed-bed reactor. The process mainly uses alumina-supported chromium oxide catalysts and platinum-based catalyst supported on zeolite molecular sieves. In 2000, Wood Company acquired Philips Petroleum's steam active reforming (STAR) process (Figure 8.1f) and made improvements by using CaO-modified $Pt/ZnO–Al_2O_3$ catalysts and a fixed-bed tubular reactor.

8.2.2 Direct Alkane Dehydrogenation Catalysts

As mentioned above, two main types of formulations are typically used for the direct alkane dehydrogenation, such as Catofin (Lummus, CrO_x-based catalysts) and Oleflex (UOP, Pt-based catalysts) technologies.

8.2.2.1 CrO_x-Based Catalysts

Supported CrO_x-based catalysts have been one of the most efficient catalysts for alkane dehydrogenation since Frey and Huppke first reported the dehydrogenation activity of Cr_2O_3 in 1933 [13]. Owing to the low price and high catalytic activity, CrO_x-based catalysts have been studied for several decades and commercially applied in the Catofin and FBD processes.

In the case of CrO_x-based catalysts, alkane molecules are thought to react at the Cr–O site. However, because chromium oxides are fiendishly complex, the reaction mechanism over such catalyst is not easy to figure out. During PDH process, propane molecules adsorbed by chromium sites may be converted into a $Cr–C_3H_8$ η3-H, H, H adduct, and heterolytic activation of a C—H bond yields $Cr^{3+}–C_3H_7$ intermediate. Subsequently, the β-H in $Cr^{3+}–C_3H_7$ intermediate would be transformed on Cr^{3+} to form $Cr^{3+}–C_3H_6$ hydride surface species. Then, propylene can be released, and H_2 is formed, thus to complete the catalytic cycle. Besides, by-products, including methane, ethane, and ethylene, would form during the PDH process due to cracking, deep dehydrogenation, and hydrogenation reactions (Figure 8.2) [14, 15].

During a catalytic cycle, coke formation and chromium species aggregation are the main deactivation causes of CrO_x-based catalysts. During the industrial processes, carbon is rapidly deposited on the chromium oxide surface causing catalyst deactivation. Consequently, the spent catalysts need to be periodically regenerated. Although the catalysts recover most of their activity after each reaction–regeneration cycle, the loss of catalytic activity is not entirely reversible. Due to the similar ionic radii of Al^{3+} and Cr^{3+}, the heat released through the combustion of coke during regeneration leads to the incorporation of chromia into the alumina framework, resulting in the loss of activity due to the formation of a spinel phase (Figure 8.3) [16].

Nature of the Active Sites On fresh CrO_x-based catalysts, there are a variety of chromium species with different valence states, including Cr^{6+}, Cr^{5+}, Cr^{3+}, and Cr^{2+}, isolated Cr^{n+}, oligomeric Cr^{n+}, and crystallite Cr_2O_3, which play different roles in the PDH process. The relative concentration of these species seems to be dependent on several factors, such as chromium loading (relative to the surface area),

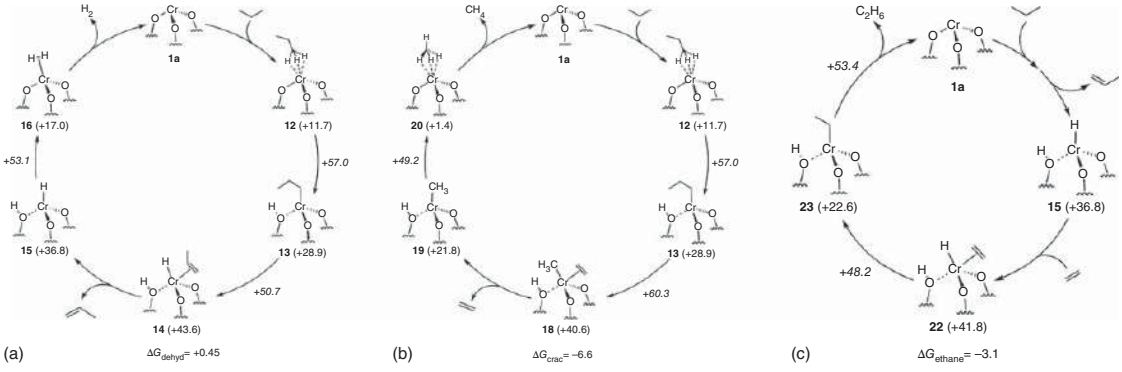

Figure 8.2 Propane dehydrogenation pathways over Cr/SiO_2. (a) Dehydrogenation of propane catalyzed by **1a**; (b) Byproduct formation for the reaction of propane with **1a**; (c) Hydrogenation of ethylene by **1a** to form ethane. The numbers in parentheses are the Gibbs free energies of the corresponding intermediates, and those on the arrows are the Gibbs free energies of the transition states, normalized with respect to that of Cr-1/SiO_2 + propane. All the energies are given in kcal mol^{-1}. Source: Reproduced with permission from Conley et al. [14]; © 2015, American Chemical Society.

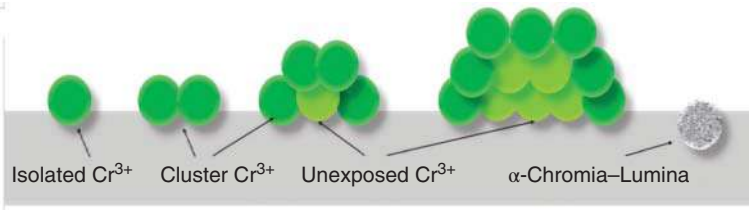

Figure 8.3 The combining process of chromium species and alumina. Weckhuysen et al. [16]/with permission from Elsevier.

calcination treatment used during catalyst preparation, and support employed. However, the high valence state chromium species would be reduced into Cr^{3+} and/or Cr^{2+} due to the reductive atmosphere during the PDH process [17, 18]. By X-ray absorption near edge structure (XANES) and UV–vis spectroscopy, Weckhuysen and coworkers found that the reduction of Cr^{6+} to Cr^{3+} at the beginning of the dehydrogenation reaction and polychromate is more easily reduced than monochromate [19]. Consequently, isolated, unsaturated, and/or clustered Cr^{3+} sites are regarded as the active sites in CrO_x-based catalysts for PDH reaction.

Role of the Support The nature of the support is important to govern the mechanical properties of the catalyst, and also the interaction of the support with the active phase has a profound impact on the catalyst activity and selectivity. A series of metal oxides such as Al_2O_3, ZrO_2, and SiO_2 have been studied as supports for CrO_x catalysts. Alumina is one of the most widely used materials in industry, by which a variety of methods have been studied for the production of chromia–alumina catalysts, e.g. the incipient wetness impregnation of alumina with CrO_3 or $Cr(NO_3)_3$ solutions, the coprecipitation of $Al(OH)_3$ and $Cr(OH)_3$ from Al^{3+} and Cr^{3+} solutions, the chemical vapor deposition (CVD) with chromium compounds on alumina, and the decomposition of complexes including both alumina and chromium [3]. However, the use of alumina as support is not free of drawbacks. For instance, Al_2O_3 can catalyze cracking and coking due to its surface acidity, causing a drop in both activity and selectivity.

Zirconia has been demonstrated as an alternative support, owing to its weak acidity and strong interaction with CrO_x species. Rossi et al. reported that catalysts with zirconia as the support were more active in the dehydrogenation of propane and isobutane than the corresponding catalysts supported on silica or alumina [20]. Nevertheless, the Cr_2O_3/ZrO_2 catalyst displayed a high coking rate, associated with rapid deactivation and short catalyst lifetime. Furthermore, another support layered double hydroxide (LDH) was also studied, and the resultant Cr-based catalyst exhibited serious side reactions and heavy carbon deposition.

Role of the Promoters Alkali metals such as K, Na, Ca, and Mg are often used as promoters to improve the activity and selectivity of chromium-based catalysts in the PDH process. Their functions are attributed to poison the acidic sites and increase the number of active chromium sites.

Potassium is by far the most widely used alkali metal for CrO_x-based catalysts. The K-modified catalysts exhibit enhanced propylene selectivity and anti-coking ability, due to the greatly decreased acidity of the catalysts, thus decreasing deactivation rate and coke formation rate. However, a proportion of the Lewis acid sites are also poisoned after the addition of alkali metals, causing a negative influence on the PDH process [3]. Transition metal species have also been studied as promoters for CrO_x-based catalysts. Different from alkali metals, transition metals have little influence on the acidic properties of CrO_x-based catalysts. However, they play important roles in influencing the dispersion, oxygen capacity, and surface properties of CrO_x-based catalysts, thus affecting their PDH performance [21].

8.2.2.2 Pt-Based Catalysts

Pt-based catalysts for PDH have been commercially applied in Oleflex (UOP) and Star (Uhde) processes. The inspiration of Pt-based catalysts catalyzes alkane dehydrogenation originating the well-known bifunctional supported metal catalysts utilized in catalytic reforming, where the noble metal catalyzes hydrogenation and dehydrogenation reactions and the acidic support provides the active sites needed for isomerization, cyclization, and hydrocracking reactions. For dehydrogenation catalysts, the acidic function must be minimized to avoid side reactions. Although all noble metals of Group VIIIB are active in the hydrogenation and/or dehydrogenation of alkanes, Pt is the only noble metal that commercially applied due to its superior activation of paraffinic C—H bonds and low activity to C–C cleavage [3]. Compared with CrO_x-based catalysts, Pt-based catalysts possess many advantages such as eco-friendliness and high stability. However, this catalyst system still suffers from catalyst deactivation due to the coke formation and the sintering of platinum species.

Nature of the Active Sites Previous studies demonstrated that Pt-based catalysts are active for dehydrogenation in the metallic state, particularly due to their affinity for paraffinic C—H bonds. During alkane dehydrogenation processes, the dehydrogenation reaction is believed to be structure insensitive, while those side reactions, such as coking, cracking, isomerization, and hydrogenolysis, are structure sensitive. Therefore, the size and structure of the Pt nanoparticles can greatly influence catalytic reactivity. Chen and coworkers synthesized a series of platinum catalysts with different cluster sizes (3–9 nm) on calcined hydrotalcite [22]. They found that the activity of propane conversion decreased with an increase in Pt cluster size, while the selectivity to propylene performed in an inverse way. By assuming that every surface atom is an active site, its reaction rate should be directly proportional to the dispersion degree. Hence, decrease of the cluster sizes will increase the amount of the active sites while the relative fraction of the exposed atoms with different local environments is also increasing, which would aggravate those side reactions (Figure 8.4).

In addition, the valence states of the Pt species have a great impact on the catalytic reactivity. Datye and coworkers reported that the conversion of propane is up to 100% with Pt^{2+} species atomically dispersed on CeO_2, while no propylene product was detected, indicating that the isolated Pt^{2+} species are not selective for PDH to propylene [23]. Gong and coworkers showed that single-atom Pt with electron

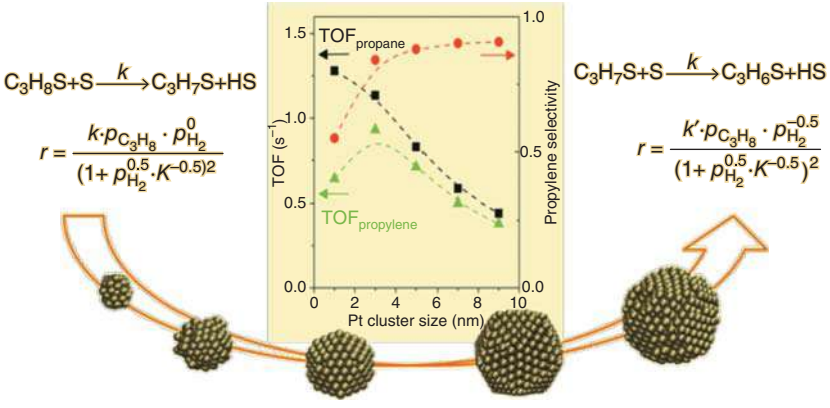

Figure 8.4 The relationships between Pt NP size and TOF. Source: Reproduced with permission from Zhu et al. [22]; © 2015, American Chemical Society.

rich on Cu metals did not desorb propylene and exhibited a higher propylene deep dehydrogenation barrier than Pt metals, leading to higher propylene selectivity but at the expense of dehydrogenation activity [24]. Therefore, every Pt surface atom is active for PDH, but the geometrically structure and electronic states can significantly influence the propylene adsorption and the possible side reactions.

Role of the Support Catalyst supports play important functions in determining the structural and electronic properties, the dispersion, and the catalytic reactivity of platinum-based catalysts. In addition, applicable supports for alkane dehydrogenation must be thermally stable, especially under the harsh conditions during the dehydrogenation and regeneration steps. A series of metal oxides, such as such as Al_2O_3, SiO_2, $MgAl_2O_4$, zeolites, and mixed oxides, have been studied as supports of Pt-based catalysts.

In those extensively studied supports, alumina with desirable textural properties (high surface area and porosity) and stability (thermal and mechanical) has been a widely used support for Pt-based catalysts in industry. However, most alumina supports are acidic, which can lead to deep dehydrogenation, cracking, and coke formation. Therefore, a series of promoters (Li, Na, and K) are used to curb support acidity. Moreover, these promoters can modify the properties of the platinum by reducing the particle size and enhancing the electronic interaction, which can then suppress the side reactions as well. To maintain high dispersion of the platinum species is crucial to attain stable catalyst performance. The weak interaction between platinum and alumina can cause the migration and growth of platinum particles. To enhance the interactions between Pt and the alumina support, sheet-like alumina with pentacoordinate Al^{3+} was synthesized as the support for stabilizing raft-like Pt–Sn clusters and guaranteeing high activity and stability in alkane dehydrogenation processes [25, 26]. Additionally, the incorporation of redox metal oxides such as CeO_2, ZrO_2, and TiO_2 as electronic additives into supports can adjust the electronic structure of active metal phases. After mixing with these metal oxides, catalytic

reactivity, stability, and anti-coking capability would be greatly improved, due to the increased interactions between Pt and the supports. For instance, doping Al_2O_3 with TiO_2 can contribute to the electron donation from partially reduced oxide species to platinum species, on which the desorption of electron-rich alkene will be promoted and coke deposits will be transferred from active platinum sites to the support. However, the addition of metal oxides enhanced the support acidity, causing higher amount of coke deposits on support and then blockage of the porosity [27]. Alternatively, MgO species can be introduced into Al_2O_3 support. Pt–Sn supported on $MgAl_2O_4$ exhibited high catalytic activity and long-term stability for PDH, owing to its hierarchical structure and weak acidity [28]. Furthermore, LDH materials are used as supports in the preparation of Pt-based catalysts that exhibit enhanced catalytic stability and anti-coking capability for PDH [29].

Zeolites have been reported as promising alternative supports for alumina due to their well-defined pores, high surface areas, and tunable acidities. Pt supported on zeolites, such as SAPO-34 [30], Zn–ZSM-5 [31], and TS-1 [32], exhibited high activity and stability for PDH. Recently, Ryoo et al. used a mesoporous zeolite as support that had pore walls with surface framework defects (called "silanol nests") and increased the catalytic lifetime 700-fold by ensuring that the supported Pt nanoparticles all presented as intermetallic compounds with La [33]. Over the last several years, some articles reported several Pt-zeolite catalysts that exhibited high performance in PDH. However, the high acidity of zeolites and the weak interaction between Pt and zeolites remain great challenges. Similarly, SiO_2 materials were unsuitable support for platinum-based catalysts as Pt–Sn nanoparticles readily sinter due to the weak metal–support interaction.

Role of the Promoters As mentioned above, monometallic Pt catalysts display very high activity in dehydrogenation reactions, while olefin selectivity and catalyst stability are not entirely satisfactory. Previous studies reported that the structural and electronic properties of Pt-based catalysts were greatly improved with the addition of promoters, which can effectivity enhance the catalytic reactivity, stability, and anti-coking capability during the alkane dehydrogenation processes.

Up to now, Sn was the most used and studied promoter, which could modify both the support and the active phase. The addition of tin can suppress unwanted side reactions by inhibiting the metal sintering and facilitating the transfer of the coke species from the metal surface to the support, due to the geometric and electronic effects. Moreover, tin species can neutralize the acidity of the support to suppress those unwanted side reactions. During the reduction treatment, SnO_2 species can be reduced to SnO and/or Sn to form a Pt–Sn alloy active phase. Density functional theory (DFT) revealed that the dehydrogenation barrier of the propylene on the Pt–Sn alloy was much higher than that on Pt particles, resulting in enhanced selectivity, stability, and anti-coking capability [34, 35]. Furthermore, Pt–Sn alloy formation effectively reduces the amount of neighboring Pt atoms within the ensembles, so as to suppress those structure-sensitive side reactions, such as isomerization, hydrogenolysis, and coke formation. On the other hand, tin species selectively cover low coordination platinum sites (such as steps, corners, edges, and defects), which

are ascribed to be the active sites for the hydrogenolysis reaction. From the electronic point of view, it has been suggested that alloyed metallic Sn or Sn^{2+} species in close contact with platinum can transfer electrons to the 5*d* band of platinum, attenuating the adsorption of the product alkene thus inhibiting coke formation. However, due to the promoter partially covering active platinum sites and meanwhile pushing down the *d* band center of platinum, the alloyed catalysts significantly lower the reaction rate of PDH, where the catalytic activity is compromised. Therefore, regulating the ratio of Pt and Sn is a crucial to balance between the two effects. There are many Pt–Sn alloy with different composition such as Pt_3Sn, PtSn, Pt_2Sn_3, and $PtSn_4$ in the Pt–Sn catalysts. Notably, DFT results revealed that the Pt_3Sn was significantly more active for the dehydrogenation reaction than other alloys (Figure 8.5) [34, 36].

In addition, other metals were also studied as promoters for platinum-based catalysts in the alkane dehydrogenation process. Zinc was used as a promoter to greatly modify the geometric and electronic properties of platinum and simultaneously poison the acid sites on the support, which can effectivity avoid side reactions and enhance catalytic activity and stability in PDH process [37]. Gallium oxide and indium oxide were also reported as good promoters for Pt-based catalysts in PDH. Those oxide additives can poison surface acid sites and alloy with platinum to modify the geometric and electronic properties of platinum, thus hindering those side reactions and coke deposition [38, 39]. Recently, transition metals, such as Cu, Mn, Fe, Co, Ni, and Ag, have been studied as promoters for improving the performance of Pt-based catalysts [40]. After the introduction of those promoters, the catalytic performance of Pt-based catalysts can be significantly improved by

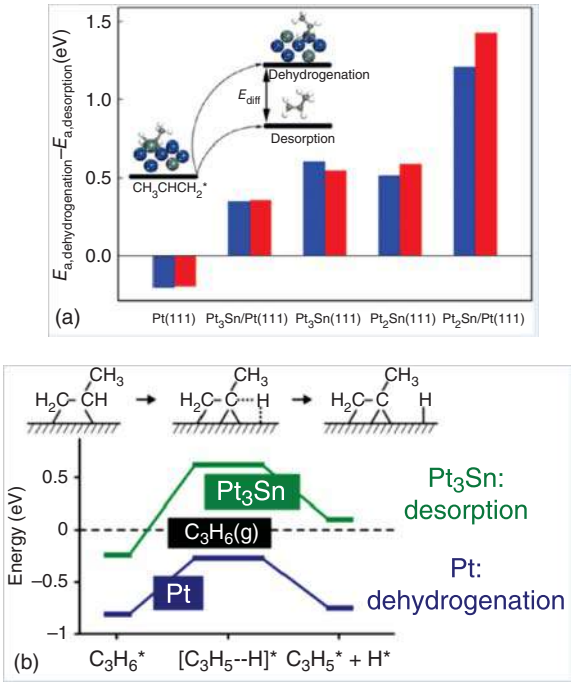

Figure 8.5 (a) Energy barrier difference (E_{diff}) between propylene dehydrogenation and propylene desorption over the Pt (111) and PtSn surfaces. Source: Reproduced with permission from Yang et al. [36]; © 2012, American Chemical Society; (b) Potential energy surface of propylene dehydrogenation. Source: Adapted from Yang et al. [34].

modifying the dispersion and structural and electronic properties of the platinum. Particularly, the presence of atomic Pt species in single Pt atom catalysts and/or geometry-isolated Pt sites in intermetallic alloys can greatly improve catalytic stability and anti-coking capability. These catalysts are highly promising for the industrialization of the PDH catalysts.

Besides the CrO_x-based and Pt-based catalyst, other metals and/or metal oxides have been studied as alkane dehydrogenation catalysts, which exhibited comparable and/or higher performance than commercial catalysts. Vanadium oxide catalysts with low price and high catalytic reactivity were reported as one of the most potential alternative catalysts with respect to commercial Pt- and CrO_x-based catalysts in PDH processes. However, the toxicity and the deactivation of VO_x catalysts still limit their application in the industrial process. Gallium oxide catalysts were also active for alkane dehydrogenation, while the exact nature of the active sites is still under debate. Furthermore, a series of transition metal catalysts (such as FeO_x-, CoO_x-, SnO_x-, ZnO_x-, and ZrO_2-based catalysts) were also tested in alkane dehydrogenation reactions. Particularly, the isolated and/or unsaturated metal species were regarded as the active sites for PDH, while those species easily aggregate into large particles, resulting in low stability.

8.3 Oxidative Dehydrogenation

In ODH reactions, the introduction of molecular oxygen makes the reaction have the advantages of not being restricted by thermodynamic equilibrium, zero carbon deposits, fast reaction rate, and low reaction temperature in comparison of direct dehydrogenation, which has attracted the attention in the academia and industry. The bottleneck of ODH is the selectivity control of olefin because of the deep oxidation of reactive olefin molecules. In the past decades, the research interest in the ODH reaction of light alkanes has been focused on transition metal oxides (e.g. V_2O_5, MoO_3, and NiO), alkaline-earth metal oxychlorides, and metal-free catalysts, such as boron-based catalysts and carbon-based catalysts [41, 42]. The following section summarizes the progress of these well-developed catalytic systems.

8.3.1 Transition Metal Oxide and Alkaline-Earth Metal Oxychloride Catalysts

8.3.1.1 Vanadium Oxide-Based Catalysts

The well-developed transition metal oxide catalysts mainly include the oxides or composite oxides from Groups VB to VIIB, such as vanadium oxide, molybdenum oxide, Mo–V–Nb composite oxide, and V–Ti composite oxide. Vanadium oxide is considered as one of the most important and useful materials to be used as an oxidative dehydrogenation of propane (ODHP) catalyst due to its reducible nature and the variable oxidation state (V^{3+}, V^{4+}, and V^{5+}). It is generally accepted that V^{5+} is the highly active initial state of the catalyst in the ODH reaction cycle. The methylene C—H bond in the propane molecule first interacts with lattice oxygen as the propane

molecule adsorbs weakly on the oxide surface. The adsorbed propane reacts with a vicinal lattice oxygen atom to form an isopropoxide species and a V–OH group. Then another hydrogen atom is abstracted on the adjacent V=O site from the isopropoxide species to form propylene and another V–OH group. The adjacent V–OH group condensates to form water, and the oxidation state of V reduces to V^{4+}. After reoxidation with oxygen, the oxidation state of V was recovered to initial V^{5+} state (Scheme 8.2) [42, 43]. This is so-called Mars-van Krevelen (MvK) mechanism for variable valence transition metal oxide catalysts [44].

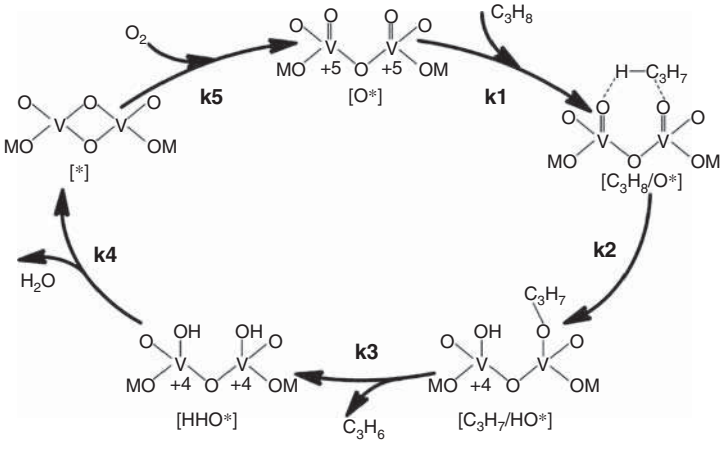

Scheme 8.2 Reaction mechanism of ODHP over VO_x-based catalyst. Source: Reproduced with permission from Chen et al. [43]; © 2002, Elsevier.

Carrero et al. [44] rigorously reviewed and compared the catalytic kinetics of supported vanadium oxide catalysts at submonolayer coverage in ODHP. They found the apparent propane ODH activation energies varied from 45 to 150 kJ mol^{-1} over different supports, indicating the critical role of the bridging V—O—Support (V—O—S) bond in the reaction kinetics and mechanism. Besides, the propane consumption TOFs were constant as a function of vanadia coverage (submonolayer coverage) over a certain oxide support, suggesting that the ratio of surface VO_4 monomers/polymers did not affect the propane ODH kinetics and the surface monomer and polymer species exhibit the same activity. The different TOFs over the specific oxide support further demonstrated the significant effect of the bridging V—O—S bond in propane activation.

Given the coexistence of these nucleophilic oxygen sites (V=O, V–O–S, or V–O–V) of the supported VO_x materials, it is difficult to identify the contribution of specific oxygen species. There is a rough conclusion that the nucleophilic species including metal bound oxo (M=O) sites and bridging oxygen atom between metal centers (M–O–M and M–O–S) play a crucial role in abstracting the initial hydrogen atom of alkanes to olefins, while the electrophilic species such as metal bound peroxo ($M > O_2$ or M–O–O–M) or superoxo ($M–O_2^-$) cause the deep oxidation of olefins to carbon oxides [45–47].

8.3.1.2 $MoVTeNbO_x$ Catalysts

$MoVTeNbO_x$ mixed metal oxide catalyst, mainly composed of the M1 and M2 crystalline phases and minor amounts of other phases such as Mo_5O_{14}-type structures or binary MoV and MoTe oxides, is active and selective in the oxidative dehydrogenation of ethane (ODHE) [48–52]. It was reported that $MoVTeNbO_x$ catalysts showed 75% ethylene yields at temperatures as moderate as 400 °C [53]. The M1 phase of $MoVTeNbO_x$ mixed oxides, consisted of eleven corner-sharing MO_6 (M = Mo or V) octahedra forming pentagonal columns aligned in the [001] direction, connected to each other by one or several corner-sharing octahedral forming hexagonal and heptagonal channels (Figure 8.6a), is the active phase in ODHE. Nieto and coworkers [54] systematically investigated the active center of $MoVTeNbO_x$ catalysts and its evolution under the reaction conditions. The multifunctional $Te_2M_{20}O_{57}$ (M = Mo, V, Nb) phase in cooperation with the (V, Nb)-substituted θ-Mo_5O_{14} phase was proposed to be responsible for ethane selective oxidation to ethylene. It should be pointed out that the reaction temperature played an important role in the stability of $MoVTeNbO_x$ catalysts. At reaction temperature over 500 °C, tellurium (melting point: 450 °C) would remove from the intercalated framework channels of the M1 phase, resulting in the partial destruction of the M1 phase and the formation of the inactive MoO_2 crystalline phase. Thus, uniform reaction temperature (below 500 °C) should be strictly controlled (i.e. no hot spots in the catalyst bed) to maintain the catalytic performance of $MoVTeNbO_x$ catalysts [48].

The advanced characterization techniques (*in situ* or *operando*) and theoretical simulations facilitate the understanding of the structural evolution and catalytic mechanism of $MoVTeNbO_x$ mixed metal oxide catalyst. Millet and coworkers [55] used the *in situ* environmental transmission electron microscopy (ETEM) to image the compositional and redox dynamics of the complex M1 phase (Figure 8.6b,c). No structural disordering was observed under reaction conditions (350 °C, $O_2/C_2H_6/N_2$ = 30/15/55, 1 mbar). The {Te–O} chains present in the hexagonal channels (acting as oxygen reservoirs) were verified to participate in the

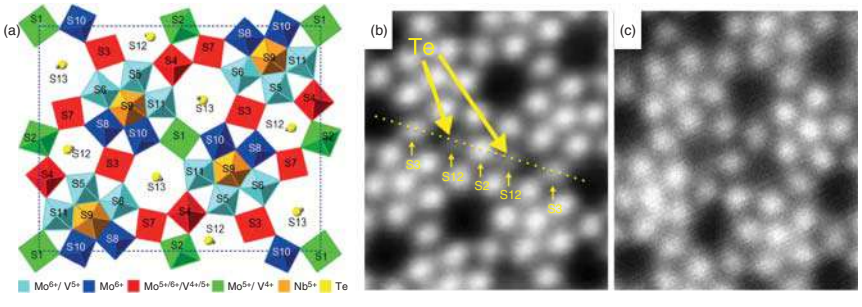

Figure 8.6 ODHE over $MoVTeNbO_x$ catalysts. (a) Two-dimensional diagram of the $MoVTeNbO_x$ M1 unit cell viewed in the [001] direction with 13 cation sites. (b) High-resolution STEM-HAADF images recorded at 350 °C under a catalytic reaction gas mixture ($O_2/C_2H_6/N_2$ = 30/15/55, 1 mbar) showing the apparent disappearance of Te peaks. (c) High-resolution STEM-HAADF images recorded at 350 °C under high vacuum (reduction by C_2H_6, 7×10^{-7} to 5×10^{-6} mbar). Source: Aouine et al. [55]/with permission from American Chemical Society.

redox process of the catalyst. Under strongly reducing conditions (high vacuum or high vacuum after reduction by C_2H_6), Te^{4+} would be reduced to Te^{2+}, leading to a high degree of freedom for displacement. The [001] basal plane of the M1 phase has generally accepted as active location to activate alkanes [56]. By combination of scanning transmission electron microscopy (STEM) with He ion microscopy images, Rietveld analysis and kinetic tests, Lercher and coworkers [57] revealed that the activation of ethane was related to the facets {001}, {120}, and {210} at the surface of M1 crystals, while the lateral facets {120} and {210} were ascribed to the typical active centers for propane oxidation. Based on the two orders of magnitude higher C_2H_6 to C_6H_{12} activation rate ratios on $MoVTeNbO_x$ than those on non-microporous vanadium oxides (VO_x/ SiO_2) and the DFT calculation on external surfaces, Deshlahra and coworkers [58] proposed that most C_2H_6 activations occurring on $MoVTeNbO_x$ were inside the micropores. These micropores tightly confined C_2H_6 molecules and stabilized C–H activation transition states via van der Waals interactions but destabilized undesired O-insertions with low CO_x emission because of the steric hindrance to proximate C–O contact in concave pore walls.

In the case of developing high-performance catalyst, the introduction of cerium oxide to phase-pure M1 phase is also reported to be an effective strategy [50, 51]. The amounts of V^{5+}active sites and the lattice oxygen species were enriched, and the reoxidation of V^{4+} to V^{5+} was also facilitated due to the incorporation of Ce. Ethane conversion of 56.2% and ethylene selectivity of 95.4% and ethylene productivity of 1.11 kg_{C2H4} kg_{cat}^{-1} h^{-1} were maintained for 200 hours over the promoted $MoVTeNbCeO_x$ catalyst [51].

8.3.1.3 Nickel Oxide-Based Catalysts

Nickel oxide is a kind of nonstoichiometric oxide with cationic vacancies, which shows excellent low-temperature reactivity in ODHE, but the main product is the deep oxidation product CO_2 due to the presence of nonstoichiometric oxygen species on the surface. V, Mo, Co, Nb, Fe, W, and Sn oxide promoters were investigated to regulate the surface nonstoichiometric oxygen species, i.e. electrophilic oxygen species, to suppress the deep oxidation [59–64]. Among these promoters, the incorporation of Nb in NiO lattice by either substitution of nickel atoms or filling of the cationic vacancies in the NiO surface led to a reduction of the electrophilic oxygen species (O^-) and showed higher ethylene selectivity [60]. The synthesis method also affects the catalyst structure, activity, selectivity, and stability of NiO-based catalysts. Caps and coworkers [65] synthesized high-surface-area NbNiO nanocomposites by slow oxidation of a nickel-rich Nb–Ni gel. This NbNiO catalyst showed a 31% ethane conversion and a 71% ethylene selectivity at 350 °C. As Nb loading over 5%, the amorphous Nb-rich oxide layers would result in lower activity and cause the deactivation of NiO catalyst. They also compared the influence in catalytic behavior of NiTaO mixed oxide catalysts between sol–gel and solid–state grinding methods. Based on the characterization results, the Ta atoms were found to insert into NiO crystal lattice to form a new Ni–Ta oxide solid solution. In the sol–gel catalyst, the selectivity decreased with the increase of conversion, indicating a consecutive pathway in the

conversion of ethane to CO_2 via an ethylene intermediate. However, the solid-state catalyst could be readily reduced and exhibited an no variation of ethylene selectivity with ethane conversion, suggesting CO_2 was directly formed from ethane [63]. Their further study found Sn, Ti, and W atoms could be individually incorporated into NiO crystal to generate solid solution phases using the solid-state grinding method, leading to the significant decrease of NiO particle size and the amount of nonstoichiometric oxygen species, which showed high selectivity to ethylene [64]. The low-temperature activity of NiO-based catalysts is also observed in ODHP [66–68]. The addition of Nb into NiO could improve the propylene selectivity, whereas the introduction of Ce can promote the propane conversion at low temperature. A propylene yield of 10.4% was obtained over the CeNbNiO catalyst at 250 °C [66].

8.3.1.4 Alkaline-Earth Metal Oxychloride Catalysts

Supported alkali metal chloride catalysts, i.e. $LiCl/Dy_2O_3/MgO$, have exhibited as high as 90% ethylene selectivity in ODHE [69]. Three factors were proposed by Lercher to result in the excellent selectivity to ethylene. The first and probably most important impact is related to the low concentration of the formed OCl^- in such catalysts. Then, the high mobility of cations and anions within the melt reduces the interactions with ethylene. The last is the spatial isolation of the hypochlorite oxidation sites in and on the dynamic melt [70]. The mechanistic insights on the concentration and dynamic genesis of the active sites under reaction conditions were further revealed by Lercher. Oxygen molecules were activated at the molten overlayer/solid support interfaces, and the active oxygen species (oxyanionic OCl^-) diffuse through the chloride melt to the surface in a low concentration. These oxygen species react more slowly with less tendency to total oxidation than the electrophilic oxygen on NiO-based catalysts. Then, the oxyanion could reactively dehydrogenate ethane at the melt–gas-phase interface with nearly ideal selectivity (Figure 8.7a) [71].

Due to the facile over oxidation of olefins, it is difficult to obtain high olefin selectivity especially at high conversion level in ODH reactions. Halogens as mild oxidants for the functionalization of light alkanes can effectively avoid the formation of CO_x. By using molecular chlorine, the selectivity toward propylene at 50% propane conversion was as high as 95% over Ru/TiO_2 catalyst in ODHP [72]. The mixed oxidizing agent of bromine–iodine also exhibited a 80% $C_3H_6 + C_3H_7X$ single-pass yield [73]. It has been reported that the addition of halogens to the feed of oxygen and propane could improve the propane conversion and the propylene selectivity. Propane conversion of 71% and propylene selectivity of 83% were obtained when introducing a small amount of Br_2 to the feed of I_2, C_3H_8, and O_2. The good performance was because molecular iodine could dissociate to form radicals more easily that facilitated the formation of Br radicals, accelerating the ODH process [74]. Wang and coworkers [75] demonstrated that NiO-modified CeO_2 nanocrystals exhibited a high ODH performance in the presence of HCl. An 80% propylene selectivity at propane conversion of 69% along with at least 100 h stability was achieved over the 8 wt% $NiO–CeO_2$ catalyst at 500 °C. The high activity and selectivity were determined to be related to the surface oxygen vacancies and

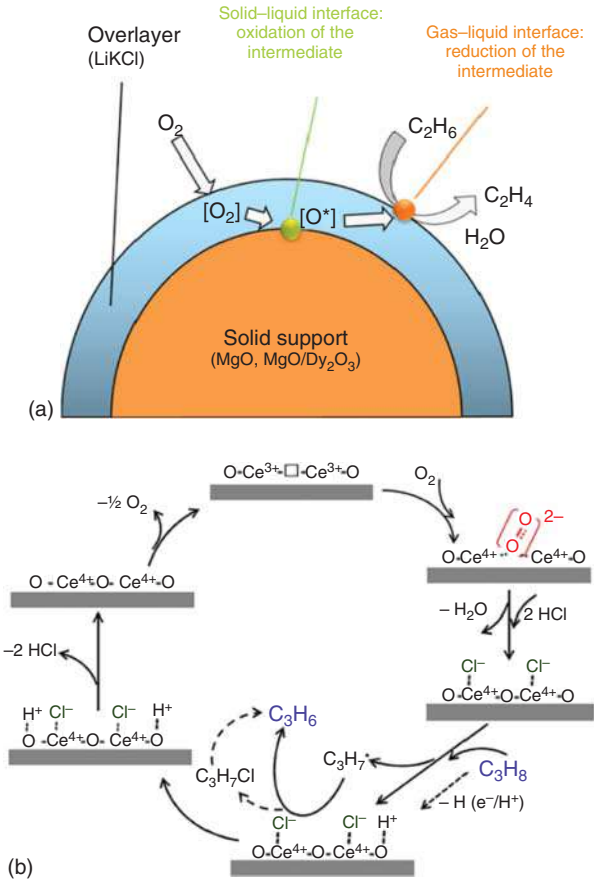

Figure 8.7 ODH on halogen-containing catalysts or atmosphere. (a) Schematic representation of the reaction sequence in ODHE over supported alkali metal chloride catalysts. Source: Reproduced with permission from Gartner et al. [71]; © 2014, American Chemical Society. (b) Proposed reaction mechanism for the oxidative dehydrogenation of C_3H_8 to C_3H_6 by O_2 in the presence of HCl over CeO_2-based catalysts. Source: Reproduced with permission from Xie et al. [75]; © 2018, American Chemical Society.

the surface chloride coverage. The peroxide species (O_2^{2-}) formed by adsorption of molecule oxygen on surface oxygen vacancies may activate chloride, generating a radical-like active chlorine species. This active chlorine species would selectively activate C—H bond of propane, forming propylene as a major product (Figure 8.7b) [75]. Pérez-Ramírez and coworkers [76] found that europium oxychloride (EuOCl) catalyst showed high yields of ethylene (90%) and propylene (40%) in ethane and propane oxychlorination reactions. The phosphates of transition metals (MPO, M = Ti, V, Cr, Mn, Fe, Co, Ni, and Cu) were also demonstrated to be active in oxychlorination of propane. Among these phosphates, $CrPO_4$ was the selective catalyst with a 95–98% propylene at ca. 20% propane conversion [77]. Recent work on *operando* electron paramagnetic spectroscopy (EPR) quantification testified a

linear correlation between the amount of redox-active center (Eu^{2+} in EuOCl or Cr^{2+} in $CrPO_4$) and the olefin space time yield, suggesting the formation of C_3H_6 was proportional to the generation of Cr^{2+} and Eu^{2+} [78].

8.3.1.5 Chemical Looping ODH

The introduction of oxygen into the dehydrogenation reaction makes a break in thermodynamic equilibrium constraints, providing a higher potential olefin yield. This has attracted great attention in the academic field. However, no industrial demonstration plant of an ODH process is reported probably due to the deficient olefin selectivity and yield, and the additional safety concerns of the oxygen-containing flammable stream. Dividing the entire the ODH process into two independent reactions (alkane cracking or dehydrogenation to olefins and reduced catalyst reoxidation), namely, chemical looping oxidative dehydrogenation (CL-ODH), is beneficial to separately feed alkanes and oxygen into individual reactor, avoiding the safety concern from the flammable mixture. Li and coworkers [79–85] presented a series of important studies in CL-ODHE reactions. The ODHE reaction was divided into ethane cracking and lattice oxygen regeneration. Hydrogen produced from ethane cracking was selectively oxidized by the lattice oxygen of the redox Mn-based catalysts (Mg_6MnO_8, Mn_7SiO_{12} [84], $SrMnO_3$, and $CaMnO_3$[82]), and the lattice oxygen was regenerated by air [80]. Due to the high temperature (>750 °C) required in ethane cracking, it is vital to selectively combust hydrogen rather than ethylene. Sodium tungstate was demonstrated to be an efficient promoter to inhibit the formation of nonselective, electrophilic oxygen species on Mg_6MnO_8 catalyst surfaces through the suppression of Mn^{4+}, showing 89.2% ethylene selectivity and 68.2% ethylene yield [81]. Further research revealed that Na_2WO_4 promoter formed a molten shell around the Mg_6MnO_8 redox catalyst and suppressed the number of basic sites on Mg_6MnO_8. Hydrogen was primarily combusted at the gas–Na_2WO_4 molten shell interface via redox reactions of the tungsten salt (Figure 8.8a), likely between WO_4^{2-} (tungstate) and WO_3^- (tungsten bronze) [85]. Compared to the low ethylene selectivity over pure $La_xSr_{2-x}FeO_{4-\delta}$ (LaSrFe), the addition of Li cations (Li-promoted LaSrFe) led to a 90% ethylene selectivity at a 61% ethane conversion in CL-ODHE. The enrichment of Li cations on the surface suppressed the diffusion of O^{2-} and the formation of electrophilic oxygen species from the bulk to surface, showing an enhanced ethylene selectivity [79]. The enhanced selectivity of ethylene was also observed in adding other alkali metal, i.e. sodium or potassium cations [83].

The direct involvement of lattice oxygen in the one-step ODH of alkanes to olefins represents the other type of CL-ODH process, which is featured with a lower operation temperature. Ostroumova and coworkers [86, 87] studied the catalytic performance of VO_x and MoO_x supported on Al_2O_3, Ga_2O_3, or Y_2O_3 in a pulsed reactor for ODHE. MoO_x/γ-Al_2O_3 showed a better catalytic performance, and 66.5% ethane conversion and 94.5% ethylene selectivity were obtained at 600 °C. VO_x-based catalyst is the most widely studied catalytic system, which can be used in both ODHP and PDH reaction. The V^{5+} sites participate in the redox of ODHP, while the activation of propane molecule is mainly occurred at V^{3+} sites [88, 89]. Gong and coworkers [90] demonstrated dual-functional Mo–V–O mixed oxides

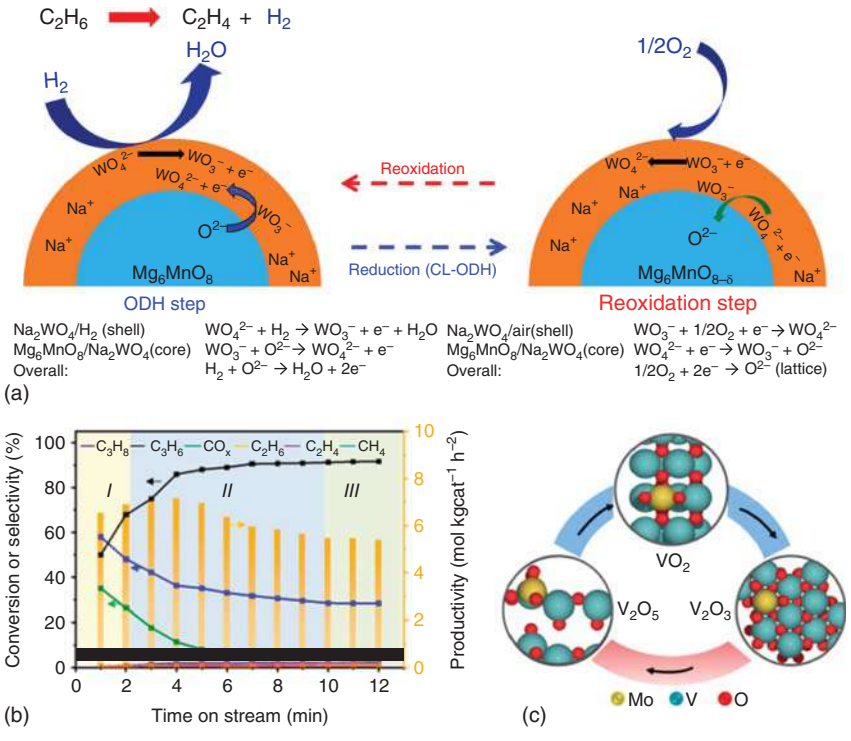

Figure 8.8 Chemical looping ODH. (a) Proposed mechanism of CL-ODHE process over NaW-promoted Mg_6MnO_8 catalysts. Source: Reproduced with permission from Yusuf et al. [85]; © 2019, American Chemical Society. (b) Product profiles over Mo–V–O (V/Mo = 6) with different reaction time. (c) Proposed CL-ODHP process over Mo–V–O mixed oxides. Source: Reproduced with permission from Chen et al. [90]; © 2019, American Chemical Society.

could selectively convert propane to propylene via the CL-ODHP approach. Due to the unique nature of the redox VO_x-based catalyst, both the features of ODH and direct dehydrogenation were apparent in chemical looping reaction. The ODH mainly occurred in the first five minutes and achieved 89% propylene selectivity at 36% propane conversion (Figure 8.8b). With the continuous consumption of lattice oxygen, the propane conversion gradually decreased. When the lattice oxygen is exhausted, the direct dehydrogenation process of propane occurs. During the overall dehydrogenation step, 80% selectivity of propylene remained stable for 100 dehydrogenation–regeneration cycle. The doping of Mo increased binding energy of V—O bonds and the fraction of V^{4+} and V^{3+} sites inhibited the lattice oxygen evolution for over-oxidation (Figure 8.9c).

8.3.2 Boron-Based Catalysts

8.3.2.1 Development of Boron-Based Catalysts

Due to its excellent antioxidation properties, high-thermal conductivity, and structural stability, hexagonal boron nitride (*h*-BN) has been extensively applied

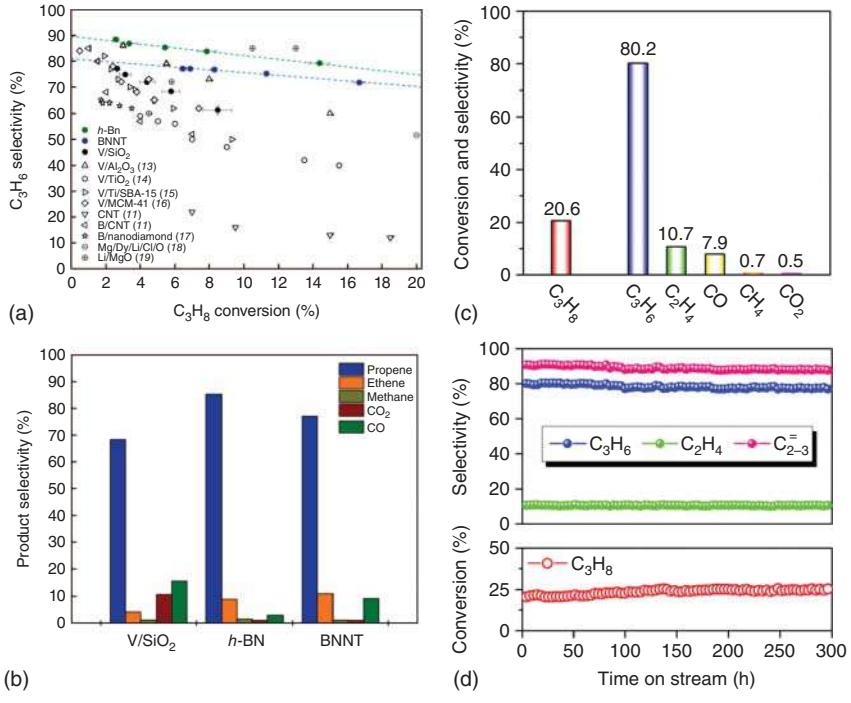

Figure 8.9 (a) Selectivity to propylene as a function of propane conversion in ODH reaction, comparing previously reported data from representative catalysts to *h*-BN and BNNTs. (b) Comparisons of product selectivity between VO_x/SiO_2, *h*-BN, and BNNTs. Source: Reproduced with permission from Grant et al. [94]; © 2016, AAAS. (c) Propane conversion and product selectivity over the BNOH catalyst. Source: Reproduced with permission from Shi et al. [95]; © 2017, Wiley. (d) Long-term stability test over the BNOH catalyst. Source: Reproduced with permission from Shi et al. [96]; © 2017, Dalian Institute of Chemical Physics, Chinese Academy of Sciences.

in the fields of physics, electronics, and aerospace. In catalysis research, *h*-BN is generally considered as an inert component due to its lack of surface defects and functional groups and has merely used as a support for different reaction systems for a long time, such as in dry reforming of methane and CO oxidation [91–93]. The understanding of the chemical inertness of boron nitride was not changed until the independent reports of Hermans's group and Lu's group in the field of oxidative dehydrogenation of light alkanes [94, 95].

Hermans's group reported that both *h*-BN and boron nitride nanotubes (BNNTs) could catalyze the oxidative dehydrogenation of propane (ODHP) with high selectivity to propylene and ethylene [94]. For example, *h*-BN delivered 79% selectivity to propylene and 12% selectivity to ethylene at 14% propane conversion. The proportion of CO_x only accounts for ~9%, far lower than that over a traditional VO_x/SiO_2 catalyst at 9% propane conversion (Figure 8.9a,b). They furthermore verified that the catalytic activity of the *h*-BN remains stable for at least 32 hours on stream. Both *h*-BN and BNNTs exhibited analogous product distribution. However, BNNTs showed a

conversion rate of propane (mol_{C3H8} kg_{cat}^{-1} h^{-1}) more than 1 order of magnitude higher than that observed with *h*-BN.

During the same period, Lu's group independently disclosed that edge-hydroxylated boron nitride can efficiently catalyze ODHP and ODHE to corresponding olefins with impressive selectivity, and with only negligible CO_2 formation [95, 96]. In the case of ODHP, the *h*-BN with edge-hydroxylation treatment (BNOH) showed high conversion of propane (20.6%) and selectivity (80.2%) to propylene. Taking the equally important product ethylene into account, the selectivity for light olefins was up to 90.9%. More significantly, the formation of CO_2 (0.5%) was lower than for the traditional ODH processes (10–60% CO_2) (Figure 8.9c). The control experiment with a feed gas of C_3H_6/O_2/He also showed almost no activity for propylene oxidation on boron nitride catalyst and suppress the occurrence of over-oxidation. Hydroxylated boron nitride (BNOH) also displayed an olefin productivity of 6.8 g_{olefin} g_{cat}^{-1} h^{-1} and stability at least 300 hours (Figure 8.9d), suggesting a promising potential for industrial implementation.

In the case of ethane [96], the ethylene selectivity was as high as 95% at 11% ethane conversion, and the ethylene selectivity maintained 90% as ethane conversion was up to 40%. At very high conversion level (63%), the ethylene selectivity still retained 80% with only negligible amounts of CO_2. These performance results are comparable with that of the industrialized ethane steam cracking process in view of the ~85% ethylene selectivity at ~60% ethane conversion, but much superior considering the much lower reaction temperature and CO_2 emission [97]. The BNOH catalyst also can exhibit high ethylene productivity (9.1 g_{C2H4} g_{cat}^{-1} h^{-1}) with >90% selectivity by modulating the reaction conditions. The remarkable stability of the BNOH catalyst was evidenced by the operation for 200 hours at 590 °C. Such stable productivity far exceeded the critical value, 1 g_{C2H4} $g_{cat}^{-1}h^{-1}$, which demonstrated its potential application for industry [41].

To further enhance the catalytic performance of boron nitride material, increasing the number of active sites may be an effective option. High-surface-area boron nitride nanosheets synthesized by the reaction of boric acid and urea also showed high activity for ODH of ethane, which not only enabled to convert ethane exclusively to ethylene at near 10% conversion but also afforded 60% ethylene selectivity at 78% ethane conversion and remained stable at least 400 hours at 575 °C [98]. High-surface-area boron nitride synthesized from boric acid and dicyanamide precursors was also showed the enhanced catalytic performance for ODHP. For example, it delivered 53% propylene selectivity and 18% ethylene selectivity at 52% propane conversion level. However, the catalytic activity of high-surface-area *h*-BN was retained for only five hours because of the oxidation of surface B—N bonds in oxygen. The addition of ammonia could regenerate the catalytic activity and maintain stable activity for more than 100 hours [99]. Ball milling was used to expose more edge sites with a significant increase of surface area. This ball-milled boron nitride, in inclusion of oxidized boron on the surface, was found to show a great improvement of selectivity to ethylene from ~42% to ~92% at 10% ethane conversion in ODH of ethane compared with pristine *h*-BN [100]. Nanostructural engineering was also employed to increase the number of active sites. 3D

spherical superstructure consisting of 2D boron nitride nanosheets derived from boron-contained metal–organic frameworks was fabricated to afford high olefin yield of 40.2% (propylene 27.8% and ethylene 12.4%) in ODHP reaction [101].

Other boron-containing materials such as borides and elemental boron were also demonstrated to be efficient ODH catalysts. Lu's group prepared an oxygenic group functionalized silicon boride (for which the main phase was SiB_6) for ODH of light alkanes including ethane, propane, and isobutane [102]. For example, in ODH of propane, the selectivity of propylene was 82.2% with only 0.3% for CO_2 when the conversion of propane approached ~19%. Moreover, 88.7% olefin selectivity was obtained at a propane conversion of 31%, showing well performance in preventing over-oxidation of olefins at high conversion. Hermans and coworkers [103] also reported a series of boron-containing materials: boron carbide (B_4C), titanium boride (TiB_2), nickel boride (NiB), cobalt boride (Co_2B/Co_3B), hafnium boride (HfB_2), tungsten boride (WB), and elemental boron all that showed catalytic activity for ODH of propane and the same product trends in their product distributions as boron nitride. High selectivity to propylene was achieved using these B-containing catalysts, with the major by-product being ethylene, rather than CO_x.

Recently, Lu's group [104] reported that a supported boron oxide catalyst synthesized by incipient wetness impregnation of boric acid on the high specific area mesoporous silica (B_2O_3/SBA-15, BOS catalyst) is selective to catalyze the ODHP. The BOS catalyst contained four types of boron species (Figure 8.10a,b), namely, boroxol ring, tricoordinated hydroxylated linear $BO_{3/2}$, and tricoordinated planar boron species, and tetracoordinated tetrahedral boron species that were fused into the silica matrix. The BOS catalyst was active at a temperature as low as 405 °C, which is about 100 °C lower than that of the BN catalyst, showing a propane conversion of 2.8% and a propylene selectivity of 84.1% ($C_{2-3}^{=}$: 94.6%). Upon raising the temperature to 450 °C, a propane conversion of 14.8% could be achieved, with a selectivity of 73.3% toward propylene or 87.4% for both propylene and ethylene ($C_{2-3}^{=}$). The mesoporous silica support offered an ideal surface to immobilize boron oxide. Thus, BOS catalyst could be stable during the 30 hours operation at 450 °C. Both experimental and theoretical studies indicated that tricoordinated boroxol ring and hydroxylated linear boron species were presently identified as the active sites being responsible for the low-temperature activity and high efficiency in catalyzing ODH of light alkanes. Hermans and coworkers [105] also reported silica-supported boron oxide catalysts (B/SiO_2) for ODHP using triisopropyl borate ($B(O^iPr)_3$) as a boron source. The propylene selectivity for B/SiO_2 catalyst was 77%, and overall olefin ($C_{2-3}^{=}$) selectivity was 91% with 5% propane conversion at 500 °C. The B/SiO_2 catalyst contained agglomerated oxidized boron species, which were made up of chains of BO_3 units formed from the decomposition of $B(O^iPr)_3$, possibly active phase for ODH reaction (Figure 8.10c,d). Although $B(O^iPr)_3$ has a large steric hindrance, it is hard to form a single-site catalysis model for the supported boron oxide system.

B_2O_3@BPO_4 sandwich-like hollow spheres acting as a liquid-phase catalyst for ODH of propane were synthesized through a one-step method without templates, and the catalysts exhibited excellent productivity of 0.79 g_{C3H6} g_{cat}^{-1} h^{-1} and superior stability for 27 hours at 550 °C. For the catalysts, BPO_4 acted as a support,

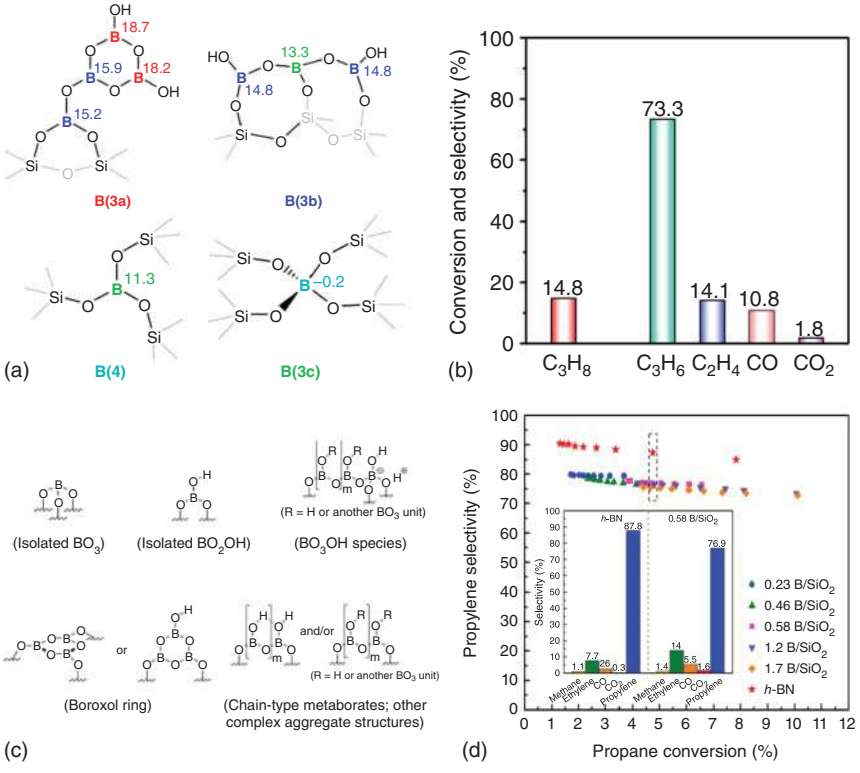

Figure 8.10 Structure of supported boron oxide catalysts and their catalytic performance for ODH of propane. (a) Schematic elucidation of four types of boron species over B_2O_3/SBA-15 catalyst; (b) Propane conversion and product selectivity; (c) Plausible boron surface structures on fresh and spent B/SiO_2 catalysts; (d) Propylene selectivity versus propane conversion data for ODHP over B/SiO_2 catalysts and *h*-BN; inset: Product distribution comparison at iso-conversion (5% propane conversion) for *h*-BN and 0.58 B/SiO_2. Source: Reproduced with permission from Lu et al. [104]; © 2019, American Chemical Society. Love et al. [105]; © 2019, American Chemical Society.

and the melted B_2O_3 supported on the surface of BPO_4 was considered as the active species [106]. The preparation of BPO_4 often requires high temperature giving rise to the formation of bulk solids with low surface areas. Considering the exposure of active sites and mass transfer issue in ODH process, Lu et al. [107] reported a three-dimensional ordered macroporous BPO_4 material with a robust framework, which exhibited excellent activity and selectivity in the ODH of propane. The selectivity for olefins was 91.5% (propylene, 82.5%; ethylene, 9.0%) at 515 °C, with a propane conversion of 14.3%. At the same time, the selectivity for the unwanted deep-oxidized CO_2 product remained less than 1.0%. Furthermore, the catalyst exhibited a remarkable olefin productivity of ~16 g_{olefin} $g_{cat}^{-1}h^{-1}$, which is much higher than most ODH catalysts.

Borosilicate zeolites with large internal surface areas, micropore structure and high thermal stability especially the distinctive boron structure could be the ideal

catalysts for application in the ODH reaction and deep understanding of the active boron sites. Recently, Lu's group reported the layered borosilicate zeolite (EniRicercheBoralite-1 [ERB-1], MCM-22 (twenty-two) [MWW] structure) with defective trigonal boron species is a highly active and selective catalyst for the ODHP [108]. The boron species in synthesized zeolites were classified into five types by solid-state ^{11}B magic-angle spinning nuclear magnetic resonance (MAS NMR) that consist of framework trigonal $B(OSi)_xOH_{3-x(x=1,2)}$, $B(OSi)_3$, tetrahedral $B(OH)_2(OSi)_2$, $B(OSi)_4$, and aggregated terminal –B–OH species. The layered borosilicate zeolites showed comparable catalytic activity with *h*-BN in the ODH of propane. With the increase of boron content, higher propane conversion was obtained under identical conditions. For example, the propane conversions of 5.6%, 9.3%, and 30.6% corresponded to boron contents of 1.54 wt% (BZEO-1), 2.48 wt% (BZEO-2), and 4.88 wt% (BZEO-3), respectively. The optimum content of boron in the borosilicate zeolite was determined as 2.48 wt% that afforded 80.4% selectivity to propylene and 91.6% selectivity to total olefins (ethylene and propylene) at 15.6% conversion of propane. Owing to the large surface area and micropore structure, the catalyst could be stable for 20 hours under ODH condition without structural collapse. Moreover, the catalysts with varied boron content showed similar apparent activation energies of propane, indicating the same active sites were involved in the reaction. Layered borosilicate zeolite can also catalyze the ethane ODH that exhibits 30.6% of ethylene yield at 37.6% ethane conversion.

8.3.2.2 Active Sites of Boron-Based Catalysts

In Lu's earliest investigation, both hexagonal boron nitride and BNNTs exhibited very low initial activity (typically <3%) for propane conversion, and there existed a catalyst activation period, i.e. a gradual increase in propane conversion along with the ODH reaction progress [109]. This period was also observed in oxidative of ethane by Wang's group [110]. Silicon boride catalysts also showed a similar induction period [102]. These phenomena suggest that it is difficult for the intact boron nitride or silicon boride to activate molecular oxygen under the ODH reaction conditions. The catalytic activity most likely originates from the *in situ* surface functionalization of boron nitride under the reaction conditions.

Detailed structural analyses verified the surface functionalization of boron nitride. Aberration-corrected transmission electron microscopy (TEM) analyses identified that the in-plane lattice retained its hexagonal symmetry with many edges (zigzag terminated configuration) that were newly created during the activation (Figure 8.11a,b). X-ray photoelectron spectroscopy (XPS) analysis identified that the surface concentrations of boron and oxygen were 44.3% and 9.2%, respectively. There were two types of boron species (Figure 8.11c); one was coordinated with nitrogen on the flat surface, whereas the other was bonded to oxygen at the edge. The chemical environment for the coordination between boron and oxygen was further verified by the 2D ^{11}B multiple-quantum magic-angle spinning (MQMAS) NMR spectrum of the BNOH catalyst. There were two types of boron—oxygen bonding at 26.0 and 24.4 ppm; the former represents the edge boron sites bonded to two bridging oxygen atoms, and the latter corresponded to B—OH bonding, which

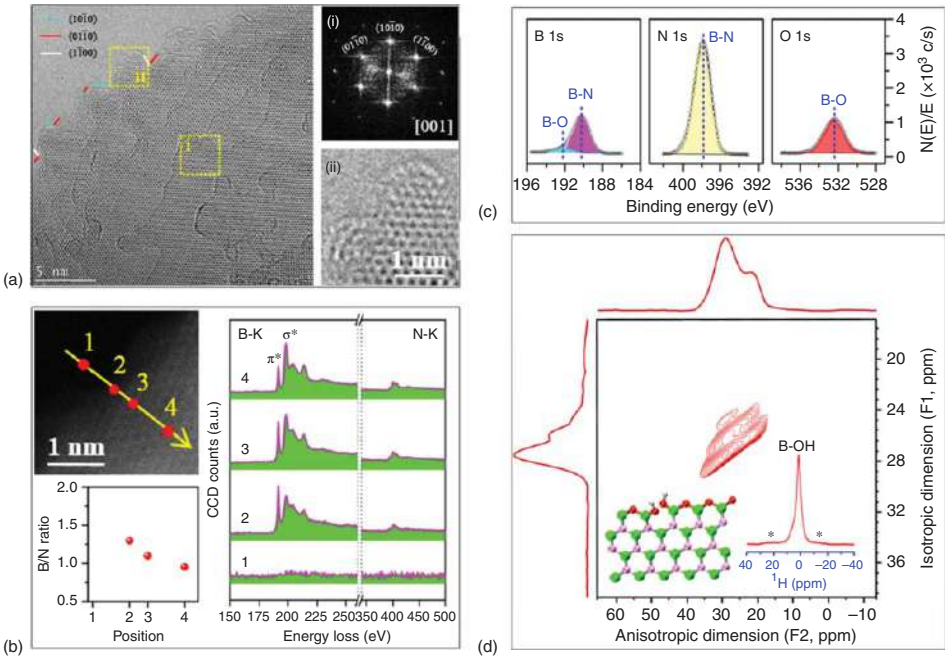

Figure 8.11 Structural characterization of the BNOH catalyst. (a) Aberration-corrected TEM images along [001] direction and FFT image of the (i) and (ii) area. (b) HAADF-STEM image (top left), boron and nitrogen K-edge EELS spectrum (right), and B/N ratio (bottom left) calculated by EELS spectrum. (c) B 1s, N 1s, and O 1s XPS spectra. (d) 2D ^{11}B MQ MAS NMR and ^{1}H MAS NMR (inset) spectra and structural model (inset) of BNOH edge. Source: Shi et al. [95]/with permission from John Wiley & Sons, Inc.

was identified by the sharp ^{1}H resonance at 1.2 ppm in the ^{1}H MAS NMR spectrum (Figure 8.11d) [95].

By comparing the results from X-ray photoelectron and IR spectroscopy of fresh and spent boron-containing materials, Hermans and coworkers suggested the analogous surface-stabilized BO_x site was formed for all tested boride catalysts under ODHP reaction conditions, which would be responsible for the selective reaction pathway to form olefins. Reactivity differences between elemental boron and boride materials might be due to active site density and electronic interactions between surface BO_x species and the subsurface bulk structure [103]. Lu's group provided *in situ* structure information of the silicon boride. As silicon boride catalyst was activated in the reaction atmosphere and then cooled down to room temperature, the characteristic peaks associated with B_2O_3 phase were observed, which implied that the origin of the unanticipated catalytic activity might be attributed to the existence of B_2O_3 species. However, the B_2O_3 signal cannot be detected at 535 °C for the low melting point of B_2O_3. In contrast, the bulk phase structure of silicon boride remained unchanged in the oxygen atmosphere at any stages, implying that the oxyfunctionalization of catalyst was facilitated under ODH reaction conditions [102].

Hermans and coworkers also employed two-dimensional correlation experiments during solid-state NMR to explain experimental spectra. Double-resonance ^{1}H–^{11}B NMR experiments suggested that *h*-BN exhibits a fraction of oxidized boron species after ODH reaction. Also, the results from ^{11}B MQMAS NMR experiments indicated that the pristine BN materials were readily oxidized and hydrolyzed under ODH reaction conditions to yield a phase consisting of three-coordinate boron sites with variable numbers of hydroxyl and bridging oxide groups denoted as $B(OH)_xO_{3-x}$ (where $x = 0$–3) (Figure 8.12). These experiments further confirmed the surface evolution of *h*-BN, that is, the oxidized layer supported on the bulk substrate [111].

Combined the induction period of catalytic activity and the advanced characterization from XPS and NMR experiments, it is demonstrated that the surface of *h*-BN (including other borides) experiences a functionalized evolution to form an oxidized layer under ODH reaction conditions. Considering the inert nature of pure boron nitride, these evolutions in structure and composition at the edge of boron nitride after the functionalization are likely to contribute to the unique catalytic function in the ODH reactions.

In the initial report, by combination of *ex situ* XPS, attenuated total reflection infrared spectroscopy (ATR-IR), and DRIFTS characterizations of fresh and spent boron nitride, Hermans and coworkers confirmed the emergence of B–OH and B–O functional groups in the ODHP reaction. Based on spectroscopic data with increased intensity at 3420 and 3250 cm^{-1} for the spent *h*-BN, they calculated that an oxygen molecule bonded to one B and one N (an oxygen-terminated armchair edge of BN [>B–O–O–N<]) acted as active site for the ODHP reaction. They suggested that the dehydrogenation initiates by the abstraction of a hydrogen atom from a secondary carbon of propane by the >B–O–O–N< sites, breaking the O—O bond while forming a B–OH species and one nitroxyl radical. A second abstraction of a hydrogen atom from a primary carbon followed another radical rebound and creates a di-propoxyl

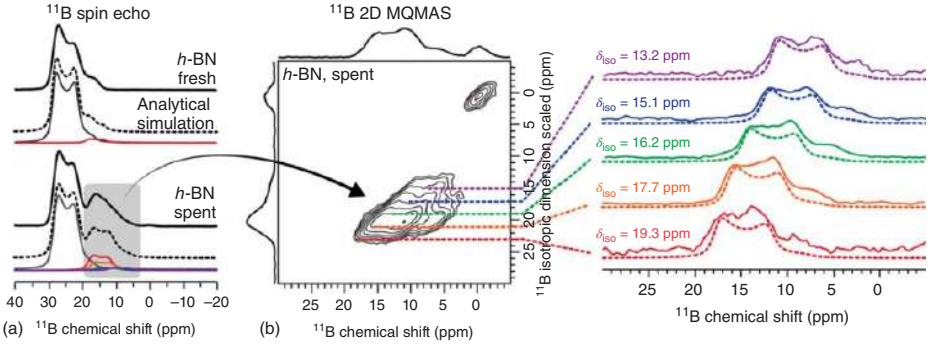

Figure 8.12 (a) 1D ^{11}B spin echo spectra. (b) 2D spectra deconvoluted based on MQMAS correlation experiments. Source: Reproduced with permission from Love et al. [111]; © 2019, American Chemical Society.

intermediate. Desorption of propylene and reorganization of hydrogen atoms along the edge form water as a side product [94].

After confirmed the dominantly exposed zigzag boron-terminated edges and the coexistence of B–O–B and B–OH groups at these edges of the active boron nitride catalyst from structural analysis (Figure 8.11), Lu and coworkers further conducted the *in situ* Fourier transform infrared spectroscopy (FTIR) to identify the roles of the B–O–B and B–OH groups under the reaction conditions. When only C_3H_8 was pulsed onto the boron nitride catalyst, the band position of the hydroxyl stretches ($\sim$3400 cm^{-1}) remained unchanged, and there was no propane conversion or generation of any products, indicating that the oxygen-containing edge boron species themselves have no catalytic activity for C–H cleavage in propane. However, the intensity of B–OH groups gradually decreased only with co-feeding of propane and oxygen, accompanied by the formation of propylene, indicating that the –OH groups interacted with molecular oxygen and were incorporated into the reaction network. The intensity of hydroxyl vibrational stretches was fully recovered upon steam activation, suggesting that the –OH groups could be readily regenerated (Figure 8.13a) [95].

Su and coworkers employed *operando* diffuse reflectance infrared Fourier-transform (DRIFT) spectroscopy and EPR to reveal that, in the presence of ethane gas, the surface of the BN catalyst was reduced and the adjacent nitrogen could stabilize the ethyl radical. However, neither ethane conversion nor ethylene product was observed under anaerobic conditions. The active sites of B–O(H) were formed at the edges of boron nitride via the aid of ethane, and molecular oxygen was indispensable for C–H dissociation. The dehydrogenation cycle could be completed with the assistance of O_2 at B–O sites (Figure 8.13b). The ^{18}O isotope tracer further verified that the dipolar B–N edges did not directly activate molecular oxygen, but only proceeded via the aid of ethane. The detailed comparison between the roles of the B–O and B–OH groups in the alkane ODH reaction was still of value for a deep understanding of the reaction mechanism [98].

Theoretical simulations also play important role in identifying the active site of *h*-BN. Zhu and coworkers selected the armchair, boron-atom-terminated zigzag (zig-B), and nitride-atom-terminated zigzag (zig-N) edges as the hypothetical active sites to simulate O_2 activation by using DFT. Computational results showed that the dissociative adsorption of O_2 is more favorable than the molecular adsorption at all selected sites. While for the mechanism of ODHP, the zig-B edge was demonstrated to be the most active site based on kinetic and thermodynamic analysis [112]. Hermans and coworkers used *ex situ* X-ray absorption spectroscopy to study the fresh and spent *h*-BN materials and further verified the increase in BO_3-coordinated species atoms after ODH [111]. However, there is no more evidence for specific active sites that are monitored under realistic reaction conditions.

8.3.2.3 Possible Reaction Pathway

Isotope-labeling measurements provided further insight into the reaction pathway, where the hydrogen atoms in the B–OH group were abstracted during the ODH reaction. Meanwhile, ^{18}O isotope tracer study demonstrated that an oxygen exchange

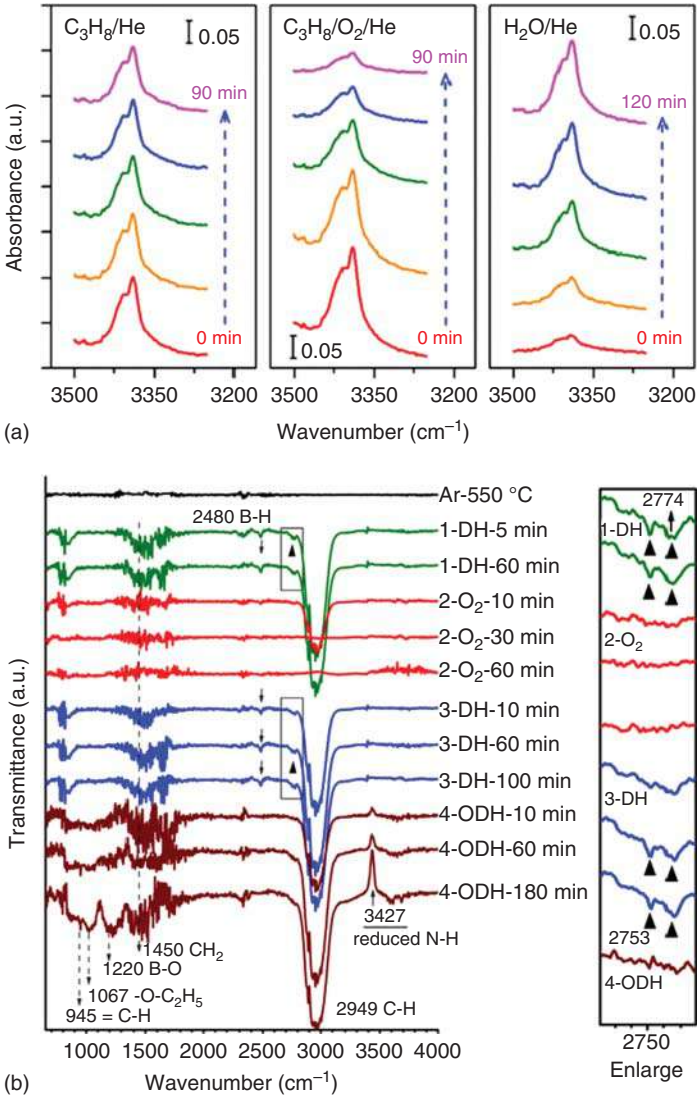

Figure 8.13 (a) FTIR spectra of the B–OH vibration over the BNOH catalyst under C_3H_8, C_3H_8/O_2/He, and H_2O/He atmospheres at 530 °C. Source: Reproduced with permission from Shi et al. [95]; © 2017, Wiley. (b) Operando DRIFT difference spectra at 550 °C under aerobic/anaerobic conditions. The flow gas was switched from Ar to C_2H_6/Ar (step 1), O_2/Ar (step 2), C_2H_6/Ar (step 3), and finally C_2H_6/O_2 (step 4). Source: Reproduced with permission from Huang et al. [98]; © 2017, Wiley.

between the surface oxygen atoms in the B–OH group and molecular oxygen occurred in the reaction process (Figure 8.14a,b). The kinetic analysis confirmed that oxygen reaction dependence followed up the L–H model, indicating a dissociative adsorption of molecular oxygen in the reaction process. These objective findings allowed us to conclude that the B–OH groups at the edge of boron nitride were

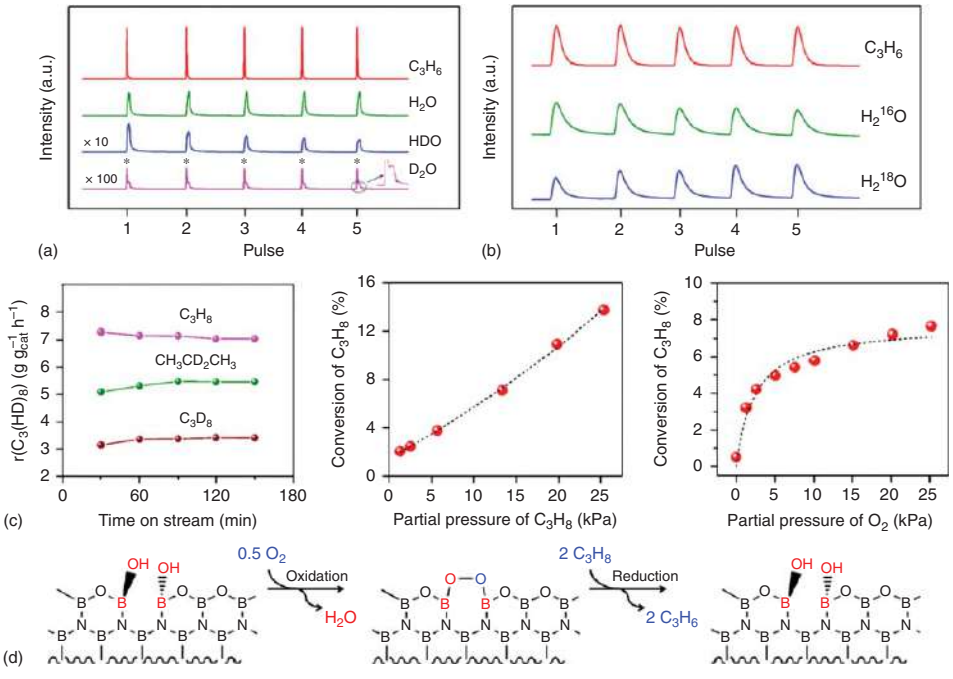

Figure 8.14 (a) Mass spectra of C_3H_6, H_2O, HDO, and D_2O species upon pulsing C_3H_8 and O_2 onto the deuterated BNOH(D) catalyst at 530 °C. (b) Mass spectra of C_3H_6, $H_2{}^{16}O$, and $H_2{}^{18}O$ species during pulsing C_3H_8 and $^{18}O_2$ onto the BNOH catalyst at 530 °C. (c) Kinetic analysis of propane ODH over the BNOH catalyst; Source: Reproduced with permission from Shi et al. [95]; © 2017, Wiley. (d) The proposed redox reaction cycle in the ODHP over the boron nitride. Source: Reproduced with permission from Shi et al. [109]; © 2018, Dalian Institute of Chemical Physics, Chinese Academy of Sciences.

initially oxidized by molecular oxygen and triggered the dehydrogenation reaction of propane. The reaction of propane was second order, and the normal kinetic H/D isotopic of 1.4~1.5 was observed, indicating that the activation of propane determined the total reaction rate (Figure 8.14c). Based on the above observations, a simple reaction pathway is proposed including a redox reaction cycle. The B–OH sites initially react with molecular oxygen, leading to the production of B–O–O–B intermediates (oxidation step). The B–O–O–B species further abstract the hydrogen atoms from propane, forming C_3H_6 and H_2O (reduction step), and then recover to B–OH sites with the assistance of water (Figure 8.14d) [109].

Zhou et al. [110] combined infrared spectroscopy, O_2 adsorption microcalorimetry, and transient analysis of products by mass spectroscopy to demonstrate the formation of hydroxyl species (B–OH species) on BN after the induction period. The quantity of these species on the activated BN can linearly increase the reaction rate of ethane conversion, suggesting that B–OH species facilitated the adsorption of O_2 and then were transformed to B–O species, which would react with ethane to produce ethylene with the aid of O_2. This results in a higher conversion rate of ethane. These findings nicely agree with Lu's viewpoints on boron nitride in the ODH reaction [109].

Su and coworkers also proposed two possible catalytic pathways based on their experimental results: at the kinetic measuring region, the ethane promoted the formation of B–OH active sites, thereby facilitating a nearly direct dehydrogenation of ethane with the aid of O_2 adsorption to produce ethylene and hydrogen, and at the non-kinetic measuring region, it cannot be ruled out that B–O active sites were formed from the adsorbed O_2, which were capable of abstracting hydrogen from ethane to C_2H_4 and H_2O. They therefore proposed that the presence of ethane promoted the activation of adsorbed O_2 at the edges of BN and the formation of B–O(H) sites. Moreover, the dehydrogenation cycle was finally completed over B–O sites. It should be emphasized that the detailed comparison between the roles of B–O and B–OH groups in the alkane ODH reaction was still of value for deep understanding the reaction mechanism [98].

Combining catalytic, spectroscopic, and kinetic data and DFT calculations, Lu and coworkers proposed the underlying possible reaction pathway. In the presence of O_2 at high temperature, the edge B–OH groups may be dehydrogenated by O_2, leading to the generation of two radical species, $BNO^{\cdot}$ and $HO_2^{\cdot}$. The $BNO^{\cdot}$ radical displays reactivity toward the hydrogen abstraction of ethane to produce $C_2H_5^{\cdot}$ radicals. The subsequent dehydrogenation of $C_2H_5^{\cdot}$ radicals, by either O_2 or H_2O_2, produces the primary C_2H_4 product. Along this pathway, the dehydrogenation of the B–OH sites appeared to be the rate-determining step. The $HO_2^{\cdot}$ radical, formed by the oxidation of either BNOH or $C_2H_5^{\cdot}$, may also be involved in the dehydrogenation of ethane. Accordingly, molecular oxygen plays crucial role in the ODH of ethane. It first abstracts one H atom from the BNOH to generate the $BNO^{\cdot}$ active species and triggers the ODH of ethane, and it may also react with $C_2H_5^{\cdot}$ to assist the formation of ethylene. This unique activation process was also observed by other independent groups [98, 110]. This explained well the O_2 dependence observed in kinetic experiments, increasing the partial pressure of O_2 favored the conversion of ethane and

the selectivity to ethylene, suggesting the participation of O_2 in the consumption of the $C_2H_5^{\cdot}$ intermediate to produce ethylene when enough O_2 was present in the reaction chamber. Moreover, the activation pathway of ethane with edge $BNO^{\cdot}$ and surface $HO_2^{\cdot}$ species nicely supported the second-order rate dependence with respect to ethane concentration in the ODH reaction over the BNOH catalyst (Figure 8.15a) [96]. Thus, it is of great urgency to apply advanced spectroscopy techniques to capture the key radicals to understand the boron-based catalysts.

Another phenomenon that should be pointed out is the surprising by-product distributions generated by *h*-BN catalysts. In the case of ODH of propane, it shows very low selectivity to CO_x and relatively higher selectivity to C_2 products (ethane, ethylene) than to C_1 products (methane, CO, and CO_2). Lu and coworkers [113] have demonstrated that boron nitride could catalyze the oxidative conversion of methane to valuable chemicals (C_2H_6, C_2H_4, CO, H_2) with minor formation of CO_2. Experimental and theoretical studies revealed that the hydroxylated *h*-BN can adsorb O_2, and then the activation of adsorbed O_2 and gaseous CH_4 occurred through a synergetic mutual activation mechanism. The CH_4 and O_2 activation triggered subsequent surface and gaseous radical reactions toward the formation of C_2H_6, C_2H_4, CO, H_2, CO_2, and H_2O. By in detail analyzing the ratio of C_2/C_1 products over *h*-BN and VO_x/γ-Al_2O_3 catalyst in the ODHP reaction, Wang and coworkers [114] proposed that the high selectivity to C_2 products was contributed to the oxidative coupling reaction of methyl that came from the cleavage of C—C bond of propane, leading to more C_2 products than C_1 products over the *h*-BN catalyst (Figure 8.15b). These results promote understanding of the reaction mechanism of ODHP over the boron-based catalysts.

Hermans and coworker also observed the potential existence of the gas-phase chemistry for the boron nitride catalyst. They found the unexpected experimental results during ODHP reaction, in which an increased propane conversion was observed with increasing diluent content of catalytically inactive SiC in the reactor. The prompted the idea that the catalytic activity of diluted *h*-BN during ODH may be included in a surface-initiated reaction that proceeds in the gas phase via radical oxidation chemistry [115]. Moreover, they also found a similar phenomenon in selective oxidative cracking of *n*-butane to light olefins over boron nitride. The adjustment of the reactant feed from O_2 rich to O_2 lean altered the product distribution in the oxidation of alkanes over *h*-BN from primarily butylenes (ODH products) to ethylene and propylene (cracking products). Lowering the O_2 concentration in the feed also reduces the selectivity to CO_x to less than 2% in most cases. Similarities in the product distribution between *h*-BN and $Li_2O/Dy_2O_3/MgO$ allowed to surmise that the cracking reactions of alkanes over the two different catalysts had closely related mechanisms, which involved in identical gas-phase reactions occurring in both systems (Figure 8.15c) [116]. These studies provide a further understanding the reaction mechanism of boron-catalyzed ODH, where gas-phase radical chemistry may be an important contributor to the high olefin selectivity observed with these materials. Thus, the capture and identification of intermediate radical species become a crucial issue to disclose the detailed reaction mechanisms over boron-based catalysts.

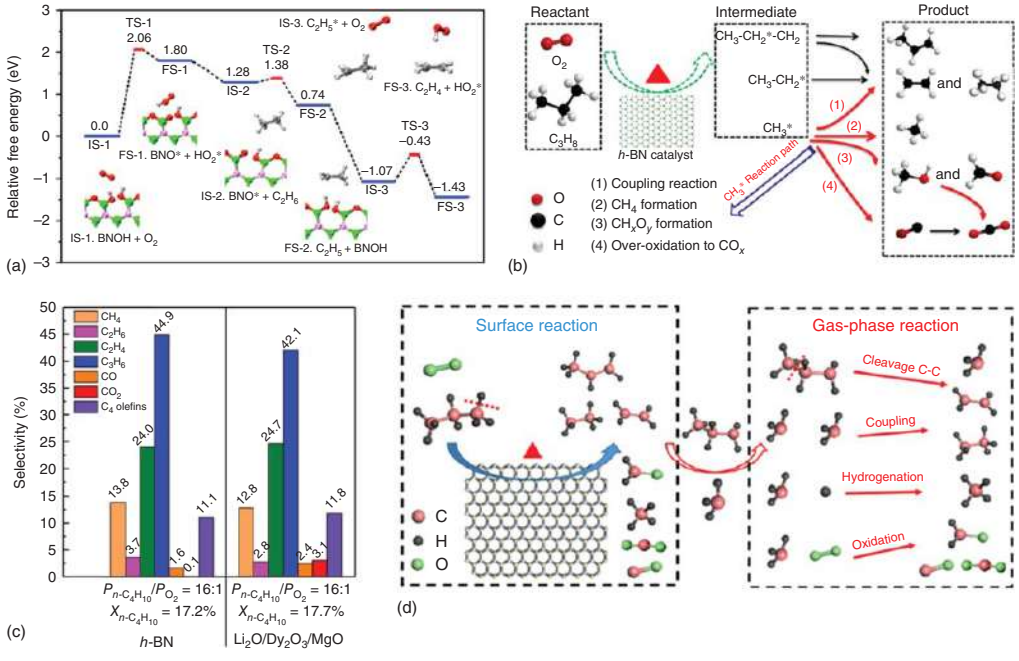

Figure 8.15 (a) Free energy profile of ODH of ethane catalyzed by BNOH from DFT calculations. Source: Reproduced with permission from Shi et al. [96]; © 2017, Dalian Institute of Chemical Physics, Chinese Academy of Sciences. (b) The proposed reaction pathways of ODHP over the *h*-BN catalyst. (c) Product distributions in the oxidation of *n*-butane over *h*-BN and Li_2O/Dy_2O_3/MgO catalysts, $T = 550\,°C$. Source: Reproduced with permission from McDermott et al. [116]; © 2020, Wiley. (d) The proposed reaction pathways of ODHP over the *h*-BN catalyst based on SVUV-PIMS studies with DFT calculations. Source: Reproduced with permission from Zhang et al. [117]; © 2020, Wiley.

Recently, Huang and coworkers [117] provided the direct experimental evidence of gas-phase methyl radicals ($CH_3^{\cdot}$) in the ODHP reaction over boron-based catalysts by using an online synchrotron vacuum ultraviolet photoionization mass spectroscopy (SVUV-PIMS), which uncovered the existence of gas-phase radical pathways. By coupling the results from kinetic SVUV-PIMS studies with DFT calculations, detailed reaction pathways are proposed for the various products from ODHP over boron-based catalysts. Gas-phase ethyl ($C_2H_5^{\cdot}$) and propyl ($C_3H_7^{\cdot}$) radicals were not detected; they proposed that propylene was mainly formed from surface reaction via the cleavage of C—H bonds of propane. Both surface-mediated and gas-phase reaction pathways can contribute to the C_1 and C_2 products (Figure 8.15d). These observations provide further insights toward understanding the ODHP reaction mechanisms over boron-based catalysts. However, the formation process of olefins is still unclear and may require higher-time-resolution techniques to address the issue.

8.3.3 Carbon-Based Catalysts

8.3.3.1 Development of Carbon-Based Catalysts

Carbonaceous materials as catalysts for the ODH of cyclohexene and ethylbenzene were first reported in the 1960s [118, 119]. Later, Velasquez [120] and Kozłowski [121] used the surface-modified activated carbons for the ODH of isobutane and found the important role of carbonyl/quinone groups on the catalyst surface. Although the manufacture of activated carbon is mature in industry, this amorphous carbon with poor crystallinity and abundant micropores usually has the risk to combust in the high-temperature and oxidative atmosphere. Nanocarbon materials with high crystallinity would be more antioxidative to act as stable catalysts in ODH reactions. Schlögl and coworkers first reported nanocarbons (carbon nanofilaments [CNFs], onion-like carbons [OLCs]) as more efficient catalysts for ODH of ethylbenzene than soot, graphite, and industrial K–Fe catalyst [122, 123]. CNFs also exhibited considerable catalytic performance in ODHP [124]. However, CNFs still suffered from severe gasification under the harsh oxidative reaction conditions. When phosphoric oxides were supported in CNFs, a stable catalytic performance of 17% propylene yield without gasification and inhibition of the over-oxidation of propane were observed. Su and coworkers first employed carbon nanotubes (CNTs) to convert 1-butene and obtained a 40% butadiene yield, superior to that of activated carbon and iron oxide [125]. Further, oxidized CNTs modified with phosphorus (P-oCNTs) exhibited a notably stable enhancement of C_4 olefin selectivity in ODH of *n*-butane for at least 100 hours in comparison with CNTs and oCNTs [126].

Considerable efforts have been made in ODH of light alkane reaction system over various nanostructured carbonaceous catalysts, such as nanodiamond (ND) [127–130], graphitic carbons (GCs) [131–135], and other carbons [136–138], which have enriched the family of carbon-based catalyst and expanded insight into traditional catalysis.

8.3.3.2 Identification of Active Sites

The complex surface compositions and structures of carbon materials, such as groups, defects, and edge sites, make the difficulty in correlating the structures between and catalytic performance. The usage of pyropolymers verified these findings that oxygen groups, especially quinone groups, played an important role in ethylbenzene (EB) ODH reaction [119]. Temperature-programmed desorption (TPD) and X-ray photoelectron spectroscopy (XPS) techniques are widely used to characterize the types and quantify the amount of surface oxygen groups of carbonaceous materials [139]. Figueiredo and coworkers selectively removed the functional groups on activated carbon by thermal treatment. A linear relationship between the EB conversion rates and the surface concentration of carbonyl/quinone groups was obtained, indicating the key role of carbonyl/quinone groups in activating ethylbenzene (Figure 8.16A) [140]. Schlögl and coworkers employed the XPS technique to detect the variation of the surface groups on CNFs and OLCs after EB ODH reaction. The basic groups (quinone groups) occurred on the spent CNFs and OLCs, indicating the important dehydrogenating function of these groups during the catalytic process [122, 123]. The near-ambient XPS technique was further used to detect the working surface of CNTs under reaction conditions with different atmosphere (*n*-butane or *n*-butane + O_2). By deconvoluting O 1s XPS in the presence of *n*-butane and O_2, a sharp increase of $I_{C-OH}/I_{C=O}$ ratio was observed after switching off the oxygen, suggesting that ketonic carbonyl groups were a critical component of the active sites (Figure 8.16B) [126].

The carbonyl/quinone groups on the surface are accepted to play a significant role of in ODH of hydrocarbons [136, 141–146]. Another different opinion on active sites was proposed by Liang and Schwartz [147]. Their studies on the ODH of isobutane using graphitized mesoporous carbon found that there were no clear relationships between the quinone-type sites and isobutene product, whereas the edge sites and defects on the carbon catalysts might be involved in the catalytic process [131, 132]. Further DFT calculations in few-layer graphene about the surface oxygen, edge sites, and defects suggested the exposed edges of carbon materials was essential and the dicarbonyls at the zigzag edges and quinones at armchair edges might be responsible for high activity (Figure 8.16C) [134, 135].

Actually, the edge sites, defect sites, and other oxygen groups (hydroxyl, carboxylic acid, and anhydride groups) of carbon could convert to carbonyl groups in the aerobic or elevated temperature environment, causing a confused understanding on actual number of active sites under the real conditions [124, 147]. Due to this ambiguity, Qi et al. proposed a chemical titration method (*ex situ* and *in situ*) using analogous organic molecule, i.e. phenylhydrazine, to selectively passivate the specific oxygen functional groups (ketonic or quinone carbonyl groups) (Figure 8.16D). The identical intrinsic catalytic activity value (turnover frequency [TOF] based on ketonic carbonyl groups) among various nanocarbon catalysts (GO materials, CNTs, and OLCs), revealed ketonic or quinone carbonyl groups were the active sites of nanocarbons for EB ODH reaction [148, 149]. Moreover, certain polymers were also synthesized to serve as model catalysts to provide an indirect evidence for identifying active sites [145, 146].

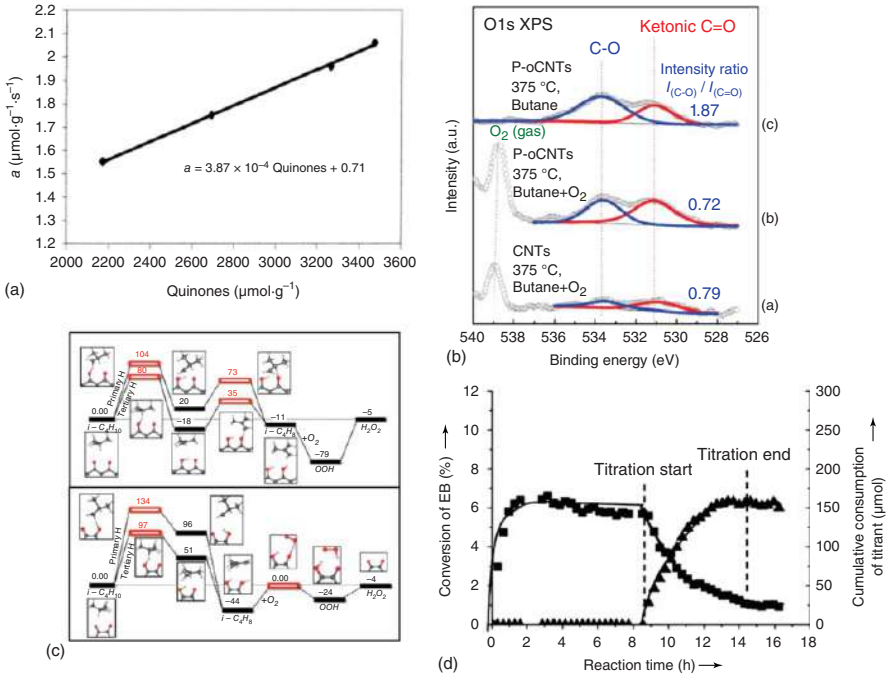

Figure 8.16 (a) Relation between the activity in the ODH of ethylbenzene and the amounts of carbonyl/quinone groups. Source: Reproduced with permission from Pereira et al. [140]; © 1999, Elsevier. (b) *In situ* O*1s* XPS spectra of working catalysts under different conditions. Source: Reproduced with permission from Zhang et al. [126]; © 2008, AAAS. (c) Calculated reaction pathways for the ODH of isobutane on dicarbonyls at zigzag edges (upper) and quinones (lower) at armchair edges. Source: Reproduced with permission from Dathar et al. [135]; © 2014, Wiley. (d) EB conversion (■) and titrant uptake (▲) as a function of time on stream during the steady-state activity measurement and *in situ* titration process. Source: Reproduced with permission from Qi et al. [149]; © 2015, Wiley.

Besides, theoretical calculation simulations have also been applied to investigate the activation of hydrocarbons on nanocarbons. By using first-principles calculations, Cao and coworker revealed the epoxy groups on the graphene oxide (GOs) surface were active sites for the C—H bond activation for ODHP [150]. The barrier for the primary C—H bond breaking in propane on the ketone, diketone, and quinone groups was calculated to be 1.07, 1.49, and 1.21 eV, respectively, demonstrating the single ketone groups on the nanostructured carbon catalysts could also be regarded as active sites in the ODHP reaction [151]. A recent computational review of nanocarbons for ODH of light alkanes appeals that the cooperation between experimental and theoretical studies could profit to promote the development of ODH reaction systems [152].

As mentioned above, the carbonyl/quinone groups could be considered as active sites, and a plausible mechanism was proposed that carbonyl/quinone groups could abstract hydrogen atoms from the C—H bonds of alkane to form olefin. Then, gas-phase oxygen molecules or dissociated oxygen species react with abstracted hydrogen atoms to form water, involving the regeneration of active sites (Scheme 8.3). A recent review of ODH on nanocarbon catalysts from *in situ* experimental accounts stressed that the behavior of oxygen molecules or dissociated oxygen species was still a question in relation to understanding the detailed catalytic mechanism of ODH process from the molecular or atomic level, which requires more *in situ* characterization to track the intermediate species during the activation process of oxygen molecules [42].

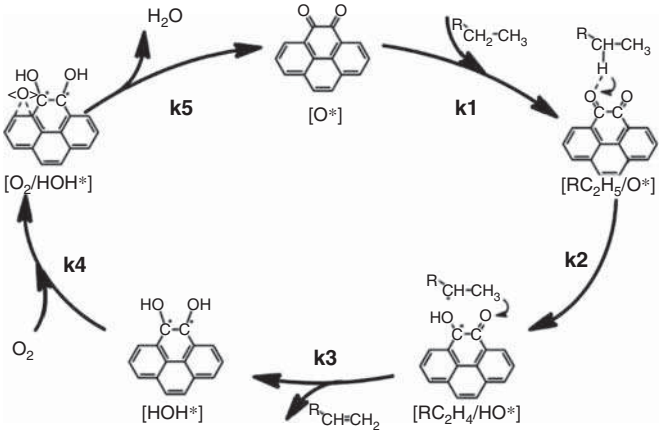

Scheme 8.3 Reaction mechanism of ODH over carbon-based catalyst. Source: Reproduced with permission from Qi et al. [42]; © 2018, American Chemical Society.

8.3.3.3 Selectivity Control of Olefins

The ODH reaction of alkanes is accepted to be a parallel-consecutive pathway, including a parallel reaction from alkanes to olefins and CO_x, and a consecutive over-oxidation of alkenes to CO_x. The surface oxygen species of nanocarbons

are typically classified into electrophilic (superoxide O_2^-, peroxide O_2^{2-}) and nucleophilic (O^{2-}) types [126]. Electrophilic oxygen species are electron deficient and prefer to attack the electron-rich C=C bonds in olefins, causing the rupture of the carbon skeleton and lowering the selectivity of olefins. In contrast, electron-rich nucleophilic oxygen species, like carbonyl/quinone groups, are selective to convert alkanes to olefins and inactive to catalyze the combustion of olefins during ODH system. Therefore, limiting the generation of electrophilic oxygen species and maintaining the amount of nucleophilic oxygen species can achieve the target for higher selectivity to olefins.

Heteroatomic (boron, nitrogen, and phosphorus elements) doping and modification are often used to modulate the electron density, acidity or basicity, and oxygen groups on the surface of nanocarbons. Frank et al. found the boron-modified CNT catalyst visibly enhanced the propylene selectivity in ODHP. Further dynamic isotope oxygen tracer experiments on the unmodified and B_2O_3–oCNTs catalysts detected no occurrence of $^{18}O^{16}O$ signal, suggesting the introduction of boron oxide could inhibit the dissociation of molecule oxygen and/or cover the combustion sites to increase the propylene selectivity (Figure 8.17a) [153]. Borate-modified nanodiamond was also chosen to catalyze ODHP, and an optimum amount of boron could interact with the defects by forming O—H bonds and suppress the formation of electrophilic oxygen species [130]. As for electron-rich nitrogen, Chen et al. tested nitrogen-doped CNTs in ODHP and found the graphitic nitrogen played an important role in promoting the catalytic activity by reducing the apparent activation energy and speeding up the activation of oxygen based on experimental results (Figure 8.17b) [154]. DFT calculation was also employed to evaluate the effect of nitrogen and boron doping on carbon catalysts in first C—H bond activation of ethane. The simulation results revealed that graphitic nitrogen and boron doping could lower the barrier for rupturing the first C—H bond, which could explain the origin of the improvement of olefin selectivity [155]. Sun et al. [129] studied the interactions between phosphate and carbon surfaces for ODHP reaction. They found phosphate could react with the phenol groups on the nanodiamond surface and selectively block the defect sites to inhibit the generation of electrophilic oxygen species (Figure 8.17c), similar to boron modification, leading to a higher propylene selectivity. It should be pointed out that the addition of boron oxide or phosphorus oxide could suppress the active sites for over-oxidation, but did not affect the active sites (ketonic carbonyl groups) for dehydrogenation.

Su et al. observed the variation of product selectivity from initial benzene to styrene over sp^3-hybridized ultra-dispersed diamond (UDD) for EB ODH with time on stream and sp^2-carbons was formed on the UDD surface during the reaction process. These phenomena suggested that sp^3-carbon would lead to the of cleavage C—C bonds, whereas sp^2-carbon would be required for styrene formation [156]. Liu et al. also found the analogous phase transformation process from the sp^3 hybridization state to the sp^2 hybridization state, the fullerene shell covered on diamond core, in ODH of *n*-butane catalyzed by UDD. They speculated that the curved and graphitic surface might be beneficial to generate the selective surface quinone groups and effectively suppress the formation of electrophilic oxygen species,

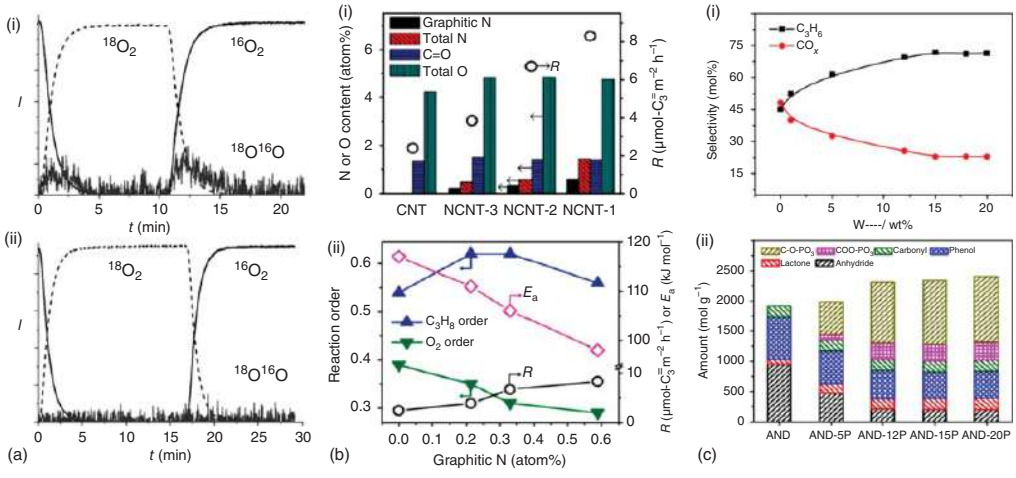

Figure 8.17 (a) Oxygen exchange on oCNTs (i) and 5B-oCNTs (ii) after the gas atmosphere was switched from 2% $^{16}O_2$/Ne to 2% $^{18}O_2$/2% Ar/ 96% Ne. Source: Reproduced with permission from Frank et al. [153]; © 2009, Wiley. (b) Structural parameters and *R* of used catalysts (i) and reaction orders *R* and E_a (ii) as a function of graphitic N content. Source: Reproduced with permission from Chen et al. [154]; © 2013, Royal Society of Chemistry. (c) Propylene and CO_x selectivity as a function of P_2O_5 loading (i) and variations in the amounts of different oxygen-containing groups (ii). Source: Reproduced with permission from Sun et al. [129]; © 2015, American Chemical Society.

resulting in the enhanced olefin selectivity [127]. The relationship between the amounts of electrophilic oxygen and side reaction rate were clarified by using iodometric titration method in ODH of *n*-butane [157]. The distinct improvement of C_4 olefin selectivity was observed by chemical reduction ($LiAlH_4$ or Grignard reagents) and annealing in nitrogen treatments due to the elimination of electrophilic oxygen species [157–159]. It should be pointed out that the carbon-based catalysts show considerable catalytic performance of ODH. However, the selectivity and yield toward olefins still need to be further improved. In addition, the stability of carbon-based catalysts in oxidative atmosphere is also a challenging problem to be solved.

8.4 Summary and Outlook

With growing demand for propylene and increasing production of propane from shale gas, direct alkane dehydrogenation has drawn particular attention and has been regarded as one of the most promising methods of propylene production. Up to now, a variety of processes have been industrialized to produce olefins, and many new PDH projects have been announced and established in recent years.

Owing to the low price and high catalytic activity, supported CrO_x is one of the most efficient catalysts for alkane dehydrogenation that has been commercially utilized in Catofin and FBD processes. However, coke formation and chromium species aggregation can lead to catalyst deactivation, which limit their application. Compared with CrO_x-based catalysts, Pt-based catalysts show slightly higher catalyst stability. Coke formation and sintering of Pt nanoparticles are two key factors affecting the performance of Pt-based catalysts. During the alkane dehydrogenation processes, two main processes cause catalyst deactivation: (i) coke formation poisoning the active sites or limiting access of the reactants to the active sites and (ii) metal sintering leading to the increase of particle size with the concomitant loss in active sites. In terms of catalysts, the development of a highly coking and sintering-resistant Pt catalyst is an important direction. A number of studies have reported that the addition of promoters can greatly modify the geometric and structural and electronic properties of Pt-based catalysts, thus improving their catalytic activity, stability, and anti-coking capability. Moreover, supports with different properties also play an important effect on the catalytic activity. Further, more detailed, systematic, and scientific studies on the roles of promoters, interactions between the active sites and supports, acidity of the support, and structural and electronic properties of active sites are highly desired.

Hydrogen energy is regarded as a clean energy with the great development potential in the twenty-first century. In alkane dehydrogenation processes, hydrogen is the main by-product, which can be a stable supply of hydrogen energy. For example, the by-product of PDH is about 0.038 tons of hydrogen per ton of propylene in the PDH. At present, the by-product of PDH in China is about 185,000 tons/yr, which is expected to reach 391,100 tons/yr in 2023. It is worth noting that the development of hydrogen storage and transportation technology is the key for by-produced hydrogen to play a more important role. Otherwise, limited by the transportation economic radius, by-produced hydrogen enterprises can only serve the surrounding areas.

ODH of light alkanes to olefins featured with nonequilibrium limitation and free of coke is a promising alternative route to industrialized direct dehydrogenation. The enhancement of olefin selectivity and productivity is still a great challenge in ODH reaction systems due to the occurrence of over-oxidation of olefin products. Transition metal oxides (e.g. V_2O_5, MoO_3, and NiO) or alkaline-earth metal oxychlorides (e.g. $LiCl/Dy_2O_3/MgO$) have shown good performance in the ODH reaction of light alkanes and provided a referential paradigm in studying ODH reaction system. It is generally accepted that ODH catalyzed by metal oxide catalysts proceeds via the Mars van Krevelen mechanism and the initial H atom abstraction is related to the rate-determining step. However, the state-of-the-art supported vanadium oxide catalysts for the ODHP only show ~17% of propylene yield even after decades of study. Given this point, alternative novel processes, such as chemical looping and halogen-containing additives, and the corresponding control techniques and reactors should be investigated to improve the selectivity and yield to olefin.

The emerging metal-free boron-based catalysts function superior selectivity toward light olefins and atom economy for olefin products by minimizing CO_2 emission. Also, boron-based catalysts are highly promising for industrial implementation because of their high productivity to light olefins ($>1\ g_{olefin}\ g_{cat}^{-1}\ h^{-1}$) and remarkable catalyst stability. Upon the development of novel boron-based catalysts and the exploration of origin of intrinsic activity based on advanced techniques, some fundamental considerations have accepted that the oxygen-containing boron species on the surface are the active sites to trigger the ODH reaction of light alkanes. It is universally acknowledged that oxygen-containing boron sites, gas-phase oxygen, and alkane molecule synergistically participate the catalytic cycle. Besides, the gas-phase radicals may play an important role in the formation of C_1 and C_2 products. A redox cycle for the main reaction based on surface B–OH sites was proposed that initially react with molecular oxygen, leading to B–O–O–B intermediates (oxidation step). Moreover, the B–O–O–B species further abstract hydrogen atoms from the alkane, forming the olefin and water (reduction step), and then recover to B–OH sites with the assistance of water. However, C_1 and C_2 products can be formed from both surface-mediated and gas-phase pathways on *h*-BN catalyst. Nevertheless, there are certainly remaining many issues needing to be addressed. First, the detailed spectroscopic evidence of key intermediates under the realistic reaction conditions is inadequate to understand the ODH reaction from molecular level. Further studies are expected to combine theoretical simulations and the capture of reaction intermediates to identify the detailed reaction mechanism. Moreover, some points on structure–performance correlation, such as the geometric and electronic characters of boron centers, the transformations of the B–O and B–OH groups, and the roles of the adjacent structure of oxygen-containing boron sites in the alkane ODH reactions, still need to be precisely determined using advanced microscopic and spectroscopic methods under *operando* conditions. Then, it is also a priority to develop new structure-tuning methods to optimize the ODH performance of boron-based materials. Maximizing the number of OH-containing boron sites may be an effective option to improve the catalytic activity of ODH reactions. Meanwhile, the stability of catalysts under high-temperature oxidation conditions may be a vital

issue in diminishing the stability of ODH reaction that hinders the application in the industry. Besides, it should also be pointed out that minimizing the cleavage of C—C bonds over boron-based catalysts remains challenging under the ODH conditions probably because of the gas-phase radicals. Thus, there is an urgent need to develop new surface-modifying methods or chemical engineering technologies to enhance the selectivity toward the targeted olefin, such as nucleophilic heteroatom doping and reactor parameter design. For practical applications, the stability of oxygen-containing boron species under high-temperature steam still needs to be improved. Overall, from the viewpoints of activity, selectivity, and stability, there is still large scope to improve the catalytic efficacy of boron-based catalysts in ODH.

Carbonaceous materials have demonstrated interesting catalytic performance in ODH of light alkanes to olefins. Considerable work has been devoted to confirming and promoting the catalytic performance over different carbon materials such as activated carbon, CNFs, CNTs, ND, and heteroatom-doped nanocarbons. Upon detailed exploration of the active sites and catalytic mechanism using TPD, XPS, DFT, and chemical titration techniques, it is generally accepted that the carbonyl/quinone groups on carbonaceous materials play an important role in activating alkane molecules. Furthermore, a redox cycle for main reaction is proposed that carbonyl/quinone groups could abstract hydrogen atoms from the C—H bonds of alkane to form olefin and carbonyl/quinone groups reduce to phenol groups. Then, gas-phase oxygen molecules or dissociated oxygen species react with abstracted hydrogen atoms to form water, and the phenol groups recover to active sites. However, there are still some issues that should be taken account. For example, the state of the intermediate of activated O_2 remains unknown, which requires the development of higher time-resolved *in situ* microscopic and spectroscopic techniques to capture the short-lived intermediates to clarify the detailed reaction mechanism on a molecular level. Although surface chemical modifications (B, P), heteroatom doping (B, N), and optimization of surface oxygen groups are demonstrated to be effective strategies to enhance objective olefins selectivity, the productivity to olefins is still far lower than 1 $g_{olefin}\ g_{cat}{}^{-1}\ h^{-1}$. Besides, the stability and antioxidation of carbonaceous materials under aerobic and high-temperature conditions should also be considered. It is of great urgency to exploit new synthesis and modification methods to address these challenges.

References

1 Corma, A., Melo, F.V., Sauvanaud, L., and Ortega, F. (2005). *Catal. Today* 107–108: 699–706.

2 Li, J., Wei, Y., Chen, J. et al. (2012). *J. Am. Chem. Soc.* 134: 836–839.

3 Sattler, J.J., Ruiz-Martinez, J., Santillan-Jimenez, E., and Weckhuysen, B.M. (2014). *Chem. Rev.* 114: 10613–10653.

4 Chen, S., Chang, X., Sun, G. et al. (2021). *Chem. Soc. Rev.* 50: 3315–3354.

5 Grosse, A.V. and Ipatieff, V. (1940). *Ind. Eng. Chem.* 32: 268–272.

6 Li, C. and Wang, G. (2018). *Sci. Sin. Chim.* 48: 342–361.

7 Sanfilippo, D., Buonomo, F., Fusco, G., and Miracca, I. (1998). *Studies in Surface Science and Catalysis*, vol. 119, 919–924. Elsevier.
8 Kotelnikov, G., Komarov, S., Bespalov, V. et al. (2004). *Studies in Surface Science and Catalysis*, vol. 147, 67–72. Elsevier.
9 Bailey, M.P. (2014). *Chem. Eng.* 121: 19.
10 Sanfilippo, D. and Miracca, I. (2006). *Catal. Today* 111: 133–139.
11 Chen, S., Chang, X., Sun, G. et al. (2021). *Chem. Soc. Rev.* https://doi.org/10.1039/d0cs00814a.
12 Vora, B.V. (2012). *Top. Catal.* 55: 1297–1308.
13 Frey, F.E. and Huppke, W.F. (1933). *Ind. Eng. Chem.* 25: 54–59.
14 Conley, M.P., Delley, M.F., Nunez-Zarur, F. et al. (2015). *Inorg. Chem.* 54: 5065–5078.
15 Delley, M.F., Silaghi, M.-C., Nuñez-Zarur, F. et al. (2017). *Organometallics* 36: 234–244.
16 Weckhuysen, B.M. and Schoonheydt, R.A. (1999). *Catal. Today* 51: 223–232.
17 Fridman, V.Z. and Xing, R. (2017). *Appl. Catal., A* 530: 154–165.
18 Fridman, V.Z., Xing, R., and Severance, M. (2016). *Appl. Catal., A* 523: 39–53.
19 Weckhuysen, B.M., Verberckmoes, A.A., Debaere, J. et al. (2000). *J. Mol. Catal. A: Chem.* 151: 115–131.
20 Rossi, S.D., Ferraris, G., Fremiotti, S. et al. (1992). *Appl. Catal. A* 81: 113–132.
21 Hu, Z.P., Yang, D., Wang, Z., and Yuan, Z.Y. (2019). *Chin. J. Catal.* 40: 1233–1254.
22 Zhu, J., Yang, M.-L., Yu, Y. et al. (2015). *ACS Catal.* 5: 6310–6319.
23 Xiong, H., Lin, S., Goetze, J. et al. (2017). *Angew. Chem. Int. Ed.* 56: 8986–8991.
24 Sun, G., Zhao, Z.J., Mu, R. et al. (2018). *Nat. Commun.* 9: 4454.
25 Gao, X.-Q., Song, W., Li, W.-C., and Lu, A.-H. (2021). *Catal. Sci. Technol.* https://doi.org/10.1039/d0cy02154g.
26 Shi, L., Deng, G.M., Li, W.C. et al. (2015). *Angew. Chem. Int. Ed.* 54: 13994–13998.
27 Jiang, F., Zeng, L., Li, S. et al. (2014). *ACS Catal.* 5: 438–447.
28 Shan, Y.-L., Wang, T., Sui, Z.-J. et al. (2016). *Catal. Commun.* 84: 85–88.
29 Xia, K., Lang, W.-Z., Li, P.-P. et al. (2016). *Chem. Eng. J.* 284: 1068–1079.
30 Nawaz, Z., Tang, X., Zhang, Q. et al. (2009). *Catal. Commun.* 10: 1925–1930.
31 Zhang, Y., Zhou, Y., Huang, L. et al. (2015). *Chem. Eng. J.* 270: 352–361.
32 Li, J., Li, J., Zhao, Z. et al. (2017). *J. Catal.* 352: 361–370.
33 Ryoo, R., Kim, J., Jo, C. et al. (2020). *Nature* 585: 221–224.
34 Yang, M.L., Zhu, Y.A., Fan, C. et al. (2011). *Phys. Chem. Chem. Phys.* 13: 3257–3267.
35 Nykänen, L. and Honkala, K. (2013). *ACS Catal.* 3: 3026–3030.
36 Yang, M.-L., Zhu, Y.-A., Zhou, X.-G. et al. (2012). *ACS Catal.* 2: 1247–1258.
37 Silvestre-Albero, J., Sanchez-Castillo, M.A., He, R. et al. (2001). *Catal. Lett.* 74: 17–25.
38 Jablonski, E.L., Castro, A.A., Scelza, O.A., and de Miguel, S.R. (1999). *Appl. Catal., A* 183: 189–198.
39 Passos, F.B., Aranda, D.A.G., and Schmal, M. (1998). *J. Catal.* 178: 478–488.

40 Ren, G.-Q., Pei, G.-X., Ren, Y.-J. et al. (2018). *J. Catal.* 366: 115–126.
41 Cavani, F., Ballarini, N., and Cericola, A. (2007). *Catal. Today* 127: 113–131.
42 Qi, W., Yan, P., and Su, D.S. (2018). *Acc. Chem. Res.* 51: 640–648.
43 Chen, K., Bell, A.T., and Iglesia, E. (2002). *J. Catal.* 209: 35–42.
44 Carrero, C.A., Schloegl, R., Wachs, I.E., and Schomaecker, R. (2014). *ACS Catal.* 4: 3357–3380.
45 Venegas, J.M., McDermott, W.P., and Hermans, I. (2018). *Acc. Chem. Res.* 51: 2556–2564.
46 Albonetti, S., Cavani, F., and TrifirÒ, F. (1996). *Catal. Rev.* 38: 413–438.
47 Grant, J.T., Venegas, J.M., McDermott, W.P., and Hermans, I. (2018). *Chem. Rev.* 118: 2769–2815.
48 Valente, J.S., Armendáriz-Herrera, H., Quintana-Solórzano, R. et al. (2014). *ACS Catal.* 4: 1292–1301.
49 Xie, Q., Chen, L.Q., Weng, W.Z., and Wan, H.L. (2005). *J. Mol. Catal. A: Chem.* 240: 191–196.
50 Dang, D., Chen, X., Yan, B. et al. (2018). *J. Catal.* 365: 238–248.
51 Yun, Y.S., Lee, M., Sung, J. et al. (2018). *Appl. Catal., B* 237: 554–562.
52 Melzer, D., Mestl, G., Wanninger, K. et al. (2019). *Nat. Commun.* 10: 4012.
53 Lopez Nieto, J.M., Botella, P., Vazquez, M.I., and Dejoz, A. (2002, https://doi.org/10.1039/b204037a). *Chem. Commun.* 1906–1907.
54 Botella, P., García-González, E., Dejoz, A. et al. (2004). *J. Catal.* 225: 428–438.
55 Aouine, M., Epicier, T., and Millet, J.-M.M. (2016). *ACS Catal.* 6: 4775–4781.
56 Shiju, N.R., Liang, X., Weimer, A.W. et al. (2008). *J. Am. Chem. Soc.* 130: 5850–5851.
57 Melzer, D., Xu, P., Hartmann, D. et al. (2016). *Angew. Chem. Int. Ed.* 55: 8873–8877.
58 Annamalai, L., Liu, Y., Ezenwa, S. et al. (2018). *ACS Catal.* 8: 7051–7067.
59 Heracleous, E., Lee, A., Wilson, K., and Lemonidou, A. (2005). *J. Catal.* 231: 159–171.
60 Heracleous, E. and Lemonidou, A. (2006). *J. Catal.* 237: 175–189.
61 Heracleous, E. and Lemonidou, A. (2006). *J. Catal.* 237: 162–174.
62 Solsona, B., Concepción, P., Demicol, B. et al. (2012). *J. Catal.* 295: 104–114.
63 Zhu, H., Rosenfeld, D.C., Anjum, D.H. et al. (2015). *J. Catal.* 329: 291–306.
64 Zhu, H., Rosenfeld, D.C., Harb, M. et al. (2016). *ACS Catal.* 6: 2852–2866.
65 Zhu, H., Ould-Chikh, S., Anjum, D.H. et al. (2012). *J. Catal.* 285: 292–303.
66 Li, J., Wang, C., Huang, C. et al. (2010). *Catal. Lett.* 137: 81–87.
67 Li, J.-H., Wang, C.-C., Huang, C.-J. et al. (2010). *Appl. Catal., A* 382: 99–105.
68 Farin, B., Eloy, P., Poleunis, C. et al. (2016). *Catal. Sci. Technol.* 6: 6046–6056.
69 Tope, B., Zhu, Y., and Lercher, J.A. (2007). *Catal. Today* 123: 113–121.
70 Kumar, C.P., Gaab, S., Müller, T.E., and Lercher, J.A. (2008). *Top. Catal.* 50: 156–167.
71 Gartner, C.A., van Veen, A.C., and Lercher, J.A. (2014). *J. Am. Chem. Soc.* 136: 12691–12701.
72 Testova, N.V., Shalygin, A.S., Kaichev, V.V. et al. (2015). *Appl. Catal., A* 505: 441–446.

73 Ding, K., Metiu, H., and Stucky, G.D. (2013). *ChemCatChem* 5: 1906–1910.
74 Upham, D.C., Kristoffersen, H.H., Snodgrass, Z.R. et al. (2019). *Appl. Catal., A* 580: 102–110.
75 Xie, Q., Zhang, H., Kang, J. et al. (2018). *ACS Catal.* 8: 4902–4916.
76 Zichittella, G., Aellen, N., Paunović, V. et al. (2017). *Angew. Chem. Int. Ed.* 56: 13670–13674.
77 Zichittella, G., Stähelin, S., Goedicke, F.M., and Pérez-Ramírez, J. (2019). *ACS Catal.* 9: 5772–5782.
78 Zichittella, G., Polyhach, Y., Tschaggelar, R. et al. (2021). *Angew. Chem. Int. Ed.* 60: 3596–3602.
79 Gao, Y., Neal, L.M., and Li, F. (2016). *ACS Catal.* 6: 7293–7302.
80 Haribal, V.P., Neal, L.M., and Li, F. (2017). *Energy* 119: 1024–1035.
81 Yusuf, S., Neal, L.M., and Li, F. (2017). *ACS Catal.* 7: 5163–5173.
82 Dudek, R.B., Gao, Y., Zhang, J., and Li, F. (2018). *AlChE J.* 64: 3141–3150.
83 Gao, Y., Haeri, F., He, F., and Li, F. (2018). *ACS Catal.* 8: 1757–1766.
84 Yusuf, S., Neal, L., Haribal, V. et al. (2018). *Appl. Catal., B* 232: 77–85.
85 Yusuf, S., Neal, L., Bao, Z. et al. (2019). *ACS Catal.* 9: 3174–3186.
86 Khadzhiev, S.N., Usachev, N.Y., Gerzeliev, I.M. et al. (2015). *Pet. Chem.* 55: 651–654.
87 Gerzeliev, I.M., Popov, A.Y., and Ostroumova, V.A. (2016). *Pet. Chem.* 56: 724–729.
88 Zhao, Z.J., Wu, T., Xiong, C. et al. (2018). *Angew. Chem. Int. Ed.* 57: 6791–6795.
89 Xiong, C., Chen, S., Yang, P. et al. (2019). *ACS Catal.* 9: 5816–5827.
90 Chen, S., Zeng, L., Mu, R. et al. (2019). *J. Am. Chem. Soc.* 141: 18653–18657.
91 Wu, J.C.S. and Lin, S.-J. (2008). *Chem. Eng. J.* 140: 391–397.
92 Lin, S., Ye, X., Johnson, R.S., and Guo, H. (2013). *J. Phys. Chem. C* 117: 17319–17326.
93 Wang, Y., Shi, L., Lu, W. et al. (2017). *ChemCatChem* 9: 1363–1367.
94 Grant, J.T., Carrero, C.A., Goeltl, F. et al. (2016). *Science* 354: 1570–1573.
95 Shi, L., Wang, D., Song, W. et al. (2017). *ChemCatChem* 9: 1788–1793.
96 Shi, L., Yan, B., Shao, D. et al. (2017). *Chin. J. Catal.* 38: 389–395.
97 Bodke, A.S., Olschki, D.A., Schmidt, L.D., and Ranzi, E. (1999). *Science* 285: 712–715.
98 Huang, R., Zhang, B., Wang, J. et al. (2017). *ChemCatChem* 9: 3293–3297.
99 Chaturbedy, P., Ahamed, M., and Eswaramoorthy, M. (2018). *ACS Omega* 3: 369–374.
100 Honda, Y., Takagaki, A., Kikuchi, R., and Oyama, S.T. (2018). *Chem. Lett.* 47: 1090–1093.
101 Cao, L., Dai, P., Tang, J. et al. (2020). *J. Am. Chem. Soc.* 142: 8755–8762.
102 Yan, B., Li, W.C., and Lu, A.H. (2019). *J. Catal.* 369: 296–301.
103 Grant, J.T., McDermott, W.P., Venegas, J.M. et al. (2017). *ChemCatChem* 9: 3623–3626.
104 Lu, W.-D., Wang, D., Zhao, Z. et al. (2019). *ACS Catal.* 9: 8263–8270.
105 Love, A.M., Cendejas, M.C., Thomas, B. et al. (2019). *J. Phys. Chem. C* 123: 27000–27011.

106 Liu, Q., Wu, Y., Xing, F. et al. (2020). *J. Catal.* 381: 599–607.
107 Lu, W.-D., Gao, X.-Q., Wang, Q.-G. et al. (2020). *Chin. J. Catal.* 41: 1837–1845.
108 Qiu, B., Jiang, F., Lu, W.-D. et al. (2020). *J. Catal.* 385: 176–182.
109 Shi, L., Wang, D., and Lu, A.-H. (2018). *Chin. J. Catal.* 39: 908–913.
110 Zhou, Y., Lin, J., Li, L. et al. (2018). *J. Catal.* 365: 14–23.
111 Love, A.M., Thomas, B., Specht, S.E. et al. (2019). *J. Am. Chem. Soc.* 141: 182–190.
112 Li, H., Zhang, J., Wu, P. et al. (2019). *J. Phys. Chem. C* 123: 2256–2266.
113 Wang, Y., Zhao, L., Shi, L. et al. (2018). *Catal. Sci. Technol.* 8: 2051–2055.
114 Tian, J., Tan, J., Xu, M. et al. (2019). *Sci. Adv.* 5: eaav8063.
115 Venegas, J.M. and Hermans, I. (2018). *Org. Process Res. Dev.* 22: 1644–1652.
116 McDermott, W.P., Venegas, J., and Hermans, I. (2020). *ChemSusChem* 13: 152–158.
117 Zhang, X., You, R., Wei, Z. et al. (2020). *Angew. Chem. Int. Ed.* 59: 8042–8046.
118 Manassen, J. and Wallach, J. (1965). *J. Am. Chem. Soc.* 87: 2671–2677.
119 Iwasawa, Y., Nobe, H., and Ogasawar, S. (1973). *J. Catal.* 31: 444–449.
120 de Jesús Díaz Velásquez, J., Suárez, L.M.C., and Figueiredo, J.L. (2006). *Appl. Catal., A* 311: 51–57.
121 Gniot, I., Kirszensztejn, P., and Kozłowski, M. (2009). *Appl. Catal., A* 362: 67–74.
122 Mestl, G., Maksimova, N.I., Keller, N. et al. (2001). *Angew. Chem. Int. Ed.* 40: 2066–2068.
123 Keller, N., Maksimova, N.I., Roddatis, V.V. et al. (2002). *Angew. Chem. Int. Ed.* 41: 1885–1888.
124 Sui, Z.-J., Zhou, J.-H., Dai, Y.-C., and Yuan, W.-K. (2005). *Catal. Today* 106: 90–94.
125 Liu, X., Su, D.S., and Schlögl, R. (2008). *Carbon* 46: 547–549.
126 Zhang, J., Liu, X., Blume, R. et al. (2008). *Science* 322: 73–77.
127 Liu, X., Frank, B., Zhang, W. et al. (2011). *Angew. Chem. Int. Ed.* 50: 3318–3322.
128 Roldán, L., Benito, A.M., and García-Bordejé, E. (2015). *J. Mater. Chem. A* 3: 24379–24388.
129 Sun, X., Ding, Y., Zhang, B. et al. (2015). *ACS Catal.* 5: 2436–2444.
130 Sun, X., Ding, Y., Zhang, B. et al. (2015). *Chem. Commun.* 51: 9145–9148.
131 Liang, C., Xie, H., Schwartz, V. et al. (2009). *J. Am. Chem. Soc.* 131: 7735–7741.
132 Xie, H., Wu, Z., Overbury, S.H. et al. (2009). *J. Catal.* 267: 158–166.
133 Schwartz, V., Xie, H., Meyer, H.M. et al. (2011). *Carbon* 49: 659–668.
134 Schwartz, V., Fu, W., Tsai, Y.T. et al. (2013). *ChemSusChem* 6: 840–846.
135 Dathar, G.K., Tsai, Y.T., Gierszal, K. et al. (2014). *ChemSusChem* 7: 483–491.
136 Michorczyk, P., Kuśtrowski, P., Niebrzydowska, P., and Wach, A. (2012). *Appl. Catal., A* 445–446: 321–328.
137 Pelech, I., Soares, O.S.G.P., Pereira, M.F.R., and Figueiredo, J.L. (2015). *Catal. Today* 249: 176–183.
138 Kwon, H.C., Yook, S., Choi, S., and Choi, M. (2017). *ACS Catal.* 7: 5257–5267.
139 Figueiredo, J.L. and Pereira, M.F.R. (2010). *Catal. Today* 150: 2–7.

140 Pereira, M.F.R., Orfao, J.J.M., and Figueiredo, J.L. (1999). *Appl. Catal., A* 184: 153–160.

141 Liu, L., Deng, Q.F., Agula, B. et al. (2011). *Chem. Commun.* 47: 8334–8336.

142 Liu, L., Deng, Q.-F., Liu, Y.-P. et al. (2011). *Catal. Commun.* 16: 81–85.

143 Schlögl, R. (2013). *Adv. Catal.* 56: 103–185.

144 Zhao, Z., Dai, Y., Lin, J., and Wang, G. (2014). *Chem. Mater.* 26: 3151–3161.

145 Zhang, J., Wang, X., Su, Q. et al. (2009). *J. Am. Chem. Soc.* 131: 11296–11297.

146 Guo, X., Qi, W., Liu, W. et al. (2017). *ACS Catal.* 7: 1424–1427.

147 Qi, W. and Su, D. (2014). *ACS Catal.* 4: 3212–3218.

148 Qi, W., Liu, W., Zhang, B. et al. (2013). *Angew. Chem. Int. Ed.* 52: 14224–14228.

149 Qi, W., Liu, W., Guo, X. et al. (2015). *Angew. Chem. Int. Ed.* 54: 13682–13685.

150 Tang, S. and Cao, Z. (2012). *Phys. Chem. Chem. Phys.* 14: 16558–16565.

151 Sun, X., Li, B., and Su, D. (2014). *Chem. Commun.* 50: 11016–11019.

152 Sun, X., Han, P., Li, B. et al. (2018). *Chem. Commun.* 54: 864–875.

153 Frank, B., Zhang, J., Blume, R. et al. (2009). *Angew. Chem. Int. Ed.* 48: 6913–6917.

154 Chen, C., Zhang, J., Zhang, B. et al. (2013). *Chem. Commun.* 49: 8151–8153.

155 Mao, S., Li, B., and Su, D. (2014). *J. Mater. Chem. A* 2: 5287.

156 Su, D., Maksimova, N.I., Mestl, G. et al. (2007). *Carbon* 45: 2145–2151.

157 Li, J., Yu, P., Xie, J. et al. (2017). *ACS Catal.* 7: 7305–7311.

158 Li, J., Yu, P., Xie, J. et al. (2018). *J. Catal.* 360: 51–56.

159 Zhang, Y., Diao, J., Rong, J. et al. (2018). *ChemSusChem* 11: 536–541.

Part IV

Zeolite Catalysis

9

Zeolites for Sustainable Chemical Transformations

Luke Harvey, Matthew Drewery, Eric Kennedy, and Michael Stockenhuber

The University of Newcastle, School of Engineering, Callaghan, NSW 2308, Australia

9.1 Introduction to Zeolites and Zeolite Chemistry

Zeolites are a class of crystalline aluminosilicates that possess a robust three-dimensional framework structure, forming a network of uniformly sized pores of molecular dimensions [1]. The structure-specific size of the pores means that large molecules are excluded. Hence, zeolites find extensive commercial use as molecular sieves. As per the IUPAC Commission on Zeolite Nomenclature 1979 [2], zeolites are classified according to their framework type whereby each is assigned a three-letter code. For example, the Linde type A (LTA) framework structure is shown in Figure 9.1 [3].

As of 2021, there are 242 distinct fully ordered and 11 partially ordered framework types recognized by the Structure Commission of the International Zeolite Association, and further 72 additional codes have been approved. However, only a handful of these find extensive commercial use, in particular AEL, CHA, FAU, LTA, MFI, MOR, and MWW.

9.1.1 Zeolite Chemistry

The zeolite framework is composed primarily of SiO_2, with isomorphic substitution of a small amount of the Si^{4+} sites by three-valent cations such as Al^{3+}, B^{3+}, and Fe^{3+} and four-valent cations such as Ti^{4+} and Ge^{4+}. Three-valent substitution results in the formation of an anionic charge in the framework. Cations (typically Na^+, K^+, NH_4^+, etc.) are present in the zeolite cavities and balance the charge. These ions are exchangeable to an extent, making them useful as ion exchangers in water treatment, as adsorbents [4, 5] or detergents [6, 7]. The performance of a zeolite used in a detergent depends upon its capacity to exchange hard Ca^{2+} and Mg^{2+} ions for Na^+ ions, preventing the agglomeration of mineral residues [1].

Heterogeneous Catalysis for Sustainable Energy, First Edition. Edited by Landong Li and Justin S. J. Hargreaves.

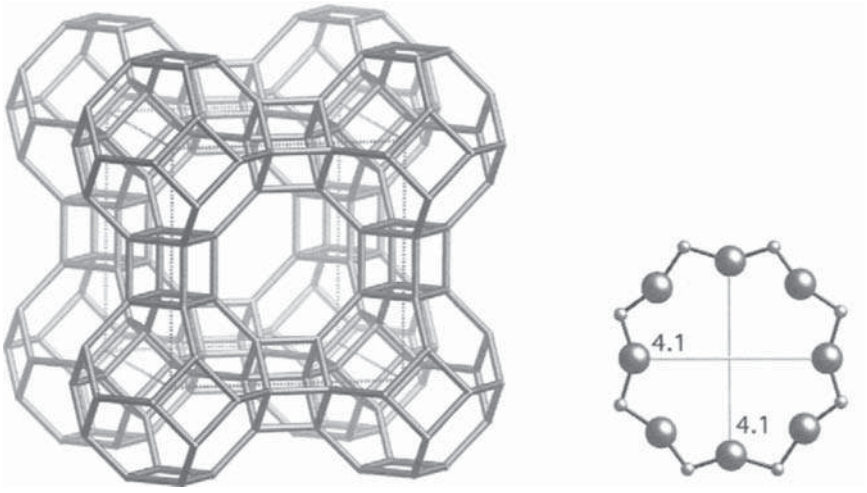

Figure 9.1 LTA framework structure, also showing pore composition with representative dimensions (Å). Source: Reproduced with permission from Baerlocher et al. [3]; © Copyright 2007, Elsevier.

9.1.2 Zeolites as Catalysts

Over the last 150 years, heterogeneous catalysis science has matured to the point where it has become integral to virtually all industrial chemical processes, with over 90% of chemical products relying on one or more catalysts at some point in their synthesis [8, 9].

As governmental and private bodies place increasingly stringent mandates upon emission control as a result of societal pressures, with significant financial penalties for noncompliance, heterogeneous catalysts in particular stand to serve a critical role in ensuring the economic viability of a chemical process. The European Emissions Trading Scheme (EU ETS), for example, has reduced the cap on greenhouse gas emissions by a reduction factor of 2.2% from 2021 levels; a significant increase from the 1.74% reduction factor introduced in Phase 3, from 2013 to 2020, essentially mandates that the CO_2 equivalent greenhouse gas generation decreases by 43 million tonnes/year. Phase 4 of the EU ETS also retains the distribution method of emission allowances by auction. In addition to emission reduction, process catalysis generally furthers economic benefits of lowering energy requirements and consuming feedstock material more efficiently. One such example of catalytically driven emission control examined in this review is the catalytic removal of low concentration methane from mining ventilation air methane (VAM). Methane is emitted from this process at concentrations below 1%, well below the flammability limit of 5%, which makes flaring the gas impossible, requiring alternative processing technologies such as catalytic oxidation. Although carbon dioxide serves as the baseline for emissions equivalents, methane is estimated to be roughly 25 times as potent in its effects on the atmosphere [10]. As such, the complete oxidation of methane to carbon dioxide is seen as a viable strategy to reduce the net greenhouse effect from emissions.

Table 9.1 Industrial applications of zeolites for chemical processing and environmental protection.

Zeolite framework	Derivative	Process
Y (FAU)	USY, CaHY, LaHY	Catalytic cracking
ZSM-5		Alkylation
		Disproportionation
	Silicalite	Beckman rearrangement [17]
	Dispersed in liquid phase	Cyclohexene hydration [18]
	Me(Cu [19], Fe [20], Co [21]) MFI	NO_x reduction
Mordenite (MOR)		Isomerization [22]
		Disproportionation [23]
	Modified	Methylamine synthesis [24]
Beta (BEA)		Benzene alkylation [25]
		Acylation [25]
SAPO-34		Methanol to olefins
MFI	Ti-MFI	Oxidation with H_2O_2

Source: Niwa et al. [26].

In fact, the bulk of heterogeneous catalysts used today are zeolites. However, only a handful of the known zeolite structures find widespread use industrially (namely, AEL, CHA, FAU, LTA, MFI, MOR, and MWW). More exotic framework structures, including "mixed" frameworks, are constantly being developed, particularly for catalytic transformations involving bulky substrates [11–16].

The zeolite catalysts used most frequently and their industrial processes are shown in Table 9.1.

Zeolites are particularly desirable as heterogeneous catalysts, whether as a support for an active center or as a catalyst themselves. They are environmentally benign, owing to their aluminosilicate chemical composition. Although some structure-directing agents (SDAs) or surfactants such as CTAB or amine heterocycles used in the synthesis of some zeolites are less environmentally benign, the finished zeolite product is itself not harmful and may last many process cycles provided that proper regeneration procedures are implemented.

9.1.3 Size Discrimination: Molecular Sieves

The rigid ring and channel structures of zeolites within the dimensional range of molecular kinetic radii make them excellent catalysts for the selective preparation of compounds by size and/or shape discrimination of reactants and products [8, 14, 27–29]. Where multiple possible transition states are possible, molecular sieves may also stabilize a particular transition state conformation [29, 30]. A classic example of this is given in Figure 9.2 [31, 32], showing the isomerization of xylene over an arbitrary pore structure (ZSM-5, within the H-MFI family of zeolite structures is commonly used for this reaction, in practice).

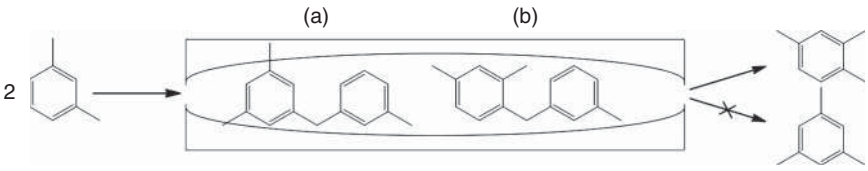

Figure 9.2 Isomerization of xylene.

The pore structure is too constricted to allow for the successful formation of transition state a due to the conformation of methyl groups, which would yield the 1,3,5 isomer. Instead, the 1,3,4 isomer is favored through selectivity of transition state b, even though it is thermodynamically less favorable in general.

It should be apparent that there is a limitation to the size of molecule a given zeolite may accommodate. The bulk of standard zeolitic materials have ring structures in the range of around 4–7 Å. Species with a kinetic diameter greater than this are generally unsuited to molecular sieving. As such there has been research activities examining the preparation of zeolites with larger pore structures through the use of more exotic SDA, and extra-large-pore zeolites with 14 member rings up to approximately 34 Å in diameter have been synthesized [33–35]. Another strategy is post-synthesis dealumination of the parent zeolite, most commonly through treatment with acid or steam [36–38]. Substitution of aluminum in the synthesis gel with a metal species having a larger atomic radius, in particular germanium, is another technique used to produce extra-large-pore zeolite structures such as ITQ or UTL [33, 39–42]. Other metals may then be introduced into the extra-large-pore zeolite framework in a post-synthesis step after removing the germanium sites in a similar method to dealumination of standard zeolite materials, retaining the extra-large-pore structure [41].

9.1.4 Zeolites as Supports for Metal Catalysts

Zeolites may be used in a given chemical reaction with little to no modification by taking advantage of inherent properties such as a well-defined pore size as in the example of xylene isomerization in Section 9.1.3 or another native property such as solid acidity, described in more detail in Section 9.2.1.1. Often, zeolites are used as supports for transition metals to introduce redox active sites and in some cases are able to exploit metals in the zeolite framework to impart bimetallic species chemistry to the catalyst [43] and bifunctional catalysts with redox and acid/base functionality [44]. The most commonly used methods for adding transition metals to a support material are known as the "ion exchange" and "incipient wetness" methods.

9.1.4.1 Methods of Metal Deposition

Ion exchange is arguably the more commonly used method, whereby a form of the zeolite support with a readily displaceable cation (typically Na^+, H^+, and NH_4^+) is stirred at a temperature usually in the order of 50–100 °C in a solution of the metal that is to be deposited. After the ion-exchange process, the zeolite is carefully filtered, dried, and calcined, immobilizing the transition metal. The ion-exchange method

offers the advantage of high dispersion of the metal and possibility of large batch processing. However, wastage of valuable noble metal salts can be high, and the amount of metal actually deposited on the zeolite is difficult to accurately predict. The ion exchange may not proceed to completion; rather it will approach a thermodynamic equilibrium [45–49].

The incipient wetness method involves coating a given quantity of the zeolite support with a monolayer of solvent (usually water, although organic solvents such as toluene are not uncommon) containing a predetermined amount of the metal to be deposited. Obtaining a monolayer coating of solvent is important in maximizing metal dispersion on the support. After the incipient wetness impregnation step is complete, the catalyst is carefully dried and calcined, similar to the ion-exchange method. Catalyst preparation by incipient wetness carries the advantages of minimizing wastage of valuable metal solutions and the ease with which a predetermined amount of metal may be deposited on the support.

Effect of Deposition Method The method of metal deposition can have marked effects on the physical and chemical properties of the catalyst. In this example [50], ruthenium catalysts supported on ZSM-5 and BEA were prepared by both ion exchange and incipient wetness methods and compared in the hydrodeoxygenation (HDO) of guaiacol – a proxy compound for biocrude. The effect of acid site concentration as an effect of the preparation method may be studied using a variety of methods, but most commonly, temperature-programmed desorption (TPD) is used. Broadly, this technique consists of probing acidic sites by adsorbing a known quantity of ammonia onto a catalyst sample, followed by desorption over a temperature range (usually somewhere between 50 and 700 °C). The quantity of ammonia desorbed, and the temperature at which this occurs, is used to measure the acid site concentration and strength, respectively. Other probe molecules such as pyridine, CO, and hydrogen are also frequently used [51–54]. In this case, TPD measurements demonstrated that the strong Brønsted acid sites in the ZSM-5 catalyst prepared by ion exchange were substantially reduced in comparison with the parent material, indicating that the bulk of NH_4^+ ions have been exchanged by ruthenium species. In contrast, the catalyst prepared by incipient wetness still exhibited Brønsted acidity, indicating that a substantial portion of acidic protons remained in the sample.

In the case of BEA catalysts, the same trend was found, in that the ion exchange method was more successful in exchanging Ru^{3+} with ammonia; a large portion of Brønsted acid sites remained, indicating that not all NH_4^+ was exchanged.

The performance of the four ruthenium zeolites in the HDO of guaiacol to cyclohexane was examined in a continuous-flow reactor. Both ion-exchange BEA and ZSM-5 catalysts exhibited substantially higher guaiacol conversion and selectivity to the target compound (Table 9.2), despite containing essentially equal levels of ruthenium content. The catalysts prepared by the incipient wetness method also demonstrated higher selectivity to undesired compounds, 1,2-dimethoxybenzene and catechol. Previous studies have demonstrated that formation of these by-products is promoted by Brønsted and Lewis acid sites [55]. Hydrogen TPD measurements indicated that ruthenium is positioned at ion-exchange sites in the more

Table 9.2 Comparison of Ru–zeolite catalyst performance in HDO reaction in flow reactor as prepared by different metal impregnation methods.[a)]

Catalyst (Ru loading, wt%)		Conversion (%)	Selectivity (%)[b)]			
		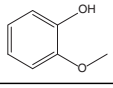		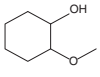		
Ion exchange	Ru–ZSM-5 (0.21)	12.6	15.6	43.2	3.5	0
	Ru–BEA (0.22)	17.7	14.6	10.4	6.7	0
Wetness impregnation	Ru–ZSM-5 (0.18)	4.3	4.1	5.2	24.2	13.0
	Ru–BEA (0.21)	9.8	1.0	2.7	43.2	26.7

a) 200 °C, weight hour space velocity (WHSV) 0.0867 min^{-1}, H_2 pressure 4.0 MPa, 120 ml min^{-1}, guaiacol flow rate 0.026 g min^{-1}.
b) Other products not listed include cyclohexanol, methylphenol, methoxy-methylphenol, dimers, etc.

effective catalysts and had much higher H_2 adsorption capacity in comparison with the catalysts prepared by incipient wetness impregnation, where the ruthenium appears to take up surface metallic positions.

9.1.5 Metals in the Zeolite Framework

A great deal of research and development has focused on the isomorphic integration of selected metals (and some non-metals such as phosphorus) into zeolite frameworks [56–60]. Although generally more complex to prepare than exchanged zeolite catalysts, catalysts with metals introduced to framework positions have several advantages, particularly the essentially complete immobilization of the metal. This arrangement prevents active metal sites from leaching out of the catalyst matrix and also deactivation by sintering (more on deactivation through sintering in Section 9.3.2).

9.1.5.1 Methods of Preparation

Direct Hydrothermal Synthesis In principle, synthetic zeolitic materials are prepared by hydrothermal synthesis of a silica and alumina source (or other T-atom, such as titanium [61, 62], iron [63, 64], germanium [65], etc.) and water in the correct ratio to form a gel, generally within a pH ranging from 10 to 13. The gel is then heated in an autoclave, normally polytetrafluoroethylene (PTFE) lined, in the presence of an SDA (also commonly referred to as a "template") for a specified period of time during which crystallization occurs. The solid material is then washed and separated by centrifugation, dried at low temperature (c. 60–100 °C), and calcined in air at around 400–650 °C to remove remaining water and organic material, in particular the SDA. Due to this high-temperature treatment step, the template is generally considered to be sacrificial; however, some large-pore zeolites offer the possibility of SDA recovery, and there is also active research into the development of SDA-free preparation methods [66–71]. Preferred metal sources include sodium salts of the oxide such as sodium aluminate or short-chain organic oxides such as titanium butoxide. The chosen silica source depends upon the required SiO_2/Al_2O_3 content of the product. Aqueous sodium silicate solutions may be used; however, contamination by aluminum generally prevents the successful preparation of zeolites with a SiO_2/Al_2O_3 ratio greater than ~600. Using commercially available colloidal silica solutions such as Ludox® from DuPont, zeolites with SiO_2/Al_2O_3 ratios of 3000–3500 can be prepared. Zeolites with still higher SiO_2/Al_2O_3 ratios, in the order of 20 000 can be obtained using fumed silica as the silica source. Tetra methyl- and tetraethylorthosilicate are obtainable in very high purity and may be used to prepare zeolites with the highest SiO_2/Al_2O_3 ratio. These materials are generally hydrolyzed prior to their addition to a synthesis mixture, the resulting alcohol having been removed by gentle heating.

Post-Synthetic Techniques Metals may also be inserted into zeolite framework positions after hydrothermal synthesis of the parent zeolite framework. Perhaps the simplest and most intuitive post-synthetic technique is heteroatom substitution.

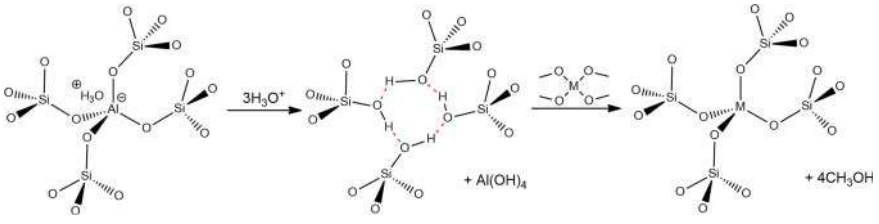

Figure 9.3 Dealumination of a generic zeolite in acid media. Water is first adsorbed at Brønsted acid sites, hydrolyzing the Al—O bonds, resulting in a silanol nest and extra-framework aluminum. In the next reaction step, a metal methoxide (for example) is added where the M—O bonds are hydrolyzed, inserting the metal into the silanol nest. Red dashed bonds in the second structure indicate hydrogen bonding between silanol groups.

This involves the removal of a framework T-atoms (most commonly aluminum, although others in particular those forming highly labile T—O bonds such as germanium are often used), forming an interstice in the framework most frequently occupied by a silanol nest (Figure 9.3).

The resulting silanol "nest" is subsequently filled by the desired catalytic metal, most often supplied with organic ligands that are hydrolyzed as the metal occupies

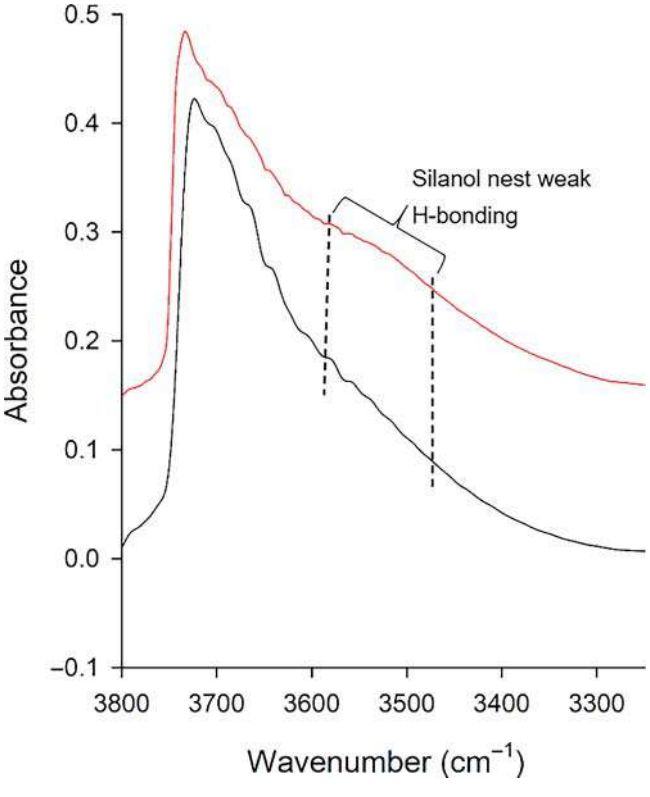

Figure 9.4 FTIR spectra of dealuminated BEA (red) and the equivalent sample after the addition of Ta into the zeolite framework (black).

the unoccupied lattice site [72–76]. Silanol nests are readily detected using Fourier transform infrared (FTIR) spectroscopy, with the hydrogen bonding between silanol groups (the second structure in Figure 9.3) presenting as a broad band at 3500–3200 cm^{-1} as distinct from the vibration assigned to the broader hydroxyl stretch of zeolite pores at 3450 cm^{-1} [77–79]. Tantalum BEA is a highly effective catalyst for the synthesis of 1,3-butadiene [74, 80, 81], an important feedstock for the manufacture of synthetic rubbers. Figure 9.4 shows the background corrected FTIR spectra of zeolite BEA after dealumination by HNO_3 (13 M, 80 °C, red spectrum) and after insertion of tantalum from tantalum(v) ethoxide (black spectrum). The near-complete removal of the silanol H-bonding vibration at 3450 cm^{-1} is an indicator of the successful insertion of tantalum into framework positions [82–84].

Another useful FTIR band for identifying framework metals is seen at 960 cm^{-1} and is attributed to a perturbation of the otherwise uniform Si–O–Si framework vibration due to the difference in reduced mass between Si and metal atoms [85, 86]. An example of this phenomena is shown in Figure 9.5, where FTIR spectra were taken of calcined samples of silicalite-1, an MFI zeolite containing only Si and O atoms (black spectrum). The red spectrum is the equivalent zeolite with titanium isomorphically replacing 1% of the silicon T sites (titanium silicalite-1, a zeotype useful in the highly selective epoxidation of olefins and in the ammoximation of

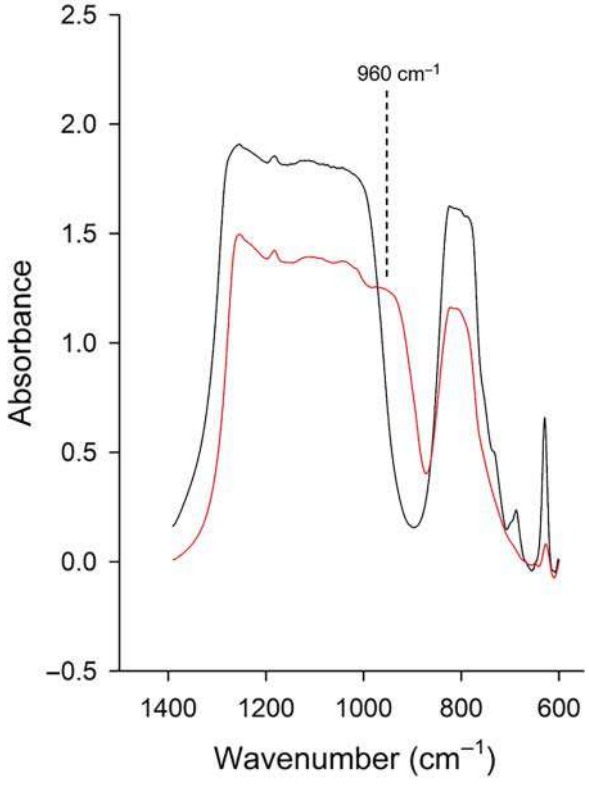

Figure 9.5 FTIR spectra of titanium silicalite-1 (TS-1) (red) and the parent titanium-free silicalite (black).

cyclic alkenes). The intensity of this vibration may also be useful in quantifying the amount of metal occupying framework sites, as discrete from extra-framework or metal oxide sites [87, 88].

More recent advances in post-synthetic techniques focus on the synthesis of extra-large-pore zeolites (those greater than 12-ring) such as ITQ, UTL, etc. through the development of exotic SDA and also "pillared" zeolites – 2D zeolite nanosheets connected by Si–O–M chains, where the "M" atom may be Si, Ti, Ge, etc. [86, 89–92]. Typically, pillared zeolites are prepared by first swelling conventional zeolites using a basic quaternary ammonium surfactant such as cetyltrimethyl ammonium ($CTMA^+$) (commonly known as CTAB in its bromide form) [93–95]. The mixture is then treated with an SDA, joining the zeolite sheets at multiple points. These materials offer strong acidity, typical of the parent zeolitic materials, combined with enhanced accessibility for large molecules.

9.2 The Nature of Active Sites and Deactivation of Zeolite-Based Catalysts

Catalyst deactivation is an issue of significant concern to the long-term success of an industrial catalytic process. The substantial environmental and economic benefits of successful catalysis were exposited in Section 9.1; however, these advantages are experienced only as long as the catalysts themselves remain suitably active. While a catalyst, by definition, undergoes no permanent chemical change, in practical applications this is not the case, with real catalysts undergoing various mechanical and chemical changes, affecting to varying degrees the detriment of their catalytic performance.

9.2.1 Active Sites in Zeolite Catalysis

As described in Sections 9.1.4 and 9.1.5, catalytically active sites in zeolites can exist either in extra-framework positions, in various oxidation states (e.g. Figure 9.6a) as hydroxides, or in framework positions, isomorphically substituting a T-atom (almost always aluminum) for the metal, giving the desired site (Figure 9.6b). Sites are either acidic (Brønsted or Lewis) or basic or provide redox chemistry.

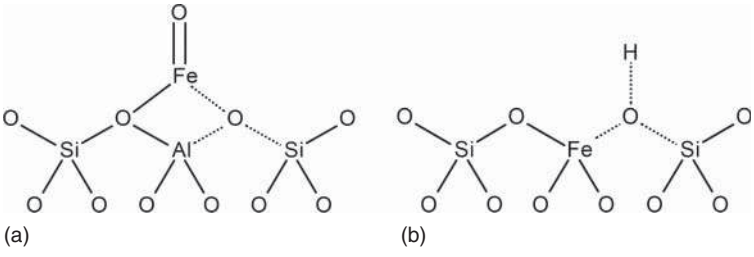

Figure 9.6 Iron site in extra-framework (a) and framework (b) positions.

9.2.1.1 Acid Sites

By a wide margin, the majority of organic transformations undertaken over zeolite catalysts are done so on sites, possessing Brønsted acid and/or Lewis acid character [96, 97]. The efficacy of the catalyst depends upon the strength of the site and its availability to the correct reactants and transition states.

A purely silica lattice, amorphous or crystalline (i.e. zeolites), comprising only Si and O with charges of 4^+ and 2^-, respectively, leads to framework with neutral charge. Where an aluminum atom being three valent is substituted for a silicon atom, an anion is created that must in each instance have its charge balanced with a corresponding cation or a hydroxyl proton forming a weak Lewis or strong Brønsted site, respectively [98, 99]. Protons with Brønsted acidity are normally located on bridging oxygen connecting silicon and alumina tetrahedra but may be present in other forms (Figure 9.7). The nature of the metal atom in the framework position opposite the silicon in Figure 9.7a (i.e. Si–OH–T, where T is the tetrahedral metal Al, Ge, Ti, etc.) influences the acid strength of the bridging hydroxyl proton and therefore the acid catalytic behavior of the zeolite [100–104]. The more electronegative the "T" atom in the Si–OH–T structure, the greater the acid strength [105].

The crystalline surface of zeolites or framework defects is terminated in silanol or aluminum hydroxide groups (Figure 9.7b), the acid strength of which is relatively low. Framework defects generally occur at sites where an aluminum atom is missing or has been intentionally removed from the framework, forming a silanol "nest" comprising four silanol groups exhibiting hydrogen bonding, as discussed in more detail in Section 9.1.5.1. The structures in Figure 9.7c represent Lewis acid sites found in extra-framework positions, the strength of which increases in the order of $Al(OH)_2^+ < AlO^+ < \equiv Si^+$, although other extra-framework structures are possible [106]. Another factor influencing the strength of Si–OH–T acid sites is the site distribution, implicitly related to the Si/Al ratio; increasing the Si/Al ratio results in increasing acid site strength [107–110]. More specifically, substitution into the next nearest neighbor (NNN) framework positions influences the acidity of bridging hydroxyl protons due to the dependency of the acid strength of those sites on the electronegativity of the cations in their second coordination sphere. The greater the population of aluminum atoms (having greater electronegativity than silicon) in NNN positions, the lower the acid strength.

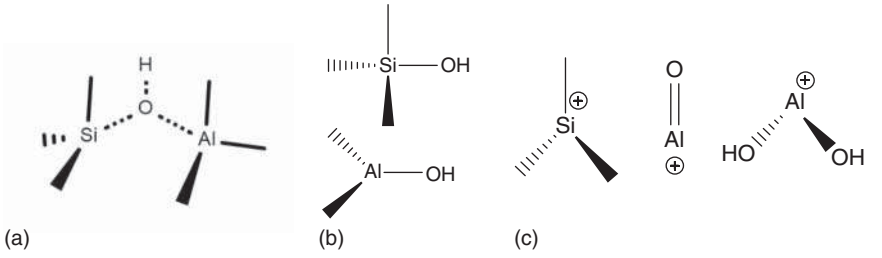

Figure 9.7 Structure of hydroxyl acid groups (a), (b) and a Lewis acid site typically arising from a framework defect (c).

The uniform crystalline structure of zeolites generally makes them superior acid catalysts to amorphous solids of similar chemical composition by virtue of providing acid sites of essentially uniform strength within well-defined pore and channel systems, greatly improving, in particular, catalyst selectivity. The example below is presented to illustrate the influence of zeolite acid concentration on catalyst performance.

The catalytic HDO of biomass-derived oxygenates (biocrude) to biofuels has quickly emerged as a significant source of renewable diesel fuels, with Finnish company Neste opening two processing plants in Finland since 2007 and another in Singapore in 2010. In 2011, a fourth such plant was brought online in The Netherlands, where it is currently the largest single renewable fuel-producing facility in Europe. Biocrudes require further processing prior to their being substituted directly for conventional crude oil from fossil fuel sources. HDO is one attractive technology for upgrading biocrude, which entails eliminating oxygen from the hydrocarbon mixture while retaining long carbon chains. Most frequently this is performed using molecular hydrogen at 2–8 MPa over Group VIII transition metals [111, 112]. The effect of acid site concentration is well demonstrated in the research emulating the HDO of biocrude to biofuels. In this case, guaiacol (*o*-methoxyphenol) is used as a surrogate compound representative of biomass oxygenates to study and optimize the catalysis of the HDO reaction over zeolite-supported nickel, with the general reaction scheme shown in Figure 9.8 [55].

The HDO catalyst contains two sites primarily involved in the reaction: redox sites (these are elaborated on in Section 9.2.1.3) and acidic sites [113, 114]. Table 9.3 illustrates a clear relationship between Si/Al ratio, catalyst acidity, and product (cyclohexane) yield. The acid site concentration is clearly correlated with Brønsted acid site concentration.

Table 9.4 shows the effect of different nickel loading onto the BEA zeolite with Si/Al ratio of 12.5, which provided the greatest cyclohexane yield for the same nickel loading. It is clear that a nickel loading between 2.3% and 3.9% is required to obtain any yield of cyclohexane. The dispersion of nickel is inversely proportional to the metal loading; hence it follows that cyclohexane yield is correlated with larger nickel clusters. This is in agreement with the literature showing that (100), (110), and (111) nickel surfaces reduce the activation energy of hydrogen

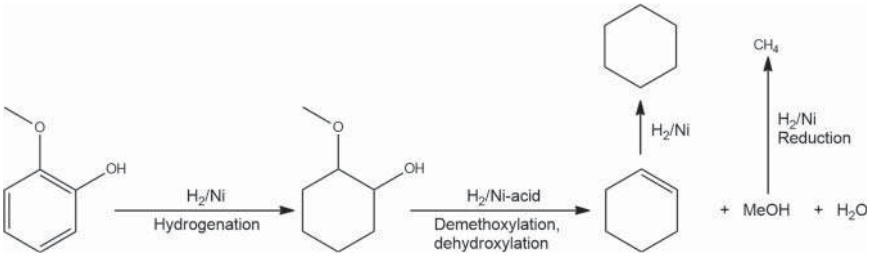

Figure 9.8 Dominant route for hydrodeoxygenation of guaiacol over Ni–zeolite catalysts. Source: Reproduced with permission from Yan et al. [55]; © Copyright 2020, Royal Society of Chemistry.

Table 9.3 Effect of acid site concentration in 15.7 wt% Ni/BEA on cyclohexane yield in HDO of guaiacol at 4.0 MPa H_2 pressure and 250 °C [55].

Si/Al	Cyclohexane yield (%)	Acid site concentration (mmol g_{cat})	
		Brønsted sites	Total
12.5	68.9	0.6	0.71
25	45.4	0.5	0.57
175	25.4	0.26	0.31

Table 9.4 Effect of nickel loading on yield of cyclohexane in guaiacol HDO reaction [55].

Ni/BEA (Ni wt%)	D_{Ni} [a] (%)	d_{Ni} [b] (nm)	Cyclohexane yield (%)	$R_{cyclohexane}$ [c] (min^{-1})
23.4	4.6	13.4	12.3	10.4
15.7	6.7	9.2	11.3	9.8
7.8	11.4	5.4	5.5	5.6
3.9	25.1	2.5	1.6	1.5
2.3	39.3	1.6	0	0

a) Dispersion of nickel on catalyst surface determined by CO chemisorption.
b) Average Ni crystallite size determined by CO chemisorption.
c) Rate of cyclohexane formation normalized to Ni loading.

[115–117] and these Ni planes were also observed over the more highly loaded catalysts [55].

The activity of the catalyst appears to reach a limit at very high nickel loading, as the increase in activity does not increase appreciably between 15.7% and 23.4% loading and the authors attribute this to the blockage of pores as Ni cluster size increases. This highlights the importance of metal loading and acidity to optimize product yield.

9.2.1.2 Basic Sites

Zeolite catalysts containing basic sites are, by far, the least studied, the bulk of reactions being acid or redox catalyzed. Furthermore, basic sites are less well defined in zeolites, and most base-catalyzed reactions involve both acid and base sites [97]. The base-catalyzed reactions most significantly studied are the Knoevenagel condensation, biocrude upgrading, and Michael additions.

Basic sites are generally imparted onto zeolites through ion exchange with large polarizable alkali metal cations, most notably cesium [118–120]. In this case, basicity arises from framework oxygen carrying the anionic charge (Lewis base) and is relatively weak. The basicity of the metal-exchanged zeolite is proportional to the electronegative charge of the metal; increasing electronegative character of the compensating metal decreases the negative charge over framework oxygen, resulting in a less strongly basic catalyst [119]. For this reason, the bulk of the literature focuses on cesium zeolite catalysts with high aluminum content that contains the most strongly

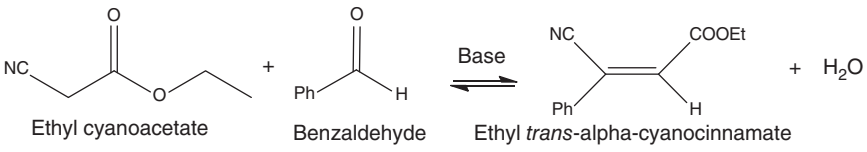

Figure 9.9 Knoevenagel condensation of ethyl cyanoacetate and benzaldehyde over base catalyst.

basic sites behind (theoretically) francium, a relatively rare, naturally occurring element, and outside of the realm of practicality for commercial catalysts. Cesium itself is relatively costly element, and this has inhibited the adoption of base zeolite catalysts in an industrial setting, particularly in those most effective supported catalysts having a cesium loading sometimes in excess of 30% [120].

Common catalysts for the Knoevenagel condensation, a coupling reaction between a carbonyl and carbanion followed by dehydration (e.g. Figure 9.9), include alkali-earth metals barium and magnesium supported on metal oxides including ZnO, γ-Al_2O_3, or Fe_2O_3. In generating basic sites expected of alkali metals, acidic sites are also formed on the support, relative to the unmodified support material [121–123].

Using *in situ* FTIR techniques, researchers found that the above reaction experienced an induction period during which an enolate intermediate formed on basic sites on the ZnO catalyst as the rate-limiting step [124]. The concentration of acidic hydroxide sites on the catalyst then participated in the condensation step of the reaction. The equivalent reaction has been undertaken using zeolites [120, 125–132] and metal organic frameworks (MOFs) [133, 134] exchanged with various alkali metal cations. Martins et al. and Hölderich and coworkers compared the efficacy of basic cesium faujasites (FAU) against faujasites exchanged with an organic cation, methylammonium, to produce an even more strongly basic catalyst [126, 135]. Selectivity to the required condensation products remained high for both Cs^+ and $MeNH_3^+$, at close to 100%. The benzaldehyde conversion however was reported at 83.1%, 66% greater than for the Cs^+ catalyst for the Knoevenagel condensation. Even more pronounced was the effect of increased catalyst basicity on the Claisen–Schmidt condensation, with conversion under the methylammonium catalyst at 40.6%, four times higher than for the Cs–FAU.

The above example illustrates the marked effect of tuning the strength of acidic/basic sites through selection of exchange species. Were it not for the decomposition of methylammonium at temperatures above 190 °C, the catalyst from this example could be used in a much broader range of applications where less mild conditions are required.

A more contemporary approach to producing basic zeolite catalysts is the synthesis of hierarchical zeolites [120, 136]. In the work by Keller and coworkers, cation-free hierarchical materials performed favorably to similar metal-exchanged traditional zeolites in the Knoevenagel condensation, among other reactions including the deoxygenation of bio-oil via aldol condensation pathways [132].

In the Knoevenagel condensation of benzaldehyde with malononitrile, the inverse of the normal principle of higher aluminum concentration leading to higher catalyst activity was found when using hierarchical USY zeolites, even in the proton form. Zeolite USY candidates with a Si/Al ratio of 385 were found to be the most effective, with Cs^+, K^+, and Na^+ forms each successfully converting c. 75% of the reactant benzaldehyde. After tuning the hierarchy factor (the relative mesopore surface area multiplied by the relative microporosity), researchers were able to achieve close to complete benzaldehyde conversion with Na–USY with Si/Al = 385 and HF = 0.10. In contrast, the cesium-exchanged zeolite X and Y were only able to convert c. 10% of the benzaldehyde. The explanation for this unexpected activity of hierarchical, high-silica zeolites is that cation exchange capacity has been previously observed on such zeolites that exceeds the alumina content, leading to the presumption of additional anionic sites in the zeolite [137]. These anionic sites were confirmed, through low-pressure alkene adsorption, to have basic characteristic [138] and through ^{1}H-NMR found to be deprotonated silanol groups stabilized by adjacent protonated silanols [139].

This work illustrates the potential to use high-silica zeolites with a tunable prevalence of site defects and pore sizes as persistent base catalysts that potentially offer a highly cost-effective alternative to cesium-exchanged zeolites.

9.2.1.3 Redox Sites in Zeolite Catalysts

Sites affecting redox catalysis may be introduced into a zeolite through introduction of an element with redox character into the zeolite framework. This may be done either during hydrothermal synthesis of the zeolite or as a post-synthesis treatment after the preparation of the parent zeolite.

Possibly the most studied family of catalysts of this type are the titanium zeotypes – ordered silicas or zeolites with a portion of the framework silicon or aluminum, usually in the order of 1–5%, isomorphically substituted for titanium. These catalysts offer exceptionally stable and selective redox sites for a range of organic transformations, most significantly the epoxidation of a wide variety of unsaturated compounds [61, 140, 141] and ammoximation reactions [42, 142, 143].

The first strictly heterogeneous catalysts utilizing a titania–silica system were developed by Sheldon [144], which were superior to the homogeneous catalysts previously synthesized, with comparable selectivity and high activity. The increased catalytic activity of the heterogeneous catalyst was attributed to an increase in the Lewis acidity contributed by Ti(IV) due to electron withdrawal by silanoxy ligands and to site isolation of Ti(IV) centers on the surface. Both the silica-supported heterocatalysts and the homogeneous ones developed previously show high sensitivity toward deactivation by strongly coordinating ligands, water in particular, making them ineffective for use in aqueous environments.

Immobilizing the titanium within a zeolite framework largely overcomes the above issues by the prevention of leaching of the titanium from Ti framework sites. Furthermore, the inherent hydrophobicity of the silica matrix allows the titanium

zeotypes, in particular TS-1, to be useful in reactions with aqueous hydrogen peroxide as the oxidizing species, rather than the harmful organic peroxides traditionally used in partial oxidations over titanium catalysts.

More recent advances in this type of material have tended to attempt to overcome the primary shortcoming of TS-1, which is the lack of bulky substrates accommodated by the relatively restrictive pore size offered by the MFI structure. This has been by way of synthesizing mesoporous TS-1 and further hierarchical TS-1 to accommodate larger organic reactants [145–147].

9.3 Causes of Deactivation in Zeolite Catalysts

All types of catalyst are susceptible to deactivation through some mechanism, leading to decreased catalytic activity in terms of turnover number, selectivity to desired species, or both. Understanding the mechanism(s) of deactivation for a given catalyst performing in an industrial chemical reaction is critical to the long-term viability of that process.

9.3.1 Poisoning

Poisoning in the context of zeolite catalyst deactivation refers to the chemisorption of some extraneous species onto the zeolite catalytic sites, blocking access of reactants to the catalytically active site. Normally, these species are present as impurities in the process. However, desired products and products from secondary reactions (in particular, coke) may also act as a catalyst poison, and in this case the reaction rate will decrease as the reaction proceeds.

9.3.1.1 Deactivation through Carbonaceous Deposits (Coking)

A mechanism of catalyst deactivation particularly prevalent in gas-phase industrial chemical processes is the formation and deposition of stable, bulky organic compounds referred to as "coke."

Catalyst deactivation via this mechanism is reported to be caused by the formation of carbonaceous deposits on the surface, blocking the active sites and preventing further oxidation. Catalytic reactions involving carbon-containing reactants are susceptible deposition through cracking or decomposition and Boudouard reaction, forming coke or carbonaceous species such as carbides [148–151]. The formation of carbonaceous surface species can be governed by the presence of different components, such as hydrogen [152]. As discussed previously, palladium is considered a highly effective catalyst for oxidation; however it has also been noted to be active in the transformation of amorphous carbon into graphitic species [153]. Understanding the surface reactions occurring is vital for maintaining catalyst activity and desired selectivities. It has been identified that the surface species formed are highly dependent on the specific active metal, the support used, and the process conditions [153], with depositions able to be considered unique and reaction specific to a certain degree.

While coke is normally composed of polyaromatics, the relatively small size of zeolite pores generally confines the generation of zeolitic coke to smaller, non-polyaromatic compounds [154–156].

9.3.1.2 Inhibition of Catalyst Activity Due to Water

The presence of water in reactant feed has been widely reported as an inhibiting agent in some catalytic processes, specifically for palladium-based catalysts [157, 158]. These studies identified that the presence of water vapor decreases activity at lower operating temperatures due to the formation of inactive hydroxyl surface species, which block the access to the active sites for dissociation. During oxidation reactions, it has been suggested that the hydroxyl groups via dissociation are likely to be more strongly bound to the surface than those adsorbed from external sources [159], with water accumulation occurring on the surface. Further, it has been hypothesized that the rate of water desorption from catalyst surfaces is slowed by an increased presence of water vapor in the gas phase. Infrared spectroscopic studies have been performed to identify the presence of stable hydroxyl species, i.e. $Pd(OH)_2$, on the catalyst surface during methane oxidation reactions. Evidence was found suggesting the formation and accumulation of hydroxyl groups on supported palladium catalysts [148]. There was also minimal change in the IR profiles when reactant flow was stopped, indicating slow desorption of surface hydroxyl species. The presence of the active oxide species (PdO) was found to have a significant impact on the hydroxyl surface bonding, hindering hydroxyl recombination and subsequent OH desorption [148]. In addition to reaction inhibition by blocking catalytically active sites, it has been shown that the presence of water can directly affect the mobility of oxygen through the catalyst support, implying that the inhibition mechanism may involve the surface hydroxyl species preventing the exchange of oxygen between support and active metal species [158].

9.3.1.3 Poisoning of Palladium Combustion Catalysts

With the use of catalysts for combustion of low-concentration methane streams, as discussed in a previous example, catalyst poisoning is the key inhibiting process for commercial application. The deactivation behavior is of particular importance to the application in ventilation air combustion and catalytic combustion to remove methane slip in gas engines and turbines. In this case, water is included in the simulated feed to emulate real catalyst working conditions. It was reported in earlier studies that water significantly inhibits the catalytic activity of supported Pd catalysts, whether the support be alumina [160, 161] or zeolites [162, 163], through competitive adsorption on active Pd sites. Further, a secondary deactivation mechanism is known to occur whereby active palladium sites are reduced to palladium hydroxide by water [164, 165]. It was proposed by Ciuparu and coworkers that the hydroxyl groups strongly bind to and accumulate on the support [158, 159]. TS-1 was described in the preceding sections as having exceptional redox activity and also greater hydrophobicity than many other zeolites [166]. It has been used both as a catalyst itself and as a support for additional catalytic materials.

For example, Au–Pd nanoparticles have been supported on hierarchical TS-1 as a catalyst for the oxidation of benzyl alcohol using hydrogen peroxide generated *in situ* [167]. It was found that the introduction of Ti into the framework improved noble metal dispersion. The properties of high dispersion and hydrophobicity made Pd/TS-1 a potential candidate for a methane oxidation catalyst also. Long-running experiments (>1900 hours) were undertaken by Setiawan et al. [168], emulating a VAM stream with a gas hourly space velocity (GHSV) of 100 000 h^{-1} of 7000 ppm methane and 40 000 ppm water, introduced using a saturator, with air as the balance.

What was found is that in comparison with the benchmark Pd/Al_2O_3 catalyst, the Pd/TS-1 was able to achieve 90% methane conversion at a consistently lower temperature (c. 430 °C, instead of 500 °C for Pd/Al_2O_3). The Arrhenius plot (Figure 9.10) indicates a change in activation energy in the case of Pd/TS-1, but not in Pd/Al_2O_3.

At c. 360 °C, the activation energy changes from 369 to 48 kJ mol^{-1} for the catalyst supported on TS-1, whereas it remains at 128 kJ mol^{-1} in the case of the alumina-based catalyst. Water TPD measurements indicated that this temperature coincides with the removal of the relatively small concentration of adsorbed water from the Pd/TS-1 surface. The change in reaction temperature is also related to the heat of adsorption of oxygen on palladium sites. Oxygen TPD showed that at 360 °C, labile oxygen desorbs, lowering the apparent activation energy [169].

The effect of water as a catalyst poison is well established, and its prevalence in both feed streams and as a reaction product in real processes has prompted the development of increasingly hydrophobic metal-substituted zeolites, for example,

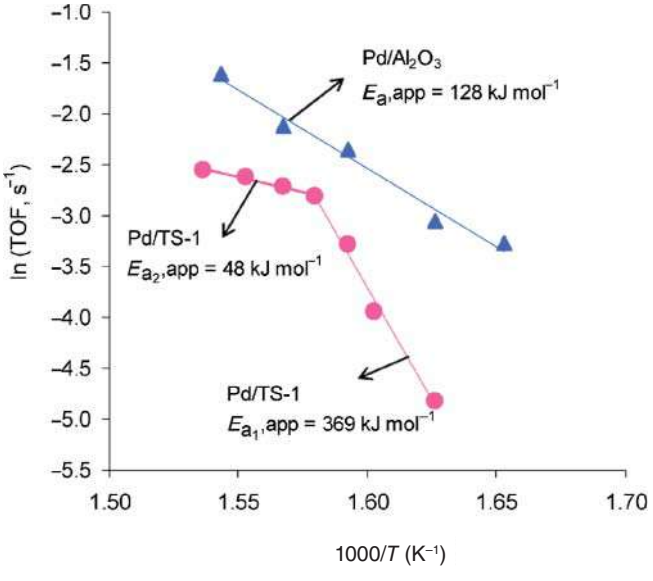

Figure 9.10 Arrhenius plot for palladium supported on TS-1 and alumina. Reaction conditions are 7000 ppm methane and 40 000 ppm water in air, with GHSV of 100 000 h^{-1}. Source: Reproduced with permission from Setiawan et al. [168]; © 2016, Royal Society of Chemistry.

Ti–BEA and Ti–MWW, by adding hydrophilic groups such as organosilanes [170] or fluoride-mediated synthesis [171–173].

Extraneous organic species are also known to poison catalytic sites. Continuing the theme of TS-1 as an oxidation catalyst, the epoxidation of allyl alcohol to glycidol using hydrogen peroxide has been well studied [174–177]. Herein [61, 140], waste glycerol from the biodiesel manufacture process was first converted to allyl alcohol using an alumina-supported iron catalyst, with the epoxidation of the unsaturated alcohol occurring subsequently. The general reaction scheme is shown in Figure 9.11.

In practice, the conversion of glycerol to allyl alcohol is not completely selective, with side products, in particular acrolein, hydroxyacetone, acetaldehyde, and acetic and propanoic acids, under some less-ideal conditions accounting for a significant portion of the total product yield [178]. From a process engineering perspective, it was important to investigate the effect of side products from the allyl alcohol synthesis on the subsequent epoxidation step. It was found that some of the side products, acrolein in particular, did have a poisoning effect on the catalyst, whereas others actually served to promote the reaction. This is illustrated in Figure 9.12.

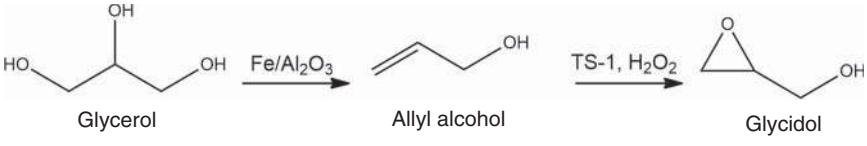

Figure 9.11 Allyl alcohol route to glycidol from glycerol.

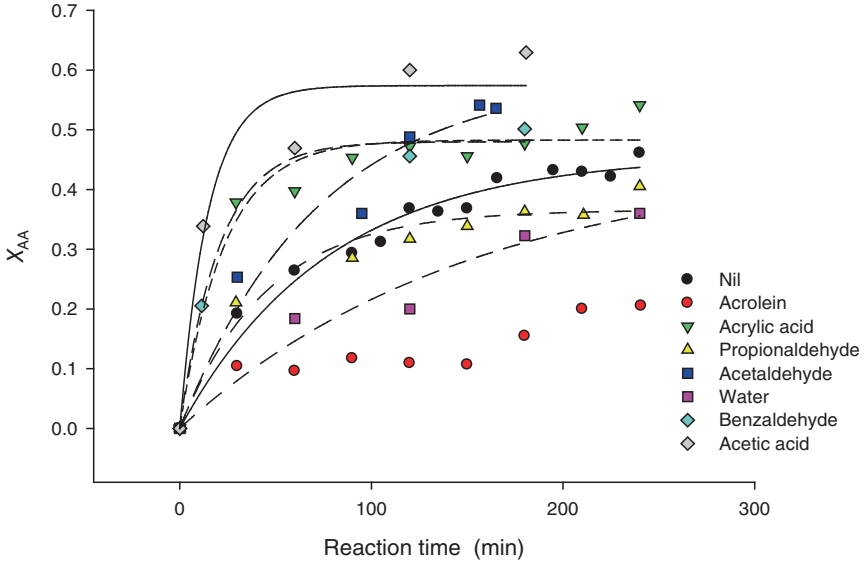

Figure 9.12 Conversion of allyl alcohol in the presence of additive species representative of process side products. Source: Reproduced with permission from Harvey et al. [140]; © 2015, Elsevier.

It was originally presumed that acrolein inhibited the reaction through competitive oxidation with allyl alcohol. However, no products of acrolein oxidation were detected in the reaction mixture and iodometric titration revealed that the corresponding amount of hydrogen peroxide remained unreacted. The specific mechanism leading to catalyst deactivation is still not fully known, yet the dipole moment for each additive species at the B3LYP/6-31G* basis set in density functional calculations showed a correlation between reaction promoters and a lower dipole moment (c. 1.8 Debye). Catalyst inhibitors tended to show a higher dipole moment at c. 3 Debye and less electronegative atomic charge on functional groups [140]. It is currently postulated that less negatively charged substrates poison the catalyst by binding to titanium Lewis acid sites. The mechanism of reaction enhancement with more electronegative functional groups is less apparent, although it is currently thought that these groups may abstract the peroxy proton, enhancing the transfer of a peroxy oxygen to the allyl moiety.

9.3.2 Particle Sintering and Agglomeration

Sintering is a thermal alteration, typically irreversible, to a solid catalyst that concerns the loss of active surface area due to the structural collapse of the support or bulk catalyst or the agglomeration of the metal catalytic phase itself. Normally, sintering is referred to as the migration in a "Brownian-like" motion and coalescence of metal particles on the surface of a catalyst support [179]. This is a different mechanism to Ostwald ripening, wherein a nanoparticle particle or "adatom" dissolves on the support surface and migrates to the surface of larger crystals due to surface species of a particle being less thermodynamically stable [179–181]. The decrease in catalytic activity can often be proportional to the decrease in metal area accessible to reactants.

9.3.2.1 Particle Agglomeration in Ventilation Air Methane Oxidation Catalysts

The stability of palladium sites in VAM oxidation catalysts supported on silicalite-1, HZSM-5, and TS-1 was studied under the same reaction conditions as described in the preceding examples [182, 183]. Gradual deactivation of Pd/silicalite-1 and Pd/HZSM-5 over 30 hours' reaction time was observed. However, this was not the case for Pd/TS-1.

X-ray absorption fine structure (XAFS) of the Pd K-edge showed that palladium in the Pd/HZSM-5 sample is partially stabilized by the zeolite framework aluminum and explains the consistent catalyst performance over the first 10 hours on stream. After further use however, the originally well-distributed nano-sized Pd–O more closely resembles the XAFS spectrum of the reference palladium oxide powder, indicating Pd agglomeration. Transmission electron microscopy (TEM) measurements obtained for fresh and used (100 hours) catalysts further show the agglomeration of Pd sites.

The silicalite-1 and TS-1 supported catalysts showed higher stability than the HZSM-5, in particular TS-1. Whereas used silicalite and HZSM-5 supports showed Pd agglomerated into c. 15–20 nm clusters, the TS-1 showed no such

clustering. This was attributed to the TS-1 providing "anchoring" sites in the form of framework Ti, which silicalite does not possess. In the case of HZSM-5, aluminum XANES shows that tetrahedral Al is lost from the zeolite framework due to the moisture in the reaction feed, resulting in the agglomeration of Pd on the remaining aluminum sites, an effect not seen on TS-1 due to its relative hydrophobicity.

9.4 Future Directions for Zeolite Catalysis

Zeolites provide a multitude of avenues for the development of catalytic materials, owing largely to their robust structure and unique chemistry. Some of the recent developments examined in this chapter included increasing catalyst hydrophobicity to mitigate catalyst deactivation, base catalysis, and production of hierarchical and pillared zeolites with a tunable mixture of meso- and micropores to accommodate bulkier organic substrates.

Steady and rapid advances in computing power have enabled realistic theoretical modeling of chemical phenomena, including zeolite chemistry and applications. Substantial progress has been made in molecular-based approaches to the design of zeolites for specific purposes [184]. For example, quantum mechanical calculations investigating the elementary steps of zeolite formation are resulting properties possibly used to predict and optimize synthesis outcomes [185–189]. Modeling of deactivation mechanisms, particularly thermodynamics of coking precursors, is also gaining much attention [190].

The accelerated effort in developing hierarchical zeolites through different routes is indicative of the popular view that this type of zeolite material offers the potential to overcome the major unresolved limitations of zeolite catalysts, namely, the accommodation of bulky substrates into pore structures. The economical design of such materials for specific chemical reactions will almost definitely work in tandem with modern computational methods to produce cutting-edge catalysts for highly selective chemical processes and waste mitigation.

References

1 Čejka, J., van Bekkum, H., Corma, A., and Schüth, F. (2007). *Introduction to Zeolite Science and Practice*, 3rde, vol. 168. Elsevier.
2 Barrer, R.M. (1979). *Pure Appl. Chem.* 51: 1091.
3 Baerlocher, C., McCusker, L.B., and Olson, D.H. (2007). Framework type datasheets. In: *Atlas of Zeolite Framework Types*, 6the (ed. C. Baerlocher, L.B. McCusker and D.H. Olson), 194. Amsterdam: Elsevier Science B.V.
4 Lonin, A.Y., Levenets, V.V., Neklyudov, I.M., and Shchur, A.O. (2015). *J. Radioanal. Nucl. Chem.* 303: 831.
5 Bacakova, L., Vandrovcova, M., Kopova, I., and Jirka, I. (2018). *Biomater. Sci.* 6: 974.

6 Ayele, L., Pérez-Pariente, J., Chebude, Y., and Díaz, I. (2015). *Microporous Mesoporous Mater.* 215: 29.
7 Koohsaryan, E., Anbia, M., and Maghsoodlu, M. (2020). *J. Environ. Chem. Eng.* 8: 104287.
8 Martínez, C. and Corma, A. (2011). *Coord. Chem. Rev.* 255: 1558.
9 Armor, J.N. (2011). *Catal. Today* 163: 3.
10 Solomon, S., Qin, D., Manning, M. et al. (2007). Climate Change 2007: The Physical Science Basis - Contribution of Working Group I to the Fourth Assessment Report of the Intergovernmental Panel on Climate Change.
11 Serrano, D.P., Escola, J.M., and Pizarro, P. (2013). *Chem. Soc. Rev.* 42: 4004.
12 Chen, L.-H., Li, X.-Y., Rooke, J.C. et al. (2012). *J. Mater. Chem.* 22: 17381.
13 Jae, J., Tompsett, G.A., Foster, A.J. et al. (2011). *J. Catal.* 279: 257.
14 Olsbye, U., Svelle, S., Bjorgen, M. et al. (2012). *Angew. Chem. Int. Ed.* 51: 5810.
15 Roth, W.J., Nachtigall, P., Morris, R.E., and Čejka, J. (2014). *Chem. Rev.* 114: 4807.
16 Čejka, J., Centi, G., Perez-Pariente, J., and Roth, W. (2012). *J. Catal. Today* 179: 2.
17 Li, W.-C., Lu, A.-H., Palkovits, R. et al. (2005). *J. Am. Chem. Soc.* 127: 12595.
18 Ishida, H. (1997). *Catal. Surv. Asia* 1: 241.
19 Burch, R. and Millington, P.J. (1993). *Appl. Catal., B* 2: 101.
20 Lobree, L.J., Hwang, I.C., Reimer, J.A., and Bell, A.T. (1999). *Catal. Lett.* 63: 233.
21 Li, Y. and Armor, J.N. (1992). *Appl. Catal., B* 1: L31.
22 Ono, Y. (2003). *Catal. Today* 81: 3.
23 Čejka, J., Kotrla, J., and Krejčí, A. (2004). *Appl. Catal., A* 277: 191.
24 Segawa, K. and Hiroyasu, T. (1991). *J. Catal.* 131: 482.
25 Cao, Y., Kessas, R., Naccache, C., and Ben Taarit, Y. (1999). *Appl. Catal., A* 184: 231.
26 Niwa, M., Katada, N., and Okumura, K. (2010). *Characterization and Design of Zeolite Catalysts: Solid Acidity, Shape Selectivity and Loading Properties*, 1. Berlin, Heidelberg: Springer-Verlag.
27 Wang, B., Côté, A.P., Furukawa, H. et al. (2008). *Nature* 453: 207.
28 Bhan, A. and Iglesia, E. (2008). *Acc. Chem. Res.* 41: 559.
29 Gounder, R. and Iglesia, E. (2013). *Chem. Commun.* 49: 3491.
30 Boronat, M., Martínez-Sánchez, C., Law, D., and Corma, A. (2008). *J. Am. Chem. Soc.* 130: 16316.
31 Guisnet, M.A.R. and Fernando, R. (2011). Zeolites as models for understanding catalyst deactivation and regeneration. In: *Deactivation and Regeneration of Zeolite Catalysts*, Catalytic Science Series (ed. M. Guisnet and F.R.A. Ribeiro), 19–38.
32 Fernandez, C., Stan, I., Gilson, J.-P. et al. (2010). *Chem. Eur. J.* 16: 6224.
33 Jiang, J., Yu, J., and Corma, A. (2010). *Angew. Chem. Int. Ed.* 49: 3120.
34 Lobo, R.F., Tsapatsis, M., Freyhardt, C.C. et al. (1997). *J. Am. Chem. Soc.* 119: 8474.
35 Férey, G., Mellot-Draznieks, C., Serre, C. et al. (2005). *Science* 309: 2040.

36 Beyer, H.K. (2002). *Post-Synthesis Modification I*, 203. Berlin, Heidelberg: Springer-Verlag.
37 Nielsen, M., Brogaard, R.Y., Falsig, H. et al. (2015). *ACS Catal.* 5: 7131.
38 Silaghi, M.-C., Chizallet, C., and Raybaud, P. (2014). *Microporous Mesoporous Mater.* 191: 82.
39 Gao, Z.-H., Chen, F.-J., Xu, L. et al. (2016). *Chem. Eur. J.* 22: 14367.
40 Corma, A., Díaz-Cabañas, M.J., and Fornés, V. (2000). *Angew. Chem. Int. Ed.* 39: 2346.
41 Přech, J. and Čejka, J. (2016). *Catal. Today* 277: 2.
42 Přech, J., Kubů, M., and Čejka, J. (2014). *Catal. Today* 227: 80.
43 Zhang, T., Liu, J., Wang, D. et al. (2014). *Appl. Catal., B* 148–149: 520.
44 Wu, S.T., She, Q.M., Tesser, R. et al. (2020). *Catal. Rev. Sci. Eng.* 62: 481.
45 Petrus, R. and Warchoł, J. (2003). *Microporous Mesoporous Mater.* 61: 137.
46 Caputo, D. and Pepe, F. (2007). *Microporous Mesoporous Mater.* 105: 222.
47 Perişanu, S. and Oancea, A.-M. (2015). *Adsorption* 21: 343.
48 Ostroski, I.C., Silva, E.A., Arroyo, P.A., and Barros, M.A.S.D. (2014). *Fluid Phase Equilib.* 372: 76.
49 Erdem, E., Karapinar, N., and Donat, R. (2004). *J. Colloid Interface Sci.* 280: 309.
50 Yan, P., Kennedy, E., and Stockenhuber, M. (2021). *J. Catal.* 396: 157–165.
51 Chao, K.-J., Chiou, B.-H., Cho, C.-C., and Jeng, S.-Y. (1984). *Zeolites* 4: 2.
52 Vaculík, J., Setnička, M., and Bulánek, R. (2016). *J. Therm. Anal. Calorim.* 125: 1217.
53 Niwa, M. and Katada, N. (2013). *Chem. Rec.* 13: 432.
54 Gould, N.S. and Xu, B. (2018). *ACS Catal.* 8: 8699.
55 Yan, P., Li, M.M.-J., Kennedy, E. et al. (2020). *Catal. Sci. Technol.* 10: 810.
56 Hartmann, M. and Kevan, L. (2002). *Res. Chem. Intermed.* 28: 625.
57 Aiello, R., Nagy, J.B., Giordano, G. et al. (2005). *C.R. Chim.* 8: 321.
58 Li, J., Corma, A., and Yu, J. (2015). *Chem. Soc. Rev.* 44: 7112.
59 Eliášová, P., Opanasenko, M., Wheatley, P.S. et al. (2015). *Chem. Soc. Rev.* 44: 7177.
60 Peters, L., Vega-Flores, G., and Depmeier, W. (2009). *Prog. Solid State Chem.* 37: 243.
61 Harvey, L., Sánchez, G., Kennedy, E.M., and Stockenhuber, M. (2015). *Asia-Pac. J. Chem. Eng.* 10: 598.
62 Uphade, B.S., Akita, T., Nakamura, T., and Haruta, M. (2002). *J. Catal.* 209: 331.
63 Fejes, P., Nagy, J.B., Lázár, K., and Halász, J. (2000). *Appl. Catal., A* 190: 117.
64 Hensen, E.J.M., Zhu, Q., and van Santen, R.A. (2003). *J. Catal.* 220: 260.
65 van de Water, L.G.A., van der Waal, J.C., Jansen, J.C., and Maschmeyer, T. (2004). *J. Catal.* 223: 170.
66 Nada, M.H. and Larsen, S.C. (2017). *Microporous Mesoporous Mater.* 239: 444.
67 Awala, H., Gilson, J.-P., Retoux, R. et al. (2015). *Nat. Mater.* 14: 447.
68 Xie, B., Song, J., Ren, L. et al. (2008). *Chem. Mater.* 20: 4533.
69 Kalipcilar, H. and Culfaz, A. (2001). *Cryst. Res. Technol.* 36: 1197.
70 Meng, X. and Xiao, F.-S. (2014). *Chem. Rev.* 114: 1521.

71 Inayat, A., Schneider, C., and Schwieger, W. (2015). *Chem. Commun.* 51: 279.

72 Chen, C.-Y. and Zones, S.I. (2010). Post-synthetic treatment and modification of zeolites. In: *Zeolites and Catalysis* (ed. J. Čejka, A. Corma and S. Zones), 155–170. Wiley-VCH https://doi.org/10.1002/9783527630295.ch6.

73 Dzwigaj, S., Millot, Y., and Che, M. (2010). *Catal. Lett.* 135: 169.

74 Kyriienko, P.I., Larina, O.V., Soloviev, S.O. et al. (2016). *Catal. Commun.* 77: 123.

75 Dijkmans, J., Demol, J., Houthoofd, K. et al. (2015). *J. Catal.* 330: 545.

76 Valtchev, V., Majano, G., Mintova, S., and Pérez-Ramírez, J. (2013). *Chem. Soc. Rev.* 42: 263.

77 Yi, F., Chen, Y., Tao, Z. et al. (2019). *J. Catal.* 380: 204.

78 Tang, B., Dai, W., Wu, G. et al. (2014). *ACS Catal.* 4: 2801.

79 Dzwigaj, S., Janas, J., Gurgul, J. et al. (2009). *Appl. Catal., B* 85: 131.

80 Kyriienko, P.I., Larina, O.V., Dzwigaj, S. et al. (2019). *Theor. Exp. Chem.* 55: 266.

81 Kyriienko, P.I., Larina, O.V., Soloviev, S.O. et al. (2017). *ACS Sustainable Chem. Eng.* 5: 2075.

82 Sushkevich, V.L. and Ivanova, I.I. (2016). *ChemSusChem* 9: 2216.

83 Gil, B., Mokrzycki, Ł., Sulikowski, B. et al. (2010). *Catal. Today* 152: 24.

84 Paukshtis, E.A., Yaranova, M.A., Batueva, I.S., and Bal'zhinimaev, B.S. (2019). *Microporous Mesoporous Mater.* 288: 109582.

85 Corma, A., Llabrés i Xamena, F.X., Prestipino, C. et al. (2009). *J. Phys. Chem. C* 113: 11306.

86 Shamzhy, M., Přech, J., Zhang, J. et al. (2020). *Catal. Today* 345: 80.

87 Shakeri, M. and Dehghanpour, S.B. (2020). *Microporous Mesoporous Mater.* 298: 110066.

88 Gao, H., Lu, W., and Chen, Q. (2000). *Microporous Mesoporous Mater.* 34: 307.

89 Zhang, X., Liu, D., Xu, D. et al. (2012). *Science* 336: 1684.

90 Na, K., Choi, M., Park, W. et al. (2010). *J. Am. Chem. Soc.* 132: 4169.

91 Fermoso, J., Hernando, H., Jana, P. et al. (2016). *Catal. Today* 277: 171.

92 Schwanke, A.J., Díaz, U., Corma, A., and Pergher, S. (2017). *Microporous Mesoporous Mater.* 253: 91.

93 Corma, A., Fornés, V., Martı´ nez-Triguero, J., and Pergher, S.B. (1999). *J. Catal.* 186: 57.

94 Vicente, M.A., Gil, A., and Bergaya, F. (2013). Chapter 10.5: Pillared clays and clay minerals. In: *Developments in Clay Science*, vol. 5 (ed. F. Bergaya and G. Lagaly), 523. Elsevier.

95 Baloyi, J., Ntho, T., and Moma, J. (2018). *RSC Adv.* 8: 5197.

96 Nicholas, C.P. (2010). Overview and recent developments in catalytic applications of zeolites. In: *Zeolites in Industrial Separation and Catalysis* (ed. S. Kulprathipanja), 355–402. Wiley-VCH.

97 Weitkamp, J. and Hunger, M. (2007). Chapter 22: Acid and base catalysis on zeolites. In: *Studies in Surface Science and Catalysis*, vol. 168 (ed. J. Čejka, H. van Bekkum, A. Corma and F. Schüth), 787. Elsevier.

98 Haw, J.F. (2002). *Phys. Chem. Chem. Phys.* 4: 5431.

99 Weitkamp, J. and Hunger, M. (2007). *Introduction to Zeolite Science and Practice*, 3rde, vol. 168. Elsevier.

100 Tielens, F. and Dzwigaj, S. (2010). *Chem. Phys. Lett.* 501: 59.

101 Yang, G., Pidko, E.A., and Hensen, E.J.M. (2013). *J. Phys. Chem. C* 117: 3976.

102 Injongkol, Y., Maihom, T., Treesukul, P. et al. (2017). *Phys. Chem. Chem. Phys.* 19: 24042.

103 Montejo-Valencia, B.D. and Curet-Arana, M.C. (2015). *J. Phys. Chem. C* 119: 4148.

104 Ouyang, X., Hwang, S.-J., Xie, D. et al. (2015). *ACS Catal.* 5: 3108.

105 Delmon, B., Delmon, B., Thomas, J.M. et al. (1997). Preparation of solid catalysts. In: *Handbook of Heterogeneous Catalysis* (ed. G. Ertl, H. Knözinger and J. Weitkamp), 264–365. Wiley-VCH.

106 Elanany, M., Koyama, M., Kubo, M. et al. (2005). *Appl. Surf. Sci.* 246: 96.

107 Liu, R., Zhang, J., Sun, X. et al. (2014). *Comput. Theor. Chem.* 1027: 5.

108 Wang, C., Wang, L., Wu, G. et al. (2020). *Catal. Lett.* 150: 429.

109 Wang, N., Zhang, M., and Yu, Y. (2013). *Microporous Mesoporous Mater.* 169: 47.

110 Liu, C., Li, G., Hensen, E.J.M., and Pidko, E.A. (2016). *J. Catal.* 344: 570.

111 Sun, J., Karim, A.M., Zhang, H. et al. (2013). *J. Catal.* 306: 47.

112 Nie, L., de Souza, P.M., Noronha, F.B. et al. (2014). *J. Mol. Catal. A: Chem.* 388–389: 47.

113 Zhang, X., Tang, W., Zhang, Q. et al. (2018). *Appl. Energy* 227: 73.

114 Zhu, X., Lobban, L.L., Mallinson, R.G., and Resasco, D.E. (2011). *J. Catal.* 281: 21.

115 Shirazi, M., Bogaerts, A., and Neyts, E.C. (2017). *Phys. Chem. Chem. Phys.* 19: 19150.

116 Liu, J., Li, C., Wang, F. et al. (2013). *Catal. Sci. Technol.* 3: 2627.

117 Foiles, S.M., Baskes, M.I., Melius, C.F., and Daw, M.S. (1987). *J. Less Common Metals* 130: 465.

118 Barthomeuf*, D. (1996). *Catal. Rev.* 38: 521.

119 Joshi, U.D., Joshi, P.N., Tamhankar, S.S. et al. (2003). *Appl. Catal., A* 239: 209.

120 Keller, T.C., Isabettini, S., Verboekend, D. et al. (2014). *Chem. Sci.* 5: 677.

121 Li, J.P.H., Adesina, A.A., Kennedy, E.M., and Stockenhuber, M. (2017). *Phys. Chem. Chem. Phys.* 19: 26630.

122 Seddigi, Z.S. (2009). *Energy Fuels* 23: 46.

123 Margelefsky, E.L., Zeidan, R.K., and Davis, M.E. (2008). *Chem. Soc. Rev.* 37: 1118.

124 Li, J.P.H., Kennedy, E.M., Adesina, A.A., and Stockenhuber, M. (2019). *J. Catal.* 369: 157.

125 Saravanamurugan, S., Palanichamy, M., Hartmann, M., and Murugesan, V. (2006). *Appl. Catal., A* 298: 8.

126 Martins, L., Vieira, K.M., Rios, L.M., and Cardoso, D. (2008). *Catal. Today* 133–135: 706.

127 Lai, S.M., Ng, C.P., Martin-Aranda, R., and Yeung, K.L. (2003). *Microporous Mesoporous Mater.* 66: 239.

128 Martins, L., Bonagamba, T.J., de Azevedo, E.R. et al. (2006). *Appl. Catal., A* 312: 77.
129 Phan, N.T.S. and Jones, C.W. (2006). *J. Mol. Catal. A: Chem.* 253: 123.
130 Murkute, A.D., Jackson, J.E., and Miller, D.J. (2011). *J. Catal.* 278: 189.
131 Xu, J., Shen, K., Xue, B., and Li, Y.-X. (2013). *J. Mol. Catal. A: Chem.* 372: 105.
132 Puértolas, B., Keller, T.C., Mitchell, S., and Pérez-Ramírez, J. (2016). *Appl. Catal., B* 184: 77.
133 Opanasenko, M., Dhakshinamoorthy, A., Shamzhy, M. et al. (2013). *Catal. Sci. Technol.* 3: 500.
134 Tran, U.P.N., Le, K.K.A., and Phan, N.T.S. (2011). *ACS Catal.* 1: 120.
135 Martins, L., Hölderich, W., and Cardoso, D. (2008). *J. Catal.* 258: 14.
136 Shanbhag, G.V., Choi, M., Kim, J., and Ryoo, R. (2009). *J. Catal.* 264: 88.
137 Chester, A.W., Chu, Y.F., Dessau, R.M. et al. (1985). *J. Chem. Soc., Chem. Commun.* 289.
138 Hufton, J.R., Ruthven, D.M., and Danner, R.P. (1995). *Microporous Mater.* 5: 39.
139 Shantz, D.F., Schmedt auf der Günne, J., Koller, H., and Lobo, R.F. (2000). *J. Am. Chem. Soc.* 122: 6659.
140 Harvey, L., Kennedy, E., Dlugogorski, B.Z., and Stockenhuber, M. (2015). *Appl. Catal., A* 489: 241.
141 Guo, Q., Sun, K., Feng, Z. et al. (2012). *Chem. Eur. J.* 18: 13854.
142 Xue, Y., Xie, Y., Wei, H. et al. (2014). *New J. Chem.* 38: 4229.
143 Lin, J., Xin, F., Yang, L., and Zhuang, Z. (2014). *Catal. Commun.* 45: 104.
144 Sheldon, R.A. (1980). *J. Mol. Catal.* 7: 107.
145 Xin, H., Zhao, J., Xu, S. et al. (2010). *J. Phys. Chem. C* 114: 6553.
146 Cheneviere, Y., Chieux, F., Caps, V., and Tuel, A. (2010). *J. Catal.* 269: 161.
147 Zhou, J., Hua, Z., Cui, X. et al. (2010). *Chem. Commun.* 46: 4994.
148 Ciuparu, D., Perkins, E., and Pfefferle, L. (2004). *Appl. Catal., A* 263: 145.
149 Bartholomew, C.H. (2001). *Appl. Catal., A* 212: 17.
150 Guisnet, M. and Magnoux, P. (2001). *Appl. Catal., A* 212: 83.
151 Guisnet, M., Costa, L., and Ribeiro, F.R. (2009). *J. Mol. Catal. A: Chem.* 305: 69.
152 Albers, P., Seibold, K., Prescher, G., and Müller, H. (1999). *Appl. Catal., A* 176: 135.
153 Albers, P., Pietsch, J., and Parker, S.F. (2001). *J. Mol. Catal. A: Chem.* 173: 275.
154 Mohamadalizadeh, A., Towfighi, J., and Karimzadeh, R. (2008). *J. Anal. Appl. Pyrolysis* 82: 134.
155 Ropital, F. and Bonnet, F. (2008). *Mater. Sci. Forum* 595–598: 681.
156 Guisnet, M.A.R. and Fernando, R. (2011). Characterization of deactivating species. In: *Deactivation and Regeneration of Zeolite Catalysts*, Catalytic Science Series (ed. M. Guisnet and F.R.A. Ribeiro), 51–81.
157 Ewen, J.P., Gattinoni, C., Morgan, N. et al. (2016). *Langmuir* 32: 4450.
158 Schwartz, W.R., Ciuparu, D., and Pfefferle, L.D. (2012). *J. Phys. Chem. C* 116: 8587.
159 Ciuparu, D., Katsikis, N., and Pfefferle, L. (2001). *Appl. Catal., A* 216: 209.
160 Burch, R., Urbano, F.J., and Loader, P.K. (1995). *Appl. Catal., A* 123: 173.
161 Liu, Y., Wang, S., Sun, T. et al. (2012). *Appl. Catal., B* 119–120: 321.

162 Gao, D., Wang, S., Zhang, C. et al. (2008). *Chin. J. Catal.* 29: 1221.
163 Shi, C., Yang, L., and Cai, J. (2007). *Fuel* 86: 106.
164 Ribeiro, F.H., Chow, M., and Dallabetta, R.A. (1994). *J. Catal.* 146: 537.
165 Zhang, F., Hakanoglu, C., Hinojosa, J.A., and Weaver, J.F. (2013). *Surf. Sci.* 617: 249.
166 Serrano, D.P., Calleja, G., Botas, J.A., and Gutierrez, F. (2007). *J. Sep. Purif. Technol.* 54: 1.
167 Moreno, I., Dummer, N.F., Edwards, J.K. et al. (2013). *J. Catal. Sci. Technol.* 3: 2425.
168 Setiawan, A., Friggieri, J., Hosseiniamoli, H. et al. (2016). *Phys. Chem. Chem. Phys.* 18: 10528.
169 Lynggaard, H., Andreasen, A., Stegelmann, C., and Stoltze, P. (2004). *Prog. Surf. Sci.* 77: 71.
170 Jin, Z., Wang, L., Zuidema, E. et al. (2020). *Science* 367: 193.
171 Luo, H.Y., Lewis, J.D., and Román-Leshkov, Y. (2016). *Annu. Rev. Chem. Biomol. Eng.* 7: 663.
172 Caullet, P., Paillaud, J.-L., Simon-Masseron, A. et al. (2005). *C.R. Chim.* 8: 245.
173 Wang, B., Lin, M., Yang, J. et al. (2018). *Microporous Mesoporous Mater.* 266: 43.
174 Hutchings, G.J., Lee, D.F., and Minihan, A.R. (1996). *Catal. Lett.* 39: 83.
175 Hutchings, G.J., Lee, D.F., and Minihan, A.R. (1995). *Catal. Lett.* 33: 369.
176 Wróblewska, A. and Fajdek, A. (2010). *J. Hazard. Mater.* 179: 258.
177 Sulimov, A., Ovcharova, A., Ovcharov, A., and Sulimova, J. (2019). *Catal. Lett.* 149: 3076.
178 Sánchez, G., Friggieri, J., Keast, C. et al. (2014). *Appl. Catal., B* 152–153: 117.
179 Hansen, T.W., DeLaRiva, A.T., Challa, S.R., and Datye, A.K. (2013). *Acc. Chem. Res.* 46: 1720.
180 Rimer, J.D., Trofymluk, O., Navrotsky, A. et al. (2007). *Chem. Mater.* 19: 4189.
181 Liu, B. and Hu, X. (2020). Chapter 1: Hollow micro- and nanomaterials: synthesis and applications. In: *Advanced Nanomaterials for Pollutant Sensing and Environmental Catalysis* (ed. Q. Zhao), 1. Elsevier.
182 Hosseiniamoli, H., Bryant, G., Kennedy, E.M. et al. (2018). *ACS Catal.* 8: 5852.
183 Hosseiniamoli, H., Setiawan, A., Adesina, A.A. et al. (2020). *Catal. Sci. Technol.* 10: 1193.
184 Van Speybroeck, V., Hemelsoet, K., Joos, L. et al. (2015). *Chem. Soc. Rev.* 44: 7044.
185 Trinh, T.T., Jansen, A.P.J., van Santen, R.A., and Jan Meijer, E. (2009). *Phys. Chem. Chem. Phys.* 11: 5092.
186 Cutini, M., Civalleri, B., and Ugliengo, P. (2019). *ACS Omega* 4: 1838.
187 Martínez-Morales, E. and Zicovich-Wilson, C.M. (2011). *Catal. Sci. Technol.* 1: 868.
188 Sánchez, M., Díaz, R.D., Córdova, T. et al. (2015). *Microporous Mesoporous Mater.* 203: 91.
189 Trinh, T.T., Rozanska, X., Delbecq, F., and Sautet, P. (2012). *Phys. Chem. Chem. Phys.* 14: 3369.
190 Bjørgen, M., Akyalcin, S., Olsbye, U. et al. (2010). *J. Catal.* 275: 170.

10

Methanol to Hydrocarbons

Weili Dai, Liu Yang, Guangjun Wu, Naijia Guan, and Landong Li

Nankai University, National Institute for Advanced Materials, School of Materials Science and Engineering, 38 Tongyan Road, Tianjin 300350, P. R. China

10.1 Background Introduction

The methanol-to-hydrocarbon (MTH) process over acidic zeolite catalysts, first discovered by Mobil in the 1970s, has attracted extensive attention in recent years from both the academia and the industry, due to the fact that methanol can be widely produced from coal, natural gas, or biomass [1–13]. As a typical acid-catalyzed reaction, methanol is first dehydrated to dimethyl ether (DME) at Brønsted acid sites (BASs). The equilibrium mixture of methanol, DME, and water is then converted to hydrocarbons. Depending on the catalyst and/or the reaction conditions, the MTH processes can be classified as methanol-to-gasoline (MTG), methanol-to-olefin (MTO), and methanol-to-aromatic (MTA) subtitles (Scheme 10.1). Among the aforementioned MTH processes, MTG was the first commercialized in New Zealand in 1985 [14, 15]. In addition, MTO processes including the SAPO-34-based hydro/UOP's MTO [16] and DICP (Dalian Institute of Chemical Physics) -MTO (DMTO) [17] and Lurgi's ZSM-5-based methanol-to-propene (MTP) process [18] have been successfully applied in industry.

The second step shown in Scheme 10.1, which represents the formation of the initial C—C bond and the subsequent hydrocarbons from the methanol molecules, has been an interesting topic in the C1 chemistry in the past decades [1–10]. There have been many debates regarding two aspects of the chemistry: (i) the formation of the first C—C bond and (ii) the subsequent reaction pathway of hydrocarbon formation. For the former, although several earlier direct routes, e.g. carbenes, free radicals, oxonium ylides, and methane–formaldehyde (FA) mechanisms, have been proposed via the direct coupling of two C1 species, they are heavily disputed problems because of the lack of experimental evidence and the higher activation energy barrier required [1, 8]. While for the latter, the indirect hydrocarbon pool (HCP) mechanism first proposed by Kolboe and Dahl has been widely accepted [5, 19]. In comparison with the former direct route, the HCP route is more favored for the MTH conversion due to the relatively lower activation barrier [7, 20]. On the basis

Heterogeneous Catalysis for Sustainable Energy, First Edition. Edited by Landong Li and Justin S. J. Hargreaves.

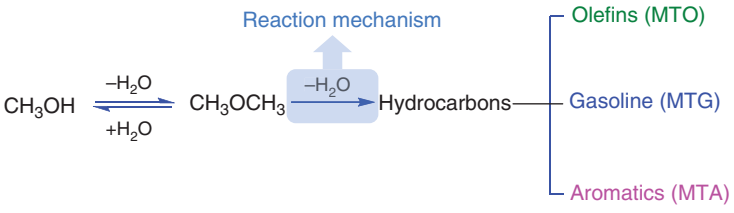

Scheme 10.1 The reaction scheme of the MTH conversion over solid acidic catalysts.

of the HCP mechanism, a modified dual-cycle mechanism involving one catalytic cycle with long olefins as intermediates and another cycle with aromatic intermediates has been proposed, and its role in controlling the product distribution is now well understood [5]. With the progress of the MTH conversion, the large compounds in the latter aromatic-based cycle, namely, polymethylbenzenes, even the polycyclic aromatics, can be rapidly formed and gradually cover the acid sites or block the zeolite cages/channels, thus causing catalytic deactivation eventually.

With the development of the spectroscopic techniques and the in-depth understanding of the reaction mechanism, interest in the direct mechanism during the initial stage of the MTH conversion has been sparked again, and several groups have provided both experimental and theoretical evidence in supporting the direct mechanism of first C—C bond formation [21–33]. With the aid of a combination between sophisticated solid-state nuclear magnetic resonance (ssNMR) technique and theoretical simulation calculation, the gap between direct and indirect mechanisms and the roadmap of the MTH conversion has been recently clarified. In this chapter, the breakthroughs that have been achieved in the reaction mechanism understanding, and high-efficiency catalyst design will be focused upon. Several key achievements in the direct mechanism of the first C—C bond formation and the stepwise roadmap of the MTH conversion will be discussed. The current challenges in the fields of academia and industry for MTH conversion and the future research directions will also be highlighted.

10.2 The Direct Mechanism for MTH Reaction

The MTH process can be divided into three time periods, namely, the induction period, the steady-state period, and the deactivation period (Figure 10.1). The induction period associated with the formation of the first C—C bond and hydrocarbons from the methanol molecules has been an interesting topic of extensive discussion in the field of C1 chemistry in the past decades. There have been many debates regarding two aspects of the chemistry: (i) the origin of the first C—C bond and (ii) the reaction mechanism of MTH conversion.

10.2.1 The Development and Milestones of the Direct Mechanism

The key problem that has puzzled researchers in the initial period of MTH conversion is the formation of the initial C—C bond. More than 20 possible mechanisms

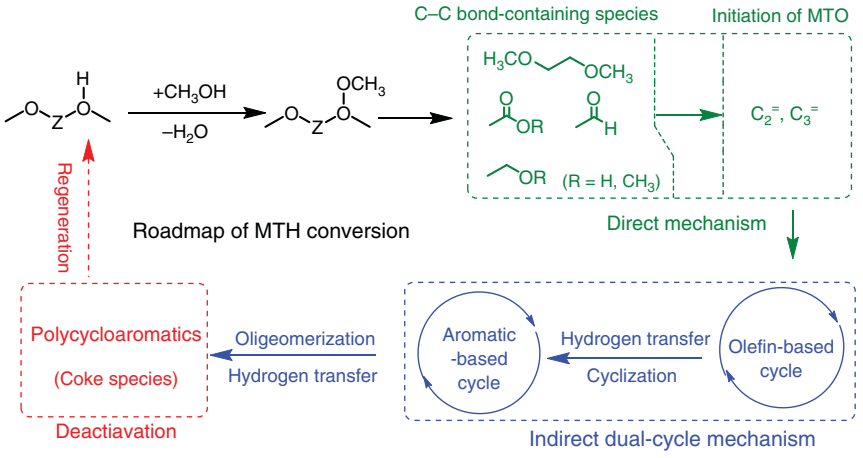

Figure 10.1 A simplified scheme of the MTH process containing the induction period, the steady-state period, and the deactivation period.

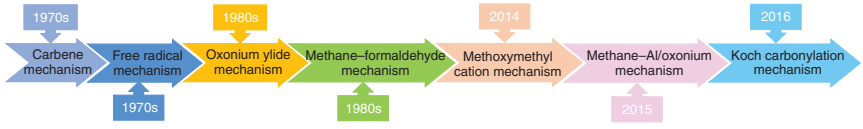

Figure 10.2 The development of direct mechanism in the MTH process in the past 40 years.

have been proposed in the past 40 years on the basis of a variety of the active intermediates such as carbenes [34–36], free radicals [37, 38], oxonium ylides [39, 40], and methane–FA [40, 41] (Figure 10.2). However, most of the aforementioned routes proposed before either lack experimental evidence or have a high energy barrier [42–46]. In 2006, Hunger and coworkers identified the reactivity of surface methoxy species (SMS) on solid acids and proposed that organic impurities had no impact on the MTH conversion [22, 23], which sparked the interest in the direct mechanism during the initial stage of the MTH conversion again [10]. In the past decade, many research groups have provided both experimental and theoretical evidence in supporting the direct mechanism of first C—C bond formation (Figure 10.3).

10.2.2 The First C—C Bond Formation

The carbene mechanism [34, 47] was proposed for the explanation of the formation of the first C—C bond in the 1970s. The carbene species, which was formed either by the dehydration of methanol through the α-elimination reaction or through the decomposition of surface methoxyl species over the acid active site, could react one by one to form olefins. However, the theoretical results indicated that the formation of carbene species had high energy barriers under real MTO reaction conditions. The free radical mechanism was proposed in the 1980s [37, 38, 47]. For instance, Rooney and coworkers have monitored the participation of the free radicals by

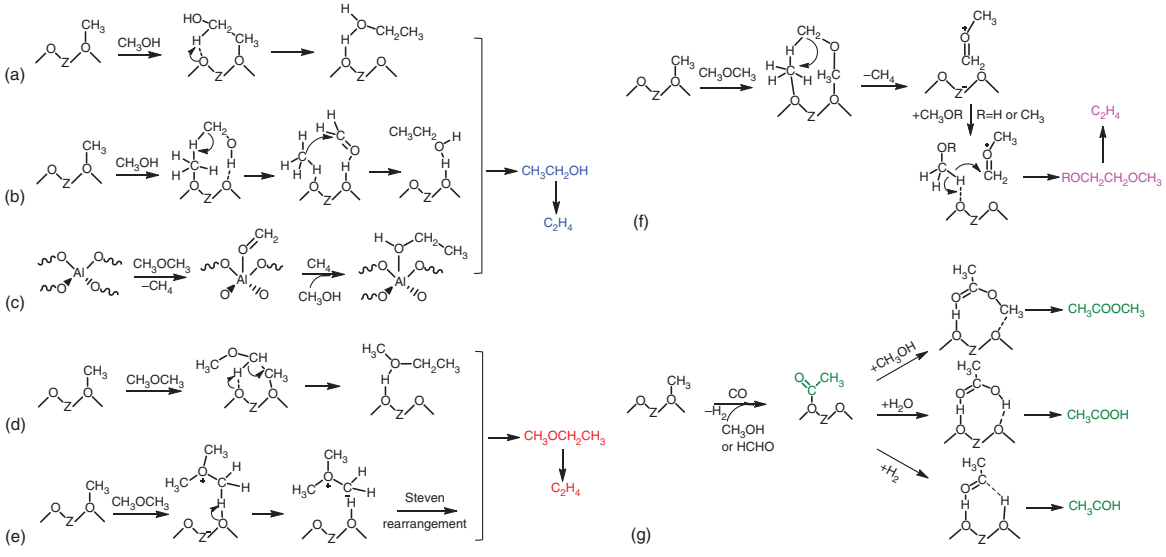

Figure 10.3 Several proposed direct reaction mechanisms for the MTH conversion over acidic zeolite catalysts.

electron paramagnetic resonance (ESR) spectroscopy during MTH conversion [38]. Clarke et al. found that the DME could react on the paramagnetic center in the zeolite to form free radicals, which could participate in the direct coupling to produce the C—C bond. However, this mechanism has not been recognized due to the limitation of characterization techniques. In the 1980s, the oxonium-ylide mechanism [39, 48] was proposed and had attracted extensive attention both in academic and industrial fields. In this mechanism, two important intermediates, i.e. trimethyloxonium ions (TMO) and dimethyl oxonium methyl ylide (DOMY), were involved. Berg et al. proposed that DME interacted with BAS to form dimethyl oxonium ions (DMO), which further reacted with another DME molecule to form TMO being subsequently deprotonated by the basic site of zeolite (ZO^-) to form DOMY. The species then transformed into methyl ethyl ether (MEE) or ethyl dimethyl oxonium ion (EDMO) via an intramolecular Stevens rearrangement or intermolecular CH_3 transfer, followed by ethene formation [49, 50].

Apart from the aforementioned direct mechanisms, methane–FA direct mechanisms have been proposed. The original methane–FA mechanism was proposed by Hutchings et al. in 1987 [40]. Recently, several similar mechanisms have been proposed (Figure 10.3), such as the energetically feasible methoxymethyl cation mechanism proposed by Fan and coworkers [25, 51]. Two intermediates are involved in this direct mechanism: (i) the methoxymethyl cation formed between SMS and DME and (ii) $CH_3OCH_2CH_2OR$ (R = H, CH_3) formed from the C–C coupling between the methoxymethyl cation and another DME/methanol molecule. Very recently, a similar methyleneoxy mechanism was proposed by Liu and coworkers, according to *in situ* ssNMR spectroscopy [32]. Three signals at 59.5, 69.0, and 80 ppm attributed to the SMS, surface-adsorbed DME, and TMO, respectively, could be observed in the initial period of MTO conversion (Figure 10.4). Simultaneously, small amounts of ethene and hydrocarbons were determined by gas chromatography–mass spectrometry (GC–MS) and ^{13}C magic angle spinning (MAS) nuclear magnetic resonance (NMR) spectroscopy. Accordingly, a direct C—C bond mechanism associated with the interaction between methanol/DME and SMS or TMO was proposed. An active methyleneoxy analog species (CH_3–O–CH_2–H–ZO) was formed via the C—H bond activation and eventually could result in the formation of olefins and methane/FA. These spectroscopic observations gave direct evidence on the formation of the first C—C bond, while the roles of methane and FA in the process of the initial C—C bond formation was not clarified. Very recently, Liu and coworkers also found the highly reactive ethene precursor, surface ethoxy species, under a real MTH reaction via *in situ* ^{13}C MAS NMR and described the complete initial C—C bond formation pathways of SMS/TMO-mediated methanol/DME conversion to olefin products [52, 53].

Very recently, Lercher and coworkers proposed the concept of the carbonylation of methoxy groups to form the acetate species in the explanation of the first C—C bond formation during the MTO conversion [28]. In this proposal, CO, as the nucleophilic carbon source, could react with the SMS (electrophilic carbon source) through the nucleophilic addition reaction to form a surface acetyl group, which subsequently dissociated into the acetate acid and methyl acetate (MA) species with the presence

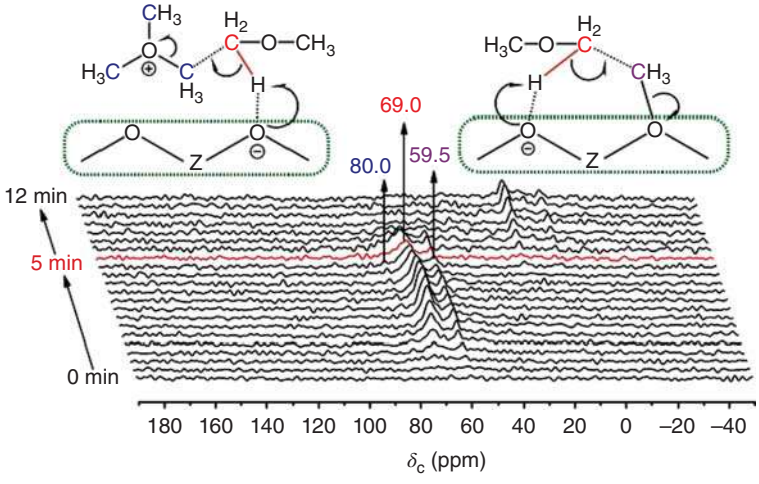

Figure 10.4 *In situ* solid-state ^{13}C MAS NMR spectra recorded during ^{13}C-methanol conversion over H–ZSM-5 at 573 K. The spectra were recorded every 20 seconds from 0 to 5 minutes and then every 60 seconds from 5 to 12 minutes. Source: Reproduced with permission from Wu et al. [32]; © 2017, Wiley-VCH.

of water and methanol, respectively. The formation of the initial C—C bond in this carbonylation mechanism had an energy barrier of 80 kJ mol^{-1}, significantly lower than the barriers of the earlier proposed direct mechanism.

Almost simultaneously, Weckhuysen and coworkers proposed the carbonylation mechanism and provided the direct spectroscopy evidence for the formation of the intermediates containing the initial C—C bond over H–SAPO-34 during the MTO process via a combination of ssNMR spectroscopy and *operando* ultraviolet–visible diffuse reflectance spectroscopy (UV–vis DRS) and online mass spectrometry [29]. Three responsible intermediates involving in the carbonylation mechanism, i.e. SMS (57.7 ppm), zeolite-bound acetate species (180.5 ppm), and MA (178.5 ppm), were identified via the 2D ^{13}C–^{13}C and ^{13}C–^{1}H NMR spectroscopies (Figure 10.5). Interestingly, besides the Koch carbonylation mechanism, the carbene route was also identified simultaneously.

Li and coworkers also identified the formation of acetaldehyde containing the C—C bond based on the surface-bound acetyl species during the MTH conversion on zeolite H–ZSM-5 via the combination of kinetic studies, spectroscopic analyses, and theoretical calculations [54]. The stepwise involvement of SMS, CO, and H_2 in the acetaldehyde formation was then confirmed by online MS and ^{13}C MAS NMR spectroscopy. That is, on the BASs of H–ZSM-5 zeolite, surface acetyl groups (181 ppm) are formed via carbonylation of SMS (58 ppm) and CO first and then transformed and dissociated into acetaldehyde (207 ppm) via hydrogenation (Figure 10.6). In addition, they proposed that the acetyl motif (CH_3CO^+) could be formed between acetaldehyde and methanol at the BAS of zeolites. The overall Gibbs free energies of the formation of acetyl motif from CO, MA, and acetaldehyde are 139, 127, and 152 kJ mol^{-1}, respectively, and the formation of acetaldehyde

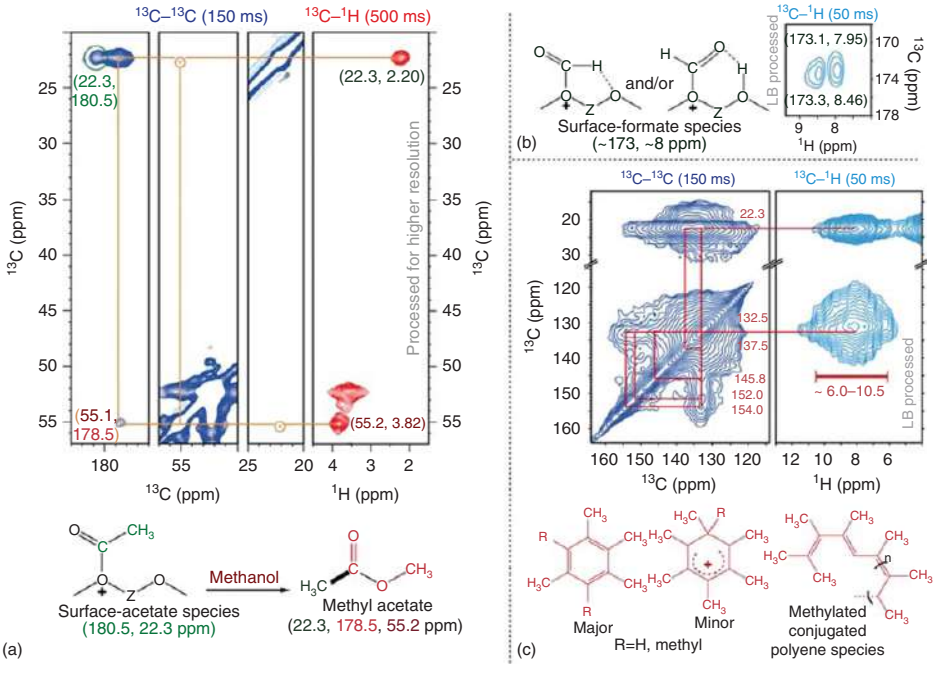

Figure 10.5 Solid-state NMR correlations of acetate, formate, and methylated polyene/benzene in H–SAPO-34 after the methanol-to-olefin (MTO) reaction for 30 minutes at 673 K. (a) Zooms from 2D $^{13}C–^{13}C$ (blue) and $^{13}C–^{1}H$ (red) MAS ssNMR spectra with long mixing (150 ms) or CP contact time (500 ms), respectively, indicating surface acetate and methyl acetate resonances. (b) ssNMR signals of surface-bound formate in the $^{13}C–^{1}H$ spectra (light blue) with a short CP contact time (50 ms). (c) Zoom of aromatic signals from 2D $^{13}C–^{13}C$ (blue) and $^{13}C–^{1}H$ (light blue) MAS NMR spectra with long mixing (150 ms) or short CP contact time (50 ms), respectively. Source: Reproduced with permission from Chowdhury et al. [29]; © 2016, Wiley-VCH.

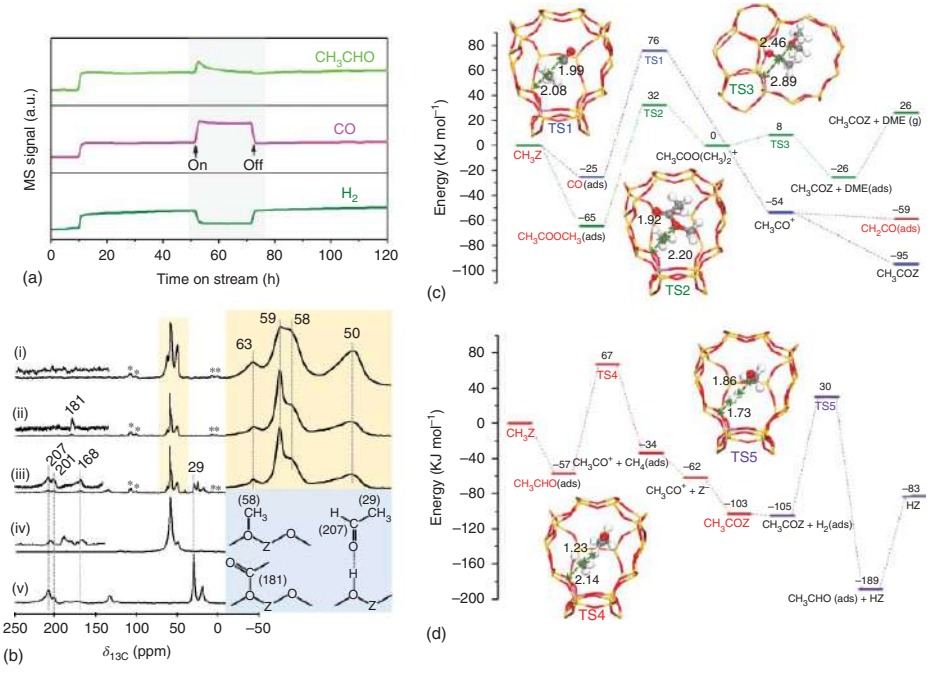

Figure 10.6 (a) Online MS monitoring of acetaldehyde, CO, and H_2 during the co-feeding of CO in methanol conversion at 523 K. (b) ^{13}C CP MAS NMR spectra of selected samples: (i) methylated H–ZSM-5 zeolite, (ii) after loading of 50 mbar ^{13}CO at 473 K for 5 minutes, (iii) of 50 mbar ^{13}CO and 50 mbar H_2 at 473 K for 5 minutes, (iv) zeolite H–ZSM-5 after methanol conversion at 523 K for 5 minutes, and (v) zeolite H–ZSM-5 loaded with 50 mbar $CH_3{}^{13}CHO$ at room temperature for 5 minutes. (c) Energy diagram at 0 K and the key transition state structures of the formation of ketene from CO and methyl acetate (CH_3COOCH_3) (d) and the key transition state structures of the evolution and formation of acetaldehyde related to the induction period of the MTH conversion in H–ZSM-5. Source: Reproduced with permission from Yang et al. [54]; © 2019, American Chemical Society.

via the hydrogenation of acetyl motif is 156 kJ mol^{-1}. All these density functional theory (DFT) calculations implied that although acetaldehyde may be slightly less reactive than MA in the case of the evolution and formation kinetics in H–ZSM-5, it could also act as stable neutral initial C—C bond species to trigger the MTH conversion via acetyl species at the BAS of zeolites.

Copéret and co-workers proposed an interesting concept that the formation of the first C—C bond could be catalyzed by extra-framework aluminum (EFAL) species in acidic zeolites [26]. In this route, a transient aluminum–oxonium species, i.e. formaldehydic oxygen coordinated to Lewis acidic aluminum, was involved in the C—C bond formation via the hydrogen abstraction from an aluminum-methoxy species. Thereafter, the aluminum–oxonium species could react with a methane molecule and generate the surface ethanolic species, which was the precursor for ethylene formation. Very recently, Wu et al. identified the surface methoxy species bound to an extra-framework aluminum (SMS-EFAL) by an advanced ^{13}C–{^{27}Al} double-resonance ssNMR technique in the MTO reaction on H–ZSM-5 zeolite [32]. The high reactivity of the SMS-EFAL led to the formation of surface ethoxy species and ethanol as the key intermediates. Based on these experimental results, a direct ethene formation route was proposed and verified by DFT calculations.

The aforementioned Koch carbonylation mechanism of the MTH reaction was recently theoretically verified by Plessow and Studt [30]. According to the theoretical calculations, this mechanism could be divided into two parts: (i) oxidation of MeOH (or DME) via FA to CO and (ii) formation of the first C—C bond through reaction of CO with MeOH to MA. Further methylation via ketenes produced ethylene, propene, and isobutene via decarbonylation of methyl esters R–CO_2–OMe with R = Et, *i*Pr, *t*Bu (Figure 10.7). Additionally, the activation barriers of the important elementary reaction steps were similar on the above four zeolites, and the order of activation barrier was found to be H–ZSM-5 < H–SSZ-13 < H–BEA < H–SAPO-34. The deviation between the most and least reactive zeolites was less than 40 kJ mol^{-1}. Thus, it was concluded that the initiation mechanism of MTO reaction on the all kinds of zeolites was probably the same at high reaction temperatures [31].

10.3 The Indirect Reaction Mechanism for MTH Reaction

10.3.1 Hydrocarbon Pool Mechanism

The autocatalytic process in the MTH reaction indicates that the presence of C—C bond-containing species can act as the active sites and enhance the reaction rate, until reaching steady state. Accordingly, an induction period is often observed [21, 55], demonstrating that methanol conversion increases with the increase of reaction time during the initial period of the MTH conversion. Dessau and LaPierre proposed an indirect reaction model on the basis of consecutive methylation and cracking [56, 57]. Once the alkenes were formed in the initial period of MTH conversion, higher alkenes would also be generated via the routes of alkene methylation,

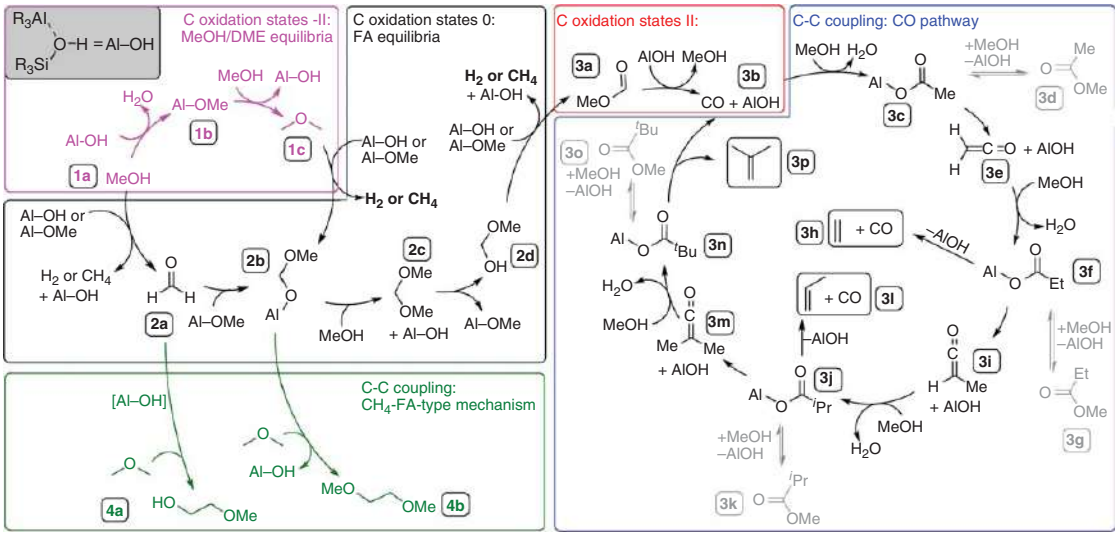

Figure 10.7 Overview of the most relevant initiation mechanisms of the MTO reaction. Al–OH and Al–OMe are used to abbreviate bridging hydroxyl and methoxy groups (for example, Al–OH–Si). Mechanisms are grouped into boxes according to the oxidation state of carbon. Formation of the surface methoxy group is shown explicitly only for the reaction 1a → 1b and is omitted for clarity in all subsequent reactions since it is not rate limiting. In the reaction of 3f to 3h, the intermediate formation of Al–OEt is omitted. Source: Reproduced with permission from Plessow and Studt [30]; © 2017, American Chemical Society.

oligomerization, and cracking. Finally, aromatics would be formed via the cyclization and hydrogen transfer reactions. Mole et al. found that the co-feeding of small amounts of toluene or *p*-xylene could greatly enhance methanol conversion and accordingly proposed aromatic co-catalysis in MTH reaction [58, 59].

Dahl and Kolboe later found that ethene and propene displayed little reactivity after co-feeding with methanol over H–SAPO-34 using isotopic labeling experiments. Based on this, the HCP mechanism was proposed (Figure 10.8) [60–62]. The HCP, with an initially specified overall stoichiometry $(CH_2)_n$, represented an adsorbate that might have many characteristics in common with ordinary coke. However, the chemical structure of the pool was not further specified.

To make a better understanding of the nature of the HCP species and their formation process and their further transformation, plentiful experimental and theoretical studies have been performed subsequently. Guisnet and coworkers developed a method to analyze the organic compounds occluded in zeolite catalysts [63]. After dissolving the spent zeolite catalysts in hydrofluoric acid (HF) solution, the occluded organic species were extracted by CH_2Cl_2 solvent, which could be qualitatively and quantitatively determined by GC–MS. Arstad and Kolboe studied the stability of organic species trapped within the cages of SAPO-34 zeolite during the MTO conversion and found that methylbenzenes were the key active HCP species [64, 65]. In a parallel study, Haw and coworkers identified methylbenzene species as the active organic reaction centers in the MTO conversion over SAPO-34 zeolite catalyst, utilizing ^{13}C cross-polarization (CP) MAS NMR. With the aid of ^{13}C MAS NMR spectroscopy, Haw and coworkers also captured pentamethylbenzenium cation over H–ZSM-5 zeolite and heptamethylbenzenium cation [66, 67] over H–Beta zeolite by co-feeding excess methanol and benzene in the MTH conversion. Bjørgen et al. studied the reactivity of polymethylbenzenes over H–Beta zeolite and identified the heptamethylbenzenium cation acting as a key intermediate in MTH conversion [68–71]. Parallel studies by Liu and coworkers detected the heptamethylbenzenium cation ($heptaMB^+$) and deprotonated heptamethylmethylenecyclohexadiene (HMMC) in the DNL-6 zeolite catalyst, a SAPO-type zeolite with larger pore cages and higher acidity than SAPO-34, via ^{13}C MAS NMR and GC–MS [72]. The representative HCP species observed in the MTH conversion over the zeolites with different topologies are summarized in Table 10.1.

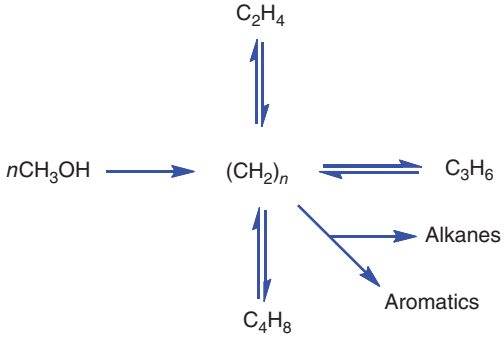

Figure 10.8 Proposed HCP mechanism. Source: Reproduced with permission from Dahl and Kolboe [60]; © 1994, Elsevier.

Table 10.1 The representative HCP species observed in the MTH conversion over the zeolites with different topologies.

Topology	CHA	MFI	BEA	RHO	TON
Cage/pore size (nm)	0.67 × 1.0	0.53 × 0.56	0.73 × 0.64	1.14 × 1.14	0.57 × 0.46
Zeolites	SSZ-13 SAPO-34	ZSM-5	H–Beta	DNL-6	H–ZSM-22
Channel structure	3D 8-ring	3D 10-ring	3D 12-ring	3D 8-ring	1D 10-ring
HCP species	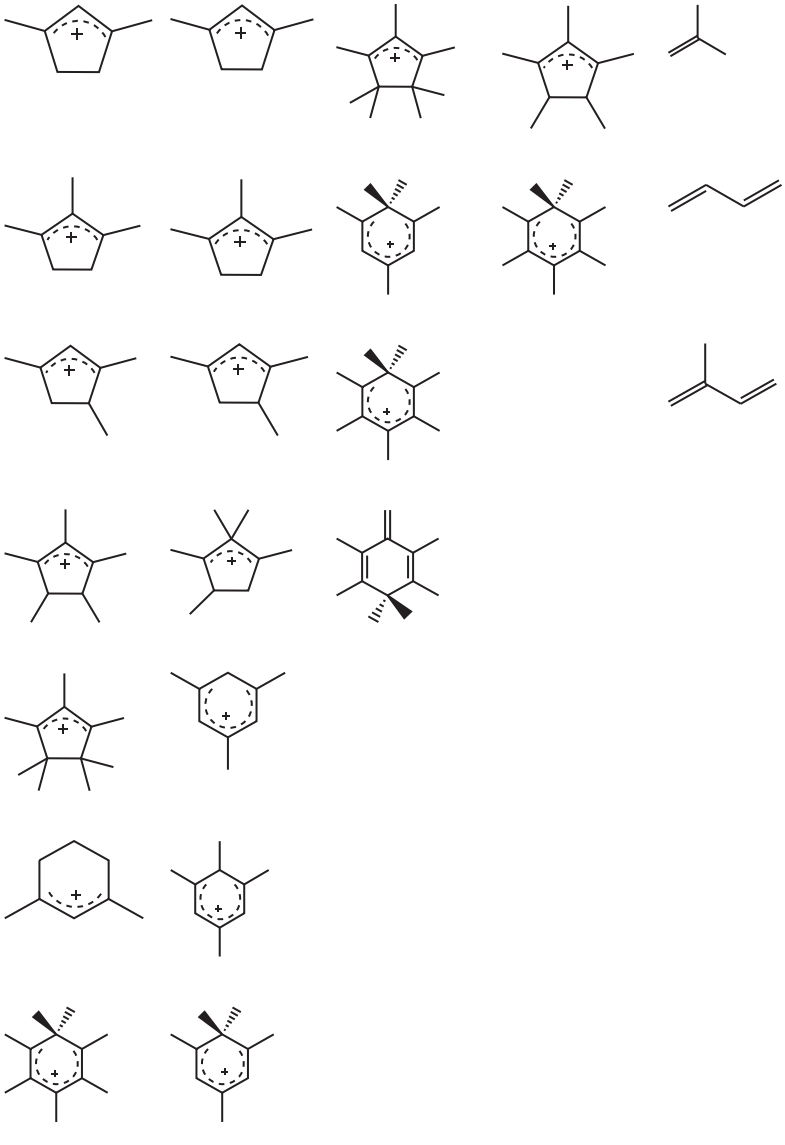				

The aforementioned results clearly indicate that polymethylbenzenes and their protonated counterparts are active intermediates for olefin formation in the MTH conversion. However, the mechanism of alkene formation on zeolite catalyst is still unclear. Two different hypotheses have been proposed, namely, the (i) side-chain methylation mechanism and (ii) paring mechanism (Figure 10.9). The paring mechanism was first proposed by Sullivan et al. to rationalize the high selectivity to isobutane in hexamethylbenzene conversion over nickel sulfide on silica–alumina [74]. The formation of the cyclopentenyl cation during this reaction was an important step. Sekiguchi and coworkers provided the direct evidence of paring mechanism in the unimolecular decomposition of protonated methylbenzenes, utilizing mass spectrometry [75, 76]. Xu and Haw first provided ssNMR evidence for the formation of the aforementioned species upon feeding cyclopentene over H–ZSM-5 zeolite [77]. Additional IR and NMR spectroscopic investigations verified the formation of persistent cyclopentenyl cations over various acid zeolites [78–81]. In addition, Haw et al. found that the presence of cyclopentenyl cations in H–ZSM-5 zeolite could completely eliminate the induction period of DME conversion [82]. These results clearly indicated the high reactivity of cyclopentenyl species in MTH conversion, but could not directly prove the paring mechanism. Later, Bjørgen et al. observed that a majority of propene and isobutane molecules contained only one ^{12}C atom after co-feeding ^{13}C-enriched methanol with ^{12}C-benzene at low temperatures of 523–543 K over H–Beta zeolite [69]. Additionally, only one aromatic ring carbon was incorporated into these products, supporting strongly the paring mechanism for olefin formation.

The alkylbenzenes with methyl, ethyl, propyl, or other alkyl groups are the key intermediates to identify the side-chain methylation mechanism. Haw and

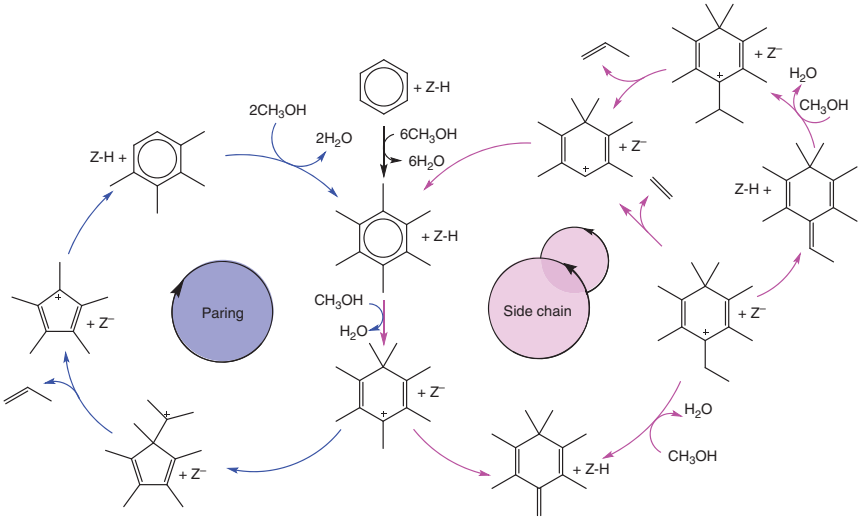

Figure 10.9 Representation of the paring and side-chain reaction concepts in MTH catalysis. Source: Reproduced with permission from Lesthaeghe et al. [73]; © 2009, Wiley-VCH.

coworkers found that significant amounts of ethene and propene could be formed after the co-reaction of ^{13}C-enriched methanol with ethylbenzene and cumene at 623 K over H–Beta zeolite [83]. Ethylbenzene alone was not reactive, while cumene alone could generate propene. In addition, with the presence of methanol, ethylbenzene and cumene were both active for olefin elimination, clearly indicating that aromatic methylation could facilitate olefin elimination. Hunger and coworkers also provided additional spectroscopic evidence for side-chain methylation over H–ZSM-5 zeolite catalysts [84–87]. Liu and coworkers [72] performed $^{12}C/^{13}C$ methanol transient switch experiments and suggested that the side-chain methylation mechanism was the major reaction route for the formation of the olefins during the MTO reaction over DNL-6 zeolite. Speybroeck and coworkers [73] suggested that side-chain methylation route occurred relatively easily in H–ZSM-5 through theoretical calculations. These results provided direct evidence that the side-chain methylation mechanism was a possible route for olefin formation from methylbenzenes (Figure 10.9).

10.3.2 Dual-Cycle Mechanism

In addition to the aforementioned aromatics and unsaturated cyclic organic species and their protonated counterparts, alkenes and the corresponding carbocations may act as another kind of active HCP species to promote the MTO reaction. Ono and Mori [88] performed ethylene and *cis*-2-butene co-feeding experiments during the MTO conversion over H–ZSM-5 at 512 K and found that both ethylene and *cis*-2-butene could significantly reduce the induction period of MTO conversion, while *cis*-2-butene showed a better effect than ethylene. Later, Dessau and LaPierre [56, 57] proposed the alkene methylation and cracking route for the first time, where alkene could be gradually methylated to long-chain alkenes by methanol or DME and subsequently cracked into light olefins. Afterward, Svelle et al. [89, 90] performed $^{12}C/^{13}C$ isotopic switch experiments and found that ^{13}C incorporation of ethene closely matched that of methylbenzenes and the ^{13}C incorporation of C_3^+ alkenes matched each other. Based on these results, a new mechanism of MTO conversion, namely, the dual-cycle mechanism, was proposed (Figure 10.10). One cycle was the olefin-based cycle, where olefins could be methylated with methanol to form the higher alkenes and subsequently be cracked into lower olefins. The other was the aromatic-based cycle, where olefins could be produced from aromatics through the paring or side-chain methylation route. In addition, the dual-cycle mechanism indicated that ethene (and propene) was formed from the lower methylbenzenes followed by re-methylation, while only the C_3^+ alkenes (not ethene) were involved in methylation/cracking.

The emergence of the dual-cycle mechanism has contributed significantly to the general understanding of the HCP mechanism. A very interesting question regarding the mechanistic understanding is highlighted since the dual-cycle concept was introduced: Can the two cycles of the dual-cycle mechanism operate completely independently, or are they intertwined in some manner [5]?

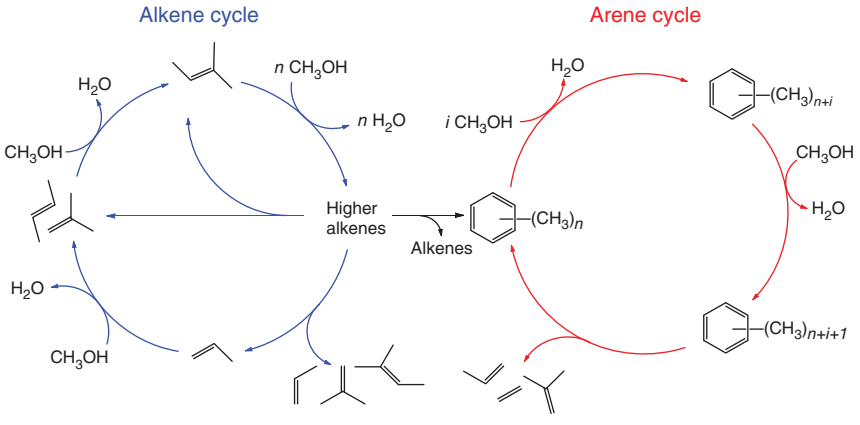

Figure 10.10 Proposed dual-cycle mode for the conversion of methanol to olefins. Source: Reproduced with permission from Olsbye et al. [5]; © 2012 Wiley-VCH.

Considering that olefins and aromatics can simultaneously exist in zeolite pores, the corresponding olefin- and aromatic-based cycles should operate in a competitive relationship. It was found that the topological structure of the zeolite catalyst had a great influence on the proportion of dual-cycle mechanism in the MTH conversion. Recently, it was indicated that the aromatic-based cycle could be suppressed in H–ZSM-22 zeolites with one-dimensional 10-ring pores (0.57 nm × 0.46 nm), and higher alkenes were detected as the main products [91–93]. In contrast, for H–ZSM5 zeolites with two-dimensional 10-ring pores (0.51 nm × 0.55 nm and 0.53 nm × 0.56 nm), the two reaction cycles were not isolated from one another and both contributed to MTH conversion [94]. Interestingly, Ahn et al. [95] and Simonetti et al. [96] indicated that the olefin-based cycle could be selectively favored over the aromatic-based cycle by altering the reaction conditions in H–Beta zeolites with 12-ring pores. Recent theoretical studies of Wang et al. demonstrated that olefins themselves were likely to be the dominant HCP species in the SAPO-34 zeolite [97]. A recent study of Li and coworkers also indicated that the olefin-based cycle was the dominant reaction mechanism during the initial stages of the MTO conversion over SAPO-34 zeolite [98]. However, with the rapid formation of aromatics, the aromatic-based cycle might start to participate in the steady state of the MTO conversion. Bhan and coworkers extended the dual-cycle mechanism over SAPO-34 via isotopic tracer studies [99]. Additionally, the olefin-based cycle was reported as the dominant mechanism during the early stages of MTO conversion over SAPO-41 and SAPO-5 with one-dimensional pores and weak BASs [100–102].

As is well known, MTH conversion is an acid-catalyzed reaction. That is, BASs play a key role as catalytically active sites in this process [103]. On the one side, the initial intermediates in the olefin-based cycle, e.g. alkenes, carbenium ions, and even the dienes, can be formed at the BASs of the zeolite catalysts during the early stages of MTO conversion. On the other side, the large compounds in the aromatic-based cycle, namely, polymethylbenzene, even the polycyclic aromatics, can also be rapidly formed at the BASs, which can lead to deactivation of MTO catalysts eventually.

Therefore, it is expected that the density of BASs should have an influence on the dual-cycle mechanism. Li and coworkers [104] investigated the role of the Brønsted acid density of AlPO-34 zeolite in the dual-cycle mechanism during the MTO conversion via several spectroscopy methods. It was found that the olefin-based cycle was the primary mechanism over AlPO-34 zeolite with very low Brønsted density, and the dominant active intermediates were C5–C6 alkenes. With the increase of Brønsted acid density, an obvious increase of aromatic species could be monitored by *in situ* UV–vis spectroscopy; the aromatic-based cycle was the dominant reaction mechanism, and a rapid transfer between C5–C6 alkenes and polymethylbenzenes could be observed. In parallel, Liu and coworkers [105] detailed the olefin-based mechanism in the MTO reaction over SAPO-18 and AlPO-18 zeolites possessing the same framework but with different Brønsted acid density. It was found that the aromatic-based mechanism was the dominant cycle over SAPO-18 zeolite, where pentaMCP$^+$ and polymethylbenzenes could be observed as the active HCP species. In contrast, the aforementioned active intermediates were absent in AlPO-18 zeolites with very low amounts of BASs, and thus the olefin-based mechanism was responsible for the olefin formation. Olsbye and coworkers [102, 106] also compared the MTH reaction over SAPO-5 and H–SSZ-24 zeolites with the same structure but different acid strength and found that the lower acid strength of H–SAPO-5 was beneficial to the olefin-based cycle, while for H–SSZ-24 zeolite with higher acid strength, the aromatic-based cycle was the dominant mechanism. Recently, Goetze and Weckhuysen [107] compared the catalytic behavior of Mg–ZSM-5 with conventional H–ZSM-5 during MTO conversion. It was found that the MTO reaction on Mg–ZSM-5 with fewer BASs exhibited a higher selectivity to C3$^+$ olefins and a longer catalyst lifetime but a lower selectivity to ethene and aromatic species. These results obviously verified that the decrease of BASs could suppress the aromatic-based cycle and, accordingly, promote the olefin-based cycle during the MTO reaction.

Furthermore, reaction temperature has been identified as an important factor influencing the dual-cycle mechanism of MTH conversion. At high reaction temperatures, the cracking of long-chain alkenes can easily take place instead of the cyclization, and it is more beneficial to the olefin-based cycle mechanism [10]. Lercher and coworkers [108] proposed that toluene methylation would play a great role in the MTO conversion at low reaction temperatures and thus the aromatic-based cycle mechanism would be the dominant mechanism. In contrast, alkenes could act as the active intermediates at high reaction temperatures, and consequently the olefin-based cycle mechanism played the key role. In addition, co-feeding the reaction reagents in the MTO conversion can influence the dual-cycle mechanism. Interestingly, recent studies from Lercher and coworkers indicated that the co-feeding of olefins or higher alcohols with methanol resulted in remarkable longer catalyst lifetime in MTO conversion. This is because the high methylation rate competed with the formation of more deactivating coke compounds [108]. Li and coworkers [109] also investigated the effect of *n*-butanol co-feeding on MTA conversion over Ga/H–ZSM-5 zeolite and found that the addition of *n*-butanol during the MTA conversion showed no impact on the deactivation mechanism

but could influence the dual-cycle mechanism, namely, *n*-butanol preferentially adsorbed on BASs over methanol, followed by dehydration to *n*-butene. The formed *n*-butene could directly participate in the olefin-based cycle and, therefore, significantly alter the proportions of the dual-cycle mechanism.

10.3.3 The Connection Between the Dual Cycles

According to the dual-cycle mechanism as shown in Figure 10.10, the two cycles are not isolated from one another. The light olefins produced by the dealkylation of the polymethylbenzenes can participate in the olefin-based cycle. On the other side, the long-chain alkenes formed from the alkene methylation can be converted to aromatics via the cyclization and the hydrogen transfer reaction, thus promoting the aromatic-based cycle. This process can be strongly proved by co-feeding experiments. Wang and coworkers [110] performed alkene (ethylene, propene, and butene) co-feeding experiments during the MTO conversion over SAPO-34 zeolite and found that the co-fed alkenes could quickly enhance the formation of the aromatics, thus greatly shortening the induction period. Deng and coworkers [111] demonstrated that cyclopentadiene formed by deprotonation of cyclopentenyl carbenium ion could be rapidly converted to aromatics via the methylation reaction. In a similar manner, Schmal and coworkers [112, 113] investigated alkenes (such as isoprene, 1,3-butadiene, cyclopentene, and isobutene) over H–ZSM-5 zeolite and found that all of these alkenes could be transformed to aromatics (benzene, toluene, and C8 and C9 aromatics) over H–ZSM-5 with strong acid sites.

The two cycles also present a competitive relationship in MTO conversion. Lercher and coworkers [114] explored the impacts of aromatics (benzene, toluene, and xylene) and alkenes (ethene, propene, 1-butene, 1-pentene, and 1-hexene) on the MTO reaction over H–ZSM-5 under industrial reaction conditions. It was found that the aromatic-based cycle could be significantly enhanced after co-feeding a few amounts of aromatics, while the olefin-based cycle was obviously suppressed simultaneously, thus leading to the higher methane, ethene formation, and aromatics methylation at the expense of $C3^+$ olefins. In contrast, co-feeding small amounts of C3–C6 alkenes did not selectively suppress the aromatic-based cycle, resulting in the unchanged selectivities to ethene and higher olefins ($C3^+$). In parallel, Ilias and Bhan [94] performed the co-feeding experiment of aromatics (^{13}C-propene, ^{13}C-toluene with ^{12}C-DME) over H–ZSM-5 under sub-conversion conditions (20.8–22.7%) at 548 K. The co-reaction of ^{13}C-propene with ^{12}C-DME showed that C5–C7 olefins were formed almost exclusively from methylation reactions, while butenes were formed from both olefin cracking and methylation reactions. Under the conditions in which the aromatic-based cycle was dominant (increasing amounts of toluene in the co-feeding), both ethene and propene contained approximately 10% ^{13}C atoms, showing that these light olefins primarily originated from the aromatic-based cycle when the olefin-based cycle was suppressed.

The aforementioned results clearly indicated the presence of the dual-cycle mechanism and its connection in MTH conversion via the indirect co-feeding

experiments while the direct spectroscopic evidence for the dual-cycle mechanism was still missing. Li and coworkers [98] investigated the formation and evolution of carbenium ions during the early stages of MTO conversion on the H–SAPO-34 model catalyst via ^{1}H MAS NMR and ^{13}C MAS NMR spectroscopies combined with theoretical calculations. For the first time, direct experimental evidence for the dual-cycle mechanism was given (Figure 10.11). Some key initial species, e.g. three-ring compounds, dienes, polymethylcyclopentenyl cations (MCP),

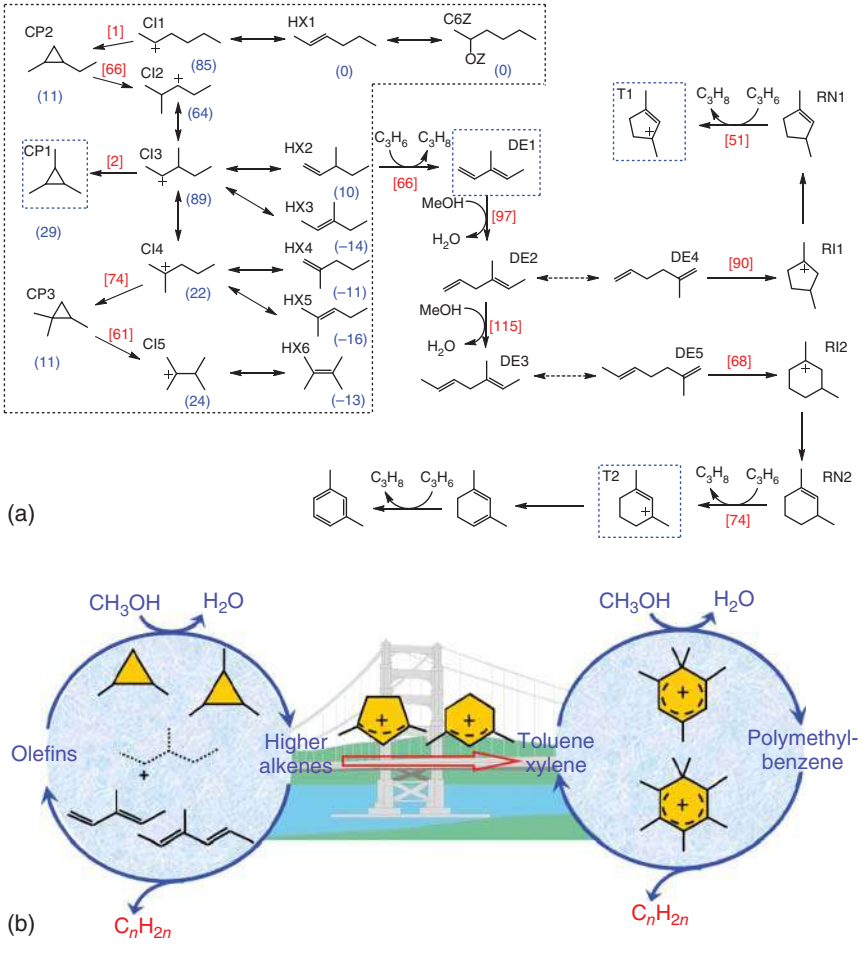

Figure 10.11 (a) Proposed reaction pathway containing the observed intermediates on H–SAPO-34 in the early stages of the MTO conversion. The blue values in parentheses are the relative energies of C6 species. The red values in square brackets are the energy barriers for each elementary step. All values are given in kJ mol^{-1}. The abbreviation OZ represents the zeolite framework. (b) Proposed route for the role of the polymethylcyclopentenyl and polymethylcyclohexenyl cations in the dual-cycle mechanism. Source: Reproduced with permission from Dai et al. [98]; © 2015, America Chemical Society.

polymethylcyclohexenyl cations, and polymethylbenzenium cations, were directly observed and identified by ssNMR spectroscopy under the real working conditions of MTO conversion. Among these species, trimethylcyclopropane and dienes were confirmed to be precursors for the production of polymethylcyclopentenyl and polymethylcyclohexenyl cations. Dimethylcyclohexenyl cations, a new type of carbenium ion in MTO conversion, were simultaneously observed with polymethylcyclopentenyl cations for the first time. According to these observations, it could be concluded that polymethylcyclopentenyl and/or polymethylcyclohexenyl cations derived from alkenes played a key role in the early stages of the MTO reaction on H–SAPO-34. Polymethylcyclopentenyl and/or polymethylcyclohexenyl cations formed before the polymethylbenzenium cations could serve as a bridge between olefin- and aromatic-based cycles at short reaction times. After the formation of aromatics, the aromatic-based cycle might participate in the reaction, which proceeded via the propagation of side alkyl chain and the succedent side-chain elimination to generate light olefins as reaction products.

Later, Liu and coworkers [115] investigated the dual-cycle mechanism in the MTO conversion over SAPO-34 zeolite by *in situ* ^{13}C MAS NMR spectroscopy and GC–MS analyses, and the methylcyclopentenyl cations and the methylcyclopentadiene were identified as the active intermediates. From these experimental results and theoretical calculations, a catalytic cycle based on cyclopentadiene species as critical intermediates for ethene and propene formation was proposed (Figure 10.12a). Cyclopentadiene species could directly participate the catalytic cycle and mediate the light olefin formation. Such a unique cyclopentadiene-based cycle serves as a bridge to link the traditional alkene- and aromatic-based cycles, in line with the results of Dai et al. [98]. More recently, Liu and coworkers [116] presented direct evidence on the formation and evolution of methylcyclopentenyl cations (MCP^+) species via *in situ* ^{13}C MAS NMR, ^{13}C-isotope tracing, co-reaction of MCP^+ and methanol experiments, and theoretical calculations. In the whole MTO reaction process, MCP^+ species were initially formed as starting HCP species and then transformed to more active intermediates, polymethylbenzenes (PMBs), at the transition stage. MCP^+ species not only could mediate the light olefin formation directly via aromatic- and cyclopentadiene-based cycles at the steady-state stage but also served as a bridge to link the direct mechanism at the initial stage and the indirect mechanism at the steady-state stage (Figure 10.12b). Independently from each other, Deng and coworkers [117] clarified the role of cycloalkenes in the aromatization of alkenes in the MTO conversion over H–ZSM-5 zeolite by ssNMR and GC–MS spectroscopies. Cyclopentene and cyclohexene formed as reactive species over H–ZSM-5 zeolite could be readily transformed into aromatics. Cyclohexene tended to form five-membered ring compound via ring contraction, followed by ring expansion to form aromatics. The promotion of cyclopentenyl cations and benzenium ion intermediates by cylcoalkenes confirmed the critical role of cylcoalkenes in triggering the aromatic-based cycle for alkene formation (Figure 10.12c).

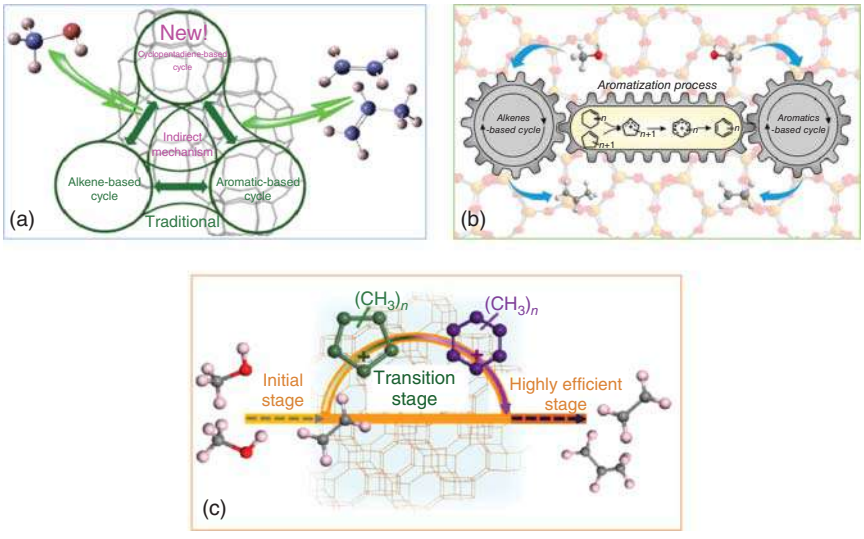

Figure 10.12 (a) Traditional dual cycles (alkene- and aromatic-based cycles) and the cyclopentadiene-based cycle. (b) Proposed route for the formation of aromatics from cyclohexene over H–ZSM-5 with detailed steps in the ring contraction process. (c) Whole mechanism of methanol to olefins. The initial ethene is generated from methanol by direct mechanism; MCP species are produced from initial ethene; PMBs species are produced from the co-reaction of MCP species and methanol; and the olefins are formed via indirect mechanism including of aromatic-, alkene-, and cyclopentadiene-based cycles. Sources: (a) Reproduced with permission from Zhang et al. [115]; © 2019, American Chemical Society. (b) Reproduced with permission from Zhang et al. [116]; © 2020, American Chemical Society. (c) Reproduced with permission from Hu et al. [117]; © 2020, American Chemical Society.

10.4 Bridging the Direct and Indirect Mechanisms

Through longtime effort, the direct route associated with the C—C bond formation in the MTH conversion has been unveiled. However, the relevance of the "direct mechanism"-derived molecules during MTH and subsequent transformation routes to the conventional HCP species is yet to be established.

Recently, Weckhuysen and coworkers [118] investigated the MTH process over a commercial SAPO-34 catalyst, utilizing a combination of advanced ssNMR spectroscopy, *operando* UV–vis spectroscopy, and online mass spectrometry. The unsaturated molecules (olefin/aromatics/carbonyls) were visible in both spectra, and clear correlations were observed between aliphatic/methyl groups and aromatic/olefinic moieties, unambiguously revealing that the acetyl group of the MA was indeed incorporated into (methylated) aromatic and olefinic compounds (Figure 10.13A–D). These spectroscopic results clearly indicated that the initial HCP species, e.g. olefins and aromatics, were derived exclusively from the direct C—C bond-containing acetyl group of MA. Based on these spectroscopic results, a catalytic roadmap for the MA to hydrocarbon conversion over SAPO-34 catalyst was proposed (Figure 10.13E). First, MA (a) could interact with the zeolite (b) to form surface acetate species (c) by acetylation of BASs of the zeolite. Simultaneously,

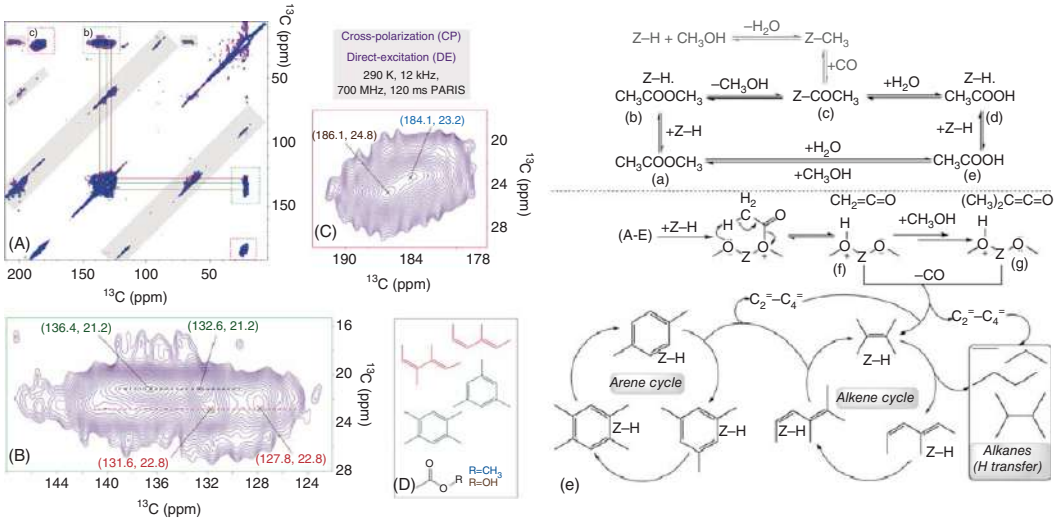

Figure 10.13 (A) 2D ^{13}C–^{13}C MAS solid-state NMR spectra of rigid molecules (290 K, 12 kHz, 700 MHz). Polarization of ^{13}C atoms was achieved through cross-polarization (CP, purple) or direct excitation (DE, blue), and a 120 ms phase alternated recoupling irradiation schemes (PARIS) mixing period was used. Gray-filled regions indicate spinning side bands. (B) Expansion of the aromatic/olefinic signals from the 2D ^{13}C–^{13}C CP MAS solid-state NMR spectrum. (C) Expansion from the 2D ^{13}C–^{13}C CP MAS solid-state NMR spectrum, indicating acetic acid and methyl acetate resonances. (D) Identified generic molecular keys/structures. (E) Proposed reaction pathways of the methyl-acetate-to-hydrocarbon (MATH) conversion catalyzed by zeolite (denoted as Z–H). Source: Reproduced with permission from Chowdhury et al. [118]; © 2018, Wiley-VCH.

(c) could be hydrolyzed to form both rigid (d, that is, zeolite adduct) and mobile (e) versions of acetic acid. According to the Koch-type carbonylation route and the recent theoretical studies of Plessow and Studt, a ketene-based route was proposed, and ketene (CH_2CO in F) could be generated from the acetyl moiety (CH_3CO^+ in a–e). Thereafter, ketene acted as the highly reactive intermediates, and lower olefins could be initially formed by decarbonylation of ketenes (f/g). Subsequently, smaller olefins oligomerize into larger olefinic and aromatic species as a part of the alkene and arene cycle of the dual-cycle/HCP mechanism, respectively, to govern the autocatalytic part of the reaction.

Subsequently, Plessow et al. investigated the initiation kinetics of the MTO conversion using a batch reactor model that consisted of both the initiation reactions and a representative part of the olefin cycle utilizing H–SSZ-13 as the model catalyst [119]. Based on these theoretical results, a simplified overview of the initial reaction mechanism of the MTO conversion including the initiation and the autocatalytic olefin-based cycle as central parts was provided in Figure 10.14. Several steps were involved in the initiation, namely, (i) the dehydrogenation of MeOH to produce CO, (ii) the subsequent methylation of CO to form MA containing first C—C bond, (iii) the decomposition of MA to ketene and methanol, (iv) the production of esters with multiple C—C bonds such as methyl isobutyrate (C4) through repeated methylation of ketene and methyl ketene, and (v) the decarbonylation of esters to yield free CO and propene. CO could be methylated again and was therefore catalytic species, but not an autocatalytic species. Propene could initiate the olefin cycle, in which the olefin was repeatedly methylated to higher olefins that could be cracked into two types of olefins as described by the HCP mechanism.

Recently, a roadmap of the MTH conversion from the formation of the initial C—C bond over H–ZSM-5 zeolite was illustrated based on the spectroscopic analyses and theoretical calculations [54]. The SMS was first formed upon adsorption of methanol onto the BAS of the H–ZSM-5 zeolite. Meanwhile, the CO and H_2 were formed

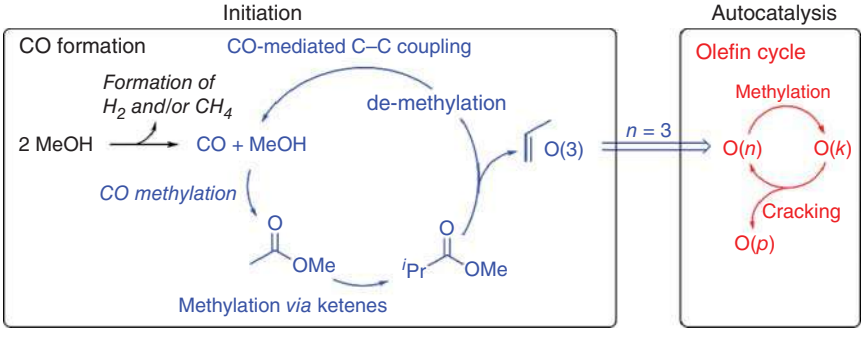

Figure 10.14 Overview of the initiation and autocatalytic part (olefin cycle only) of the MTO process. The initiation part is further broken down into a part responsible for CO formation and CO-mediated C–C coupling. O(*n*) is an abbreviation for any isomer of an olefin C_nH_{2n}. Sources: Reproduced with permission from Plessow et al. [119]; © 2019, American Chemical Society.

through dehydrogenation of methanol/FA. Subsequently, the surface-bound acetyl species containing the direct C—C bond were formed through the carbonylation reaction of SMS and CO, which could be further converted to acetaldehyde via hydrogenation with the co-presence of H_2. Thereafter, the formed acetaldehyde could be immediately involved in the subsequent reaction and induced the formation of HCP species at 523 K, which could initiate the MTH conversion. On the one side, acetaldehyde and methanol could react at the BAS of H–ZSM-5 zeolite and lead to the formation of methane and acetyl motif (CH_3CO^+). The formed acetaldehyde could also be rapidly involved in a subsequent aldol condensation reaction and lead to the formation of coupling products. The coupling products could be further converted to aromatics via hydrogen transfer/decarbonylation and cyclization route or direct cyclization and dehydration route, thus initiating the MTH conversion.

The aforementioned results clearly indicated the Koch-type carbonylation route was involved in the initial C—C bond formation. In the Koch-type carbonylation route, CO was the key intermediate, which could be formed from methanol dehydrogenation via FA intermediate with the presence of Al–OH or EFAL species. In acidic zeolites, the framework Al species were associated with the BASs, and the EFAL could act as the Lewis acid sites (LAS). A clear roadmap of the MTH conversion over H–ZSM-5 catalyst with the participation of both BAS and LAS was proposed on the basis of spectroscopic results (Figure 10.15). First, CO and H_2 were formed through methanol/FA dehydrogenation at the LAS (EFAL species), and the SMS was formed at the BAS (Si–OH–Al) of H–ZSM-5 zeolite. Subsequently, the surface-bound acetyl species were formed via the carbonylation of SMS and CO over BAS, which could be further converted to acetic acid or MA with the presence of water and methanol/DME. Additionally, the surface-bound acetyl species could be hydrogenated to acetaldehyde with the co-presence of H_2. The formed acetaldehyde and acetic acid were immediately involved in the subsequent reactions. The acetic acid could be immediately converted to acetone at BAS/LAS. On the other hand, the formed acetaldehyde could be converted to acetone at LAS via aldol condensation pathway. With the involvement of both BAS and LAS, the self- and cross-condensations of acetaldehyde and acetone would occur, resulting in the formation of chain or cyclic unsaturated aldehydes/ketones. The unsaturated aldehydes/ketones could be further converted to alkenes via the decarbonylation route or cracking route, thus initiating the MTH conversion via the alkene cycle. The formed chain alkenes could be converted to five/six-ring carbenium ions and aromatics via the cyclization, deprotonation, and hydride transfer steps over BAS. With the presence of BAS, the chain coupling products could also be converted to aromatics via hydrogen transfer/decarbonylation and cyclization routes or direct cyclization and dehydration routes. Meanwhile, the cyclic unsaturated ketones, e.g. 2-MCP and 3,4-diMCP, could be converted to aromatics via protonation, dehydration, and isomerization, thus initiating the MTH conversion via the aromatic cycle. Finally, with the formation of alkenes and aromatics, the dual-cycle mechanism would dominate the MTH conversion. In summary, three cycles, namely, the aldol cycle, the alkene cycle, and the aromatic cycle, were involved in the roadmap of MTH conversion over H–ZSM-5 zeolite with the participation of both BAS and LAS,

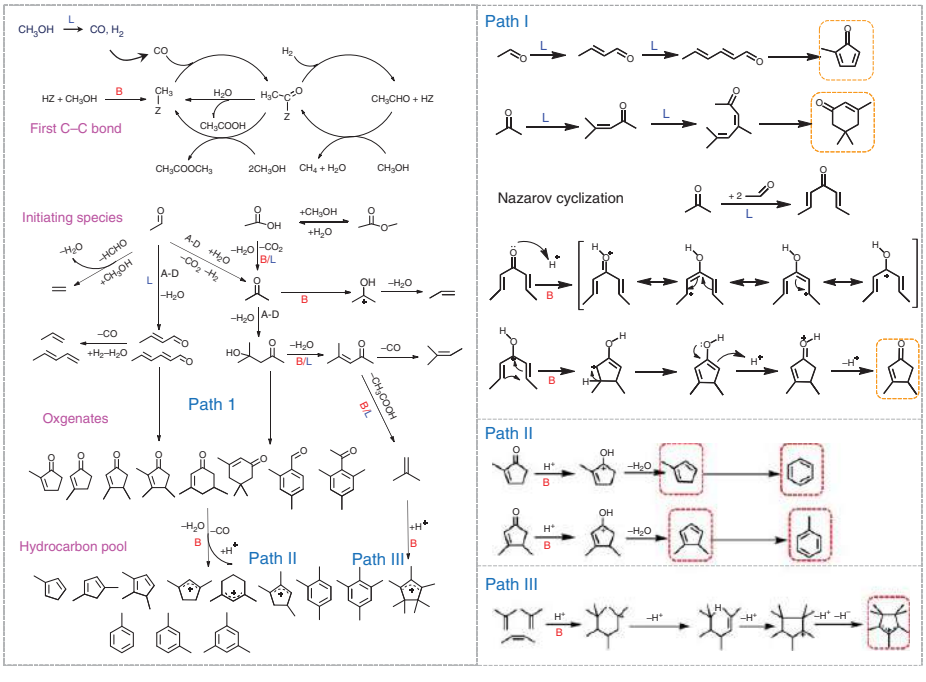

Figure 10.15 Proposed roadmap of the MTH conversion over H−ZSM-5 (denoted as HZ) with the participation of both Brønsted (denoted as B) and Lewis acid sites (denoted as L).

and the initial aldol cycle could bridge the dual-cycle mechanism during the MTH conversion.

10.5 Zeolite Catalysts for MTH Conversion

Shape selectivity is a key to the success of zeolite catalysis. Product selectivity in the MTH conversion can be rationally explained in terms of zeolite topologies. In the past few decades, the MTO reaction has received extensive attention due to its large-scale industrial application. According to the aforementioned descriptions of the reaction mechanism, we can recognize that the topologies and acidity of zeolite catalysts are two important factors influencing the product distribution and MTO activity. The channel and cavity structure of zeolites can impose spatial confinement effect on the type/reactivity of active intermediates, thus affecting the reaction routes and product selectivity. On the other hand, the BASs are the essential driving force for the realization of MTO conversion. The generation and evolution of the active intermediates are closely related to the acidic properties of zeolite catalysts. Accordingly, the choice of topology and the adjustment of acidity are vital for improving the catalytic performance of the zeolite catalysts for the MTO reaction [9, 17].

Through comprehensive screenings on a large variety of zeolites with different pore structures, zeolites with the eight-membered ring (8-MR) pores and large cages are believed to exhibit better shape selectivity toward light olefins. The large cages are beneficial to the formation of the large active intermediates, e.g. polymethylbenzenes, thus promoting the MTO conversion. On the other side, the small-pore windows can hinder the diffusion of products with large kinetic sizes, e.g. long-chain alkenes, out of the channels, deriving high selectivity toward ethene and propene. Among the 8-MR zeolites, silicoaluminophosphate SAPO-34 with 3D channels and moderate acid strength exhibits remarkable catalytic performance with high lower olefin yield of >90% (Figure 10.16a) [120]. SAPO-34 has

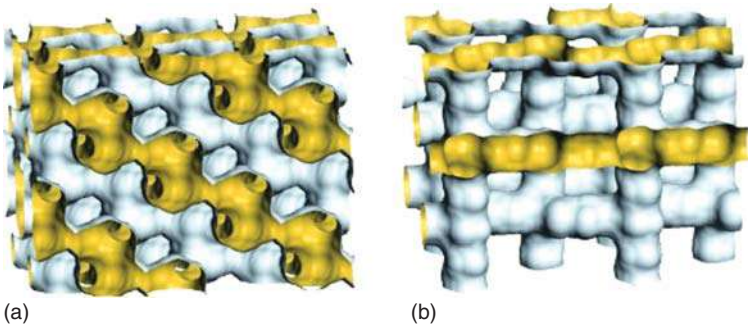

Figure 10.16 Shape and connection of the internal surface to the two zeolites that are in industrial use: (a) H–SAPO-34 and (b) H–ZSM-5. Both materials have a three-dimensional channel structure, but the shape is very different. The surface in H–ZSM-5 is best described as interconnected tubes, while H–SAPO-34 has larger cavities with narrow connections. Source: Reproduced with permission from Olsbye et al. [5]; © 2012, Wiley-VCH.

been utilized as a commercial MTO catalyst in UOP, Norsk Hydro, DMTO, and Sinopec-MTO (SMTO) technologies [9]. The synthesis and optimization of SAPO-34 zeolite catalyst for MTO conversion are available in the review article by Liu and coworkers and the references therein [17].

In addition to SAPO-34, silicoaluminate H–ZSM-5 zeolite with 3D intersected 10-membered ring (10-MR) pore structures attracts extensive attention (Figure 10.16b) and has been utilized as a commercial catalyst for the MTP reaction. Up to now, two strategies have been employed in optimizing H–ZSM-5 catalyst for the MTP reaction: (i) decreasing the acid density to enhance the olefin-based cycle and to improve the propene selectivity and (ii) decreasing the crystal size or constructing the mesoporosity to shorten the diffusion path and consequently prolong the catalyst lifetime. A variety of direct synthesis and post-synthesis strategies have been proposed for preparing H–ZSM-5 zeolite samples to improve their catalytic performance in the MTP reaction (see Ref. [121] and references therein).

Although SAPO-34 and H–ZSM-5 are the exclusive two zeolites utilized in the industrial MTH process up to now, various zeolites with different topologies (channels/cavities), framework compositions (strength and density of acidic sites), and morphologies (crystal dimensions and microporosity and mesoporosity) have been screened from potential industrial applications in the past few decades. Representative zeolites with the different topologies and compositions are summarized in Table 10.2.

Zeolites with 8-MR windows and large cages have received extensive attention, owing to the high selectivity to lower olefins in the MTO reaction. Besides the pore windows, the shape of the cavities plays an important role in the MTO reaction. Liu and coworkers investigated the catalytic performance of the MTO conversion over SAPO-35 (LEV), SAPO-34 (CHA), SAPO-18 (AEI), and DNL-6 (RHO) zeolites with different cavity dimensions [72, 122, 123]. According to the spectroscopic and theoretical calculations, it was concluded that the types of the confined active intermediates were governed by the cavity space, which would determine the product distribution. In other words, lower methylbenzenes acting as the dominant active intermediates would be formed in the smaller cavities, which are beneficial to the ethane formation. While in lager cavities, higher methylbenzenes would be formed and acted as the active intermediates, thus favoring the production of propene and butene. Therefore, under the similar reaction conditions, SAPO-35 with the smallest cavity space (7.3×6.3 Å) showed higher selectivity toward ethene, while SAPO-34 (10.9×6.7 Å) delivered high selectivity to ethene and propene and SAPO-18 (12.7×11.6 Å) and DNL-6 (11.4×11.4 Å) with the larger cavity space yielded more propene and butene. In addition, in zeolites with large cavities but combined with narrow-pore windows, higher selectivity toward ethene could be obtained. For example, AFX zeolite with very small-pore windows (3.4×3.6 Å) yielded higher selectivity to ethene, but the larger cavity space (13.0×8.3 Å) would promote the rapid accumulation of the polycyclic aromatics, thus causing rapid deactivation [124]. Similarly, ERI zeolite with narrow-pore windows (3.6×5.1 Å) also delivered higher selectivity to ethene [125]. Very recently, Zones and coworkers investigated the product distributions over the small-pore (8-MR), cage-containing

Table 10.2 Representative zeolites with the different topologies and compositions employed in the MTH conversion.

Topology	Material	Channel structure	Composition
TON	ZSM-22	1D, 10-ring	Si/Al = 30, 50
MTT	ZSM-23	1D, 10-ring	Si/Al = 23, 26
MRE	ZSM-48	1D, 10-ring	Si/Al = 40
EUO	EU-1	1D, 10-ring	Si/Al = 30
AFI	SAPO-5	1D, 12-ring	Al(50)P(34)Si(16)
UFI	UZM-5	2D, 8-ring	Si/Al = 5–12
RTH	RUB-13	2D, 8-ring	Si/Al = 12–15
ITE	ITQ-3	2D, 8-ring	Si/Al = 13
FER	ZSM-35	2D, 10-ring	Si/Al = 5–∞
CON	B-CON	2D, 12-ring, 10-ring	Si/Al = 100–∞
CHA	**H–SAPO-34**	**3D, 8-ring**	**Al(50)P(34)Si(16)**
	H-SSZ-13		Si/Al = 15–25
ERI	UZM-12	3D, 8-ring	Si/Al = 6
RHO	DNL-6	3D, 8-ring	Al(50)P(36)Si(14)
LEV	SSZ-17	3D, 8-ring	Si/Al = 14–17
	SAPO-35	3D, 8-ring	Al(48)P(40)Si(12)
AFX	SSZ-16	3D, 8-ring	Si/Al = 14–17
	SAPO-56	—	Si/Al = 0.2
DDR	DDR	3D, 8-ring	Si/Al = 22–168
AFN	SAPO-14	3D, 8-ring	Al(50)P(48)Si(2)
AEI	SAPO-18	3D, 8-ring	Al(49)P(49)Si(2)
	SSZ-98	—	Si/Al = 13.5
	SSZ-39	—	Si/Al = 15–25
SFW	STA-18	3D, 8-ring	Si/Al = 0.3
SAV	STA-7	3D, 8-ring	Si/Al = 0.2
LTA	SAPO-42	3D, 8-ring	Si/Al = 28.8
KFI	STA-14	3D, 8-ring	Si/Al = 4
UFI	UZM-5	3D, 8-ring	Si/Al = 6
MFI	**ZSM-5**	**3D, 10-ring**	**Si/Al = 10–∞**
MEL	ZSM-11	3D, 10-ring	Si/Al = 10–∞
TUN	TNU-9	3D, 10-ring	Si/Al = 20
IMF	IM-5	3D, 10-ring	Si/Al = 9–16
BEA	Beta	3D, 12-ring	Si/Al = 8–25

Zeolites utilized in the commercial MTO plants

zeolites, including LEV, ERI, CHA, AFX, SFW, AEI, DDR, RTH, ITE, SAV, LTA, RHO, KFI, and UFI, in the MTO conversion and found that the cage-defining ring size correlated well with the distribution of light olefin products [126, 127].

Medium-pore 10-MR zeolites composed of straight and/or curved channels can also be utilized as MTO catalysts with high selectivity toward propene. For catalysts with channel intersections, e.g. ZSM-5, the dual-cycle mechanism works in parallel, and propagation of one cycle over the other can be achieved by many approaches, such as co-feeding of olefins or higher alcohols [105]. The types of aromatic intermediates and their reactivity highly depend on the space of the intersection cavities, similar to those of the 8-MR cage-containing zeolites. In the case of ZSM-22 zeolite with TON topology and one-dimensional channels, the absence of channel intersections greatly suppresses the aromatic-based cycle and makes the olefin-based cycle the dominant mechanism, resulting in the formation of predominant C_{5+} products (50–75%) [91, 127]. Svelle and coworkers investigated the shape selectivity in the MTH conversion over the one-dimensional 10-MR zeolites including ZSM-22 (TON), ZSM-23 (MTT), ZSM-48 (*MRE), and EU-1 (EUO) and found that small differences in the channel system showed notable influences on the product distribution. High selectivity toward C_{5+} hydrocarbons could be achieved over all the employed zeolites, but the aromatics were absent over ZSM-22 (TON) and ZSM-23 (MTT) with the narrow-pore windows of 5.7×4.6 Å and 5.2×4.5 Å, respectively [128], in line with previous reports.

Large-pore 12-membered ring (12-MR) zeolites are commonly utilized for the elucidation of MTH reaction mechanism. Owing to the large cavity space and pore windows, the aromatic-based cycle works as the major route in the MTH conversion, thus yielding C_{4+} alkenes and aromatics as the dominant products. Mechanistic investigations indicate that reducing the acid density can greatly promote the olefin-based cycle, thus enhancing the selectivity toward propene. Accordingly, high-silica Beta zeolites (Si/Al > 100) with low acid density have been widely studied as MTH catalysts. Bjørgen et al. employed dealuminated Beta zeolite (Si/Al = 120) in MTH conversion at 623 K. Although a high propene/ethene ratio of 21 could be achieved, the selectivity to propene (22.7%) was still very low [129]. In a similar manner, Otomo et al. prepared several dealuminated Beta zeolites and found that high propene selectivity of 37.4–49.7% could be achieved over the sample with a Si/Al ratio of 112 [130]. Recently, Liu and coworkers synthesized a series of high-silica Beta zeolites with Si/Al ratios of 136–340, and the propene selectivity could reach up to 58.3% [131]. However, the total selectivity of ethene and propene (~65%) over 10-MR and 12-MR zeolites is still much lower than that over 8-MR zeolites (>80%), owing to their larger pore windows.

The acidity, including the density and strength, is an important factor influencing the MTH performance over zeolite catalysts. In principle, excess BASs or high acid strength can increase the contribution of the aromatic-based cycle, thus enhancing the secondary reaction rates and aggravating the retention of coke precursors. In contrast, low acid density or weak acid strength can increase the contribution of the olefin-based cycle, consequently declining the deactivation rate and prolonging the catalyst lifetime. Liu and coworkers investigated the MTO activity and reaction

mechanism on 8-MR AlPO-18 and low-silica SAPO-18 zeolites. For SAPO-18 with high BAS density, MTO conversion took place followed by the aromatic-based cycle. While for SAPO-18 with low Brønsted acid density, two cycles were involved in parallel. Over non-acidic AlPO-18 catalyst, the methanol conversion was very low, and the reaction mainly followed the olefin-based route [105]. Li and coworkers also investigated the catalytic cycle and activity of MTO reaction over low-silica AlPO-34 zeolites with controllable Brønsted acid density [104]. For the catalysts with low BAS densities, the olefin-based cycle was the dominant mechanism during MTO conversion. Long-chain alkenes, e.g. C5–C6 alkenes, acted as intermediates that could be cracked to lower olefins. While for catalysts with slightly higher BAS densities, the long-chain alkenes were rapidly transformed to aromatics, and, subsequently, the aromatic-based cycle mechanism contributed to the MTO conversion. In a similar manner, an increase in the amounts of BASs in H–ZSM-5 zeolite would enhance the chance of methanol molecules to interact with each other, thus increasing the chance for aromatics and ethene formation based on the aromatic-based cycle [132]. It was also shown that the modifications with alkaline-earth metals could greatly decrease the BASs of H–ZSM-5 zeolite, thus suppressing the aromatic-based cycle and greatly prolonging the catalyst lifetime [107, 133–135].

10.6 Summary and Outlook

For more than 40 years, the MTH reaction remains an interesting topic in the field of C1 chemistry. Recently, the development of industrial implementation has sparked even more attention from the academic and industrial communities, and the formation of the direct C—C bond has received extensive attention in fundamental studies. Several research groups have provided experimental and/or theoretical evidence for the feasibility of direct mechanisms, including the developed oxonium and methane–FA mechanism, methyleneoxy mechanism, and Koch carbonylation mechanism. However, owing to the lack of authentic experimental evidence and the complexity of the induction period of the MTH conversion, there remain ongoing debates about the formation of C—C bond. Accordingly, the further transformation of C—C bonds to the HCP species during the induction period of the MTH conversion has also not been fully understood. To boost the further studies in this field, the current achievements in the direct mechanism of MTH chemistry have been highlighted, and the picture of the reaction mechanism of MTH conversion has been outlined in the present chapter.

In the next mechanistic step, the dual-cycle mechanism containing two competing cycles is now well understood and can be used as an effective means to control the product selectivity and catalyst lifetime. With the development of advanced spectroscopic techniques, the nature and the evolution of the active HCP species in the dual cycle have been clarified. The dominant reaction cycle and the reactivity of the active intermediates highly depend on zeolite topology. Channel/cage dimensions can cause spatial restrictions preventing certain intermediates to participate in the mechanistic cycle. By adjusting the reaction conditions (temperature),

feed composition (co-feeding olefins or aromatics), zeolite topology, and acidity, the product selectivity and catalyst lifetime can be well tuned. Extensive efforts have been devoted to the high selectivity of propene and the enhancement of the propene/ethene ratio. In the MTH industry, C_4 alkene recycling unit is also applied to maximize the propene yield. How to achieve this objective without compromising catalyst lifetime is, however, still an open question, as ethene is mainly produced via the aromatic-based cycle. In addition, the potential fluctuations in the olefin market require the controllable product selectivity in MTH process.

Up to now, SAPO-34 zeolite is still the most suitable catalyst for MTO. Although significant achievements have been made in the development of SAPO-34 zeolite catalysts, many issues are still to be improved, and several future research directions are given as follows: (i) a general strategy to synthesize high-quality nanosized or mesoporous SAPO-34 with the controllable Si content, distribution, and higher hydrothermal stability, (ii) a SAPO-34 zeolite with tunable product selectivity in the MTO reaction, and (iii) a cost-efficient and environment-friendly strategy for scalable production in industry.

The combination of syngas or CO_2 to methanol and the MTH process to produce olefins, gasoline, and aromatics is a new promising route. A bifunctional system containing metal oxides and zeolite catalysts is generally employed as catalyst for this new route. Although significant achievements have been made in this direction over the past years, a series of obstacles still need to overcome, for example, the over-hydrogenation of olefins to paraffins and high selectivity toward CO and methane by-products.

References

1 Stöcker, M. (1999). Methanol-to-hydrocarbons: catalytic materials and their behavior. *Microporous Mesoporous Mater.* 29: 3–48.

2 Stöcker, M. (2010). *Zeolite and Catalysis: Synthesis, Reactions and Applications* (ed. J. Čejka, A. Corma and S. Zones), 687. Weinheim: Wiley-VCH.

3 White, J.L. (2011). Methanol-to-hydrocarbon chemistry: the carbon pool (r)evolution. *Catal. Sci. Technol.* 1: 1630–1635.

4 Haw, J.F., Song, W.G., Marcus, D.M., and Nicholas, J.B. (2003). The mechanism of methanol to hydrocarbon catalysis. *Acc. Chem. Res.* 36: 317–326.

5 Olsbye, U., Svelle, S., Bjørgen, M. et al. (2012). Conversion of methanol to hydrocarbons: how zeolite cavity and pore size controls product selectivity. *Angew. Chem. Int. Ed.* 51: 5810–5831.

6 Ilias, S. and Bhan, A. (2013). Mechanism of the catalytic conversion of methanol to hydrocarbons. *ACS Catal.* 3: 18–31.

7 Van Speybroeck, V., De Wispelaere, K., Van der Mynsbrugge, J. et al. (2014). First principle chemical kinetics in zeolites: the methanol-to-olefin process as a case study. *Chem. Soc. Rev.* 43: 7326–7357.

8 Olsbye, U., Svelle, S., Lillerud, K.P. et al. (2015). The formation and degradation of active species during methanol conversion over protonated zeotype catalysts. *Chem. Soc. Rev.* 44: 7155–7176.

9 Tian, P., Wei, Y., Ye, M., and Liu, Z. (2015). Methanol to olefins (MTO): from fundamentals to commercialization. *ACS Catal.* 5: 1922–1938.

10 Yarulina, I., Chowdhury, A.D., Meirer, F. et al. (2018). Recent trends and fundamental insights in the methanol-to-hydrocarbons process. *Nat. Catal.* 1: 398–411.

11 Schulz, H. (2018). About the mechanism of methanol conversion on zeolites. *Catal. Lett.* 148: 1263–1280.

12 Wang, C., Xu, J., and Deng, F. (2020). Mechanism of methanol-to-hydrocarbon reaction over zeolites: a solid-state NMR perspective. *ChemCatChem* 12: 965–980.

13 Hwang, A. and Bhan, A. (2019). Deactivation of zeolites and zeotypes in methanol-to-hydrocarbons catalysis: mechanisms and circumvention. *Acc. Chem. Res.* 52: 2647–2656.

14 Chang, C.D. (1992). The New Zealand gas-to-gasoline plant: an engineering tour de force. *Catal. Today* 13: 103–111.

15 Yurchak, S. (1988). Development of Mobil's fixed-bed methanol-to-gasoline (MTG) process. *Stud. Surf. Sci. Catal.* 36: 251–272.

16 Vora, B.V., Marker, T.L., Barger, P.T. et al. (1997). Economic route for natural gas conversion to ethylene and propylene. *Stud. Surf. Sci. Catal.* 107: 87–98.

17 Yang, M., Fan, D., Wei, Y. et al. (2019). Recent progress in methanol-to-olefins (MTO) catalysts. *Adv. Mater.* 31: 1902181.

18 Koempel, H. and Liebner, W. (2007). Lurgi's methanol to propylene (MTP) report on a successful commercialization. *Stud. Surf. Sci. Catal.* 167: 261–267.

19 Kolboe, S. and Dahl, I.M. (1995). Methanol conversion to hydrocarbons. Use of isotopes for mechanism studies. *Stud. Surf. Sci. Catal.* 94: 427–434.

20 Hemelsoet, K., Van der Mynsbrugge, J., Wispelaere, K.D. et al. (2013). Unraveling the reaction mechanisms governing methanol-to-olefins catalysis by theory and experiment. *ChemPhysChem* 14: 1526–1545.

21 Wang, W., Buchholz, A., Seiler, M., and Hunger, M. (2003). Evidence for an initiation of the methanol-to-olefin process by reactive surface methoxy groups on acidic zeolite catalysts. *J. Am. Chem. Soc.* 125: 15260–15267.

22 Jiang, Y., Hunger, M., and Wang, W. (2006). On the reactivity of surface methoxy species in acidic zeolites. *J. Am. Chem. Soc.* 128: 11679–11692.

23 Wang, W. and Hunger, M. (2008). Reactivity of surface alkoxy species on acidic zeolite catalysts. *Acc. Chem. Res.* 41: 895–904.

24 Yamazaki, H., Shima, H., Imai, H. et al. (2011). Evidence for a "carbene-like" intermediate during the reaction of methoxy species with light alkenes on H–ZSM-5. *Angew. Chem. Int. Ed.* 50: 1853–1856.

25 Li, J., Wei, Z., Chen, Y. et al. (2014). A route to form initial hydrocarbon pool species in methanol conversion to olefins over zeolites. *J. Catal.* 317: 277–283.

26 Comas-Vives, A., Valla, M., Copéret, C., and Sautet, P. (2015). Cooperativity between Al sites promotes hydrogen transfer and carbon—carbon bond formation upon dimethyl ether activation on alumina. *ACS Cent. Sci.* 1: 313–319.

27 Muller, S., Liu, Y., Kirchberger, F.M. et al. (2016). Hydrogen transfer pathways during zeolite catalyzed methanol conversion to hydrocarbons. *J. Am. Chem. Soc.* 138: 15994–16003.

28 Liu, Y., Muller, S., Berger, D. et al. (2016). Formation mechanism of the first carbon—carbon bond and the first olefin in the methanol conversion into hydrocarbons. *Angew. Chem. Int. Ed.* 55: 5723–5726.

29 Chowdhury, A.D., Houben, K., Whiting, G.T. et al. (2016). Initial carbon—carbon bond formation during the early stages of the methanol-to-olefin process proven by zeolite-trapped acetate and methyl acetate. *Angew. Chem. Int. Ed.* 55: 15840–15845.

30 Plessow, P.N. and Studt, F. (2017). Unraveling the mechanism of the initiation reaction of the methanol to olefins process using ab initio and DFT calculations. *ACS Catal.* 7: 7987–7994.

31 Plessow, P.N. and Studt, F. (2018). Theoretical insights into the effect of the framework on the initiation mechanism of the MTO process. *Catal. Lett.* 148: 1246–1253.

32 Wu, X., Xu, S., Zhang, W. et al. (2017). Direct mechanism of the first carbon—carbon bond formation in the methanol-to-hydrocarbons process. *Angew. Chem. Int. Ed.* 56: 9039–9043.

33 Wang, C., Chu, Y., Xu, J. et al. (2018). Extra-framework aluminum-assisted initial C—C bond formation in methanol-to-olefins conversion on zeolite H-ZSM-5. *Angew. Chem. Int. Ed.* 57: 10197–10201.

34 Chang, C.D. and Silvestri, A.J. (1977). The conversion of methanol and other O-compounds to hydrocarbons over zeolite catalysts. *J. Catal.* 47: 249–259.

35 Chang, C.D. (1981). A reply to Kagi: mechanism of conversion of methanol over ZSM-5 catalyst. *J. Catal.* 69: 244–245.

36 Swabb, E.A. and Gares, B.C. (1972). Diffusion, reaction, and fouling in H-mordenite crystallites. The catalytic dehydration of methanol. *Ind. Eng. Chem. Fundam.* 11: 540–545.

37 Zatorski, W. and Krzyzanowski, S. (1978). Conversion of methanol to hydrocarbons over natural mordenite. *Acta Phys. Chem.* 24: 347–352.

38 Clarke, J.K.A., Darcy, R., Hegarty, B.F. et al. (1986). Free radicals in dimethyl ether on H-ZSM-5 zeolite. A novel dimension of heterogeneous catalysis. *J. Chem. Soc., Chem. Commun.* 5: 425–426.

39 Olah, A.G. (1981). Higher coordinate (hypercarbon containing) carbocations and their role in electrophilic reactions of hydrocarbons. *Pure Appl. Chem.* 53: 201–207.

40 Hutchings, G.J., Gottschalk, F., Hall, M.V.M., and Hunter, R. (1987). Hydrocarbon formation from methylating agents over the zeolite catalyst ZSM-5. Comments on the mechanism of carbon—carbon bond and methane formation. *J. Chem. Soc., Faraday Trans.* 83: 571–583.

41 Tajima, N., Tsuneda, T., Toyama, F., and Hirao, K. (1998). A new mechanism for the first carbon—carbon bond formation in the MTG process: a theoretical study. *J. Am. Chem. Soc.* 120: 8222–8229.

42 Blaszkowski, S.R. and van Sante, R.A. (1995). Density functional theory calculations of the activation of methanol by a Brønsted zeolitic proton. *J. Phys. Chem.* 99: 11728–11738.

43 Blaszkowski, S.R. and van Sante, R.A. (1997). Theoretical study of C—C bond formation in the methanol-to-gasoline process. *J. Am. Chem. Soc.* 119: 5020–5027.

44 Lesthaeghe, D., Speybroeck, V.V., Marin, G.B., and Waroquier, M. (2006). Understanding the failure of direct C–C coupling in the zeolite-catalyzed methanol-to-olefin process. *Angew. Chem. Int. Ed.* 45: 1714–1719.

45 Lesthaeghe, D., Van Speybroeck, V., Marin, G.B., and Waroquier, M. (2007). The rise and fall of direct mechanisms in methanol-to-olefin catalysis: an overview of theoretical contributions. *Ind. Eng. Chem. Res.* 46: 8832–8838.

46 Venuto, P.B. and Landis, P.S. (1971). Formation of stilbenes and related compounds from reaction of benzyl-type mercaptans over zeolites. *J. Catal.* 21: 330–335.

47 Chang, C.D., Hellring, S.D., and Pearson, J.A. (1989). On the existence and role of free radicals in methanol conversion to hydrocarbons over HZSM-5: 1. Inhibition by NO. *J. Catal.* 115: 282–285.

48 Olah, G.A., Doggweiler, H., and Felberg, J.D. (1984). Ylide chemistry. 3. Evidence for competing oxonium ylide formation with carbon-hydrogen insertion in Meerwein's reaction of methylene and methylene-d_2 with dialkyl ethers. *J. Org. Chem.* 49: 2116–2120.

49 van den Berg, J.P., Wolthuizen, J.P., and van Hooff, J.H.C. (1980). The conversion of dimethyl ether to hydrocarbons on zeolite H-ZSM-5: the reaction mechanism for formation of primary olefins. In: *Proceedings of the Fifth International Conference on Zeolites, Naples, Italy, 2–6 June 1980* (ed. L.V.C. Rees), 649–660. London: Heyden.

50 Olah, G.A., Doggweiler, H., Felberg, J.D. et al. (1984). Onium ylide chemistry. 1. Bifunctional acid-base-catalyzed conversion of heterosubstituted methanes into ethylene and derived hydrocarbons. The Onium ylide mechanism of the $C_1 \rightarrow C_2$ conversion. *J. Am. Chem. Soc.* 106: 2143–2149.

51 Wei, Z., Chen, Y., Li, J. et al. (2016). Methane formation mechanism in the initial methanol-to-olefins process catalyzed by SAPO-34. *Catal. Sci. Technol.* 6: 5526–5533.

52 Wu, X., Chen, W., Xu, S. et al. (2021). Dynamic activation of C1 molecules evoked by zeolite catalysis. *ACS Cent. Sci.* 7: 681–687.

53 Sun, T., Chen, W., Xu, S. et al. (2021). The first carbon—carbon bond formation mechanism in methanol-to-hydrocarbons process over chabazite zeolite. *Chemistry* 7: 1–14.

54 Yang, L., Yan, T., Wang, C. et al. (2019). Role of acetaldehyde in the roadmap from initial carbon—carbon bonds to hydrocarbons during methanol conversion. *ACS Catal.* 9: 6491–6501.

55 Kolboe, S. (1988). On the mechanism of hydrocarbon formation from methanol over protonated zeolites. *Stud. Surf. Sci. Catal.* 36: 189–193.

56 Dessau, R.M. and LaPierre, R.B. (1982). On the mechanism of methanol conversion to hydrocarbons over HZSM-5. *J. Catal.* 78: 136–141.

57 Dessau, R.M. (1986). On the H-ZSM-5 catalyzed formation of ethylene from methanol or higher olefins. *J. Catal.* 99: 111–116.

58 Mole, T., Whiteside, J.A., and Seddon, D. (1983). Aromatic co-catalysis of methanol conversion over zeolite catalysts. *J. Catal.* 82: 261–266.

59 Mole, T., Bett, G., and Seddon, D. (1983). Conversion of methanol to hydrocarbons over ZSM-5 zeolite: an examination of the role of aromatic hydrocarbons using ^{13}carbon- and deuterium-labeled feeds. *J. Catal.* 84: 435–445.

60 Dahl, I.M. and Kolboe, S. (1993). On the reaction mechanism for propene formation in the MTO reaction over SAPO-34. *Catal. Lett.* 20: 329–336.

61 Dahl, I.M. and Kolboe, S. (1994). On the reaction mechanism for hydrocarbon formation from methanol over SAPO-34: 1. Isotopic labeling studies of the co-reaction of ethene and methanol. *J. Catal.* 149: 458–464.

62 Dahl, I.M. and Kolboe, S. (1996). On the reaction mechanism for hydrocarbon formation from methanol over SAPO-34: 2. Isotopic labeling studies of the co-reaction of propene and methanol. *J. Catal.* 161: 304–309.

63 Magnoux, P., Roger, P., Canaff, C. et al. (1987). New technique for the characterization of carbonaceous compounds responsible for zeolite deactivation. *Stud. Surf. Sci. Catal.* 34: 317–330.

64 Arstad, B. and Kolboe, S. (2001). Methanol-to-hydrocarbons reaction over SAPO-34. Molecules confined in the catalyst cavities at short time on stream. *Catal. Lett.* 71: 209–212.

65 Arstad, B. and Kolboe, S. (2001). The reactivity of molecules trapped within the SAPO-34 cavities in the methanol-to-hydrocarbons reaction. *J. Am. Chem. Soc.* 123: 8137–8138.

66 Xu, T., Barich, D.H., Goguen, P.W. et al. (1998). Synthesis of a benzenium ion in a zeolite with use of a catalytic flow reactor. *J. Am. Chem. Soc.* 120: 4025–4026.

67 Song, W., Nicholas, J.B., Sassi, A., and Haw, J.F. (2002). Synthesis of the heptamethylbenzenium cation in zeolite-β: in situ NMR and theory. *Catal. Lett.* 81: 49–53.

68 Bjørgen, M., Olsbye, U., and Kolboe, S. (2003). Coke precursor formation and zeolite deactivation: mechanistic insights from hexamethylbenzene conversion. *J. Catal.* 215: 30–44.

69 Bjørgen, M., Olsbye, U., Petersen, D., and Kolboe, S. (2004). The methanol-to-hydrocarbons reaction: insight into the reaction mechanism from [^{12}C] benzene and [^{13}C] methanol coreactions over zeolite H-beta. *J. Catal.* 221: 1–10.

70 Bjørgen, M., Olsbye, U., Svelle, S., and Kolboe, S. (2004). Conversion of methanol to hydrocarbons: the reactions of the heptamethylbenzenium cation over zeolite H-Beta. *Catal. Lett.* 93: 37–40.

71 Bjørgen, M., Bonino, F., Kolboe, S. et al. (2003). Spectroscopic evidence for a persistent benzenium cation in zeolite H-Beta. *J. Am. Chem. Soc.* 125: 15863–15868.

72 Li, J., Wei, Y., Chen, J. et al. (2012). Observation of heptamethylbenzenium cation over SAPO-type molecular sieve DNL-6 under real MTO conversion conditions. *J. Am. Chem. Soc.* 134: 836–839.

73 Lesthaeghe, D., Horré, A., Waroquier, M. et al. (2009). Theoretical insights on methylbenzene side-chain growth in ZSM-5 zeolites for methanol-to-olefin conversion. *Chem. Eur. J.* 15: 10803–10808.

74 Sullivan, R.F., Egan, C.J., Langlois, G.E., and Sieg, R.P. (1961). A new reaction that occurs in the hydrocracking of certain aromatic hydrocarbons. *J. Am. Chem. Soc.* 83: 1156–1160.

75 Svelle, S., Bjørgen, M., Kolboe, S. et al. (2006). Intermediates in the methanol-to-hydrocarbons (MTH) reaction: a gas phase study of the unimolecular reactivity of multiply methylated benzenium cations. *Catal. Lett.* 109: 25–35.

76 Sekiguchi, O., Mayer, V., Letzel, M.C. et al. (2009). Energetics and reaction mechanisms for the competitive losses of H_2, CH_4 and C_2H_4 from protonated methylbenzenes—implications to the methanol-to-hydrocarbons (MTH) process. *Eur. J. Mass Spectrom.* 15: 167–181.

77 Xu, T. and Haw, J.F. (1994). Cyclopentenyl carbenium ion formation in acidic zeolites: an in situ NMR study of cyclic precursors. *J. Am. Chem. Soc.* 116: 7753–7759.

78 Stepanov, A.G., Luzgin, M.V., Arzumanov, S.S. et al. (2002). *n*-Butene conversion on H-ferrierite studied by ^{13}C MAS NMR. *J. Catal.* 211: 165–172.

79 Luzgin, M.V., Stepanov, A.G., Arzumanov, S.S. et al. (2006). Mechanism studies of the conversion of ^{13}C-labeled *n*-butane on zeolite H-ZSM-5 by using ^{13}C magic angle spinning NMR spectroscopy and GC-MS analysis. *Chem. Eur. J.* 12: 457–465.

80 Long, J.L., Wang, X., Ding, Z. et al. (2008). Cyclopentadiene transformation over H-form zeolites: TPD and IR studies of the formation of a monomeric cyclopentenyl carbenium ion intermediate and its role in acid-catalyzed conversions. *J. Catal.* 255: 48–58.

81 Song, W., Nicholas, J.B., and Haw, J.F. (2001). A persistent carbenium ion on the methanol-to-olefin catalyst HSAPO-34: acetone shows the way. *J. Phys. Chem. B* 105: 4317–4323.

82 Haw, J.F., Nicholas, J.B., Song, W. et al. (2000). Roles for cyclopentenyl cations in the synthesis of hydrocarbons from methanol on zeolite catalyst HZSM-5. *J. Am. Chem. Soc.* 122: 4763–4775.

83 Sassi, A., Wildman, M.A., Ahn, H.J. et al. (2002). Methylbenzene chemistry on zeolite HBeta: multiple insights into methanol-to-olefin catalysis. *J. Phys. Chem. B* 106: 2294–2303.

84 Seiler, M., Wang, W., Buchholz, A., and Hunger, M. (2003). Direct evidence for a catalytically active role of the hydrocarbon pool formed on zeolite H-ZSM-5 during the methanol-to-olefin conversion. *Catal. Lett.* 88: 187–191.

85 Hunger, M. and Horvath, T. (1996). Adsorption of methanol on Brønsted acid sites in zeolite H-ZSM-5 investigated by multinuclear solid-state NMR spectroscopy. *J. Am. Chem. Soc.* 118: 12302–12308.

86 Seiler, M., Wang, W., and Hunger, M. (2001). Local structure of framework aluminum in zeolite H-ZSM-5 during conversion of methanol investigated by in situ NMR spectroscopy. *J. Phys. Chem. B* 105: 8143–8148.

87 Wang, W., Seiler, M., and Hunger, M. (2001). Role of surface methoxy species in the conversion of methanol to dimethyl ether on acidic zeolites investigated by in situ stopped-flow MAS NMR spectroscopy. *J. Phys. Chem. B* 105: 12553–12558.

88 Ono, Y. and Mori, T. (1981). Mechanism of methanol conversion into hydrocarbons over ZSM-5 zeolite. *J. Chem. Soc., Faraday Trans.* 77: 2209–2221.

89 Svelle, S., Joensen, F., Nerlov, J. et al. (2006). Conversion of methanol into hydrocarbons over zeolite H-ZSM-5: ethene formation is mechanistically separated from the formation of higher alkenes. *J. Am. Chem. Soc.* 128: 14770–14771.

90 Bjørgen, M., Svelle, S., Joensen, F. et al. (2007). Conversion of methanol to hydrocarbons over zeolite H-ZSM-5: on the origin of the olefinic species. *J. Catal.* 249: 195–207.

91 Cui, Z., Qiang, L., Song, W., and Wan, L. (2006). Insights into the mechanism of methanol-to-olefin conversion at zeolites with systematically selected framework structures. *Angew. Chem. Int. Ed.* 45: 6512–6515.

92 Cui, Z., Qiang, L., Ma, Z. et al. (2008). Direct observation of olefin homologations on zeolite ZSM-22 and its implications to methanol to olefin conversion. *J. Catal.* 258: 83–86.

93 Wei, F., Cui, Z., Meng, X. et al. (2014). Origin of the low olefin production over HZSM-22 and HZSM-23 zeolites: external acid sites and pore mouth catalysis. *ACS Catal.* 4: 529–534.

94 Ilias, S. and Bhan, A. (2012). Tuning the selectivity of methanol-to-hydrocarbons conversion on H-ZSM-5 by co-processing olefin or aromatic compounds. *J. Catal.* 290: 186–192.

95 Ahn, J.H., Temel, B., and Iglesia, E. (2009). Selective homologation routes to 2,2,3-trimethylbutane on solid acids. *Angew. Chem. Int. Ed.* 48: 3814–3816.

96 Simonetti, D.A., Ahn, J.H., and Iglesia, E. (2011). Mechanistic details of acid-catalyzed reactions and their role in the selective synthesis of triptane and isobutane from dimethyl ether. *J. Catal.* 277: 173–195.

97 Wang, C., Wang, Y., and Xie, Z. (2013). Insights into the reaction mechanism of methanol-to-olefins conversion in HSAPO-34 from first principles: are olefins themselves the dominating hydrocarbon pool species? *J. Catal.* 301: 8–19.

98 Dai, W., Wang, C., Dyballa, M. et al. (2015). Understanding the early stages of the methanol-to-olefin conversion on H-SAPO-34. *ACS Catal.* 5: 317–326.

99 Hwang, A., Prieto-Centurion, D., and Bhan, A. (2016). Isotopic tracer studies of methanol-to-olefins conversion over HSAPO-34: the role of the olefins-based catalytic cycle. *J. Catal.* 216–256.

100 Dai, W., Dyballa, M., Wu, G. et al. (2015). Intermediates and dominating reaction mechanism during the early period of the methanol-to-olefin conversion on SAPO-41. *J. Phys. Chem. C* 119: 2637–2645.

101 Westgård Erichesen, M., Svelle, S., and Olsbye, U. (2013). H-SAPO-5 as methanol-to-olefins (MTO) model catalyst: towards elucidating the effects of acid strength. *J. Catal.* 298: 94–101.

102 Westgård Erichesen, M., De Wispelaere, K., Hemelsoet, K. et al. (2015). How zeolitic acid strength and composition alter the reactivity of alkenes and aromatics towards methanol. *J. Catal.* 328: 186–196.

103 Dai, W., Wang, X., Wu, G. et al. (2012). Methanol-to-olefin conversion catalyzed by low-silica AlPO-34 with traces of Brønsted acid sites: combined catalytic and spectroscopic investigations. *ChemCatChem* 4: 1428–1435.

104 Dai, W., Cao, G., Liu, Y. et al. (2017). Insights into the catalytic cycle and activity of methanol-to-olefin conversion over low-silica AlPO-34 zeolites with controllable Brønsted acid density. *Catal. Sci. Technol.* 7: 607–618.

105 Chen, J., Li, J., Yuan, C. et al. (2014). Elucidating the olefin formation mechanism in the methanol to olefin reaction over AlPO-18 and SAPO-18. *Catal. Sci. Technol.* 4: 3268–3277.

106 Westgård Erichesen, M., Svelle, S., and Olsbye, U. (2013). The influence of catalyst acid strength on the methanol to hydrocarbons (MTH) reaction. *Catal. Today* 215: 216–223.

107 Goetze, J. and Weckhuysen, B.M. (2018). Spatiotemporal coke formation over zeolite ZSM-5 during the methanol-to-olefins process as studied with operando UV-vis spectroscopy: a comparison between H–ZSM-5 and Mg–ZSM-5. *Catal. Sci. Technol.* 8: 1632–1644.

108 Sun, X., Mueller, S., Liu, Y. et al. (2014). On reaction pathways in the conversion of methanol to hydrocarbons on HZSM-5. *J. Catal.* 317: 185–197.

109 Dai, W., Yang, L., Wang, C. et al. (2018). Effect of *n*-butanol cofeeding on the methanol to aromatics conversion over Ga-modified nano H–ZSM-5 and its mechanistic interpretation. *ACS Catal.* 8: 1352–1362.

110 Zhu, J., Li, Y., Muhammad, U. et al. (2017). Effect of alkene co-feed on the MTO reactions over SAPO-34. *Chem. Eng. J.* 316: 187–195.

111 Wang, C., Chu, Y., Zheng, A. et al. (2014). New insight into the hydrocarbon-pool chemistry of the methanol-to-olefins conversion over zeolite H-ZSM-5 from GC-MS, solid-state NMR spectroscopy, and DFT calculations. *Chem. Eur. J.* 20: 12432–12443.

112 Nunes, M.G.O., Silva, V.T., and Schmal, M. (2004). The influence of the acid sites on the methylamines synthesis with Cu-HZSM-5 zeolite. *Catal. Lett.* 97: 1–2.

113 Song, Y., Zhu, X., and Xu, L. (2006). Study on the process of transformation of olefin into aromatics over HZSM-5. *Catal. Commun.* 7: 218–223.

114 Sun, X., Mueller, S., Shi, H. et al. (2014). On the impact of co-feeding aromatics and olefins for the methanol-to-olefins reaction on HZSM-5. *J. Catal.* 314: 21–31.

115 Zhang, W., Zhi, Y., Huang, J. et al. (2019). Methanol to olefins reaction route based on methylcyclopentadienes as critical intermediates. *ACS Catal.* 9: 7373–7379.

116 Zhang, W., Zhang, M., Xu, S. et al. (2020). Methylcyclopentenyl cations linking initial stage and highly efficient stage in methanol-to-hydrocarbon process. *ACS Catal.* 10: 4510–4516.

117 Hu, M., Wang, C., Gao, X. et al. (2020). Establishing a link between the dual cycles in methanol-to-olefins conversion on H–ZSM-5: aromatization of cycloalkenes. *ACS Catal.* 10: 4299–4305.

118 Chowdhury, A.D., Paioni, A.L., Houben, K. et al. (2018). Bridging the gap between the direct and hydrocarbon pool mechanisms of the methanol-to-hydrocarbons process. *Angew. Chem. Int. Ed.* 57: 8095–8099.

119 Plessow, P.N., Smith, A., Tischer, S., and Studt, F. (2019). Identification of the reaction sequence of the MTO initiation mechanism using ab initio-based kinetics. *J. Am. Chem. Soc.* 141: 5908–5915.

120 Liu, Z. and Liang, J. (1999). Methanol to olefin conversion catalysts. *Curr. Opin. Solid State Mater. Sci.* 4: 80–84.

121 Galadima, A. and Muraza, O. (2015). Recent developments on silicoaluminates and silicoaluminophosphates in the methanol-to-propylene reaction: a mini review. *Ind. Eng. Chem. Res.* 54: 4891–4905.

122 Chen, J., Li, J., Wei, Y. et al. (2014). Spatial confinement effects of cage-type SAPO molecular sieves on product distribution and coke formation in methanol-to-olefin reaction. *Catal. Commun.* 46: 36–40.

123 Li, J., Wei, Y., Chen, J. et al. (2015). Cavity controls the selectivity: insights of confinement effects on MTO reaction. *ACS Catal.* 5: 661–665.

124 Bhawe, Y., Moliner-Marin, M., Lunn, J.D. et al. (2012). Effect of cage size on the selective conversion of methanol to light olefins. *ACS Catal.* 2: 2490–2495.

125 Kang, J., Walter, R., Xie, D. et al. (2018). Further studies on how the nature of zeolite cavities that are bounded by small pores influences the conversion of methanol to light olefins. *ChemPhysChem* 19: 412–419.

126 Kang, J., Alshafei, F.H., Zones, S.I., and Davis, M.E. (2019). Cage-defining ring: a molecular sieve structural indicator for light olefin product distribution from the methanol-to-olefins reaction. *ACS Catal.* 9: 6012–6019.

127 Teketel, S., Svelle, S., Lillerud, K.P., and Olsbye, U. (2009). Shape-selective conversion of methanol to hydrocarbons over 10-ring unidirectional-channel acidic H-ZSM-22. *ChemCatChem* 1: 78–81.

128 Teketel, S., Skistad, W., Benard, S. et al. (2012). Shape selectivity in the conversion of methanol to hydrocarbons: the catalytic performance of one-dimensional 10-ring zeolites: ZSM-22, ZSM-23, ZSM-48, and EU-1. *ACS Catal.* 2: 26–37.

129 Bjørgen, M., Joensen, F., Lillerud, K.P. et al. (2009). The mechanisms of ethene and propene formation from methanol over high silica H-ZSM-5 and H-beta. *Catal. Today* 142: 90–97.

130 Otomo, R., Müller, U., Feyen, M. et al. (2016). Development of a post-synthetic method for tuning the Al content of OSDA-free Beta as a catalyst for conversion of methanol to olefins. *Catal. Sci. Technol.* 6: 713–721.

131 Zhao, X., Wang, L., Li, J. et al. (2017). Investigation of methanol conversion over high-Si beta zeolites and the reaction mechanism of their high propene selectivity. *Catal. Sci. Technol.* 7: 5882–5892.

132 Khare, R., Liu, Z., Han, Y., and Bhan, A. (2017). A mechanistic basis for the effect of aluminum content on ethene selectivity in methanol-to-hydrocarbons conversion on HZSM-5. *J. Catal.* 348: 300–305.

133 Yarulina, I., Bailleul, S., Pustovarenko, A. et al. (2016). Suppression of the aromatic cycle in methanol-to-olefins reaction over ZSM-5 by post-synthetic modification using calcium. *ChemCatChem* 8: 3057–3063.

134 Yarulina, I., De Wispelaere, K., Bailleul, S. et al. (2018). Structure–performance descriptors and the role of Lewis acidity in the methanol-to-propylene process. *Nat. Chem.* 10: 804–812.

135 Bailleul, A.S., Yarulina, I., Hoffman, A.E.J. et al. (2019). A supramolecular view on the cooperative role of Brønsted and Lewis acid sites in zeolites for methanol conversion. *J. Am. Chem. Soc.* 141: 14823–14842.

Part V

Carbon Dioxide as C1 Building Block

11

Overview on CO_2 Emission and Capture

Wanlin Gao and Qiang Wang

Beijing Forestry University, Department of Environmental Science and Engineering, 35 Qinghua East Road, Haidian District, Beijing 100083, P. R. China

11.1 Introduction

Nowadays, the global air environmental problems are mainly reflected in three aspects, which are the greenhouse gas (GHG) effect, the destruction of ozone layer, and acid rain. However, global warming has an obvious influence on the worldwide global climate change [1]. Excessive emission of carbon dioxide (CO_2), as one of the major GHG, is the primary cause for severe global warming. According to the Intergovernmental Panel on Climate Change (IPCC) report, the atmospheric CO_2 concentration has increased from 292 ppm before the industrial evolution to 386 ppm [2]. If the concentration level continues to rise to 450–550 ppm, the worldwide average temperature would have an increment of 2–3 °C. This would cause severe extreme weather conditions, such as sea-level rise, glacier melting, high temperature, serious drought, and storms, which would bring immeasurable loss to all the countries in the world [3, 4]. Therefore, carbon emission reduction and global warming mitigation have become the common concerns for all human beings.

Carbon capture or separation, from industrial emission sources, is a critical endeavor to mitigate challenging climate change [5–7]. Fossil fuel-burning power plants are the largest point sources of anthropogenic CO_2 emissions and will largely rely on CO_2 capture to reduce emissions [8–10]. It is expected that the energy demand will further increase by 53% by 2030, and fossil fuels will still be the dominant energy source over the next few decades [11, 12]. The continuing and even accelerating increase in anthropogenic CO_2 emission and its adverse impact on our planet's climate necessitate the near-term implementation of strategies relating to the reduction of CO_2 emission [13–15]. Currently, a variety of technological approaches have been developed to reduce CO_2 emission from power plants, including precombustion capture, postcombustion capture, oxy-fuel combustion, and chemical-looping combustion [16, 17]. Carbon capture for fossil-fuel power plants is perceived as a critical technology for climate change mitigation [18, 19].

In this chapter, we will critically summarize the latest developments and advanced achievements in the field of CO_2 capture, along with a systematic demonstration of

Heterogeneous Catalysis for Sustainable Energy, First Edition. Edited by Landong Li and Justin S. J. Hargreaves.

the current CO_2 emission circumstances since 2010. Capturing materials including a variety of solvents and solid adsorbents that show superior adsorption capacity toward CO_2 are presented, as well as simulated processes for the deployment of fabricated adsorbents and technoeconomic analyses. Overall, there is much new progress for carbon capture in terms of material fabrication and process application.

11.2 CO_2 Emission and Related Problems

The Paris Agreement on climate change has set out a legally binding commitment to keep the increase in global average temperature to well below 2 °C above preindustrial levels, with an ambition to limit the rise to 1.5 °C [20]. In 2016, around 42% of the global CO_2 emissions were from electricity and heat generation, and 30.7% of these emissions occurred in China. The majority of the CO_2 emission increment during 2007–2012 can be attributed to electricity generation (96.2%) driven by the changes in power demand, the key to power sector decarbonization. Additionally, all power grids exhibited an increase in CO_2 emissions from electricity generation, with the east and central grids accounting for 64% of the national increase. The power transmission structure had only a small impact on CO_2 emissions from power generation.

As the largest industrial CO_2 emission sectors of coal chemical industry in the world, China faces tremendous pressure to reduce its carbon emission. The provincial-level spatial pattern of the CO_2 emission of the chemical industry implies that the industry is strongly influenced by coal resource and the majority of the CO_2 emission is distributed in northern China, where coal is relatively abundant. The market demand for chemicals is also an important driving factor. Considering the development of the modern coal chemical industry, its CO_2 emission was predicted to be as high as 416.52 Mt in 2020. However, the CO_2 emission could be reduced by 317.98 Mt when carbon capture, utilization, and storage are applied to process and energy systems simultaneously [21]. The implementation plan and technological roadmap for China's 2050 renewable energy development are critical for China to achieve its CO_2 emission goals. Power transmission has an important role in securing a stable electricity supply. The potential for improving energy use efficiency remains high, especially for renewable energy such as solar and wind for time-variant characteristics. Changes in the power transmission structure in the northwest and northeast grids promoted CO_2 emissions by 31.2 and 4.8 million tons, respectively [13].

Chemical production is set to become the single largest driver of global oil consumption by 2030 [22, 23]. To reduce oil consumption and the resulting GHG emissions, carbon dioxide can be captured from stacks or air and utilized as an alternative carbon source for chemicals (Figure 11.1). Carbon capture and utilization (CCU) has the technical potential to decouple chemical production from fossil resources, reducing annual GHG emissions by up to 3.5 Gt CO_2-eq in 2030, leading to a carbon-neutral chemical industry and decoupled chemical production from fossil resources. This transition, however, will cause largely increased mass

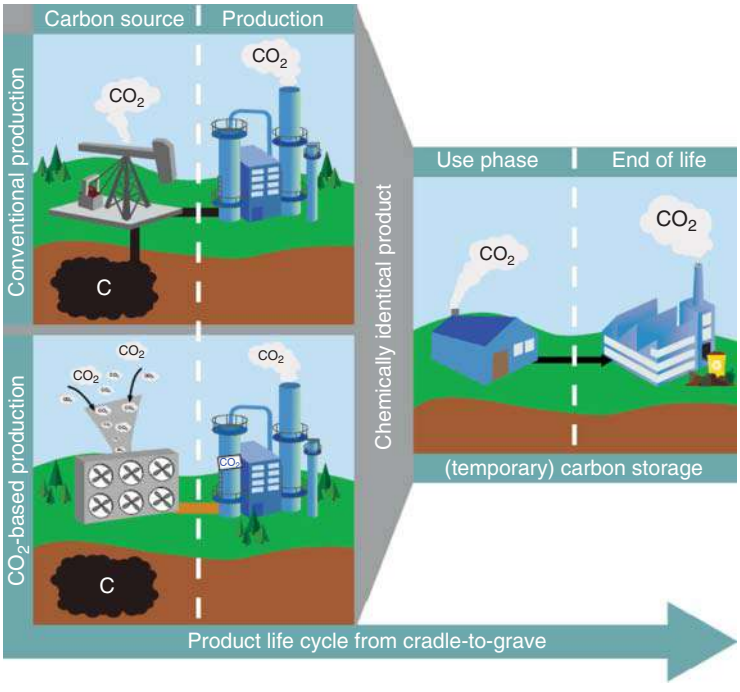

Figure 11.1 Changes in the life cycle of established chemicals through the implementation of CCU technologies. Source: Reproduced with permission from Katelhon et al. [24]; © 2019, National Academy of Sciences.

flows and demand of more than 18.1 PWh for low-carbon electricity, corresponding to 55% of the projected global electricity production in 2030. Most large-scale CCU technologies are found to be less efficient in reducing GHG emissions per unit low-carbon electricity when benchmarked to power-to-X efficiencies reported for other large-scale applications including electro-mobility (e-mobility) and heat pumps. Once and where these other demands are satisfied, CCU in the chemical industry could efficiently contribute to climate change mitigation [24].

11.3 CO_2 Capture Technology

Global warming is an international issue caused by the increasing GHG emissions [25, 26]. The Paris Agreement called for an urgent action to limit warming levels well below 2 °C, pursuing efforts to limit it to 1.5 °C. Among various anthropogenic GHG emitted into the atmosphere, CO_2 accounts for the largest percentage due to human activities [27, 28]. Since the preindustrial era, the CO_2 level in the atmosphere has increased from ~280 to ~407 ppm. Efficient CO_2 capture is of great significance for the GHG reduction and the control of global warming [29, 30]. The CO_2 emission reduction from anthropogenic sources will require a higher reliance on carbon capture technologies [31, 32]. Most of the CO_2 release comes from the combustion of fossil fuels, and industries with high CO_2 emissions are mainly centered on power

generation, the cement industry, communication and transportation, the steel industry, chemical engineering, etc. Among them, the carbon footprint from power generation accounts for more than 40% of the total emission amount of CO_2 in China. Except for the transportation industry, the other large-scale CO_2 emission sources are all stationary point sources, which is favorable for focusing on the implementation of carbon release reduction. Therefore, one of the most effective methods to curb carbon emission is to capture CO_2 from coal-fired power plants.

According to different CO_2 capture locations for coal-fired power plants, there are three main CO_2 capture processes, which are postcombustion, precombustion, and oxy-fuel combustion, respectively, for industrial applications [32]. At present, there are several solid adsorbents that are commonly deployed for CO_2 capture, namely, carbon-based materials, zeolites, metal–organic frameworks (MOFs), and metal oxides [33]. Different types of adsorbents show diverse CO_2 capture performance under various operation temperatures, pressures, CO_2 concentration, and relative humidity. Therefore, the deployment of adsorbent should be carefully determined by its practical application. An ideal adsorbent should have high CO_2 capture capacity, rapid desorption rate, good regenerability, good mechanical strength, and low fabrication cost [34]. For the selection of a suitable adsorbent, both the advantages and disadvantages of the adsorbent should be taken into consideration, and the economic impact should be carefully analyzed according to the practical application.

11.3.1 Precombustion CO_2 Capture

Precombustion capture involves reacting fuel with oxygen or air and/or steam to give mainly a "syngas" composed of carbon monoxide and hydrogen. The CO is reacted with steam in a catalytic reactor to give CO_2 and more H_2. CO_2 is then separated, usually by a physical or chemical absorption process, resulting in a H_2-rich fuel (Figure 11.2) [35]. The high pressure of the water–gas shift product

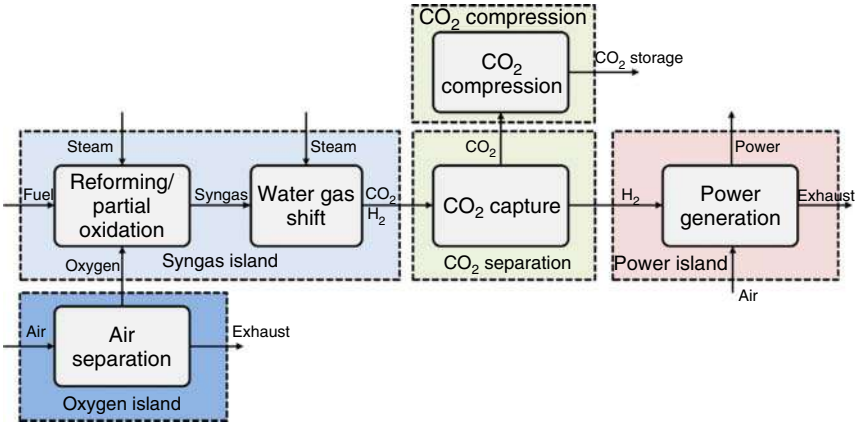

Figure 11.2 Schematic of precombustion capture for power generation.
Source: Reproduced with permission from Jansen et al. [35]; © 2015, Elsevier.

gas stream facilitates the CO_2 removal. The CO_2 concentration at the inlet of the CO_2/H_2 separation stage can be in the range of 15–60% at a total pressure, typically between 2 and 7 MPa. The syngas composition and pressure are highly suitable for precombustion CO_2 capture, due to the high attainable partial pressure of CO_2 through the water-gas shift (WGS) reaction [36]. In the WGS section, excess steam is conventionally utilized to drive the WGS equilibrium to high CO conversion, limit the adiabatic temperature rise within the reactors, and minimize side reactions avoiding damage in the catalyst and the reactors. Commonly, there are two general precombustion routes to capture CO_2 in power generation, namely, natural gas combined cycles (NGCC) and integrated gasification combined cycles (IGCC) [13]. The operation condition for the precombustion process contains CO_2 of high concentration and partial pressure. In general, considerable investment is strongly necessary in the early stage, and the operating cost is rather low.

For natural gas reforming used in a precombustion CO_2 capture system, there are several technologies available including conventional steam methane reforming (SMR), heat exchange reforming (HER)/gas-heated reforming (GHR), non-catalytic partial oxidation (POX), catalytic partial oxidation (CPO), and autothermal reforming (ATR). For another, a typical IGCC system consists of a gasifier, an air separation unit, an extensive gas cleanup system, and a combined cycle for power production. In the coal-based chemical industries and IGCC power plants, the syngas produced by coal gasification has a high pressure (2–7 MPa) and high temperature (250–500 °C). Compared with the conventional Selexol process, elevated temperature pressure swing adsorption (ET-PSA) can save sensitive heat both from syngas for regeneration with the application potential to capture CO_2 in a real IGCC power plant and relatively low energy consumption in some chemical industries (e.g. ammonia synthesis) to adjust the CO_2/H_2 ratio. An effective way to further reduce the energy consumption is to add rinse and purge steps, whose energy loss mainly comes from the consumption of high-temperature steam [37].

11.3.1.1 Intermediate-Temperature Adsorbents

MgO-Based Adsorbents Discovering sustainable materials that can efficiently capture CO_2 is a crucial step toward mitigating anthropogenic GHG emissions. Metal oxide-based adsorbents such as magnesium oxide (MgO) have received special attention as suitable basic solid adsorbents for precombustion process, which can capture CO_2 through chemical reaction [38, 39]. CO_2, as a typical acidic gas, can be easily trapped by the basic sites exposed on the metal oxide surface, and thus metal oxide adsorbents usually show higher CO_2 uptake and higher selectivity [40]. The fabrication of metal oxide-based materials has been regarded as a research hotspot toward CO_2 capture for their high CO_2 capture capacity, good selectivity, low cost, and broad source. MgO adsorbent, obtained from preconcentration of natural minerals, has simple access to mass production with low cost [41]. It shows excellent adsorption selectivity toward CO_2 under wet conditions and is easy to regenerate through operation temperature manipulation [42]. The acidic CO_2 molecule can interact with basic

active sites on the surface of MgO, generating bicarbonate and mono- and bidentate carbonate species, which is highly dependent on the adsorption condition and surface chemistry.

Among various CO_2 adsorbents, recently MgO-based adsorbents have received significant attention due to their high theoretical capture capacity, wide availability, low cost, nontoxicity, and wide operation temperatures [43]. However, the main obstacle in the way of the practical application of MgO adsorbents for CO_2 capture lies in their low actual capture capacity and poor sorption kinetics, which are usually attributed to the barren basic active sites and intrinsically high lattice enthalpy. Therefore, to improve the performance of MgO sorbents for efficient CO_2 capture, various approaches have been proposed, and significant progresses have been achieved. The approaches reported include alkaline metal carbonate/nitrate modification [44], dispersion of MgO on porous supports [45], mesoporous MgO fabrication [42], construction of MgO-based mixed oxides [46], and microstructural modification [47]. In addition, some researchers have paid attention to the granulation, the influences of impurity gases and other applications of MgO adsorbents, etc. Microstructures are of substantial importance to the sorption process with MgO adsorbents [40]. Selecting suitable magnesium precursors is an effective strategy toward producing efficient MgO adsorbents for CO_2 capture [48] and preparing MgO adsorbents from natural minerals that have drawn special attention. Small particle sizes, large surface areas, and high and well-exposed surface basic sites are crucial to the CO_2 capture performance of MgO adsorbents. The operation conditions including CO_2 concentration, pressure, and gas impurities vary significantly depending on the application scenarios, while these are important factors affecting the CO_2 adsorption performance [36, 49]. In 2019, Hu and coworkers published a timely overview of the state-of-the-art research on MgO adsorbents [39].

To optimize the CO_2 capture performance, Creamer and coworkers incorporated biomass during the sample preparation to ensure the formation of dispersed MgO nanoparticles from the decomposition of $MgCl_2$ hydrate. The carbon-supported activated MgO nanoparticles efficiently captured CO_2 at low temperature by physisorption on the pristine MgO and carbon surfaces and $MgCO_3$ formation on the activated defect sites on MgO [50]. For CO_2 adsorbents, a fast adsorption rate is as important as the adsorption capacity to enable the efficient CO_2 capture in the treatment of large amounts of emission gas, where the contact time between the adsorbent and gas is limited. Jin and coworkers fabricated triple salt-promoted MgO adsorbents developed by incorporating $CaCO_3$ with a bi-disperse pore distribution with different ranges, contributing to the fast adsorption rate. The incorporation of Ca into the salt-promoted MgO was effective for controlling the lattice parameter, the textural properties, and the basicity. As a result, the Ca-doped adsorbent could efficiently capture CO_2 at rapid intermediate temperature swing sorption, where pure MgO exhibited a low working capacity [46]. Among these promoting strategies, alkali doping, especially doping of alkaline metal eutectic mixtures, seems to be the most effective [51, 52]. The promoting effect of alkali nitrate molten salt on the CO_2 capture capacity of a commercial MgO was investigated by Wang and coworkers. The MgO sample doped with 10 mol% $(Li_{0.3}Na_{0.6}K_{0.1})NO_3$ was demonstrated to possess the highest

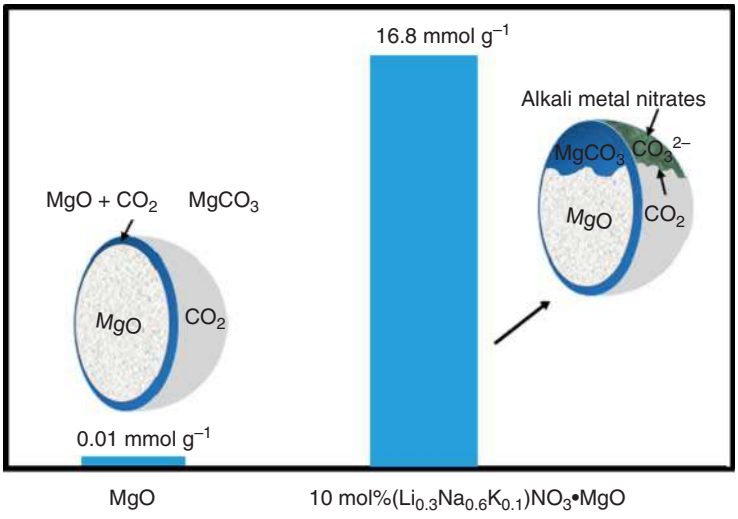

Figure 11.3 The comparison of the CO_2 uptake between neat MgO and 10 mol% $(Li_{0.3}Na_{0.6}K_{0.1})NO_3$·MgO adsorbents. Source: Reproduced with permission from Qiao et al. [53]; © 2017, ACS Publications.

CO_2 uptake (up to 16.8 mmol g^{-1}), as depicted in Figure 11.3. The phase status of the molten salts is crucial for the marked improvement in CO_2 capture capacity of MgO [53]. In 2017, Gao et al. published a review summarizing the advances in the fabrication of molten salt-modified MgO-based CO_2 adsorbents, which is the dominant approach to improve the performance of MgO adsorbents [38].

The granulation of MgO sorbents is necessary prior to realistic application [54]. The MgO granules should be fabricated with good mechanical properties and CO_2 sorption performance using relatively easily accessible raw materials. Future work needs to evaluate a particular sorbent under the test conditions similar to those typically known in the targeted applications. In terms of the economy, the costs of raw materials, manufacturing process, operating process, and energy consumption should be taken into full consideration and carefully optimized.

LDH-Derived Adsorbents Layered double hydroxides (LDHs) are a class of ionic lamellar compounds that are made up of stacked positively charged brucite-like layers, with the interlayer spaces containing charge compensating anions and solvation molecules. Due to their well-defined layer structure with interlayer distance of nanometers, large surface areas, high anion exchange capacities, and pH buffering capacities, LDHs have been intensively studied for a wide range of important applications, e.g. catalysis, photochemistry, gas adsorption, electrochemistry, polymerization, magnetization, biomedical science, and metal corrosion inhibition. In particular, LDH-derived mixed metal oxides have been investigated as promising CO_2 absorbents because they possess good thermal stability, relatively fast CO_2 adsorption kinetics, and moderate regeneration temperatures [55]. They show desired properties as CO_2 adsorbents in precombustion capture

applications and have been identified as particularly suited adsorbent materials for CO_2 adsorption in the sorption-enhanced water-gas shift (SEWGS) and sorption enhanced biomass reforming (SEBR) technologies that operate in the temperature range of 200–400 °C [56]. For LDH-derived CO_2 adsorbents, starting from the natural mineral (Mg–Al–CO_3), extensive studies have been focused on the effects of divalent cations, trivalent cations, charge compensating anions, Mg/Al ratio, synthesis method, the presence of SO_2 and H_2O, particle size, and alkali metal (K, Cs) doping on CO_2 adsorption. In addition to changing the composition of LDHs, another effective way to improve the CO_2 capture capacities is to control the particle size of the LDHs [57]. For the adsorbents, decreasing the particle size or increasing the specific surface area can enhance the surface adsorption sites, which accordingly improves the CO_2 capture capacity [58].

The structure of LDHs consists of positively charged brucite-like layers, with interlayer spaces containing charge compensating anions and water molecules [59]. The metal cations occupy the center of an octahedral structure whose vertices contain hydroxide ions, and the octahedra are connected by sharing edges to form an infinite sheet [60]. Upon calcination, the sheet structure of LDHs can be well preserved in the obtained mixed metal oxides. Gao and coworkers have performed comprehensive investigations on the CO_2 adsorption characteristics of Mg–Al–CO_3 LDH-derived mixed metal oxides and proposed the possible adsorption sites and the mechanisms for CO_2 adsorption. The active Mg–O species could be induced either by the substitution of Mg^{2+} by Al^{3+} in the periclase MgO lattice or by the diffusion of Al^{3+} out of the octahedral brucite layers, as depicted in Figure 11.4 [61]. The anions affect the thermal stability and morphology and the surface area of LDHs, consequently influencing the CO_2 adsorption capacity. LDHs can be fabricated by many methods including coprecipitation, structure reconstruction, reverse microemulsion, sol–gel routes, ion exchange, urea hydrolysis, etc. The calcination temperature is a key parameter determining the number of active Mg–O species. Too low calcination temperature cannot break the Mg—O bonds, and the hydroxide phase of LDHs will be preserved. On the other hand, too high calcination temperature will induce the reaction between Mg and Al species to form the $MgAl_2O_4$ spinel oxide. Since each LDH possesses specific thermal stability, the optimal calcination temperatures for different LDHs are different [4].

11.3.1.2 High-Temperature Adsorbents

CaO-Based Adsorbents CaO is a promising high-temperature CO_2 adsorbent for some CO_2-free sorption-enhanced steam reforming (SESR) processes. It has been proposed to be applied in both pre and postcombustion capture processes based on the reversible carbonation/calcination cycles and SESR reaction, which is a candidate technique for producing pure H_2 via simultaneous reforming and adsorptive separation of CO_2. Moreover, the reaction temperature can be reduced to around 500–600 °C, which is much lower than those used in conventional steam reforming (~800 °C). Hence, CaO is regarded as one of the most promising high-temperature CO_2 sorbents [62].

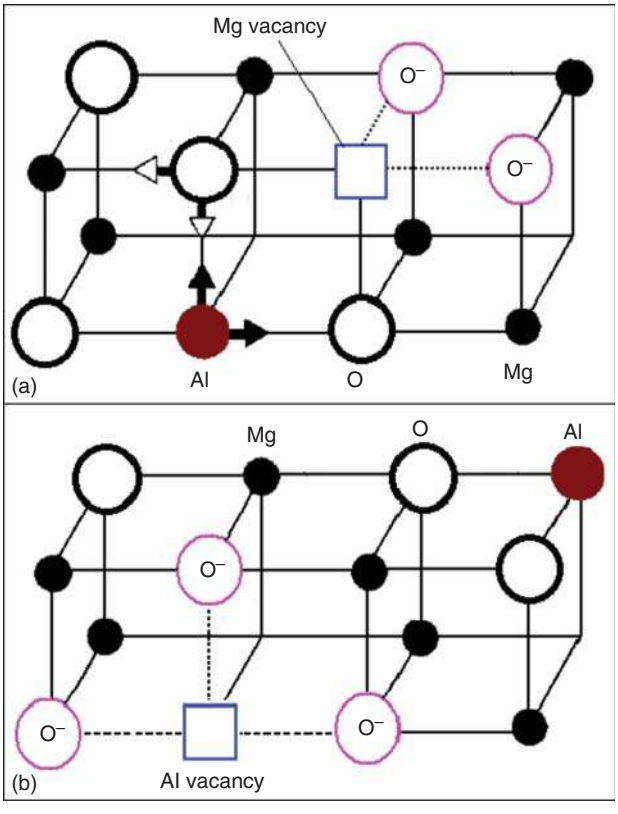

Figure 11.4 The proposed mechanisms for the formation of active Mg–O species induced by (a) the substitution of Mg by Al and (b) the diffusion of Al atoms out of the octahedral brucite layers. Source: Reproduced with permission from Gao et al. [61]; © 2013, The Royal Society of Chemistry.

CaO reacts with CO_2 molecules to form calcium carbonate $CaCO_3$, which will decompose to CaO for regeneration at high temperatures of 500–900 °C [63, 64]. Calcium looping, a CO_2 capture technique, may offer a mid-term, if not a near-term, solution to mitigate climate change, triggered by the yet increasing anthropogenic CO_2 emissions [65–67]. For CaO-based high-temperature CO_2 sorbents, good cyclic stability is highly desired for their practical applications. Calcium looping is based on the reversible carbonation and calcination of CaO ($CaO + CO_2 \leftrightarrow CaCO_3$) and has been demonstrated in pilot-scale facilities. Unfortunately, the poor cyclic stability of CaO at high temperatures is a non-negligible issue for the successful development of this process. The sorption/desorption processes are normally performed at high temperatures (600–950 °C), but the Tammann temperature is lower than that for either carbonation or calcination in calcium looping, which leads to irreversible and detrimental changes to the textural properties of CaO during cycles. In this context, the CO_2 diffusion becomes difficult, resulting in only partial carbonation. For this reason, great effort has been devoted to the improvement of the sintering resistance of CaO over recent years.

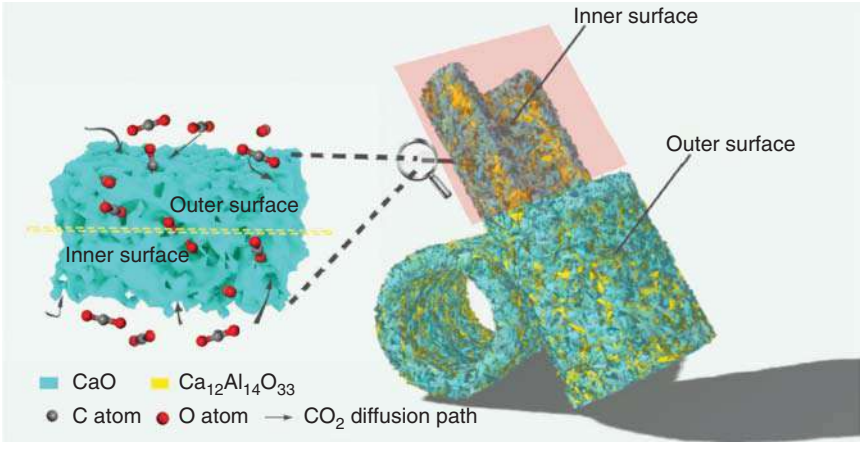

Figure 11.5 Model diagram and CO_2 capture mechanism of the morphogenetic CaO-based adsorbent. Source: Reproduced with permission from Ma et al. [69]; © 2019, Elsevier.

To overcome the loss-in-capacity problems of Ca-based adsorbents with multiple calcium looping cycles, Ma and coworkers fabricated a novel $CaO/Ca_{12}Al_{14}O_{33}$ adsorbent with a microtube-like structure, providing a low CO_2 diffusion resistance in the adsorbent [68]. The utilization of the bio template is useful to retain the high cyclic CO_2 capture reactivity of the synthetic adsorbent. CO_2 could penetrate through the microtube-like structure of the synthetic sorbent from two directions, i.e. from the outer surface and inner surface, as shown in Figure 11.5. This phenomenon effectively enlarged the contact area between CO_2 and CaO. Therefore, the morph-genetic CO_2 adsorbent possessed a high porosity and exhibited a high CO_2 capture capacity during multiple cycles [69]. A key requirement for the economic operation of calcium looping is the availability of highly effective CaO-based CO_2 adsorbents. Naeem and coworkers reported hollow and MgO-stabilized CaO microspheres featuring highly porous multi-shelled morphologies, retaining 83% of its initial CO_2 uptake over 30 CO_2 adsorption/desorption cycles under practically relevant operating conditions. As a thermal stabilizer, MgO minimized the sintering-induced decay of the adsorbents' CO_2 capacity and ensured a stable CO_2 uptake over multiple operation cycles. The compositional homogeneity and the formation of a multi-shelled morphology, containing excess porosity and being composed of small nanoparticles, are key requirements to obtain effective CO_2 adsorbents [70]. Sun and coworkers synthesized dual functional materials, containing a CaO adsorbent coupled with a catalytic component CeO_2, displaying almost 100% CO selectivity and 51.8% CO_2 conversion in the reverse WGS reaction and a remarkable cyclic stability after 20 cycles of integrated CO_2 capture and conversion [71].

Lithium-Containing Ceramic Adsorbents Lithium-containing ceramic-based high-temperature CO_2 sorbents have received tremendous attention due to their high CO_2 capture capacity, low regeneration temperatures, and relatively high stability.

Li_4SiO_4, Li_2ZrO_3, and many other lithium-containing ceramics exhibit advantages in terms of relatively high sorption capacity, fast sorption rate, good cycling stability, and also reasonable material costs. Typically, Li_4SiO_4 sorbent captures CO_2 at temperatures between 450 and 700 °C, with a theoretical maximum CO_2 capacity of 36.7 wt%. According to the double-shell sorption mechanism, an external shield of alkaline carbonate will form during the process CO_2 of sorption. Once the shield is formed, the lithium and oxygen elements have to diffuse throughout the external layer and continue to react with CO_2. Regeneration performance is an important evaluation standard for lithium-containing ceramic adsorbents while the high production cost represents another limitation of the sorbents for practical applications [72].

Compared with many other high-temperature CO_2 sorbents, Li_4SiO_4 has been considered as one of the most promising sorbents [73]. The Li_4SiO_4 sorbent mainly works in the temperature range of 500–750 °C for the SESR process [74]. Despite the high theoretical maximum CO_2 sorption capacity of 36.7 wt%, the CO_2 capture capacities of practical Li_4SiO_4 reported in the literature are often much lower due to the mass transport limitation and severe sintering issues [72]. To achieve appreciable CO_2 capture performance with Li_4SiO_4 sorbents, several attempts have been made, including but not limited to microstructural modification, alkali promotion, transition metal doping, and Li substitution by Na [75]. Zhang and coworkers prepared a novel Li_4SiO_4-based high-temperature CO_2 sorbent directly from the cheap raw material vermiculite (expanded vermiculite [EXVMT]) for the first time, possessing better dispersion of Li_4SiO_4 nanoparticles and higher porosity, which accordingly resulted in the greatly enhanced CO_2 sorption/desorption cycling stability due to the separating effect by the existing impurity phases in EXVMT [11]. The sorbent showed lower activation energies for both the chemisorption and the diffusion processes, enabling it much less affected by CO_2 concentration. The optimized sorbent gave a high CO_2 sorption capacity of 20.7 wt% at 650 °C under 100 vol% CO_2 for 2 hours. The highly porous microstructure favored the CO_2 diffusion, and separating effect of impurity phases prevented the sintering of Li_4SiO_4, making the vermiculite (VMT)-derived Li_4SiO_4-based high-temperature CO_2 sorbent potential for practical applications (Figure 11.6).

Alkali Titanate-Based Adsorbents Alkali metal and alkali earth metal titanates are important inorganic materials, showing great potential and vital application prospects as novel energy materials due to their superior physical and chemical properties. Among them, alkali metal titanates with the spinel structure are very attractive and exhibit good regenerability and structural stability. The investigations on the fabrication of inorganic materials with nanostructures, the establishment of the generation mechanism model, and the relationship between the structure and performance of these inorganic materials are of significant importance for both theoretical investigation and practical applications.

The fabrication methods for titanates are mainly based on solid-state, hydrothermal, sol–gel, and template processes. The sol–gel method to prepare titanates is one of the important wet chemical routes. The main procedure includes the mixing

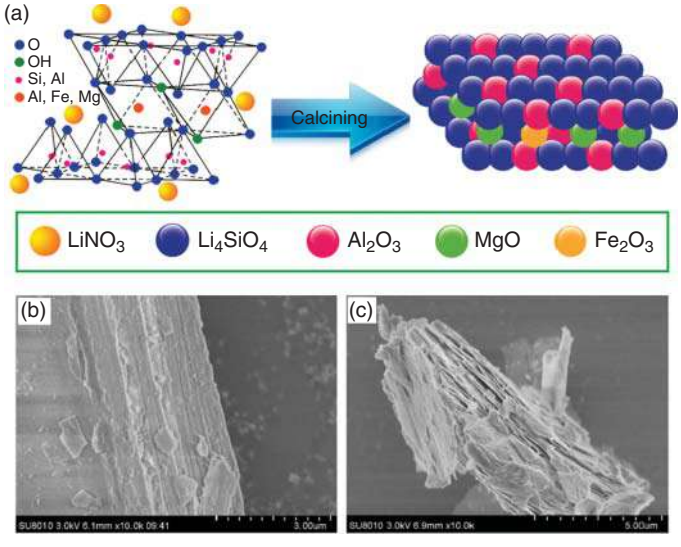

Figure 11.6 (a) Schematic illustration of the synthesis of Li_4SiO_4-based CO_2 sorbent from vermiculite precursor and SEM images of (b) raw VMT and (c) EXVMT. Source: Reproduced with permission from Zhang et al. [11]; © 2018, Elsevier.

of the titanium alkoxide, soluble titanium tetrachloride, and accessory ingredient to form a sol for a certain period. After an aging process, the gel turns to titanate powder upon calcination. The titanates obtained by the sol–gel method show high purity, uniform particle size distribution, and small particles, but the preparation method is costly and difficult for scale-up. Similar to the sol–gel method, titanates can be synthesized via a hydrothermal route. The morphology and structure of the titanates prepared via the hydrothermal route are highly dependent upon the crystallization temperature, the time, the type of alkali, and the titanium source. The solid-state sintering technology is the most commonly employed method and is also practical for industrialization. Compared with other methodologies, the solid-state sintering technology has lower cost and larger production and is easy to operate that is available for real applications.

Alkali titanates have attracted much attention as one kind of emerging high-temperature CO_2 sorbent. Potassium dititanate ($K_2Ti_2O_5$) was revealed to possess an unexpected, highly reversible CO_2 sorption/desorption capacity at ~750 °C, suitable for sorption-enhanced hydrogen production (SEHP) processes. A reversible structure switching mechanism between $K_2Ti_2O_5$ and $K_2Ti_4O_9$ accompanied by the formation of K_2CO_3 species was recently reported by Zheng and coworkers [76]. In addition to $K_2Ti_2O_5$, a new type of high-temperature CO_2 capture material potassium sodium titanate $KNaTiO_3$ was discovered by the same group for the first time [77], which exhibited excellent sorption performance, including a superior CO_2 capture capacity and a fast sorption rate under different concentrations of CO_2 (Figure 11.7). It exhibited outstanding thermal stability even up to 800 °C and a quite high CO_2 capture capacity of 19.0 wt% at 700 °C. Even under

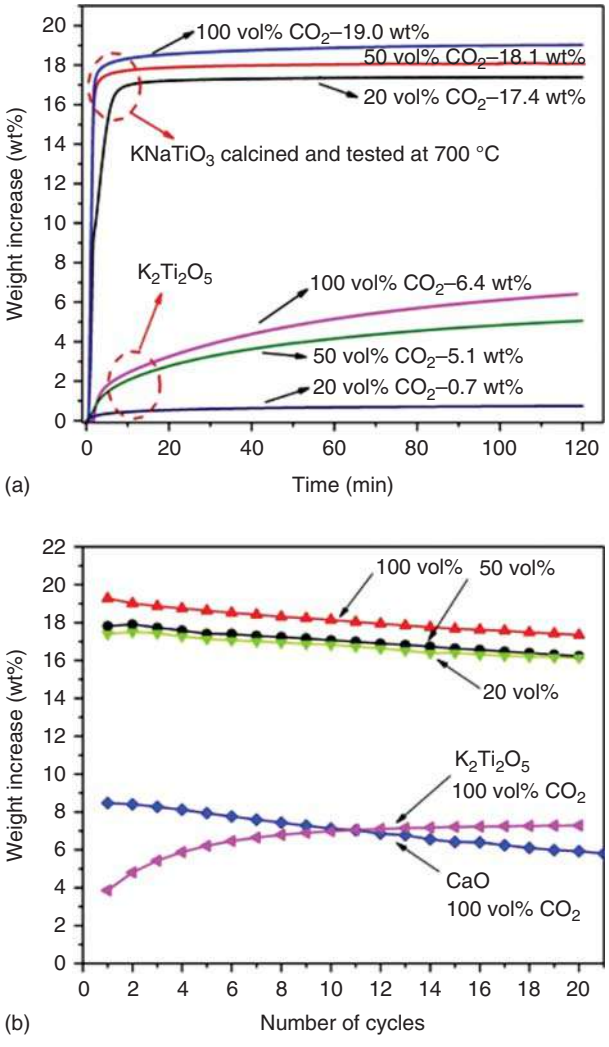

Figure 11.7 (a) The influence of different CO_2 concentrations on the CO_2 capture capacity of $KNaTiO_3$ and $K_2Ti_2O_5$. (b) Comparison of the CO_2 sorption/desorption cycling performance of $KNaTiO_3$ with other sorbents ($K_2Ti_2O_5$ and CaO) at different CO_2 partial pressure. Source: Reproduced with permission from Zheng et al. [77]; © 2020, Elsevier.

low CO_2 concentrations such as 20 and 50 vol% CO_2, the CO_2 capture capacity could reach 17.4 and 18.1 wt%, respectively. The performance achieved is very critical for practical applications for CO_2 removal under various concentration conditions.

11.3.2 Postcombustion CO_2 Capture

Postcombustion capture based on a regenerative chemical absorption is considered a mature and close-to-market option in the near term and mid-term, which can be applied to most of the CO_2 stationary emission sources, for example, the flue gas

of coal-fired power plants [78]. In fact, absorption technology is presently the most available and effective approach for postcombustion CO_2 capture [79]. Solvents are key to the performance of absorption technology. The process has been widely applied as conventional CO_2 capturing methodology due to its low economy input in the early stage, and it is regarded as the dominant procedure to curb carbon emission, taking current technologies and circumstances into consideration. For the postcombustion process, the CO_2 concentration in the flue gas is relatively low and therefore imposes severe restrictions upon the CO_2 capture procedure.

The swing adsorption reactor cluster is a promising new method for postcombustion CO_2 capture using a synergistic combination of temperature and pressure swings. The pressure swing is carried out by a vacuum pump and allows for 90% CO_2 capture using only a small temperature swing, which is carried out by a heat pump. The small temperature swing allows the heat pump to transfer heat from carbonation to regeneration at very high efficiency, minimizing the energy penalty. Higher CO_2 concentrations allow a given CO_2 capture ratio achieved with a smaller temperature swing, thus further improving the heat pump efficiency. Primary energy consumption will continue to decline as the electricity sector decarbonizes, increasing the attractiveness of the swing adsorption reactor cluster in the coming decades [79]. System-wide integration of the postcombustion CO_2 capture process into a coal-fired power plant is an effective and practical strategy to improve cost-effectiveness for capturing CO_2 emissions from the power sector. Considerable reduction of the net energy efficiency of a power plant by 20–40% is inevitable due to the energy requirements for the CO_2 capture and the power requirement for the CO_2 compression. The net efficiency penalty can be significantly reduced by exploiting the choice of steam quality for the solvent regeneration and accommodating further power generation [80].

11.3.2.1 Amine-Based Solvents

The amine-based capturing process is one of the most commonly adopted methods for the relatively low CO_2 concentration in flue gas. A very active chemical solvent is necessary, and relatively high energy is imperative for regeneration for real applications. The process is widely applied to produce CO_2 of high purity and improves the oil recovery rate and is applied to urea production and in the food and beverage industry. Amine-based absorption is the primary candidate for postcombustion CO_2 absorption for its long-term operational experience from natural gas and hydrogen and its suitability for retrofitting existing fossil fuel-fired power plants (Figure 11.8) [8]. However, the amine-based CO_2 capture processes have drawbacks including low CO_2 absorption capacity, energy penalty correlated with absorbent regeneration, monoethanolamine (MEA) degradation, higher operating costs, and equipment corrosion, thus limiting their further application [81, 82]. Research hotspots in amine-based CO_2 absorption include environmental impact minimization, amine loss reduction, and energy efficiency improvement [83, 84]. Major concerns have arisen regarding the formation and the subsequent release of toxic nitrosamine and nitramine byproducts from amine systems to impact the environment [85]. Recently, phase change solvents have attracted growing

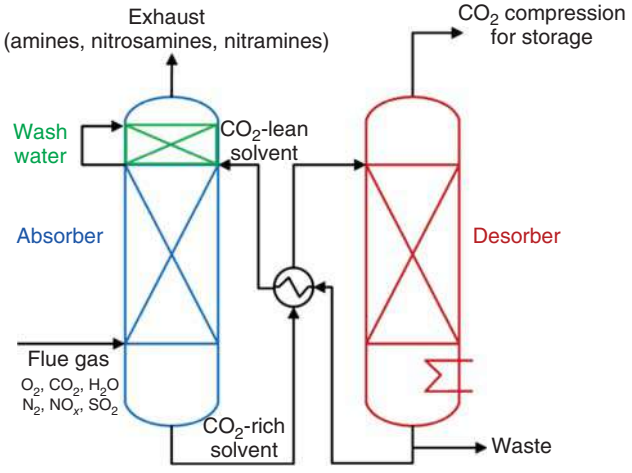

Figure 11.8 Amine-based CO_2 capture system. Source: Reproduced with permission from Yu et al. [8]; © 2017, ACS Publications.

interests for their potential to substantially reduce the energy requirement for CO_2 capture. Phase change solvents are homogeneous solvents under normal conditions but undergo a phase transition into a heterogenic system, triggered by changes in polarity, hydrophilicity, ionic strength, or hydrogen bond strength to form a CO_2-lean liquid phase and a CO_2-enriched liquid or solid phase [42].

11.3.2.2 Amine-Functionalized Adsorbents

Amine-functionalized nanomaterials have significant potential in CO_2 capture technology because of their low energy consumption, stable performance, and high regeneration capacity [86, 87]. Porous organic polymers show distinct advantages of large pore volume, diversified structure, high specific surface area, excellent stability, robust and hydrophobic all-carbon skeleton, and low density, making them good candidates for the incorporation of amines. Yang and coworkers converted cost-effective porous organic polymers into robust CO_2 adsorbents through functionalization with polyamine, which have strong potential in postcombustion CO_2 capture [88]. Organic molecular cages (OMCs) have attracted great attention in the field of porous organic materials for their intrinsic porosity and the solution-processible properties. Recently, Wang and coworkers demonstrated a strategy of "cage to frameworks" to synthesize fluorescent porous networked tetraphenylethylene-based oxacalixarene (TOC) with enhanced porous properties for the polymerization, overcoming the window-to-arene packing modes of cages (Figure 11.9). Porous TOC, by virtue of its strong fluorescence and the shape-persistent intrinsic cavity, displayed prominent reversible fluorescence enhancement in response to CO_2 in different dispersion systems and fluorescence recovery for CO_2 release in the presence of $NH_3 \cdot H_2O$ and was therefore very effective to detect and quantify the fractions of CO_2 in a gaseous mixture [89]. Novel amine-functionalized adsorbents composed of copper silicate nanospheres grafted

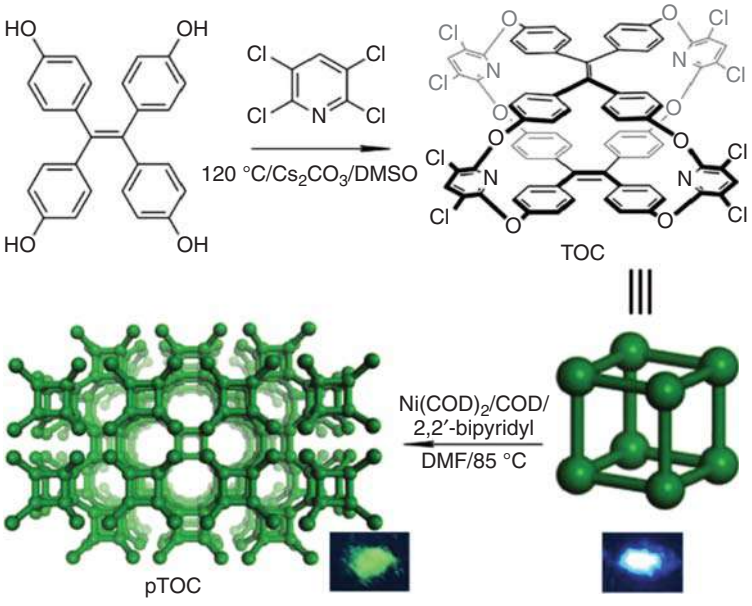

Figure 11.9 Graphical representation of synthesis of TOC and pTOC. Source: Reproduced with permission from Wang et al. [89]; © 2018, John Wiley & Sons, Inc.

with mono-, di-, and tri-aminosilanes were synthesized by Ren and coworkers. The copper silicates with rich surface hydroxyl groups, significant surface areas, and mesoporous structures facilitated chemical modifications by amines, resulting in a high CO_2 adsorption capacity (a maximum CO_2 uptake of 47.88 mg g^{-1}) and excellent cyclic regenerability (maximum deviation of 3.51% after a 20-times test). The types of amines, the number of amine groups, and the steric hindrance of the molecular chain significantly influence the CO_2 adsorption capacity and the amine efficiency [90].

11.3.2.3 MOF-Based Adsorbents

MOFs are one kind of novel porous material with crystalline structure composed of metal atoms or clusters to form coordination bonds and multidentate ligand, which are typically prepared by hydrothermal or solvothermal method [91, 92]. The key point for the fabrication of MOFs is the suitable selection of the metal center and the design of the organic ligand. There are a variety of organic ligands that could be selected to manipulate the pore diameter, pore structure, and chemical potential to adjust the selectivity, kinetic property, and capture capacity [93, 94]. MOFs show superior CO_2 capture capacity under high pressure and rather good capturing performance under ambient temperature and pressure (Figure 11.10) [95], in comparison with carbon- and zeolite-based adsorbents [96, 97]. However, the organic chelating ligands for the fabrication of MOFs typically contain aromatic rings modified with hydroxyl, carboxyl, and amino groups, which are of high cost and complicated structure, restricting studies to the laboratory scale [98]. Besides,

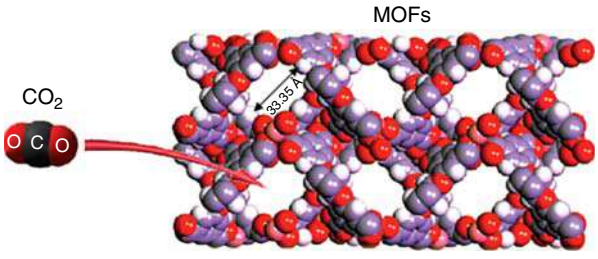

Figure 11.10 Metal–organic frameworks for CO_2 adsorption. Source: Reproduced with permission from Zhuang et al. [95]; © 2011, ACS Publications.

the moisture stability, regenerability, and competitive adsorption capacity of MOFs need further enhancement from the view point of practical application. Recently, Yan and coworkers deployed ZIF-8/mIm-glycol-water slurry in the continuously cycled setup of pilot-scale separation experiments. More than 92% of CO_2 could be removed, and the performance remained stable for more than 100 hours of cycling. The slurry could be regenerated under very mild conditions and thus required relatively low energy cost [94].

11.3.2.4 Zeolite Adsorbents

Zeolites are a kind of originally naturally occurring porous silicate framework material with well-defined crystal structure, which have been now industrially manufactured on the large scale [92]. The pore sizes of zeolites are uniformly distributed in the range of 0.3–1.5 nm, which make them readily available for gas adsorption and separation. Zeolites can be used to selectively adsorb molecules with higher dipole and quadrupole energies [99, 100]. CO_2 has a very high quadrupole moment and can strongly interact with the electric field generated by the cations present in zeolites such as Li^+ and Na^+ [101]. In this context, zeolites are regarded as a type of good CO_2 adsorbent. The separation capacity of zeolites depends on many factors, such as topology, framework composition, ionic form, the purity of gas, and the properties of gas molecules (size, shape, and the molecular polarity) [102, 103]. Generally, low-cost zeolite-based adsorbents possess excellent adsorption kinetics and high adsorption capacity, making them promising for large-scale industrial applications [104, 105]. However, similarly to the carbon-based adsorbents, the effect of temperature on CO_2 adsorption capacity is non-negligible [106, 107]. Higher temperatures may cause the lower adsorption capacities during the adsorption processes. Meanwhile, the competitive adsorption of water vapor vitally impacts on the CO_2 adsorption capacities of zeolite-based absorbents, which is the key issue to address before further considerations for practical CO_2 adsorption [108, 109].

11.3.2.5 Carbon-Based Adsorbent

Carbon-based materials are the most commonly applied adsorbents, being composed of only one element but showing so many advantages like good thermal and chemical stability, excellent conductivity for heat and electricity, and adequate mechanical strength and flexibility. Carbon-based materials with low density,

high specific surface area, and high pore volume are particularly favorable for CO_2 adsorption and capture. Moisture shows no obvious influence on the capture performance of carbon-based materials, and the preparation cost of carbon-based materials is rather low. The adsorption/desorption temperatures are both below 100 °C with low CO_2 adsorption energy consumption under ambient pressures. Carbon-based materials also have a wide range of sources, giving perfect access to massive production at very low cost. For instance, active carbon could be made from coal, industrial by-product, and biomass materials. However, carbon-based materials can exhibit different pore diameter distribution, pore structure, and surface features according to the source of the raw material from which they are prepared. The capture mechanism of CO_2 on carbon-based materials relies on physisorption. The capture capacity of carbon-based materials is low in complex flue gas environments, which is not favorable for power generation plant application.

An adsorption system based on a physical adsorbent, i.e. the activated carbon, was assessed by Jiang and coworkers in the capture of CO_2 emissions from an NGCC. The net efficiency of NGCC using activated carbon increased slightly from 50.8% to 51.1% due to the low regeneration temperature of 85 °C. Although the thermal energy required to regenerate the activated carbon is relatively low, a significant improvement of net efficiency could be observed with increasing partial pressure. Activated carbon shows significant advantages over amine, for example, monoethanolamine, in terms of efficiency and cost, which could be further improved with enhanced heat and mass recovery. From an economic perspective, a postcombustion capture plant based on activated carbon represents a competitive and promising alternative for CO_2 capture in a NGCC [78]. Under typical flue gas conditions (0.15 bar of CO_2 at 40–70 °C), the adsorption capacity and selectivity toward CO_2 over N_2 remain poor on traditional porous adsorbents due to the weak adsorbent–adsorbate interactions. Guo and coworkers reported the synthesis of hierarchically structured porous carbon composites via an interfacial assembling strategy. This fabrication strategy allowed fine-tuning of the surface chemistry and pore network of porous carbons with the aim of enhancing the CO_2 capture capacity at elevated temperatures. The obtained carbon composites reached a record-high CO_2/N_2 selectivity (114.3) at 70 °C, associated with a high adsorption capacity of 1.7 mmol g^{-1} at 1.1 bar. The inorganic substance integrated 3D carbon framework was responsible for such superior CO_2 capture capability by enhancing adsorbent–adsorbate interactions. The inorganic additive also contributed significantly to the enhancement of CO_2 adsorption and separation performance at elevated temperatures in two ways: (i) generating strong interaction sites with CO_2 molecules and (ii) tailoring the pore size and architecture [110].

11.3.3 Oxy-Fuel Combustion CO_2 Capture

CO_2 capture can not only have ecological benefits by reducing CO_2 emissions into the air but also cause direct economic benefits with the high-quality liquid CO_2 for squeezing the remaining oil out from underground in the oil industry. Thus, energy

storage and CO_2 capture interact with increased feasibility and a reduced energy penalty for CO_2 capture. In the gas and steam mixture cycle (GSMC), the combustion products of natural gas (NG) are H_2O and CO_2 while the turbine working medium is also H_2O-CO_2. The oxy-fuel combustion mainly utilizes oxygen of high purity (without nitrogen, obtained from membrane separation or low-temperature separation) rather than air to burn fossil fuels, from which CO_2 with high concentration is generated. Despite the abovementioned advantages, the technique is still far from maturity and needs further investigations on pollution emission, boiler reformation design, and flue gas recovery. The combustion products are basically CO_2 and moisture, which could be further separated by condensation.

Volatile compound emissions and solvent degradation are two major concerns about the deployment of carbon capture technologies based on chemical absorption. Partial oxy-combustion might mitigate the solvent degradation by utilization of a higher CO_2 concentration in the flue gas. Partial oxy-combustion can substantially decrease the reboiler duty due to the increase in the CO_2 partial pressure in the flue gas and the driving force in the absorber thereof. Vega and coworkers evaluated the oxidative degradation of a novel 2-amino-2-methyl-1-propanol (AMP)/aminoethyl piperazine (AEP) blend for CO_2 absorption, showing high resistance to degradation. The presence of higher CO_2 content in the flue gas decreased the NH_3 production, and ~70% reduction of NH_3 emissions was achieved as the CO_2 concentration shifted from 15% to 60% [111]. Later on, they explored the potentialities of partial oxy-combustion in a bench-scale CO_2 capture unit to evaluate the benefits on the CO_2 separation stage, achieving CO_2 removal efficiencies over 95% and lowered energy consumptions. The lowest specific energy requirement was achieved using 60% CO_2 where the energy requirement for the regeneration stage was 4.74 GJ/t CO_2 [112]. Besides, Wu and coworkers simulated a novel GSMC power generation system integrated the technologies of NG/O_2 combustion, energy storage, peak shaving, and CO_2 capture with NG/O_2 cold energy utilization, which exhibited remarkable features such as high efficiency, low first/operation/maintenance costs, zero CO_2 and NO_x emission, and massive off-peak power shifting [113]. As a way of enhancing the potential of this technology to support the decarbonization of energy systems, Eveloy and coworkers investigated a high-temperature electrolysis-based PtM process and its integration with oxy-fuel combustion to cogenerate synthetic methane, heat, and power. The system incorporated *in situ* heat, oxygen, CO_2, and water recycling, as depicted in Figure 11.11. The PtM–oxy-fuel hybridization investigated could effectively contribute to raise the electricity GHG emission threshold below which synthetic natural gas (SNG) could environmentally compete with natural gas, relative to low-temperature electrolysis-based PtM and conventional postcombustion CO_2 capture [114].

11.3.4 Chemical Looping Combustion

Chemical looping combustion (CLC) is a promising technique to capture CO_2 at reduced cost [115]. In CLC, a solid oxygen carrier, typically a transition metal oxide, provides the oxygen to oxidize a carbonaceous fuel yielding a mixture of steam

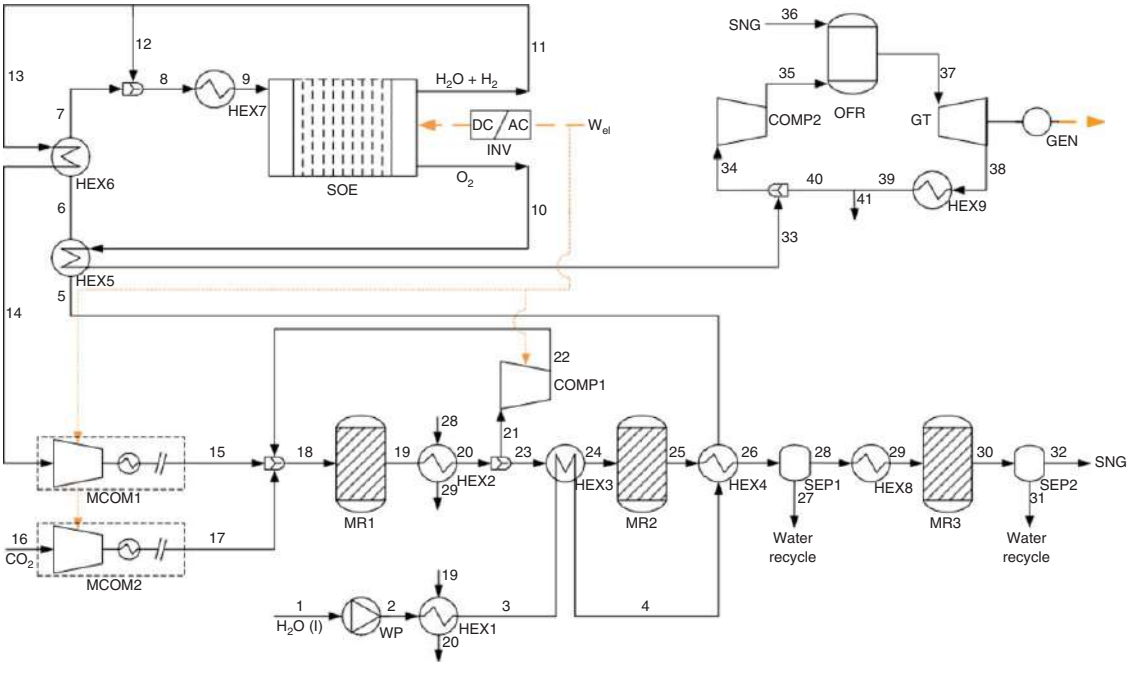

Figure 11.11 Schematic process flow diagram for the hybrid PtM–oxy-fuel system. Note: COMP, compressor; GEN, generator; GT, gas turbine; HEX, heat exchanger; INV, inverter; MCOM, multistage compressor; MR, methanation reactor stage; OFR, oxy-fuel reactor; SEP, separator; SOE, solid oxide electrolyzer; WP, water pump. Source: Reproduced with permission from Eveloy [114]; © 2019, Elsevier.

and CO_2. A pure CO_2 stream is readily obtained after the steam condensation. The reduced oxygen carrier is regenerated and oxidized back to its original oxidation state by air. By mixing the active component and the stabilizer, Yüzbasi and coworkers fabricated highly porous Cu model oxygen carriers with stable redox characteristics for CLC, which appeared to be sufficient to ensure the excellent redox cyclic stability and exhibited capacity retention of 96% over 10 redox cycles. The presence of a conformal Al_2O_3 overcoat offers an effective means to stabilize the oxygen carriers against sintering-induced deactivation during repeated redox cycles [116].

11.3.5 Direct Air Capture of CO_2

Direct air capture (DAC) of CO_2 offers the prospect of permanently lowering the atmospheric CO_2 on a large scale (Figure 11.12) [117]. However, DAC of CO_2 has hitherto been deemed unviable for the higher energy associated with capture at low atmospheric concentrations. High-temperature aqueous solution-based direct air capture (HT DAC) and low-temperature solid sorbent-based direct air capture (LT DAC) are the two main categories of commercially available technologies. LT DAC systems are favorable due to the lower heat supply costs and the possibility of using waste heat from other systems. Despite the technical advances in the past decade, there are still some misconceptions about DAC's current and long-term costs and energy, water, and area demand. This could undermine DAC's anticipated role in a neutral or negative GHG emission system and influence the policymakers. DAC system costs could be lowered significantly with commercialization in the 2020s followed by massive implementation in the 2040s and 2050s, making them cost competitive with point source carbon capture and an affordable climate change mitigation solution. DAC is competitive to point source carbon capture (PSCC) with fewer restrictions on capacity and location. The fossil fuel-based CO_2 may induce further costs than the capturing costs alone, since later emissions to the atmosphere are most likely to be included, in particular for a net zero emission system. That is, the DAC capturing costs may be the minor cost fraction for PSCC. Such freedom could

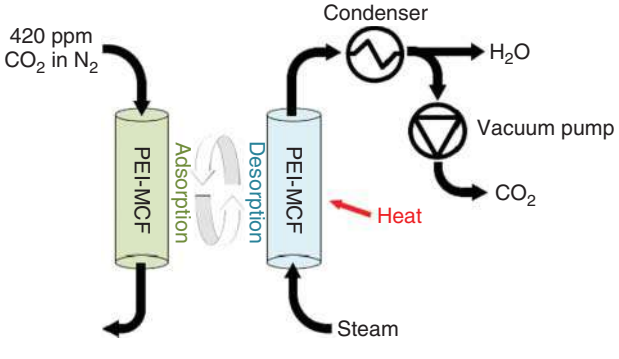

Figure 11.12 Adsorption and desorption process for capturing CO_2 from air.
Source: Reproduced with permission from Wijesiri et al. [117]; © 2019, ACS Publications.

further increase the competitiveness of DAC in projects associated with CO_2 storage or utilization, by minimizing the transportation costs [118].

Regarding cost, electricity consumption, water, and makeup sorbent filters using Marathon A would yield direct operational costs of $42 per ton CO_2. Humidity swing DAC does not require difficult processing conditions such as high temperatures, nor does it need rare or expensive materials or equipment [119]. Brethomé and coworkers reported a hybrid DAC approach combining the benefits of an aqueous sorbent (such as relatively high CO_2 absorption rates, easy handling, and low maintenance requirements) with the advantages of solid-state CO_2 desorption (such as lower energy penalty and minimal sorbent evaporation and degradation). Combining the amino acid sorbents with better air–liquid contactors that optimize the interfacial area and minimize the water loss will promisingly lead to more efficient DAC systems [120].

11.3.6 Carbon Capture, Storage, and Utilization

Carbon capture and storage (CCS) has been discussed intensively in the past decades. However, the CCS technology lock-in risk has been neglected for long and may have a negative impact on the understanding the potential of CCS for applications [3, 121]. From the perspectives of avoiding the CCS technology lock-in risk, the second-generation CCS technology should be commercially applied by 2035. Conversely, if the second-generation CCS technology being commercially applied by 2040, the coal-fired power plants would face a high risk of being locked in by the first-generation CCS technology or lose their best opportunity to retrofit CCS technologies. To promote the development of the first-generation CCS technology and the commercialization of the second-generation CCS technology, the government and the power enterprises should pay particular attention to the following two aspects. One aspect is the total input of CCS commercialization, and the other is the investment allocation between the first- and second-generation CCS technologies. Generally, the second-generation CCS technology should share more than 92% of the total input. The carbon price, which can be regarded as an important tool to promote CCS development and has a large influence on the application of CCS technologies for coal-fired power plants, is still at a very low level [122].

CO_2 capture and conversion to fuel using renewable energy is being promoted as a climate change mitigation measure that reduces fossil fuel use by effectively recycling carbon. The mitigation potential of CCU for fuel production is limited to 50% of the original emissions of the reference system without CCU. The main challenge to CCU cost reduction is not the CO_2-to-fuel conversion step but the production of required carbon-free electricity at very low cost [2]. Biomass-to-power generation is an alternative for fossil fuel-to-power pathways and plays a significant role in electricity supply and CO_2 emission reduction in the United Kingdom [123]. Ye and coworkers assessed the overall cost of a typical 600MW supercritical coal-fired power plant using amine adsorption via an Integrated Environmental Control Model (IECM). The CO_2 capture cost for a newly constructed power plant is 150 yuan/t, whereas for an existing CCS retrofitted power plant, this cost ranges from 162 to

185 yuan/t. The sulfur concentration in the exhaust gases of a power plant shows an especially critical impact on the capture and electricity generation costs [124].

European large stationary sources are currently emitting more than 1.4 Gt of CO_2 every year. CO_2 transportation is intrinsically characterized by the risk of leakage. In the most conservative scenario, mitigation actions represented 10% of total cost for installing and operating the transport network. For the two additional scenarios being considered, mitigation costs never represent more than 11% of the transport costs (less than 1.5% of the overall costs for deploying CCS infrastructure). The offshore sequestration potential is only exploited when limitations on inshore storage are taken into account according to local legislations. No feasible solution can be found for a carbon reduction target higher than 50% because of the unacceptable level of societal risk [125].

CCU has the technical potential to decouple chemical production from fossil resources, reducing annual GHG emission by up to 3.5 Gt CO_2-eq in 2030 [126]. The climate change mitigation potential of CCU in the chemical industry is neither determined by the amount of CO_2 use nor stored in chemicals, but by the substitution of conventional technologies [127]. There is a lack of demand to not only determine emission reductions compared with conventional technologies but to also compare climate change mitigation measures regarding their power-to-X efficiency [128]. The government should formulate targeted subsidy policies for the CO_2 utilization, which is beneficial to the development of full-chain CCU project, the improvement of oil production, and the progress of CO_2 utilization technologies [129].

From a commercial and policy perspective, CCU should be encouraged only when CO_2 is useful as a cheap feedstock. That is when it can be robustly and reliably shown that the CO_2 product could deliver the same service at the same price and also would not result in an increase in the emission of CO_2-derived products. The driving force should be feedstock substitution and the production of materials at a lower cost and with lower fossil carbon content. Underpinning research into CO_2, as this can never happen at the required magnitude without conversion, should continue to expand options and reduce costs. CO_2-enhanced oil recovery (EOR), while no panacea, can be deployed at a sufficient scale to facilitate the deployment of CO_2 transport infrastructure and potentially stacked CO_2 storage options. Any proposals for its large-scale deployment should be accompanied by a careful and thorough analysis of associated primary and opportunity costs [130].

11.4 Conclusions

In this chapter, the latest developments and advanced achievements since 2010 in the field of CO_2 capture was systematically summarized. It is concluded that the CO_2 capture technique has real potential to achieve large-scale carbon emission reduction for coal-fired power plants. Though CO_2 capture-based processes have made considerable progress in recent years for coal-fired power plants, related mature technology programs that can be applied for large-scale commercialization are still not available. The core technology of CO_2 capture is the development of

adsorbent/absorbent with low energy consumption. To achieve the CO_2 separation economically and efficiently from the flue gas is a severe challenge, the solution of which will largely mitigate the damages caused by the GHG effects. The fabrication of adsorbents with high capture capacity and the optimization of the technological conditions have become the research hot spots. The development of coupling of various separation procedures to further decrease the cost by multistage separation and coupling technology is of significant importance to achieve better separation performance. However, the deployment of CO_2 capture process still faces problems including high investment and high energy efficiency, which is far from large-scale industrialization and needs further in-depth study.

Acknowledgments

This work was supported by the Fundamental Research Funds for the Central Universities (2019JQ03015), the National Natural Science Foundation of China (U1810209), the International Science and Technology Cooperation Project of Bingtuan (2018BC002), and the Beijing Municipal Education Commission for their financial support through Innovative Transdisciplinary Program "Ecological Restoration Engineering."

References

1 Wang, Q., Luo, J., Zhong, Z., and Borgna, A. (2011). CO_2 capture by solid adsorbents and their applications: current status and new trends. *Energy Environ. Sci.* 4 (1): 42–55.
2 Abanades, J.C., Rubin, E.S., Mazzotti, M., and Herzog, H.J. (2017). On the climate change mitigation potential of CO_2 conversion to fuels. *Energy Environ. Sci.* 10 (12): 2491–2499.
3 Bui, M., Adjiman, C.S., Bardow, A. et al. (2018). Carbon capture and storage (CCS): the way forward. *Energy Environ. Sci.* 11 (5): 1062–1176.
4 Wang, J., Huang, L., Yang, R. et al. (2014). Recent advances in solid sorbents for CO_2 capture and new development trends. *Energy Environ. Sci.* 7 (11): 3478–3518.
5 Zhu, X., Shi, Y., and Cai, N. (2017). CO_2 residual concentration of potassium-promoted hydrotalcite for deep CO/CO_2 purification in H_2-rich gas. *J. Energy Chem.* 26 (5): 956–964.
6 Parkinson, B., Balcombe, P., Speirs, J.F. et al. (2019). Levelized cost of CO_2 mitigation from hydrogen production routes. *Energy Environ. Sci.* 12 (1): 19–40.
7 Chen, Y., Guerschman, J.P., Cheng, Z., and Guo, L. (2019). Remote sensing for vegetation monitoring in carbon capture storage regions: a review. *Appl. Energy* 240: 312–326.
8 Yu, K., Mitch, W.A., and Dai, N. (2017). Nitrosamines and nitramines in amine-based carbon dioxide capture systems: fundamentals, engineering implications, and knowledge gaps. *Environ. Sci. Technol.* 51 (20): 11522–11536.

9 Apergis, N., Christou, C., and Gupta, R. (2017). Are there environmental Kuznets curves for US state-level CO_2 emissions? *Renewable Sustainable Energy Rev.* 69: 551–558.

10 Deutz, S., Bongartz, D., Heuser, B. et al. (2018). Cleaner production of cleaner fuels: wind-to-wheel–environmental assessment of CO_2-based oxymethylene ether as a drop-in fuel. *Energy Environ. Sci.* 11 (2): 331–343.

11 Zhang, Y., Yu, F., Louis, B., and Wang, Q. (2018). Scalable synthesis of the lithium silicate-based high-temperature CO_2 sorbent from inexpensive raw material vermiculite. *Chem. Eng. J.* 349: 562–573.

12 Creutzig, F., Breyer, C., Hilaire, J. et al. (2019). The mutual dependence of negative emission technologies and energy systems. *Energy Environ. Sci.* 12 (6): 1805–1817.

13 Wang, S., Zhu, X., Song, D. et al. (2019). Drivers of CO_2 emissions from power generation in China based on modified structural decomposition analysis. *J. Cleaner Prod.* 220: 1143–1155.

14 Szima, S., Nazir, S.M., Cloete, S. et al. (2019). Gas switching reforming for flexible power and hydrogen production to balance variable renewables. *Renewable Sustainable Energy Rev.* 110: 207–219.

15 Bhatia, S.K., Bhatia, R.K., Jeon, J.-M. et al. (2019). Carbon dioxide capture and bioenergy production using biological system – a review. *Renewable Sustainable Energy Rev.* 110: 143–158.

16 Wang, X., Akhmedov, N.G., Hopkinson, D. et al. (2016). Phase change amino acid salt separates into CO_2-rich and CO_2-lean phases upon interacting with CO_2. *Appl. Energy* 161: 41–47.

17 von der Assen, N., Muller, L.J., Steingrube, A. et al. (2016). Selecting CO_2 sources for CO_2 utilization by environmental-merit-order curves. *Environ. Sci. Technol.* 50 (3): 1093–1101.

18 Sgouridis, S., Carbajales-Dale, M., Csala, D. et al. (2019). Comparative net energy analysis of renewable electricity and carbon capture and storage. *Nat. Energy* 4 (6): 456–465.

19 Ren, Z., Zheng, H., He, X. et al. (2019). Changes in spatio-temporal patterns of urban forest and its above-ground carbon storage: implication for urban CO_2 emissions mitigation under China's rapid urban expansion and greening. *Environ. Int.* 129: 438–450.

20 Bellamy, R., Lezaun, J., and Palmer, J. (2019). Perceptions of bioenergy with carbon capture and storage in different policy scenarios. *Nat. Commun.* 10 (1): 743.

21 Zhang, Y., Yuan, Z., Margni, M. et al. (2019). Intensive carbon dioxide emission of coal chemical industry in China. *Appl. Energy* 236: 540–550.

22 Zhou, K., Chaemchuen, S., and Verpoort, F. (2017). Alternative materials in technologies for Biogas upgrading via CO_2 capture. *Renewable Sustainable Energy Rev.* 79: 1414–1441.

23 Costa, I., Rochedo, P., Costa, D. et al. (2019). Placing hubs in CO_2 pipelines: an application to industrial CO_2 emissions in the Iberian Peninsula. *Appl. Energy* 236: 22–31.

24 Katelhon, A., Meys, R., Deutz, S. et al. (2019). Climate change mitigation potential of carbon capture and utilization in the chemical industry. *Proc. Natl. Acad. Sci. U.S.A.* 116 (23): 11187–11194.

25 Zhang, Y., Ji, X., Xie, Y., and Lu, X. (2016). Screening of conventional ionic liquids for carbon dioxide capture and separation. *Appl. Energy* 162: 1160–1170.

26 Lim, J., Choi, W., Mok, J., and Seo, Y. (2019). Kinetic CO_2 selectivity in clathrate-based CO_2 capture for upgrading CO_2-rich natural gas and biogas. *Chem. Eng. J.* 369: 686–693.

27 Zheng, J., Bhatnagar, K., Khurana, M. et al. (2018). Semiclathrate based CO_2 capture from fuel gas mixture at ambient temperature: effect of concentrations of tetra-*n*-butylammonium fluoride (TBAF) and kinetic additives. *Appl. Energy* 217: 377–389.

28 Hu, Y., Liu, W., Yang, Y. et al. (2019). CO_2 capture by Li_4SiO_4 sorbents and their applications: current developments and new trends. *Chem. Eng. J.* 359: 604–625.

29 Xie, H., Liu, T., Wang, Y. et al. (2017). Enhancement of electricity generation in CO_2 mineralization cell by using sodium sulfate as the reaction medium. *Appl. Energy* 195: 991–999.

30 Skorek-Osikowska, A., Bartela, Ł., and Kotowicz, J. (2017). Thermodynamic and ecological assessment of selected coal-fired power plants integrated with carbon dioxide capture. *Appl. Energy* 200: 73–88.

31 Subha, P.V., Nair, B.N., Visakh, V. et al. (2018). Germanium-incorporated lithium silicate composites as highly efficient low-temperature sorbents for CO_2 capture. *J. Mater. Chem. A* 6 (17): 7913–7921.

32 Luis Míguez, J., Porteiro, J., Pérez-Orozco, R. et al. (2018). Evolution of CO_2 capture technology between 2007 and 2017 through the study of patent activity. *Appl. Energy* 211: 1282–1296.

33 Pardakhti, M., Jafari, T., Tobin, Z. et al. (2019). Trends in solid adsorbent materials development for CO_2 capture. *ACS Appl. Mater. Interfaces* 11: 34533–34559.

34 Wilberforce, T., Baroutaji, A., Soudan, B. et al. (2019). Outlook of carbon capture technology and challenges. *Sci. Total Environ.* 657: 56–72.

35 Jansen, D., Gazzani, M., Manzolini, G. et al. (2015). Pre-combustion CO_2 capture. *Int. J. Greenhouse Gas Control* 40: 167–187.

36 Gao, W., Zhou, T., Gao, Y., and Wang, Q. (2019). Enhanced water gas shift processes for carbon dioxide capture and hydrogen production. *Appl. Energy* 254: 113700.

37 Zhu, X., Shi, Y., and Cai, N. (2016). Integrated gasification combined cycle with carbon dioxide capture by elevated temperature pressure swing adsorption. *Appl. Energy* 176: 196–208.

38 Gao, W., Zhou, T., Gao, Y. et al. (2017). Molten salts-modified MgO-based adsorbents for intermediate-temperature CO_2 capture: a review. *J. Energy Chem.* 26 (5): 830–838.

39 Hu, Y., Guo, Y., Sun, J. et al. (2019). Progress in MgO sorbents for cyclic CO_2 capture: a comprehensive review. *J. Mater. Chem. A* 7 (35): 20103–20120.

40 Gao, W., Zhou, T., Louis, B., and Wang, Q. (2017). Hydrothermal fabrication of high specific surface area mesoporous MgO with excellent CO_2 adsorption potential at intermediate temperatures. *Catalysts* 7 (12): 116.

41 Gao, W., Zhou, T., Gao, Y. et al. (2018). Study on MNO_3/NO_2 (M = Li, Na, and K)/MgO composites for intermediate-temperature CO_2 capture. *Energy Fuels* 33 (3): 1704–1712.

42 Gao, W., Zhou, T., and Wang, Q. (2018). Controlled synthesis of MgO with diverse basic sites and its CO_2 capture mechanism under different adsorption conditions. *Chem. Eng. J.* 336: 710–720.

43 Jin, S., Ko, K.-J., and Lee, C.-H. (2019). Direct formation of hierarchically porous MgO-based sorbent bead for enhanced CO_2 capture at intermediate temperatures. *Chem. Eng. J.* 371: 64–77.

44 Harada, T., Brown, P., and Hatton, T.A. (2019). Nonvolatile colloidal dispersion of MgO nanoparticles in molten salts for continuous CO_2 capture at intermediate temperatures. *ACS Sustainable Chem. Eng.* 7 (8): 7979–7986.

45 Li, P., Liu, W., Dennis, J.S., and Zeng, H.C. (2017). Synthetic architecture of MgO/C nanocomposite from hierarchical-structured coordination polymer toward enhanced CO_2 capture. *ACS Appl. Mater. Interfaces* 9 (11): 9592–9602.

46 Jin, S., Ho, K., and Lee, C.-H. (2018). Facile synthesis of hierarchically porous MgO sorbent doped with $CaCO_3$ for fast CO_2 capture in rapid intermediate temperature swing sorption. *Chem. Eng. J.* 334: 1605–1613.

47 Cui, H., Zhang, Q., Hu, Y. et al. (2018). Ultrafast and stable CO_2 capture using alkali metal salt-promoted MgO-$CaCO_3$ sorbents. *ACS Appl. Mater. Interfaces* 10 (24): 20611–20620.

48 Guo, Y., Tan, C., Wang, P. et al. (2020). Structure-performance relationships of magnesium-based CO_2 adsorbents prepared with different methods. *Chem. Eng. J.* 379: 122277.

49 Hu, Y., Cui, H., Cheng, Z., and Zhou, Z. (2019). Sorption-enhanced water gas shift reaction by in situ CO_2 capture on an alkali metal salt-promoted MgO-$CaCO_3$ sorbent. *Chem. Eng. J.* 377: 119823.

50 Creamer, A.E., Gao, B., Zimmerman, A., and Harris, W. (2018). Biomass-facilitated production of activated magnesium oxide nanoparticles with extraordinary CO_2 capture capacity. *Chem. Eng. J.* 334: 81–88.

51 Lee, H., Triviño, M.L.T., Hwang, S. et al. (2018). In situ observation of carbon dioxide capture on pseudo-liquid eutectic mixture-promoted magnesium oxide. *ACS Appl. Mater. Interfaces* 10 (3): 2414–2422.

52 Wang, K., Zhao, Y., Clough, P.T. et al. (2019). Structural and kinetic analysis of CO_2 sorption on $NaNO_2$-promoted MgO at moderate temperatures. *Chem. Eng. J.* 372: 886–895.

53 Qiao, Y., Wang, J., Zhang, Y. et al. (2017). Alkali nitrates molten salt modified commercial MgO for intermediate-temperature CO_2 capture: optimization of the Li/Na/K ratio. *Ind. Eng. Chem. Res.* 56 (6): 1509–1517.

54 Jin, S., Ko, K.-J., Song, Y.-G. et al. (2019). Fabrication and kinetic study of spherical MgO agglomerates via water-in-oil method for pre-combustion CO_2 capture. *Chem. Eng. J.* 359: 285–297.

55 Garcés-Polo, S.I., Villarroel-Rocha, J., Sapag, K. et al. (2018). Adsorption of CO_2 on mixed oxides derived from hydrotalcites at several temperatures and high pressures. *Chem. Eng. J.* 332: 24–32.

56 Coenen, K., Gallucci, F., Mezari, B. et al. (2018). An in-situ IR study on the adsorption of CO_2 and H_2O on hydrotalcites. *J. CO_2 Util.* 24: 228–239.

57 Wang, J., Huang, L., Zheng, Q. et al. (2016). Layered double hydroxides/oxidized carbon nanotube nanocomposites for CO_2 capture. *J. Ind. Eng. Chem.* 36: 255–262.

58 Wang, J., Mei, X., Huang, L. et al. (2015). Synthesis of layered double hydroxides/graphene oxide nanocomposite as a novel high-temperature CO_2 adsorbent. *J. Energy Chem.* 24: 127–137.

59 Kim, S. and Lee, K.B. (2019). Impregnation of hydrotalcite with $NaNO_3$ for enhanced high-temperature CO_2 sorption uptake. *Chem. Eng. J.* 356: 964–972.

60 Zhu, X., Chen, C., Wang, Q. et al. (2019). Roles for K_2CO_3 doping on elevated temperature CO_2 adsorption of potassium promoted layered double oxides. *Chem. Eng. J.* 366: 181–191.

61 Gao, Y., Zhang, Z., Wu, J. et al. (2013). Comprehensive investigation of CO_2 adsorption on Mg–Al–CO_3 LDH-derived mixed metal oxides. *J. Mater. Chem. A* 1 (41): 12782–12790.

62 Huang, L., Xu, C., Ren, R. et al. (2018). Revealing how molten salts promote CO_2 capture on CaO via an impedance study and sorption kinetics simulation. *Sustain. Energy Fuel* 2 (1): 68–72.

63 Ortiz, C., Chacartegui, R., Valverde, J.M., and Becerra, J.A. (2016). A new integration model of the calcium looping technology into coal fired power plants for CO_2 capture. *Appl. Energy* 169: 408–420.

64 Antzara, A.N., Arregi, A., Heracleous, E., and Lemonidou, A.A. (2018). In-depth evaluation of a ZrO_2 promoted CaO-based CO_2 sorbent in fluidized bed reactor tests. *Chem. Eng. J.* 333: 697–711.

65 Kim, S.M., Abdala, P.M., Broda, M. et al. (2018). Integrated CO_2 capture and conversion as an efficient process for fuels from greenhouse gases. *ACS Catal.* 8 (4): 2815–2823.

66 Huang, L., Zhang, Y., Gao, W. et al. (2017). Alkali carbonate molten salt coated calcium oxide with highly improved carbon dioxide capture capacity. *Energy Technol.* 5: 1328–1336.

67 Kierzkowska, A.M., Pacciani, R., and Muller, C.R. (2013). CaO-based CO_2 sorbents: from fundamentals to the development of new, highly effective materials. *ChemSusChem* 6 (7): 1130–1148.

68 Huang, L., Zheng, Q., Louis, B., and Wang, Q. (2018). A facile solvent/nonsolvent preparation of sintering-resistant MgO/CaO composites for high-temperature CO_2 capture. *Energy Technol.* 6 (12): 2469–2478.

69 Ma, X., Li, Y., Yan, X. et al. (2019). Preparation of a morph-genetic CaO-based sorbent using paper fibre as a biotemplate for enhanced CO_2 capture. *Chem. Eng. J.* 361: 235–244.

70 Naeem, M.A., Armutlulu, A., Imtiaz, Q. et al. (2018). Optimization of the structural characteristics of CaO and its effective stabilization yield high-capacity CO_2 sorbents. *Nat. Commun.* 9 (1): 2408.

71 Sun, H., Wang, J., Zhao, J. et al. (2019). Dual functional catalytic materials of Ni over Ce-modified CaO sorbents for integrated CO_2 capture and conversion. *Appl. Catal., B* 244: 63–75.

72 Zhang, Y., Gao, Y., Pfeiffer, H. et al. (2019). Recent advances in lithium containing ceramic based sorbents for high-temperature CO_2 capture. *J. Mater. Chem. A* 7 (14): 7962–8005.

73 Zhang, Y., Gao, Y., Louis, B. et al. (2019). Fabrication of lithium silicates from zeolite for CO_2 capture at high temperatures. *J. Energy Chem.* 33: 81–89.

74 Zhang, Y., Gao, Y., Yu, F., and Wang, Q. (2019). Synthesis of hierarchical Li_4SiO_4 nanoparticles/flakers composite from vermiculite/MCM-41 hybrid with improved CO_2 capture performance under different CO_2 concentrations. *Chem. Eng. J.* 371: 424–432.

75 Zhang, Y., Zhou, T., Louis, B. et al. (2017). Environmental benign synthesis of lithium silicates and Mg-Al layered double hydroxide from vermiculite mineral for CO_2 capture. *Catalysts* 7 (12): 105.

76 Zheng, Q., Huang, L., Zhang, Y. et al. (2016). Unexpected highly reversible topotactic CO_2 sorption/desorption capacity for potassium dititanate. *J. Mater. Chem. A* 4 (33): 12889–12896.

77 Zheng, Q., Huang, L., Zhong, Z. et al. (2020). Development of $KNaTiO_3$ as a novel high-temperature CO_2 capturing material with fast sorption rate and high reversible sorption capacity. *Chem. Eng. J.* 380: 122444.

78 Jiang, L., Gonzalez-Diaz, A., Ling-Chin, J. et al. (2019). Post-combustion CO_2 capture from a natural gas combined cycle power plant using activated carbon adsorption. *Appl. Energy* 245: 1–15.

79 Cloete, S., Giuffrida, A., Romano, M.C., and Zaabout, A. (2019). The swing adsorption reactor cluster for post-combustion CO_2 capture from cement plants. *J. Cleaner Prod.* 223: 692–703.

80 Oh, S.-Y., Yun, S., and Kim, J.-K. (2018). Process integration and design for maximizing energy efficiency of a coal-fired power plant integrated with amine-based CO_2 capture process. *Appl. Energy* 216: 311–322.

81 Ullah, A., Soomro, M.I., and Kim, W.-S. (2019). Ammonia-based CO_2 capture parameters optimization and analysis of lean and rich vapor compression processes. *Sep. Purif. Technol.* 217: 8–16.

82 Chen, X., Huang, G., An, C. et al. (2018). Emerging *N*-nitrosamines and *N*-nitramines from amine-based post-combustion CO_2 capture – a review. *Chem. Eng. J.* 335: 921–935.

83 Ge, K., Yu, Q., Chen, S. et al. (2019). Modeling CO_2 adsorption dynamics within solid amine sorbent based on the fundamental diffusion-reaction processes. *Chem. Eng. J.* 364: 328–339.

84 Afonso, R., Sardo, M., Mafra, L., and Gomes, J.R.B. (2019). Unravelling the structure of chemisorbed CO_2 species in mesoporous aminosilicas: a critical survey. *Environ. Sci. Technol.* 53 (5): 2758–2767.

85 Widger, L.R., Combs, M., Lohe, A.R. et al. (2017). Selective removal of nitrosamines from a model amine carbon-capture waterwash using low-cost activated-carbon sorbents. *Environ. Sci. Technol.* 51 (18): 10913–10922.

86 Lai, Q., Diao, Z., Kong, L. et al. (2018). Amine-impregnated silicic acid composite as an efficient adsorbent for CO_2 capture. *Appl. Energy* 223: 293–301.

87 Liu, Y. and Yu, X. (2018). Carbon dioxide adsorption properties and adsorption/desorption kinetics of amine-functionalized KIT-6. *Appl. Energy* 211: 1080–1088.

88 Yang, Y., Chuah, C.Y., and Bae, T.-H. (2019). Polyamine-appended porous organic polymers for efficient post-combustion CO_2 capture. *Chem. Eng. J.* 358: 1227–1234.

89 Wang, Z., Ma, H., Zhai, T.L. et al. (2018). Networked cages for enhanced CO_2 capture and sensing. *Adv. Sci.* 5 (7): 1800141.

90 Ren, Y., Ding, R., Yue, H. et al. (2017). Amine-grafted mesoporous copper silicates as recyclable solid amine sorbents for post-combustion CO_2 capture. *Appl. Energy* 198: 250–260.

91 Qasem, N.A.A. and Ben-Mansour, R. (2018). Energy and productivity efficient vacuum pressure swing adsorption process to separate CO_2 from CO_2/N_2 mixture using Mg-MOF-74: a CFD simulation. *Appl. Energy* 209: 190–202.

92 Qasem, N.A.A. and Ben-Mansour, R. (2018). Adsorption breakthrough and cycling stability of carbon dioxide separation from $CO_2/N_2/H_2O$ mixture under ambient conditions using 13X and Mg-MOF-74. *Appl. Energy* 230: 1093–1107.

93 Qasem, N.A.A., Ben-Mansour, R., and Habib, M.A. (2018). An efficient CO_2 adsorptive storage using MOF-5 and MOF-177. *Appl. Energy* 210: 317–326.

94 Yan, S., Zhu, D., Zhang, Z. et al. (2019). A pilot-scale experimental study on CO_2 capture using zeolitic imidazolate framework-8 slurry under normal pressure. *Appl. Energy* 248: 104–114.

95 Zhuang, W., Yuan, D., Liu, D. et al. (2011). Robust metal–organic framework with an octatopic ligand for gas adsorption and separation: combined characterization by experiments and molecular simulation. *Chem. Mater.* 24 (1): 18–25.

96 Bahamon, D., Díaz-Márquez, A., Gamallo, P., and Vega, L.F. (2018). Energetic evaluation of swing adsorption processes for CO_2 capture in selected MOFs and zeolites: effect of impurities. *Chem. Eng. J.* 342: 458–473.

97 Ghanbari, T., Abnisa, F., and Wan Daud, W.M.A. (2019). A review on production of metal organic frameworks (MOF) for CO_2 adsorption. *Sci. Total Environ.* 707: 135090.

98 Masala, A., Vitillo, J.G., Mondino, G. et al. (2017). CO_2 capture in dry and wet conditions in UTSA-16 metal-organic framework. *ACS Appl. Mater. Interfaces* 9 (1): 455–463.

99 Jiang, Y., Ling, J., Xiao, P. et al. (2018). Simultaneous biogas purification and CO_2 capture by vacuum swing adsorption using zeolite NaUSY. *Chem. Eng. J.* 334: 2593–2602.

100 Ke, Q., Sun, T., Wei, X. et al. (2019). Economical synthesis strategy of RHO zeolites with fine-tuned composition and porosity for enhanced trace CO_2 capture. *Chem. Eng. J.* 359: 344–353.

101 Kodasma, R., Fermoso, J., and Sanna, A. (2019). Li-LSX-zeolite evaluation for post-combustion CO_2 capture. *Chem. Eng. J.* 358: 1351–1362.

102 Minelli, M., Papa, E., Medri, V. et al. (2018). Characterization of novel geopolymer-zeolite composites as solid adsorbents for CO_2 capture. *Chem. Eng. J.* 341: 505–515.

103 Ramya, G., Crittenden, B., Smith, M. et al. (2019). Synthesis of novel regenerable 13X zeolite-polyimide adsorbent foams. *Chem. Eng. J.* 361: 736–750.

104 Sun, M., Gu, Q., Hanif, A. et al. (2019). Transition metal cation-exchanged SSZ-13 zeolites for CO_2 capture and separation from N_2. *Chem. Eng. J.* 370: 1450–1458.

105 Thakkar, H., Lawson, S., Rownaghi, A.A., and Rezaei, F. (2018). Development of 3D-printed polymer-zeolite composite monoliths for gas separation. *Chem. Eng. J.* 348: 109–116.

106 Xu, M., Chen, S., Seo, D.-K., and Deng, S. (2019). Evaluation and optimization of VPSA processes with nanostructured zeolite NaX for post-combustion CO_2 capture. *Chem. Eng. J.* 371: 693–705.

107 Zeleňák, V., Skřínska, M., Zukal, A., and Čejka, J. (2018). Carbon dioxide adsorption over amine modified silica: effect of amine basicity and entropy factor on isosteric heats of adsorption. *Chem. Eng. J.* 348: 327–337.

108 Zhao, Q., Wu, F., Men, Y. et al. (2019). CO_2 capture using a novel hybrid monolith (H-ZSM5/activated carbon) as adsorbent by combined vacuum and electric swing adsorption (VESA). *Chem. Eng. J.* 358: 707–717.

109 Zhao, Q., Wu, F., Xie, K. et al. (2018). Synthesis of a novel hybrid adsorbent which combines activated carbon and zeolite NaUSY for CO_2 capture by electric swing adsorption (ESA). *Chem. Eng. J.* 336: 659–668.

110 Guo, L.-P., Li, W.-C., Qiu, B. et al. (2019). Interfacial assembled preparation of porous carbon composites for selective CO_2 capture at elevated temperatures. *J. Mater. Chem. A* 7 (10): 5402–5408.

111 Vega, F., Cano, M., Sanna, A. et al. (2018). Oxidative degradation of a novel AMP/AEP blend designed for CO_2 capture based on partial oxy-combustion technology. *Chem. Eng. J.* 350: 883–892.

112 Vega, F., Camino, S., Gallego, L.M. et al. (2019). Experimental study on partial oxy-combustion technology in a bench-scale CO_2 capture unit. *Chem. Eng. J.* 362: 71–80.

113 Wu, J., Chen, Y., Zhu, Z. et al. (2017). Performance simulation on NG/O_2 combustion gas and steam mixture cycle with energy storage and CO_2 capture. *Appl. Energy* 196: 68–81.

114 Eveloy, V. (2019). Hybridization of solid oxide electrolysis-based power-to-methane with oxyfuel combustion and carbon dioxide utilization for energy storage. *Renewable Sustainable Energy Rev.* 108: 550–571.

115 Adnan, M.A., Azis, M.M., Quddus, M.R., and Hossain, M.M. (2018). Integrated liquid fuel based chemical looping combustion–parametric study for efficient power generation and CO_2 capture. *Appl. Energy* 228: 2398–2406.

116 Yuzbasi, N.S., Armutlulu, A., Abdala, P.M., and Muller, C.R. (2018). Atomic layer deposition of a film of Al_2O_3 on electrodeposited copper foams to yield

highly effective oxygen carriers for chemical looping combustion-based CO_2 capture. *ACS Appl. Mater. Interfaces* 10 (44): 37994–38005.

117 Wijesiri, R.P., Knowles, G.P., Yeasmin, H. et al. (2019). Desorption process for capturing CO_2 from air with supported amine sorbent. *Ind. Eng. Chem. Res.* 58: 15606–15618.

118 Fasihi, M., Efimova, O., and Breyer, C. (2019). Techno-economic assessment of CO_2 direct air capture plants. *J. Cleaner Prod.* 224: 957–980.

119 van der Giesen, C., Meinrenken, C.J., Kleijn, R. et al. (2017). A life cycle assessment case study of coal-fired electricity generation with humidity swing direct air capture of CO_2 versus MEA-based postcombustion capture. *Environ. Sci. Technol.* 51 (2): 1024–1034.

120 Brethomé, F.M., Williams, N.J., Seipp, C.A. et al. (2018). Direct air capture of CO_2 via aqueous-phase absorption and crystalline-phase release using concentrated solar power. *Nat. Energy* 3 (7): 553–559.

121 Fajardy, M. and Mac, D.N. (2018). The energy return on investment of BECCS: is BECCS a threat to energy security? *Energy Environ. Sci.* 11 (6): 1581–1594.

122 Fan, J.-L., Xu, M., Li, F. et al. (2018). Carbon capture and storage (CCS) retrofit potential of coal-fired power plants in China: the technology lock-in and cost optimization perspective. *Appl. Energy* 229: 326–334.

123 Yi, Q., Zhao, Y., Huang, Y. et al. (2018). Life cycle energy-economic-CO_2 emissions evaluation of biomass/coal, with and without CO_2 capture and storage, in a pulverized fuel combustion power plant in the United Kingdom. *Appl. Energy* 225: 258–272.

124 Ye, B., Jiang, J., Zhou, Y. et al. (2019). Technical and economic analysis of amine-based carbon capture and sequestration at coal-fired power plants. *J. Cleaner Prod.* 222: 476–487.

125 d'Amore, F., Mocellin, P., Vianello, C. et al. (2018). Economic optimisation of European supply chains for CO_2 capture, transport and sequestration, including societal risk analysis and risk mitigation measures. *Appl. Energy* 223: 401–415.

126 Nowicki, D.A., Skakle Janet, M.S., and Gibson, I.R. (2018). Nano-scale hydroxyapatite compositions for the utilization of CO_2 recovered using post-combustion carbon capture. *J. Mater. Chem. A* 6 (13): 5367–5377.

127 Roh, K., Lim, H., Chung, W. et al. (2018). Sustainability analysis of CO_2 capture and utilization processes using a computer-aided tool. *J. CO_2 Util.* 26: 60–69.

128 Meys, R., Kätelhön, A., and Bardow, A. (2019). Towards sustainable elastomers from CO_2: life cycle assessment of carbon capture and utilization for rubbers. *Green Chem.* 21 (12): 3334–3342.

129 Norhasyima, R.S. and Mahlia, T.M.I. (2018). Advances in CO_2 utilization technology: a patent landscape review. *J. CO_2 Util.* 26: 323–335.

130 Mac Dowell, N., Fennell, P.S., Shah, N., and Maitland, G.C. (2017). The role of CO_2 capture and utilization in mitigating climate change. *Nat. Clim. Change* 7 (4): 243–249.

12

CO_2 Reduction to Fuels and Chemicals

Jian Sun[1] *and Lisheng Guo*[2]

[1] *Chinese Academy of Sciences, Dalian Institute of Chemical Physics, Dalian National Laboratory for Clean Energy, 457 Zhongshan, Dalian 116023, P.R. China*
[2] *Anhui University, School of Chemistry and Chemical Engineering, 111 Jiulong, Hefei 230601, P.R. China*

12.1 Introduction

For the past two centuries, the utilization of carbon-rich fossil fuels, such as coal and natural gas, has promoted the development of economic society. As a consequence, it has caused massive CO_2 emission that results in a series of ecological problems, such as global warming and ocean acidification [1, 2]. Hence, various strategies have been adapted for the utilization, storage, and capture of CO_2 to mitigate the concentration of CO_2 in air [2–7].

Rather than a waste resource, CO_2 turns out to be a promising C1 building block with which to fabricate a series of value-added chemicals [6, 8]. Compared with the capture and storage of CO_2, the transformation and utilization of CO_2 are more attractive in the long term [9]. The utilization of CO_2 can provide an alternative route to convert renewable raw materials into useful chemicals or fuels and achieve the effective recycling of global carbon resources at the same time [1]. At the end of the 1920s, Fischer and Tropsch published their first report relating to hydrocarbon synthesis from CO hydrogenation [10]. From then on, Fischer–Tropsch synthesis (FTS) has been regarded as an alternative pathway to produce fuels and chemicals from non-petroleum sources [11–13]. In recent decades, a modified CO_2 hydrogenation process based on methanol intermediate (methanol synthesis followed by methanol dehydration to hydrocarbons, denoted as CO_2-MSR) or Fischer–Tropsch intermediates (CO_2-fed FTS), where CO_2 is used instead of CO, has been used in CO_2 conversion to produce hydrocarbons and attracts considerable attention from both academia and industry [14–18]. The corresponding routes to synthesize valuable hydrocarbons from CO_2 hydrogenation are compared in Figure 12.1.

It should be noted that CO_2 is a stable molecule, and thus it demands high energy input and/or a high energy density reductant (H_2) to break the C—O bonds. However, nearly 95% of H_2 is derived from petroleum sources and natural gas steam reforming [19]. These methods are all energy-intensive processes requiring high

Heterogeneous Catalysis for Sustainable Energy, First Edition. Edited by Landong Li and Justin S. J. Hargreaves.

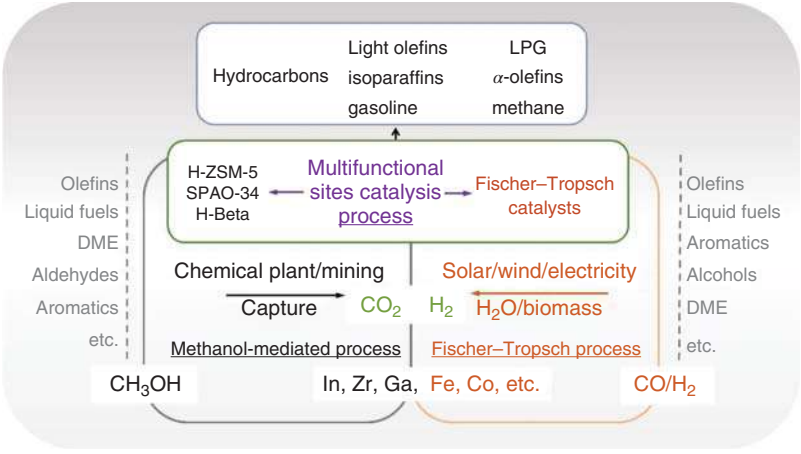

Figure 12.1 Possible routes to synthesize valuable hydrocarbons from CO_2 hydrogenation and possible derivatives from CH_3OH and CO intermediate.

temperatures, which are not sustainable in the long run. In the case of sustainable development, the production of H_2 from renewables such as wind, biomass, solar energy, and tidal energy is environmentally friendly [20, 21]. However, the choice of catalyst and process design strategies to improve performance is a critical aspect to be considered for achieving higher H_2 production [22]. Although renewable hydrogen production from natural resources is an alternative and promising process, high costs still limit large-scale application. Therefore, the sustainable supply of H_2 is also a vital issue for the catalytic hydrogenation of CO_2. In terms of products, CO_2 hydrogenation processes occurring via modified FT processes usually produce a relatively wide spectrum of products, and the product distribution is in most cases described by the Anderson–Schulz–Flory (ASF) model. The ASF distribution is not conducive to attain high selectivity for target products as shown in Figure 12.2a. For example, the selectivity of liquid fuels (C_{5+}) is about 53% (38%

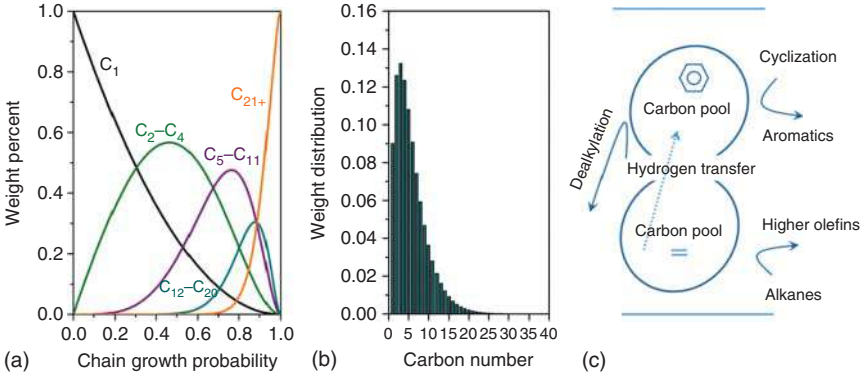

Figure 12.2 (a) Product distributions of an FT process according to the Anderson–Schulz–Flory (ASF) model. (b) A typical theoretical FT synthesis distribution, $\alpha = 0.70$. (c) Mechanism for hydrocarbon formation from a methanol-mediated process.

for C_2–C_4 hydrocarbons) when the chain growth probability (α) is 0.7, as shown in Figure 12.2b. Therefore, breaking the limitations imposed by ASF distribution is a key issue for increasing the selectivity toward target products. Moreover, the low activity of C–C coupling is another challenge that further hinders the production of desired hydrocarbons (C_{2+} hydrocarbons) from CO_2 hydrogenation. Thus, most products produced from the CO_2 hydrogenation process have been usually light hydrocarbons and especially methane. To solve this problem and meet the demand of product diversity simultaneously, modification of catalysts via various methods has been investigated by different researchers.

Given that the product distribution is limited by the ASF model for a modified FTS process, the integration of the conversion of CO_2 to methanol and methanol to hydrocarbons (MTH) via a methanol-mediated process has been used to break such a limitation (Figure 12.2c). The MTH process can also be further divided to methanol to gasoline (MTG), methanol to olefins (MTO), and other processes. Previously, mixtures of CO_2 and H_2 reacted over Cu-based catalysts to produce methanol, followed by its subsequent dehydration to produce hydrocarbons over a zeolite catalyst [23]. Although considerable efforts were made in the development of such Cu-based composite catalysts, the major products were usually light alkanes [24, 25]. Recently, other methanol synthesis catalysts such as In–Zr, Cr–Zn, Zn–Ga, and Zn–Zr have been used to replace Cu-based catalysts for the fabrication of bifunctional catalysts. Actually, significant breakthroughs have recently been achieved in the direct conversion of CO_2 into target products with excellent selectivity using the strategy of reaction coupling over these catalysts [26–28]. However, for these composite catalysts, the integration manner and spatial distribution of active sites play an important role for the catalytic performance [25–27, 29]. Therefore, it is crucial to arrange active sites in a reasonable and reliable way to optimize catalytic performance.

Although many reviews focus on heterogeneous catalytic hydrogenation of CO_2 and developments in CO_2 technologies over the past decade [1, 2, 5, 8, 30–36], these reviews focus on the general aspects of CO_2 conversion route and reaction mechanism rather than the direct conversion of CO_2 to valuable hydrocarbons or chemicals. More recently, some reviews on CO_2 hydrogenation have been published by different groups [36–40], but the direct and highly selective formation of specific target products is not yet achieving sufficient attention. Therefore, a chapter regarding the highly selective hydrogenation of CO_2 to C_{2+} hydrocarbons and alcohol products will contribute to deepening understanding about CO_2 utilization and the upgrading of end products. In this critical chapter, we discuss the developments made over the past decade, with emphasis on the type of catalysts, and the key factors influencing the product selectivity of CO_2 hydrogenation. Besides we also provide an overview regarding the challenges and opportunities for future research in the selective conversion of CO_2.

12.2 Methanation of Carbon Dioxide

Excessive emission of CO_2 has had a severe impact on the climate. Accordingly, the development of effective ways for the reclamation of CO_2 is gaining increasing

interest. One attractive route is CO_2 methanation, which shows great potential in environmental remediation and renewable energy storage. In a typical FTS reaction, both cobalt- and iron-based catalysts have been extensively used [12, 13, 41, 42]. When switching the feed gas from syngas (CO/H_2) to CO_2 and H_2 gas mixtures, the selectivity of products changed sharply over cobalt-based catalysts. In fact, cobalt-based catalysts are usually regarded as methanation catalysts in CO_2 hydrogenation. The reaction is listed in Eq. (12.1). Owen et al. fabricated a range of noble metal or alkali metal promoter-modified Co-based catalysts and tested their ability to hydrogenate CO_2 at atmospheric pressure [43]. Although the conversion of CO_2 was reduced upon the introduction of noble metals and alkali metal promoters, these catalysts still possessed an advantage compared with other cobalt catalysts and even iron-based catalysts being studied for CO_2 hydrogenation. To further improve reaction performance, some researchers investigated the role of the support properties (for example, pore size, structure, metal–support interaction) on carbon dioxide methanation [44]. ZrO_2 as support imparts superior activity and stability to Co catalysts for CO_2 methanation compared with the inert Al_2O_3 support. The ZrO_2 support shows strong adsorption for reactant H_2, CO_2, and intermediate product CO, which benefits CO_2 methanation [44]:

$$CO_2 + 4H_2 \rightarrow CH_4 + 2H_2O, \quad \Delta H_{298\,K} = -252.9\ \text{kJ mol}^{-1}. \tag{12.1}$$

In addition to the Co-based catalysts, Ni-based catalysts have been extensively exploited for CO_2 methanation, owing to the high activity and low price of Ni. The Ni–support interaction also has a significant influence on the methanation process. The support material plays key roles not only in the dispersion of Ni catalysts but also in the enhancement of CO_2 adsorption, activation, and conversion. SiO_2, MgO, Al_2O_3, TiO_2, CeO_2, ZrO_2, and many other supports have been exploited for Ni catalysts in CO_2 methanation [45, 46]. Among these oxide supports, the basic ZrO_2 shows superior properties with enhanced activity, high thermal stability, and low carbon deposition rate, because of its rich surface active sites, basic sites (OH groups, adsorbed O^{2-}), acid–base Zr^{4+}–O^{2-} pairs, and oxygen vacancies [44]. Similarity, monolith-coated Ni/GDC (gadolinium-doped ceria) catalysts for CO_2 methanation also presented superior activity resulting from the existence of Ce^{3+}/Ce^{4+} ion pairs and surface oxygen vacancies in the GDC support [47]. Dreyer et al. designed a series of metal oxide-supported Ru catalysts spanning from irreducible supports to reducible supports and investigated the effects of the supports on catalytic performance [48]. The catalytic activity of the systems comprising the pristine oxide supports (Al_2O_3, CeO_2, MnO_x, and ZnO) was directly linked to the strength of basic sites, which resulted in large amounts of CO formed through the reverse water–gas shift (RWGS) reaction. Enhanced support reducibility decreased the Ru–CO coverage and increased H_2 dissociation sites. It in turn could strengthen the C—O bonds due to a lower electron density in the π*antibonding orbital of CO. Thus, delicate tuning of the Ru–CO adsorption strength by adjusting the support properties is crucial for modifying methanation behavior [48].

As mentioned above, the presence of oxygen vacancies in the surface of support materials is one of the most interesting parameters in the methanation process

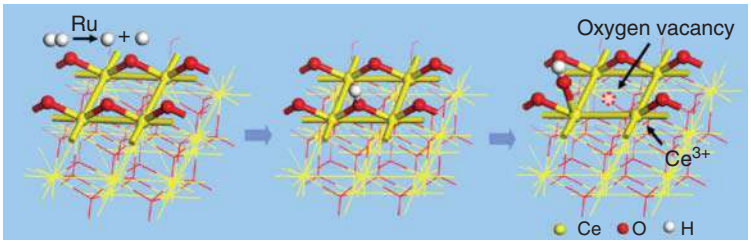

Figure 12.3 Schematic illustration of the generation process for oxygen vacancies, Ce^{3+}, and surface hydroxyls in Ru/CeO_2 catalyst in the reduction process. Source: Wang et al. [49] © 2016, American Chemical Society.

by storing and releasing oxygen or promoting the dispersion degree and activity of the supported noble metal. Given that the critical role of oxygen vacancies in the reaction mechanism is insufficiently well understood, Wang et al. conducted comparative experiments for CO_2 methanation over Ru/CeO_2 (with oxygen vacancies in CeO_2) and $Ru/\alpha\text{-}Al_2O_3$ (without oxygen vacancies) catalysts [49]. CO_2 methanation occurs via the formate route over Ru/CeO_2 catalyst, and the formate dissociation to methanol catalyzed by oxygen vacancies is the rate-determining step. In contrast, CO_2 methanation occurs via the CO route over the Ru surface in $Ru/\alpha\text{-}Al_2O_3$ in the absence of oxygen vacancies, thereby demonstrating active site-dependent catalytic mechanism toward CO_2 methanation. Oxygen vacancies catalyze the rate-determining step at a much lower activation temperature. Figure 12.3 illustrates the formation of oxygen vacancies during reaction processes.

Doping catalysts with promoters is another route to boost methanation performance. Yan et al. designed a novel Ni–W–Mg mixed oxide catalyst ($NiWMgO_x$) prepared by homogeneous precipitation for application to the methanation of CO_2 [50]. Therein, W increased the number of stable CO_2 adsorption sites and helped in anchoring the Ni sites as a result of strengthened Ni–Mg interaction. Both factors were responsible for the enhanced CO_2 methanation activity and improved resistance against sintering. Consequently, it exhibited improved stability, anti-CO-poisoning ability, and resistance against coke formation. Currently, the urgent requirement for efficient CO_2 methanation is the development of a catalyst with high activity, high stability, and high selectivity and at the same time operational under moderate reaction conditions (especially low reaction temperature). In this regard, a research trend has been to design alloy catalysts with good metal–support interaction by utilizing oxygen vacancies and regulating CO_2 adsorption and surface properties. In addition, the modification of alloy catalysts with promoters can also further improve the reaction performance:

$$CO_2 + CH_4 \rightarrow 2CO + 2H_2, \quad \Delta H_{298\,K} = +247\ \text{kJ mol}^{-1}. \tag{12.2}$$

Besides Co-based catalysts, other related noble metal catalysts such as $Pd–Mg/SiO_2$ have also been used in the CO_2 methanation process [51, 52]. These non-cobalt/non-nickel catalysts have also presented excellent performance in CO_2 methanation but will not be discussed here [51]. In addition, the CO_2 reforming of methane (CRM) reaction is beneficial for the reaction of two greenhouse

gases (CO_2 and CH_4) to generate syngas [53]. Thus the CRM reaction (Eq. (12.2)) has also gained the attention from academia. However, the fast deactivation of catalysts, which results from carbon deposition, e.g. via Boudouard reaction and methane thermal decomposition, hinders large-scale application. Investigations of the CRM reaction have extensively reported [54–56], and the CRM reaction will be an important supplement for the utilization of CO_2.

12.3 Synthesis of C_{2+} Hydrocarbons

12.3.1 Alkenes

Lower olefins, i.e. ethylene, propylene, and butane, are key building blocks for the current chemical industry and are crucial for the formation of plastics, synthetic textiles, rubbers, solvents, and coatings. Thus, the direct conversion of CO_2 into lower olefins would offer an attractive route for efficient utilization of CO_2 as a renewable feedstock to replace petroleum for the synthesis of key building block chemicals.

More recently, researchers have paid greater attention toward the conversion of CO_2 into lower olefins, gasoline, and other chemicals over composite catalysts and bifunctional catalysts [26–29]. The most important challenge for a methanol-mediated composite catalyst is how to suitably match the two or more components such as a methanol synthesis catalyst and MTO catalyst in terms of the different optimum operational conditions. Many types of catalysts have been designed rationally to achieve excellent catalytic performance and stability. Liu et al. designed a bifunctional catalyst comprising $ZnGa_2O_4$ and SAPO-34 catalyzing the direct conversion of CO_2 to C_2–C_4 olefins with a selectivity of 86% [29]. Oxygen vacancies existing on the surface of $ZnGa_2O_4$ played a pivotal role for the activation of CO_2 to methanol via intermediate formate and methoxide species, and the combination of $ZnGa_2O_4$ with SAPO-34 suppressed the RWGS reaction. Thus, Zn–Ga–O/SAPO-34 presented a unique selectivity for light olefins coupled to low selectivity for undesired products such as methane and CO (Figure 12.4a–c). Similar oxygen vacancies on an In–Zr/SAPO-34 catalyst surface also played an important role in the activation of CO_2 [28]. The incorporation of Zr into In-based catalysts not only enhanced the reaction activity by creating new kinds of vacancies but also improved the catalytic stability by preventing sintering. Thus the integration of indium–zirconium composite oxides (In–Zr oxide) and SAPO-34 zeolites exhibited unique light olefin selectivity. The incorporation of Zr for stabilizing intermediates especially CH_3O^* was beneficial for formation of methanol based on density function theory (DFT) calculations (Figure 12.4d). Therefore, precise control of oxygen vacancies on the oxide surface is important for improving the CO_2 hydrogenation performance. As for the In–Zr/SAPO-34 catalyst, what should not be ignored is the enormous waste of carbon atoms, owing to the significant formation of CO without further conversion. Similarly, Li et al. reported a ZnZrO/SAPO tandem catalyst that achieved a high light olefin selectivity of 80% in hydrocarbons (Figure 12.5) [25]. Based on a chemical trapping-mass spectrometry method, it

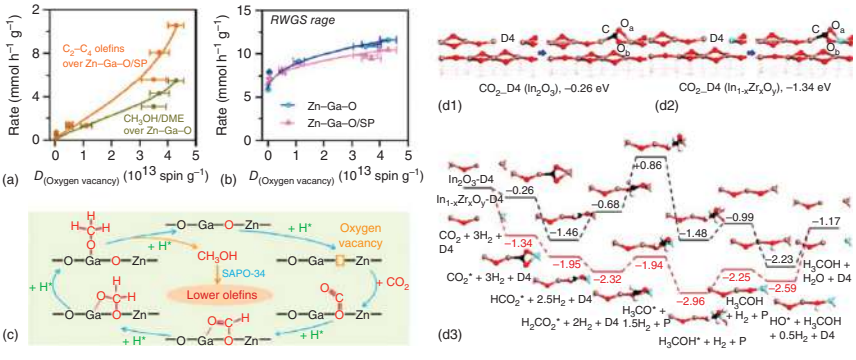

Figure 12.4 (a) Correlation of the formation rates of CH_3OH/DME (Zn–Ga–O) and C_2–C_4 olefins (Zn–Ga–O/SAPO-34) with the density of oxygen vacancies. (b) Correlation of the CO formation rate with the density of oxygen vacancies. (c) A possible reaction mechanism for the conversion of CO_2 into methanol on the Zn–Ga–O catalyst. Source: Liu et al. [29] © 2018, The Royal Society of Chemistry. (d) CO_2 adsorption energy at the O_{4a} surface oxygen vacancy (D_4) site on (d1) the pure In_2O_3 and (d2) Zr-doped $In_{1-x}Zr_xO_y$ surfaces. (d3) Energy profiles of CO_2 hydrogenation to form CH_3OH on the In_2O_3 and $In_{1-x}Zr_xO_y$ surfaces shown in black and red, respectively. D and P stand for defective and perfect surfaces with and without the oxygen vacancy, respectively. Source: Reprinted with permission from Gao et al. [28]; © 2017, American Chemical Society.

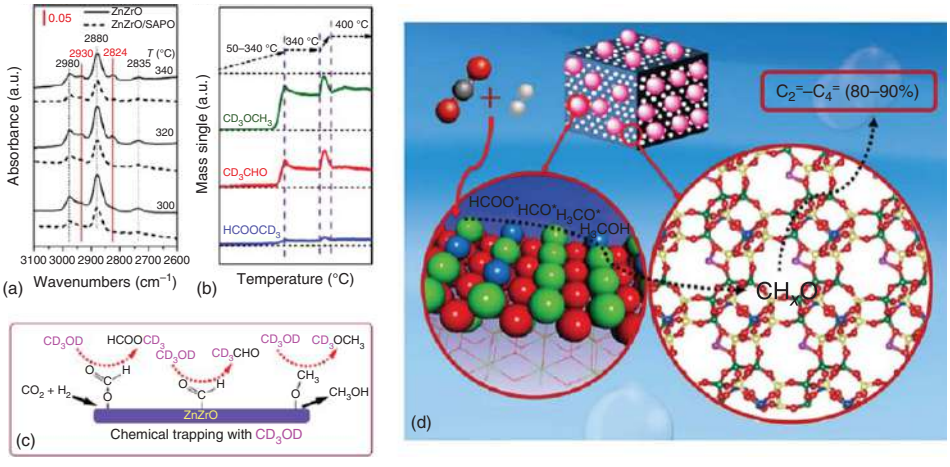

Figure 12.5 Reaction intermediate species. (a) *In situ* DRIFT spectra from CO_2 hydrogenation over ZnZrO and ZnZrO/SAPO at different temperatures. (b) Chemical trapping-mass spectrometry results with a trapping reagent CD_3OD during the CO_2 hydrogenation over ZnZrO at reaction temperatures of 50–400 °C. (c) Scheme of chemical trapping using CD_3OD as trapping reagent during CO_2 hydrogenation. (d) Schematic for the proposed reaction mechanism of CO_2 hydrogenation on the tandem catalyst, ZnZrO/SAPO. Source: Li et al. [25] © 2017, American Chemical Society.

was found that the CH_xO species (mainly CH_3O*, CHO*, and CH_3OH species) were produced on the ZnZrO surface and then migrated to the SAPO surface and formed hydrocarbons. Furthermore, the catalyst exhibited stability toward sulfur treatment, thereby demonstrating promise for industrial application. Besides that, a similar bifunctional catalyst composed of a methanol synthesis (In_2O_3/ZrO_2) catalyst and an MTO (SAPO-34) catalyst was used to directly produce ethylene and propylene from CO_2 and H_2 with a high selectivity of 80–90% in hydrocarbons [57].

More recently, Guo et al. reported a bio-promoter-modified Fe-based catalyst, which achieved a high linear α-olefin (LAO) selectivity – 80% selectivity in C_{4-18} alkenes [58]. A similar phenomenon of hydrogenation inhibition was observed over a Na-modified FeZn catalyst for improving the selectivity of syngas-derived alkenes [59], which is beneficial for the formation of long-chain alkenes. A similar promoter migration phenomenon has also been reported by different groups [60, 61], and the migration action was able to influence the activity and selectivity effectively. Tuning promoter migration in heterogeneous catalysis is an important tool for enhancing activity and product selectivity. Generally, the formed olefins as primary products will undergo secondary steps under the reaction conditions to form a series of hydrocarbon products. Lee et al. reported that the addition of Ru dopant increased the re-adsorption ability of α-olefins and resulted in the enhancement of secondary reactions. Thus, the Ru dopant could be applied to modify chain length of hydrocarbons and produce higher carbon number hydrocarbons [62]. Contrary to the finding reported by Lee et al., Niemelä and Nokkosmäki suggested that Ru did not provide any benefit for selectivity and activity of CO_2 hydrogenation [63].

Generally, CO_2 adsorption occurs on basic sites; thus various metal oxides as promising dopants have been applied to enhance the CO_2 adsorption capability and/or activation ability, such as K, Zr, and Ru. Thus, when it comes to increasing light olefin selectivity, generally, the addition of alkali metal is indispensable. As an alkali metal, K can donate electron density to the vacant d orbital of iron, so that increases the catalyst surface basicity, resulting in a decrease in H_2 adsorption and an increase in CO_2 adsorption [64–66]. Choi et al. reported that CO_2 is most likely adsorbed on the K sites while Fe adsorbs H_2 according to chemisorption studies, and thus the preference for CO_2 rather than hydrogen increases the probability of C—C bond formation [67]. The formation of more C—C bonds coupled to low surface concentration of hydrogen would be also a favorable condition for olefin formation. Indeed, Zhao and coworkers reported a high olefin distribution (c. 54 wt%) over iron-based catalysts with K promotion [16]. Wang and coworkers found that an appropriate amount of B existing in the K-modified iron catalysts could enhance light olefin selectivity and decrease the selectivity of higher hydrocarbons without changing the activity of catalysts [68]. In addition, sodium-containing Fe_3O_4 catalysts exhibited higher activity and produced more C_2–C_4 olefins and C_{5+} hydrocarbons likewise [69]. The electron density of oxygen is expected to be high on basic sites; thus the strength of the basicity can relate to the binding energy of O_{1s} for the carbonate species. According to this principle, Ando et al. investigated the catalytic performance of CO_2 hydrogenation over Fe–Cu catalysts and disclosed the relationship between basicity and olefin content [70]. It is well accepted that

carbide has been considered as the active phase in the modified FTS process [71], similarly to the catalytic hydrogenation of CO via FTS [59, 72]. Furthermore, some researchers found that the addition of K could also promote the formation of Hägg carbide that further influenced the selectivity of products [68, 73, 74]. Recently, Fischer et al. confirmed that the addition of K had a direct promotional effect on the formation of Hägg carbide via the application of novel *in situ* techniques [74]. In addition, Lee and coworkers investigated the promoter effect of V, Cr, Mn, and Zn on Fe-based catalysts, in which V prevented the formation of carbides while Cr, Mn, and Zn exhibited the opposite function [75].

12.3.2 Liquefied Petroleum Gas (LPG)

Early, Fujiwara et al. reported a process with a high selectivity of ethylene and propene over Cu–Zn-chromate/HY zeolite composite catalyst [24]. Afterward they investigated the effect of HY zeolite on a composite catalyst comprising Fe–ZnO/HY zeolite [76]. Fe–ZnO possessed two kinds of active site, which are one kind for FT reaction and the other for methanol synthesis. The addition of HY zeolite influenced the catalytic activity of Fe–ZnO and changed the product selectivity significantly. In other words, the utilization of HY zeolite decreased the activity of sites for the FT reaction without deactivating the sites for methanol synthesis and thus led to non-ASF product distribution and was beneficial for the formation of unsaturated hydrocarbons. As described above, the correct zeolite in the composite catalysts is crucial for the formation of target products. A composite catalyst composed of Pd-β zeolite and Zr-modified CuZn catalyst for liquefied petroleum gas (LPG) production was reported by Li et al. [77] Hydrogen spillover phenomenon over Pd-β zeolite made it possible to convert methanol into paraffinic hydrocarbons at low temperature, and the main product was isobutane.

12.3.3 Liquid Fuels

Previously, direct synthesis of gasoline from CO_2 with a practical conversion level had not been achieved, owing to some intrinsic weakness such as high selectivity to methane, poor performance of CO_2 hydrogenation compared with syngas conversion, and strong hydrogen-transfer action of H-ZSM-5. Recently, it was reported that a high selectivity of gasoline-range hydrocarbons could also be achieved on such composite catalysts based on a methanol-mediated process [27].The author prepared a bifunctional catalyst composed of reducible indium oxide (In_2O_3) and zeolites toward CO_2 hydrogenation to liquid fuels, and the proposed reaction pathway was that the activation of H_2 and CO_2 over oxygen vacancies on the In_2O_3 surfaces combined the C–C coupling process in zeolite process. This achieves 78.6% C_5–C_{11} hydrocarbons with a high octane number. Gasoline-range hydrocarbons were formed over the acidic sites of the zeolite via the hydrocarbon-pool mechanism, as shown in Figure 12.6.

Besides gasoline-range hydrocarbons production from a methanol-mediated process, Wei et al. utilized the cooperatively catalysis of multi-types of active

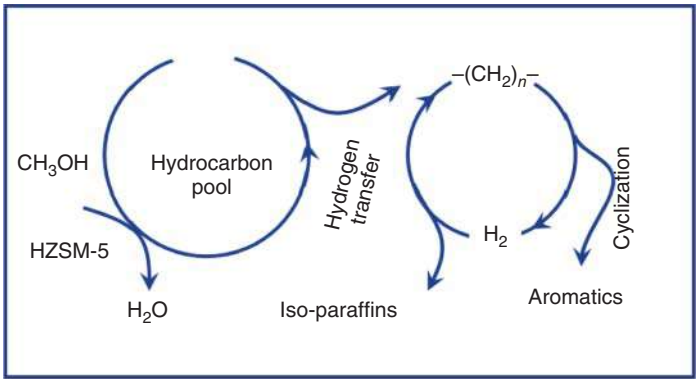

Figure 12.6 Schematic of the hydrocarbon-pool mechanism for CH_3OH conversion into hydrocarbons inside H-ZSM-5.

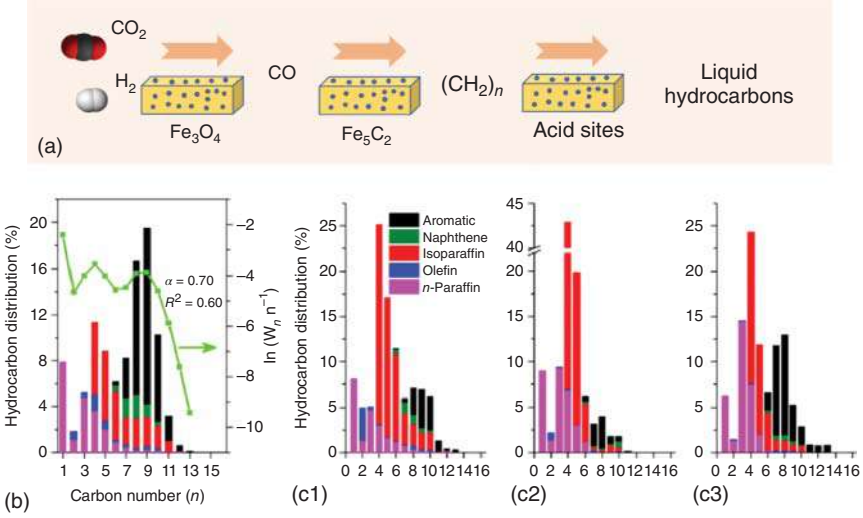

Figure 12.7 (a) Multi-active sites for catalyzing CO_2 into liquid hydrocarbons. (b) The detailed hydrocarbon product distribution obtained over Na–Fe_3O_4/H-ZSM-5(160) composite catalyst. Source: Wei et al. [26] © 2017, Springer Nature. (c) Detailed hydrocarbon product distribution obtained over different catalysts (c1, Na–Fe_3O_4/HMCM-22; c2, Na–Fe_3O_4/H-Beta; c3, Na–Fe_3O_4/H-ZSM-5). Source: Wei et al. [78] © 2018, American Chemical Society.

sites to catalyze CO_2 hydrogenation to gasoline-range hydrocarbons based on a non-methanol-mediated process, and the reaction scheme is shown in Figure 12.7 [26, 78]. Three types of active site (Fe_3O_4, Fe_5C_2, and acid sites) cooperatively catalyzed a tandem reaction. Thus, Na–Fe_3O_4/zeolite achieved an excellent performance. The design of proper spatial arrangement of active sites provided an effective route for designing a high-performance catalyst, not just for the CO_2 hydrogenation process [27]. Not limited to CO_2 hydrogenation, which also generally shows high selectivity toward desired products (aromatics, olefins, isoparaffins, etc.), the

utilization of two or more types of catalyst especially combinations involving zeolite in CO hydrogenation demonstrates the great prospect of multifunctional catalysts [79–84]. Currently, composite/hybrid catalysts generally include a methanol synthesis catalyst and a zeolite based on a methanol-mediated process for higher hydrocarbon production. The main reason is that methanol-mediated process is more conducive to breaking the rate-limiting step of C–C coupling.

The integration method and spatial distribution (that is proximity of active sites) of the active components have a profound effect on the catalytic performance for CO_2 hydrogenation over bifunctional catalysts [25–28]. The different proximity of active sites led to an evidently difference in product distribution, as shown in Figure 12.8. Although the closest proximity between metal sites and zeolite acid sites can be created by simple powder mixing, CO_2 conversion and C_{5+} hydrocarbon selectivity was significantly lower than the levels in a granule-mixing bifunctional catalyst with a moderate distance between the two kinds of active sites as compared in Figure 12.8. This loss of activity and C_{5+} hydrocarbon selectivity may originate from the coverage or poisoning effect of different active sites such as the poisoning of metal sites resulting from zeolite acid sites and thus the two active sites not being utilized to the maximum extent. Previously, the effects of proximity between metallic sites and acid sites on catalytic performance including selectivity and activity were investigated [85–90]. Francis et al. ascribed the middle distillate selectivity improvement and enhanced conversion to efficient synergy between metal sites and acid sites, owing to

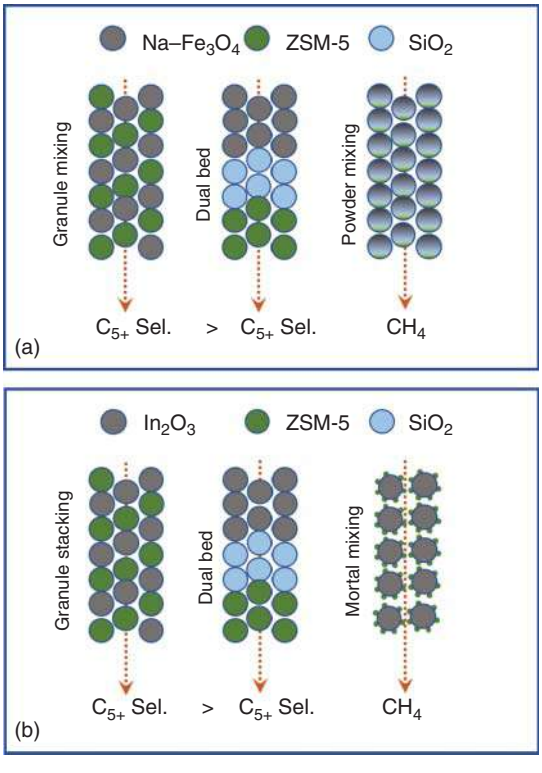

Figure 12.8 CO_2 hydrogenation performances over the multifunctional catalysts with different proximity.

an increased proximity [85]. Kim et al. regarded that the short diffusion path lengths between metal sites and acid sites is beneficial for further reaction of intermediate products before their escape [87]. Afterward, Zecevic et al. demonstrated that the closest proximity between metal sites and acid sites was detrimental to the catalytic performance by investigating hydrocarbon hydrocracking reactions and argued that a suitable method for tailoring catalyst properties should be associated with process requirements rather than a simple "the closer the better" notion of intimacy [91]. Similarly, Samad et al. demonstrated that optimized bifunctional catalytic performance of metal–acid catalysts for *n*-heptane isomerization reaction can be achieved with a nanometer to micrometer-scale site proximity [92]. Based on these reports, we can learn that a moderate distance among different active is crucial for the synergistic effect of multifunctional catalysts, and this property needs to be considered as the key factor and difficulty for the design and fabrication of multifunctional catalysts achieving high performance.

Although iso-alkanes are regarded as a fuel additive both for enhancing the octane value of gasoline and for improving automobile exhaust, few studies have been conducted on the CO_2 hydrogenation conversion to iso-alkanes. Tan and coworkers investigated the CO_2 hydrogenation process over a mechanically mixed catalyst comprising Fe–Zn–Zr oxide and HY zeolite [93, 94]. Fe–Zn–Zr in the composite catalyst was not only a methanol synthesis catalyst but was beneficial for the formation of iso-alkanes based on reaction results [93]. Although these composite catalysts were used to produce iso-alkanes from CO_2, the selectivity of iso-alkanes was still unsatisfied, owing to the poor synergistic effect of metal oxide and zeolite via the mechanical mixture preparation route. To overcome this disadvantage, a new kind of capsule catalyst with Fe–Zn–Zr as the core and a zeolite (H-ZSM-5, H-Beta, and HY) as the shell was synthesized by a simple cladding method to enhance the catalytic performance (Figure 12.9) [95]. The excellent synergistic effect between H-ZSM-5 and H-Beta zeolites in the shell and the confinement effect resulted in a high selectivity of iso-alkanes (81.3% of iso-alkanes among hydrocarbons). Furthermore, the capsule structure/core–shell catalysts usually exhibited a benign stability and product selectivity in C1 chemistry as previously reported [80, 96]. Thus, a rational design of capsule catalyst would play a positive role in the utilization of CO_2 and directed formation of desired products.

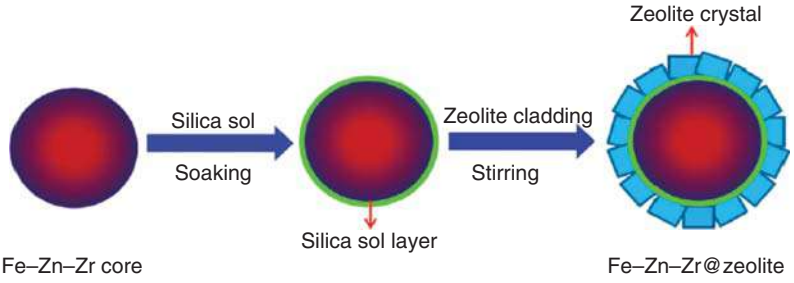

Figure 12.9 Scheme for the Fe–Zn–Zr@zeolite core–shell catalyst preparation by a simple cladding method. Source: Wang et al. [95] © 2016, The Royal Society of Chemistry.

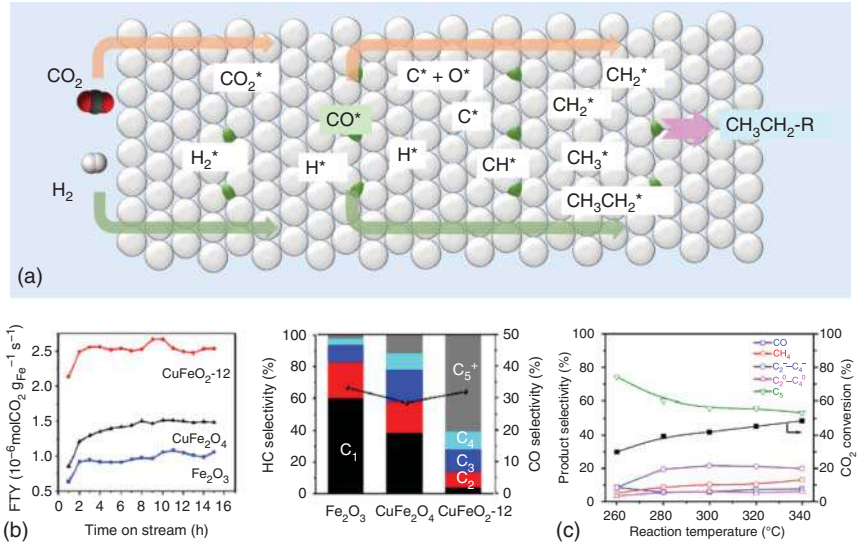

Figure 12.10 (a) Reaction scheme for CO_2 hydrogenation to liquid hydrocarbons over promoted iron-based catalyst. (b) Fe time yield (FTY) against time on stream for catalysts derived from Fe_2O_3, $CuFe_2O_4$, and $CuFeO_2$-12 precursors [97]. Source: © 2017, Elsevier. (c) Influence of reaction temperature on the catalytic performance of 10Fe0.8K catalyst. Source: Jiang et al. [98] © 2018, The Royal Society of Chemistry.

In addition to a hybrid system for catalyzing CO_2 into liquid hydrocarbons, modified iron-based catalysts without any zeolite utilization were also applied to convert CO_2 into liquid fuels, based on the conventional FTS process (Figure 12.10a). Choi et al. used delafossite ($CuFeO_2$) as the catalyst precursor for converting CO_2 hydrogenation into liquid fuels, producing liquid hydrocarbon (C_{5+}) selectivity of 65% and greatly suppressing CH_4 formation to 2–3% (Figure 12.10b) [97]. Jiang et al. designed a K^+-doped iron-based catalyst for liquid fuel formation (Figure 12.10c) [98]. The catalyst also presented a high C_{5+} selectivity exceeding 50%. In fact, the pure iron catalyst does not show good selectivity for high-carbon hydrocarbon products. To solve this problem, alkali metal doping, especially K^+ or Na^+, is widely used. Choi et al. fabricated sodium-containing spinel zinc ferrite as a catalyst precursor for the selective synthesis of liquid hydrocarbon fuels (58%) [99]. The combination of Zn and Na with Fe increases the CO_2 adsorption properties and promotes the *in situ* formation of carbide, which is the active phase for the formation of heavy hydrocarbons in CO_2 hydrogenation.

As mentioned earlier, cobalt-based catalysts are often methanation catalysts, which convert CO_2 to CH_4. Contrary to expectation, a recent study showed that cobalt-based catalysts can also achieve good selectivity for high carbon-containing products [100]. He et al. constructed a simple Co_6/MnO_x nanocatalyst that could efficiently catalyze CO_2 hydrogenation to normal C_{5+} hydrocarbons at a lower temperature (Figure 12.11). Co was the major catalyst, while the Mn promoter enhanced CO_2 adsorption and weakened H_2 adsorption on the catalyst. During

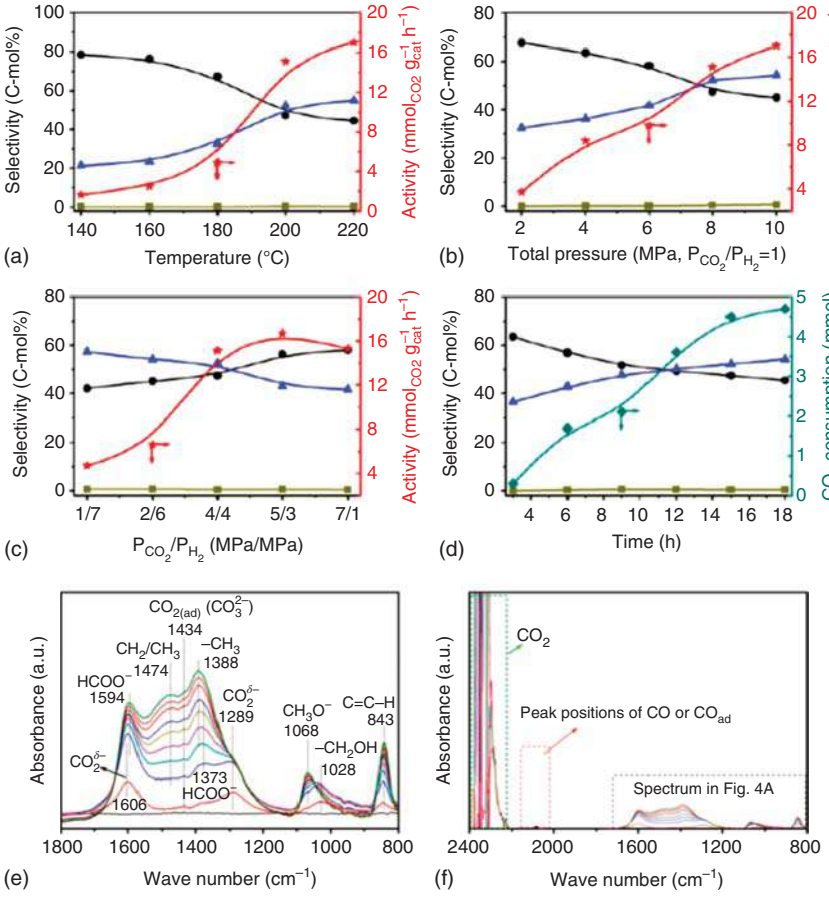

Figure 12.11 (a) Reaction temperature, (b) total pressure, (c) CO_2/H_2 ratio, and (d) reaction time on the CO_2 hydrogenation using 20 mg of Co_6/MnO_x and 1 ml of squalane. Other conditions: (a) 4 MPa of CO_2 and 4 MPa of H_2, 15 h; (b) $PCO_2/PH_2 = 1$, 200 °C, 15 h; (c) initial pressure 8 MPa, 200 °C, 15 h; and (d) 4 MPa of CO_2 and 4 MPa of H_2, 200 °C. Symbols: triangle, C_{5+} selectivity; circle, C_{1-4} selectivity; square, CO selectivity; star, activity; diamond, CO_2 consumption. (e) *In situ* Fourier-transform infrared (FTIR) spectra key intermediates and (f) wide band recorded during the CO_2 adsorption on Co_6/MnO_x. The catalyst was pretreated with H_2 at 200 °C for 2 h before the adsorption test. The black straight line at the bottom was the baseline recorded before CO_2 adsorption. The spectra were recorded after the CO_2 was introduced to the catalyst, and the time sequence, from bottom to top, was 2, 2.5, 4.5, 7.5, 15, 25, 35, 45, and 55 min. Source: He et al. [100] © 2019, Proceedings of the National Academy of Sciences, American Institute of Physics.

the reaction, CO_2 adsorbed on the catalyst and was reduced by H atoms to CH_2 monomer and CH_3 species, via $CO_2^{\delta-}$, $HCOO^-$, $-CH_2OH$, and/or CH_3O^- intermediates instead of CO intermediate. The liquid hydrocarbons were generated by further chain growth steps, which are similar to those of the well-known Co^0 catalyzed FTS reaction. The reaction could proceed by avoiding CO, which opens an avenue for liquid fuel synthesis and CO_2 transformation.

At present, the formation of liquid fuels by hydrogenation of carbon dioxide mainly occurs through three pathways: (i) the reaction pathway with methanol as the intermediate over a composite catalyst, (ii) the reaction pathway with low carbon olefin as the intermediates on the hybrid catalyst, and (iii) the simple traditional FTS. For pathway (i), the characteristics of the zeolite and the contact intimacy between the methanol synthesis catalyst and the zeolite are the prerequisites to achieve good performance. For route (ii), in addition to the above factors, the choice of iron-based catalyst with benign olefin selectivity is also a key factor. However, for the last pathway, promoter modification (i.e. K^+) doping or synthesis of catalysts with unique structures (such as spinel-like structure) is a key element. Especially recently, through the improvement of reaction equipment, it is possible to also achieve a good reaction yield (multistage reactor system). Hence combining the rational design of catalyst and device improvement will be an important trend for CO_2 industrialization [101].

12.3.4 Aromatics

Aromatics are used mainly for the production of polymers, constituting about one-third of the market for commodity petrochemicals. The worldwide demand for benzene derivatives, polyester fibers, and resins is growing rapidly at a rate of 6% per year. In the current chemical industry, the production of aromatics heavily relies on petroleum. Therefore, the directed production of aromatic compounds from the hydrogenation of carbon dioxide is an alternative route. In fact, this process from one carbon to a compound of six to eight carbon atoms involves a great challenge. The activation of carbon dioxide and the effective growth of the carbon chain are the key to solving this problem.

Ni et al. took the lead in preparing a highly efficient composite catalyst composing of nano-scaled spinel structural $ZnAlO_x$ oxide and H-ZSM-5 zeolite for highly selective aromatic hydrocarbon generation from CO_2 hydrogenation, achieving 73.9% aromatic selectivity with only 0.4% CH_4 selectivity among the carbon products without CO in the CO_2 hydrogenation reaction occurring through a methanol-mediated process (Figure 12.12a) [102]. Zn^{2+} in $ZnAlO_x$ activates CO_2 hydrogenation, and the shield of the external Brønsted acid sites of H-ZSM-5 is beneficial to aromatization. Similarly, a ZnZrO solid solution combined with H-ZSM-5 zeolite was also successfully prepared for directly converting CO_2 hydrogenation to aromatics with aromatic selectivity up to 73% at a CO_2 conversion of 14% [105]. The tandem catalyst ZnZrO/ZSM-5 favors the thermodynamic coupling between CO_2 hydrogenation over ZnZrO and the formation of aromatics over H-ZSM-5 through the transfer of CH_xO intermediates from the surface of ZnZrO to the pore structure of H-ZSM-5. Zhou et al. utilized a similar hybrid system containing ZnO–ZrO_2 aerogel and zeolite H-ZSM-5 for the hydrogenation of CO_2 into aromatics with 76% selectivity at a single pass CO_2 conversion of 16% [103]. By applying advanced electron paramagnetic resonance (EPR) measurements, they demonstrated that the adsorption of CO_2 and formation rates of methanol/dimethyl ether (DME) are governed by the total amount of oxygen vacancies (Figure 12.12b).

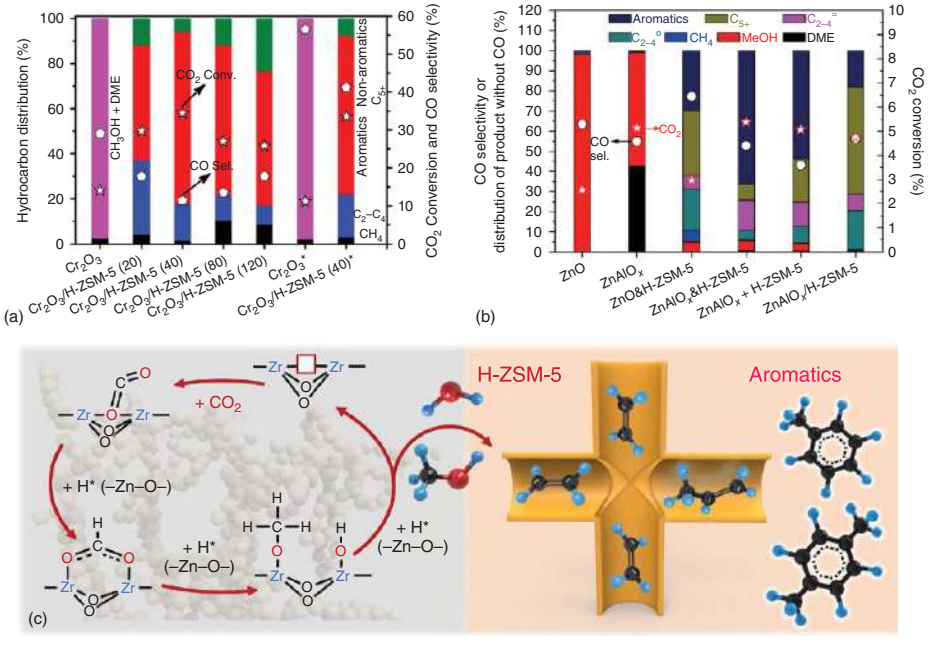

Figure 12.12 (a) Comparisons of the CO_2 conversion and product selectivity over various catalysts. Reaction conditions: space velocity = 12 000 (for ZnO and $ZnAlO_x$) or 6000 (for composite catalysts) ml g^{-1} h^{-1}, 3.0 MPa, 593 K, $H_2/CO_2/Ar$ = 3/1/0.2. Note that the C_{5+} excludes aromatics. $C_{2-4}{}^{=}$ and $C_{2-4}{}^{\circ}$ refer to C_2-C_4 olefins and paraffins, respectively; $ZnAlO_x$&H-ZSM-5 prepared by grinding; $ZnAlO_x$ + H-ZSM-5 prepared by granules mixing; $ZnAlO_x$/H-ZSM-5 denoted as dual-bed catalysts. Source: Ni et al. [102] © 2018, Springer Nature. (b) Possible mechanism of direct hydrogenation of CO_2 into aromatics over bifunctional catalyst. Source: Zhou et al. [103] © 2020, American Chemical Society. (c) Catalytic performance of various catalysts for CO_2 conversion to aromatics. CH_4, black; CH_3OH + DME, magenta; C_2-C_4, blue; aromatics, red; non-aromatics C_{5+}, green. The number in parentheses in the catalyst name corresponds to the Si/Al ratio of H-ZSM-5. Reaction conditions: 350 °C, 3 MPa, H_2/CO_2 = 3 (5.42 vol% CO), 10 ml min^{-1}, time of stream (TOS) = 6 h. Catalyst weight, 0.5 g, oxide/zeolite mass ratio = 1, 0.25 g Cr_2O_3 for methanol synthesis. $^*CO_2$ hydrogenation reaction over Cr_2O_3 or Cr_2O_3/H-ZSM-5 without CO contained in the feed gas. Source: Wang et al. [104] © 2019, American Chemical Society.

In addition, Wang et al. designed a bifunctional catalyst composed of Cr_2O_3 and H-ZSM-5 for CO_2 hydrogenation to aromatics directly through a tandem catalysis process, in which a high aromatic selectivity of 75.9% with only 1.5% CH_4 and 11.4% CO selectivity was achieved at a CO_2 conversion of 34.5% (Figure 12.12c) [104]. Additionally, they provided a very promising strategy for an efficient conversion of CO_2 to *p*-xylene by applying core–shell-structured H-ZSM-5@S-1 zeolite capsule catalyst (S-1 refers to silicalite-1). Zhang et al. synthesized $ZnCrO_x$–zeolite composite catalysts for CO_2 hydrogenation into aromatics, also accomplishing a good aromatic selectivity [106]. Through the introduction of a small amount of Zn into the ZSM-5 zeolite, the formation of aromatics was improved [106]. Obviously, direct conversion of CO_2 into aromatics with high selectivity can be further regulated by tailor-made zeolites such as by applying a coating film or using ion exchange. In another words, acid site density, strength, and SiO_2/Al_2O_3 ratio are crucial factors for boosting catalytic performance.

In contrast, recently, the direct conversion of carbon dioxide hydrogenation into aromatics through the conventional Fischer–Tropsch route (olefins intermediates) instead of the methanol-mediated route has attracted attention [107–109]. Xu et al. designed a composite Na/Fe and H-ZSM-5 catalyst system, which presented a high aromatic selectivity [108]. Additionally, SiO_2-coated H-ZSM-5 can suppress the isomerization of *para*-xylene and *para*-ethyltoluene. Not limited to this, a dual-layer packing configuration of composite catalyst (FeK1.5/HSG-H-ZSM-5 zeolite) achieved an unprecedentedly high space–time yield of aromatics of 11.8 μmol CO_2 $gcat^{-1}$ s^{-1} [107]. Ramirez et al. reported the combination of a series of catalysts comprising potassium superoxide-doped iron oxide and a highly acidic zeolite (ZSM-5 and MOR) that directly convert CO_2 to either light olefins (in MOR) or aromatics (in ZSM-5). The space–time yields of $STYC_2$–$C_4^=$ and STYAROM achieved 11.4 and 9.2 mmol g^{-1} h^{-1}, respectively, at 375 °C, $P = 30$ bar, $H_2/CO_2 = 3$, and 5000 ml g^{-1} h^{-1} [109].

12.3.5 Synthesis of Alcohol

Alcohol is a key building block in the chemical industry, with prospects as a sustainable energy carrier (alternative next-generation clean fuel) if its production is accomplished from CO_2 and H_2 [110–114]. Currently, the leading catalysts used in industry for hydrogenation of CO_2 to methanol ($CO_2 + 3H_2 \rightarrow CH_3OH + H_2O$) are $Cu/ZnO/Al_2O_3$ catalysts. One of the main challenges is that as the reaction process progresses, the Cu nanoparticles (NPs) will gradually aggregate and separate from ZnO, thereby exhibiting poor catalytic performance. Thus, stabilizing intimately mixed Cu and Zn species is crucial to maintaining efficient conversion including reaction activity and product formation [114]. In response to this problem, a series of studies have been launched.

Based on the above considerations, An et al. used strong metal–support interactions (SMSIs) and confinement effects to stabilize Cu NPs to enhance catalytic activity. Ultrasmall Cu/ZnO_x NPs in metal–organic framework (MOF) cavities was designed to catalyze CO_2 hydrogenation into methanol (Figure 12.13a) [112].

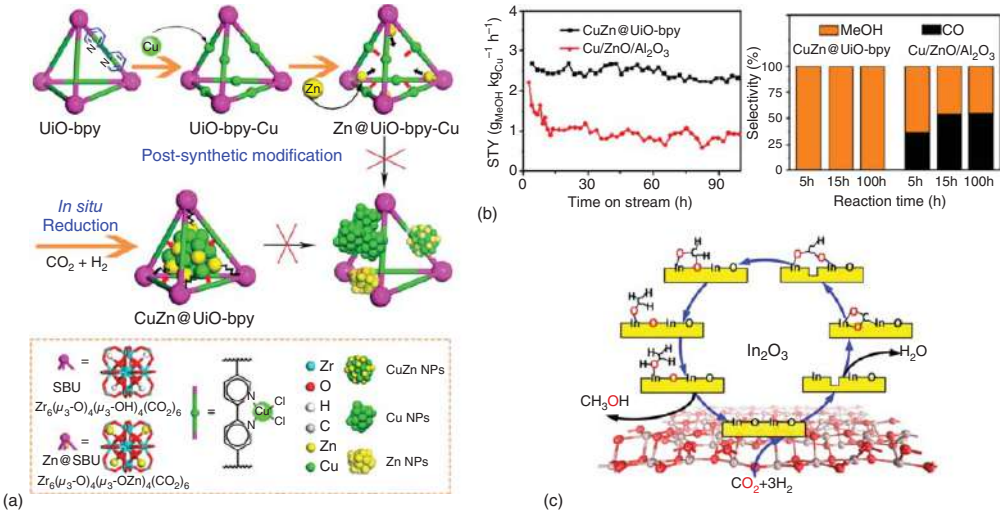

Figure 12.13 (a) Preparation of CuZn@UiO-bpy via *in situ* reduction of post-synthetically metalated UiO-bpy. Source: An et al. [112] © 2017, American Chemical Society. (b) STY of MeOH and selectivity of product vs. reaction time over a period of 100 h on stream. Source: An et al. [112] © 2013, American Chemical Society. (c) Methanol synthesis from CO_2 hydrogenation on the defective In_2O_3 [110] surface with surface oxygen vacancies. Source: Ye et al. [115] © 2013, American Chemical Society.

The special structure can stabilize these ultrasmall NPs and prevent the agglomeration under reaction conditions, achieving high activity and selectivity for methanol synthesis (Figure 12.13b). MOFs as excellent supports pave new opportunities by taking advantage of tunable and specific SMSIs. Although a large number of catalysts are widely used in the methanol synthesis process, the efforts to understand the nature of the active sites in Cu/ZnO led to debate about the role of ZnO. Kattel et al. demonstrated that ZnCu undergoes surface oxidation under reaction conditions so that surface Zn transforms into ZnO allowing ZnCu to reach the activity of ZnO/Cu with the same Zn coverage. Meanwhile, the synergy effect of Cu and ZnO at the interface promotes methanol synthesis through formate intermediates [114]. Similarly, a tunable copper–ceria interface by combining metal and oxide sites in the interface affords complementary properties that lead to efficient synthesis of methanol. In addition to Cu-based catalysts, In_2O_3 was also applied to methanol synthesis, in which the oxygen vacancies on the In_2O_3 [110] surface assist CO_2 activation and hydrogenation and also stabilize the key intermediates involved in methanol formation (Figure 12.13c) [115].

Besides, Li et al. developed a hybrid oxide catalyst comprising manganese oxide NPs supported on mesoporous spinel cobalt oxide as a highly active and selective methanol synthesis catalyst [116]. In this hybrid system, the existence of a MnO/CoO interface facilitated an activity enhancement toward methanol synthesis, presenting potential industrial applications. As mentioned above, the oxygen vacancies on the In_2O_3 surface significantly improve the catalytic performance of synthesis. On this basis, Martin et al. designed the supported metal hybrid system (In_2O_3/ZrO_2) for the hydrogenation of CO_2 to methanol featuring outstanding activity and 100% selectivity under industrially relevant conditions (Figure 12.14a,b) [117]. It is worth noting

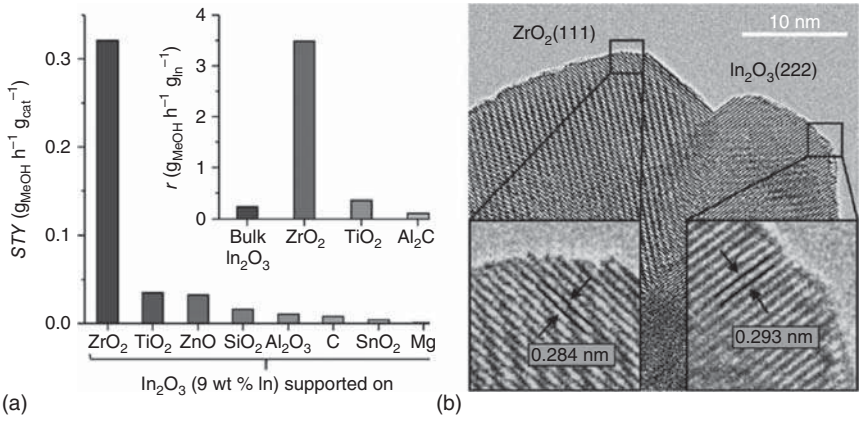

Figure 12.14 (a) Methanol STY for different supported catalysts after 4 h on stream. Source: Martin et al. [117] © 2016, Wiley-VCH. (b) High-resolution transmission electron microscopy (HRTEM) micrograph of the In_2O_3/ZrO_2 catalyst obtained after 4 h on stream. Reaction conditions: $T = 573$ K, $P = 5.0$ MPa, $H_2/CO_2 = 4:1$, and gas hourly space velocity (GHSV) = 16 000 h^{-1}. Source: Martin et al. [117] Figure 03 [p. 6264]/with permission from John Wiley & Sons, Inc.

that the cyclic release of oxygen vacancies and the electronic interaction with the carrier have been further strengthened, and these factors are of great significance for the efficient selective synthesis of methanol.

Especially recently, Li et al. achieved efficient methanol production by designing an advanced reaction system (water-conduction membrane incorporated dehydration membrane reactor for high-purity methanol direct synthesis) (Figure 12.15A) [113]. For this reaction system, highly efficient *in situ* water removal through water-conduction nanochannels led to a substantial increase in CO_2 conversion and methanol yield in CO_2 hydrogenation for methanol production. This phenomenon of *in situ* water removal enhancing catalytic performance provides a new concept for involving catalysts or reaction systems. In addition to low-carbon alcohols (methanol), the direct generation of high-carbon alcohols (C_{2+} alcohol) from the hydrogenation of CO_2 is another research hotspot of carbon dioxide utilization. The higher alcohols ($C_{2+}OH$), which are well-known commodity chemicals and have higher energy densities than methanol, have wide applications. Compared with methanol, the synthesis of $C_{2+}OH$ from CO_2 and H_2 is a more difficult owing to the chemical inertness of CO_2 and chain propagation [120]. Xu et al. reported efficient and selective CO_2 hydrogenation to C_{2+} alcohols with STY of 73.4 $mg\,g_{cat}^{-1}\,h^{-1}$ and $C_{2+}OH/ROH$ percentage of 93.8% over a Cs-modified CuFeZn catalyst, which contains synergetic active sites [118]. *In situ* diffuse reflectance infrared Fourier transform spectroscopy (DRIFTS) analysis confirms that ethanol follows the tandem reaction mechanism of RWGS and C(H)O* insertion via CH_3CHO* intermediates. Iron carbide is responsible for CO dissociation to form surface alkyl intermediates, while Cu is responsible for CO non-dissociative activation (Figure 12.15B). Similarly, Bai et al. reported highly ordered Pd–Cu NPs to be highly active, highly selective, and stable catalysts toward CO_2 hydrogenation to C_2H_5OH [119]. With optimization of the Pd/Cu ratio and the support, the Pd_2Cu NPs/P25 catalyst delivered high selectivity to C_2H_5OH of 92.0% and exhibited the highest turnover frequency (TOF) of 359.0 h^{-1}, outperforming all previous catalysts (Figure 12.15C). Mechanistic studies demonstrated the Pd_2Cu NPs/P25 underwent CO_2 adsorption/activation, formation of formate intermediates, transformation or hydrogenation of intermediates (formate, *CO, $*CH_3$, *CO insertion to form $*CH_3CO$), and hydrogenation to C_2H_5OH finally. Notably, *CO hydrogenation to *HCO is likely to be the rate-determining step for the CO_2 hydrogenation to C_2H_5OH. To replace the scarce and expensive noble metals with inexpensive and abundant first-row transition metals, such as cobalt, Wang et al. designed an alumina-supported cobalt particle ($CoAlO_x$) catalyst with tunable Co–CoO_x phases [120]. The investigators have investigated $C_{2+}OH$ synthesis from CO_2 hydrogenation over Pt/Co_3O_4 catalyst in different solvents. It is also found that the existence of reaction solvent plays a crucial role in the higher alcohol synthesis reaction. Water as solvent can enhance the reaction significantly, and it also promotes selectivity of the reaction in other solvents effectively [121]. More importantly, heterogeneous catalyst/water (or aqueous solution) catalytic systems that are effective at low temperature have great potential for application in the reaction, and the strategy

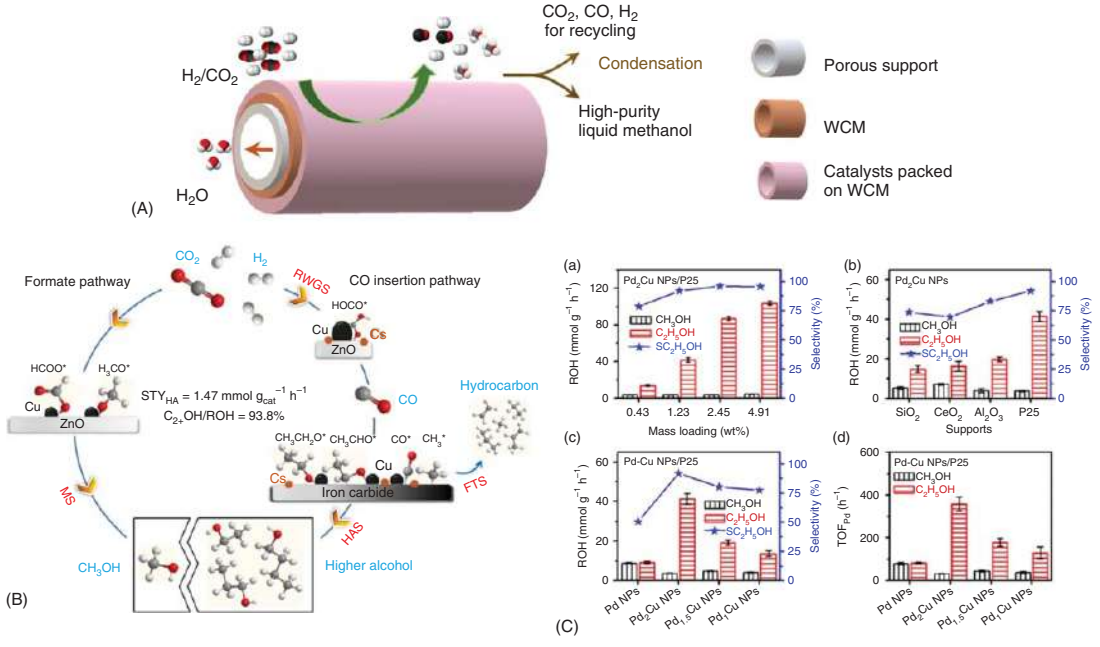

Figure 12.15 (A) Schematics of water-conduction membrane (WCM)-incorporated dehydration membrane reactor for high-purity methanol direct synthesis from renewable resources. (B) Illustration for the reaction pathways of CO_2 hydrogenation over the Cs–CuFeZn catalysts. Source: Xu et al. [118] © 2020, American Chemical Society. (C) Achieved product yields of CH_3OH and C_2H_5OH (ROH) and selectivity of C_2H_5OH of Pd_2Cu NPs with different loadings on P25 or over different support in CO_2 hydrogenation at 200 °C for 5 h or achieved product yields of ROHs and selectivities of C_2H_5OH and comparisons of the TOF Pd values of Pd–Cu NPs/P25. Source: Bai et al. [119] © 2017, American Chemical Society.

to use the synergistic effect of water and metallic catalysts can also be used to explore other catalytic systems for efficiently producing $C_{2+}OH$ at mild conditions. Achieving high selectivity and yields toward C_{2+} alcohols is urgently desired in future CO_2 utilization. The key to the selective production of alcohol products from the hydrogenation of carbon dioxide is how to design the alloy interface with adjustable stability so that the catalyst can maintain good structural performance under reaction conditions. The combination of improvement of the reaction unit and modification of catalyst should be one of the future development trends.

12.3.6 Synthesis of Other Valuable Chemicals

Formate is very desirable product with many useful applications, including as fuel, fuel additives, H_2 storage media, energy carriers, and more [122, 123]. Heterogeneous single-atom catalysts (SACs) composed of atomically dispersed active metal centers on a support have attracted much interest in recent years. Heterogeneous SACs with atomically dispersed active metal centers represent an intermediary between heterogeneous and homogeneous catalysis. More recently, Shao et al. designed a stable, atomically dispersed Ir catalyst for the liquid-phase hydrogenation of CO_2 to formate (Figure 12.16a). Subsequently, they proposed that single-atom catalysis has a high potential for catalyzing CO_2 to formate [126]. Gunasekar et al. synthesized a novel covalent triazine framework functionalized with an Ir(III)-*N*-heterocyclic carbene complex for efficiently catalyzing the hydrogenation of CO_2 to formate with a TOF of up to 16 000 h^{-1} and a turnover number of up to 24 300 [127].The strong σ-donating and poor π-accepting characters of the N-heterocyclic carbene (NHC) site in the covalent triazine framework (CTF) enhance the electron density on the central metal Ir(III) cation, consequently presenting the highest TOF values.

Besides that, Ru pincer complex Ru(PNN)CO(H) was also designed for efficiently converting CO_2 into formate with an ultrahigh TOF value (Figure 12.16b) [124]. Afterward, Rohmann et al. constructed a novel [Ru(Acriphos)(PPh_3)(Cl)($PhCO_2$)] [1; Acriphos = 4,5-bis (diphenylphosphino) acridine] as an excellent pre-catalyst for the hydrogenation of CO_2 to formic acid in dimethyl sulfoxide (DMSO) and DMSO/H_2O without the need for amine bases as co-reagents [128]. Ingeniously, inspired by nature, which utilizes an ortho-OH-substituted pyridine motif in Fe-containing hydrogenases, Dubey et al. synthesized a Mn complex with a simple *N*-donor ligand, 6,6′-dihydroxy-2,2′-bipyridine, that acts as an efficient catalyst for CO_2 hydrogenation, achieving a turnover number of 6250 for hydrogenation of CO_2 to formate in the presence of 1,8-diazabicyclo[5.4.0]undec-7-ene (DBU) [125]. It should be noted that SACs can maintain the advantages of homogeneous and heterogeneous catalysis well. Hence, the development of high-performance SACs for the conversion of carbon dioxide to formate is also a promising route.

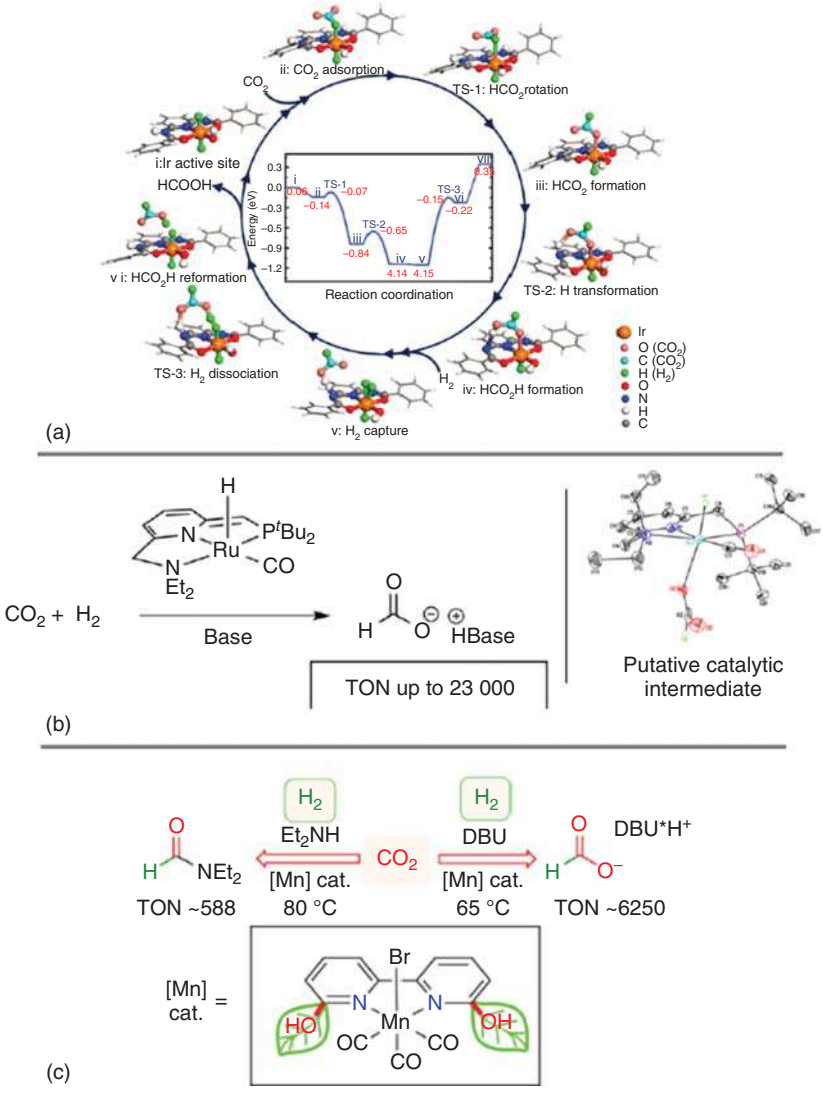

Figure 12.16 (a) The proposed reaction mechanism for CO_2 hydrogenation over the oppositely H bonding Ir single-atom active sites. Gaseous CO_2 is activated by Ir-hydride active sites (ii) and preferentially transferred to O-binding sites (iii) with a 0.07 eV barrier (TS-1). This is followed by hydrogenation by amide-H to give formic acid (iv) via a 0.19 eV transition state (TS-2). The H_2 molecule is then activated by the Ir single-atom active site (v) and dissociated to produce formic acid (vi) after passing through a 1.00 eV barrier (TS-3), with H transfer back to the amide to recover the catalyst (i). The inset in the cycle shows the calculated energy profile as a reference (in eV). Source: Shao et al. [122] © 2019, Elsevier. (b) Proposed reaction mechanism for CO_2 hydrogenation to formate over a Ru pincer complex Ru(PNN)CO(H). Source: Huff and Sanford [124] © 2013, American Chemical Society. (c) Proposed reaction mechanism for CO_2 hydrogenation to formate over a Mn complex with a simple *N*-donor ligand, 6,6′-dihydroxy-2,2′-bipyridine. Source: Dubey et al. [125] © 2017, American Chemical Society.

12.4 Photocatalytic and Electrocatalytic Conversion of CO_2 into Valuable Fuels or Chemicals

In addition to conventional thermocatalytic conversion of CO_2, photocatalysis and electrocatalysis have been identified as the ideal methods to convert CO_2 into selective products (e.g. methane, ethane, formate, methanol, ethanol, etc.) under solar light irradiation, especially for liquid products at ambient temperature and pressure [129–133]. This technology is also called artificial photosynthesis because it mimics nature's energy cycle (Figure 12.17).

In fact, there are also as many problems with the photocatalytic process as exist in the thermocatalytic process. Taking electrocatalysis as an example, the diffusion of gas molecules is a huge challenge. To overcome this challenge, recently, García de Arquer et al. presented a catalyst:ionomer bulk heterojunction (CIBH) architecture that decouples gas, ion, and electron transport [131]. By applying this design strategy, CO_2 electroreduction to multi-carbon products on copper in 7 M potassium hydroxide electrolyte (pH ≈ 15) with an ethylene partial current density of 1.3 A cm^{-2} at 45% cathodic energy efficiency was achieved (Figure 12.18). In the past decade, photoelectric catalysis has made great progress and solved a series of problems, but there are still many problems that need to be solved to push the development of these related fields. Although photoelectric catalysis of carbon dioxide to high value-added products has attracted much attention in the recent years, the reaction products are usually concentrated in low-carbon products, that is, the carbon atom number is less than 4. In comparison, the current thermal catalytic conversion of carbon dioxide has more scale and industrialization prospects than photoelectric catalysis processes. Therefore, in the near future, how to further broaden the product range (such as high carbon products) and achieve a large-scale yield will be a research focus and a challenge.

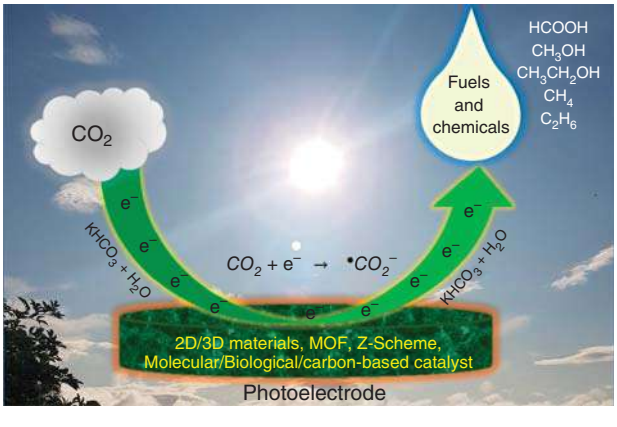

Figure 12.17 Schematic of the photocatalysis and electrocatalysis CO_2 conversion into fuels and value-added products under solar light irradiation. Source: Kumaravel et al. [129] Figure 01 [p. 487]/with permission from American Chemical Society.

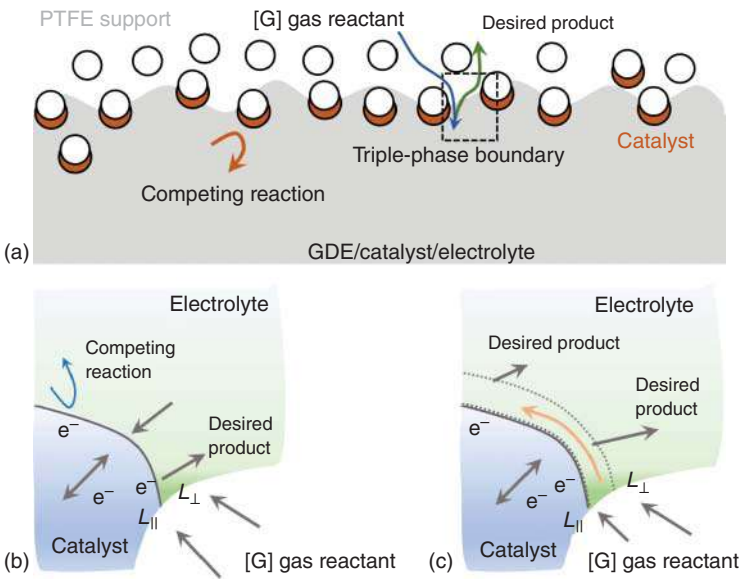

Figure 12.18 (a) In a gas-diffusion electrode, catalysts are deposited onto a hydrophobic support. (b) The volume in which gas reactants, active sites, and water and ions coexist determines the maximum available current for gas electrolysis. (c) When gas and electrolyte transport is decoupled, the three-phase reaction interface can be extended so that all electrons participate in the desired electrochemical reaction.

References

1 Porosoff, M.D., Yan, B., and Chen, J.G. (2016). Catalytic reduction of CO_2 by H_2 for synthesis of CO, methanol and hydrocarbons: challenges and opportunities. *Energy Environ. Sci.* 9: 62–73.

2 Wang, W., Wang, S., Ma, X., and Gong, J. (2011). Recent advances in catalytic hydrogenation of carbon dioxide. *Chem. Soc. Rev.* 40: 3703–3727.

3 Datta, S.J., Khumnoon, C., Lee, Z.H. et al. (2015). CO_2 capture from humid flue gases and humid atmosphere using a microporous coppersilicate. *Science* 50: 302–306.

4 Landau, M.V., Vidruk, R., and Herskowitz, M. (2014). Sustainable production of green feed from carbon dioxide and hydrogen. *ChemSusChem* 7: 785–794.

5 Kondratenko, E.V., Mul, G., Baltrusaitis, J. et al. (2013). Status and perspectives of CO_2 conversion into fuels and chemicals by catalytic, photocatalytic and electrocatalytic processes. *Energy Environ. Sci.* 6: 3112–3135.

6 Rodemerck, U., Holeña, M., Wagner, E. et al. (2013). Catalyst development for CO_2 hydrogenation to fuels. *ChemCatChem* 5: 1948–1955.

7 Song, C. (2006). Global challenges and strategies for control, conversion and utilization of CO_2 for sustainable development involving energy, catalysis, adsorption and chemical processing. *Catal. Today* 115: 2–32.

8 Centi, G. and Perathoner, S. (2009). Opportunities and prospects in the chemical recycling of carbon dioxide to fuels. *Catal. Today* 148: 191–205.

9 Trainham, J.A., Newman, J., Bonino, C.A. et al. (2012). Whither solar fuels? *Curr. Opin. Chem. Eng.* 1: 204–210.

10 Fischer, F. and Tropsch, H. (1926). Über die direkte Synthese von Erdöl-Kohlenwasserstoffen bei gewöhnlichem Druck. *Ber. Dtsch. Chem. Ges.* 59: 830–831.

11 Galvis, H.M.T., Bitter, J.H., Khare, C.B. et al. (2012). Supported iron nanoparticles as catalysts for sustainable production of lower olefins. *Science* 335: 835–838.

12 Zhang, Q., Kang, J., and Wang, Y. (2010). Development of novel catalysts for Fischer–Tropsch synthesis: tuning the product selectivity. *ChemCatChem* 2: 1030–1058.

13 Jiao, F., Li, J., Pan, X. et al. (2016). Selective conversion of syngas to light olefins. *Science* 351: 1065–1068.

14 Visconti, C.G., Martinelli, M., Falbo, L. et al. (2017). CO_2 hydrogenation to lower olefins on a high surface area K-promoted bulk Fe-catalyst. *Appl. Catal., B* 200: 530–542.

15 Gnanamani, M.K., Jacobs, G., Hamdeh, H.H. et al. (2016). Hydrogenation of carbon dioxide over Co-Fe bimetallic catalysts. *ACS Catal.* 6: 913–927.

16 Zhang, J., Lu, S., Su, X. et al. (2015). Selective formation of light olefins from CO_2 hydrogenation over Fe-Zn-K catalysts. *J. CO2 Util.* 12: 95–100.

17 Al-Dossary, M., Ismail, A.A., Fierroa, J.L.G. et al. (2015). Effect of Mn loading onto MnFeO nanocomposites for the CO_2 hydrogenation reaction. *Appl. Catal., B* 165: 651–660.

18 Pérez-Alonso, F.J., Ojeda, M., Herranz, T. et al. (2008). Carbon dioxide hydrogenation over Fe-Ce catalysts. *Catal. Commun.* 9: 1945–1948.

19 Ahmad, H., Kamarudin, S.K., Minggu, L.J., and Kassim, M. (2015). Hydrogen from photo-catalytic water splitting process: a review. *Renewable Sustainable Energy Rev.* 43: 599–610.

20 Elsharnouby, O., Hafez, H., Nakhla, G., and El Naggar, M.H. (2013). A critical literature review on biohydrogen production by pure cultures. *Int. J. Hydrogen Energy* 38: 4945–4966.

21 Osterloh, F.E. (2013). Inorganic nanostructures for photoelectrochemical and photocatalytic water splitting. *Chem. Soc. Rev.* 42: 2294–2320.

22 Tentu, R.D. and Basu, S. (2017). Photocatalytic water splitting for hydrogen production. *Curr. Opin. Electrochem.* 5: 56–62.

23 Fujiwara, M., Kieffer, R., Ando, H., and Souma, Y. (1995). Development of composite catalysts made of Cu-Zn-Cr oxide/zeolite for the hydrogenation of carbon dioxide. *Appl. Catal., A* 121: 113–124.

24 Fujiwara, M., Ando, H., Tanaka, M., and Souma, Y. (1995). Hydrogenation of carbon dioxide over Cu-Zn-chromate/zeolite composite catalyst: the effects of reaction behavior of alkenes on hydrocarbon synthesis. *Appl. Catal., A* 130: 105–111.

25 Li, Z., Wang, J., Qu, Y. et al. (2017). Highly selective conversion of carbon dioxide to lower olefins. *ACS Catal.* 7: 8544–8548.

26 Wei, J., Ge, Q., Yao, R. et al. (2017). Directly converting CO_2 into a gasoline fuel. *Nat. Commun.* 8: 15174–15181.

27 Gao, P., Li, S., Bu, X. et al. (2017). Direct conversion of CO_2 into liquid fuels with high selectivity over a bifunctional catalyst. *Nat. Chem.* 9: 1019–1024.

28 Gao, P., Dang, S., Li, S. et al. (2017). Direct production of lower olefins from CO_2 conversion via bifunctional catalysis. *ACS Catal.* 8: 571–578.

29 Liu, X., Wang, M., Zhou, C. et al. (2018). Selective transformation of carbon dioxide into lower olefins with a bifunctional catalyst composed of $ZnGa_2O_4$ and SAPO-34. *Chem. Commun.* 54: 140–143.

30 Olajire, A.A. (2013). Valorization of greenhouse carbon dioxide emissions into value-added products by catalytic processes. *J. CO2 Util.* 3–4: 74–92.

31 Li, Y., Chan, S.H., and Sun, Q. (2015). Heterogeneous catalytic conversion of CO_2: a comprehensive theoretical review. *Nanoscale* 7: 8663–8683.

32 Klankermayer, J., Wesselbaum, S., Beydoun, K., and Leitner, W. (2016). Selective catalytic synthesis using the combination of carbon dioxide and hydrogen: catalytic chess at the Interface of energy and chemistry. *Angew. Chem. Int. Ed.* 7296–7343.

33 Aresta, M., Dibenedetto, A., and Angelini, A. (2014). Catalysis for the valorization of exhaust carbon: from CO_2 to chemicals, materials, and fuels. Technological use of CO_2. *Chem. Rev.* 114: 1709–1742.

34 Razali, N.A.M., Lee, K.T., Bhatia, S., and Mohamed, A.R. (2012). Heterogeneous catalysts for production of chemicals using carbon dioxide as raw material: a review. *Renewable Sustainable Energy Rev.* 16: 4951–4964.

35 Yu, K.M.K., Curcic, I., Gabriel, J., and Tsang, S.C.E. (2008). Recent advances in CO_2 capture and utilization. *ChemSusChem* 1: 893–899.

36 Yang, H., Zhang, C., Gao, P. et al. (2017). A review of the catalytic hydrogenation of carbon dioxide into value-added hydrocarbons. *Cat. Sci. Technol.* 7: 4580–4598.

37 Li, W., Wang, H., Jiang, X. et al. (2018). A short review of recent advances in CO_2 hydrogenation to hydrocarbons over heterogeneous catalysts. *RSC Adv.* 8: 7651–7669.

38 Prieto, G. (2017). Carbon dioxide hydrogenation into higher hydrocarbons and oxygenates: thermodynamic and kinetic bounds and progress with heterogeneous and homogeneous catalysis. *ChemSusChem* 10: 1056–1070.

39 Li, J., Wang, L., Cao, Y. et al. (2018). Recent advances on the reduction of CO_2 to important C_{2+} oxygenated chemicals and fuels. *Chin. J. Chem. Eng.* https://doi.org/10.1016/j.cjche.2018.07.008.

40 Huang, K., Zhang, J.-Y., Liu, F., and Dai, S. (2018). Synthesis of porous polymeric catalysts for the conversion of carbon dioxide. *ACS Catal.* 8: 9079–9102.

41 Prieto, G., De Mello, M.I.S., Concepción, P. et al. (2015). Cobalt-catalyzed Fischer–Tropsch synthesis: chemical nature of the oxide support as a performance descriptor. *ACS Catal.* 5: 3323–3335.

42 Khodakov, A.Y., Chu, W., and Fongarland, P. (2007). Advances in the development of novel cobalt Fischer–Tropsch catalysts for synthesis of long-chain hydrocarbons and clean fuels. *Chem. Rev.* 107: 1692–1744.

43 Owen, R.E., O'Byrne, J.P., Mattia, D. et al. (2013). Cobalt catalysts for the conversion of CO_2 to light hydrocarbons at atmospheric pressure. *Chem. Commun.* 49: 11683–11685.

44 Jia, X., Zhang, X., Rui, N. et al. (2019). Structural effect of Ni/ZrO_2 catalyst on CO_2 methanation with enhanced activity. *Appl. Catal., B* 224: 159–169.

45 Zhou, R., Rui, N., Fan, Z., and Liu, C.-J. (2016). Effect of the structure of Ni/TiO_2 catalyst on CO_2 methanation. *Int. J. Hydrogen Energy* 41: 22017–22025.

46 Bacariza, M.C., Graca, I., Lopes, J.M., and Carlos, H. (2018). Ni-Ce/zeolites for CO_2 hydrogenation to CH_4: effect of the metal incorporation order. *ChemCatChem* 10: 2773–2781.

47 Vita, A., Italiano, C., Pino, L. et al. (2018). Activity and stability of powder and monolith-coated Ni/GDC catalysts for CO_2 methanation. *Appl. Catal., B* 226: 384–395.

48 Dreyer, J.A.H., Li, P., Zhang, L. et al. (2017). Influence of the oxide support reducibility on the CO_2 methanation over Ru-based catalysts. *Appl. Catal., B* 219: 715–726.

49 Wang, F., He, S., Chen, H. et al. (2016). Active site dependent reaction mechanism over Ru/CeO_2 catalyst toward CO_2 methanation. *J. Am. Chem. Soc.* 138: 6298–6305.

50 Yan, Y., Dai, Y., He, H. et al. (2016). A novel W-doped Ni-Mg mixed oxide catalyst for CO_2 methanation. *Appl. Catal., B* 196: 108–116.

51 Aziz, M.A.A., Jalil, A.A., Triwahyono, S., and Ahmad, A. (2015). CO_2 methanation over heterogeneous catalysts: recent progress and future prospects. *Green Chem.* 17: 2647–2663.

52 Sharm, S., Hu, Z., Zhang, P. et al. (2011). CO_2 methanation on Ru-doped ceria. *J. Catal.* 278: 297–309.

53 Zhang, L., Wang, F., Zhu, J. et al. (2019). CO_2 reforming with methane reaction over $Ni@SiO_2$ catalysts coupled by size effect and metal–support interaction. *Fuel* 256: 115954.

54 Xu, L., Wang, F., Chen, M. et al. (2017). Alkaline-promoted Co-Ni bimetal ordered mesoporous catalysts with enhanced coke-resistant performance toward CO_2 reforming of CH_4. *J. CO2 Util.* 18: 1–14.

55 Pegios, N., Schroer, G., Rahimi, K. et al. (2016). Design of modular Ni-foam based catalysts for dry reforming of methane. *Cat. Sci. Technol.* 6: 6372–6380.

56 Pakhare, D. and Spivey, J. (2014). A review of dry (CO_2) reforming of methane over noble metal catalysts. *Chem. Soc. Rev.* 43: 7813–7837.

57 Gao, J., Jia, C., and Liu, B. (2017). Direct and selective hydrogenation of CO_2 to ethylene and propene by bifunctional catalysts. *Cat. Sci. Technol.* 7: 5602–5607.

58 Guo, L., Sun, J., Ji, X. et al. (2018). Directly converting carbon dioxide to linear α-olefins on bio-promoted catalysts. *Commun. Chem.* 1: 11.

59 Zhai, P., Xu, C., Gao, R. et al. (2016). Highly tunable selectivity for syngas-derived alkenes over zinc and sodium-modulated Fe_5C_2 catalyst. *Angew. Chem. Int. Ed.* 55: 1–7.

60 Li, J., Cheng, X., Zhang, C. et al. (2017). Alkalis in iron-based Fischer–Tropsch synthesis catalysts: distribution, migration and promotion. *J. Chem. Technol. Biotechnol.* 92: 1472–1480.

61 Pedersen, E.Ø., Svenum, I.-H., and Blekkan, E.A. (2018). Mn promoted Co catalysts for Fischer–Tropsch production of light olefins—an experimental and theoretical study. *J. Catal.* 361: 23–32.

62 Lee, S.-C., Jang, J.-H., Lee, B.-Y. et al. (2004). Promotion of hydrocarbon selectivity in CO_2 hydrogenation by Ru component. *J. Mol. Catal. A: Chem.* 210: 131–141.

63 Niemelä, M. and Nokkosmäki, M. (2005). Activation of carbon dioxide on Fe-catalysts. *Catal. Today* 100: 269–274.

64 Yang, Y., Xiang, H.-W., Xu, Y.-Y. et al. (2004). Effect of potassium promoter on precipitated iron-manganese catalyst for Fischer–Tropsch synthesis. *Appl. Catal., A* 266: 181–194.

65 Wang, J., You, Z., Zhang, Q. et al. (2013). Synthesis of lower olefins by hydrogenation of carbon dioxide over supported iron catalysts. *Catal. Today* 215: 186–193.

66 Satthawong, R., Koizumi, N., Song, C., and Prasassarakich, P. (2015). Light olefin synthesis from CO_2 hydrogenation over K-promoted Fe-Co bimetallic catalysts. *Catal. Today* 251: 34–40.

67 Choi, P.H., Jun, K.W., Lee, S.J. et al. (1996). Hydrogenation of carbon dioxide over alumina supported Fe-K catalysts. *Catal. Lett.* 40: 115–118.

68 You, Z., Deng, W., Zhang, Q., and Wang, Y. (2013). Hydrogenation of carbon dioxide to light olefins over non-supported iron catalyst. *Chin. J. Catal.* 34: 956–963.

69 Wei, J., Sun, J., Wen, Z. et al. (2016). New insights into the effect of sodium on Fe_3O_4-based nanocatalysts for CO_2 hydrogenation to light olefins. *Cat. Sci. Technol.* 6: 4786–4793.

70 Ando, H., Xu, Q., Fujiwara, M. et al. (1998). Hydrocarbon synthesis from CO_2 over Fe-Cu catalysts. *Catal. Today* 45: 229–234.

71 Saeidi, S., Amin, N.A.S., and Rahimpour, M.R. (2014). Hydrogenation of CO_2 to value-added products—a review and potential future developments. *J. CO2 Util.* 5: 66–81.

72 Yang, C., Zhao, H., Hou, Y., and Ma, D. (2012). Fe_5C_2 nanoparticles: a facile bromide-induced synthesis and as an active phase for Fischer–Tropsch synthesis. *J. Am. Chem. Soc.* 134: 15814–15821.

73 Visconti, C.G., Martinelli, M., Falbo, L. et al. (2016). CO_2 hydrogenation to hydrocarbons over Co and Fe-based Fischer–Tropsch catalysts. *Catal. Today* 277: 161–170.

74 Fischer, N., Henkel, R., Hettel, B. et al. (2016). Hydrocarbons via CO_2 hydrogenation over iron catalysts: the effect of potassium on structure and performance. *Catal. Lett.* 146: 509–517.

75 Prasad, P.S.S., Bae, J.W., Jun, K.-W., and Lee, K.-W. (2008). Fischer–Tropsch synthesis by carbon dioxide hydrogenation on Fe-based catalysts. *Catal. Surv. Asia* 12: 170–183.

76 Fujiwara, M., Kieffer, R., Ando, H. et al. (1997). Change of catalytic properties of Fe-ZnO/zeolite composite catalyst in the hydrogenation of carbon dioxide. *Appl. Catal., A* 154: 87–101.

77 Li, C., Yuan, X., and Fujimoto, K. (2014). Direct synthesis of LPG from carbon dioxide over hybrid catalysts comprising modified methanol synthesis catalyst and β-type zeolite. *Appl. Catal., A* 475: 155–160.

78 Wei, J., Yao, R., Ge, Q. et al. (2018). Catalytic hydrogenation of CO_2 to isoparaffins over Fe-based multifunctional catalysts. *ACS Catal.* 8: 9958–9967.

79 Zhao, B., Zhai, P., Wang, P. et al. (2017). Direct transformation of syngas to aromatics over Na-Zn-Fe_5C_2 and hierarchical HZSM-5 tandem catalysts. *Chem* 3: 323–333.

80 Zhang, P., Tan, L., Yang, G., and Tsubaki, N. (2017). One-pass selective conversion of syngas to para-xylene. *Chem. Sci.* 8: 7941–7946.

81 Yang, J., Pan, X., Jiao, F. et al. (2017). Direct conversion of syngas to aromatics. *Chem. Commun.* 53: 11146–11149.

82 Cheng, K., Zhou, W., Kang, J. et al. (2017). Bifunctional catalysts for one-step conversion of syngas into aromatics with excellent selectivity and stability. *Chem* 3: 334–347.

83 Jiao, F., Pan, X., Gong, K. et al. (2018). Shape-selective zeolites promote ethylene formation from syngas via a ketene intermediate. *Angew. Chem. Int. Ed.* 130: 1–6.

84 Yang, T., Cheng, L., Li, N., and Liu, D. (2017). Effect of metal active sites on the product distribution over composite catalysts in the direct synthesis of aromatics from syngas. *Ind. Eng. Chem. Res.* 56: 11763–11772.

85 Francis, J., Guillon, E., Bats, N. et al. (2011). Design of improved hydrocracking catalysts by increasing the proximity between acid and metallic sites. *Appl. Catal., A* 409–410: 140–147.

86 Batalha, N., Pinard, L., Bouchy, C. et al. (2013). *n*-Hexadecane hydroisomerization over Pt-HBEA catalysts. Quantification and effect of the intimacy between metal and protonic sites. *J. Catal.* 307: 122–131.

87 Kim, J., Kim, W., Seo, Y. et al. (2013). *n*-Heptane hydroisomerization over Pt/MFI zeolite nanosheets: effects of zeolite crystal thickness and platinum location. *J. Catal.* 301: 187–197.

88 Mendes, P.S.F., Gregório, A.F.C., Daudin, A. et al. (2017). Elucidation of the zeolite role on the hydrogenating activity of Pt-catalysts. *Catal. Commun.* 89: 152–155.

89 Mendes, P.S.F., Lapisardi, G., Bouchy, C. et al. (2015). Hydrogenating activity of Pt/zeolite catalysts focusing acid support and metal dispersion influence. *Appl. Catal., A* 504: 17–28.

90 Knaeble, W. and Iglesia, E. (2016). Acid strength and metal-acid proximity effects on methylcyclohexane ring contraction turnover rates and selectivities. *J. Catal.* 344: 817–830.

91 Zecevic, J., Vanbutsele, G., de Jong, K.P., and Martens, J.A. (2015). Nanoscale intimacy in bifunctional catalysts for selective conversion of hydrocarbons. *Nature* 528: 245–248.

92 Samad, J.E., Blanchard, J., Sayag, C. et al. (2016). The controlled synthesis of metal-acid bifunctional catalysts: the effect of metal: acid ratio and metal-acid proximity in Pt silica-alumina catalysts for *n*-heptane isomerization. *J. Catal.* 342: 203–212.

93 Ni, X., Tan, Y., Han, Y., and Tsubaki, N. (2007). Synthesis of isoalkanes over Fe–Zn–Zr/HY composite catalyst through carbon dioxide hydrogenation. *Catal. Commun.* 8: 1711–1714.

94 Tan, Y., Fujiwara, M., Ando, H. et al. (1999). Syntheses of isobutane and branched higher hydrocarbons from carbon dioxide and hydrogen over composite catalysts. *Ind. Eng. Chem. Res.* 38: 3225–3229.

95 Wang, X., Yang, G., Zhang, J. et al. (2016). Synthesis of isoalkanes over a core (Fe–Zn–Zr)–shell (zeolite) catalyst by CO_2 hydrogenation. *Chem. Commun.* 52: 7352–7355.

96 Yang, G., Xing, C., Hirohama, W. et al. (2013). Tandem catalytic synthesis of light isoparaffin from syngas via Fischer–Tropsch synthesis by newly developed core–shell-like zeolite capsule catalysts. *Catal. Today* 215: 29–35.

97 Choi, Y.H., Jang, Y.J., Park, H. et al. (2017). Carbon dioxide Fischer–Tropsch synthesis: a new path to carbon-neutral fuels. *Appl. Catal., B* 202: 605–610.

98 Jiang, F., Liu, B., Geng, S. et al. (2018). Hydrogenation of CO_2 into hydrocarbons: enhanced catalytic activity over Fe-based Fischer–Tropsch catalysts. *Cat. Sci. Technol.* https://doi.org/10.1039/C8CY00850G.

99 Choi, Y.H., Ra, E.C., Kim, E.H. et al. (2017). Sodium-containing spinel zinc ferrite as a catalyst precursor for the selective synthesis of liquid hydrocarbon fuels. *ChemSusChem* 10: 4764–4770.

100 He, Z., Cui, M., Qian, Q. et al. (2019). Synthesis of liquid fuel via direct hydrogenation of CO_2. *Proc. Natl. Acad. Sci. U.S.A.* 116: 12654–12659.

101 Guo, L., Cui, Y., Zhang, P. et al. (2018). Enhanced liquid fuel production from CO_2 hydrogenation: catalytic performance of bimetallic catalysts over a two-stage reactor system. *ChemistrySelect* 3: 13705–13711.

102 Ni, Y.M., Chen, Z.Y., Fu, Y. et al. (2018). Selective conversion of CO_2 and H_2 into aromatics. *Nat. Commun.* 9: 3457.

103 Zhou, C., Shi, J., Zhou, W. et al. (2020). Highly active ZnO-ZrO_2 aerogels integrated with H-ZSM-5 for aromatics synthesis from carbon dioxide. *ACS Catal.* 10: 302–310.

104 Wang, Y., Tan, L., Tan, M.H. et al. (2019). Rationally designing bifunctional catalysts as an efficient strategy to boost CO_2 hydrogenation producing value-added aromatics. *ACS Catal.* 9: 895–901.

105 Li, Z., Qu, Y., Wang, J. et al. (2019). Highly selective conversion of carbon dioxide to aromatics over tandem catalysts. *Joule* 3: 570–583.

106 Zhang, J., Zhang, M., Chen, S. et al. (2019). Hydrogenation of CO_2 into aromatics over a $ZnCrO_x$–zeolite composite catalyst. *Chem. Commun.* 55: 973–976.

107 Wang, S., Wu, T., Lin, J. et al. (2019). FeK on 3D graphene–zeolite tandem catalyst with high efficiency and versatility in direct CO_2 conversion to aromatics. *ACS Sustainable Chem. Eng.* 7: 17825–17833.

108 Xu, Y.B., Shi, C.M., Liu, B. et al. (2019). Selective production of aromatics from CO_2. *Cat. Sci. Technol.* 9: 593–610.

109 Ramirez, A., Chowdhury, A.D., Dokania, A. et al. (2019). Effect of zeolite topology and reactor configuration on the direct conversion of CO_2 to light olefins and aromatics. *ACS Catal.* 9: 6320–6334.

110 Xiong, S., Lian, Y., Xie, H., and Liu, B. (2019). Hydrogenation of CO_2 to methanol over Cu/ZnCr catalyst. *Fuel* 256: 115975.

111 Graciani, J., Mudiyanselage, K., Xu, F. et al. (2014). Highly active copper-ceria and copper-ceria-titania catalysts for methanol synthesis from CO_2. *Nature* 345: 6196.

112 An, B., Zhang, J., Cheng, K. et al. (2017). Confinement of ultrasmall Cu/ZnO_x nanoparticles in metal–organic frameworks for selective methanol synthesis from catalytic hydrogenation of CO_2. *J. Am. Chem. Soc.* 139: 3834–3840.

113 Li, H., Qiu, C., Ren, S. et al. (2020). Na+-gated water-conducting nanochannels for boosting CO_2 conversion to liquid fuels. *Science* 367: 667–671.

114 Kattel, S., Ramírez, P.J., Chen, J.G. et al. (2017). Active sites for CO_2 hydrogenation to methanol on Cu/ZnO catalysts. *Science* 355: 1296–1299.

115 Ye, J., Liu, C., Mei, D., and Ge, Q. (2013). Active oxygen vacancy site for methanol synthesis from CO_2 hydrogenation on In_2O_3(110): a DFT study. *ACS Catal.* 3: 1296–1306.

116 Li, C.-S., Melaet, G., Ralston, W.T. et al. (2015). High-performance hybrid oxide catalyst of manganese and cobalt for low-pressure methanol synthesis. *Nat. Commun.* 6: 6538.

117 Martin, O., Mart, A.J., Mondelli, C. et al. (2016). Indium oxide as a superior catalyst for methanol synthesis by CO_2 hydrogenation. *Angew. Chem. Int. Ed.* 55: 6261–6265.

118 Xu, D., Ding, M., Hong, X. et al. (2020). Selective C_{2+} alcohol synthesis from direct CO_2 hydrogenation over a Cs-promoted Cu-Fe-Zn catalyst. *ACS Catal.* 10: 5250–5260.

119 Bai, S., Shao, Q., Wang, P. et al. (2017). Highly active and selective hydrogenation of CO_2 to ethanol by ordered Pd–Cu nanoparticles. *J. Am. Chem. Soc.* 139: 6827–6830.

120 Wang, L.X., Wang, L., Zhang, J. et al. (2018). Selective hydrogenation of CO_2 to ethanol over cobalt catalysts. *Angew. Chem. Int. Ed.* 130: 1–6.

121 He, Z., Qian, Q., Ma, J. et al. (2016). Water-enhanced synthesis of higher alcohols from CO_2 hydrogenation over a Pt/Co_3O_4 catalyst under milder conditions. *Angew. Chem. Int. Ed.* 55: 737–741.

122 Shao, X.Z., Yang, X.F., Xu, J.M. et al. (2019). Iridium single-atom catalyst performing a quasi-homogeneous hydrogenation transformation of CO_2 to formate. *Chem* 5: 1–13.

123 Kar, S., Goeppert, A., and Prakash, G.K.S. (2019). Integrated CO_2 capture and conversion to formate and methanol: connecting two threads. *Acc. Chem. Res.* 52: 2892–2903.

124 Huff, C.A. and Sanford, M.S. (2013). Catalytic CO_2 hydrogenation to formate by a ruthenium pincer complex. *ACS Catal.* 3: 2412–2416.

125 Dubey, A., Nencini, L., Fayzullin, R.R. et al. (2017). Bio-inspired Mn(I) complexes for the hydrogenation of CO_2 to formate and formamide. *ACS Catal.* 7: 3864–3868.

126 Su, X., Yang, X.-F., Huang, Y. et al. (2019). Single-atom catalysis toward efficient CO_2 conversion to CO and formate products. *Acc. Chem. Res.* 52: 656–664.

127 Gunasekar, G.H., Park, K., Ganesan, V. et al. (2017). A covalent triazine framework, functionalized with Ir/N-heterocyclic carbene sites, for the efficient hydrogenation of CO_2 to formate. *Chem. Mater.* 29: 6740–6748.

128 Rohmann, K., Kothe, J., Haenel, M.W. et al. (2016). Hydrogenation of CO_2 chemie to formic acid with a highly active ruthenium Acriphos complex in DMSO and DMSO/water. *Angew. Chem. Int. Ed.* 55: 8966–8969.

129 Kumaravel, V., Bartlett, J., and Pillai, S.C. (2020). Photoelectrochemical conversion of carbon dioxide (CO_2) into fuels and value-added products. *ACS Energy Lett.* 5: 486–519.

130 Xia, Y. and Yu, J. (2020). Reaction: rational design of highly active photocatalysts for CO_2 conversion. *Chem* 6: 1–2.

131 García De Arquer, F.P., Dinh, C.-T., Ozden, A. et al. (2020). CO_2 electrolysis to multicarbon products at activities greater than 1 A cm^{-2}. *Science* 367: 661–666.

132 Wang, H., Tzeng, Y.-K., Ji, Y. et al. (2019). Synergistic enhancement of electrocatalytic CO_2 reduction to C_2 oxygenates at nitrogen-doped nanodiamonds/Cu interface. *Nat. Nanotechnol.* 15: 131–137.

133 Nielsen, D.U., Hu, X.-M., Daasbjerg, K., and Skrydstrup, T. (2018). Chemically and electrochemically catalysed conversion of CO_2 to CO with follow-up utilization to value-added chemicals. *Nat. Catal.* 1: 244–254.

Part VI

Biomass Conversion

13

Lipids to Fuels and Chemicals

Bolong Li, Arif Ali, Shutao Lei, and Chen Zhao

East China Normal University, Shanghai Key Laboratory of Green Chemistry and Chemical Processes, School of Chemistry and Molecular Engineering, 3663 N. Zhongshan Rd, Shanghai 200062, P. R. China

13.1 Introduction

Alternative energy sources are being developed due to increasing energy demand and fossil fuel depletion, particularly in relation to the direct transformation of biomass to green hydrocarbon fuels. Lipids and fatty acids are considered as promising renewable biocarriers that can be further deoxygenated to diesel-range alkanes. The deoxygenation of lipids can be catalyzed by a variety of catalysts producing diesel-range alkanes, linear and cyclic paraffins and olefins, and oxygenated compounds including aldehydes, ketones, and carboxylic acids. The lipid deoxygenating catalysts can be classified into two types, namely, supported metal sulfide catalysts and supported sulfur-free metal catalysts. Lipids serve as precursors for the production of jet fuels through the cracking process and for alkenes via fatty alcohol dehydration. In addition, lipids can produce olefins in the presence of homogeneous and heterogeneous catalysts. Likewise, the selective hydrogenation of lipids yields commodity chemical fatty alcohols.

Over the years, great effort has been directed toward the efficient production of high-value-added chemicals and fuels from lipids. In this context, diesel-range hydrocarbons were synthesized efficiently via the hydrodeoxygenation process in the presence of supported metal sulfide catalysts or sulfur-free metal catalysts. Lipid hydrodeoxygenation is an efficient process yielding diesel-range hydrocarbons through the hydrogenolysis followed by hydrogenation, decarboxylation, decarbonylation, and hydrogenation–dehydration processes. Catalytic deoxygenation processes provide an alternative approach for upgrading fatty acids and triglycerides [1–7]. The important pathways for the conversion of lipids such as fatty acids to linear alkanes entail decarboxylation, decarbonylation, and hydrodeoxygenation while methanation and water–gas shift reaction are the main reactions in the vapor phase. The hydrodeoxygenation comprises several consecutive reaction steps, in which oxygen is lost as H_2O and in which the resultant *n*-alkane shows the same carbon number as the

Heterogeneous Catalysis for Sustainable Energy, First Edition. Edited by Landong Li and Justin S. J. Hargreaves.

corresponding fatty acid [8–28]. In addition, the ketonization, carboxylation, and decarnonylation pathways lead to the formation of ketones, paraffins, and aldehydes during fatty acid conversion in a nitrogen atmosphere. Importantly, the other processes such as decarbonylation, hydrogenation–decarbonylation, and hydrogenation–dehydration–hydrogenation are observed as main reaction pathways under hydrogen atmospheres during fatty acid conversion, yielding paraffins as the final products.

The thermocatalytic cracking conversion of lipids has been performed in batch reactors yielding jet fuels over $AlCl_3$ and Al_2O_3 (acidic catalysts) and MgO, CaO, and NaOH (basic catalysts) at relatively high reaction temperatures in the order of 400–500 °C. Catalytic cracking and deoxygenation over various zeolite catalysts are the most widely employed alternatives to upgrade the triglycerides producing jet fuels. Catalysts derived from silica–alumina and zeolites such as HZSM-5 and HY are found to be effective for the production of fuel via the catalytic cracking of lipids. Importantly, hydrogen was not required in contrast with hydrodeoxygenation undertaken with hydrotreating catalysts, which is a significant advantage. Triglyceride cracking over acidic zeolites entails the conversion of fatty acids to green gasoline initiated by the protonation of the unsaturated bond of the fatty acid. The decarboxylation and decarbonylation of lipids produce gaseous products such as CO_2 and CO during cracking, and other resulting reaction intermediates such as linear alkanes and alkenes are further cracked into smaller hydrocarbons.

The sustainable and selective catalytic conversion of renewable feedstocks such as plant oil via deoxygenation results in the formation of linear α-olefins (LAOs). In this regard, ethenolysis or alkenolysis processes directly lead to the formation of value-added α-olefins. Various homogeneous or heterogeneous catalysts have been used in the deoxygenation of fatty acids and their derivatives through dehydration, decarbonylation, and decarboxylation. The decarboxylation of fatty acids produces paraffins and alkenes while dehydration combined with decarbonylation and decarboxylation leads to the formation of ketones and alkenes, respectively.

The alkane products such as paraffins are highly effective chemical compounds for biodiesel, jet fuel, and renewable diesel. A number of homogeneous catalysts based upon Pd produce olefins at 200 °C along with CO and HCl. Such reaction occurs by the oxidative addition of the acyl chloride to Pd^0, forming an acyl Pd^{II} species. Carbon monoxide liberation results in an alkyl Pd^{II} species that undergoes β-hydride elimination to yield the olefin product regenerating the active Pd^0 catalyst after HCl reductive elimination. The decarbonylation of fatty acids with $PdCl_2$ and phosphine at 280 °C can produce olefins. Heterogeneous catalysts have been introduced to obtain olefin products from lipids due to their easy separation from the reaction products and higher thermal stability in general.

13.2 Lipids to Diesel-Range Hydrocarbons

Lipids show great potential to produce the diesel-range hydrocarbons via the hydrodeoxygenation process in the presence of supported metal sulfide catalysts

or sulfur-free metal catalysts. Lipid hydrodeoxygenation leads to the formation of diesel-range hydrocarbons through hydrogenolysis followed by hydrogenation, decarboxylation, decarbonylation, and hydrogenation–dehydration processes.

13.2.1 Deoxygenation of Lipids over Supported Metal Sulfide Catalysts

The hydroprocessing of pure sunflower oil over sulfided $NiMo/Al_2O_3$ at 350 °C using 5 MPa H_2 for nine hours led to complete conversion with a 71% yield of straight-chain C_{15}–C_{18} alkanes (see Table 13.1) [8]. The hydrotreating of these triglycerides entails (i) hydrogenation of double bonds in olefins, (ii) the

Table 13.1 Alkane product distribution by hydrotreatment from pure sunflower oil over sulfided metal catalysts.

Catalyst	*T* (°C)	H_2 (MPa)	Time (h)	Conv. (%)	Yield (%)						
					n-C_{18}	*n*-C_{17}	*n*-C_{16}	*n*-C_{15}	C_3	CO_x	CO
Sulfided $NiMo/Al_2O_3$	300	5	6	58	34	15	3.4	2	3.6	–	–
Sulfided $NiMo/Al_2O_3$	350	5	6	71	40	25	1.0	1.2	3.8	–	–
Sulfided $NiMo/Al_2O_3$	400	5	6	62	28	20	4	3	3.9	1.6	1.5
Sulfided $NiMo/Al_2O_3$	450	5	6	47	16	15	5	4.5	4	1	1.5
$NiMoS/Al_2O_3$	270	7	6	100	90	10	–	–	–	–	–
Sulfided NiW/SiO_2-Al_2O_3	300	1	6	65	35	15	6	3	3	2	1
Sulfided NiW/SiO_2-Al_2O_3	325	1	6	62	24	15	5	2	12	3	1
Sulfided NiW/SiO_2-Al_2O_3	350	1	6	60	9.5	6.5	4	3	28	5	4

Source: Based on Huber et al. [8].

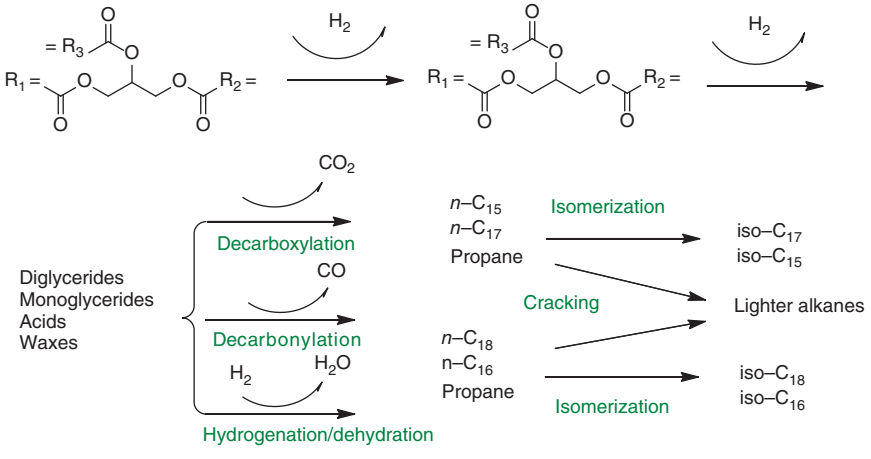

Figure 13.1 Reaction pathways and main reaction steps for lipid conversion to alkanes with sulfided catalysts.

hydrogenolysis of saturated triglycerides to fatty acids, and (iii) the hydrodeoxygenation, decarbonylation, or decarboxylation of fatty acids to alkenes (Figure 13.1). Firstly, the tryiglycerides of fatty acids, and further the oxygen removal from fatty acids, can be accomplished either through decarboxylation/decarbonylation yielding CO_2/CO or through hydrodeoxygenation yielding CO_2/CO or hydrodeoxygenation producing water. Nevertheless, these sulfided catalysts can contaminate the products via sulfur leaching and thus be deactivated due to desulfurization by a reverse Mars van Krevelen reaction [9].

The hydrotreating of oils such as jatropha oil, palm oil, and canola oil was performed over Ni/Mo-based catalysts in a high-pressure fixed-bed flow reactor at 350 °C under 4 MPa H_2 [10]. Ni–Mo/SiO_2 catalyst produced paraffins such as *n*-$C_{18}H_{38}$, *n*-$C_{17}H_{36}$, *n*-$C_{16}H_{34}$, and *n*-$C_{15}H_{32}$ as the main products in the hydrotreatment of jatropha oil. These paraffins have quite high melting points and pour points. In addition, Ni–Mo/HY and Ni–Mo/HZSM-5 produced a large amount of gasoline-range hydrocarbons due to the presence of the strong acid sites associated with zeolites. SiO_2–Al_2O_3-supported Ni–Mo catalyst yielded liquid hydrocarbon products with suitable pour points (−10 °C) similar to commercially available diesel.

The hydroprocessing of rapeseed oil was explored for the production of biocomponents in the diesel fuel range [11–14]. Rapeseed oil was hydroprocessed at temperatures of 260–340 °C under 7 MPa H_2 in a continuous flow reactor. Three Ni–Mo/Al_2O_3 sulfide hydrotreating catalysts were evaluated thoroughly. Reaction products comprised hydrogen-rich gas, water, and organic liquid products. The main components in the organic liquid product consisted of the long-chain C_{17} and C_{18} *n*-alkanes. The free fatty acids and unconverted triglycerides were also found in organic liquid products at low reaction temperature.

The hydrogenation of vegetable oils using Ni–Mo/γ-Al_2O_3 catalyst was thoroughly studied [14]. The soy oil decomposed, whereas vegetable oils such as maracuja, buritimtucha, and babassu oils were hydrogenolyzed. The main product found was *n*-alkanes (66–76 wt%) after two hours treatment at 360 °C under 14 MPa hydrogen in a batch reactor. The yields of gaseous products and H_2O were recorded as 9–13 and 5 wt%, respectively. In addition to the main product *n*-alkanes, the fraction of iso-paraffins increased from 5% to 38%, and the lighter C_8–C_{14} alkanes increased to 22% from 330 to 398 °C. After hydrotreating, it was observed that the white diesel had a cetane number of 77 with a low water content of 13 ppm and high oxidation stability for 22 h. However, a major disadvantage of this liquid fuel is its poor flow properties in cold winter. Blending with fossil diesel can control the shortcomings of low density and poor cold flow properties.

The hydrotreatment of triglycerides over conventional NiMo and CoMo sulfide catalysts can be performed in petroleum refineries to produce straight-chain alkanes ranging from C_{12} to C_{18} at 350–450 °C in the presence of 4–15 MPa H_2 [16, 27]. Hydrotreating is more selective toward diesel-range hydrocarbons than catalytic cracking. Hydroprocessing results in high conversion of triglyceride oils and high yields of hydrocarbon middle distillate, which are beneficial as an alternative diesel fuel. Owing to high cetane number in the range of 55–90, such fuel is described as super cetane diesel [28].

13.2.2 Deoxygenation of Lipids over Sulfur-Free Metal Catalysts

Catalytic deoxygenation processes provide an alternative approach for upgrading fatty acids and triglycerides [29–42]. The possible reaction routes for the conversion of fatty acids to linear alkanes consist of decarboxylation, decarbonylation, and hydrodeoxygenation, whereas methanation and water–gas shift reactions are the important reactions occurring in the vapor phase. The hydrodeoxygenation comprises several consecutive reaction steps, in which oxygen is removed in the form of H_2O, and the resulting *n*-alkane shows the same carbon number as the corresponding fatty acid [30, 31]. Hydrocarbonylation is a process in which the oxygen is removed as CO, and the resultant *n*-alkane contains one carbon atom less compared with the original fatty acid. Decarboxylation does not require hydrogen consumption. Catalytic deoxygenation has several advantages, including the lower-temperature requirement (250–300 °C), higher selectivity to the target linear hydrocarbons, and little or no H_2 requirement than that of hydrotreating [31, 32].

Supported noble metal catalysts such as Pd/C are frequently used for decarboxylation and decarbonylation of fatty acids [29, 33–44]. For instance, 5 wt% Pd/C produced 100% C_{17} hydrocarbons from C_{18} stearic acid (SA) at 300 °C [35]. The noble metal catalysts showed high activities and selectivities toward the target product alkanes in fatty acid conversion. However, they showed much lower activities and selectivities for triglyceride conversion [30, 45–47]. The high price of noble metals limits their commercial application. Base metal catalysts such as Ni supported on zeolites were then used for the hydrodeoxygenation of fatty acids [48]. In this regard, Ni/HZSM-5 (10 wt%, Si/Al = 45) catalyzed the complete conversion of SA in dodecane at 260 °C for six hours under 4.0 MPa H_2 (Table 13.2) while significant cracking of the produced alkanes (43% yield) was observed. Ni/HZSM-5 catalysts with higher Si/Al ratios of 120 and 200 exhibited lower activities. Ni/HBEA (Si/Al = 75) of 5 wt% showed quantitative conversion of SA with high selectivity to

Table 13.2 Stearic acid conversion to hydrocarbons using Ni/zeolite catalysts, from Refs. [47, 48].

Catalyst	*T* (°C)	H_2 (MPa)	Time (h)	Conv. (%)	Yield (%)				
					n-C_{18}	Iso-C_{18}	*n*-C_{17}	Iso-C_{17}	Cracking
10 wt% Ni/HZSM-5 45	260	4	6	100	41	6.3	9.2	0.4	43
10 wt% Ni/HZSM-5120	260	4	6	65	44	5	6	–	10
10 wt% Ni/HZSM-5200	260	4	6	60	48	4	3	–	5
5 wt% Ni/HBEA 75	260	4	6	96	64	14	13	4	1
10 wt% Ni/HBEA 75	260	4	6	100	73	10	15	1.6	0.6
5 wt% Ni/HBEA 180	260	4	6	96	80	6	8.8	0.2	1
10 wt% Ni/HBEA 180	260	4	6	98	83	5.4	9.3	–	0.3
10 wt% Ni/TPA-HBEA	260	4	1	60	44	5	5	6	–
10 wt% Ni/TPA-HBEA	260	4	2	70	55	4	6	5	–
10 wt% Ni/TPA-HBEA	260	4	3	78	60	3	10	7	–

C_{18} alkane (82%) and some minor production of C_{17} alkane (18%), and almost no cracking of the hydrocarbon chain was observed. The higher rate of cracking using Ni/HZSM-5 was due to the higher effective residence time caused by the higher Brønsted acid site concentration and the narrower pores of HZSM-5 than HBEA. Subsequently, the synthesis of Ni/HBEA was updated to deposition precipitation and nanoparticle grafting methods from the conventional impregnation methods, and the resultant small-sized Ni nanoparticles ($d = 3$ nm) showed fivefold higher hydrodeoxygenation activities in SA and microalgae oil conversion [49].

The individual hydrodeoxygenation kinetics of SA reactant and 1-octadecanol intermediate over Ni/HBEA under identical conditions were investigating thoroughly [50, 51]. The reaction routes for deoxygenation of SA were suggested to proceed from the hydrogenation of the carboxylate group through the corresponding aldehyde, e.g. octadecanal (rate-determining step), followed by either decarbonylation of octadecanal to *n*-heptadecane and carbon monoxide (minor route) or hydrogenation to 1-octadecanol (major route). Thus, the produced 1-octadecaol showed the sequential acid-catalyzed dehydration or metal-catalyzed hydrogenation yielding the final *n*-octadecane product. In the gaseous phase, CO reacted with hydrogen to produce methane and water. On the other hand, the multifunctional Ni catalyst potentially catalyzed the hydrogenolysis of the fatty acid ester, the decarbonylation of aldehyde intermediates, and the hydrogenation of –COOH, –CHO, and C=C double bonds in the oxygenated reactants and intermediates. It should be noted that the acid sites catalyzed the dehydration of alcohol intermediates and the hydrocracking and hydro-isomerization of alkane products.

The catalytic conversion of SA on catalysts consisting of 3–15 wt% Ni and various supports was investigated at 260 °C under 4 MPa H_2 in batch mode [52]. It was observed that all Ni/ZrO_2 catalysts produced a high yield of *n*-heptadecane, whereas the pure ZrO_2 support gave a low conversion of 13%. The 10% Ni/TiO_2 and 10% Ni/CeO_2 catalysts showed quantitative conversion under identical conditions, with slightly lower selectivities to C_{17} *n*-heptadecane of 87% and 93%, respectively. Ni/Al_2O_3 and Ni/SiO_2 were found to be less reactive and selective, showing 45–63% conversion with 80–90% hydrocarbon selectivity.

The hydrodeoxygenation of SA over Pd/C catalyst showed 5% selectivity to *n*-heptadecane at a higher temperature of 300 °C with 95% selectivity in a semi-batch mode under 0.51 MPa of 5% H_2 in Ar [30, 45–47]. The results revealed that deoxygenation activity decreased in the following sequence: Pd > Pt > Ni > Rh > Ir > Ru > Os [35]. The carbon-supported Pd, Pt, and Rh catalysts showed 90% selectivity after six hours, and deoxygenation products (*n*-heptadecane, 1-heptadecene, and other C_{17} products) at nearly full conversion were obtained. In contrast, Ni/SiO_2 and Ni/Cr_2O_3 catalysts showed selectivities > 60% toward deoxygenation products such as *n*-heptadecane. 5 wt% Pd/C exhibits a higher initial reaction rate than Pd/Al_2O_3 and Pt/Al_2O_3, Ni/Al_2O_3, and NiMo/Al_2O_3 catalysts. However, the selectivities to ketone were relatively high with Al_2O_3-supported catalysts. Thus, it could be concluded that the ketonization of fatty acids occurred preferably on the surfaces of Al_2O_3 supports.

The higher initial rates over carbon-supported catalysts can be attributed to the catalyst structure, i.e. higher specific surface areas than silica and alumina supports. The influence of catalyst deactivation due to sintering and/or coking could be therefore minimized [35]. Ru/SiO_2 and RANEY Ni showed low activities in fatty acid deoxygenation, giving 7.2% and 14% conversion, respectively. The low acidity supports (C, SiO_2, and Al_2O_3) showed negligible cracking with Pt, Pd, Rh, and Ir (selectivity < 5%) while the cracking was pronounced when Ni was used (selectivity > 15%) due to the strong C–C hydrogenolysis ability of Ni sites. Notably, cracking was almost absent in the deoxygenation of methyl stearate over Pt/Al_2O_3. Compared to Pd/C, Pd supported on SBA-15 was active and selective for SA deoxygenation, with a much higher turnover frequency (TOF) on Pd/SBA-15 than on Pd/C (0.72 vs 0.13 s^{-1}) [53, 54]. These results also revealed that Pd and Pt catalysts are efficient for either decarbonylation or decarboxylation of fatty acids or fatty acid esters. The low activity of highly dispersed Pd was suggested to be caused by the strong interaction of Pd with the supports. Likewise, the acidity/basicity of Pd/C catalysts (measured from the pH of the catalyst slurry) influenced the deoxygenation of ethyl stearate.

Noticeably, the supports used for hydrodeoxygenation of fatty acids can be categorized into four classes: (i) carbon; (ii) solid Brønsted acids including HBEA and HZSM-5 zeolites; (iii) refractory oxides such as SiO_2, Al_2O_3, and MgO; and (iv) reducible oxides such as ZrO_2, TiO_2, and CeO_2 (Table 13.3). The neutral C support showed no catalytic function and led to the direct decarbonylation/decarboxylation of carboxylic acid functional groups on metal sites. Ni/HBEA and Ni/HZSM-5 produced C_{18} octadecane as the main product, because the elementary step of alcohol dehydration was very fast. Interestingly, when Al_2O_3 and SiO_2 were used as supports, C_{17} heptadecane was found as major product via the hydrogenation–decarbonylation route. Moreover, the side reaction of ketonization was promoted on these oxide supports. The bifunctional ZrO_2-, TiO_2-, and CeO_2-supported Ni catalysts showed almost quantitative conversion to *n*-heptadecane [51, 55] (Table 13.3).

In the presence of hydrogen, the deoxygenation rate of palmitic acid followed the sequence of (r = rate): r (Ni/HBEA or Ni/HZSM-5) > r (Ni/ZrO_2 or Ni/TiO_2 or Ni/CeO_2) > r (Ni/Al_2O_3 or Ni/SiO_2) [53] (Table 13.4). It was found that the TOF on Ni/ZrO_2, Ni/TiO_2, and Ni/CeO_2 catalysts (12 h^{-1}) were over two times higher than that on Ni/Al_2O_3 and Ni/SiO_2 catalysts (5.0 h^{-1}) [51, 56].

These results suggested that Ni provides reasonable active sites for SA hydrogenation to octadecanal (route 1 in Figure 13.2). The higher activity with reducible supports revealed that the support played a key role in the reductive conversion of SA to octadecanal. The hydrogenation of carboxylic acids to aldehydes can be catalyzed by reducible oxides ZrO_2, TiO_2, and CeO_2, proceeding with concerted adsorption of acid at oxygen vacancies to form carboxylates and H_2 activation via dissociative adsorption on the oxygen vacancy sites of oxide surfaces like ZrO_2. Subsequently, α-H atoms of the carboxylate can be cleaved to yield the ketene intermediate, which was hydrogenated to octadecanal on Ni nanoparticles. The two residual protons involve the one generated in the adsorption of the SA and the other from the abstraction of the α-H atom of the alkyl chain, which recombined with the oxygen bound at

Table 13.3 Stearic acid conversion to hydrocarbons using oxide-supported catalysts.

Catalyst	*T* (°C)	H_2 (MPa)	Time (h)	Conv. (%)	Yield (%)						References
					C_{17}	C_{18}	Cracking	C_{18}-OH	C_{35}-stearone	Stearyl stearate	
ZrO_2	260	4	8	13	0.4	–	–	4	7	1.6	[50]
3% Ni/ZrO_2	260	4	8	96	49	4	3	32	–	8	[50]
5% Ni/ZrO_2	260	4	8	100	90	2	1	6.7	–	–	[50]
10% Ni/ZrO_2	260	4	8	100	96	1.5	1.2	1.2	–	–	[50]
15% Ni/ZrO_2	260	4	8	100	96	1.5	1.3	1.4	–	–	[50]
10% Ni/TiO_2	260	4	8	98	85	5	0.8	6.5	–	0.7	[50]
10% Ni/CeO_2	260	4	8	100	93	0.4	2.8	3.5	–	–	[50]
10% Ni/Al_2O_3	260	4	8	63	51	0.4	0.6	9	–	2	[50]
10% Ni/SiO_2	260	4	8	45	26	0.6	0.6	15.3	–	2.5	[50]
10% Ni/ZnO	260	4	8	42	13	0.3	0.3	14.4	–	14	[50]
RANEY Ni	300	4	6	14	7	0.07	2.6	–	–	4.5	[50]
16% Ni/Al_2O_3	300	1.2	6	18	8	0.05	2	–	3	5	[52]
60% Ni/SiO_2	300	1.2	6	18	10	0.2	4	–	–	3.8	[52]
60% Ni/Cr_2O_3	300	1.2	6	12	7	–	2	–	–	3	[52]
3%, 9% NiMo/Al_2O_3	300	1.2	6	8.6	2	–	0.3	–	–	6.3	[52]
5% Ru/SiO_2	300	1.2	6	7.2	1.6	–	0.5	–	4.3	0.8	[52]
5% Ru/MgO	300	1.2	6	96	–	–	–	–	95	1	[52]
5% Ru/C	300	1.2	6	13	8.5	0.06	1.4	–	1	2	[52]
5% Pd/Al_2O_3	300	1.2	6	24	10	–	0.3	–	11.7	2	[52]
5% Pd/SiO_2	300	–	6	37	100	–	–	–	–	–	[53]
5% Pd/SiO_2	300	–	6	85	100	–	–	–	–	–	[53]
5% Pd/SiO_2	300	–	6	89	100	–	–	–	–	–	[53]
Pd/SBA-15	300	1.7	6	100	100	–	–	–	–	–	[54]
1% Pd/C	300	0.6	6	33	31	0.5	0.5	–	–	1	[55]
10% Pd/C	300	0.6	6	48	45	0.2	0.48	–	2.5	–	[55]
5% Pd/C	300	0.6	6	100	99	–	1	–	–	–	[55]
5% Pd/C	300	0.6	6	100	100	–	–	–	–	–	[55]
8%, 2% PdPt/C	300	0.6	6	62	59	0.3	1.7	–	–	1	[55]
5% Pt/Al_2O_3	300	0.6	6	20	9.2	0.1	0.4	–	7.5	2.8	[55]
5% Pt/C	300	0.6	6	86	82	0.5	3	–	–	0.5	[55]
2% Ir/Al_2O_3	300	0.6	6	17	0.3	–	–	–	14	2.7	[55]
2% Ir/SiO_2	300	0.6	6	5	3.4	–	0.1	–	–	1.5	[55]
5% Os/C	300	0.6	6	7	3.7	–	0.1	–	–	3.2	[55]
3% Rh/SiO_2	300	0.6	6	16	3.5	–	0.5	–	9	3	[55]
1% Rh/C	300	0.6	6	18	15.2	0.08	0.71	0.71	1.3	–	[55]

Table 13.4 Catalytic conversion of vegetable, jatropha, and microalgae oils to hydrocarbons in hydrogen, from Refs. [48, 50, 53].

Feedstock	Catalyst	*T* (°C)	H_2 (MPa)	Time (h)	Conv. (%)	Yield (%)					
						C_1	C_2-C_4	C_5-C_9	C_{10}-C_{20}	C_{21}^+	CO_x
Vegetable oil	1% Pt/SiO_2	300	2	12	2.4	0.3	1.4	0.5	0.04	0.12	0.05
	1% Pt/SiO_2-Al_2O_3	300	2	12	5.6	0.5	1.12	–	3.3	–	0.67
	1% Pt/HZSM-5 (23)	300	2	12	68	1.7	3.5	4.8	55	0.90	2.1
	1% Pt/HZSM-5 (30)	300	2	12	43	2.6	4.3	5.1	28	1.2	1.8
	1% Pt/USY (6.3)	300	2	12	90	1	3.5	0.18	81	2.7	2.7
	1% Pt/USY (5.1)	300	2	12	75	1	2.3	0.05	67.5	1.2	3
	1% Pt/BEA (5.1)	300	2	12	25	1	1	4.7	16.7	0.85	0.75
	1% Pt/HY (5.1)	300	2	12	30	0.51	0.51	0.06	17.1	10	1.82
	1% Pt/HMOR (18.3)	300	2	12	2.3	0.3	1	0.30	0.7	0.07	0.06
	1% Pt/FER (20)	300	2	12	52	2	2.6	0.1	45	0.67	1.63
	1% Pt/L (6.0)	300	2	12	1	0.16	0.36	0.05	0.19	0.07	0.22
	5% Pd/C	350	–	10	23	–	2	4	17	–	–
	1% Pt/C	350	–	10	30	–	0.15	5.4	21.6	–	–
	20% Ni/C	350	–	10	92	1	10	50	18	–	–
	RANEY Ni	340	2.1	9	85	46	–	–	39	–	–
	27% Ni/Al_2O_3	340	2.1	9	90	44	–	–	46	–	–
	5% Pt/Al_2O_3	325	2	5	46	–	–	–	46	–	–
Jatropha oil	1% Pt/HZSM-5 (23)	270	4	12	100	1.7	6	7.1	83	1.7	1
	1% Pt/USY (6.3)	270	4	12	31	0.4	1.84	–	21	5.9	1.86
	1% Pt/Tube	270	4	12	14	0.8	–	–	5	8	–
	1% Pt/HZSM-5 (23)	270	4	12	22	–	–	–	–	–	–
Microalgae oil	10% Ni/HBEA (150)	260	4	8	100	3	3	–	93	–	1
	10% Ni/ZrO_2	270	4	8	100	4.6	3.6	–	91	–	1

the ZrO_2 defect site and lost in the form of H_2O. The presence of the ketene intermediate has been studied by *in situ* IR spectroscopy probing with a diamond detector [51]. Under a H_2 atmosphere, the ketene intermediates were hydrogenated on the Ni sites to hexadecanal. In the absence of H_2, the ketene intermediate produces palmitone via interaction with the neighboring palmitate over the ZrO_2 support

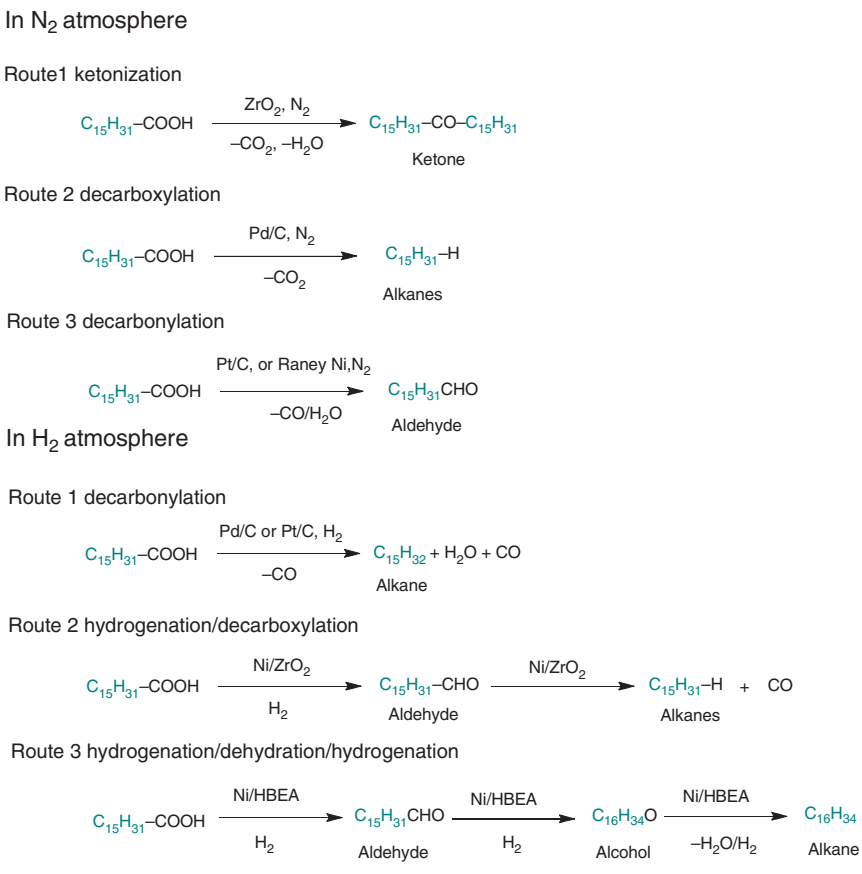

Figure 13.2 Reaction network for deoxygenation of palmitic acid on oxide-supported metal catalysts in the presence or absence of hydrogen.

while eliminating CO_2. Thereby, the H coverage on the active sites determined either the hydrogenation–decarbonylation or the self-condensation (ketonization) pathway.

The reaction rates and product distributions over the Ni/ZrO_2 catalyst were greatly affected by the composition of reaction system [53]. In this regard, the palmitic acid conversion decreased from 100% to 3.5% when the proportion of H_2 in the carrier gas was decreased from 100% to 0%. These results suggested that the deoxygenation rate was much higher in a H_2 atmosphere due to the promoted hydrogenation of the acid in the primary step. When the partial pressure of H_2 declined, the selectivity toward *n*-pentadecane also decreased from 90% to 16%, whereas the selectivity to palmitone increased from 0% to 60%. Reducing the partial pressure of H_2 altered the individual reaction rates and the pathways.

The ketonization, carboxylation, and decarbonylation reaction steps occurred during fatty acid (for example, palmitic acid) conversion in a nitrogen atmosphere, leading to the formation of ketones, paraffins, and aldehydes. On the other

side, the decarbonylation, hydrogenation–decarbonylation, and hydrogenation–dehydration–hydrogenation steps occurred during fatty acid conversion in hydrogen atmosphere, giving paraffins as the final products (see Figure 13.2) [51, 53, 55–58].

Even if conversion of SA and esters was observed in the inert nitrogen atmosphere, the presence of hydrogen was found to be beneficial for catalyst stability [31, 59]. The fast deactivation in the inert atmosphere was attributed to the formation of heavy products and unsaturated hydrocarbons. Due to the fast saturation of the unsaturated intermediates in the hydrogen atmosphere, the catalyst deactivation by coking was significantly reduced [59]. Identical results were reported for the fixed-bed deoxygenation of SA over Pd/C (360 °C, 1 MPa Ar, or 5% H_2 in Ar), where stable conversion was observed in the hydrogen atmosphere [49]. Reducing the H_2 pressure in the reaction atmosphere (using different H_2–He mixture compositions) also suppressed the initial reaction rate in ethyl stearate deoxygenation and decreased the selectivity to *n*-heptadecane [39]. Importantly, ethyl stearate decomposed into ethene and SA in the absence of a catalyst at temperatures around 300 °C [60]. Hydrogen consumption showed positive responses to retain the catalyst activity due to alkene intermediate hydrogenation observed in methyl octanoate deoxygenation [59].

The importance of hydrogen for the deoxygenation of carboxylic acids was further illustrated by investigating the solvent effect [31, 61]. It was reported that some solvents might act as the hydrogen donors via hydrogenation–dehydrogenation equilibrium and consequently affect the deoxygenation. In this regard, dodecane was found to undergo dehydrogenation (conversion of ~2%) over Pd/C under typical deoxygenation conditions (300 °C, 1.5 MPa H_2), and dihydrogen was formed [31]. Moreover, the initial rate of SA formation from ethyl stearate in the inert atmosphere was higher in dodecane than that in mesitylene, whereas dodecane acted as an H-donor solvent irrespective to that of mesitylene. The initial rate of *n*-heptadecane formation remained changed by the solvent employed, suggesting that the initial deoxygenation was not affected by the presence of hydrogen [44].

The deoxygenation of several fatty acids (C_{17}–C_{22}) in dodecane under Ar (300 °C, 1.7 MPa, Pd/C) was found to be independent of chain length. In this context, the initial deoxygenation rates of C_{17}, C_{18}, and C_{20} fatty acids displayed similar results [62]. The same conclusion can be arrived at for palmitic and SA deoxygenation under 5% H_2 in Ar [48]. Likewise, different deoxygenation rates were reported for the conversion of C_{19} or C_{22} fatty acids due to the presence of unsaturated fatty acids and phosphorus as impurities. Typically, the conversion decreased from about 90% to approximately 20% in the presence of these impurities.

The hydrotreating of crude microalgae oil to produce hydrocarbon fuels was performed in a batch mode using 10 wt% Ni/HBEA catalyst (Si/Al = 180) at 260 °C in the presence of 4 MPa H_2 [54]. The results displayed 78 wt% liquid alkane yield after eight hours (including 60 wt% yield of C_{18} octadecane), which was found to be very close to the theoretical maximum liquid hydrocarbon yield (84 wt%). In addition, propane (3.6 wt%) and methane (0.6 wt%) were detected as the main products in the gas phase. Furthermore, Ni/ZrO_2 catalyst achieved quantitative conversion of microalgae oil to C_{17} alkanes as the final products at 270 °C under 4 MPa H_2 pressure [51].

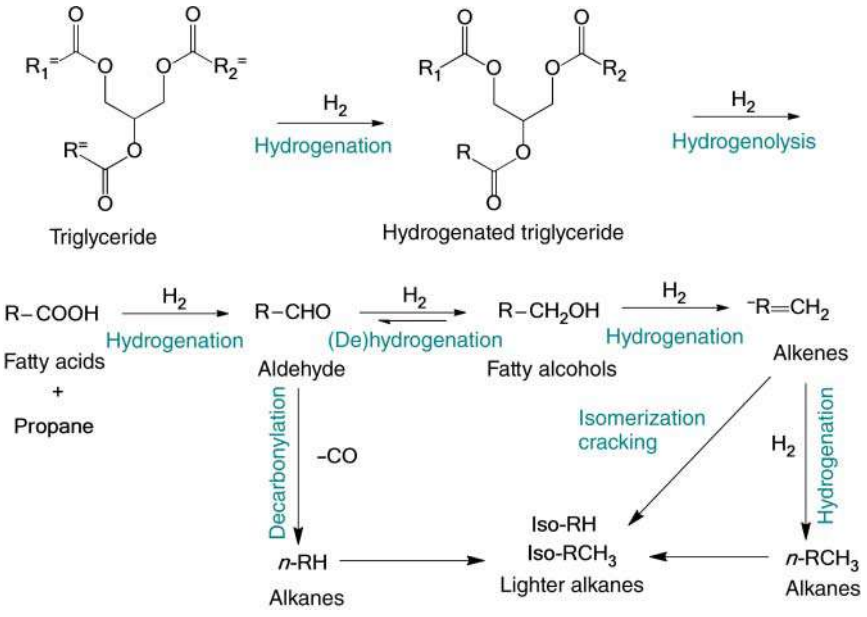

Figure 13.3 Proposed reaction pathway for the transformation of microalgae oil to alkanes over bifunctional Ni/HBEA catalysts. Source: Reproduced with permission from Song et al. [55]; © 2013, Wiley.

The overall reaction pathways for microalgae oil conversion over Ni/HBEA catalyst are presented in Figure 13.3 [55]. Conversion of microalgae oil proceeds via the hydrogenation of the double bonds to single bonds in the alkyl chain over metal catalyst, followed by the hydrogenolysis of the saturated triglyceride to release fatty acids and propane. The hydrogenation of the carboxylate group of the fatty acids produces the corresponding aldehyde as the rate-determining step, followed by either decarbonylation of octadecanal to *n*-heptadecane and carbon monoxide (minor route) or hydrogenation of octadecanal to 1-octadecanol (major route). The produced 1-octadecanol undergoes sequential acid-catalyzed dehydration and metal-catalyzed hydrogenation to give *n*-octadecane as the final product. Notably, the acidic sites in the zeolite favor the alkane hydro-isomerization and hydrocracking. Thus, C_{17} alkanes can be identified as the major products catalyzed by Ni/ZrO_2, while C_{18} alkanes are the dominant products produced by Ni/HBEA.

In addition to supported Ni catalysts, a non-pyrophoric RANEY® Ni type catalyst has been tested for the hydroconversion of sunflower oil [63]. The catalyst showed 85% conversion with 58% hydrocarbon selectivity in the model reaction of octanoic acid transformation at 340 °C and 2.1 MPa H_2 via hydrodecarbonylation and decarboxylation routes. In addition to this route, Ni-based catalysts were found to be active in CO methanation and C—C bond cleavage of alkenes producing methane as the by-product in high concentration and with high consumption of hydrogen. The non-pyrophoric RANEY Ni catalyst was more effective than Ni/Al_2O_3, in particular for the C–C hydrogenolysis reaction. These catalysts were further modified using the metal cations to exclude the possible active sites responsible for the side

reactions. Typically, the addition of In_2O_3 was found to be quite effective to promote deoxygenation, resulting in high alcohol yield.

Carbon-supported metals with 20 wt% Ni/C, 5 wt% Pd/C, and 1 wt% Pt/C catalysts were tested in the deoxygenation of triglycerides such as tristearin, triolein, and soybean oil in a nitrogen atmosphere [53]. The Ni/C catalyst led to quantitative conversion of the triglyceride producing linear C_5–C_{17} alkanes and alkenes. The oxygen was lost in the form of CO and CO_2, whereas small amounts of light alkanes (C_1–C_4) and hydrogen could be detected. The reaction of soybean oil deoxygenation revealed the pathways for triglyceride deoxygenation that entailed the conversion of fatty acids via C—O bond scission and hydrogen transfer, followed by the elimination of CO_2 from the acids. Overall, Pd/C and Pt/C catalysts showed lower activities for both triglyceride deoxygenation and C—C bond cleavage in fatty acid chains than Ni/C catalyst.

SA obtained from hydrogenolysis and hydrogenation of oils and triglycerides (lipids) can be employed to produce alkanes (for example, *n*-heptadecane and *n*-octadecane) as kerosene additives for aviation fuel. The selective deoxygenation of lipids and fatty acids are potentially promising sustainable energy sources for biomass conversion to biofuels [64, 65]. Zhao and coworkers introduced the one-pot tandem process involving the dehydroaromatization of the terpene limonene and the hydrodeoxygenation of SA over Pd-Ni/HZSM-5 catalyst at 280 °C under 0.2 MPa H_2 pressure (Figure 13.4). Importantly, this process entails the formation of *p*-cymene from terpene with the concomitant generation of hydrogen and the

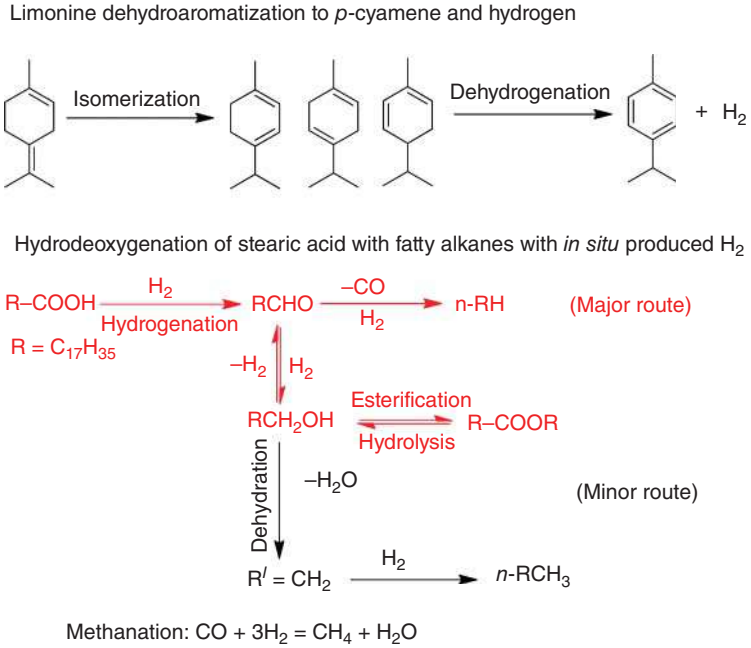

Figure 13.4 A one-pot process combining limonene dehydroaromatization and stearic acid hydrodeoxygenation in the absence of hydrogen. Source: Reproduced with permission from Luo et al. [64]; © 2016, Royal Society of Chemistry.

subsequent hydrodeoxygenation of SA. With respect to the bimetallic Pd–Ni catalyst loaded on the HZSM-5, Pd was necessary to cause the limonene hydrodearomatization to *p*-cymene, while Ni exhibited high catalytic activity for hydrodeoxygenation of SA to alkanes [66].

In summary, herein the triglyceride deoxygenation approaches are discussed on the basis of supported metal catalysts employed. Noble metals like Pt and Pd and base metals like Ni have been explored, and the various supports from activated carbon to oxides such as Al_2O_3, SiO_2, SiO_2–Al_2O_3, and H-zeolite (HZSM-5, HBEA, HY, and HUSY) have been used.

13.3 Lipids to Jet Fuel Hydrocarbons

In the 1920s, the thermocatalytic cracking processes of vegetable oils were reported in batch reactors over acidic catalysts such as $AlCl_3$ and Al_2O_3 and basic catalysts such as MgO, CaO, and NaOH catalysts at the relatively high temperatures of 400–500 °C [67–69]. Acidic catalysts based on silica–alumina and zeolites like HZSM-5 and HY were also employed [70], whereas the cracking and deoxygenation over various zeolite catalysts were found to be the most promising alternatives to upgrade triglycerides to fuels [71–73]. Hydrogen is not required in cracking, which is its significant advantage compared than hydrodeoxygenation with hydrotreating catalysts.

Zeolites such as HZSM-5, HBEA, and HUSY were tested for the cracking of palm oils at 350–450 °C in a fixed-bed reactor at atmospheric pressure [71–73]. Notably, the application of the three zeolites resulted in 99%, 82%, and 53% conversion with gasoline selectivity of 28%, 22%, and 7%, respectively. In comparison, HZSM-5 favored gasoline-range hydrocarbons and gaseous products while HUSY produced diesel-like product. Due to high acidity and unique pore dimensions and architecture, HZSM-5 produced high yields of aromatic hydrocarbons, i.e. benzene and toluene, of 80–95 wt% in the liquid phase. Increasing pore diameter and the cavities led to the formation of coke products inside zeolite pores, whereas the rate of coke production increased in the order of HZSM-5 < HBEA < HUSY. In contrast, acidic amorphous silica–alumina produced a high yield of aliphatic hydrocarbons (10–30 wt%) and aromatics (25–50 wt%) as organic liquid products [74]. Likewise, SAPO-5 and SAPO-11 produced C_6–C_9 aromatics as the main hydrocarbons in the organic phase, whereas the nonacidic aluminophosphate Mg–AlPO-36 delivered about the same fraction of aromatics and aliphatic hydrocarbons [73].

Consistently, the yield of organic liquid products for biofuel applications decreased with the increasing concentration and strength of acid sites, due to overcracking to gaseous products [74]. Likewise, high yields of kerosene and gasoline were obtained at the expense of gases and diesel when the Si/Al ratio of HZSM-5 was increased from 50 to 400. Meanwhile, the aromatic content in the organic phase decreased from 52 to 35 wt% with small yields of coke (2 wt%) [75]. The amorphous silica–alumina and MCM-41 delivered high yields of organic liquid products up to 65 wt% with higher amount of coke formation (9–12 wt%) [74, 75]. Subsequently,

increasing the temperature from 450 to 500 °C lowered the yield of organic liquid products from 54 to 40 wt% over HZSM-5 zeolite [76], revealing that the yields of organic liquid products were significantly affected by reaction temperature. The influence of the density of acid sites and their strength were investigated and illustrated using potassium-loaded ZSM-5 [75]. The impregnation of HZSM-5 with potassium decreased the triglyceride conversion and gasoline-range hydrocarbon yield, particularly aromatics [76], owing to the lower concentration of Brønsted acid sites. The different product distribution over HZSM-5 and KZSM-5 zeolites revealed that the catalyst acidity played a key role in the aromatization and oligomerization reactions.

Mesoporous MCM-41 catalyst exhibited an enhanced gasoline selectivity to 40% [77]. In comparison, the catalytic cracking of a fatty acid mixture and used palm oil over HZSM-5 and HZSM-5/MCM-41 composite catalyst presented significantly enhanced conversion of used palm oil at 400 °C when the HZSM-5 fraction increased from 50% to 70%. The advantage of HZSM-5 rests in the reduced diffusion that decreased with respect to high cracking temperature. Expectedly, the conversion over the neat mesoporous materials was significantly lowered (60–70%) due to the lower density and strength of acidic sites [78]. The gasoline yield was reported to be the highest (44 wt%) for composite catalysts containing 10–30% of the mesoporous phase [77], probably due to the balance between initial cracking in the mesoporous material and secondary cracking in the micropores of HZSM-5 zeolite. Likewise, an enhanced gasoline yield was observed for palm oil cracking over HZSM-5/MCM-41 composite catalysts [75].

Subsequently, the zeolite-catalyzed cracking of triglycerides resulted in linear and cyclic olefins and paraffins and oxygenated compounds including aldehydes, ketones, and carboxylic acids [79]. The wide molecular-weight distribution of products is not considered as beneficial with selective processes because a more complex downstream treatment of the products is required to make use of all the products efficiently. Several reactions such as cracking, hydrolysis, isomerization, dehydrogenation, aromatization mainly by the Diels–Alder reaction, and coking proceed via a free radical or carbocation-based mechanism [80]. Likewise, thermal catalytic cracking represents a route to gasoline rather than to diesel in terms of the fractional composition. The optimization of catalytic cracking process produces relatively low green diesel yields. Moreover, these products often contain carboxylic acids and other oxygenates that probably cause difficulty in storage and distribution and their ignition in engines [81].

The reaction pathways of triglyceride cracking over acidic zeolites have been investigated and overviewed thoroughly [82–84]. The reaction pathways for the conversion of oleic acid to green gasoline probably start with the protonation of the unsaturated bond of the fatty acid on HZSM-5 (Figure 13.5). Afterward, the proton charge can shift through the fatty acid carbon chain. β-Scission results in cracking of the fatty acid. The narrow channels of ZSM-5 are speculated to continue the protonation toward the pore mouth of a zeolite catalyst. Moreover, molecular pattern reveals the cracking of fatty acids starts on acid sites at the pore mouth [84]. The resultant species are sufficiently small to enter the catalyst pores

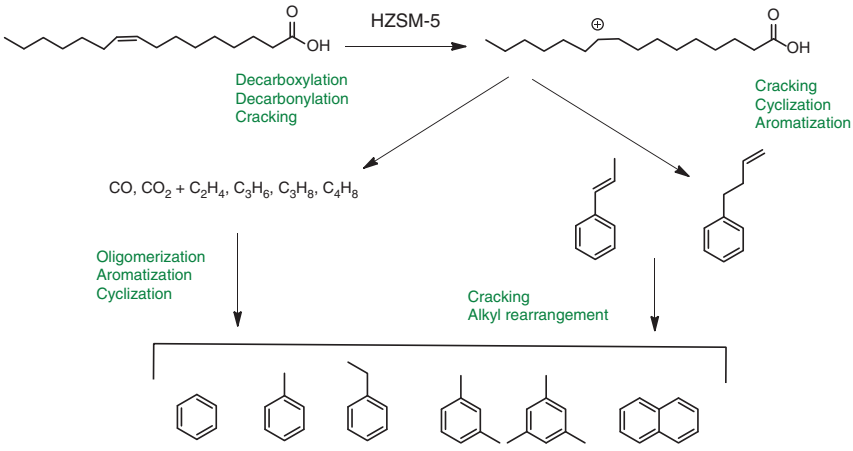

Figure 13.5 Reaction routes for oleic acid cracking and aromatization to aromatics. Source: Based on Vinh et al. [85].

and consequently undergo aromatization and cyclization steps to produce aromatic compounds mainly from propenylbenzene and phenylbutene in the overall mechanism [86].

Decarboxylation and decarbonylation produce gaseous products such as CO_2 and CO, respectively, and other resulting reaction intermediates such as linear alkanes and alkenes are cracked into smaller hydrocarbons (Figure 13.5) [85]. Light olefins (C_2–C_4) rapidly oligomerize, cyclize, and aromatize inside the pores of HZSM-5 zeolite producing aromatic compounds [87]. The generated aromatic molecules can either diffuse out or stay inside the pores forming coke as the side reactions. This can be illustrated well by the fact that the addition of single aromatic compounds can yield naphthalene and methylnaphthalene, which favor coking [88, 89]. Likewise, coke aggregates in the catalyst pores block the catalyst and prevent access to catalytic sites, and therefore, oxidation is required for their removal [66, 90].

Lipids are well-known precursors of valuable products such as jet aviation fuels and other commodity chemicals [48, 64, 91–96] through processing at 350–400 °C and in the absence of hydrogen. The resulting bio-jet fuels are very important strategic natural resources [97]. In addition, cyclic alkanes such as C_6–C_9 ring compounds can be achieved by the hydrodeoxygenation of lignin, which further coactivate deoxygenation of triglycerides under hydrogen-free conditions in an integrated process (Table 13.5). Hydrogen is released from cycloalkanes, and aromatic hydrocarbons are produced. Importantly, the as-produced hydrogen will cause the hydrodeoxygenation of lignin, and the heat required for endothermic dehydrogenation of cycloalkanes is provided by the exothermic lipid deoxygenation reactions to maximize the energy utilization. This strategy, as shown in Figure 13.6, favors the potential production of high-quality jet fuels possessing arenes from lignin and lipids.

Table 13.5 Conversion of stearic acid (SA) in ethyl-cyclohexane (ECH) under different reaction conditions, from Ref. [97].

			Arenes	Light alkanes		Liquid yield from SA (C%)			Gas component (%)			
Catalyst	SA (g)	ECH Conv. (%)	Yield from ECH (C%)		SA conv. (%)	C_{17} alkane/alkene	C_9–C_{16}	$C_{19}H_{38}O$	CH_4	H_2	CO	CO_2
–	0.5	0.8	0.1	0.7	100	44: 11	30	15	26	0	50	24
γ-Al_2O_3	0.5	1.4	0.3	1.1	100	17: 3	78	2	20	0	67	13
1.5% Pt-2.0% Ir	0	32	24	7	–	–	–	0	70	30	0	0
1.5% Pt-2.0% Ir	0.5	47	35	12	100	48: 0	52	0	80	19	0.8	0.2
1.5% Pt+2.0% Ir	0.5	37	30	7	100	38: 0	62	0	84	16	0.7	0.3
1.5% Pt	0	26	10	16	–	–	–	0	7	93	0	0
1.5% Pt	0.05	15	10	5	100	81: 0	19	0	3	97	0	0
1.5% Pt	0.1	2	1	1	100	43: 0	57	0	23	0	77	0
1.5% Pt	0.5	1.8	0.6	1.2	100	61: 0	39	0	12	0	80	8
2.0% Ir	0	25	19	6	–	–	–	0	74	26	0	0
2.0% Ir	0.05	2	1	1	100	34: 0	66	0	68	0	32	0
2.0% Ir	0.1	3	2	1	100	55: 0	45	0	79	0	21	0
2.0% Ir	0.5	1.8	0.6	1.2	100	46: 0	54	0	77	0	21	2

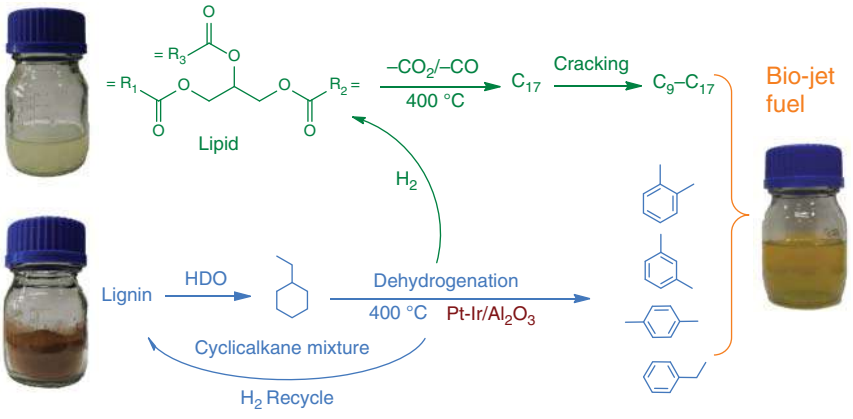

Figure 13.6 Production of bio-jet fuels from lignin and lipids. Source: Lu et al. [97]/with permission from Royal Society of Chemistry.

13.4 Lipids to Alkenes

The long-chain terminal olefins or LOFs having odd carbon numbers can be synthesized more sustainably and selectively from renewable feedstocks such as plant oil via deoxygenation process [98]. Unsaturated plant oil triglycerides can also be selectively converted to α-olefins via ethenolysis or alkenolysis, which shows potential application in the petrochemical industry [99–108]. The conversion routes of lipids to olefins over homogeneous or heterogeneous catalysts are shown in Figure 13.7.

The deoxygenation of fatty acids and their derivatives entails dehydration, decarbonylation, and decarboxylation [98]. The decarboxylation of fatty acids (C_n) produces linear alkanes and alkenes (C_{n-1}), whereas the combination between

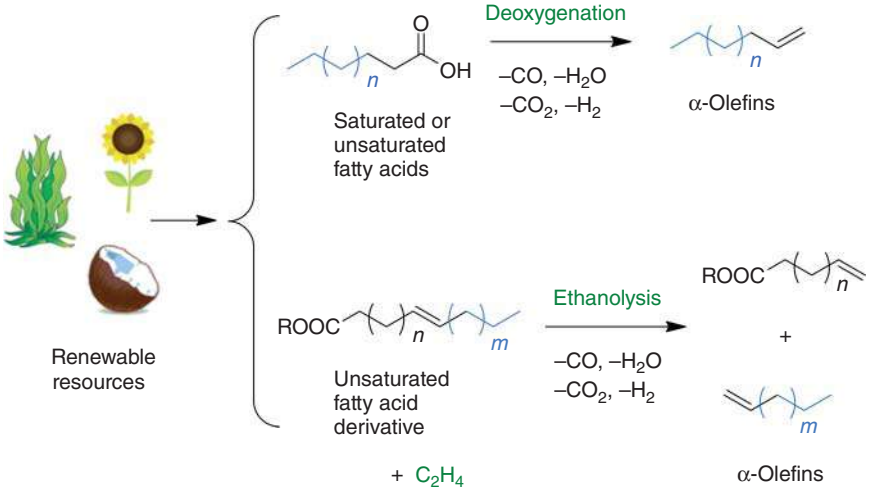

Figure 13.7 Synthesis of LAOs from renewable resources.

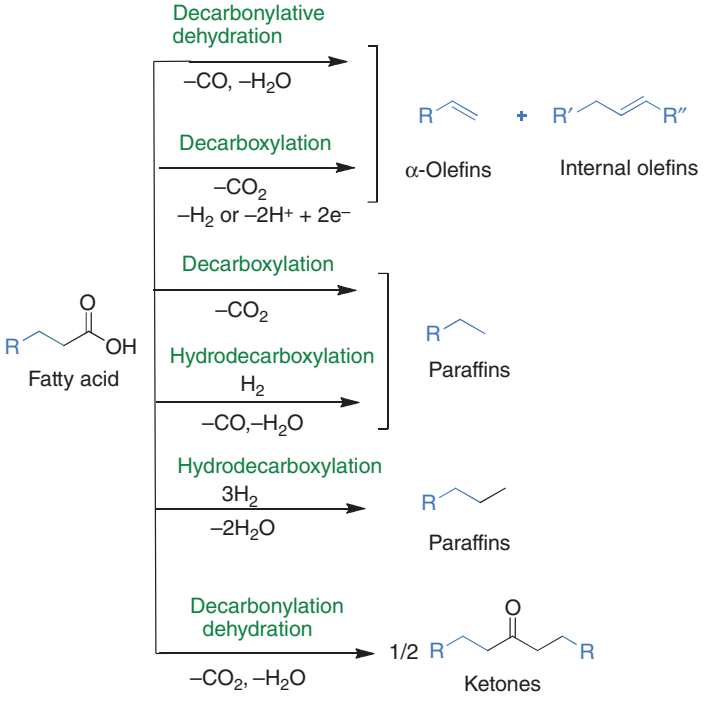

Figure 13.8 Fatty acid deoxygenation reaction network.

dehydration and decarbonylation and decarboxylation results in the formation of alkenes and ketones, respectively (Figure 13.8). The alkane products (paraffins) are also highly useful chemicals compounds for biodiesel, jet fuel, and renewable diesel.

13.4.1 Lipids to Alkenes over Homogeneous Catalysts

In 1965, the first palladium catalyst was reported to perform decarbonylation of aliphatic acyl chlorides to yield olefins along with CO and HCl (Figure 13.9) [102, 103]. The reaction proceeded via oxidative addition of the acyl chloride to Pd^0, forming an acyl Pd^{II} species. Subsequently, carbon monoxide liberation resulted in the alkyl Pd^{II} species that underwent β-hydride elimination to yield the olefin product and, after HCl reductive elimination, regenerated the active Pd^0 catalyst. This reaction required a high temperature of 200 °C. However, the product was a mixture of double-bond positional isomers.

The decarbonylation of fatty acids with $PdCl_2$ and phosphine was investigated at 280 °C [104]. This process produced a mixture of olefin isomers with quite low α-olefin selectivity, and low activity (turnover number [TON] < 10, TOF < 3 h^{-1}, α-olefin selectivity < 50%) was observed over 10 mol% $PdCl_2$ in a large excess of PPh_3 ligand (PPh_3/Pd = 50/1). It was proposed that the decarbonylation presumably proceeded via the anhydride considering that heating of the acid anhydride gave twice amount of product compared with that of acid.

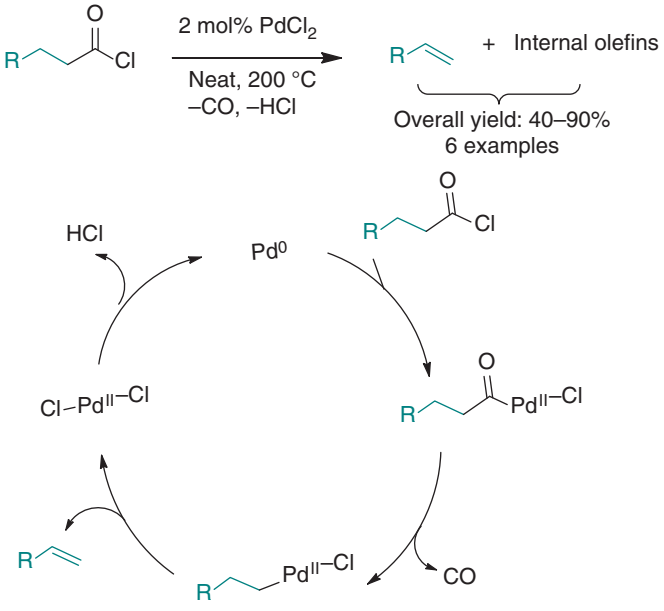

Figure 13.9 Palladium-catalyzed decarbonylation of aliphatic acyl chlorides.
Source: Reproduced with permission from Tsuji et al. [102]; © 1968, American Chemical Society.

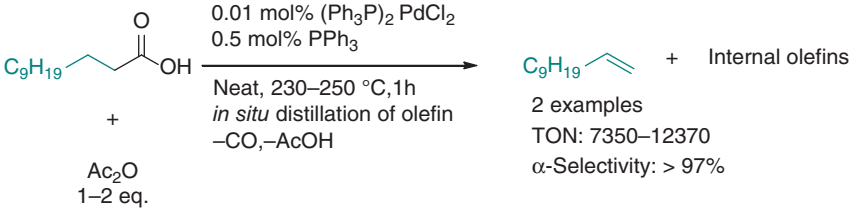

Figure 13.10 Decarbonylative dehydration with the lowest catalyst loading.
Source: Reproduced with permission from Miller et al. [105]; © 1993, American Chemical Society.

Subsequently, the "mixed anhydride system" was reported to improve catalytic activity when using an equimolar mixture of carboxylic acid and acetic anhydride [105, 106]. This led to the efficient decarbonylative dehydration with highest activity (TON = 104, TOF = 104 h^{-1}, and α-olefin selectivity > 97%) (Figure 13.10). However, the reaction required a high temperature of ~250 °C and continuous distillation of the olefin products to maintain the high selectivity. Thereby, only volatile olefins can be synthesized in this way. $(PPh_3)_2PdCl_2$ (TON = 12370, α-olefin selectivity > 97%) were found to be much more active than $(PPh_3)_4Pd$ (TON = 1550, α-olefin selectivity > 97%), revealing that Pd^{II} compounds were superior as decarbonylation initiators than Pd^0.

The variations of reaction conditions, for example, using PPh_3/Pd ratio of 25/1 instead of 50/1, could significantly improve the performance of $(PPh_3)_4Pd$ [107].

Nevertheless, high temperature of > 200 °C and continuous distillation of the olefin product were still needed to maintain the high selectivity. In addition, a sacrificial anhydride in equimolar amounts was required to activate the carboxylic acids.

Several carboxylic acids such as fatty acids were converted into olefins using an anhydride-induced activation with Pd^{II} initiator [108]. The strategy involved the use of pivalic anhydride and a catalyst system obtained from $PdCl_2$ and DPEPhos (bis(2-diphenylphosphinophenyl) ether) in *N*,*N*′-dimethylpropyleneurea (DMPU) at a low temperature of 110 °C. The low temperature would not cause isomerization, and high α-olefin selectivity could be obtained without *in situ* distillation. Subsequently, high activity and α-olefin selectivity were achieved using trialkylamine additives with the same *in situ* catalytic system and low reaction temperatures of 100–110 °C [109]. The total conversion of SA into α-heptadecene with 96% selectivity was obtained within 16 hours using equimolar amounts of Et_3N. Replacement of the cost-intensive pivalic anhydride (Piv_2O) by the more readily available acetic anhydride was also accomplished with comparable conversion and selectivity (TON ≤ 33, TOF = 2 h^{-1}, α-olefin selectivity > 95%). Notably, by changing the solvent from DMPU to acetonitrile, the selectivity also altered from 1-alkene to 2-alkene products, due to the *in situ* formation of a bis-(acetonitrile) Pd^{II} complex assisting as a tandem catalyst for the decarbonylative dehydration and isomerization.

The acidic additives and part-wise addition of the acetic anhydride were investigated, which produced low yield of double-bond olefin isomerization products [110]. Compared with Pd-catalyzed decarbonylation [108–113], this system could be successfully applied with a wide range of functional groups at relatively low temperature of 132 °C with excellent α-olefin selectivity (TON ≤ 600, TOF ≤ 533 h^{-1}, α-olefin selectivity = 80–99%). It was illustrated that the decarbonylative dehydration served as promising reaction not only for producing commodity LAOs but also in multistep organic synthesis of more useful molecules [111]. In this regard, the decarbonylative dehydration was applied as a key step for the enantioselective total synthesis of (−)-aspewentins A–C.

The decarbonylative dehydration reaction of SA could be operated over well-defined Pd-based catalysts in phosphine at the relatively low temperature of 110 °C (Figure 13.11) [114]. The reaction showed high selectivity for a wide range of substrates without *in situ* distillation. More importantly, the availability of molecular catalyst structures facilitated the improvement via structure–activity analogy. Likewise, density functional theory (DFT)-derived information showed that excess phosphine should increase the rate-determining barrier.

Rh-based catalysts were active in the decarbonylative dehydration of fatty acids without any sacrificial anhydride [104], in significant contrast to the above-described Pd catalysts. For example, SA was quantitatively converted into 1-heptadecene and isomer mixtures over a catalyst system of $RhCl_3$ (1 mol%) and triphenylphosphine (10 mol%). These results were obtained for neat substrate under a nitrogen flow at temperatures of 280 °C (TON ≤ 250, TOF ≤ 250 h^{-1}, α-olefin selectivity < 50%), and the reaction proceeded via a decarbonylative dehydration sequence instead of the alternative decarboxylation process. The feasible reaction route was presented in

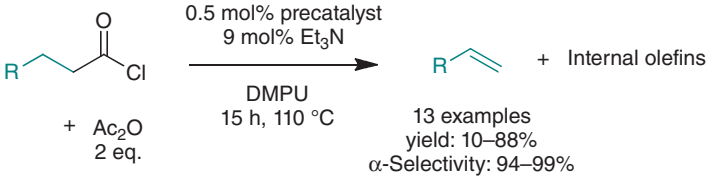

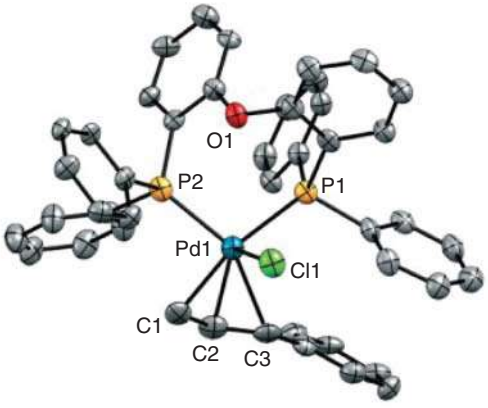

Figure 13.11 Decarbonylative dehydration of fatty acids over palladium precatalyst. Source: Reproduced with permission from Chatterjee et al. [114]; © 2016, American Chemical Society.

which the key step was the formation of the acid anhydride due to removal of water. The *in situ* formed acid anhydride probably reacted with the metal center to generate the olefin product, carbon monoxide, and carboxylic acid. The acid could, afterward, generate another anhydride molecule and start the next catalytic cycle. Acetic anhydride was applied as an acid activator that increased the overall yield and selectivity by an *in situ* distillation strategy. In addition, acetic anhydride further averted olefin isomerization [105] and achieved good yield of up to 97%, whereas no isomerization could be observed [106]. However, the stoichiometric amount of acetic acid was obtained as an unwanted by-product, and an additional purification step was required for its removal.

Even though anhydride addition enhanced the TON for Rh, the conversion to α-olefins could be obtained on Rh metal without the wasteful stoichiometric addition of the acidic anhydride [104, 105]. The excess of phosphine ligand was not used on Rh unlike Pd [105], and thereby, Rh catalysts were employed in the decarbonylative dehydration of fatty acids despite their lower activity. The catalytic activity of Rh relative to Pd was further studied via the DFT-based investigations to understand the mechanism of Rh-catalyzed decarbonylative dehydration using an anhydride-activated model carboxylic acid [113]. Calculation results revealed that the overall reaction barrier was higher for Rh than that of Pd, consistent with the superior activity of Pd-based catalysts, and also explained the difference in mechanism to inspire the future improvement in Rh-based catalysts.

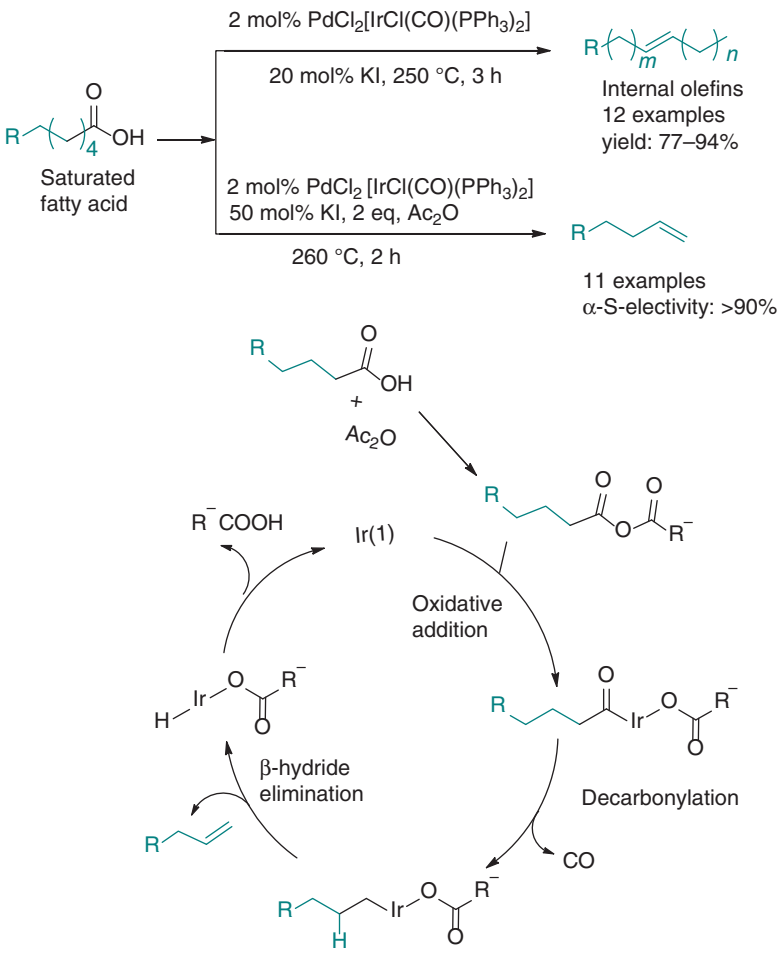

Figure 13.12 Iridium-catalyzed decarbonylative dehydration of aliphatic carboxylic acids to internal and α-olefins and its plausible mechanism. Source: Reproduced with permission from Maetani et al. [115]; © 2011, American Chemical Society.

The reaction conditions and additives for Vaska's complex were changed for the decarbonylative dehydration of a variety of saturated fatty acids, and both α-olefins and mixtures of internal olefins could be achieved in good yields (Figure 13.12) [115]. Likewise, a mixture of internal olefins (yields 90–94%, selectivity of internal olefins > 98%) was obtained at a relatively high temperature of 250 °C with KI as the sole promoter and in the absence of acetic anhydride. In addition, sufficient anhydride was obtained from the fatty acids at high temperature, and adding an anhydride activator could lower the reaction temperature to ~160 °C, which accordingly led to high selectivity to α-olefins (TON < 20, TOF < 4 h^{-1}, α-selectivity > 95%) by suppressing the formation of isomerization products.

Vaska's complex was replaced by 2.5 mol% $[Ir(COD)Cl]_2$ in the presence of 15 mol% PPh_3 at the same temperature (~160 °C), promoter (2 equi. Ac_2O),

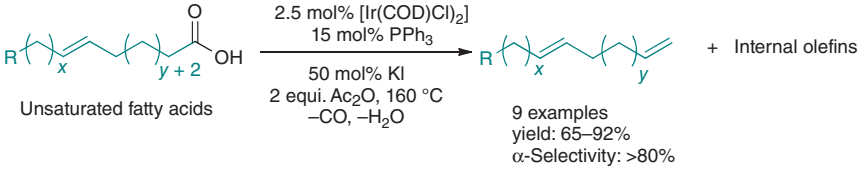

Figure 13.13 Iridium-catalyzed decarbonylative dehydration of unsaturated fatty acids. Source: Reproduced with permission from Ternel et al. [116]; © 2018, Royal Society of Chemistry.

and additives (50 mol% KI), (Figure 13.13) [116]. Comparatively, this catalyst showed similar catalytic performance (TON < 40, TOF < 8 h^{-1}) to that of Vaska's complex [98]. Likewise, the α-olefin selectivity was observed to be ≤ 90% in the transformation of unsaturated fatty acids.

Ru can decarboxylate the fatty acids irrespective to the other transition metals. The tandem isomerization–decarboxylation process for unsaturated fatty acids over $[Ru(CO)_2EtCO_2]_n$ and $Ru_3(CO)_{12}$ produced mixtures of alkene isomers (Figure 13.14) [117–119]. Importantly, no anhydride additive was needed to activate the substrate in this process. Nevertheless, the substrate scope was very limited, and almost no selectivity to α-olefins was observed. The activity at ~250 °C (TON ≤ 377, TOF ≤ 93 h^{-1}) was reported to be lower than that of Pd and Rh catalysts under similar conditions [64].

Stoichiometric amounts of $NiCl_2$ and zinc dust resulted in the decarbonylation of thioesters to alkene products [109, 110]. Nevertheless, the thioesters should be prepared from the carboxylic acid prior to decarbonylation. This, together with the stoichiometric amounts of the catalyst, limits the application of this approach. More promising results were observed with respect to the catalytic properties of nickel [111]. Likewise, a combination of 5 mol% $Ni(COD)_2$ and 7.5 mol%

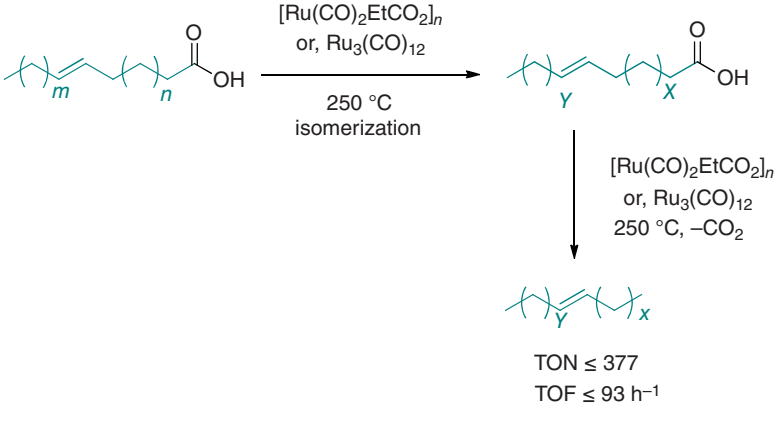

Figure 13.14 Ruthenium-catalyzed tandem isomerization–decarboxylation of unsaturated fatty acids to alkenes. Source: Reproduced with permission from Knothe et al. [117]; © 2017, American Chemical Society.

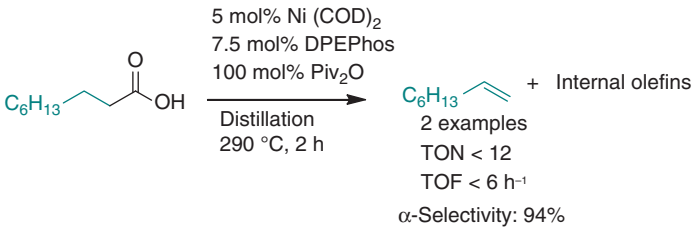

Figure 13.15 Ni-catalyzed the decarbonylative dehydration of nonanoic acid. Source: Reproduced with permission from John et al. [120]; © 2016, American Chemical Society.

DPEPhos ligand produced 1-octene in 56% yield (TON < 12, TOF < 6 h^{-1}, α-olefin selectivity = 94%) at 190 °C (Figure 13.15).

α-Olefins could be obtained over $Ni(OAc)_2$ and stoichiometric amounts of PPh_3 as reductant without using substrate-activating anhydride [112]. Despite the low reactivity, the results appeared to be very promising with respect to developing base metal catalysts without stoichiometric additives (TON < 9, TOF < 0.6 h^{-1}, α-olefin selectivity ≤ 71%). In addition, the amount of phosphine could be reduced using 1,1,3,3-tetramethyldisiloxane (TMDS) as a terminal reductant and catalytic $Cu(OTf)_2$, with a noticeable loss in α-olefin selectivity (Figure 13.16).

The decarbonylative dehydration of a variety of saturated fatty acids was also performed over $FeCl_2$ as a catalyst. It was revealed that a high CO pressure was acquired for the *in situ* formation of the active catalyst, an iron-carbonyl species (Figure 13.17) [122]. High α-olefin selectivity was observed using this approach, but the catalyst stability was very low (TON < 10, TOF < 3.3 h^{-1}). Other nickel, cobalt, and iron complexes were investigated for the decarbonylation of carboxylic acids, in the presence of either KI or other iodide precursors [115, 123]. However, the observed acid conversions were much lower than using Pd or Rh catalyst precursors.

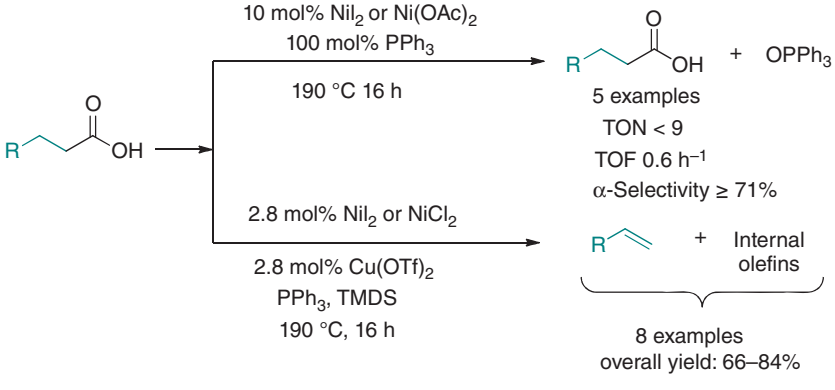

Figure 13.16 Deoxygenation of carboxylic acids over anhydride additive-free Ni. Source: Reproduced with permission from John et al. [121]; © 2017, American Chemical Society.

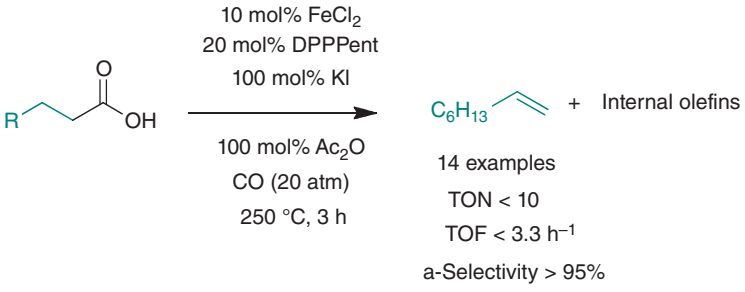

Figure 13.17 Decarbonylative dehydration of aliphatic carboxylic acids to terminal alkenes over iron catalyst. Source: Reproduced with permission from Maetani et al. [122]; © 2012, Royal Society of Chemistry.

Generally, homogeneous catalysts exhibit moderate activity and stability in the conversion of acids to α-olefins. High TONs have been achieved at high temperatures using precious metals and stoichiometric amounts of an anhydride promoter. In addition, the formation of internal olefins can be suppressed by *in situ* distillation. Overall TON can be promoted by recycling the catalyst, but this is rather difficult in homogenous catalysis. An aqueous biphasic system is more beneficial in this case, as the catalyst remained in the water phase, whereas the product resided in the organic phase [118]. After the reaction, the catalyst can be recovered and recycled by simple phase separation.

13.4.2 Lipids to Alkenes over Heterogeneous Catalysts

Compared with homogeneous catalysts, heterogeneous catalysts can be easily separated from the reaction products, and, in general, they show higher thermal stability [119]. Despite these benefits, only very few reports relate to the conversion of fatty acids and their derivatives to α-olefins over heterogeneous catalysts so far.

To hinder catalyst deactivation, the deoxygenation of fatty acids over supported metal catalysts should be performed in hydrogen, which results in the rapid hydrogenation of alkenes from the deoxygenation process, and thereby high selectivity toward paraffins has been reported [29, 39, 43, 98, 107, 116, 117, 120, 121, 124–129]. The α-olefins are obtained at selectivity of < 30% in some deoxygenation processes [98, 130], and the product contains a mixture of olefins, saturated hydrocarbons, ketones, and cracking products. Obviously, the extraction of α-olefins from such mixtures is quite difficult.

The decarbonylation of heptanoic acid was undertaken using carbon-supported Pd and Pt nanoparticles as catalysts, and low TOF of $< 19\,h^{-1}$ and low α-olefin selectivity of < 15% in the liquid phase were obtained, owing to the rapid catalyst deactivation (Figure 13.18) [130, 131]. The rapid conversion of α-olefins into internal olefins was observed in the liquid phase, whereas the highest α-olefin selectivity in the gas phase was recorded at 57% [131].

Supported Ni catalysts containing at least one of the additional elements Sn, Ge, and Pb led to the formation of α-olefins at 200–400 °C (Figure 13.19) [132]. However,

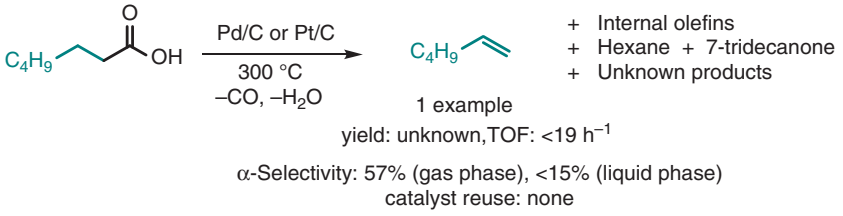

Figure 13.18 α-Olefin production over heterogeneous catalysts from fatty acids and their derivatives. Source: Reproduced with permission from Lopez-Ruiz and Davis [131]; © 2014, Royal Society of Chemistry.

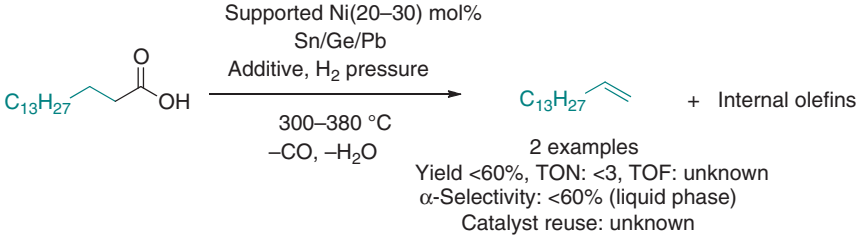

Figure 13.19 α-Olefins from fatty acids and their derivatives over Ni-based heterogeneous catalysts.

the data about catalyst activity and recyclability were not reported, and the TON was found to be very low (< 3). Further studies revealed that Pd on activated carbon (Pd/C) produced cracking products, with no selectivity toward α-olefins. LAOs might be obtained with high selectivity (> 90%) over heterogeneous acid catalysts in aqueous phase reactions at 400–500 °C [133]. However, the process is limited for unsaturated carboxylic acids and their lactones as substrates and showed low reaction rate (TOF < 6 h^{-1}) (Figure 13.20).

Commercial Pd/C catalyst produced the α-olefin with higher activity (TOF = 420 h^{-1}) and selectivity (> 95%) in the presence of phosphine ligands (Figure 13.21) [114]. The advantages of this process entail solvent-free conditions and easy catalyst recycling, and there is no need of *in situ* product distillation to

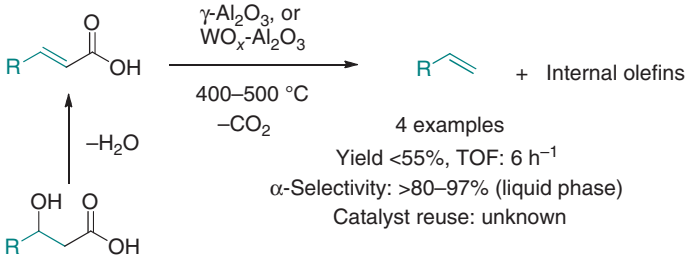

Figure 13.20 α-Olefin production from fatty acids and their derivatives over heterogeneous acids. Source: Reproduced with permission from Chatterjee et al. [106]; © 2018, Royal Society of Chemistry.

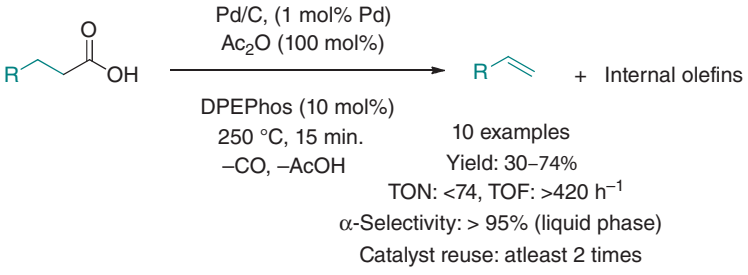

Figure 13.21 Heterogeneous catalysis to yield α-olefins from fatty acids and their derivatives. Source: Reproduced with permission from Chatterjee et al. [114]; © 2016, American Chemical Society.

get high selectivity. However, a fresh batch of phosphine ligands was introduced in each recycling step.

Heterogeneous catalysts have shown potential to convert fatty acids and their derivatives to α-olefins in the above-discussed processes. In fact, well-defined organometallic precatalysts might be grafted onto inorganic supports [134, 135] such as silica or aluminum oxide or linked covalently into porous organic polymers [136] such as polystyrene for the production of α-olefins by linking homogeneous catalysis and heterogeneous catalysis.

13.5 Lipids to Fatty Alcohols

The selective catalytic reduction of triglycerides, methyl esters, and carboxylic acids leads to the formation of fatty alcohols by utilizing molecular hydrogen as the reducing agent. Vegetable and seed oils are considered as reasonable bio-based resources for the fatty alcohol production. The value-added chemical fatty alcohols are applied as intermediates in synthesis of fragrances, pharmaceuticals, detergents, emulsifiers, and lubricants. In addition, fatty alcohols can be used as raw materials to prepare alkyl polyglycosides (APG), fatty alcohol ethoxylates, fatty alcohol sulfates, ether sulfates, amines, alkyl halides, acrylates, and sulfosuccinates [137].

13.5.1 Hydrogenation of Oils

Liquid vegetable oils such as soybean oil, cotton seed oil, corn oil, sunflower oil, rapeseed oil, and palm oil can be selectively hydrogenated to corresponding fatty alcohols over Ni/γ-Al_2O_3 catalysts. Other metals like Co, Rh, Ru, Os, Ir, and Pt were investigated for the hydrogenation of oils and fats under batch reactor hydrogenation conditions with a hydrogen pressure from atmospheric to about 3.4 MPa and a temperature ranging from 100 to about 300 °C [138, 139]. Commercially, the fatty alcohol production entails the methanolysis of triglycerides or fatty acids, followed by hydrogenolysis over copper chromite catalysts at temperatures of 200–400 °C and hydrogen pressures of 20–30 MPa [140, 141]. In addition, chromium-free catalysts

are more acceptable to reduce concerns related to environmental pollution. In this context, doping Cu with promoters such as boron has led to the replacement of Cr and also to performing the reaction at lower hydrogen pressures (in the level of ~10 MPa) while retaining the moderate reaction temperatures (240 °C) [142]. In this context, Cu-B_2O_3/SiO_2 serves as an effective catalyst for synthesis of fatty alcohols from the hydrogenolysis of fatty acid esters. Boron oxide can increase the dispersion of copper as a textural promoter and decrease the activation energy of hydrogenolysis by 10 kJ mol^{-1}.

The quantitative transformation of natural oils and methyl esters to fatty alcohols was performed with N-modified carbon (N–C)-supported RuSn catalysts in water at relatively low temperatures of 140–180 °C and under a hydrogen pressure of 5 MPa [143]. The unsaturated triglycerides were first hydrogenated and then underwent hydrogenolysis to produce fatty acids. The fatty acids could transform to aldehyde intermediates in the presence of hydrogen before being converted into the final product fatty alcohols over RuSn/N-C catalyst (Figure 13.22). The N–C support acted as a basic medium favoring the adsorption of fatty acids by interaction with the nitrogen functionalities. Ru and Sn nanoclusters constituted the principal active sites for the hydrogenation of acid. Sn nanoparticles interacted with the carbonyl group of fatty acids strongly, while Ru catalyzed the cleavage of molecular hydrogen into free radical hydrogen species, which could add to the C=C double bond of the carbonyl group and thereby convert the fatty acid to aldehyde intermediate. The aldehyde intermediate then underwent easy hydrogenation to fatty alcohol as the final product [144].

13.5.2 Hydrogenation of Esters or Methyl Esters

The hydrogenation or reduction of methyl esters (carboxylic acid derivatives) is a potential route to produce the fatty alcohols in synthetic organic chemistry. Notably, stoichiometric methods were applied for the reduction of esters and acids in early studies. The Bouveault–Blanc reduction, one of the early methods reported to reduce esters, entails the reaction with elemental Na in absolute ethanol [139, 145].

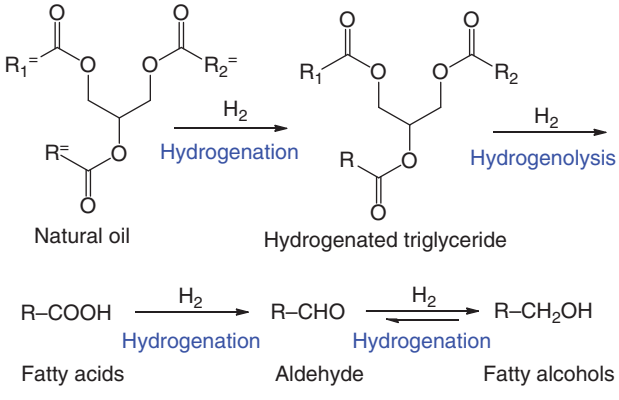

Figure 13.22 Direct transformation of natural to fatty alcohols. Source: Reproduced with permission from Ali et al. [143]; © 2019, Royal Society of Chemistry.

In this reaction, a total of four equivalents of Na are used to convert the ester into the corresponding alcohols. Owing to the risks related with the handling of alkali metals and the huge waste production, the Bouveault–Blanc reduction has been replaced by other processes such as metal hydrides as reducing agents [146]. Typical hydrides employed are lithium aluminum hydride ($LiAlH_4$) or sodium borohydride ($NaBH_4$), which have been successfully applied in the reduction of a large range of esters. Nevertheless, the stoichiometric nature of the reduction reactions led by metal hydrides also produces a lot of waste [147]. In addition, other disadvantages including the tedious workup method and quite harmful handling of these highly reactive metal hydride compounds have been pinpointed [148]. Compared with stoichiometric reduction methods, catalytic processes are more attractive from both environmental and economic perspectives.

The use of molecular hydrogen as reducing agent facilitates the achievement of complete efficiency of 100%. However, the catalytic hydrogenation of carboxylic acids and their esters is quite challenging, in particular due to the low electrophilicity of the carbonyl carbon and the difficulties related with polarizing the carbonyl group from acid derivates [149]. Nevertheless, the catalytic reduction of esters can yield a wide range of useful chemicals or fine synthesis intermediates such as fatty alcohols.

Compared with other derivatives of carboxylic acids, acid anhydrides are the most reactive toward reduction, followed by imides, esters, lactones, free acids, and, finally, amides (Figure 13.23). Therefore, imides, acids, esters, and lactones show different reactivities toward hydrogenation, and the product distribution in the catalytic reaction might be different conclusively based on the extent of the interconversion process. Esters and lactones offer catalytic reduction at harsh conditions with temperatures ranging from 200 to 300 °C and hydrogen pressures of 14–30 MPa [150]. Meanwhile, the side reactions and degradation of the reaction substrates and products can be observed.

Methyl esters such methyl oleate could be selectively hydrogenated to oleyl alcohol in the presence of the $NaBH_4$-reduced Ru–Sn–B/Al_2O_3 (Ru/Sn = 1 : 2) catalyst at 270 °C and 4.4 MPa hydrogen pressure [151]. Under such conditions, 80% methyl oleate conversion and 62% selectivity toward oleyl alcohol were recorded in seven hours. Detailed characterization revealed the importance of an intimate contact between boron and catalytically active Ru phases. Further investigation revealed that the role of the boron promoter was to enhance the electron density of surface Ru species, whereas the presence of Sn favored a high dispersion of metallic Ru in alumina support.

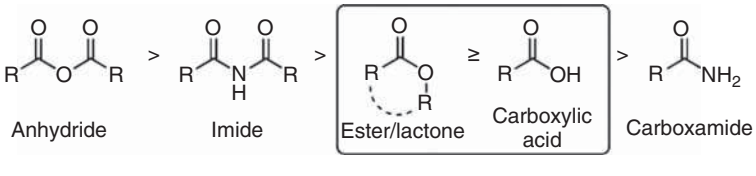

Figure 13.23 Comparison of the order of polarizability of the carbonyl group.

In the proposed reaction mechanism, metallic Ru sites catalyze the H_2 dissociation. However, the adjacent Sn^{2+}/Sn^{4+} Lewis acid sites polarized the carbonyl group of the methyl oleate and promoted the hydride transfer from the adjacent Ru–H sites to generate anionic species. These anionic species could be rapidly hydrogenated to alcohol via the formation of reactive aldehyde intermediate. Simultaneously, the OR moieties adjacent to the carbonyl group are eliminated and converted to fatty alcohol as the final product [152]. Further analyses revealed the involvement of mixed Ru–Sn sites and their importance in the hydrogenation reaction that proceeded via a hemiacetal intermediate (Figure 13.24) [153].

Rh–Sn catalysts have been investigated for the partial hydrogenation of pure methyl laurate ($C_{13}H_{26}O_2$) and methyl palmitate ($C_{17}H_{34}O_2$) esters. The formation of transesterification products was observed in the absence of catalyst and at temperatures above 200 °C [154]. Nevertheless, this effect could be reversed to some extent by employing catalysts suited for the hydrogenation of transesterification products. Notably, the evaluation and comparison of several other transition metals revealed that bimetallic catalysts such as Ru–Co, Ru–Zn, Co–Zn, and Ru–Cu could not efficiently catalyze the hydrogenation of fatty acid methyl ester due to the formation of lauric acid. The importance and participation of solvent and catalyst support in ester reduction were investigated in detail over $Ru/ZrO_2{\cdot}xH_2O$ catalyst (Figure 13.25) [155]. It was revealed that water served as a proton acceptor facilitating the heterolytic H_2 cleavage. Subsequently, the reaction relied on the synergic effect between Zr-bound hydroxyl groups, Ru sites, and water as solvent. Likewise, the hydrogen bonding of the substrate with surface hydroxyl groups (**A**, Figure 13.25) could polarize the carbonyl moiety, thereby facilitating quite difficult hydride insertion step (**C**). The mechanism for hydrogen activation greatly depended on the solvent used. In water, the H_2O molecules serve as base mediators (**D**) that could shift the H^+ formed by the heterolytic cleavage of H_2 to the

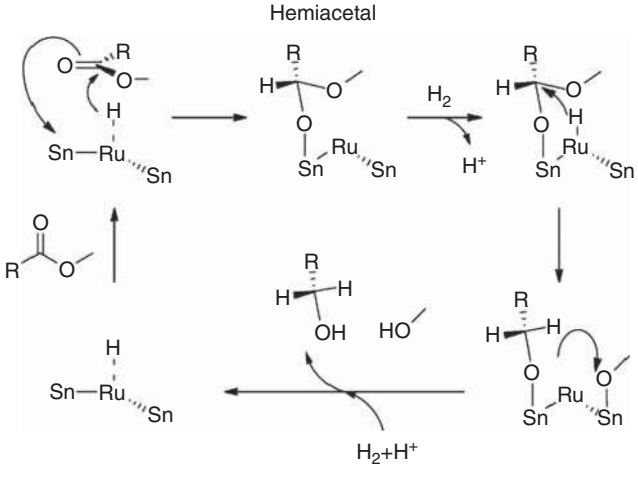

Figure 13.24 Mechanism for methyl oleate hydrogenation to alcohol. Source: Reproduced with permission from Pouilloux et al. [153]; © 1998, Elsevier.

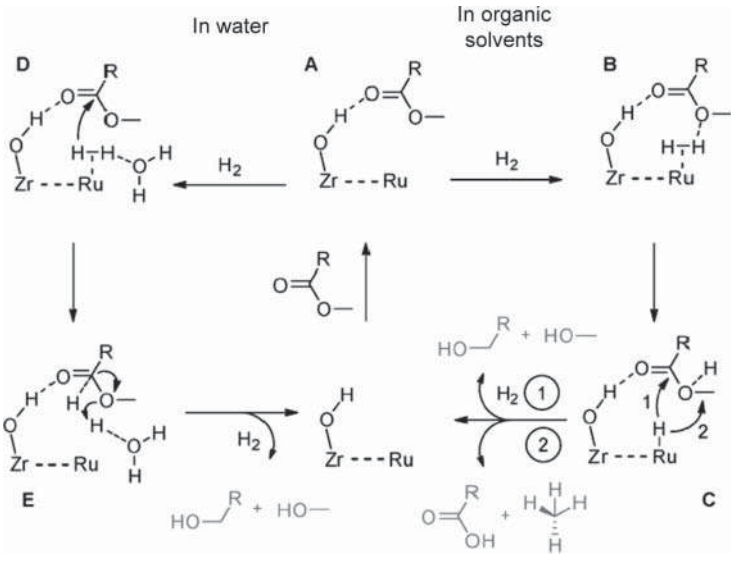

Figure 13.25 Mechanism of methyl propionate hydrogenation over $Ru/ZrO_2 \cdot xH_2O$ catalyst in water or organic solvents. Source: Fan et al. [155].

pre-coordinated substrate molecules (**E**). Thereby, the subsequent hydrogenation of the substrate molecule occurred. When the reaction was performed in an organic phase, the ester functionality itself acted as a base in the heterolytic H_2 cleavage (**B**), making the overall process less efficient. Experimental observations revealed strong promoting effects of polar solvent such as water compared with hexane, different short-chain alcohols, and other diol solvents. A 1-propanol yield of ~95% could be achieved at relatively low temperatures of 150 °C in the aqueous phase.

A series of aluminum-pillared clay-related catalysts were evaluated for the hydrogenation of diesters such as dimethyl adipate [156]. These catalysts showed 95% ester conversion with no selectivity toward diol products in the absence of Ru and Sn. The activity was probably due to a high concentration of surface acid sites in the clay structure. The hydrogenation of diesters can produce a wide range of products as carbonyl groups, which could be transformed to acid, alcohol, and alkane (Figure 13.26). The formation of other products apart from 1,6-hexanediol using Ru-supported aluminum-pillared clay-related catalysts could be suppressed to ~50% by the addition of Ba to reduce the acidity of the clay. The addition of Sn to Ru was very beneficial to enhance the conversion and selectivity toward important cyclic products, such as ε-caprolactone, methyl caproate, and caproic acid. It was speculated that Sn increased 1,6-hexanediol formation on bimetallic Ru–Sn (Ru/Sn = 1/2) catalysts, whereas no diol formation was observed over monometallic Ru catalysts [156, 157].

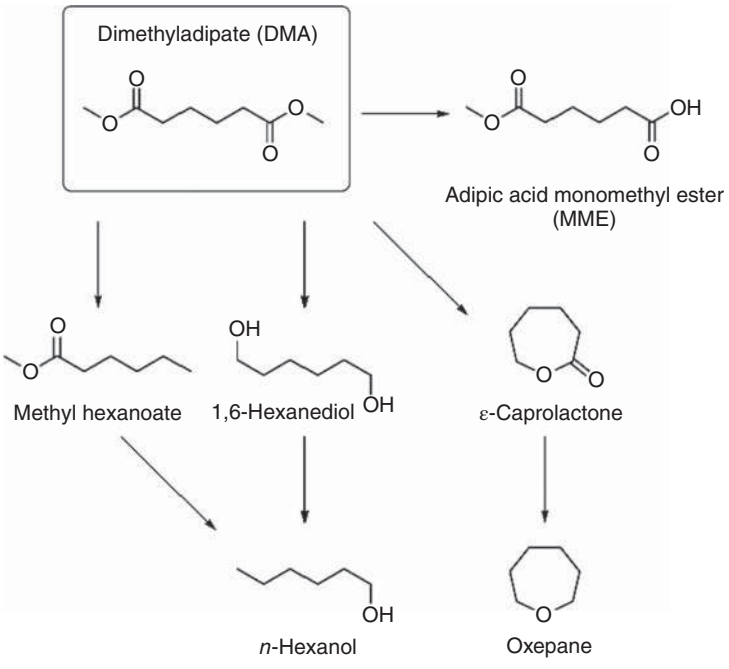

Figure 13.26 Products derived from the hydrogenation of dimethyl adipate.
Source: Reproduced with permission from Figueiredo et al. [156]; © 2009, Elsevier.

13.5.3 Hydrogenation of Fatty Acids

The selective hydrogenation of fatty acids to fatty alcohols showed well-known industrial application. Fatty alcohols have important applications in this regard as plasticizers, surfactants, food additives, cosmetics, and pharmaceuticals. The global demand for fatty alcohols has reached 3.1 million tons per year with a projected growth rate of 3.2% [158]. The well-known non-noble metal catalytic systems for the hydrogenation of fatty acids to fatty alcohols are based on bimetallic Cu–Cr [159]. To achieve high performance, harsh reaction conditions, i.e. temperatures of 250–400 °C and hydrogen pressures of 20–30 MPa, were employed [160]. Besides, the environmental pollution related to the disposal of Cr in these catalytic systems makes them less suitable for large-scale application in industry.

The synthetic routes of fatty alcohols from fatty acids over various heterogeneous catalysts under different reaction conditions are presented in Figure 13.27 [143, 159–164]. In particular, Ru/TiO_2 catalysts are well-known for effective hydrogenation of the C=O bonds in fatty acids. The surface Ti^{3+} defect sites in the TiO_2 support might participate in the hydrogenation of the carbonyl group of the carboxylic acid [165]. Reaction mechanistic study revealed that strong metal–support interactions could stabilize highly dispersed Ru particles for hydrogenation and TiO_2 played an important role in the reaction by polarizing the carbonyl part during hydrogenation. The supports should play key roles in the selective hydrogenation of fatty acids to fatty alcohols (Table 13.6). Experimental results suggested the involvement of metal

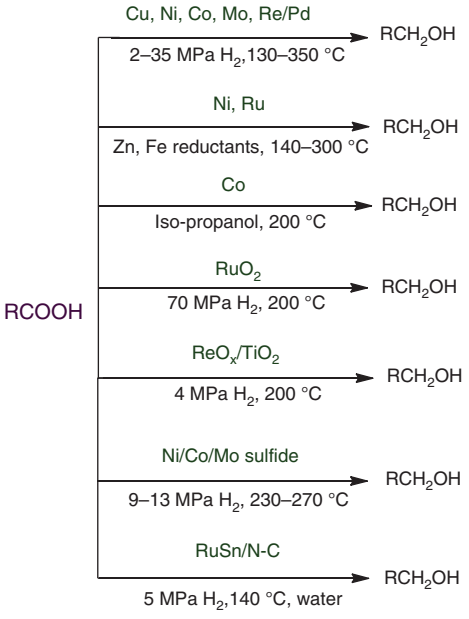

Figure 13.27 Selective hydrogenation of fatty acids to fatty alcohols over heterogeneous catalysts under different conditions.

oxide support in the hydrogenation of carboxylic acid such as acetic acid over Pt catalysts and pointed out that TiO_2 was better than SiO_2, Al_2O_3, and Fe_2O_3 supports [167]. Obviously, the hydrogenation reaction can proceed via the direct involvement and the interaction of carbonyl group with the sites on the reducible oxide surface.

13.6 Summary

In recent decades, the synthesis of new catalysts and their applications for the conversion of lipids into useful products via green routes has remained a major target in the field of catalysis. Supported metal sulfide and sulfur-free metal catalysts were applied to the synthesis of diesel-range hydrocarbons via hydrodeoxygenation of lipids, including individual steps of hydrogenolysis, hydrogenation, decarboxylation, decarbonylation, and hydrogenation–dehydration. Catalytic cracking of lipids yielded gasoline over acidic zeolite via protonation of the unsaturated bonds. During the cracking, gaseous products such as CO_2, CO, and smaller hydrocarbons were observed. Silica–alumina and zeolites are the most feasible catalysts for catalytic cracking of lipids into jet-fuels.

Lipids can be catalytically and selectively hydrogenated to fatty alcohols over Cu- and Ru-based catalysts. Also, they can be converted into alkenes and α-olefins by the alkenolysis using homogeneous catalysts or heterogeneous catalysts. A number of Pd homogeneous catalysts produce olefins at 200 °C along with CO and HCl. Such reaction occurs by the oxidative addition of the acyl chloride to Pd^0, forming an acyl Pd^{II} species. Heterogeneous catalysts are a better choice to catalyze olefin formation from lipids due to their easy separation and better recycling capability. It can

Table 13.6 Synthesis of stearyl alcohol from carboxylic acids and their derivatives over various catalysts.

						Yield (%)					
Catalyst	**Substrate**	***T* (°C)**	**H_2 (MPa)**	**Time (h)**	**Conv. (%)**	**Stearic acid**	**C_{18}-OH**	**C_{17}–C_{18}**	**C_{17}-CHO**	**Ester**	**References**
Co	Oleic acid	200	–	4	100	23.9	–	–	–	49.3	[166]
Co-350	Oleic acid	200	–	4	100	–	91.9	2.5	–	5.7	[166]
Co/CoO	Oleic acid	200	–	4	90	22	2.5	–	–	34.5	[166]
CoO/Co_3O_4	Oleic acid	200	–	4	46.3	–	–	–	–	27.5	[166]
$Co/CoO/Co_3O_4$	Oleic acid	200	–	4	80.9	–	6.1	–	–	21.8	[166]
4% ReO_x/TiO_2	Stearic acid	180	2	2	20	80	16.6	3.5	–	–	[163]
4% ReO_x/TiO_2	Stearic acid	200	2	2	80	20	72	4	2	2	[163]
4% ReO_x/TiO_2	Stearic acid	220	2	2	80	20	70	3	3	4	[163]
4% ReO_x/TiO_2	Stearic acid	200	3	2	80	20	72	4	2	2	[163]
4% ReO_x/TiO_2	Stearic acid	200	4	2	80	20	72	4	2	2	[163]
2.5% Ru 2.5% Sn/NC	Stearic acid	140	5	6	100	–	96	4	–	–	[143]

be expected that in the future, more important and highly desirable products will be catalytically produced from sustainable inexpensive lipid bioresources.

References

1 Wang, D., Ma, B., Wang, B. et al. (2015). One-pot synthesized hierarchical zeolite supported metal nanoparticles for highly efficient biomass conversion. *Chem. Commun.* 51 (82): 15102–15105.

2 Kong, J., He, M., Lercher, J.A., and Zhao, C. (2015). Direct production of naphthenes and paraffins from lignin. *Chem. Commun.* 51 (99): 17580–17583.

3 Arif, A. and Chen, Z. (2020). Direct liquefaction techniques on lignite coal. *Chin. J. Catal.* 41: 375–389.

4 Luo, Z. and Zhao, C. (2016). Mechanistic insights into selective hydrodeoxygenation of lignin-derived β-O-4 linkage to aromatic hydrocarbons in water. *Catal. Sci. Technol.* 6 (10): 3476–3484.

5 Kong, J., Li, B., and Zhao, C. (2016). Tuning Ni nanoparticles and the acid sites of silica-alumina for liquefaction and hydrodeoxygenation of lignin to cyclic alkanes. *RSC Adv.* 6 (76): 71940–71951.

6 Li, B., Li, L., Sun, H., and Zhao, C. (2018). Selectie deoxygenation of aqueous furfural to 2-methylfuran over Cu^0/Cu_2O-SiO_2 sites via a copper phyllosilicate precursor without extraneous gas. *ACS Sustainable Chem. Eng.* 6: 12096–12103.

7 Wu, L., Li, B., and Zhao, C. (2018). Direct synthesis of hydrogen and dimethoxylmethane from methanol on copper/silica catalysts with optimal Cu^+/Cu^0 sites. *ChemCatChem* 10 (5): 1140–1147.

8 Huber, G.W., O'Connor, P., and Corma, A. (2007). Processing biomass in conventional oil refineries: production of high quality diesel by hydrotreating vegetable oils in heavy vacuum oil mixtures. *Appl. Catal., A* 329: 120–129.

9 Gutiérrez, O.Y., Kaufmann, C., and Lercher, J.A. (2011). Influence of potassium on the synthesis of methanethiol from carbonyl sulfide on sulfided Mo/Al_2O_3 catalyst. *ChemCatChem* 3 (9): 1480–1490.

10 Topsøe, H., Clausen, B.S., and Massoth, F.E. (1996). *Hydrotreating Catalysis*, 1–269. Berlin, Heidelberg: Springer-Verlag.

11 Kubička, D. and Kaluža, L. (2010). Deoxygenation of vegetable oils over sulfided Ni, Mo and NiMo catalysts. *Appl. Catal., A* 372 (2): 199–208.

12 Šimáček, P., Kubička, D., Šebor, G. et al. (2010). Fuel properties of hydroprocessed rapeseed oil. *Fuel* 89 (3): 611–615.

13 Smejkal, Q., Smejkalová, L., and Kubička, D. (2009). Thermodynamic balance in reaction system of total vegetable oil hydrogenation. *Chem. Eng. J.* 146 (1): 155–160.

14 Melero, J.A., Iglesias, J., and Morales, G. (2009). Heterogeneous acid catalysts for biodiesel production: current status and future challenges. *Green Chem.* 11 (9): 1285–1308.

15 Gusmao, J., Brodzki, D., Djéga-Mariadassou, G. et al. (1989). Utilization of vegetable oils as an alternative source for diesel-type fuel: hydrocracking on reduced Ni/SiO_2 and sulphided $Ni\text{-}Mo/\gamma\text{-}Al_2O_3$. *Catal. Today* 5 (4): 533–544.

16 Bezergianni, S. and Dimitriadis, A. (2013). Temperature effect on co-hydroprocessing of heavy gas oil–waste cooking oil mixtures for hybrid diesel production. *Fuel* 103: 579–584.

17 Bezergianni, S., Kalogianni, A., and Dimitriadis, A. (2012). Catalyst evaluation for waste cooking oil hydroprocessing. *Fuel* 93: 638–641.

18 Bezergianni, S., Dimitriadis, A., Kalogianni, A. et al. (2011). Toward hydrotreating of waste cooking oil for biodiesel production. Effect of pressure, H_2/oil ratio, and liquid hourly space velocity. *Ind. Eng. Chem. Res.* 50 (7): 3874–3879.

19 Karonis, D., Siagos, I.Z., and Bezergianni, S. (2018). Characterization of hydroprocessed used cooking oils as high cetane number blending component for automotive diesel. SAE Technical Paper.

20 Bezergianni, S., Dimitriadis, A., Kalogianni, A. et al. (2010). Hydrotreating of waste cooking oil for biodiesel production. Part I: effect of temperature on product yields and heteroatom removal. *Bioresour. Technol.* 101 (17): 6651–6656.

21 Bezergianni, S., Voutetakis, S., and Kalogianni, A. (2009). Catalytic hydrocracking of fresh and used cooking oil. *Ind. Eng. Chem. Res.* 48 (18): 8402–8406.

22 Bezergianni, S. and Kalogianni, A. (2009). Hydrocracking of used cooking oil for biofuels production. *Bioresour. Technol.* 100 (17): 3927–3932.

23 Zhang, Y., Dubé, M.A., McLean, D. et al. (2003). Biodiesel production from waste cooking oil: 2. Economic assessment and sensitivity analysis. *Bioresour. Technol.* 90 (3): 229–240.

24 Bezergianni, S., Kalogeras, K., and Pilavachi, P.A. (2011). On maximizing biodiesel mixing ratio based on final product specifications. *Comput. Chem. Eng.* 35 (5): 936–942.

25 Kalogeras, K., Bezergianni, S., Kazantzi, V. et al. (2010). On the prediction of properties for diesel/biodiesel mixtures featuring new environmental considerations. *Comput. Aided Chem. Eng.* 28: 973–978.

26 Choudhary, T.V. and Phillips, C.B. (2011). Renewable fuels via catalytic hydrodeoxygenation. *Appl. Catal., A* 397 (1–2): 1–12.

27 Donnis, B., Egeberg, R.G., Blom, P. et al. (2009). Hydroprocessing of bio-oils and oxygenates to hydrocarbons. Understanding the reaction routes. *Top. Catal.* 52 (3): 229–240.

28 Lapuerta, M., Villajos, M., Agudelo, J.R. et al. (2011). Key properties and blending strategies of hydrotreated vegetable oil as biofuel for diesel engines. *Fuel Process. Technol.* 92 (12): 2406–2411.

29 Snåre, M., Kubičková, I., Mäki-Arvela, P. et al. (2006). Heterogeneous catalytic deoxygenation of stearic acid for production of biodiesel. *Ind. Eng. Chem. Res.* 45 (16): 5708–5715.

30 Snåre, M., Kubičková, I., Mäki-Arvela, P. et al. (2008). Catalytic deoxygenation of unsaturated renewable feedstocks for production of diesel fuel hydrocarbons. *Fuel* 87 (6): 933–945.

31 Immer, J.G., Kelly, M.J., and Lamb, H.H. (2010). Catalytic reaction pathways in liquid-phase deoxygenation of C_{18} free fatty acids. *Appl. Catal., A* 375 (1): 134–139.

32 Maier, W.F., Roth, W., Thies, I. et al. (1982). Hydrogenolysis, IV. Gas phase decarboxylation of carboxylic acids. *Chem. Ber.* 115 (2): 808–812.

33 Kubičková, I., Snåre, M., Eränen, K. et al. (2005). Hydrocarbons for diesel fuel via decarboxylation of vegetable oils. *Catal. Today* 106 (1–4): 197–200.

34 Immer, J.G. and Lamb, H. (2010). Fed-batch catalytic deoxygenation of free fatty acids. *Energy Fuels* 24 (10): 5291–5299.

35 Ping, E.W., Wallace, R., Pierson, J. et al. (2010). Highly dispersed palladium nanoparticles on ultra-porous silica mesocellular foam for the catalytic decarboxylation of stearic acid. *Microporous Mesoporous Mater.* 132 (1–2): 174–180.

36 Ping, E.W., Pierson, J., Wallace, R. et al. (2011). On the nature of the deactivation of supported palladium nanoparticle catalysts in the decarboxylation of fatty acids. *Appl. Catal., A* 396 (1–2): 85–90.

37 Arend, M., Nonnen, T., Hoelderich, W.F. et al. (2011). Catalytic deoxygenation of oleic acid in continuous gas flow for the production of diesel-like hydrocarbons. *Appl. Catal., A* 399 (1–2): 198–204.

38 Fu, J., Lu, X., and Savage, P.E. (2011). Hydrothermal decarboxylation and hydrogenation of fatty acids over Pt/C. *ChemSusChem* 4 (4): 481–486.

39 Ford, J.P., Immer, J.G., and Lamb, H.H. (2012). Palladium catalysts for fatty acid deoxygenation: influence of the support and fatty acid chain length on decarboxylation kinetics. *Top. Catal.* 55 (3–4): 175–184.

40 Zhang, J. and Zhao, C. (2016). Development of a bimetallic Pd-Ni/HZSM-5 catalyst for the tandem limonene dehydrogenation and fatty acid deoxygenation to alkanes and arenes for use as bio-jet fuel. *ACS Catal.* 6 (7): 4512–4525.

41 Ma, B., Yi, X., Chen, L. et al. (2016). Interconnected hierarchical HUSY zeolite-loaded Ni nano-particles probed for hydrodeoxygenation of fatty acids, fatty esters, and palm oil. *J. Mater. Chem. A* 4 (29): 11330–11341.

42 Cui, H., Zhang, J., Luo, Z. et al. (2016). Mechanisms into dehydroaromatization of bio-derived limonene to *p*-cymene over Pd/HZSM-5 in the presence and absence of H_2. *RSC Adv.* 6 (71): 66695–66704.

43 Snåre, M., Kubičková, I., Mäki-Arvela, P. et al. (2007). Production of diesel fuel from renewable feeds: kinetics of ethyl stearate decarboxylation. *Chem. Eng. J.* 134 (1–3): 29–34.

44 Mäki-Arvela, P., Kubickova, I., Snåre, M. et al. (2007). Catalytic deoxygenation of fatty acids and their derivatives. *Energy Fuels* 21 (1): 30–41.

45 Lestari, S., Simakova, I., Tokarev, A. et al. (2008). Synthesis of biodiesel via deoxygenation of stearic acid over supported Pd/C catalyst. *Catal. Lett.* 122 (3–4): 247–251.

46 Rozmysłowicz, B., Mäki-Arvela, P., Lestari, S. et al. (2010). Catalytic deoxygenation of tall oil fatty acids over a palladium-mesoporous carbon catalyst: a new source of biofuels. *Top. Catal.* 53 (15–18): 1274–1277.

47 Ma, B. and Zhao, C. (2015). High-grade diesel production by hydrodeoxygenation of palm oil over a hierarchically structured Ni/HBEA catalyst. *Green Chem.* 17 (3): 1692–1701.

48 Peng, B., Yao, Y., Zhao, C. et al. (2012). Towards quantitative conversion of microalgae oil to diesel-range alkanes with bifunctional catalysts. *Angew. Chem. Int. Ed.* 51 (9): 2072–2075.

49 Lestari, S., Maki-Arvela, P., Bernas, H. et al. (2009). Catalytic deoxygenation of stearic acid in a continuous reactor over a mesoporous carbon-supported Pd catalyst. *Energy Fuels* 23 (8): 3842–3845.

50 Ma, B., Hu, J., Wang, Y. et al. (2015). Ni nanoparticles encapsulated into mesoporous single-crystalline HBEA: application for drainage oil hydrodeoxygenation to diesel. *Green Chem.* 17 (9): 4610–4617.

51 Peng, B., Yuan, X., Zhao, C. et al. (2012). Stabilizing catalytic pathways via redundancy: selective reduction of microalgae oil to alkanes. *J. Am. Chem. Soc.* 134 (22): 9400–9405.

52 Peng, B., Zhao, C., Kasakov, S. et al. (2013). Manipulating catalytic pathways: deoxygenation of palmitic acid on multifunctional catalysts. *Chem. Eur. J.* 19 (15): 4732–4741.

53 Morgan, T., Grubb, D., Santillan-Jimenez, E. et al. (2010). Conversion of triglycerides to hydrocarbons over supported metal catalysts. *Top. Catal.* 53 (11–12): 820–829.

54 Lestari, S., Mäki-Arvela, P., Simakova, I. et al. (2009). Catalytic deoxygenation of stearic acid and palmitic acid in semibatch mode. *Catal. Lett.* 130 (1–2): 48–51.

55 Song, W., Zhao, C., and Lercher, J.A. (2013). Importance of size and distribution of Ni nanoparticles for the hydrodeoxygenation of microalgae oil. *Chem. Eur. J.* 19 (30): 9833–9842.

56 Hasan, M.A., Zaki, M.I., and Pasupulety, L. (2003). Oxide-catalyzed conversion of acetic acid into acetone: an FTIR spectroscopic investigation. *Appl. Catal., A* 243 (1): 81–92.

57 Hendren, T.S. and Dooley, K.M. (2003). Kinetics of catalyzed acid/acid and acid/aldehyde condensation reactions to non-symmetric ketones. *Catal. Today* 85 (2–4): 333–351.

58 Dooley, K.M., Bhat, A.K., Plaisance, C.P. et al. (2007). Ketones from acid condensation using supported CeO_2 catalysts: effect of additives. *Appl. Catal., A* 320: 122–133.

59 Do, P.T., Chiappero, M., Lobban, L. et al. (2009). Catalytic deoxygenation of methyl-octanoate and methyl-stearate on Pt/Al_2O_3. *Catal. Lett.* 130 (1–2): 9–18.

60 Colson, A. (1999). Formation of ethylene hydrocarbon from esters. *C.R. Acad. Sci., Ser. IIc: Chim.* 147: 1054–1057.

61 Zhao, C., Brück, T., and Lercher, J.A. (2013). Catalytic deoxygenation of microalgae oil to green hydrocarbons. *Green Chem.* 15 (7): 1720–1739.

62 Simakova, I., Simakova, O., Mäki-Arvela, P. et al. (2010). Decarboxylation of fatty acids over Pd supported on mesoporous carbon. *Catal. Today* 150 (1–2): 28–31.

63 Onyestyák, G., Harnos, S., Szegedi, Á. et al. (2012). Sunflower oil to green diesel over Raney-type Ni-catalyst. *Fuel* 102: 282–288.

64 Luo, Z., Zheng, Z., Wang, Y. et al. (2016). Hydrothermally stable Ru/HZSM-5-catalyzed selective hydrogenolysis of lignin-derived substituted phenols to bio-arenes in water. *Green Chem.* 18 (21): 5845–5858.

65 Luterbacher, J.S., Rand, J.M., Alonso, D.M. et al. (2014). Nonenzymatic sugar production from biomass using biomass-derived γ-valerolactone. *Science* 343 (6168): 277–280.

66 Ragauskas, A.J., Williams, C.K., Davison, B.H. et al. (2006). The path forward for biofuels and biomaterials. *Science* 311 (5760): 484–489.

67 Dos Anjos, J.R.S., Gonzalez, W.D.A., Lam, Y.L. et al. (1983). Catalytic decomposition of vegetable oil. *Appl. Catal.* 5 (3): 299–308.

68 Leung, A., Boocock, D.G.B., and Konar, S.K. (1995). Pathway for the catalytic conversion of carboxylic acids to hydrocarbons over activated alumina. *Energy Fuels* 9 (5): 913–920.

69 Idem, R.O., Katikaneni, S.P.R., and Bakhshi, N.N. (1997). Catalytic conversion of canola oil to fuels and chemicals: roles of catalyst acidity, basicity and shape selectivity on product distribution. *Fuel Process. Technol.* 51 (1–2): 101–125.

70 Di Renzo, F. and Fajula, F. (2005). Introduction to molecular sieves: trends of evolution of the zeolite community. *Stud. Surf. Sci. Catal.* 157: 1–12.

71 Twaiq, F.A., Zabidi, N.A.M., and Bhatia, S. (1999). Catalytic conversion of palm oil to hydrocarbons: performance of various zeolite catalysts. *Ind. Eng. Chem. Res.* 38 (9): 3230–3237.

72 Zhang, J. and Zhao, C. (2015). A new approach for bio-jet fuel generation from palm oil and limonene in the absence of hydrogen. *Chem. Commun.* 51 (97): 17249–17252.

73 Katikaneni, S.P.R., Adjaye, J.D., and Bakhshi, N.N. (1995). Catalytic conversion of canola oil to fuels and chemicals over various cracking catalysts. *Can. J. Chem. Eng.* 73 (4): 484–497.

74 Benson, T.J., Hernandez, R., White, M.G. et al. (2008). Research article heterogeneous cracking of an-unsaturated fatty acid and reaction intermediates on HZSM-5 catalyst. *Clean* 36: 652–656.

75 Twaiq, F.A.A., Mohamad, A.R., and Bhatia, S. (2004). Performance of composite catalysts in palm oil cracking for the production of liquid fuels and chemicals. *Fuel Process. Technol.* 85 (11): 1283–1300.

76 Katikaneni, S.P.R., Adjaye, J.D., Idem, R.O. et al. (1996). Catalytic conversion of canola oil over potassium-impregnated HZSM-5 catalysts: C_2–C_4 olefin production and model reaction studies. *Ind. Eng. Chem. Res.* 35 (10): 3332–3346.

77 Ooi, Y.S., Zakaria, R., Mohamed, A.R. et al. (2005). Catalytic conversion of fatty acids mixture to liquid fuel and chemicals over composite microporous/mesoporous catalysts. *Energy Fuels* 19 (3): 736–743.

78 Ooi, Y.S., Zakaria, R., Mohamed, A.R. et al. (2004). Catalytic cracking of used palm oil and palm oil fatty acids mixture for the production of liquid fuel: kinetic modeling. *Energy Fuels* 18 (5): 1555–1561.

79 Degnan, T.F. (2000). Applications of zeolites in petroleum refining. *Top. Catal.* 13 (4): 349–356.

80 Tanabe, K. and Hölderich, W.F. (1999). Industrial application of solid acid–base catalysts. *Appl. Catal., A* 181 (2): 399–434.

81 Stadlbauer, E.A., Altensen, R., Bojanowski, S. et al. (2006). Production of hydrocarbons from animal fat by thermocatalytic cracking; Herstellung von Kohlenwasserstoffen aus Tierfett durch Thermokatalytisches Spalten.

82 Benson, T.J., Hernandez, R., French, W.T. et al. (2009). Elucidation of the catalytic cracking pathway for unsaturated mono-, di-, and triacylglycerides on solid acid catalysts. *J. Mol. Catal. A: Chem.* 303 (1–2): 117–123.

83 Benson, T.J., Hernandez, R., White, M.G. et al. (2008). Heterogeneous cracking of an unsaturated fatty acid and reaction intermediates on H-ZSM-5 catalyst. *Clean Soil Air Water* 36: 652–656.

84 Kloprogge, J.T., Duong, L.V., and Frost, R.L. (2005). A review of the synthesis and characterisation of pillared clays and related porous materials for cracking of vegetable oils to produce biofuels. *Environ. Geol.* 47 (7): 967–981.

85 Vinh, T.Q., Loan, N.T.T., Yang, X.Y. et al. (2011). Preparation of bio-fuels by catalytic cracking reaction of vegetable oil sludge. *Fuel* 90 (3): 1069–1075.

86 Vedrine, J.C., Dejaifve, P., Garbowski, E.D. et al. (1980). Aromatics formation from methanol and light olefins conversions on HZSM-5 zeolite: mechanism and intermediate species. *Stud. Surf. Sci. Catal.* 5: 29–37.

87 Ong, Y.K. and Bhatia, S. (2010). The current status and perspectives of biofuel production via catalytic cracking of edible and non-edible oils. *Energy* 35 (1): 111–119.

88 Wojciechowski, B.W. (1998). The reaction mechanism of catalytic cracking: quantifying activity, selectivity, and catalyst decay. *Catal. Rev.* 40 (3): 209–328.

89 Cumming, K.A. and Wojciechowski, B.W. (1996). Hydrogen transfer, coke formation, and catalyst decay and their role in the chain mechanism of catalytic cracking. *Catal. Rev.* 38 (1): 101–157.

90 Forzatti, P. and Lietti, L. (1999). Catalyst deactivation. *Catal. Today* 52 (2–3): 165–181.

91 Ma, B., Cui, H., Wang, D. et al. (2017). Controllable hydrothermal synthesis of Ni/H-BEA with a hierarchical core–shell structure and highly enhanced biomass hydrodeoxygenation performance. *Nanoscale* 9 (18): 5986–5995.

92 Wu, L., Li, L., Li, B. et al. (2017). Selective conversion of coconut oil to fatty alcohols in methanol over a hydrothermally prepared Cu/SiO_2 catalyst without extraneous hydrogen. *Chem. Commun.* 53 (45): 6152–6155.

93 Ma, B., Cui, H., and Zhao, C. (2017). A nickel-phyllosilicate core–echinus catalyst via a green and base additive free hydrothermal approach for hydrogenation reactions. *Chem. Commun.* 53 (75): 10358–10361.

94 Luo, Z., Zheng, Z., Li, L. et al. (2017). Bimetallic Ru–Ni catalyzed aqueous-phase guaiacol hydrogenolysis at low H_2 pressures. *ACS Catal.* 7 (12): 8304–8313.

95 Zheng, Z., Luo, Z., and Zhao, C. (2018). Morphologically cross-shaped Ru/HZSM-5 catalyzes tandem hydrogenolysis of guaiacol to benzene in water. *ChemCatChem* 10 (6): 1376–1384.

96 Kumar, R., Rana, B.S., Tiwari, R. et al. (2010). Hydroprocessing of jatropha oil and its mixtures with gas oil. *Green Chem.* 12 (12): 2232–2239.

97 Lu, Y., Ma, B., and Zhao, C. (2018). Integrated production of bio-jet fuel containing lignin-derived arenes via lipid deoxygenation. *Chem. Commun.* 54 (70): 9829–9832.

98 Dawes, G.J.S., Scott, E.L., Le Notre, J. et al. (2015). Deoxygenation of bio-based molecules by decarboxylation and decarbonylation—a review on the role of heterogeneous, homogeneous and bio-catalysis. *Green Chem.* 17 (6): 3231–3250.

99 Higman, C.S., Lummiss, J.A.M., and Fogg, D.E. (2016). Olefin metathesis at the dawn of implementation in pharmaceutical and specialty-chemicals manufacturing. *Angew. Chem. Int. Ed.* 55 (11): 3552–3565.

100 Chikkali, S. and Mecking, S. (2012). Refining of plant oils to chemicals by olefin metathesis. *Angew. Chem. Int. Ed.* 51 (24): 5802–5808.

101 van der Klis, F., Le Nôtre, J., Blaauw, R. et al. (2012). Renewable linear alpha olefins by selective ethenolysis of decarboxylated unsaturated fatty acids. *Eur. J. Lipid Sci. Technol.* 114 (8): 911–918.

102 Tsuji, J. and Ohno, K. (1968). Organic syntheses by means of noble metal compounds. XXXIV. Carbonylation and decarbonylation reactions catalyzed by palladium. *J. Am. Chem. Soc.* 90 (1): 94–98.

103 Tsuji, J. and Kiyotaka, O. (1969). Decarbonylation reactions using transition metal compounds. *Synthesis* 04: 157–169.

104 Foglia, T.A. and Barr, P.A. (1976). Decarbonylation dehydration of fatty acids to alkenes in the presence of transition metal complexes. *J. Am. Oil Chem. Soc.* 53 (12): 737–741.

105 Miller, J.A., Nelson, J.A., and Byrne, M.P. (1993). A highly catalytic and selective conversion of carboxylic acids to 1-alkenes of one less carbon atom. *J. Org. Chem.* 58 (1): 18–20.

106 Chatterjee, A., Eliasson, S.H.H., and Jensen, V.R. (2018). Selective production of linear α-olefins via catalytic deoxygenation of fatty acids and derivatives. *Catal. Sci. Technol.* 8 (6): 1487–1499.

107 Kraus, G.A. and Riley, S. (2012). A large-scale synthesis of α-olefins and α, ω-dienes. *Synthesis* 44 (19): 3003–3005.

108 Gooßen, L.J. and Rodríguez, N. (2004). A mild and efficient protocol for the conversion of carboxylic acids to olefins by a catalytic decarbonylative elimination reaction. *Chem. Commun.* 6: 724–725.

109 Le Nôtre, J., Scott, E.L., Franssen, M.C.R. et al. (2010). Selective preparation of terminal alkenes from aliphatic carboxylic acids by a palladium-catalysed decarbonylation–elimination reaction. *Tetrahedron Lett.* 51 (29): 3712–3715.

110 Liu, Y., Kim, K.E., Herbert, M.B. et al. (2014). Palladium-catalyzed decarbonylative dehydration of fatty acids for the production of linear alpha olefins. *Adv. Synth. Catal.* 356 (1): 130–136.

111 Liu, Y., Virgil, S.C., Grubbs, R.H. et al. (2015). Palladium-catalyzed decarbonylative dehydration for the synthesis of α-vinyl carbonyl compounds and total synthesis of (−)-aspewentins A, B, and C. *Angew. Chem. Int. Ed.* 54 (40): 11800–11803.

112 Ortuño, M.A. and López, N. (2018). Creating cavities at palladium–phosphine interfaces for enhanced selectivity in heterogeneous biomass conversion. *ACS Catal.* 8 (7): 6138–6145.

113 John, A., Dereli, B., Ortuño, M.A. et al. (2017). Selective decarbonylation of fatty acid esters to linear α-olefins. *Organometallics* 36 (15): 2956–2964.

114 Chatterjee, A., Hopen Eliasson, S.H., Törnroos, K.W. et al. (2016). Palladium precatalysts for decarbonylative dehydration of fatty acids to linear alpha olefins. *ACS Catal.* 6 (11): 7784–7789.

115 Maetani, S., Fukuyama, T., Suzuki, N. et al. (2011). Efficient iridium-catalyzed decarbonylation reaction of aliphatic carboxylic acids leading to internal or terminal alkenes. *Organometallics* 30 (6): 1389–1394.

116 Ternel, J., Léger, B., Monflier, E. et al. (2018). Amines as effective ligands in iridium-catalyzed decarbonylative dehydration of biosourced substrates. *Catal. Sci. Technol.* 8 (15): 3948–3953.

117 Knothe, G., Steidley, K.R., Moser, B.R. et al. (2017). Decarboxylation of fatty acids with triruthenium dodecacarbonyl: influence of the compound structure and analysis of the product mixtures. *ACS Omega* 2 (10): 6473–6480.

118 Gao, Y., Ou, Y., and Gooßen, L.J. (2019). Pd-catalyzed synthesis of vinyl arenes from aryl halides and acrylic acid. *Chem. Eur. J.* 25 (37): 8709–8712.

119 Doll, K.M., Bantchev, G.B., Walter, E.L. et al. (2017). Parameters governing ruthenium sawhorse-based decarboxylation of oleic acid. *Ind. Eng. Chem. Res.* 56 (4): 864–871.

120 John, A., Miranda, M.O., Ding, K. et al. (2016). Nickel catalysts for the dehydrative decarbonylation of carboxylic acids to alkenes. *Organometallics* 35 (14): 2391–2400.

121 John, A., Hillmyer, M.A., and Tolman, W.B. (2017). Anhydride-additive-free nickel-catalyzed deoxygenation of carboxylic acids to olefins. *Organometallics* 36 (3): 506–509.

122 Maetani, S., Fukuyama, T., Suzuki, N. et al. (2012). Iron-catalyzed decarbonylation reaction of aliphatic carboxylic acids leading to α-olefins. *Chem. Commun.* 48 (19): 2552–2554.

123 Ternel, J., Lebarbé, T., Monflier, E. et al. (2015). Catalytic decarbonylation of bio-sourced substrates. *ChemSusChem* 8 (9): 1585–1592.

124 Li, Z., Gentry, Z., Murphy, B. et al. (2019). Scalable synthesis of orthogonally protected β-methyllanthionines by indium (III)-mediated ring opening of aziridines. *Org. Lett.* 21 (7): 2200–2203.

125 Zachos, I., Gaßmeyer, S.K., Bauer, D. et al. (2015). Photobiocatalytic decarboxylation for olefin synthesis. *Chem. Commun.* 51 (10): 1918–1921.

126 Miranda, M.O. (2014). *Polymerization kinetics of cyclic esters by metal alkoxide complexes and catalystic decarbonylation of bio-drived carboxylic acids to commodity alkenes*. University of Minnesota.

127 Sheldon, R.A., Arends, I., Hanefeld, U. (2007). *Green Chemistry and Catalysis*. Wiley.

128 Choudary, B.M., Kantam, M.L., Neeraja, V. et al. (2001). Layered double hydroxide fluoride: a novel solid base catalyst for C—C bond formation. *Green Chem.* 3 (5): 257–260.

129 Schlögl, R. (2015). Heterogeneous catalysis. *Angew. Chem. Int. Ed.* 54 (11): 3465–3520.

130 Lopez-Ruiz, J.A., Pham, H.N., Datye, A.K. et al. (2015). Reactivity and stability of supported Pd nanoparticles during the liquid-phase and gas-phase decarbonylation of heptanoic acid. *Appl. Catal., A* 504: 295–307.

131 Lopez-Ruiz, J.A. and Davis, R.J. (2014). Decarbonylation of heptanoic acid over carbon-supported platinum nanoparticles. *Green Chem.* 16 (2): 683–694.

132 Stern, R. and Hillion, G. (1985). Process for manufacturing a linear olefin from a saturated fatty acid or fatty acid ester. US Patent 4, 554, 397, 19 November 1985.

133 Wang, D., Hakim, S.H., Alonso, D.M. et al. (2013). A highly selective route to linear alpha olefins from biomass-derived lactones and unsaturated acids. *Chem. Commun.* 49 (63): 7040–7042.

134 Thomas, S.J.M. (2010). The advantages of exploring the interface between heterogeneous and homogeneous catalysis. *ChemCatChem* 2 (2): 127–132.

135 Severn, J.R., Chadwick, J.C., Duchateau, R. et al. (2005). "Bound but not gagged" immobilizing single-site α-olefin polymerization catalysts. *Chem. Rev.* 105 (11): 4073–4147.

136 Lu, J. and Toy, P.H. (2009). Organic polymer supports for synthesis and for reagent and catalyst immobilization. *Chem. Rev.* 109 (2): 815–838.

137 Kuiper, J. (1981). Process for the selective hydrogenation of triglyceride oils with a metallic catalyst in the presence of ammonia. US Patent 4, 278, 609, 14 July 1981.

138 Qualeatti, G.M. and Arena, B.J. (1985). Selective reduction of fatty materials using a supported group VIII metal in eggshell distribution. US Patent 4, 519, 951, 28 May 1985.

139 Bouveault, L. and Blanc, G. (1903). Preparation of primary alcohols by means of the corresponding acids. *Compt. Rend* 136: 1676–1678.

140 Pritchard, J., Filonenko, G.A., van Putten, R. et al. (2015). Heterogeneous and homogeneous catalysis for the hydrogenation of carboxylic acid derivatives: history, advances and future directions. *Chem. Soc. Rev.* 44 (11): 3808–3833.

141 Pohl, J., Carduck, F.J., and Goebel, G. (1989). Acid-resistant catalysts for the direct hydrogenation of fatty acids to fatty alcohols. US Patent 4, 855, 273, 8 August 1989.

142 Turek, T., Trimm, D.L., and Cant, N.W. (1994). The catalytic hydrogenolysis of esters to alcohols. *Catal. Rev. Sci. Eng.* 36 (4): 645–683.

143 Ali, A., Li, B., Lu, Y. et al. (2019). Highly selective and low-temperature hydrothermal conversion of natural oils to fatty alcohols. *Green Chem.* 21: 3059–3064.

144 Luo, Z., Bing, Q., Kong, J. et al. (2018). Mechanism of supported Ru_3Sn_7 nanocluster-catalyzed selective hydrogenation of coconut oil to fatty alcohols. *Catal. Sci. Technol.* 8 (5): 1322–1332.

145 Li, J.J. and Corey, E.J. (2007). *Name Reactions of Functional Group Transformations*. Wiley.

146 Bodnar, B.S. and Vogt, P.F. (2009). An improved bouveault–blanc ester reduction with stabilized alkali metals. *J. Org. Chem.* 74 (6): 2598–2600.

147 Smith, A.M. and Whyman, R. (2014). Review of methods for the catalytic hydrogenation of carboxamides. *Chem. Rev.* 114 (10): 5477–5510.

148 Urben, P.G. (2017). *Bretherick's Handbook of Reactive Chemical Hazards*. Elsevier.

149 Clayden, J., Warren, S., Greeves, N. et al. (2000). Reactions of enolates with aldehydes and ketones: the aldol reaction. *Org. Chem.* 691–694.

150 Adkins, H. and Connor, R. (1931). The catalytic hydrogenation of organic compounds over copper chromite. *J. Am. Chem. Soc.* 53 (3): 1091–1095.

151 Deshpande, V.M., Patterson, W.R., and Narasimhan, C.S. (1990). Studies on ruthenium-tin boride catalysts I. characterization. *J. Catal.* 121 (1): 165–173.

152 Deshpande, V.M., Ramnarayan, K., and Narasimhan, C.S. (1990). Studies on ruthenium-tin boride catalysts II. Hydrogenation of fatty acid esters to fatty alcohols. *J. Catal.* 121 (1): 174–182.

153 Pouilloux, Y., Autin, F., Guimon, C. et al. (1998). Hydrogenation of fatty esters over ruthenium–tin catalysts; characterization and identification of active centers. *J. Catal.* 176 (1): 215–224.

154 Miyake, T., Makino, T., Taniguchi, S. et al. (2009). Alcohol synthesis by hydrogenation of fatty acid methyl esters on supported Ru–Sn and Rh–Sn catalysts. *Appl. Catal., A* 364 (1–2): 108–112.

155 Fan, G., Zhou, Y., Fu, H. et al. (2011). Highly efficient hydrogenation of methyl propionate to propanol over hydrous zirconia supported ruthenium. *Chin. J. Chem.* 29 (2): 229–236.

156 Figueiredo, F.C.A., Jordão, E., Landers, R. et al. (2009). Acidity control of ruthenium pillared clay and its application as a catalyst in hydrogenation reactions. *Appl. Catal., A* 371 (1–2): 131–141.

157 dos Santos, S.M., Silva, A.M., Jordão, E. et al. (2005). Performance of RuSn catalysts supported on different oxides in the selective hydrogenation of dimethyl adipate. *Catal. Today* 107: 250–257.

158 Zhang, Z., Zhou, F., Chen, K. et al. (2017). Catalytic *in situ* hydrogenation of fatty acids into fatty alcohols over Cu-based catalysts with methanol in hydrothermal media. *Energy Fuels* 31 (11): 12624–12632.

159 Church, J.M. and Abdel-Gelil, M.A. (1957). Catalytic hydrogenation of methyl laurate to lauryl alcohol. *Ind. Eng. Chem.* 49 (5): 813–817.

160 Voeste, T. and Buchold, H. (1984). Production of fatty alcohols from fatty acids. *J. Am. Oil Chem. Soc.* 61 (2): 350–352.

161 Tan, X., Wang, Y., Liu, Y. et al. (2015). Highly efficient tetradentate ruthenium catalyst for ester reduction: especially for hydrogenation of fatty acid esters. *Org. Lett.* 17 (3): 454–457.

162 Carnahan, J.E., Ford, T.A., Gresham, W.F. et al. (1955). Ruthenium-catalyzed hydrogenation of acids to alcohols. *J. Am. Chem. Soc.* 77 (14): 3766–3768.

163 Rozmysłowicz, B., Kirilin, A., Aho, A. et al. (2015). Selective hydrogenation of fatty acids to alcohols over highly dispersed ReO_x/TiO_2 catalyst. *J. Catal.* 328: 197–207.

164 Potts, T.M., Durant, K., Hestekin, J. et al. (2014). Catalytic production of 1-octadecanol from octadecanoic acid by hydrotreating in a plug flow reactor. *J. Am. Oil Chem. Soc.* 91 (9): 1643–1650.

165 Mendes, M.J., Santos, O.A.A., Jordao, E. et al. (2001). Hydrogenation of oleic acid over ruthenium catalysts. *Appl. Catal., A* 217 (1–2): 253–262.

166 Wang, J., Nie, R., Xu, L. et al. (2019). Catalytic transfer hydrogenation of oleic acid to octadecanol over magnetic recoverable cobalt catalysts. *Green Chem.* 21 (2): 314–320.

167 Rachmady, W. and Vannice, M.A. (2000). Acetic acid hydrogenation over supported platinum catalysts. *J. Catal.* 192 (2): 322–334.

14

Lignin Upgrading

Yong Guo and Yanqin Wang

East China University of Science and Technology, Shanghai Key Laboratory of Functional Materials Chemistry, Research Institute of Industrial Catalysis, School of Chemistry and Molecular Engineering, No. 130 Meilong Road, Shanghai, 200237, P. R. China

14.1 Introduction

Biomass is the only renewable organic carbon resource on earth. It is a promising resource from which to obtain fuels and carbon-containing chemicals, especially in the context of the increasingly severe climate change, because biomass is considered as a carbon neutral resource [1]. In the utilization of biomass, the biorefinery of lignocellulose has been paid significant attention, because it is most abundant among the various biomass resources available. Lignocellulose comprises three dominant components, cellulose, hemicellulose, and lignin, which is constituted by C6 sugar, C6/C5 sugars, and aromatic monomers, respectively. In an ideal lignocellulosic biorefinery, it is expected to fractionate the lignocellulose into its three primary components with high efficiency and then convert them into fuels or chemicals separately.

In the concept of lignocellulosic biorefinery, the utilization of lignin is very important because it is the most abundant aromatic carbon resource in nature and accounts for 10–35% by weight and up to 40% by energy of lignocellulose. However, the robustness and complexity of lignin make the efficient conversion of lignin very difficult and challenging. Over the past few decades, and especially in the most recent decade, studies on the catalytic conversion of lignin to renewable fuels, value-added chemicals, and platform compounds have grown rapidly, owing to the importance of lignin in the lignocellulosic biorefinery. In this chapter, we focus on the utilization of lignin via the catalytic approaches applied over the last decade and present an overview of its structure, depolymerization, and upgrading, and finally outline a brief perspective for its further future development.

Heterogeneous Catalysis for Sustainable Energy, First Edition. Edited by Landong Li and Justin S. J. Hargreaves.

14.1.1 Structure of Lignin

During evolutionary adaptation, land-based plants developed the ability to synthesize lignin gradually. Lignin is essential for the structural integrity of the cell wall and can waterproof cell walls, allowing water and solutes to be transported through the vascular system. Lignin plays a crucial role in plant life, and consequently the biosynthetic formation of monolignols and their polymerization and the final structure of lignin have been widely studied for decades [2].

Lignin is a polymer with an amorphous tridimensional structure consisting of various methoxylated phenylpropanoid units, including sinapyl (3,5-dimethoxy 4-hydroxycinnamyl), coniferyl (3-methoxy 4-hydroxycinnamyl), and *p*-coumaryl (4-hydroxycinnamyl) alcohols, named as S, G, and H, respectively (Figure 14.1) [3]. These units are connected by ether or C—C bonds. Owing to the nature of the different plant sources, the proportion of these three momolignols differs. In general, grass lignin contains all three of these units; hardwood lignin comprises mainly the two guaiacyl and syringyl alcohol units, while guaiacyl alcohol is dominant in softwood lignin [4].

As shown in Figure 14.1, all the primary building blocks contain a phenyl unit and a propyl side chain containing a C=C bond. These C=C bonds in the propyl side chain play a key role in the coupling of monolignols, i.e. the formation of dimers. The formation pathway of dimers is referred to as "radical generation and radical coupling" as described by Ralph et al. [2]. The most important cross-couplings are presented in Figure 14.2 [2]. These are crucial to the polymer growth and the extension of the complex three-dimensional network. The most important reaction during the coupling of monolignols is the cross-coupling via connecting the β carbon in the side chain and the O atom attached to the C_4 position of the aromatic moiety. Therefore, β-O-4 linkages are the most abundant in native lignin. In addition to β-O-4 linkages, there are two other major linkages in lignin: β-β and β-5 [5]. Some other linkages, such as α-O-4, α-O-γ, 5-5, and β-1, also occur in native lignin. Over all the linkages, ether bonds account for about two thirds with the remaining linkages being C—C bonds. Many studies on the linkages in lignin have been conducted in the field of the chemistry of forest products [6, 7]. The typical linkages and their proportions

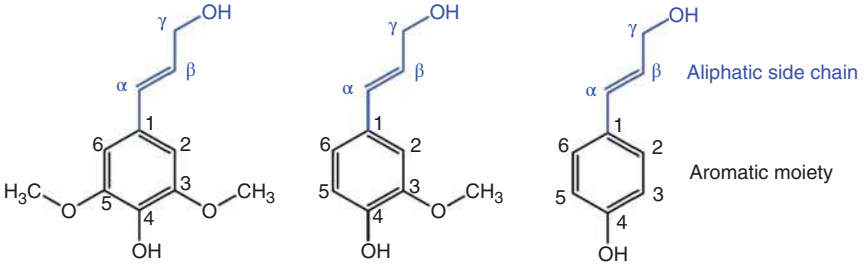

Figure 14.1 The primary building blocks of lignin. Source: Reproduced with permission from Li et al. [3]; © 2015, American Chemical Society.

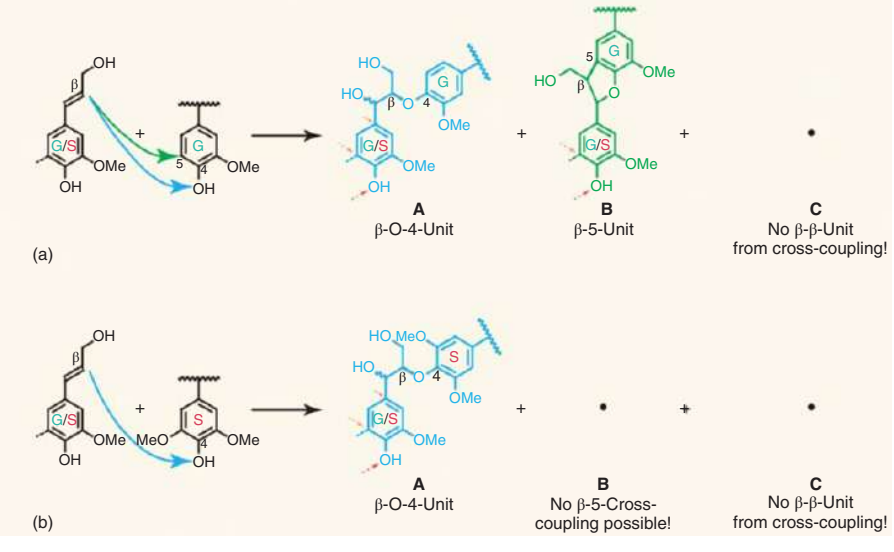

Figure 14.2 Two typical couplings of monolignols: (a) monolignol cross-coupling with a G-end unit and (b) monolignol cross-coupling with an S-end unit. Source: Reproduced with permission from Ralph et al. [2]; © 2007, Wiley.

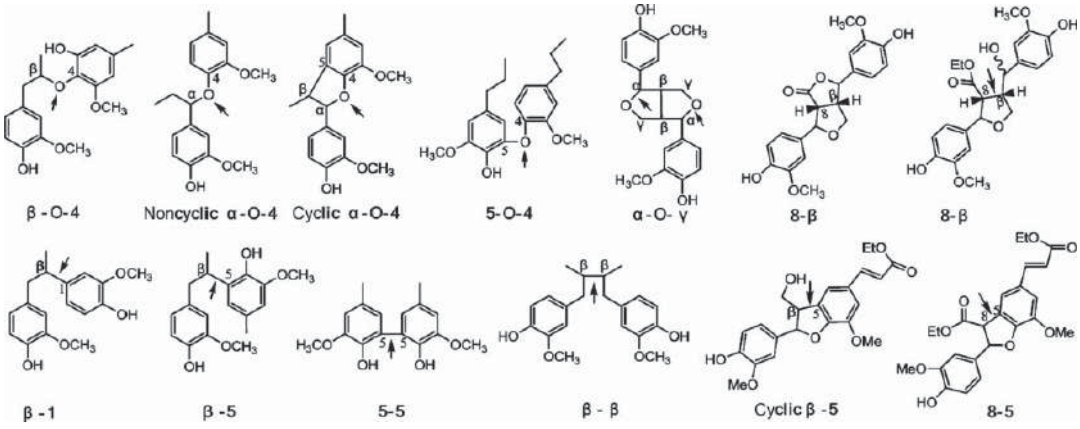

Figure 14.3 Typical linkages between monolignols in native lignin. Source: Reproduced with permission from Li et al. [3]; © 2015, American Chemical Society.

Table 14.1 Typical linkages and functional groups in various lignins.

Linkage	Number 100 ppu^{-1}		Functional group	Number 100 ppu^{-1}	
	Softwood	Hardwood		Softwood	Hardwood
β-O-4	43–50	50–65	Methoxyl	92–96	132–146
α-O-4	6–8	4–8	Phenolic hydroxyl	20–28	9–20
4-O-5	4	6–7	Benzene hydroxyl	16	—
β-5	9–12	4–6	Aliphatic hydroxyl	120	—
β-β	2–4	3–7	Carbonyl	20	3–17
5-5	10–25	4–10	Carboxyl		11–13
β-1	3–7	5–7	—	—	—
Others	16	7–8	—	—	—

Source: Data are collected from Refs. [6, 7].

in lignin have been identified and measured and are summarized in some recent reviews [3, 8–11]. The details of typical linkages and their proportions are shown in Figure 14.3 and Table 14.1, respectively.

After the formation of dimers, there are still some functional groups, such as the OH group attached to the aromatic moiety or unreacted side chains, which can undergo cross-coupling reaction with other monolignols or dimers. With the increasing numbers of linked units, the polymer grows gradually to form the three-dimensional structure. The final structure of native lignin polymers is extremely complex, and some representative structures of these polymers in terms of 20–25 units in softwood and hardwood have been presented by Brunow [12] and Boerjan [13]. Figure 14.4 depicts the lignin polymer models for spruce (softwood) and poplar (hardwood). These models contain most of the linkages in lignin, including ether bonds and C—C bonds. It must be noted that these are only models and do not imply any primary structure sequencing in lignin. However, these models could accommodate the main linkage types and their approximate relative proportions.

Besides the complex and resistant structure of lignin, there are strong connections between lignin and cellulose or hemicellulose in plants. To fractionate and obtain lignin, several strategies have been developed, and different kinds of lignin have been obtained. Based on the fractionation/isolation methods, specific names are applied, such as Klason lignin, Kraft lignin, lignosulfonate, organosolv lignin, cellulolytic enzyme lignin, enzymatic mild acidolysis lignin, ionic liquid lignin, steam explosion lignin, mechanocatalytic lignin, and alkaline wet oxidation lignin. These lignin structures have been modified during the fractionation/isolation process, giving the different lignin feedstocks unique characteristics. Therefore, to improve the economics of biorefinery, for the lignins with different characteristics, targeted depolymerization and upgrading strategies need to be adopted.

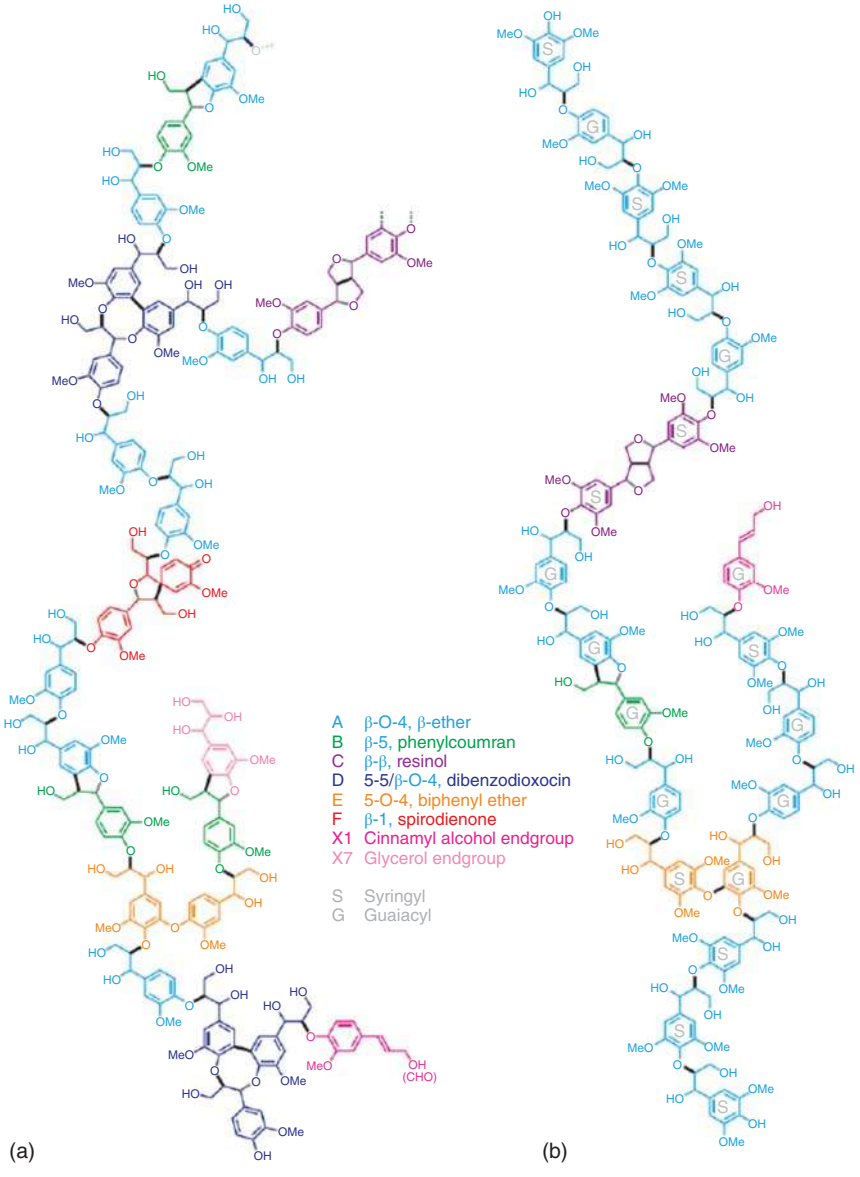

Figure 14.4 Lignin polymer models for a softwood and a hardwood, respectively. (a) Spruce lignin model and (b) poplar lignin model. Source: Reproduced with permission from Ralph et al. [2]; © 2007, Wiley.

14.2 Catalytic Depolymerization

Valorization of lignin is of great significance to the production of renewable fuels and chemicals, and it is currently one of the hot topics in biomass utilization. In general, the strategy for valorization of lignin is to depolymerize lignin to monomers that are then further transformed into value-added chemicals or alternative fuels via upgrading.

Many depolymerization processes for lignin have been developed, including catalytic and noncatalytic processes. The noncatalytic depolymerization processes usually refer to the direct pyrolysis or gasification of lignin, which are conducted at high temperature with the products generally being polyhydroxylated phenol compounds, volatile light hydrocarbons and char, or syngas. These processes severely damage the aromatic structure in lignin and do not conform to the concept of green chemistry and suffer from poor economy.

Catalytic lignin depolymerization processes are generally carried out under relatively mild conditions. These processes do not change the structure of lignin as much as the noncatalytic processes and can preserve more aromatic compounds in the products. There have been several catalytic depolymerization processes developed, such as acid, alkaline, reductive, and oxidative catalytic depolymerization processes, etc. A number of illustrative depolymerization processes are described in detail in the following sections.

14.2.1 Acid Catalytic Depolymerization

Acid catalytic depolymerization, also named as acidolysis, has been widely used in biomass conversion. In general, acid catalytic treatment of biomass is adopted to fractionate the lignocellulose into the main three components. Historically, acid pulping was predominantly used for isolating the reduced molecular weight lignin fractions from the lignocellulose matrix [14]. Acid catalytic polymerization has been extensively applied over a long period to transform cellulose and hemicellulose, which could produce sugars or furfural by hydrolyzing the C—O linkages between the monosaccharide units.

Since the acid catalyst can break the ether bonds in cellulose and hemicellulose, it should also be able to catalyze the cleavage of ether bonds in lignin. In very early studies, it was found that there were some aromatic monomers generated in the fractions of lignin from lignocellulose by using acid treatment. However, the aim of this treatment is not to gather more valuable aromatic monomer products.

With the increasing demand for obtaining aromatic compounds from lignin in recent years, more and more studies have been conducted on the conversion of lignin to monomers by acid catalytic depolymerization, including mechanistic studies employing model compounds. Many acid catalysts such as mineral acids, Lewis acids, zeolites, acidic ILs, and organic acids have been evaluated in the acidolysis of lignin or the typical model compounds (dimers or oligomers).

Barta and coworkers designed a novel approach to catalytic lignin depolymerization by acidolysis [15]. In their work, triflic acid was used as the acid catalyst to

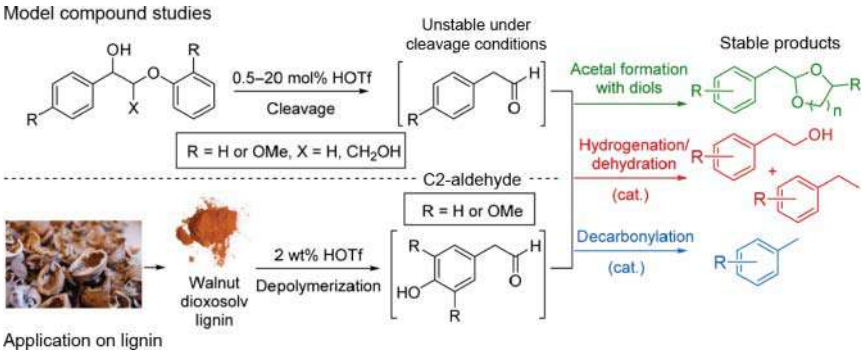

Figure 14.5 C_2-aldehyde stabilization strategy in acidolysis of lignin. Source: Deuss et al. [15], Figure 02/with permission from American Chemical Society.

accomplish the efficient depolymerization of walnut dioxosolv lignin to aromatic monomer. As shown in Figure 14.5, the unstable aldehyde intermediates were captured by reaction with diols or by *in situ* catalytic hydrogenation or decarbonylation. They also undertook very detailed studies by using β-O-4 linkage model compounds to gain the insight into the pathway and chemistry. The aldehyde products were identified as the main cause of the side reactions under the acidolysis conditions, reacting with aromatic moieties via condensation to produce undesirable higher molecular weight side products. To suppress the side reactions, they innovatively introduced protection reactions to transform the unstable products into stable ones with specific functional groups. They also emphasized that future research should focus on in-depth mechanistic understanding of lignin conversion pathways and the role of intermediates to maximize the production of aromatic monomers from lignin.

In fact, much effort has been undertaken by others to clarify the acid catalytic depolymerization mechanism. In 2010, Ekerdt and coworkers demonstrated efficient acid catalytic depolymerization for the cleavage of β–O–4 bonds of phenolic (guaiacylglycerol-β-guaiacyl ether, shorted as GG) and non-phenolic (veratrylglycerol-β-guaiacyl ether, shorted as VG) lignin model compounds in an acidic ionic liquid [16]. More than 70% of the β–O–4 bonds of both GG and VG reacted with water to produce guaiacol at 150 °C. In particular, the substrate concentration could be up to 32 wt% with a similar yield of guaiacol. The possible pathway was studied carefully, and the enol aryl ether (EE), generated via dehydration, was detected and proposed as a possible intermediate in the acid depolymerization of GG or VG. Accordingly, one possible acid catalytic mechanism for the acidolysis of β–O–4 bonds of GG and VG via the possible EE and dimer intermediates was proposed (Scheme 14.1). In this proposed mechanism, the dehydration step initiated by a proton was the rate-determination step for the total acidolysis while the intermediate of EE was hydrolyzed to guaiacol and α-ketocarbinol rapidly. Finally, α-ketocarbinol was converted to a mixture of ketones also called "Hibbert's ketones." The mechanism was also proved in their later work [17]. Beckham and coworkers also reported the same mechanism for

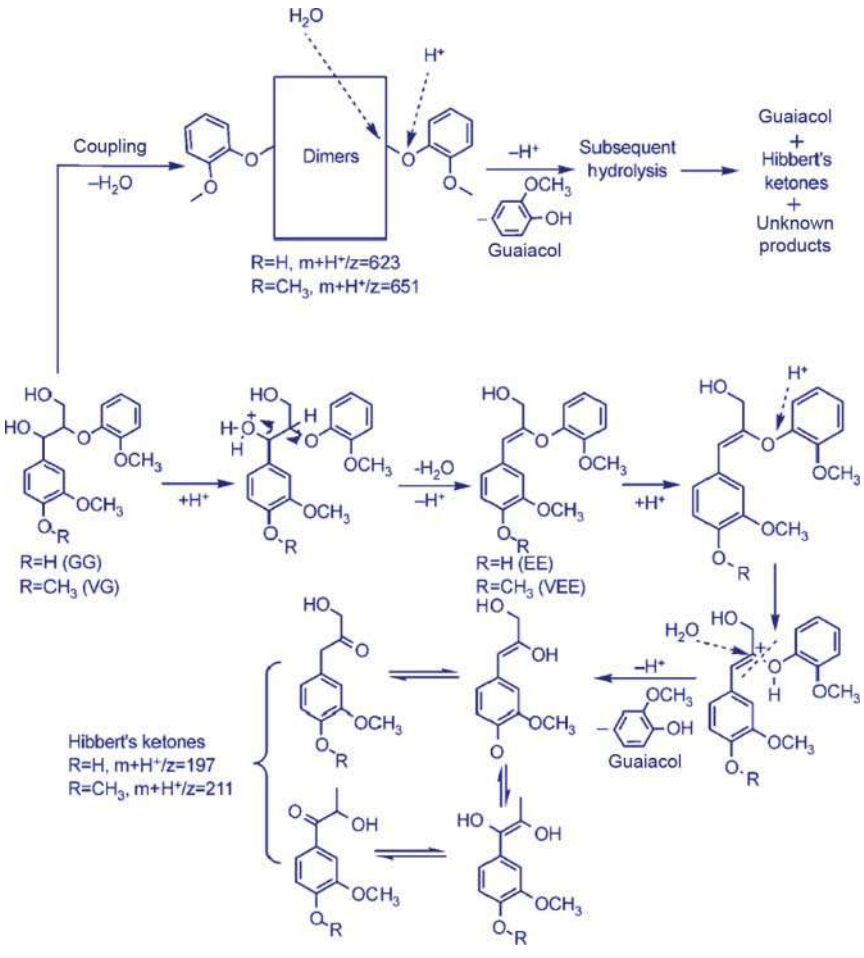

Scheme 14.1 The possible mechanism for acidolysis of β-O-4 bonds in lignin model compounds. Source: Reproduced with permission from Jia et al. [16]; © 2010, Wiley.

the acidolysis of lignin based on a more detailed study in a sulfuric acid catalytic system, in which they used four kind of different dimers as model compounds (Figure 14.6) [18].

Model compounds based upon β–O–4 linkages are the most popular in mechanistic studies relating to the depolymerization because the β–O–4 linkage dominates over all linkages in lignin. However, overly simplified model compounds of β–O–4 dimers often lack relevance to the chemistry of lignin, as there also are some other types of linkage especially C—C linkages that should be considered. Certainly, the ideal situation is to directly investigate native lignin as the reactant, but the analytical issues are a huge challenge, owing to the complexity and diversity of lignin. To develop a more precise mechanism, new kinds of advanced model compounds containing both β–O–4 and β–5 linkages (Figure 14.7) have been synthesized and applied to study the acidolysis of lignin by Barta and coworkers [19].

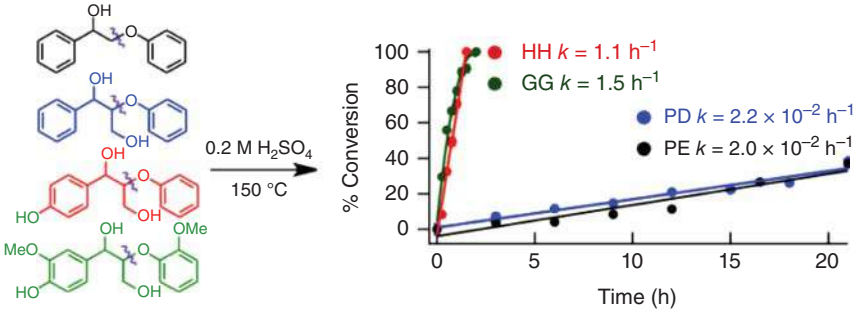

Figure 14.6 Acidolysis of different types of lignin compounds. Source: Reproduced with permission from Sturgeon et al. [18]; © 2014, American Chemical Society.

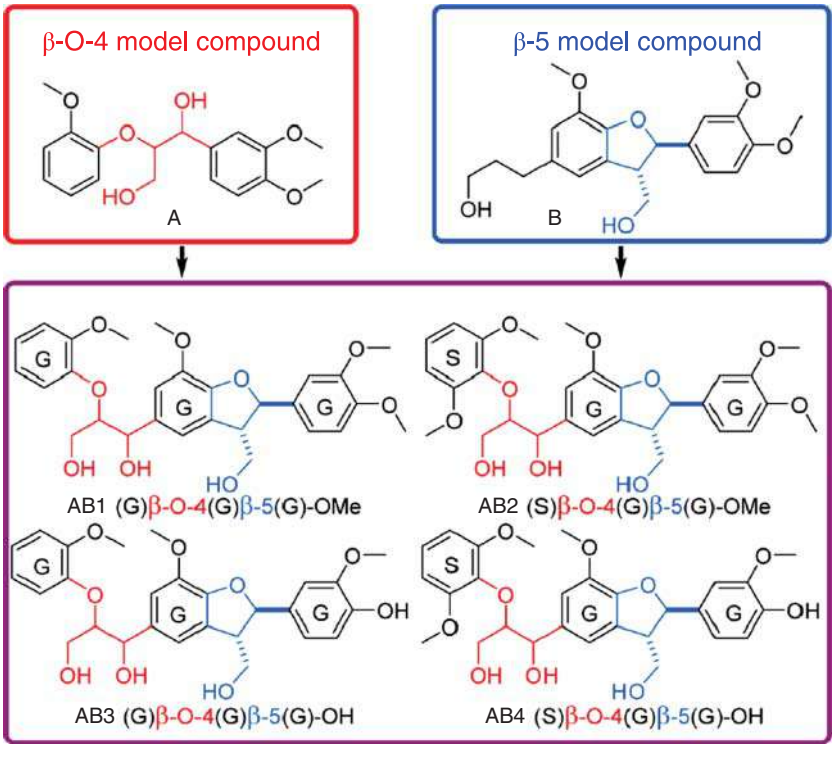

Figure 14.7 Model compounds containing β-O-4 and β-5 linkages. Source: Reprinted with permission from Lahive et al. [19], © 2016, American Chemical Society.

Using well-designed model compounds, detailed insight into the acid catalytic depolymerization of β-O-4, β-5 and β–β linkages can be gained, and a possible reaction mechanism has been presented in Scheme 14.2. The triflic acid catalytic system was highly efficient in terms of the cleavage of C—O bonds, whereas the main C—C linkages in the β-5 and β-β units were left intact, with the only C—C bond scission being the release of formaldehyde. In addition, some novel dimers

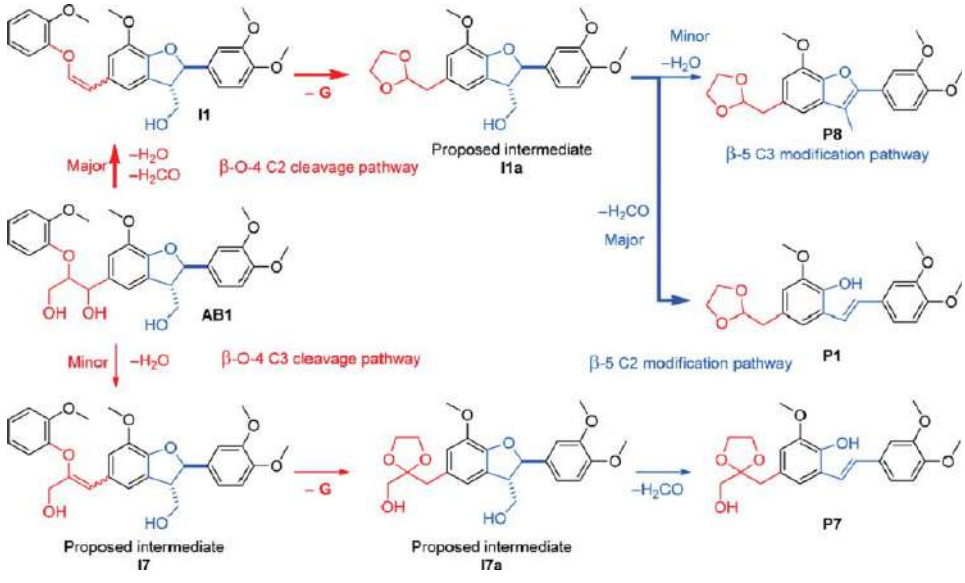

Scheme 14.2 A proposed mechanism for depolymerization of an oligomer model compound in lignin. Source: Reproduced with permission from Lahive et al. [19], © 2016, American Chemical Society.

were identified for the first time in the depolymerization mixtures generated from pine and walnut lignin.

Many results on the acidolysis of lignin and its model compounds have been reported, in which the cleavage of α- and β-aryl ether bonds plays a dominant role because the aryl—aryl ether bonds, phenolic C—O bond, and C—C bonds linked in aromatic monomers are more stable. To design and develop more advanced acidolysis aiming to maximize the aromatic monomer production by breaking these bonds is a highly desired target for future work. A drawback of acidolysis is recondensation, and diols are used to protect the products. Another is that pure lignin is required. It is difficult to achieve the fractionation and depolymerization from lignocellulosic biomass because of the difficulties associated with separation and condensation.

14.2.2 Alkaline Catalytic Depolymerization

Alkaline treatment is well known as being highly efficient for the depolymerization of lignin because it has been adopted in the Kraft pulping process to degrade lignin to fragments and enhance its dissolution, achieving the purpose of separating from cellulose. Alkaline catalytic depolymerization is an exceptional route for the production of simple aromatic chemicals under mild conditions. Similar to the Kraft process, using alkaline catalysts to treat lignin could depolymerize it with a fast rate and high conversion. Usually, alkali, alkali carbonate, and organic bases have been employed as catalysts in depolymerization of lignin. These alkaline catalysts are low cost and are commercially available.

As described in the acid catalytic depolymerization section, the cleavage of ether bonds is also the dominant reaction in the alkaline catalytic depolymerization of lignin because the aryl—alkyl ether bonds, including β–O–4 bonds, are the weakest bonds in lignin [20, 21]. An apparent drawback of alkaline catalytic depolymerization is related to the high solid residue content after reaction due to repolymerization [22], including condensation reactions that can be catalyzed by alkali with extremely high efficiency. Additionally, there are many acidic compounds generated in the alkaline catalytic depolymerization, which can react with the alkaline catalyst. Acid–base neutralization is responsible for two disadvantages for depolymerization: (i) it gradually consumes and deactivates the alkaline catalyst during the depolymerization, and (ii) it leads to the formation of salts, which influence the product quality.

Investigations on alkaline catalytic depolymerization are less numerous than those on other depolymerization methods, especially in relation to mechanistic considerations. The conventional mechanism for alkaline catalytic depolymerization originates from studies of the Kraft pulping process. In the conventional Kraft process, an aqueous solution of sodium hydroxide and sodium sulfide, also known as white liquor, reacts with the wood chips in a digester. Chakar and Ragauskas summarized the chemistry involved in the Kraft lignin process and reported a mechanism for alkaline catalytic depolymerization [23]. The α-aryl ether bonds in the phenol unit are easily cleaved by transformation of the phenolate unit to the

corresponding quinone methylate intermediate, while the cleavage of β-aryl ether linkages in non-phenolic units occurs via the attack of an ionized hydroxyl group present on the α- or γ-carbon (Scheme 14.3).

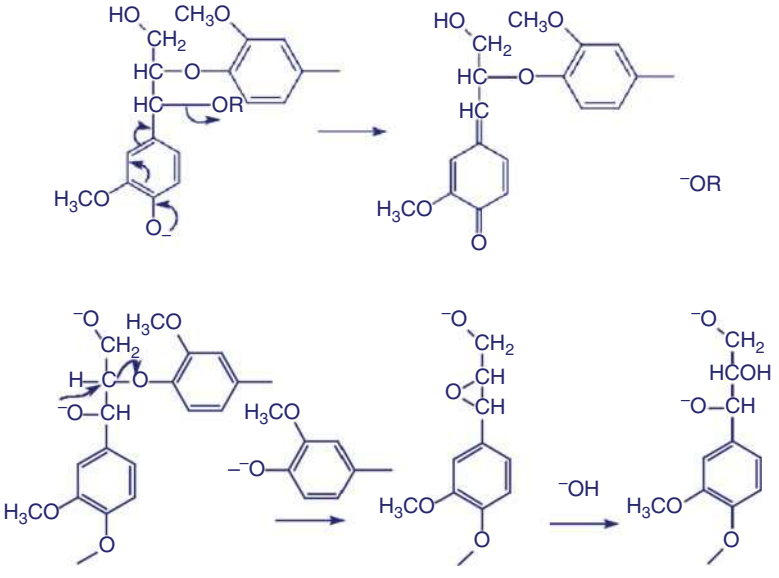

Scheme 14.3 Alkaline cleavage of α- (top) and β-aryl (bottom) ether bonds in phenolic (top) and non-phenolic (bottom) arylpropane units, respectively. Source: Reproduced with permission from Chakar and Ragauskas [23], © 2004, Elsevier.

A similar mechanism was also proposed by Ekerdt and coworkers when studying the depolymerization of phenolic lignin model compounds with an organic catalyst system [24], as shown in Scheme 14.4.

The early alkaline catalytic depolymerization of lignin directly used aqueous solutions of base as catalysts, including sodium hydroxide [25] and potassium hydroxide [26]. As the condensation of unstable intermediates is very rapid and the production of aromatic monomers is very low, a novel mechanochemical technique using solid base-assisted ball milling for alkaline catalytic depolymerization of lignin was developed by Bolm and coworkers [27]. Studying model compounds in this work led to an understanding of the underlying cleavage processes, in which lignin predominantly involved in the breaking of β-O-4 linkages, as shown in Scheme 14.5. Meanwhile, the drawback of this process was stated to be the consumption of too much base, which might be reduced by subsequent reaction process optimization.

Presently, few studies on the catalytic depolymerization of lignin with solely base catalysts have been reported while their role as co-catalysts in other depolymerization processes have been reported [28, 29]. The implementation of NaOH could enhance the delignification, but it has serious consequences on the obtained lignin oil [28]. Alkaline conditions enhance (i) repolymerization leading to low monomer yields and (ii) C2-substituted phenolics instead of C3-substituted phenolics with the loss of hydroxyl groups. The first effect is most pronounced when

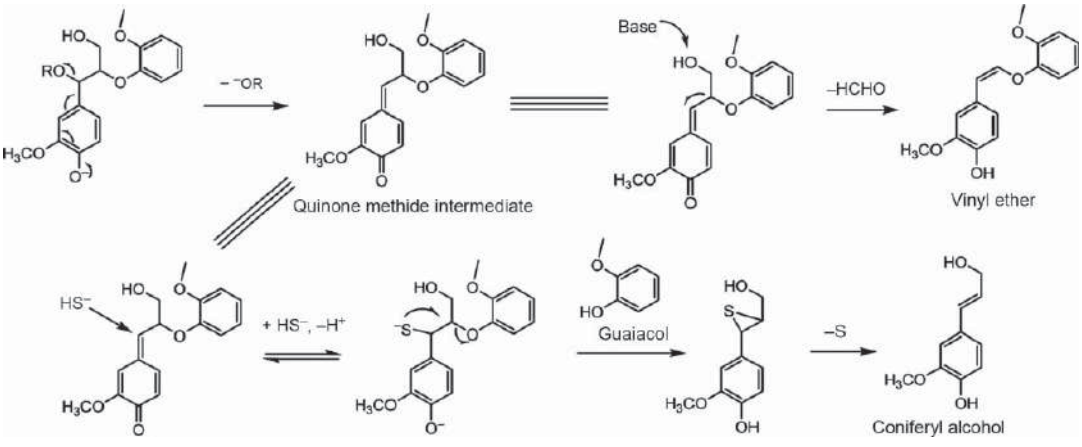

Scheme 14.4 A mechanism for alkaline catalytic depolymerization of lignin compound. Source: Reproduced with permission from Jia et al. [24], © 2010, De Gruyter.

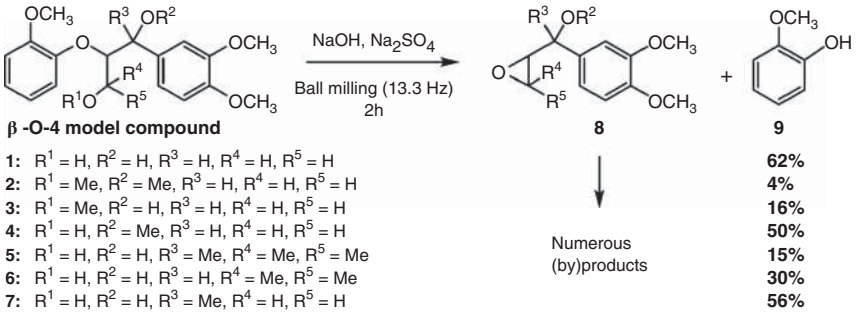

Scheme 14.5 Mechanochemical alkaline catalytic depolymerization of β-O-4 linkage compounds. Source: Reproduced with permission from Kleine et al. [27], © 2013, Royal Society of Chemistry.

lignins rich in G units (softwoods) are processed because of the reactivity-free ortho-position, producing lignin oil with a broad molecular weight distribution and a low monomer yield. A hypothesis to explain both of these effects is presented involving the alkaline-induced formation of quinone methide intermediates. Additionally, another disadvantage of employing NaOH is a significant loss of cellulose exerting a negative effect on the fractionation efficiency.

Song and Li systematically studied the influence of alkaline $CsCO_3$ for the reductive depolymerization of lignin with a Ru/C catalyst [29]. A mechanism for the alkaline regime shifting the selectivity from C3-fragmented phenols to C2-fragmented phenols was proposed (Figure 14.8). The type of base, reaction temperature, and time have significant impact on both the activity and the selectivity of lignin hydrogenolysis. Under optimized conditions, a high proportion of C2 phenols (44%) could be produced with a desirable total monomer yield (26.6 wt%).

14.2.3 Reductive Catalytic Depolymerization

Reductive catalytic depolymerization usually refers to the depolymerization of lignin by a hydrotreating process in a hydrogen atmosphere. It is one of the most popular and effective methods for depolymerization of lignin because it is feasible for it to be conducted in a refinery integrating biomass with petroleum and it gives a relatively high yield of lignin oil product and a good distribution of aromatic monomers. Besides, during the catalytic reductive process, fractionation and depolymerization could be achieved simultaneously.

Hydrogen and metal species that can activate hydrogen are essential in reductive catalytic depolymerization. Due to the assistance of hydrogen and metal sites, lignin not only is depolymerized (cleavage of interunit C—O linkages, even C—C linkages) to low-molecular-weight aromatic compounds under relatively mild conditions but also can be further upgraded to targeted compounds through hydrogenation and hydrodeoxygenation (HDO). In this section, we will focus on the depolymerization, and the upgrading of lignin monomers via HDO or other reductive techniques will be discussed in detail in Section 14.3. In general, the product is a mixture of

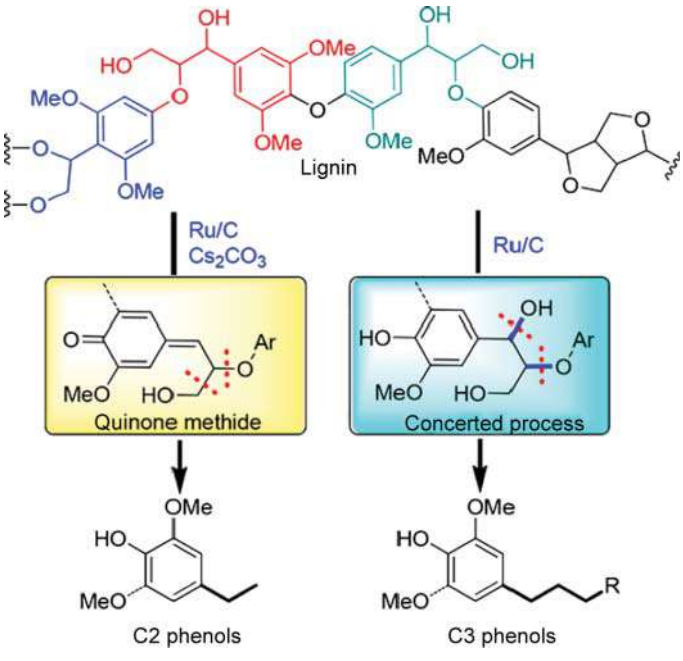

Figure 14.8 The effect of alkaline additive upon reductive depolymerization of lignin. Source: Reproduced with permission from Li and Song [29], © 2019, American Chemical Society.

various oxygen-containing aromatic compounds, also known as "lignin oil." This oil usually cannot be utilized directly as a fuel or for chemicals and needs to be further upgraded.

Due to the preservation of methoxy groups under mild conditions, oxygen-containing aromatics are often produced at low temperatures via the one-step method. In general, these oxygen-containing aromatics include 4-*n*-propylguaiacol, 4-*n*-propylsyringol, 4-*n*-propanolguaiacol, 4-*n*-propanol syringol, and other compounds. Generally, the product distribution is affected by both catalysts and solvents [30].

In 2008, Kou and coworkers [31] reported that a Pd/C catalyst can selectively cleave the aromatic C—O bonds of aryl ethers in lignin in the aqueous phase to produce monomers and dimers, which were then further transformed to alkanes via hydrogenation. Subsequently, Pd-based catalysts or Pd-based bimetallic catalysts have been widely applied to the hydrogenolysis of lignin under mild conditions. Interestingly, the product distributions can be tuned by the choice of noble metal. For example, Sels and coworkers [32] found that changing the catalyst from Pd/C to Ru/C could decrease the OH content of the lignin-derived products, in particular in the phenolic monomers. The different product distributions originated from the low C—O hydrogenolysis activity of the Pd/C catalyst, which could retain γ-OH in the side chain with high selectivity to 4-*n*-propanolguaiacol and 4-*n*-propanolsyringol (total up to 91%), while over Ru/C, the γ-OH in side chain was easily removed,

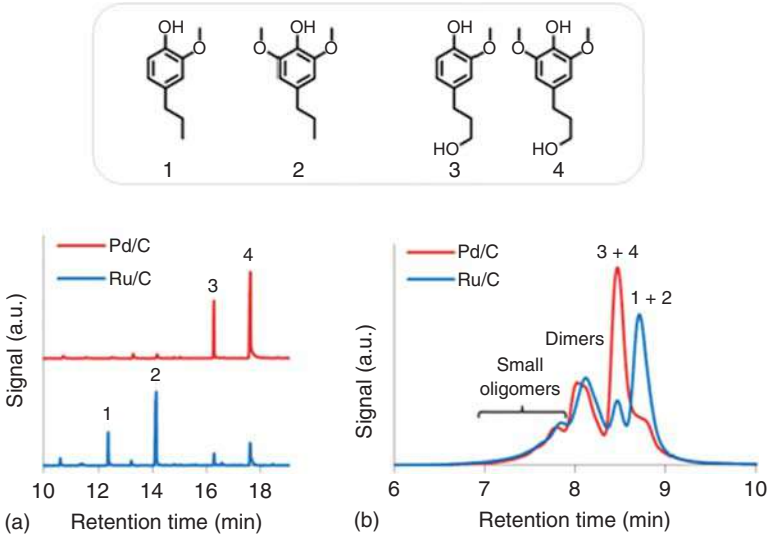

Figure 14.9 Comparing the lignin products after Ru/C- and Pd/C-catalyzed processing of birch wood in MeOH. (a) Peak identification of the monomers via GC-MS (Gas Chromatography-Mass Spectrometry). (b) MW (molecular weight) distribution of the "lignin oil" via GPC (Gel Permeation Chromatography). Source: Reproduced with permission from Van den Bosch et al. [32], © 2015, Royal Society of Chemistry.

leading to the major products of 4-*n*-propylguaiacol and 4-*n*-propylsyringol (total up to 75%) (Figure 14.9). In fact, Ru-based catalysts were not only used in the reductive depolymerization of lignin [29, 33, 34] but also applied in the reductive lignocellulose fractionation into soluble lignin-derived phenolic monomers and dimers [35]. At the same time, processable carbohydrate pulps were obtained with almost quantitative retention of the original cellulose and hemicellulose.

Apart from noble metals, some non-noble metals have been also used for reductive depolymerization. In particular, Ni-based catalysts showed excellent hydrogenolysis activity in lignin depolymerization, whenever carbon, SiO_2, Al_2O_3, SiC, and ZrP were used as supports or Raney Ni was used as the catalyst [36–39]. Recently, Li and coworkers [40] presented an efficient hydrogenolysis process for the selective decomposition of organosolv lignin and char elimination over a nickel-supported zirconium phosphide (Ni/ZrP) catalyst. Besides, metallic oxides or sulfides are possible choices that have been attracting increasing attention. Very recently, Zhang et al. developed a ReO_x/AC catalytic system that achieved a high yield of aromatic monomers (about 98.0%) from model compounds and up to 80.1% from lignin oil and 24.5% yield of monomers from native lignin [41].

Including hydrogen gas, it can also be derived from hydrogen donors, such as formic acid, methanol, ethanol, isopropanol, or the lignin itself. In view of the safety considerations and cost associated with hydrogen gas, *in situ* generated hydrogen from lignin has been extensively studied, employing hydrogen-donor solvents as hydrogen sources. For example, Ford and coworkers [42] demonstrated that the highly efficient hydrogenolysis of lignin could be achieved over Cu-based catalysts

in supercritical methanol through hydrogen transfer. Xu et al. demonstrated that Ni-based catalysts were highly active and selective in native lignin conversion into monomeric phenols, propylguaiacol, and propylsyringol. The best selectivity of 97% toward monomeric phenols was achieved at 50% conversion of birch wood lignin with methanol as the hydrogen source (Scheme 14.6) [37]. Subsequently, a Raney Ni catalyst system with isopropanol as hydrogen source was developed [43]. Jae and coworkers [44] further investigated the use of combined Ru/C and MgO/ZrO_2 catalysts in supercritical ethanol for the depolymerization of lignin through a synergy of base-catalyzed solvolysis and metal-catalyzed hydrogenolysis. Very recently, a mild redox-neutral lignin depolymerization system featuring a water-soluble binuclear Rh complex has been developed by Wang and coworkers [45]. Interestingly, the hydrogen used here for the cleavage of C—O bond originates from the alcohol moiety in lignin itself.

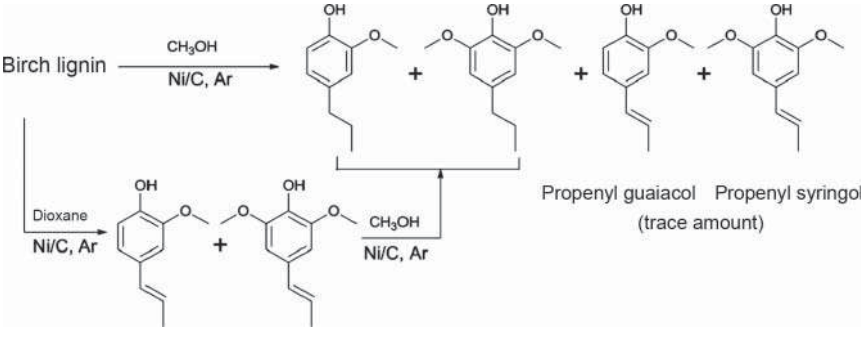

Scheme 14.6 Reductive depolymerization of lignin over a Ni/C catalyst in methanol. Source: Reproduced with permission from Song et al. [37], © 2013, Royal Society of Chemistry.

Besides the conventional metal catalysts, metal sulfide catalysts have been adopted in the hydrogenolysis of lignin. Laurenti and coworkers studied the reaction pathway over a $NiMoS/Al_2O_3$ catalyst and gave a very comprehensive reaction scheme, as shown in Scheme 14.7 [46]. They assumed that the initial degradation of the lignin was mostly thermal and then became catalytically driven as soon as oligomers could interact with the catalyst. During the initial thermal step, the carboxylic acidic functions of initial feed started decarboxylation, the weakest β-O-4 and α-O-4 ether linkages were cleaved, and dehydration of the aliphatic OH groups took place. Then, in the second phase, the catalytic stage started with the hydrogenation of double bonds on aliphatic chains and the demethoxylation, demethylation, and dehydroxylation of phenols to form progressively phenolic, aromatic, and naphthene monomers and oligomers in the liquid phase.

In addition to the one-step reductive catalytic depolymerization of lignin, two-step strategies have also been developed to achieve high yields of aromatic monomers under mild conditions. One excellent example is shown in Figure 14.10, in which Luterbacher and coworkers reported that adding formaldehyde during the pretreatment of biomass could significantly improve the yield of lignin monomer by avoiding

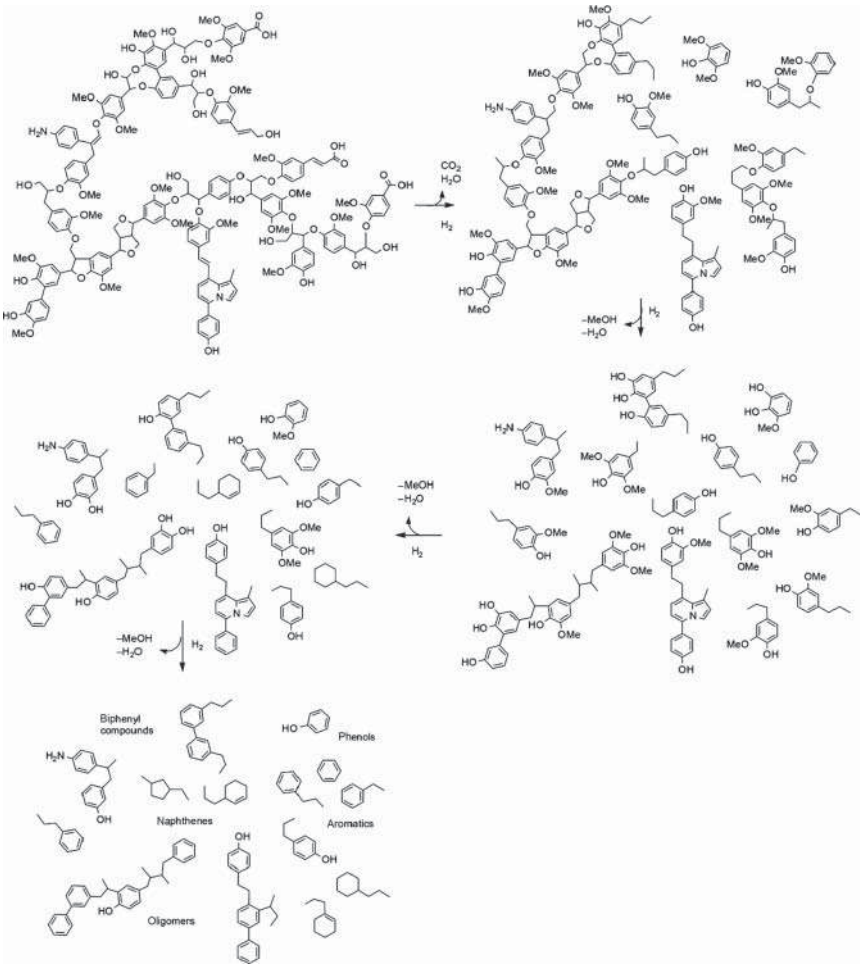

Scheme 14.7 The progressive transformation scheme of lignin to oligomers and monomers under catalytic hydrotreating with $NiMoS/Al_2O_3$. Source: Reproduced with permission from Joffres et al. [46], © 2016, Elsevier.

the interunit C—C coupling. In this strategy, formaldehyde hindered the formation of new C—C bonds through forming a stable six-membered 1,3-dioxane structure with 1,3-diols on lignin side chains, which blocked the formation of benzylic cations, thus preventing repolymerization [47].

As the most abundant linkages in lignin, β-O-4 model compounds also have been studied to derive the pathways and mechanism in the hydrogenolysis of lignin. Abu-Omar and coworkers developed a Pd–Zn bimetallic catalyst, in which Pd and Zn did not alloy while they were in the form of Pd and Zn^{2+}, respectively [48]. This catalyst could selectively cleave the recalcitrant ether bonds of model lignin dimers and polymers, remove alcohol oxygen atoms on the alkyl chains, and maintain the valuable aromaticity of the starting materials, under relatively mild conditions. There were two proposed pathways (Figure 14.11):

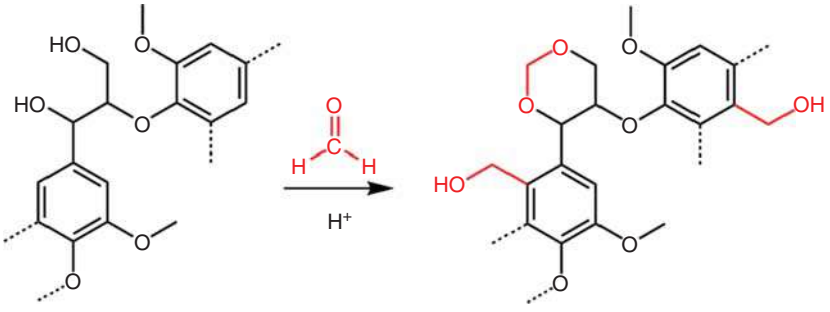

Figure 14.10 Lignin monomer production by extraction followed by hydrogenolysis.

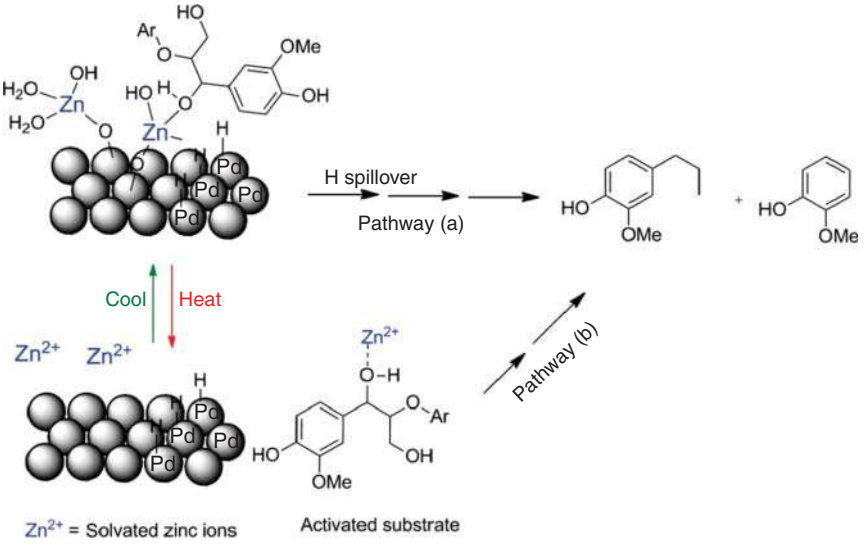

Figure 14.11 Proposed pathways for hydrogenolysis of β-O-4 lignin model compounds. Source: Reproduced with permission from Parsell et al. [48], © 2013, Royal Society of Chemistry.

pathway (a) involved substrate binding to Zn^{2+} sites and hydrogen spillover from Pd sites, and pathway (b) represented the desorption of Zn ions into solution, activation of substrate via binding, and Zn-bound substrate reaction with Pd sites on the catalyst surface. This developed sequentially: the primary step being the formation of a benzylic carbenium ion through dehydration (removal of the OH group) that often occurred at the acidic site to afford enol ether as the intermediate, the subsequent cleavage of the C—O bond of enol ether through hydrogenolysis to yield the 1-(4-hydroxy-3-methoxyphenyl)-2-propanone intermediate, and the final occurrence of hydrogenation/dehydration or direct hydrogenolysis (DDO) events. The cleavage of C—O–C bonds depolymerized the lignin polymer into its oligomers, dimers, and monomers. Hence, the released fragments of lignin were then cleaved by Ru-catalyzed reductive reaction involving molecular hydrogen to form 2-methoxy-4-propylphenol as the major compound.

14.2.4 Oxidative Catalytic Depolymerization

Oxidative catalytic depolymerization is one strategy to convert lignin by oxidation. Although it has been widely used for the pulp bleaching in the paper industry, its purpose is to remove lignin from lignocellulose, while not to produce useful products from lignin. During this process, lignin is depolymerized to oligomers or monomers, which can be dissolved in an aqueous phase. As people pay more attention to the valorization of lignin, the production of useful fuels or chemicals by the oxidative catalytic depolymerization of lignin has become a research trend. Many methods have been adopted for oxidative catalytic depolymerization of lignin, including heterogeneous catalysis [49], ionic liquids [50], photocatalysis [51], and electrocatalysis [52]. Nitrobenzene, metal oxides, molecular oxygen, and hydrogen peroxide are the most popular oxidants for the oxidative catalytic depolymerization of lignin. The products obtained from the oxidative catalytic depolymerization are some of oxygen-containing aromatics, such as phenols, alcohols, aldehydes, or carboxylic acids. These products could be used directly as chemicals or can be further upgraded to alternative fuels and chemicals.

The production of vanillin from lignin by oxidation has been achieved for a long time, and some researchers have taken it as a typical case in the utilization of lignin to produce value-added chemicals. However, the feedstock used for vanillin production is lignosulfonate originating from acidic catalytic depolymerization. Strictly speaking, it does not belong to the category of oxidative catalytic depolymerization of lignin. Herein, only the cases involving bond cleavage between monomers by oxidation reaction will be detailed.

Production of vanillin from lignin by oxidative catalytic depolymerization has been studied extensively in the last few decades. Lin and coworkers developed a series of perovskite-type oxide catalysts and used them in the wet oxidative depolymerization of lignin to produce aromatic aldehydes, including vanillin [53, 54]. The lignin conversion and yield of each aromatic aldehyde were significantly enhanced by the catalytic process over $LaMnO_3$ or $LaCoCO_3$ catalyst, compared with the noncatalytic process. In particular, they conducted very detailed study on the mechanism and proposed a convincing mechanism over $LaCoCO_3$ catalyst (Scheme 14.8).

The adsorbed oxygen surface sites, $Co_{(surf)}{}^{3+}O^{2-}$, were proposed as active sites. Based on the experimental observations, they claimed that there was a cycle of $Co_{(surf)}{}^{3+} \rightarrow Co_{(surf)}{}^{2+} \rightarrow Co_{(surf)}{}^{3+}O^{2-} \rightarrow Co_{(surf)}{}^{3+}$. The formation rates of the intermediates quinonemethide and hydroperoxide were the rate-determining steps. In addition to the relative high activity, the $LaCoO_3$ catalyst had good stability, which did not undergo obvious changes after the five successive reactions. There are also many other catalysts used for oxidative catalytic depolymerization of lignin, for example, La-SBA-15 [55] and ionic liquids [56].

In addition to obtaining vanillin from lignin, some other kinds of aromatic compounds could be obtained from the oxidative catalytic depolymerization. Wang and coworkers reported that cerium oxide-supported palladium nanoparticles (Pd/CeO_2) could efficiently catalyze the organosolv lignin depolymerization to vanillin,

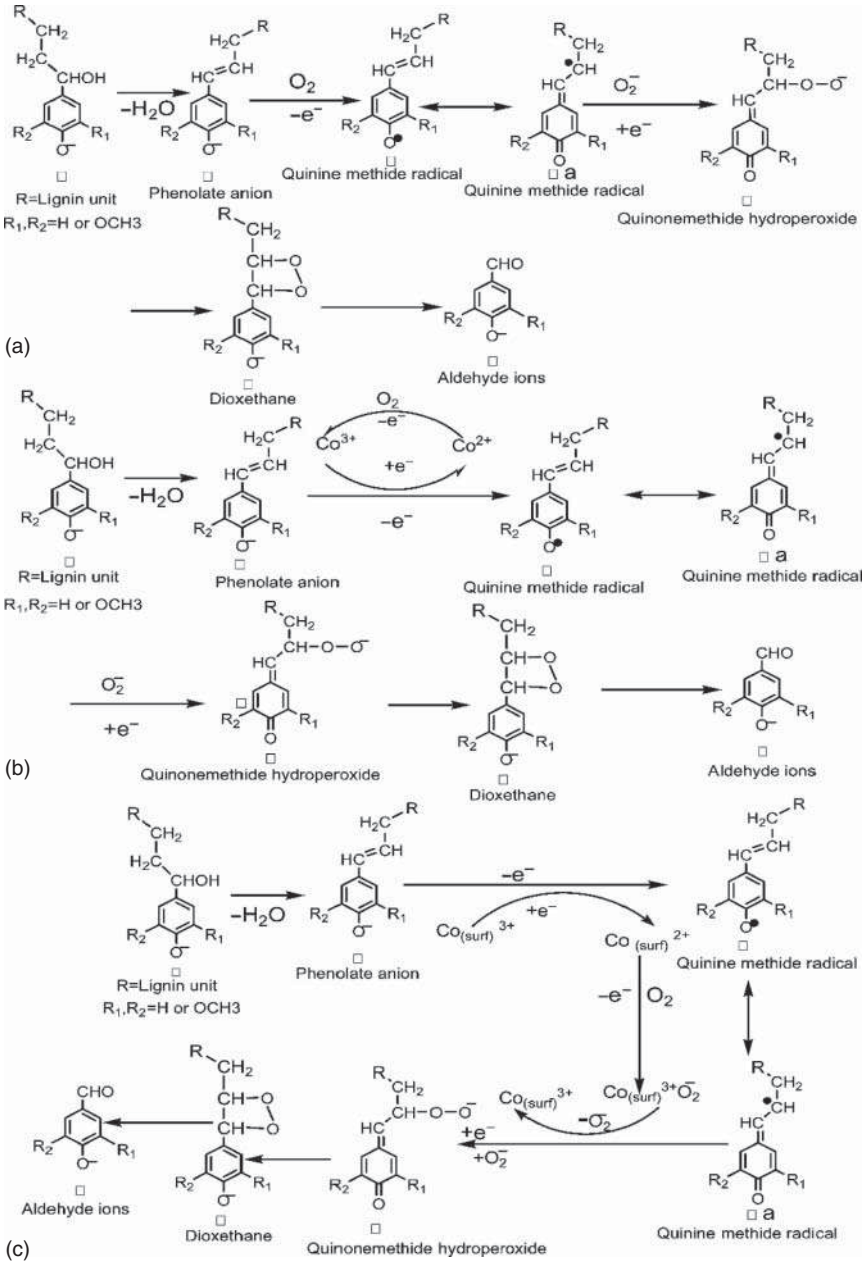

Scheme 14.8 The proposed mechanism of oxidative depolymerization of lignin in the (a) noncatalytic process, (b) Co^{2+} catalytic process, and (c) $LaCoO_3$ catalytic process. Source: Reproduced with permission from Deng et al. [54], © 2009, American Chemical Society.

guaiacol, and 4-hydroxybenzaldehyde [57]. They also used 2-phenoxy-1-phenylethanol, a lignin model compound containing a β-O-4 bond and a C_α-hydroxyl group, to investigate the reaction pathway and mechanism. It was proposed that Pd nanoparticles played a crucial role in the oxidation of the C_α–OH group into C_α=O, which weakened the β–O–4 bond. The activated β–O–4 bond might either undergo hydrogenolysis to product acetophenone and phenol or undergo oxidative cleavage to produce phenol and oxidized intermediates such as 2-hydroxyacetophenone and a small fraction of acetophenone.

Most of the efforts on the oxidative catalytic depolymerization focus on the cleavage of the β–O–4 bond, since it is the most abundant linkage in native lignin. However, with the aim of maximizing the monomer yield, the cleavage of C—C linkage is also worthy of investigation for the oxidative catalytic depolymerization of lignin. Fang and Meier have investigated the oxidative depolymerization of the β-1 and β-5 lignin linkages, using four β-1 and β-5 model compounds [58]. They observed that direct oxidative cleavage of C—C bonds occurred in metal-catalyzed TEMP [(2,2,6,6-tetramethylpiperidin-1-yl)oxyl] oxidation systems and with iron porphyrin oxidations, which was different to those with β-O-4 models. In the study of C—C bond cleavage, Wang and coworkers presented a very interesting study on the cleavage the C—C bond by oxidative catalytic depolymerization of lignin [59]. They focused on the C_α–C_β cleavage in β-O-4 models. In their work, they undertook a two-step strategy for the oxidative cleavage of lignin C—C bond to aromatic acids and phenols with molecular oxygen as oxidant (Figure 14.12). In the first step, lignin β-O-4 alcohol was oxidized to β-O-4 ketone over a $VOSO_4$/TEMPO catalyst. In the second step, the C—C bond of β-O-4 linkages were selectively cleaved to acids and phenols by the oxidation over a Cu/1,10-phenanthroline catalyst. Computational investigations suggested a copper-oxo-bridged dimer was the catalytically active site for hydrogen-abstraction from C_β–H bond, which was the rate-determining step for the C—C bond cleavage.

Compared with other catalytic or noncatalytic depolymerization of lignin procedures, oxidative catalytic depolymerization has the great advantage that

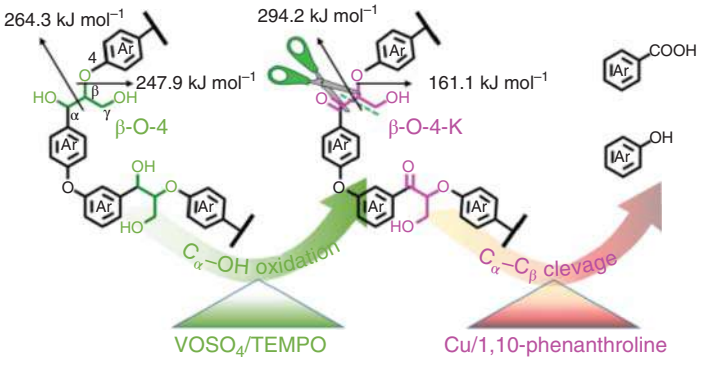

Figure 14.12 Two-step strategy for β–O–4 bond cleavage by oxidative method. Source: Reproduced with permission from Wang et al. [59], © 2016, American Chemical Society.

it can be conducted under relatively mild conditions. Although it shows great potential in the depolymerization of lignin, there are also some big challenges that need to be solved. One challenge is to control the oxidation reaction and avoid the over-oxidation, since during the oxidative catalytic depolymerization, over-oxidation will convert the partial lignin substrate to gaseous products and thus lower the yield of monomers. Another is to prevent the repolymerization because the radical species generated during the oxidation reaction will facilitate the repolymerization of lignin monomers and decrease the efficiency of depolymerization. Moreover, the oxidation reaction could add new functional groups to the aromatics and make the product composition more complex, increasing the difficulty in separation. Although many efforts have been devoted to oxidative catalytic depolymerization of lignin to monomers, including lignin or its model compounds, the products usually contain several aromatics that can be very difficult to be separated from one another. These mixtures cannot be utilized directly as fuels as they contain high amount of oxygen. On the other hand, even if upgrading is undertaken to deal with these mixtures, it is still difficult to convert them into one pure chemical. It is therefore required to develop more highly efficient oxidative catalytic depolymerization to convert lignin to oxygen-containing products.

14.2.5 Other Catalytic Depolymerization

Apart from the above acid, alkaline, reductive, and oxidative depolymerization of lignin routes, some other depolymerization methods also have been reported, such as catalytic pyrolysis and photocatalysis.

Pyrolysis is a very common and simple approach for the transformation of lignin to bio-oil. The process is usually conducted with a rapid heating rate to a high temperature, achieving the cleavage of C—C and C—O bonds. With promotion by catalysts, the pyrolysis rate can be enhanced, and the reaction temperature can be lowered. Zeolites and alkalis are usually used as catalysts for the catalytic pyrolysis of lignin [60–62].

Photocatalysis is usually conducted under mild conditions and is considered as an alternative means for conventional catalysis. There are also some studies on photocatalysis for the depolymerization of lignin [63]. Wang and coworkers reported the fractionation and valorization of lignocellulose via solar energy-driven conversion of native lignin at room temperature [64]. The cadmium sulfide quantum dots not only catalyzed the cleavage of β–O–4 bonds in lignin models quantitatively but also efficiently converted the native lignin within biomass into functionalized aromatics under visible light with cellulose/hemicellulose remaining almost intact. The mechanism for this photocatalysis process was investigated, and it was clarified that the β–O–4 bond in lignin was cleaved by an electron–hole-coupled photoredox mechanism based on a C_α radical intermediate, in which both photogenerated electrons and holes participate in the reaction (Figure 14.13). Although this work shows a great breakthrough in the utilization of lignin, the efficiency of photocatalysis still needs to be further improved, in relation to future industrial application.

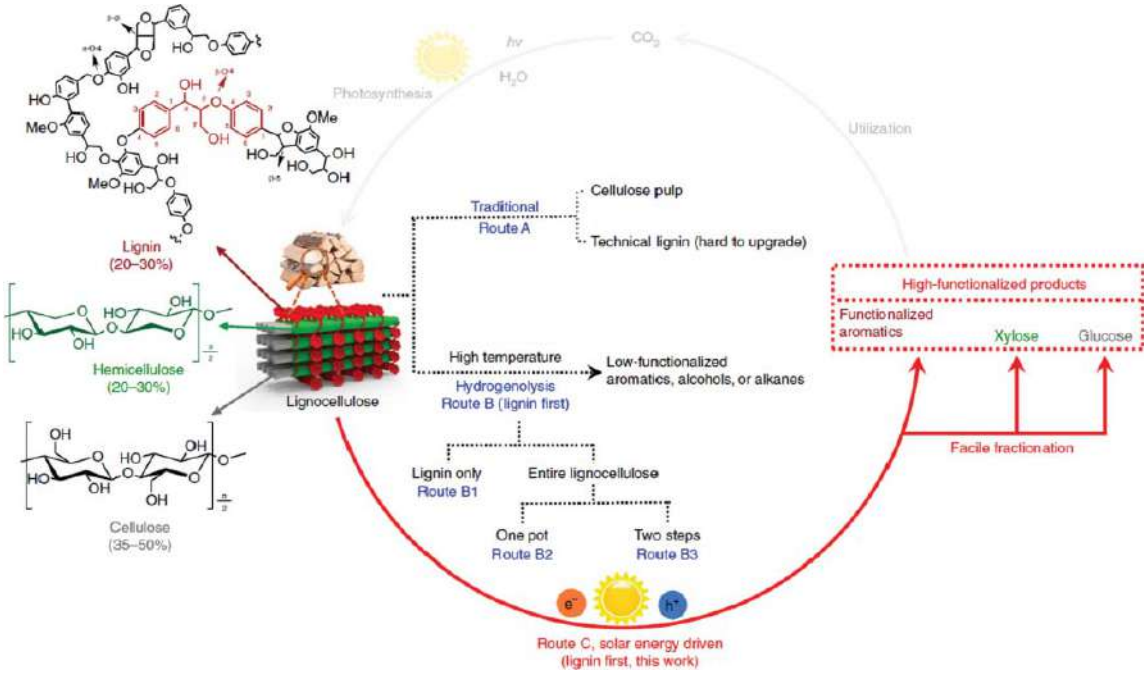

Figure 14.13 Photocatalysis of lignin to functionalized aromatics. Source: Wu et al. [64], Figure 01/with permission from Springer Nature.

14.3 Upgrading of Monomers to Fuels and Chemicals

The products obtained from the depolymerization of lignin exist as a mixture of phenolic compounds. Generally, the phenolic compounds contain a phenolic body, substituted with one or two ortho-methoxy groups and a para-propyl hydroxyl group. The complexity and diversity of these mixtures limit their utility as chemicals. Moreover, the high oxygen content in these mixtures lowers the heat value dramatically, making them unsuitable for use as fuels. Therefore, it is essential to upgrade these monomers to fuels or value-added chemicals by various techniques. Currently, the common upgrade products include cycloalkanes, aromatic hydrocarbons, and phenols. Recently, the generation of other value-added chemicals from lignin-derived monomers has also drawn significant attention. Among the techniques adopted for the upgrading of lignin-derived monomers, hydroprocessing is the most popular and efficient strategy as it can transform lignin monomers into various products, such as cycloalkanes, aromatic hydrocarbons, and phenols, by adjusting catalysts and processing conditions.

14.3.1 Upgrading Lignin Monomers to Cycloalkanes

Lignin monomers can transform into cycloalkanes by breaking the C—O bonds and hydrogenating the unsaturated carbon–carbon bonds [65] including the unsaturated bonds formed by the cleavage of C—O units and the native benzene ring. It has been extensively demonstrated that these cycloalkanes can be generated with very high yield from lignin oil or lignin monomer model compounds over various kinds of catalytic systems. In general, this conversion requires catalysts not only to have the ability to activate H_2 but also to have the ability to activate the C—O bonds or dehydration, i.e. the bifunctional catalysts. Metal active sites, especially noble metals like Ru, Rh, Pd, and Pt, have been shown to provide excellent activity in this kind of reaction. Cheaper metals with high activity in hydrogenation, for example, Ni and Co, have also been successfully applied. Acidic active sites are known to promote the cleavage of C—O bonds or dehydration. The acidic active sites can be provided by homogeneous acids, such as H_3PO_4, H_2SO_4, CH_3COOH, and acidic ionic liquids, and heterogeneous acids, such as acidic zeolites and other solid oxide acids.

In 2009, Kou's and Lercher's group jointly developed an efficient catalytic route for the production of alkanes by upgrading the aqueous phenolic bio-oil [65]. A carbon-supported noble metal Pd catalyst in combination with the mineral acid H_3PO_4 was employed as the bifunctional catalytic system for the one-pot conversion of bio-oil through the multistep reactions consisting of hydrogenation, hydrolysis, and dehydration. The mixture of alkane products (C_{1-3}-alkylated cyclohexanes) formed an organic phase, which could be easily separated from the aqueous phase. This novel route provides a feasible approach for the direct use of crude aqueous bio-oil mixture, facilitating an energy-efficient and atom-economic process.

Subsequently, Kou worked with Dyson and achieved the transformation of lignin-derived phenolic compounds to cycloalkanes in ILs in 2010 [66]. The catalytic

system applied was composed of metal nanoparticles and a functionalized Brønsted acidic IL immobilized in a nonfunctionalized IL. This allows hydrogenation and dehydration reactions to occur in tandem. Compared with previous systems that were performed either with metal sulfite or with mineral acid/supported metal catalysts in water, this system allowed lignin derivatives to be upgraded in an efficient and less energy-demanding process. In addition, they proposed a mechanism for the formation of cycloalkanes from phenolic monomers using phenol as a model compound (Scheme 14.9).

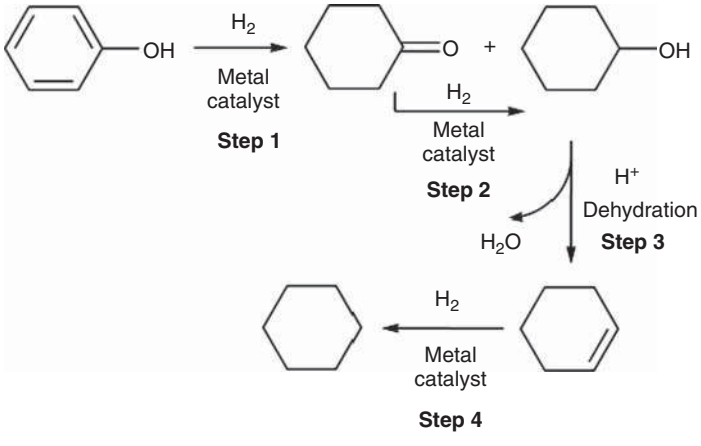

Scheme 14.9 Key steps involved in the formation of cyclohexane from phenol. Source: Reproduced with permission from Yan et al. [66], © 2010, Wiley.

Lignin oil usually contains many phenolic compounds. Taking one or two model compounds of lignin monomer as feedstock cannot genuinely represent the ability of these catalytic systems for real lignin oil. Zhao and Lercher used the aqueous phenolic mixture (nine different phenol, guaiacol, and syringol derivatives, which are made up 14.2 wt% of the phenols in the water solution) as feedstock and evaluated their conversion over the catalyst combined with Pd/C and H–ZSM-5 at 473 K and 5 MPa H_2 for four hours [67]. After evaluation, they obtained an upper organic layer consisting of 87% C_6–C_9 cycloalkanes and an aqueous layer containing 11% methanol at a conversion of 85% (Scheme 14.10), suggesting that the catalyst system could efficiently suppress the polymerization of the phenolic mixture even at high reactant concentrations.

In addition to Pd, Ru is another metal commonly used in the upgrading of lignin monomers to cycloalkanes. Among the reported Ru catalysts, zeolite-supported Ru catalyst possesses high efficiency [68, 69]. Zhang et al. reported that Ru/H–ZSM-5 (Si/Al = 25), a bifunctional catalyst of Ru supported using zeolite H–ZSM-5, exhibited excellent HDO ability for the conversion of lignin-derived phenolic monomers to cycloalkanes in aqueous solutions [69]. To gain the insight of this reaction, the reaction pathway was investigated in detail with phenol as model compound. The elementary reactions for phenol HDO were divided into three processes, and

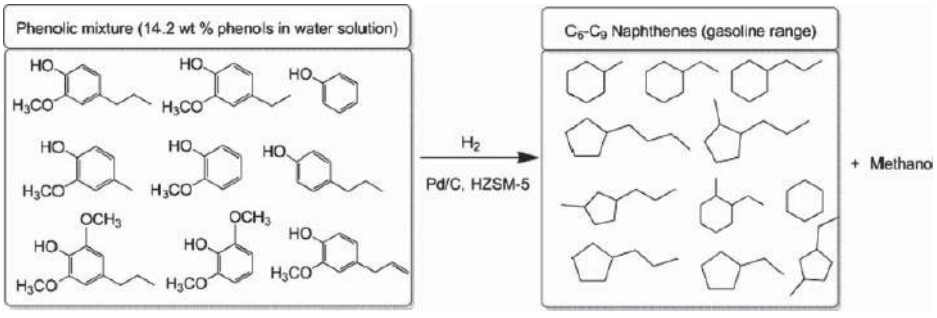

Scheme 14.10 HDO of the phenolic mixture with Pd/C and H–ZSM-5 catalysts in water at 473 K. Source: Reproduced with permission from Zhao and Lercher [67], © 2012, Wiley.

the turnover frequencies (TOFs) were measured separately. The three processes are shown in Scheme 14.11, namely, (i) direct phenol hydrogenation to cyclohexanol over Ru/H–ZSM-5, (ii) cyclohexanol dehydration to cyclohexene over H–ZSM-5, and (iii) cyclohexene hydrogenation to cyclohexane over Ru/H–ZSM-5. The direct cyclohexanol hydrogenolysis to cyclohexane (iv) was also considered, which might be another elementary reaction involved in phenol HDO.

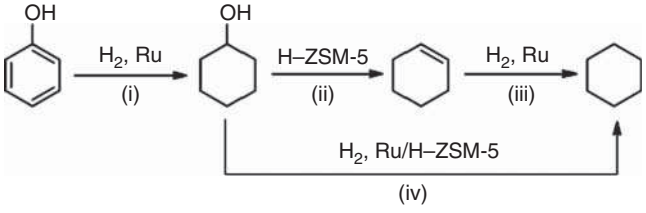

Scheme 14.11 The proposed reaction pathway for HDO of phenol. Source: Reproduced with permission from Zhang et al. [69], © 2014, American Chemical Society.

The TOF of phenol hydrogenation over Ru/H–ZSM-5 was 118 mol_{phenol} mol_{Ru}^{-1} h^{-1} at 393 K at a low phenol conversion level of 10%. Under the above conversions, cyclohexanol was observed to be the predominant product with a selectivity of 86.5%. The rate of cyclohexanol dehydration over H–ZSM-5 was about 15 $mol_{cyclohexanol}$ mol_{acid}^{-1} h^{-1} with observed selectivity of 99.9% to cyclohexene. The TOF of cyclohexene hydrogenation to cyclohexane over Ru/H–ZSM-5 was 2.1×10^3 $mol_{cyclohexene}$ mol_{Ru}^{-1} h^{-1}, a far higher value than that of the phenol hydrogenation. In the case of cyclohexanol conversion, the rate of cyclohexanol hydrogenolysis was very inferior over Ru/H–ZSM-5 with a TOF value of about 7 $mol_{cyclohexanol}$ mol_{Ru}^{-1} h^{-1} and cyclohexane selectivity of 52.3%. From the TOF values for different elementary steps, it is proposed that the dehydration, i.e. the cleavage of C—O bond, should be the rate-limiting step in the HDO of phenol. The oxygen-containing groups in phenolic compounds were removed by cleaving the C—O bond in the phenolic form, followed by integrated metal and acid-catalyzed hydrogenation and dehydration. As a bifunctional catalyst Ru/H–ZSM-5, the presence of both the Brønsted acid sites in the pores of H–ZSM-5 for dehydration and a metallic function of Ru for hydrogenation is responsible for the formation of cycloalkanes from lignin-derived phenolics. Furthermore, the Ru/H–ZSM-5 with the lowest H–ZSM-5 Si/Al ratio proved to be most the selective to cycloalkanes, indicating that more acid sites over the zeolite were favorable for the dehydration of cyclohexanol during the HDO process, leading to the higher selectivity to hydrocarbons. This work presents a good example of the investigation of the reaction pathway of phenol conversion by HDO and can guide the design and preparation of more highly efficient catalysts.

Besides phenol, other phenolic compounds are employed as model compounds of lignin monomers. 2-Methoxyphenol (guaiacol) is one of the prototypical models as it is considered to represent a large number of substituted phenols found in bio-oils derived from soft or hard wood lignin. Gates and coworkers studied

the reaction network of guaiacol over a Pd/Al_2O_3 catalyst [70]. They derived a detailed qualitative network by using selectivity–conversion data to determine an approximate quantitative reaction network accounting for the primary products (Scheme 14.12). The rate constants for the formation of primary products were measured, and the three major classes of reactions were demonstrated, namely, hydrogenolysis (including HDO), hydrogenation, and trans-alkylation. It was inferred that the metal function catalyzed the two former reaction classes and that the alumina support catalyzed the latter. Higher temperatures favored trans-alkylation, while higher H_2 partial pressure was beneficial for the selectivity for HDO.

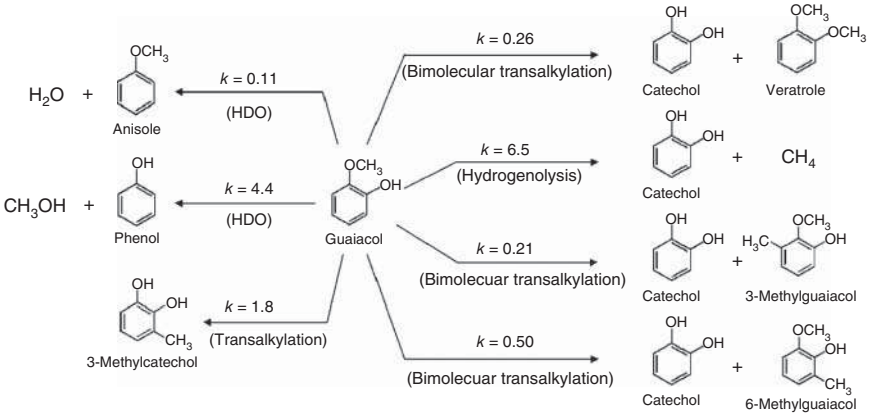

Scheme 14.12 The reaction network accounting for the formation of primary products determined from analysis of selectivity–conversion plots for the conversion of guaiacol and H_2 catalyzed by Pt/γ-Al_2O_3 at 573 K. Source: Reproduced with permission from Nimmanwudipong et al. [70], © 2011, American Chemical Society.

Apart from noble metal catalysts, non-noble metal catalysts have been applied in many investigations of the upgrading of lignin monomers to cycloalkanes. Ma and coworkers developed bifunctional $Ni/SiO_2–ZrO_2$ catalysts, which gave a maximum 100% guaiacol conversion and 96.8% cyclohexane selectivity [71]. Subsequently, another Ni-based catalytic system was developed and used in the upgrading of lignin to cycloalkanes by the same group [72]. The Ni component obtained in situ from the thermal decomposition of $Ni(HCOO)_2$ acted as the hydrogenation and hydrogenolysis catalyst, while H–ZSM-5, Nb_2O_5, and SiZr oxide acted as the solid acid for dehydration. Fang et al. have taken an integrated dual catalyst strategy to upgrade lignin-derived oxygenates over Ni-containing catalytic systems [73]. In their work, almost 100% conversion of various oxygenates was obtained, and the product distribution could be tuned using the integration approach and active catalysts. High cyclohexane selectivity of 87.9–100% was achieved by using integrated dual catalysts. In addition to metal catalysts, metal sulfide catalysts have been reported to be effective for the hydrotreating of lignin monomers [74].

14.3.2 Upgrading Lignin Monomers to Aromatic Hydrocarbons

As described above, although hydrocarbons can be generated by upgrading of lignin monomers via hydrotreating to remove oxygen, these hydrocarbons are saturated, losing the aromatic moiety originating from the lignin structure. It is more desirable to produce aromatic hydrocarbons from lignin as compared with cycloalkanes. As gasoline blend, aromatic hydrocarbons are more desirable in terms of the demand for octane number. As jet fuel blend, aromatic hydrocarbons are also more favorable because they not only have a high density that means the airplane carries more fuel but also have good compatibility with rubber that can prevent fuel leakage from the tank. Moreover, it consumes less hydrogen from lignin to produce aromatic hydrocarbons than that required to produce cycloalkanes. Therefore, many efforts have been devoted to the conversion of lignin to aromatic hydrocarbons. Generally, one of great challenges is how to facilitate the hydrogenolysis of C—O bonds and meanwhile keep aromatic ring intact.

In general, three reaction mechanisms for the conversion of phenolic compounds into aromatic hydrocarbons have been demonstrated [75], namely, (i) DDO of phenolic hydroxyl groups to arenes; (ii) the hydrogenation route involving three tandem steps including hydrogenation to cyclohexanol or cyclohexanone, then dehydration to cyclohexene, and finally dehydrogenation to aromatic hydrocarbons; and (iii) the tautomerization-hydrogenation-dehydration (THD) route that is proposed to proceed via tautomerization followed by hydrogenation to cyclohexadienol and finally dehydration to generate aromatic hydrocarbons (Scheme 14.13). These three parallel pathways are usually affected by various factors including the reaction conditions like the temperature and hydrogen pressure, the hydrogenation activity of the metal, and the role of the support. The first two pathways, i.e. DDO and hydrogenation, are relatively common. The DDO route is more desirable for the production of aromatic hydrocarbons from phenolic compounds, which is favored by operating at high temperature and low hydrogen pressure.

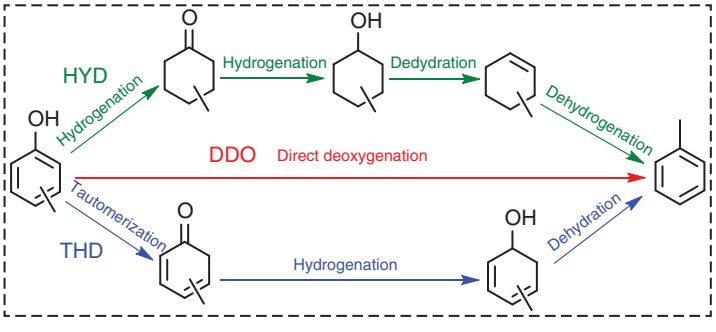

Scheme 14.13 The reaction pathway for the conversion of cresol to toluene. Source: Reproduced with permission from Jing et al. [75], © 2020, Wiley.

Significant attention has been paid to the development of heterogeneous catalysts for the removal of phenolic hydroxyl groups, owing to their strongest bond energy

among all C—O bond groups within lignin. Cresol and phenol are the simplest among the widely investigated compounds representative of lignin oils, incorporating the aromatic ring and hydroxyl group that are typical groups of lignin and lignin-derived compounds. In addition, guaiacol is applied as a more complex model compound.

Many catalysts have been developed for the HDO of phenolic compounds to produce aromatic hydrocarbons. The developed phenolic HDO catalysts can be divided into four categories, i.e. (i) metal sulfides, (ii) noble metal catalysts, (iii) non-noble metal catalysts, and (iv) metal carbides, nitrides, and phosphides.

Sulfided $NiMo/Al_2O_3$ and $CoMo/Al_2O_3$ catalysts have been used in the petroleum refineries for many decades, and the main purpose is eliminating the sulfur-containing compounds from distillation oil by hydrodesulfurization (HDS) to produce clean fuels. During this process, the nitrogen- and oxygen-containing compounds can also be converted to hydrocarbons by hydrodenitrogenation (HDN) and HDO.

In 1995, Delmon and coworkers employed a Al_2O_3-supported CoMo sulfide catalyst to upgrade lignin oil via HDO [76, 77]. Recently, many metal sulfide catalysts have been reported for the HDO of lignin-derived phenolic compounds [78]. For example, Liu et al. developed a CoMoS catalyst with a large number of basal sulfur vacancies within Co-doped single-layer MoS_2 through high-temperature treatment in H_2 [79]. This catalyst, with a sufficient number of Co–S–Mo active sites for the HDO reaction to occur at a low operating temperature, was extremely active, selective, and stable for the conversion of 4-methylphenol to toluene. Consequently, $Co–{}^{S}MoS_2$ displayed superior activity and selectivity (99.2%) to non-promoted conventional catalysts, as shown in Figure 14.14. A similar study has also been reported

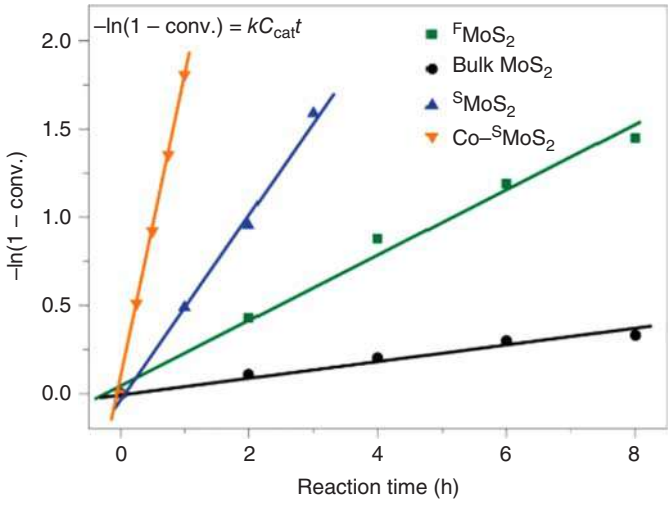

Figure 14.14 Kinetic studies for HDO of 4-methylphenol to toluene showing the activity order of $Co–{}^{S}MoS_2 > {}^{S}MoS_2 > {}^{F}MoS_2 >$ bulk MoS_2. Source: Reproduced with permission from Liu et al. [79], © 2017, Nature.

by Jiang and coworkers, in which they proposed the surface atom engineering strategy to design an efficient CoMoS nanosulfide for HDO of lignin-derived phenols to aromatic hydrocarbons [80]. Typically, a self-induced method was taken to substitute S sites by Co effectively, leading to the good incorporation of Co atoms onto the top surface of MoS_2 nanosheets while maintaining its original morphology. Thus, a highly dispersed active phase Co–Mo–S was created successfully and exhibited excellent performance in HDO of lignin-derived phenolic compounds with >85% yield of aromatic hydrocarbons.

Although metal sulfide catalysts exhibit excellent activity in the HDO of lignin-derived phenolics, the stability of such catalysts needs to be improved. There are two main reasons for the catalyst deactivation. One is that during the hydrogenation process, the sulfur in metal sulfides is easily taken away in the form of hydrogen sulfide, resulting in the loss of active phase components. Another is that such catalysts are prone to carbon deposition, which can block the active sites. Efforts have been made to develop alternative sulfur-free catalysts, including noble metal catalysts, non-noble metal catalysts, and metal carbides, nitrides, and phosphides.

Ru, Pd, and Pt are the most common noble metals employed in the HDO of phenolics to aromatic hydrocarbons. Among them, Ru is considered to be the most efficient because Ru possesses a proper hydrogenation activity, leading to the high selectivity to aromatic hydrocarbons. For the metal catalysts, supports also play a significant role as substrates need to be adsorbed and activated on them. The oxophilic sites are critical to the supports. In this respect, the high-valence and strong Lewis acidity metal oxides, such as TiO_2, MoO_3, Nb_2O_5, Re_2O_7, and WO_3, are desirable candidates. Particularly, Nb_2O_5 shows distinctive performance on generating aromatic hydrocarbons from phenolics by HDO. Undoubtedly, both metal sites and supports are responsible for the performance of a supported catalyst.

Wang and coworkers have developed a series of Nb-based catalysts and used them in the upgrading of lignin or its derivatives, showing amazing activity and selectivity to aromatic hydrocarbons [1, 75, 81, 82]. A porous Ru/Nb_2O_5 was capable of converting organosolv lignin into arenes with high selectivity, and the Nb_2O_5 support enabled the selective activation of the phenolic hydroxyl groups, resulting in a significant reduction of the disassociation energy for the phenolic hydroxyl groups. The adsorption and binding of phenol molecules on the $Nb_2O_5(001)$, $ZrO_2(010)$, $Al_2O_3(110)$, and $TiO_2(101)$ surfaces confirm that Nb_2O_5 has strong adsorption of phenol and low dissociation energy of $C_{aromatic}$–OH bonds among them [81], as shown in Figure 14.15. Subsequent investigations including the metal size effect, electronic effect, and Nb_2O_5 surface properties revolved around the activation of the phenolic hydroxyl groups over Nb-based catalysts [83–85]. It is found that the size of the Ru nanoparticles strongly affects the lignin hydrogenolysis activities and product distribution [83, 84]. The exploration of the relationships between Nb_2O_5 surface properties and its catalytic performance in HDO of lignin and its derived compounds revealed that the coordination states of Nb (NbO_x sites) affected the catalytic activity, while Ru nanoparticle size was responsible for the product selectivity [84, 86]. More unsaturated NbO_x species show stronger

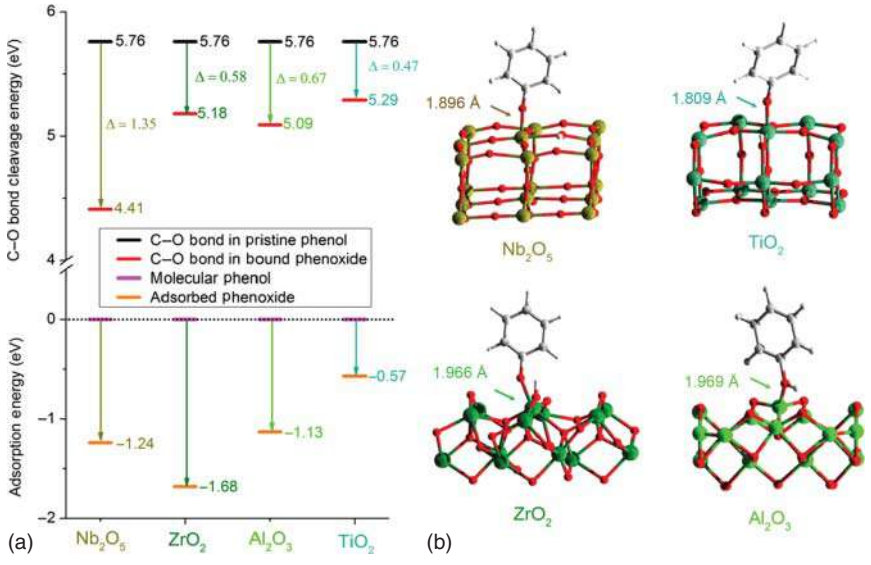

Figure 14.15 Calculated energies and views of the optimized structural models for phenol binding on catalyst surfaces. (a) Calculated energies for phenol adsorption (that is, a combination of deprotonation of $C_{aromatic}$–OH to form phenoxide bound to the vacant surface metal sites and the formation of surface-OH groups and dissociation of the C—O bonds upon adsorption over Nb_2O_5, ZrO_2, Al_2O_3, and TiO_2). (b) Views of the corresponding DFT-optimized structural models for the phenoxide bound on Nb_2O_5 (001), ZrO_2 (010), Al_2O_3 (110), and TiO_2 (101) surfaces. Source: Reproduced with permission from Shao et al. [81].

adsorption and activation ability for C—O bonds, thus promoting the HDO reaction of lignin-derived compounds.

By modifying the Ru/Nb_2O_5 catalyst, other specific aromatic hydrocarbons can be obtained from lignin oil or lignin. Li et al. designed an efficient FeO_x-modified Ru/Nb_2O_5 catalyst for the highly selective production of ethylbenzene from birch lignin oil (BLO) through the integration of dehydrogenative decarbonylation (DHDC) and HDO processes [87]. Compared with Ru/Nb_2O_5 catalyst, $RuFe/Nb_2O_5$ exhibited higher selectivity to ethylbenzene from both lignin model compound (78.5%) and BLO (63.4%). The introduction of FeO_x species decreased the ratio of metallic Ru species that retarded the DDO of $C_{propanol}$—O bonds and enhanced the DHDC process. Moreover, the modification of FeO_x enhanced the oxygen vacancies on the surface of Nb_2O_5, thus promoting the cleavage of $C_{aromatic}$—O bonds. Both of these two factors led to the highly selective production of ethylbenzene, as shown in Figure 14.16. More interestingly, weakening the hydrogenolysis ability of Ru through the strong interaction created by the decoration of CH_2Cl_2 favors another parallel route, namely, the intramolecular cyclization reaction, rather than the DDO of propyl hydroxyl groups, achieving a high yield of indane and its derivatives [88].

Compared with Ru, HDO catalysts involving Pt and Pd are generally favorable for the saturation of aromatic rings instead of the removal of phenolic hydroxyl groups, resulting in a high yield of cycloalkanes due to their strong hydrogenation

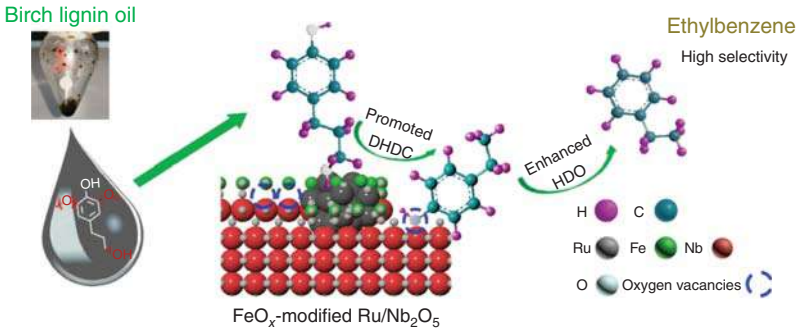

Figure 14.16 Selective production ethylbenzene from lignin oil. Source: Li et al. [87] (2020)/with permission from Elsevier.

activity. Interestingly, three completely different pathways for the HDO of phenol over Ru/Nb_2O_5, Pd/Nb_2O_5, and Pt/Nb_2O_5, respectively, have been confirmed by experimental and vibrational analysis [81, 89]. When employing Ru/Nb_2O_5 as catalyst, the direct cleavage of C—O bonds is overwhelming, owing to a combination of strong adsorption, selective activation of the phenolic hydroxyl groups, and synergistic effect between the Ru and NbO_x species, leading to a distinct selectivity to benzene [81]. While with Pd/Nb_2O_5, the aromatic ring saturation shows higher selectivity than the DDO of C—O bonds because of stronger bonding of the aromatic ring with catalyst surface and the higher hydrogenation ability of Pd than that of Ru. In contrast, a combination of a direct dehydroxylation and a tandem route with fast kinetics over Pt/Nb_2O_5 results in a higher benzene selectivity than that of Pd/Nb_2O_5 at the beginning of the reaction [89]. Even so, the aromatic hydrocarbons selectivity over Pt/Nb_2O_5 is still lower than that of Ru/Nb_2O_5, owing to its stronger hydrogenation activity.

Non-noble metals are generally inexpensive and environmentally benign; thus, they are promising candidates for selective HDO. Among the non-noble metal catalysts, Ni has been extensively studied for HDO of phenols not only to cycloalkanes but also to aromatic hydrocarbons, owing its excellent ability to dissociate hydrogen. However, it is still difficult to convert phenolics to aromatic hydrocarbons over Ni-based catalysts in comparison with conversion to cycloalkanes, because of the strong hydrogenation ability of Ni. In general, to use Ni catalysts to obtain aromatic hydrocarbons, modifications are required to decrease their hydrogenation ability. For example, Resasco and coworkers developed a catalyst comprising a highly dispersed Ni core decorated with MoO_x that sterically and chemically modify its surface [90]. The catalyst shows a huge increase in the activity in HDO of *m*-cresol and higher selectivity toward desired aromatic hydrocarbons than the unmodified Ni catalyst.

Apart from the obstacle to selectivity caused by the over-hydrogenation on non-noble catalysts, deactivation is another barrier for their application in the HDO of lignin or its derivatives. This is because non-metal catalysts are prone to aggregation during reaction, especially at high temperatures, leading to the loss of

activity. Recently, metal carbides, nitrides, and phosphides have been employed in the upgrading of lignin monomers. It is considered that these catalysts exhibit similar properties to noble metal catalysts in hydrogenation. In addition, their stability is superior to the non-metal catalysts as the aggregation will not occur as severely as non-metal catalysts. For example, Ni_2P/SiO_2 showed excellent HDO ability in the conversion of lignin model compounds [91]. The active site of Ni_2P catalysts is composed of threefold hollow Ni and P sites, which are favorable for the adsorption of H or OH groups.

14.3.3 Upgrading Lignin Monomers to Phenols

In addition to completely eliminating the monomer oxygen functionality, upgrading aims to retain the phenolic OH group to produce phenols. In industry, phenols are produced via oxidation of benzene. Compared with producing hydrocarbons from lignin, the production of phenols is more economically beneficial as it consumes less hydrogen and phenols are more valuable than hydrocarbons. Thus, phenol production from lignin is a potential and green alternative route for lignin upgrading that is gaining much current attention for the utilization of lignin.

Guaiacol or 4-propylguaiacol is commonly used as a prototype molecule representing lignin-derived monomers to study the selective cleavage of C—O bonds because they all contain a methoxy group, a phenolic hydroxyl group, and an aromatic ring. It is important to selectively remove methoxy groups and para-side chain groups in the upgrading of lignin monomers to phenol.

As shown in Scheme 14.14, guaiacol can be converted to phenol through three routes. First, it is converted to catechol intermediates by demethylation and then dehydroxylated to phenol. Second, it shows direct demethoxylation to phenol. Third, the anisole is first formed by dehydroxylation and then demethylated to phenol [75]. Based on the bond energy of the three groups in guaiacol, the corresponding first two approaches are proposed and have been proven by most studies. That is, the mechanism of demethoxylation is a point of focus.

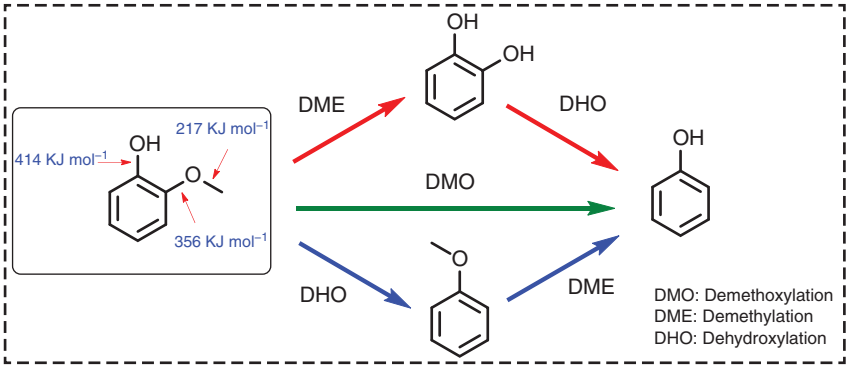

Scheme 14.14 Reaction pathways in the conversion of guaiacol to phenol. Source: Reproduced with permission from Jing et al. [75], © 2020, Wiley.

There are several apparent competitive reactions in producing phenol from lignin monomers, i.e. the desired removal of methoxy groups and undesired hydrogenolysis of the phenolic hydroxyl group and hydrogenation of benzene ring. Therefore, it is necessary to carefully design and prepare the catalyst to achieve the demethoxylation while retaining the phenolic hydroxyl group and aromatic moiety. Many types of catalyst (including metal sulfides $NiMoS/Al_2O_3$ and $CoMoS/ZrO_2$; TiO_2-supported Au, Ag, or Ni; Au/Nb_2O_5; molybdenum supported on carbon; and Ru/CeO_2) have been developed for upgrading lignin monomers to phenols (as summarized in Table 14.2).

Among the abovementioned catalysts, supported gold catalysts have exhibited excellent performance for hydrotreating lignin monomers to phenols. The remarkable performance of gold is attributed to its relatively low hydrogenation activity, which avoids hydrogenation of the benzene ring and hydrogenolysis of the phenolic hydroxyl group. In 2017, Zhang and coworkers identified a strikingly active Au/TiO_2 catalyst with high selectivity to phenolics [95]. The catalyst hindered guaiacol conversion to aromatic hydrocarbons or cycloalkanes by inhibiting the hydrogenolysis of phenolic hydroxyl group or hydrogenation of benzene ring, as shown in Scheme 14.15, leading to the high phenol selectivity of 87.1%. In comparison, neither the Au nanoparticles nor the TiO_2 support was active for the hydrogenation of guaiacol. In contrast to other supports such as TiO_2 (rutile), activated carbon, silica, gamma alumina, and zirconia, only the specific anatase phase of TiO_2 appeared to be suitable for the production of active Au nanoparticles.

Undoubtedly, supports play a significant role in the removal of the methoxy groups. Whatever the elimination of methoxy group achieved by directly hydrogenolyzing or hydrolyzing followed by hydrogenolyzing of one phenolic hydroxyl group, good oxophility of supports is required to adsorb and activate the oxygen in methoxy group. As described in Section 14.3.2, niobium oxide has been confirmed to show high activity in the activation of C—O bonds in lignin monomers. Very recently, Wang and coworkers developed Au/Nb_2O_5 catalyst and evaluated its performance in the upgrading lignin monomers and lignin oils to phenols [98]. Compared with other metal oxide supports, Nb_2O_5 shows the best performance with complete conversion and selectivity of 84.2% toward 2-methoxy-4-propylphenol (Figure 14.17). Apart from the contribution of Nb_2O_5 in the adsorption and activation of substrates, the electronic effect of gold plays a crucial role in the efficient production of phenolics from 4-propylguaiacol. The gold in Au/Nb_2O_5 is electron richer, as confirmed by the X-ray photoelectron spectroscopy (XPS) and X-ray absorption spectroscopy (XAS) characterization. Both the electron-rich Au nanoparticles and the Nb_2O_5 support are responsible for the efficient cleavage of the $C_{aromatic}$–O linkage and high production of phenols from lignin monomers and lignin oils. Very recently, similar work was reported about the synergistic effect between metal and support in the upgrading of guaiacol to phenol [96]. Silver supported on TiO_2 was found to promote H_2 dissociation and spillover onto the TiO_2 surface. The spillover hydrogen can reduce the TiO_2 surface to create oxygen vacancies as the active sites for HDO, resulting in the efficient performance for the selective conversion of guaiacol into phenol.

Table 14.2 Overview of the synthesis of phenols from lignin model compounds.

Feedstock	Conversion (%)	Catalyst	Reaction conditions	Major product	Yield (%)	References
Guaiacol	100	$CoMoS/ZrO_2$	A partial pressure of guaiacol of 2.7 kPa, 300 °C, 4 MPa H_2	Phenol	60	[92]
Guaiacol	98	MoO_2/AC	0.035 g ml^{-1} in tetral, 300 °C, 3 MPa H_2, 3 h	Phenol	71	[93]
Guaiacol	~90	Au/TiO_2	60 Nml min^{-1}, 300 °C, 6 h, 4 MPa H_2, 2.7 kPa guaiacol	Phenol	~63	[94]
Guaiacol	100	Au/TiO_2	0.16 mol l^{-1} in toluene, 300 °C, 6.5 MPa H_2, 700 rpm, 3 h	Phenol	50	[95]
Guaiacol	~75	Ag/TiO_2	1.5/18.5 g g^{-1} in heptane, 300 °C, 3 MPa H_2, 700 rpm, 3 h	Phenol	~45	[96]
Guaiacol	100	Ni/TiO_2	0.048 g ml^{-1} in decane, 300 °C, 4 MPa H_2, 500 rpm, 6 h	Phenol	~85	[97]
2-Methoxy-4-propylphenol	100	Au/Nb_2O_5	5% g ml^{-1} in water, 300 °C, 8 h, 6.5 MPa H_2	Propylphenol	84	[98]
Vanillin	100	ZnO/Co@N-CNTs	250/30 mg ml^{-1} in water, 300 °C, 6 h, 5 MPa H_2	*p*-Cresol	82	[99]
4-Ropylguaiacol	~65	Au/TiO_2 + H-ZMS-5	10% g ml^{-1} in benzene, 350 °C, 2 h, 5 MPa H_2	Phenol	~60	[100]
2-Methoxy-4-propylphenol	~100	Pt/C + H-ZMS-5	Feedstock injection rate 240 µl h^{-1}, water injection rate 240 µl h^{-1}, H_2 10 ml min^{-1}, 375 °C	Phenol	60	[101]

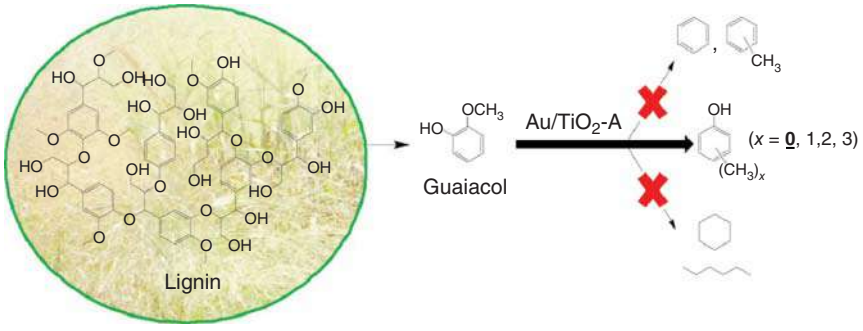

Scheme 14.15 Production of phenol from guaiacol over Au/TiO_2 catalyst. Source: Mao et al. [95]/with permission from American Chemical Society.

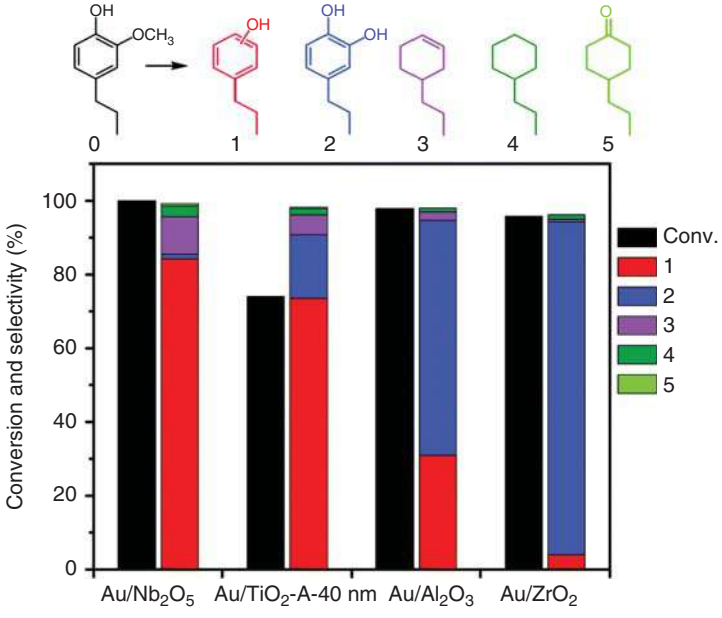

Figure 14.17 Conversion of 4-propylguaiacol over gold supported on various metal oxides catalysts. Source: Reproduced with permission from Dong et al. [98], © 2019, Royal Society of Chemistry.

Although guaiacol has been employed as a model compound to investigate the possibility to generate phenol, there still is an obvious difference between guaiacol and real lignin monomers obtained by depolymerization. That is, the real lignin monomers usually contain a para-propyl group. Thus, when taking lignin oil as substrate, the products obtained by the above techniques used in upgrading guaiacol to phenol are some phenols with alkyl groups in the para-position. Selective conversion of alkylphenols to phenol and olefins is presented as a challenging step in the upgrading of lignin. To obtain phenol, several groups have made efforts on stripping the alkyl group in alkylphenols. For example, Sels and coworkers took

4-ethylphenol and 4-propalphenol as substrates, respectively, to study the phenol production over zeolite catalysts [102, 103]. A high yield of phenol and olefins (ethylene and propene) was obtained by dealkylation. Yan and coworkers also succeeded in the single-step conversion of lignin monomers to phenol by combining two catalysts, namely, Pt/C and H–ZSM-5, to simultaneously break the C—O bond of the methoxy groups and the C—C bond of the alkyl group. However, the deactivation of the dealkylation catalyst limits its application [101]. Very recently, Sels and coworkers reported that 20 wt% of phenol and 9 wt% of propylene (on the basis of lignin weight) were obtained using crude lignin oil as feedstock. Importantly, the residual phenolic oligomers (30 wt%) might be used in printing ink as replacements for controversial para-nonylphenol [104].

Wang et al. employed a unique strategy and developed a completely different approach to produce phenol from lignin [105]. As shown in Scheme 14.16, the C_α–C_β bond was first oxidized to cleave and generate a carboxylic group. Then, subsequent decarboxylation occurred to form phenol. This strategy is also capable of converting raw biomass including poplar, birch, pine, peanut, bamboo willow, and straw into phenol.

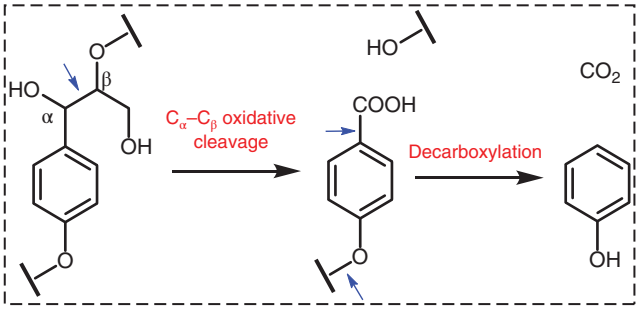

Scheme 14.16 Production of phenol from lignin via an oxidation–hydrogenation route. Source: Reproduced with permission from Wang et al. [105], © 2018, American Chemical Society.

14.3.4 Upgrading Lignin Monomers to Other Chemicals

Although most of the studies on lignin upgrading focus on the production of cycloalkanes, aromatic hydrocarbons, and phenols, the synthesis of other types of value-added chemicals is also an interesting topic. As a great example, Yan and coworkers developed a three-step strategy for the production of terephthalic acid (TA) from lignin-derived monomer mixtures [106]. As shown in Figure 14.18, this strategy started with the hydrotreating of corn stover-derived lignin oil over a supported molybdenum catalyst to selectively remove methoxy groups. The generated 4-alkylphenols were converted to 4-alkylbenzoic acids by carbonylation with carbon monoxide. Then, a Co–Mn–Br catalyst oxidized various alkyl chains into carboxy groups, transforming the 4-alkylbenzoic acid mixture into a single-product TA. From this route, the overall yield of TA based on lignin content of corn stover could reach 15.5 wt%, and importantly, TA with greater than 99% purity was obtained

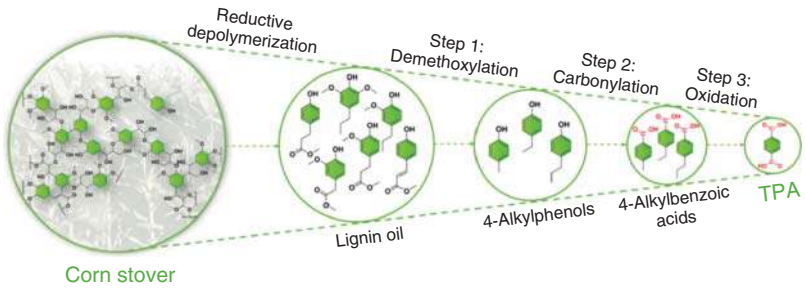

Figure 14.18 Production of pure terephthalic acid (PTA) from lignin oil. Source: Song et al. [106], Scheme 01/with permission from John Wiley & Sons, Inc.

simply by first decanting the reaction mixture and then washing the solid product with water. Apart from TA, ethanol, acetic acid, and methyl-substituted amine production from lignin also have been reported by Han's group [107–109].

14.4 Direct Conversion of Lignin to Fuels and Chemicals

Recently, routes to convert lignin via integrating depolymerization and subsequent upgrading in a one-pot reaction have also been reported. Compared with the two-step process of depolymerization and following upgrading, one-pot reactions not only are convenient in terms of operation but are also lower in cost. Although there are not as many examples as for the traditional two-step process, they represent an increasing trend in the valorization of lignin.

In 2016, pioneering work was reported by Wang and coworkers, who developed a novel route to achieve the full conversion of lignocellulose, including cellulose, hemicellulose, and lignin, to alkanes in one-pot process [110]. They designed a highly efficient $Pt/NbOPO_4$ catalyst with multifunctionality, i.e. activation of C—O bond, dehydration, and hydrogenation contributed by NbO_x species, acidic sites, and Pt, respectively. As shown in Figure 14.19, lignin was converted to alkylcycloalkanes. Investigations on the molecular mechanism employing *in situ* inelastic neutron scattering (INS) and density functional theory (DFT) calculations revealed that a synergistic effect between Pt, NbO_x species, and acidic sites promoted the highly efficient HDO of bulk lignocellulose. Subsequently, they reported a one-pot lignin conversion over a Ru/Nb_2O_5 catalyst in water to directly produce liquid hydrocarbons with a mass yield of 35.5 wt% and a near-quantitative carbon yield based on lignin monomers [81]. Significantly, this process combines the depolymerization of raw lignin and the hydrogenolysis of depolymerized compounds and affords an exceptional selectivity of 71 wt% to aromatic hydrocarbons. The combination of in situ INS and DFT calculations unambiguously confirmed the unique activity of the Nb_2O_5 species, thus rationalizing the observed high reactivity and unusual selectivity for Ru/Nb_2O_5. They demonstrated that it is the combination of strong adsorption, selective activation of the $C_{aromatic}$–OH bonds in phenolics, and synergistic effect between the Ru and NbO_x species that resulted in the high

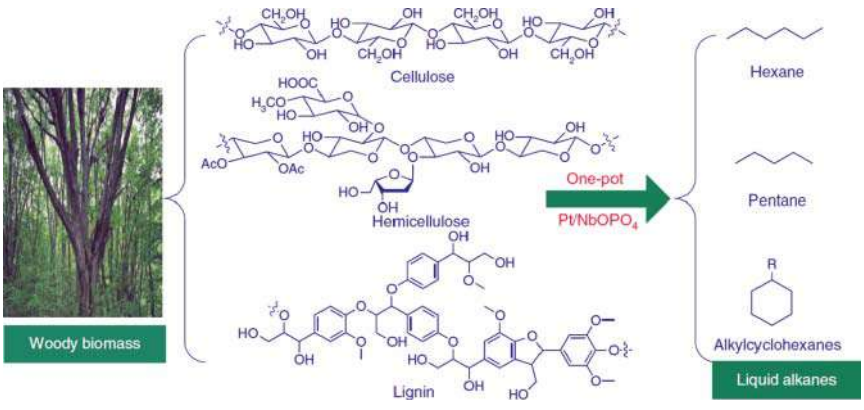

Figure 14.19 Direct conversion of raw woody biomass into liquid alkanes over $Pt/NbOPO_4$ catalyst. Source: Xia et al. [110], Figure 01/Springer Nature/CC BY 4.0

selectivity to yield aromatic hydrocarbons. To control the morphology of Nb_2O_5, they further improved the performance of Ru/Nb_2O_5 catalyst [84]. Over a layered Nb_2O_5 supported Ru catalyst, an important result was obtained with enzymatic lignin as the feedstock. The selectivity to aromatic hydrocarbons could reach up to 94.8% with the hydrocarbon yield of 99.6%. It is inferred that the unsaturated NbO_x species play a crucial role via promoting the adsorption and activation of C—O bonds in lignin. Some other Nb-based catalysts also have been demonstrated to be effective in the direct conversion of lignin to hydrocarbons, especially to aromatic hydrocarbons [82, 83, 86].

Apart from the Nb-based catalysts, several other types of catalysts have been reported to catalyze lignin to hydrocarbons in a one-pot process. Zhao and coworkers used Ni supported on amorphous silica alumina to convert enzyme lignin by hydrotreating in one-pot process [111]. Under optimized conditions (300 °C and 6.0 MPa H_2), the yield of transparent liquid product was up to 46.2%. The product mainly comprised naphtha and paraffins with a selectivity of 80.8% C_3–C_9 (gasoline range), 6.5% C_{10}–C_{14} (kerosene range), and 12.7% C_{14}–C_{17} (diesel range). Yang and coworkers employed a Ru–Cu/HY catalyst to hydrotreat the softwood lignin and obtained hydrocarbon products with a total yield of approximately 26–32 wt% [112]. The products were mainly monocyclic and bicyclic cycloalkanes. Rinaldi and coworker reported that a Ni/Al-SBA-15 catalyst could convert organosolv lignin by hydrotreating in a one-pot reaction, resulting in a selectivity to cycloalkanes higher than 99%. Besides Nb-based catalysts, the reported catalysts can only convert lignin to cycloalkanes by one-pot processes, but not to aromatic hydrocarbons. This may be due to the unique adsorption of benzene ring on NbO_x species.

The abovementioned cases for conversion of lignin in one-pot processes involve the depolymerization of lignin by only breaking the C—O–C ether bonds in lignin, followed by HDO. As known that except for the monomer building blocks connected by C—O–C linkages, there are also large amounts of monomers linked by C—C bonds. To maximize the production of monocyclic aromatic hydrocarbons from lignin upgrading, it is greatly desired to break not only the C—O linkage but also the

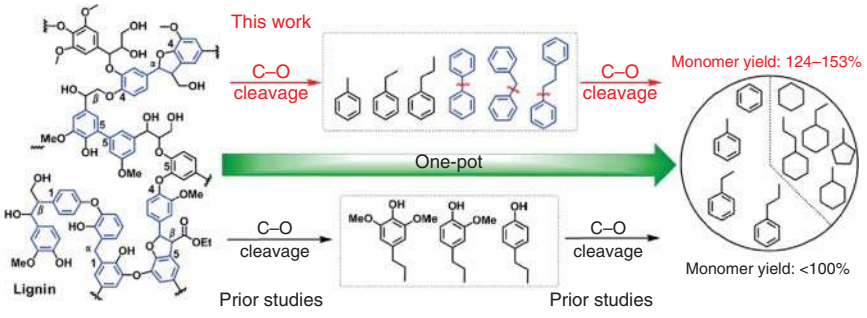

Figure 14.20 A representative structure of a lignin fragment showing various intramolecular linkages and a schematic representation of the one-pot depolymerization and hydrodeoxygenation of lignin into monocyclic aromatic hydrocarbons. Source: Reproduced with permission from Dong et al. [113]; © 2019, Elsevier.

C—C linkage. Very recently, Wang and coworkers employed a novel strategy for the valorization of lignin, aiming to maximize the production of monocyclic aromatic hydrocarbons via the utilization of the monomers connected by both C—O–C and C—C bonds, as shown in Figure 14.20 [113]. Using a multifunctional $Ru/NbOPO_4$ catalyst, they achieved the first example of catalytic cleavage of both interunit C—C and C—O bonds in lignin in a one-pot reaction to yield 153% of monocyclic C6–C9 hydrocarbons from Kraft lignin, which is 1.5 times the theoretical yield obtained from the established nitrobenzene oxidation (NBO) method. More significantly, the aromatic hydrocarbons dominate in the products, accounting for approximately 70%. Interestingly, the catalytic system is very efficient for the cleavage of $C_{aromatic}$–$C_{aliphatic}$ bonds but inert for the cleavage of $C_{aliphatic}$–$C_{aliphatic}$ bonds.

Until now, the reports on the direct conversion of lignin by one-pot processes mainly focus on the production of hydrocarbons, including cycloalkanes and aromatic hydrocarbons, via hydrotreating techniques. Direct conversion of lignin to other products, especially to oxygen-containing chemicals, is limited because of the complexity of the products obtained via other techniques. Great efforts are needed to improve the selectivity, though it will be a challenging task. Li and coworkers reported a new catalytic system to promote the selective oxidation of lignin to synthesize diethyl maleate with a selectivity of 72.7% [114]. However, in 2020, there are still many other by-products needing to be separated. Encouragingly, an innovative study has been reported to produce oxygen-containing chemicals via directly converting lignin in a one-pot process. Han and coworkers achieved the selective catalytic transformation of lignin with guaiacol as the only liquid product with a yield of 25.5 wt% [115].

14.5 Conclusions and Perspective

Lignin, as a major renewable aromatic resource, is attracting much attention in terms of its formation, structure, and utilization. Regarding the formation of lignin,

biologists and botanists have conducted fruitful research and revealed its formation mechanism. For the structure of lignin, forestry scientists and chemists have done a lot of work to analyze its structure and reveal its building blocks, i.e. sinapyl, coniferyl, and *p*-coumaryl alcohols. These achievements have produced a solid foundation upon which to build the valorization of lignin. In this decade, with the emphasis on alternative resource development, the production of alternative fuels and value-added chemicals from lignin by catalysis has become a research hotspot in the field of biomass utilization. In general, the depolymerization of lignin to monomers (also named lignin oil) and upgrading of monomers are the two main steps for lignin utilization. Various catalytic depolymerization strategies have been developed, including acidic, alkaline, reductive, and oxidative catalytic depolymerization. These possess different requirements for the treatment of lignin. By upgrading lignin monomers, various products, such as cycloalkanes, aromatic hydrocarbons, phenols, and other chemicals, have been obtained via specific catalytic techniques, especially the hydrotreating techniques (hydrogenation and hydrogenolysis). It is of great significance to design and prepare efficient catalysts to achieve the selective transformation of lignin monomers to target products. Integrating the depolymerization of lignin and upgrading of monomers into one pot have shown great superiority to the conventional two-step process, owing to its convenient operation and low cost.

The chemistry involved in the valorization of lignin is mainly the activation of C—O and C—C bonds, especially the $C_{aromatic}$–O bonds, whether in the depolymerization or in the upgrading by hydrotreating. Miscellaneous multifunctional catalysts with activation of hydrogen and C—O bonds have been developed. In general, noble metals such as Ru, Pt, and Pd are often employed in the production of cycloalkanes or aromatic hydrocarbons, which require catalysts to have high ability to activate hydrogen. In contrast, the metals with relative lower ability to activate hydrogen, including Au and Ag, can be used for the production of phenols. Ni catalysts have also been successfully applied in both above cases, owing their moderate ability to activate hydrogen. For the activation of C—O bonds, early transition metal oxides (TiO_2, CeO_2, ZrO_2, MoO_3, and Nb_2O_5) and solid acids (zeolites, silica–alumina oxides, and $NbOPO_4$) are usually used as supports. Among them, NbO_x has proven to be very effective for the activation and cleavage of C—O bonds.

Considering the industrial valorization of lignin, great effort is required both in the fundamental and applied contexts. The formation and controlled structure of lignin could be achieved by genetic engineering, making one building block dominant, and possibly the occurrence of only this building block. For the depolymerization of lignin, the detailed mechanism needs to be more fully understood. In addition, more efficient and environmentally friendly techniques are desirable, especially for the acidic and alkaline catalytic depolymerization processes. In terms of lignin monomer upgrading, the structure–activity relationship should be paid more attention, especially to improve the selectivity through the design of advanced catalysts. Integrating the depolymerization of lignin and upgrading of lignin monomers, which meet the requirement of industrial application, will be a trend in the development for valorization of lignin. Finally, the economy is crucial to the application of lignin valorization, especially in the context of low oil price.

References

1 Jing, Y.X., Guo, Y., Xia, Q.N. et al. (2019). Catalytic production of value-added chemicals and liquid fuels from lignocellulosic biomass. *Chem* 5: 2520–2546.
2 Ralph, J., Brunow, G., and Boerjan, W. (2007). Lignins. In: *Encyclopedia of Life Sciences*, 1–10. Wiley.
3 Li, C.Z., Zhao, X.C., Wang, A.Q. et al. (2015). Catalytic transformation of lignin for the production of chemicals and fuels. *Chem. Rev.* 115: 11559–11624.
4 Lewin, M. and Goldstein, I.S. (1991). *Wood Structure and Composition*, 183–261. Boca Raton: *CRC Press*.
5 Yue, F.X., Lu, F.C., Sun, R.C., and Ralph, J. (2012). Synthesis and characterization of new 5-linked pinoresinol lignin models. *Chem. Eur. J.* 18: 16402–16410.
6 Evtuguin, D.V., Neto, C.P., Silva, A.M.S. et al. (2001). Comprehensive study on the chemical structure of dioxane lignin from plantation *Eucalyptus globulus* wood. *J. Agric. Food Chem.* 49: 4252–4261.
7 Pinto, P.C.R., da Silva, E.A.B., and Rodrigues, A.E. (2011). Insights into oxidative conversion of lignin to high-added-value phenolic aldehydes. *Ind. Eng. Chem. Res.* 50: 741–748.
8 Xu, C.P., Arancon, R.A.D., Labidi, J., and Luque, R. (2014). Lignin depolymerisation strategies: towards valuable chemicals and fuels. *Chem. Soc. Rev.* 43: 7485–7500.
9 Zhang, Z.R., Song, J.L., and Han, B.X. (2017). Catalytic transformation of lignocellulose into chemicals and fuel products in ionic liquids. *Chem. Rev.* 117: 6834–6880.
10 Sun, Z.H., Fridrich, B., de Santi, A. et al. (2018). Bright side of lignin depolymerization: toward new platform chemicals. *Chem. Rev.* 118: 614–678.
11 Schutyser, W., Renders, T., Van den Bosch, S. et al. (2018). Chemicals from lignin: an interplay of lignocellulose fractionation, depolymerisation, and upgrading. *Chem. Soc. Rev.* 47: 852–908.
12 Brunow, G. (2001). Methods to reveal the structure of lignin. In: *Lignin, Humic Substances and Coal*, 89–119. Wiley: Weinheim.
13 Boerjan, W., Ralph, J., and Baucher, M. (2003). Lignin biosynthesis. *Annu. Rev. Plant Biol.* 54: 519–546.
14 Adler, E. (1977). Lignin chemistry—past, present and future. *Wood Sci. Technol.* 11: 169–218.
15 Deuss, P.J., Scott, M., Tran, F. et al. (2015). Aromatic monomers by *in situ* conversion of reactive intermediates in the acid-catalyzed depolymerization of lignin. *J. Am. Chem. Soc.* 137: 7456–7467.
16 Jia, S.Y., Cox, B.J., Guo, X.W. et al. (2010). Cleaving the beta-O-4 bonds of lignin model compounds in an acidic ionic liquid, 1-H-3-methylimidazolium chloride: an optional strategy for the degradation of lignin. *ChemSusChem* 3: 1078–1084.
17 Jia, S.Y., Cox, B.J., Guo, X.W. et al. (2011). Hydrolytic cleavage of beta-O-4 ether bonds of lignin model compounds in an ionic liquid with metal chlorides. *Ind. Eng. Chem. Res.* 50: 849–855.

18 Sturgeon, M.R., Kim, S., Lawrence, K. et al. (2014). A mechanistic investigation of acid-catalyzed cleavage of aryl-ether linkages: implications for lignin depolymerization in acidic environments. *ACS Sustainable Chem. Eng.* 2: 472–485.

19 Lahive, C.W., Deuss, P.J., Lancefield, C.S. et al. (2016). Advanced model compounds for understanding acid-catalyzed lignin depolymerization: identification of renewable aromatics and a lignin-derived solvent. *J. Am. Chem. Soc.* 138: 8900–8911.

20 Minami, E., Kawamoto, H., Saka, S. et al. (2003). Reaction behavior of lignin in supercritical methanol as studied with lignin model compounds. *J. Wood Sci.* 49: 158–165.

21 Tsujino, J., Kawamoto, H., and Saka, S. (2003). Reactivity of lignin in supercritical methanol studied with various lignin model compounds. *Wood Sci. Technol.* 37: 299–307.

22 Yuan, Z.S., Cheng, S.N., Leitch, M., and Xu, C.B. (2010). Hydrolytic degradation of alkaline lignin in hot-compressed water and ethanol. *Bioresour. Technol.* 101: 9308–9313.

23 Chakar, F.S. and Ragauskas, A.J. (2004). Review of current and future softwood Kraft lignin process chemistry. *Ind. Crops Prod.* 20: 131–141.

24 Jia, S.Y., Cox, B.J., Guo, X.W. et al. (2010). Decomposition of a phenolic lignin model compound over organic N-bases in an ionic liquid. *Holzforschung* 64: 577–580.

25 Nenkova, S., Vasileva, T., and Stanulov, K. (2008). Production of phenol compounds by alkaline treatment of technical hydrolysis lignin and wood biomass. *Chem. Nat. Compd.* 44: 182–185.

26 Miller, J.E., Evans, L., Littlewolf, A., and Trudell, D.E. (1999). Batch microreactor studies of lignin and lignin model compound depolymerization by bases in alcohol solvents. *Fuel* 78: 1363–1366.

27 Kleine, T., Buendia, J., and Bolm, C. (2013). Mechanochemical degradation of lignin and wood by solvent-free grinding in a reactive medium. *Green Chem.* 15: 160–166.

28 Renders, T., Schutyser, W., Van den Bosch, S. et al. (2016). Influence of acidic (H_3PO_4) and alkaline (NaOH) additives on the catalytic reductive fractionation of lignocellulose. *ACS Catal.* 6: 2055–2066.

29 Li, H.L. and Song, G. (2019). Ru-catalyzed hydrogenolysis of lignin: base-dependent tunability of monomeric phenols and mechanistic study. *ACS Catal.* 9: 4054–4064.

30 Li, Y.D., Li, S., Kim, H. et al. (2018). An "ideal lignin" facilitates full biomass utilization. *Sci. Adv.* 4: eaau2968.

31 Yan, N., Zhao, C., Dyson, P.J. et al. (2008). Selective degradation of wood lignin over noble-metal catalysts in a two-step process. *ChemSusChem* 1: 626–629.

32 Van den Bosch, S., Schutyser, W., Koelewijn, S.F. et al. (2015). Tuning the lignin oil OH-content with Ru and Pd catalysts during lignin hydrogenolysis on birch wood. *Chem. Commun.* 51: 13158–13161.

33 Verziu, M., Tirsoaga, A., Cojocaru, B. et al. (2018). Hydrogenolysis of lignin over Ru-based catalysts: the role of the ruthenium in a lignin fragmentation process. *Mol. Catal.* 450: 65–76.

34 Ullah, N., Odda, A.H., Liang, K. et al. (2019). Metal-acid nanoplate-supported ultrafine Ru nanoclusters for efficient catalytic fractionation of lignin into aromatic alcohols. *Green Chem.* 21: 2739–2751.

35 Van den Bosch, S., Schutyser, W., Vanholme, R. et al. (2015). Reductive lignocellulose fractionation into soluble lignin-derived phenolic monomers and dimers and processable carbohydrate pulps. *Energy Environ. Sci.* 8: 1748–1763.

36 Gao, F., Webb, J.D., and Hartwig, J.F. (2016). Chemo- and regioselective hydrogenolysis of diaryl ether C—O bonds by a robust heterogeneous Ni/C catalyst: applications to the cleavage of complex lignin-related fragments. *Angew. Chem. Int. Ed.* 55: 1474–1478.

37 Song, Q., Wang, F., Cai, J.Y. et al. (2013). Lignin depolymerization (LDP) in alcohol over nickel-based catalysts via a fragmentation–hydrogenolysis process. *Energy Environ. Sci.* 6: 994–1007.

38 Song, Q., Wang, F., and Xu, J. (2012). Hydrogenolysis of lignosulfonate into phenols over heterogeneous nickel catalysts. *Chem. Commun.* 48: 7019–7021.

39 He, J.Y., Zhao, C., and Lercher, J.A. (2012). Ni-catalyzed cleavage of aryl ethers in the aqueous phase. *J. Am. Chem. Soc.* 134: 20768–20775.

40 Ma, H.W., Li, H.W., Zhao, W.J. et al. (2019). Selective depolymerization of lignin catalyzed by nickel supported on zirconium phosphate. *Green Chem.* 21: 658–668.

41 Zhang, B., Qi, Z.J., Li, X.X. et al. (2019). ReO_x/AC-catalyzed cleavage of C—O bonds in lignin model compounds and alkaline lignins. *ACS Sustainable Chem. Eng.* 7: 208–215.

42 Barta, K., Matson, T.D., Fettig, M.L. et al. (2010). Catalytic disassembly of an organosolv lignin via hydrogen transfer from supercritical methanol. *Green Chem.* 12: 1640–1647.

43 Wang, X.Y. and Rinaldi, R. (2013). A route for lignin and bio-oil conversion: dehydroxylation of phenols into arenes by catalytic tandem reactions. *Angew. Chem. Int. Ed.* 52: 11499–11503.

44 Limarta, S.O., Ha, J.M., Park, Y.K. et al. (2018). Efficient depolymerization of lignin in supercritical ethanol by a combination of metal and base catalysts. *J. Ind. Eng. Chem.* 57: 45–54.

45 Liu, Y.X., Li, C.Z., Miao, W. et al. (2019). Mild redox-neutral depolymerization of lignin with a binuclear Rh complex in water. *ACS Catal.* 9: 4441–4447.

46 Joffres, B., Nguyen, M.T., Laurenti, D. et al. (2016). Lignin hydroconversion on MoS_2-based supported catalyst: comprehensive analysis of products and reaction scheme. *Appl. Catal., B* 184: 153–162.

47 Shuai, L., Amiri, M.T., Questell-Santiago, Y.M. et al. (2016). Formaldehyde stabilization facilitates lignin monomer production during biomass depolymerization. *Science* 354: 329–333.

48 Parsell, T.H., Owen, B.C., Klein, I. et al. (2013). Cleavage and hydrodeoxygenation (HDO) of C—O bonds relevant to lignin conversion using Pd/Zn synergistic catalysis. *Chem. Sci.* 4: 806–813.

49 Behling, R., Valange, S., and Chatel, G. (2016). Heterogeneous catalytic oxidation for lignin valorization into valuable chemicals: what results? What limitations? What trends? *Green Chem.* 18: 1839–1854.

50 Chatel, G. and Rogers, R.D. (2014). Review: oxidation of lignin using ionic liquids—an innovative strategy to produce renewable chemicals. *ACS Sustainable Chem. Eng.* 2: 322–339.

51 Li, S.H., Liu, S.Q., Colmenares, J.C., and Xu, Y.J. (2016). A sustainable approach for lignin valorization by heterogeneous photocatalysis. *Green Chem.* 18: 594–607.

52 Pan, K., Tian, M., Jiang, Z.H. et al. (2012). Electrochemical oxidation of lignin at lead dioxide nanoparticles photoelectrodeposited on TiO_2 nanotube arrays. *Electrochim. Acta* 60: 147–153.

53 Deng, H.B., Lin, L., Sun, Y. et al. (2008). Perovskite-type oxide $LaMnO_3$: an efficient and recyclable heterogeneous catalyst for the wet aerobic oxidation of lignin to aromatic aldehydes. *Catal. Lett.* 126: 106–111.

54 Deng, H.B., Lin, L., Sun, Y. et al. (2009). Activity and stability of perovskite-type oxide $LaCoO_3$ catalyst in lignin catalytic wet oxidation to aromatic aldehydes process. *Energy Fuels* 23: 19–24.

55 Gu, X.L., Cheng, K.H., He, M. et al. (2012). La-modified SBA-15/H_2O_2 systems for the microwave assisted oxidation of organosolv beech wood lignin. *Maderas-Cienc. Tecnol.* 14: 31–42.

56 Yang, Y.Y., Fan, H.L., Song, J.L. et al. (2015). Free radical reaction promoted by ionic liquid: a route for metal-free oxidation depolymerization of lignin model compound and lignin. *Chem. Commun.* 51: 4028–4031.

57 Deng, W.P., Zhang, H.X., Wu, X.J. et al. (2015). Oxidative conversion of lignin and lignin model compounds catalyzed by CeO_2-supported Pd nanoparticles. *Green Chem.* 17: 5009–5018.

58 Fang, Z. and Meier, M.S. (2018). Toward the oxidative deconstruction of lignin: oxidation of beta-1 and beta-5 linkages. *Org. Biomol. Chem.* 16: 2330–2341.

59 Wang, M., Lu, J.M., Zhang, X.C. et al. (2016). Two-step, catalytic C—C bond oxidative cleavage process converts lignin models and extracts to aromatic acids. *ACS Catal.* 6: 6086–6090.

60 Yu, Y.Q., Li, X.Y., Su, L. et al. (2012). The role of shape selectivity in catalytic fast pyrolysis of lignin with zeolite catalysts. *Appl. Catal., A* 447: 115–123.

61 Yang, H.P., Yan, R., Chen, H.P. et al. (2007). Characteristics of hemicellulose, cellulose and lignin pyrolysis. *Fuel* 86: 1781–1788.

62 Ma, Z.Q., Troussard, E., and van Bokhoven, J.A. (2012). Controlling the selectivity to chemicals from lignin via catalytic fast pyrolysis. *Appl. Catal., A* 423: 130–136.

63 Nguyen, J.D., Matsuura, B.S., and Stephenson, C.R.J. (2014). A photochemical strategy for lignin degradation at room temperature. *J. Am. Chem. Soc.* 136: 1218–1221.

64 Wu, X.J., Fan, X.T., Xie, S.J. et al. (2018). Solar energy-driven lignin-first approach to full utilization of lignocellulosic biomass under mild conditions. *Nat. Catal.* 1: 772–780.

65 Zhao, C., Kou, Y., Lemonidou, A.A. et al. (2009). Highly selective catalytic conversion of phenolic bio-oil to alkanes. *Angew. Chem. Int. Ed.* 48: 3987–3990.

66 Yan, N., Yuan, Y.A., Dykeman, R. et al. (2010). Hydrodeoxygenation of lignin-derived phenols into alkanes by using nanoparticle catalysts combined with bronsted acidic ionic liquids. *Angew. Chem. Int. Ed.* 49: 5549–5553.

67 Zhao, C. and Lercher, J.A. (2012). Selective hydrodeoxygenation of lignin-derived phenolic monomers and dimers to cycloalkanes on Pd/C and H–ZSM-5 catalysts. *ChemCatChem* 4: 64–68.

68 Yao, G., Wu, G.J., Dai, W.L. et al. (2015). Hydrodeoxygenation of lignin-derived phenolic compounds over bi-functional Ru/H-beta under mild conditions. *Fuel* 150: 175–183.

69 Zhang, W., Chen, J.Z., Liu, R.L. et al. (2014). Hydrodeoxygenation of lignin-derived phenolic monomers and dimers to alkane fuels over bifunctional zeolite-supported metal catalysts. *ACS Sustainable Chem. Eng.* 2: 683–691.

70 Nimmanwudipong, T., Runnebaum, R.C., Block, D.E., and Gates, B.C. (2011). Catalytic conversion of guaiacol catalyzed by platinum supported on alumina: reaction network including hydrodeoxygenation reactions. *Energy Fuels* 25: 3417–3427.

71 Zhang, X.H., Zhang, Q., Chen, L.A. et al. (2014). Effect of calcination temperature of $Ni/SiO_2–ZrO_2$ catalyst on its hydrodeoxygenation of guaiacol. *Chin. J. Catal.* 35: 302–309.

72 Zhang, X.H., Wang, T.J., Zhang, Q. et al. (2015). Production of alkanes from lignin-derived phenolic compounds over *in situ* formed Ni catalyst with solid acid. *Chem. Lett.* 44: 648–650.

73 Fang, H.H., Chen, W.K., Li, S. et al. (2019). Tandem hydrogenolysis-hydrogenation of lignin-derived oxygenates over integrated dual catalysts with optimized interoperations. *ChemSusChem* 12: 5199–5206.

74 Bui, V.N., Laurenti, D., Afanasiev, P., and Geantet, C. (2011). Hydrodeoxygenation of guaiacol with CoMo catalysts. Part I: promoting effect of cobalt on HDO selectivity and activity. *Appl. Catal., B* 101: 239–245.

75 Jing, Y.X., Dong, L., Guo, Y. et al. (2020). Chemicals from lignin: a review of catalytic conversion involving hydrogen. *ChemSusChem* 13: 1–19.

76 Centeno, A., Laurent, E., and Delmon, B. (1995). Influence of the support of CoMo sulfide catalysts and of the addition of potassium and platinum on the catalytic performances for the hydrodeoxygenation of carbonyl, carboxyl, and guaiacol-type molecules. *J. Catal.* 154: 288–298.

77 Ferrari, M., Maggi, R., Delmon, B., and Grange, P. (2001). Influences of the hydrogen sulfide partial pressure and of a nitrogen compound on the hydrodeoxygenation activity of a CoMo/carbon catalyst. *J. Catal.* 198: 47–55.

78 Zhang, J.H., Sun, J.M., and Wang, Y. (2020). Recent advances in the selective catalytic hydrodeoxygenation of lignin-derived oxygenates to arenes. *Green Chem.* 22: 1072–1098.

79 Liu, G.L., Robertson, A.W., Li, M.M.J. et al. (2017). MoS_2 monolayer catalyst doped with isolated Co atoms for the hydrodeoxygenation reaction. *Nat. Chem.* 9: 810–816.

80 Song, W.J., Zhou, S.J., Hu, S.H. et al. (2019). Surface engineering of CoMoS nanosulfide for hydrodeoxygenation of lignin-derived phenols to arenes. *ACS Catal.* 9: 259–268.

81 Shao, Y., Xia, Q.N., Dong, L. et al. (2017). Selective production of arenes via direct lignin upgrading over a niobium-based catalyst. *Nat. Commun.* 8: 16104.

82 Guo, T.Y., Xia, Q.N., Shao, Y. et al. (2017). Direct deoxygenation of lignin model compounds into aromatic hydrocarbons through hydrogen transfer reaction. *Appl. Catal., A* 547: 30–36.

83 Dong, L., Yin, L.L., Xia, Q.N. et al. (2018). Size-dependent catalytic performance of ruthenium nanoparticles in the hydrogenolysis of a β-O-4 lignin model compound. *Catal. Sci. Technol.* 8: 735–745.

84 Xin, Y., Dong, L., Guo, Y. et al. (2019). Correlation of the catalytic performance with Nb_2O_5 surface properties in the hydrodeoxygenation of lignin model compound. *J. Catal.* 375: 202–212.

85 Han, Q., Rehman, M.U., Wang, J.H. et al. (2019). The synergistic effect between Ni sites and Ni-Fe alloy sites on hydrodeoxygenation of lignin-derived phenols. *Appl. Catal., B* 253: 348–358.

86 Ma, D., Lu, S.L., Liu, X.H. et al. (2019). Depolymerization and hydrodeoxygenation of lignin to aromatic hydrocarbons with a Ru catalyst on a variety of Nb-based supports. *Chin. J. Catal.* 40: 609–617.

87 Li, L.X., Dong, L., Liu, X.H. et al. (2020). Selective production of ethylbenzene from lignin oil over FeO_x modified Ru/Nb_2O_5 catalyst. *Appl. Catal., B* 260: 118143.

88 Xin, Y., Jing, Y.X., Dong, L. et al. (2019). Selective production of indane and its derivatives from lignin over a modified niobium-based catalyst. *Chem. Commun.* 55: 9391–9394.

89 Dong, L., Shao, Y., Han, X. et al. (2018). Comparison of two multifunctional catalysts M/Nb_2O_5 (M = Pd, Pt) for one-pot hydrodeoxygenation of lignin. *Catal. Sci. Technol.* 8: 6129–6136.

90 Yang, F.F., Libretto, N.J., Komarneni, M.R. et al. (2019). Enhancement of *m*-cresol hydrodeoxygenation selectivity on Ni catalysts by surface decoration of MoO_x species. *ACS Catal.* 9: 7791–7800.

91 Moon, J.S., Kim, E.G., and Lee, Y.K. (2014). Active sites of Ni_2P/SiO_2 catalyst for hydrodeoxygenation of guaiacol: a joint XAFS and DFT study. *J. Catal.* 311: 144–152.

92 Bui, V.N., Laurenti, D., Delichere, P., and Geantet, C. (2011). Hydrodeoxygenation of guaiacol part II: support effect for CoMoS catalysts on HDO activity and selectivity. *Appl. Catal., B* 101: 246–255.

93 Cai, Z., Wang, F.M., Zhang, X.B. et al. (2017). Selective hydrodeoxygenation of guaiacol to phenolics over activated carbon supported molybdenum catalysts. *Mol. Catal.* 441: 28–34.

94 Nguyen, T.S., Laurenti, D., Afanasiev, P. et al. (2016). Titania-supported gold-based nanoparticles efficiently catalyze the hydrodeoxygenation of guaiacol. *J. Catal.* 344: 136–140.

95 Mao, J.B., Zhou, J.X., Xia, Z. et al. (2017). Anatase TiO_2 activated by gold nanoparticles for selective hydrodeoxygenation of guaiacol to phenolics. *ACS Catal.* 7: 695–705.

96 Liu, K.R., Yan, P.F., Jiang, H. et al. (2019). Silver initiated hydrogen spillover on anatase TiO_2 creates active sites for selective hydrodeoxygenation of guaiacol. *J. Catal.* 369: 396–404.

97 Zhang, X.Q., Yan, P.F., Zhao, B. et al. (2019). Selective hydrodeoxygenation of guaiacol to phenolics by Ni/anatase TiO_2 catalyst formed by cross-surface migration of Ni and TiO_2. *ACS Catal.* 9: 3551–3563.

98 Dong, L., Xin, Y., Liu, X.H. et al. (2019). Selective hydrodeoxygenation of lignin oil to valuable phenolics over Au/Nb_2O_5 in water. *Green Chem.* 21: 3081–3090.

99 Ranaware, V., Verma, D., Insyani, R. et al. (2019). Highly-efficient and magnetically-separable ZnO/Co@N-CNTs catalyst for hydrodeoxygenation of lignin and its derived species under mild conditions. *Green Chem.* 21: 1021–1042.

100 Huang, X.M., Ludenhoff, J.M., Dirks, M. et al. (2018). Selective production of biobased phenol from lignocellulose-derived alkylmethoxyphenols. *ACS Catal.* 8: 11184–11190.

101 Zhang, J.G., Lombardo, L., Gozaydin, G. et al. (2018). Single-step conversion of lignin monomers to phenol: bridging the gap between lignin and high-value chemicals. *Chin. J. Catal.* 39: 1445–1452.

102 Verboekend, D., Liao, Y.H., Schutyser, W., and Sels, B.F. (2016). Alkylphenols to phenol and olefins by zeolite catalysis: a pathway to valorize raw and fossilized lignocellulose. *Green Chem.* 18: 297–306.

103 Liao, Y.H., d'Halluin, M., Makshina, E. et al. (2018). Shape selectivity vapor-phase conversion of lignin-derived 4-ethylphenol to phenol and ethylene over acidic aluminosilicates: impact of acid properties and pore constraint. *Appl. Catal., B* 234: 117–129.

104 Liao, Y.H., Koelewijn, S.F., Van den Bossche, G. et al. (2020). A sustainable wood biorefinery for low-carbon footprint chemicals production. *Science* 367: 1385–1390.

105 Wang, M., Liu, M.J., Li, H.J. et al. (2018). Dealkylation of lignin to phenol via oxidation-hydrogenation strategy. *ACS Catal.* 8: 6837–6843.

106 Song, S., Zhang, J.G., Gozaydin, G., and Yan, N. (2019). Production of terephthalic acid from corn stover lignin. *Angew. Chem. Int. Ed.* 58: 4934–4937.

107 Mei, Q.Q., Liu, H.Z., Shen, X.J. et al. (2017). Selective utilization of the methoxy group in lignin to produce acetic acid. *Angew. Chem. Int. Ed.* 56: 14868–14872.

108 Zhang, J.J., Qian, Q.L., Wang, Y. et al. (2019). Synthesis of ethanol from aryl methyl ether/lignin, CO_2 and H_2. *Chem. Sci.* 10: 10640–10646.

109 Mei, Q.Q., Shen, X.J., Liu, H.Z. et al. (2019). Selective utilization of methoxy groups in lignin for N-methylation reaction of anilines. *Chem. Sci.* 10: 1082–1088.

110 Xia, Q.N., Chen, Z.J., Shao, Y. et al. (2016). Direct hydrodeoxygenation of raw woody biomass into liquid alkanes. *Nat. Commun.* 8: 16104.

111 Kong, J.C., He, M.Y., Lercher, J.A., and Zhao, C. (2015). Direct production of naphthenes and paraffins from lignin. *Chem. Commun.* 51: 17580–17583.

112 Wang, H.L., Ruan, H., Feng, M.Q. et al. (2017). One-pot process for hydrodeoxygenation of lignin to alkanes using Ru-based bimetallic and bifunctional catalysts supported on zeolite Y. *ChemSusChem* 10: 1846–1856.

113 Dong, L., Lin, L.F., Han, X. et al. (2019). Breaking the limit of lignin monomer production via cleavage of interunit carbon–carbon linkages. *Chem* 5: 1521–1536.

114 Cai, Z.P., Long, J.X., Li, Y.W. et al. (2019). Selective production of diethyl maleate via oxidative cleavage of lignin aromatic unit. *Chem* 5: 2365–2377.

115 Shen, X.J., Meng, Q.L., Mei, Q.Q. et al. (2020). Selective catalytic transformation of lignin with guaiacol as the only liquid product. *Chem. Sci.* 11: 1347–1352.

Index

Heterogeneous Catalysis for Sustainable Energy, First Edition. Edited by Landong Li and Justin S. J. Hargreaves.